AD609104

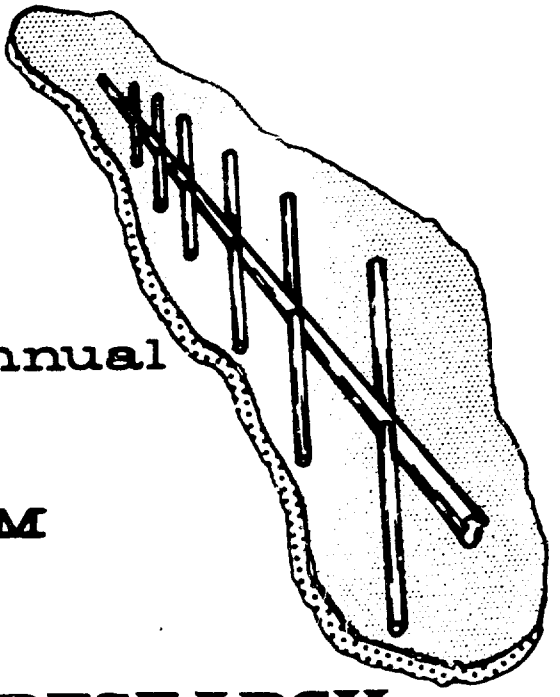

abstracts of the

Fourteenth Annual

SYMPOSIUM

USAF ANTENNA RESEARCH

and

DEVELOPMENT PROGRAM

20010703009

DDC
DEC 2 2 1964
DDC-IRA B

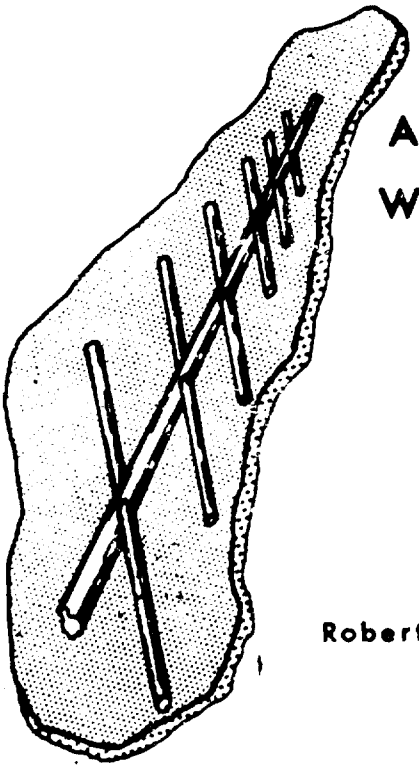

Sponsored by

AIR FORCE AVIONICS LABORATORY

WRIGHT PATTERSON AIR FORCE BASE, OHIO.

In cooperation with the

UNIVERSITY of ILLINOIS.

October 6, 7, 8, 1964.

Robert Allerton Park, Monticello, Illinois.

UNCLASSIFIED

CLEARINGHOUSE FOR FEDERAL SCIENTIFIC AND TECHNICAL INFORMATION CFSTI
DOCUMENT MANAGEMENT BRANCH 410.11

LIMITATIONS IN REPRODUCTION QUALITY

ACCESSION # AD609104

☒ 1. WE REGRET THAT LEGIBILITY OF THIS DOCUMENT IS IN PART UNSATISFACTORY. REPRODUCTION HAS BEEN MADE FROM BEST AVAILABLE COPY.

☐ 2. A PORTION OF THE ORIGINAL DOCUMENT CONTAINS FINE DETAIL WHICH MAY MAKE READING OF PHOTOCOPY DIFFICULT.

☐ 3. THE ORIGINAL DOCUMENT CONTAINS COLOR, BUT DISTRIBUTION COPIES ARE AVAILABLE IN BLACK-AND-WHITE REPRODUCTION ONLY.

☐ 4. THE INITIAL DISTRIBUTION COPIES CONTAIN COLOR WHICH WILL BE SHOWN IN BLACK-AND-WHITE WHEN IT IS NECESSARY TO REPRINT.

☐ 5. LIMITED SUPPLY ON HAND: WHEN EXHAUSTED, DOCUMENT WILL BE AVAILABLE IN MICROFICHE ONLY.

☐ 6. LIMITED SUPPLY ON HAND: WHEN EXHAUSTED DOCUMENT WILL NOT BE AVAILABLE.

☐ 7. DOCUMENT IS AVAILABLE IN MICROFICHE ONLY.

☐ 8. DOCUMENT AVAILABLE ON LOAN FROM CFSTI (TT DOCUMENTS ONLY).

☐ 9.

PROCESSOR: L. Lee

TSL-107-10 64

UNCLASSIFIED

Abstracts of the

FOURTEENTH ANNUAL SYMPOSIUM

ON

THE USAF ANTENNA RESEARCH AND DEVELOPMENT PROGRAM

SPONSORED BY

AIR FORCE AVIONICS LABORATORY

WRIGHT-PATTERSON AIR FORCE BASE, OHIO

ROBERT ALLERTON PARK

(University of Illinois)

Monticello, Illinois

6, 7, 8, October, 1964

UNCLASSIFIED

NOTICES

When Government drawings, specifications, or other data are used for any purpose other than in connection with a definitely related government procurement operation, the United States Government thereby incurs no responsibility nor any obligation whatsoever; and the fact that the Government may have formulated, furnished, or in any way supplied the said drawings, specifications, or other data is not to be regarded by implication or otherwise as in any manner licensing the holder or any other person or corporation, or conveying any rights or permission to manufacture, use or sell any patented invention that may in any way be related thereto.

CONTENTS

POLARIZATION CONTROL

An Automatic Microwave Polarization Analyzer	J. A. Kaiser and K. L. Hanlin, NATIONAL AERONAUTICS AND SPACE ADMINISTRATION, WASHINGTON, D.C.
Far Field Pattern for Reflector Antennas with Displaced Feed	Benedikt A. Munk, NORTH AMERICAN AVIATION, COLUMBUS, OHIO
A Simplified Variable Polarization Antenna	John L. Kerr, U. S. ARMY ELECTRONICS LABORATORIES, FORT MONMOUTH, N. J.

NEW TECHNIQUES

On the Design and Evaluation of HF Airplane Communications Antennas	A. E. Lipp and D. D. Hutchinson, THE BOEING CO. AIRPLANE DIVISION, SEATTLE, WASHINGTON
A New Class of Electrically Small Antennas	Richard C. Fenwick, COLLINS RADIO COMPANY, RICHARDSON, TEXAS
Broadband Antennas Utilizing Ferrites	J. A. M. Lyon, J. E. Herman and S. B. Rhee, UNIVERSITY OF MICHIGAN, ANN ARBOR, MICHIGAN
Variable Prism Scanning Lens	Scott H. Walker, MOTOROLA, INC., SCOTTSDALE, ARIZONA
Tandem Couplers and Phase Shifters: A New Class of Unlimited Components	J. P. Shelton, R. Van Wagoner and J. J. Wolfe, RADIATION SYSTEMS, INC. ALEXANDRIA, VIRGINIA
A New Scimitar Antenna	E. M. Turner, AVWE, WRIGHT-PATTERSON AFB, OHIO
*Simulation of RF Far-Field Conditions Using a Microwave Lens	P. Zuzulo, S. Jurczak, and J. Castri REPUBLIC AVIATION CORP., FARMINGDALE NEW YORK
*HF Shunt Antennas for Electrically Short Aircraft	Donald G. Gordon, NORTH AMERICAN AVIATION, INC., LOS ANGELES, CALIF.

*paper not presented

CONTENTS (Continued)

THEORY

The Self and Mutual Admittances of Circular and Dipole Arrays	Richard B. Mack, AIR FORCE CAMBRIDGE RESEARCH LABORATORIES, BEDFORD, MASSACHUSETTS
Near-Field Measurements on the Planar Four-Arm Log-Spiral Antenna	P. L. Ransom and J. D. Dyson, UNIVERSITY OF ILLINOIS, URBANA, ILLINOIS
Advanced Antennas for Space Applications	A. M. Berkman and W. M. Young, LOCKHEED MISSILES AND SPACE CO., SUNNYVALE, CALIF.
Interference Coupling Factors for Pairs of Antennas	J. A. M. Lyon, A. I. Simanyi and W. R. Heath, UNIVERSITY OF MICHIGAN, ANN ARBOR, MICHIGAN
The Equivalent Radius of Arbitrarily-Shaped Antennas	Charles W. Su, NORTHROP CORP., NORAIR DIVISION, HAWTHORNE, CALIF.
Transverse Focal Region Properties of a Spherical Reflector	G. Hyde, RADIO CORPORATION OF AMERICA, MOORESTOWN, N. J.
*Dual Mode Pattern and Reciprocity Studies with a Simple Waveguide Feed and Reflector Antenna	M. W. Scheldorf, IITRI, ANTENNA RESEARCH FACILITY, GENEVA, ILLINOIS
*Some Geodetic Lenses and Their Application	J. L. McFarland, NORTH AMERICAN AVIATION, ANAHEIM, CALIF.

HI-GAIN ANTENNAS

A Survey of Side Lobe Optimization, Suppression, and Cancellation Techniques	John B. Damonte, DALMO VICTOR COMPANY, BELMONT, CALIF.
Lightweight Large-Aperture Arrays for Airborne Applications	B. M. Bowman, W. O. Klever, and A. E. Marble, GOODYEAR AEROSPACE CORP., AKRON, OHIO
Antenna Range Evaluation for Measurements of Gemini Track Radar	J. H. Diel, NEW MEXICO STATE UNIVERSITY, UNIVERSITY PARK, N. M.

*paper not presented

ENVIRONMENTAL

Design and Evaluation of Antennas for Use in a Thermal Environment of 2000°F	Godfrey F. Buranich, CORNELL AERO NAUTICAL LABORATORY, INC., BUFFAL , NEW YORK
Design, Evaluation and Performance of Modern Microwave Anechoic Chambers for Antenna Measurements	Elery F. Buckley, EMERSON & CUMIN INC., CANTON, MASSACHUSETTS
R. F. Corona on Titanium Surfaces at Elevated Temperature	Paul F. Stang, LOCKHEED-CALIFORNI CO., BURBANK, CALIF.
A Precision Ground-Reflection Antenna Boresight Test Range	J. S. Hollis, R. E. Pidgeon, SCIENTIFIC-ATLANTA, INC., ATLANTA GEORGIA, and R. M. Schutz, McDONN AIRCRAFT CORP., ST. LOUIS, MISSOU
Effect of Ambient Plasma on Antenna Breakdown Radiation Characteristic	J. B. Chown and D. W. Weissman, STANFORD RESEARCH INSTITUTE, MENL PARK, CALIF.
*RF Breakdown in a Space Environment	R. F. Vance and J. E. Nanevicz, STANFORD RESEARCH INSTITUTE, MENL PARK, CALIF.
*Integrated Low Profile Antennas	E. R. Murphy and D. R. Wehner, MOTOROLA, INC., SCOTTSDALE, ARIZO
*A High Temperature C-Band Annular Slot Antenna	C. R. Bitter, J. W. Pool and W. E. Porteus, MOTOROLA, INC., SCOTTSDAI ARIZONA

SCANNING TECHNIQUE

The Use of Strip-Transmission Line Techniques at X-Band	W. Bryant, D. Canaday, and G. Mons ADVANCED DEVELOPMENT LABORATORIES, INC., NASHUA, N. H.
Helix Frequency Scanning Feed	G. H. Okubo, HUGHES AIRCRAFT CO., FULLERTON, CALIF.
Wide Scan Short Focus Millimeter Wave Dielectric Lenses	A. Mayer, NATIONAL ENGINEERING SCIENCE CO., PASADENA, CALIF.

*paper not presented

CONTENTS (Continued)

Antennafiers for Beam-Steering Arrays	Jonathan D. Young, OHIO STATE UNIVERSITY, COLUMBUS, OHIO
High-Power Beam Switching Techniques for Multibeam Array Antennas	Helmut E. Schrank, WESTINGHOUSE DEFENSE AND SPACE CENTER, BALTIMORE, MARYLAND
*The Design of a Broadband Rotating Feed for a Low Noise Temperature Antenna with Auto-Track Capability	D. G. Henry, NEW MEXICO STATE UNIVERSITY, UNIVERSITY PARK, N. M.
*A High Dielectric Constant Phasing Lens for Electronically-Scanned Antenna Arrays	R. Scott Brazil, MOTOROLA, INC., SCOTTSDALE, ARIZONA

*paper not presented

An Automatic Microwave Polarization Analyzer

J. A. Kaiser and K. L. Hanlin

Introduction

A method whereby the polarization characteristics of an incident wave may be instantaneously and continuously measured and indicated is described. It is possible to analyze either modulated or unmodulated signals whose frequencies are within the operating range of the individual system components. The system comprises an antenna which receives and separates the two senses of circular polarization, a microwave phase comparator, and a means for making amplitude ratio measurements. The method described differs from previous methods in that it utilizes the two senses of circular polarization in conjunction with a phase measurement to obtain "tilt" angle rather than using two orthogonal linearly polarized fields in conjunction with a phase shifter.

Polarization Relationships

An arbitrarily polarized wave incident on a receiving antenna, in terms of two orthogonal linear components, may be written in the form

$$E = E\phi + jE\theta = C \cos Wt + jD \sin Wt. \tag{1}$$

As shown by Rumsey,[1] these two orthogonal linearly polarized fields can be represented in terms of two circular fields:

$$E_L = Ae^{+jWt}$$

$$E_R = Be^{-jWt}. \tag{2}$$

In a plane normal to the direction of propagation, the circular fields are periodically in-phase, i.e., they add constructively in one direction, twice during the course of one cycle. In the orthogonal direction, the circular fields add destructively, i.e., they are anti-phase. Figure 1 shows a representation of the two circular fields in a X - Y plane at an instant of time when they are in-phase and so add to produce the major axis of the polarization ellipse. It may be seen that 90 degrees later in time the two fields will be anti-phase because of their opposite senses of rotation, producing the minor axis of the polarization ellipse.

An amplitude envelope of the resultant field is generally an ellipse which has a major and a minor axis. $E\phi$ assumes the direction of the major axis while $E\theta$, which is orthogonal to $E\phi$, is in the direction of the minor axis of the polarization ellipse. In terms of the circular fields, the linear components are:

$$E\phi = \mathrm{Re}\ (E_L + E_R) = (A + B) \cos Wt$$
that is, $C = A + B$

$$\text{and } E\theta = \mathrm{Im}\ (E_L + E_R) = (A - B) \sin Wt$$
that is, $D = A - B$.

It may be noted that if $P = 0$, then $A = C = D$. In this case (1) reduces to left circular as represented in (2). Similarly for $A = 0$, (1) reduces to right circular polarization. When $A = B$, $E\theta$ disappears which is the case for linear polarization.

The ellipticity of a wave may be expressed as a ratio of the maximum value of field to the minimum value of field:

$$E\phi/E\theta = C/D = \frac{A + B}{A - B} .$$

This ratio ranges from infinite for linear polarization to one for circular polarization.

Polarization Analyzer

Automatic polarization analysis can be accomplished with the aid of the circuitry shown in Figure 2. In order to analyze polarization characteristi it is first necessary to transfer the wave in space into fields in transmiss lines. For the purposes of this paper, an antenna such as a turnstile array selected which separates a received signal into its two circular components. For a given orientation of the receiving antenna, the two fields in the tran mission lines will be in-phase for only one orientation of the major axis of incident polarization ellipse. This direction of the major axis may be established as a reference direction. As the polarization ellipse tilts in space from this reference direction, the phase of the field in one transmission line will be advanced an angle equal to the angle of tilt while the phase of the field on the other transmission line will be retarded a like amount. The signal intensities in the transmission lines from the antenna may be written:

$$E_L \sim A \cos (Wt + \gamma)$$
$$E_R \sim B \cos (Wt - \gamma)$$
where γ is the angle between the major axis of the polarization ellipse and a reference direction.

In Figure 1 the reference direction is shown as the X-axis. It may be noted that the reference direction may be changed at will by an observer who can simply rotate the receiving antenna.

A portion of each field in (6) is detected to provide quantities proportional to component amplitudes. The remainder goes to a phase comparator to be used for determination of the ellipse tilt angle.

Ratio of Amplitudes

The detected amplitudes P_L and P_R shown in Figure 2 are proportional to the squares of the absolute amplitudes of left and right circular components. Recalling that the ellipticity ratio is given by $E\phi/E\theta$, a computer which solves the equation

$$\frac{A + B}{A - B} \approx \frac{\sqrt{P_L} + \sqrt{P_R}}{\sqrt{P_L} - \sqrt{P_R}} \tag{7}$$

provides two factors of interest concerning polarization characteristics of a wave: (1) degree of ellipticity (2) dominant sense of circular polarization (by noting whether the ratio is positive or negative).

It is somewhat simpler to determine the ratio P_R/P_L and in some applications is sufficient. The degree of ellipticity--for a limited range of values of P_R/P_L--can be determined if required with the aid of Figure 3. The dominant sense of circular polarization is determined by noting whether the ratio is greater than or less than one.

Determination of Tilt Angle

The tilt angle of the polarization ellipse is the remaining unknown and is determined easily by measuring the phase difference between the two senses of circular polarization with a microwave phase comparator.[2] Assuming the signals of (6) as inputs to the phase comparator shown in Figure 2, the signal intensity at terminal a is proportional to:

$$\begin{aligned} Ea &\approx A \cos (Wt + \gamma) + B \cos (Wt + \gamma) \\ &\approx (A + B) \cos Wt \cos \gamma + (A - B) \sin Wt \sin \gamma. \end{aligned} \tag{8}$$

The detected signal is proportional to the square of the signal intensity:

$$\begin{aligned} Pa &\approx Ea^2 \\ &\approx (A^2 + B^2 + 2AB) \cos^2 Wt \cos^2 \gamma \\ &\quad + (A^2 + B^2 - 2AB) \sin^2 Wt \sin^2 \gamma \\ &\approx (A^2 + B^2) (\cos^2 Wt \cos^2 \gamma + \sin^2 Wt \sin^2 \gamma) \\ &\quad + 2AB (\cos^2 Wt \cos^2 \gamma - \sin^2 Wt \sin^2 \gamma) \\ Pa &\approx (A^2 + B^2) + 2AB \cos 2\gamma. \end{aligned} \tag{9}$$

Similarly, the other detected outputs from the phase comparator are:

$$\begin{aligned} Pb &\approx A^2 + B^2 - 2AB \cos 2\gamma \\ Pc &\approx A^2 + B^2 + 2AB \sin 2\gamma \\ Pd &\approx A^2 + B^2 - 2AB \sin 2\gamma. \end{aligned} \tag{10}$$

Differencing the outputs from each of the hybrids produces:

$$\begin{aligned} Pa - Pb &\approx 4AB \cos 2\gamma \\ Pc - Pd &\approx 4AB \sin 2\gamma. \end{aligned} \tag{11}$$

Displaying these difference amplitudes orthogonally, i.e., Pa - Pb on the X-axis and Pc - Pd on the Y-axis of an X - Y indicator, which may be an X - Y recorder or oscilloscope, yields the indication:

$$Pt \approx 4AB\ (\cos 2\gamma + j \sin 2\gamma)$$
$$4ABe^{j2\gamma}.$$

Thus, the product of the amplitudes of the two circular components is the radius to a circle which is described by the phase difference (2γ) between the circular components. See Figure 4. If either A or B is zero, which means that only one sense of circular polarization is received, the radius of the phase circle goes to zero, showing no elliptical polarization present.

The X - Y indicator serves here as a computer, taking as inputs the functions of an angle and displaying the angle itself.

It may be observed that as the tilt angle γ ranges through 180 degrees, a complete circle is traced on the indicator, meaning that the relative phase of the fields in the transmission lines has undergone a change of 360 degrees. The X - Y indicator thus does not automatically display the tilt angle in the sense that it yields a change in displayed angle of twice the change in tilt angle.

Tilt angle can be automatically displayed if quantities proportional to (11) are applied to a two-phase motor whose rotor is connected to a pointer through a 2:1 gear reducer.

Conclusion

It has been shown how to determine automatically and continuously all of the polarization characteristics of a wave. The degree of ellipticity and domi sense of rotation are obtained from a ratio derived from the circular component amplitudes and the direction of polarization is obtained from a measurement of the phase difference between the two components. The method described requires moving parts or active phasing devices.

References

1. H. G. Booker, V. H. Rumsey, G. A. Deschamps, M. L. Kales, and J. I. Bohnert "Techniques for Handling Elliptically Polarized Waves with Special Referenc to Antennas." Proceedings of the IRE, Vol. 39, No. 5, pp 533-552, May, 195

2. J. A. Kaiser, H. B. Smith, Jr., W. H. Pepper, and J. H. Little, "An Automatic Microwave Phase Comparator." IRE Transactions on MTT, MTT-10(6), pp 548-550, November, 1962.

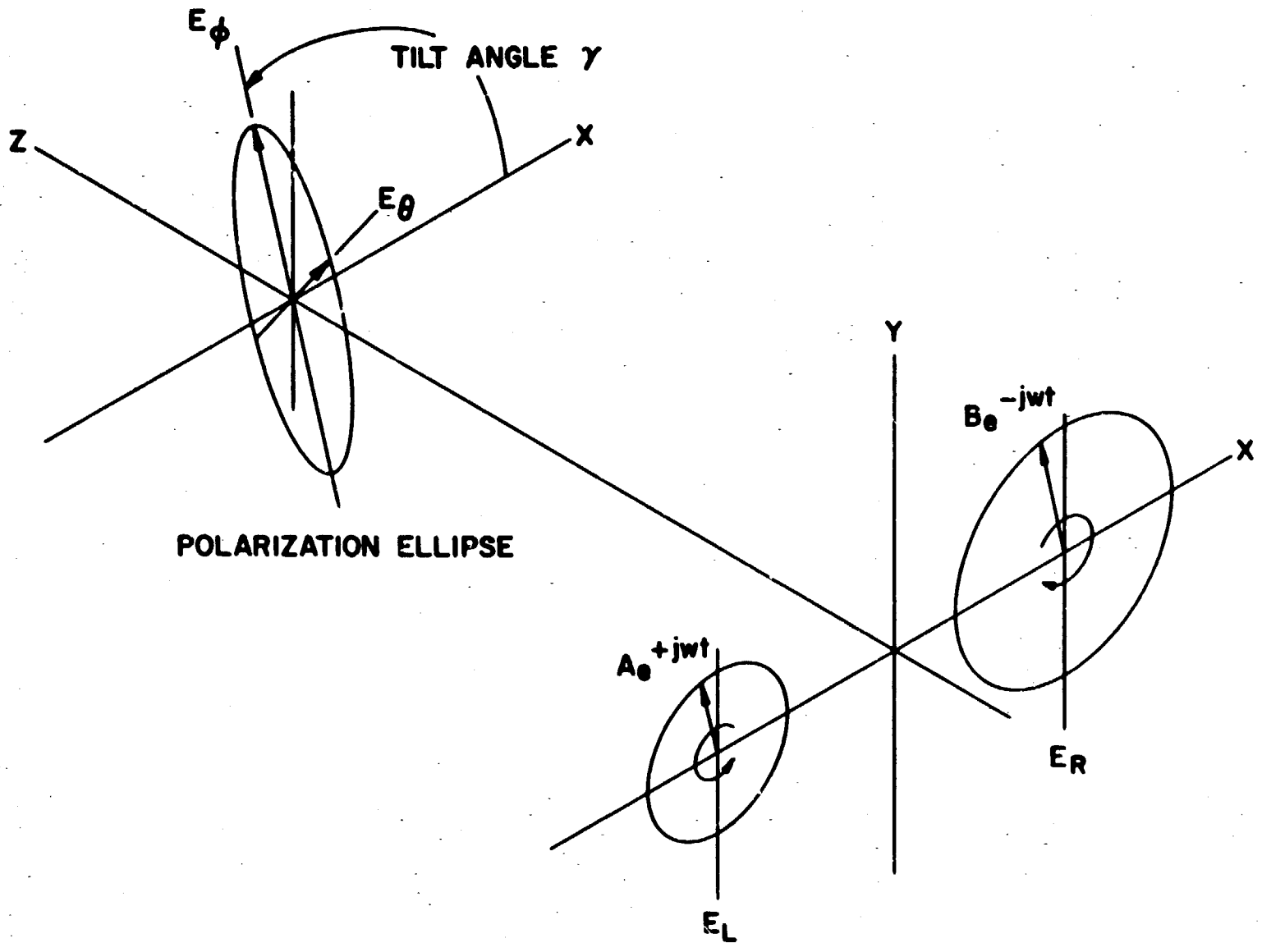

Fig. 1 — THE POLARIZATION ELLIPSE AND ITS CIRCULAR COMPONENTS

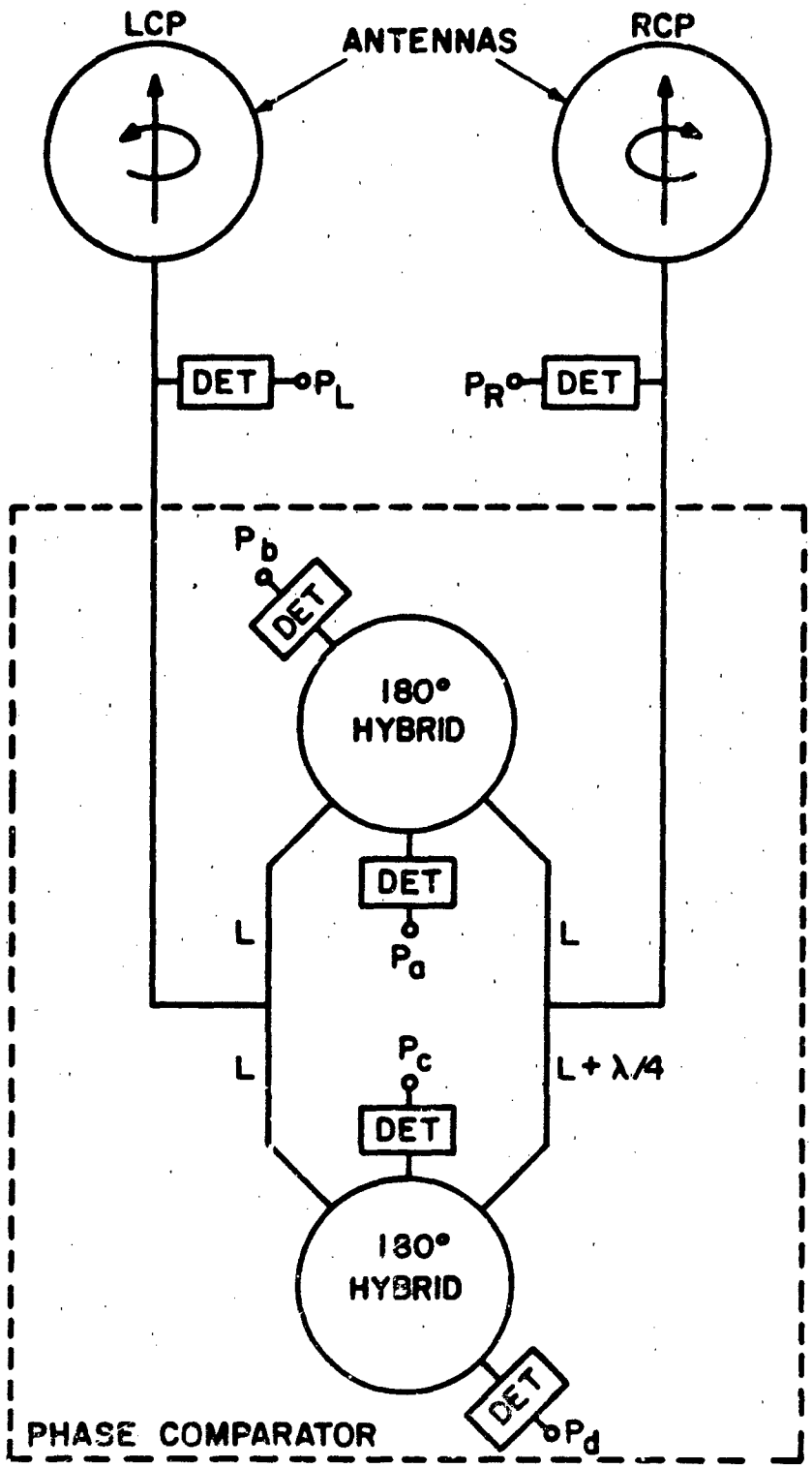

Figure 2 — Automatic polarization analyzer.

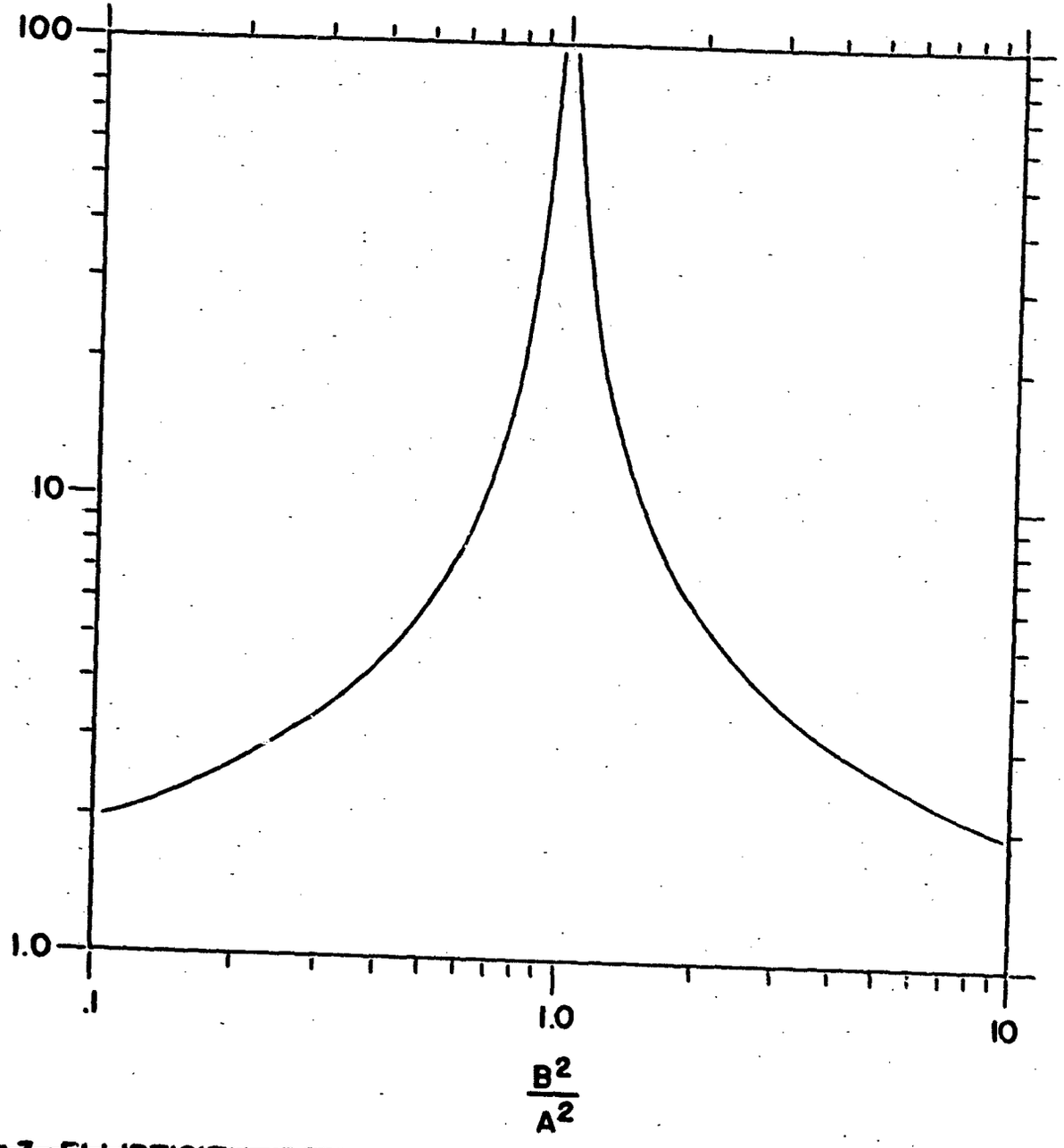
100
10
1.0
$\frac{E_\phi}{E_\theta}$
.1
1.0
10
$\frac{B^2}{A^2}$

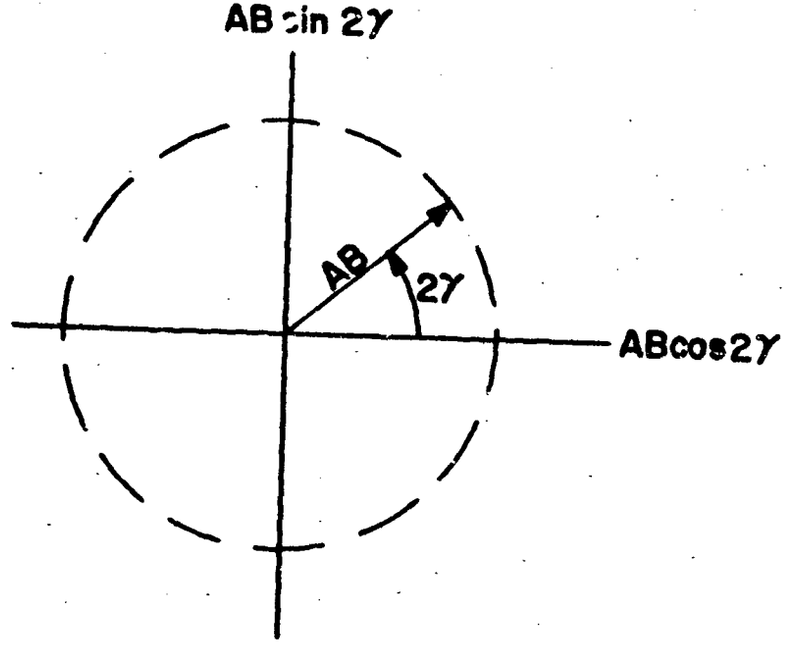

Fig.4 – PHASE COMPARATOR OUTPUT DISPLAYED ON X–Y INDICATOR

Far Field Pattern for Reflector Antennas with Displaced Feed

by

B. A. Munk

North American Aviation, Inc.,

Columbus, Ohio

Abstract

Far field patterns for a paraboloidal dish with the feed displaced either transversely or axially are determined analytically. The results obtained are displayed graphically, in plots including the first three side lobes.

INTRODUCTION

This paper presents an analytical treatment of the far field pattern of a paraboloidal reflector, in which the feed is displaced from the focus either transversely or axially. Although the transverse method has been investigated both experimentally and by use of various computer programs, only one other analytical study of this method has been found by the author. (See reference 3.) The transverse method presented here differs from the previously published one in that expansion is performed around an axis nearly coinciding with the displaced beam, rather than around the boresight axis of the dish. The advantage of this approach lies in the simplification that only a few correcting terms need be added to the unperturbed beam. Previous studies of axial displacement show that approximately to a quadratic phase-distortion. The problem is thus reduced to the classical one first treated by Lommel. (See reference 7) However, in this paper, a slightly different approach is used.

FEED DISPLACED IN THE FOCAL PLANE.

In figure 1, an aperture S is shown with a coordinate system. It is generally accepted that the far field pattern for such an aperture is given by the diffraction integral

$$E = \int_S f(r_1\phi)\, e^{j\beta r \sin\theta \cos\phi}\, d\,S \qquad (1)$$

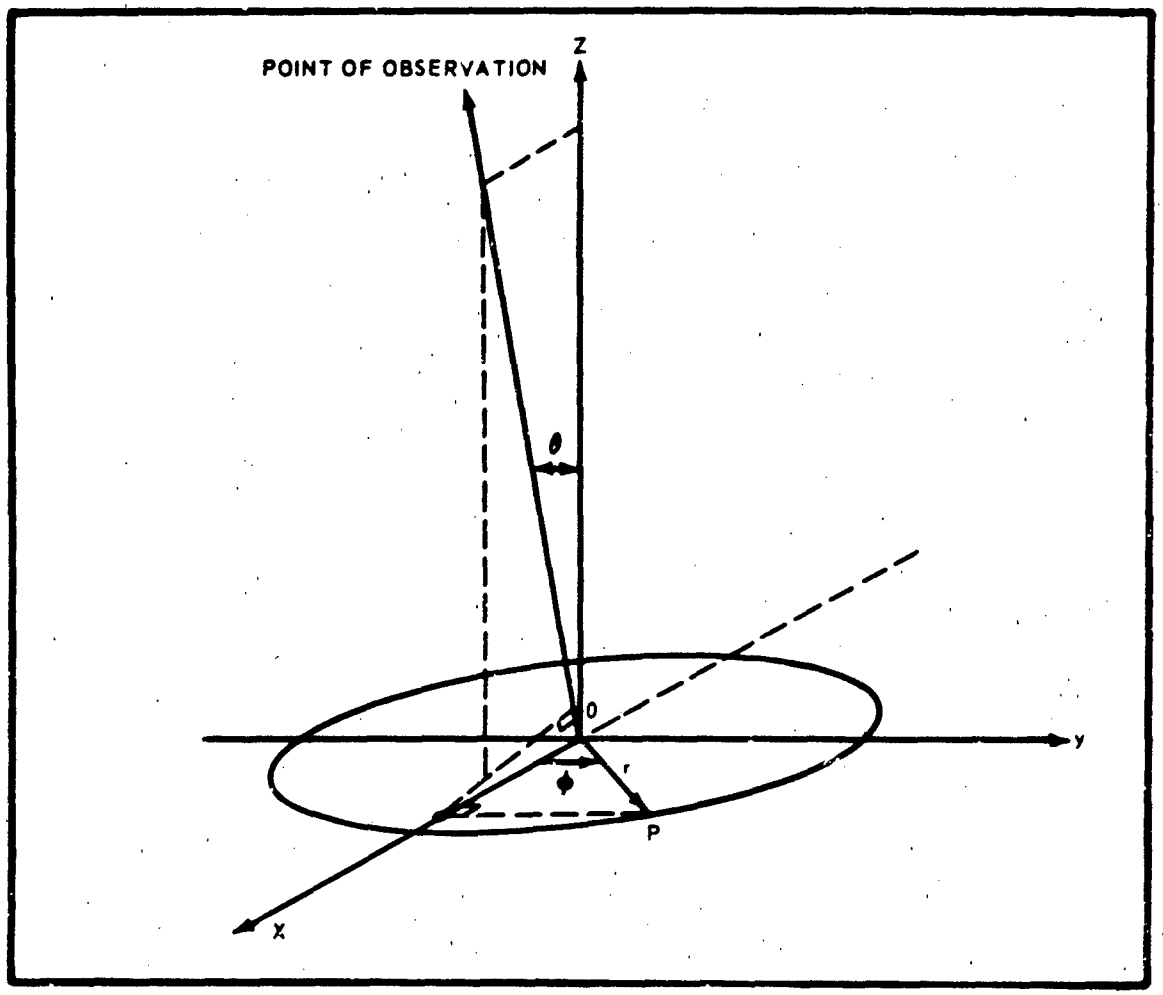

FIG 1

Here $f(r_1\phi)$ is the illuminating function defining the field strength across the aperture, both in amplitude and phase. Selecting the circular aperture with radius R, assume that $f(r_1\phi)$ has the magnitude

$$/f(r_1\phi)/ = 1-K(^{r}/R)^2 \qquad (2)$$

Here, K is a constant, for determining the taper across the aperture. For example, for K=0 we obtain a constant illumination; for K=2/3, the illumination taper is approximately 10 db.

The problem is now to determine the complex phase of $f(r,\phi)$ with the feed displaced in the focal plane as shown in figure 2. Here, F is the focal point of the paraboloidal dish and F' the actual location of the feed. We now note that if the feed had been located at F, then all rays would have arrived at the aperture plane with the same phase. With the feed actually located at F' the difference in phase is mainly due to the path difference between FB and F'B. This is a very good approximation because BP=BP' are both nearly perpendicular to the aperture plane. Further, BP is appreciably smaller than the focal length f of the dish (unless the f/D-ratio is extremely small).

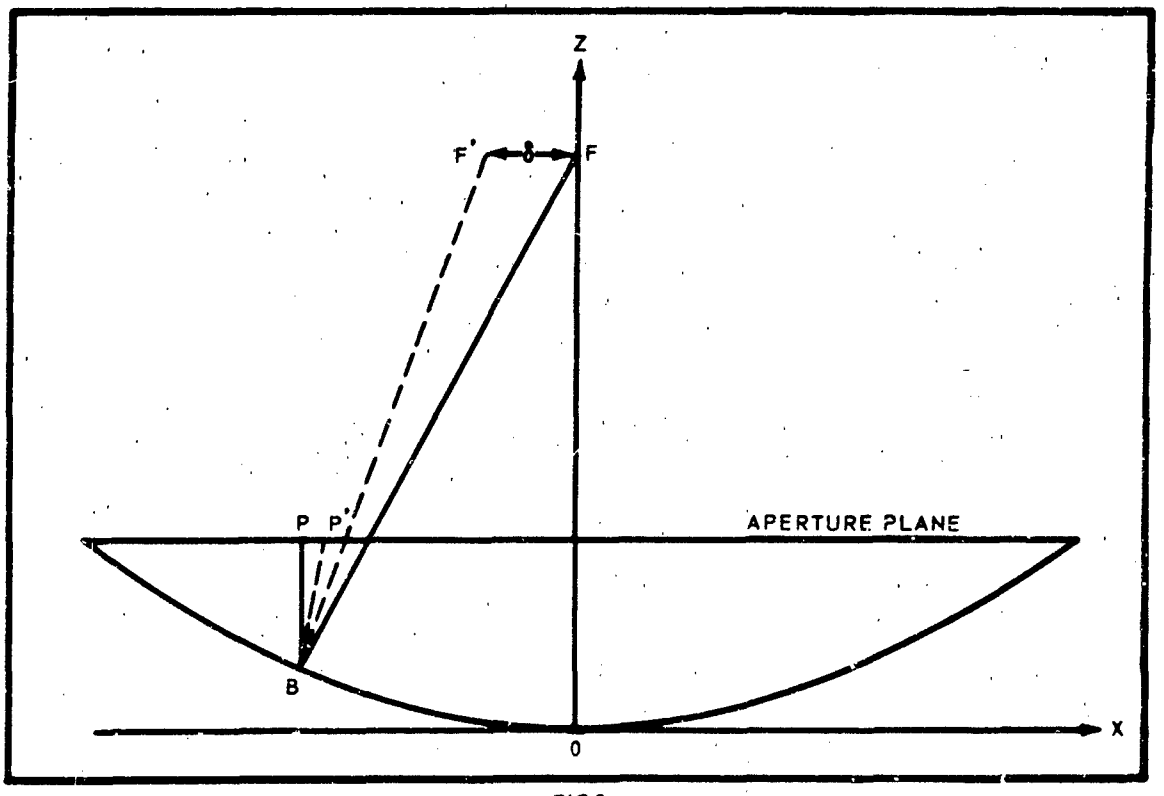

FIG 2

The evaluation of FB and F'B is illustrated in the more general three-dimensional figure 3. Again, the arbitrary point on the paraboloidal surface i designated by B, and we find from triangle ABF

$$BF^2 = r^2 + (f-2)^2$$

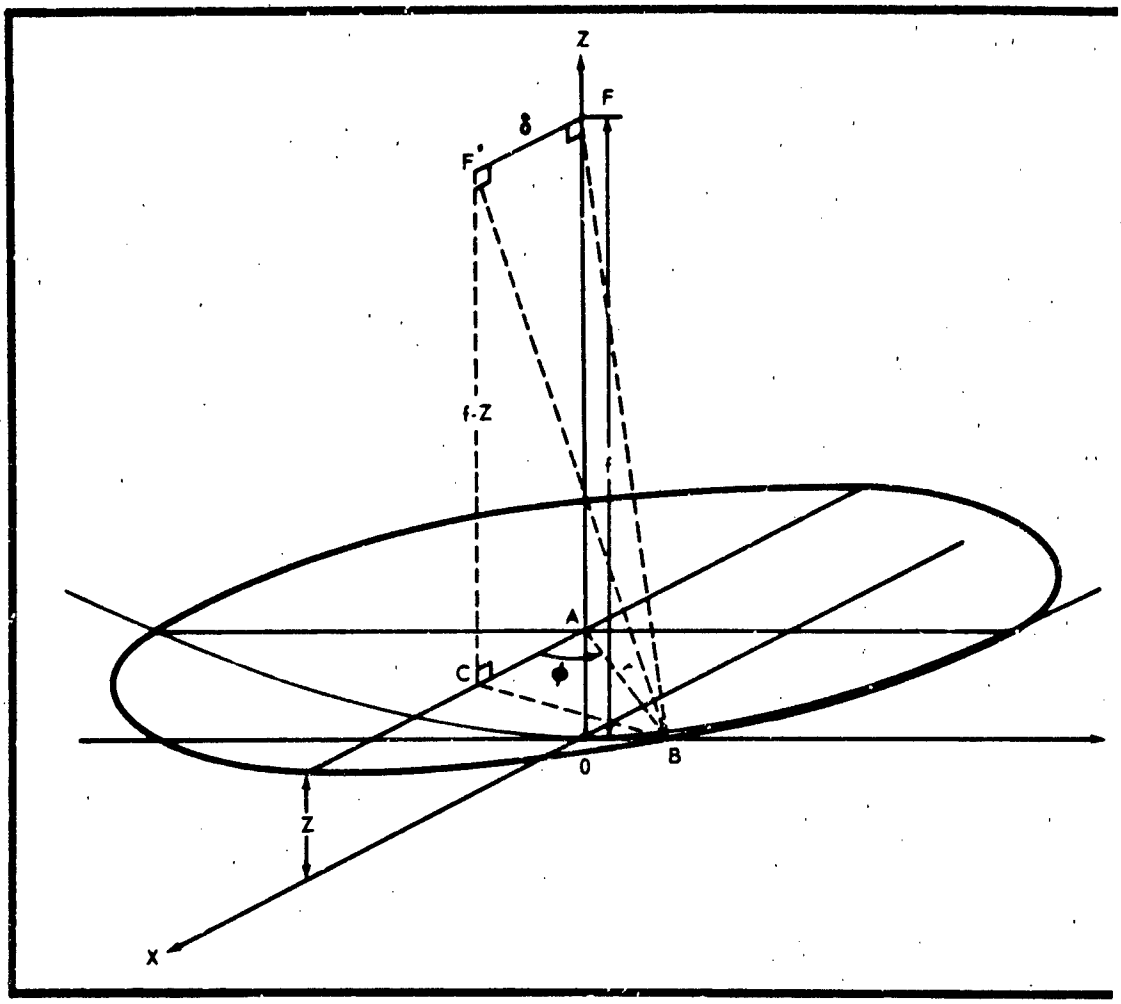

FIG 3

Substituting the parabolic equation

$$r^2 = 4fz$$

into (3) yields

$$BF = f\left[1 + (r/2f)^2\right]$$

Similarly, from triangles BCF and ABC we obtain

$$BF'^2 = BC^2 + CF'^2 = r^2 + \delta^2 - 2r\delta \cos\phi + (f - Z)^2$$

or with (4)

$$BF'^2 = f^2 \left(1 + \left(\frac{r}{2f}\right)^2\right)^2 + \delta^2 - 2r\delta \cos\phi \tag{6}$$

Now, since $\delta << f$, by applying the expansion

$$\sqrt{1-y} = 1 - \frac{y}{2} - \frac{y^2}{8}$$

and substituting the first two terms we obtain

$$BF' \cong f \left(1 + (r/2f)^2\right) \left[1 - \frac{\delta r}{f^2\left(1f(r/2f)^2\right)^2} \cos\phi\right] \tag{7}$$

Thus, from (5) and (7) we obtain for the phase function $\Delta(r,\phi)$ for the illuminating function $f(r,\phi)$ across the aperture

$$\Delta(r,\phi) = \beta \left[BF - BF'\right]$$

$$\Delta(r,\phi) = \frac{\delta}{f\left(1 + (r/2f)^2\right)} \beta r \cos\phi \tag{8}$$

For brevity we will introduce

$$q = \frac{\delta}{f(1 + (r/2f)^2)} \tag{9}$$

Thus, (8) can be written

$$\Delta(r,\phi) = \beta r q \cos\phi \tag{10}$$

We now substitute (10) into the defraction integral (1) and obtain

$$E = \int_0^R |f(r)| r dr \int_0^{2\pi} e^{j\beta r (\sin\theta\, fq) \cos\phi} d\phi \tag{11}$$

Applying the formula

$$J_n(Z) = \frac{i^n}{2\pi} \int_0^{2\pi} e^{iz\cos\phi}\, e^{in\phi}\, d\phi \tag{11a}$$

Where $J_n(Z)$ is the Bessel function of the first kind of order n and argument Z, we obtain from (11)

$$E = 2\pi \int_0^R /f(r)/r \quad J_0\left[\beta r (\sin\theta + q)\right] dr \tag{12}$$

Our next task is to obtain a suitable approximation for q. We may rewrite (9)

$$q = \frac{\delta}{f}\,\frac{1}{1+(r/2f)^2} = \frac{\delta}{f}\left[1 - \frac{1}{\left(\frac{2f}{R}\right)^2 + (r/R)^2}\,(r/R)^2\right] \qquad (13)$$

In this way we have managed to get q into a form consisting of a constant term plus a smaller term depending only on r. Thus, for a typical example, wi an f/D-ratio of 0.4 we obtain from (13)

$$q \to \begin{cases} \frac{\delta}{f}\left[1 - \frac{1}{2.56}\,(r/R)^2\right] & \text{for } r/R \to 0 \\ \frac{\delta}{f}\left[1 - \frac{1}{3.56}\,(r/R)^2\right] & \text{for } r/R \to 1 \end{cases} \qquad (14$$

and a reasonable approximation for q in this case will be

$$q \sim \delta/f\left[1 - \frac{1}{3}(r/R)^2\right] \qquad (14$$

Similarly, for a f/D = 0.6 we find

$$q \to \begin{cases} \delta/f\left[1 - \frac{1}{5.8}\,(r/R)^2\right] & \text{for } r/R \to 0 \\ \delta/f\left[1 - \frac{1}{6.8}\,(r/R)^2\right] & \text{for } r/R \to 1 \end{cases}$$

Thus, in this case, a good approximation is

$$q \sim \delta/f\left[1 - \frac{1}{6}\,(r/R)^2\right] \qquad (14$$

In the following calculations, we will substitute only (14a). As shall be see the final result can easily be modified to include also (14b).

Substituting (14a) into (12) now yields

$$E = 2\pi \int_0^R |f(r)|\, r\, J_0\left(x - t\left(\frac{r}{R}\right)^3\right) dr \qquad (15$$

where we for convenience have denoted

$$X = \beta r(\sin\theta + \delta/f) \text{ and } t = \frac{\beta \delta R}{3f} \qquad (16$$

We now apply to (15) one of the addition theorems related to Bessel functions, namely

$$J_p(x+y) = \left(1+\frac{y}{x}\right)^p \sum_{\gamma=0}^{\infty} \frac{(-1)^\gamma y^\gamma}{\gamma!}\left(1+\frac{y}{2x}\right)^\gamma J_{p+\gamma}(x) \qquad (17$$

Further, we substitute (2) into (16), integrate term by term and finally obtain after some reduction of the first terms:

$$
\begin{aligned}
E/\pi R^2 &= (1-K)\,\Lambda_1 + \frac{K}{2}\,\Lambda_2 \\
&+ \frac{tx_1}{4}\left[(1-K)\,\Lambda_2 - \tfrac{1}{3}(1-2K)\,\Lambda_3 - \tfrac{1}{6}K\,\Lambda_4\right] \\
&- \tfrac{1}{8}t^2\left[(1-K)\,\Lambda_2 - \tfrac{2}{3}(1-\tfrac{3}{2}K)\,\Lambda_3 + \tfrac{1}{6}(1-3K)\,\Lambda_4 + \tfrac{K}{10}\,\Lambda_5\right] \\
&+ \tfrac{1}{48}t^2x_1^2\left[(1-K)\,\Lambda_3 - \tfrac{1}{2}(1-\tfrac{3}{2}K)\,\Lambda_4 + \tfrac{1}{10}(1-3K)\,\Lambda_5 + \tfrac{K}{20}\,\Lambda_6\right] \\
&- \tfrac{1}{48}t^3x_1\left[(1-K)\,\Lambda_3 - \tfrac{3}{4}(1-\tfrac{4}{3}K)\,\Lambda_4 + \tfrac{3}{10}(1-2K)\,\Lambda_5 - \tfrac{1}{20}(1-4K)\,\Lambda_6 - \tfrac{K}{35}\,\Lambda_7\right] \\
&+ \tfrac{1}{1152}t^3x_1^3\left[(1-K)\,\Lambda_4 - \tfrac{3}{5}(1-\tfrac{4}{3}K)\,\Lambda_5 + \tfrac{1}{5}(1-2K)\,\Lambda_6 - \tfrac{1}{35}(1-4K)\,\Lambda_7 - \tfrac{K}{70}\,\Lambda_8\right] \\
&+ \tfrac{1}{192}t^6\left[(1-K)\,\Lambda_3 - \tfrac{7}{4}(1-\tfrac{8}{7}K)\,\Lambda_4 + \tfrac{21}{10}(1-\tfrac{4}{3}K)\,\Lambda_5 - \tfrac{7}{4}(1-\tfrac{8}{5}K)\,\Lambda_6 + (1-2K)\,\Lambda_7\right]
\end{aligned}
\qquad (18)
$$

where

$$\Lambda_n = n!\,\frac{J_n(x_1)}{(x_1/2)^n}$$

$$X_1 = \beta R\,(\sin\theta + \delta/f)$$

$$t = \begin{cases} \dfrac{\beta\,\delta R}{3f} & \text{for } f/D = 0.4 \\ \dfrac{\beta\,\delta R}{6f} & \text{for } f/D = 0.6 \end{cases}$$

It is interesting to note that the first two terms in (18) represent exactly the well known far field from circular aperture with no phase distortion present. Yet, the argument is not $x = \beta R \sin\theta$ but $x_1 = \beta R(\sin\theta + \delta/f)$, i.e., the pattern has been displaced by the angle

$$\theta_o = \sin^{-1}\delta/f$$

This is what one intuitively might anticipate and the rest of the terms in (18 can thus be considered to be merely smaller correcting terms yielding directly an expression for the distortion of the pattern. This is further illustrated in figure 4 where (18) has been plotted for $t = 1/2$ rad corresponding to $\delta = 0.1915\lambda$,

$x_o = 3t = 1.5$ for $f/D = 0.4$ or

$\delta = 0.574\lambda$, $x_o = 6t = 3$ for $f/D = 0.6$.

For the purpose of comparison, the undistorted pattern is also shown corresponding to the first two terms in (18). It clearly shows that the side lobes increase on the side of the beam closest to the boresight axis and that the displacement of the main beam is somewhat smaller than θ_o; this is in agreement with beam deviation factor introduced in references 2 and 8. It is also seen that a large f/D-ratio permits a greater displacement δ for a given distortion. Similarly, figure 5 shows a plot of equation (18) for $t = 1$ rad.

FEED DISPLACED IN THE AXIAL DIRECTION

This situation is shown in figure 6. Again, applying the same approach as in the case above, it is readily seen that the rays emerging from F^1 will be delayed by an amount corresponding to the path $F^1S \cong \delta \cos\gamma$. However, as the feed is moved from F to F^1 the phase reference at the origin 0 is changed by an amount δ, so that the actual phase function is given

$$\Delta(r) = \beta\delta(1-\cos\gamma) \tag{19}$$

From the geometry of a paraboloid it is further known that

$$\cos\gamma = \frac{4f^2-r^2}{4f^2+r^2} \tag{20}$$

Substituting (20) into (19) yields

$$\Delta(r) = \frac{\beta\delta}{2f^2}\,\frac{r^2}{1+(r/2f)^2} \tag{21}$$

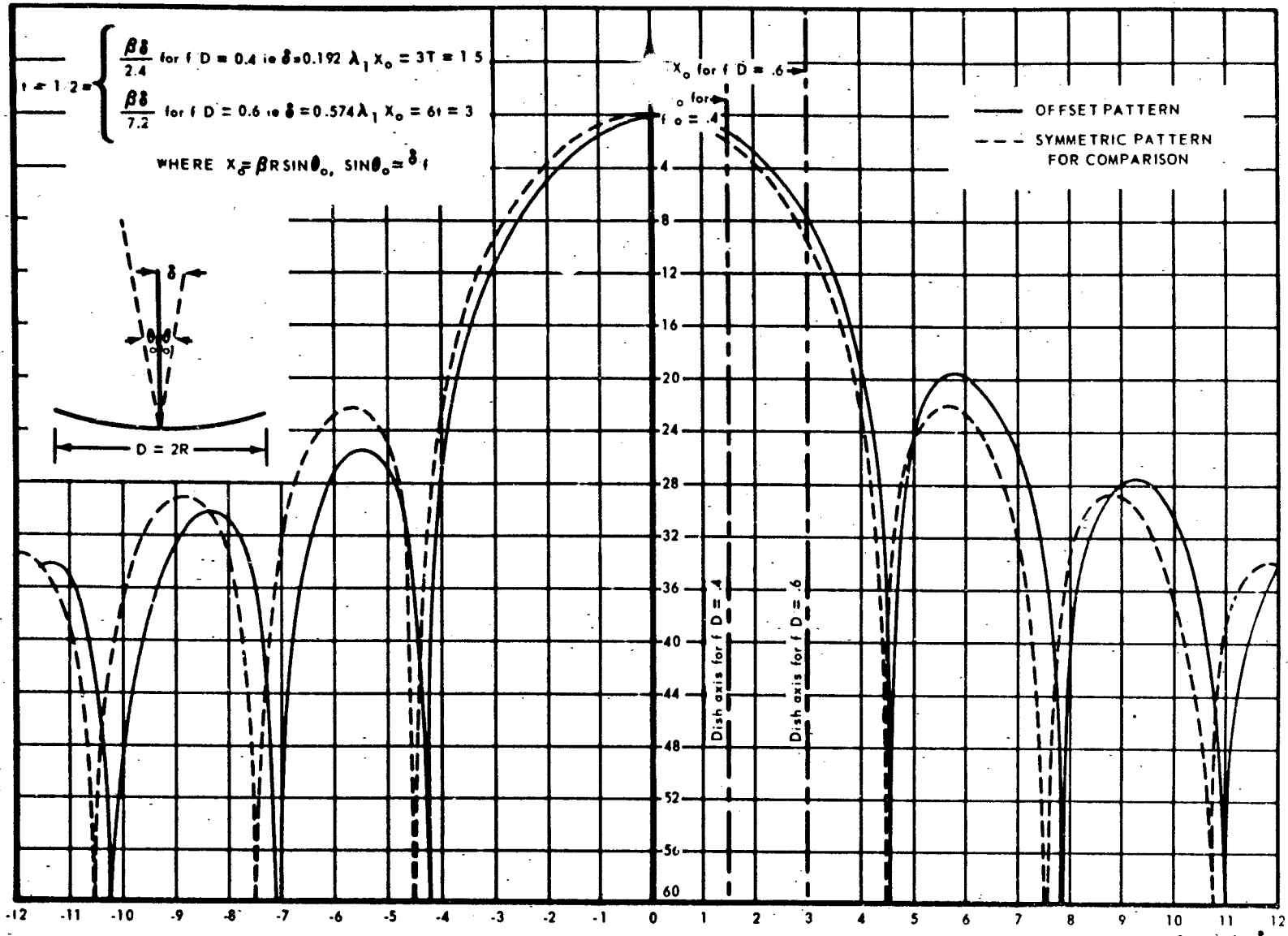

Fig 4. Radiation pattern for circular dish with offset feed. Illumination f(r) = 1-2 3(r R)^2 i.e. 10db taper

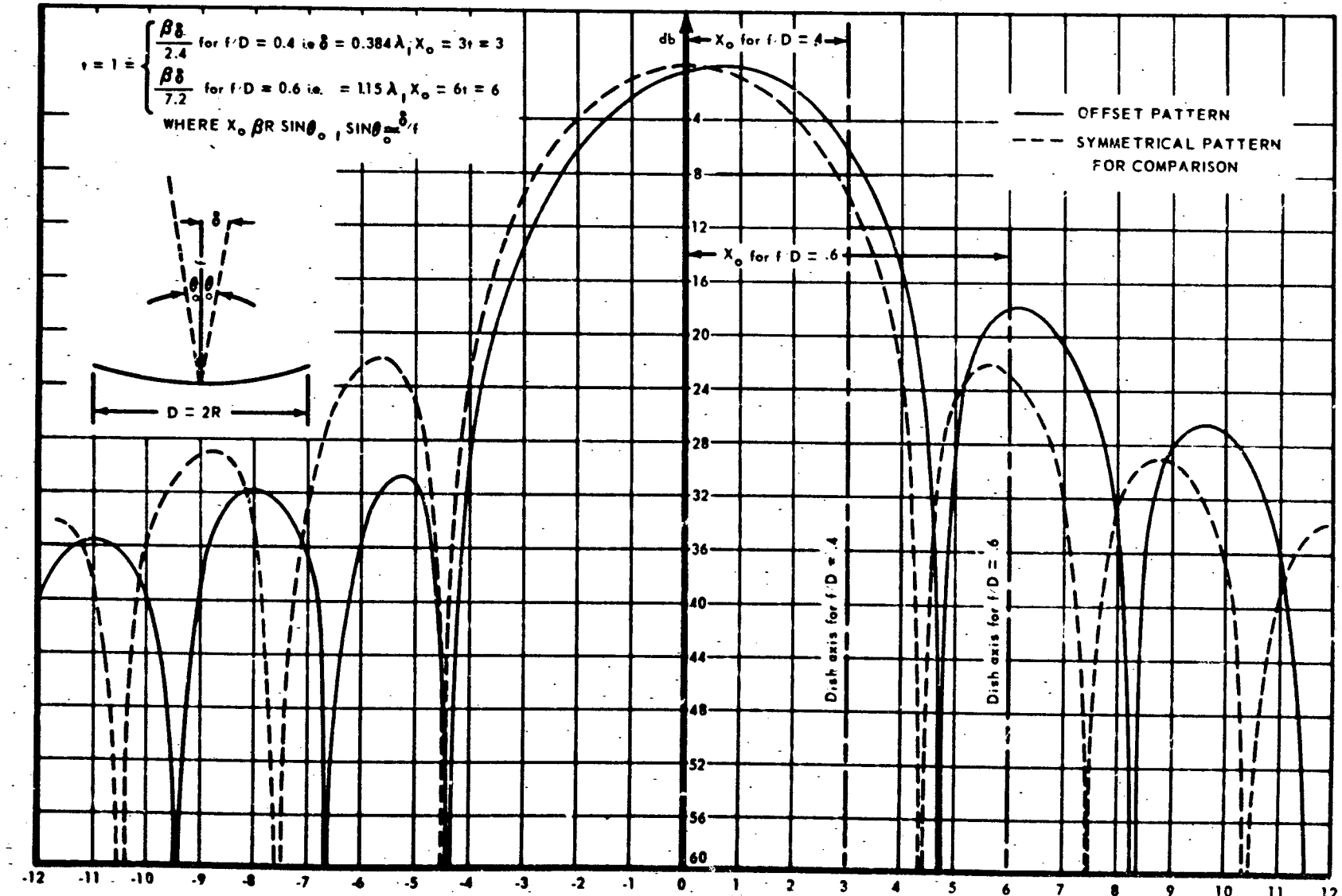

Fig 5 Radiation pattern for circular dish with offset feed. Illumination $f(r) = 1 \cdot 2\ 3(r\ R)^2$ i.e. 10db taper

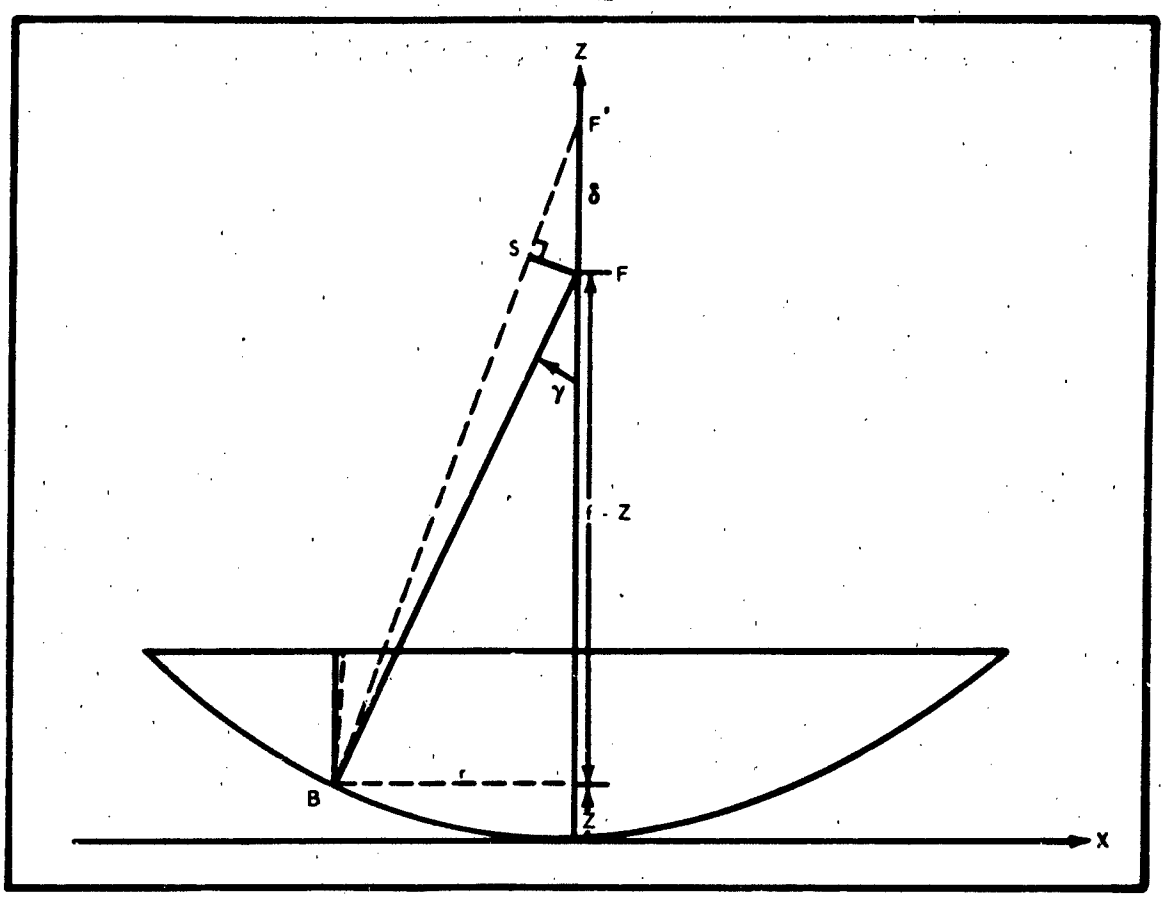

FIG 6

To obtain a clear picture of $\Delta(r)$ as a function of r it has been plotted in figure 7 and compared with $(r/R)^2$. It will be observed that $\Delta(r)$ does not deviate very much, particularly for large values of f/D-ratio. Some comments are in order in regard to evaluation of the diffraction integral when the phase function is defined as

$$\Delta(r) = a. \left(\frac{r}{R}\right)^p.$$

The writer has evaluated the integral for values of p of 1, 2, and 4, and it can be shown that the changes in the secondary radiation pattern for $1 \leq p \leq 4$ are gradual and continuous if "a" is held constant. In other words, the error resulting from the assumption that $\Delta(r)$ is of the form

$$\Delta(r) = a \left(\frac{r}{R}\right)^2 \qquad (22)$$

is not great.

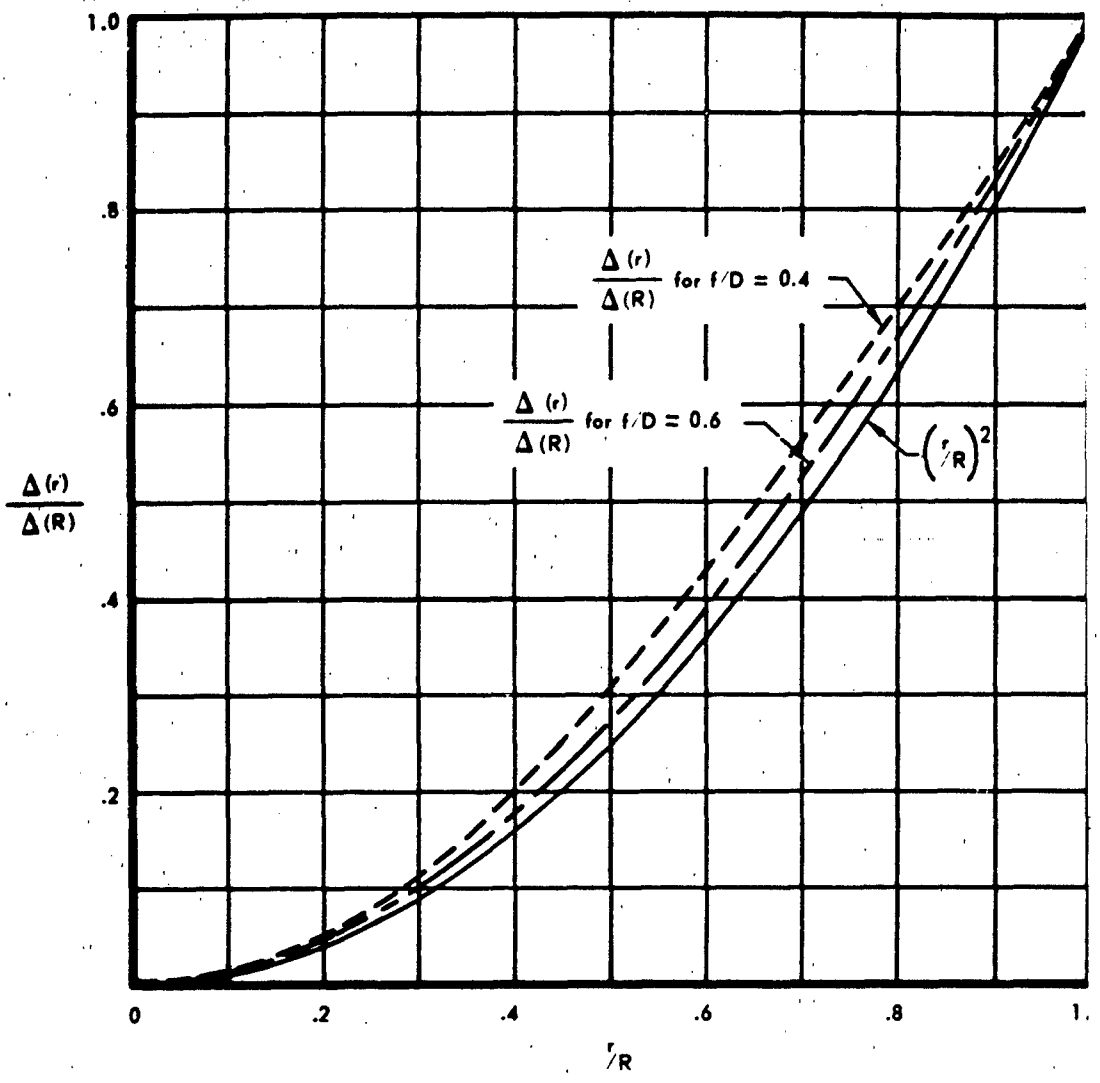

FIG 7

The constant "a" is simply given by

$$a = \Delta(R) = \frac{2\beta\delta}{1 + 16\left(\frac{f}{D}\right)^2} \qquad (2$$

Substituting (22) and (2) into the diffraction integral (1) yields

$$E = \int_0^R \int_0^{2\pi} |f(r)|\, e^{j\beta r \sin\theta \cos\phi + ja\left(\frac{r}{R}\right)^2} r\,dr\,d\phi \qquad (2$$

Now applying (11a) on (24) gives

$$E = 2\pi \int_0^R |f(r)|\, r\, J_0(\beta r \sin\theta)\, e^{ja\left(\frac{r}{R}\right)^2} dr \qquad (2$$

The evaluation of (25) can now be performed in a number of ways. For $|f(r)| = 1$ an obvious approach is the application of the Lommel functions in two variables (see reference 4, page 434 and reference 5 page 537), which were introduced by Lommel for this purpose. However, in this presentation the writer chooses to expand the exponential factor in the well known form

$$e^{x} = \sum_{n=0}^{\infty} \frac{x^n}{n!}$$

and thus to integrate by parts, term by term after first substituting (2) into (25). After reduction we obtain:

$$\begin{aligned} E &= (1-K)\,\Lambda_1 + \frac{K}{2}\,\Lambda_2 \\ &+ j\,a\left[(1-K)\,\Lambda_1 - (\tfrac{1}{2}-K)\,\Lambda_2 - \tfrac{K}{3}\,\Lambda_3\right] \\ &-\tfrac{1}{2!}\,a^2\left[(1-K)\Lambda_1 - (1-\tfrac{3}{2}K)\,\Lambda_2 + (\tfrac{1}{3}-K)\,\Lambda_3 + \tfrac{K}{4}\,\Lambda_4\right] \\ &\frac{-j}{3!}\,a^3\left[(1-K)\,\Lambda_1 - (\tfrac{3}{2}-2K)\,\Lambda_2 + (1-2K)\,\Lambda_3 - (\tfrac{1}{4}-K)\,\Lambda_4 - \tfrac{K}{5}\,\Lambda_5\right] \\ &+ \frac{1}{4!}\,a^4\left[(1-K)\,\Lambda_1 - (2-\tfrac{5}{2}K)\,\Lambda_2 + (2-\tfrac{10}{3}K)\,\Lambda_3 - (1-\tfrac{5}{2}K)\,\Lambda_4\right. \\ &\left. + (\tfrac{1}{5}-K)\,\Lambda_5 + \frac{K}{6}\,\Lambda_6\right] \end{aligned} \qquad (26)$$

where $\Lambda_n = n!\,\dfrac{J_n(x)}{(x)^n}$

and $x = \beta R \sin\theta$.

Expression (26) is plotted in figure 8 for $a = 1$ and 2 radians. For an $^f/_D$-ratio equal to 0.4 this corresponds according to (23) to a $\delta = 0.284\,\lambda$ and $0.568\,\lambda$ respectively. With an $^f/_D$-ratio equal to 0.6, this corresponds to $\delta = .54\,\lambda$ and $1.08\,\lambda$ respectively.

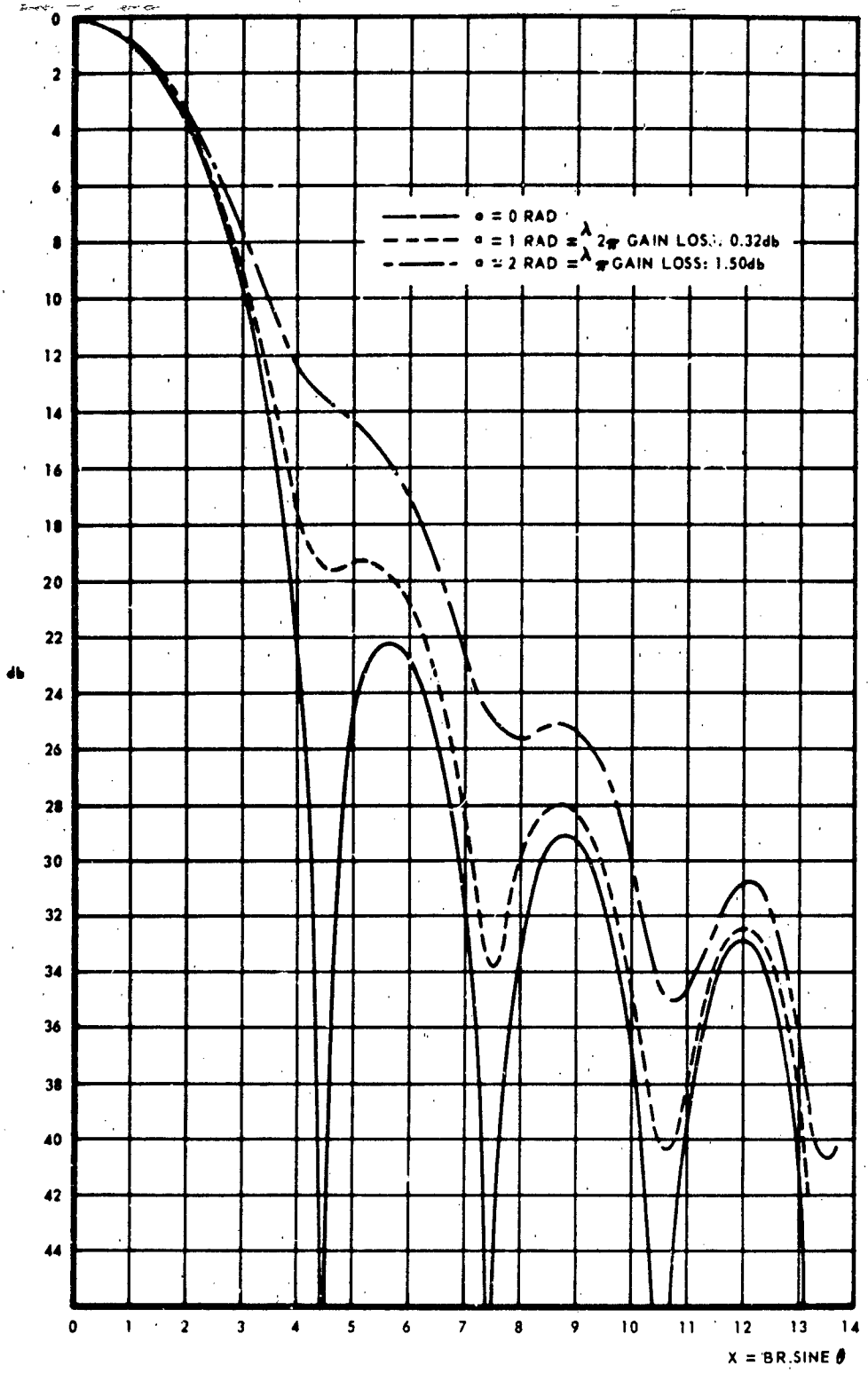

Fig 8 Radiation pattern for circular aperture with phase deviation function

$$\Delta(r) = \sigma\left(\frac{r}{R}\right)^2$$

Illumination $f(r) = 1\text{-}2.3\left(\frac{r}{R}\right)^2$ *i.e. 10db taper.*

Conclusion

An expansion for the far field for a paraboloidal dish with the feed displaced either axially or transversely in the focal plane has been obtained. In both cases the expansion produces an expression the individual terms of which are the product of a polynomial dependent only on $x = \beta R \sin\theta$ and an exponential factor $\beta\delta$ depending only on the displacement of the feed. Thus, once the polynomials have been evaluated, patterns for arbitrary displacement of the feed can be readily obtained.

References

1. D. K. Cheng and S. T. Moseley: On axis Defocus Characteristics of the parabolic reflector. IRE Trans. on Antennas and Propagation 1955 Oct.

2. Y-T Lo: On the Beam Deviation Factor of a Parabolic Reflector. Trans. IRE Vol. AP-8, May 1960, p.p. 347-349.

3. S. S. Sandler: Paraboloidal Reflector for Off-Axis Feed. IRE Trans. Ant. & Prop. July 1960 p. 368.

4. Born and Wolf: Principle of Optics. Pergamon Press. 1959.

5. Watson: Theory of Bessel Function Cambridge At The University Press, 1958.

6. Jahnke and Emde: Table of functions. Dover Publications.

7. Lommel: Abh. der math. phys. classe der K. b. A Kad. der Wiss. (Munchen) XV (1886) p.p. 229-328. 529-664

8. S. Silver: Microwave Antennas and Techniques, MIT Rad. Lab.series, Vol. 12.

9. MING-KUEI HU: Fresnel Region Field Distribution of Circular Ape Antennas. IRE Trans. Ant. & Prop. May 1960 p. 344.

Acknowledgement:

The author wishes to express his thanks to his supervisor Dr. Horsc his advisor at Ohio State University Dr. Kouyoumjian for many fruitful and iating discussions. Also, I am indebted to Mr. A. E. Joost for a critical r of this paper.

A SIMPLIFIED VARIABLE POLARIZATION ANTENNA

by

John L. Kerr

Presented at the Fourteenth Annual Symposium
on USAF Antenna Research and Development

University of Illinois
6, 7, 8 October 1964

U. S. ARMY ELECTRONICS LABORATORIES
U. S. ARMY ELECTRONICS COMMAND
FORT MONMOUTH, N. J.

A SIMPLIFIED VARIABLE POLARIZATION ANTENNA

INTRODUCTION

In applications where changes in polarization are required, it has been the practice to effect these changes through one of the following methods: use of multiple antennas, transmission-line switching, rotating quarter-wave and half-wave plates, and insertion or removal of various components such as polarizing elements, various feeds for reflector-type antennas, and waveguide twist sections. Effort was directed toward development of a simplified variable-polarization antenna in which any type of polarization – linear, circular, or elliptical – would be readily available. Many of the disadvantages of previously used techniques would thereby be eliminated.

Design of the antenna was based on a waveguide feed arrangement in which a polarizing element and the input field were independently rotatable about the axis of propagation.

Perhaps the most commonly used waveguide polarizers are the lumped-reactance and dielectric-delay-section types. At millimeter wavelengths, however, difficulties arise in fabrication of the required components and in reproduction of electrical characteristics.

The elliptical-waveguide or squeeze-section polarizer[1] appears to have significant advantages over other types. Therefore, additional effort was directed toward developing a relatively simple means of transforming a round waveguide into a waveguide with a cross section which approaches an ellipse.

THEORY OF OPERATION

In a waveguide of elliptical cross section,[1-3] if the input electric vector is not aligned with either axis of the ellipse, the field is resolved into two orthogonal components. The electric vector of one wave is aligned with the major axis of the ellipse and the electric vector of the other wave is aligned with the minor axis. These two waves are classified as the odd ($_oTE_{11}$) and the even ($_eTE_{11}$) waveguide modes. The cut-off wavelength (λ_c) differs for the two modes, and in general the amplitudes are unequal. The exception to the inequality of amplitudes occurs when the input electric vector is aligned at an angle of 45 degrees with respect to the axes of the ellipse.

Linear Polarization

When the input electric vector is aligned with the major axis of the elliptical waveguide, the $_oTE_{11}$ wave results. The $_eTE_{11}$ wave is obtained when the input electric vector is aligned with the minor axis of the ellipse. In either case, the alternate wave is not propagated and linear polarization is obtained.

Circular Polarization

The guide wavelength (λ_g) of a signal propagating in the fundamental mode in a hollow air-filled waveguide is given by

$$\lambda_g = \frac{\lambda}{\sqrt{1-\left(\frac{\lambda}{\lambda_c}\right)^2}} \quad , \qquad (1)$$

where λ = free space wavelength

and λ_c = cutoff wavelength .

Since λ_c is different for the even and odd modes in an elliptical waveguide, or squeeze section, the two waves propagate through this section with different phase velocities.

The parameters of the squeeze section are then so chosen that

$$2\pi L\left(\frac{1}{\lambda_{ge}} - \frac{1}{\lambda_{go}}\right) = \frac{\pi}{2} \quad , \qquad (2)$$

where L = length of the squeeze section

λ_{ge} = guide wavelength for the even mode

λ_{go} = guide wavelength for the odd mode.

With the polarizer so adjusted and the input electric vector fixed at an angle of 45 degrees with respect to the axes of the ellipse, the two waves will emerge from the polarizer essentially equal in amplitude and in phase quadrature, the required condition for circular polarization.[1,4]

Elliptical Polarization

Elliptical polarization is obtained when the angle between the input electric vector and either axis of the polarizer is other than 0 degrees or 45 degrees. The ratio of the amplitudes of the even and odd waveguide modes varies for each such angle of orientation, and therefore elliptical polarization of any axial ratio between linear and circular polarization may be obtained.

DESCRIPTION

The variable polarization antenna assembly consists of a waveguide rotary joint, a transition from rectangular to round waveguide, a polarizing element, and a radiator. These are arranged so that the polarizer and the input field are independently rotatable about the axis of propagation (Figure 1). Figure 2 is a photograph of the experimental model.

The waveguide rotary joint is of a conventional, continuously rotatable type. At least one arm is collinear with the axis of propagation. The antenna used in the experimental model was a conical horn with an aperture approximately 7λ in diameter. In addition to the conical horn, many other antenna types may be used. They include, but are not limited to, circularly symmetric vertex feeds, cassegrain systems, and dielectric rod antennas.

Squeeze-Section Polarizer

The squeeze-section polarizer was formed by squeezing round copper tubing with an outer diameter of 0.375 inch and an inner diameter of 0.291 inch in a roller device in which the amount and length of squeeze could be precisely controlled. Since results vary for different metals, wall thicknesses, and so forth, it was necessary to determine experimentally the squeeze-section parameters required for the type of tubing used.

The tubing was first compressed in an amount and over a length known to be less than required for the 90-degree differential phase shift. Then, the amount and length of the squeeze were increased by small increments and the results measured electrically until the 90-degree differential phase shift was obtained. A smooth transition at the beginning and at the end of the squeeze section was obtained by using rollers of relatively large diameter.

The tubing used for the experimental model was compressed 0.050 inch over a length of 1.25 inches. (The length here is defined as the center-to-center travel of the rollers along the tubing.) This compression resulted in a measured inner cross section with a major axis of 0.301 inch and a minor axis of 0.266 inch. Electrical measurements indicated that the required 90-degree differential phase shift was obtained at the design frequency of 33.6 gigacycles with the dimensions given above.

The parameters as determined by the above procedure were used in the fabrication of additional squeeze sections. The electrical characteristics were easily reproduced with a minimum of time and effort.

EXPERIMENTAL PROCEDURES

Polarization patterns were measured by means of the experimental setup diagrammed in Figure 4. The variable-polarization antenna was used as a receiver. The transmitting antenna was a pyramidal horn with approximately 22-db gain, which was arranged to rotate about the axis of propagation. The position information was fed to a polar recorder by a synchro link. The patterns were plotted on a relative voltage scale at the design frequency of 33.6 gigacycles. The receiver gain was adjusted to maintain the amplitude near full scale for each polarization; hence, these patterns do not show the variation in signal strength as the polarization changes from linear to circular.

Linear Polarization

To demonstrate the availability of linear polarization and to show its rotation about the axis of propagation, the input electric vector was fixed in alignment with the minor axis of the squeeze section. The polarizer and rotary joint were then rotated in unison in discrete steps through the range $\delta = -90°$ to $\delta = +90°$, where δ is defined as the angle between the polar axis and the minor axis of the squeeze section. (Refer to Figure 5.) The polarization patterns taken are shown in Figures 6 through 10.

Elliptical Polarization

In the case of elliptical polarization, any axial ratio between linear and circular may be chosen. The polarization ellipse may be fixed in any position about the axis of propagation or may be continuously rotated. Rotation of the polarization ellipse is accomplished as follows: The input electric vector and the minor axis of the polarizer (taken as the reference) are first aligned at the angle corresponding to the desired axial ratio. The rotary joint and the polarizer are then rotated in unison continuously, or turned to any position about the axis of propagation.

To measure the variations in elliptical polarization, the orientation of the input electric vector was fixed and the polarizer rotated in discrete steps through the range $\gamma = -45°$ to

$\gamma = +45°$, where γ is defined as the angle between the input electric vector and the minor axis of the polarizer (Figure 11).

The polarization patterns for $\gamma = -45°$ (Figure 12) and $\gamma = +45°$ (Figure 13) show essentially circular polarization with an axial ratio less than 0.5 db. The patterns for angles between $\gamma = 0°$ and $\gamma = -45°$ (Figures 14 through 17) and for angles between $\gamma = 0°$ and $\gamma = +45°$ (Figures 18 through 21) indicate the range of elliptical polarizations between linear and circular.

The sense of the circular or elliptical polarization (right or left) is dependent upon whether γ is positive or negative. (See Figure 22.)

Bandwidth and VSWR

A bandwidth of approximately 10 percent where the axial ratio did not exceed 1.5 db was measured for the squeeze-section polarizer investigated. The bandwidth for rotating linear polarization in the variable polarization antenna is limited only by the bandwidth of the circular waveguide used, in contrast to the extremely narrow bandwidth obtained by devices which utilize a half-wave plate to effect rotating linear polarization.

In order to determine the effect of the transitions formed in squeezing the round waveguide into an elliptical shape, the waveguide rotary joint was removed from the system and VSWR measurements were made at the input to the rectangular-to-round waveguide transition. The VSWR curves for various orientations of the squeeze-section polarizer with respect to the input electric vector, as shown in Figure 23, indicate a well-matched device.

CONCLUSIONS

A relatively simple technique was devised for forming an elliptical waveguide or squeeze-section polarizer that demonstrates the capacity for excellent reproduction of electrical characteristics. This device was combined with a waveguide rotating joint to form the variable polarization antenna. Experiments showed that with this antenna any type of polarization is readily available. Linear polarization may be fixed in any plane about the axis of propagation or may be continuously rotated. Right or left elliptical polarization of any desired axial ratio between linear and circular may be selected. The polarization ellipse may be fixed in any direction about the axis of propagation or may be continuously rotated. This variable polarization antenna will have many practical applications in the fields of radar, communications, and countermeasures.

REFERENCES

1. Hatkin, Dr. Leonard, "Circularly Polarized Radio Waves," USASRDL Technical Report 2127, pp. 1-5 (January 1961).
2. Moreno, Theodore, *Microwave Transmission Design Data* pp. 118-122, Dover Publications, Inc., New York (1958).
3. Chu, L. J., "Electromagnetic Waves in Hollow Pipes of Metal," Journal of Applied Physics, Vol. 9, pp. 483-591 (1938).
4. Kraus, John D., *Antennas*, pp. 464-477, McGraw-Hill Electrical and Electronic Engineering Series, McGraw-Hill Book Company, Inc., New York (1950).

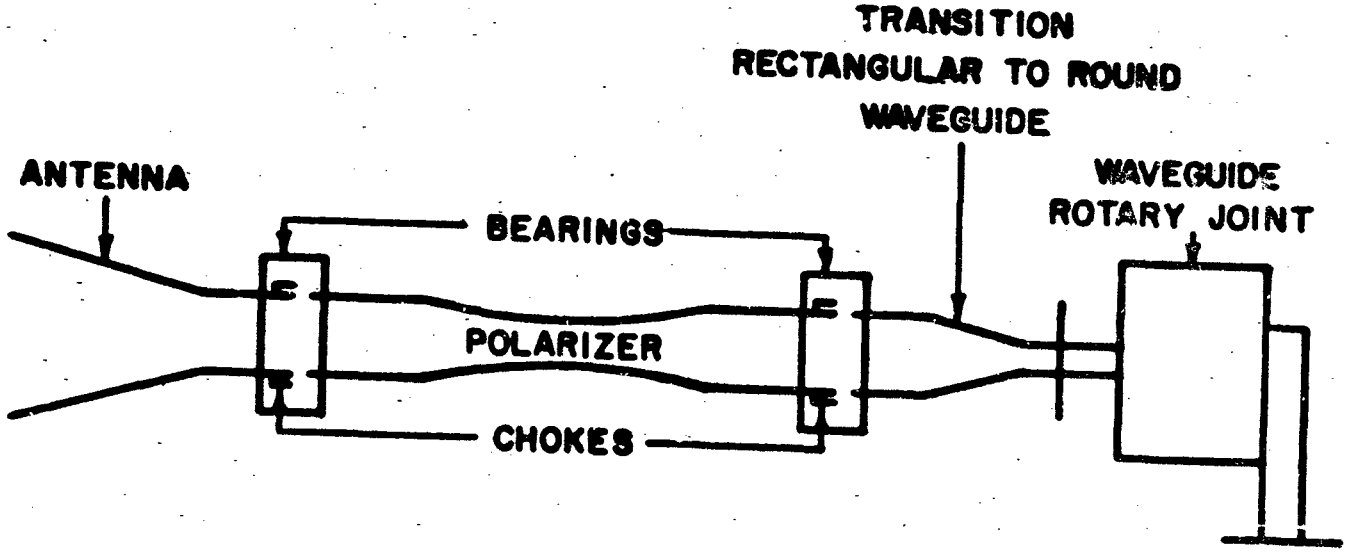

FIGURE 1. VARIABLE POLARIZATION ANTENNA

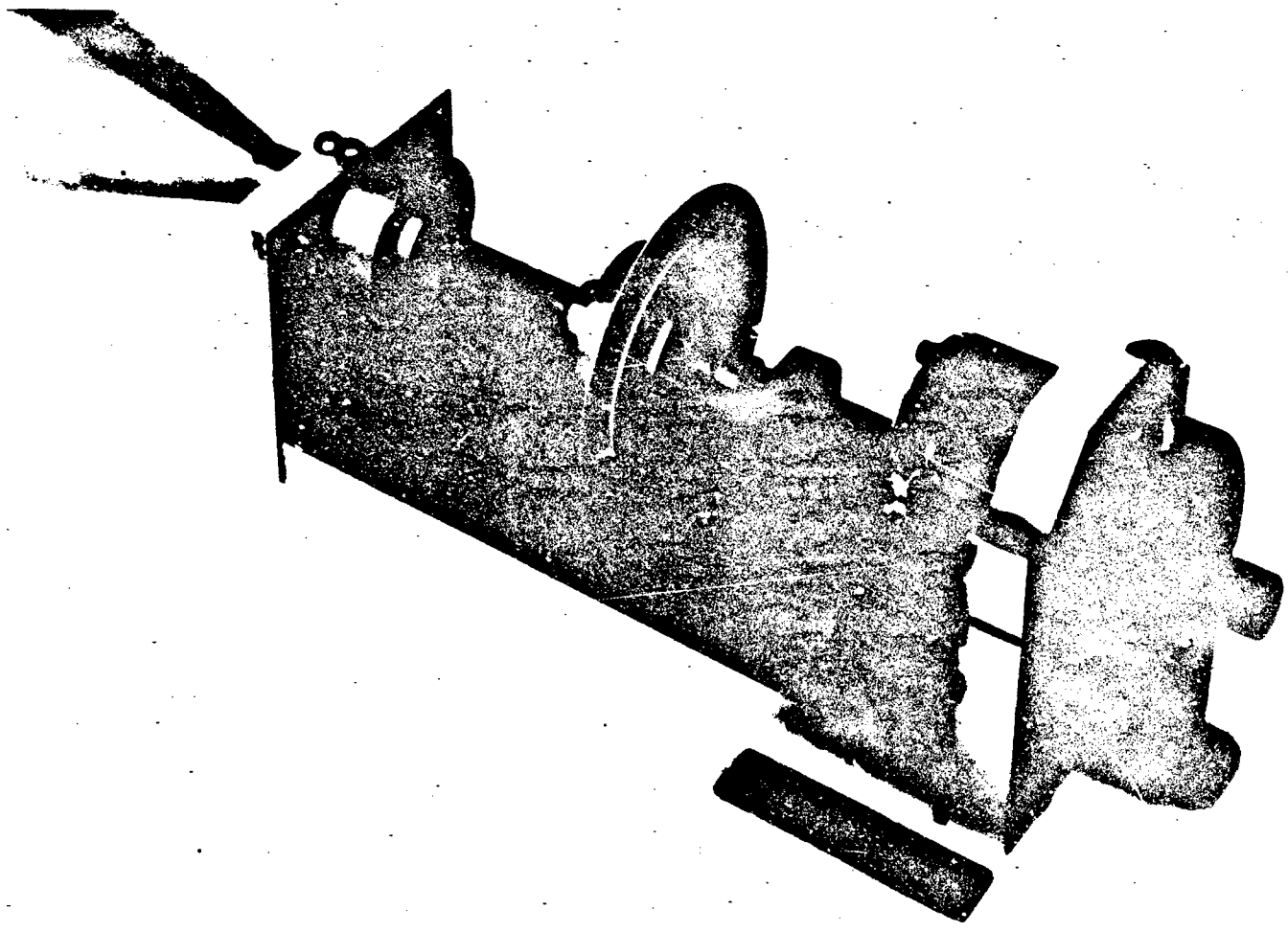

FIGURE 2. VARIABLE POLARIZATION ANTENNA: EXPERIMENTAL MODEL



FIGURE 3. TUBING CONVERSION DEVICE

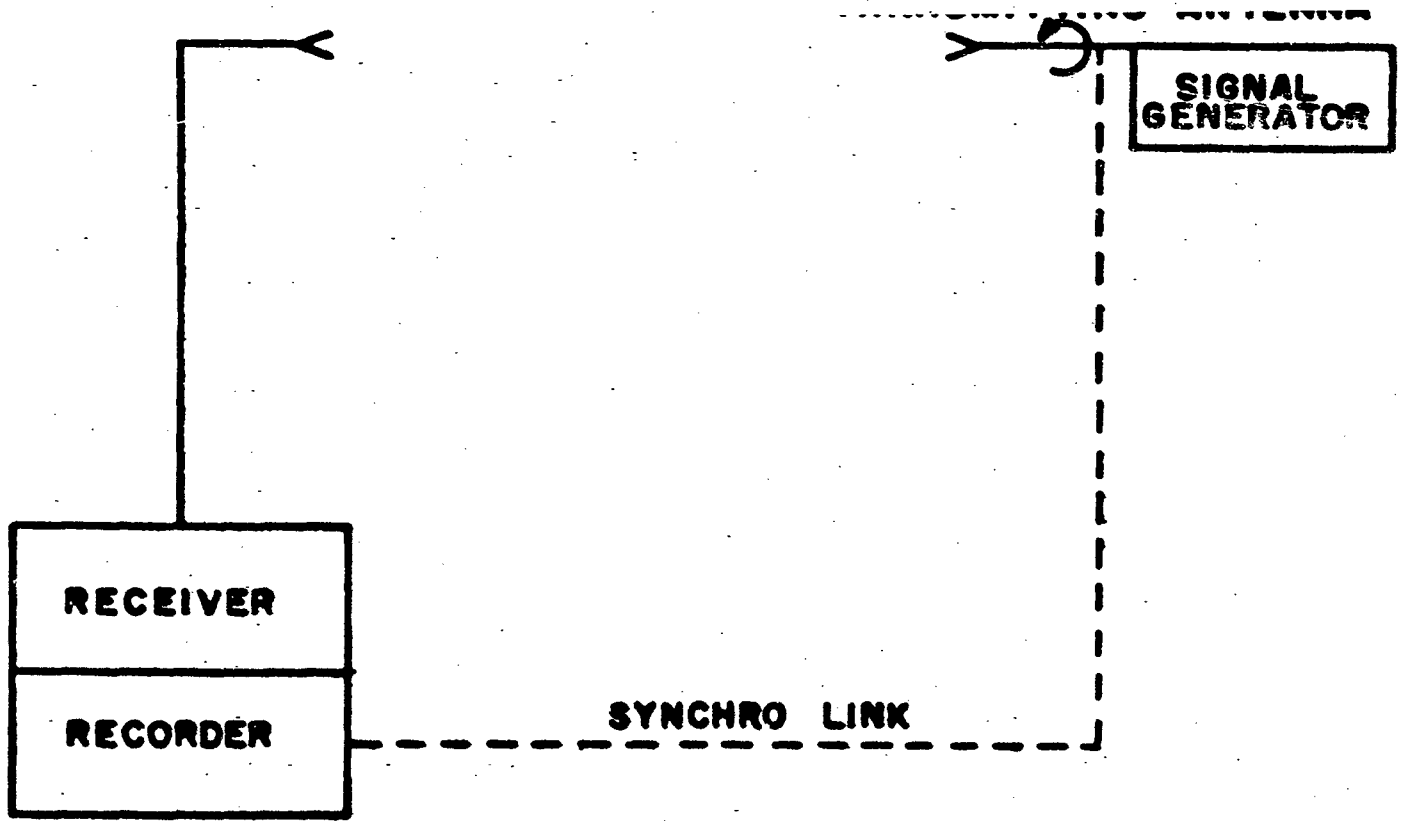

FIGURE 4. EXPERIMENTAL SETUP FOR RECORDING POLARIZATION PATTERNS

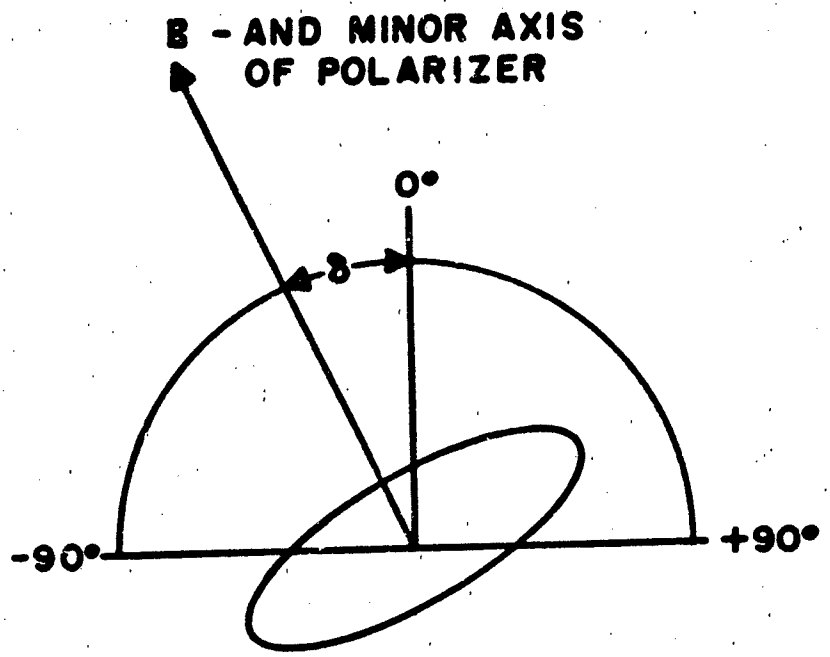

FIGURE 5. DEFINITION OF THE ANGLE θ
LINEAR POLARIZATION

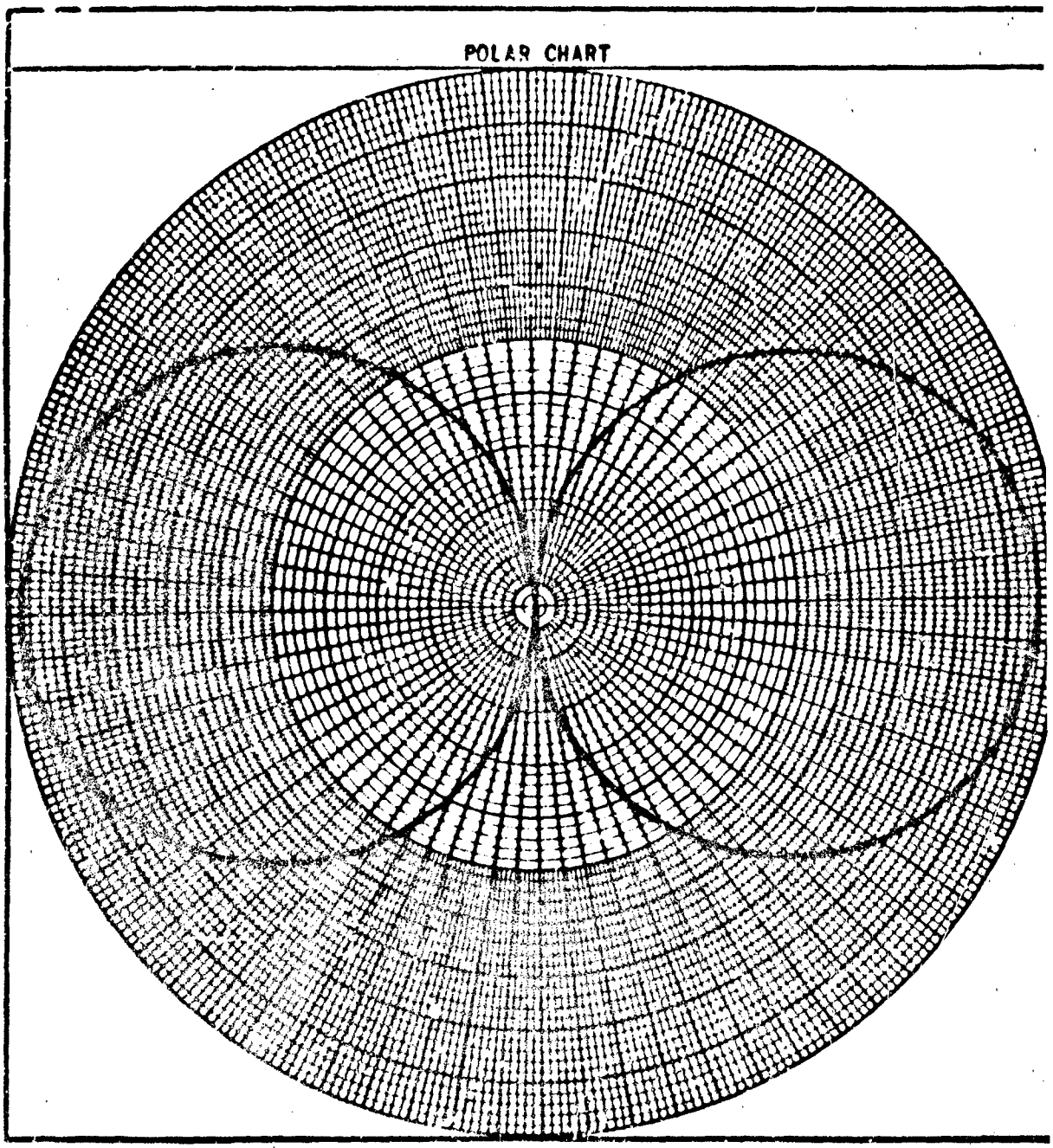

FIGURE 6. VARIABLE POLARIZATION ANTENNA: POLARIZATION PATTERNS
LINEAR POLARIZATION

$\delta = -90^{\circ}$

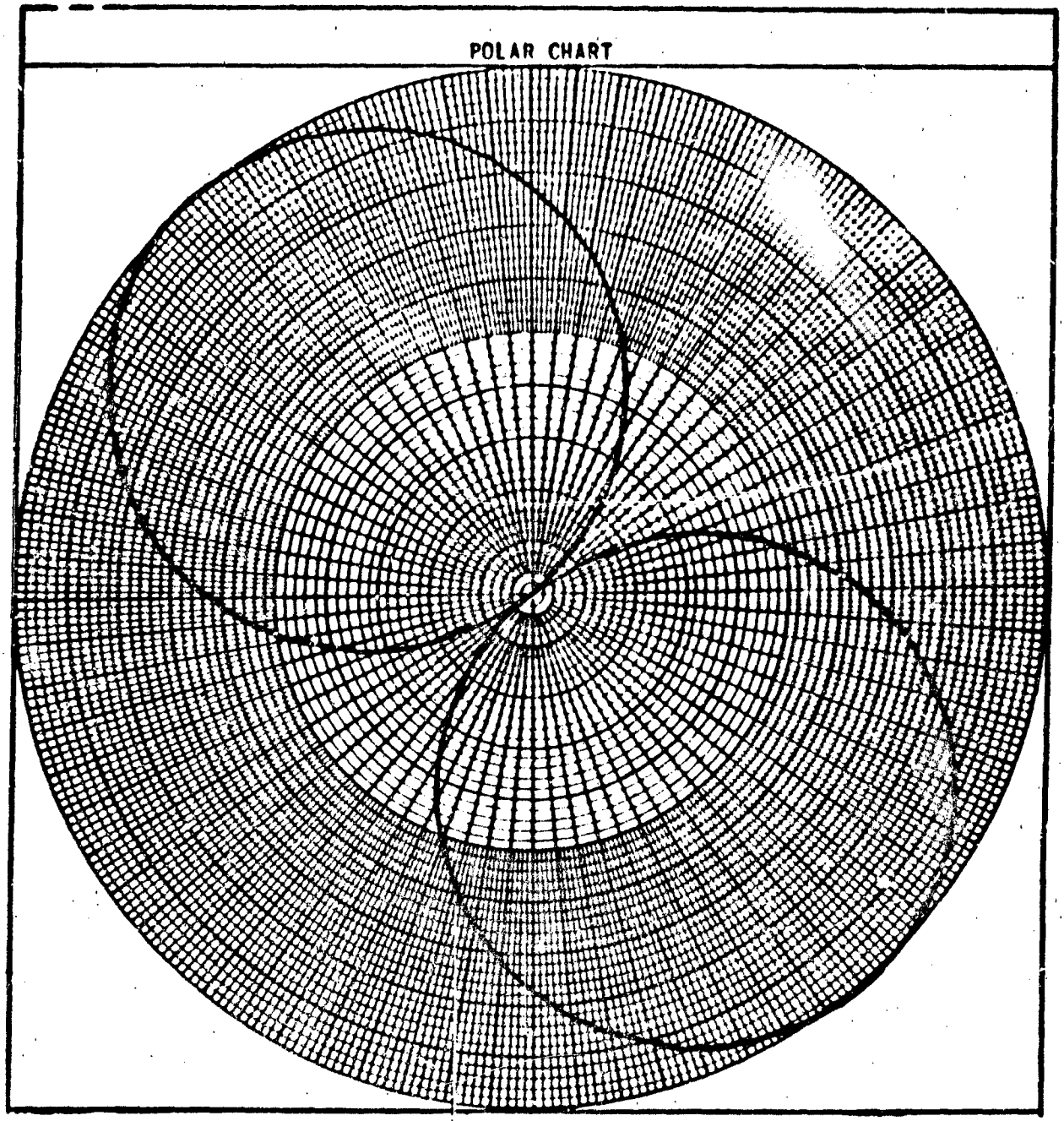

FIGURE 7. VARIABLE POLARIZATION ANTENNA: POLARIZATION PATTERN
LINEAR POLARIZATION

$\beta = -45°$

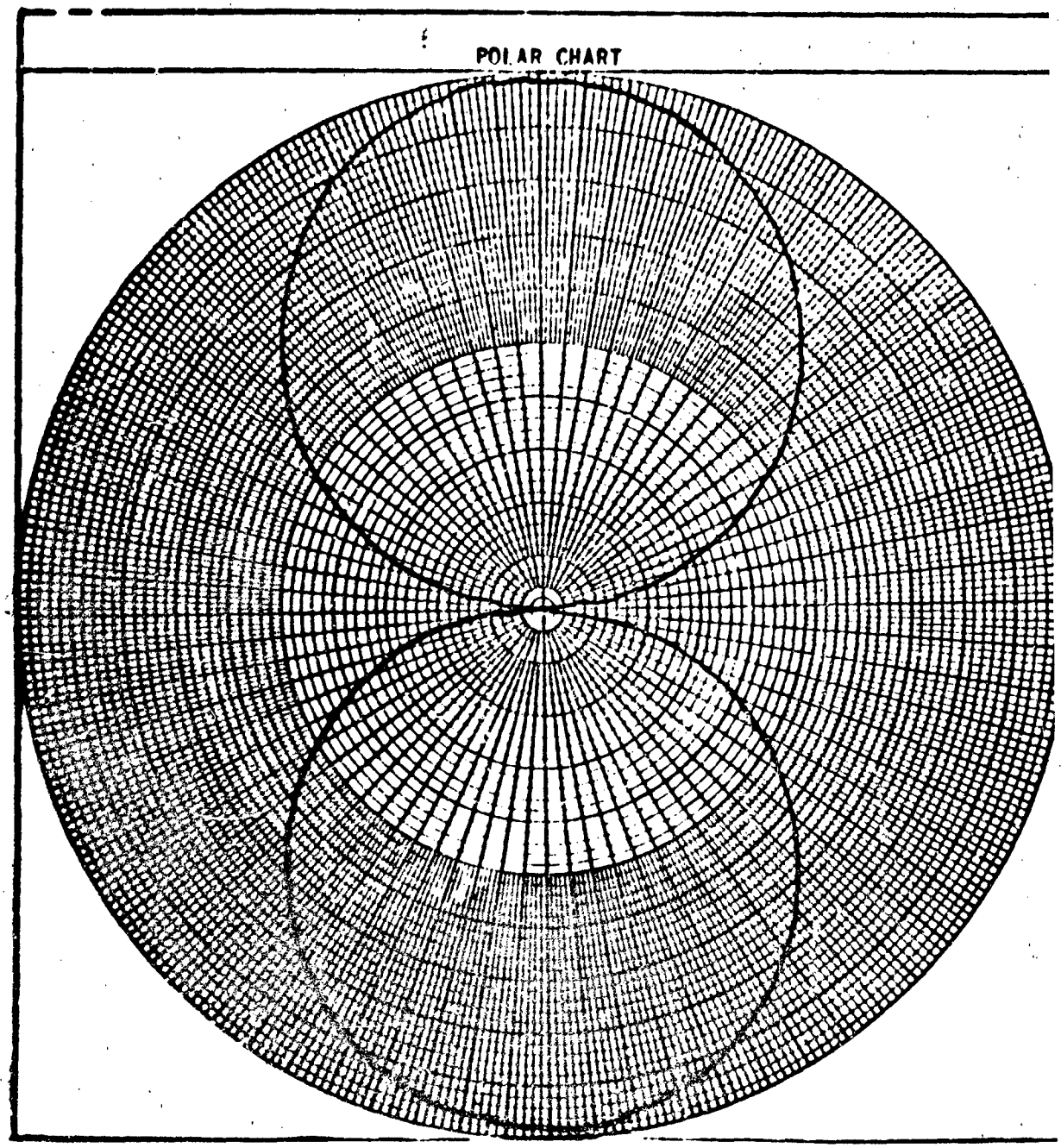

FIGURE 6. [illegible] POLARIZATION ANTENNA: POLARIZATION PATTERN
[illegible] POLARIZATION

$\theta = 0^{\circ}$

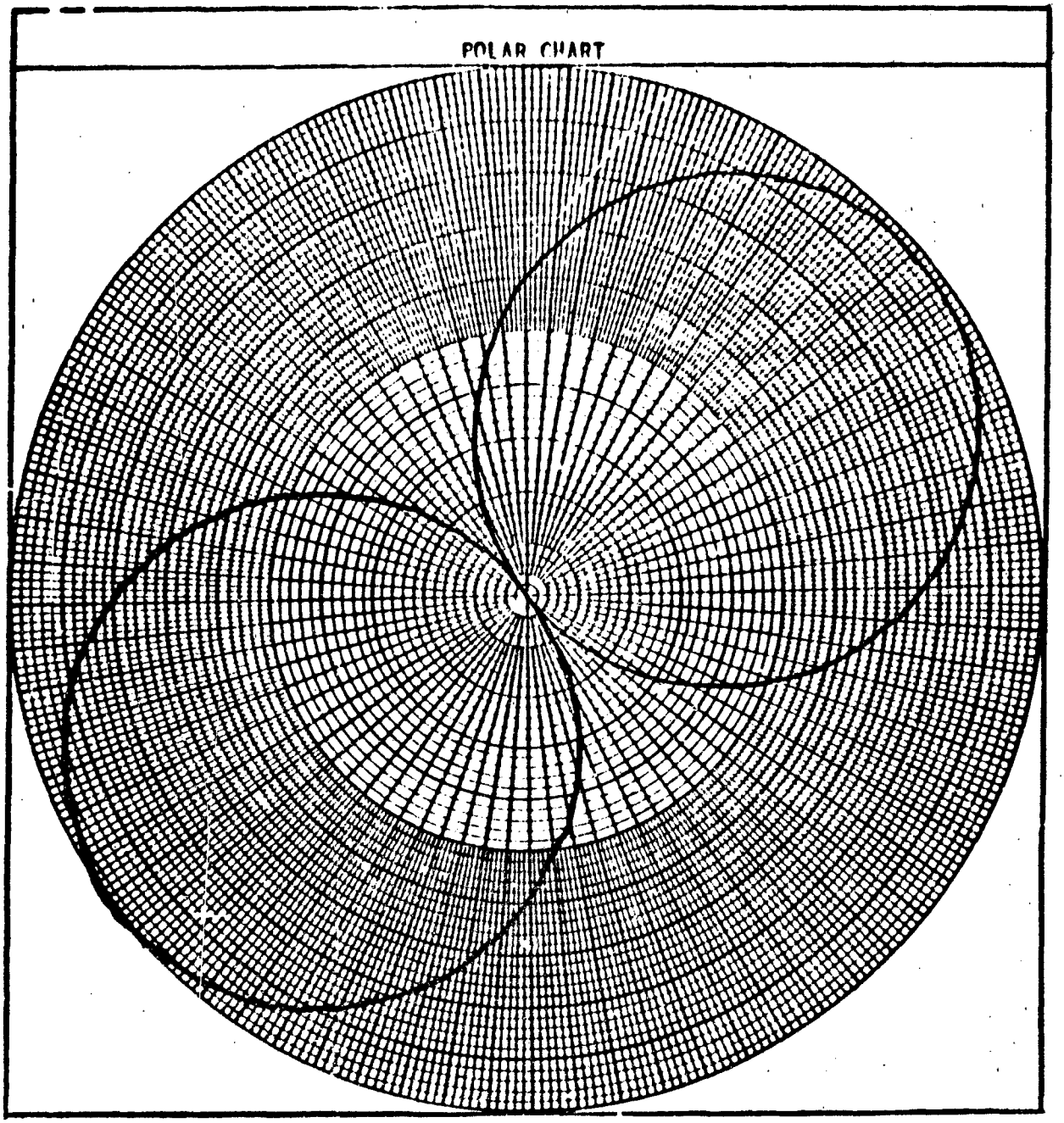

FIGURE 9. VARIABLE POLARIZATION ANTENNA: POLARIZATION PATTERN
LINEAR POLARIZATION

$\beta = +45^{\circ}$

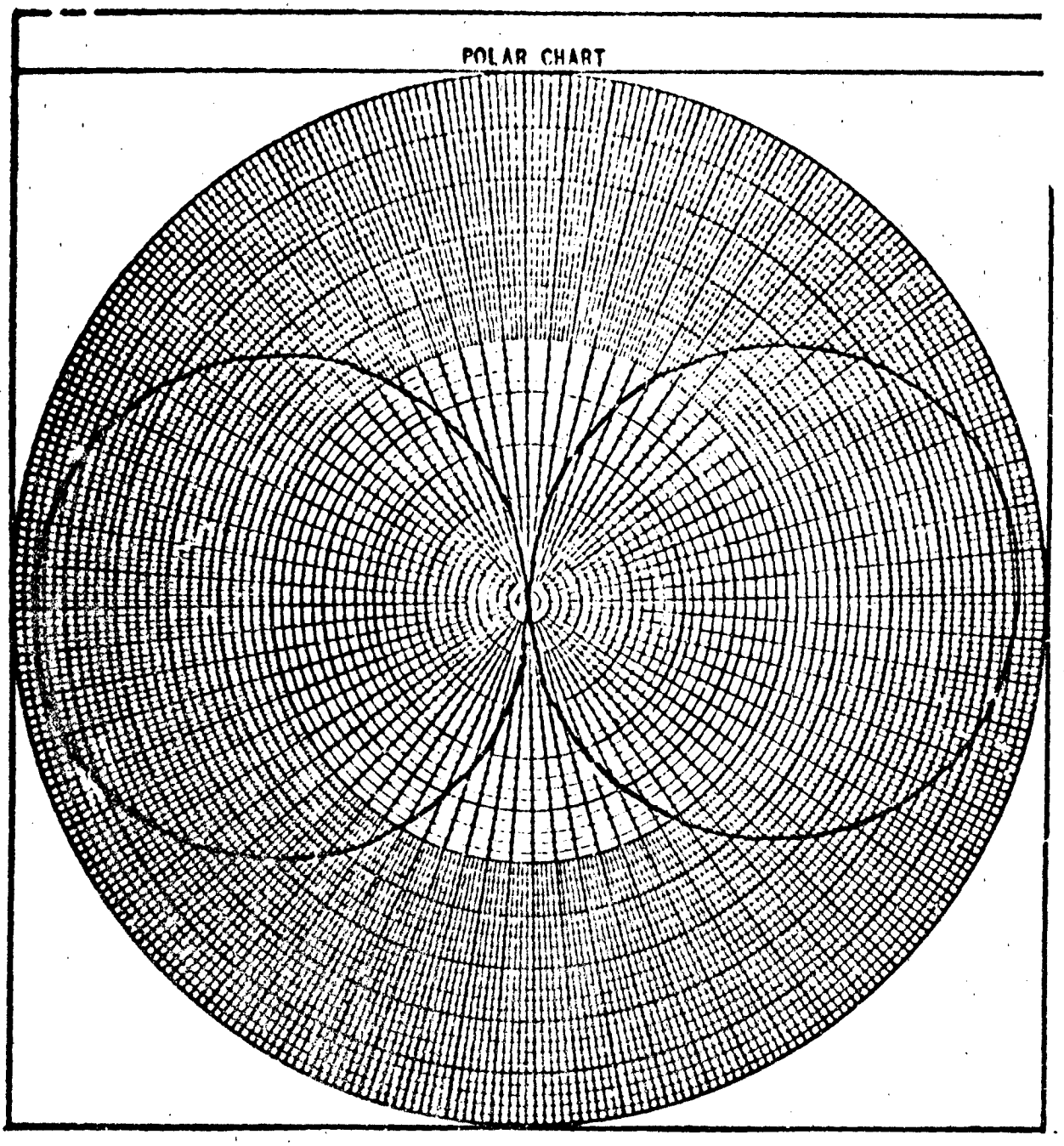

FIGURE 10. VARIABLE POLARIZATION ANTENNA: POLARIZATION PATTERN
LINEAR POLARIZATION

$\theta = +50^{\circ}$

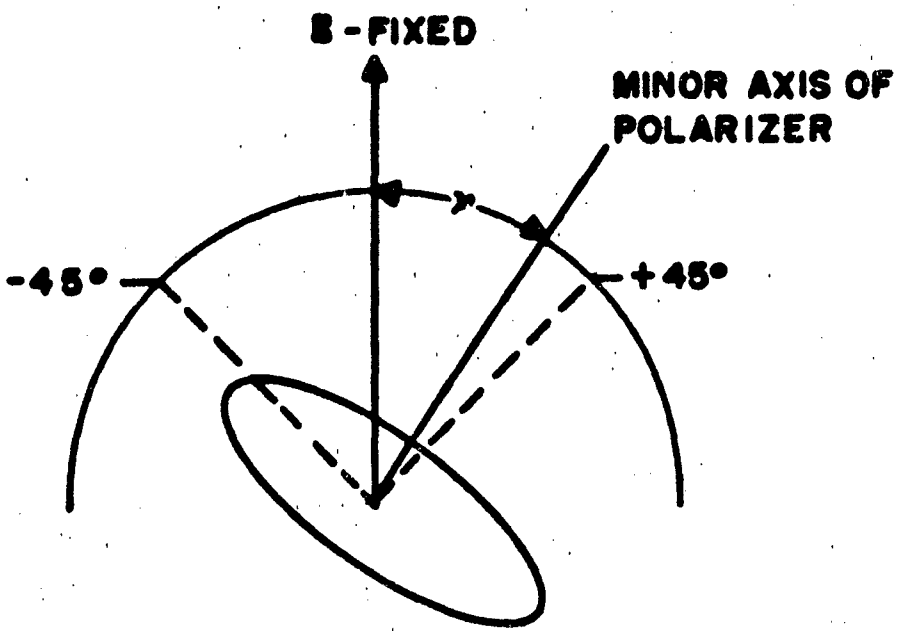

FIGURE 11. DEFINITION OF THE ANGLE γ
ELLIPTICAL POLARIZATION

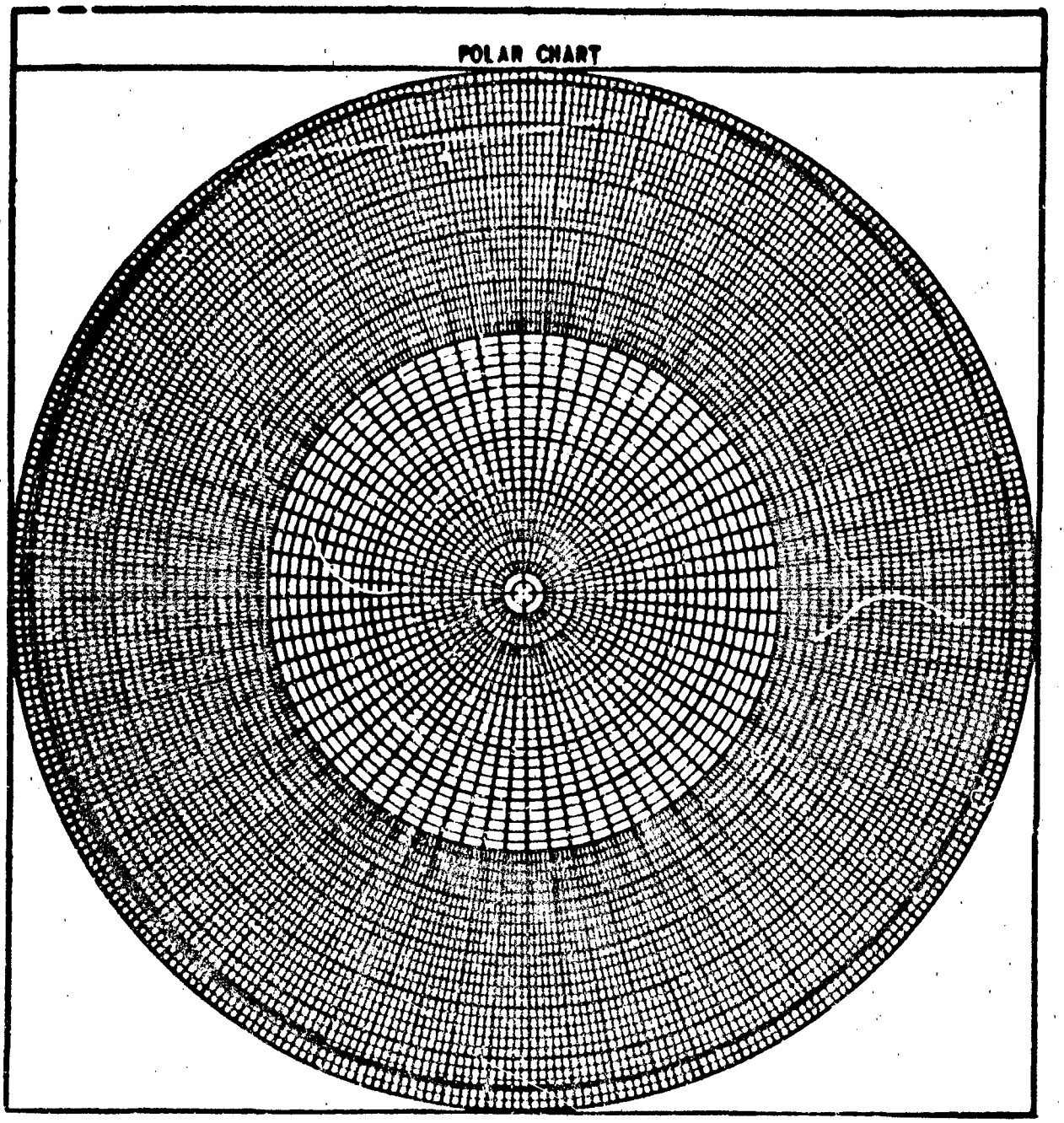

FIGURE 12. VARIABLE POLARIZATION ANTENNA: POLARIZATION PATTERN
CIRCULAR POLARIZATION

$\gamma = -45^{\circ}$

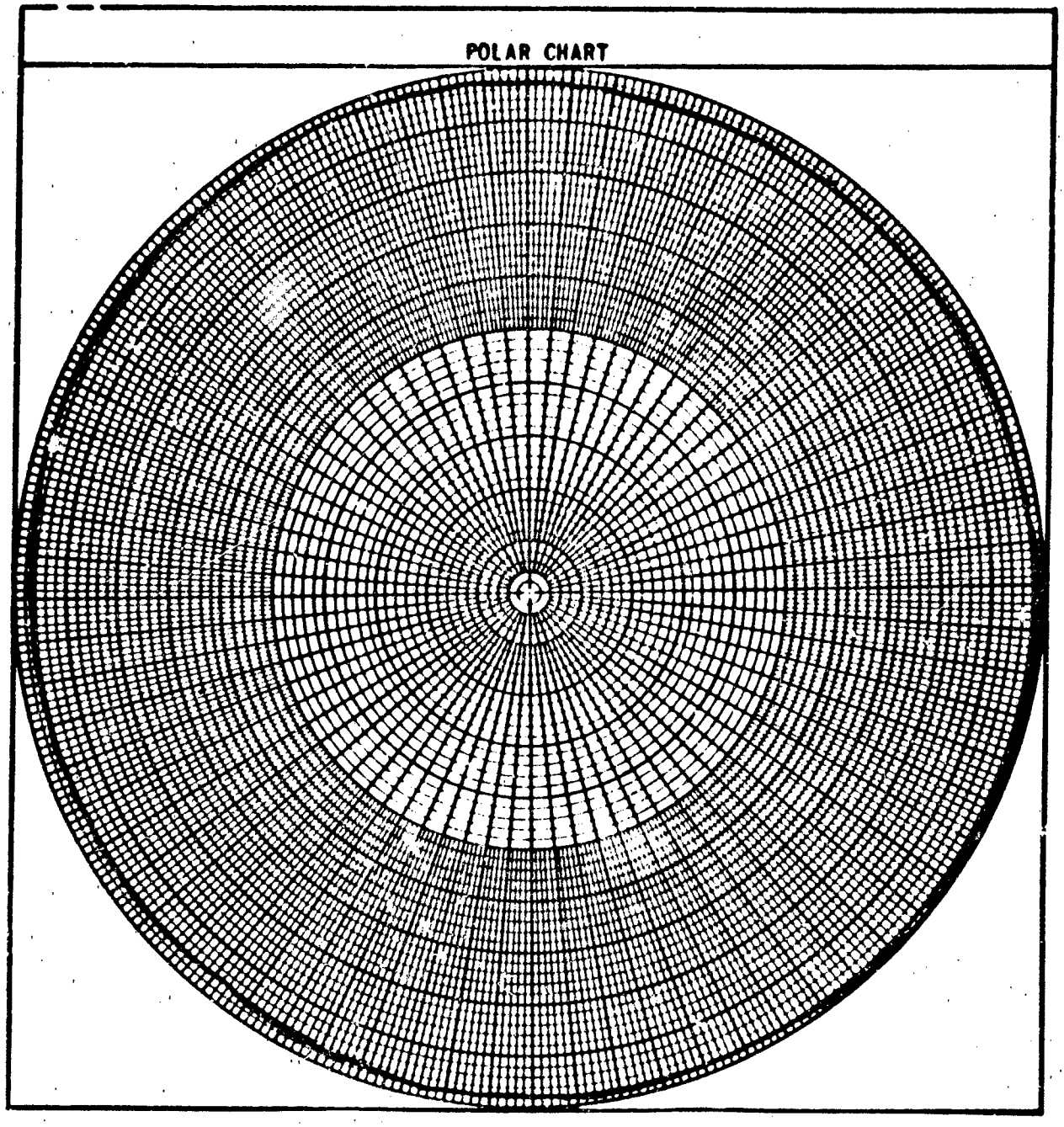

FIGURE 13. VARIABLE POLARIZATION ANTENNA: POLARIZATION PATTERN
CIRCULAR POLARIZATION

$\gamma = +45^{\circ}$

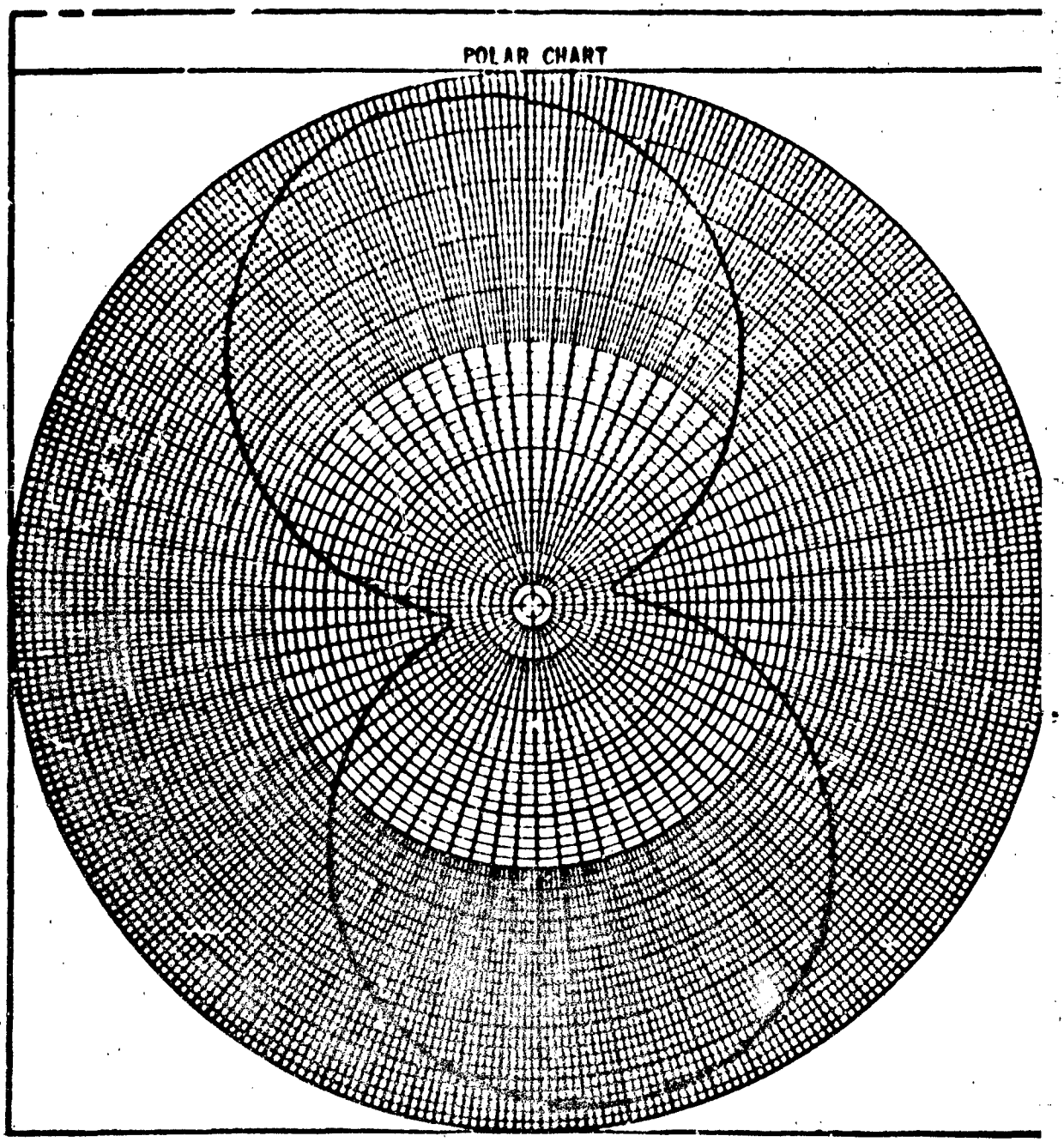

FIGURE 14. VARIABLE POLARIZATION ANTENNA: POLARIZATION PATTERN
ELLIPTICAL POLARIZATION

$\gamma = -10^{\circ}$

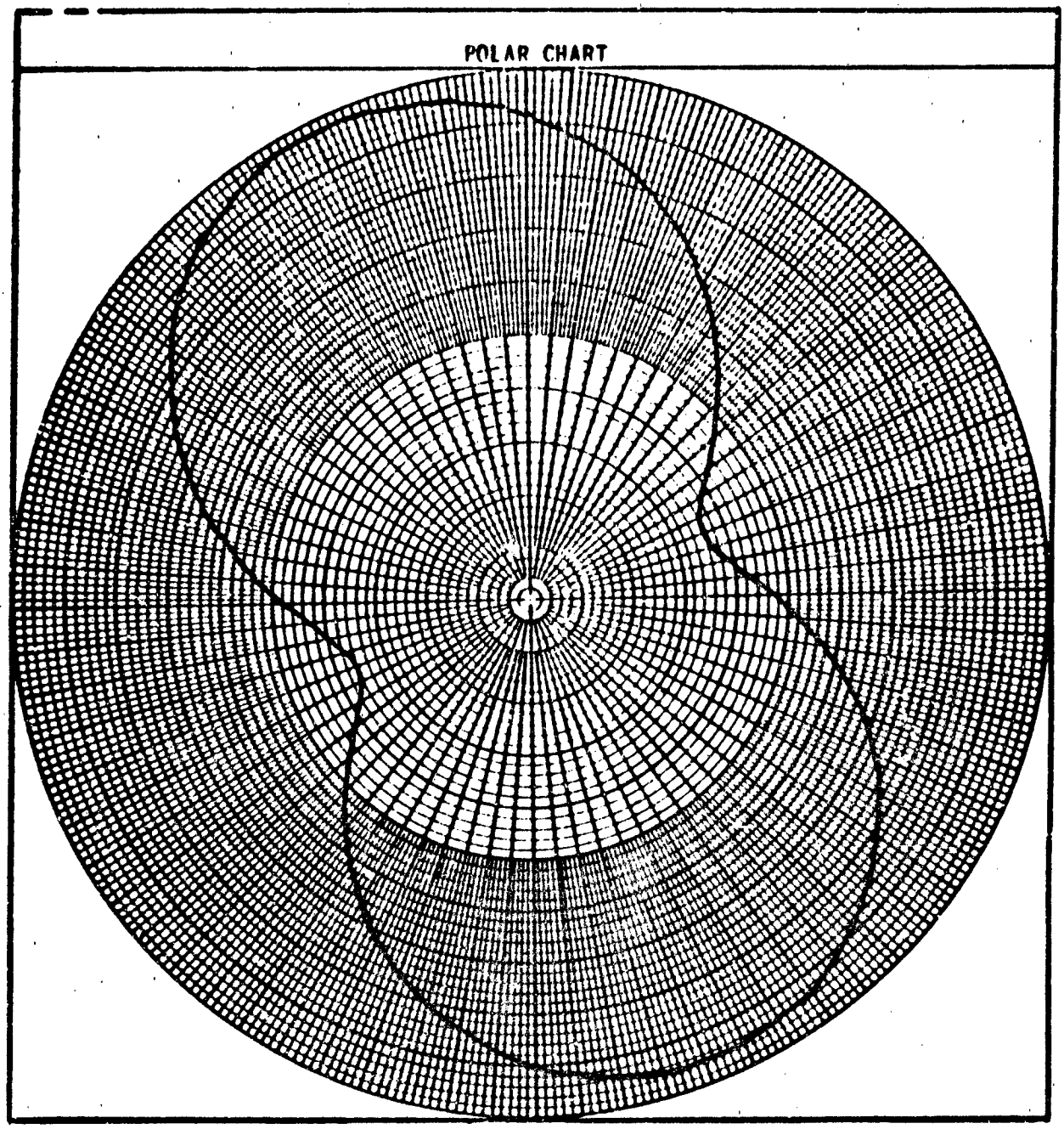

FIGURE 15. VARIABLE POLARIZATION ANTENNA: POLARIZATION PATTERN
ELLIPTICAL POLARIZATION

$\gamma = -80^{\circ}$

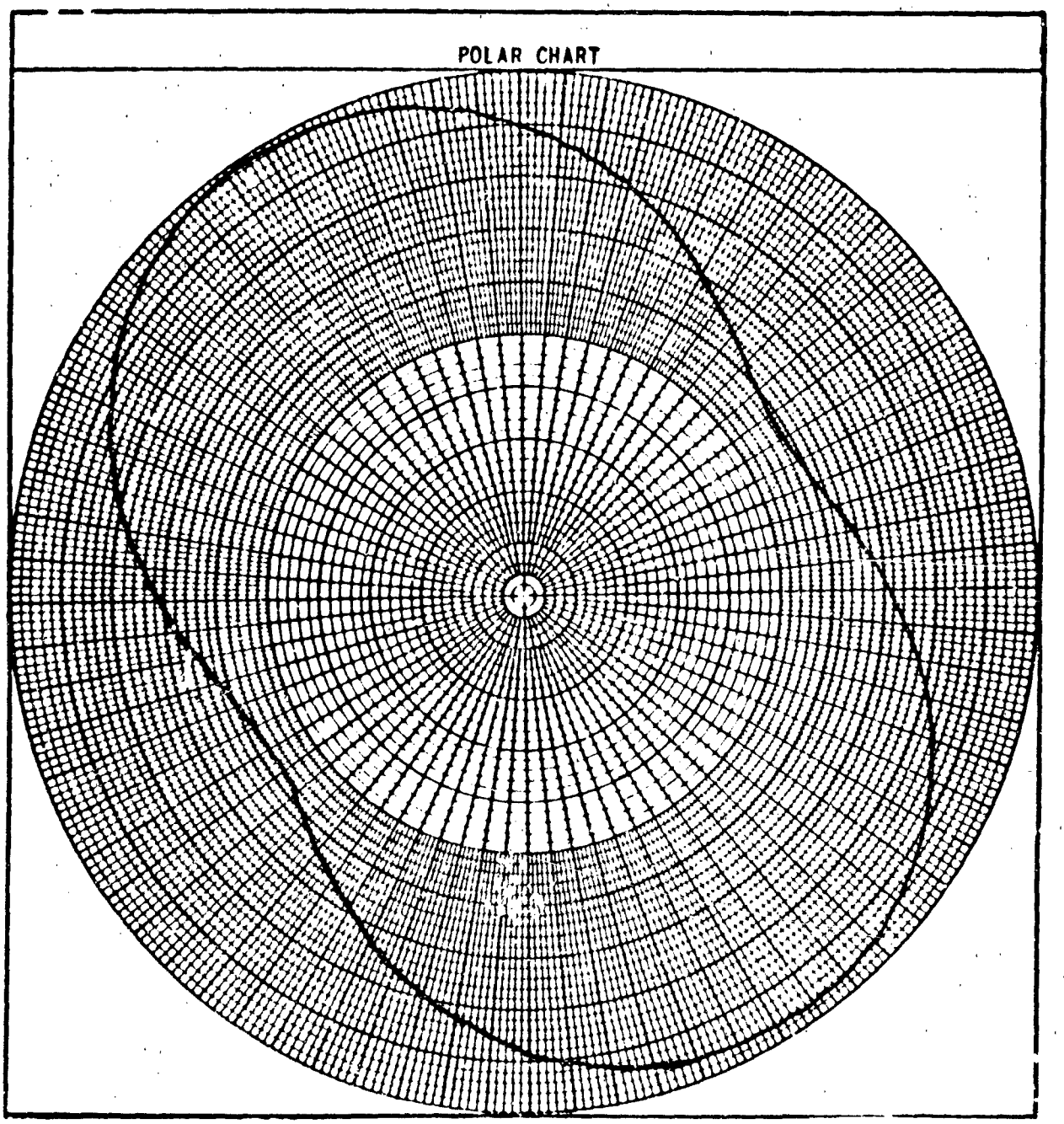

FIGURE 16. VARIABLE POLARIZATION ANTENNA: POLARIZATION PATTERN
ELLIPTICAL POLARIZATION

$\gamma = -30^{\circ}$

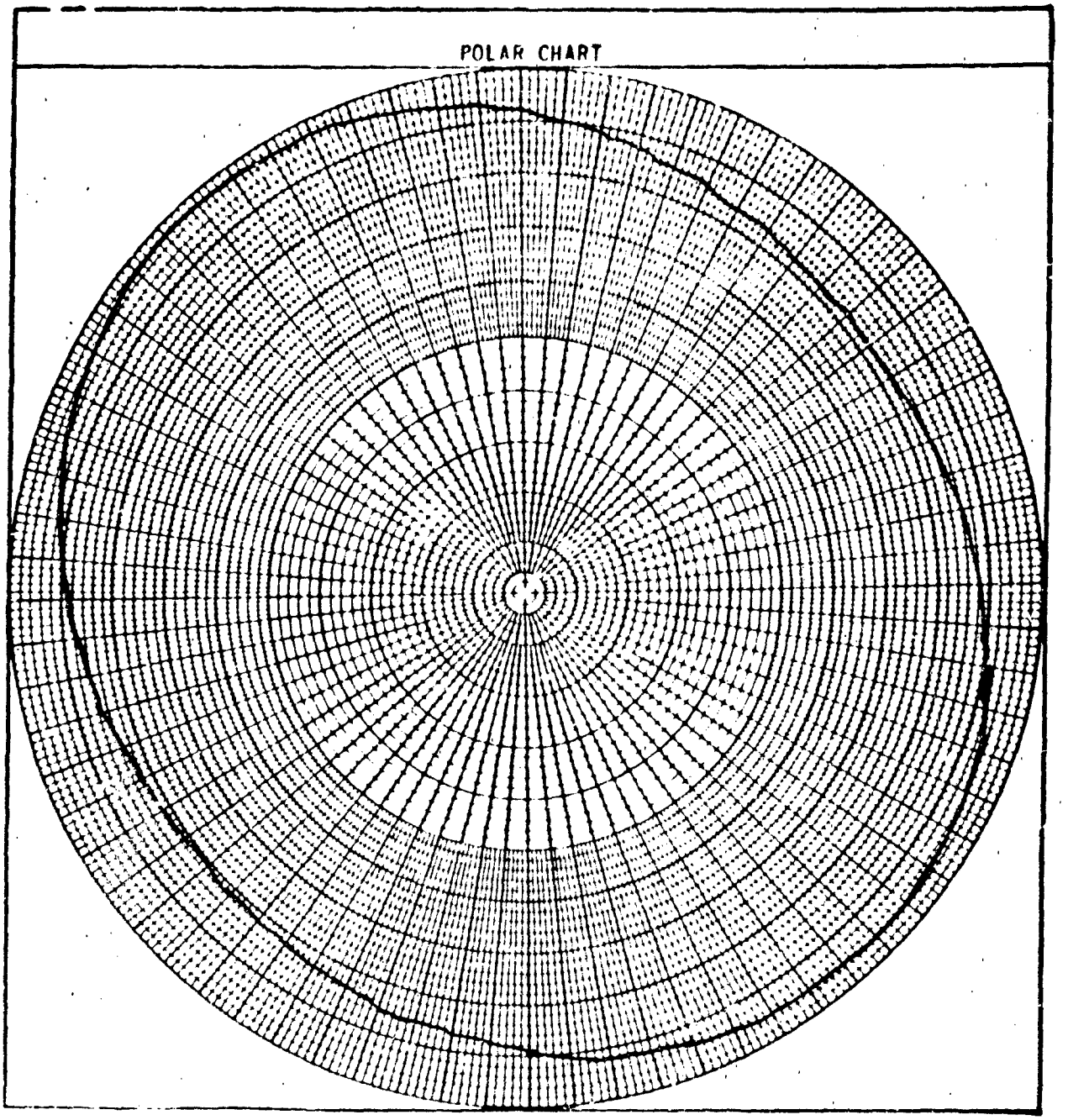

FIGURE 17. VARIABLE POLARIZATION ANTENNA: POLARIZATION PATTERN
ELLIPTICAL POLARIZATION

$\gamma = -40^{\circ}$

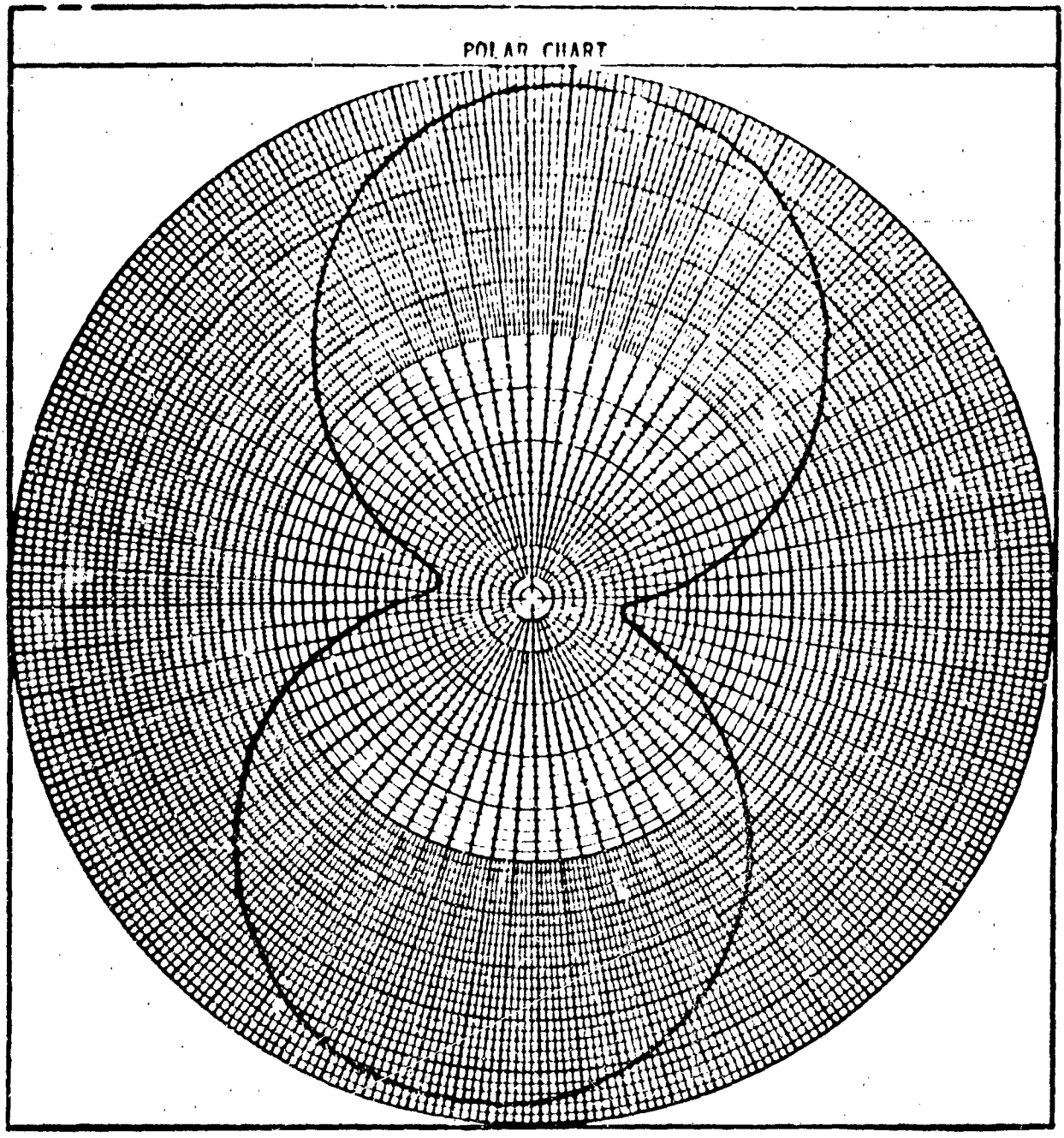

FIGURE 18. VARIABLE POLARIZATION ANTENNA: POLARIZATION PATTERN
ELLIPTICAL POLARIZATION

$\gamma = +10^{\circ}$

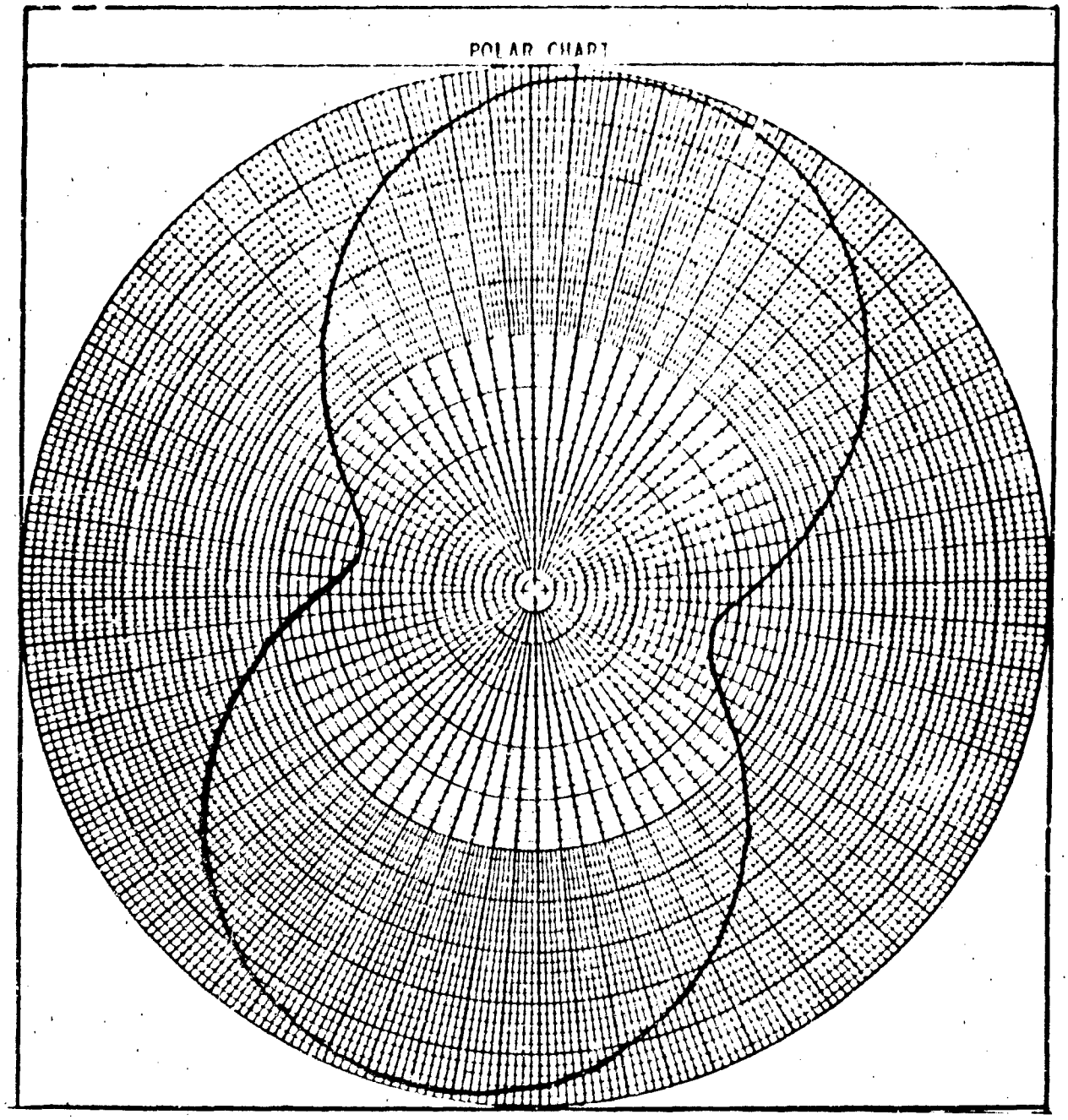

FIGURE 19. VARIABLE POLARIZATION ANTENNA: POLARIZATION PATTERN
ELLIPTICAL POLARIZATION

$\gamma = +20^{\circ}$

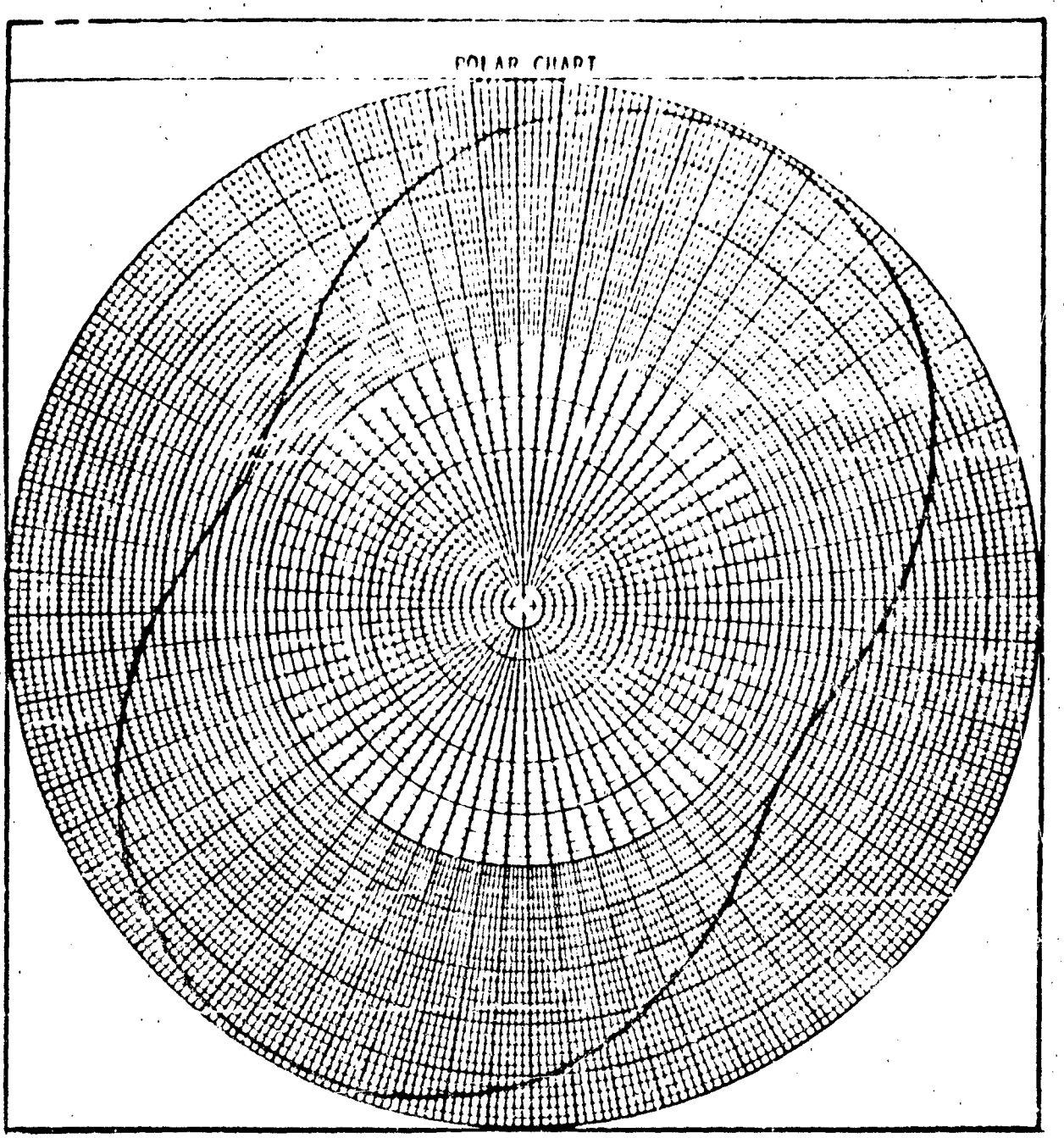

FIGURE 80. VARIABLE POLARIZATION ANTENNA: POLARIZATION PATTERN
ELLIPTICAL POLARIZATION

$\gamma = +30^{\circ}$

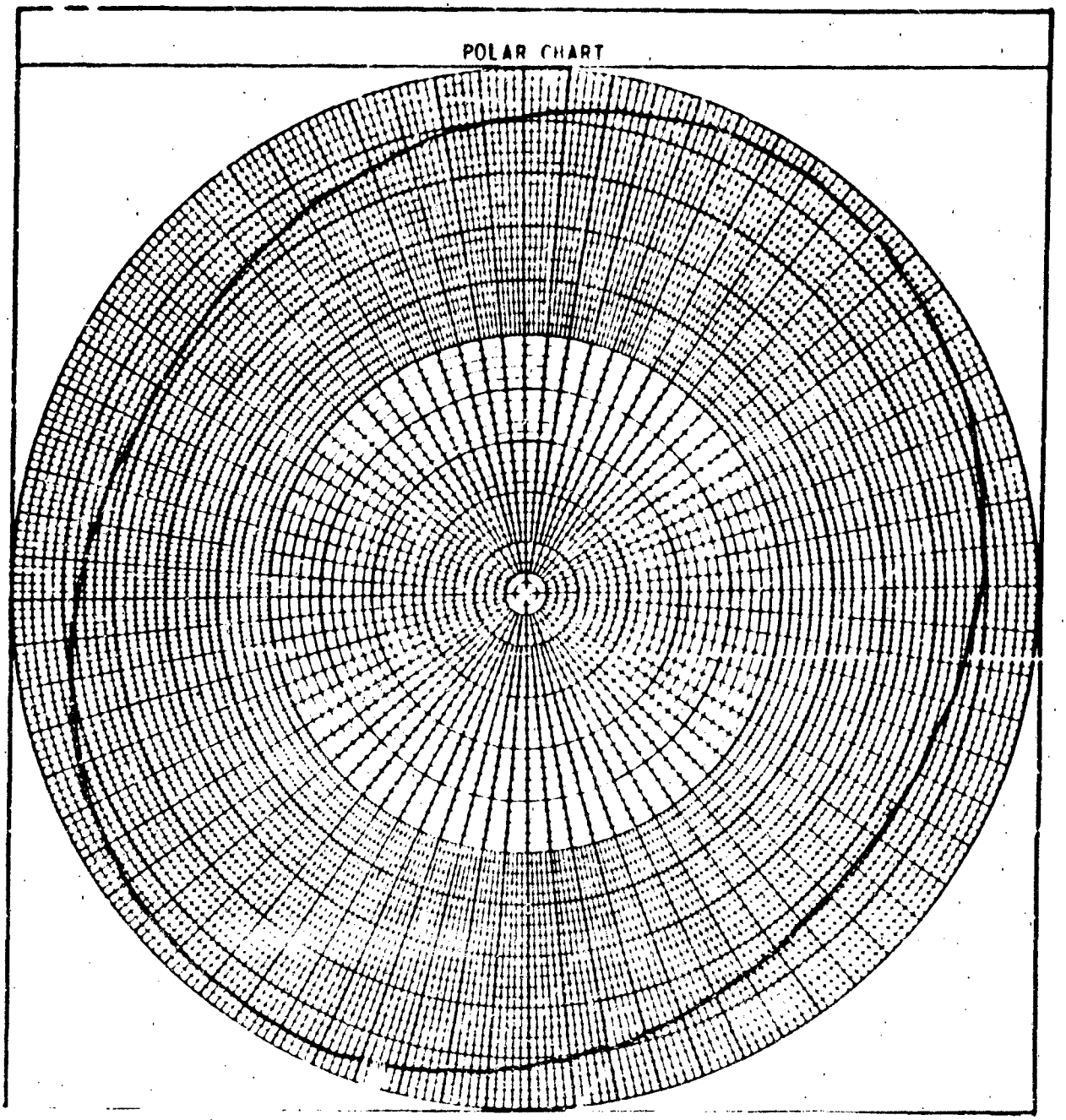

FIGURE 21. VARIABLE POLARIZATION ANTENNA: POLARIZATION PATTERN
ELLIPTICAL POLARIZATION

$\gamma = +40^{\circ}$

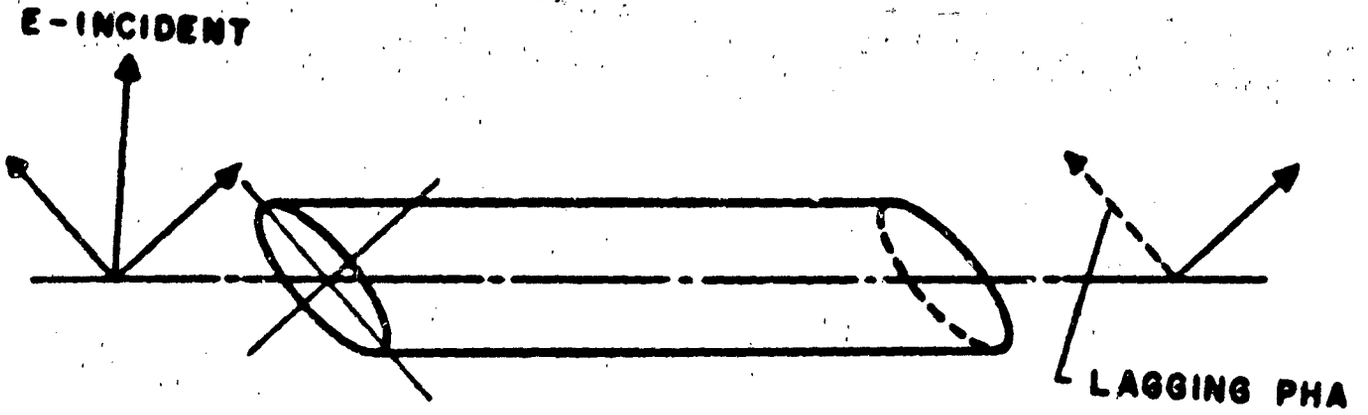

γ - POSITIVE
RIGHT HAND SENSE

DIRECTION OF PROPAGATION

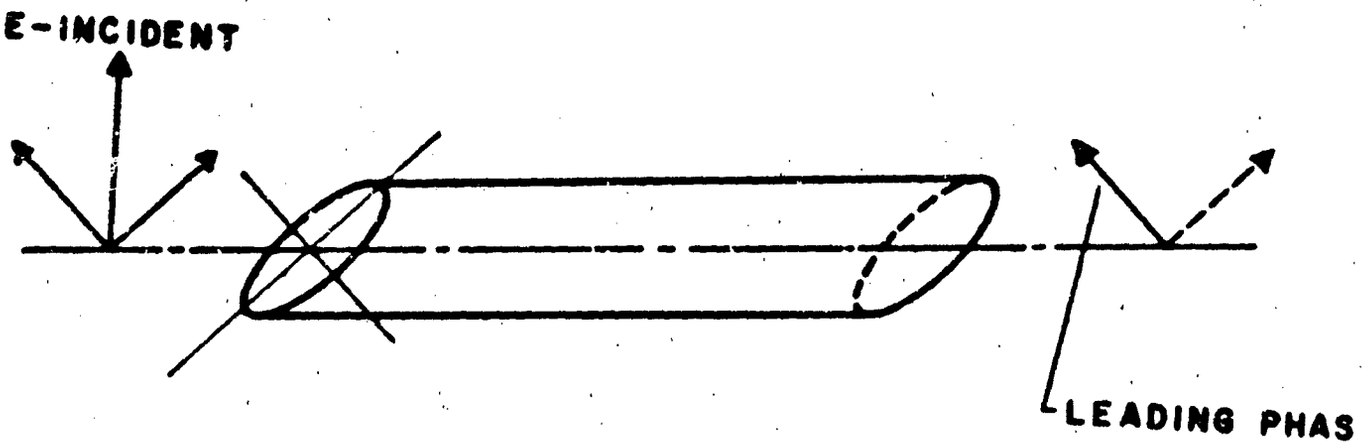

γ -NEGATIVE
LEFT HAND SENSE

FIGURE 22. [illegible]-SECTION POLARIZER
[illegible] OF POLARIZATION

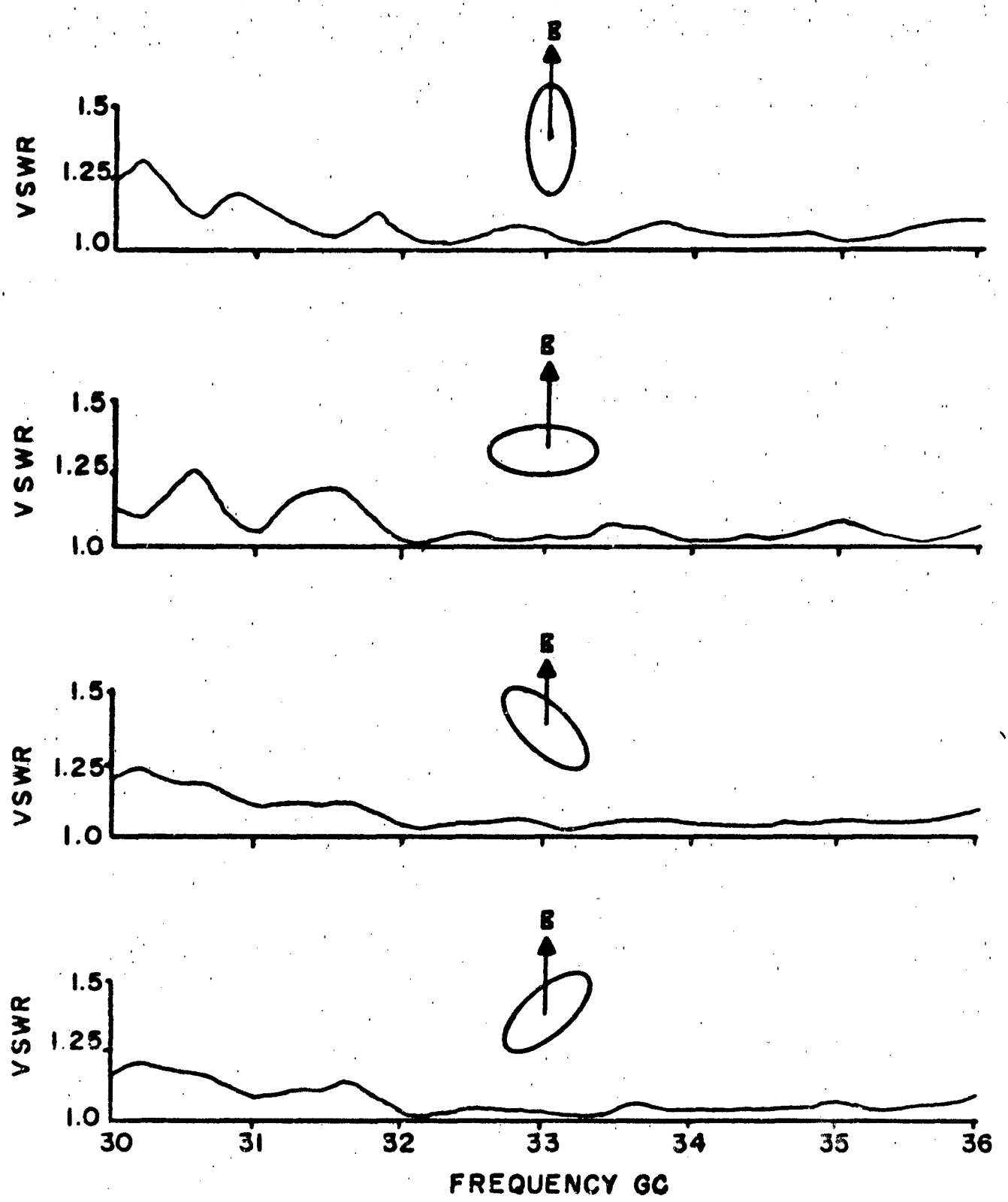

FIGURE 23. VSWR VERSUS FREQUENCY

Army-Fort Monmouth NJ-MON 4201-64

ON THE DESIGN AND EVALUATION OF HF AIRPLANE COMMUNICATIONS ANTENNAS

A. E. Lipp and D. E. Hutchinson

Boeing Airplane Division Renton, Washington

SUMMARY

This paper describes a method of determining the system power gain required by an HF airborne system to provide a prescribed communications circuit reliability. The method includes the effects of carrier power, skywave propagation loss, noise, receiver bandwidth, antenna radiation pattern and required signal-to-noise ratio. The modes of propagation considered are F-layer, E-layer, and mixed E and F layers of the ionosphere. The method can also be used to predict the reliability of existing or proposed antenna systems.

INTRODUCTION

The HF antenna systems generally used on subsonic aircraft such as the KC-135 have been well defined. However, for high performance airplanes, Figure 1, where variable geometry is employed, these systems present certain problems and in some cases become impractical. In view of these problems, a program was initiated at The Boeing Company to determine suitable methods of exciting radiating currents on both small and large variable geometry airplanes. Since a new generation of electronics would be used on these airplanes a method of predicting the system power gain and thus the carrier power required to provide a prescribed circuit reliability was sought. A number of methods have been developed for the evaluation of HF airplane antennas. 1,2,3,4,5,6* Five of the methods 1,2,3,4,5, however, tend to rate all antennas the same such that it is usually possible to select the one that is most convenient. Reference 6 presents a method whereby a factor of merit can be determined for amplitude modulation, a 200 to 3000 mile communications range, a zero db signal-to-noise ratio (SNR), and for reflections from the F-layer of ionosphere. With the event of the use of digital communications systems, requiring higher SNR, and the use of HF on fighter airplanes, where the communication ranges may be less than 1000 miles, it was felt an approach whereby the time availability of a prescribed signal-to-noise ratio could be predicted would be more applicable.

A search of the literature was made and was found that the National Bureau of Standards had an existing digital computer program capable of predicting HF skywave communications circuit reliability. This report deals primarily with the implementation of this program such that the reliability of a large number of circuits taken to be typical of those that would be encountered in practice could be calculated and thus predict the system performance of airplane HF skywave communications systems.

---

* The references are listed at the end of the report

Calculations to date show that for short path lengths, 90 to 720 nautical miles, emphasis is placed on high angles of radiation and the low end of the 2 to 30 mc frequency range. At the longer ranges 200 to 1800 nautical miles, emphasis is placed on low angles of radiation and the upper end of the HF frequency range. For the short path lengths a single antenna and 1000 watt carrier or two antennas and a 250 watt carrier will provide, in the majority of the cases, a 90 percent circuit reliability where the required signal-to-noise (SNR) is 3 db in a 3 KC bandwidth. For the longer communication ranges, 200 to 1800, calculations show that, in some instances, the power gain required to provide a 90 percent circuit reliability are impractical for airborne systems.

III SAMPLE CALCULATIONS AND RESULTS

In HF Skywave communications circuits the available signal power and noise power are subject to day-to-day variations; therefore, when the required signal-to-noise ratio (hourly median signal to average noise within the hours) equals the available signal-to-noise ratio (monthly median of the hourly median signal relative to the median noise within the time block) the circuit may be expected to have acceptable quality on half of the days within the month, or the probability of satisfactory performance on any given day will be 0.5. This probability of satisfactory signal-to-noise ratio at a given hour is defined as circuit reliability. As the available signal-to-noise ratio exceeds the required signal-to-noise, circuit reliability will increase. Figures 2 through 6 give the estimated reliability for circuits having their control point(s) (ionospheric reflection point) at various geomagnetic latitudes. These reliability contours were determined from the amplitude probability distribution of the signal and the amplitude probability distribution of the noise and were calculated by the National Bureau of Standards[7]. These curves were used to predict both the required antenna gain and the reliability for a given antenna system.

A. Required Antenna Gain

In the design of an antenna system it is necessary to know the required antenna radiation pattern coverage. For HF Skywave circuits the required antenna gain and direction of radiation is a function of ionospheric conditions and is not readily calculated. Therefore, using the curves in Figures 2 through 6 and the digital computer program on HF Skywave propagation[7] a composite program was written whereby the antenna pattern gain, Figures 7, 8, and 9, required to provide a prescribed circuit reliability for large number of postulated paths could be calculated. Each circuit was described by 13 parameters; path length, path direction, receiver location, time at receiving site, season, sunspot number, best operating frequency, noise, receiver bandwidth, carrier power, antenna radiation patterns, required signal-to-noise ratio and circuit reliability. For each path the best operating frequency, incidence angle at the ionosphere, corresponding airplane elevation and azimuth angle, and available median signal-to-noise ratio (SNR) were calculated. The required available SNR, at

the frequency corresponding to the best operating frequency, was then determined, for a prescribed circuit reliability, from Figures 2 through 6. The required SNR, in a one cycle per second band, is the SNR required by the receiver to perform properly. For example in voice communication a 38 db SNR in a one cycle per second band, depending on the vocabulary used, will result in an 82 percent word intelligibility. The required antenna gain, relative to a prescribed carrier power and an isotropic radiator, is the difference between the required available SNR and the corresponding calculated available SNR. After each calculation the required gain was compared to -1000 db and the maximum and average values grouped according to airplane elevation angle (θ) and frequency. The airplane elevation angle θ was measured from the zenith while the airplane azimuth angle (ϕ) was measured counterclockwise from the airplane nose.

The required antenna gain, Figures 7, 8, and 9, was calculated for two cases; one for short ranges where the control points are below 60 degrees geomagnetic latitude, temperate zone, and one for long range communications where the control points are both in the temperate and in the auroral zone, above 60 degrees geomagnetic latitude. Table one gives the positions of the transmitter, the receiver location being the variable, and the parameters defining each circuit.

Both man-made and atmospheric noise were considered.[7,8] Figure 10 shows the median level of typical man-made noise, and for two atmospheric noise grades. The atmospheric noise levels are shown for comparison purposes only. The man-made noise in the case of the short ranges, which were taken to be typical of a fighter airplane, was taken to be that typical of a rural area, while in the case of the longer ranges, which were taken to be typical of a commercial overseas airliner, the man-made noise was taken to be that of a typical remote area. In both cases the computer selected which ever was greater, man-made or atmospheric noise, and used this value in calculating available signal-to-noise ratio. The reason for selecting different man-made noise levels, was that in the tactical case the receiving antenna may not be located remotely from the transmitter or be placed in a remote area. This would be especially true in the case of aircraft carriers and mobile ground units. Since the noise was considered to be equal in all directions and the receiver to be external noise limited, the receiving antenna gain was taken to be zero.

The distribution of the required antenna gain shows that for the short ranges 90 to 720 nautical miles importance is placed on high angles of radiation, small airplane elevation angles, and low frequencies; while for the longer communications ranges importance is placed on low angles of radiation, high airplane elevation angles, and high frequencies. In the case of small airplanes, were the airframe members are small in terms of radio wavelengths, this is a disadvantage in that it may be

difficult to obtain a reasonable power transfer efficiency. This is somewhat offset in that the gain at the low frequencies, 2 to 4 mc, is lower than that required in the remaining portion of the band. For operation in the temperate zone the required gain values are reasonable for airborne systems. However, for circuits that have their control points in the auroral zones the maximum gains become high and are not practical for airborne systems. However, it is felt that the maximum gains are required for a small number of paths and that a lower gain may not greatly degrade the overall system performance. This will be examined in the next section.

Since reliability is a function of the difference between the available and required one cycle band SNR the distributions shown in Figures 7 through 9 can be used to determine the carrier power or maximum antenna gain for other required SNR. The one cycle band SNR can be converted to other bandwidths. For example a 38 db one cycle band SNR is equivalent to a 3 db SNR in a 3 KC bandwidth. Thus for a carrier power of 200 watts one has the maximum antenna gain for a one cycle band SNR of 38 db.

Figures 11 through 16 show the directive pattern gains of a notch fed vertical stabilizer and shunt fed wing strakes on a typical variable wing fighter airplane. The gains are for the wings in the swept position and a power transfer efficiency of 100 percent. The shunts, placed in each wing strake, were fed such that symmetric modes of currents were excited on the wings. Comparison of the required antenna gain and the gain values in Figures 11 through 16 shows that the notch antenna will provide the better radiation pattern coverage and that a carrier power of 1200 watts is required to provide a reliability of 90 percent for a one cycle band SNR of 38 db.

B. Antenna System Evaluation

To predict the performance of a given antenna system the reliability was calculated for a large number of postulated communications circuits. For each circuit the best operating frequency, incident angle at the ionosphere and available one cycle band signal-to-noise ratio was calculated for isotropic radiators and a prescribed carrier power. The antenna gain at the corresponding frequency, airplane elevation and azimuth angle was selected from a table of antenna gains and was added to the calculated available SNR. The greater of the direct wave or the ground reflected wave (a - 3 db ground loss was assumed) was used as the antenna gain value. The reliability was then determined from Figures 2 through 6 and the required one cycle band SNR. Figures 17 and 18 show the circuit reliability distribution for a 100 to 700 nautical communications range, a 100 watt carrier power, two airplane headings, a required one cycle band SNR of 38 db and the notch fed stabilizer radiation patterns shown in Figures 11, 12, and 13. The airplane headings were north and west respectively. The distributions show that the number of circuits, for each heading, having a reliability of 90 percent, are approximately equal. Examination of the required antenna gain data prior to being sorted into angle-frequency groups

showed that, for short length circuits having their ionospheric reflection points below 60 degrees geomagnetic latitude, the gain in most of the circuits varied only slightly with direction. For long range circuits where the reflections can fall both in the temperate zone and auroral zone the gain as a function of direction varied as much as 15 db, and as a result of radiation pattern nulls the reliability for some headings would be reduced and at least four airplane headings should be used. Figure 19 shows the circuit distribution for a 1200 watt carrier power, a north airplane heading and the notch antenna. Figure 20 shows the circuit reliability for a 200 watt carrier and an antenna gain pattern consisting of the maximum values of the gain for the notch and shunt fed wing strakes. The distribution indicates that by using two antenna systems and a switching arrangement the transmitter carrier power required to provide a given reliability could be approximately 6 db lower than for a single antenna.

It is felt that this would be more applicable to large airplanes where weight and space is not as critical. For airplanes where communications is predominately off the nose and tail the antenna locations and design could be such that a moderate, 4 db, forward and aft gain could be maintained. This would be especially applicable to long and short auroral circuits where high power gains are required.

It was previously mentioned that the overall system performance, as a result of the high required maximum gains (Figures 7 and 8), may not be greatly degraded. To illustrate this the circuit reliability distribution Figure 21 was calculated for an airplane antenna having a zero db gain, required one cycle band SNR of 35 db, and a carrier power of 250 watts. The distribution shows that 82 percent of the circuits have a calculated reliability of 90 percent or greater, 97 percent have a reliability 75 percent or greater, 98 percent have a reliability of 50 percent and that only 2 percent have a reliability less than 50 percent. Table 2 gives the condition for which the distributions were calculated. The distributions shown in Figures 17, 18, 19, 20, and 21 hold for other required SNR's if the transmitter power is increased or decreased accordingly. In each case equal importance was given to all azimuth angles. However, pattern weighting in the azimuth plane can be accomplished by making calculations only at the airplane angles desired. For example one may desire only to include the azimuth angles plus and minus 60 degrees from the nose and tail of the airplane.

CONCLUSIONS

A method of predicting the communications circuit reliability of airborne HF systems has been outlined. The method takes into account antenna patterns, carrier power and required signal-to-noise ratio. There are some areas open to discussion. The level of man-made noise in the case of the short ranges may be too high and in the case of the long ranges may be too low. It was assumed the man-made noise at the airplane is less than that of the ground site such that air-to-air circuit reliability would be equal to or greater than the air-to-ground reliability. This infers that the airplane is designed such that the man-made noise is less than that of the ground sites. In either case the man-made noise is less than that of the ground sites. In either case the man-made noise should be minimized and the level determined prior to circuit reliability predictions. The method shows that air-to-ground communications carrier power required for relatively long aurora circuits are prohibitive for airborne use and that the required antenna gain distribution would be more useful if the maximum, 90 percentile and, 70 percentile level of the gain were determined. It is anticipated that the program will be up-dated to include the above values and to determine the actual ground losses associated with the antenna gain used in the calculations.

ACKNOWLEDGMENT

The concept of using a large number of postulated circuits to obtain a reasonable sample of what would take place in practice was introduced by Mr. J. F. Cline. The digital program on HF Skywave predictions was purchased from the National Bureau of Standards and its operation explained by Mr. D. L. Lucas. The composite program on required antenna gain and circuit reliability distribution was written by Mr. G. S. Tsiang of The Boeing Company.

REFERENCES

1. J. V. N. Granger, "Systems Considerations in Aircraft Antenna Design", IRE Trans., PGAE-1, PP. 1 - 12, December 1951.

2. E. J. Moore, "Factor of Merit for Aircraft Antenna Systems for the Frequency Range from 3 to 30 MC", IRE Trans., PGAP-3, PP. 67 - 74, August 1952.

3. E. J. Moore, "Performance Specifications and Evaluation of Liaison Antennas", Final Report, Task III, SRI Project 606, Contract AF33(616)-82, SRI, Menlo Park, California, November 1953.

4. E. J. Moore, "Performance Evaluation of HF Aircraft Antenna Systems" IRE Trans., PGAP-6, PP. 254-260 July 1958.

5. W. S. Lucke, "Antenna Evaluation Methods", IRE Trans., PGAP-6, PP. 251 - 254, July 1958.

6. J. F. Cline, "A New Approach to the Evaluation of HF Aircraft Antennas", Technical Report 72, Contract AF 19(604)-3458, SRI, Menlo Park, California, March 1961.

7. G. W. Haydon, D. L. Lucas, and R. A. Hanson, "Technical Considerations in the Selection of Optimum Frequencies for High Frequency Sky-Wave Communication Services", NBS Report 7249, Project 8530-12-85431, National Bureau of Standards, Boulder, Colorado, November 1962.

8. Report on Revision of Atmospheric Noise Data, "CCIR Study Group VI Report", National Bureau of Standards, Boulder Colorado, July 1956.

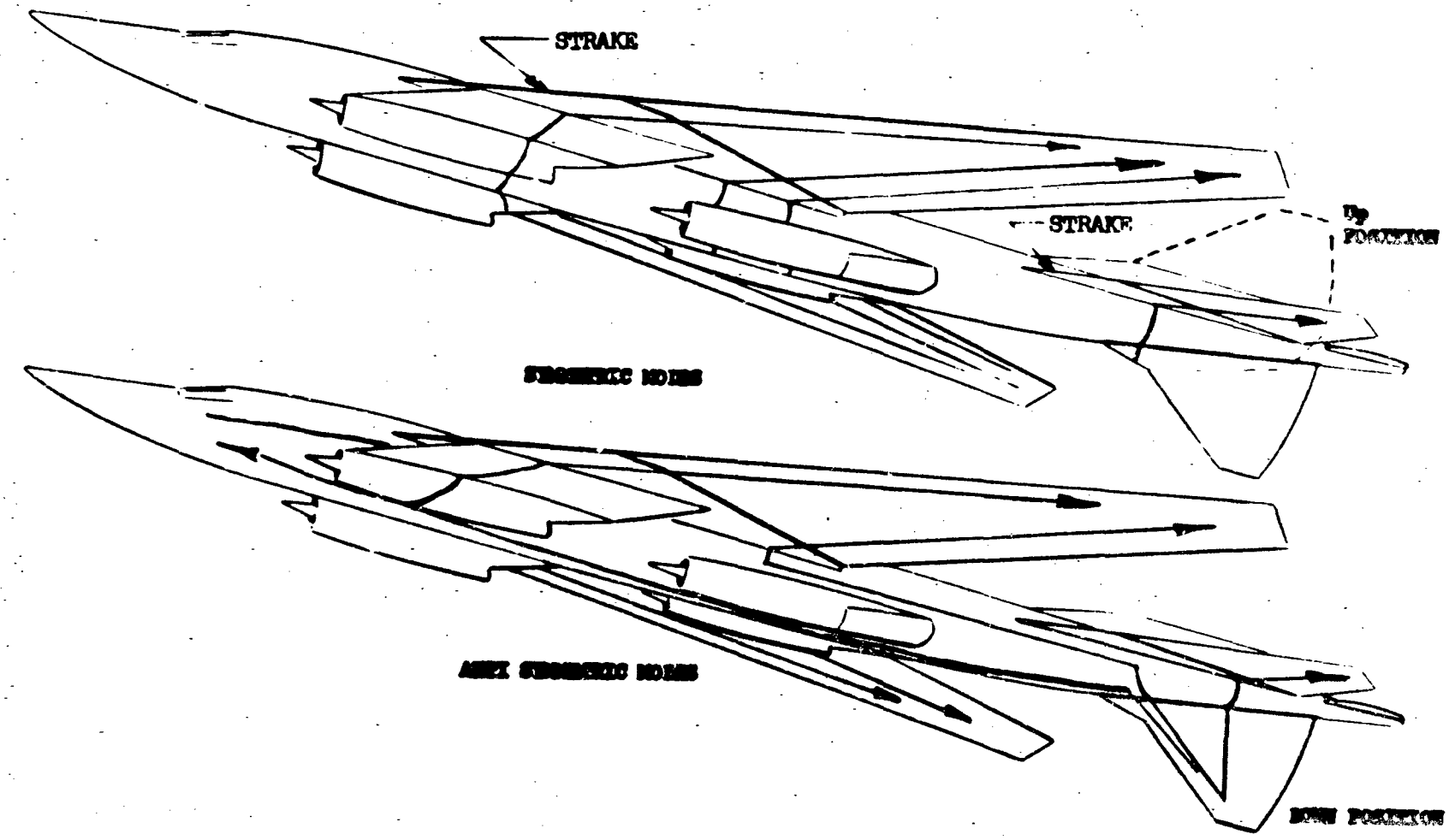

CURRENT MODES ON A TYPICAL VARIABLE GEOMETRY AIRPLANE

FIGURE 1

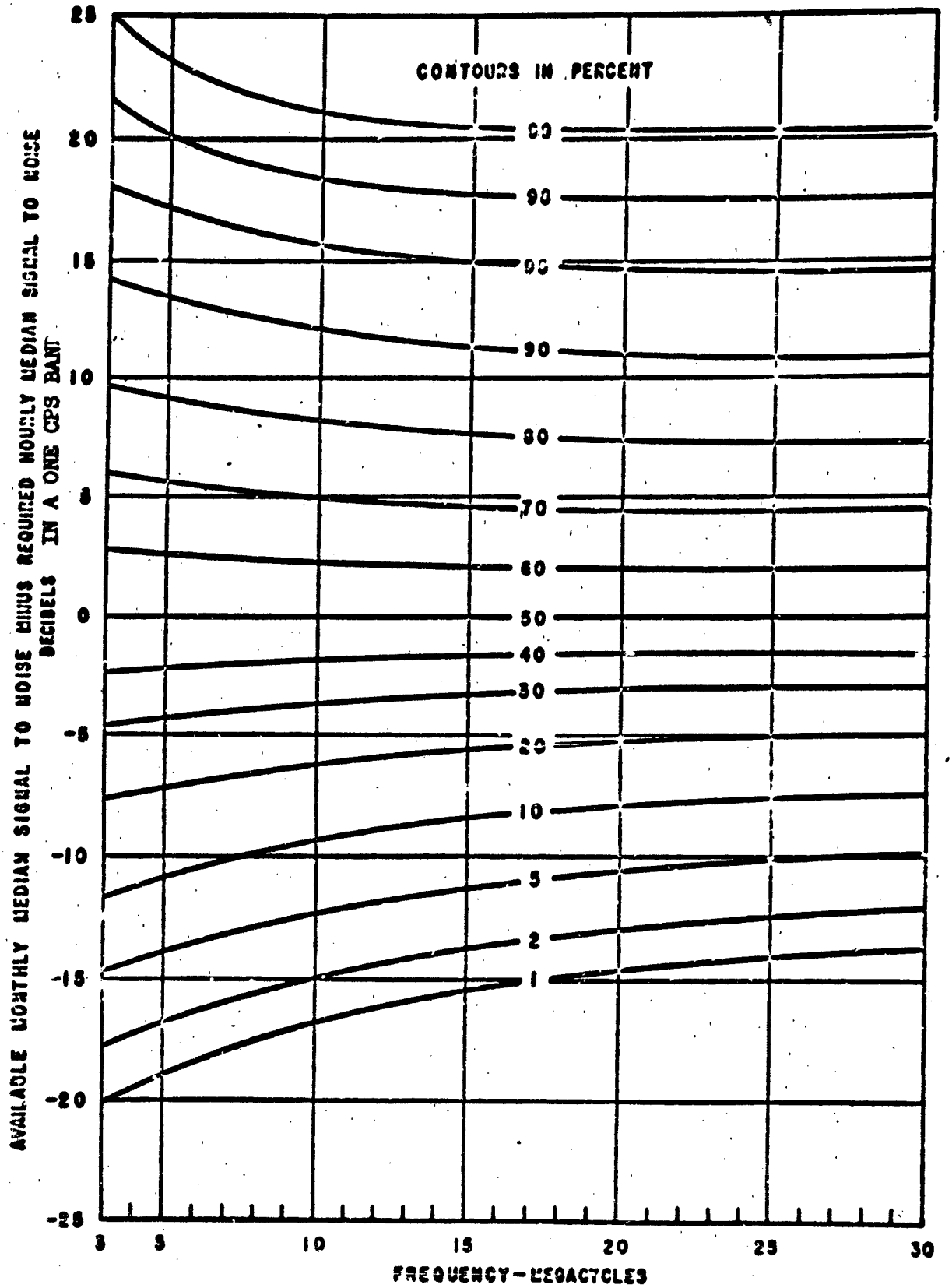

Chart to Estimate Nighttime Reliability of Sky-Wave Circuits Below 60° Geomagnetic Latitude

FIGURE 2

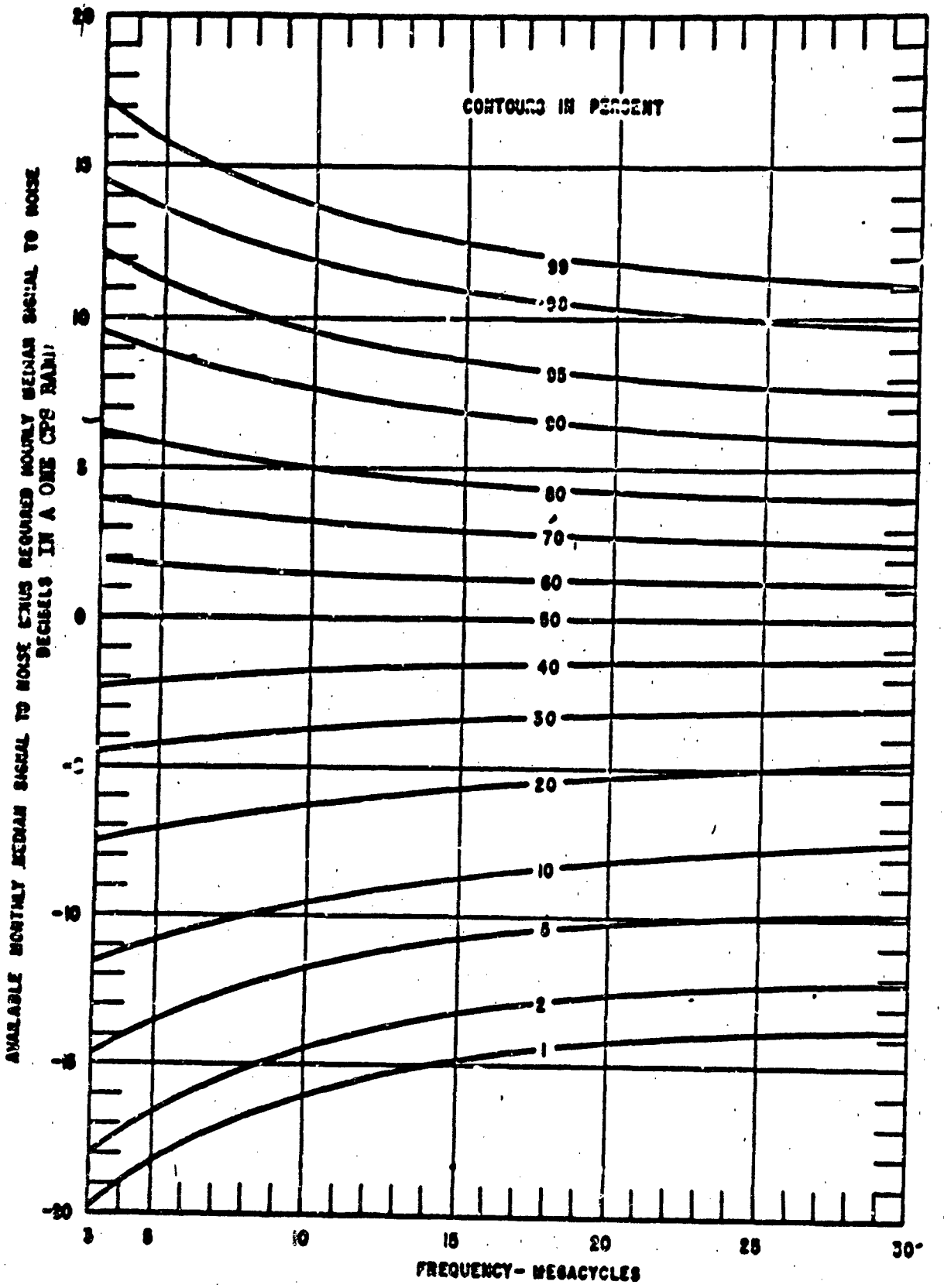

Chart to Estimate Daytime Reliability of Sky-Wave Circuits Below 60° Geomagnetic Latitude

FIGURE 3

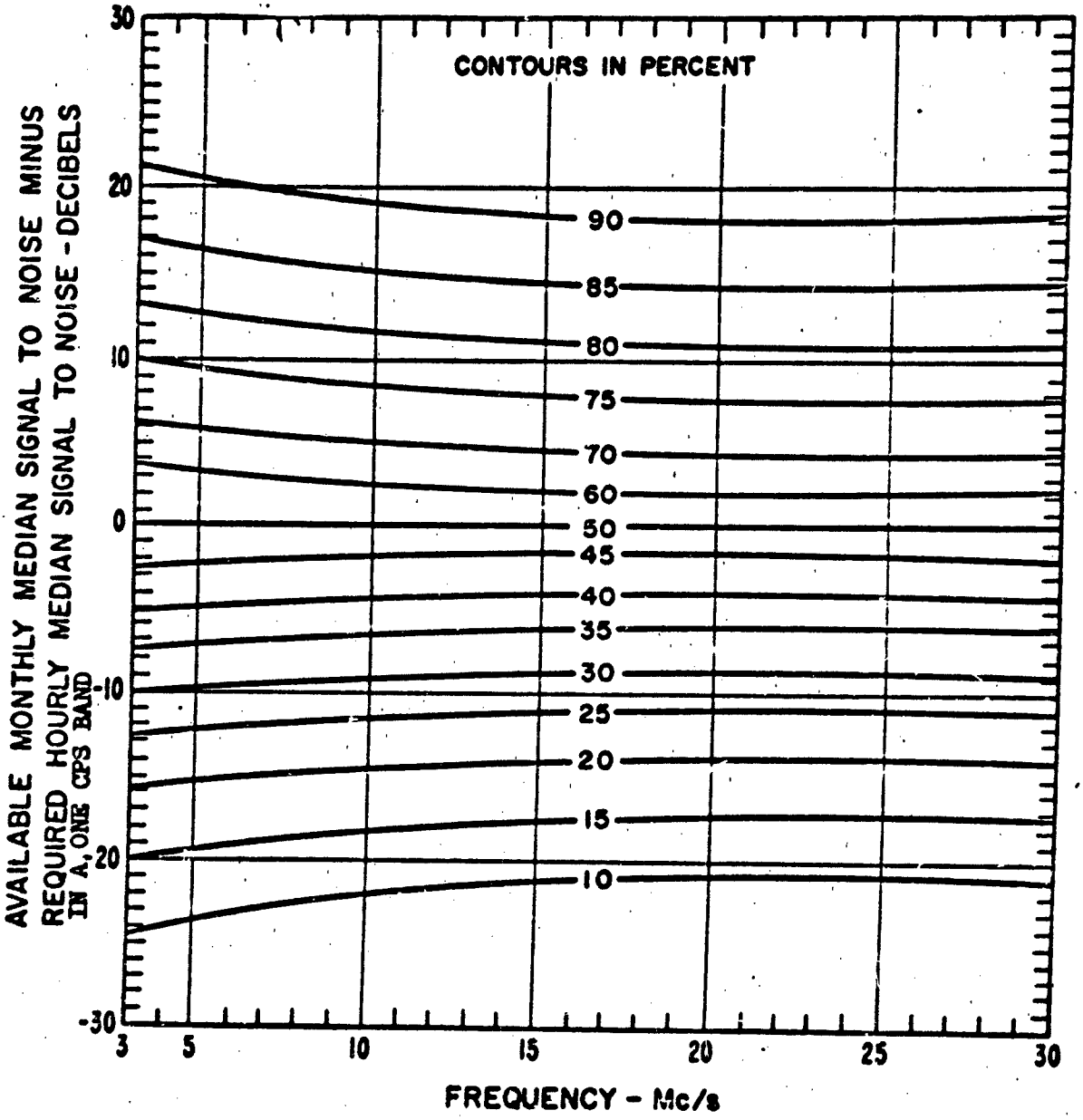

Chart to Estimate Reliability of Short Auroral Circuits (Circuits 4000 Km or Less with Circuit Mid Point Between 60° and 70° Geomagnetic Latitude).

FIGURE 4

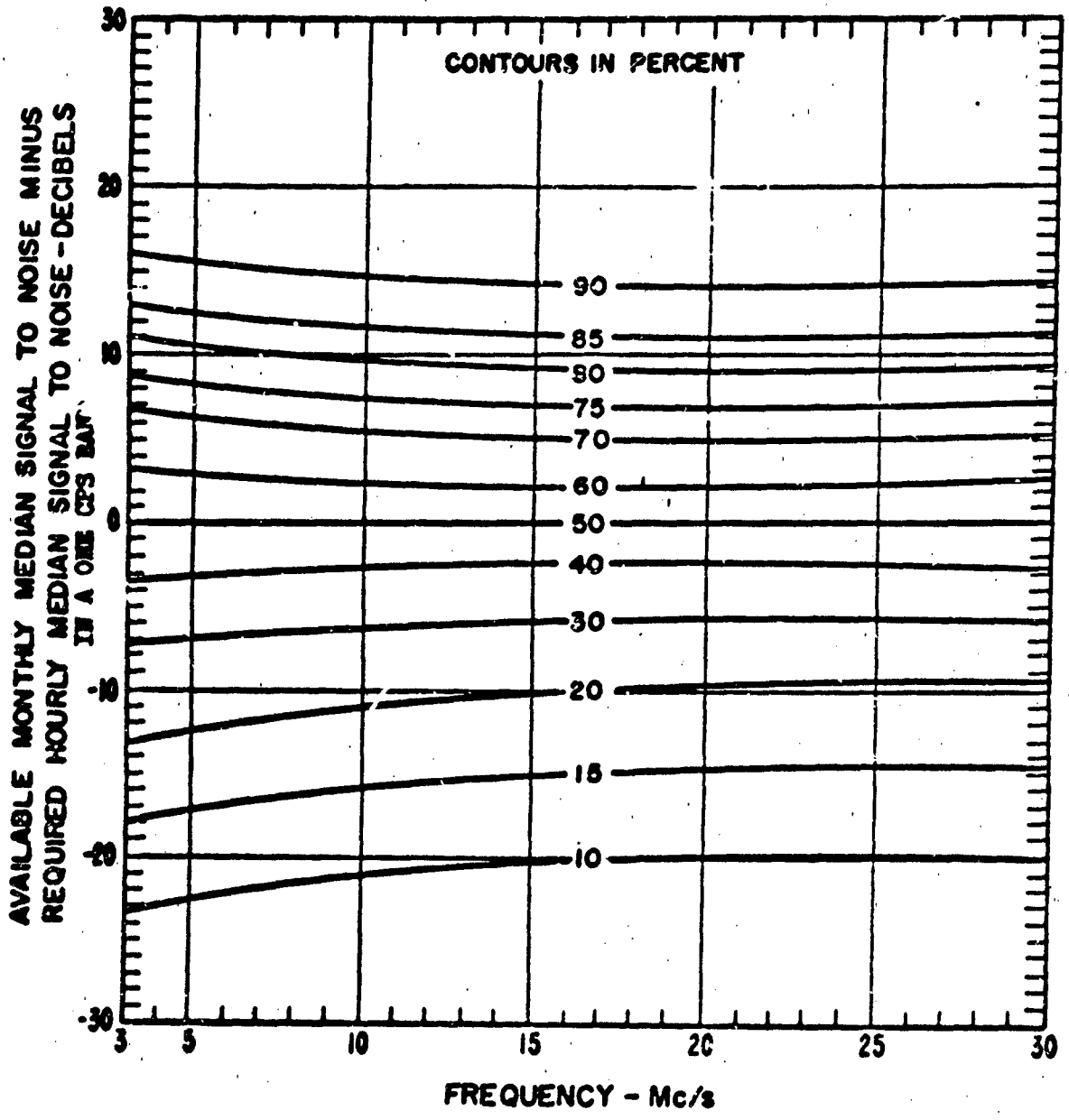

Chart to Estimate Reliability of Long Auroral Circuits (Circuits Greater than 4000 Km with One or Both Control Points Between 60° and 70° Geomagnetic Latitude).

FIGURE 5

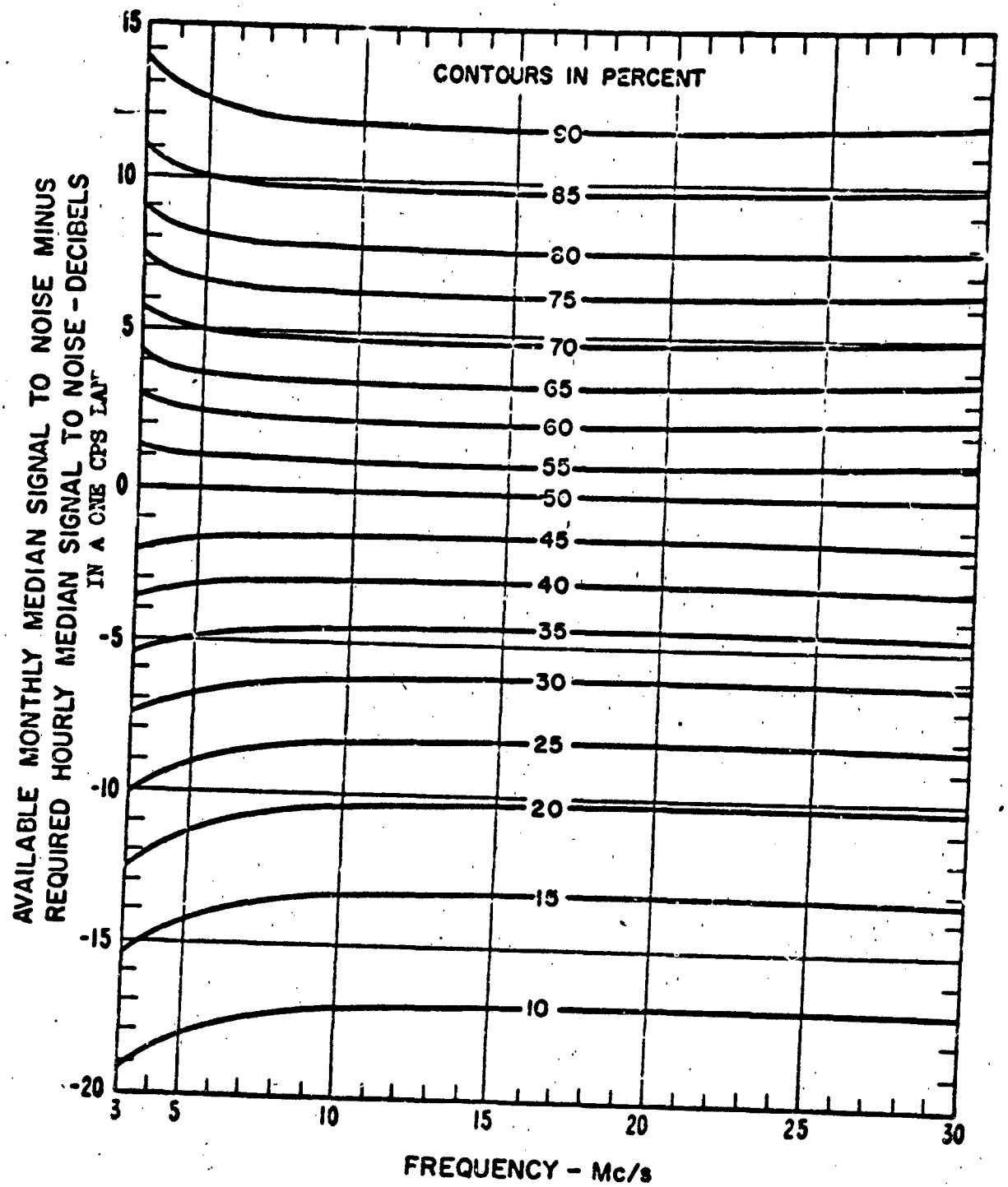

Chart to Estimate Reliability of Polar Circuits (All Circuit Control Points Above 70° Geomagnetic Latitude).

FIGURE 6

AIRPLANE ELEVATION ANGLE θ (DEGREES)	FREQUENCY (MEGACYCLES) 0.00 TO 2.00	2.10 TO 2.80	2.90 TO 4.00	4.10 TO 5.60	5.70 TO 8.00	8.10 TO 11.3	11.4 TO 16.0	16.1 TO 22.6	22.7 TO 32.0	32.1 TO INFINITY	TOTALS
0-32	0 0. 0.	98 -17.0 -27.0	160 -18.0 -25.8	433 -13.0 -22.4	39 -23.0 -25.6	0 0. 0.	0 0. 0.	0 0. 0.	0 0. 0.	0 0. 0.	730
33-47	2 -26.0 -31.0	141 -19.0 -30.0	505 -13.0 -27.4	473 -17.0 -29.3	294 -21.0 -33.1	68 -25.0 -35.7	2 -29.0 -34.5	0 0. 0.	0 0. 0.	0 0. 0.	1485
48-49	0 0. 0.	98 -14.0 -26.4	555 -9.0 -23.9	367 -14.0 -24.6	237 -18.0 -28.2	65 -24.0 -31.5	24 -24.0 -33.2	0 0. 0.	0 0. 0.	0 0. 0.	1346
50-69	0 0. 0.	2 -16.0 -19.0	381 -8.0 -21.2	565 -8.0 -21.2	404 -8.0 -24.0	124 -21.0 -28.7	53 -22.0 -31.2	0 0. 0.	0 0. 0.	0 0. 0.	1509
70-79	0 0. 0.	0 0. 0.	114 -3.0 -19.7	898 1.0 -18.3	1273 -5.0 -19.9	1166 -5.0 -21.8	379 -8.0 -23.9	93 -9.0 -28.5	4 -28.0 -29.0	0 0. 0.	3927
80-90	0 0. 0.	4 -24.0 -28.7	8 -21.0 -24.0	353 3.0 -14.7	1827 5.0 -15.6	2801 5.0 -17.2	4661 11.0 -17.0	1762 9.0 -21.0	317 35.0 -20.6	6 35.0 35.0	11739
TOTALS	2	343	1723	3069	4074	4224	5119	1855	321	6	20736

In each square the three numbers reading from top to bottom are the total number of circuits, maximum gain, and average gain, required to provide a 50 percent reliability for a one cycle band SNR of 36 db and a 100 watt carrier.

Required Antenna Gain Distribution (200 to 1800 N.M.)

FIGURE 7

AIRPLANE ELEVATION ANGLE θ (DEGREES)	FREQUENCY (MEGACYCLES)										
	0.00 TO 2.00	2.10 TO 2.80	2.90 TO 4.00	4.10 TO 5.60	5.70 TO 8.00	8.10 TO 11.3	11.4 TO 16.0	16.1 TO 22.6	22.7 TO 32.0	32.1 TO INFINITY	TOTALS
0-32	0 0. 0.	98 4.3 -8.6	160 2.6 -8.5	433 7.0 -8.5	39 -14.3 -17.1	0 0. 0.	0 0. 0.	0 0. 0.	0 0. 0.	0 0. 0.	730
33-47	2 -4.0 -15.0	141 2.6 -13.7	505 3.6 -12.1	473 3.1 -14.9	294 -1.0 -22.5	68 -5.6 -24.6	2 -10.1 -21.1	0 0. 0.	0 0. 0.	0 0. 0.	1485
48-49	0 0. 0.	98 7.3 -9.1	555 7.0 -8.0	367 6.3 -9.0	237 2.0 -15.5	65 -4.5 -22.6	24 -5.3 -24.1	0 0. 0.	0 0. 0.	0 0. 0.	1346
60-69	0 0. 0.	2 5.3 2.3	381 12.9 -4.6	545 11.0 -6.2	404 12.0 -10.8	124 -1.6 -17.8	53 -3.8 -21.9	0 0. 0.	0 0. 0.	0 0. 0.	1509
70-79	0 0. 0.	0 0. 0.	114 17.6 -2.6	898 21.3 -2.9	1273 15.0 -5.7	1166 14.0 -9.7	379 10.7 -13.7	93 9.0 -20.0	4 -22.0 -22.0	0 0. 0.	3927
80-90	0 0. 0.	4 -2.6 -12.0	8 -1.0 -12.0	353 23.0 1.7	1827 20.0 -1.2	2801 24.0 -3.9	4661 29.0 -5.7	1762 27.0 -12.7	317 53.0 -12.8	6 41.0 41.0	11739
TOTALS	2	343	1723	3069	4074	4224	5119	1855	321	6	20736

In each square the three numbers reading from top to bottom are the total number of circuits, maximum gain, and average gain required, to provide a 90 percent reliability for a one cycle band SNR of 35 db and a 100 watt carrier

Required Antenna Gain Distribution (200 to 1000 N.M.)

FIGURE 8

AIRPLANE ELEVATION ANGLE θ (DEGREES)	FREQUENCY (MEGACYCLES)										
	0.00 TO 2.00	2.10 TO 2.80	2.90 TO 4.00	4.10 TO 5.60	5.70 TO 8.00	8.10 TO 11.3	11.4 TO 16.0	16.1 TO 22.6	22.7 TO 32.0	32.1 TO INFINITY	TOTALS
0-32	4 -25.0 -25.2	32 -18.0 -20.2	623 -8.3 -17.0	838 5.0 -12.4	646 -0.4 -13.9	169 -11.0 -19.5	0 0. 0.	0 0. 0.	0 0. 0.	0 0. 0.	2312
33-47	8 -22.0 -23.1	36 -16.0 -18.7	704 -8.3 -15.6	618 -5.2 -15.6	801 -7.6 -14.6	259 -3.0 -17.7	16 -17.0 -17.7	0 0. 0.	0 0. 0.	0 0. 0.	2442
48-49	1 -21.0 -21.0	24 -14.0 -16.8	518 -9.3 -13.8	585 -7.7 -13.9	574 2.5 -14.8	336 -9.0 -14.8	61 -10.0 -14.7	0 0. 0.	0 0. 0.	0 0. 0.	2099
60-69	0 0. 0.	6 -13.0 -14.8	248 -8.3 -12.0	1106 -7.5 -11.9	803 0. -12.4	562 0. -12.9	311 -9.0 -13.1	8 -10.0 -12.7	0 0. 0.	0 0. 0.	3044
70-79	0 0. 0.	1 -19.0 -19.0	36 -8.1 -10.1	462 -5.9 -10.5	545 -5.0 -11.3	965 -2.0 -8.5	409 -3.0 -10.0	53 -10.0 -13.5	0 0. 0.	0 0. 0.	2451
80-90	0 0. 0.	8 -13.0 -14.0	3 -11.0 -11.0	7 -5.9 -6.4	63 -6.0 -7.3	351 -4.4 -7.4	958 -4.0 -5.1	86 -5.0 -5.5	0 0. 0.	0 0. 0.	1476
TOTALS	13	107	2132	3616	3432	2622	1755	147	0	0	13824

In each square the three numbers reading from top to bottom are the total number of circuits, maximum gain and average gain, required to provide a 90 percent reliability for a one cycle band SNR of 35 db and a 100 watt carrier

Required Antenna Gain Distribution (90 to 720 N.M.)

FIGURE 9

TABLE 1

Conditions for Required Antenna Gain Calculation

	Short Range (90 to 720 N.M.)		Long Range (200 to 1800 N.M.)	
Locations:	Latitude	Longitude	Latitude	Longitude
	15 N	105 E	40 N	73 W
	36 N	52 E	48 N	2 E
	48 N	12 E	51 N	27 W
	30 N	80 W	37 N	25 W
	35 N	68 W	65 N	148 W
	33 N	107 W	59 N	18 E
			49 N	54 W
			64 N	22 W
Directions:	North, South, East and West		North, South, East and West	
Distance Increments:	8 at 90 N.M. Each		9 at 200 N.M. each	
Times of Day:	0200 - 0600 - 1000 1400 - 1800 - 2200		0200 - 0600 - 1000 1400 - 1800 - 2200	
Seasons:	January - April July - October		January - April July - October	
Carrier Power:	100 Watts		100 Watts	
Man-Made Noise:	Rural		Rural	
Required SNR:	35 db in 1 CPS Band		35 db in 1 CPS Band	
Sunspot Numbers:	10 - 50 - 130		10 - 50 - 130	
Total Circuits:	13,824		20,736	

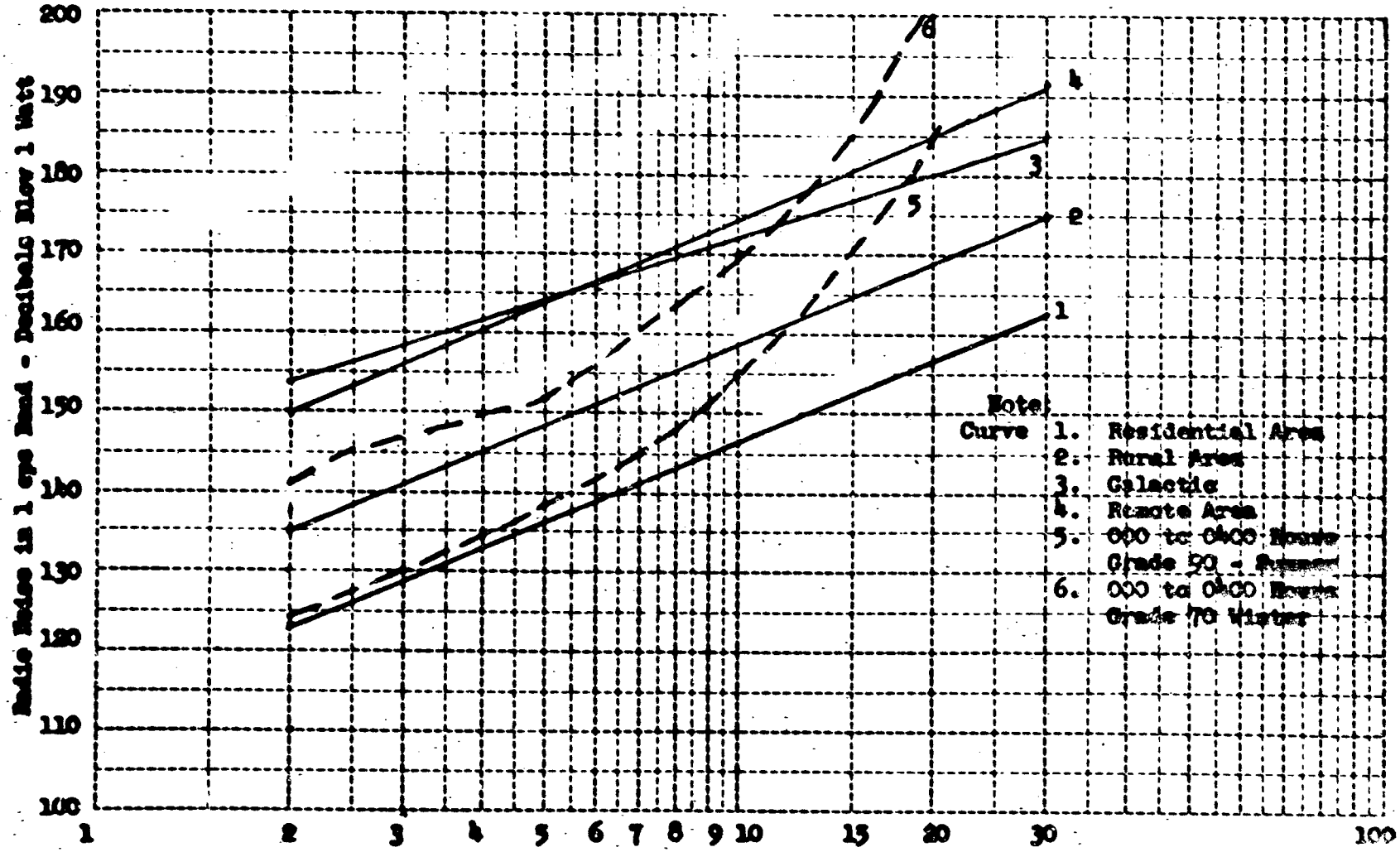

TYPICAL MAN-MADE, GALACTIC AND ATMOSPHERIC RADIO NOISE

FIGURE 10

TIME	θ	0	15	30	45	60	75	90	105	120	135	150	165	180	195	210	225	240	255	270	285	300	315	330	345
2.4	15	2.	3.	2.	3.	3.	3.	3.	3.	3.	2.	1.	1.	2.	3.	2.	3.	3.	2.	3.	2.	4.	2.	2.	2.
	25	2.	3.	2.	3.	3.	2.	3.	2.	3.	2.	1.	0.	1.	2.	2.	2.	2.	2.	2.	2.	2.	2.	1.	1.
	35	1.	2.	2.	3.	2.	2.	2.	2.	2.	1.	0.	0.	0.	1.	2.	2.	2.	2.	2.	2.	2.	1.	1.	1.
	45	0.	1.	2.	2.	2.	2.	2.	2.	1.	0.	-1.	-2.	-1.	-0.	0.	1.	2.	2.	2.	2.	1.	1.	0.	0.
	55	-1.	-0.	1.	1.	2.	2.	2.	2.	1.	-1.	-2.	-3.	-2.	-1.	-0.	0.	1.	1.	1.	1.	1.	1.	-1.	-1.
	65	-2.	-1.	-0.	0.	1.	1.	1.	1.	0.	-2.	-3.	-4.	-4.	-3.	-1.	-0.	0.	1.	1.	1.	1.	-0.	-2.	-3.
	75	-5.	-3.	-1.	-0.	1.	1.	1.	1.	0.	-3.	-4.	-6.	-6.	-4.	-2.	-1.	0.	1.	1.	1.	1.	-1.	-3.	-5.
	85	-6.	-4.	-2.	-0.	0.	1.	1.	1.	-1.	-3.	-6.	-8.	-7.	-5.	-3.	-1.	0.	0.	1.	0.	-0.	-3.	-5.	-8.
	95	-7.	-4.	-2.	-0.	0.	1.	1.	0.	-1.	-4.	-6.	-9.	-7.	-5.	-3.	-1.	-0.	0.	0.	0.	-0.	-3.	-5.	-8.
	105	-7.	-4.	-3.	-1.	0.	0.	0.	0.	-2.	-4.	-6.	-9.	-8.	-5.	-3.	-2.	-0.	1.	0.	0.	-1.	-3.	-6.	-9.
	115	-8.	-5.	-3.	-1.	-1.	0.	0.	0.	-2.	-4.	-5.	-8.	-8.	-6.	-3.	-2.	-1.	-0.	0.	0.	-1.	-3.	-6.	-9.
	125	-6.	-5.	-3.	-1.	-1.	0.	0.	0.	-0.	-3.	-4.	-6.	-6.	-5.	-4.	-2.	-1.	-0.	0.	0.	-1.	-3.	-5.	-7.
	135	-4.	-3.	-2.	-1.	-0.	0.	0.	0.	-0.	-1.	-2.	-3.	-4.	-4.	-3.	-1.	-0.	-0.	0.	0.	0.	-1.	-3.	-4.
	145	-2.	-2.	-1.	-0.	-0.	0.	0.	0.	1.	0.	-1.	-1.	-2.	-1.	-1.	0.	0.	-0.	0.	0.	0.	-0.	-1.	-2.
	155	5.	5.	5.	4.	4.	4.	3.	3.	3.	4.	4.	4.	5.	5.	5.	4.	4.	2.	3.	3.	4.	4.	5.	5.
	165	5.	5.	5.	4.	4.	3.	3.	2.	3.	3.	4.	3.	4.	4.	4.	4.	3.	2.	2.	3.	3.	0.	4.	4.
3.4	15	2.	3.	2.	3.	3.	3.	3.	3.	3.	2.	1.	1.	2.	3.	2.	3.	3.	2.	3.	2.	4.	2.	2.	2.
	25	2.	3.	2.	3.	3.	2.	3.	2.	3.	2.	1.	0.	1.	2.	2.	2.	2.	2.	2.	2.	2.	2.	1.	1.
	35	1.	2.	2.	3.	2.	2.	2.	2.	2.	1.	0.	0.	0.	1.	2.	2.	2.	2.	2.	2.	2.	2.	1.	1.
	45	0.	1.	2.	2.	2.	2.	2.	2.	1.	0.	-1.	-2.	-1.	-0.	0.	1.	2.	2.	2.	2.	1.	1.	0.	0.
	55	-1.	-0.	1.	1.	2.	2.	2.	2.	1.	-1.	-2.	-3.	-2.	-1.	-0.	0.	1.	1.	1.	1.	1.	1.	-1.	-1.
	65	-2.	-1.	-0.	0.	1.	1.	1.	1.	0.	-2.	-3.	-4.	-4.	-3.	-1.	-0.	0.	1.	1.	1.	1.	-0.	-2.	-3.
	75	-5.	-3.	-1.	-0.	1.	1.	1.	1.	0.	-3.	-4.	-6.	-6.	-4.	-2.	-1.	0.	1.	1.	1.	1.	-1.	-3.	-5.
	85	-6.	-4.	-2.	-0.	0.	1.	1.	1.	-1.	-3.	-6.	-8.	-7.	-5.	-3.	-1.	0.	0.	1.	0.	-0.	-3.	-5.	-8.
	95	-7.	-4.	-2.	-0.	0.	1.	1.	0.	-1.	-4.	-6.	-9.	-7.	-5.	-3.	-1.	-0.	0.	0.	0.	-0.	-3.	-5.	-8.
	105	-7.	-4.	-3.	-1.	0.	0.	0.	0.	-2.	-4.	-6.	-9.	-8.	-5.	-3.	-2.	-0.	1.	0.	0.	-1.	-3.	-6.	-9.
	115	-8.	-5.	-3.	-1.	-1.	0.	0.	0.	-2.	-4.	-5.	-8.	-8.	-6.	-3.	-2.	-1.	-0.	0.	0.	-1.	-3.	-6.	-9.
	125	-6.	-5.	-3.	-1.	-1.	0.	0.	0.	-0.	-3.	-4.	-6.	-6.	-5.	-4.	-2.	-1.	-0.	0.	0.	-1.	-3.	-5.	-7.
	135	-4.	-3.	-2.	-1.	-0.	0.	0.	0.	-0.	-1.	-2.	-3.	-4.	-4.	-3.	-1.	-0.	-0.	0.	0.	0.	-1.	-3.	-4.
	145	-2.	-2.	-1.	-0.	-0.	0.	0.	0.	1.	0.	-1.	-1.	-2.	-1.	-1.	0.	0.	-0.	0.	0.	0.	-0.	-1.	-2.
	155	5.	5.	5.	4.	4.	4.	3.	3.	3.	4.	4.	4.	5.	5.	5.	4.	4.	2.	3.	3.	4.	4.	5.	5.
	165	5.	5.	5.	4.	4.	3.	3.	2.	3.	3.	4.	3.	4.	4.	4.	4.	3.	2.	2.	3.	3.	0.	4.	4.
4.76	15	2.	3.	2.	3.	3.	3.	3.	3.	3.	2.	1.	1.	2.	3.	2.	3.	3.	2.	3.	2.	4.	2.	2.	2.
	25	2.	3.	2.	3.	3.	2.	3.	2.	3.	2.	1.	0.	1.	2.	2.	2.	2.	2.	2.	2.	2.	2.	1.	1.
	35	1.	2.	2.	3.	2.	2.	2.	2.	2.	1.	0.	0.	0.	1.	2.	2.	2.	2.	2.	2.	2.	2.	1.	1.
	45	0.	1.	2.	2.	2.	2.	2.	2.	1.	0.	-1.	-2.	-1.	-0.	0.	1.	2.	2.	2.	2.	1.	1.	0.	0.
	55	-1.	-0.	1.	1.	2.	2.	2.	2.	1.	-1.	-2.	-3.	-2.	-1.	-0.	0.	1.	1.	1.	1.	1.	1.	-1.	-1.
	65	-2.	-1.	-0.	0.	1.	1.	1.	1.	0.	-2.	-3.	-4.	-4.	-3.	-1.	-0.	0.	1.	1.	1.	1.	-0.	-2.	-3.
	75	-5.	-3.	-1.	-0.	1.	1.	1.	1.	0.	-3.	-4.	-6.	-6.	-4.	-2.	-1.	0.	1.	1.	1.	1.	-1.	-3.	-5.
	85	-6.	-4.	-2.	-0.	0.	1.	1.	1.	-1.	-3.	-6.	-8.	-7.	-5.	-3.	-1.	0.	0.	1.	0.	-0.	-3.	-5.	-8.
	95	-7.	-4.	-2.	-0.	0.	1.	1.	0.	-1.	-4.	-6.	-9.	-7.	-5.	-3.	-1.	-0.	0.	0.	0.	-0.	-3.	-5.	-8.
	105	-7.	-4.	-3.	-1.	0.	0.	0.	0.	-2.	-4.	-6.	-9.	-8.	-5.	-3.	-2.	-0.	1.	0.	0.	-1.	-3.	-6.	-9.
	115	-8.	-5.	-3.	-1.	-1.	0.	0.	0.	-2.	-4.	-5.	-8.	-8.	-6.	-3.	-2.	-1.	-0.	0.	0.	-1.	-3.	-6.	-9.
	125	-6.	-5.	-3.	-1.	-1.	0.	0.	0.	-0.	-3.	-4.	-6.	-6.	-5.	-4.	-2.	-1.	-0.	0.	0.	-1.	-3.	-5.	-7.
	135	-4.	-3.	-2.	-1.	-0.	0.	0.	0.	-0.	-1.	-2.	-3.	-4.	-4.	-3.	-1.	-0.	-0.	0.	0.	0.	-1.	-3.	-4.

6.73	15	3.	3.	3.	3.	3.	3.	3.	3.	3.	3.	2.	2.	3.	3.	3.	3.	3.	3.	3.	3.	3.	4.
	25	3.	3.	3.	3.	3.	3.	3.	3.	3.	2.	1.	2.	2.	2.	2.	3.	2.	2.	3.	3.	3.	3.	2.	3.
	35	2.	2.	2.	3.	3.	2.	3.	3.	3.	2.	1.	1.	1.	1.	1.	2.	2.	2.	3.	3.	3.	3.	2.	2.
	45	1.	1.	2.	2.	2.	3.	3.	2.	3.	1.	0.	-0.	0.	0.	0.	1.	2.	2.	2.	2.	2.	2.	2.	1.
	55	0.	0.	1.	2.	2.	2.	2.	2.	1.	0.	-1.	-1.	-2.	-2.	-1.	0.	1.	1.	2.	2.	2.	2.	1.	1.
	65	-1.	-0.	-0.	1.	1.	2.	2.	2.	1.	-0.	-1.	-3.	-4.	-3.	-2.	-1.	1.	1.	2.	2.	2.	2.	-0.	-1.
	75	-3.	-2.	-1.	0.	1.	1.	2.	2.	1.	-0.	-2.	-3.	-4.	-4.	-4.	-3.	-1.	0.	1.	2.	2.	1.	-0.	-2.
	85	-4.	-4.	-2.	-0.	1.	2.	2.	2.	1.	-0.	-3.	-4.	-6.	-6.	-4.	-3.	-0.	1.	1.	2.	2.	1.	-1.	-3.
	95	-6.	-4.	-2.	-0.	1.	2.	2.	2.	0.	-1.	-3.	-5.	-5.	-6.	-4.	-2.	-0.	1.	2.	2.	1.	0.	-2.	-4.
	105	-5.	-4.	-2.	-0.	1.	2.	2.	2.	0.	-0.	-3.	-4.	-5.	-5.	-3.	-1.	-0.	2.	2.	2.	1.	0.	-2.	-4.
	115	-5.	-3.	-2.	-1.	0.	1.	2.	2.	0.	-0.	-2.	-4.	-5.	-4.	-3.	-1.	0.	1.	1.	2.	1.	0.	-2.	-4.
	125	-4.	-3.	-2.	-1.	0.	1.	2.	2.	2.	0.	-1.	-3.	-4.	-4.	-3.	-1.	0.	1.	1.	2.	1.	0.	-1.	-3.
	135	-2.	-3.	-1.	-1.	0.	1.	2.	2.	2.	1.	0.	-1.	-2.	-2.	-1.	-0.	1.	2.	2.	2.	2.	2.	-0.	-1.
	145	0.	0.	-0.	1.	1.	1.	2.	2.	2.	2.	1.	1.	0.	0.	1.	1.	1.	2.	2.	2.	2.	2.	0.	0.
	155	6.	6.	6.	5.	4.	4.	3.	3.	4.	5.	5.	5.	6.	6.	6.	5.	4.	4.	3.	4.	4.	5.	6.	5.
	165	6.	6.	6.	5.	5.	4.	3.	3.	3.	4.	4.	5.	5.	5.	5.	4.	3.	3.	3.	4.	4.	0.	5.	6.
9.5	15	5.	5.	5.	5.	5.	5.	4.	4.	4.	4.	3.	3.	2.	2.	3.	4.	4.	4.	4.	4.	4.	4.	4.	4.
	25	5.	5.	5.	6.	5.	5.	4.	4.	3.	3.	3.	2.	2.	2.	3.	3.	4.	4.	4.	4.	5.	5.	5.	4.
	35	5.	5.	5.	5.	4.	5.	4.	4.	3.	3.	2.	1.	1.	1.	2.	2.	3.	4.	4.	4.	5.	5.	6.	4.
	45	4.	4.	4.	5.	4.	5.	4.	4.	3.	2.	1.	-0.	0.	0.	1.	1.	2.	3.	4.	4.	5.	5.	5.	4.
	55	3.	3.	3.	5.	5.	5.	4.	3.	2.	1.	-1.	-1.	-2.	-2.	-1.	1.	1.	3.	3.	4.	5.	4.	4.	3.
	65	2.	2.	3.	4.	4.	5.	4.	3.	1.	-1.	-2.	-3.	-4.	-3.	-2.	-1.	0.	2.	3.	4.	5.	4.	3.	3.
	75	1.	1.	2.	3.	4.	4.	3.	2.	-0.	-2.	-4.	-5.	-6.	-5.	-4.	-2.	-1.	1.	2.	3.	4.	3.	3.	1.
	85	-2.	-1.	1.	3.	3.	4.	4.	2.	-0.	-3.	-5.	-7.	-9.	-7.	-6.	-3.	-1.	0.	2.	3.	3.	3.	1.	-1.
	95	-7.	-5.	-1.	1.	3.	4.	4.	2.	-0.	-3.	-6.	-10.	-11.	-10.	-7.	-5.	-2.	0.	2.	3.	3.	2.	1.	-3.
	105	-13.	-7.	-1.	2.	3.	4.	4.	2.	-0.	-3.	-7.	-13.	-16.	-12.	-7.	-4.	-2.	1.	2.	3.	3.	2.	-1.	-5.
	115	-16.	-7.	-2.	1.	3.	4.	4.	2.	-0.	-3.	-7.	-12.	-16.	-12.	-7.	-4.	-1.	1.	2.	3.	3.	1.	-2.	-7.
	125	-10.	-7.	-2.	0.	2.	3.	3.	2.	0.	-2.	-5.	-8.	-10.	-9.	-7.	-4.	-1.	0.	2.	2.	2.	1.	-1.	-4.
	135	-5.	-4.	-2.	-0.	2.	3.	3.	2.	0.	-1.	-2.	-4.	-5.	-5.	-5.	-2.	-1.	1.	1.	2.	2.	1.	0.	-2.
	145	-1.	-1.	0.	1.	2.	3.	3.	2.	1.	1.	-1.	-1.	-2.	-2.	-2.	-1.	0.	1.	2.	2.	2.	2.	1.	-1.
	155	8.	8.	8.	7.	6.	5.	5.	5.	5.	5.	5.	5.	5.	5.	6.	5.	5.	5.	5.	5.	5.	6.	7.	7.
	165	8.	8.	8.	7.	6.	5.	5.	5.	5.	5.	5.	5.	5.	5.	5.	5.	5.	5.	5.	5.	5.	0.	7.	7.
11.6	15	3.	3.	4.	4.	2.	1.	1.	1.	0.	1.	-0.	-1.	-1.	-1.	-0.	-0.	0.	-0.	0.	1.	2.	2.	3.	2.
	25	3.	3.	4.	4.	2.	2.	1.	1.	-0.	-1.	-2.	-3.	-3.	-3.	-2.	-2.	-1.	0.	0.	1.	2.	3.	3.	3.
	35	4.	4.	4.	4.	3.	2.	1.	1.	-1.	-2.	-2.	-4.	-4.	-3.	-4.	-3.	-2.	-1.	0.	1.	3.	3.	3.	4.
	45	4.	3.	4.	4.	3.	2.	1.	-0.	-1.	-4.	-4.	-5.	-6.	-5.	-5.	-4.	-3.	-1.	1.	1.	3.	4.	4.	4.
	55	3.	3.	3.	3.	3.	2.	1.	-0.	-2.	-5.	-5.	-7.	-7.	-6.	-7.	-5.	-4.	-2.	-0.	1.	3.	3.	4.	3.
	65	2.	2.	2.	3.	3.	2.	1.	-0.	-3.	-5.	-6.	-7.	-8.	-8.	-7.	-7.	-6.	-3.	-0.	2.	4.	4.	3.	5.
	75	0.	0.	1.	2.	3.	2.	1.	-1.	-4.	-5.	-6.	-8.	-8.	-7.	-7.	-7.	-6.	-3.	-0.	2.	3.	4.	3.	1.
	85	-2.	-2.	0.	1.	3.	2.	1.	-1.	-4.	-6.	-7.	-8.	-9.	-7.	-6.	-6.	-7.	-4.	-0.	2.	3.	4.	3.	0.
	95	-7.	-6.	-2.	1.	3.	2.	1.	-1.	-4.	-6.	-7.	-9.	-9.	-7.	-6.	-6.	-7.	-4.	-0.	3.	3.	3.	2.	-2.
	105	-12.	-9.	-3.	0.	2.	2.	1.	-2.	-5.	-7.	-8.	-10.	-10.	-8.	-7.	-7.	-6.	-3.	-0.	3.	3.	3.	1.	-4.
	115	-13.	-8.	-3.	0.	1.	1.	1.	-2.	-5.	-8.	-9.	-11.	-10.	-9.	-9.	-8.	-5.	-3.	-0.	2.	2.	2.	0.	-4.
	125	-8.	-5.	-2.	0.	1.	1.	1.	-1.	-5.	-8.	-9.	-11.	-11.	-11.	-10.	-9.	-6.	-3.	-0.	2.	2.	1.	-0.	-5.
	135	-4.	-3.	-1.	-0.	1.	1.	0.	-1.	-3.	-7.	-9.	-11.	-11.	-11.	-10.	-9.	-5.	-3.	-0.	2.	2.	1.	-1.	-3.
	145	-1.	-0.	0.	0.	1.	1.	0.	-1.	-2.	-5.	-7.	-8.	-9.	-9.	-8.	-6.	-3.	-1.	-0.	1.	2.	1.	0.	-0.
	155	6.	6.	6.	6.	4.	2.	1.	2.	2.	2.	3.	2.	2.	2.	2.	2.	1.	0.	1.	2.	4.	5.	5.	
	165	6.	6.	7.	5.	4.	2.	1.	1.	1.	1.	1.	0.	0.	0.	0.	1.	1.	1.	1.	1.	2.	0.	5.	6.

DIRECTIVE GAINS FOR NOTCH FFO VERTICAL STABILIZER
FIGURE [illegible]

TIME	θ	0	15	30	45	60	75	90	105	120	135	150	165	180	195	210	225	240	255	270	285	300	315	330	345
		-6.	-6.	-7.	-8.	-9.	-11.	-13.	-12.	-10.	-9.	-6.	-6.	-5.	-5.	-5.	-7.	-9.	-11.	-11.	-11.	-10.	-8.	-7.	-6.
13.5		-1.	-1.	-2.	-3.	-5.	-7.	-8.	-7.	-6.	-5.	-3.	-2.	-2.	-2.	-2.	-4.	-6.	-7.	-8.	-6.	-5.	-4.	-3.	-1.
		1.	1.	1.	0.	-1.	-4.	-6.	-6.	-4.	-3.	-1.	-1.	0.	0.	-1.	-2.	-4.	-6.	-5.	-3.	-2.	-1.	-0.	1.
		2.	3.	2.	2.	1.	-2.	-5.	-4.	-3.	-2.	-0.	-0.	0.	1.	1.	-1.	-2.	-5.	-5.	-2.	-0.	1.	2.	1.
		2.	3.	4.	3.	3.	0.	-4.	-3.	-2.	-1.	0.	-1.	0.	1.	1.	1.	-1.	-4.	-4.	-0.	2.	3.	2.	1.
		1.	2.	3.	4.	3.	1.	-3.	-3.	-1.	0.	0.	-2.	-2.	0.	1.	2.	0.	-3.	-4.	0.	3.	4.	3.	1.
		-1.	1.	3.	4.	4.	2.	-4.	-4.	-1.	0.	-0.	-2.	-4.	-1.	0.	-0.	0.	-4.	-4.	1.	4.	4.	3.	0.
		-3.	0.	3.	4.	3.	2.	-4.	-5.	-1.	0.	-0.	-4.	-7.	-4.	-1.	1.	-1.	-5.	-5.	2.	3.	4.	3.	-1.
		-4.	-1.	2.	4.	5.	3.	-2.	-4.	-1.	-0.	-1.	-5.	-10.	-6.	-2.	-0.	-1.	-5.	-4.	1.	4.	4.	3.	-1.
		-3.	-0.	3.	5.	5.	3.	-1.	-4.	-2.	-1.	-2.	-6.	-10.	-5.	-2.	-0.	-1.	-4.	-2.	3.	4.	5.	4.	0.
		-1.	1.	3.	5.	5.	3.	-1.	-3.	-1.	-1.	-2.	-5.	-7.	-4.	-1.	-0.	-1.	-3.	-2.	3.	4.	6.	4.	2.
		2.	2.	4.	5.	5.	3.	-0.	-3.	-2.	-2.	-3.	-5.	-6.	-3.	-1.	-1.	-1.	-3.	-1.	3.	4.	5.	5.	3.
		3.	4.	4.	4.	5.	3.	-0.	-3.	-5.	-4.	-5.	-6.	-6.	-4.	-2.	-2.	-3.	-3.	-1.	2.	4.	5.	5.	3.
		4.	4.	4.	4.	4.	3.	1.	-3.	-5.	-8.	-10.	-10.	-9.	-7.	-5.	-5.	-5.	-3.	-1.	1.	3.	4.	5.	4.
		-3.	-3.	-5.	-7.	-9.	-10.	-10.	-10.	-10.	-8.	-5.	-3.	-2.	-2.	-4.	-6.	-8.	-9.	-9.	-8.	-8.	-8.	-6.	-4.
		2.	2.	1.	-1.	-4.	-5.	-5.	-5.	-6.	-5.	-1.	0.	1.	1.	-0.	-3.	-5.	-6.	-5.	-4.	-4.	-0.	-1.	1.
19.0		2.	2.	2.	2.	1.	0.	-1.	-1.	-1.	-1.	-1.	-2.	-2.	-1.	-1.	-1.	-1.	-2.	0.	0.	2.	2.	2.	2.
		4.	4.	3.	3.	3.	2.	-0.	-2.	-1.	-2.	-2.	-1.	-1.	0.	-0.	-1.	-1.	-1.	-1.	0.	1.	2.	3.	3.
		4.	4.	2.	4.	3.	2.	-1.	-2.	-3.	-3.	-2.	-1.	0.	1.	1.	-0.	-1.	-2.	-1.	-0.	1.	3.	4.	4.
		5.	5.	5.	4.	3.	1.	-1.	-3.	-3.	-3.	-1.	-0.	1.	2.	1.	0.	-1.	-2.	-2.	-1.	1.	3.	3.	4.
		4.	4.	2.	1.	0.	-0.	-1.	-2.	-2.	-0.	2.	2.	2.	-1.	-2.	-3.	-3.	-3.	-2.	1.	3.	4.	5.	4.
		4.	4.	4.	3.	3.	1.	0.	-1.	-3.	-4.	-1.	1.	1.	2.	1.	0.	-1.	-3.	-3.	-1.	1.	3.	3.	2.
		3.	3.	3.	2.	2.	0.	0.	-1.	-3.	-3.	-1.	1.	1.	1.	1.	0.	-1.	-2.	-3.	-0.	1.	2.	3.	2.
		2.	2.	2.	2.	2.	1.	0.	-0.	-2.	-4.	-2.	0.	1.	1.	1.	-0.	-1.	-1.	-2.	-2.	1.	1.	2.	1.
		1.	1.	1.	1.	1.	1.	1.	0.	-2.	-3.	-3.	-2.	0.	0.	0.	1.	-0.	-1.	-1.	0.	0.	-1.	-0.	0.
		0.	1.	0.	-0.	-1.	-0.	-0.	0.	-1.	-2.	-3.	-2.	-2.	-1.	-1.	0.	0.	-1.	-1.	-0.	-1.	-2.	-2.	-1.
		-1.	-1.	-2.	-2.	-3.	-2.	-1.	-1.	-1.	-2.	-1.	-1.	-1.	-1.	0.	0.	0.	-1.	-2.	-2.	-2.	-3.	-4.	-2.
		-3.	-3.	-4.	-5.	-5.	-3.	-2.	-2.	-3.	-2.	-2.	-1.	-1.	0.	0.	0.	-1.	-2.	-3.	-2.	-3.	-5.	-8.	-6.
		-6.	-6.	-8.	-8.	-7.	-5.	-3.	-3.	-3.	-3.	-2.	-2.	-1.	-1.	-1.	-1.	-2.	-3.	-4.	-4.	-5.	-8.	-9.	-8.
		-8.	-9.	-10.	-11.	-10.	-9.	-6.	-5.	-4.	-3.	-3.	-2.	-1.	-1.	-1.	-2.	-1.	-3.	-5.	-6.	-7.	-11.	-13.	-10.
		5.	5.	5.	5.	3.	1.	-0.	-1.	-1.	0.	0.	1.	1.	2.	1.	1.	1.	-1.	0.	0.	2.	3.	3.	5.
		7.	7.	6.	6.	4.	3.	0.	-2.	-1.	-1.	-0.	2.	2.	3.	2.	1.	1.	-0.	-0.	1.	2.	0.	5.	5.
26.9		-1.	-2.	-2.	-3.	-3.	-4.	-4.	-4.	-4.	-4.	-5.	-5.	-6.	-7.	-5.	-5.	-5.	-4.	-4.	-3.	-2.	-2.	-1.	-2.
		1.	1.	-0.	-1.	-2.	-3.	-3.	-3.	-3.	-4.	-4.	-5.	-5.	-5.	-4.	-5.	-4.	-3.	-3.	-2.	-1.	0.	0.	1.
		3.	2.	1.	1.	-1.	-2.	-2.	-2.	-3.	-3.	-4.	-4.	-4.	-4.	-4.	-3.	-3.	-2.	-1.	-1.	0.	1.	2.	2.
		4.	-3.	3.	2.	1.	0.	-1.	-1.	-2.	-3.	-2.	-2.	-2.	-2.	-2.	-2.	-2.	-2.	-2.	-1.	-0.	1.	3.	4.	4.
		4.	4.	3.	3.	2.	1.	-0.	-1.	-1.	-1.	-1.	-1.	-1.	-1.	-1.	-2.	-1.	-0.	1.	2.	4.	3.	4.	
		3.	3.	3.	3.	2.	2.	0.	-0.	-0.	-1.	-1.	-1.	-1.	-1.	-1.	-1.	-1.	-0.	1.	1.	2.	4.	3.	3.
		2.	2.	2.	3.	2.	2.	1.	1.	-1.	0.	0.	-1.	-1.	-1.	-1.	-1.	-1.	0.	1.	1.	2.	3.	3.	2.
		2.	2.	2.	2.	2.	1.	1.	1.	0.	0.	0.	0.	0.	0.	0.	0.	0.	1.	1.	1.	2.	2.	2.	2.
		2.	1.	1.	1.	1.	1.	0.	1.	1.	0.	0.	-1.	-1.	0.	0.	0.	1.	1.	1.	0.	1.	2.	2.	2.
		1.	1.	0.	1.	1.	1.	-0.	0.	1.	1.	0.	-1.	-2.	-1.	-1.	1.	1.	0.	0.	-0.	1.	2.	1.	1.
		1.	1.	1.	2.	1.	1.	0.	-1.	-1.	-1.	-2.	-2.	-2.	-3.	-2.	-1.	-0.	0.	0.	1.	2.	2.	1.	1.
		-1.	-1.	-1.	-0.	0.	1.	0.	-1.	-1.	-2.	-2.	-5.	-5.	-6.	-4.	-2.	-1.	-1.	-1.	0.	1.	0.	-0.	-1.
		-4.	-4.	-3.	-2.	-1.	-1.	-1.	-2.	-2.	-2.	-3.	-4.	-6.	-7.	-5.	-3.	-2.	-2.	-2.	-0.	0.	-0.	-2.	-3.
		-5.	-5.	-4.	-2.	-1.	-1.	-2.	-3.	-3.	-3.	-4.	-5.	-6.	-5.	-4.	-2.	-2.	-2.	-2.	-1.	-1.	-2.	-3.	-4.
		2.	1.	0.	-0.	-1.	-2.	-3.	-4.	-3.	-3.	-3.	-3.	-3.	-4.	-2.	-3.	-4.	-3.	-3.	-1.	-0.	1.	1.	1.
		4.	4.	2.	2.	-0.	-1.	-2.	-2.	-2.	-2.	-1.	-2.	-2.	-2.	-2.	-2.	-2.	-1.	-1.	-0.	1.	0.	3.	4.

DIRECTIVE GAINS FOR NOTCH FED VERTICAL STABILIZER

FIGURE 12

2.4	15	-4.	-4.	-5.	-5.	-4.	-4.	-2.	-3.	-3.	-3.	-4.	-5.	-5.	-5.	-6.	-5.	-6.	-5.	-5.	-5.	-5.	-5.	-5.
	25	-4.	-4.	-5.	-5.	-4.	-4.	-2.	-2.	-3.	-3.	-4.	-4.	-5.	-5.	-5.	-5.	-5.	-6.	-6.	-5.	-5.	-5.	-4.
	35	-2.	-2.	-2.	-2.	-2.	-2.	-2.	-2.	-2.	-2.	-2.	-2.	-2.	-2.	-3.	-3.	-3.	-3.	-3.	-2.	-1.	-1.	-1.
	45	-1.	-1.	-1.	-2.	-1.	-1.	-1.	-1.	-1.	-1.	-1.	-1.	-1.	-2.	-2.	-2.	-3.	-3.	-3.	-2.	-2.	-2.	-1.
	55	0.	0.	0.	0.	0.	0.	0.	-0.	-0.	-0.	-0.	0.	0.	0.	0.	-1.	-1.	-1.	-1.	-1.	-2.	-1.	0.
	65	1.	1.	1.	1.	1.	1.	0.	0.	0.	0.	1.	1.	1.	1.	1.	1.	1.	0.	0.	0.	0.	0.	0.
	75	1.	2.	2.	2.	1.	1.	1.	1.	1.	1.	1.	1.	1.	1.	2.	1.	1.	1.	1.	1.	1.	1.	1.
	85	2.	1.	2.	1.	1.	1.	1.	1.	1.	1.	1.	2.	2.	2.	2.	2.	2.	1.	1.	1.	1.	1.	1.
	95	1.	1.	1.	1.	1.	1.	1.	1.	1.	1.	1.	2.	2.	2.	2.	2.	2.	2.	1.	1.	1.	1.	1.
	105	1.	1.	1.	1.	1.	1.	1.	1.	1.	1.	1.	2.	2.	2.	2.	2.	2.	2.	1.	1.	1.	1.	1.
	115	0.	0.	0.	1.	0.	0.	0.	0.	0.	0.	0.	1.	1.	1.	1.	1.	1.	1.	1.	1.	1.	1.	1.
	125	-1.	-1.	-1.	-1.	-2.	-2.	-2.	-2.	-1.	-1.	0.	0.	0.	1.	1.	1.	1.	0.	0.	0.	0.	0.	0.
	135	-3.	-3.	-3.	-2.	-3.	-3.	-3.	-3.	-3.	-2.	-2.	-2.	-2.	-1.	-1.	-1.	-1.	-1.	-1.	-1.	-0.	-1.	-1.
	145	-4.	-4.	-4.	-5.	-5.	-5.	-4.	-4.	-5.	-4.	-5.	-5.	-5.	-5.	-5.	-4.	-4.	-3.	-3.	-3.	-3.	-3.	-3.
	155	-7.	-6.	-7.	-7.	-7.	-6.	-6.	-6.	-6.	-5.	-4.	-5.	-5.	-5.	-5.	-4.	-4.	-4.	-4.	-5.	-5.	-5.	-6.
	165	-9.	-8.	-8.	-8.	-8.	-10.	-9.	-8.	-9.	-12.	-9.	-9.	-10.	-10.	-9.	-9.	-9.	-9.	-8.	-8.	-8.	-8.	-8.
3.4	15	-4.	-4.	-4.	-4.	-5.	-6.	-6.	-6.	-5.	-5.	-5.	-5.	-6.	-7.	-9.	-10.	-10.	-9.	-8.	-7.	-5.	-4.	-5.
	25	-4.	-3.	-3.	-3.	-3.	-4.	-4.	-4.	-5.	-5.	-5.	-5.	-6.	-6.	-8.	-8.	-9.	-9.	-9.	-7.	-7.	-5.	-4.
	35	-2.	-2.	-1.	-2.	-2.	-2.	-2.	-3.	-3.	-3.	-3.	-3.	-3.	-4.	-4.	-4.	-5.	-5.	-5.	-5.	-5.	-4.	-3.
	45	0.	0.	0.	-0.	-0.	-1.	-1.	-1.	-2.	-2.	-2.	-2.	-3.	-3.	-4.	-4.	-14.	-4.	-5.	-5.	-4.	-3.	-1.
	55	2.	2.	2.	1.	1.	1.	1.	1.	1.	0.	0.	0.	0.	-1.	-1.	-2.	-2.	-3.	-3.	-2.	-1.	0.	1.
	65	3.	3.	3.	2.	2.	2.	1.	1.	1.	1.	1.	1.	1.	0.	0.	-1.	-1.	-1.	-1.	-1.	0.	1.	2.
	75	3.	3.	3.	3.	2.	2.	2.	2.	2.	2.	2.	2.	1.	1.	1.	0.	0.	0.	0.	0.	1.	2.	2.
	85	3.	3.	3.	3.	3.	2.	2.	2.	2.	2.	2.	2.	2.	1.	1.	1.	0.	0.	0.	1.	1.	2.	3.
	95	3.	3.	3.	3.	2.	2.	2.	2.	2.	2.	2.	2.	2.	1.	1.	1.	0.	0.	0.	1.	1.	2.	3.
	105	3.	3.	3.	3.	2.	2.	2.	2.	2.	2.	2.	2.	2.	2.	1.	1.	1.	0.	0.	1.	1.	2.	3.
	115	2.	2.	2.	2.	1.	1.	1.	1.	1.	1.	2.	2.	2.	2.	1.	1.	1.	0.	0.	1.	1.	2.	3.
	125	2.	1.	1.	1.	0.	0.	0.	1.	1.	1.	1.	1.	1.	1.	0.	0.	0.	-1.	-1.	0.	0.	1.	2.
	135	-1.	-1.	-1.	-2.	-2.	-2.	-2.	-1.	-1.	-0.	-1.	0.	-1.	-1.	-2.	-2.	-2.	-3.	-3.	-2.	-2.	-1.	-1.
	145	-3.	-3.	-3.	-3.	-2.	-2.	-3.	-3.	-3.	-3.	-3.	-2.	-3.	-4.	-4.	-4.	-4.	-3.	-2.	-3.	-4.	-3.	-4.
	155	-4.	-4.	-5.	-5.	-6.	-5.	-5.	-4.	-4.	-4.	-4.	-3.	-4.	-4.	-4.	-5.	-5.	-3.	-4.	-4.	-4.	-3.	-4.
	165	-6.	-6.	-6.	-5.	-5.	-4.	-4.	-4.	-4.	-4.	-5.	-6.	-6.	-7.	-7.	-7.	-6.	-5.	-5.	-5.	-6.	-7.	-7.
4.76	15	-3.	-2.	-3.	-2.	-3.	-2.	-2.	-2.	-1.	-1.	-2.	-1.	-3.	-4.	-7.	-8.	-7.	-7.	-5.	-4.	-3.	-2.	-3.
	25	-2.	-1.	-2.	-6.	-1.	-2.	-2.	-2.	-2.	-1.	-2.	-1.	-2.	-2.	-3.	-4.	-5.	-5.	-6.	-6.	-5.	-4.	-3.
	35	-1.	-1.	-0.	-1.	-1.	-2.	-1.	-1.	-1.	-2.	-1.	0.	0.	0.	-1.	-2.	-2.	-3.	-4.	-2.	-1.	-1.	0.
	45	0.	0.	1.	-0.	-1.	-1.	-1.	-1.	-1.	-1.	-0.	0.	0.	0.	-1.	-2.	-2.	-3.	-4.	-4.	-2.	-2.	-1.
	55	2.	2.	1.	1.	-0.	-1.	-1.	-1.	-1.	-0.	0.	0.	1.	1.	1.	1.	-1.	-2.	-2.	-2.	-2.	-2.	0.
	65	2.	2.	2.	1.	0.	-0.	-1.	-1.	-0.	0.	1.	1.	2.	2.	1.	1.	0.	-1.	-2.	-2.	-2.	-1.	0.
	75	3.	2.	2.	1.	0.	-1.	-1.	-1.	0.	1.	1.	2.	2.	2.	1.	1.	0.	-1.	-2.	-2.	-2.	-1.	0.
	85	3.	3.	2.	2.	1.	0.	-1.	-1.	0.	1.	2.	2.	3.	2.	1.	0.	-1.	-1.	-2.	-1.	0.	1.	2.
	95	3.	3.	2.	1.	0.	-1.	-2.	-2.	0.	1.	2.	2.	2.	2.	1.	0.	-1.	-1.	-2.	-1.	0.	1.	2.
	105	3.	2.	2.	1.	0.	-1.	-1.	-1.	0.	1.	2.	2.	2.	2.	1.	1.	0.	-1.	-2.	-2.	0.	1.	2.
	115	2.	2.	2.	1.	0.	-0.	-1.	-1.	-0.	0.	1.	2.	2.	2.	1.	1.	0.	-1.	-1.	-1.	0.	1.	2.
	125	2.	2.	1.	1.	-0.	-1.	-1.	-2.	-1.	-0.	0.	1.	1.	1.	1.	0.	-1.	-1.	-2.	-1.	0.	1.	2.
	135	1.	1.	1.	-0.	-0.	-1.	-1.	-1.	-1.	-1.	-0.	0.	0.	0.	0.	-1.	-1.	-2.	-1.	-1.	-1.	1.	2.
	145	1.	1.	1.	-0.	-0.	-1.	-1.	-1.	-1.	0.	1.	1.	1.	1.	-0.	-1.	-3.	-3.	-4.	-2.	-2.	-1.	1.
	155	-1.	-0.	-1.	-1.	-1.	-1.	-1.	-1.	-2.	-2.	-2.	-2.	-2.	-2.	-3.	-3.	-2.	-3.	-2.	-2.	-2.	-2.	-1.
	165	-1.	-0.	-1.	-1.	-1.	-1.	-1.	-1.	-2.	-2.	-2.	-2.	-2.	-2.	-3.	-3.	-2.	-3.	-2.	-2.	-2.	-2.	-1.

DIRECTIVE GAIN FOR SHUNT FED WING STRAKES

FIGURE 14

FREQ	θ	0	15	30	45	60	75	90	105	120	135	150	165	180	195	210	225	240	255	270	285	300	315	330	345	360
6.73	15	0.	0.	1.	1.	-3.	-1.	-3.	-4.	-5.	-5.	-3.	-1.	-1.	-1.	-1.	-3.	-4.	-4.	-4.	-4.	-3.	-2.	-1.	0.	0.
	25	1.	1.	1.	1.	1.	-1.	-3.	-4.	-5.	-4.	-2.	-1.	0.	-1.	-0.	-1.	-3.	-4.	-4.	-4.	-3.	-2.	-1.	1.	1.
	35	2.	1.	0.	-1.	-3.	-4.	-5	-6.	-5.	-4.	-2.	-1.	0.	-2.	-3.	-5.	-5.	-5.	-5.	-4.	-2.	0.	1.	1.	2.
	45	3.	2.	1.	-0.	-2.	-4.	-5.	-6.	-5.	-3.	-1.	0.	1.	0.	-1.	-2.	-4.	-5.	-6.	-5.	-4.	-1.	1.	2.	3.
	55	4.	3.	2.	0.	-2.	-5.	-7.	-8.	-6.	-2.	-1.	1.	2.	1.	0.	-1.	-4.	-6.	-6.	-5.	-2.	0.	2.	3.	4.
	65	4.	3.	2.	0.	-3.	-5.	-8.	-8.	-5.	-3.	0.	1.	2.	1.	0.	-2.	-4.	-6.	-7.	-5.	-3.	0.	2.	4.	4.
	75	4.	4.	2.	0.	-2.	-6.	-8.	-8.	-6.	-15.	0.	2.	2.	2.	1.	-2.	-4.	-6.	-7.	-5.	-2.	0.	3.	4.	5.
	85	4.	4.	2.	0.	-2.	-6.	-8.	-8.	-6.	-2.	0.	2.	2.	2.	1.	-1.	-4.	-7.	-7.	-4.	-2.	0.	3.	4.	5.
	95	4.	4.	2.	1.	-2.	-5.	-8.	-8.	-5.	-2.	0.	2.	2.	2.	0.	-2.	-5.	-7.	-7.	-6.	-3.	0.	2.	4.	4.
	105	4.	3.	3.	1.	-2.	-5.	-6.	-7.	-6.	-3.	0.	1.	2.	1.	0.	-2.	-5.	-8.	-8.	-6.	-3.	0.	2.	3.	4.
	115	4.	3.	2.	0.	-2.	-4.	-7.	-7.	-5.	-3.	-1.	0.	1.	1.	-1.	-3.	-6.	-7.	-9.	-6.	-3.	0.	2.	3.	4.
	125	3.	3.	2.	0.	-1.	-4.	-4.	-4.	-5.	-3.	-2.	0.	0.	0.	-1.	-3.	-3.	-7.	-7.	-6.	-3.	-1.	2.	3.	4.
	135	3.	3.	2.	1.	-2.	-3.	-4.	-4.	-4.	-3.	-1.	-1.	-1.	0.	-2.	-3.	-4.	-5.	-5.	-4.	-3.	-0.	1.	2.	3.
	145	3.	3.	2.	1.	-2.	-3.	-4.	-4.	-4.	-3.	-1.	-1.	-1.	0.	-2.	-3.	-4.	-5.	-5.	-4.	-3.	-0.	1.	2.	3.
	155	2.	2.	1.	-1.	-1.	-1.	-0.	-1.	-1.	-2.	-1.	0.	1.	0.	-0.	-1.	-2.	-2.	-2.	-2.	-1.	-1.	0.	2.	2.
	165	2.	2.	1.	-1.	-1.	-1.	-0.	-1.	-1.	-2.	-1.	0.	1.	0.	-0.	-1.	-2.	-2.	-2.	-2.	-1.	-1.	0.	2.	2.
9.5	15	0.	-1.	-1.	-1.	-2.	-1.		-2.	-2.	-2.	-2.	-2.	-2.	-2.	-2.	-4.	-5.	-5.	-5.	-5.	-4.	-3.	-1.	-1.	0.
	25	0.	-1.	-1.	-1.	-2.	-1.		-2.	-2.	-2.	-2.	-2.	-2.	-2.	-2.	-4.	-5.	-5.	-5.	-5.	-4.	-3.	-1.	-1.	0.
	35	2.	1.	1.	-0.	-1.	-2.	-3.	-2.	-2.	-2.	-0.	-1.	0.	-1.	-3.	-5.	-7.	-7.	-4.	-3.	-2.	0.	1.	2.	3.
	45	2.	1.	1.	-0.	-1.	-2.	-3.	-2.	-2.	-2.	-0.	-1.	0.	-1.	-3.	-5.	-7.	-10.	-6.	-3.	-2.	0.	1.	2.	3.
	55	3.	3.	2.	0.	-0.	-2.	-3.	-3.	-3.	-1.	0.	1.	1.	1.	-1.	-4.	-5.	-6.	-5.	-2.	0.	1.	2.	3.	4.
	65	3.	3.	3.	1.	0.	-2.	-3.	-3.	-2.	-1.	1.	2.	2.	1.	0.	-3.	-5.	-6.	-4.	-2.	1.	2.	3.	3.	4.
	75	4.	4.	3.	2.	1.	-1.	-3.	-4.	-3.	-1.	1.	2.	2.	2.	1.	-1.	-4.	-5.	-4.	-2.	0.	2.	3.	4.	5.
	85	4.	4.	3.	2.	1.	-1.	-3.	-3.	-2.	-1.	1.	2.	2.	2.	1.	-1.	-3.	-5.	-4.	-2.	0.	2.	3.	4.	5.
	95	4.	4.	3.	2.	1.	-1.	-3.	-4.	-3.	-1.	1.	2.	2.	2.	1.	-1.	-3.	-5.	-4.	-1.	1.	2.	3.	4.	5.
	105	4.	4.	3.	2.	0.	-1.	-4.	-4.	-20.	-1.	1.	2.	2.	2.	1.	-1.	-3.	-4.	-3.	-1.	1.	2.	3.	4.	5.
	115	4.	3.	3.	1.	0.	-3.	-4.	-4.	-4.	-2.	0.	1.	2.	2.	1.	-1.	-3.	-4.	-3.	-2.	0.	2.	3.	4.	5.
	125	3.	3.	2.	0.	-2.	-5.	-5.	-5.	-3.	-1.	0.	1.	2.	1.	0.	-2.	-3.	-9.	-9.	-0.	1.	2.	3.	3.	4.
	135	3.	3.	2.	-0.	-2.	-3.	-4.	-3.	-3.	-2.	-1.	0.	1.	0.	-1.	-3.	-3.	-4.	-2.	-1.	-0.	1.	2.	2.	3.
	145	3.	3.	2.	-0.	-2.	-3.	-4.	-3.	-3.	-2.	-1.	0.	1.	0.	-1.	-3.	-3.	-4.	-2.	-1.	-0.	1.	1.	2.	3.
	155	1.	1.	-1.	-2.	-3.	-3.	-3.	-2.	-3.	-2.	-1.	-1.	-1.	-2.	-2.	-4.	-4.	-3.	-2.	-2.	-1.	-0.	0.	1.	2.
	165	1.	1.	-1.	-2.	-3.	-3.	-3.	-2.	-3.	-2.	-1.	-1.	-1.	-2.	-2.	-4.	-4.	-3.	-2.	-2.	-1.	-0.	0.	1.	2.
11.6	15	7.	7.	7.	6.	5.	2.	-4.	-10.	-10.	-3.	2.	4.	4.	4.	2.	-2.	-7.	-13.	-7.	-1.	3.	5.	5.	6.	6.
	25	6.	7.	6.	6.	4.	1.	-3.	-7.	-8.	-4.	0.	3.	4.	3.	1.	-3.	-8.	-10.	-6.	-2.	2.	4.	5.	6.	6.
	35	7.	7.	6.	5.	4.	1.	-2.	-4.	-6.	-7.	-0.	2.	3.	3.	3.	-2.	-6.	-8.	-6.	-2.	1.	4.	5.	6.	7.
	45	7.	7.	6.	4.	3.	2.	1.	0.	-1.	0.	1.	2.	3.	3.	1.	-1.	-2.	-2.	-0.	1.	3.	4.	6.	7.	7.
	55	7.	7.	6.	4.	3.	2.	1.	0.	-1.	0.	1.	2.	3.	3.	1.	-1.	-2.	-2.	-0.	1.	3.	4.	6.	7.	7.
	65	6.	6.	5.	4.	3.	3.	3.	3.	-0.	2.	3.	3.	3.	3.	2.	1.	1.	3.	3.	7.	5.	5.	5.	5.	6.
	75	6.	6.	5.	4.	3.	3.	3.	2.	-0.	2.	3.	3.	3.	3.	2.	1.	1.	3.	3.	7.	5.	5.	5.	5.	6.
	85	6.	5.	4.	3.	3.	3.	2.	2.	-1.	1.	2.	4.	4.	4.	3.	1.	-0.	-1.	-2.	-1.	1.	3.	4.	4.	5.
	95	6.	5.	4.	3.	3.	3.	2.	2.	1.	2.	3.	4.	4.	4.	3.	1.	-1.	-1.	-1.	-3.	1.	3.	4.	4.	5.
	105	6.	6.	5.	4.	2.	0.	-2.	-2.	-2.	0.	3.	4.	5.	4.	2.	-1.	-4.	-4.	-3.	-1.	2.	4.	5.	6.	6.
	115	6.	6.	5.	4.	2.	0.	-2.	-2.	-2.	0.	3.	4.	5.	4.	2.	-1.	-4.	-4.	-8.	-2.	2.	4.	5.	6.	6.
	125	7.	7.	6.	5.	3.	-1.	-4.	-6.	-4.	0.	3.	5.	5.	4.	2.	-2.	-5.	-5.	-3.	1.	3.	5.	5.	7.	7.
	135	7.	7.	7.	6.	3.	-0.	-5.	-8.	-10.	0.	3.	5.	5.	4.	2.	-1.	-6.	-7.	-4.	1.	4.	5.	6.	7.	7.
	145	8.	8.	7.	7.	4.	1.	-6.	-13.	-8.	-1.	2.	5.	6.	5.	3.	-1.	-7.	-9.	-5.	0.	4.	6.	7.	7.	8.
	155	7.	7.	7.	6.	5.	1.	-4.	-12.	-11.	-2.	3.	5.	5.	5.	3.	-1.	-8.	-14.	-12.	0.	2.	5.	6.	7.	7.
	165	7.	7.	7.	6.	6.	3.	-4.	-12.	-11.	-2.	2.	4.	5.	4.	3.	-2.	-8.	-15.	-7.	0.	3.	5.	6.	7.	7.

DIRECTIVITY DATA FOR SHORT FED WIRE STRAKES

FREQ	θ	φ																					
								105						210	225	240							
13.5	15	-1.	-1.	-1.	-1.	-2.	-2.	-1.	-1.	-2.	-3.	-3.	-2.	-1.	-1.			-2.	-2.	-2.	-2.	-1.	-1.	-1.	-1.
	25	-1.	-1.	-1.	-2.	-2.	-2.	-1.	-1.	-2.	-3.	-3.	-2.	-1.	-1.			-1.	-2.	-2.	-2.	-2.	-1.	-1.	-1.
	35	-1.	-2.	-1.	-1.	-0.	0.	-0.	-1.	-3.	-3.	-3.	-3.	-2.	-2.	-3.	-3.	-2.	-2.	-2.	-1.	-1.	0.	-1.	-1.
	45	-1.	-2.	-1.	-1.	-0.	0.	-0.	-1.	-3.	-2.	-3.	-3.	-2.	-2.	-3.	-3.	-2.	-2.	-2.	-1.	-1.	0.	-1.	-1.
	55	-2.	-2.	-1.	0.	1.	1.	1.	-1.	-3.	-3.	-5.	-4.	-3.	-4.	-5.	-5.	-4.	-4.	-2.	1.	2.	2.	1.	0.	-1.
	65	-2.	-2.	0.	1.	3.	3.	2.	-0.	-4.	-7.	-7.	-5.	-3.	-5.	-7.	-8.	-7.	-8.	-4.	-0.	2.	3.	3.	2.	1.	-1.
	75	-1.	-1.	1.	3.	4.	4.	3.	1.	-4.	-9.	-10.	-7.	-4.	-5.	-8.	-10.	-6.	-1.	2.	4.	4.	3.	4.	0.
	85	0.	0.	0.	1.	2.	5.	5.	4.	1.	-4.	-10.	-13.	-6.	-6.	-9.	-12.	-7.	-2.	2.	4.	4.	3.	2.	0.
	95	-1.	0.	2.	4.	5.	5.	3.	0.	-5.	-13.	-14.	-8.	-6.	-7.	-10.	-12.	-5.	0.	3.	4.	4.	3.	1.	0.
	105	-1.	0.	2.	4.	5.	5.	3.	-1.	-6.	-16.	-15.	-9.	-7.	-8.	-10.	-11.	-5.	0.	2.	4.	3.	2.	1.	-1.
	115	-1.	-1.	1.	3.	4.	4.	2.	-1.	-7.	-13.	-12.	-8.	-7.	-7.	-8.	-8.	-4.	0.	2.	3.	3.	2.	0.	-1.
	125	-2.	-1.	1.	2.	3.	3.	1.	-2.	-8.	-10.	-10.	-7.	-6.	-6.	-7.	-6.	-3.	-0.	2.	3.	2.	1.	0.	-1.
	135	-1.	0.	0.	2.	2.	1.	-0.	-2.	-5.	-7.	-8.	-6.	-4.	-2.	-2.	-1.	-1.	1.	1.	2.	2.	2.	1.	0.
	145	-1.	0.	0.	2.	2.	1.	-0.	-2.	-5.	-4.	-4.	-4.	-7.	-5.	-1.	1.	2.	2.	2.	2.	1.	1.	1.	0.
	155	2.	1.	1.	0.	-0.	-1.	-2.	-3.	-4.	-5.	-5.	-3.	-1.	-0.	-0.	-0.	-0.	-0.	-1.	-1.	-0.	0.	1.	2.	1.
	165	2.	1.	1.	0.	-0.	-1.	-2.	-3.	-4.	-5.	-5.	-3.	-1.	-0.	-0.	-0.	-0.	-0.	-1.	-1.	-0.	0.	1.	2.	1.
19.0	15	-7.	-7.	-7.	-6.	-4.	-3.	-3.	-3.	-3.	-4.	-5.	-5.	-4.	-4.	-5.	-4.	-3.	-3.	-3.	-3.	-4.	-5.	-7.	-6.
	25	-7.	-7.	-7.	-6.	-4.	-3.	-3.	-3.	-3.	-4.	-5.	-5.	-4.	-4.	-5.	-4.	-3.	-3.	-3.	-3.	-4.	-5.	-7.	-6.
	35	-4.	-4.	-4.	-3.	-0.	1.	2.	-0.	-1.	-3.	-4.	-3.	-3.	-3.	-4.	-3.	-1.	1.	2.	1.	-2.	-4.	-4.	-5.
	45	-4.	-4.	-4.	-3.	-0.	1.	2.	-0.	-1.	-3.	-4.	-3.	-3.	-3.	-4.	-3.	-1.	1.	2.	1.	-2.	-4.	-5.	-5.
	55	-1.	-2.	-4.	-2.	1.	3.	4.	3.	-0.	-3.	-4.	-16.	-3.	-4.	-4.	-3.	-0.	2.	3.	1.	-1.	-5.	-4.	-3.
	65	-1.	-1.	-3.	-2.	2.	5.	5.	4.	1.	-3.	-5.	-4.	-3.	-4.	-5.	-3.	0.	3.	4.	2.	0.	-5.	-5.	-2.
	75	-1.	-2.	-3.	-2.	2.	5.	5.	4.	1.	-3.	-5.	-4.	-3.	-4.	-6.	-4.	1.	4.	4.	3.	-2.	-3.	-3.	-2.
	85	-1.	-2.	-2.	-2.	2.	5.	5.	4.	1.	-4.	-5.	-4.	-2.	-3.	-5.	-4.	1.	4.	5.	4.	-1.	-5.	-5.	-3.
	95	-1.	-2.	-4.	-2.	2.	5.	5.	4.	0.	-4.	-5.	-3.	-1.	-3.	-5.	-4.	1.	4.	5.	4.	0.	-4.	-5.	-3.
	105	-1.	-2.	-3.	-2.	2.	4.	5.	3.	0.	-4.	-5.	-3.	-2.	-3.	-5.	-4.	1.	4.	5.	3.	0.	-3.	-4.	-2.
	115	-1.	-2.	-3.	-2.	2.	4.	4.	3.	1.	-3.	-4.	-4.	-3.	-4.	-6.	-4.	-1.	3.	4.	3.	0.	-3.	-4.	-2.
	125	-1.	-2.	-3.	-2.	1.	4.	4.	3.	1.	-2.	-4.	-4.	-5.	-6.	-6.	-4.	-0.	2.	3.	3.	-1.	-3.	-4.	-3.
	135	-4.	-4.	-4.	-2.	0.	2.	2.	2.	0.	-2.	-4.	-6.	-6.	-6.	-5.	-4.	-1.	1.	2.	1.	-1.	-2.	-4.	-5.
	145	-4.	-5.	-3.	0.	2.	2.	1.	-1.	-2.	-2.	-3.	-5.	-7.	-9.	-5.	-1.		3.	1.	-1.	-3.	-4.	-4.	-5.
	155	-4.	-5.	-5.	-4.	-3.	-2.	-1.	-1.	-1.	-2.	-5.	-6.	-5.	-5.	-5.	-3.	-2.	-3.	-1.	-2.	-1.	-2.	-3.	-4.
	165	-4.	-5.	-5.	-4.	-3.	-2.	-1.	-1.	-1.	-2.	-5.	-6.	-5.	-5.	-5.	-3.	-2.	-3.	-1.	-2.	-1.	-2.	-4.	-4.
26.9	15	3.	2.	0.	0.	1.	1.	0.	0.	-0.	-1.	-2.	-3.	-3.	-3.	-2.	-1.	-1.	-1.	-0.	1.	1.	2.	4.	4.
	25	3.	2.	0.	0.	1.	1.	0.	0.	-0.	-1.	-2.	-3.	-3.	-3.	-2.	-1.	-1.	-1.	-0.	1.	1.	2.	4.	3.
	35	4.	4.	2.	1.	-1.	-0.	1.	1.	0.	-2.	-3.	-3.	-2.	-2.	-2.	-1.	-0.	0.	-0.	-0.	1.	3.	4.	4.
	45	4.	4.	2.	1.	-1.	-0.	1.	1.	0.	-2.	-3.	-3.	-2.	-2.	-2.	-1.	-0.	0.	-0.	-0.	1.	3.	4.	4.
	55	3.	2.	0.	-2.	-4.	-1.	1.	2.	1.	-2.	-3.	-3.	-2.	-4.	-4.	-1.	1.	1.	-2.	-3.	-1.	1.	2.	3.
	65	2.	1.	0.	-3.	-6.	-2.	1.	1.	0.	-5.	-6.	-4.	-3.	-6.	-7.	-2.	1.	1.	-3.	-6.	-5.	-1.	1.	1.
	75	1.	1.	1.	-5.	-8.	-5.	-1.	1.	-1.	-7.	-8.	-4.	-1.	-3.	-8.	-5.	0.	1.	-1.	-7.	-6.	-2.	0.	1.
	85	2.	2.	-1.	-4.	-10.	-7.	-1.	1.	-1.	-6.	-8.	-3.	-1.	-2.	-7.	-4.	1.	2.	-1.	-7.	-6.	-1.	1.	2.
	95	1.	0.	0.	-6.	-11.	-7.	-1.	1.	0.	-5.	-8.	-5.	-4.	-5.	-8.	-3.	1.	2.	-2.	-8.	-7.	-2.	0.	1.
	105	-1.	-2.	-4.	-7.	-10.	-6.	-1.	1.	0.	-5.	-9.	-7.	-5.	-8.	-10.	-4.	0.	1.	-1.	-6.	-8.	-4.	-2.	-1.
	115	-1.	-1.	-3.	-6.	-7.	-5.	-1.	0.	-1.	-4.	-7.	-6.	-3.	-5.	-8.	-6.	-1.	1.	-1.	-5.	-5.	-5.	-3.	-1.
	125	1.	0.	-2.	-5.	-6.	-5.	-2.	-1.	-2.	-4.	-6.	-4.	-3.	-4.	-6.	-5.	-1.	0.	-1.	-3.	-4.	-2.	0.	1.
	135	1.	0.	-2.	-4.	-6.	-4.	-3.	-1.	-1.	-1.	-3.	-4.	-5.	-6.	-7.	-5.	-3.	-1.	-1.	-4.	-4.	-3.	-1.	1.
	145	1.	0.	-2.	-4.	-6.	-4.	-3.	-1.	-1.	-1.	-3.	-4.	-5.	-6.	-7.	-5.	-3.	-1.	-1.	-4.	-4.	-3.	-1.	1.
	155	4.	3.	2.	2.	2.	2.	2.	2.	2.	2.	2.	1.	0.	0.	0.	-1.	-0.	1.	2.	1.	2.	2.	2.	3.	3.
	165	4.	3.	2.	2.	2.	2.	2.	2.	2.	2.	2.	1.	0.	0.	0.	-1.	-0.	1.	2.	1.	2.	2.	2.	3.	3.

DIRECTIVE GAIN FOR SHUNT FED WIRE STRAKES

FIGURE 16

AIRPLANE ELEVATION ANGLE-Θ (DEGREES)	FREQUENCY (MEGACYCLES)										
	0.00 TO 2.00	2.10 TO 2.80	2.90 TO 4.00	4.10 TO 5.60	5.70 TO 8.00	8.10 TO 11.3	11.4 TO 16.C	16.1 TO 22.6	22.7 YO 32.0	32.1 TO INFINITY	TOTALS
0 - 32	12 12 0 0	60 60 0 0	609 609 0 0	1322 981 336 5	808 672 136 0	240 240 0 0	0 0 0 0	0 0 0 0	0 0 0 0	0 0 0 0	3051
33 - 47	12 12 0 0	58 58 0 0	749 744 5 0	994 964 30 0	741 741 0 0	326 326 0 0	11 11 0 0	0 0 0 0	0 0 0 0	0 0 0 0	2891
48 - 59	14 14 0 0	52 52 0 0	673 652 21 0	931 898 33 0	848 843 5 0	506 505 1 0	193 193 0 0	0 0 0 0	0 0 0 0	0 0 0 0	3217
60 - 69	0 0 0 0	15 12 3 0	226 162 64 0	1329 985 344 0	1095 980 83 32	783 732 51 0	465 426 39 0	0 0 0 0	0 0 0 0	0 0 0 0	3913
70 - 79	0 0 0 0	10 10 0 0	47 21 26 0	418 220 198 0	1016 568 434 14	1295 678 537 90	725 407 246 70	85 85 0 0	0 0 0 0	0 0 0 0	3596
80 - 90	0 0 0 0	12 9 3 0	11 6 5 0	12 0 12 0	80 8 72 0	339 178 159 2	930 309 582 39	92 33 59 0	0 0 0 0	0 0 0 0	1476
TOTALS	38	207	2315	5006	4588	3489	2324	177	0	0	18144

In each square the four numbers reading from top to bottom are the total number of circuits, the number of circuits having a reliability greater than 90, 50, and 25 percent respectively for a

ELEVATION ANGLE θ (DEGREES)	0.00 TO 2.00	2.10 TO 2.80	2.90 TO 4.00	4.10 TO 5.60	5.70 TO 8.00	8.10 TO 11.3	11.4 TO 16.0	16.1 TO 22.6	22.7 TO 32.0	32.1 TO INFINITY	TOTAL EVENTS
0-32	12	60	609	1322	808	240	0	0	0	0	3051
	12	60	597	891	617	240	0	0	0	0	
	0	0	12	112	102	0	0	0	0	0	
	0	0	0	255	89	0	0	0	0	0	
33-47	12	58	749	994	741	326	11	0	0	0	2891
	12	58	688	869	737	326	11	0	0	0	
	0	0	49	97	4	0	0	0	0	0	
	0	0	12	28	0	0	0	0	0	0	
48-49	14	52	673	931	848	506	193	0	0	0	3217
	14	47	444	733	801	506	190	0	0	0	
	0	5	200	181	40	0	3	0	0	0	
	0	0	29	17	7	0	0	0	0	0	
60-69	0	15	226	1329	1095	783	465	0	0	0	3913
	0	10	73	449	750	682	413	0	0	0	
	0	5	97	554	241	64	32	0	0	0	
	0	0	56	320	36	37	20	0	0	0	
70-79	0	10	47	418	1016	1295	725	85	0	0	3596
	0	6	2	53	329	458	283	85	0	0	
	0	3	27	153	257	241	93	0	0	0	
	0	1	16	193	342	399	206	0	0	0	
80-90	0	12	11	12	80	339	930	92	0	0	1476
	0	6	0	0	0	85	72	16	0	0	
	0	3	5	0	13	85	102	17	0	0	
	0	2	5	4	65	132	467	57	0	0	
TOTALS	38	207	2315	5006	4588	3489	2324	177	0	0	18144

In each square the four numbers reading from top to bottom are the total number of circuits, the number of circuits having a reliability greater than 90, 50, and 25 percent respectively for a carrier power of 100 watts, a required one cps band SNR of 38 db and a west airplane heading.

Circuit Reliability Distribution (100 to 700 N.M.) for the Notch Antenna

FIGURE 18

AIRPLANE ELEVATION ANGLE θ (DEGREES)	FREQUENCY (MEGACYCLES)										
	0.00 TO 2.00	2.10 TO 2.80	2.90 TO 4.00	4.10 TO 5.60	5.70 TO 8.00	8.10 TO 11.3	11.4 TO 16.0	16.1 TO 22.6	22.7 TO 32.0	32.1 TO INFINITY	TOTALS
0-32	12 12 0 0	60 60 0 0	609 609 0 0	1322 1306 16 0	808 808 0 0	240 240 0 0	0 0 0 0	0 0 0 0	0 0 0 0	0 0 0 0	3051
33-47	12 12 0 0	58 58 0 0	749 749 0 0	994 994 0 0	741 741 0 0	326 326 0 0	11 11 0 0	0 0 0 0	0 0 0 0	0 0 0 0	2891
48-59	14 14 0 0	52 52 0 0	673 673 0 0	931 931 0 0	848 848 0 0	506 506 0 0	193 193 0 0	0 0 0 0	0 0 0 0	0 0 0 0	3217
60-69	0 0 0 0	15 15 0 0	226 226 0 0	1329 1329 0 0	1095 1063 23 9	783 783 0 0	465 465 0 0	0 0 0 0	0 0 0 0	0 0 0 0	3913
70-79	0 0 0 0	10 10 0 0	47 47 0 0	418 411 7 0	1016 1001 15 0	1295 1258 35 2	725 690 28 7	85 85 0 0	0 0 0 0	0 0 0 0	3598
80-90	0 0 0 0	12 12 0 0	11 11 0 0	12 11 1 0	80 72 8 0	339 333 6 0	930 927 3 0	92 92 0 0	0 0 0 0	0 0 0 0	1476
TOTALS	38	207	2315	5006	4588	3489	2324	177	0	0	18144

In each square the four numbers reading from top to bottom are the total number of circuits, the number of circuits having a reliability greater than 95, 90, and 70 percent respectively, for a carrier power of 1200 watts and a required one cps band SNR of 38 db.

Circuit Reliability Distribution (100 to 700 N.M.) for the Notch Antenna

FIGURE 10

ELEVATION ANGLE θ (DEGREES)	FREQUENCY (MEGACYCLES) 0.00 TO 2.00	2.10 TO 2.80	2.90 TO 4.00	4.10 TO 5.60	5.70 TO 8.00	8.10 TO 11.3	11.4 TO 16.0	16.1 TO 22.6	22.7 TO 32.0	32.1 TO INFINITY	TOTALS
0-32	12 12 0 0	60 60 0 0	609 609 0 0	1322 1011 179 118	808 708 97 3	240 240 0 0	0 0 0 0	0 0 0 0	0 0 0 0	0 0 0 0	3051
33-47	12 12 0 0	58 58 0 0	749 743 6 0	994 961 33 0	741 741 0 0	326 326 0 0	11 11 0 0	0 0 0 0	0 0 0 0	0 0 0 0	2891
48-59	14 14 0 0	52 52 0 0	673 665 8 0	931 908 23 0	848 847 1 0	506 506 0 0	193 193 0 0	0 0 0 0	0 0 0 0	0 0 0 0	3217
60-69	0 0 0 0	15 15 0 0	226 219 7 0	1329 1279 50 0	1095 1021 5 50	783 777 5 1	465 464 1 0	0 0 0 0	0 0 0 0	0 0 0 0	3913
70-79	0 0 0 0	10 10 0 0	47 42 5 0	418 356 52 10	1016 776 176 64	1295 1016 146 130	725 583 71 60	85 85 0 0	0 0 0 0	0 0 0 0	3596
80-90	0 0 0 0	12 12 0 0	11 10 1 0	12 1 5 6	80 15 63 2	339 281 48 10	930 591 204 134	92 73 17 2	0 0 0 0	0 0 0 0	1476
TOTALS	38	207	2315	5006	4588	3489	2324	177	0	0	18144

In each square the four numbers reading from top to bottom are the total number of circuits, the number of circuits having a reliability greater than 95, 90, and 70 percent respectively, for a carrier power of 200 watts and a required one cps band SNR of 30 db.

Circuit Reliability Distribution (100 to 700 N.M.) for a Combined Notch-Shunt Antenna Pattern

FIGURE 20

AIRPLANE ELEVATION ANGLE θ (DEGREES)	FREQUENCY (MEGACYCLES)										
	0.00 TO 2.00	2.10 TO 2.80	2.90 TO 4.00	4.10 TO 5.60	5.70 TO 8.00	8.10 TO 11.3	11.4 TO 16.0	16.1 TO 22.6	22.7 TO 32.0	32.1 TO INFINITY	TOTALS
0-32	0 0 0 0	75 75 0 0	289 288 1 0	810 673 137 0	31 31 0 0	0 0 0 0	0 0 0 0	0 0 0 0	0 0 0 0	0 0 0 0	1205
33-47	6 6 0 0	203 203 0 0	656 653 3 0	605 605 0 0	325 325 0 0	202 202 0 0	7 7 0 0	0 0 0 0	0 0 0 0	0 0 0 0	2004
48-59	0 0 0 0	160 151 9 0	645 631 14 0	619 613 6 0	371 371 0 0	102 102 0 0	71 71 0 0	0 0 0 0	0 0 0 0	0 0 0 0	1968
60-69	0 0 0 0	6 4 2 0	420 351 69 0	859 735 124 0	774 707 67 0	272 272 0 0	140 140 0 0	0 0 0 0	0 0 0 0	0 0 0 0	2471
70-79	0 0 0 0	2 2 0 0	167 118 46 3	1101 868 228 5	1860 1572 284 4	1960 1681 279 0	724 673 51 0	242 238 4 0	11 11 0 0	0 0 0 0	6067
80-90	0 0 0 0	10 10 0 0	17 17 0 0	483 245 211 27	2304 1731 505 67	4151 3357 746 38	6926 4891 1452 160	2757 2372 343 7	719 638 3 0	22 0 0 0	17389
TOTALS	6	456	2194	4477	5665	6687	7868	2999	730	22	31104

In each square the four numbers reading from top to bottom are the total number of circuits, the number of circuits having a reliability greater than 90, 70, and 50 percent respectively, for a carrier power of 250 watts and a required one cps band SNR of 35 db.

Circuit Reliability Distribution (200 to 1800 N.M.) for an Isotropic Transmitting Antenna

TABLE 2

Conditions for Circuit Reliability Calculations

	Short Range (100 to 700 N.M.)		Long Range 200 to 1800 N.	
Locations:	**Latitude**	**Longitude**	**Latitude**	**Longitude**
	15 N	105 E	40 N	73 W
	36 N	52 E	48 N	2 E
	48 N	12 E	51 N	27 W
	30 N	80 W	37 N	25 W
	35 N	68 W	65 N	148 W
	33 N	107 W	59 N	18 E
			49 N	54 W
			64 N	22 W
Directions:	12 in 30 degree increments		12 in 30 degree increm	
Distance Increments:	7 at 100 N.M. Each		9 at 200 N.M. Each	
Times of Day:	0200 - 0600 - 1000 1400 - 1800 - 2200		0200 - 0600 - 1000 1400 - 1800 - 2200	
Seasons:	January and July		January and July	
Man-Made Noise:	Rural		Remote	
Required SNR:	38 db in 1 CPS Band		35 db in 1 CPS Band	
Sunspot Numbers:	10, 50 and 130		10, 50 and 130	
Antenna:	Stabilizer Notch and Wing Strake Shunts		Omni-directional Zero db gain	
Airplane Heading:	North and West		North	
Carrier Power:	100, 200, and 1200 watts		250 watts	
Total Circuits Each Condition:	18,144		31,104	

A NEW CLASS OF ELECTRICALLY SMALL ANTENNAS

by

Richard C. Fenwick
Collins Radio Company
Dallas, Texas

Presented at the Fourteenth Annual Symposium
on USAF Antenna Research and Development

University of Illinois
6-8 October 1964

A NEW CLASS OF ELECTRICALLY SMALL ANTENNAS

by Richard C. Fenwick
Collins Radio Company
Space Systems and Antennas Division
Dallas, Texas

ABSTRACT

This paper describes a new class of electrically small antennas which incorporate resonant, half wave windings. The principal advantages of these antennas are the resistive input impedance and the radiation resistance transformation which may be obtained within the structure. A simple transmission line theory is presented, by which antenna efficiency and bandwidth may be calculated to a useful accuracy. Experimental methods and results are described for antennas in the order of .01 wavelength in height and .05 wavelength in diameter.

INTRODUCTION

One form of electrically short antenna which has been commonly used in the past in a variety of configurations is a transmission line fed against a ground plane, as shown in Figure 1.

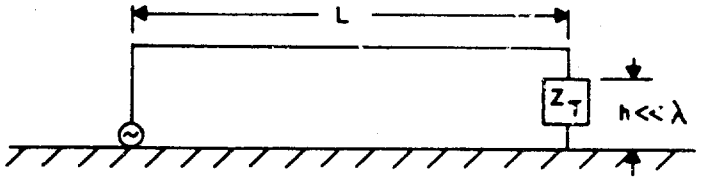

Figure 1. Basic electrically small antenna structure

The terminating impedance Z_T, is frequently an open circuit, and L is approximately a quarter wave long to give a resonant input impedance. Also, Z_T is often a capacitance, tunable to obtain a resonant input over a band of frequencies. In other instances Z_T is a short circuit, and L is a quarter wave long or less, so that an anti-resonant input is obtained over a band of frequencies by tuning a shunt capacitance at the feedpoint. This configuration is sometimes called a "strap antenna." The tuning range can be extended by shorting the transmission line with relays. Another condition is that where Z_T is a short circuit and L is of proper length,

approximately a half wave, so that the input is resonant. Such a structure is shown in Figure 2, with its current distribution. Note that the currents in the vertical members are equal in amplitude and in space phase.

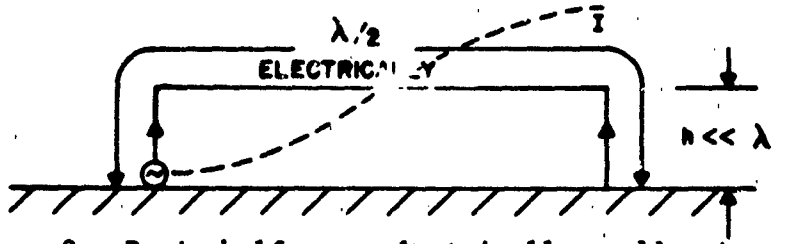

Figure 2. Basic half wave electrically small antenna

This antenna offers several advantages over the quarter wave open circuited structure, the principal one being the possibility of obtaining a large radiation resistance transformation at the input.

The structure of Figure 2 radiates a predominantly vertically polarized wave, due to the phase reversal in the horizontal conductor. The azimuthal pattern is bidirectional, in directions perpendicular to the plane of the structure. If the horizontal conductor is wound up in some manner parallel to the ground plan so that the vertical leads are brought within a quarter wavelength or so of each other, the azimuthal radiation patterns will be substantially omnidirectional. In addition, the overall dimensions of the structure can be substantially reduced by the winding technique without necessarily affecting the electrical properties of the antenna. Such wound, half wave structures are the subject of this paper. Figure 3 illustrates one form that the winding may take.

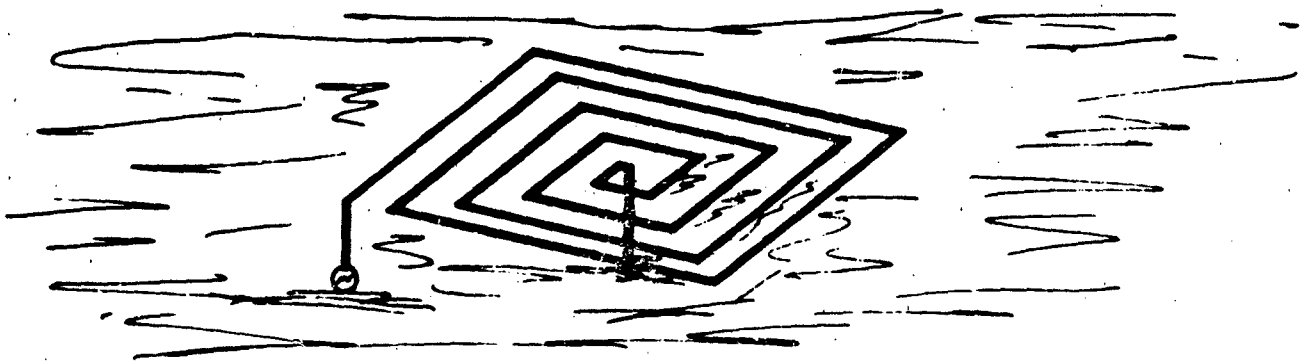

Figure 3. Electrically small antenna with simple flat spiral winding, an electrical half wave long

THEORETICAL MODEL

Even though the transmission line connecting the two vertical radiators is wound up, hence coupled to itself, it has been found satisfactory to consider that for a uniform winding a unique characteristic impedance Z_o for the transmission line exists. The value of Z_o depends on the coupling, of course, and is not strictly constant along the winding in many configurations, including that of Figure 3.

From an impedance transformation standpoint it is advantageous to employ two quarter wave resonant windings in series of different characteristic impedance in place of a uniform half wave winding. Figure 4 shows the transmission line

equivalent circuit applicable to all configurations employing planar windings.

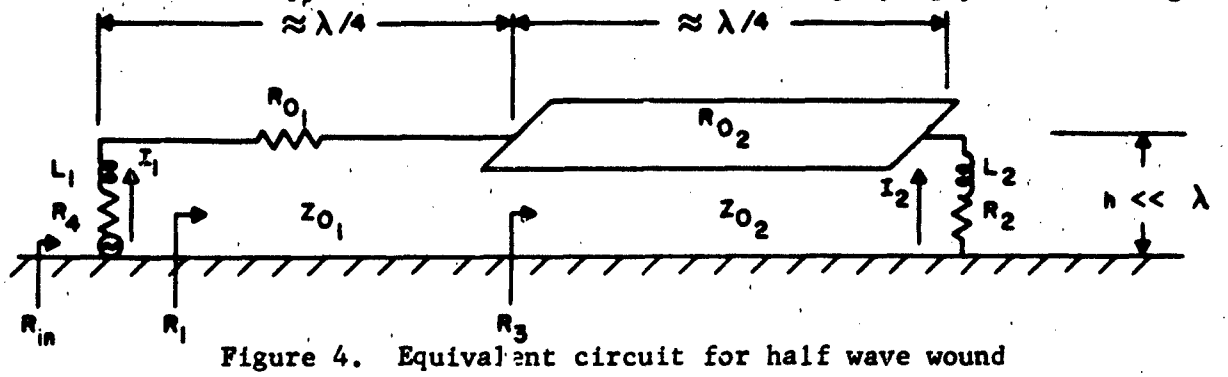

Figure 4. Equivalent circuit for half wave wound electrically small antennas

For purposes of the following analysis the vertical members in Figure 4 are considered to be closely coupled, and the transmission line between these members is wound so that the over-all width of the structure is much less than a half wave. Physical length of the winding required for resonance depends on the winding configuration. As an example, approximately a length 15% greater than a half wave is required for antennas .01λ high and .04λ diameter, provided that the conductor width is small in relation to the spacing between adjacent conductors. Length is closer to a half wave for larger diameter. Resistances R_{o_1} and R_{o_2} represent dissipative losses in the winding, the ground plane is considered lossless, and R_2 and R_4 are radiation resistances. Radiation resistance of the winding itself is considered negligible. Inductances L_1 and L_2 are considered to affect only the required winding length for resonance.

By familiar transmission line relationships for lossless quarterwave transformers,

$$Z_{o_2'} = \sqrt{R_3 R_2}\,, \quad \text{whence } R_3 = \frac{Z_{o_2}^2}{R_2};$$

similarly, $$R_1 = \frac{Z_{o_1}^2}{R_3}\,, \quad \text{whence } R_1 = \frac{Z_{o_1}^2}{Z_{o_2}^2} R_2. \quad \text{Thus, } R_{in} = R_4 + \frac{Z_{o_1}^2}{Z_{o_2}^2} R_2.$$

It readily follows from a consideration of the power distribution in the equivalent circuit that $I_2 = \frac{Z_{o_1}}{Z_{o_2}} I_1$. The same result is obtained if dissipative losses are relatively low. In the lossless case, all the input power is radiated, so $P_{in} = (I_1 + I_2)^2 R_r = I_1^2 R_{in}$, where R_r is the radiation resistance, given by

$$R_r \cong 1600 \left(\frac{h}{\lambda}\right)^2$$

assuming uniform current in the vertical leads. Substituting for I_2, we find that

$$\boxed{R_{in} = \left(1 + \frac{Z_{o_1}}{Z_{o_2}}\right)^2 R_r} \quad \text{(lossless case)}$$

Note that if $Z_{o_1} = Z_{o_2}$ (uniform winding), $R_{in} = 4R_r$ regardless of the value of Z_o. Note also that R_{in} can be made very much greater than the radiation resistance by making $Z_{o_1} >> Z_{o_2}$. As the ratio of the characteristic impedances becomes large, it is necessary that each transmission line be very nearly an electrical quarter wave in length, or the expected input resistance will not be realized.

Now consider the effect of losses. If the current in each quarter wave section is sinusoidal, the effective loss resistance of each section referred to the point of current maximum is one half the total resistance of that section. Since the current maxima presumably occur at the vertical leads, the total dissipation is

$$P_d = \frac{I_1^2 R_{o_1}}{2} + \frac{I_2^2 R_{o_2}}{2} = I_1^2 \left[\frac{R_{o_1}}{2} + \frac{R_{o_2}}{2} \left(\frac{Z_{o_1}}{Z_{o_2}} \right)^2 \right]$$

so the loss resistance referred to the input terminals is

$$R_{o_{input}} = \frac{R_{o_1}}{2} + \frac{R_{o_2}}{2} \left(\frac{Z_{o_1}}{Z_{o_2}} \right)^2$$

The total input resistance is thus

$$\boxed{R_{in} = \left(1 + \frac{Z_{o_1}}{Z_{o_2}} \right)^2 R_r + \frac{R_{o_1}}{2} + \frac{R_{o_2}}{2} \left(\frac{Z_{o_1}}{Z_{o_2}} \right)^2} \quad \text{(includes loss)}$$

The radiation efficiency is simply given by the first term divided by R_{in}. For some purposes it is desirable to know the values of R_2 and R_4 in the equivalent circuit. Without going through the calculations,

$$R_2 = \left(1 + \frac{Z_{o_2}}{Z_{o_1}} \right) R_r \text{ and } R_4 = \left(1 + \frac{Z_{o_1}}{Z_{o_2}} \right) R_r$$

An expression for the bandwidth can be readily calculated for the circuit of Figure 4 for the case where $Z_{o_1} = Z_{o_2}$. The result is

$$\boxed{\text{Bandwidth} = \frac{2 R_{in} f_o}{Z_o \pi}} \left(Z_{o_1} = Z_{o_2} \right)$$

where f_o is the resonant frequency and bandwidth is understood as that between frequencies of equal resistance and reactance. Note that the bandwidth is inversely proportional to Z_o. Low values of Z_o imply large conductor widths and spacings, hence large winding areas. Thus, increased bandwidth implies greater antenna

volume. This seems to be a fundamental property of small antennas.

The voltage in the center of the half wave winding can be quite large. Assuming a sinusoidal distribution on the winding,

$$\frac{V_{max}}{V_{input}} = \frac{Z_{o_1}}{R_{in}} \sqrt{\frac{R_1 - \frac{R_{o_1}}{2}}{R_1 + \frac{R_{o_1}}{2}}} \cong \frac{Z_{o_1}}{R_{in}} \quad \text{usually,}$$

where $$R_1 = \left(\frac{Z_{o_1}}{Z_{o_2}}\right)^2 \left(R_2 + \frac{R_{o_2}}{2}\right) = \left(\frac{Z_{o_1}}{Z_{o_2}}\right)^2 \left[\left(1 + \frac{Z_{o_2}}{Z_{o_1}}\right) R_r + \frac{R_{o_2}}{2}\right].$$

DETERMINATION OF CHARACTERISTIC IMPEDANCES

An interesting feature of the transmission line approach to the analysis is that the impedance transformations of the windings can be determined experimentally simply by using known resistances as "loads" and then measuring the input resistance. The value of $\frac{Z_{o_1}}{Z_{o_2}}$ can be found from the relation

$$\frac{Z_{o_1}}{Z_{o_2}} = \sqrt{\frac{R_{in_1} - R_{in_2}}{R_{L_1} - R_{L_2}}}$$

where R_{in_1} and R_{in_2} are the input resistances with loads R_{L_1} and R_{L_2} respectively placed at the normally grounded end of the half wave winding.

The characteristic impedances can be determined to a useful accuracy by calculating the capacitance per foot and inductance per foot of the winding. Then $Z_o = \sqrt{\frac{L}{C}}$. The value of C is found by calculating the capacitance of an equivalent wire grid containing the same length of wires and wire spacing as the winding, and then dividing by the length of the winding. The capacitance of the grid is found by standard handbook techniques. The average inductance is determined by calculating the inductance for the middle of the winding, taking into account the mutual inductances of the nearby wires. Again, standard handbook formulas are used.

TUNING AND MATCHING SCHEMES

The simplest arrangement for obtaining a resonant input over a wide band is shown schematically in Figure 5.

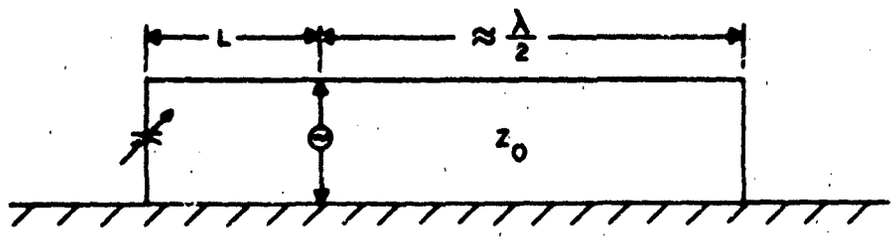

Figure 5. Simplest arrangement for tuning over a wide band, schematically

The only purpose of the variable capacitor is to prevent length L from being res This would cause an impedance discontinuity at the input. A switch can be substituted for the capacitor. The tuning arrangement of Figure 6 allows a grea input resistance than can be obtained with a uniform Z_o.

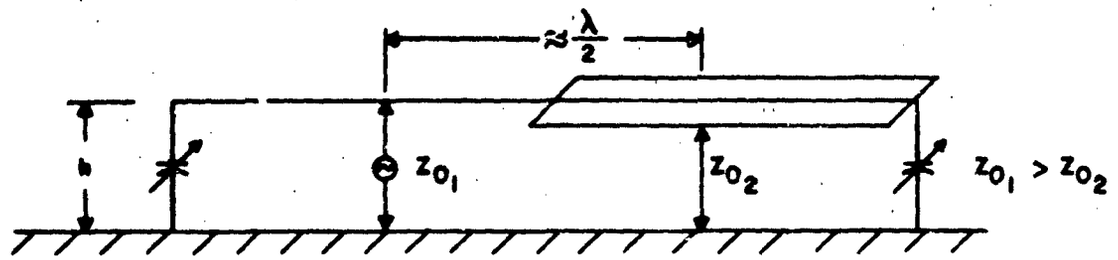

Figure 6. Tuning arrangement where $Z_{o_2} \neq Z_{o_1}$, giving greater input resistance

Even if $\frac{h}{\lambda}$ is as small as .01, sufficiently large input resistances can be obtained by the latter arrangement to allow use of an autotransformer to match the input to usual transmission lines. For example, if $\frac{h}{\lambda} = .01$, $R_r \cong 1600\left(\frac{h}{\lambda}\right)^2$ = .16 ohm. If $\frac{Z_{o_1}}{Z_{o_2}} = 3$ is achieved, and there are no dissipative losses,

$$R_{in} = \left(1 + \frac{Z_{o_1}}{Z_{o_2}}\right)^2 R_r = 16R_r = 2.56 \text{ ohms.}$$

If the structure is 50% efficient, the input resistance is 5.12 ohms. If the structure were converted into a top loaded vertical monopole by shorting out all the "turns" and opening the grounded end, the input resistance would be only .32 oh for 50% efficiency.

PLANAR WINDING CONFIGURATIONS

Up to this point specific winding designs have been scarcely mentioned, for a reason. This being that the number of possible winding configurations are

legion. The type of antenna being described is truly a wirebender's delight. It is initially surprising that such a divergence of structures can give such similar impedance and radiation properties. It is not surprising that some of the members of this wide class of structures have been used in the past.

Some winding configurations are preferrable to others, of course. Figure 7 shows top views of three windings, and their resonant frequencies. Each was 3 x 3 feet, located 8 inches above a ground plane, and containing 42 feet of wire.

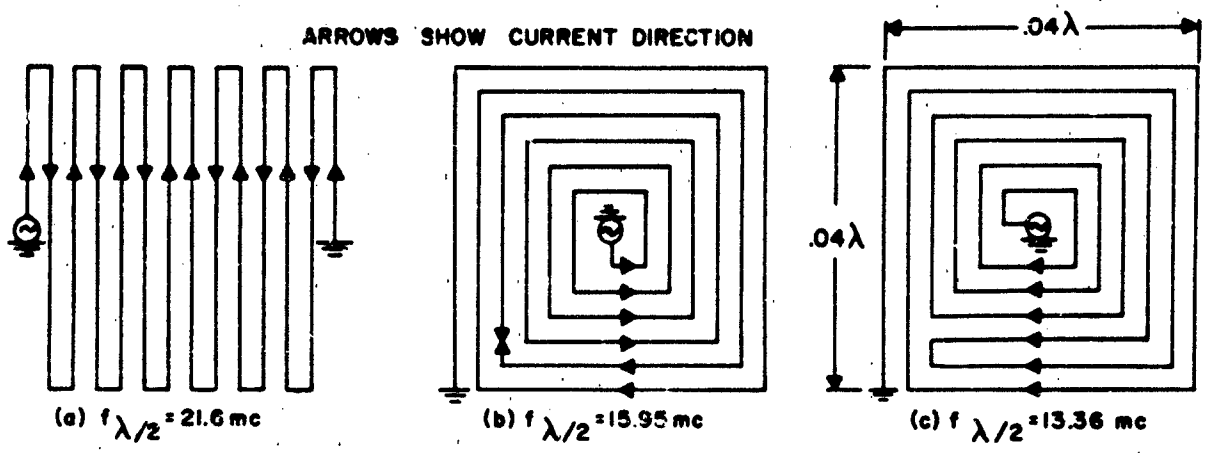

Figure 7. Three windings of same dimensions and containing the same length of wire, with their resonant frequencies

In winding (c) the sense of winding is reversed at the winding midpoint, where the current phase reversal occurs. Thus winding (c) is the only structure of the three which has positive mutual inductances between all adjacent wires. The required winding length for resonance is only between 14 and 17% longer than a physical half wave, depending on whether the vertical leads are considered as part of the windings. Exact winding lengths required must in general be determined experimentally. Windings (a) and (b) would require more conductor length to resonate at 13.36 mc, so that their loss resistance would be greater and their radiation efficiency lower. Configurations which give positive mutual inductances can be considered optimum in the sense that minimum winding length is required. Figure 8 illustrates two additional structures having this property (top views).

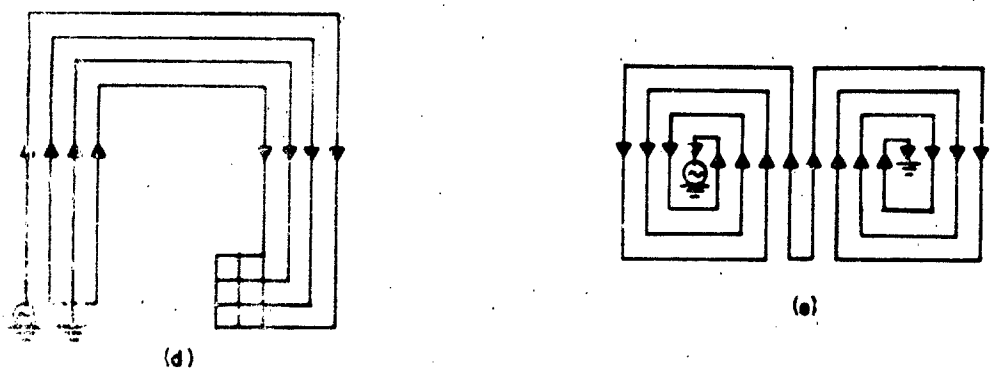

Figure 8. Windings in which mutual inductances between adjacent wires are positive

Winding (d) is recognized as a bent folded monopole, in this case multiply folded to obtain a greater input resistance.

NON-PLANAR WINDINGS

Since the net vertical current moment is reduced, hence the radiation resistance, non-planar windings are to be avoided unless allowable antenna dimensic are severely limited, or mechanical considerations rule out a planar winding. Efficiencies can be just as large with non-planar windings, however, since wider conductors can be used, giving lower winding resistance than could be obtained with a planar winding. Two types of structures which have been studied extensively experimentally are shown in Figure 9.

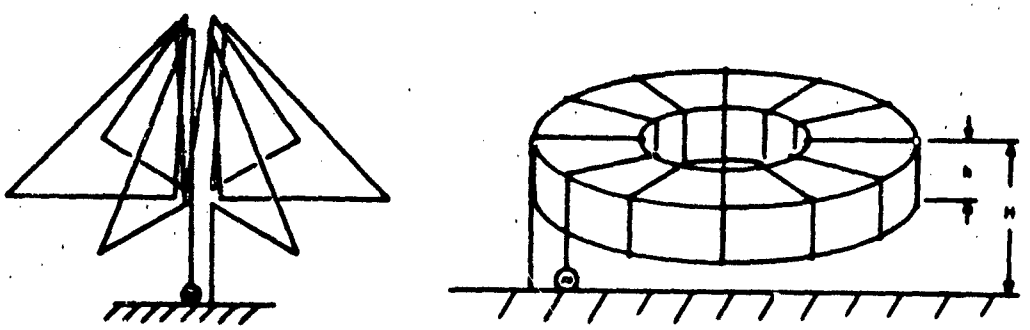

Figure 9. Non-planar half wave resonant structures

The EMR has been studied with a ferrite core as well as air. Inductance per unit length of winding is much greater with the ferrite, of course, but the loss is also greater. A straight solenoidal winding has also been studied, as have several other winding configurations for the Wound Umbrella. The one shown is preferrable to most due to positive mutual impedances and a more favorable mechanical arrangement. Use of a grounded supporting tower makes the wound umbrella attractive at low frequencies.

EXPERIMENTAL RESULTS

The efficiency and impedance properties of a wide variety of wound structures have been measured over the last two years. The electrical similarity of all of the described winding configurations has become apparent as a result of the measurements. In Table I the theoretical and measured performance data are presented for several planar wound structures, shown in Figures 3, 10, and 11. Relative Communication Efficiency (RCE) is for surface waves, with reference being a perfect short vertical monopole. Calculated RCEs and bandwidths in Table I are those obtained assuming uniform current in the vertical leads, and using the measured input resistances, which are seen to be not drastically different from the calculated values. The latter have been calculated assuming a sinusoidal current distribution, the measured value of Z_{o_1}/Z_{o_2}, and lossless ground screen and dielectrics. Resistances of connections were ignored, also, but an attempt was made to take proximity effect into account. Not surprisingly, then, observed

input resistances are greater than the calculated values. The last two antennas described in Table I gave unbelievably high efficiencies, which were as great as +1 db rather commonly at frequencies near resonance for the 12 inch height. This represents a discrepancy of 2 db or so from the expected value, which is not very serious considering the errors which can attend field strength measurements, as discussed later. It appears that an additional explanation is needed, however. A slight departure from an omnidirectional pattern probably accounts for some of the discrepancy. Also, measurements of field strength with a top loaded vertical monopole suggest that the field strength at 17.4 mc may be about 1 db higher than the value obtained with the calibrated loop antenna. If so, the antenna efficiency given should be 1 db lower.

Efficiencies of non-planar windings can be similar to that of planar windings. For example, an air core 11 turn "Elevated Magnetic Ring" (Figure 9b) with dimensions 4 feet OD, 1 foot ID, 4" high, and 8" high over-all gave efficiency within 1 db of a planar structure as in Figure 3, described in Table I. Input resistance of the EMR antenna was somewhat lower, but bandwidth was about the same. Some advantage was found in going to various configurations of multiple windings on the same core.



Figure 10. Planar half-wave spiral winding, with sense reversed in center

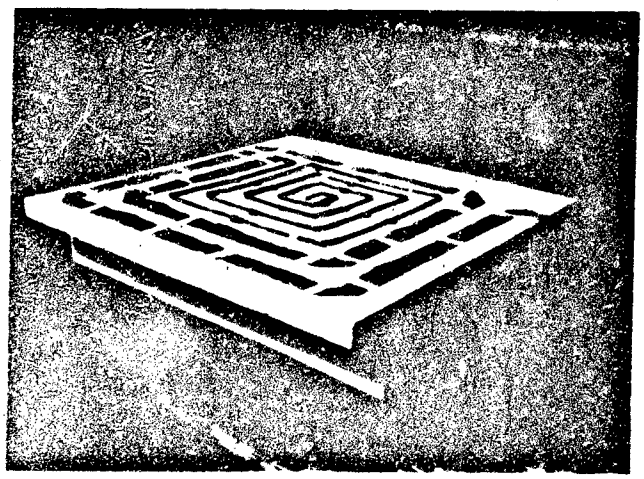

Figure 11. Planar half-wave spiral winding designed for greater resistance transformation

Table 1. Relative Communication Efficiency (RCE)

and Bandwidth Calculations and Measurements

on Half Wave Wound Antennas

Antenna Type	Winding Dimensions	Overall Height	Meas. $f_{\frac{\lambda}{2}}$ mc	Meas. R_{in} ohms	Calc. R_{in} ohms	Calc. R_T ohms	Meas. RCE db	Calc. RCE db	Meas. BW kc	Calc. BW kc	Meas. Z_{o_1}/Z_{o_2}	Calc. Z_o ohms
Fig. 3	36 x 36"	8"	15.95	2.0	1.2	.19	-4.2	-3.7	--	--	1.1	--
Fig. 10	36 x 36"	8"	14.3	1.5	0.9	.15	-5.6	-4.0	20	25.6	(assumed) 1.0	533
Fig. 10	36 x 36"	12"	14.4	2.4	1.6	.34	-3.6	-2.5	26	33.5	(assumed) 1.0	659
Fig. 11	36 x 32"	8"	17.4	3.2	2.3	.22	- .1	-2.3	--	--	1.95	--
Fig. 11	36 x 32"	12"	17.5	5.9	4.8	.51	- .2	-1.2	--	--	1.96	--

RADIATION PATTERNS

Elevation and azimuth patterns were taken on a 1/10 scale model of the antenna shown in Figure 10. These were compared with those of a top loaded vertical monopole of the same dimensions. For all practical purposes the two sets of data were identical, as expected. Radiation overhead was at least 20 db down from that at the horizon. H-plane patterns should be nearly omnidirectional for spacings between vertical leads up to an eighth wavelength. H-plane patterns for non-planar windings have been observed to be omnidirectional within about ± 1 db where the winding height was as much as 90% of the over-all height. Based on rather limited evidence, it appears that patterns will not depart seriously from omnidirectional regardless of the configuration.

METHOD OF MEASURING EFFICIENCY

The efficiency of the models is determined by measuring the available power, P_{av}, from the antenna when placed in a known (measured) surface wave field. The Relative Communication Efficiency (RCE) is defined as

$$RCE = \frac{P_{av,\text{test antenna}}}{P_{av,\text{standard antenna}}} = \frac{P_{av,t}}{P_{av,s}}$$

The standard antenna is normally taken as a perfect quarter wave or short vertical monopole, for which the available power is readily calculated from a knowledge of the field strength. For a quarter wave vertical reference,

$$RCE = 1.62 \times 10^{-2} f_{mc}^2 \left(\frac{V_m}{E_{inc}}\right)^2 \frac{1}{R_a} \left[\left(\frac{R_a}{50} + 1\right)^2 + \left(\frac{X_a}{50}\right)^2\right]$$

where f_{mc} is the frequency in megacycles

V_m is the measured voltage delivered from the antenna to a 50 ohm load

E_{inc} is the field strength at the position of the antenna, with the antenna removed, in volts/meter

R_a is the input resistance of the antenna

X_a is the input reactance of the antenna.

A surface wave signal is generated at a distance of 550 feet from the models. A remote reference antenna is used to insure that the field at the model has not changed between the time when V_m is measured and when the model is removed and E_{inc} is measured. Care is taken to determine that the incident field does not vary over the model. Accurate measurement of E_{inc} has been the greatest problem. An Empire Devices NF105 field strength meter is used, with the LP105 loop antenna. The "loop factors" have recently been revised by the manufacturer (January 6, 1964), and the accuracies readily obtainable now appear to be within ± 1 db at the frequencies where the factors have been extensively used (Table I), or better if extreme care is taken.

FUTURE WORK

Nothing has been said about arrays of the half wave, wound structures. Arrays are useful to increase power handling capability in a tuned system using sliding contacts, and to increase the bandwidth. Up to 4 element stagger tuned arrays have been built, with some success. Arrays to obtain unidirectional patterns will also receive attention in the future. Development of tuning and matching schemes deserves additional attention. A general theory for non-planar structures has yet to be worked out, and the simple theory for planar structures cannot account for the efficiency variations with frequency which have been frequently observed.

ACKNOWLEDGEMENT

Credit and appreciation are due Dr. Walter L. Weeks of Purdue University, formerly of Collins Radio Company, who initially conceived and directed the Collins electrically small antenna study program.

BROADBAND ANTENNAS UTILIZING FERRITES

J. A. M. Lyon
J. E. Herman
S. B. Rhee
The University of Michigan, Radiation Laboratory, Ann Arbor, Michigan

INTRODUCTION

This paper represents a continuation of studies dealing with the utilization of ferrite material with various types of antennas. The antenna types considered include the rectangular slot and the log conical antennas.

Data and a brief analysis are presented dealing with the effects of magnetic bias on the operation of the rectangular ferrite-filled slot antenna. At the 13th Annual Symposium on USAF Antenna Research and Development, information on the rectangular ferrite-filled slot was presented. In this paper additional information is presented showing that a shift of the operating frequency of the rectangular slot utilizing ferrite can be obtained through the introduction of magnetic bias.

Various arrangements of the log conical spiral antenna have been made using ferrite material and the results are compared with that of the same antenna without the material. It has been found that the lower frequency end of the operating band has been lowered through the use of ferrite.

Preliminary data on the variation of the magnetic properties of the ferrite with temperature are presented.

GENERAL DISCUSSION

At the last conference, a paper dealing with the ferrite-filled rectangular slot antenna with some mathematical detail was presented. This paper indicated the

possible size reduction as well as the corresponding reduction in efficiency. For review purposes a brief resume of results on such antennas is now given. Figure 1 shows three rectangular slot antennas. Further data including the dimensions of these antennas and bandwidths are shown in Table I. For comparison purposes the Table gives information for an air-filled slot, a slot filled with powdered ferrite, and a slot filled with solid ferrite. This latter slot is the smallest shown in Fig. 1. It is believed by the authors that for some uses the reductions in efficiency shown for the two ferrite antennas, one being of powdered ferrite and the other having solid ferrite, are tolerable when it is considered that there is an appreciable reduction in lineal dimensions and weight. The bandwidth of these antennas is given in Table I, and it is noted that the bandwidth of the rectangular slot filled with solid ferrite is approximately 19 Mc. Although this is sufficient for some purposes, such as telemetry on a space vehicle, it is recognized that the bandwidth may cause severe limitations in other possible applications. With this in mind, additional studies were made wherein the solid ferrite material was magnetized with a steady magnetic bias field.

In Fig. 2 is shown the solid ferrite-filled slot with permanent magnets used in experiments involving a shift of the center frequency of the operating band. The permanent magnets can be placed in various positions with respect to the housing of this rectangular slot. It was found that in each position used the permanent magnet and the accompanying magnetic field caused a rise of the center frequency. The actual operating bandwidth remained approximately the same. Figure 3 shows the amount of shift possible for two values of magnetic field. It appears that the primary factor in the shift of center frequency has been the change in the incremental permeability corresponding to the positioning of the permanent magnet. It has also been observed that

other orientations of the magnet could be used with a shift in frequency in the same direction as shown in the curves of Fig. 3.

In Figure 4 are shown several radiation patterns that have been taken with the rectangular ferrite-loaded slot with and without the application of magnetic fields. It is interesting that there is very little change in the shape of the radiation pattern of the basic slot, although some minor variations in sidelobes have been observed.

Efficiency measurements were made upon the ferrite-filled slot having solid rods of ferrite both with and without magnetic bias. The application of magnetic bias in the manner shown in Fig. 3, case 3, has resulted in the efficiency dropping from thirty percent to approximately twenty-five percent. It was encouraging to see that the drop in efficiency was small, and upon this basis more extended studies in magnetic bias control of the position of the operating frequency band are contemplated.

Figure 5 shows a log conical spiral antenna which was used for radiation pattern, VSWR, and efficiency tests. Figure 6 shows the VSWR curves for this antenna with and without loading. The inset in Fig. 6 indicates the arrangement of the antenna in a cavity with ferrite. Figure 7 shows a number of radiation patterns taken on this log conical spiral antenna as mounted in the metal cavity; both loaded and unloaded cases are shown. One of the remarkable aspects of these studies has been that the use of ferrite has lowered the low frequency limit of this antenna. Furthermore, this lowering has been accomplished while keeping the antenna operating in the desired axial beam mode. It is recognized that antennas of this type degenerate at the low frequency end as the operation passes from an axial beam into a split beam mode. Measurements of this antenna show that it has an efficiency of 13 percent with

ferrite loading at 400 Mc. Quite obviously this cavity imposes a very severe restriction on the operation of the log conical antenna inserted. Figure 8 shows two log conical spiral antennas. The small antenna on the right contained powdered ferrite which was inserted within the conical structure. The powdered ferrite material was retained by putting a thin sheet of polyethylene plastic over the smaller log conical spiral. The ferrite powder completely filled all space inside the spiralled conducting elements. Ferrite extends just outside of the conducting elements since the supporting wood structure extends approximately 1/8" beyond the metal conducting elements. This ferrite-loaded antenna operated with VSWR characteristics as shown in Fig. 9 which also shows the VSWR for the air-filled case. Figure 10 shows the radiation patterns with and without ferrite loading at various frequencies.

The efficiency of the larger log conical antenna without ferrite shown on the left of Fig. 8 was compared with that of the small ferrite-filled log conical antenna on the right. The small ferrite-filled log conical antenna has an efficiency of 23 percent at 400 Mc compared to an efficiency of 92 percent for the large log conical antenna at the same frequency. This decrease in efficiency is accompanied by a decrease in lineal antenna dimensions of approximately a factor of two and a volume decrease of about a factor of 7. This means that a much smaller antenna of the general log conical type can be made at the sacrifice of approximately 6 db in efficiency. The radiation patterns indicate that otherwise the operating performance is at least as good as that of the corresponding air-filled log conical antenna.

The ferrite antenna characteristics described above have been obtained at very low power levels and at room temperature. In anticipation of possible uses of ferrite antennas at either higher power levels or higher ambient temperatures,

studies have been made recently of the magnetic properties of the ferrite used at various temperatures and frequencies. The ferrite used is described by the formula:

$$Ni_{.9696}\ Zn_{.0404}\ Co_{.03}\ Fe_{1.84}\ Al_{.04}\ O_4 \quad .$$

Figure 11 shows complex permeability as a function of temperature for various frequencies. It is quite apparent that temperature may impose a severe restriction on the use of ferrite antennas on aerospace vehicles unless special precautions are taken to limit the temperature of the ferrite material to less than 150° C. Some of the means now used for protecting apparatus on aerospace vehicles on reentry could possibly be applied to these antennas. For antennas which do not have to pass through temperatures corresponding to reentry, it might be that the antennas would perform satisfactorily. Additional studies are necessary for very low temperatures.

CONCLUSIONS

The results achieved using ferrite material have been very encouraging as far as reduction in the size of a given antenna type. It has been shown that reduction in size is possible both for broadbanded antennas and for antennas which are essentially narrow band. Furthermore, it has been shown that through the application of magnetic bias substantial shifts of the position of the operating band of frequencies can be achieved. It is interesting that these shifts can be provided with very little reduction in the efficiency of the antenna. It is also recognized that the use of ferrite material causes in some cases a marked reduction in efficiency. However, these reductions in efficiency possibly can be tolerated in specific practical applications because of the great improvement represented by the reduction in physical dimensions of a given antenna.

ACKNOWLEDGEMENTS

The work was performed under Contract AF33(657)-10607 under the particular guidance of Mr. E. M. Turner and Mr. O. E. Horton, Avionics Laboratory, Wright Patterson Air Force Base, Ohio.

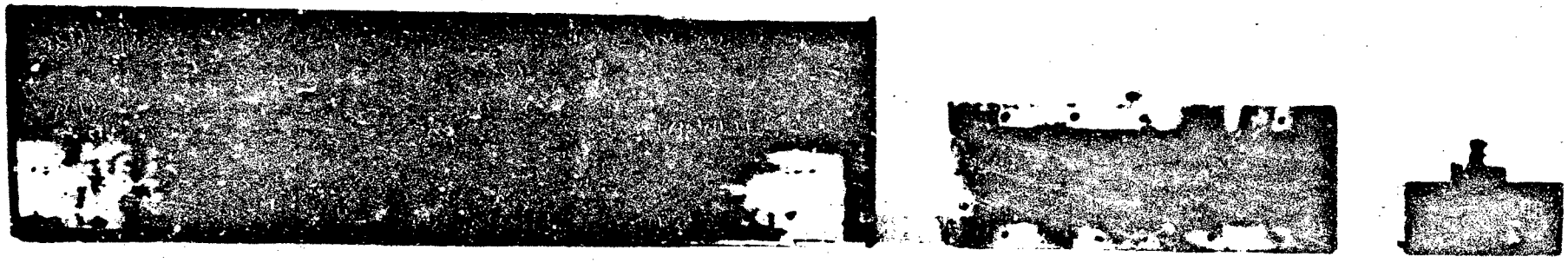

Fig. 1. Physical comparison of loaded-slot antennas.

	Size	Volume	Bandwidth With Flange		Bandwidth - No Flange		Efficiency	Directivity	Weight	(Mc) Operating Frequency
			VSWR = 3.0	VSWR = 6.0	VSWR = 3.0	VSWR = 6.0				
Air Loaded Antenna	30" x 7½" x 10"	2250 cu. in.			64 Mc	90 Mc	90%	5.8	25-3/4 pounds	300
Ferrite Powder Loaded Antenna	12" x 3" x 9"	144 cu. in.	22 Mc	50 Mc	20 Mc	36 Mc	65%	5.0	16-3/4 pounds	320
Solid Ferrite Loaded Antenna	5" x 2" x 1½"	15 cu. in.	19 Mc	34 Mc	19 Mc	32 Mc	30%	5.0	3.6 pounds	352

Table I. Performance comparison of rectangular cavity-slot antennas.

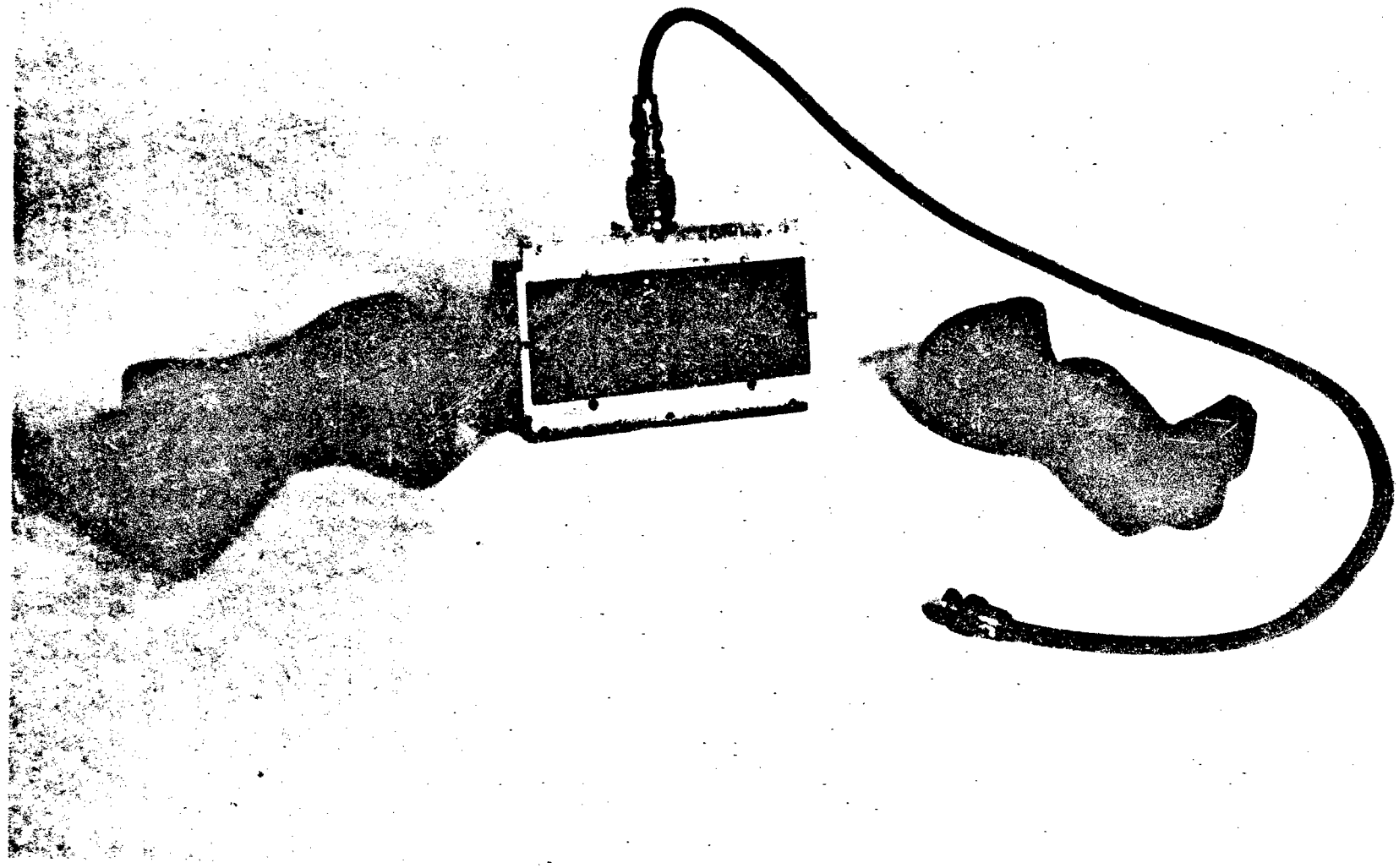

FIG. 2. Ferrite Loaded Slot Antenna with Permanent Magnets

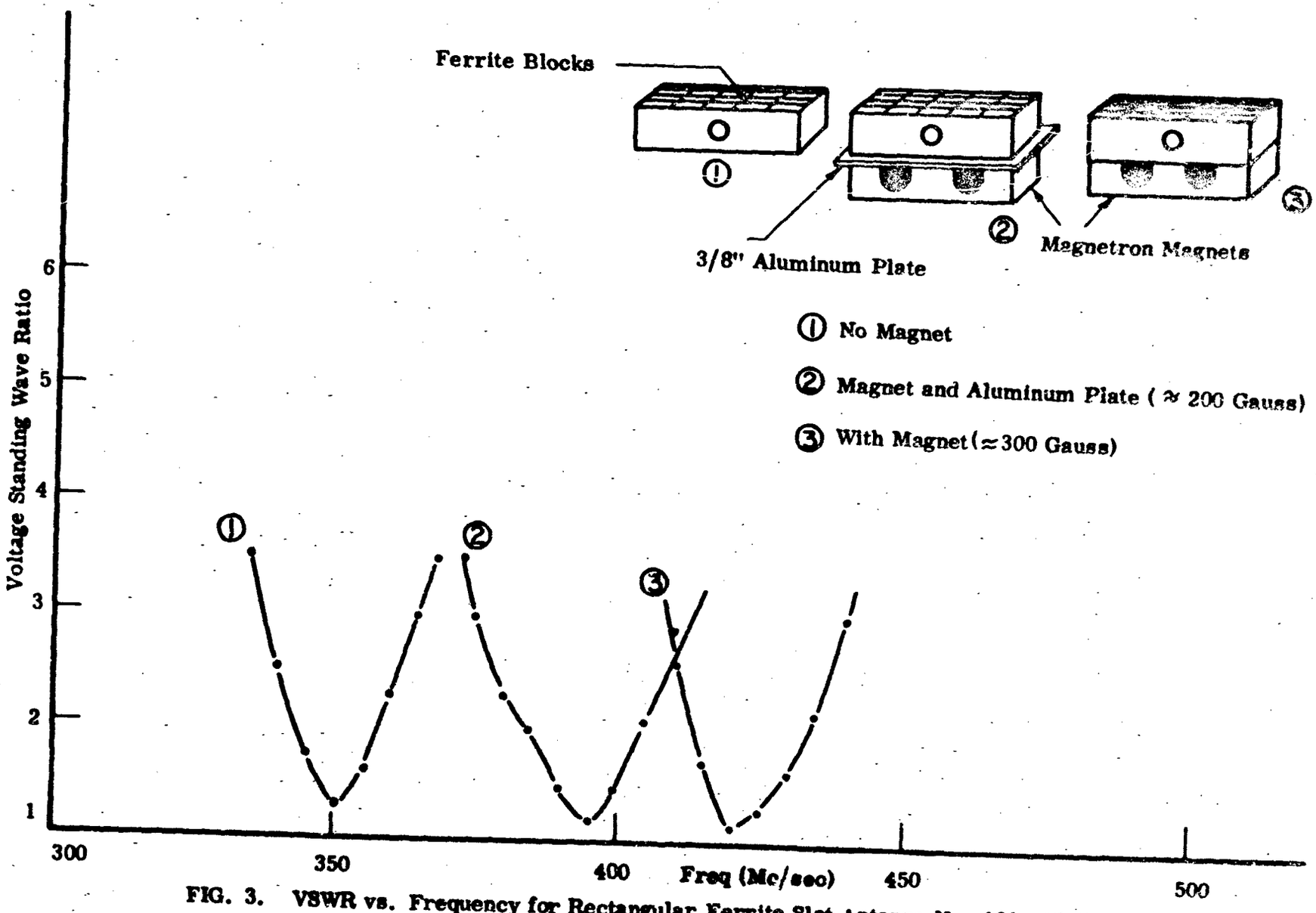

FIG. 3. VSWR vs. Frequency for Rectangular Ferrite Slot Antenna No. 101 with Permanent Magnets

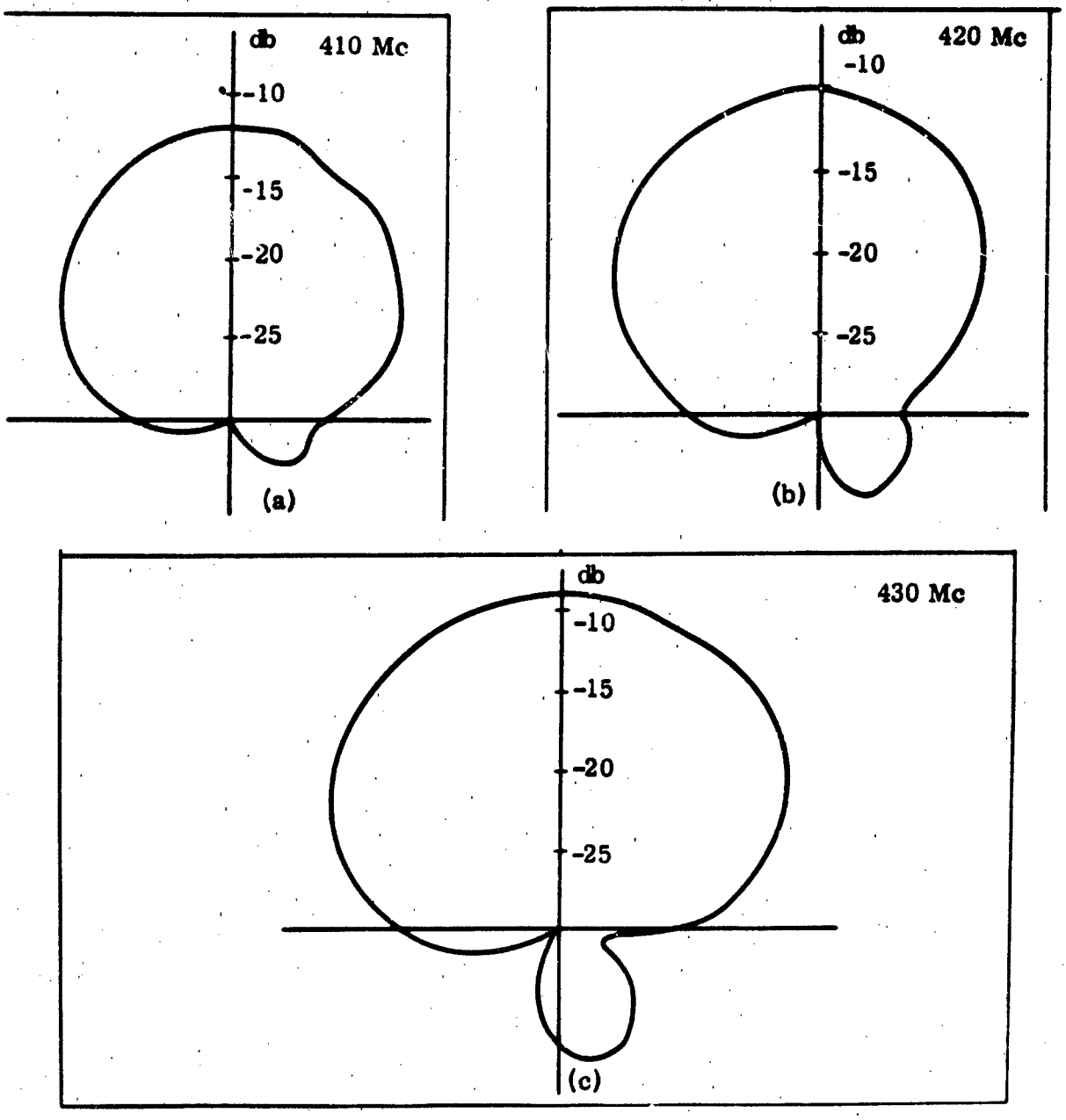

Resonant Frequency = 420 Mc

FIG. 4a - 4c: Radiation Patterns (E_ϕ) for Antenna No. 101 with Magnet

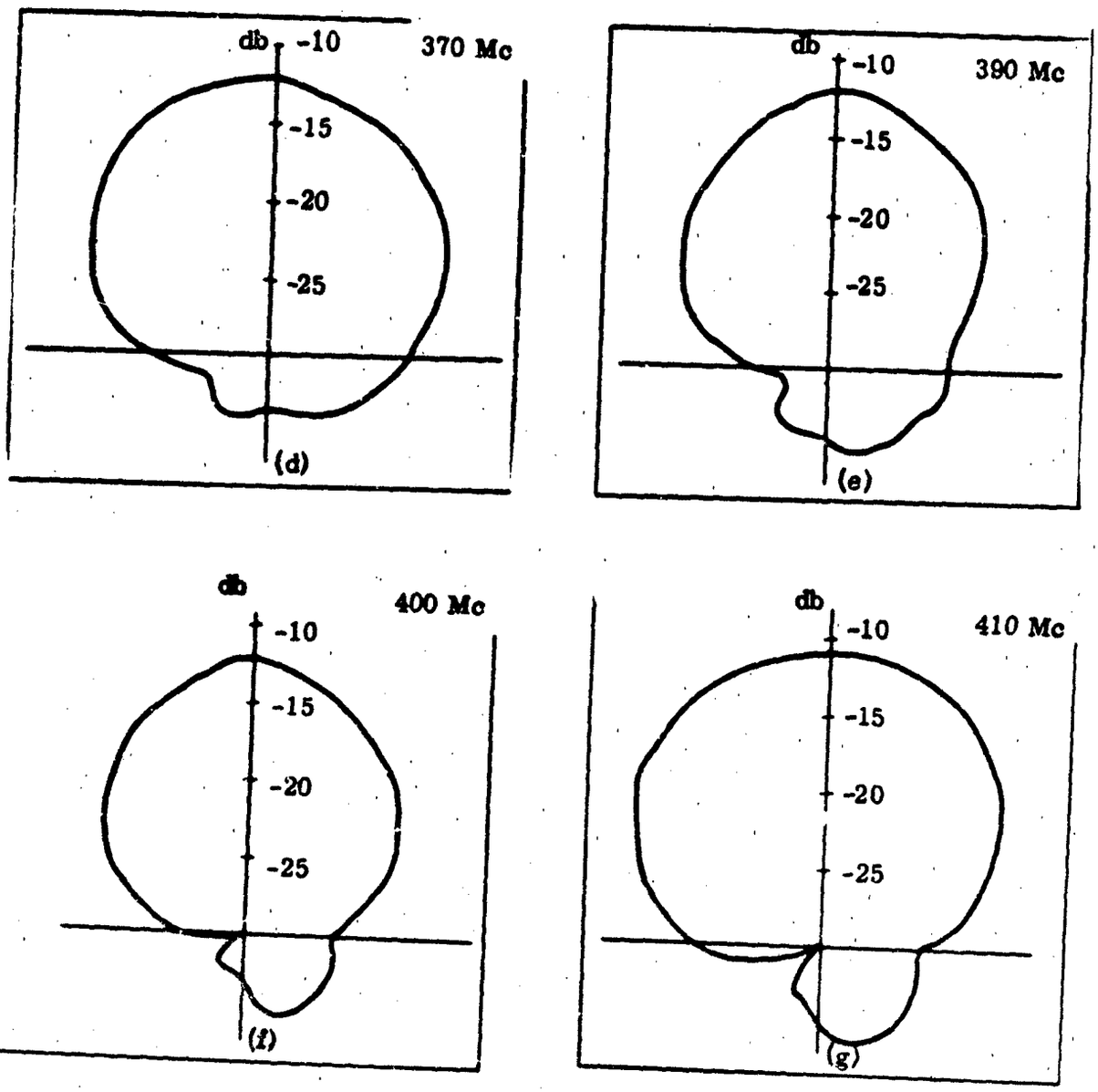

Resonant Frequency = 395 Mc

FIG. 4d-4g: Radiation Patterns (E_ϕ) for Antenna No. 101 with Magnet and Aluminum Plate

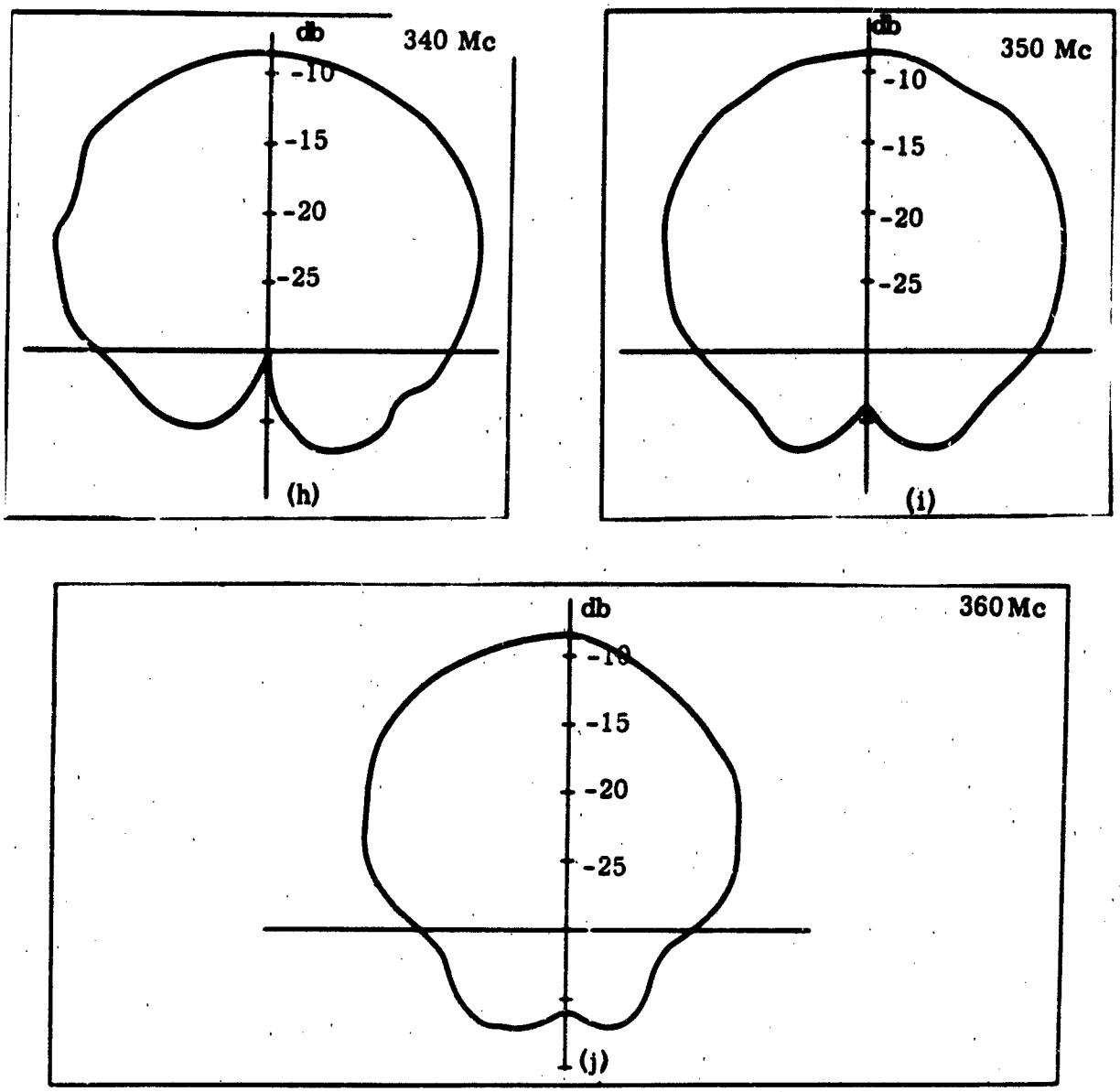

Resonant Frequency = 350 Mc

FIG 4h-4j: Radiation Patterns (E_ϕ) for Antenna No. 101 Without Magnet

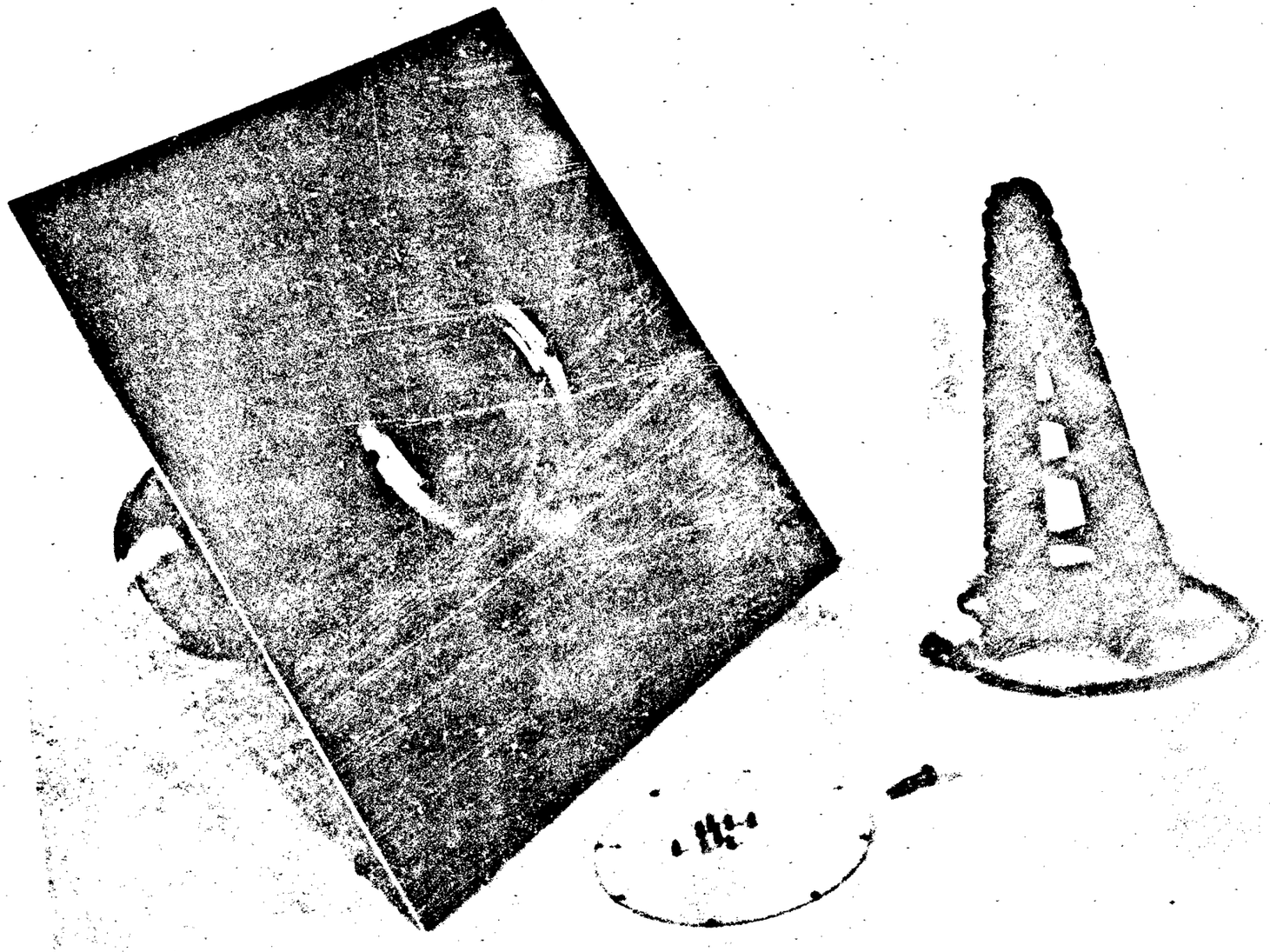

FIG. 5. Log Conical Spiral Antenna with Cavity.

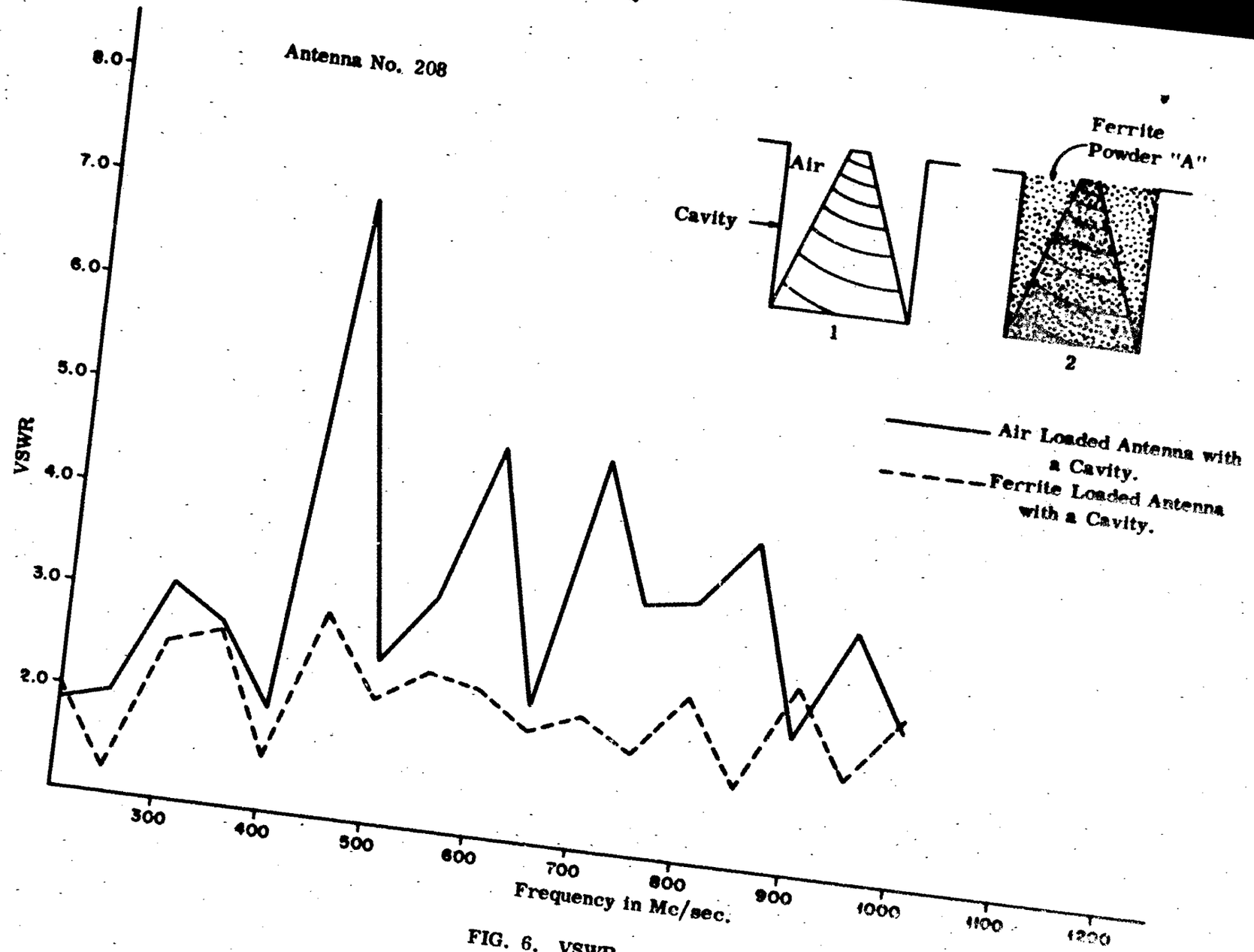

FIG. 6. VSWR vs. Frequency

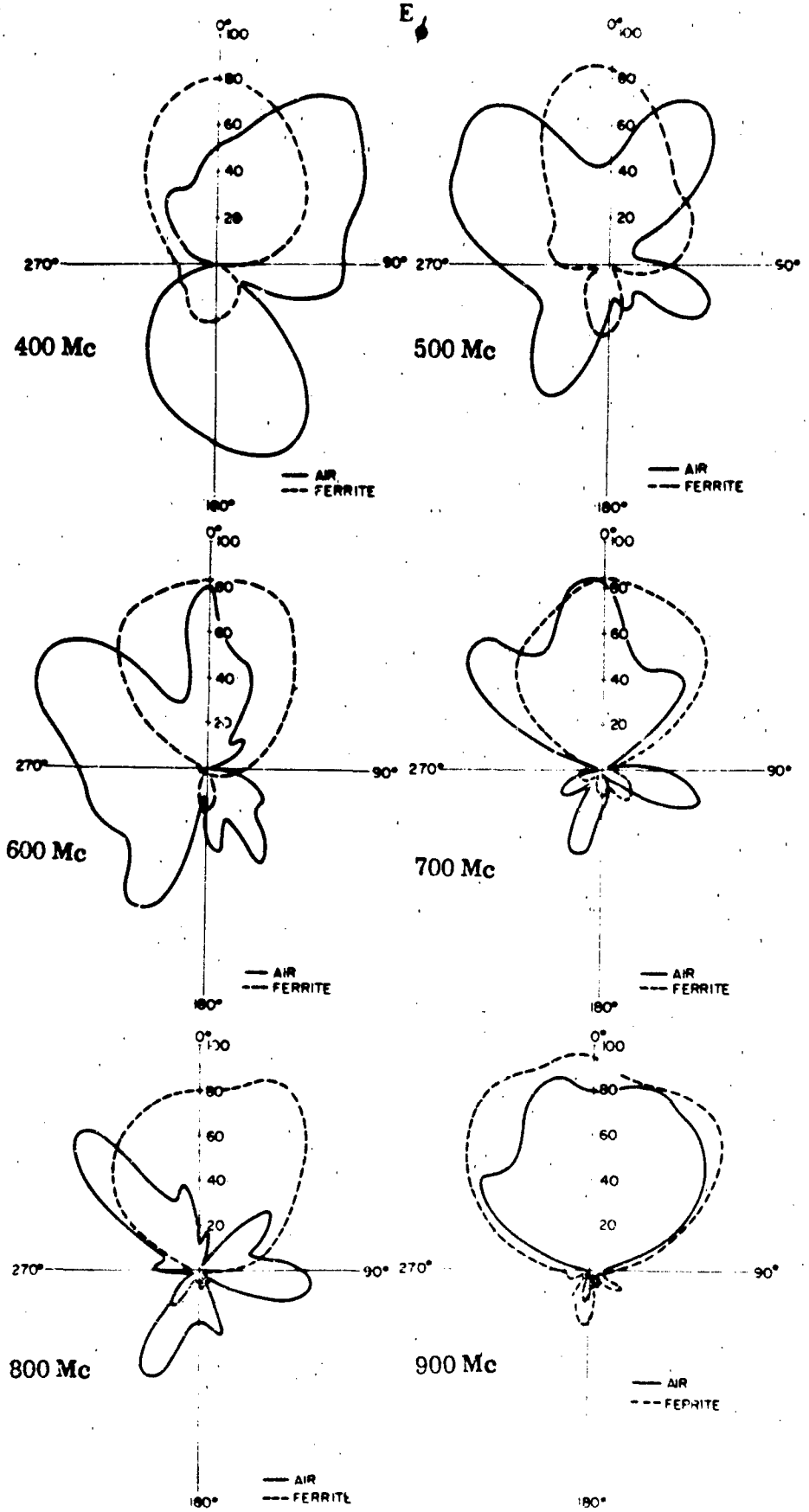
E
0°
100
80
60
40
20
270°
90°
180°
400 Mc
500 Mc
600 Mc
700 Mc
800 Mc
900 Mc
AIR
FERRITE

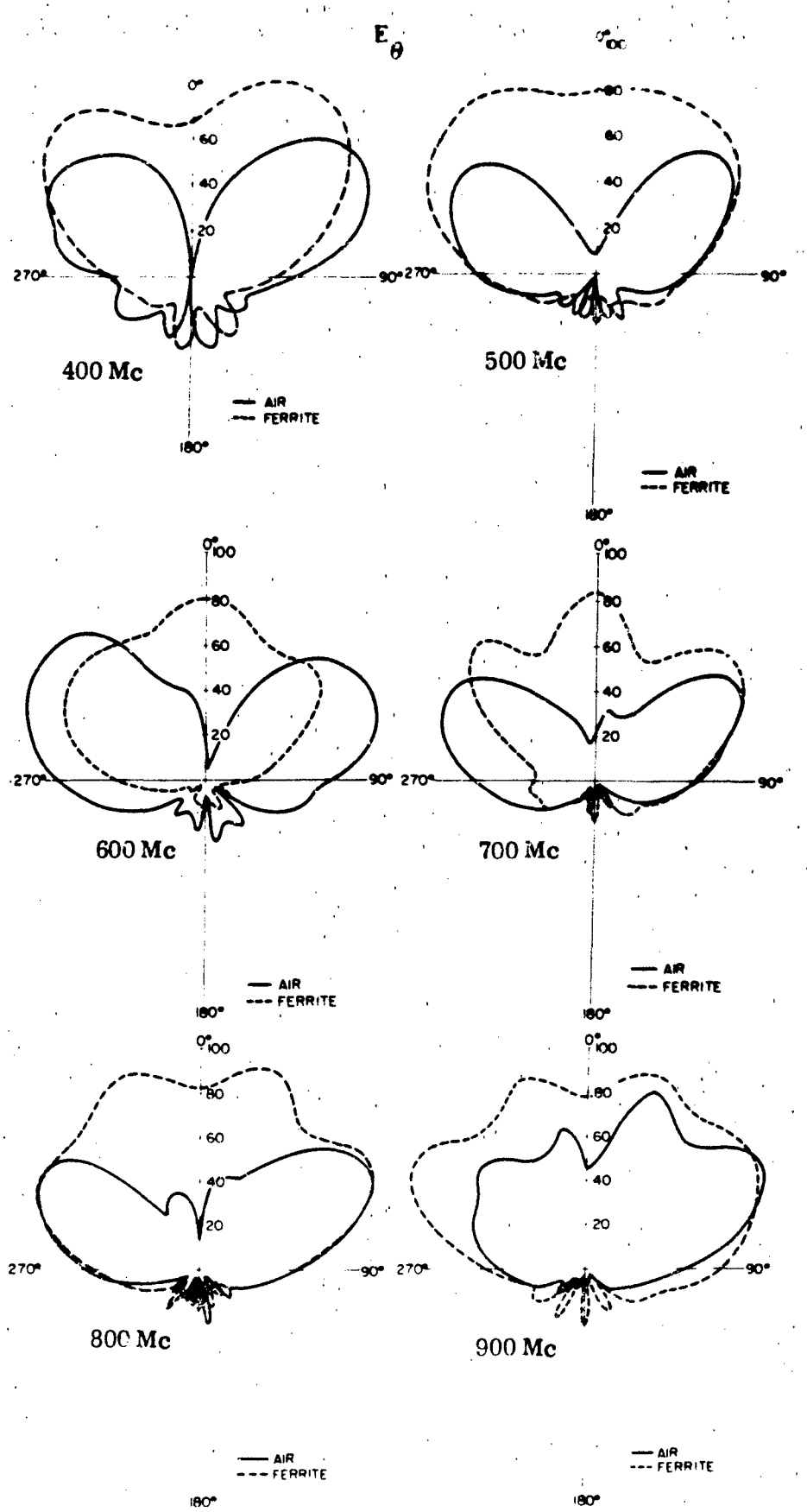

FIG. 7b. Radiation Patterns with Cavity

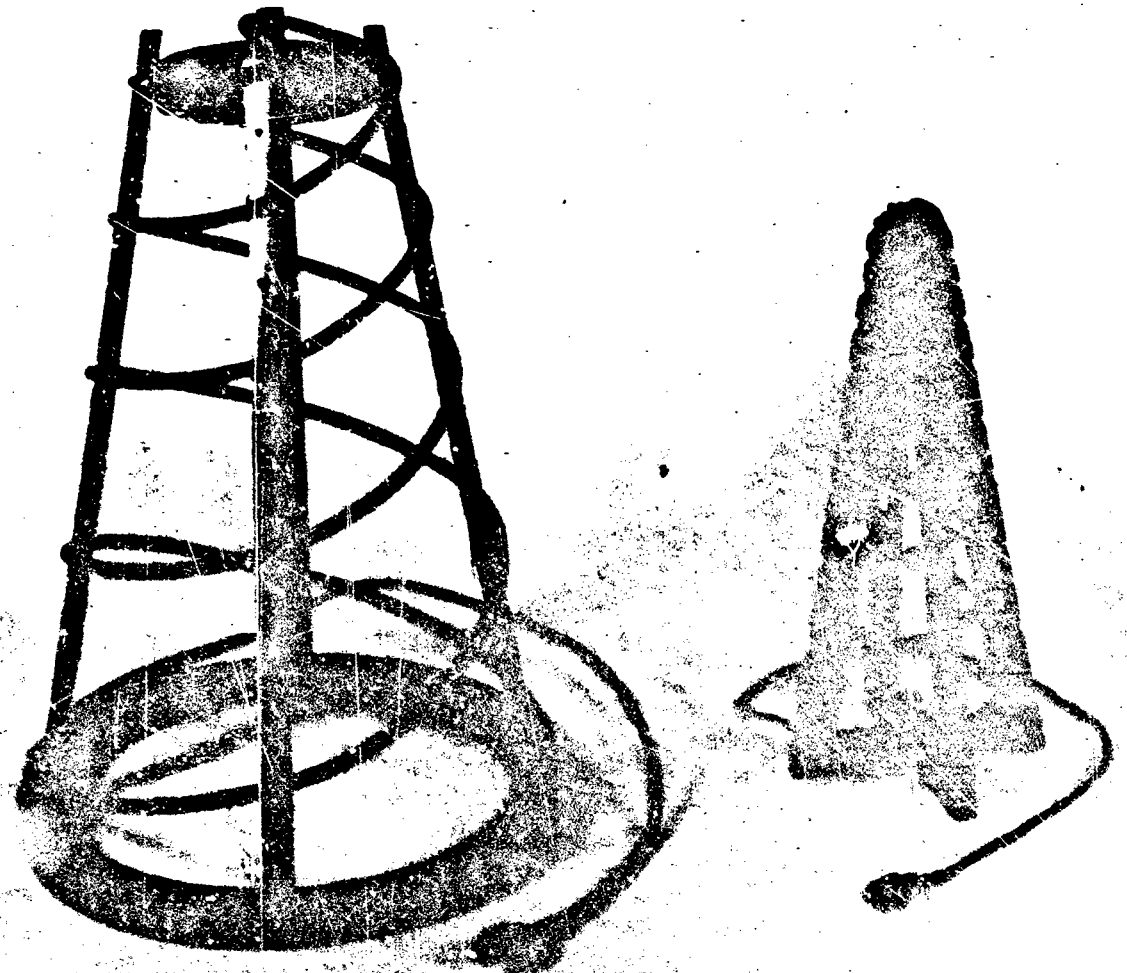

FIG. 8. Large and Small Log Conical Spiral Antennas

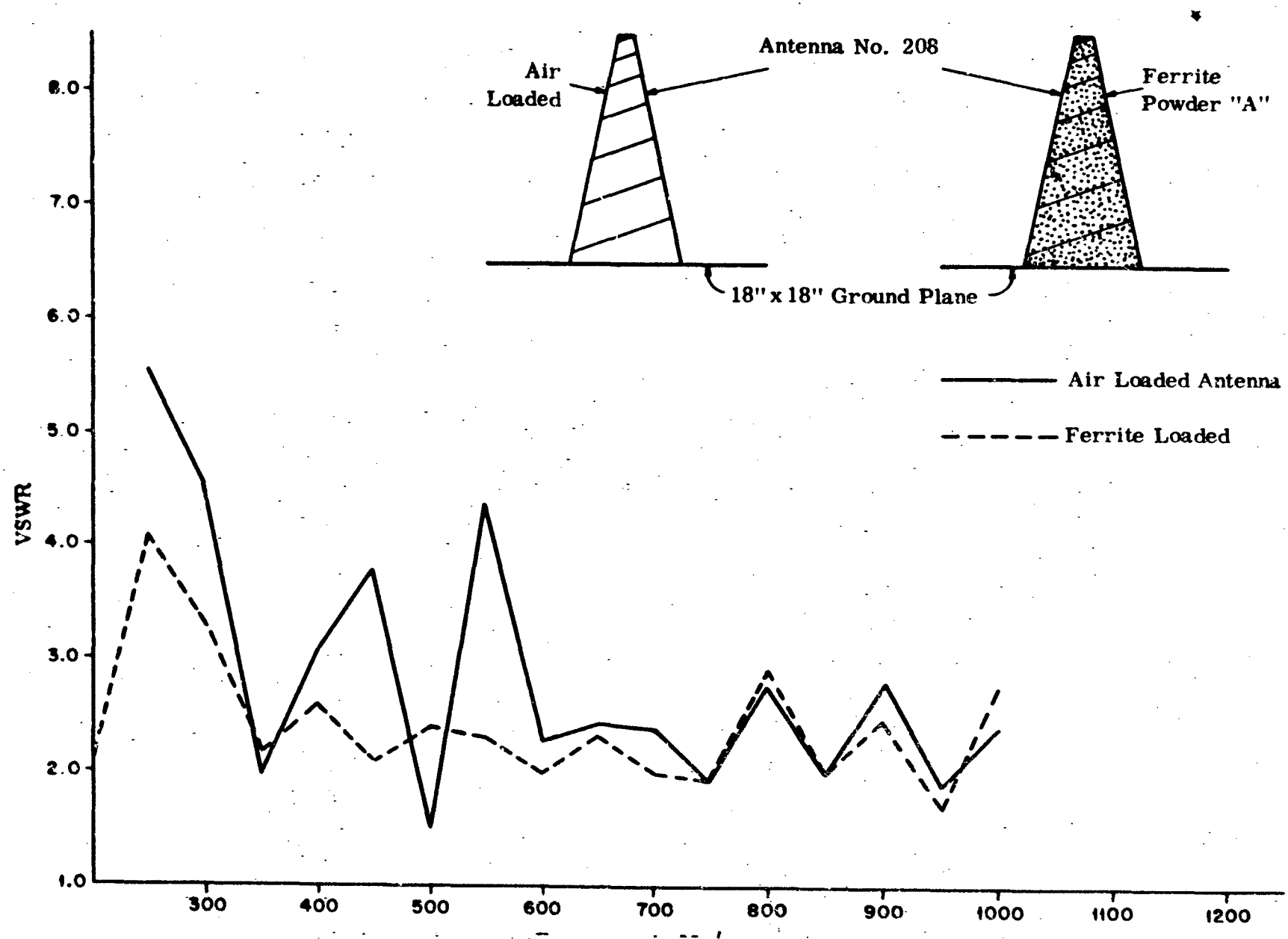
Antenna No. 208
Air Loaded
Ferrite Powder "A"
18" x 18" Ground Plane
Air Loaded Antenna
Ferrite Loaded
VSWR
8.0
7.0
6.0
5.0
4.0
3.0
2.0
1.0
300
400
500
600
700
800
900
1000
1100
1200

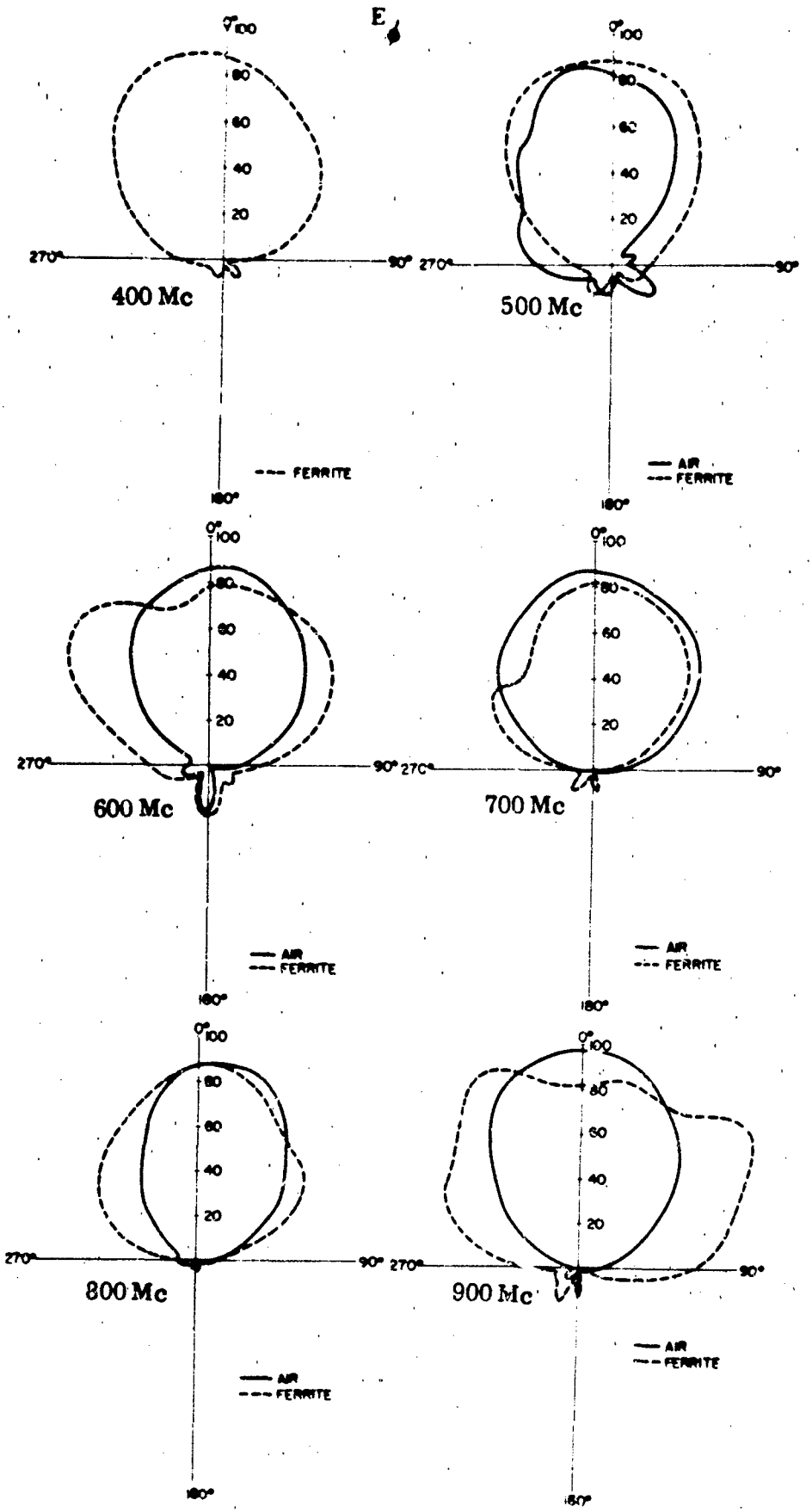

FIG. 10a. Radiation Patterns without Cavity.

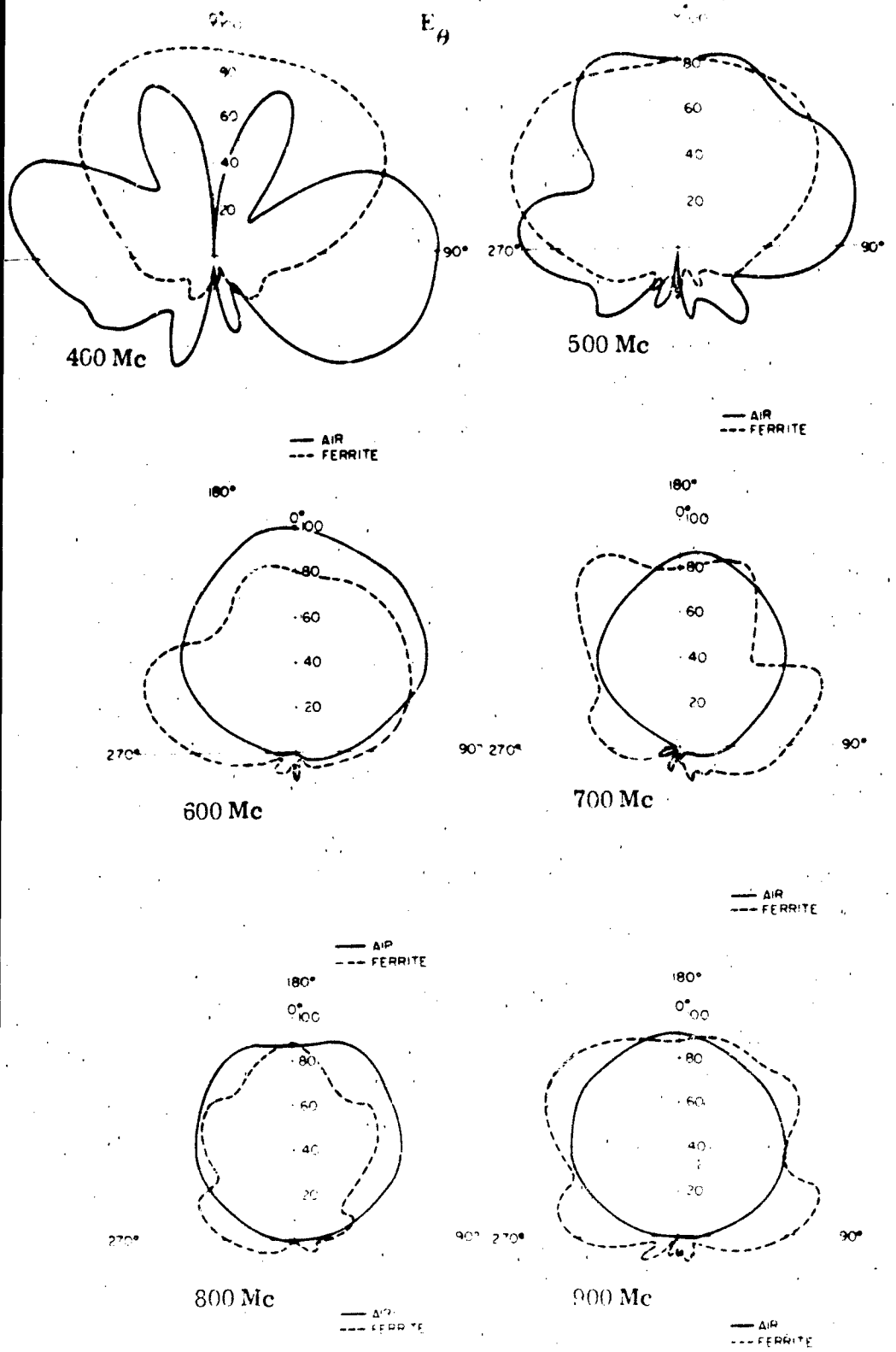

FIG. 10b. Radiation Patterns without Cavity.

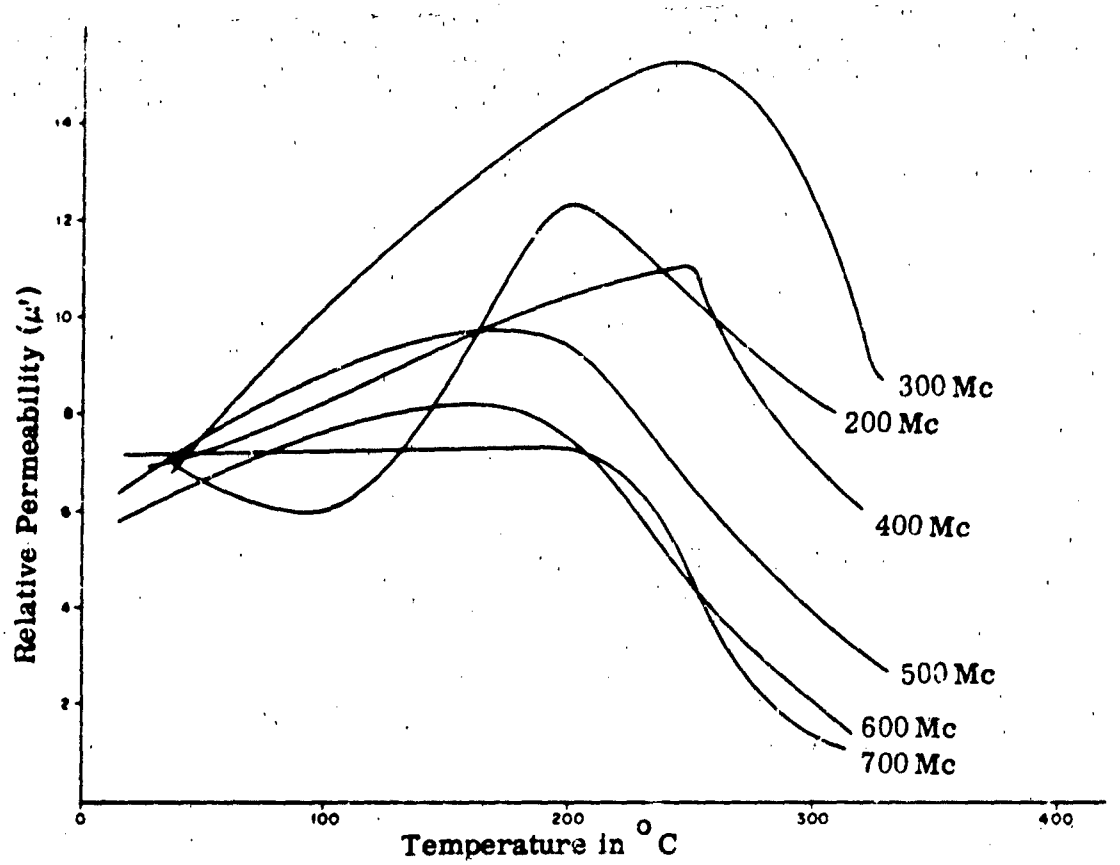

FIG. 11a. Relative Permeability (μ') versus Temperature for Co_2Z .

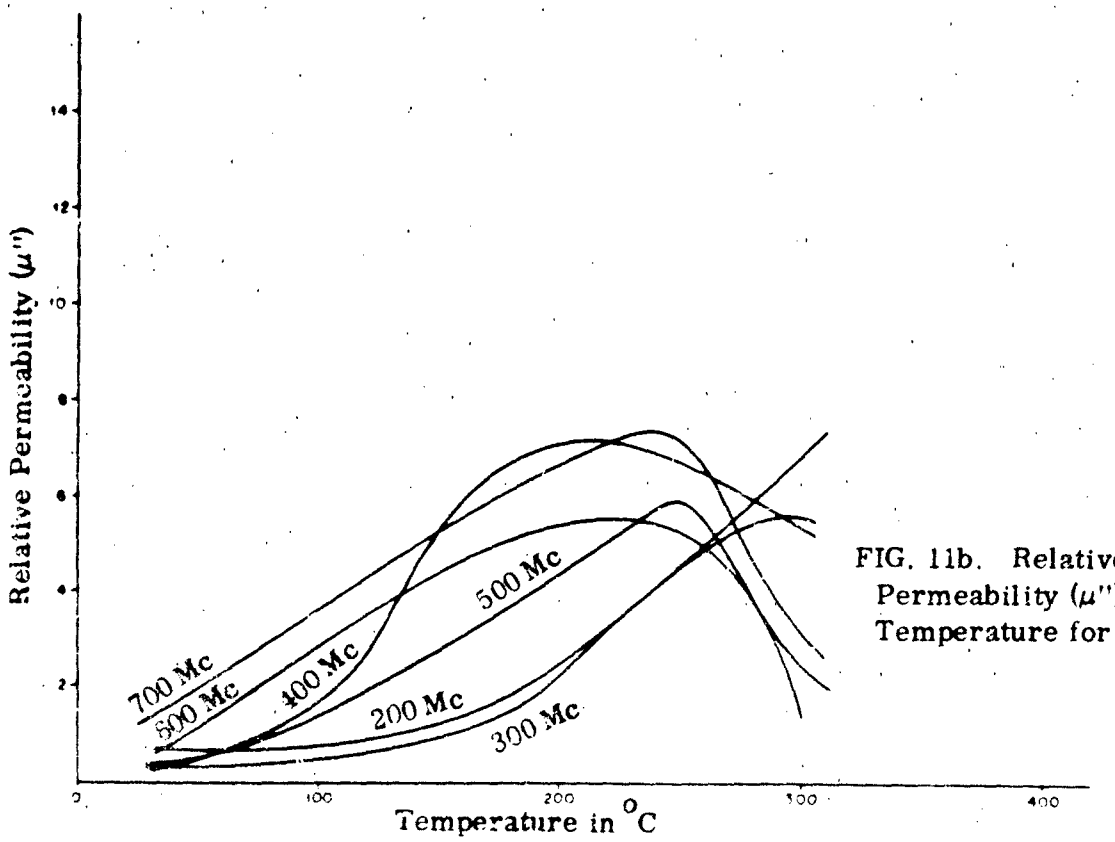

FIG. 11b. Relative Permeability (μ'') versus Temperature for Co_2Z.

VARIABLE PRISM SCANNING LENS

By

Scott H. Walker

MOTOROLA INC.
Military Electronics Division
WESTERN CENTER
8201 EAST McDOWELL ROAD SCOTTSDALE ARIZONA

I INTRODUCTION

The capability of narrow beam antennas tc scan through large angular sectors has become increasingly important in modern radar and communications systems. In some cases it is desirable to use a single antenna for the performance of many functions at widely different look angles. It is also important to locate the antenna apertures around the periphery of a vehicle so that the presence of the vehicle structure will have little affect on the performance of the antenna.

Two dimensional Luneberg or geodesic lenses are often considered for these applications as they are capable of 360 degrees scan and provide apertures which can be flushmounted to many vehicles. The circular line apertures of these antennas, however, result in off-axis pattern deterioration which is not acceptable in many applications. For example, a circular line source has a narrow beamwidth in elevation (the plane normal to the plane of the aperture) making beam shaping over an appreciable angular sector extremely difficult. Also, although a narrow beamwidth may be achieved in the azimuth plane (plane of the aperture) the beamwidth widens rapidly for pattern cuts through planes tilted at increasing elevations. Such antennas are therefore not well suited to applications requiring fan shaped beams.

The obvious solution to the problem is to employ a number of flushmounted scannable linear apertures which together can cover the required angular sector. Electronic scanning techniques are commonly considered for such applications but their size, weight and cost frequently make their use impractical. Mechanically scanned linear aperture such as pillboxes have recently achieved 100 to 120 degrees of beam scan, but the use of three to four such large and heavy structures to achieve large angular coverage is undesirable.

The prism antenna technique to be discussed makes it possible to scan the beam from a number of linear apertures with a relatively simple mechanical system. The beam forming capabilities of amplitude tapered arrays can be utilized for the antenna feed since a point source feed is not required. A mechanical advantage between feed and beam rotation is accomplished. In addition, the elevation beam can be shaped and scanned independently of azimuth beam characteristics.

II BASIC PRISM THEORY

The basic operation of the prism can be explained through Snell's law as illustrated in Figure 1. A prism having a refractive index η_2 is outlined by B, D, E. A wave front FB is shown impinging on the EB surface of the prism. A normal to this surface is shown by BD. An incident ray (AB) of the wave is at an angle of incidence α with respect to the normal BD. The angle $\emptyset$ to which the ray is refracted upon entering the higher dielectric prism is by Snell's law

$$\emptyset = \sin^{-1}\left(\frac{\eta_1 \sin\alpha}{\eta_2}\right) \tag{1}$$

where η_1 and η_2 are the refractive indices of the medium through which the incident and refractive rays propagate.

$$\eta_1 = \sqrt{\epsilon_1} = 1 \text{ for air} \tag{2}$$

$$\eta_2 = \sqrt{\epsilon_2} \tag{3}$$

therefore,

$$\frac{\sin\alpha}{\sin\emptyset} = \sqrt{\epsilon_2} \tag{4}$$

and for very small angles

$$\alpha \cong \sqrt{\epsilon_2}\ \emptyset \tag{5}$$

If the angle BED is made equal to $\emptyset$ then all refracted rays are perpendicular to the second prism face ED and ED will then correspond to a constant phase front.

From (4)

$$\sin\alpha = \sqrt{\epsilon_2}\ \sin\phi \tag{6}$$

multiplying by length BE

$$BE \sin\alpha = \sqrt{\epsilon_2}\ BE \sin\phi \tag{7}$$

but

$$BE \sin\alpha = FE \tag{8}$$

and

$$BE \sin\phi = BC \tag{9}$$

therefore

$FE = \sqrt{\epsilon_2}$ BC with the result that the electrical length from F to E is the same as that from B to C yielding a constant phase front across ED. (10

If a linear array is placed along the ED surface and phased to provide a beam in the dielectric perpendicular to this surface the actual beam in free space will be refracted at the EB surface at an angle α with respect to the normal. Since the beam pointing angle, α, is related to the prism angle, ϕ, by equation 6 a mechanical advantage exists between the mechanical feed rotatio and the beam rotation. For example, if $\epsilon_2 = 9$ the array would have to be mov only 13.6 degrees for a beam scan of 45 degrees from the normal.

While it would appear difficult to change the angle BED = ϕ in a solid diele tric prism, a method has been devised which accomplishes this task as shown in Figure 2. The dielectric material between the refracting surface and feed array is divided along a circular arc. The feed and a section of dielectric are free to rotate with respect to the refracting surface. The consequences of the resultant small air gap will be discussed in Section V.

There is a degradation of effective array aperture with scan equal to $\frac{\cos \alpha}{\cos \beta}$ which for high dielectric constants is very nearly equal to the normal cosine law. For example, if $\epsilon_2 = 9$ and $\alpha = 45^\circ$ the effective aperture is .727 of the feed aperture; slightly greater than the .707 expected from phase scanning a linear aperture.

For practical reasons TEM parallel plate operation was chosen for an experimental model. The wavelength or phase delay in TEM mode propagation is not dependent upon plate spacing, allowing more reasonable tolerances in the construction of such an antenna. For some applications other modes of operation are useful. For instance, operation in two modes which are separable at the output and coupled to two displaced (stacked in elevation) radiating apertures would allow electronic elevation beam scanning as the relative phases of the two modes were changed at the input.

Figure 3 illustrates one particular geometry for a prism antenna which allows full 360° scan. Each side of the four sided figure is an aperture. The beam scan for each aperture is shown versus relative feed position. It should be noted that the scan is discontinuous between apertures. The radiating apertures must be longer than the feed array to allow extreme rays from the end of the array to pass through the refracting aperture at the scan limits of $\pm 45^\circ$.

While the square shape shown in Figure 3 is optimum (minimum size for 360° scan) many variations of this shape can be envisioned for other applications. Some applications might not be able to tolerate the effective aperture degradation associated with scanning 45° from one side. Six sides could be used with only $\pm 30^\circ$ scan required of each side for total 360° scan. The aperture degradation would then be only .880 for $\epsilon_2 = 9$, which is quite an improvement over the prior .727 degradation. The overall size of the antenna must now be increased considerably, so a tradeoff between these two opposing

criteria would have to be made for each application. Another application might require less scan in some quadrants reducing the required size of that one aperture.

It should be emphasized that the prism does no focusing, but merely redirects the radiation. Thus, any technique that can be used with a line source feed can be used with the prism. For this reason electronic scan of the prism feed can be incorporated in addition to the mechanical scan already discussed. The prism will not cause any multiplication of electronic scan. This is the case since it requires as much phase shift per unit length of the array to scan the beam X degrees in the dielectric medium as it does to scan KX degrees in air where K is $\frac{\alpha}{\beta}$. Monopulse operation could also be included in the prism feed. More than one feed can be used for a number of simultaneous beams either from the same aperture of a combination of apertures.

III FEED TECHNIQUES

A number of techniques for feeding the prism have been considered. A simple H-plane sectoral horn with correcting lens has been used on test models to date. The designs of such a feed are very simple and are easily integrated into the dielectric filled parallel plate prism, since the dielectric is merely an extension of the correcting lens. The horn, however, is inefficient, large, heavy, and it is difficult to design for low sidelobes. These disadvantages can be eliminated with the use of waveguide type feeds, either of leaky wave or resonant slot design.

Prior discussions have always assumed a beam in the dielectric normal to the feed surface. It has been pointed out, however, that scanning of the feed beam in the dielectric may be used in addition to mechanical scan of the feed. In all cases the dielectric is assumed contiguous with the feed, and the necessity of this condition will be explored shortly. Figure 4 shows an arrangement employing two feed arrays each producing non-broadside beams. The weight of

the feed in this case is very much reduced by the reduced amount of dielectric employed. Leaky wave structures would be ideal for such a feed system although calculations have shown the design parameters (especially attenuation per unit length along the traveling wave antenna) to be difficult to realize physically.

A resonant slot array feed as pictured in Figure 5 can be easily designed as a feed for free space operation, but the additional requirement of parallel plate operation, particularly with a high dielectric loading, imposes some restrictions in the design not normally considered. Obviously if the dielectric is contiguous to the array, the slot spacing for high efficiency (absence of grating lobes) must be less than $\frac{\lambda_o}{\sqrt{\epsilon}}$. For high dielectric constant prisms this condition cannot be fulfilled without also loading the waveguide with a high dielectric material. Appendix A shows that if an air space of a certain minimum thickness is allowed between the dielectric and the array much larger slot spacings can again be allowed.

It can be shown that such a dielectric air transition is allowable and can be matched if the interface is on a constant phase front so that no refraction will occur. Since the interface is rotated with the array for beam scanning, this condition is always met for the design shown in Figure 5. A quarterwave step in the dielectric will provide a narrow band match at the interface. Assuming the step must match air filled guide to dielectric filled guide (ϵ_2), the step dimensions are

$$L = \frac{\lambda_o}{4\sqrt[4]{\epsilon_2}} \tag{11}$$

and

$$\frac{t}{w} = \frac{\frac{1}{\sqrt{\epsilon_2}} - 1}{\frac{1}{\epsilon_2} - 1} \tag{12}$$

where

L is the length of the step, t is the thickness of the step, and

ω is the thickness of the parallel plate region.

For TEM operation of the parallel plate region broad wall shunt slots are used in the feed array. Normally such slots have low mutual impedances, but the presence of the parallel plates introduce image slots which cause effectively high mutual impedances. The design must therefore be based upon experimentally determined incremental slot conductances.

IV RADIATING APERTURE

Means of radiating from the dielectric filled parallel plate transmission line to free space are varied and each serves a particular application. Where the best possible match over broadbands and wide angular regions is required, a long taper from dielectric to air coupled with an exponential horn could be used. This involves considerable added weight and size, however, and a number of compromises have been studied. A single quarter-wave step to air is easily calculated and constructed, but the match depends on both frequency and angle of arrival. An even simpler method is available which has little or no angular sensitivity and is also broadband. The thickness of the parallel plate is changed from W_1 with the dielectric to $W_2 = \frac{W_1}{\sqrt{\epsilon_2}}$ in air. This equalizes the characteristic impedance in the two media since

$$Z_o = \frac{377_W}{\sqrt{\epsilon_r}\, b} \tag{13}$$

and therefore

$$Z_{o_1} = \frac{377_{W1}}{\sqrt{\epsilon_r}\, b} = \frac{377_{W2}}{b} = Z_{o_2} \tag{14}$$

and

$$W2 = \frac{W1}{\sqrt{\epsilon_r}} \tag{15}$$

The match at this junction is still not optimum because of the capacitive discontinuity associated with the sharp change of guide dimensions. Whinnery and Jamieson[1] have derived values for the equivalent shunt capacitive reactances due to such steps in parallel plate line. Methods of cancelling this reactance include undercutting the dielectric, or adding a second short step with increased inductance.

A simple horn can then be used to transform from the air loaded parallel plate to free space radiation at this prism output surface. The horn could be used as the primary feed of a parabola whereby movement of the parabola would cause scanning of the beam in the elevation plane.

V CONSTRUCTION TECHNIQUES

Construction tolerances are difficult to analyze, but a few guidelines are available. Inhomogeneities in the dielectric material can be analyzed as in Appendix B. It is shown by means of an example that 20 db sidelobes will be degraded by 0.5 db or less in a prism in which the dielectric constant is held between 9 ±.03. Although such a sidelobe requirement is rather stringent it does represent the degree of homogeneity required for some applications. It has been determined experimentally that small air gaps between the dielectric and the metal parallel plates, which cause an effective inhomogeneity, are intolerable. The conductors must be plated or fired intimately to the dielectric surface or beam distortion, servere beam broadening, and large increases in sidelobe levels will result.

The circular interface between the rotating feed and stationary prism must not leak appreciable rf energy or cause a standing wave to be set up in the feed. A quarter-wave choke of standard design will acceptably reduce the radiation from this interface. The maximum air gap allowable, between the stationary and rotating dielectrics for $\epsilon = 9$ and a VSWR of 1.14, would be $.010\,\lambda_o$. This is a difficult but attainable gap tolerance over limited temperature ranges.

VI TEST RESULTS

Results of tests on a lens compensated horn fed prism have verified the basic operation of the antenna. A picture of the test antenna is shown in Figure 6. The dielectric was G-7 silicone fiberglass with a dielectric constant of 4.1 at 1 mc. Figure 7 shows patterns for mechanical scan angles of ±18 degrees and 0 degrees. From Snell's law then; $\epsilon_r = \left(\frac{\sin 40^o}{\sin 18^o}\right)^2 = 4.2$. Originally the aluminum sheets were used as the two conducting plates but the patterns were sensitive to plate pressure and at best sidelobes were only 6 db below the main beam. Copper was then plated to both sides of the dielectric with results as shown. It should be noted that the sidelobes are not imaged at extreme scan angles nor are they symmetric at 0 degrees scan indicating that non-symmetric phase errors are present. Such phase errors are associated with random inhomogeneities in the prism dielectric.

VII CONCLUSIONS

This paper has described the operation of a scanning antenna based on the properties of a prism. Operation over one quadrant of the proposed 360° ultimate scanning range has been experimentally verified. Construction accuracies have been shown to be critical but realizable. Techniques for improvement of the antenna system particularly in feed and aperture design have been discussed.

ACKNOWLEDGEMENTS

This work was sponsored by Research and Technology Division, Air Force Systems Command, United States Air Force.

The author wishes to thank Dr. T. Charlton for his guidance and many helpful suggestions and Mr. R. Eckstein for his suggestions and corrections to the test.

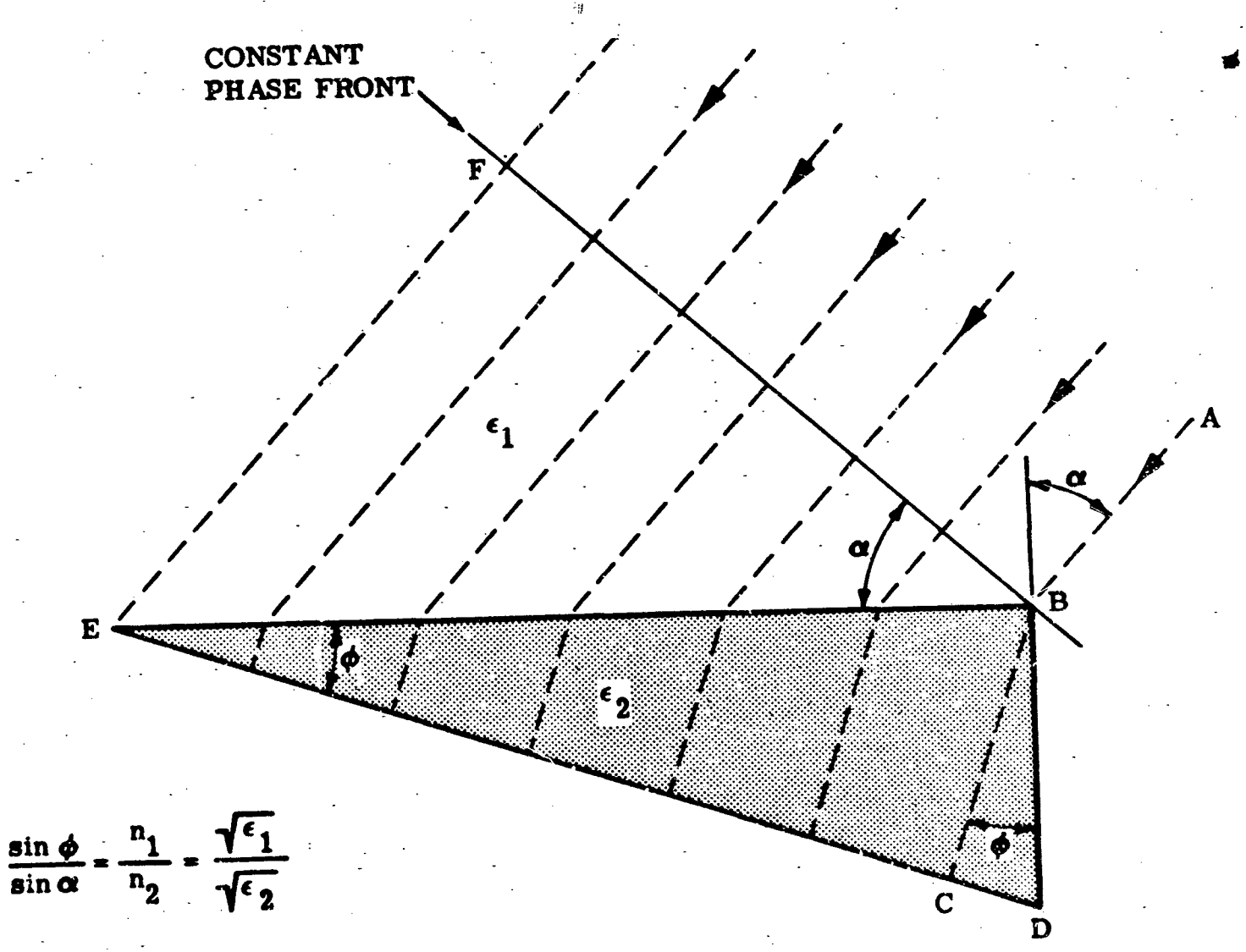

Figure 1. Basic Prism Operation

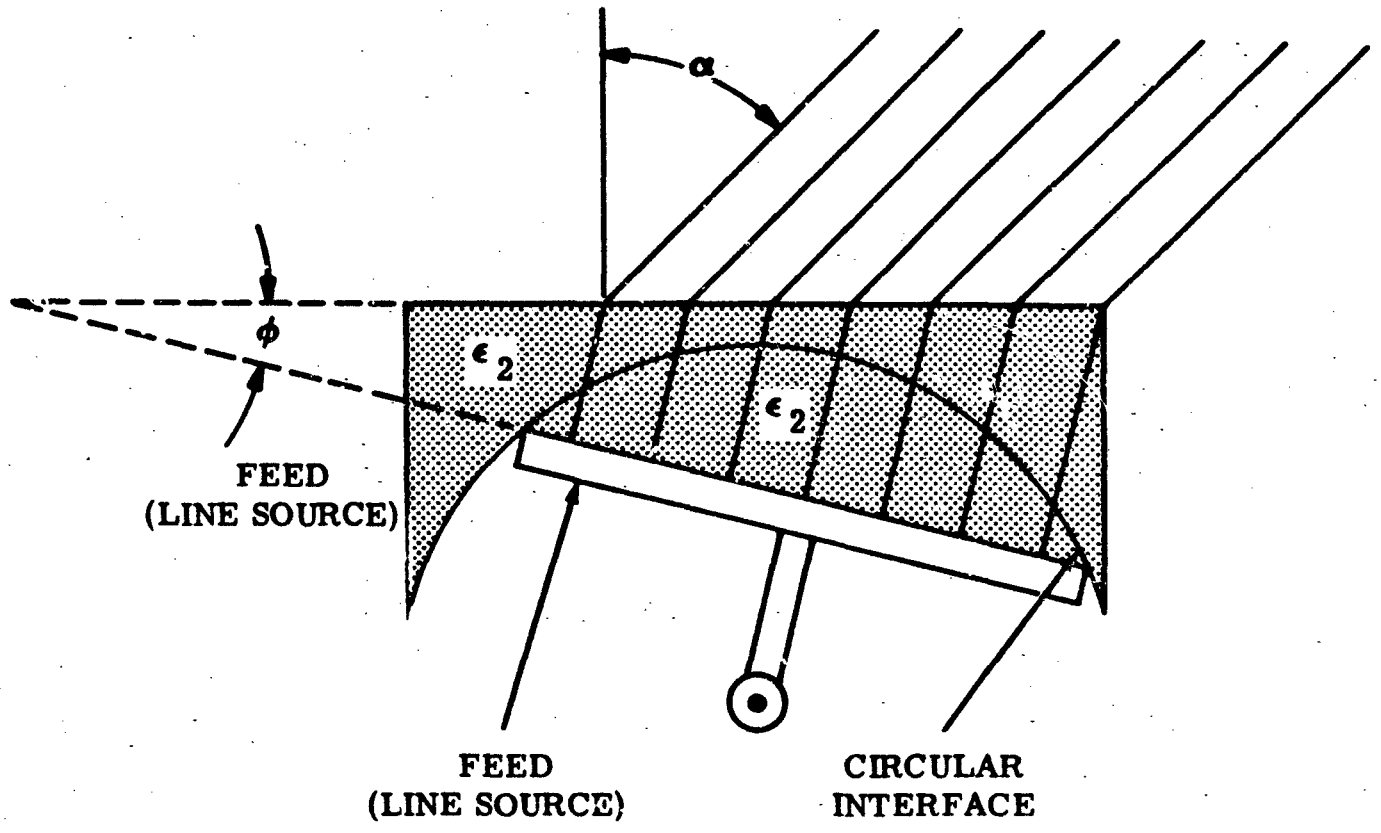

Figure 2. Variable Prism Circular Interface

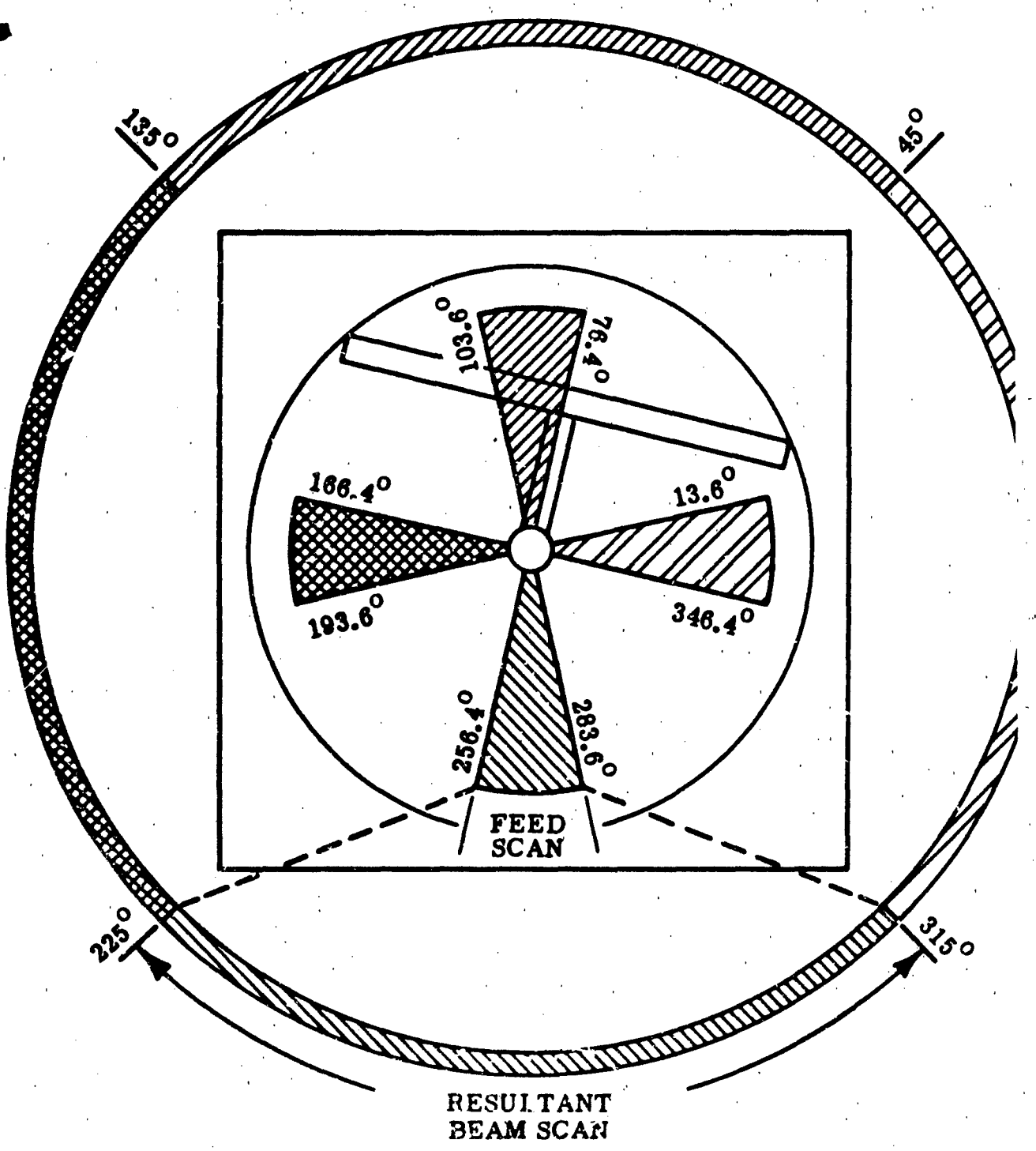

Figure 3. Beam Scan Versus Feed Scan

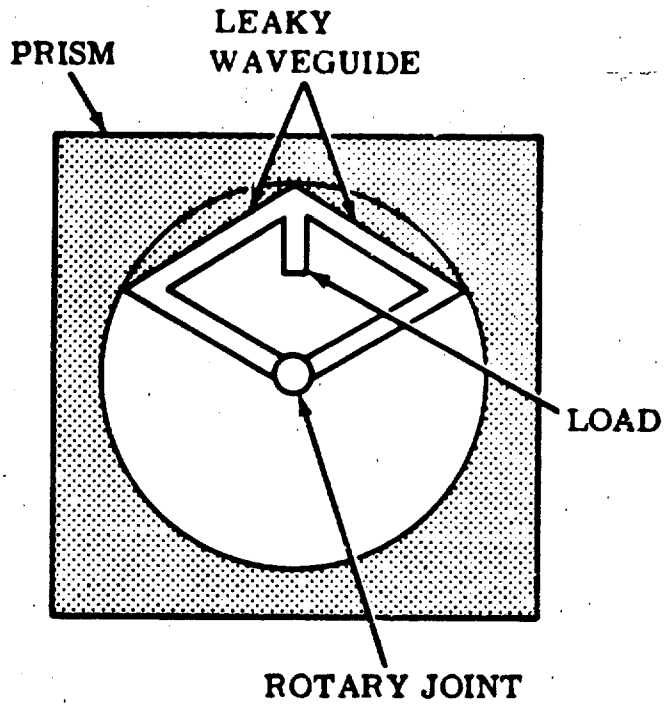

Figure 4. Leaky Waveguide Feed

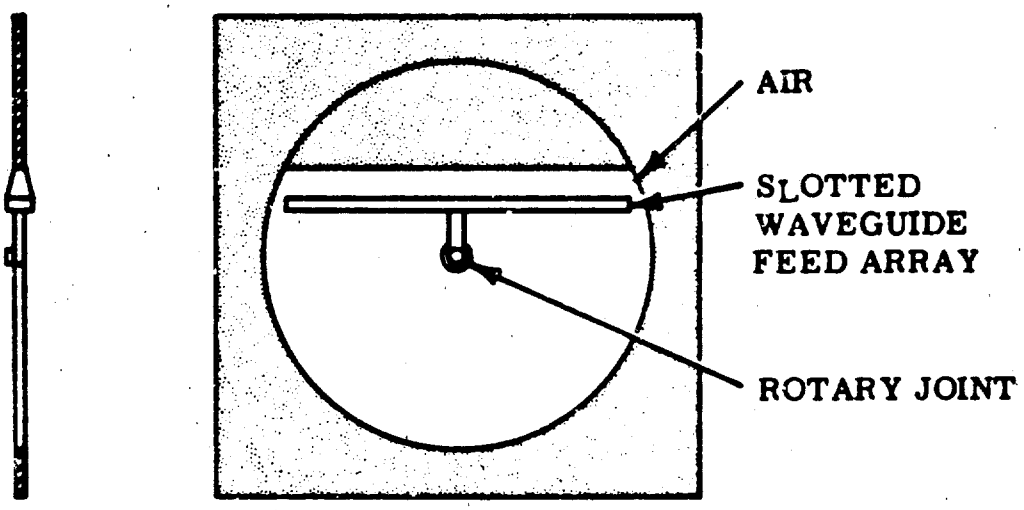

Figure 5. Resonant Slot Array Feed

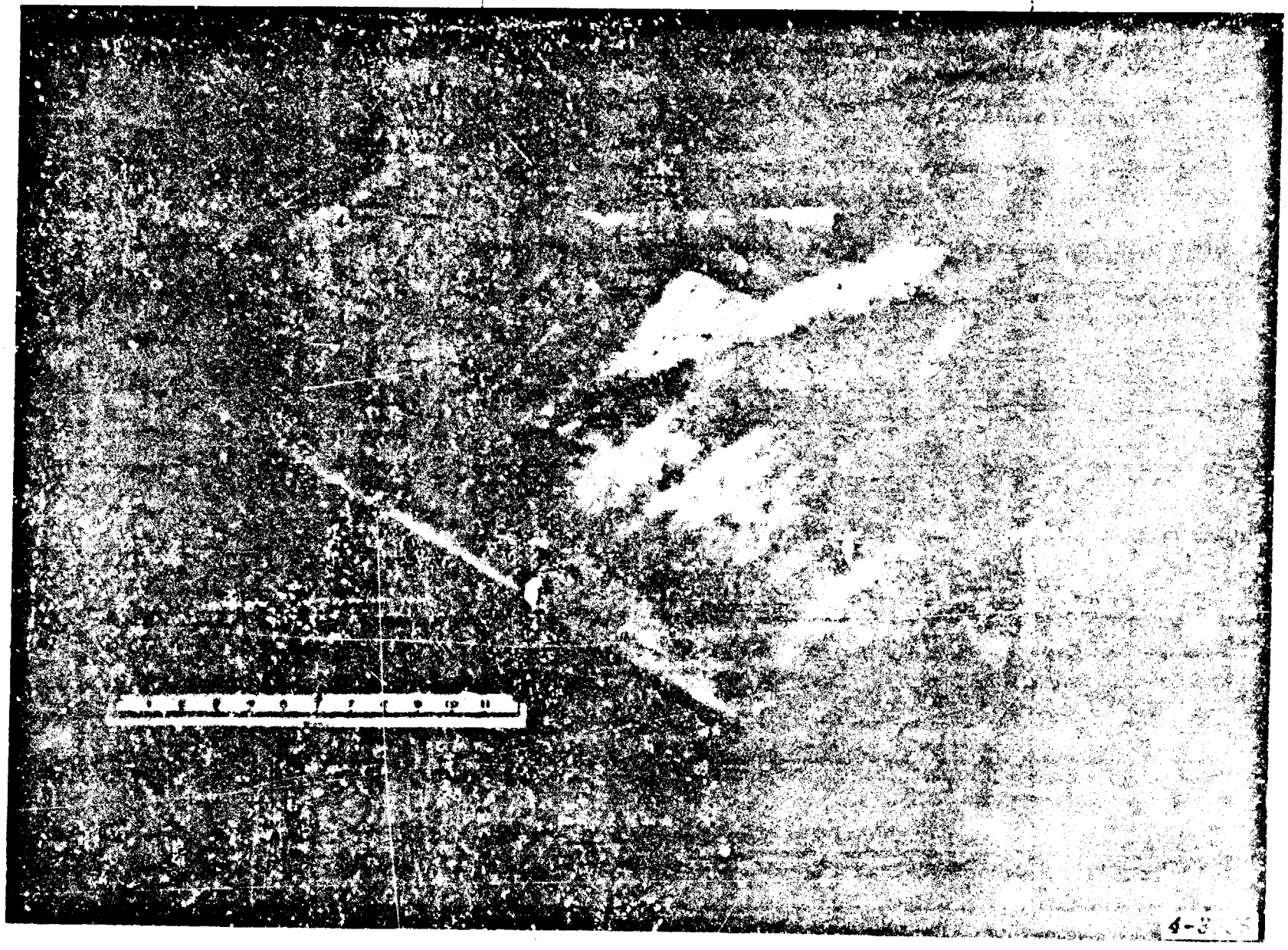

Figure 6. Variable Prism Antenna Test Model

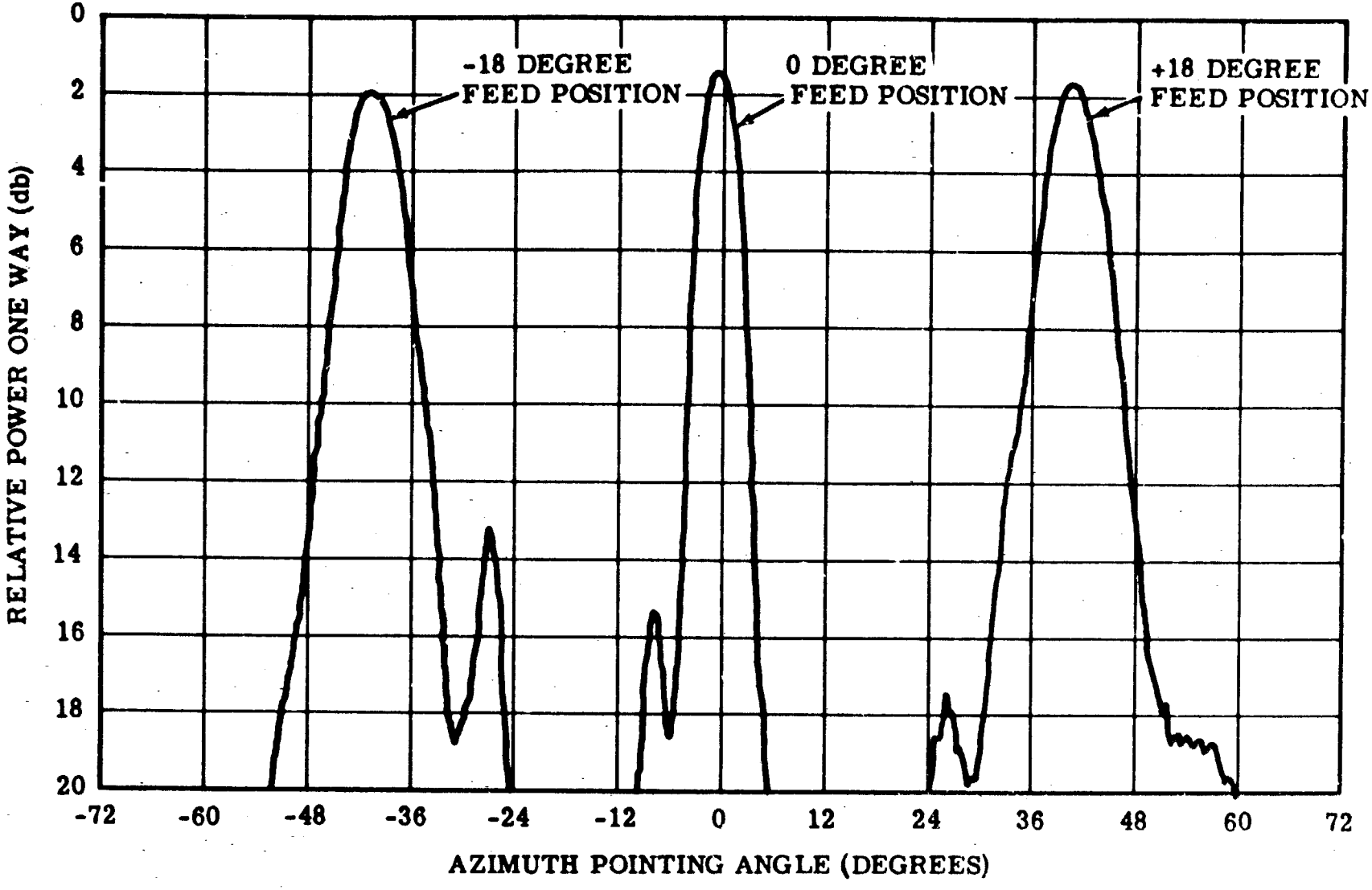

Figure 7. Measured Patterns of a Horn Fed Silicone Fiberglass Prism

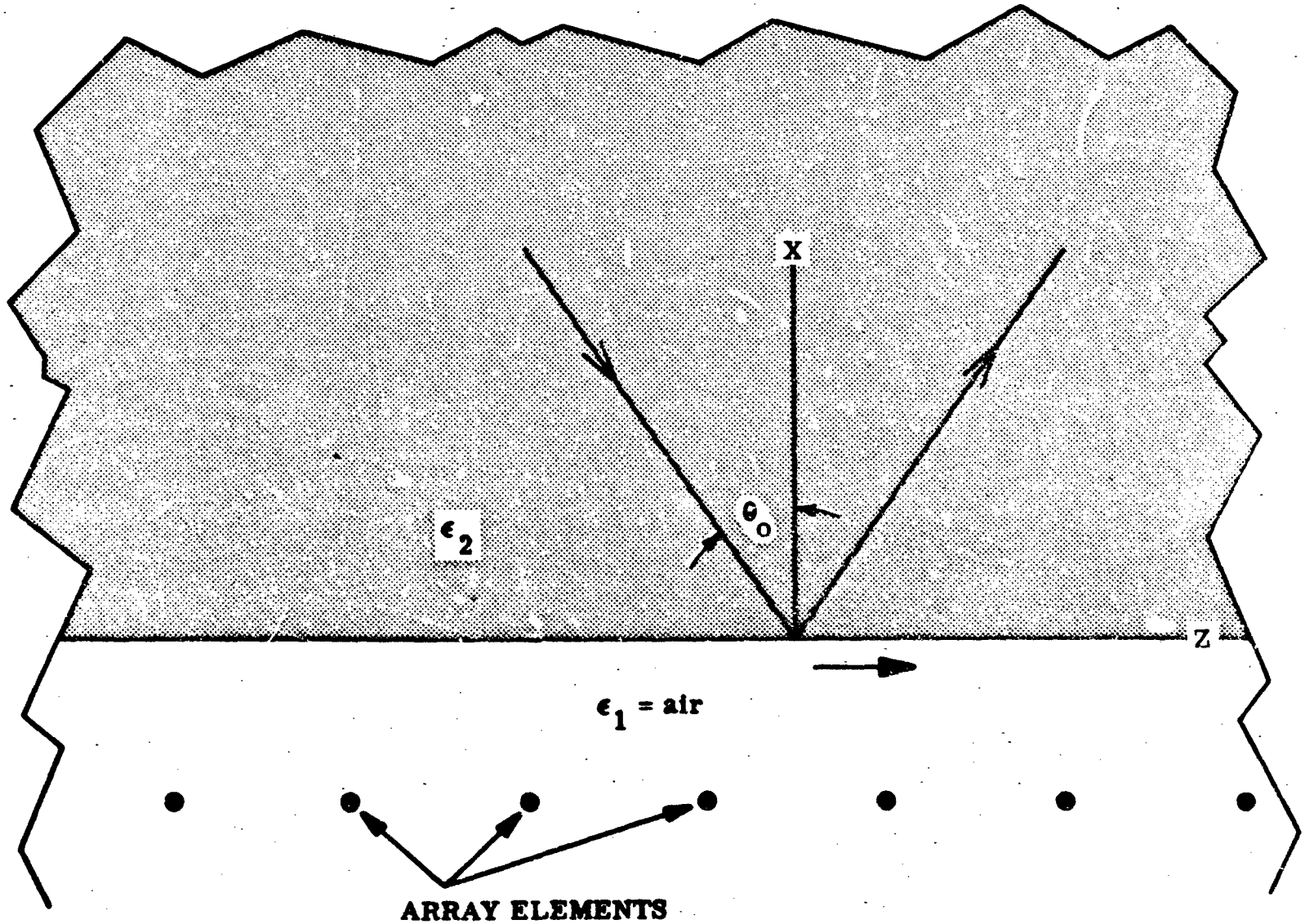

Figure 8. Derivation of Element Spacing

REFERENCES

1. Whinnery, J.R., and Jamieson, H.W., "Equivalent Circuits for Discontiniuties in Transmission Lines" Proc. IRE, February 1944, pp 98-114

2. Stratton, J.A., "Electromagnetic Theory" McGraw-Hill Publishing Co., 1941, pp 497-500

3. Skolnik, M.I., "Introduction to Radar Systems" McGraw-Hill Publishing Co., 1962, pp 336-343

APPENDIX A

OPTIMUM SPACING OF FEED ARRAY ELEMENTS FOR HIGH EFFICIENCY ANTENNA PERFORMANCE

The determination of the appropriate spacing between elements of an array in close proximity to a dielectric interface can be handled on the basis of the generation of grating lobes. Obviously, when such an array is designed to produce only one main lobe it will be very efficient, neglecting delectric and copper losses in the antenna mechanism.

Consider an array having a Taylor distribution yielding 20 db sidelobes. The Taylor distribution implies that the source is continuous. However, it can be shown that discrete elements with a certain maximum spacing can closely approximate the theoretical ideal. As the spacing is increased beyond the allowable maximum another lobe called a grating lobe will appear in the pattern very quickly (for long apertures) and move towards the main beam as spacing is increased. As the spacing is further increased more grating lobes are produced. A particular antenna design based on discrete elements must therefore be closely examined and a spacing determined to suppress such grating lobes. If the -20 db sidelobes limit is held then the production of as many as ten such sidelobes would reduce the gain (efficiency) of the antenna by less than 0.5 db.

Figure 8 illustrates the geometry of such a prism feed problem. Snell's law requires that a ray impinging on the dielectric-air ($\epsilon_2 - \epsilon_1$) interface at an angle $\theta_o = \sin^{-1}\left(\frac{1}{\sqrt{\epsilon_2}}\right)$ (where θ_o is the critical angle) would be transmitted parallel to the array at a velocity equal to that of light in air. The total suppression of a grating lobe in a direction θ_o in this system would then require $\frac{\lambda_o}{2}$ spacing of the elements, where λ_o is the wavelength in air and the array elements are fed in phase with one another.

For a long array such a grating lobe would be suppressed for any spacing slightly less than one wavelength, just as for an array in free space.

Thus, for such a broadside array radiation impinging at any angle between broadside and the critical angle, $\theta_o = \sin^{-1}\left(\frac{1}{\sqrt{\epsilon_2}}\right)$, will not result in a beam of greater than -20 db level if a nominal spacing of 0.5 λ or less is employed. At angles greater than the critical angle, however, the effect of total internal reflection is encountered. This effect corresponds to surface waves characterized by no time average flow of energy into the medium of lesser refractive index. There is, however, a field which decays exponentially with distance away from the interface into the lower dielectric. The time average flow of energy in the lower refractive medium is parallel to the interface and does not vanish. This energy flow is unattenuated in its direction of propagation. It decays exponentially ($e^{B_1 X}$) as the distance from the interface increases since x is negative.

From Stratton [2] the field intensity of the transmitted wave is given by

$$E_t = E_1 e^{(B_1 X + i \alpha Z - i \omega t)} \tag{A1}$$

where

$$\alpha = \frac{2\pi}{\lambda_2} \sin\theta = \text{phase velocity in Z direction and for } \epsilon_1 = 1, \tag{A2}$$

$$B_1 = \frac{2\pi}{\lambda_2} \sqrt{\sin^2\theta - \frac{1}{\epsilon_2}} = \text{attenuation in X direction.} \tag{A3}$$

When $B_1 = 0$

$$\sin^2\theta_o = \frac{1}{\epsilon_2} \text{ or } \sin\theta_o = \frac{1}{\sqrt{\epsilon_2}} \text{ (the critical angle).} \tag{A4}$$

The phase velocity in medium 1 (air) is then

$$\alpha = \frac{2\pi}{\lambda_2 \sqrt{\epsilon_2}} = \frac{2\pi}{\lambda_1} \tag{A5}$$

where λ_1 is the wavelength of the energy flow parallel to the array and sinc

$$\lambda_o = \sqrt{\epsilon_2}\ \lambda_2 \tag{A6}$$

then

$$\lambda_1 = \lambda_o \text{ at the critical angle.} \tag{A7}$$

If the elements are spaced $\frac{\lambda_o}{2}$ apart they will not give rise to this surfac wave. However, for such a spacing any surface wave for which $\lambda_1 = \lambda_o/2$ would be coupled to the array. This would occur when the phase velocity or sin θ is equal to 2 sin θ_o. For example, using a dielectric constant of 9

$$\sin \theta_o = \frac{1}{\sqrt{9}} = 0.333. \tag{A8}$$

Thus, when sin θ = 0.666 the array would be coupled efficiently to the surface wave.

But then

$$B_1 = \frac{2\pi}{\lambda_2} \sqrt{\sin^2 \theta - \frac{1}{9}} \tag{A9}$$

$$= \frac{2\pi}{\lambda_2} \sqrt{.443 - .111} = \frac{2\pi\ (0.576)}{\lambda_2}.$$

If the dielectric interface is one half of a free space wavelength from the array then the field incident upon the array will be attenuated by

$$e^{-\frac{2\pi\,(.576)\,\lambda_o}{2\lambda_2}} \tag{A10}$$

$$= e^{-5.45} = -26 \text{ db.}$$

This is greater than the -20 db level of the other antenna sidelobes and is therefore satisfactory.

A signal at any angle θ greater than this is attenuated even more, so the condition of no grating lobes greater that -20 db has been fulfilled. Thus, when the dielectric interface is at least one half of one free space wavelength from the array an element spacing of one half free space wavelength will be great enough to insure a very high efficiency.

APPENDIX B

DIELECTRIC PRISM PHASE ERROR ANALYSIS

In order to gain some insight into the effect of inhomogeneities in the dielectric materials of the prism, the phase error analysis of Skolnik[3] is used. Changes in the dielectric constant over small regionsof the prism will have their greatest effect on the velocity and resultant output phase of coherent energy traveling from the feed array to the radiating aperture.

For small phase errors the statistical average power pattern of a two dimensional source is

$$\overline{P_{(\theta,\phi)}} = P_o\ (\theta,\phi) + S\ (\theta,\phi)\ \frac{4C^2\ \pi^2\ \bar{\delta}^2}{\lambda^2\ G_o}\ \exp\ \left(-\ \frac{\pi^2\ u^2\ C^2}{\lambda^2}\right) \qquad \text{(B1}$$

where $u = \sin\theta$

$$S\ (\theta,\phi) = \cos\theta\ (\cos^2\theta\cos^2\phi + \sin^2\phi) \qquad \text{(B2}$$

G_o = no error antenna gain

$P_o(\theta, \phi)$ = no error array power pattern

$\bar{\delta}^2$ = mean square phase error in radians

C = correlation interval

Both $\bar{\delta}^2$ and C are fixed by the dielectric properties of the material employed and must be interpreted for a specific prism design. A large statistical analysis of typical or available materials that would determine these parameters is not available. Most high frequency measurements use sample pieces approximately $\frac{\lambda}{2}$ x $\frac{\lambda}{4}$ for insertion into waveguide. The smallest correlation interval, C, which can be used for this analysis is therefore $\frac{\lambda}{2}$.

The mean square phase error will be affected by the total path length through which the wave travels. If a particular phase error, δ_ρ , is associated with a sample path length L , the total phase error, δ . associated with a total path length NL will be

$$\delta = \sqrt{N}\ \delta_\rho \tag{B3}$$

This assumes a normal probability distribution for the errors and independence of the errors.

For example, given a sample path of length $\frac{\lambda}{2}$, which is equal to the correlation interval, then for a total path length of 10 λ the allowable error over the $\frac{\lambda}{2}$ path length sample (δ_ρ) would be

$$\delta_\rho = \delta/\sqrt{20} = .223\ \delta\ . \tag{B3a}$$

Assuming a small azimuth beamwidth of 2° then from equation (2) S $(\theta, \phi) \approx 1$. Also, since $u \approx 0$, $\exp\left(\frac{-\pi^2 u^2 C^2}{\lambda^2}\right) \approx 1$. Therefore (1) may be written

$$\overline{P_{(\theta,\phi)}} = P_o(\theta,\phi) + \frac{4C^2\pi^2\ \bar{\delta}^2}{\lambda^2\ G_o} \tag{B4}$$

If we allow 0.5 db maximum degradation of 20 db sidelobes we then have at this -19.5 db sidelobe

$$\overline{P_{(\theta,\phi)}} = .0112 \qquad (-19.5\ \text{db}) \tag{B5}$$

$$P_o(\theta,\phi) = .0100 \qquad (-20\ \text{db}) \tag{B6}$$

therefore from 4, 5, and 6 and remembering that $C = \frac{\lambda}{2}$

$$.0112 - .0100 = \frac{\pi^2\ \bar{\delta}^2}{G_o} = .0012 \tag{B7}$$

then assuming a gain G_o of 26 db (2° beamwidth line source)

$$\bar{\delta}^2 = \frac{.0012 \times 400}{\pi^2} = .0487 \text{ radians RMS} \quad \text{(B8}$$

from (3) and (8)

$$\delta_\rho^2 = 1.09 \times 10^{-2} \text{ radians RMS} \quad \text{(B9)}$$

$$= \pm 0.9^o \text{ peak phase error.}$$

The phase delay through the small path $\frac{\lambda}{2}$ is $\sqrt{\epsilon_r} \times 180^o$. Therefore over two parallel but equal length paths in which a nominal dielectric constant of 9 varies by some amount X it must be true that

$$\sqrt{9.00}\ (180) - \sqrt{9.00-X}\ (180) \leq 0.90 \quad \text{(B10}$$

solving for X

$$|X| \leq 0.03 \quad \text{(B11}$$

and the dielectric constant must therefore be held to 9.00 ±.03 in order to ins 19.5 db sidelobes. While this criteria is certainly quite restrictive there are a few materials such as alumina creamic which have this homogeneity.

TANDEM COUPLERS AND PHASE SHIFTERS: A NEW CLASS OF UNLIMITED BANDWIDTH COMPONENTS

By

J. P. Shelton*, R. Van Wagoner and J. J. Wolfe
Radiation Systems, Incorporated
Alexandria, Virginia

1.0 INTRODUCTION

A new class of tandem couplers and phase shifters has been developed. The bandwidths of these components may be extended almost without limit. These components consist of a series of coupling sections, having relatively low coupling coefficients, arranged in tandem to achieve overall coupling values of any desired strength. When used for octave bandwidths of operation, the advantage of this technique is that it allows the fabrication tolerance to be relaxed by a factor of five or six. This same technique, by virtue of the increased spacings between the tandem coupling sections, allows components to be developed for high average power applications. For example, RSI has developed and tested a 3-db quadrature coupler capable of handling 7.5 kw of average power.

Perhaps the most important asset of the tandem technique is that it allows almost unlimited bandwidths of operation to be achieved. This broad bandwidth capability is made possible by the fact that the requirement for increased coupling ratios for increased bandwidths may now be alleviated by the use of a series of tandem coupled sections. For example, an eight-to-one bandwidth coupler has been developed with a coupling variation of less than $\pm$0.5 db. Complementary to the development of these quadrature couplers has been the development of the fixed phase shifters for similar bandwidth.

Measured data are given for octave bandwidths, eight-to-one bandwidths, and preliminary data on 17-to-1 bandwidth couplers and phase shifters. The technique used to integrate these hybrid couplers and phase shifters into feed matrix assemblies is also illustrated.

2.0 REVIEW OF THEORY OF SIMPLE DIRECTIONAL COUPLER

The basic theory of operation of the parallel-coupled directional coupler is reviewed briefly for the benefit of those unfamiliar with this general

*Mr. Shelton is now a member of the staff of the Institute for Defense Analyses, Washington, D. C.

type of component. Figure 1 illustrates the operation in terms of the even and odd modes of the coupled region. The concept of even and odd mode for such a structure is very powerful because it allows analysis of the network as a two-port rather than as a four-port. From the illustration it is that the coupled region represents a low impedance for one mode and a high impedance for the other. Thus, each mode is reflected by the coupled region the magnitude of the reflection depending upon the length of the region and the mode impedance.

The reverse coupling characteristic is achieved by the opposite sign of the reflection coefficients for the two modes. The voltage reflection coefficient from an upward impedance step is positive, while that from a downward step is negative. It is this characteristic that accomplishes the transfer of energy from the input port to the opposite port. The analysis of the component for energy fed into a given port is outlined below.

Input amplitudes	1	0
Even Mode component	+1/2	+1/2
Odd Mode component	+1/2	-1/2
Reflected Even Mode component	+1/2 r	+1/2 r
Reflected Odd Mode component	-1/2 r	+1/2 r
Total Reflected (coupled) Amplitudes	0	r

The transmission coefficients for the two modes are both positive, so that the energy emerging from the other end of the coupled region maintains the same relative distribution as at the input end. Thus, in order to insure the proper cancellation of reflected components at the input port, the reflection coefficients of the even and odd modes must be of the same magnitude. If the characteristic impedance of the uncoupled transmission line is Z_o, the even-mode impedance of the coupled region is Z_{oe}, and the odd-mode impedance of the coupled region is Z_{oo}, the reflection coefficients will have the same magnitude if $Z_o/Z_{oo} = Z_{oe}/Z_o$. This leads directly to the well-known expression, $Z_{oe}Z_{oo} = Z_o^2$, which guarantees perfect match and isolation for these directional couplers.

Therefore, the performance of any parallel-coupled directional coupler can be described in terms of the reflection characteristics of a single mode provided the required inverse relationship between even and odd mode impedances is maintained. For the single coupled region with $Z_{oe}/Z_{oo} = \rho$ and length = θ, a straightforward transmission-line calculation yields

$$V_c = \frac{j\,k \sin\theta}{\sqrt{1 - k^2}\cos\theta + j\sin\theta},$$

where: $$k = \frac{\rho - 1}{\rho + 1}$$

For loose coupling, that is for $\rho - 1$ small, the voltage coupling coefficient V_C is nearly sinusoidal with frequency. For stronger coupling, the curve tends to be flatter than a sine curve.

3.0 THEORY OF OPERATION OF WIDEBAND COUPLERS

The coupler can be further analyzed for the case of loose coupling. For $\rho \approx 1$, $V_C \approx j\, k \sin\theta$. Another way of looking at the operation of the component is to consider the reflections from the individual impedance steps. For loose coupling these reflections can be added separately, since the second-order reflections will be negligible. Thus, the reflection coefficient for the even mode at the input to the coupled region, for example, is given by

$$\Gamma = \frac{\rho - 1}{\rho + 1}$$

and the total reflected amplitude from both ends of the coupled region is given by

$$V_C = j2\Gamma \sin\theta \ .$$

It is seen upon examination that

$$2\,\frac{\sqrt{\rho - 1}}{\sqrt{\rho + 1}} \approx \frac{\rho - 1}{\rho + 1} \quad \text{or} \quad 2\Gamma \approx k .$$

Therefore, as one would expect, the operation of the coupler for the case of loose coupling can be analyzed in terms of the reflection coefficients at the impedance steps.

It is now possible to consider the techniques that are available for broadbanding the directional coupler. From past experience it can be expected that a broadband component will contain several coupled regions. One configuration for a broadband prototype is shown in Figure 2. The coupler is symmetrical in order to insure phase quadrature of the outputs in applications with close tolerance on phase. Please note the crossover of coupled lines at the center. The need for this detail will be clarified later. As with most multisection or multielement arrays, the operation can be described in terms of harmonics. The innermost steps contribute a term proportional to sin θ, the next steps out contribute a term proportional to sin 3θ, and so forth for as many odd harmonics as one wishes.

The synthesis procedure will not be described here. Shelton has recently presented the synthesis of wideband directional couplers and fixed

type of component. Figure 1 illustrates the operation in terms of the even and odd modes of the coupled region. The concept of even and odd mode for such a structure is very powerful because it allows analysis of the network as a two-port rather than as a four-port. From the illustration it is that the coupled region represents a low impedance for one mode and a hi impedance for the other. Thus, each mode is reflected by the coupled re the magnitude of the reflection depending upon the length of the region an the mode impedance.

The reverse coupling characteristic is achieved by the opposite si of the reflection coefficients for the two modes. The voltage reflection efficient from an upward impedance step is positive, while that from a do ward step is negative. It is this characteristic that accomplishes the tra of energy from the input port to the opposite port. The analysis of the co ponent for energy fed into a given port is outlined below.

Input amplitudes	1	0
Even Mode component	+1/2	+1/2
Odd Mode component	+1/2	-1/2
Reflected Even Mode component	+1/2 r	+1/2 r
Reflected Odd Mode component	-1/2 r	+1/2 r
Total Reflected (coupled) Amplitudes	0	r

The transmission coefficients for the two modes are both positive, so that the energy emerging from the other end of the coupled region maintains the same relative distribution as at the input end. Thus, in order to insure t proper cancellation of reflected components at the input port, the reflectic coefficients of the even and odd modes must be of the same magnitude. I the characteristic impedance of the uncoupled transmission line is Z_o, th even-mode impedance of the coupled region is Z_{oe}, and the odd-mode impedance of the coupled region is Z_{oo}, the reflection coefficients will hav the same magnitude if $Z_o/Z_{oo} = Z_{oe}/Z_o$. This leads directly to the well-known expression, $Z_{oe}Z_{oo} = Z_o^2$, which guarantees perfect match and isolation for these directional couplers.

Therefore, the performance of any parallel-coupled directional cou can be described in terms of the reflection characteristics of a single mod provided the required inverse relationship between even and odd mode impedances is maintained. For the single coupled region with $Z_{oe}/Z_{oc} = \rho$ and length = θ, a straightforward transmission-line calculation yields

$$V_c = \frac{j k \sin\theta}{\sqrt{1 - k^2}\cos\theta + j\sin\theta},$$

where: $$k = \frac{\rho - 1}{\rho + 1}$$

in general, the lower ρ, the greater the separation between transmission lines, with resultant difficulty in stepping in to more tightly coupled sections.

Of course, the first instance in which the tandem configuration was used was the single-section coupler, in which the relatively strong coupling coefficient associated with a three-db coupler was avoided by using two 8.3 db couplers in tandem. The primary reason for this design approach was the improvement in strip-transmission-line mechanical tolerance, which is outlined in the table of Figure 4 (a). By coincidence, the 8.3 db coupled regions can be realized quite conveniently with a three-layer sandwich in which the thicknesses of the layers are the same. In addition to improved reproducibility which results from the superior mechanical tolerances, the tandem realization allows the design of three-db couplers at relatively high microwave frequencies without the use of elaborate tuning adjustments. For example, a commercially available three db coupler operating in the S-band region contains six tuning screws. Furthermore, the increased spacing between center conductors in the coupled regions enables the use of these components at increased power levels.

In the case of single-section components, a small price is paid for the use of the tandem configuration in the form of slight degradation of the bandwidth-vs-coupling tolerance curve, as shown in Figure 4 (b). It is seen that an octave-bandwidth three db coupler has a tolerance of $\pm$ .31 db for a single coupled region and $\pm$ .45 db for the tandem arrangement.

5.0 COMPONENT DESIGNS AND TEST RESULTS

Tandem components of widely varied design and construction have been fabricated and tested at Radiation Systems, Incorporated since early 1962. These components vary from relatively narrow-band units to components that cover 17:1 bandwidths. Frequencies of operation vary from V.H.F. through X-band. In all cases the results have been satisfactory and, it is felt, better than might have been obtained through previously available techniques. The tables in Figures 5 and 6 list design values for the coupling coefficients of several couplers and phase shifter designs.

5.1 Octive Bandwidth Units

The performance data for a typical octave-band coupler fabricated of three-layer strip transmission-line, are shown in Figure 7. Twelve of these couplers were fabricated for a particular hardware requirement. Performance data on all units were identical within the measurement tolerances of the equipment used. These couplers were not tuned or adjusted in any manner during the fabrication and testing process. This experience is by no means unusual for tandem components.

The data shown in Figure 8 illustrates the performance of a 90 degr phase shifter that was designed to be used with the 3 db couplers discusse in the above paragraph.

5.2 High Power Units

Tandem couplers have been designed and constructed to oper with rather high power levels. The photograph of Figure 9 illustrates three three db couplers that have been fully tested at an average power of 7.5 kv at a frequency of 136 mc. The three db coupling tolerance is within ± 0.1 d the VSWR is less than 1.1 to 1, and the isolation is greater than 28 db ove the 30 percent band of operation. This coupler is designed utilizing conve tional three-layer strip transmission techniques; however, the center condu are machined from 1/16 inch brass and the dielectric material is machined solid teflon sheets. The overall package is 1 3/16 inches thick, 17 7/8 in long and 6 1/8 inches wide.

5.3 Eight to One Bandwidth Component Design and Data

The general design procedure outlined in the previous section was used to determine the ρ values and hence the even and odd mode impec of a seven section 8.3 db coupler with tolerance of ± .35 db and a four sec 45° phase shifter with tolerance of ± 3°. It was decided to fabricate the u on copper clad polyolefin base material because of its low insertion loss a negliable dielectric constant variation. The units were designed for a 3 la strip transmission line package with a s/b ratio of 1/9, using s = .031 a b = .281. The strip widths and gap spacings of the units were calculated a follows:

Seven Section Coupler

ρ	Strip Width	Strip Overlap
4.4470	.133	.085
1.6256	.197	.020
1.2197	.215	-.087
1.0708	.219	-.187

Four Section Phase Shifter

ρ	Strip Width	Strip Overlap
5.033	.128	.106
2.202	.171	.013
1.462	.204	-.037
1.158	.218	-.113

Once these units were realized, they were combined in the previously discuss tandem technique to form the final 3 db hybrid coupler and 90° shifter. Photog of these units are shown in Figures 10 and 11.

The forty five degree miters situated between the quarter wavelength sections were found to lessen impedance discontinuity caused by large changes in gap spacings from one section to the next. Final test data of the units are shown in Figures 12 and 13. The power division data recorded for the hybrid coupler is very close to the calculated curve. The relative phase data recorded for the 90° phase shifter indicates wider phase tolerance than anticipated. However, part of this discrepancy was attributed to measurement errors, and part to the imperfect realization of the calculated strip widths and spacings. It is noteworthy to mention that it was found that strip widths and gap spacing tolerances must be held to within ± .005" on the loosely coupled sections and ± .002" on the tightly coupled sections. Also, it was found that a slight variation in thickness of the center dielectric layer had an appreciable affect on the coupling valve of the tightly coupled section.

5.4 Excitation Assembly

One of the prime advantages of developing printed circuit hybrid junctions and phase shifters is the ease and practicability of integrating these units into matrix feed networks or excitation assemblies. Figure 14 illustrates RSI's technique for laying out a four part matrix using the 8 to 1 components discussed on the previous section. The network was used in conjunction with a four-arm equalangular conical spiral antenna to afford radiation in the sum (Σ), Difference (Δ) and acquisition (3) modes of operation. A block diagram of the four part matrix and resultant radiation patterns are shown in Figure 15.

5.5 Seventeen to One Bandwidth Hybrid Coupler

Within the last few weeks a 17:1 band 3 db coupler has been designed, fabricated, and tested. A photograph of the unit is shown in Figure 16. The experimental results of this initial effort are shown in Figures 17 and 18. It is very encouraging to notice that the measured ripple position and magnitude very nearly correspond to the theoretical curve plotted in Figure 17. The loss of coupling at the high end of the band is due to a fabrication difficulty. If the design synthsis was faulty the coupling curve would have been symmetrically poor around the center frequency of the coupler. It is expected that slight layout adjustments will bring the coupling curve very close to the theoretical performance.

6.0 BIBLIOGRAPHY

1. Paul Shelton, "Synthesis and Design of Wideband TEM Directional Couplers", presented at International Conference on Microwaves, Circuit Theory, and Information Theory, 10 September 1964, Tokyo, Japan.

2. B. M. Shiffman, "A New Class of Broadband Microwave 90-Degree Phase Shifters, "IRE Trans. Vol. MTT-6, pp. 232-237, April 1958.

3. S. B. Cohn, "The Re-Entrant Cross Section and Wide-band 3 db Hybrid Couplers, "IEEE Trans. Vol. MTT-11, No. 4, pp. 254-257; July 1963.

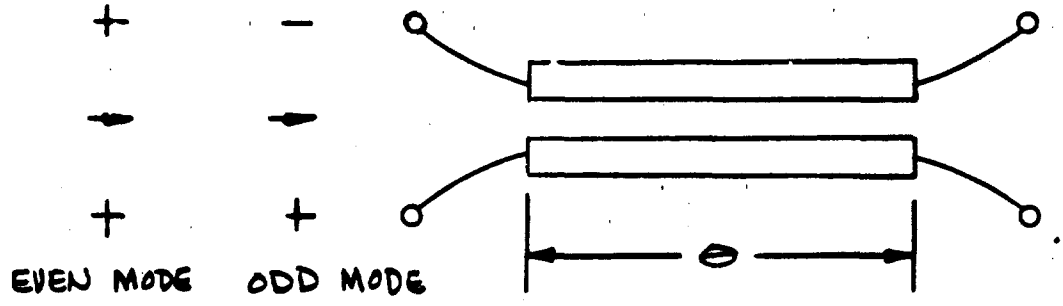

(a) EVEN AND ODD MODES FOR PARALLEL-COUPLED REGION

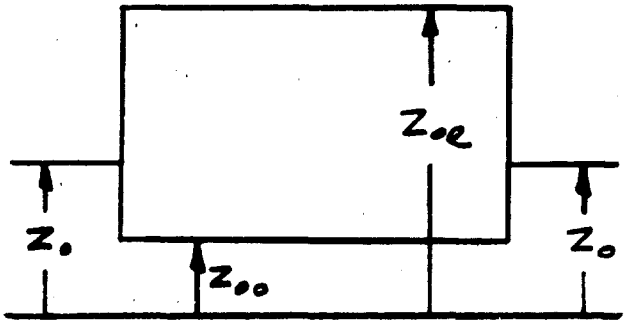

(b) IMPEDANCES FOR EVEN AND ODD MODES

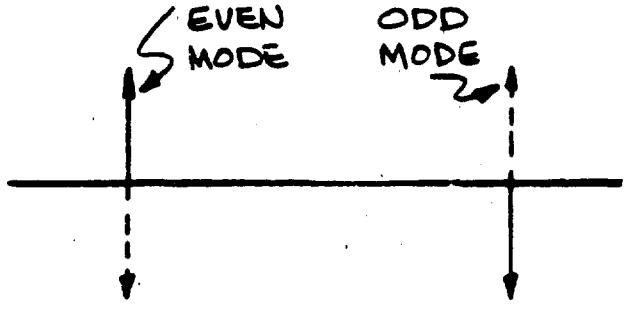

(c) REFLECTION COEFFICIENTS FOR EVEN AND ODD MODES

Figure 1. Operation of Directional Coupler on Mode Basis

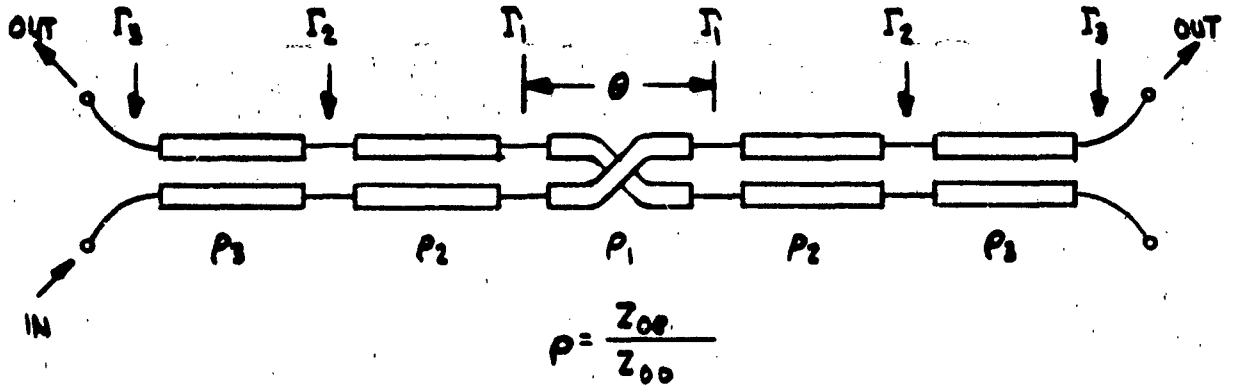

FIG 2a CONFIGURATION OF MULTISECTION DIRECTIONAL COUPLER

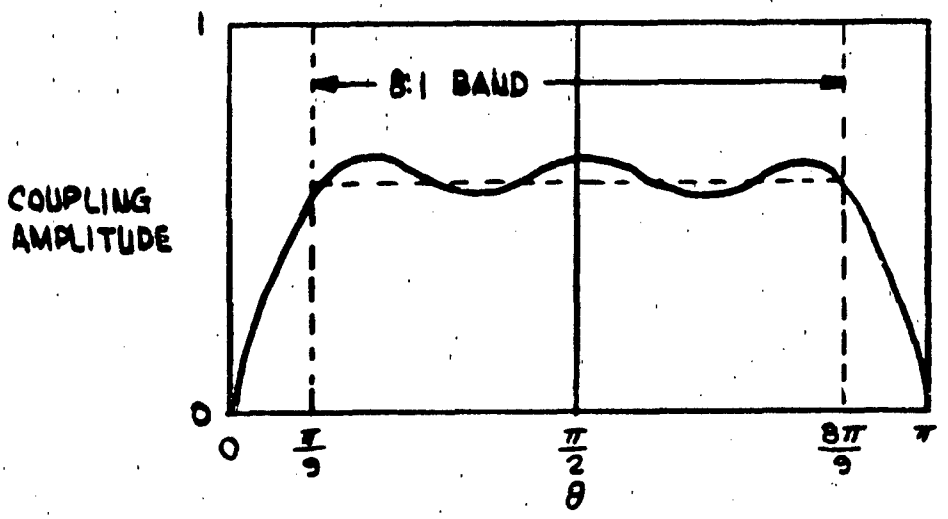

FIG 2b REQUIRED COUPLING RESPONSE OF MULTISECTION COUPLER

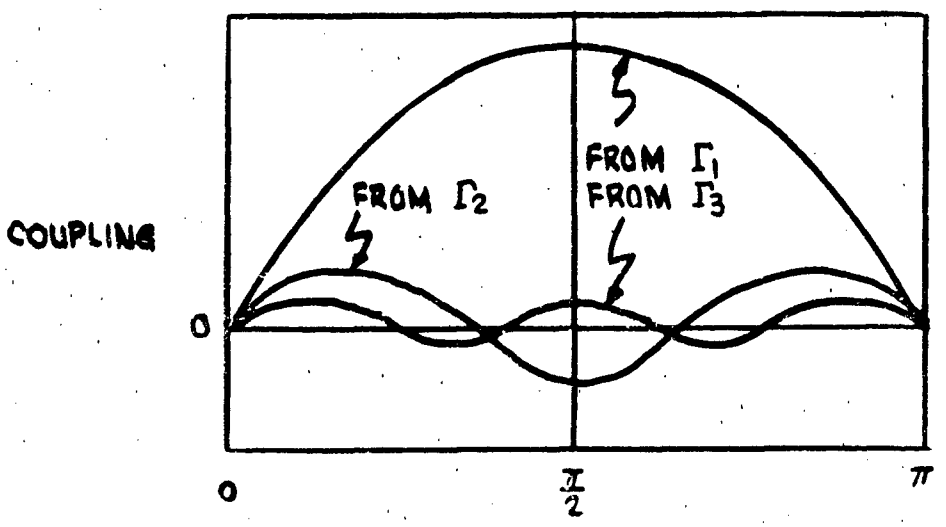

FIG 2c DECOMPOSITION OF COUPLING RESPONSE

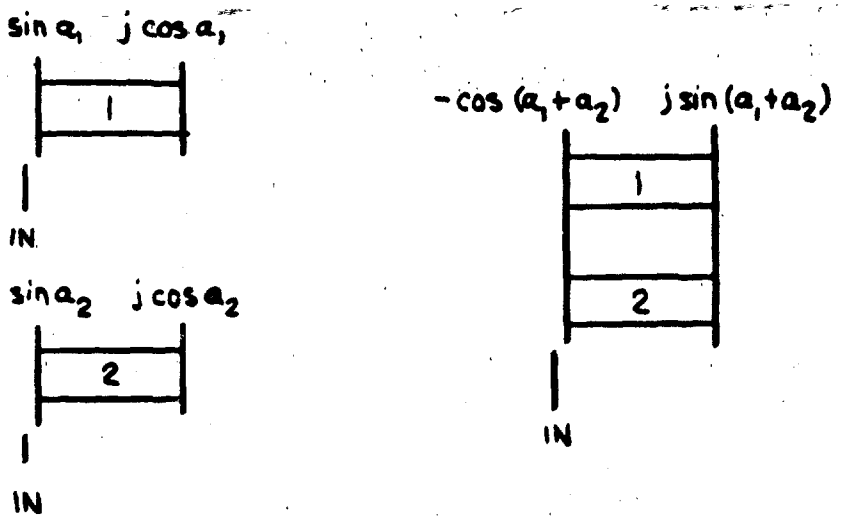

FIG 3a OPERATION OF DIRECTIONAL COUPLERS CONNECTED IN TANDEM

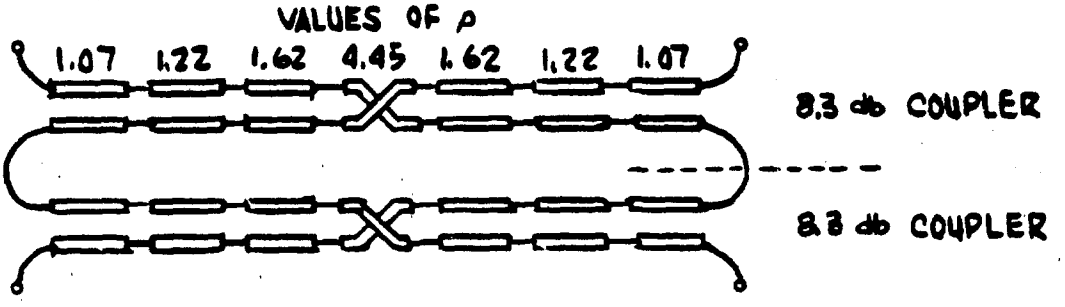

FIG 3b TANDEM CONNECTION OF TWO IDENTICAL UNITS

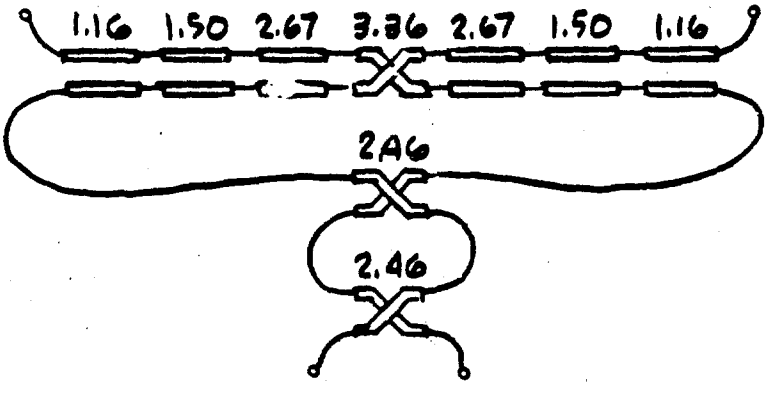

FIG 3c TANDEM CONNECTION OF DISSIMILAR UNITS

FIG.3. LAYOUT OF DIRECTIONAL COUPLERS WITHOUT EXTREMELY TIGHT COUPLING

Figure 4(a) Effects of Mechanical Tolerances in Coupling Tolerances

Physical Characteristics	Performance RSi Design	Conventional Design
Strip Width, S-	S = 0.062	S = 0.014
Groundplane separation, b -	b = 0.188	b = 0.204
Strip width tolerance -	0.027 db change/mil	0.1 db change/mil
Material thickness tolerance (Center layer)	0.140 db change/mil	0.4 db change/mil

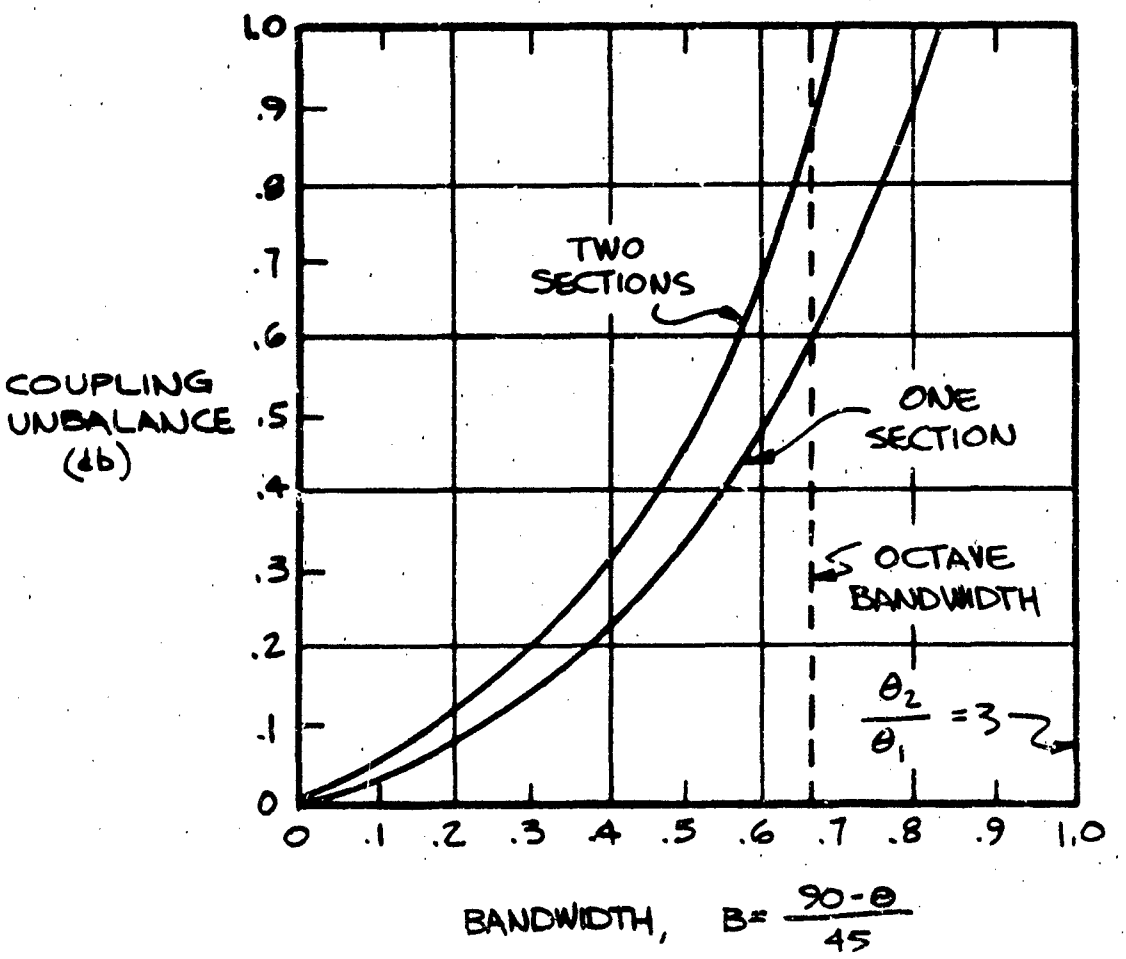

Figure 4(b) Bandwidth versus Coupling Unbalance.

Nominal Coupling Value		3 db	3 db	3 db	3 db	3 db
Coupling Tolerance, + db		0.01	0.5	0.23	0.24	0.4
Bandwidth		0.3:1	2:1	8:1	8:1	17:1
Voltage Coupling Coefficient for each λ/4 Section	K11	.382	.406	.636	.542	.542
	K12			.238	.453	.542
	K13			.099	.208	.436
	K14			.034	.073	.286
	K15					.181
	K16					.116
	K17					.061
	K21	.382	.406	.636	.412	.542
	K22			.238		.162
	K23			.099		
	K24			.034		
	K31				.412	.506

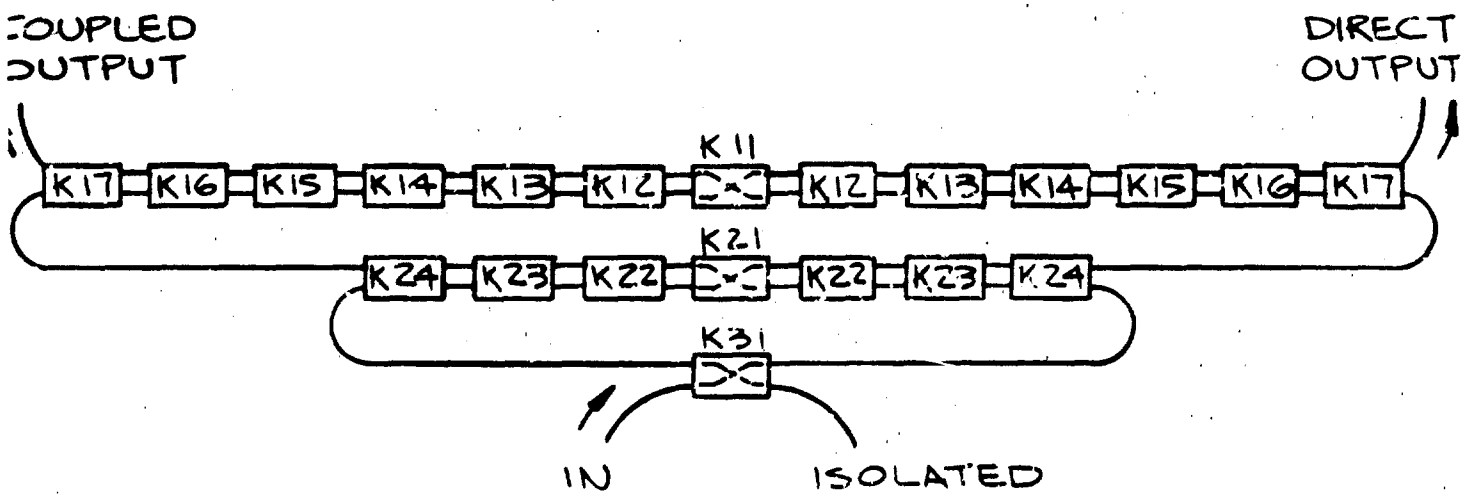

Figure 5. Coupling Sections Required for Various Tandem Quadrature Couplers

Nominal Phase Shift, degrees		90	45	90	90
Phase Tolerance, + degrees		3	4	4	6
Bandwidth		2:1	8:1	8:1	17:1
Voltage Coupling Coefficient for Each λ/4 Section	K11	.480	.638	.658	.542
	K12		.332	.375	.542
	K13		.140	.187	.542
	K14			.079	.483
	K15				.315
	K16				.180
	K21			.658	.542
	K22			.375	.542
	K23			.187	.199
	K24			.079	
	K31				.542
	K32				.156
	K41				.421

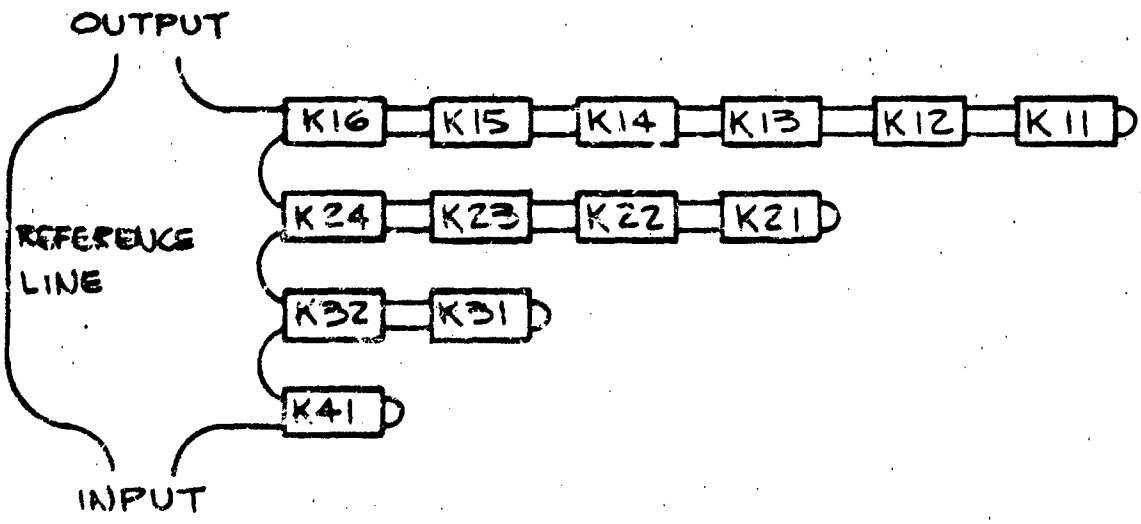

Figure 6. Coupling Sections Required for Various Tandem F

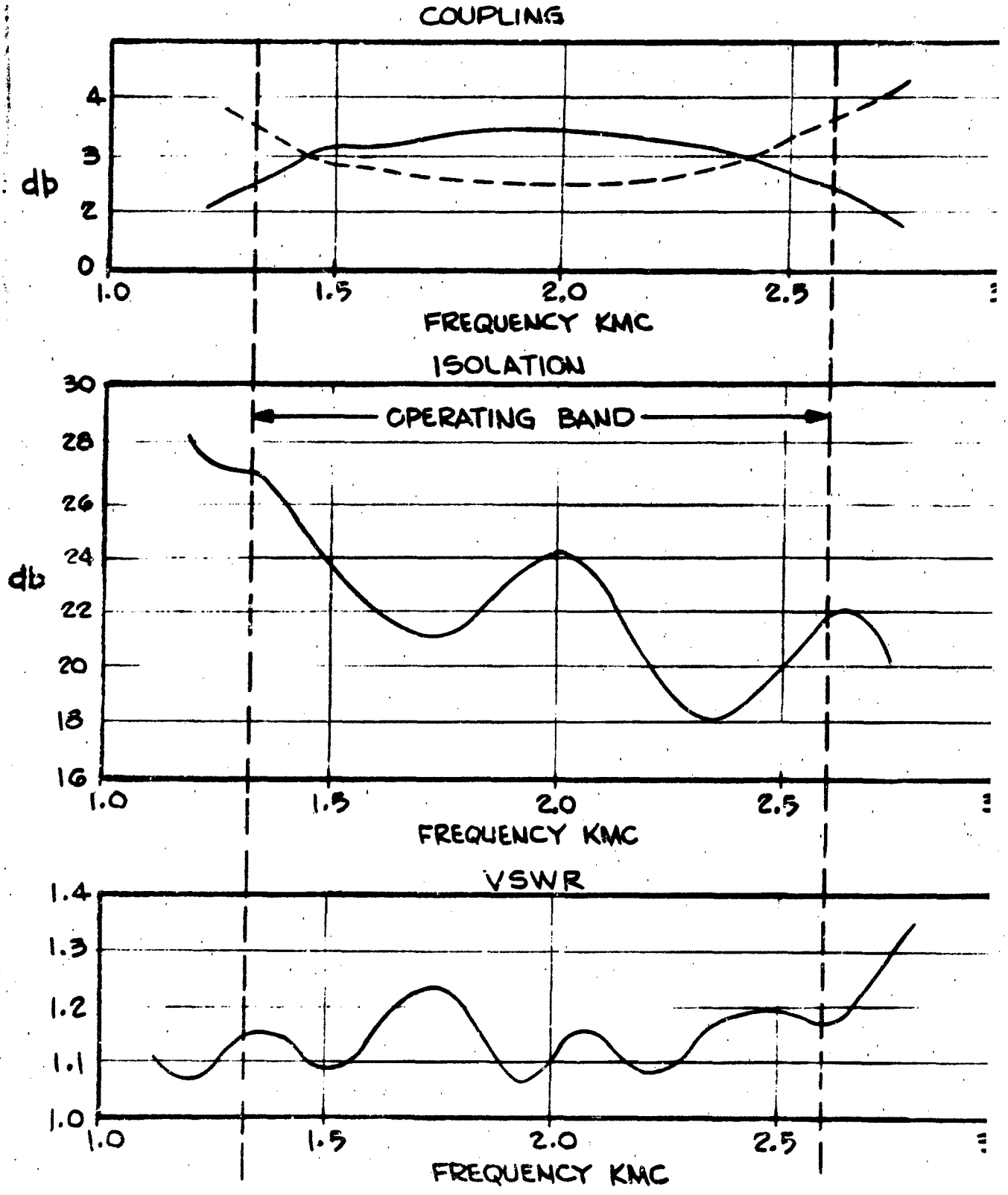

Figure 7. Performance of Octave-Band Tandem Coupler.

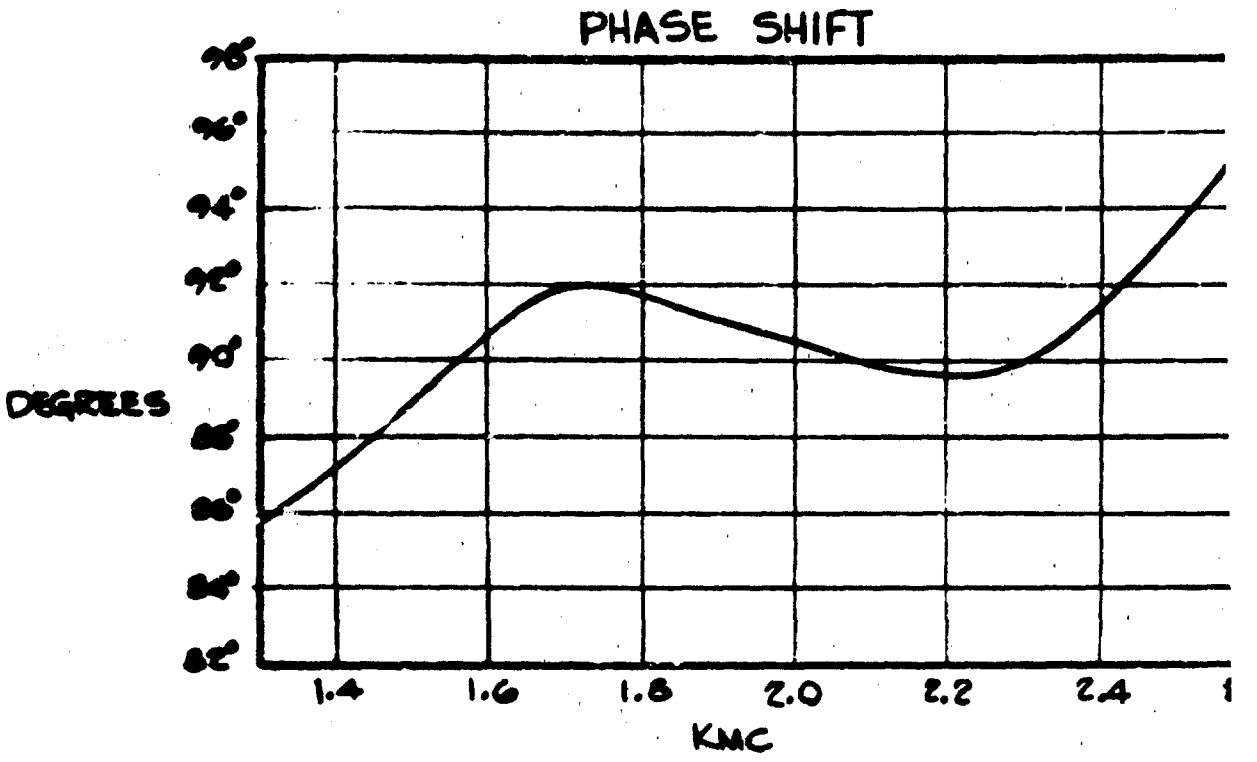

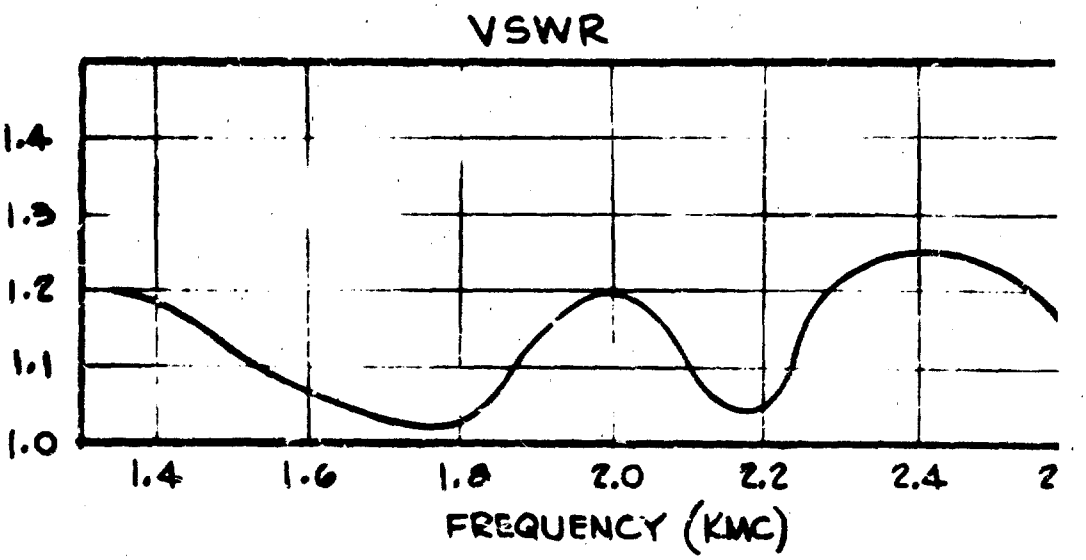

Figure 9. Performance of Octave-Band 90° Phase Shifter.

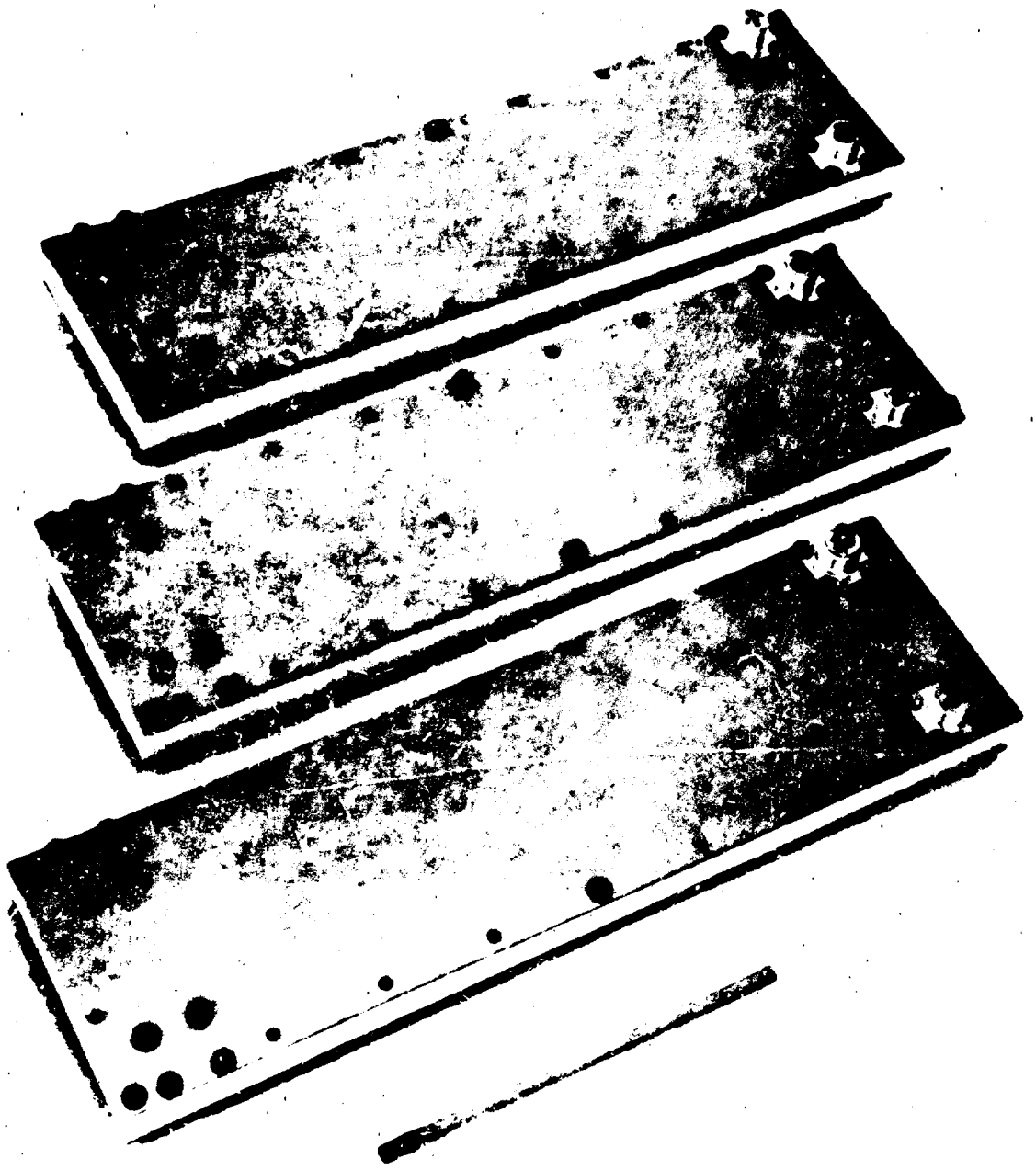

Figure 9. High Power 3 db Couplers

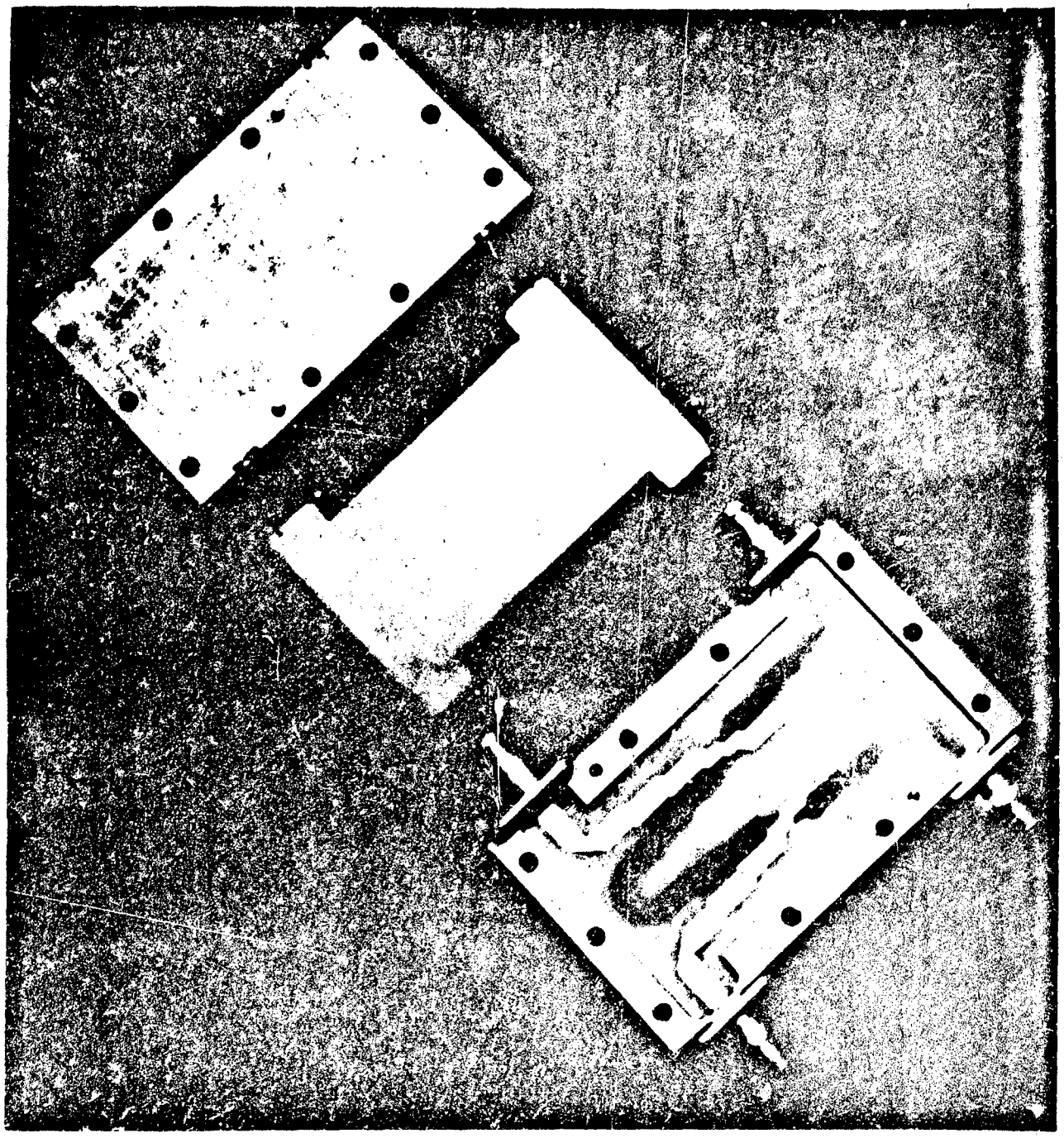

Figure 10. Eight to One Bandwidth Hybrid Coupler.

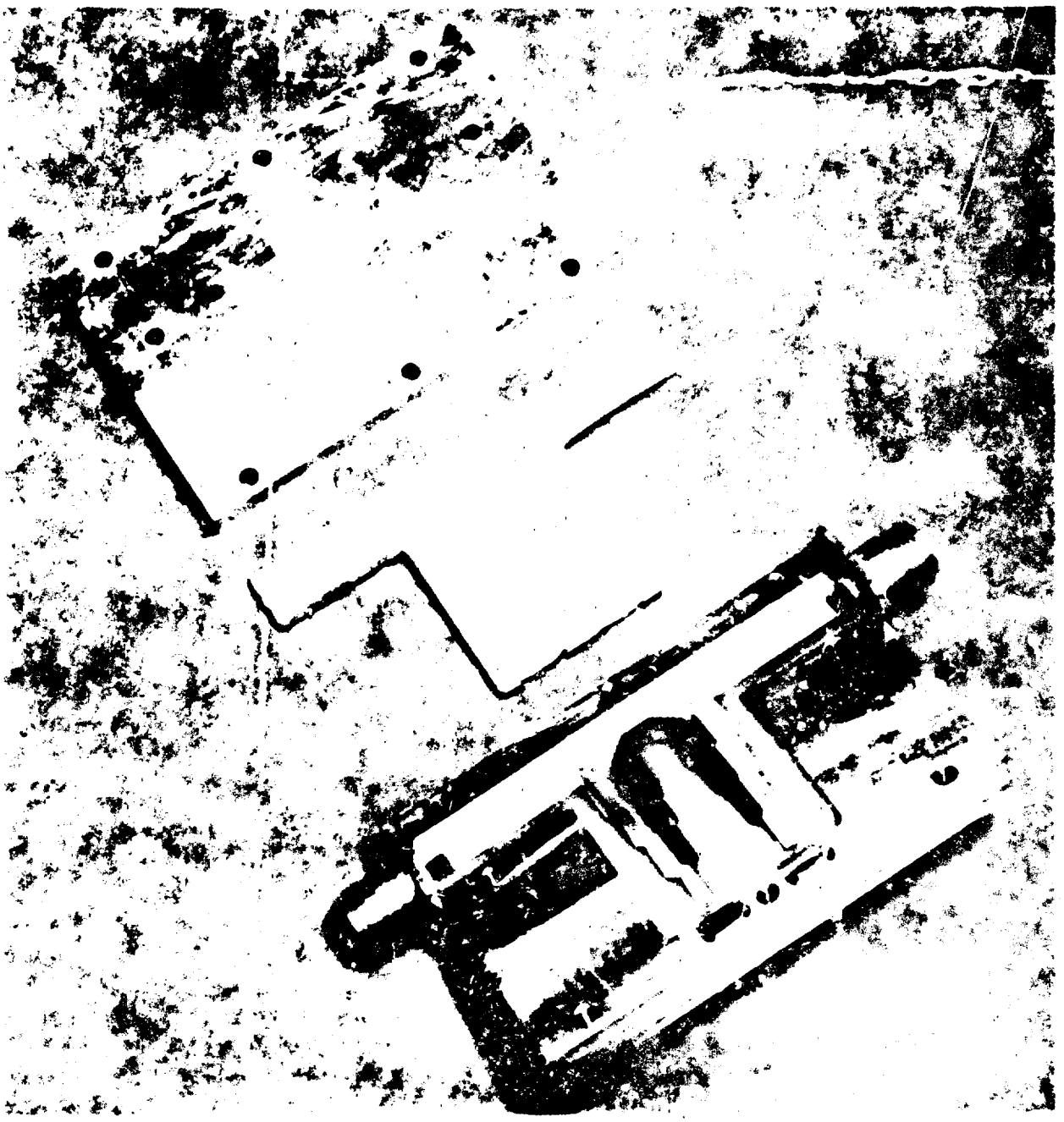

Figure 11. Eight to One Bandwidth 90° Phase Shifter.

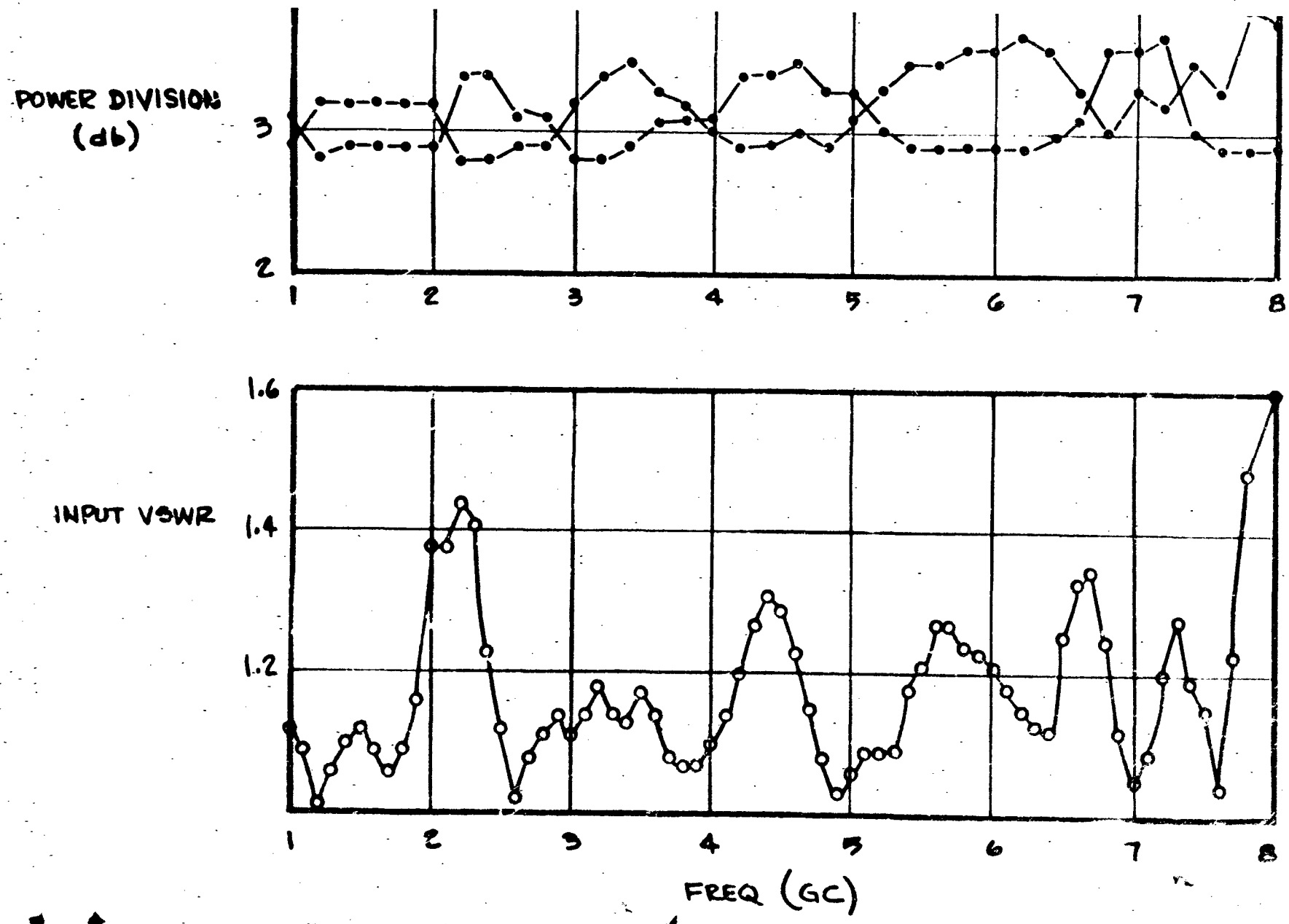

Figure 12. Performance Data of 8 to 1 Bandwidth Hybrid Coupler.

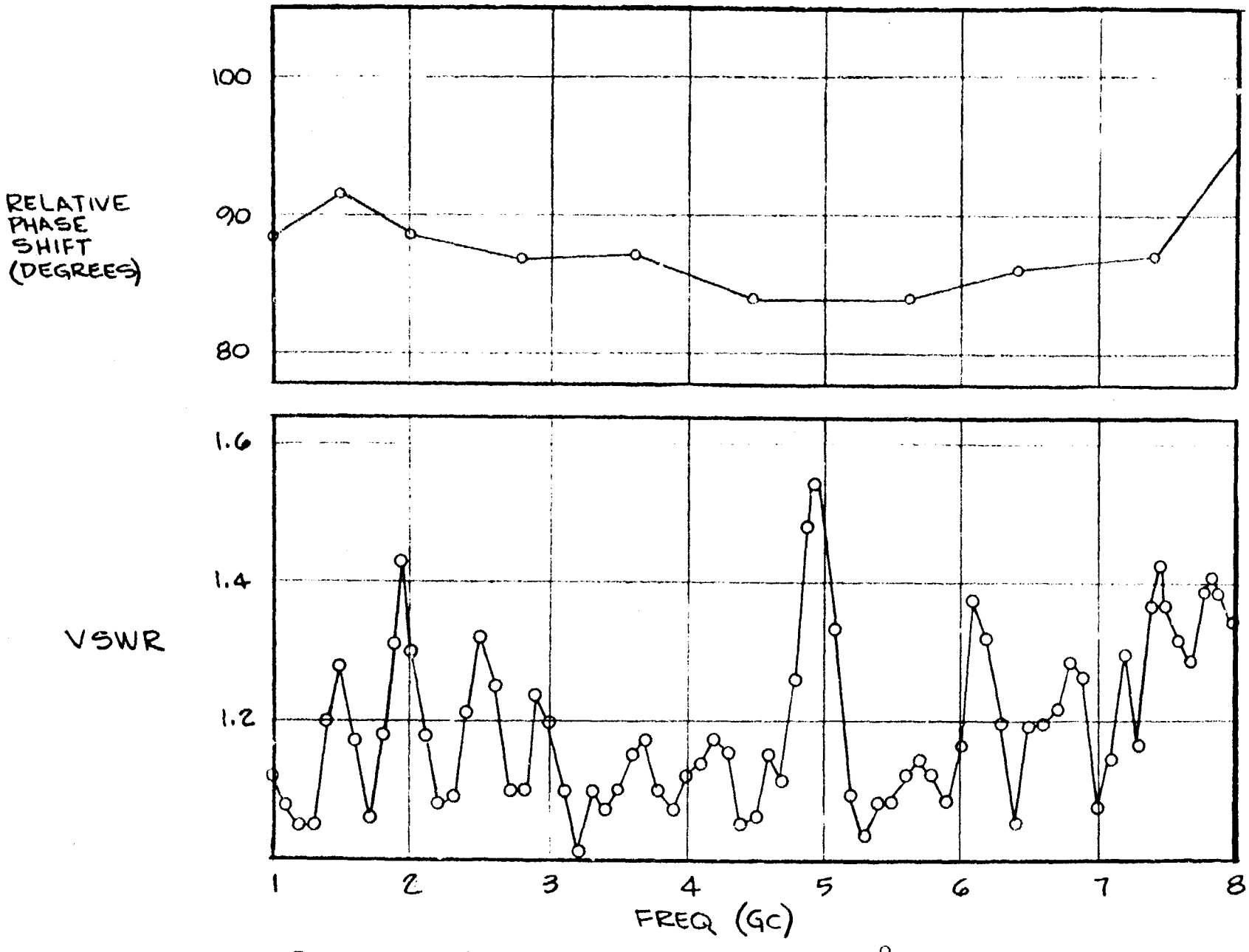

Figure 13. Performance Data of 8 to 1 Bandwidth 90° Phase Shifter.

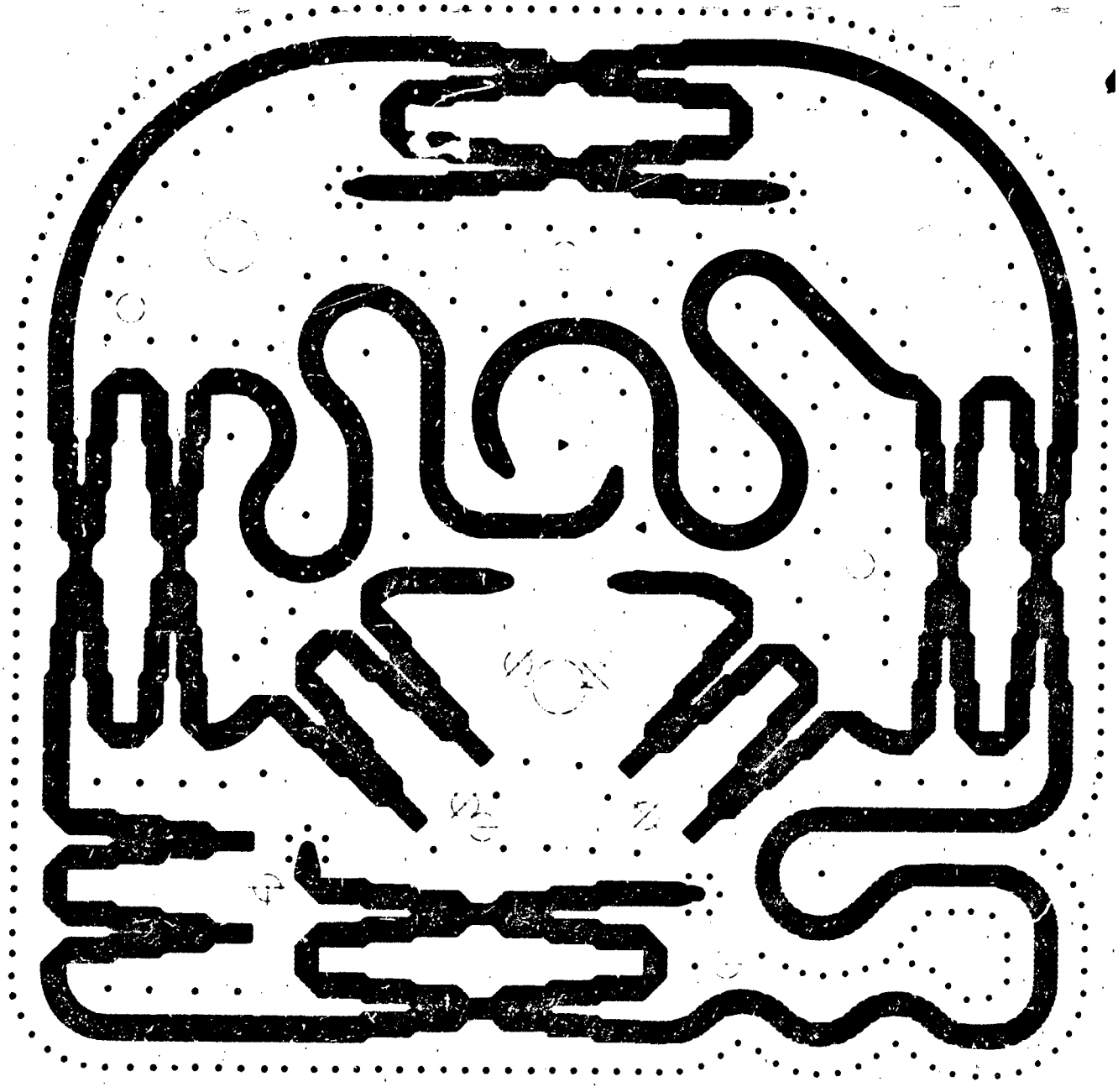

Figure 14. Layout of Four-Port Excitation Assembly.

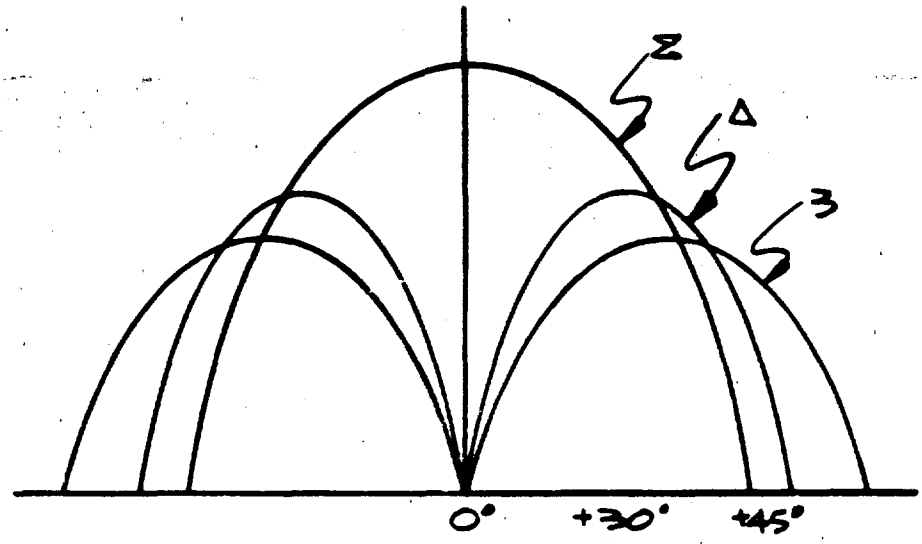

TYPICAL RADIATION PATTERN
OF 4 ARM SPIRAL FOR A GIVEN INPUT.

RELATIVE PHASE AT
SPIRAL TERMINAL INPUTS

Δ	0	180	0	180
3	0	-90	-180	-270
Σ	0	90	180	270

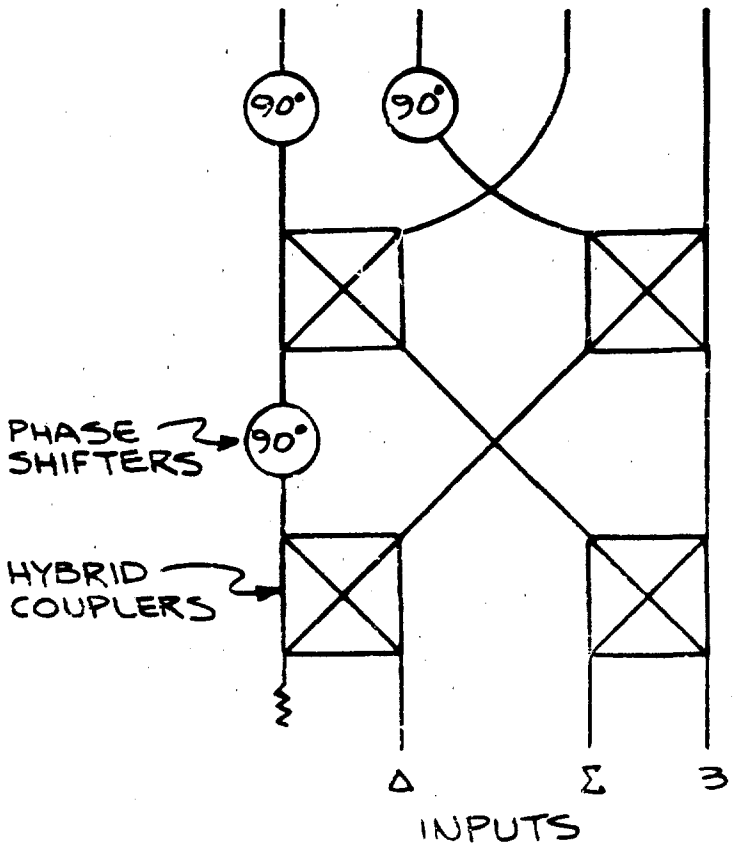

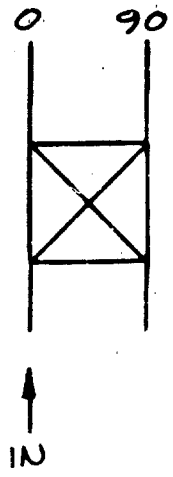

HYBRID COUPLER
PHASE CHARACTERIS

Figure 15. Block Diagram of Excitation Assembly and Resultant Radiation Pattern of Wideband Antenna.

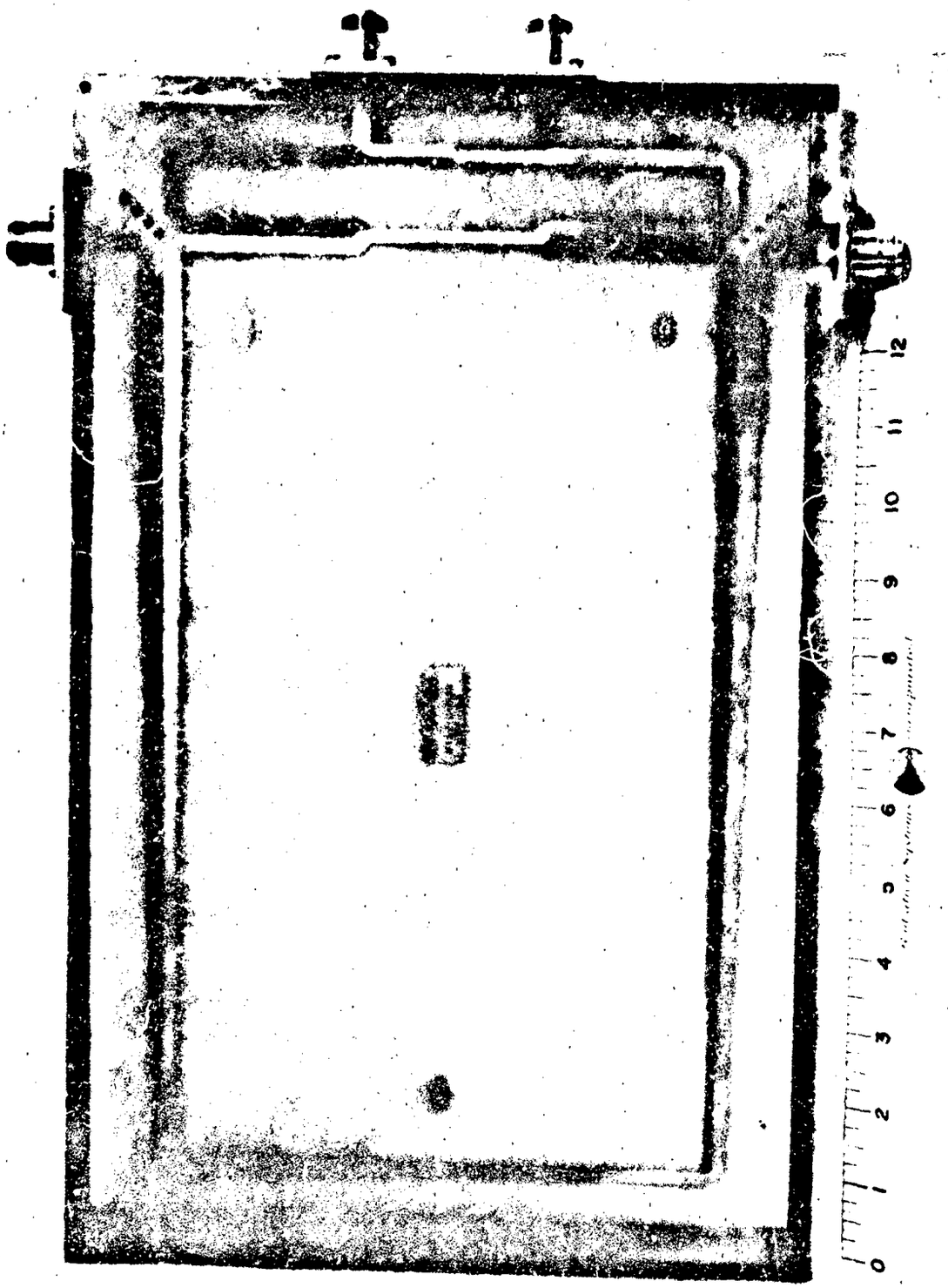

Figure 16. Center section of a 17 to 1 Bandwidth 3 db Coupler.

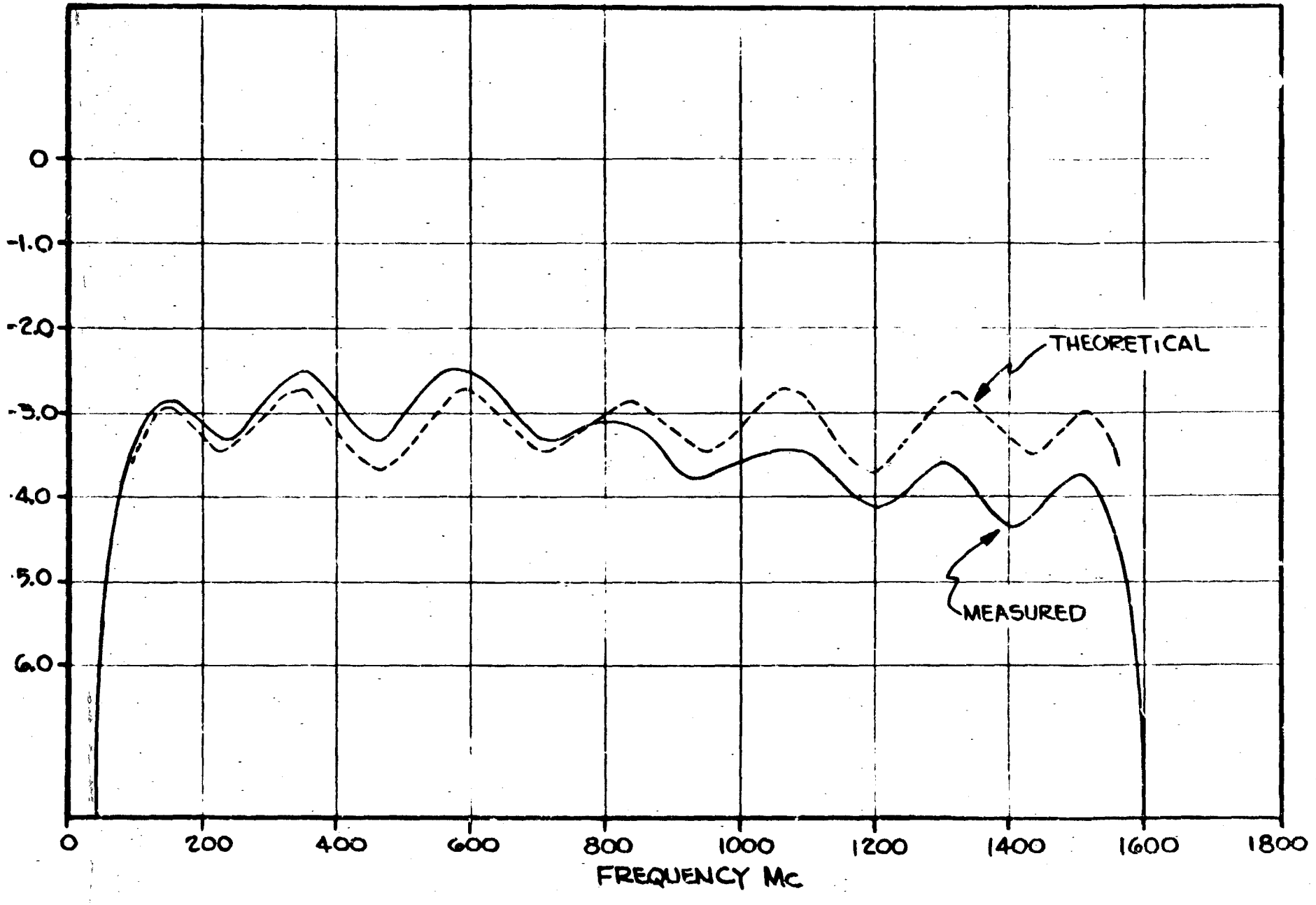

Figure 17. Comparison of Theoretical and Measured Performance of Seventeen to one 3 db Coupler.

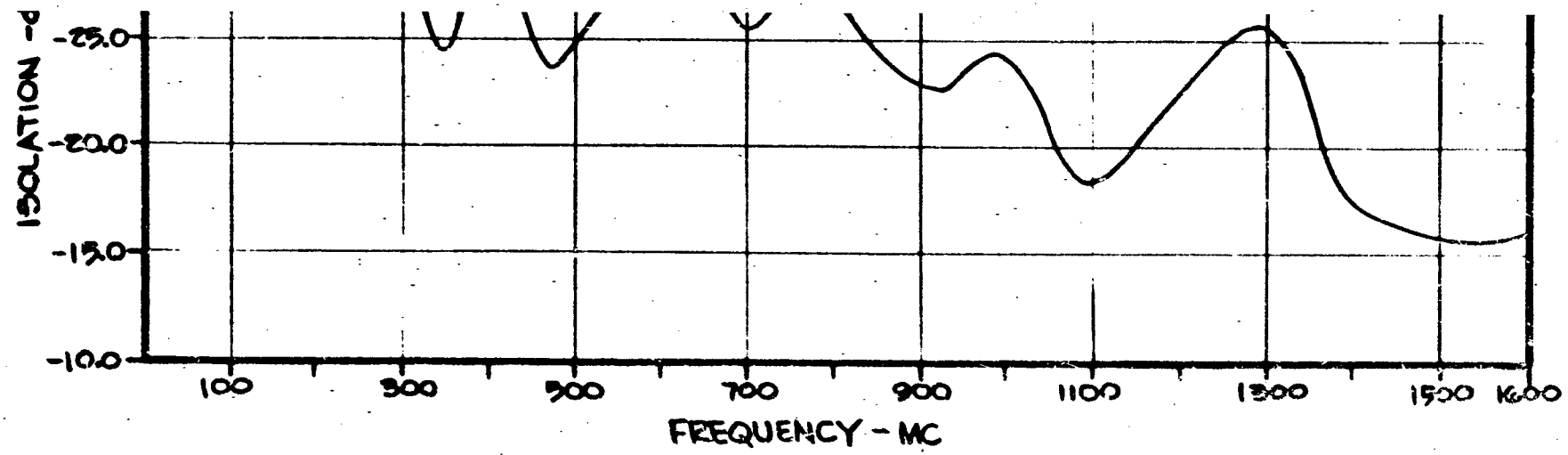

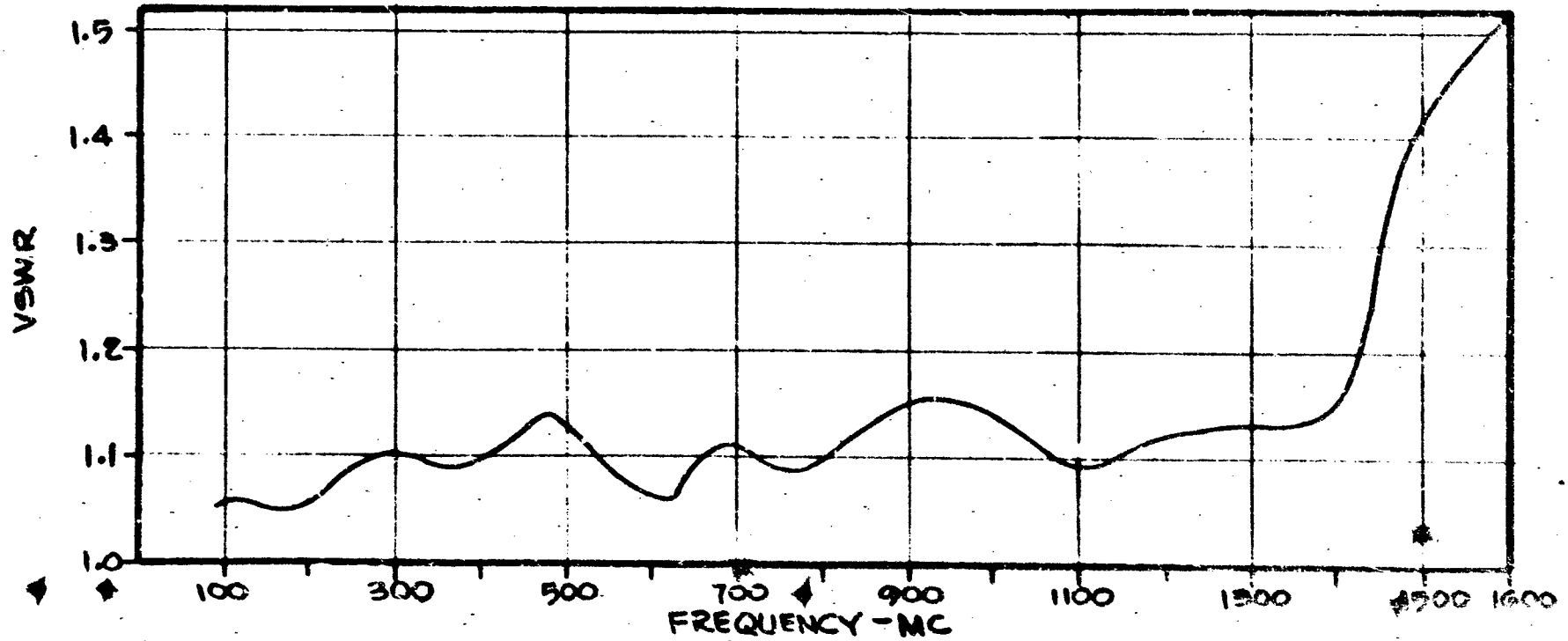

Figure 18. VSWR and Isolation Data for Seventeen to one 3 db Coupler.

A New Scimitar Antenna

By E. M. Turner
AFWL, Wright-Patterson AFB, O.

Introduction

The Scimitar Antenna was discovered by E. M. Turner and W. P. Turner at WPAFB, Ohio in 1956, while feeding one leg of a log periodic spiral over a ground plane. The antenna from the start displayed excellent broadband properties, particularly with respect to impedance. The patterns while consistent were not always the most desirable for certain operational requirements, since approximately 85 percent of the radiated energy was in the vertical plane and 15% in the horizontal plane. The excellent efficiency (approximately 95%), the extreme simplicity, the ruggedness of construction, and the low cost, however, caused it to find immediate application. Since that date many thousands have been manufactured for many uses, and across the entire frequency spectrum from 2 mc/s to 20 gc, and for temperatures exceeding 2000°F. The natural impedance of the configuration defined by the equation $\zeta = Ke^{(a_1 - a_2)\theta}$ (Fig 2) lies between 60 and 120 ohms depending upon the thickness and tapering of the conductor. By using the proper matching techniques it is practical to obtain VSWR's less than 1.25 over an octave of bandwidth with a 50 ohm line, or less than 1.5 over a 10:1 bandwidth. The patterns can be modified considerably by the a and θ factors of the equation, however, the general pattern configurations remained similar.

It was known from the beginning that the attenuation from the feed point was extremely high, thus little energy was left at the end opposite the feed point to cause reflections. An exact analysis of the near field currents on the structure has remained, however, a matter of speculation until recently when Dr. Hans Meinke, Institut fur Hochfrequenstechnik, Munich was commissioned by R&T Division under contract AF 61(052)-506 to study the scimitar configuration and determine the current and voltage distributions, and to make recommendations for an optimum structure. While the study is still in progress, a considerable amount of valuable information has been released and a summary is being presented here. The far field patterns of the new antenna (See Fig 1) were made on a model constructed at WPAFB, and are not necessarily the optimum in design, nor does it explore all parameters which may effect the patterns.

Factual Data

To obtain the desired data the antenna was split into two symmetrical sections with holes being drilled into the walls and also in the ground plane (See Fig's 2, 3, and 4) Small loops were used to determine the magnetic field, and probes were used to obtain the electrical field. The phase distribution was also obtained and is shown in Fig 5. See figure 6 for

for a plot of the phase, E vectors in the near field. Fig 7 shows a plot of the surface currents on scimitar. Investigations must be made over a wide frequency band, however, to get a complete insight into the operatio of the antenna. It is known that changes are slow and orderly for the far field patterns, and in the Smith Chart plot of impedance, thus it is concluded that the same is true for the near field parameter.

Fig 8a, b, and c show Smith Chart plots of the old, the new, and the new antenna configuration compensated. You will note particularly (a) th orderliness of the impedance behavior, (b) the impedance is inductive eve when antenna is less than .1 λ in length, (c) the rapid rate at which the impedance normalises to its basic value, and (d) how it is possible by a simple RC network to compensate the antenna at fantastically low values of frequency.

Figures 9a and b give samples of the far field patterns of a convent scimitar antenna. Figures 11 through 14 give samples of the far field patterns for the new configuration. You will note that the major differe in the patterns are that both the vertical and horizontal patterns lay ne the ground plane, with very little energy emerging near the geometrical center of the antenna. This can be a decided advantage in some applicati Many variations of the scimitar can be made to change the orientation of t patterns, and to shift the energy from the vertical to the horizontal polarization. From earlier studies of impedance matching Dr. Meinke determined that a 35° taper from the ground plane will provide an almost perfect impedance match for a 50 ohm transmission line feed through a grou plane. It can readily be seen from the impedance plots, that this has be achieved and needs little additional work. Dr. Lyons, University of Michi has demonstrated that by selectively loading the scimitar with ferrite material, thus reducing its size, it can have several octaves of bandwidth and still remain over 80% efficient at all frequencies. In view of the inductive nature of this antenna at the lower frequencies, it is doubtful, however, if any additional compensation beyond the RC network shown is required or desired.

Conclusions

(1) Both the old and the new configurations of the scimitar have fantastic abilities to radiate energy with little or no end effects, and with efficiencies above 95%.

(2) The impedances can be matched to approach that of a transmission line over several octaves of bandwidth.

(3) The polarization is linear, but is oriented differently for all points in space.

(4) The patterns are complex and require cuts in all principal planes for both E_θ and E_ϕ polarizations to get a comprehensive three dimensional picture of the energy distribution. A considerable shift in patterns can be achieved by an angler rotation of the configuration over the ground plane and by a tapering of the conductor from the feed point to the termination.

(5) The scimitar can radiate efficiently when less than .1 λ in length.

(6) Its unique properties should make it an important tool in the antenna art for many applications.



FIG 1 NEW SCIMITAR CONFIGURATION

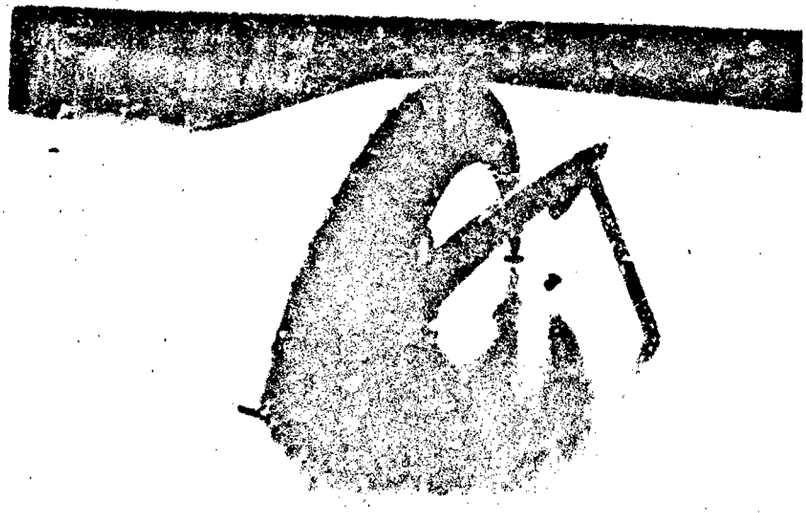

FIG 2 CONVENTIONAL SCIMITAR OPENED FOR THE PLACEMENT OF PROBES



FIG 3 CONVENTIONAL SCIMITAR WITH HOLES IN SURFACE FOR PROBES



FIG 4 CONVENTIONAL SCIMITAR WITH HOLES IN GROUND PLANE FOR PROBES

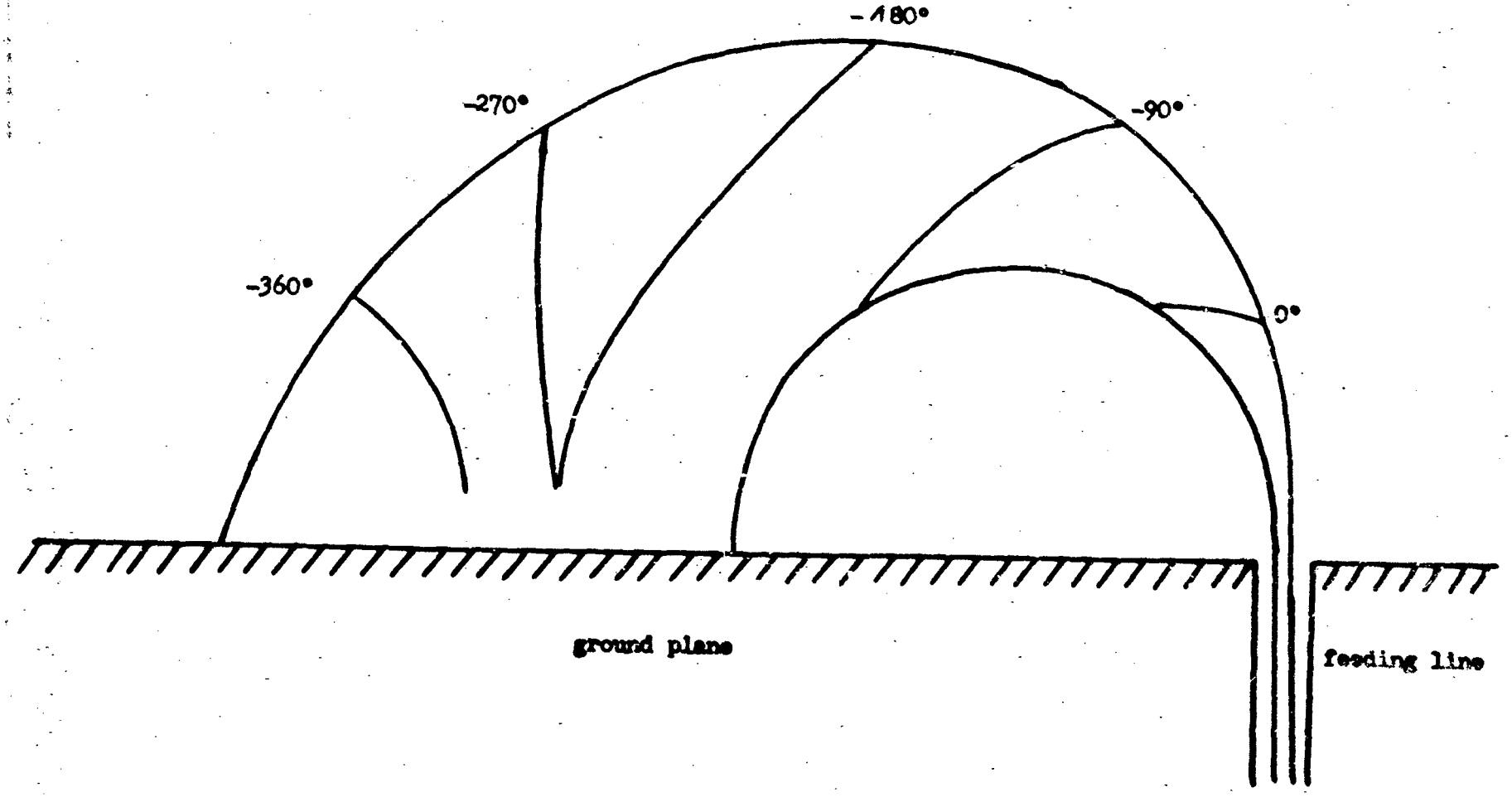

FIG 5 E-FIELD PHASE (F = 1000 Mc/S)

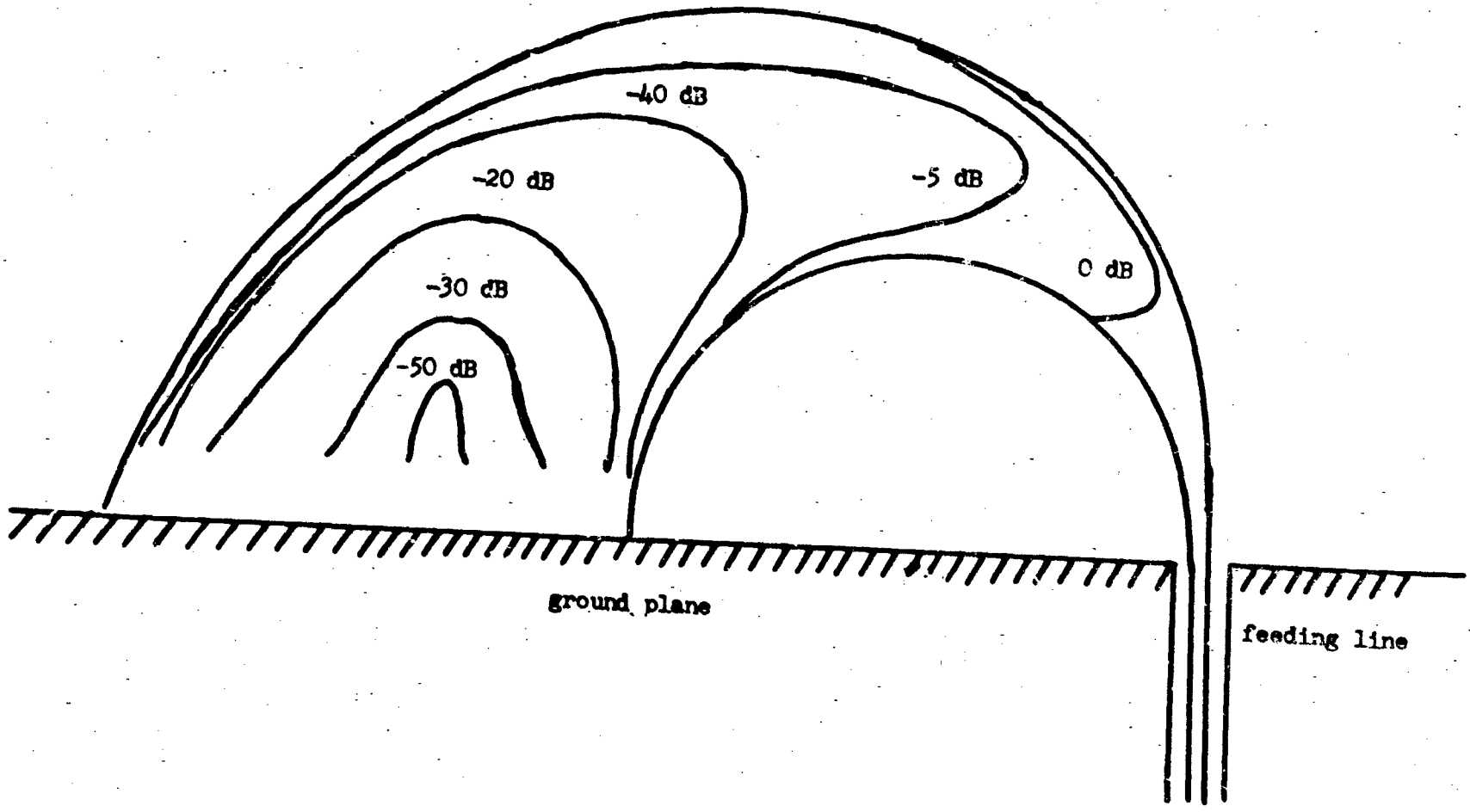
-40 dB
-20 dB
-5 dB
0 dB
-30 dB
-50 dB
ground plane
feeding line

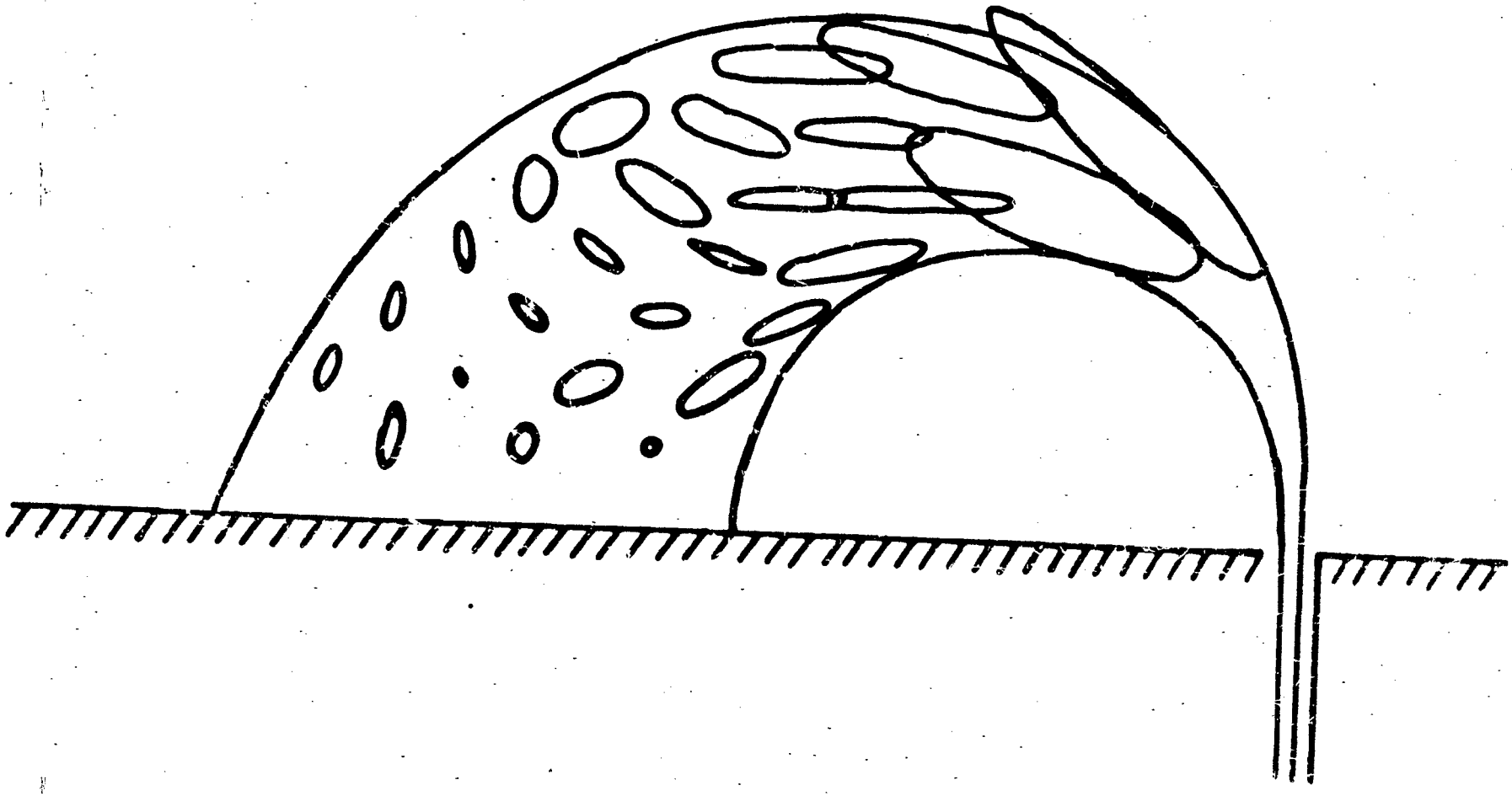

FIG 7 ELLIPTICAL POLARIZATION OF CURRENT

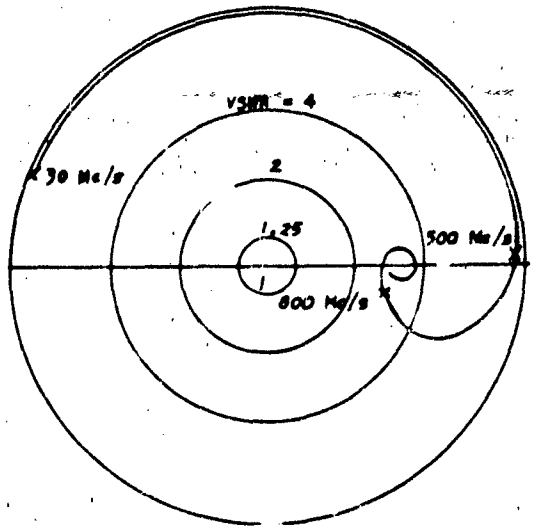

FIG 6a IMPEDANCE OF MODIFIED SCIMITAR IN A SMITH-CHART

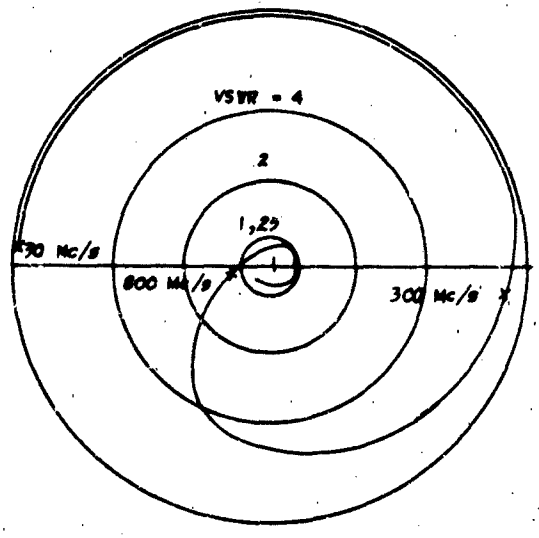

FIG 6b IMPEDANCE OF MODIFIED SCIMITAR WITH MC-COMBINATION IN A SMITH-CHART

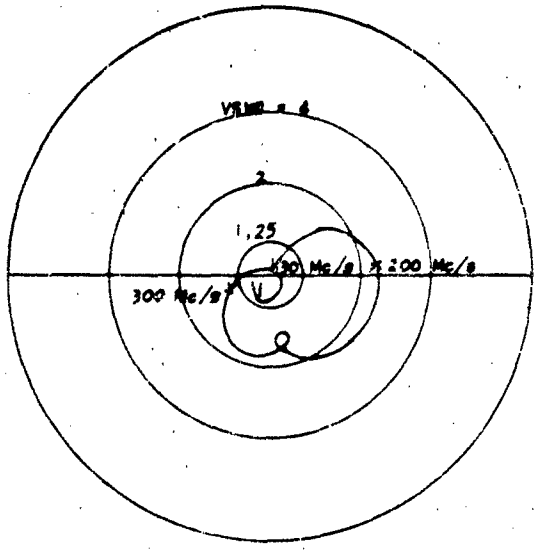

FIG 6c IMPEDANCE OF COMMON SCIMITAR IN A SMITH-CHART

FULL SCALE X
ANTENNA TYPE
NOMENCLATURE
VARIABLE ANGLE ϕ(X) θ( )
CONSTANT ANGLE ϕ( ) θ(20)
CURVE MEASURED IN VOLTS (X)
POWER ( ) LINEAR ( ) DB ( )
TRANSMITTER POLARIZATION
Eθ( ) Eϕ( )
OTHER ( )

MODEL
MODEL SCALE
MODEL FULL SCALE FREQ. 1000 g
MODEL FREQ.
ANTENNA LOCATION
PLANE TYPE
AIRCRAFT NOSE AT
θ = 90° ϕ = 0

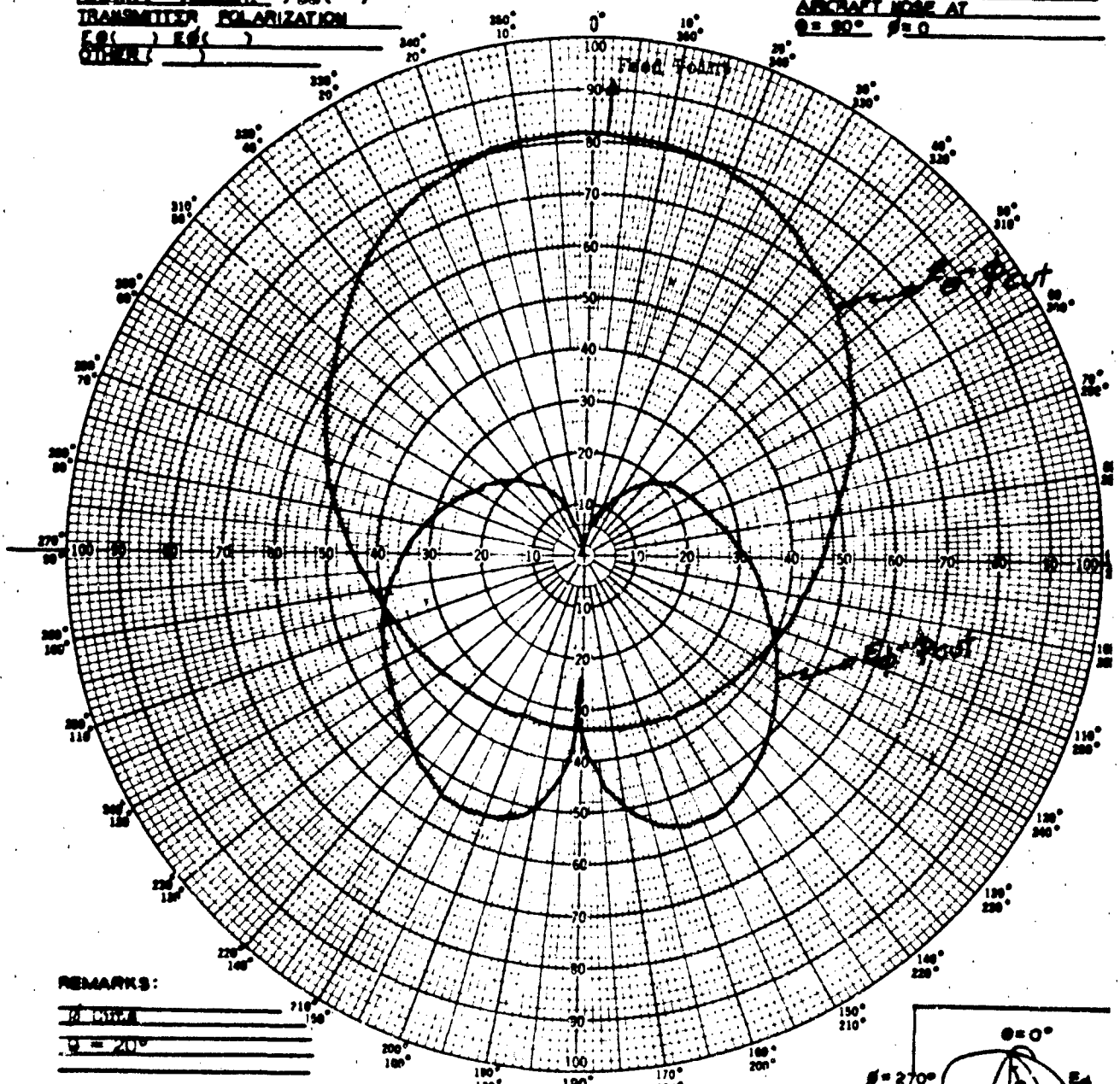

REMARKS:
ϕ CUTS
θ = 20°

ACCOUNT #
GAIN
HALF POWER BEAM WIDTH ϕ( ) θ( )
GROUND PLANE DIMENSIONS

TYPICAL FAR FIELD PATTERNS OF A CONVENTIONAL SCIMITAR ANTENNA

SPHERICAL COORDINATE SYSTEM (USED IN MEASUREMENT)

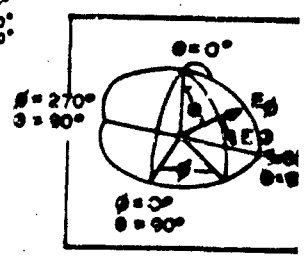

FIG 9a

POLAR PATTERN

AF-WP-S-JUL 62 [illegible]

ASD-O FORM JUN 62 241

Replaces WADD-O Form 241 which may be used.

OPERATOR DATE
ENGINEER DATE

FULL SCALE X
ANTENNA TYPE
NOMENCLATURE
VARIABLE ANGLE ϕ( ) θ(X)
CONSTANT ANGLE ϕ( ) θ( )
CURVE MEASURED IN VOLTS (X)
POWER ( ) LINEAR ( ) DB ( )
TRANSMITTED POLARIZATION
E θ(X) E ϕ(X)
OTHER ( )

MODEL SCALE
MODEL FULL SCALE FREQ. 1000 gc
MODEL FREQ.
ANTENNA LOCATION
PLANE TYPE
AIRCRAFT ATTITUDE AT
θ = 90° ϕ = 0

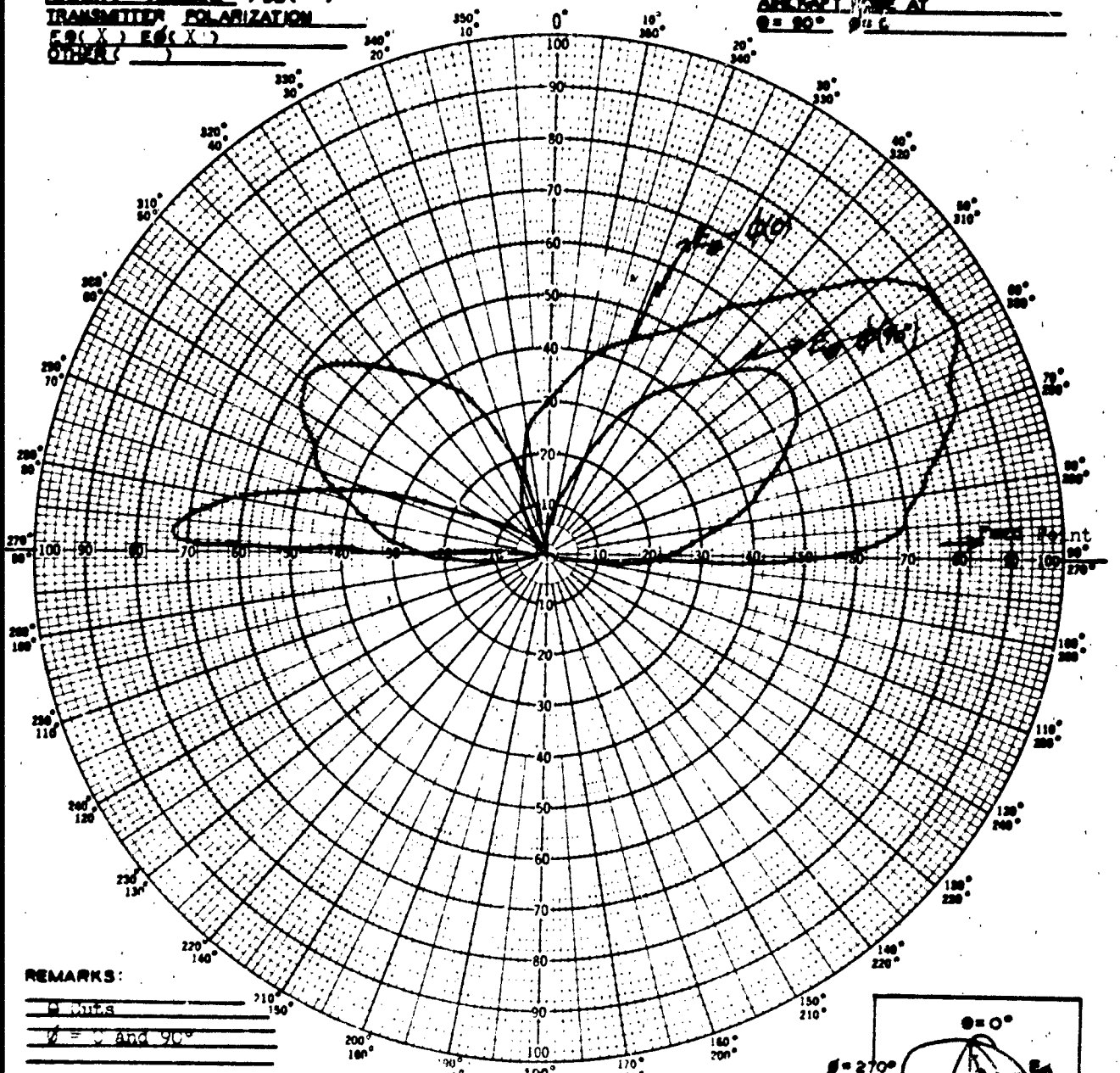

REMARKS:
Cuts
ϕ = 0 and 90°

ACCOUNT #
GAIN
ONE HALF POWER BEAM WIDTH ϕ( ) θ( )
GROUND PLANE DIMENSIONS

TYPICAL FAR FIELD PATTERNS OF A CONVENTIONAL SCIMITAR ANTENNA

SPHERICAL COORDINATE SYSTEM (USED IN MEASUREMENT)

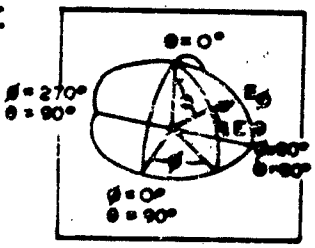

FIG 9b

POLAR PATTERN
AF-WP-8-JUN 62 388
ASD-O FORM 241 JUN 62
Replaces ASDD-O Form 241 which may be used.

OPERATOR DATE
ENGINEER DATE

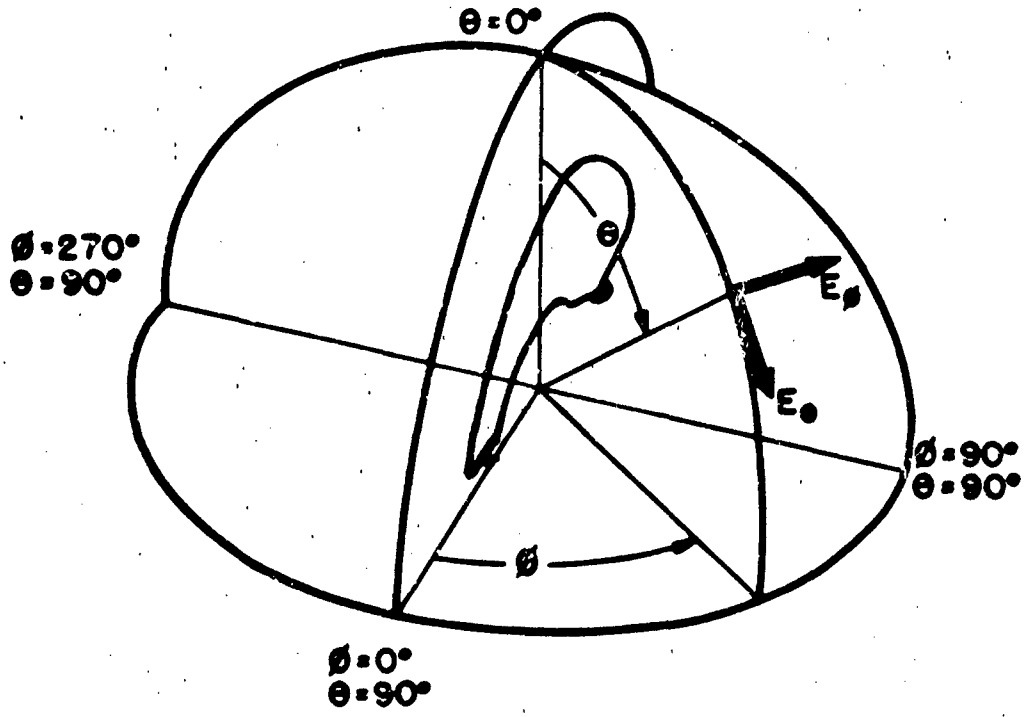

SPHERICAL COORDINATE SYSTEM
USED IN MEASUREMENTS

FIG 10

FULL SCALE
ANTENNA TYPE
NOMENCLATURE
VARIABLE ANGLE ϕ( ) θ( )
CONSTANT ANGLE ϕ( ) θ( )
CURVE MEASURED IN VOLTS ( )
POWER ( ) LINEAR ( ) DB ( )
TRANSMITTER POLARIZATION
E θ( ) E ϕ( )
OTHER ( )

MODEL
MODEL SCALE
MODEL FULL SCALE FREQ. 500MC.
MODEL FREQ.
ANTENNA LOCATION
PLANE TYPE
AIRCRAFT NOSE AT
θ = 90° ϕ = 0

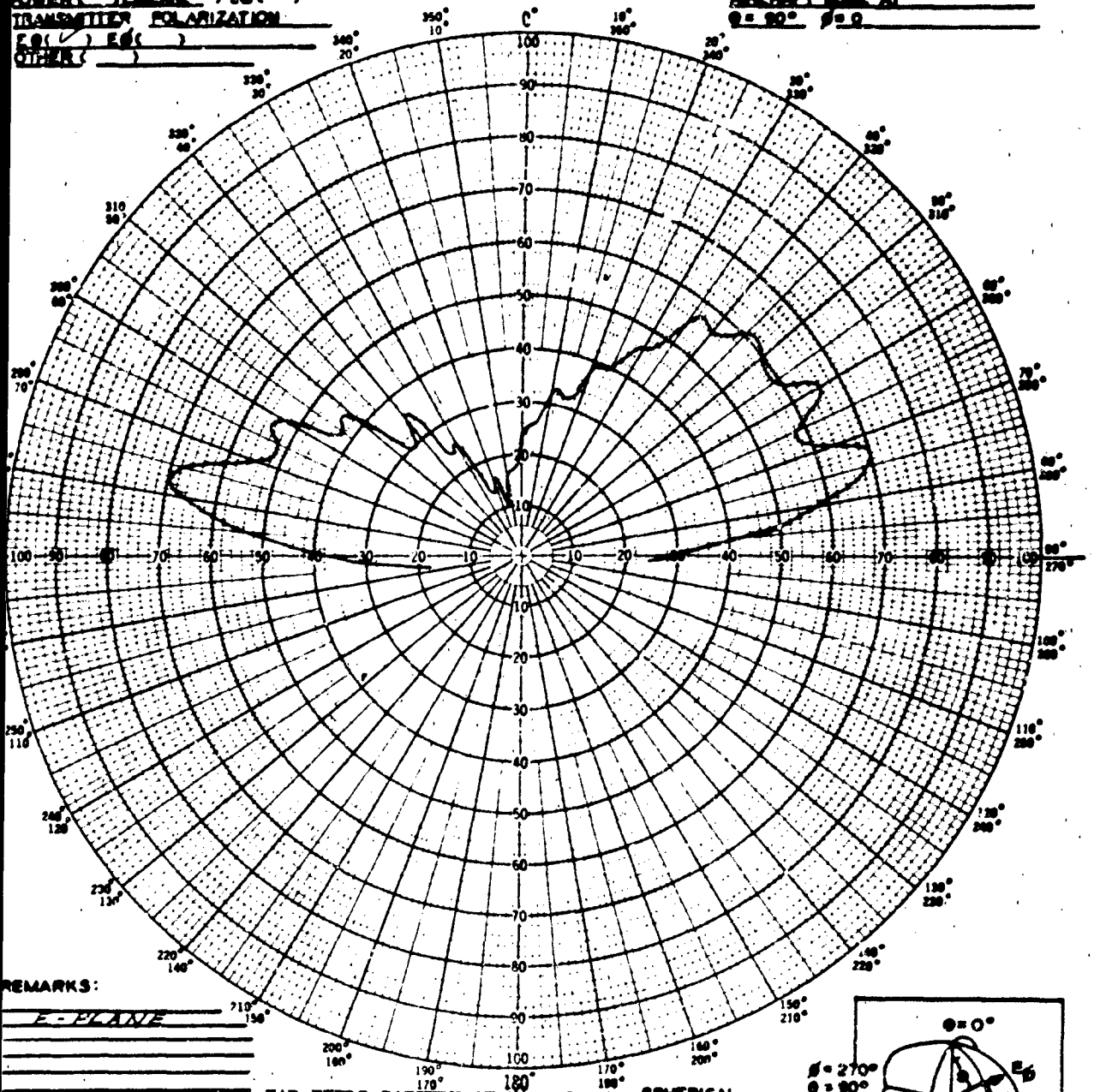

REMARKS:
E - PLANE

ACCOUNT #
BAM
ONE HALF POWER BEAM WIDTH ϕ( ) θ( )
GROUND PLANE DIMENSIONS

FAR FIELD PATTERN OF NEW SCIMITAR ANTENNA AT 500 MC

SPHERICAL COORDINATE SYSTEM (USED IN MEASUREMENT)

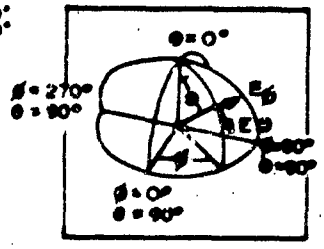

POLAR PATTERN

FIG 11a

OPERATOR _____ DATE _____
ENGINEER _____ DATE _____

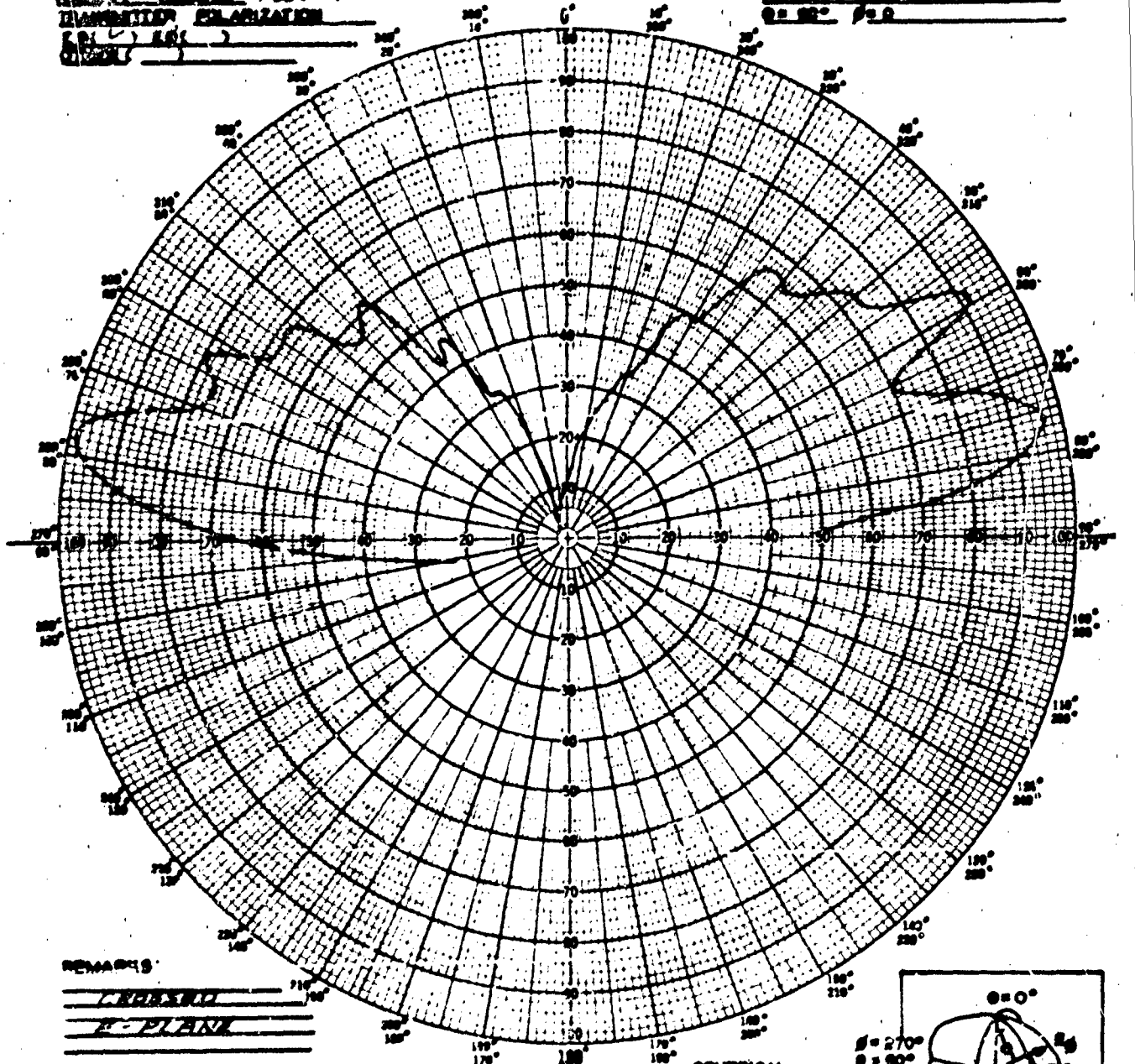

FAR FIELD PATTERN OF NEW SCIMITAR ANTENNA AT 500 MC

FIG 11b

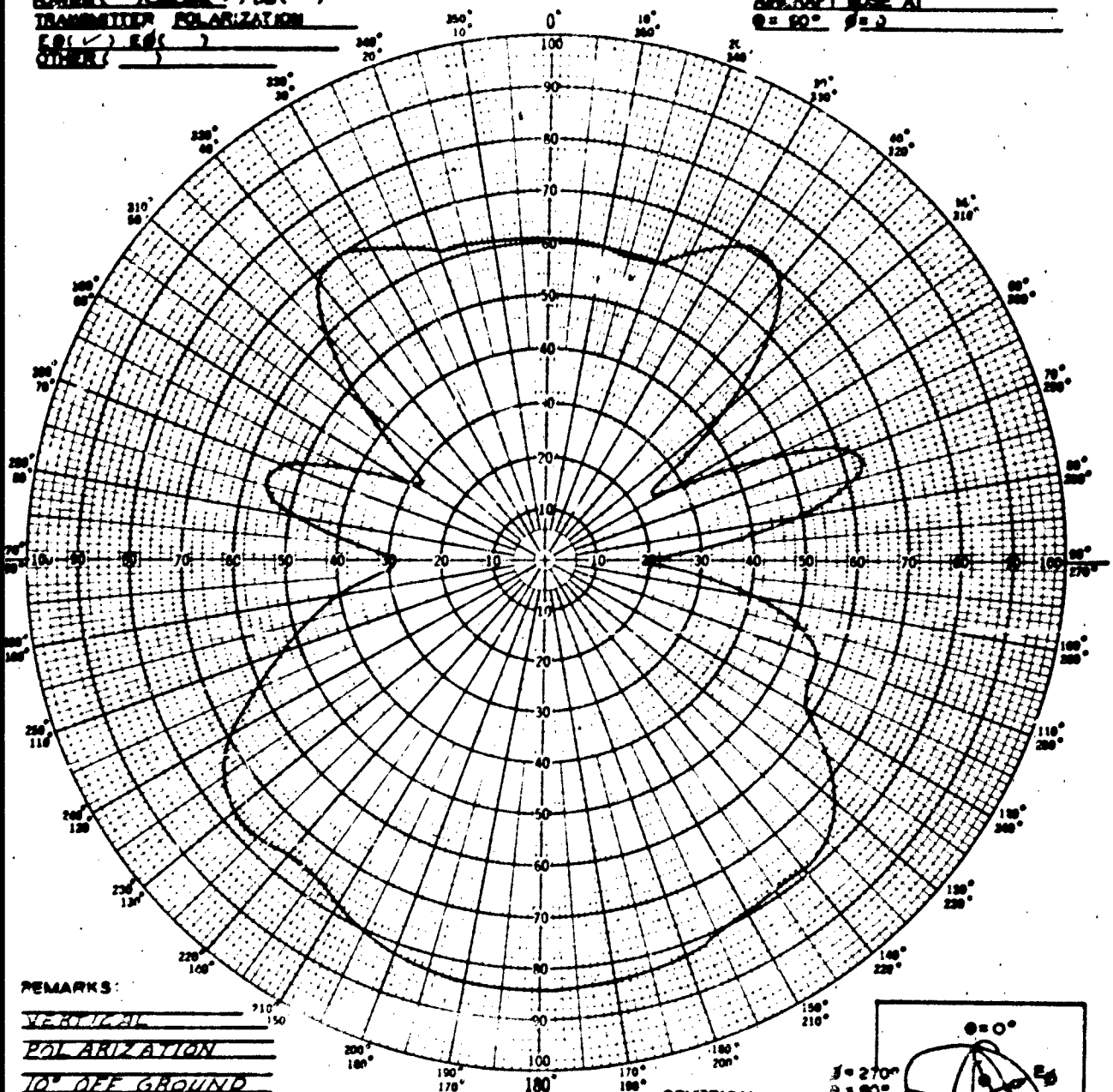

CURV. SCALE
ANTENNA TYPE
NOMENCLATURE
VARIABLE ANGLE ϕ(✓) θ( )
CONSTANT ANGLE ϕ( ) θ: 80°
CURVE MEASURED IN VOLTS (✓)
POWER ( ) LINEAR (✓) DB ( )
TRANSMITTER POLARIZATION
E θ (✓) E ϕ ( )
OTHER ( )

MODEL
MODEL SCALE
MODEL FULL SCALE FREQ. 4000 MC
MODEL FREQ.
ANTENNA LOCATION
PLANE TYPE
AIRCRAFT NOSE AT
θ = 90° ϕ = 0

REMARKS:
VERTICAL
POLARIZATION
10° OFF GROUND
PLANE
ACCOUNT #
GAIN
ONE HALF POWER BEAM WIDTH ϕ( ) θ( )
GROUND PLANE DIMENSIONS

FAR FIELD PATTERNS OF NEW SCIMITAR ANTENNA AT 4 GC

SPHERICAL COORDINATE SYSTEM (USED IN MEASUREMENT)

POLAR PATTERN

OPERATOR _____ DATE _____
ENGINEER _____ DATE _____

FIG 12a

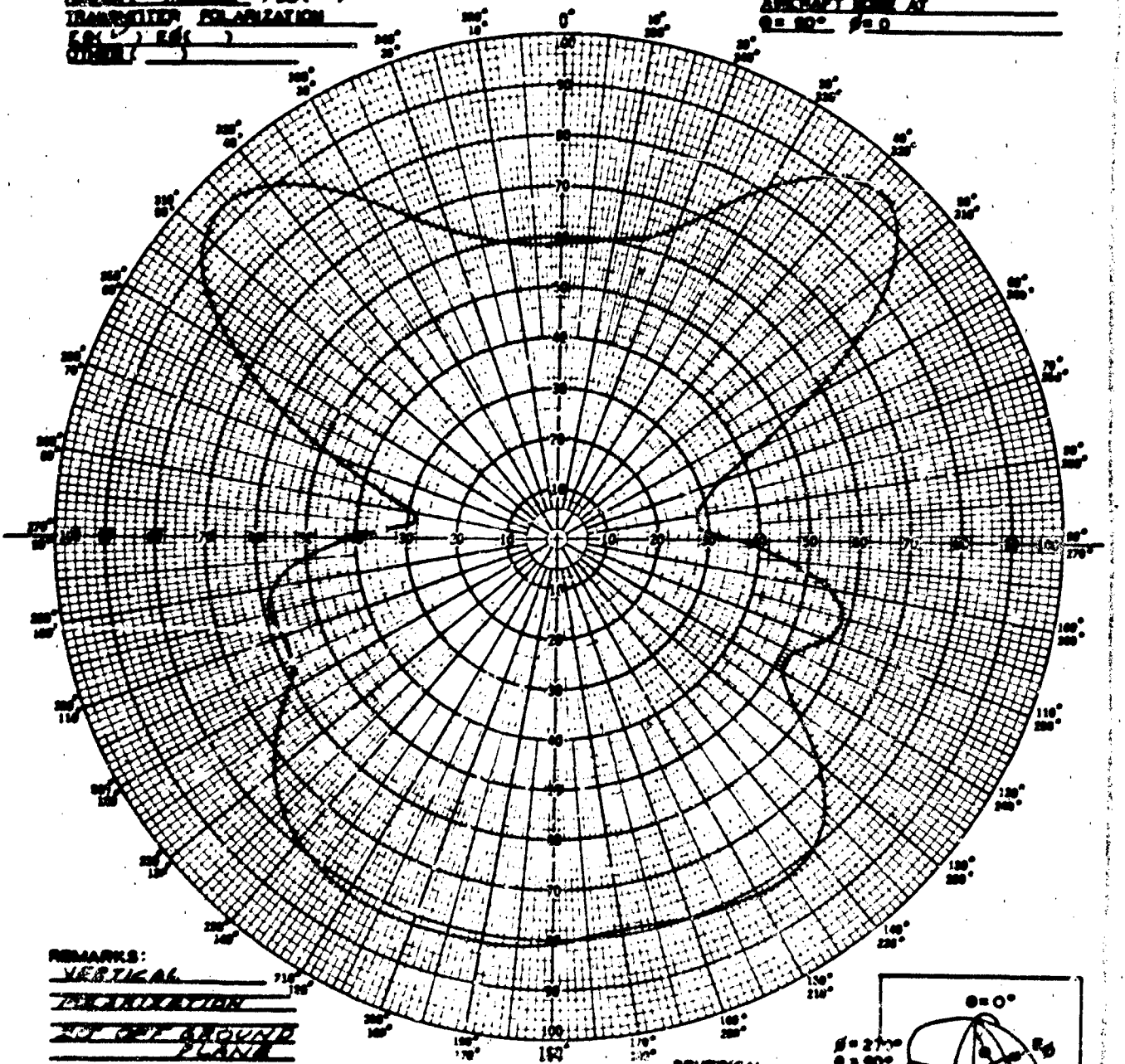

FAR FIELD PATTERNS OF NEW SCIMITAR ANTENNA AT 4 GC

POLAR PATTERN

VIII 12b

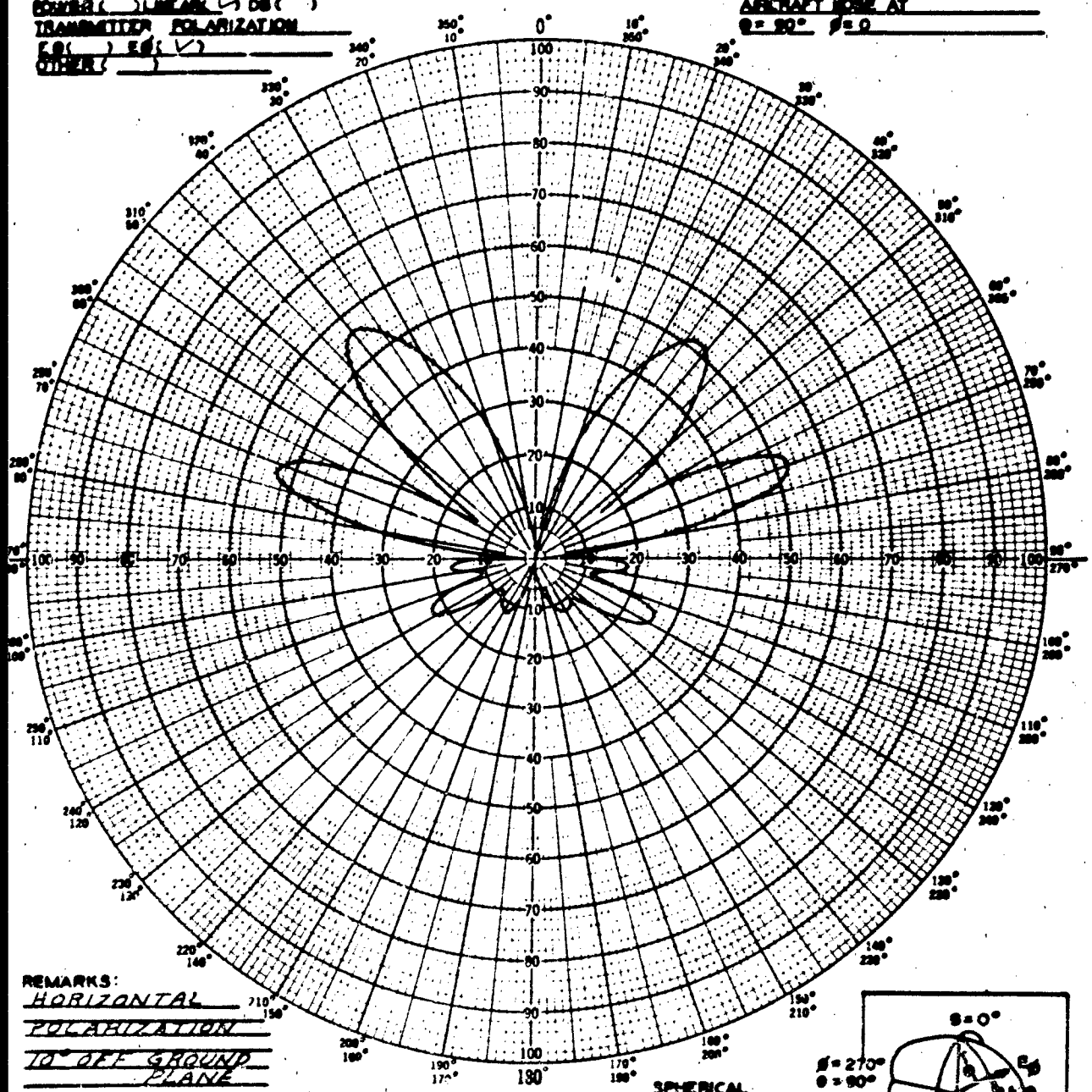

DBL. SCALE
ANTENNA TYPE
NOMENCLATURE
VARIABLE ANGLE ϕ(✓) θ( )
CONSTANT ANGLE ϕ( ) θ=90°
CURVE MEASURED IN VOLTS (✓)
POWER ( ) LINEAR (✓) DB ( )
TRANSMITTER POLARIZATION
E θ ( ) E ϕ (✓)
OTHER ( )

MODEL
MODEL SCALE
MODEL FULL SCALE FREQ. 4000 MC
MODEL FREQ.
ANTENNA LOCATION
PLANE TYPE
AIRCRAFT NOSE AT
θ = 90° ϕ = 0

REMARKS:
HORIZONTAL POLARIZATION
10° OFF GROUND PLANE

ACCOUNT #
GAIN
HALF POWER BEAM WIDTH ϕ( ) θ( )
GROUND PLANE DIMENSIONS

FAR FIELD PATTERNS OF NEW SCIMITAR ANTENNA AT 4 GC

SPHERICAL COORDINATE SYSTEM (USED IN MEASUREMENT)

POLAR PATTERN

OPERATOR _____ DATE _____
ENGINEER _____ DATE _____

FIG 12c

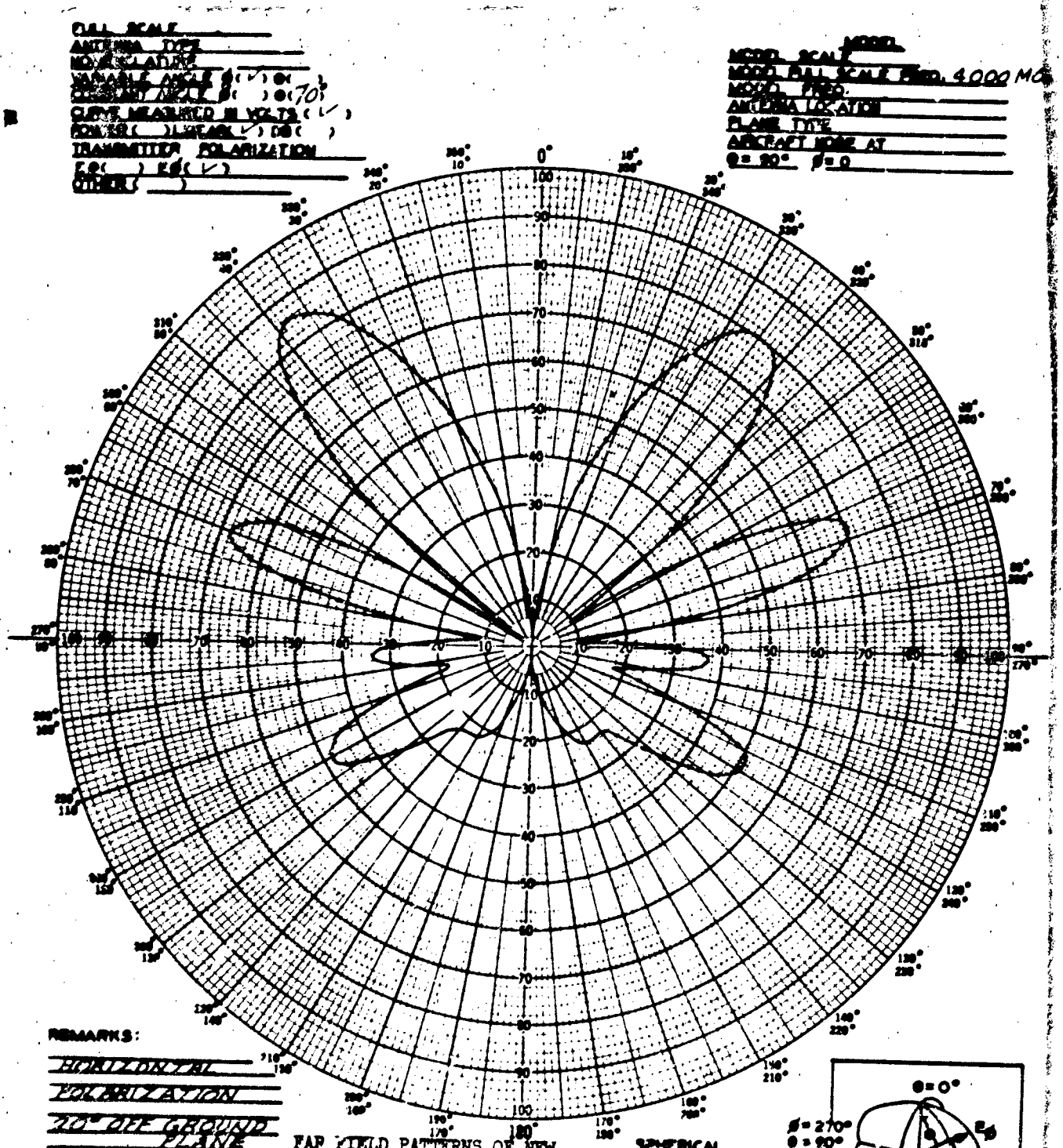

FAR FIELD PATTERNS OF NEW GCDMTTAR ANTENNA AT 4 GC

FIG 12d

FULL SCALE
ANTENNA TYPE
NOMENCLATURE
VARIABLE ANGLE ϕ( ) θ(✓)
CONSTANT ANGLE ϕ(0) θ( )
CURVE MEASURED IN VOLTS (✓)
POWER ( ) LINEAR (✓) DB ( )
TRANSMITTER POLARIZATION
Eθ(✓) Eϕ( )
OTHER ( )

MODEL
MODEL SCALE
MODEL FULL SCALE FREQ. 4000 MC.
MODEL FREQ.
ANTENNA LOCATION
PLANE TYPE
AIRCRAFT NOSE AT
θ = 90° ϕ = 0

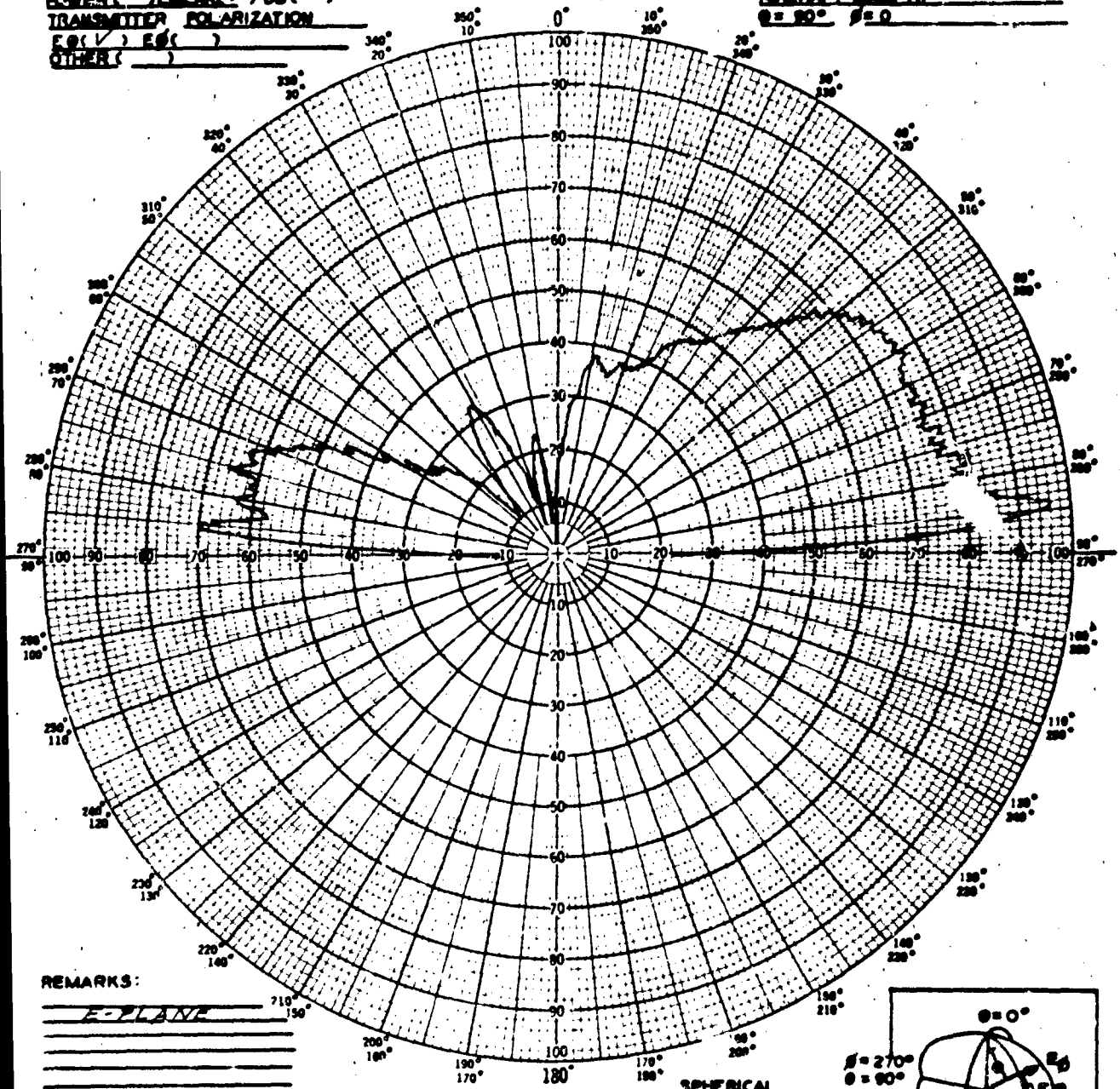

REMARKS:
E-PLANE

ACCOUNT #
GAIN
ONE HALF POWER BEAM WIDTH ϕ( ) θ( )
GROUND PLANE DIMENSIONS

FAR FIELD PATTERNS OF NEW SCIMITAR ANTENNA AT 4 GC

SPHERICAL COORDINATE SYSTEM (USED IN MEASUREMENT)

POLAR PATTERN

OPERATOR _____ DATE _____
ENGINEER _____ DATE _____

FIG 13a

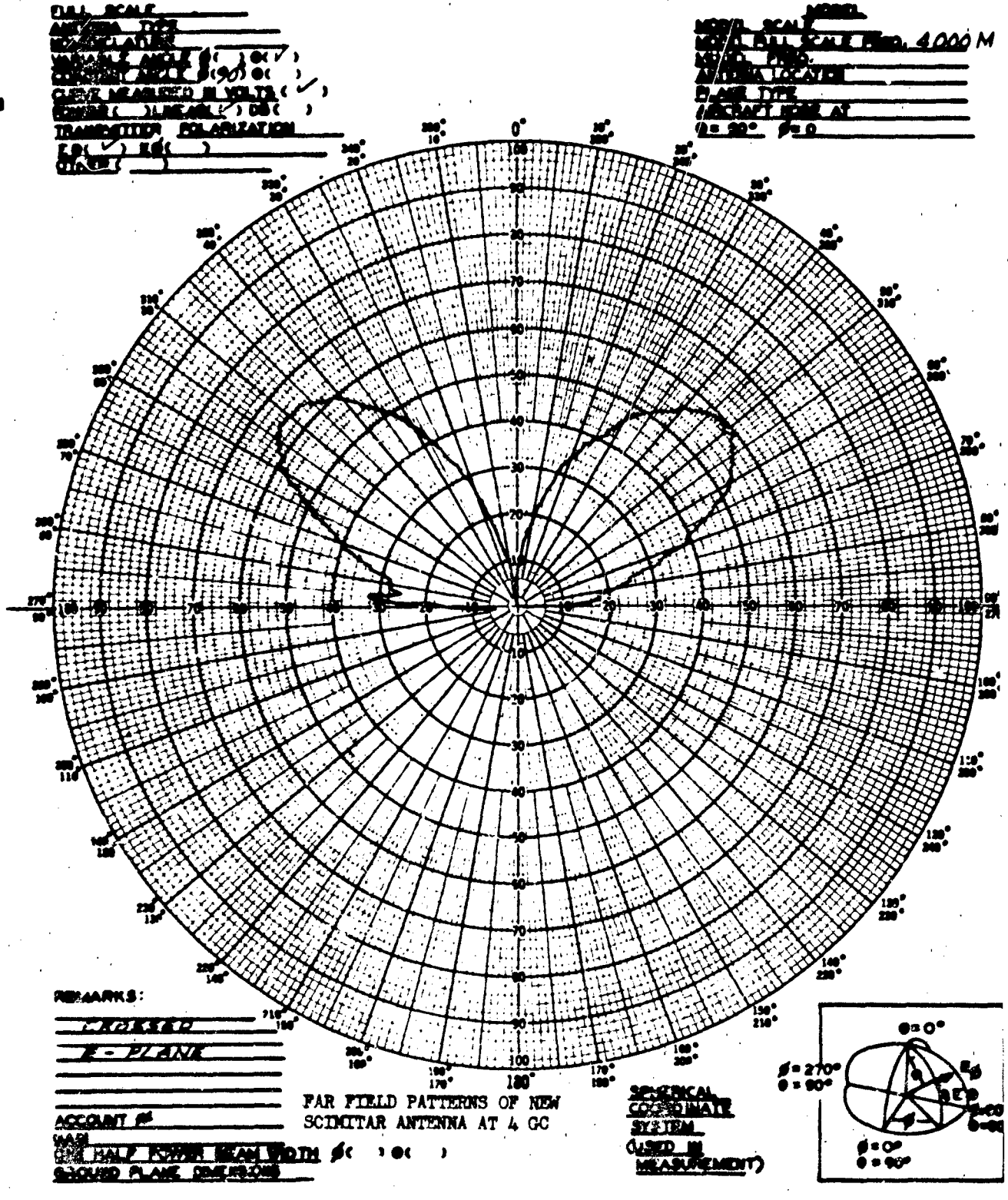

FAR FIELD PATTERNS OF NEW SCIMITAR ANTENNA AT 4 GC

FIG 13b

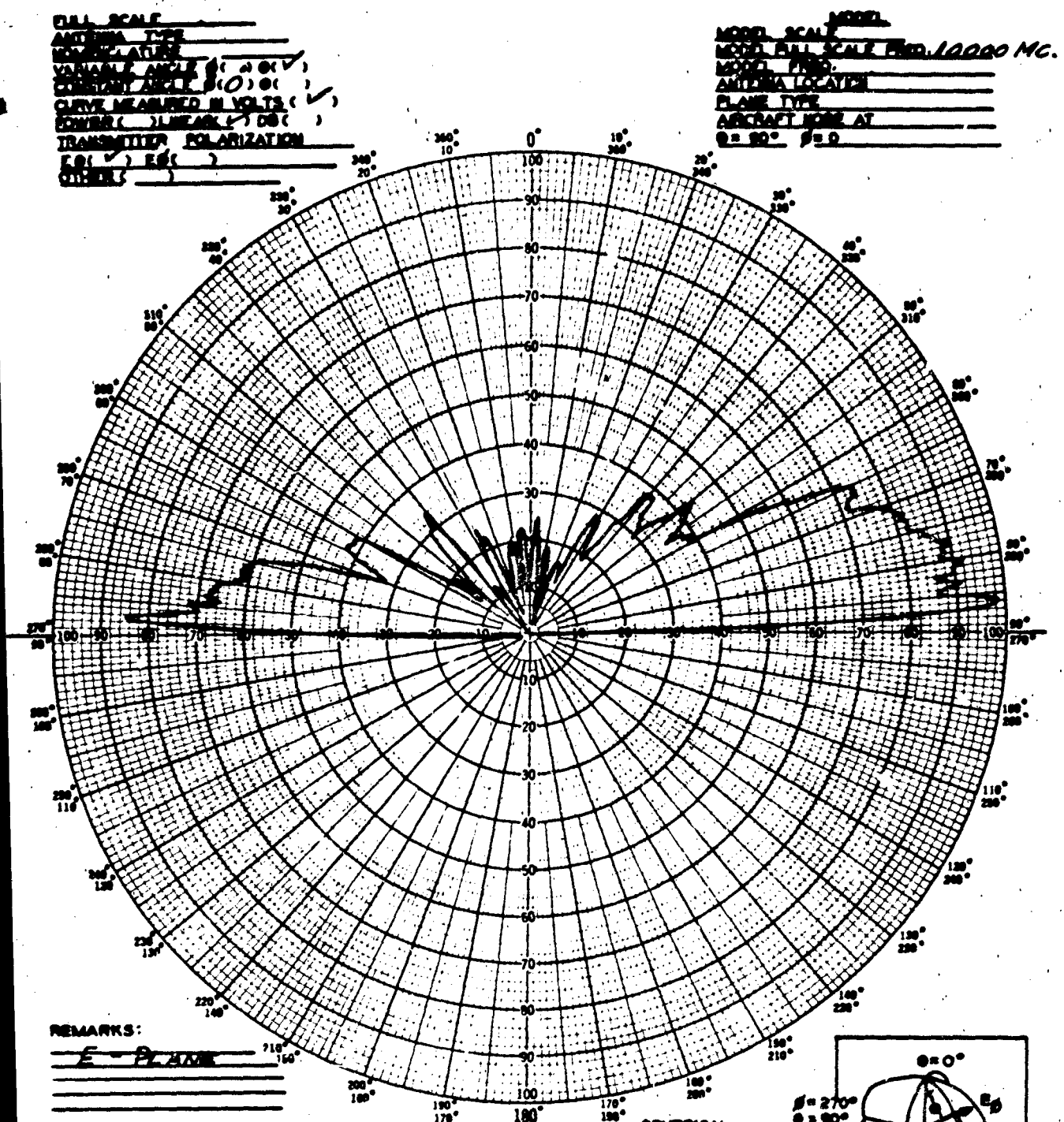
FULL SCALE
ANTENNA TYPE
NOMENCLATURE
VARIABLE ANGLE ϕ( ) θ( )
CONSTANT ANGLE ϕ( ) θ( )
CURVE MEASURED IN VOLTS ( )
POWER ( ) LINEAR ( ) DB ( )
TRANSMITTER POLARIZATION
E θ( ) E ϕ( )
OTHER ( )
MODEL
MODEL SCALE
MODEL FULL SCALE FREQ. 10000 MC.
MODEL FREQ.
ANTENNA LOCATION
PLANE TYPE
AIRCRAFT HORIZ AT
θ = 90° ϕ = 0
0°
90°
180°
270°
REMARKS:
E - PLANE
ACCOUNT #
DATE
ONE HALF POWER BEAM WIDTH ϕ( ) θ( )
GROUND PLANE DIMENSIONS
POLAR PATTERN
FAR FIELD PATTERNS OF NEW
SCIMITAR ANTENNA AT 10 GC
SPHERICAL COORDINATE SYSTEM (USED IN MEASUREMENT)
θ = 0°
ϕ = 270°
θ = 90°
ϕ = 0°
θ = 90°
OPERATOR
DATE
ENGINEER
DATE

FIG 14a

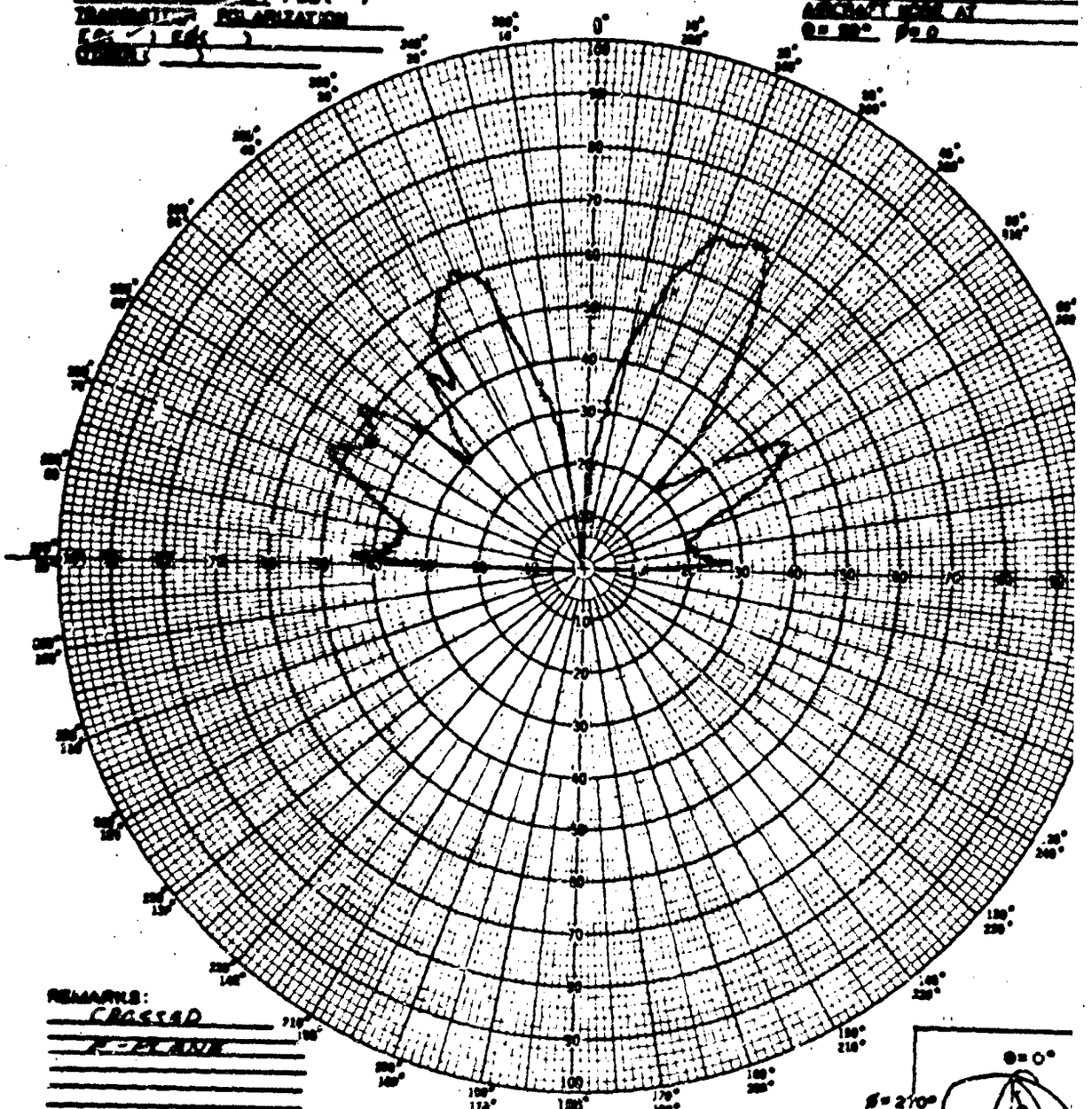

FAR FIELD PATTERNS OF NEW SCIMITAR ANTENNA AT 10 GC

FIG 14b

ESD 64-170R

RAC 2576

Simulation of RF Far-Field Conditions Using a Microwave Lens

By

Peter Zusolo

Stanley Jurczak

Joseph Castrigno

7 September 1964

Prepared for

The Fourteenth Annual Symposium on

U.S.A.F. Antenna Research and Development

University of Illinois

Monticello, Illinois

6 to 8 October 1964

Republic Aviation Corporation

Aircraft Division

Farmingdale, New York

ABSTRACT

For testing and calibration of radar systems, the available space and distance becomes a major problem. The far-field criteria generally requires that large distances separate the two antennas under consideration. In order to overcome this obstacle, Republic has investigated the near-field characteristics of a monopulse antenna in both "free-space" and anechoic chambers (reference 1). The findings indicated that phase correction of the near-field is required in order to properly simulate the far-field at short distances. This paper describes the utilization of a microwave lens for phase compensation of the near-field errors.

Geometric-optical techniques are employed for establishing the well known far-field criteria and the magnitude of phase errors encountered. The collimation of microwave energy by a lens is presented. This collimation action is verified by amplitude and phase data taken from near-field probe measurements of a microwave lens.

Far-field data taken on a 125 feet "free-space" range is presented. This data is compared to near-field data taken with a microwave lens at an antenna distance separation of 18 inches. A four horn X-band monopulse antenna was utilized for all tests. Therefore the data includes both elevation and azimuth radiation patterns for the sum and difference channels. Also presented are data for the amplitude and phase of the difference-to-sum channel ratio in the elevation plane. Boresight error measurements and calibration technique to eliminate these errors is described.

It is concluded that a microwave lens in the near-field is an effective method for accurately simulating the RF conditions of the far-field

A. INTRODUCTION

One of the problems often encountered in the testing and calibration of radar systems is the large space required. The far-field criteria established allowable quadratic phase errors across the aperture of the radar antenna. This, in turn, determines the antenna separation which must be used. Republic has investigated the near-field characteristics of a monopulse antenna in both free-space and anechoic chambers (reference 1). The calculated minimum test range was 40 feet. The data obtained indicated that a range of 40 feet was marginal, while results at 50 feet were satisfactory for boresight measurements. Pattern measurements require greater ranges.

For an antenna being tested in the near field, some means of correcting the incident phase front is necessary if meaningful data is to be obtained. Republic utilizes a dielectric microwave lens in a small anechoic chamber for flight line testing of airborne radar systems. The microwave lens converts the incident phase front from the feed horn into a plane phase front which illuminates the antenna of the radar system. The radar operates in a normal fashion and all modes of operation and necessary calibrations are checked. Of primary interest is clearance plane calibration for terrain avoidance. This requires accurate boresight axis measurements. The use of the dielectric microwave lens in this application has eliminated the necessity of a flight test for clearance plane calibration.

B. DIELECTRIC LENS

1. Lens Design

The function of the dielectric lens as used in radar testing and calibration is to modify the phase fronts of a radiating

source. The contour of the lens surface is designed using the principles of geometrical optics, a procedure commonly referred to as ray tracing. The electrical path length of a ray is determined by the product of the physical path length and the index of refraction (η) of the medium in which the ray is propagating. The index of refraction (η) is equal to the square-root of the dielectric constant (ϵ_r). Lens design is based on the principle of equality of electrical paths along rays between pairs of wavefronts and on Snell' Law of refraction. The theory of reciprocity will apply to a dielectric lens. If the lens converts to a spherical equiphase surface from the source located to its left into a plane equiphase surface on its right, it will bring to a focus the energy in a plane wave incident from the right.

If one surface of the lens coincides with an equiphase front, then the rays are refracted only at the other surface. Consider a lens with one plane surface and rotational symmetry about an axis. A cross section is shown in figure 1. The equation of the refracting surface necessary to convert a spherical phase front into a plane front may be obtained from the condition that the electrical path length through an arbitrary point (P) shall be equal to the electrical path length on the axis. This condition is

$$(FP) = (FQ) + (QQ')\eta \qquad (1)$$

where η is the index of refraction of the dielectric material ($\eta = \sqrt{\epsilon_r}$). These path lengths are illustrated in figure 1. The distance (FQ) is the focal length (f) of the lens. Equation (1) can be re-written in polar coordinate (r,θ) form as

$$r = f + \eta(r\cos\theta - f) \qquad (2)$$

or, solving for r

$$r = (\eta - 1)f / \eta\cos\theta - 1 \qquad (3)$$

When η is greater than one, equation (3) is that of a hyperbola of eccentricity η. Although Snell's Law of refraction was not used in deriving the equation of the lens surface, it can be shown to be satisfied.

The thickest part of the lens is on the axis. The thickness (t) of the lens at this point is given by

$$t = \frac{R(1-\cos\theta_0)}{\eta-1} \qquad (4)$$

where R and θ_0 are the coordinates of the lens apex where the dielectric reaches zero thickness. The thickness (t) can be found in terms of the focal length (f), the refractive index (η) and the lens diameter (D) by means of the equation

$$t = -\frac{f}{\eta+1} + \frac{\left\{f^2(\eta-1)^2 + (\eta^2-1)\left(\frac{D}{2}\right)^2\right\}^{1/2}}{\eta^2-1} \qquad (5)$$

The thickness (d) at any point on the lens surface defined by the coordinates (r, θ) is given by

$$d = \frac{r(\cos\theta-1)}{\eta-1} + t \qquad (6)$$

2) Design Approach

The lens to be used in the test system has two fixed parameters determined by size considerations. Typical values of these parameters are a focal length (f) of 20 inches and a diameter (D) of 36 inches. The design approach suggested is outlined below.

a) Determine a maximum allowable thickness (t max.) for the lens. Weight, dielectric losses and overall dimension requirements will limit (t). The coordinates of the lens apex (R and θ_0) may be found geometrically.

b) Solve equation (4) for the index of refraction (η).

$$\eta = \frac{R(1-\cos\theta_0) + t_{max}}{t_{max}} = \sqrt{\epsilon_r} \qquad (7)$$

This results in a minimum allowable value of dielectric constant (ϵ_r min).

c) Determine a minimum allowable thickness (t min) for the lens. The lens must remain structurally sound at the minimum thickness. Again, determine R and θ_0 geometrically.

d) Solve equation (7) for the index of refraction. This results in a maximum allowable value of dielectric constant (ϵ_r max).

Following the above procedure, a range of allowable thickness

$$t \text{ min} \leq t \leq t_{max}$$

will determine a range of allowable dielectric constant

$$\eta^2 \text{min} = \epsilon_r \text{ min} \leq \epsilon \leq \epsilon_r \text{max} = \eta^2 \text{m}$$

The final step in the design is then to choose a material whose dielectric constant is in the allowable range and determine the equation of the hyperboloidal surface.

When material of a given dielectric constant is specified the parameters available for design are the lens diameter (D) the lens thickness (t) and the focal length (f). One of these parameters may then be fixed to a given value and ranges of allowable values determined for the remaining two parameters. The procedure is essentially the same as outlined above.

The lens utilized in the test program was made of plexiglass ($\epsilon_r = 2.56$). It has a diameter (D) of 36 inches, a thickness (t) of 8.6 inches, and a focal length (f) of 20 inches.

3. Lens Performance

The illumination across the aperture of the lens is a result of the primary illumination of the feed horn and the effects of the lens on this primary pattern. The lens not only changes the shape of the incident phase fronts but also introduces an amplitude variation across its aperture. The effect of the lens on the illumination of an isotropic source is shown in figure 2 (see reference 2). Experimental data (figure 3) indicates that the lens forms phase fronts plane to within $\lambda/16$ (2 millimeters) and introduces an amplitude taper of 10 DB which includes the primary feed illumination taper. The lens accounts for 7.4 DB and the feed horn introduces approximately 2 DB.

The variation in illumination over the aperture of the radar antenna being tested will be about 5 DB. This taper is added to the illumination taper already designed into the radar antenna. An increase in measured beamwidth and sidelobe level is expected.

C. ANTENNA TESTS WITH DIELECTRIC LENS

A four-horn monopulse antenna was tested on a free-space 125 foot range and at a distance of 16 inches from the face of the dielectric lens. The data taken includes radiation patterns and difference-to-sum channel ratio curves. Figure 4 illustrates the test set-up utilizing the dielectric lens.

The patterns presented in Figures 5 to 8 verify original expectations. The half-power beamwidths show little or no increase when measured with the lens, but beam broadening is evident at larger scan angles. Sidelobe levels increase at scan angles of 10 degrees or greater with some changes in sidelobe structure. In the region of interest for radar system testing, ie. the boresight region, the patterns are virtually identical when measured in free space or with the lens.

The difference channel information of a monopulse radar antenna system consists of two radiation lobes of opposite phase. The crossover point or null is used to define the location of the boresight axis. Any apparent shift of this null from the defined boresight axis as determined by the antenna gimballing is considered to be a boresight error (BSE). The processed signal used by the radar system in locating targets consists of the ratio of difference to sum signal amplitudes multiplied by cosine of the phase of the difference signal. This phase is referenced to the sum channel lobe. One difference channel lobe is in phase, the other is 180 degrees out of phase. In the boresight region, the phase changes rapidly. A phase error in this region will shift the crossover point left or right, resulting in boresight errors.

The ratio of the difference channel amplitude to the sum channel amplitude (E_Δ / E_Σ) and the phase difference of the two channels (θ)

were measured on the 125 foot free space range and with the lens. The results of the measurement is shown in Figure 9. Again, the data are virtually identical when measured in free space or with the lens.

By displacing the feed horn off the lens axis, the radar receives a signal from a different apparent direction. This is due to the resulting tilt in the incident phase front. For radar system calibration purposes, a maximum phase front tilt of 6 degrees was required. Tests were conducted relating horn displacement to angular tilt of the phase front and a calibration chart was generated for the lens. The calibration curve was used in subsequent flight line tests.

D. CONCLUSIONS

Republic has conducted an extensive test program to prove the validity of radar system check-out utilizing a microwave dielectric lens. The program included tests on the lens as a phase-front forming device and its effect on antenna measurements such as patterns and boresight error. The lens has also been used as an integral part of an automatic radar tester. Comparisons have been made to testers which use a small anechoic chamber without phase correcting devices. Evaluation of the data obtained has shown the lens system to be the most suitable of the short range techniques available. Appreciation is extended to Dr. Henry Jasik who conducted this independent evaluation

REFERENCES

1. Abstracts of the Thirteenth Annual Symposium on the USAF Research and Development Program "Boresight Errors in the Near-Field of a Monopulse Antenna" by P. Zusolo, S. Jurcsak and J. Castrigno dated October 1963

2. S. Silver "Microwave Antenna Theory and Design" McGraw Hill Book Company, 1949

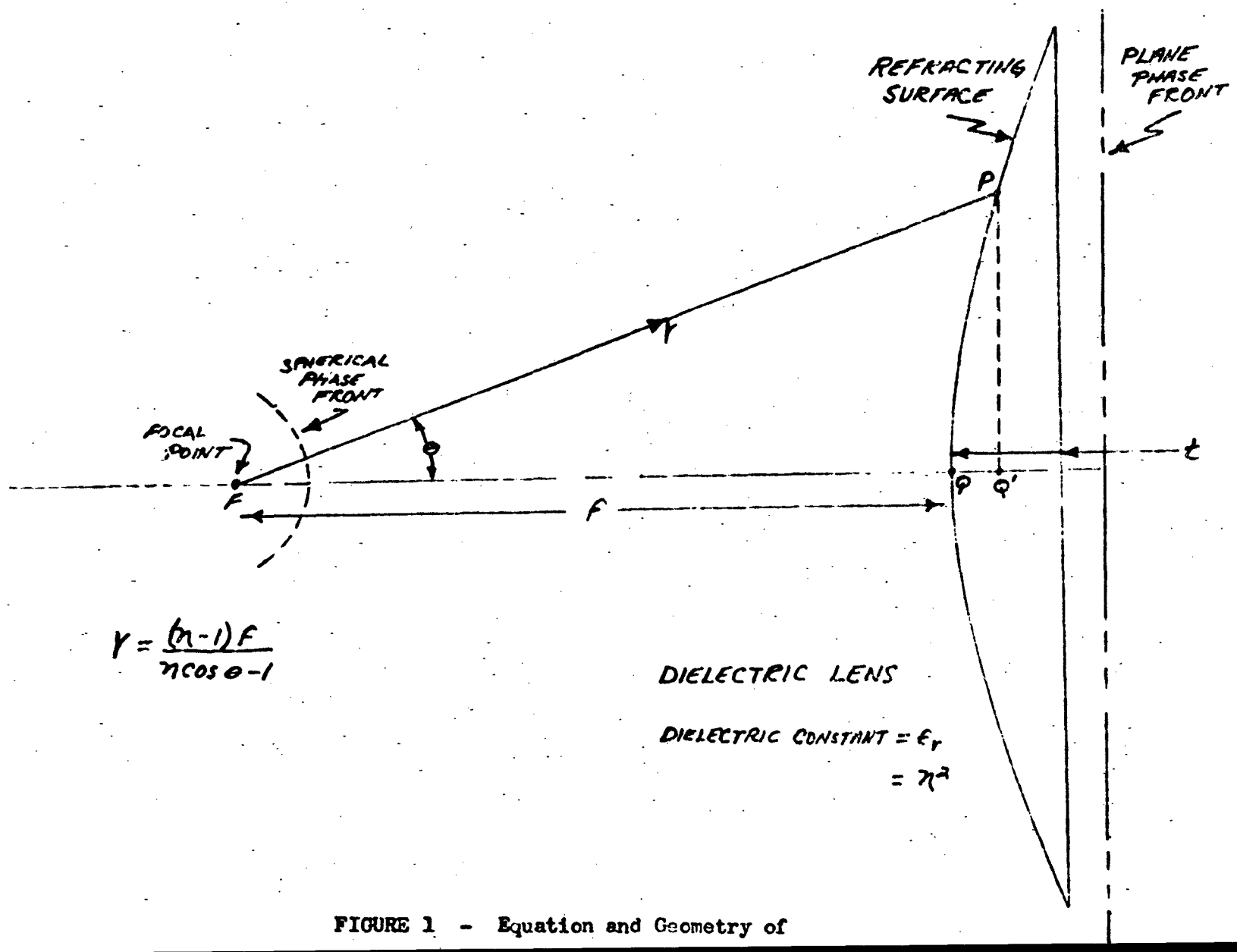

FIGURE 1 - Equation and Geometry of

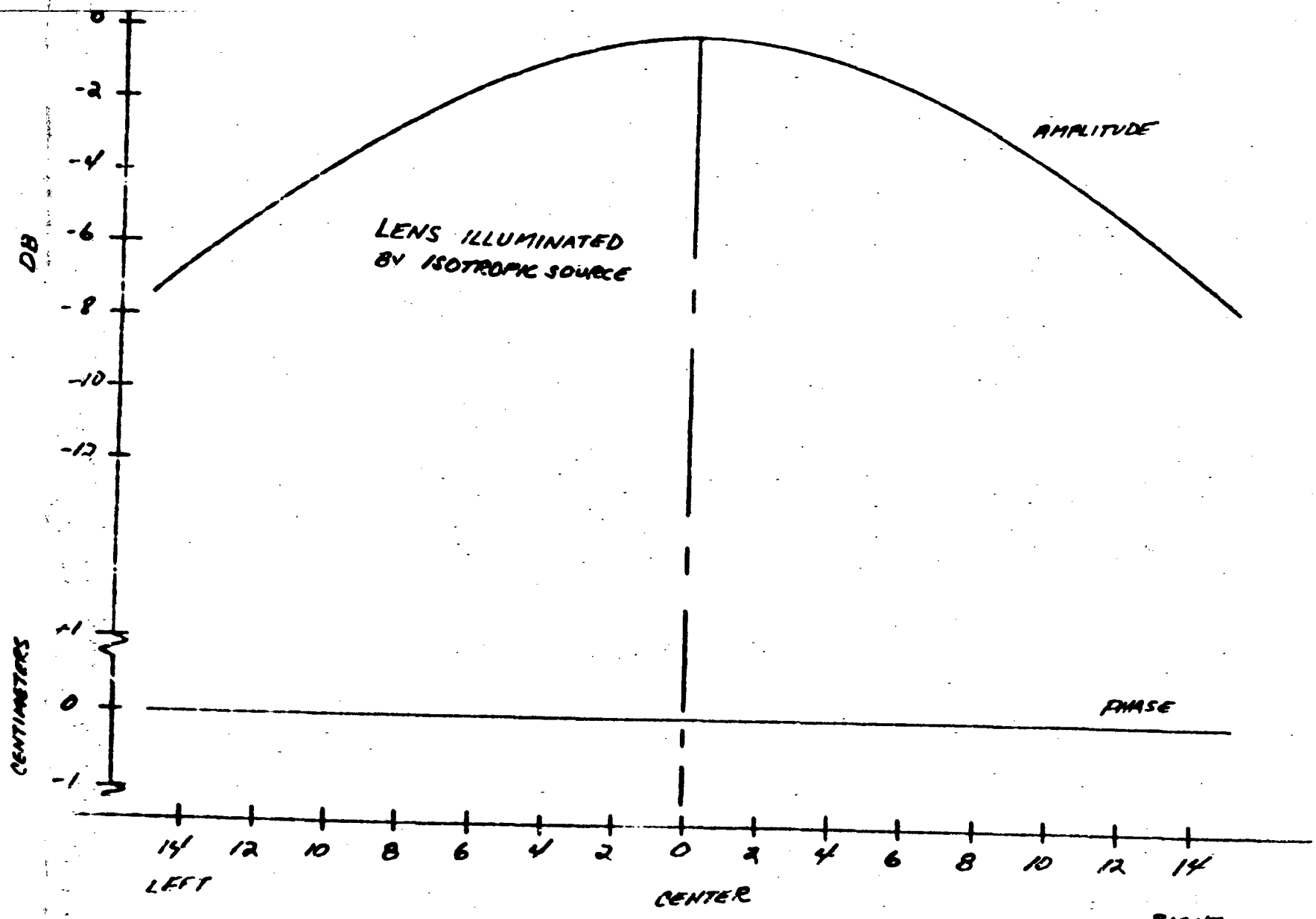

FIGURE 2 - Theoretical Amplitude and Phase Variation Across The Face Of A Dielectric Microwave Lens

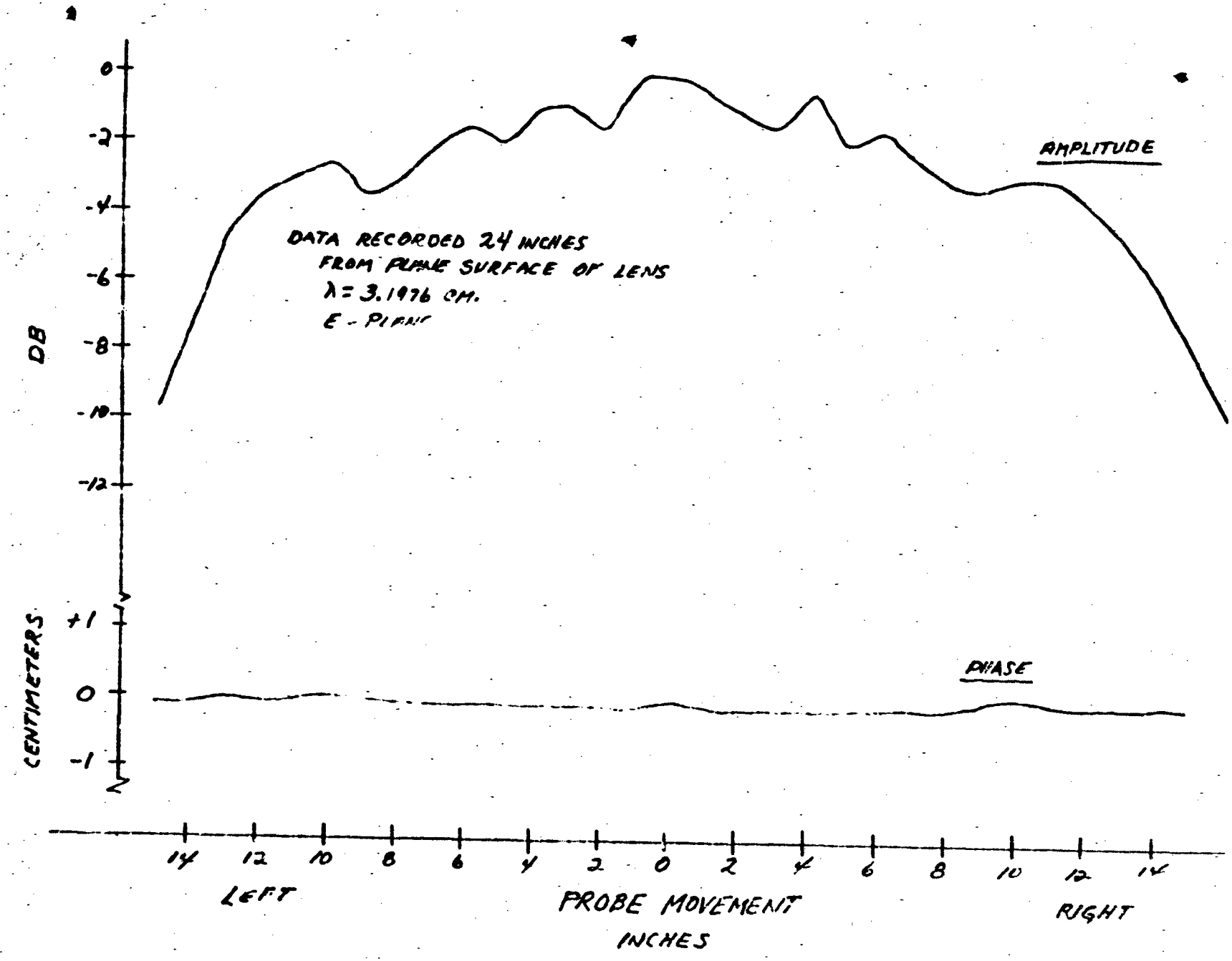

FIGURE 3 - Experimental Amplitude And Phase

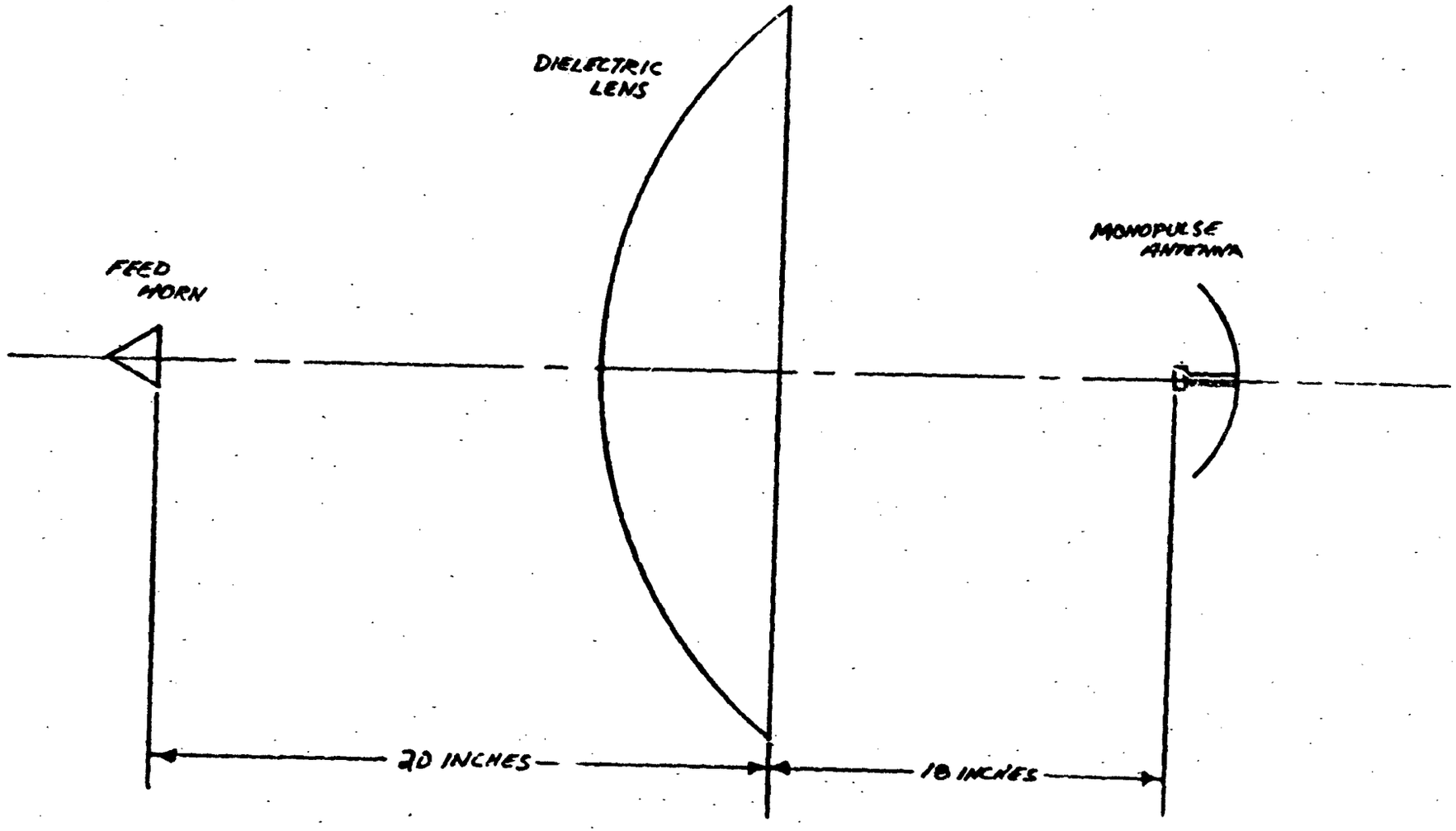

FIGURE 4 - Test Set-Up With Microwave Lens

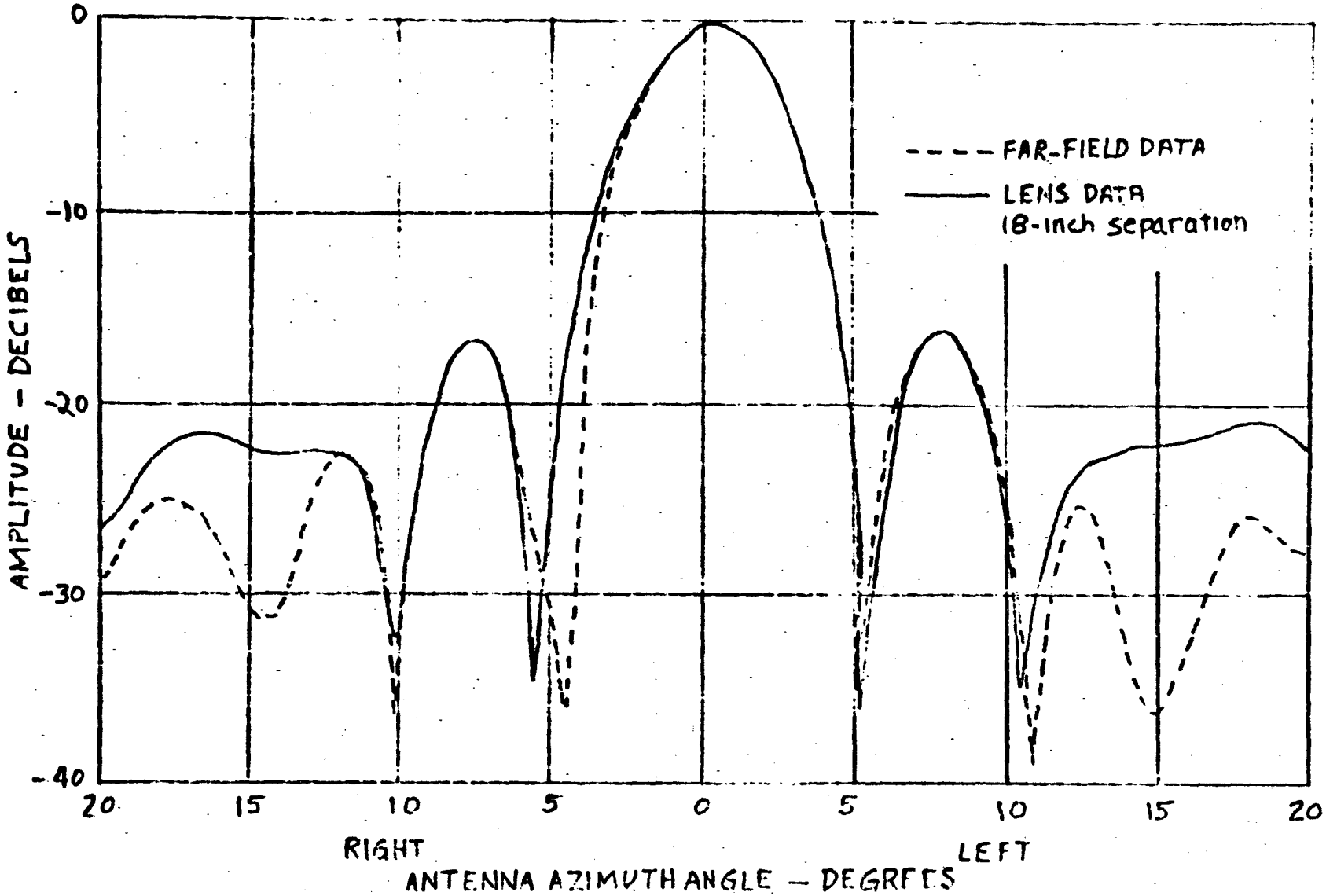

FIGURE 5 - Far-Field Data and Lens Data On

Azimuth Plane Sum Patterns

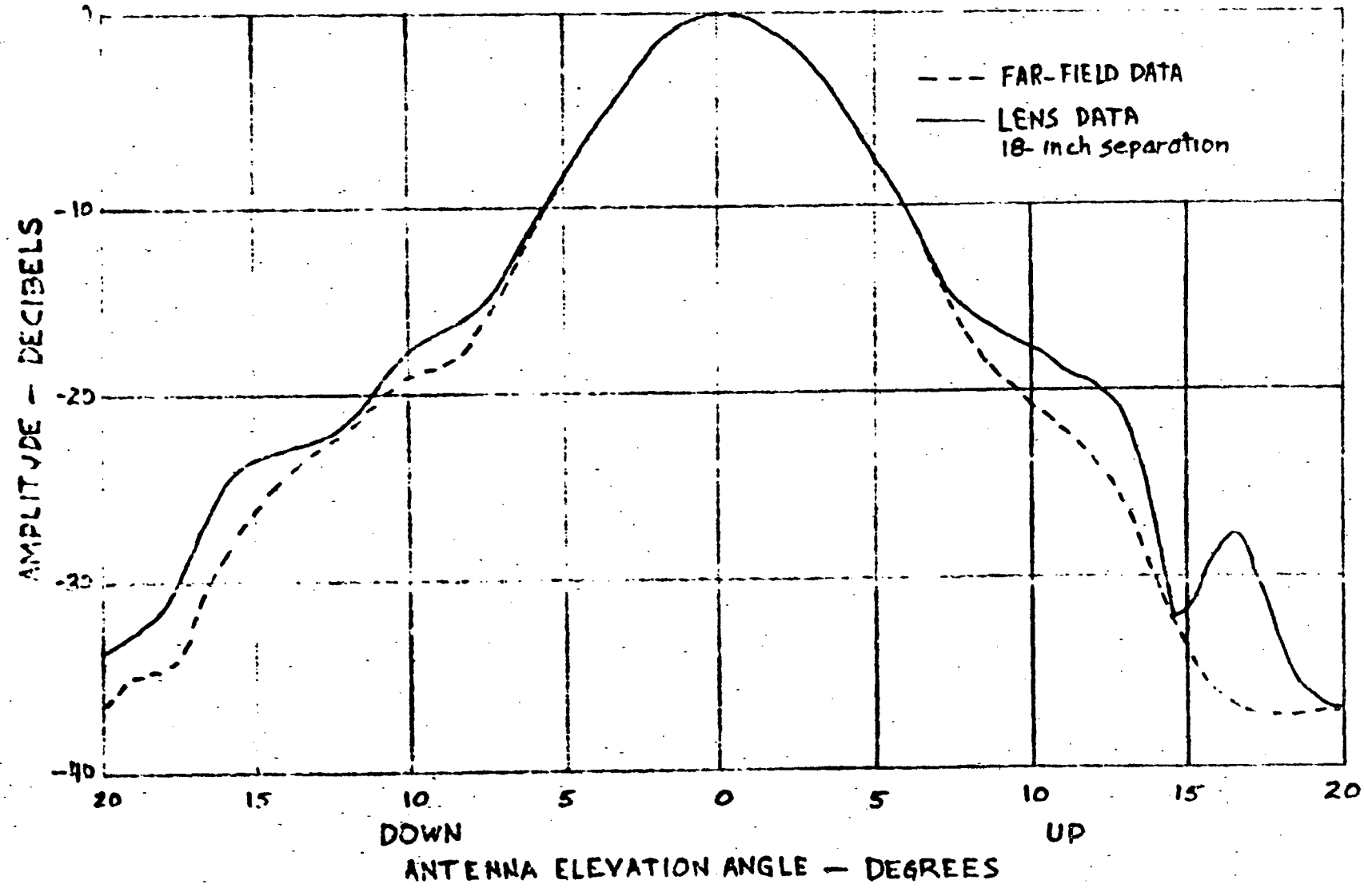

FIGURE 6 - Far-Field Data and Lens Data on Elevation Plane Sum Pattern

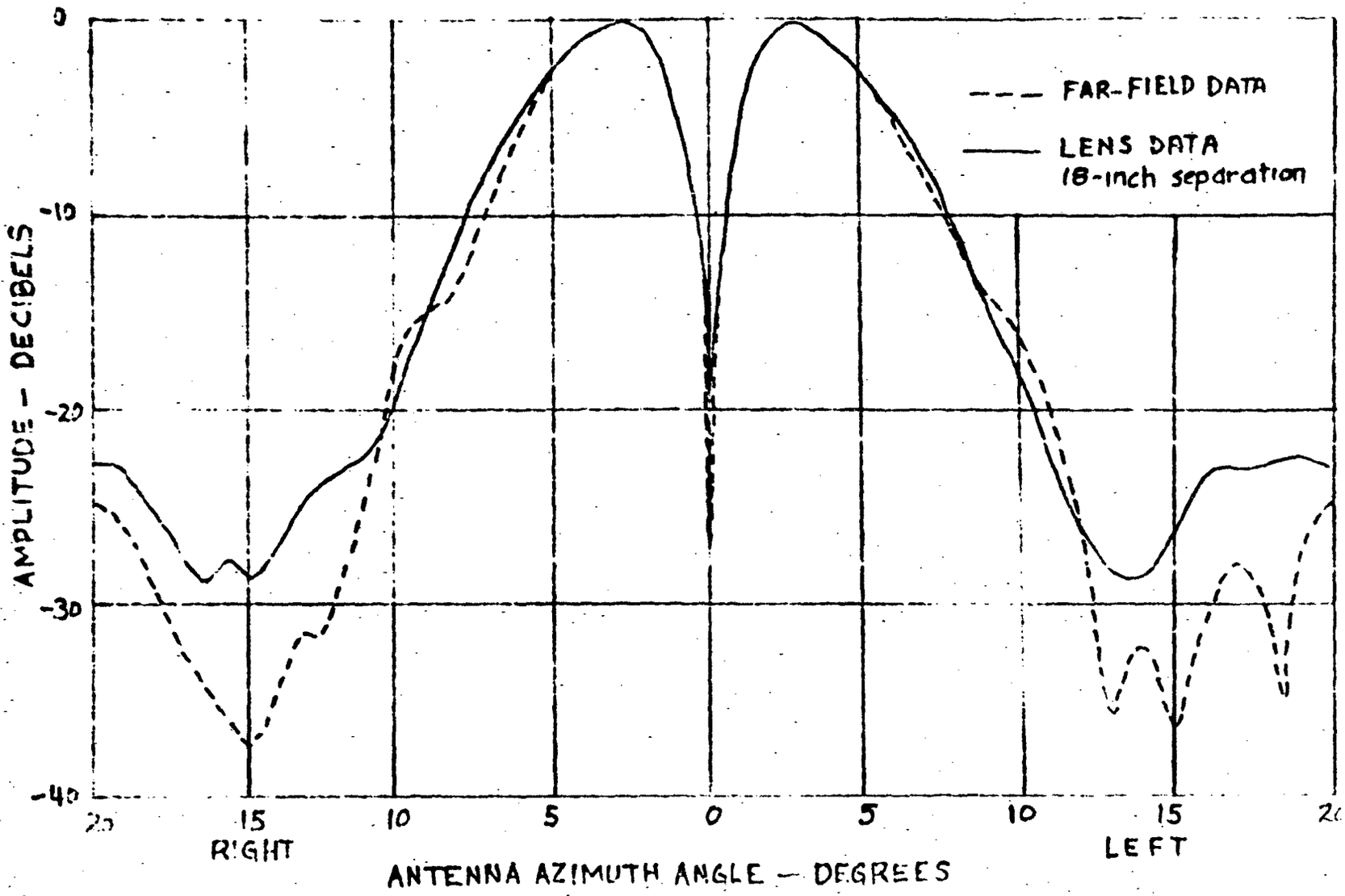

FIGURE 7 - Far-Field Data and Lens Data

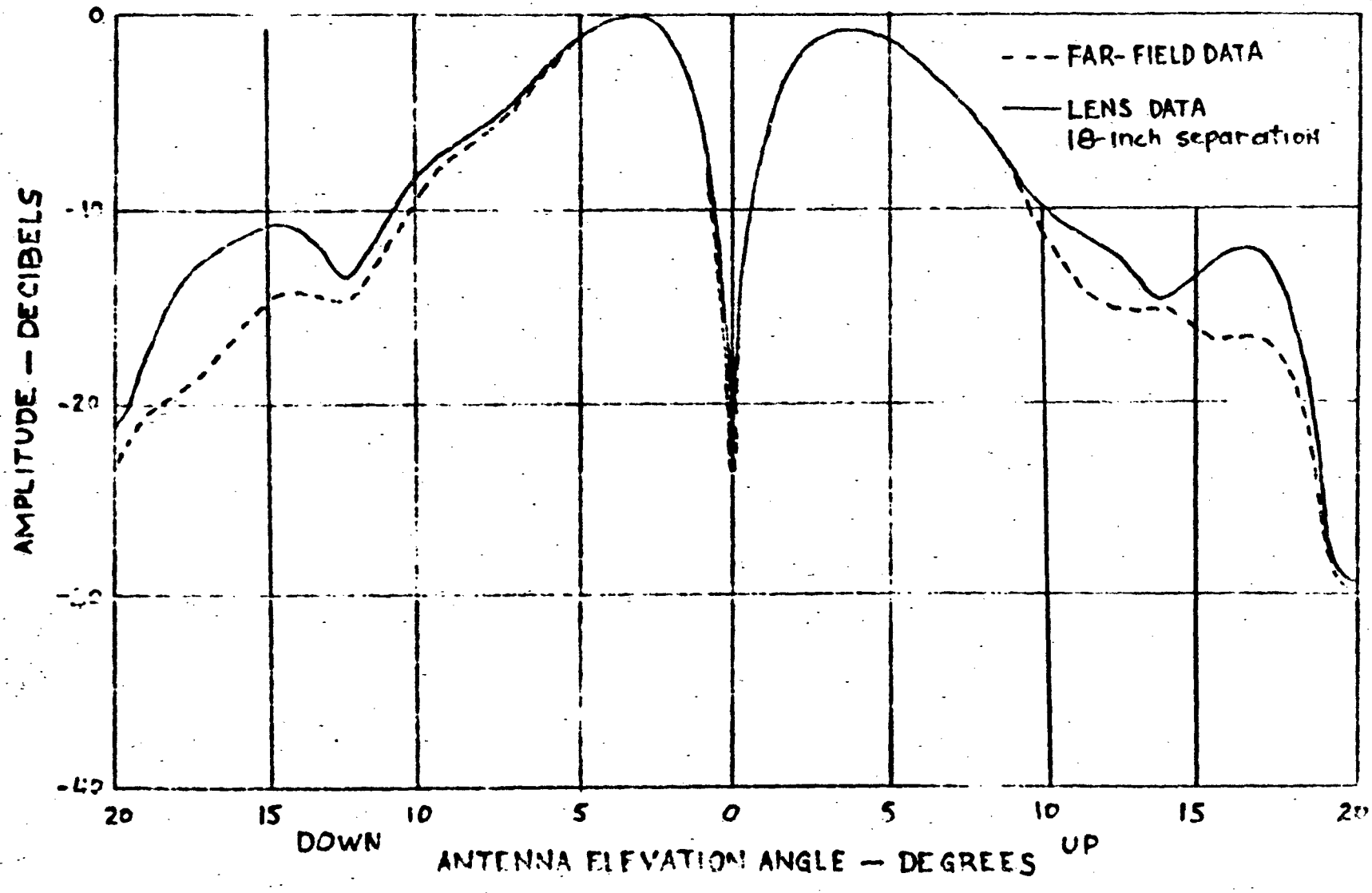

FIGURE 8 - Far-Field Data and Lens Data on Elevation Plane Difference Pattern

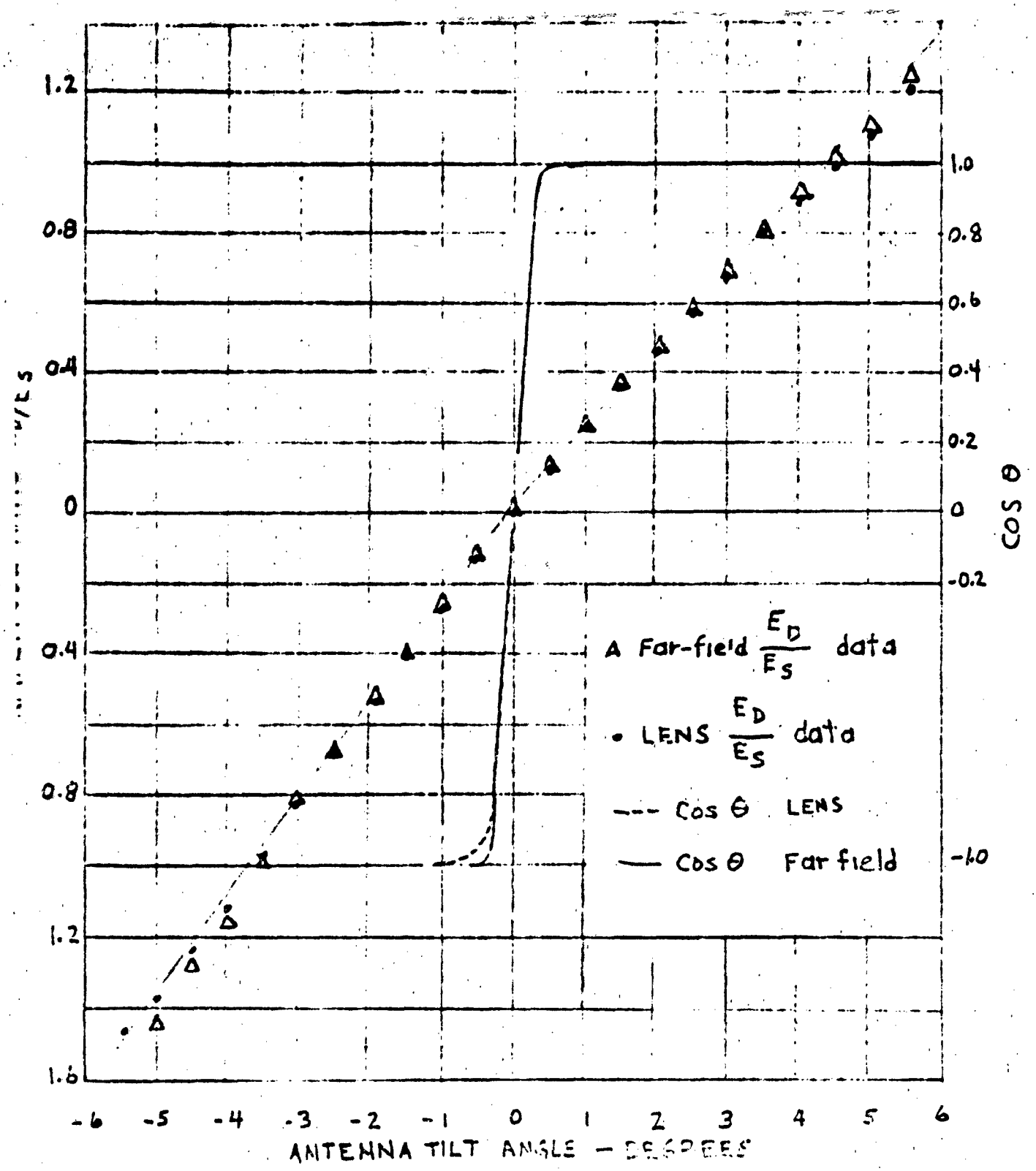

FIGURE 9 - Far-Field Data and Lens Data on Channel Amplitude Ratio and Phase Difference

HF SHUNT ANTENNAS FOR ELECTRICALLY SHORT AIRCRAFT

BY

DONALD G. GORDON
DESIGN ENGINEER
NORTH AMERICAN AVIATION, INC/LOS ANGELES DIVISION

A PAPER PRESENTED AT THE 14TH ANNUAL SYMPOSIUM ON
USAF ANTENNA RESEARCH AND DEVELOPMENT

I INTRODUCTION

This paper discusses an HF antenna concept, enumerates its advantages for high-speed aircraft, and presents data resulting from a research study on this antenna type. This research is continuing at the Los Angeles Division of North American Aviation with the objective of antenna design parameter development.

It is well established that an airborne HF antenna operates by coupling to the resonant modes of the aircraft structure so that, in effect, the entire vehicle functions as an antenna. There are two basic ways to excite an airframe - the shunt feed method and the series feed method. The series feed method consists of electrically isolating a portion of the aircraft from the main body and feeding the antenna between the gap. This is a high-voltage device and is often called a voltage-type antenna. The probe- and cap-type antennas are the familiar examples which have comprised the most often used solution of the HF excitation problem.

The shunt feed method utilizes a type of shunt strip that is shorted to the airframe at one end and runs parallel to the aircraft surface to the feed point. This is a high current device and is therefore often called a current-type antenna. This paper concerns itself mainly with the shunt antenna concept.

II ADVANTAGES OF SHUNT ANTENNAS

Structural

Series-type antennas, as previously stated, involve the electrical isolation of a portion of the aircraft structure by means of dielectric materials. This structural problem becomes very difficult to solve for high-speed aircraft. At speeds above Mach 2, air friction causes very high temperature on the aircraft skin. At Mach 3, temperatures in excess of 600 °F are encountered. A great thermal and/or structural stress is put on the dielectric materials used for isolation. Shunt-type antennas, however, can have their shunt element centrally located, even on the fuselage itself. This fact results in a much greater structural integrity for shunt antennas since the shunt element can be located in regions of lower temperature and less structural stress.

Efficiency

The systems efficiency of an HF antenna depends in large measure on the efficiency of the coupling circuit used to match the antenna to the transmission line from the transmitter. The series-type antennas need coils in their

coupler circuits and these coils are very large and lossy at the lower frequencies. Shunt antennas at these frequencies, however, can be matched with low loss circuits composed solely of capacitors. This advantage becomes very useful in the case of HF antennas for electrically short aircraft.

Lightning Protection

Shunt antennas have an inherent protection against lightning strikes since the feed can be located away from the extremities of the aircraft; therefore, in most cases, lightning arrestors are not needed for shunt antennas. For high-speed aircraft this is a decided advantage over series-type antennas, since high-temperature lightning arrestors are usually very costly.

Voltage Breakdown

Series-type antennas are high-voltage devices and are thus subject to voltage breakdown, especially at high altitudes. Shunt-type antennas, being high-current devices, have relatively low voltages at their terminals for a given power level. Although high voltages may be encountered at frequencies for which the shunt element approaches a quarter wavelength, this effect can be avoided by shorting the shunt element to a shorter length as one proceeds higher in frequency.

Cooling Advantages

The coupler of an HF antenna for a high-speed aircraft must be cooled because of the high skin temperature and the heat which is dissipated due to inherent coupler losses. Since shunt-type antennas can be more centrally located, the cooling systems for the coupler can be more closely related to the main cooling system. In fact, for the fuselage shunt, the coupler can be placed in the main body of the fuselage with no special cooling apparatus needed.

III FUSELAGE SHUNT ANTENNAS FOR A LONG SUPERSONIC AIRCRAFT

An external fuselage shunt was proposed by NAA for the HF communications requirement of its SST design. This antenna consisted of a shunt strap approximately 15 feet long, supported by a dorsal fin and located on the dorsal midline near the tail (see figure 1). It was this antenna that was mentioned in a recent issue of Aviation Daily. (Refer to Reference 1.)

A flush shunt antenna in the same location was also studied. A photograph of this antenna is shown in figure 2. This design incurs no aerodynamic penalty, but has a greater effect on the basic aircraft structure. The antenna consists of a dielectric filled trough in the airframe partially covered with a conducting strap narrower than the trough width and shorted to the airframe at one end. (See figure 3.) The feed is as shown in figure 4.

A 9-1/2-foot model (figure 5) of delta wing aircraft was constructed and the fuselage shunt antennas tested on it. This simplified shape should have characteristics common to many delta wing aircraft.

Magnetic Field Strength Tests

Magnetic field strength measurements were made in order to determine the current flow patterns and the relative degree of coupling when the antenna feed was placed in different locations. These measurements were made with an electrically shielded loop probe. The flush shunt antenna was tested in two positions - forward and aft with the feed point forward of the strap. The external shunt (figure 6) was tested in the same two positions and also in the aft position with the strap forward of the feed.

The excitation frequency was 123.5 mc model frequency, or about 6.2 mc full scale. This simulates an aircraft about 190 feet in length. In MKS units, the H vector immediately adjacent to a conductor has the same magnitude as the current density. Relative current magnitude profiles can therefore be constructed by using the loop probe. Figures 7 through 11 show these magnitude profiles for the flush and external shunt in the feed positions previously mentioned. The readings were taken with the capacitor and variable resistor of the detecting circuit set in the same position. The current values are normalized to 100 for the largest measureable value.

Figures 7 and 10 indicate that the flush and external shunts in the aft position have essentially the same degree of coupling with slightly better excitation of the vertical stabilizer in the case of the flush shunt.

Figures 9 and 10 show that a disadvantage is suffered by placing the strap forward of the feed when the antenna is in the aft position. About the same wing area is strongly excited, but the vertical stabilized is excited considerably less.

Figures 8 and 11 show that the forward location of the antenna feed gives much better excitation of the wing than the aft position. The mode at the test frequency consists of strong excitation of the leading and trailing edge of the wing. The vertical stabilizer is only weakly excited.

The considerable difference in magnitude between the flush and external shunt for the forward position is not understood at this time. Figures 9, 10, and 11 were taken under identical conditions and it is therefore felt that these profiles provide valid comparison of the two feed positions. In any case, the wing excitation mode is indicated in both figures 8 and 11, and the superiority of the forward feed position for excitation of the wing is shown.

The aft position does have the advantage of a strong excitation of the vertical stabilizer which may give rise to somewhat more favorable radiation patterns than the forward feed position.

Impedance Measurements

The impedance of the flush shunt antenna in the aft position was measured for the 2.5 to 8 mc range, full-scale, using a Boonton 160A Q-Meter. The test setup is shown in figure 12. A computer program was developed to calculate the transformation of impedance by the transmission line. The program assumed that the line was lossless.

The object of these tests was to establish an estimate of coupler size and weight. For such a goal, it was felt that the inexpensive model shown in figure 5 would suffice. The antenna feed structure itself was accurately dimensioned, but the general airframe shape was not made to close tolerance. The model was made of galvanized steel, and the antenna feed structure was made of copper.

The parallel resistance R_p and reactance X_p were calculated using the standard Q-Meter formulas (Refer to Reference 2)

$$R_p = \frac{Q_1 Q_2}{\omega C_1 (Q_1 - Q_2)}$$

$$X_p = \frac{1}{\omega (C_2 - C_1)}$$

where: Q_1 = Q of work coil and circuits
C_1 = capacitance necessary to resonate work coil
Q_2 = Q of antenna plus work coil and circuit
C_2 = capacitance necessary to resonate antenna plus work coil
ω = 2π x frequency

The series resistance R_s and the series reactance X_s were calculated from

$$R_s = \frac{R_p X_p^2}{R_p^2 + X_p^2}$$

$$X_s = \frac{R_p^2 X_p}{R_p^2 + X_p^2}$$

Impedance curves calculated from the data obtained for the 2.5 to 8 mc range, full scale, are shown in figure 13. Two resistance peaks have tentatively been identified as half wave resonance of the fuselage and trailing edge of the wing. As with all shunt antennas, below quarter wavelength resonance, the reactance is inductive.

Coupler Evaluation

Shunt antennas are inductive at frequencies below the quarter wave resonance of the shunt element. To match such an antenna a shunt capacitor is needed to transform the resistance to the characteristic impedance of the transmission line and a series capacitor to tune out the inductive reactance of the parallel combination. If the antenna resistance is greater than the characteristic impedance of the transmission line (typically 52 Ω) or if the antenna resistance is capacitive, a variable inductor is needed in parallel with the shunt capacitor. These circuits, with their theoretical tuning ranges, are shown in figure 14. From the impedance curves of figure 13 and data from similar aircraft, required tuning ranges of 30-3000 pf, shunt capacitance, and 5-500 pf, series capacitance, were calculated.

Since no power is reflected back to the transmitter when the antenna is matched, all the power is dissipated in the antenna resistance Ra. The peak current I_p through Ra and Xa (the antenna reactance), can thus be found by setting I_p^2 Ra = the peak input power. For a 100-watt carrier and 100 percent modulation, the peak input power will be 400 watts. From the peak current, the peak voltage can be found which is the voltage across all parallel coupler components. Finally, the current through the coupler components can be found.

Results of calculations based on the impedance data measured to date on the 1/20 scale SST model are shown in figure 15. These results, together with data from other delta wing aircraft, indicate that current through the parallel coupler capacitor will not exceed 35 amperes, rms, for 400-watt peak power. These calculations also show that voltages across the coupler components and the antenna feed should not exceed 4 kv, peak.

The above requirements of tuning range, voltage rating, and curr can be met with off-the-shelf capacitors. One possible coupler config is shown in figure 16. Preliminary calculations indicate that the coup should have a range of 0.1-15 μ h. At frequencies for which the impe capacitive and of low resistance, high current through the required in will cause large losses. This effect can be avoided by shorting the sh ment to half its length when the frequency is near primary resonance (10 mc, full scale).

For higher powers, the coupler must handle quite high currents. kw, PEP for example, over 180 amps must flow through the shunt cap Large currents, such as this, will require advances in coupler technol

Conclusions

In order to fulfill the HF communications requirement for today's speed aircraft, a change from series-fed to shunt-fed antennas is indic The high structural integrity of shunt antennas and their resistance to breakdown and lightning strikes are the main advantages which dictate change.

This change from series to shunt feed systems is a change from a voltage to a high current device. New design problems will therefore p themselves. For powers greater than 1 kw, couplers must be designed will withstand hundreds of amperes. The large current flowing in the the aircraft might create an ohmic loss problem that may require spec platings of low loss metals for its solution.

At North American Aviation, these problems are being considered connection with a continuing research and development project on HF an nas. The goal of this project is to exploit to the fullest, all methods wh will extend HF communications capability to shorter and faster aircraft.

IV REFERENCES

1. Aviation Daily, April 2 issue, p 210

2. BRC Notebook, Winter 1955, p 4

3. NA-64-34, "Impedance and Field Strength of SST HF Flush Shunt Antenna," North American Aviation, 16 January 1964, Los Angel Division

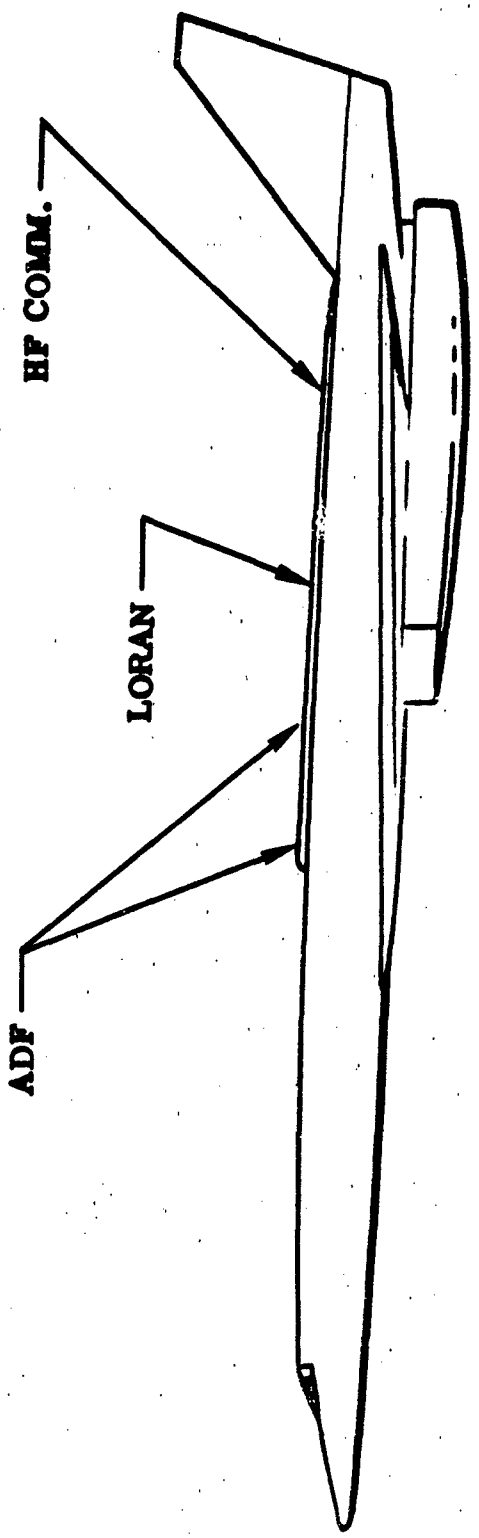

Figure 1. HF Antenna Housed in Dorsal Fin

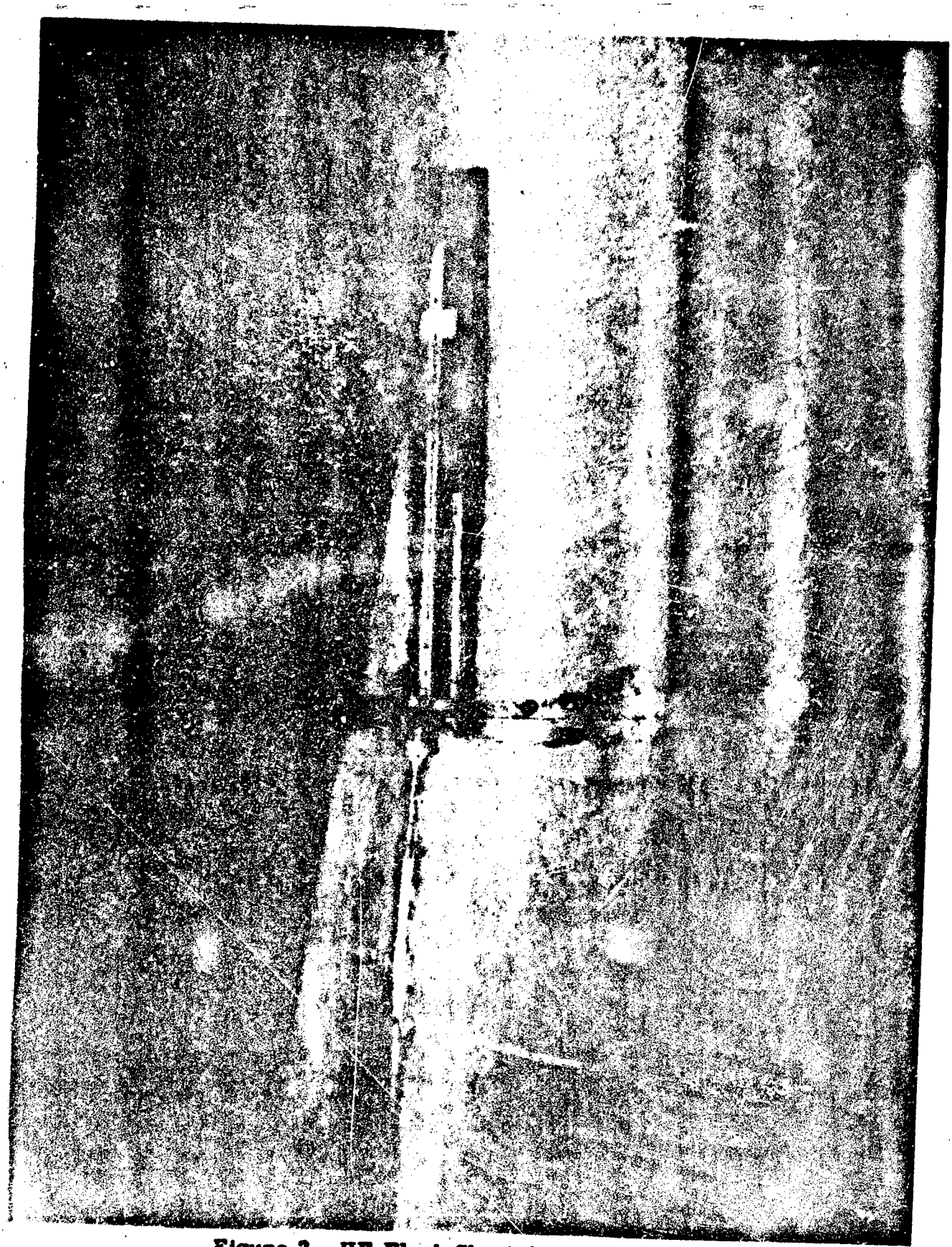

Figure 2. HF Flush Shunt Antenna

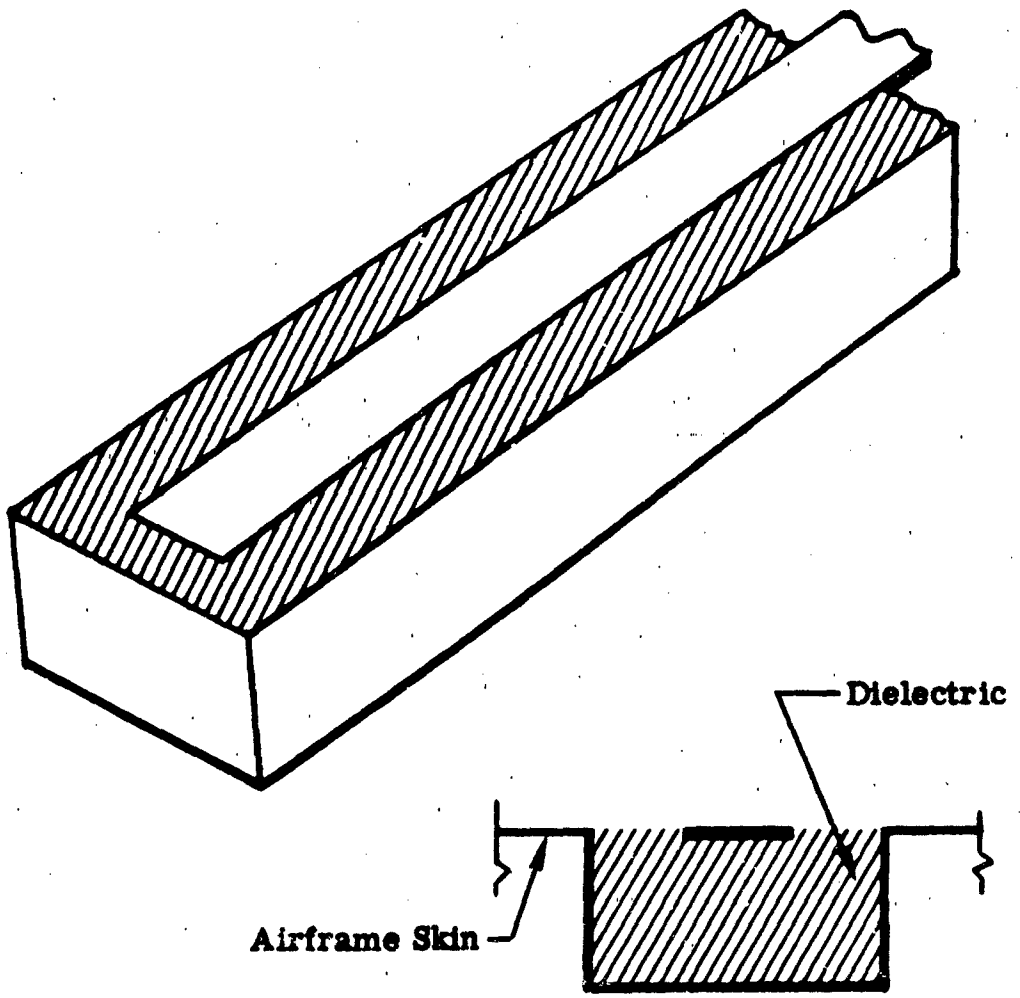

Figure 3.
The HF Flush Shunt Antenna

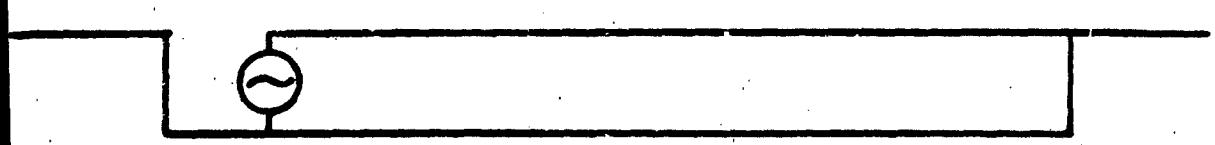

Figure 4. Method of Feed



Figure 5. 9-foot Delta Wing Impedance and Field Strength Model

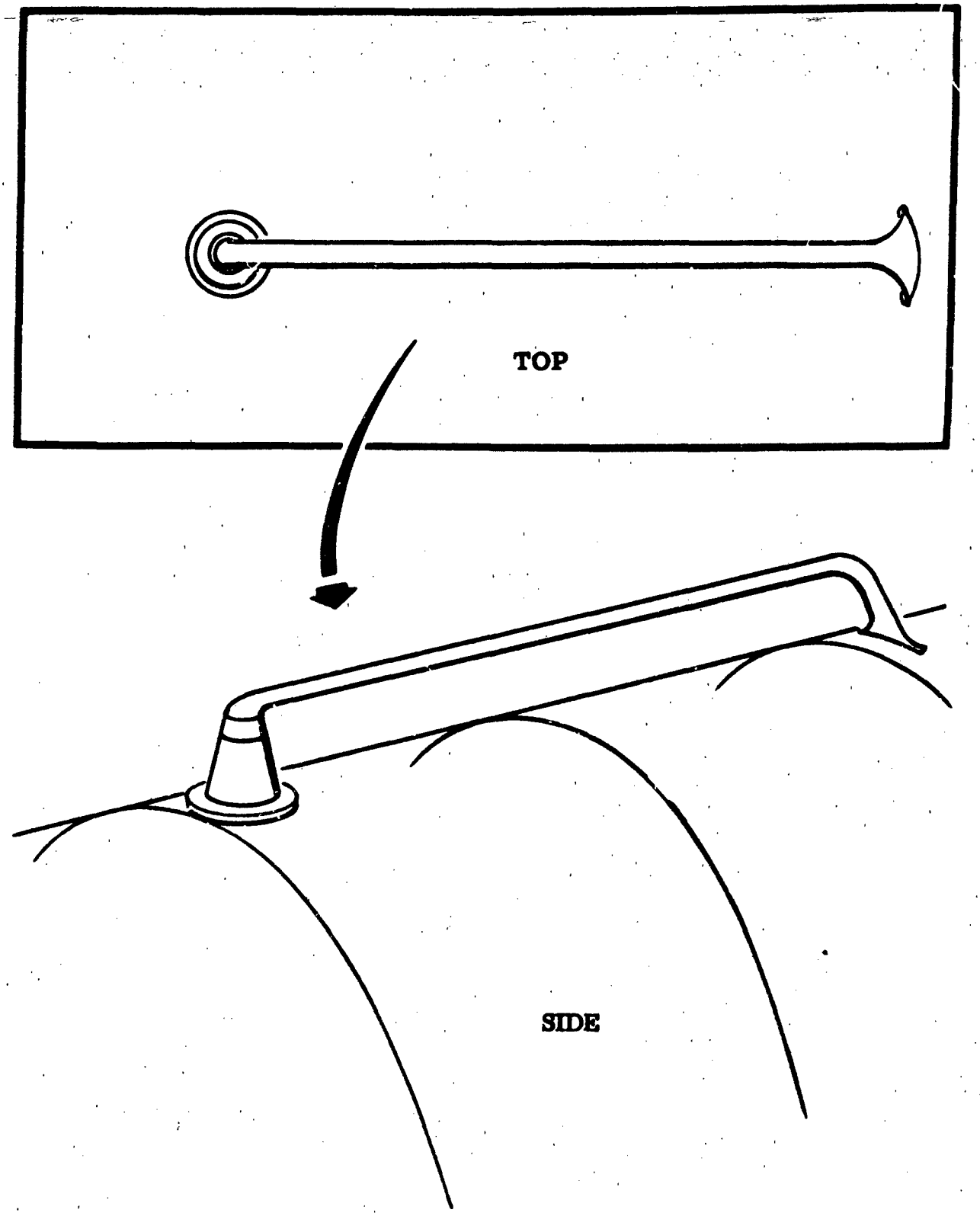

Figure 6. External Fuselage Shunt Antenna

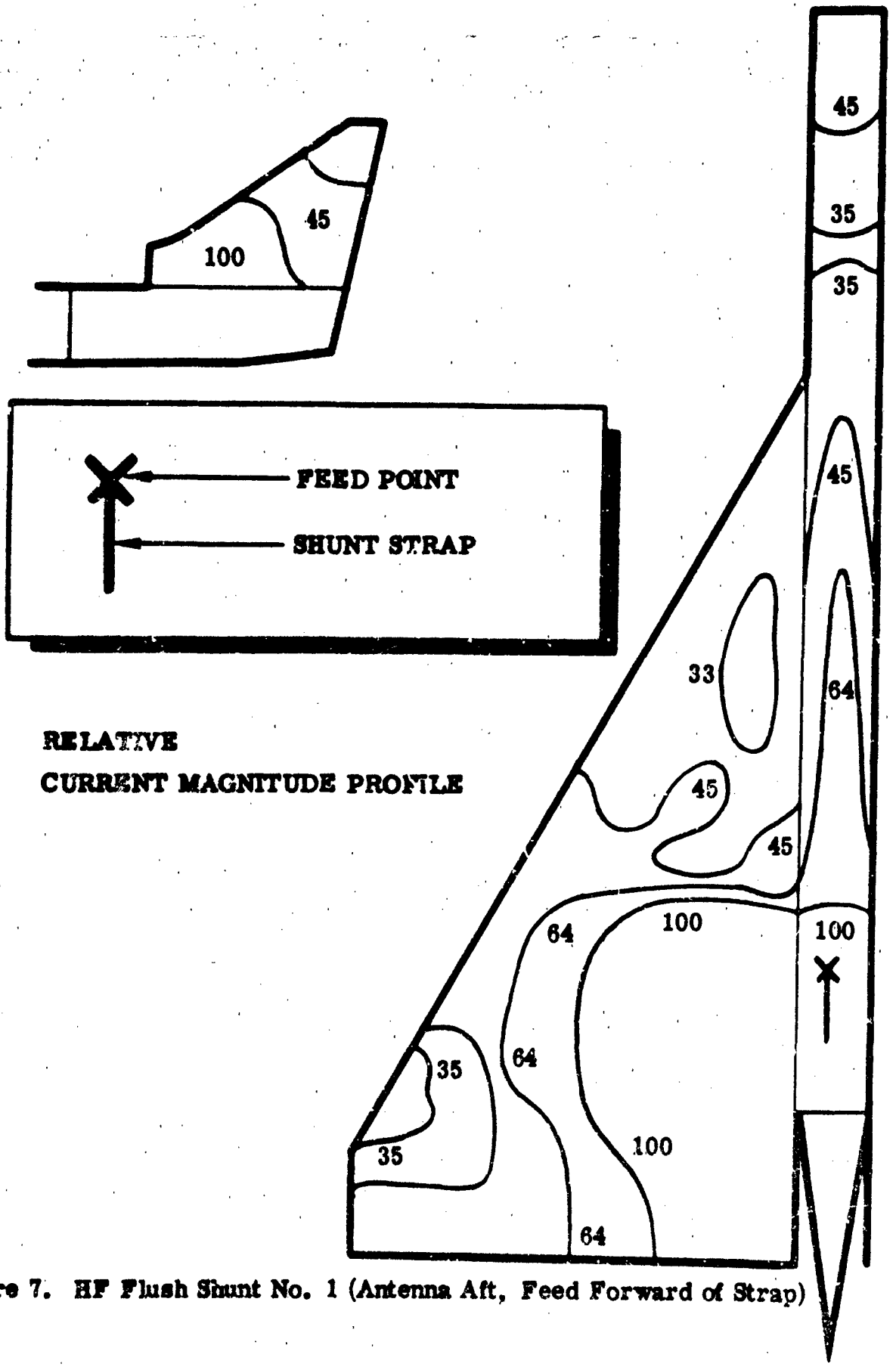

Figure 7. HF Flush Shunt No. 1 (Antenna Aft, Feed Forward of Strap)

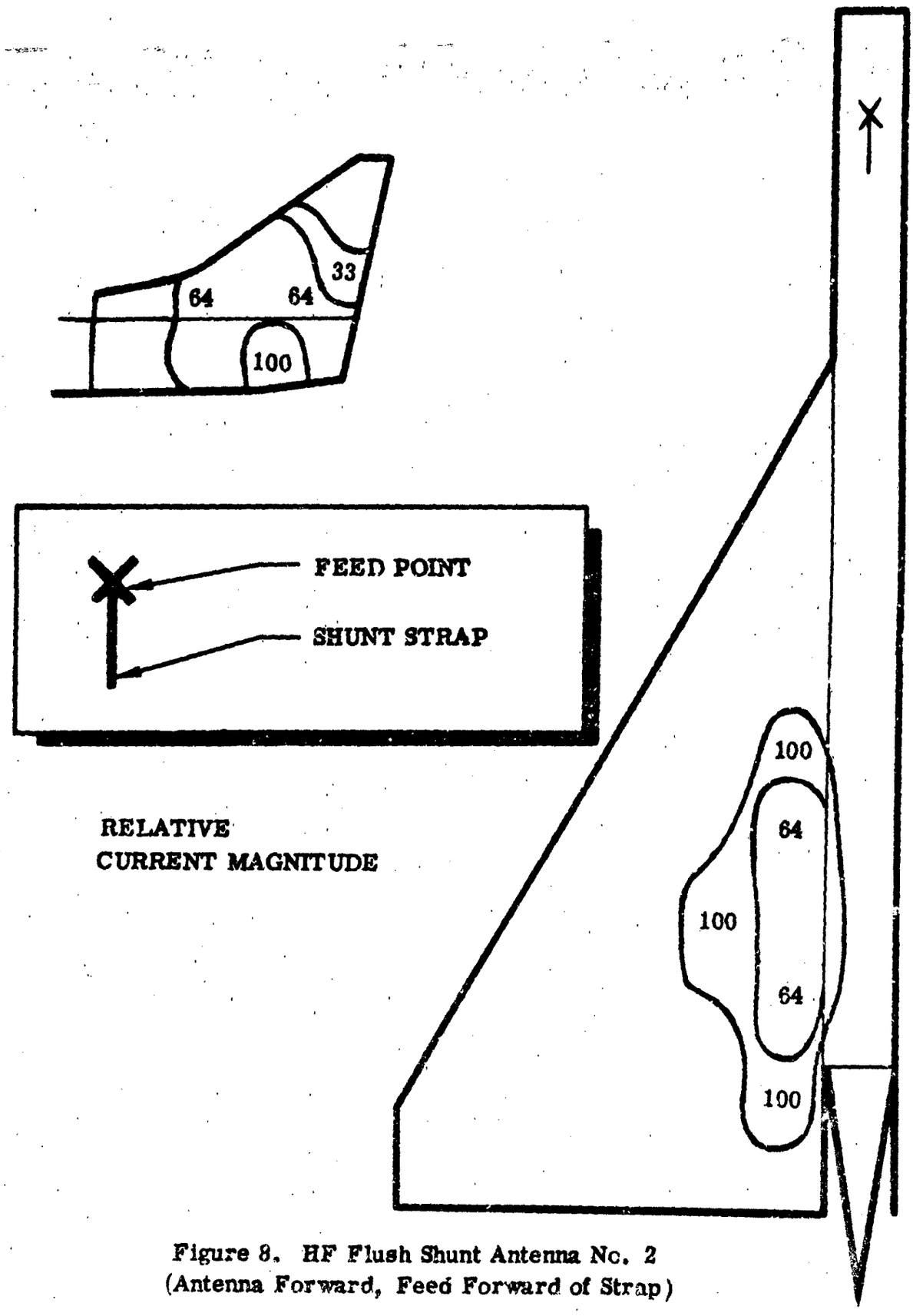

Figure 8. HF Flush Shunt Antenna No. 2
(Antenna Forward, Feed Forward of Strap)

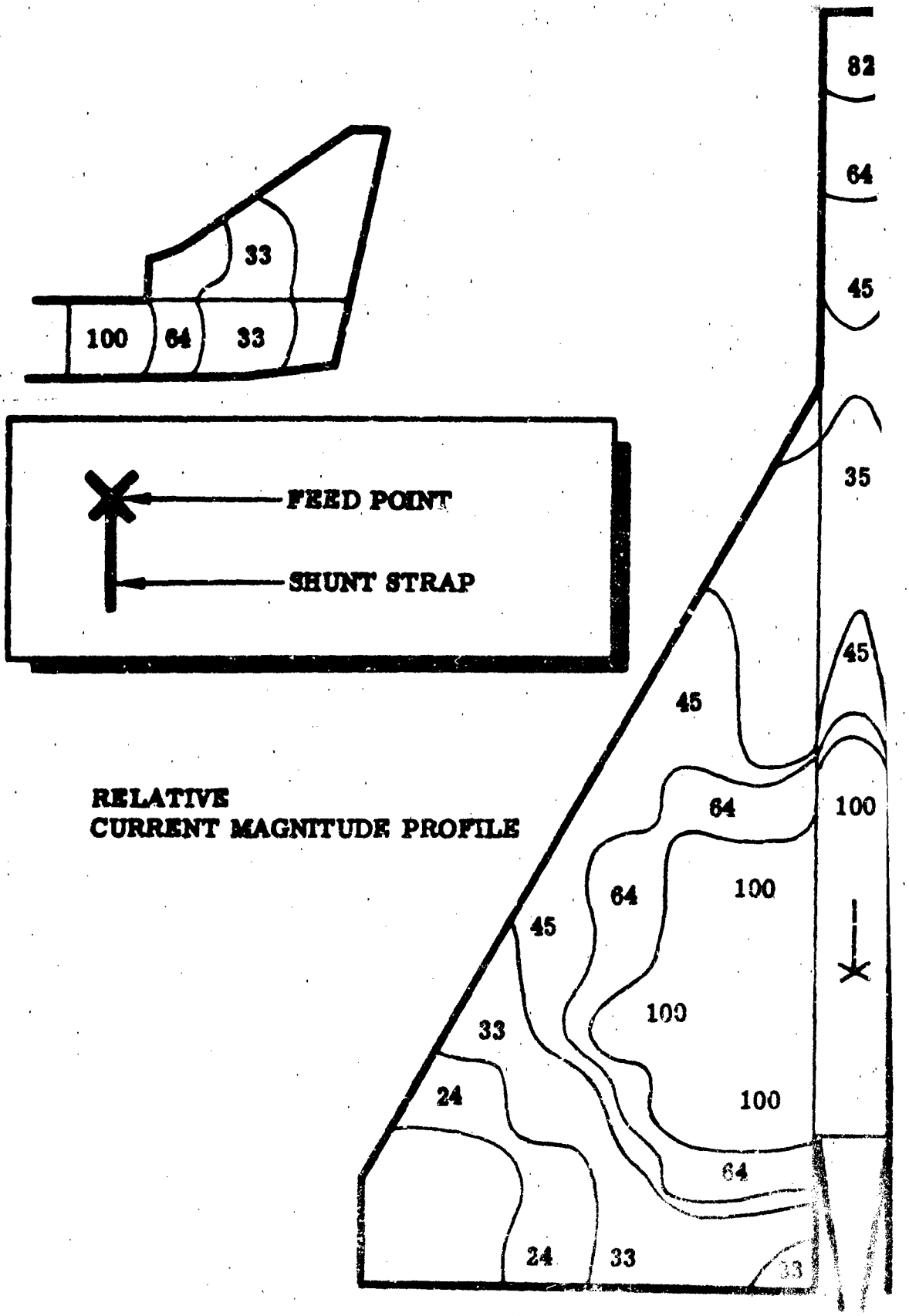

Figure 9. HF External Shunt Antenna No. 1 (Antenna Aft, Feed Aft of Strap

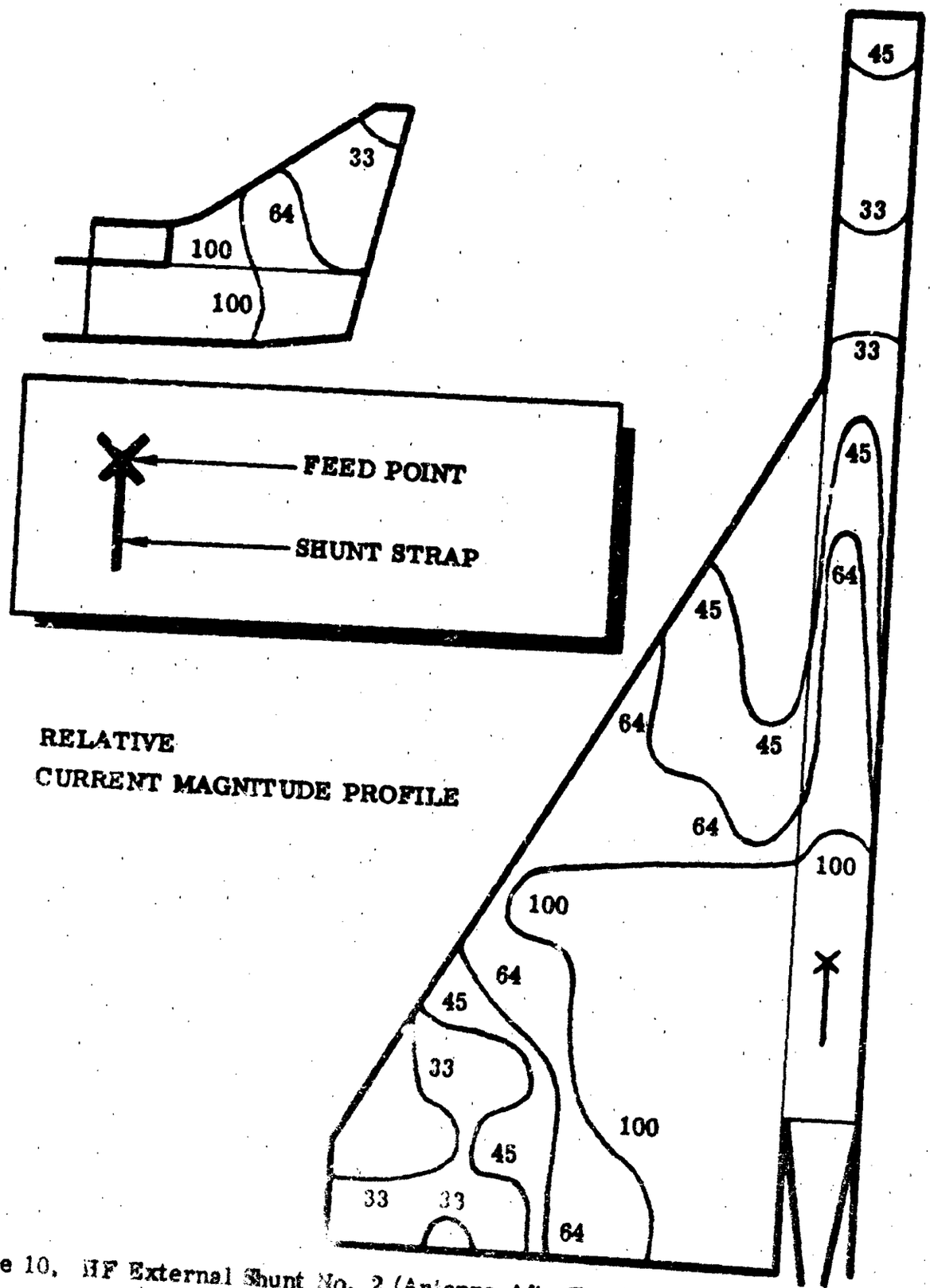

Figure 10. HF External Shunt No. 2 (Antenna Aft, Feed Forward of Strap)

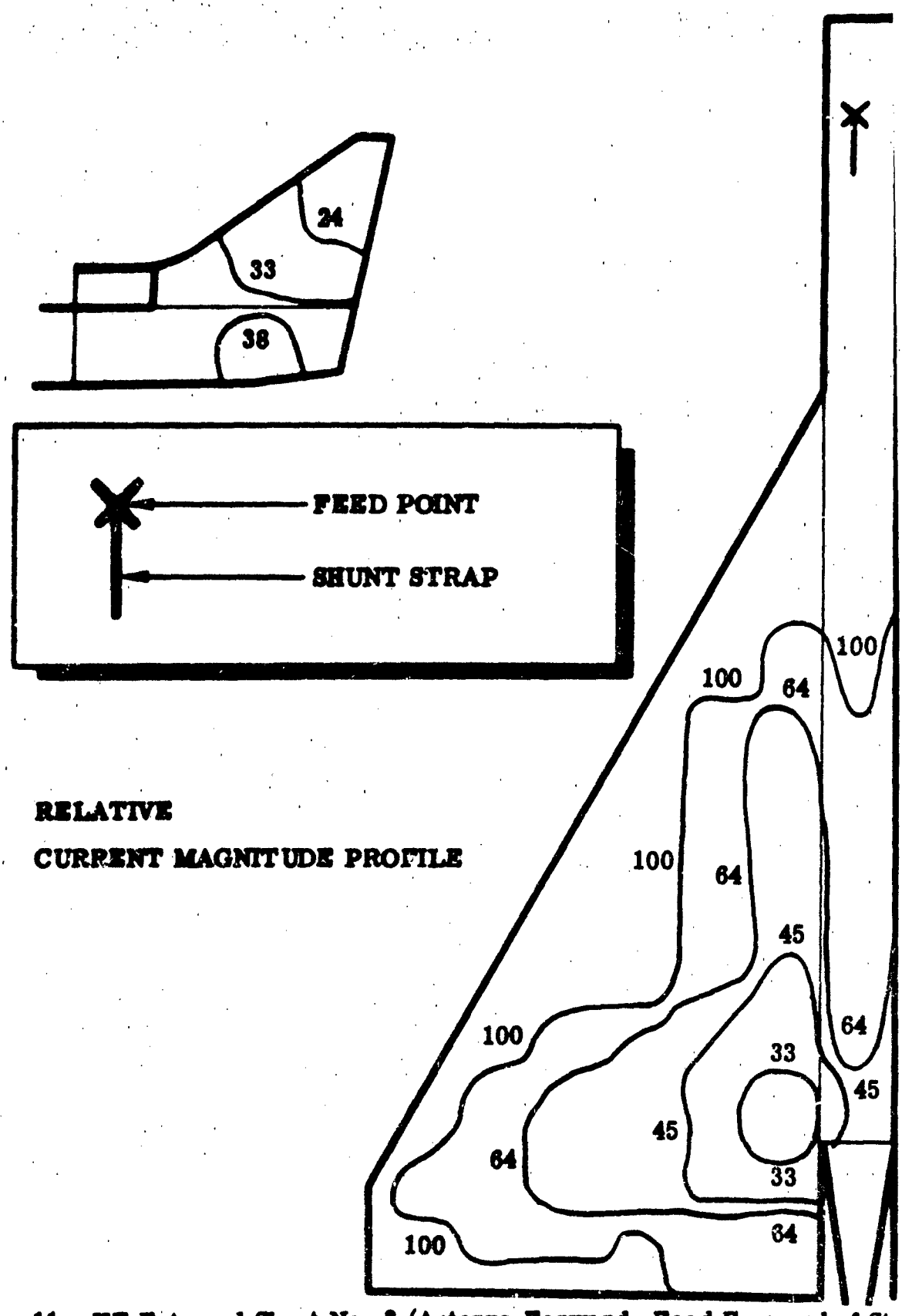

Figure 11. HF External Shunt No. 3 (Antenna Forward, Feed Forward of Str

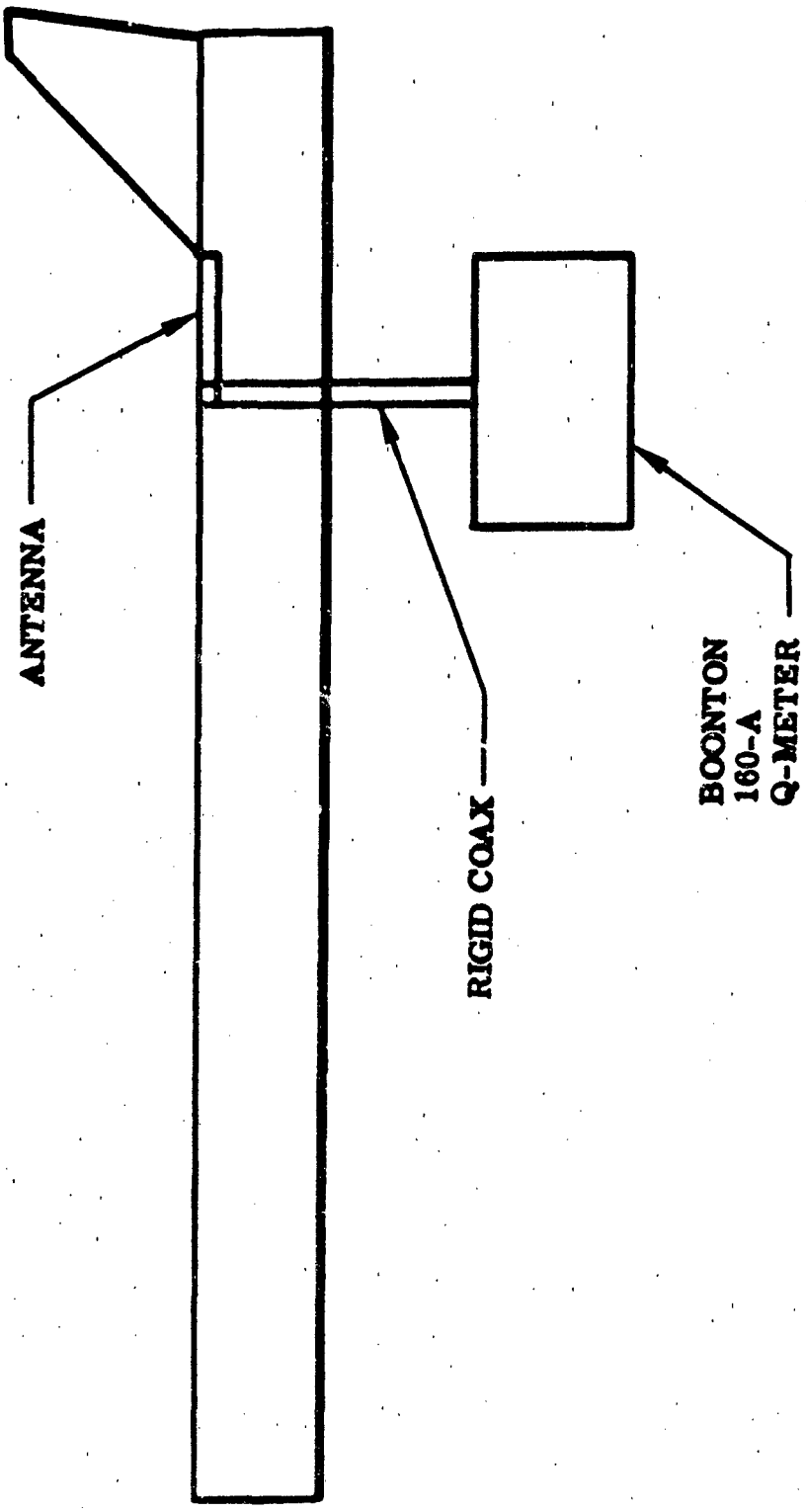

Figure 12. Impendance Measurement Setup

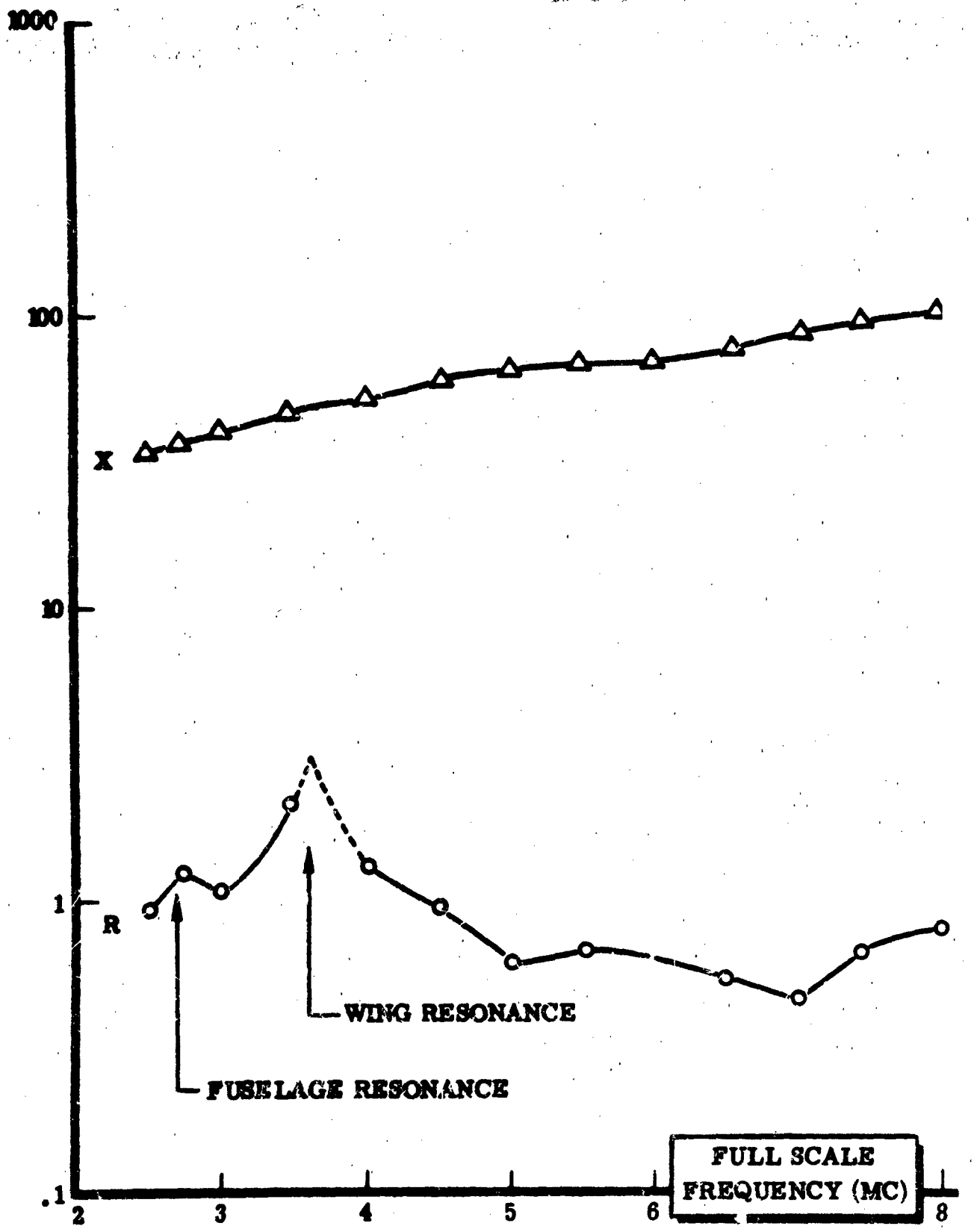

Figure 13. Flush Shunt Antenna Impedance (Aft)

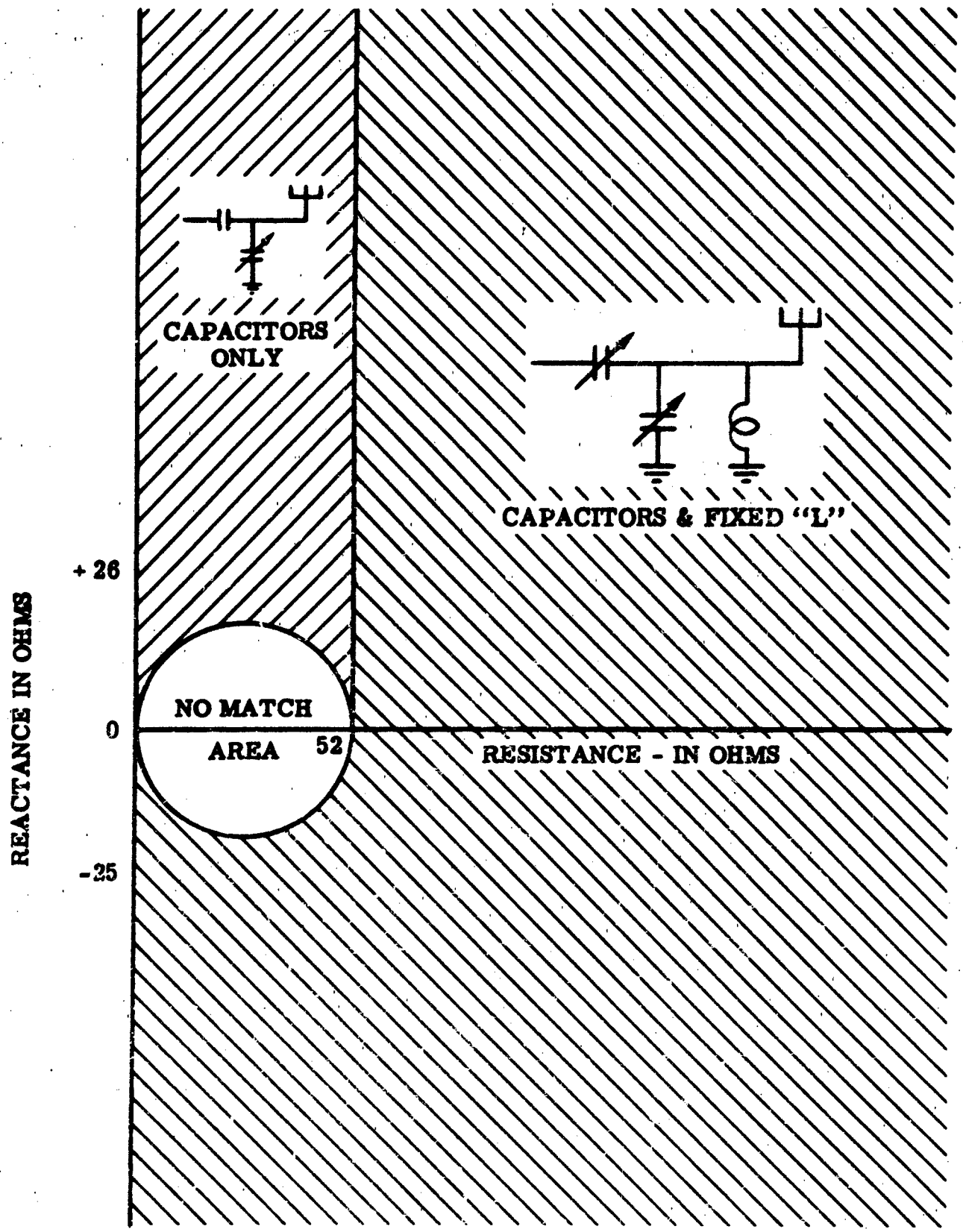

Figure 14. Network Tuning Range (Theoretical)
Characteristic Impendance of Transmission Line = 52 Ω

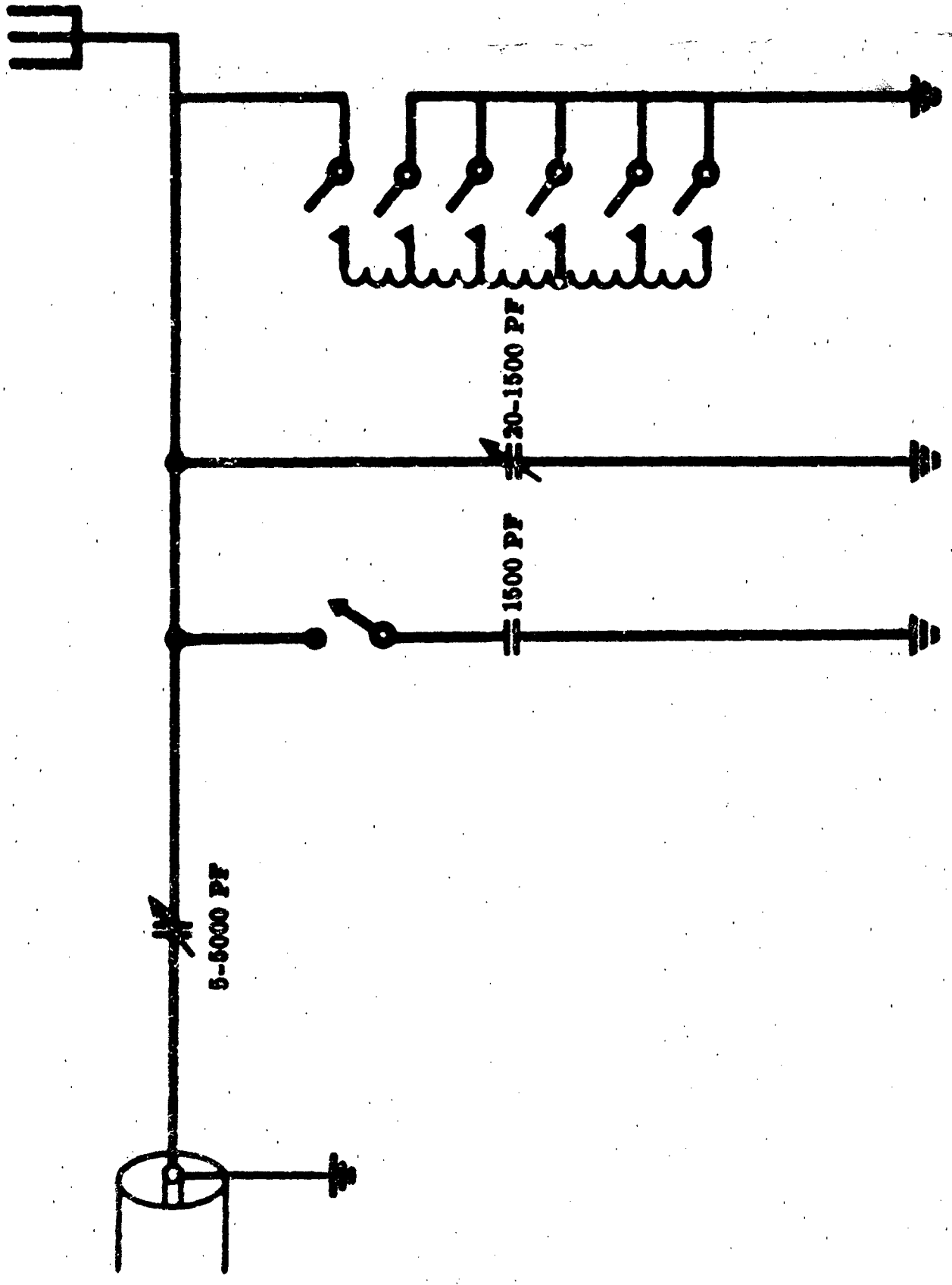

Figure 16. HF Flush Shunt Antenna Coupler Configuration

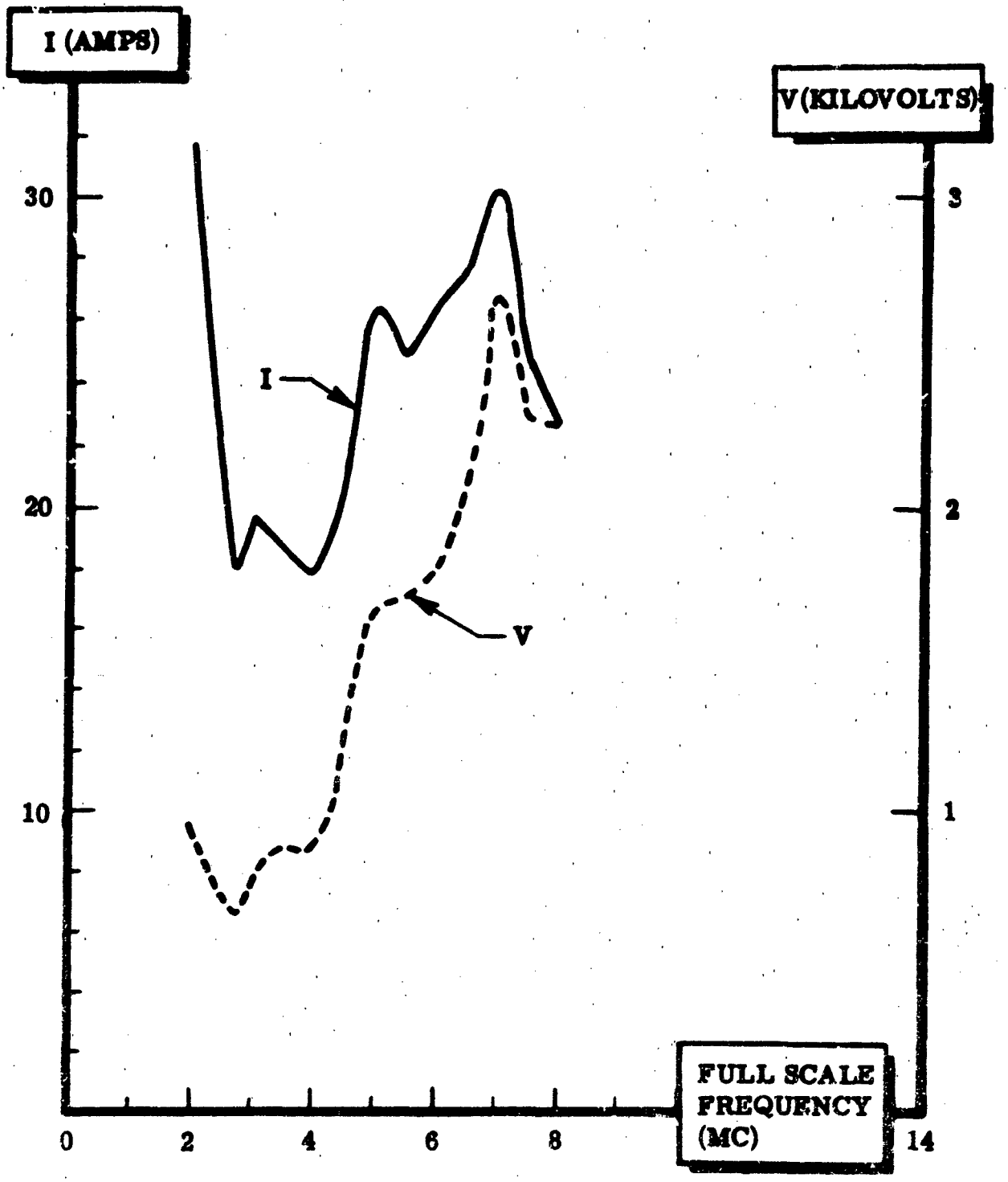

Figure 15. RMS Voltage and Current For Flush Shunt Antenna During Modulation Peaks Assuming 100- watt Carrier or 400-Watt PEP

THE SELF AND MUTUAL ADMITTANCES OF CIRCULAR DIPOLE ARRAYS

Richard B. Mack*
Microwave Physics Laboratory
Air Force Cambridge Research Laboratories
Office of Aerospace Research
Laurence G. Hanscom Field, Bedford, Massachusetts

Summary

Although circular arrays of dipoles have been given considerable attention in the past, the experimental results generally have been confined to dipoles very nearly a half wavelength in length, have considered only pairs of dipoles, or have been obtained from experimental models not reconcilable to the usual theoretical models. The King-Middleton theory which gives the most accurate theoretical results has been too complicated for application to large arrays. The purpose of the present work has been to examine the circuit properties of circular arrays over a fairly wide range of dipole lengths and spacings, to correlate the measured results with corresponding results calculated from the King quasi-zeroth order theory, and to package the latter theory in a form suitable for practical application to the design of circular dipole arrays.

The following discussion and results apply to thin, center-driven dipoles of lengths less than $3\lambda/2$ where λ is the free space wavelength. In a given array, all of the dipoles are assumed to be parallel, identical, non-staggered, and evenly spaced about a circle. Thus, an array of N elements has the dipoles located at the vertices of an N-sided equilateral polygon. The side of this polygon is designated by d/λ, and the radius of the circle passing through the vertices is

$$r = \frac{d/\lambda}{\sin \pi/N} \qquad (1)$$

Circular arrays exhibit some interesting properties which are characteristic of the array as a unit. For example, there are resonant spacings at which the self and mutual conductances are at or near maximum values and at which the self and mutual susceptances are zero or have small values. Such spacings appear to exist for all of the dipole lengths considered, but

* This study was carried out while the author was at Gordon McKay Laboratory, Harvard University, and was supported by Joint Service Contract NoNR 1866(32).

the resonances become less pronounced as the dipole length is increased beyond $\lambda/2$. As the number of array elements is increased, the resonances occur at smaller values of d/λ and become more distinct. For a 2-element array of any dipole length these space resonances are not well defined. For an array of five half-wave dipoles the resonant spacing is $d/\lambda = 0.475$. If the dipole length is $3\lambda/4$, more than five elements are required to produce a well defined space resonance. For a given array, there is only one spacing which produces a space resonance. When the element spacings are near the resonant spacings, the circuit properties are very sensitive to small changes in any of the array parameters. Thus, in arrays with driven elements, these spacings are best avoided. In arrays with parasitic elements, the parasitic elements have maximum excitation near the resonant spacings.

If there is only one driven element in the array, spacings can be found at which the driven element is nearly completely uncoupled from the parasitic elements. As the number of array elements increases, the value of d/λ at which this occurs decreases. For a 5-element array of full-wave dipoles, it occurs at about $d/\lambda = 0.49$.

For dipoles of length $2h$ not greater than λ, there also are spacings at which many of the circuit properties change very slowly as the number of array elements is changed. For example, when $2h = \lambda$, curves of self and mutual conductances vs. d/λ all intersect near $d/\lambda = 0.150$ for a wide range of N and the corresponding susceptance curves are very close from $d/\lambda = 0.150$ to 0.200. Here again the results for $N = 2$ are found to be quite different from those for larger N.

Similar graphs of the admittances indicate that, when d/λ is decreased from about 0.200, the conductances decrease slowly, but the self and some mutual susceptances increase very rapidly. It is in this region that the storage fields become very large with the attendant high Q's and frequency sensitivity.

The results also indicate a two-element array to be a somewhat degenerate example which lacks many characteristics of larger arrays. Thus, the approximation of applying the results from a two-element array to pairs of elements in a larger array cannot produce results which are more than qualitatively correct, and in many cases, even the qualitative behavior will not be correctly described.

The results further show that the mutual admittances are significant in magnitude compared to the self admittance for nearly all useful spacings and dipole sizes. Hence, simply ignoring the mutuals is a very poor approximation.

In the experimental model, antennas were actually monopoles over a 24 x 48 ft. aluminum ground plane. They were formed by extending the slotted center conductor of a coaxial line above the groundplane. Below

the groundplane, the coaxial line served as a regular slotted line with a balanced loop probe to measure the current standing wave. The measurement frequency was about 660 Mcps. This model has received considerable use and quite detailed analysis. It differs from the usual theoretical model primarily in having a generator region which extends over a small but finite distance near the groundplane surface. The extent of this region depends upon the b/a ratio of the coaxial line where b and a are the radii of the outer and inner conductors respectively. Its principal effect is to make measured values of the input susceptance more negative than the theoretical values. The equipment had a b/a of 3.

Measurement procedures for determining the self and mutual admittances of an array are based on the coupled circuit equations. For circular arrays of identical elements, symmetries reduce this set of equations to a single equation which can be written

$$Y_{in} = \frac{I_1(0)}{V_1} = Y_{11} + \frac{V_2}{V_1} Y_{12} + \ldots \frac{V_k}{V_1} Y_{1k} + \ldots \frac{V_N}{V_1} Y_{1N} \quad (2)$$

If Y_{in} is measured for $\frac{N+1}{2}$ (N odd) or $\frac{N}{2} + 1$ (N even) different sets of known voltage ratios and an equation like (2) written for each measurement, the resulting set can always be solved for the self and mutual admittances in terms of the measured input admittances. However, any uncertainty or error in the experimental adjustment of the voltages will be present in the final admittances. Therefore, the voltages should be set with an accuracy that is an order of magnitude better than that desired in the measured admittances. The following sets of voltages can be established with high accuracy and were used in the measurements:

$$V_1 = V_1, \; V_2 = V_3 = \ldots . \; V_N = 0 \qquad Y_{in\,1} = Y_{11} \quad (3)$$

$$V_1 = V_1, \; V_2 = V_3 = V_{k-1} = 0, \; V_k = -V_1, \; V_{k+1} = \ldots \; V_N = 0$$

$$Y_{in\,k} = Y_{11} - Y_{1k} \quad (4)$$

$$Y_{11} = Y_{in\,1} \; ; \quad Y_{1k} = Y_{in\,1} - Y_{in\,k} \quad (5)$$

Driving voltages can be set equal to zero simply by short-circuiting the antenna to the groundplane. The antisymmetric condition can be set by placing an electric field probe at the array center and adjusting the phase and amplitude of one driven element until a deep null is obtained at the probe.

Data was obtained by recording current distributions near the standing wave minima, graphing these to an enlarged scale, and reading 3 db curve widths and minimum shifts from the graph. With these precautions, the results could easily be repeated within ±0.2 millimhos when h/λ was near 0.2500, and within ±0.02 millimhos for other lengths; most of the results were repeatable within much closer limits.

Theoretical results were calculated from the King quasi zeroth order theory. In this theory, current along the k th antenna can be written as

$$\frac{I_k(z)}{V_k} = s_k \sin\beta(h - |z|) + c_k \left[\cos\beta z - \cos\beta h\right], \quad \beta h \neq \pi/2$$

$$= s_k' (1 - \sin\beta |z|) - c_k' \cos\beta z, \quad \beta h = \pi/2$$

$\beta = \frac{2\pi}{\lambda}$, $2h$ = dipole length, z measures position along the antenna.

The coefficients s_k and c_k involve all of the array parameters and can readily be defined through four or five pages of equations. Although the theory does involve some intricate mathematical considerations, it still is sufficiently simple to be practical for applications to even large arrays, and will provide an accurate description of both the radiation patterns and input admittances. For applications to array design, the theory has been packaged as a Fortran program to which the user need only supply the array parameters as input data. In this form the theory can be used without detailed considerations of the underlying mathematics.

When measured and theoretical values of the admittances are compared, very good agreement is found for the self conductance and for the mutual admittances. The theoretical self susceptance has the correct variation with d/λ but differs from the measured values by an amount which is essentially constant for a given h/λ and which is essentially equal to the differences found for a single isolated antenna. These differences are primarily due to the presence of a finite generator region in the experimental model. If the difference between experimental and theoretical input susceptances are determined for an isolated antenna of the desired length and thickness, this may be applied as a correction for the same antenna when used in an array to produce very good agreement between theoretical and experimental values of either self susceptances or input susceptances.

Additional details, graphs, and tables of the results are given in the references.

References

1. King, R.W.P., "Linear Arrays: Currents, Impedances, and Fields, I", PGAP, Special Supplement, AP-7, S4A1, December, 1959.

2. King, R.W.P., "The End Correction for a Coaxial Line When Driving an Antenna Over a Ground Screen", PGAP, AP-3, p. 66, April, 1955.

3. Mack, R.B., "A Study of Circular Arrays. 1. Experimental Equipment", TR No. 381, The Cruft Laboratory, Harvard University, Cambridge, Mass. May, 1963. Contract Nonr-1866(32).

4. Mack, R.B., "A Study of Circular Arrays. 2. Self and Mutual Admittances", TR No. 382, The Cruft Laboratory, Harvard University, Cambridge, Mass. May, 1963. Contract Nonr-1866(32).

5. Mack, R.B., "A Study of Circular Arrays. 4. Tables of Quasi-Zeroth Order $\psi_{dR}^{m}(h)$, $T^{m}(h)$, $T'^{m}(\lambda/4)$, Admittances and Quasi-First-Order Susceptances", TR No. 384, The Cruft Laboratory, Harvard University, Cambridge, Mass. May, 1963. Contract Nonr-1866(32).

6. Mack, R.B. and Mack, E.W., "A study of Circular Arrays. 6. Plan for Practical Application to Arrays of Twenty or Fewer Elements", TR No. 386, The Cruft Laboratory, Harvard University, Cambridge, Mass. May 1963. Contract Nonr-1866(32).

NEAR-FIELD MEASUREMENTS ON THE PLANAR FOUR-ARM LOG-SPIRAL ANTENNA

Preston L. Ransom

and

John D. Dyson

University of Illinois

Urbana, Illinois

Introduction

The multi-mode logarithmic spiral antennas radiate far-fields with amplitude and phase characteristics that make this class of antennas of use in homing, direction-finding, and related systems.[1] The greatest possible utilization of these antennas, however, requires a detailed knowledge of their basic characteristics. To provide this knowledge on the four-arm planar antenna, an investigation of the near-field amplitudes was undertaken.

This paper, an interim report, gives information on the position and extent of the active regions for the three possible modes of excitation and the relationship between the characteristics of these regions and the far-field radiation characteristics of the antenna. This information, which was obtained for a representative range of parameters, over a four to one range of frequencies, provides a conservative definition of the usable modal bandwidth of the antenna.

The Antenna

A sketch of the four-arm planar logarithmic spiral antenna is shown in Figure 1, together with the defining parameters. The radius of the truncation of the arms at the feed region is denoted by ρ_o, the maximum radius of the antenna by ρ_m, the angular width of the arms by δ, and the spiral angle or angle of wrap by the symbol α. Three antennas, with spiral angles of 75, 80 and 85°, were used in this investigation. All antennas were self-complementary (i.e., $\delta = 45^\circ$) and had $\rho_o = 0.8$ cm, $\rho_m = 20$ cm. The planar antennas investigated are formally labelled in the figures by the notation 4p-α -δ -2 ρ_m - 2 ρ_o where 4p denotes the "four-arm planar" antenna and ρ_m and ρ_o are in centimeters. However, since the spiral angle, α, is the only varying parameter, the antennas may be referred to as the "75, 80, or 85° spiraled antenna."

The antennas were constructed by photographically reducing a precision drawing to the desired physical size. The negative, so obtained, was used to

Presented at 14th Annual USAF Antenna Res. and Dev. Conference, Oct. 1964

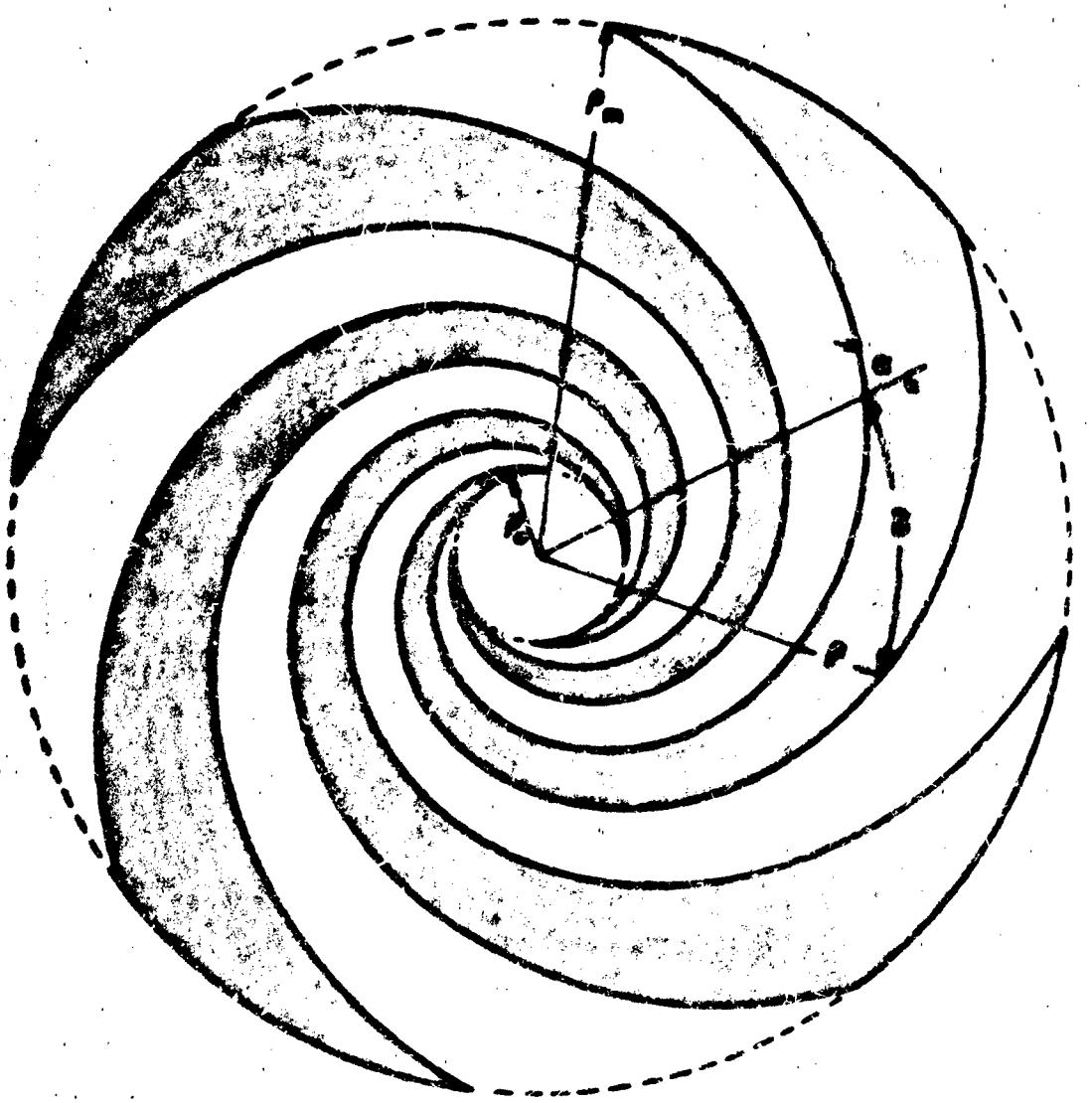

Figure 1. Sketch of Four-Arm Planar Logarithmic Spiral Antenna and Defining Parameters.

expose to ultra-violet light a chemically treated sheet of copper-clad, fiberglass impregnated teflon. The undesired copper was then etched away, leaving the finished antenna. Photographs of the 75, 80, and 85° spiraled antennas are shown in Figure 2.

The Modal Excitation

The theory of excitation of multi-mode log-spiral antennas (both planar and conical) has been presented by Dyson and Mayes.[2] It provides three possible modes of excitation for antennas with four-fold rotational symmetry about the polar or antenna axis. Namely,

$$A_1 = (1, j, -1, -j)$$
$$A_2 = (1, -1, 1, -1)$$
$$A_3 = (1, -j, -1, j),$$

where $A_n = (I_1, I_2, I_3, I_4)$ is the current vector notation for the excitation at the four input terminals, and the input terminals are numbered in the clockwise direction around the inner truncation (radius = ρ_o) of the antenna.

In keeping with the IRE standard, the polarization sense of the log-spiral antenna may be determined from the hand used when pointing the fingers in the direction of the spiraled arm currents and the thumb in the direction of the radiated fields. Since the currents are assumed to travel away from the input terminals, right-hand circular polarization corresponds to phase delay in the direction of increasing ϕ in the positive half-space; left-hand circular polarization corresponds to phase advance in the direction of increasing ϕ. Consequently, spiral antennas wound in the right-hand sense (see 85° spiraled antenna in Figure 2) will produce primarily fields with phase variation of the form $e^{-jm\phi}$ and those wound in the left-hand sense (see 75° and 80° spiraled antennas in Figure 2), $e^{+jm\phi}$. Notice that in all cases, $e^{\pm jm\psi}$, m must be an integer for the field to be single-valued.

Consider the excitation (1, j, -1, -j). This produces a field whose azimuthal variation is such that a rotation of π 2 radians about the antenna in the direction of increasing ϕ is accompanied by:

(a) a phase delay of $\pi/2$ radians

(b) a phase advance of 3 $\pi/2$ radians

Case (a) requires a field with azimuthal variation of the form $e^{-j\phi}$, where m = 1. But right-hand wound spiral antennas produce such fields, so this excitation is said to yield mode 1 for the right-hand wound, four-arm log-spiral antenna.

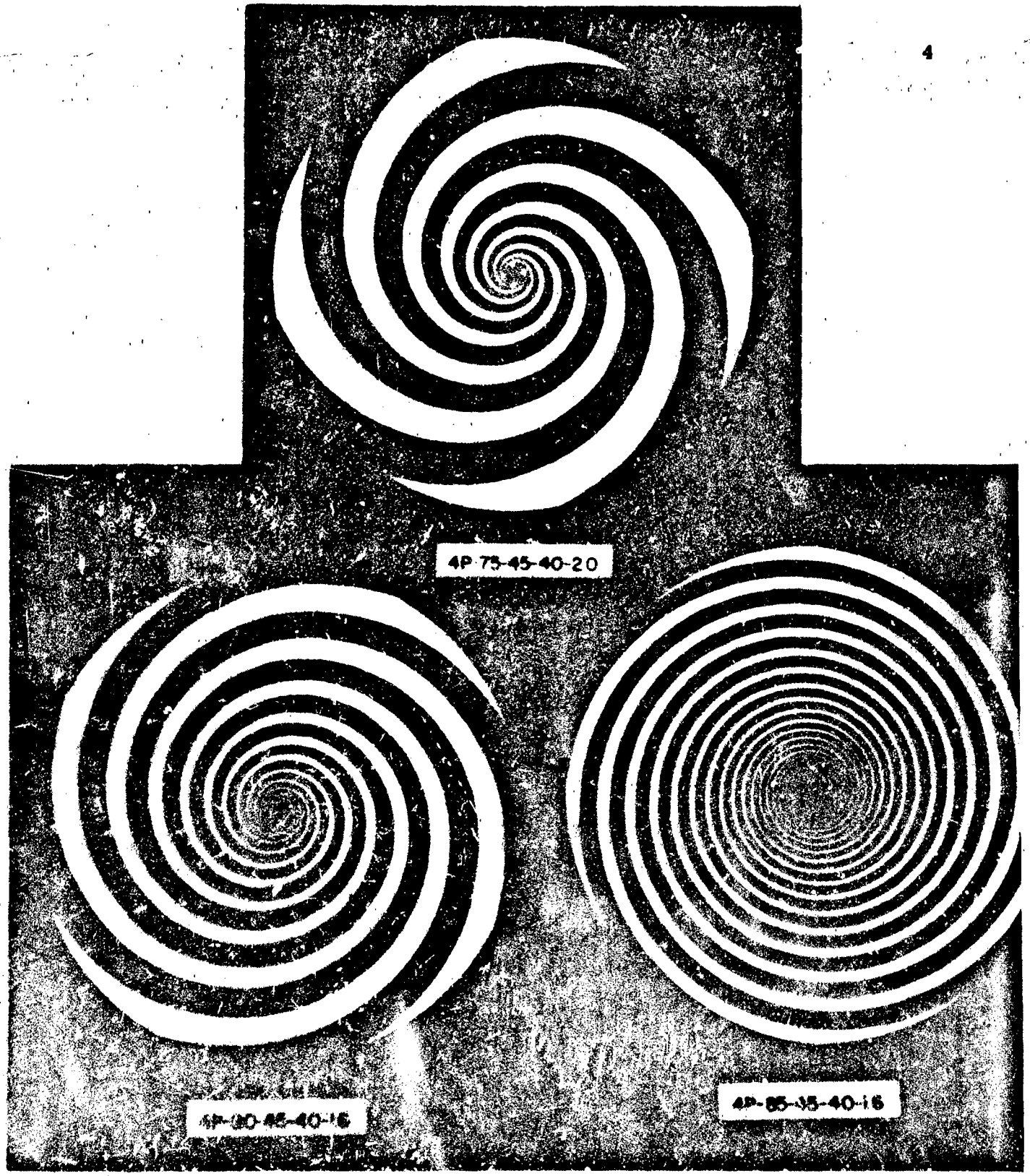

Figure 2. Photographs of Antennas used in Experimental Program.

Case (b) requires a field with azimuthal variation of the form $e^{+j3\phi}$, where m = 3. Since left-hand wound spiral antennas produce such fields, this excitation is said to yield mode 3 for the left-hand wound, four-arm log-spiral antenna.

The modes excited by the remaining two excitations are identified by similar analysis. The results are listed below and depicted in Figure 3.

Relation Between Sense of Wrap and Modal Excitation

L-H Wound	Excitation	R-H Wound
m = 3	(1, j, -1, -j)	m = 1
m = 2	(1, -1, 1, -1)	m = 2
m = 1	(1, -j, -1, j)	m = 3

It has been pointed out that for $m \neq 1$ the far-fields always have a null along the polar or antenna axis.[2, 3]. Hence modes 2 and 3 are characterized by a conical beam, while mode 1 exhibits a broad lobe perpendicular to the plane of the log-spiral antenna as shown in Figure 4.

To obtain this excitation, a feed system employing one 90° hybrid and three 180° hybrids may be used with interconnections as shown in Figure 5.

The Near-Field Amplitude

The amplitude of the field along the antennas was measured by moving a small shielded loop probe along a path spaced .03λ from the plane of the antenna and parallel to an antenna diameter. A block diagram of the experimental measuring system is shown in Figure 6.

Figure 7 displays the near-field structure corresponding to three excitations for the 80° spiraled antenna at 1300 Mc. On all the near-field plots, the vertical axis is the relative magnitude of the probed field in decibels and the horizontal axis is the distance from the antenna center, ρ, and the circumference at ρ, C.

As observed for the conical log-spiral antenna,[4] there is a region of closely bound waves near the origin. With increasing radius, ρ, these waves become more loosely bound, and more energy is coupled to the probe until the waves become so loosely bound that this energy is rapidly lost through radiation. In this latter region the measured amplitude of the near field decays to a negligible value. It is apparent that the region of rapid

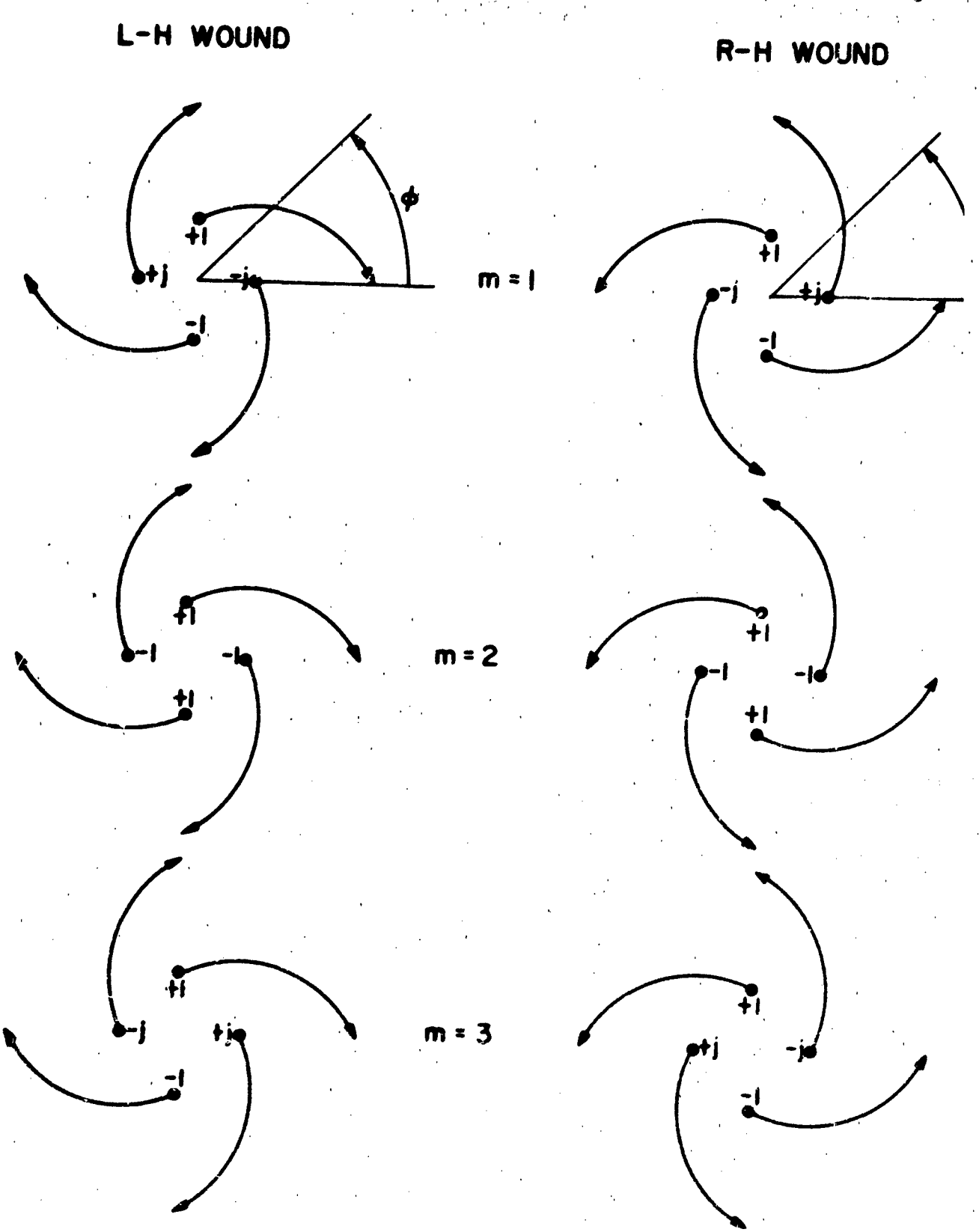

Figure 3. Relation Between Sense of Wrap and Modal Excitation.

E_ϕ - - - - -

E_θ ——————

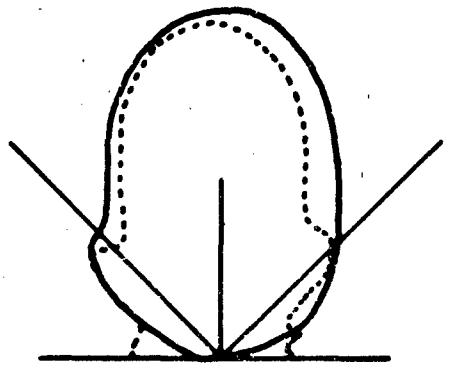

MODE 1

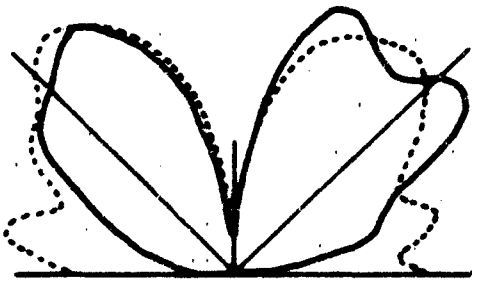

MODE 2

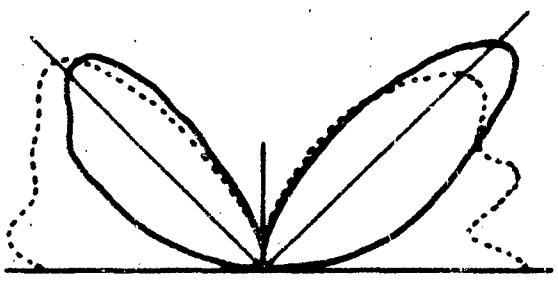

MODE 3

Figure 4. Typical Radiation Patterns with Modal Excitation.

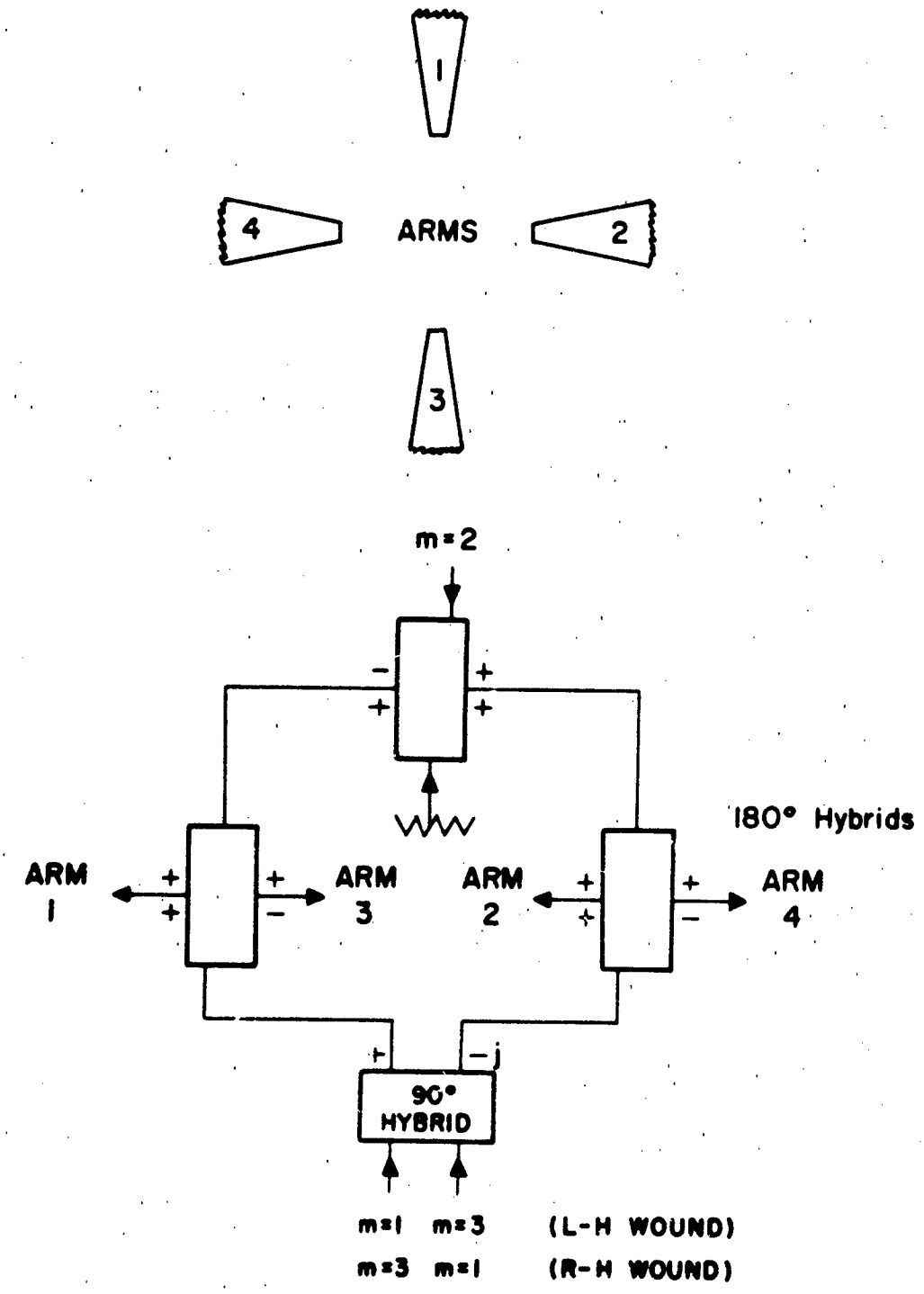

Figure 5. Hybrid Feed System for Four-Arm Log-Spiral Antennas.

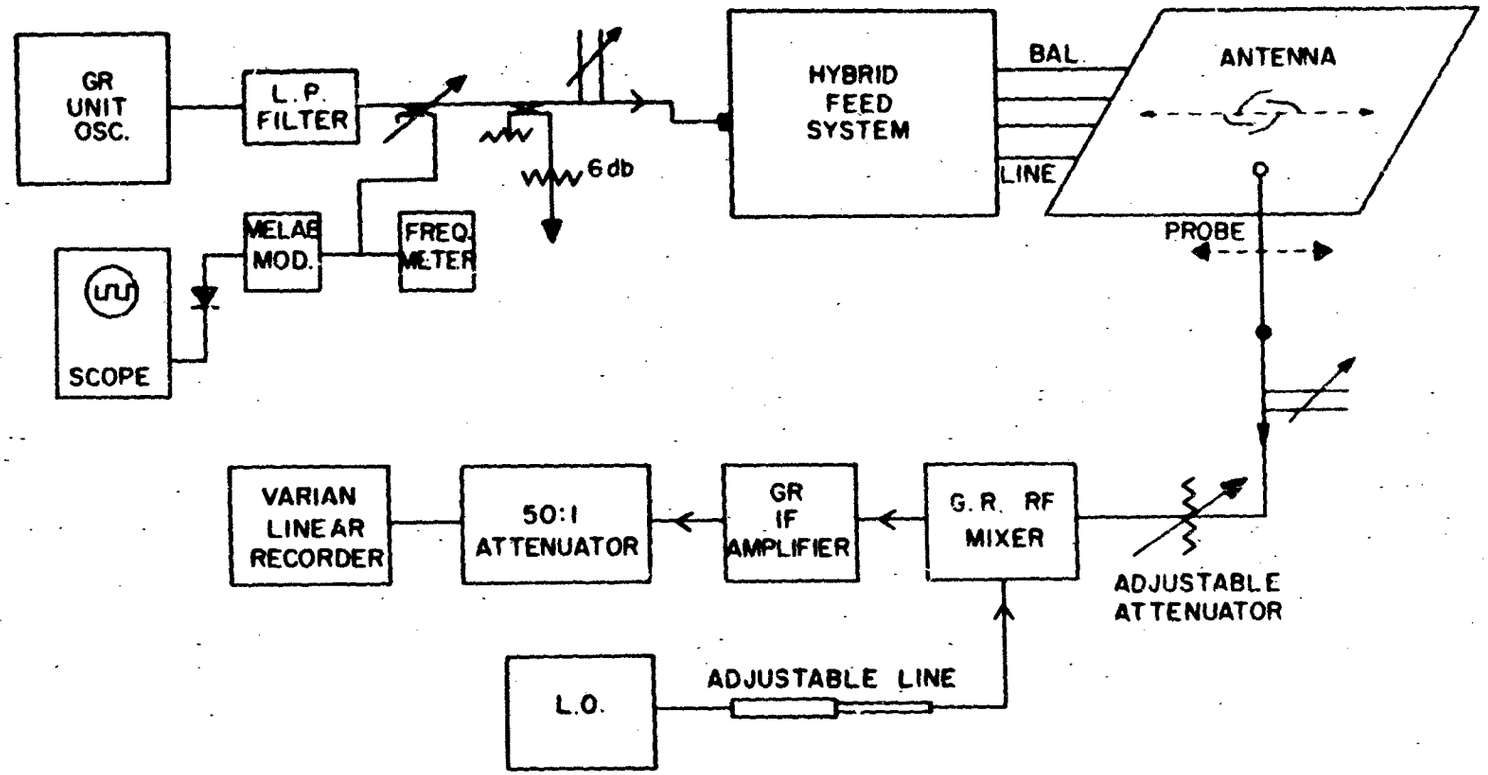

Figure 6. Block Diagram of Near Field Amplitude Measuring System.

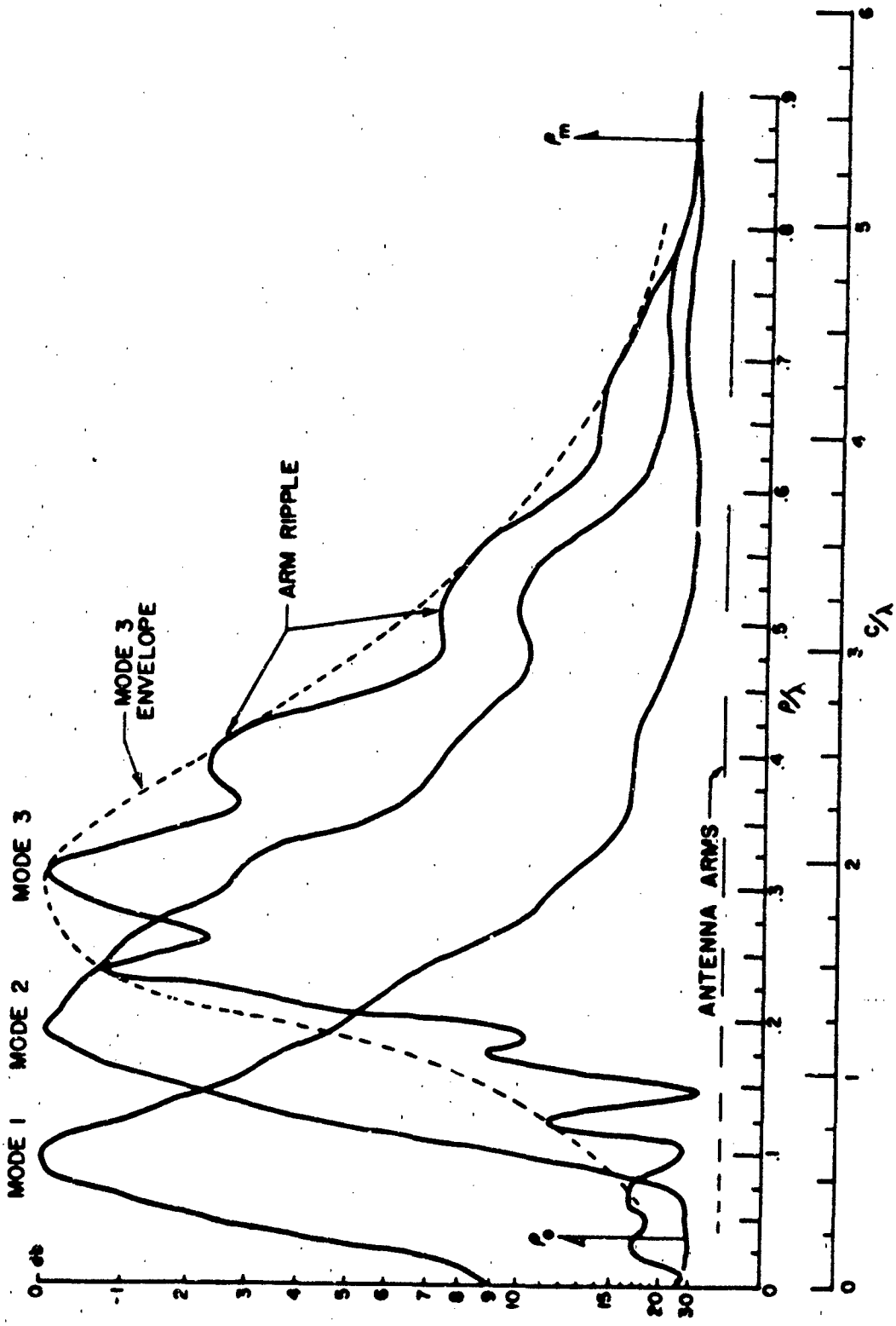

Figure 7. Near-Field Amplitude of 4P-80-45-40-1.6 at 1300 Mc for each Mode of Excitation.

decay occurs at an increasing value of ρ as the order of mode is increased.

The probe-antenna spacing of $.03\lambda$ is arbitrary. Obviously, the probe must be in the near-field region. However, the closer it is to the antenna, the more the presence of the probe will disturb the current distribution on the arms. One effect of moving the probe closer to the antenna is to increase the "arm-ripple" in the measured amplitudes of the fields. This is already quite evident in the mode 3 plot. Conversely, the arm-ripple effect is less apparent with increased spacing.

As the probe path line is rotated around the antenna through an angle of 22.5° the position of the arms intersected by this line undergoes a translation of one-half period. The "arm-ripple" similarly shifts along the horizontal axis. The envelope of these ripples remains constant and hence all data used to define the characteristics of the active region were obtained from such envelopes.

The well-known scaling property of the log-spiral antennas is demonstrated by the measured fields of mode 2 of the 80° spiraled antenna shown in Figure 8. Figure 8a, with a horizontal axis with length units, illustrates the movement of the near-field structure toward the origin of the antenna, i.e., toward ρ_o as the frequency of operation increases from 1000 to 1800 Mc. Figure 8b shows the constancy of the same fields when plotted on a normalized ρ/λ, scale.

The observations of the plot of the mode 2 near-fields, representative of all the mode plots of the 80° spiraled antenna, leads to the conclusion that the modal active regions, in wavelengths, are essentially constant in position and extent for a range of frequencies such that the inner and outer truncation of the arms does not cause distortion of these fields.

To determine the position of the outer edge of the active region, the modal near field plots and corresponding radiation patterns were observed as the outer diameter, ρ_m, of the 80° spiraled antenna was incrementally reduced. When a definite change in the radiation patterns was observed, the reduced radius was taken as the outer radius of the active region for the mode of excitation. This radius in wavelengths is denoted as ρ_+^m, where the + sign signifies the outer extent of the active region and the letter, m, will have values 1, 2, or 3 for the mode. The superscript m should not be confused with the subscript m used to denote the outer radius of the antenna structure, ρ_m, where m signifies "maximum". The increment of radius reduction was $.06\lambda$ at 1000 Mc for mode 1

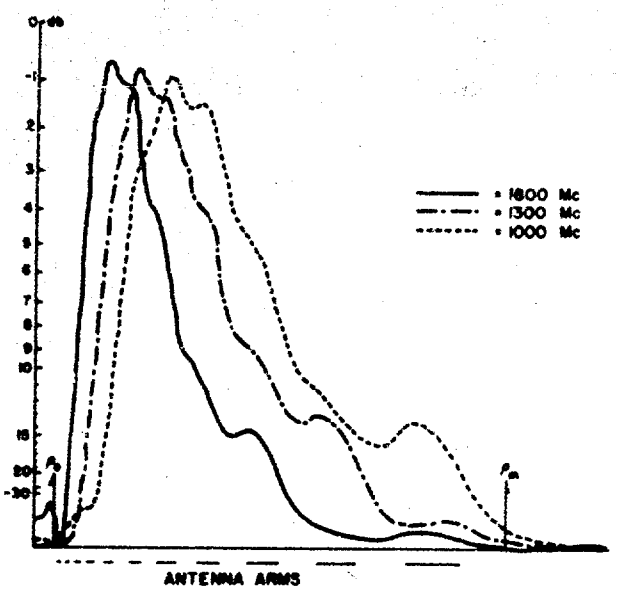

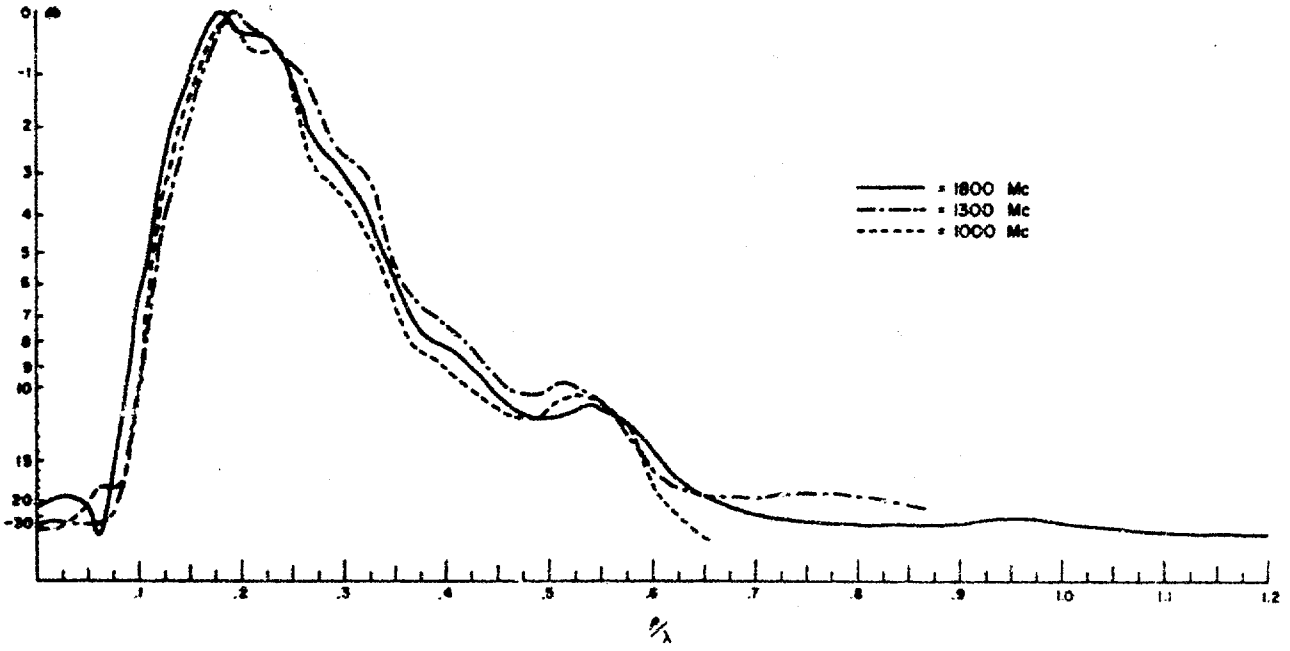

Figure 8. Near-Field Amplitude of 4P-80-45-40-1.6 with Mode 2 Excitation as a Function of Frequency

and 0.1^{λ} at 1600 Mc for modes 2 and 3.

For mode 1, a definite change in the radiation patterns appeared when the reduced radius was at the point of 14.5 db down from peak on the near-field plot of the unreduced antenna (see Figure 9a). For modes 2 and 3 the effect of reduction was obvious at 15 db down as illustrated in Figure 9b and c. So the modal radii at 15 db were selected as the outer extent of the active region. These radii are tabulated below.

Outer Radius of Active Region of 4P-80-45-40-1.6

Mode	DB	Radius /λ
1	15	0.35
2	15	0.67
3	15	0.83

It should be noted that the values listed above will be conservative in design use, since they indicate the point at which a change in radiated fields become apparent and not the point at which radiation patterns deteriorate to the point of becoming unusable. This fact is shown in Figure 9.

To determine the inner extent of the active retion in wavelengths, ρ_1^m, the inner radius of the antenna, ρ_o, was incrementally enlarged. This technique did not yield desired results since, as ρ_o increased, the four-balanced and phased excitation lines were spread apart and, so separated, radiated a circularly polarized beam, much as a turnstile antenna. To date, this experimental problem has not been solved on the four-arm log-spiral antenna. However, two facts justify selecting the radius at a point 6 db below the maximum, on the increasing slope of the near fields, as the inner extent of the active region.

First, there is remarkable consistency in the results obtained, thus far, on this four-arm planar antenna and the results obtained on the two-arm antennas, both conical and planar. Under the same experimental conditions, the outer extent of the active region was found to be at 15 db on both the two-arm conical and planar antennas. The inner extent of the active region occurred at approximately 3 db for the two-arm conical with small included cone angles (15°) and decreased with larger included cone angles (45°). Correspondingly, the inner edge of the active region on the two-arm planar was determined to be at a radius such that the amplitude of the fields as measured was approximately 6 db. below the maximum recorded value.

Secondly, on the four-arm antenna being considered, the amplitude of the fields coupled to the probe increases rapidly with distance from the

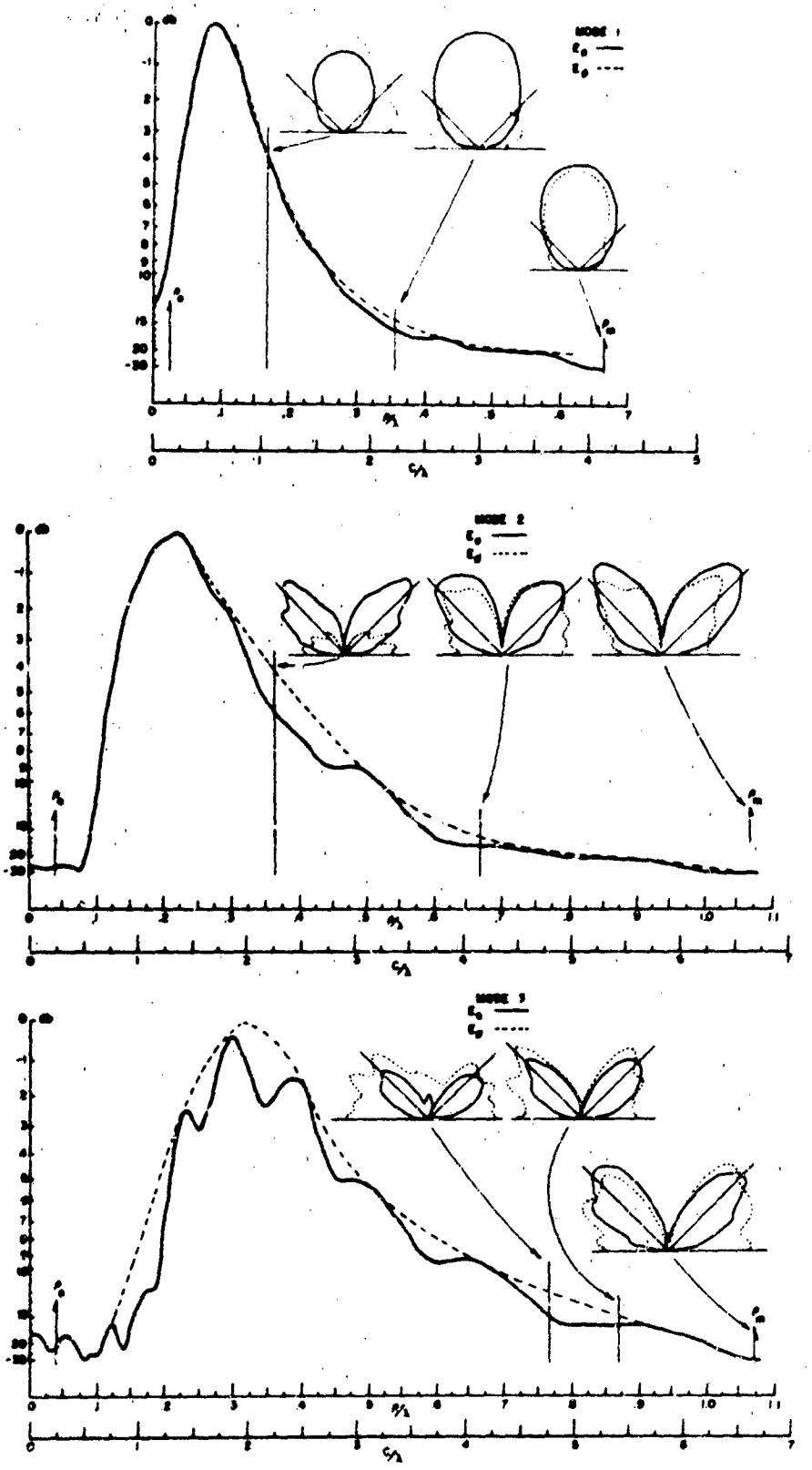

Figure 9. Relation of Far-Fields of Reduced Antenna to Near-Field of Unreduced Antenna for Each Mode of Excitation.

origin of the antenna causing a very small change between radii at 10 db and radii at 3 db below the following maximum recorded value. This fact is evidenced on all near-field plots. These variations in radii are listed below.

Radii in Wavelengths to DB Points on Increasing Slope of Near-Fields of 4P-80-45-40-1.6

	Modes		
DB	1	2	3
3	.045	.134	.21
6	.03	.12	.17
10	.02	.11	.15
$\Delta\rho$ =	.025,	.024,	.06

Hence, to define the inner extent of the active region, those modal radii at 6 db. down from peak of the near fields were selected.

Inner Radius of Active Region - on 4P-80-45-40-1.6

Modes	DB	Radius/λ
1	6	.03
2	6	.12
3	6	.17

Knowledge of the extent and position of the modal active region allows calculation of the usable or operating bandwidth, B of the antenna. At the high frequency limit of B, f_H,

$$f_H = c/\lambda_H, \text{ and } \rho_-^m = \rho_o/\lambda_H \quad (1)$$

and at the low frequency limit of B, f_L,

$$f_L = c/\lambda_L, \text{ and } \rho_+^m = \rho_m/\lambda_L \quad (2)$$

where c is the velocity of propagation in free space. Thus the operating bandwidth, B, is given by,

$$B = \frac{f_H}{f_L} = \frac{\rho_m}{\rho_o} \quad \frac{\rho_-^m}{\rho_+^m} \tag{3}$$

In keeping with Carrel's[4] definition we shall denote the structure bandwidth as B_S and the modal active region bandwidth as B_{ar}^m and interpret them as follows:

$$B_s = \rho_m/\rho_o \ , \ B_{ar}^m = \rho_+^m/\rho_-^m \tag{4}$$

$$B = B_s/B_{ar}^m \tag{5}$$

Near field measurements, at the 0.03λ probe to antenna spacing, were taken on the 75 and 85° spiraled antennas at 1000 Mc for mode 1 and 1600 Mc for modes 2 and 3. The 6 db and 15 db criteria for ρ_-^m, ρ_+^m was applied, and the results including the calculated values for the modal active regions and operating bandwidth are tabulated below.

Calculated Bandwidths of the 75, 80, 85° Spiraled Antennas

(B_s = 25)

α	Mode	ρ_-^n	ρ_+^m	B_{ar}^m	B
75°	1	----	0.405	----	----
	2	0.100	0.730	7.30	3.40
	3	0.163	0.950	5.83	4.28
80°	1	0.030	0.350	11.65	2.14
	2	0.120	0.670	5.56	4.50
	3	0.170	0.830	4.88	5.12
85°	1	0.052	0.410	7.90	3.16
	2	0.168	0.670	4.05	6.17
	3	0.260	0.895	3.44	7.27

Curves that indicate the trend in the operating bandwidth as a function of the spiral angle are shown in Figure 10.

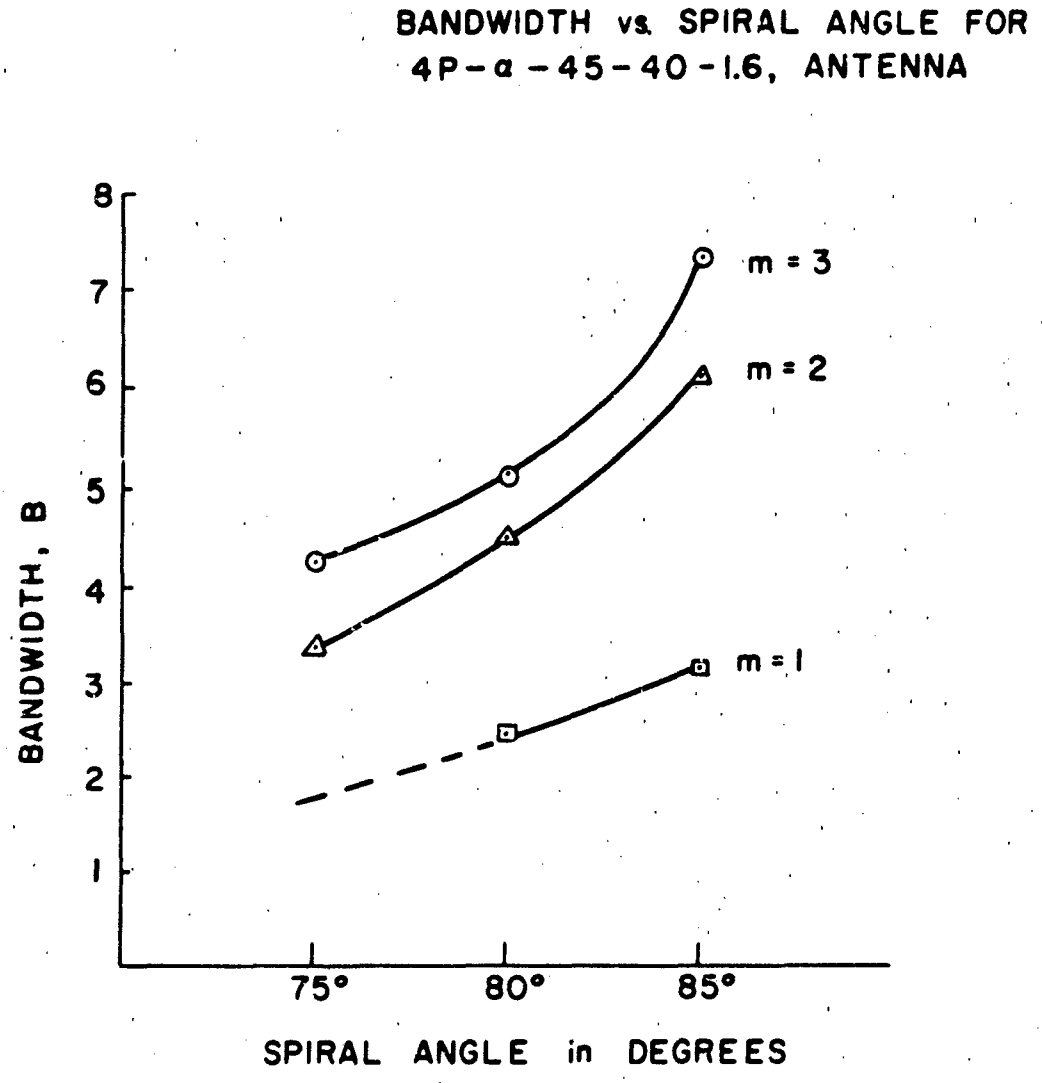

Figure 10. Trend in bandwidth of Antenna as a function the spiral Angle α.

The circumference of the antenna at the extremites of the modal active region, as defined here, is shown in Figure 11. It is interesting to note that the active region increases in width as the spiral angle, α, decreases This is in further agreement with the results found on the two-arm conical log-spiral antenna.[4]

Conclusion

The near-field structure of the four-arm log-spiral antenna has been experimentally investigated as a function of frequency and spiral angle. An active region, based on radiation characteristics, has been defined and used to interpret the operating bandwidth of these antennas.

Acknowledgment

It is a pleasure to acknowledge the assistance of Forrest Green and Richard Slaughter in the construction and testing program. This work was supported by the Air Force Avionics Laboratory under Contract AF33(657)10474.

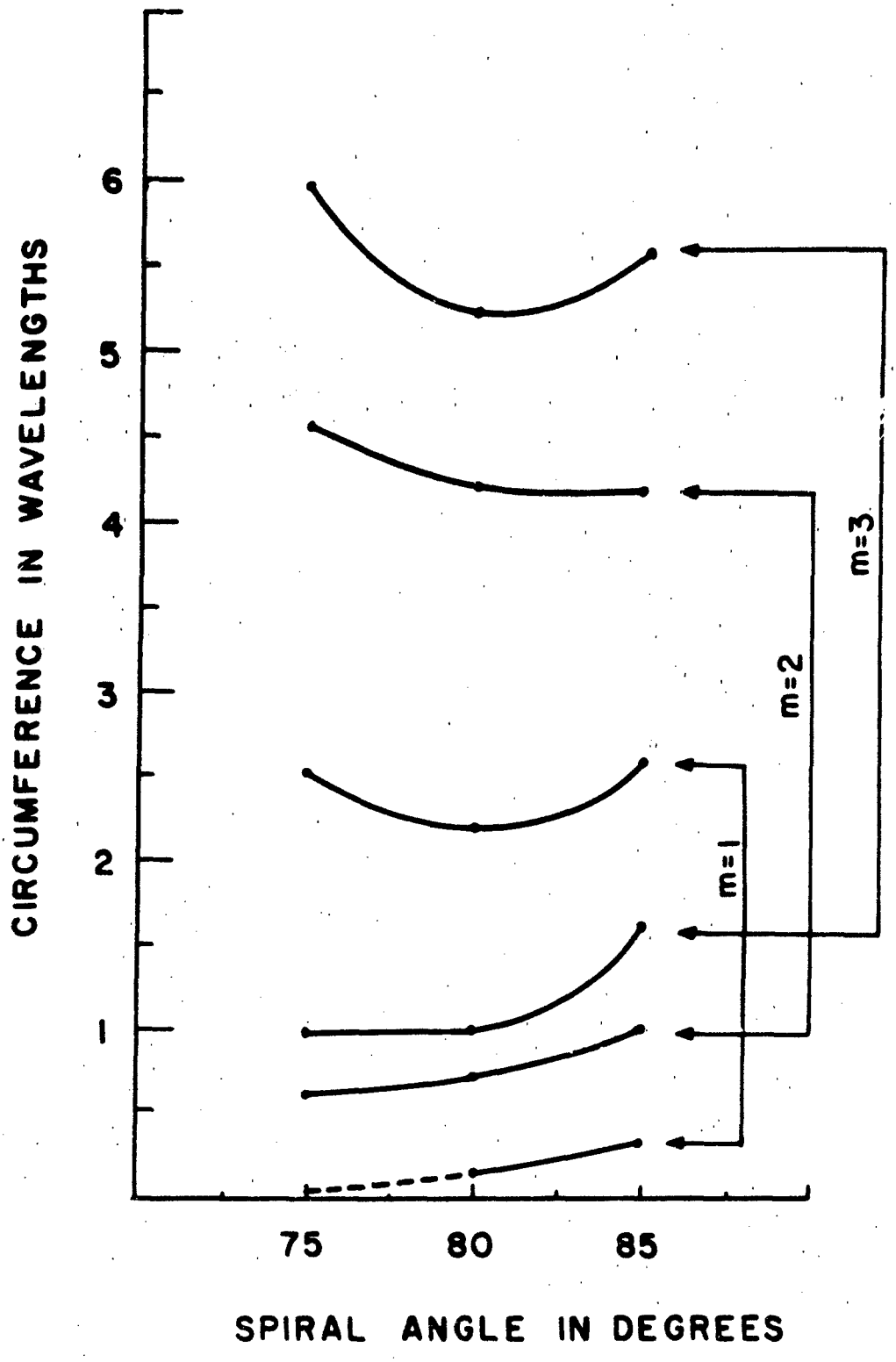

Figure 11. Circumference at Extremities of the Modal Active Regions.

REFERENCES

1. Dyson, J. D., "Multi-Mode Logarithmic Spiral Antennas - - Possible Applications," Proceedings of the N. E. C., October 1961, pp. 206-213.

2. Dyson, J. D. and Mayes, P. E., "New Circularly-Polarized Frequency-Independent Antennas With Conical Beam or Omnidirectional Patterns," IRE Transactions on Antennas and Propagation, Vol. AP-9, No. 4, July 1961, pp. 334-342.

3. Cheo, R. R. S., Rumsey, V. H., and Welch, W. J., "A Solution to the Frequency-Independent Antenna Problem," Trans. IRE., Vol. AP-9, Nov. 1961, pp. 527-534.

4. Dyson, J. D., "The Design of Conical Log-Spiral Antenna," 1964 IEEE Convention Record, Part 6, pp. 259-273.

5. Carrel, R. L., "Analysis & Design of Log-Periodic Dipole Antennas," University of Illinois Antenna Laboratory, Technical Report No. 52, October 1961.

ADVANCED ANTENNAS FOR SPACE APPLICATION

A. M. Berkman and W. M. Young

Lockheed Missiles and Space Company
Sunnyvale, California

The engineer faces two basic challenges in design of satellite antennas. These are the interrelated problems of mechanical and electrical feasibility and their compatibility with the space vehicle. This paper discusses several well known antenna designs and the techniques developed for their application to space vehicles.

The basic mechanical problem in the design of a satellite antenna is to achieve a package that is at once small and light enough to be launched aboard a space vehicle and which, once in space, will have sufficient structural integrity and accuracy to withstand the environment and to perform its intended mission.

In the stowed condition the package must be able to withstand the environment of the space vehicle during pre-launch, launch and exit. Some of the conditions encountered during this phase are extremes in vibration, shock, acceleration, temperature and rapid depressurization. Upon deployment the antenna must function in the vacuum of space, as well as survive the effects of radiation and thermal extremes.

The electrical requirements of pattern, gain, impedance, frequency bandwidth, etc., determine the size, configuration and in some cases, the type of antenna that must be constructed.

If, for example, the satellite antenna must produce a high gain pencil beam, the engineer has a number of choices of the type of antenna to obtain this pattern, but the choice must be tempered with the mechanical considerations. Is the space available? Will the antenna withstand the environment, and so forth.

A number of antennas were built at Lockheed to meet these specific problems. A short description of various antennas and the outstanding mechanical and electrical characteristics of each will follow.

I. Antenna Farm

The following is a brief description of an antenna system known as the "Antenna Farm". The system consists of a grouping of two equiangular spiral antennas and a flush mounted discone. The antennas are located on a swing out circumferential segment of the vehicle.

The electrical requirements specified a circularly polarized group of antennas operating from 150 to 2500 megacycles with a VSWR less than 3:1 over the band. The pattern requirement called for a single lobe beam with the coverage at 72° from the axis in a figure of revolution to be no less than -12 db below isotropic.

Also required was a linearly polarized antenna to operate from 2700 to 2800 megacycles with a VSWR below 3:1 over the band. The pattern was to possess a null on axis with a main lobe describing a figure of revolution at approximately 60° from the axis.

A study of the available space on the vehicle indicated that flush mounted antennas located on the side of the vehicle would be the most desirable type. Almost without exception the electrical requirement called for the use of a frequency independent antenna. The flush mounting desirability suggested the use of the planar equiangular spiral. While it was recognized that the planar equiangular spiral possesses bidirectional radiation characteristics its use was justified on the following bases: Space available, simplicity of construction and its ability to meet the gain, VSWR and broad band coverage requirement.

The 2700 to 2800 megacycle pattern coverage and gain requirement suggested the use of a flush mounted discone.

Space allocation for this antenna was the aft area just inside the clearance circle for the vehicle booster shroud. The antenna structure formed a section of a 30" radius cylinder, to fit this space in the stowed condition. For operation the antenna is rotated 90 degrees about one hinged side, the operating force being provided by a spring loaded, hydraulically damped actuator. Release is provided by a squib actuated pin pulling device. This is illustrated in Figure 1.

II. Vertical Multirange System

The Vertical Multirange Antenna System may be briefly described as three pyramidal spiral antennas clustered at the end of an inflatable aluminum/Mylar boom. In the vertically positioned vehicle a long boom is necessary to place the antenna system clear of the vehicle.

The electrical specifications required a circularly polarized group of antennas operating over an 18:1 bandwidth with a VSWR below 3:1 over the band. In the frequency range from 150 to 2500 megacycles a single lobe beam was required with the gain level at 70° from the axis in a figure of revolution to be no more than 12 db below isotropic. In the 2700 - 2800 megacycle range the pattern required a null on axis with the main lobe describing a figure of revolution at approximately 60° from the axis. The main lobe gain was to be greater than 0 db.

A study of the space allocated for the Vertical Multirange Antenna System indicated that flush mounting of the antennas would not be practical for the following reason. As the longitudinal axis of the vehicle is perpendicular to the Earth's surface and the antenna system is located at the rear of the vehicle, shadowing of the antenna by the vehicle body would be excessive. This would be the case for all antennas mounted close to the vehicle body. The solution chosen was to extend the antennas from the vehicle on an inflatable aluminum/Mylar laminate boom.

In order to operate over the required bandwidth it is necessary to use two frequency independent antennas. Both of the pattern coverage requirements, i.e. the unidirectional pattern and the beacon type pattern, suggested the use of conical spiral antennas fed in different manners.

The space allocated was in the vehicle aft rack area. The dimensions were approximately 34" long, 8" wide and 10" high, maximum.

It was decided the best design approach to meet the stated requirements would be to use an unfurlable antenna for the 150 - 1000 megacycle range and attach smaller 1000 - 2500 and S-band fixed antennas to the base of the larger one.

In order to deploy the antennas to the best operating position the boom had to extend out 3 feet and bend to trail 11 feet aft of the vehicle flight path. The antennas were directed toward Earth. See Figures 2 and 3.

III. Flex-Rib Antenna

The Flex-Rib Antenna as developed for space vehicles is an extremely light parabolic reflector which is furled into a small package for ascent.

The electrical requirements specified a high gain circularly polarized pencil beam, to operate in the 1500 megacycle region.

This 6' parabola design consists of a thin metallic rib structure covered with a flexible fabric which is gold plated by the patented LMSC Lockspray process to form a reflective surface.

Radial ribs carry and maintain the parabolic contour on their upper edge by virtue of their depth in the axial direction. Because of their cross section, however, they may be wrapped around the hub in the furled condition. The reflective surface is attached to and folded with the ribs, and when unfurled provides lateral stability as an integrally stressed part of the antenna structure. Additional stability and erection response is provided by cupping or "oil canning" the ribs.

The 6' parabola illustrated in Figures 4 and 5 weighs 11 pounds complete, and furls into a 10" diameter container. Deployment from the container is accomplished through the release of a compressed spring, the hub sliding out in a shaft. The spring loaded center feed arm folds down and also serves the function of restraining the reflector in the container.

The feed antenna for the parabola is a pyramidal spiral fed by a tapered microstrip balun. The balun is supported by the center feed arm.

IV. P-3 Antenna

This is a circularly polarized pyramidal spiral with hexagonal cross section. It is mounted in the aft rack of the vehicle at the end of an inflatable aluminum/Mylar boom. The spiral is deployed in orbit by the inflation of the boom and spiral framework.

The electrical specifications required a circularly polarized antenna to operate in the 60 megacycle range. The VSWR was to be less than 3:1. The antenna pattern was to have an on axis gain of no less than 0 db with the horizon level to be no lower than -10 db.

A space in the shape of a rectangular box was allotted. It was 24" long, 8" wide and 10" high. Once again the longitudinal axis of the vehicle is perpendicular to the Earth's surface.

The antenna as deployed is illustrated in Figures 6 and 7. The boom and hexagonal framework are composed of 3" aluminum/Mylar tubing and the antenna diameter is 20 inches greater than that of the vehicle itself. A significant feature is that it demonstrates effectively one of the basic principles used in many of these unfurlable designs, the ability of an inflatable device to maintain its physical shape after the inflation-erection process is completed and the unit is depressurized.

V. Inflatable Waveguide

Work is currently in process toward development of an inflatable rectangular waveguide for spacecraft application. This technique makes use of Mylar hemispherical balloon segments to apply proper tensioning to the aluminized Mylar waveguide walls. To date an eight foot section has been successfully constructed and tested and the technique shows promise for early application to lightweight linear arrays.

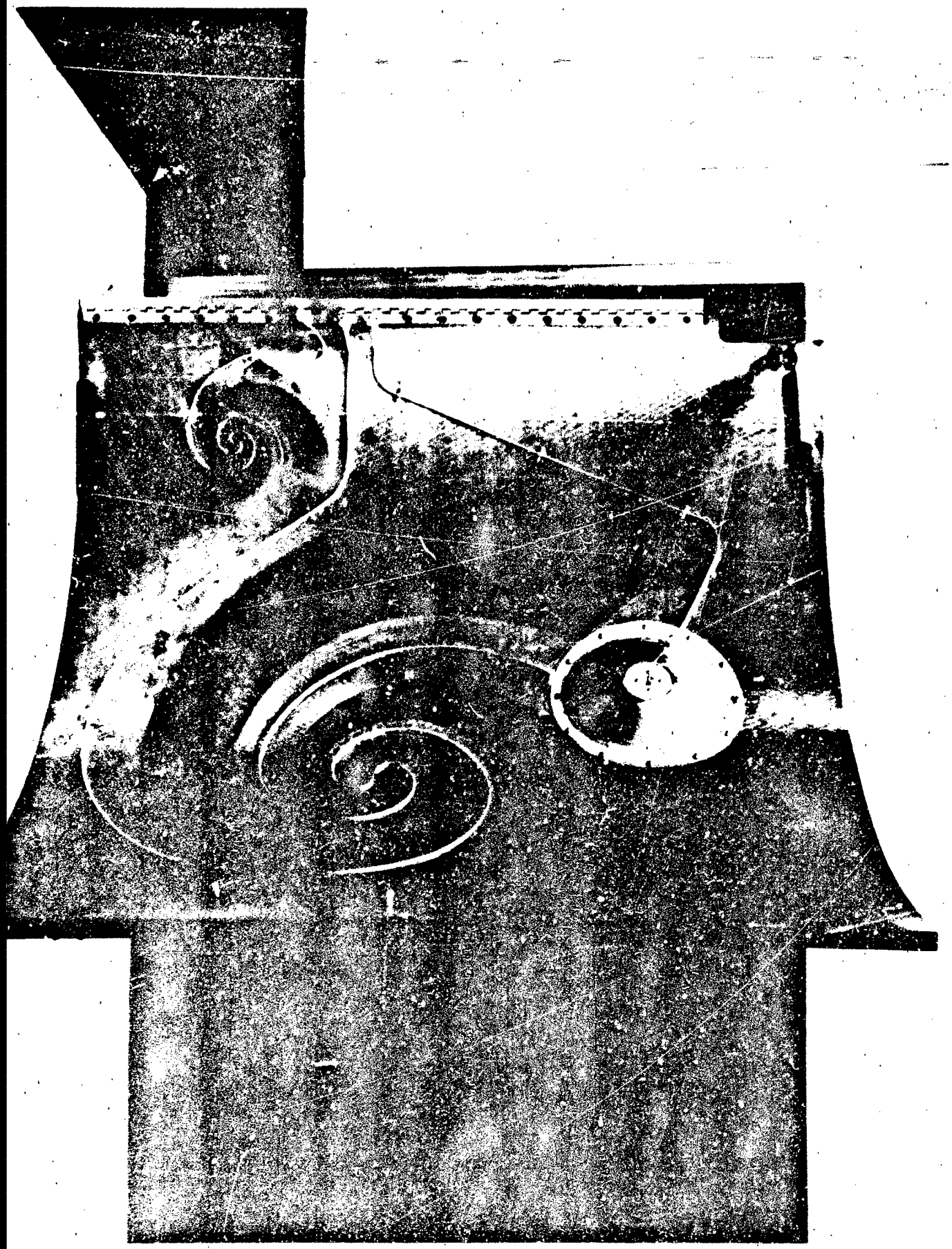

FIGURE 1

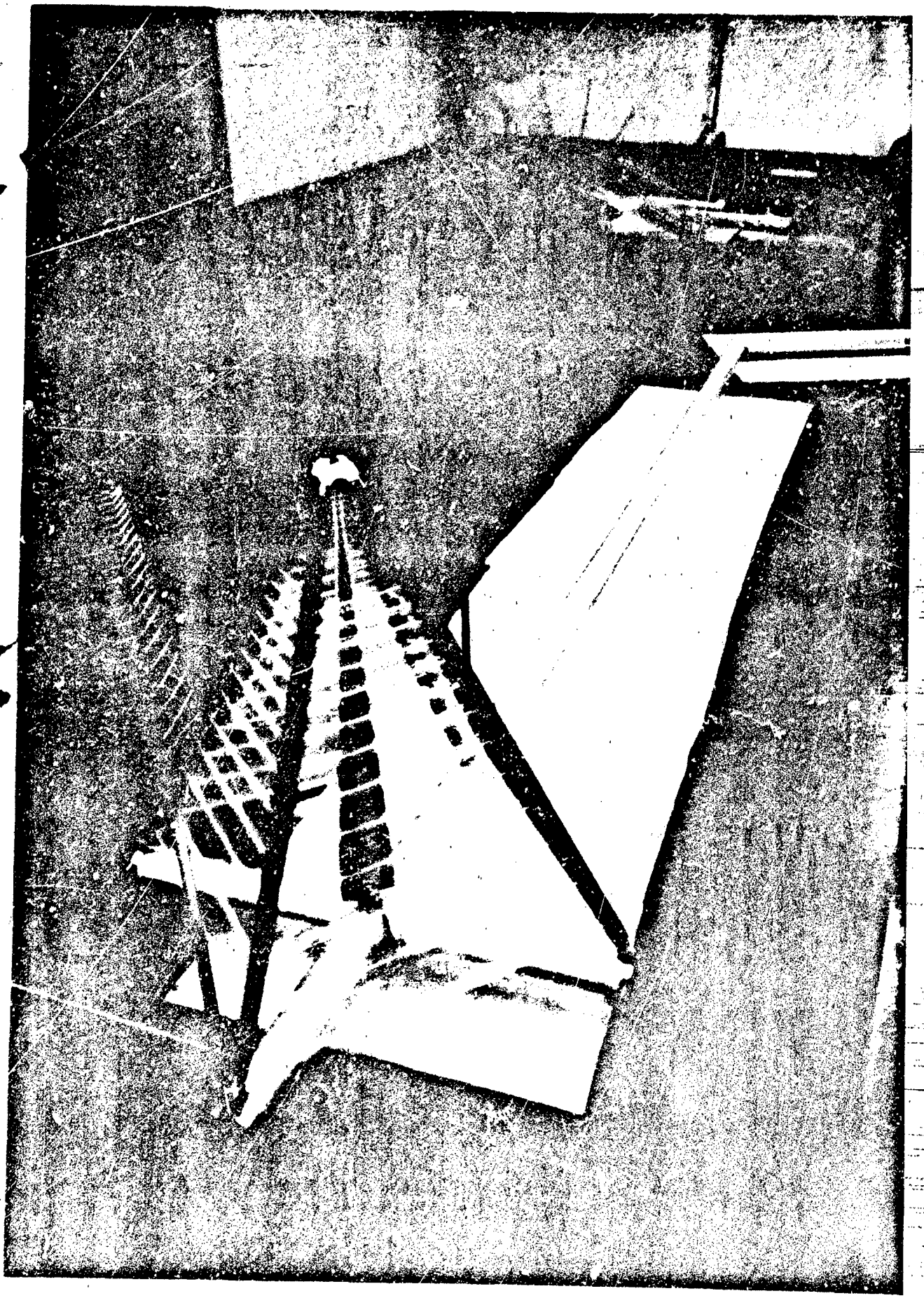

FIGURE 2



FIGURE 3

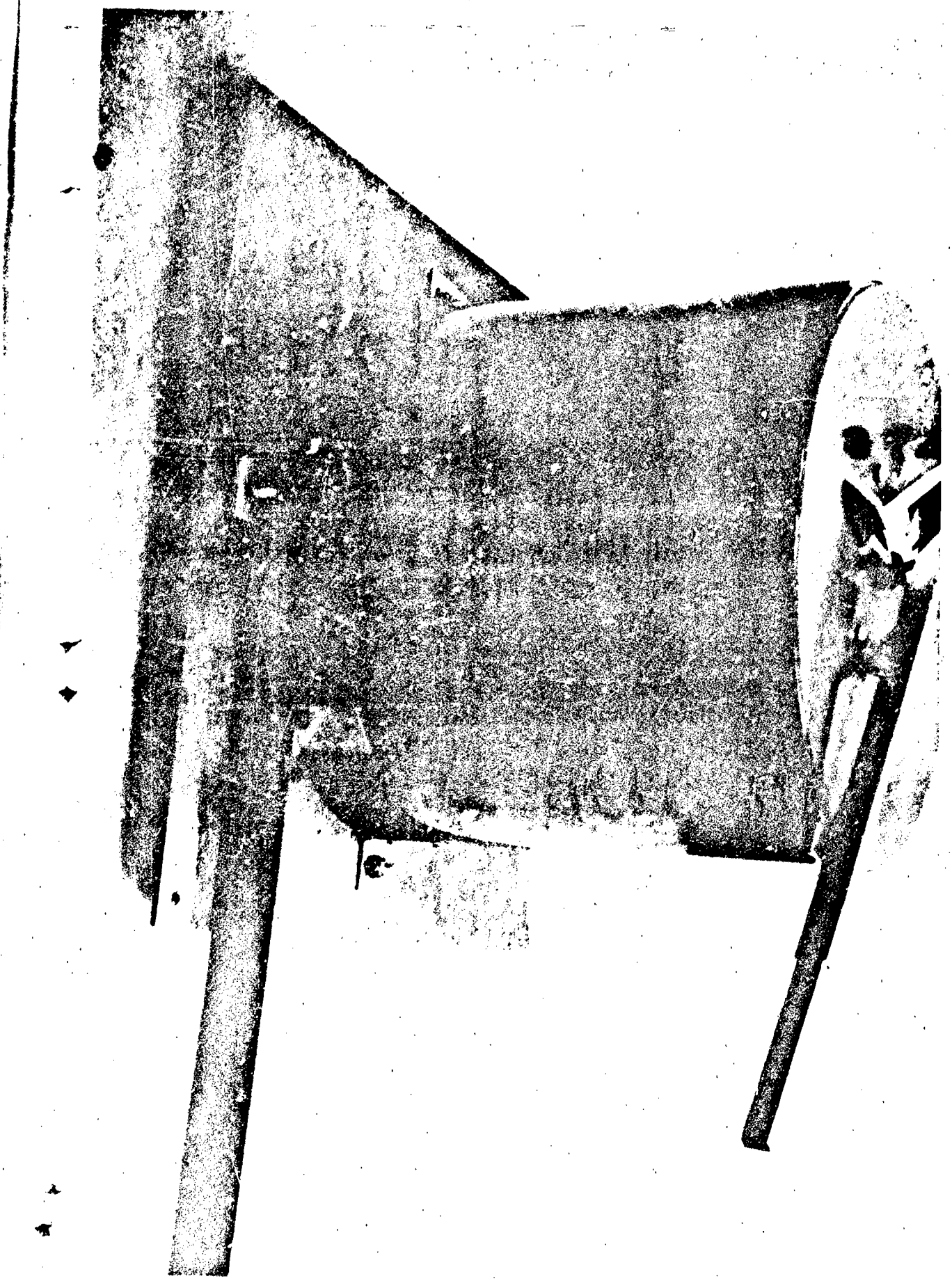

FIGURE 4

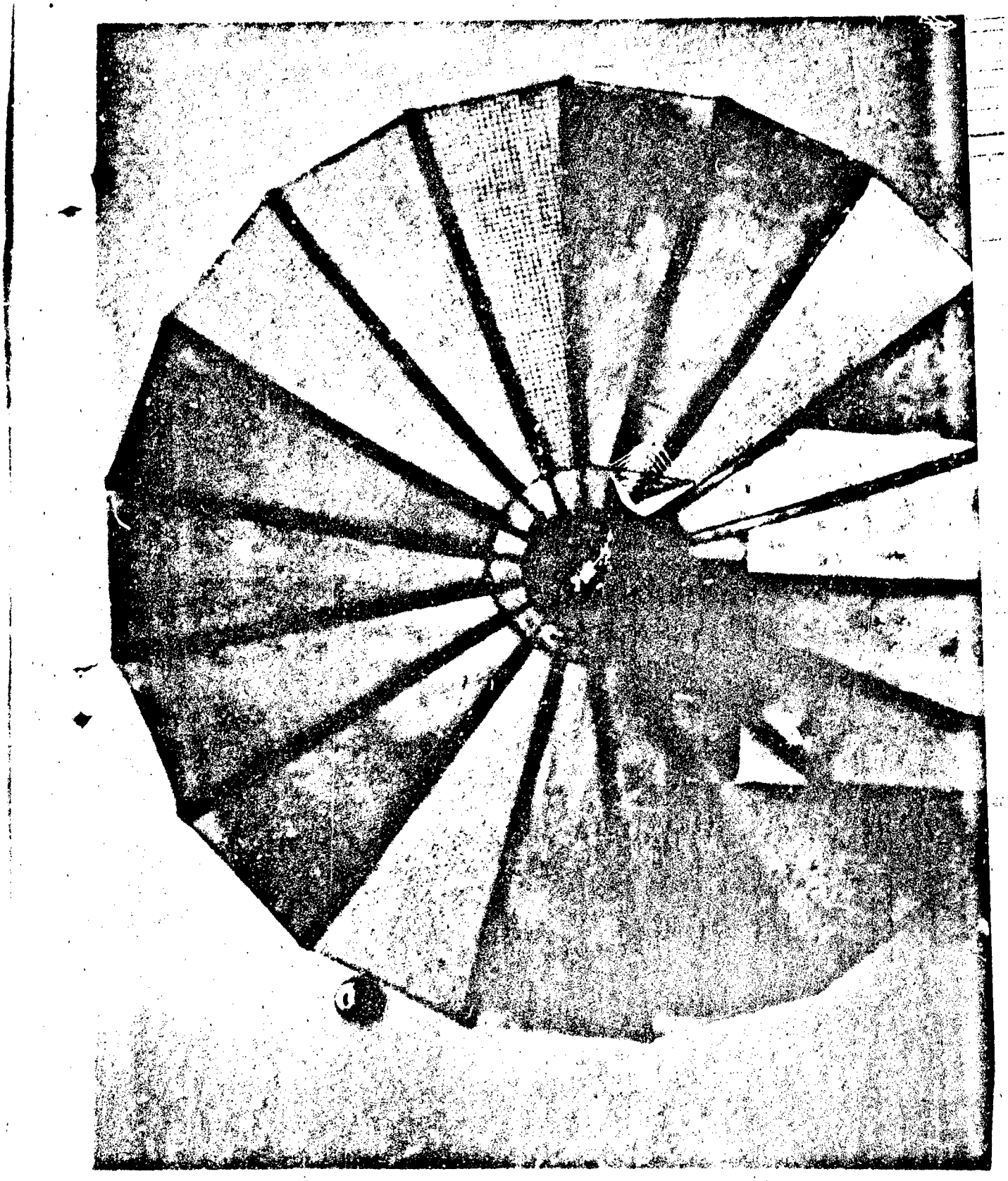

FIGURE 5

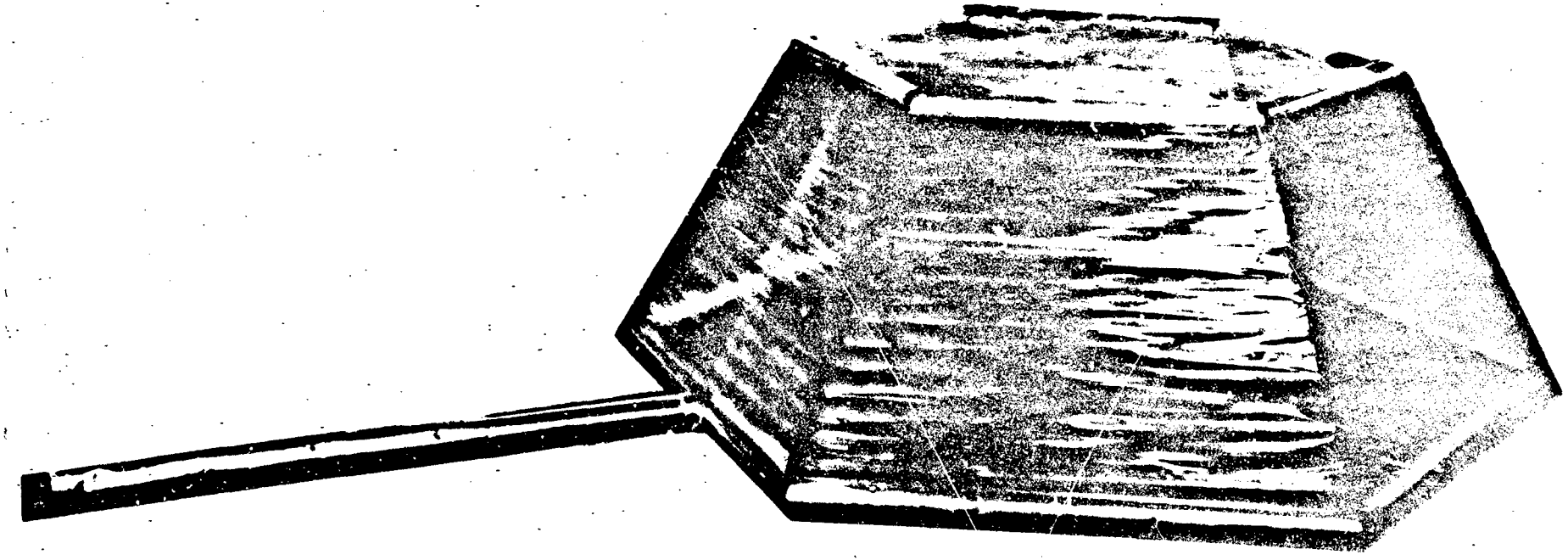

FIGURE 6



INTERFERENCE COUPLING FACTORS FOR PAIRS OF ANTENNAS

J. A. M. Lyon
A. I. Simanyi
W. R. Heath

The Radiation Laboratory
The University of Michigan

INTRODUCTION

This paper represents a continuation of the power coupling* interference studies which were presented in part at the conference one year ago.** At that time a detailed mathematical analysis was given for the case of two rectangular slots operating in a common metal ground plane. Further analysis was also presented with these two slots in a curved metal surface. Experimental data was given for two rectangular slots and also for two circular Archimedean spiral antennas. The study of power interference coupling has been continued with additional data available on these two types of antennas. Further information has also been obtained for two square spiral antennas. In addition, coupling studies have been made on E-sectoral, pyramidal, and conical horn antennas. Altogether, information is presented here on the power coupling between two antennas where each of the antennas involved is one of the four types mentioned.

Besides considering a pair of similar antennas, studies were made between a given antenna and a monopole antenna. Results of coupling between a square spiral and monopole are shown here.

The Square Archimedean Spiral. Right-hand and left-hand wound square spirals were experimentally tested on the 12 ft. by 12 ft. ground plane in an anechoic

---

* For a definition of power coupling, see Appendix A.

**Kalafus, R. M., et al, see List of References.

chamber. Pertinent data follow:

Type: Cavity-backed, two-arm, twenty turns.

Frequency range: 2 - 4 Gc.

Balun type: Strip-line, Roberts, located in cavity.

Manufacturer: Advanced Development Laboratories.

Model No. : 1 L (left-hand wound)

3 R (right-hand wound).

Overall dimensions (antenna and cavity): 2 in. x 2 in. x 1 in.

Coupling measurements were taken between the square spiral antenna and a quarter-wave monopole. The monopole was perpendicular to the ground plane and located 11.3 in. from the center of the square spiral antenna. Coupling patterns were recorded for frequencies from 2 to 4 Gc at 100-Mc intervals. Typical curves for Spiral 1 L are shown in Fig. 1.

Further studies of these coupling patterns reveal a preponderance of maxima at locations radially out from the antenna corners (at $\phi = 0^{\circ}$, 90°, 180°, and 270°).

Figure 2 indicates the maximum and minimum coupling between the 1 L spiral antenna and the quarter-wave monopole, normalized such that the spacing between these two antennas is 1.92 wavelengths. These curves indicate:

a) A relatively small variation in coupling as a function of frequency.

b) A relatively constant difference between maximum and minimum coupling levels over the frequency range.

c) A trend toward increased average coupling as the frequency is increased.

Radiation patterns indicate:

a) A greater beam width than that observed for the circular spiral.

b) A relatively constant gain over the frequency range of the antenna.

A theoretical analysis of the fields from a square spiral antenna is presented in Appendix B. In this analysis it is assumed that current waves travel out from the center terminals of the antenna with a wave propagation factor β which is constant. In addition, it is assumed that the current does not experience reflection at the spiral corners and that it is attenuated in the "radiation region" of the antenna.

The equations resulting from this analysis were programmed for the IBM 7090 computer and radiation patterns were calculated. These patterns were found to check quite well in many respects with those obtained experimentally. Both theoretical and experimental coupling patterns have maxima at positions radially out from the corners of the antenna.

The equations from Appendix B for the electric fields of the square spiral antenna were used to try to predict the fields from the square photo-etched spiral. This spiral has twenty turns and a spacing of .01 in. It is designed to operate between 2 Gc and 4 Gc. Since the width of the wires and the spacing between wires are equal, the antenna and the ground plane can be considered as being the complement of a square spiral in free space. The free space spiral has the same geometry as the spiral formed by the spaces between wires on the spiral. Equations for predicting the fields of the ADL spiral in a ground plane are then found by interchanging E_ϕ and E_θ in the equations for the complementary free-space spiral.

It should be noted that the radiation from any spiral is affected by the cavity and the photo-etched balun in the feed system. These effects are not considered in the derivation of the field equations and hence do not appear in the computed patterns. Both theoretical and experimental patterns are shown in Fig. 3. The

absolute levels of the theoretical curves are arbitrary since they depend on the current at the terminals, which is not known exactly. Note that in Fig. 3 the experimental pattern has higher directivity than the computed pattern. This is due to the fact that the cavity radiates more power directly outward than in directions near the ground plane.

In Fig. 4 there are definite maxima at locations near the spiral corners in both the experimental and computed patterns. Note, however, that the experimental pattern does not contain a great degree of symmetry for field points 180° apart. This deviation from the theory is primarily due to the imbalance in the feed caused by the balun and by direct radiation from the balun.

An attempt to simulate this imbalance was made by calculating a pattern for the case of unbalanced currents at the feed terminals. Since no information was available concerning the amount of imbalance the balun caused, a guess was made. A six-degree error in the phase and a two-to-one ratio in the amplitudes of the terminal currents were assumed. The resulting field pattern is shown at the top of Fig. 4. The curve suggests that if the actual imbalance in the feed were known, then closer correlation with experimental results could be realized.

The pattern for the component of electric field in the plane of the spiral (Fig. 5) is symmetric with respect to the origin; that is, the magnitudes of the electric fields at points 180° apart are equal. This result was predicted since diametrically opposite points on the spiral (points reflected through the origin) carry identical currents. Computer results also revealed a 360° phase shift for E_{ϕ} as ϕ is varied from zero to 2π radians.

Automatic Positioning Apparatus. In order to facilitate the rapid acquisition of power interference coupling data, it was decided to build an apparatus which would allow the continuous measurement of power coupling as a function of distance. In making this decision it was necessary to first decide that only the amplitude of coupling was to be determined. Figure 6 shows a front view of this automatic spacing equipment in which are mounted two pyramidal horns. Basically, the apparatus utilizes a sliding brass belt containing the movable antenna with one of the antennas remaining fixed as shown in the bottom of the picture of Fig. 6, part A. As shown, provision has been made to minimize the effects of any cracks between the moving metal belt and the adjoining conducting ground plane. Figure 6, part B shows details behind the ground plane of the automatic spacing device. It is to be noticed that there is a servo-mechanism take-off of the position information providing one to one correspondence between chart paper advance and movement of the one antenna with respect to the other antenna. An additional servo-mechanism take-off is provided so that the rotation of the bottom antenna in Fig. 6, part A may be recorded.

The output of this servo-mechanism is used to drive the abscissa of an X-Y plotter. The resulting pattern is that of coupling versus rotation for any given spacing of the antennas.

Pyramidal Horn Antenna. A number of measurements were made of the power interference coupling between two pyramidal horns. Figure 7, parts A, B, and C show drastic changes in the level of coupling between two such horns as the receiving horn is changed in its orientation with respect to the transmitting horn. Each part is for a given spacing and orientation as indicated in the legend on the individual parts. The same two horns were used in another test involving the

automatic positioning equipment previously described. For this test the E-fields of the two horns were in line. Figure 7, part D shows the variation of the coupling as the spacing is changed from a minimum of 8 inches to a maximum of 21 inches. The coupling level is lowered 6 db for each doubling of the spacing between the antennas as shown by the calculated curve in this figure. This calculated curve corresponds to the dependence of electric field upon the reciprocal of distance, or power density falling off inversely as R squared.

Very low levels of coupling were observed when the two pyramidal horn antennas were aligned with the H-fields colinear. The general level of coupling in this case was in the neighborhood of 80 db which is substantially lower than the general level of coupling observed in the previous case (E-fields colinear). At this extremely low level of coupling, because of the sensitivity of the measurement apparatus, small variations of power level become prominent. It has been these small variations which have been difficult to explain. (It is expected that in the oral presentation it will be possible to clarify the variations in couplings observed and therefore to present detailed data on the actual coupling through the use of slides at that time.)

E-Sectoral Horns. Numerous tests were performed on E-sectoral horns, each horn having a directivity of approximately 8 db. Figure 8 shows the coupling for two E-sectoral horns with two different orientations corresponding to E-plane coupling and H-plane coupling. The data in the figure have been taken for a spacing of 11.2 cm. A frequency of 10 Gc was used in the test. Later a series of tests for various spacings in the two orientations were made for the coupling of the same two E-sectoral horns. The information on the latter tests are

described by the curves of Fig. 9.

Conical Horn Antennas. Two circularly polarized conical horns were used in a series of coupling measurements. Figure 10, part A, shows the power interference coupling to have a minor variation about a level 71 db down from the power entering the transmitting antenna. Part B shows a similar measurement with the orientation of the transmitting horn changed by an angle of 90°. It is noted that the average level here has now been lowered to about 73 db down. The variations observed in these two curves are due at least in part to polarization ellipticity present on either or both of the horns. The results shown in this figure were for a frequency of 7.57 Gc and a spacing of 31.0 cm. Subsequently, coupling measurements were made on these same conical antennas at various spacings and frequencies. Figure 11, curves A and B show the radiation patterns in two orthogonal planes for the conical horns used. The directivity of each of these conical horns is approximately 20 db.

CONCLUSIONS

Much data has been obtained upon each of several pairs of antennas. Details in the construction and feed arrangements of the antennas appear to be of great importance in the power interference coupling level existing between two antennas. In the application of coupling information to the power interference between two systems, additional data on coupling antennas operating at frequencies other than the design frequency must be obtained. The results of this paper are useful in assessing the interference of the particularly difficult problem of two systems using antennas mounted in a common metal surface.

REFERENCES

Curtis, W. L., "Spiral Antennas," IRE Trans. on Ant. and Prop., May 1960, pp. 298-306.

Kaiser, J. A., "The Archimedean Two-Wire Spiral Antenna," IRE Trans. on Ant. and Prop., May 1960, pp. 312-323.

Kalafus, R. M., R. B. Harris, Y. K. Kwon and J. A. M. Lyon, "Coupling Effects with Slot and Spiral Antennas," The University of Michigan, Ann Arbor Michigan.

Wolfe, J. J. and R. Bawer, "Printed-Circuit Spiral Antennas," Electronics, April 1961.

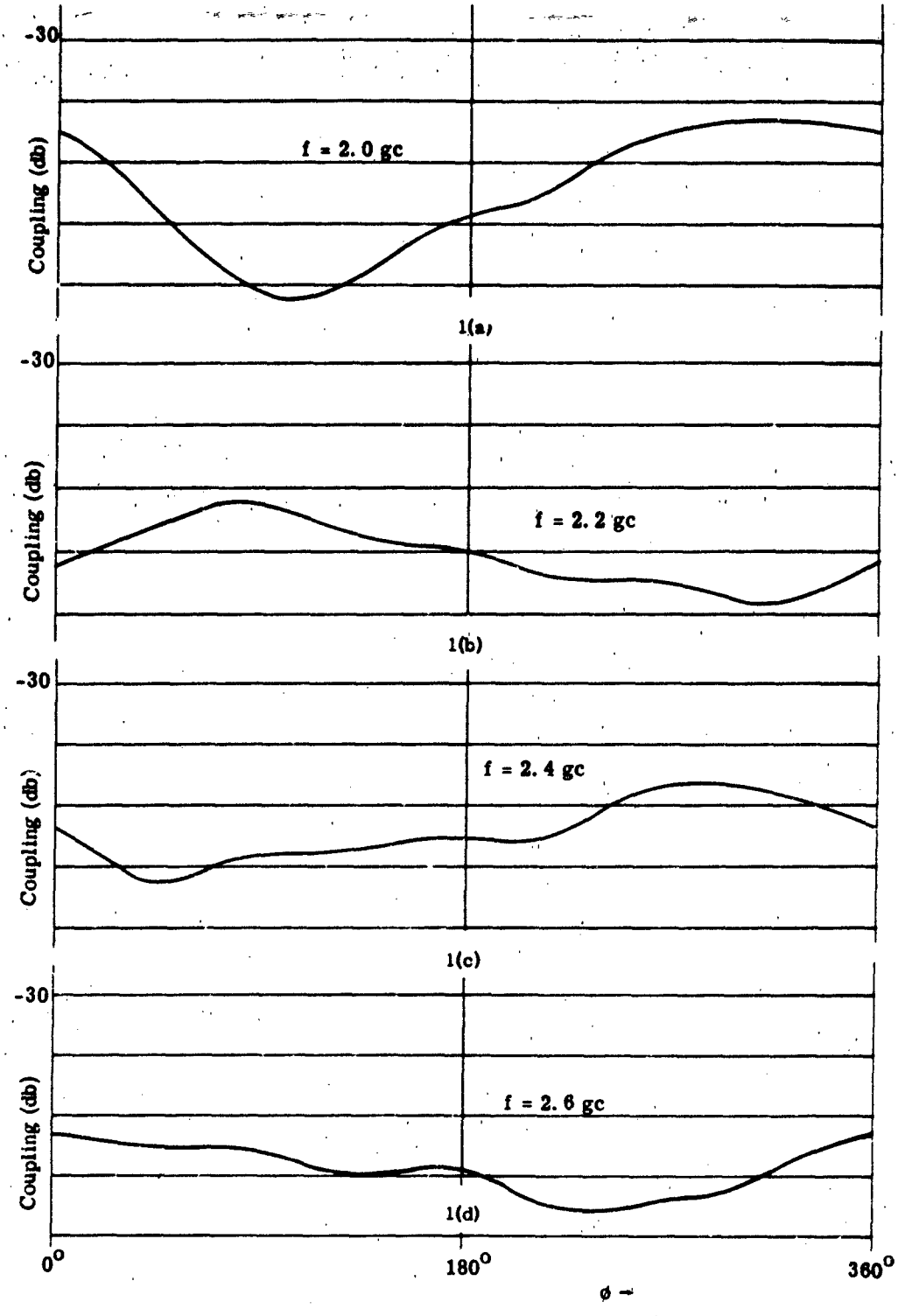

Fig. 1. Coupling patterns for Square Spiral "1L" normalized.

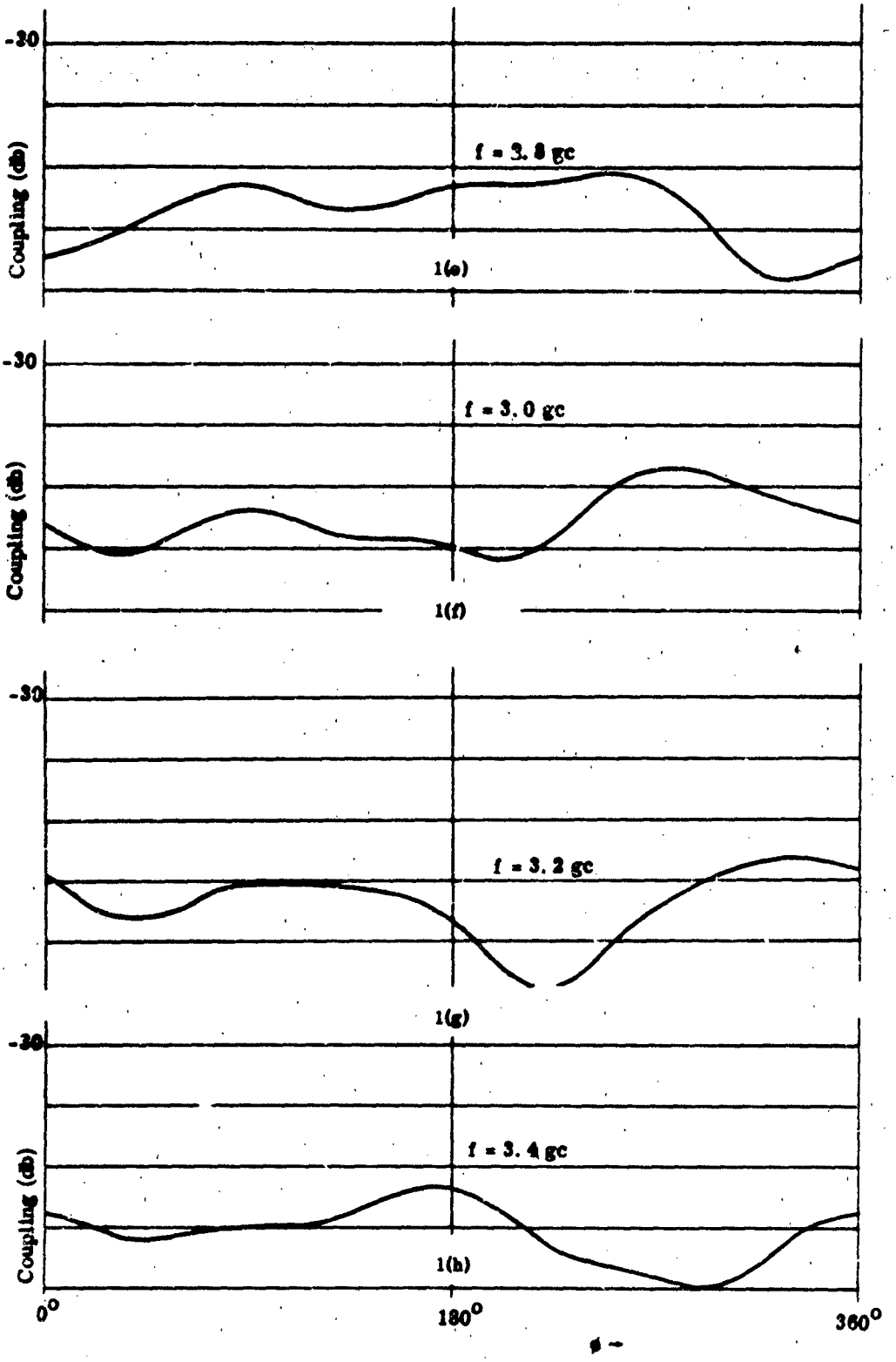

Fig. 1 (Cont.). Coupling patterns for Square Spiral "1L" normalized.

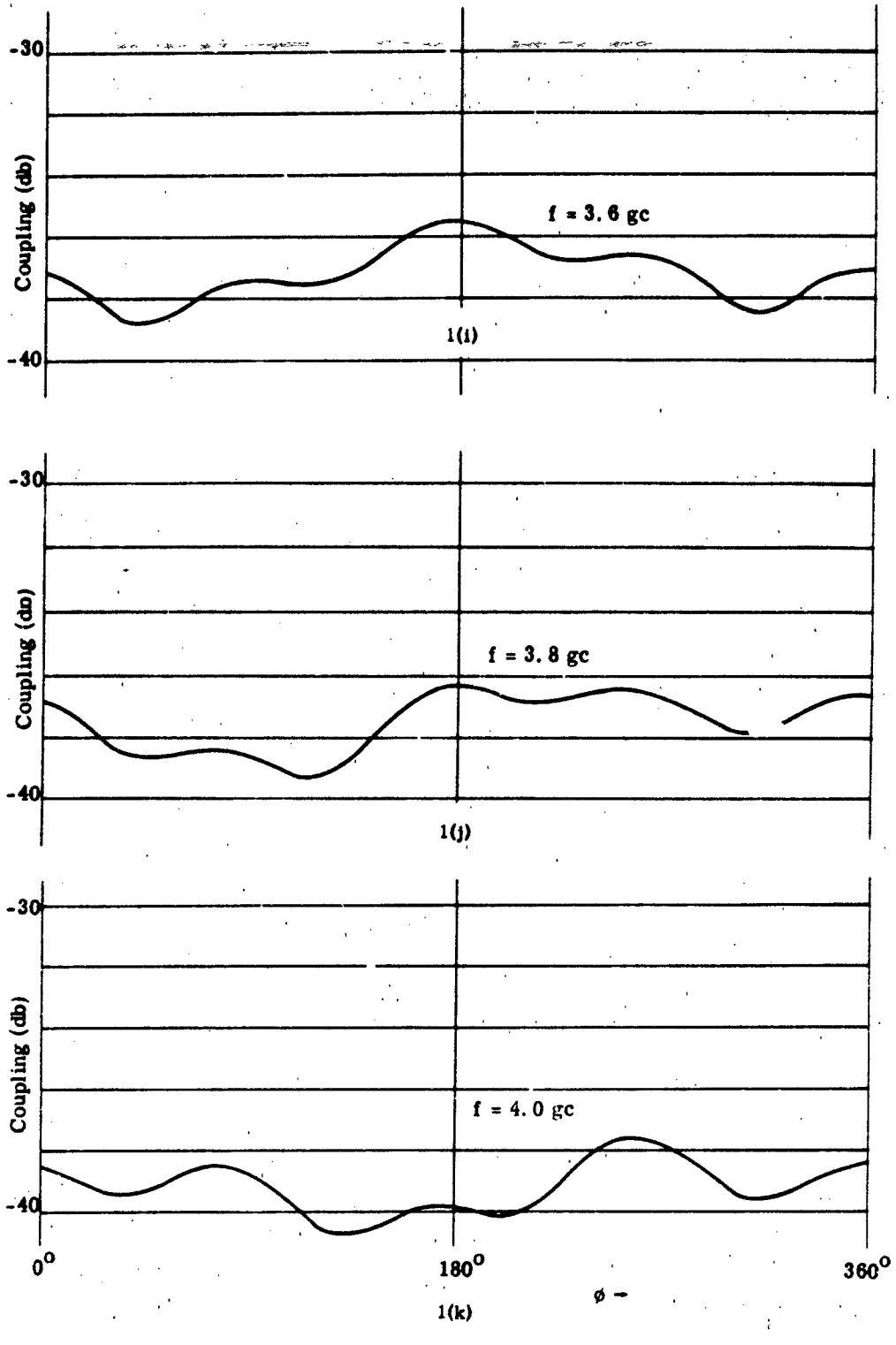

Fig. 1 (Cont.). Coupling patterns for Square Spiral "1L" normalized.

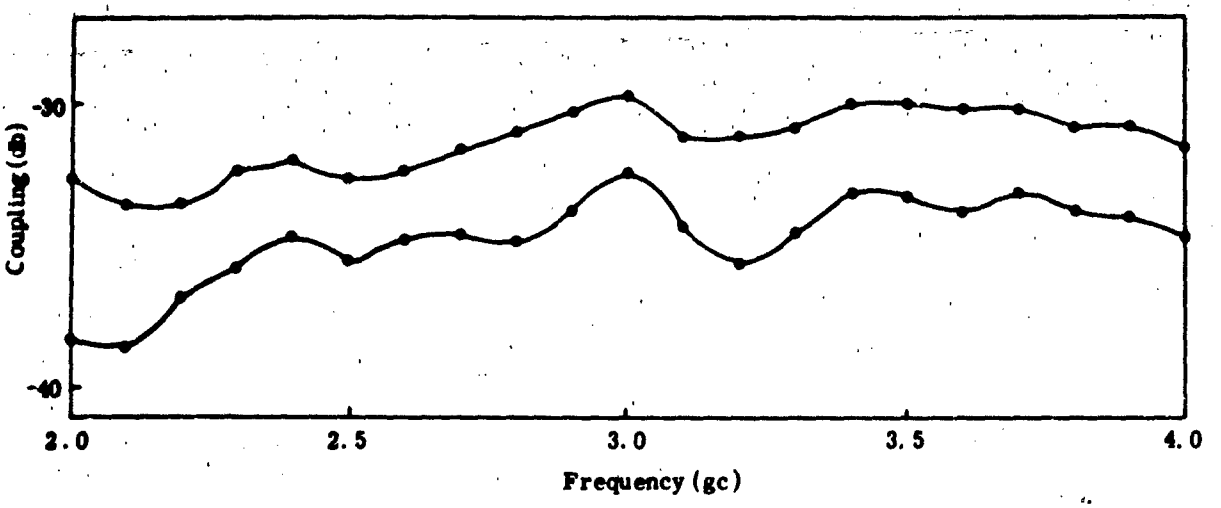

Fig. 2. Total variation of coupling vs. frequency, square spiral "1L".

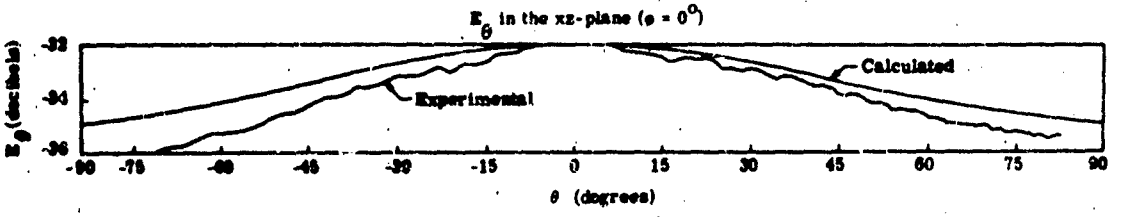

Fig. 3. Experimental and theoretical radiation patterns, square spiral.

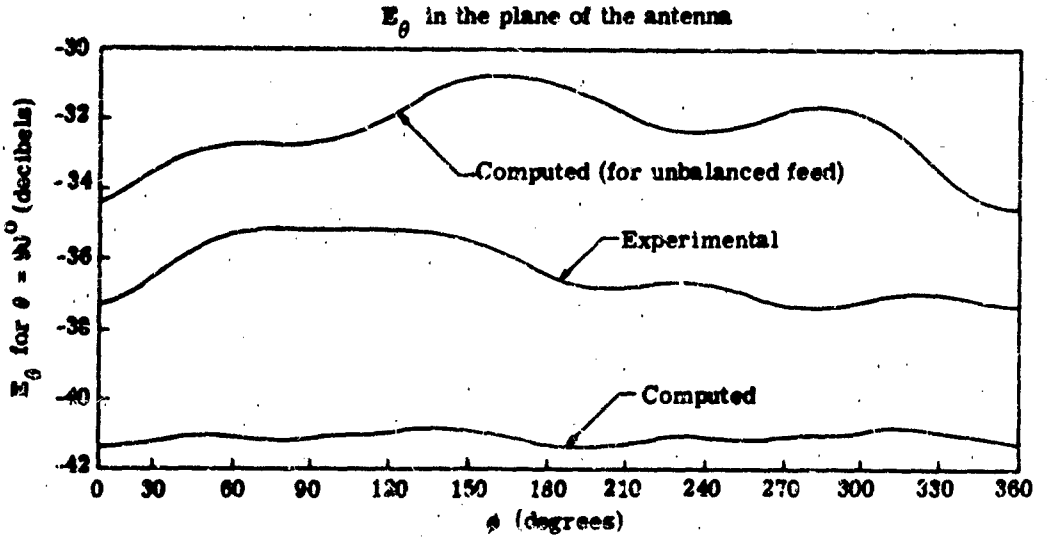

Fig. 4. Experimental and theoretical coupling patterns, square spiral.

(a) E_ϕ in the xz Plane

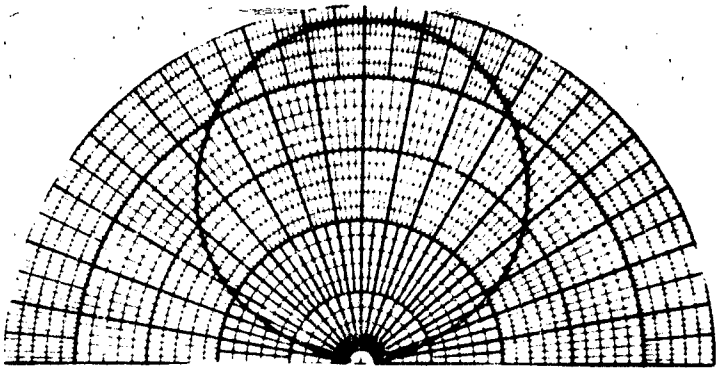

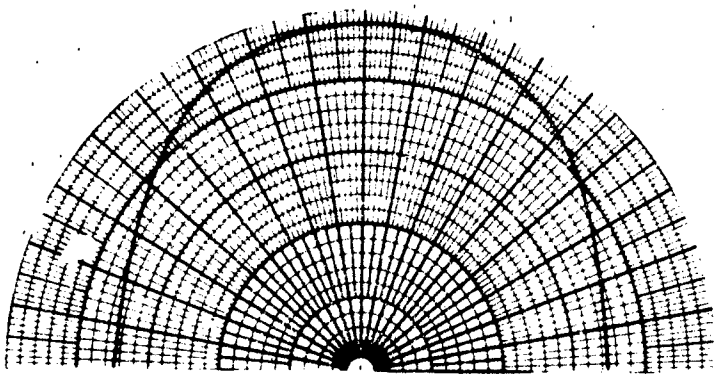

(b) E_θ in the xz Plane

(c) E_θ in the Plane of the Spiral (xy Plane)

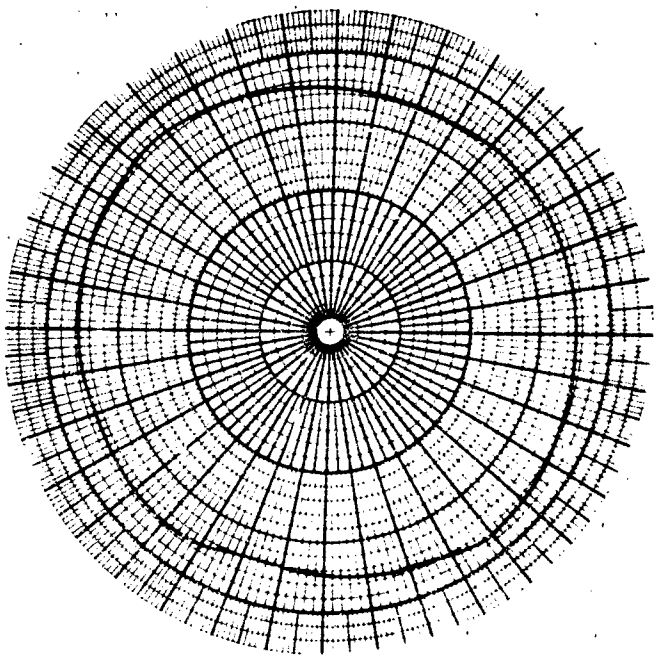

Fig. 5. Predicted patterns of square spiral.



FIG. 6a. Front View of Automatic Positioning Apparatus.

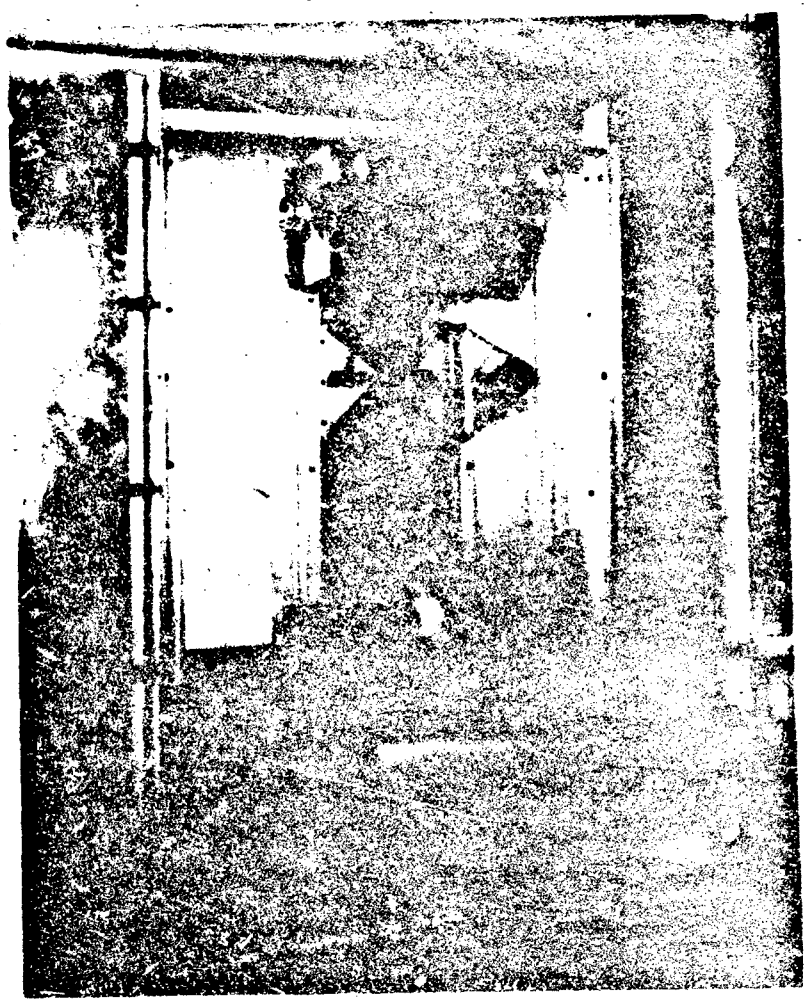

FIG. 6b. Rear View of Automatic Positioning Apparatus.

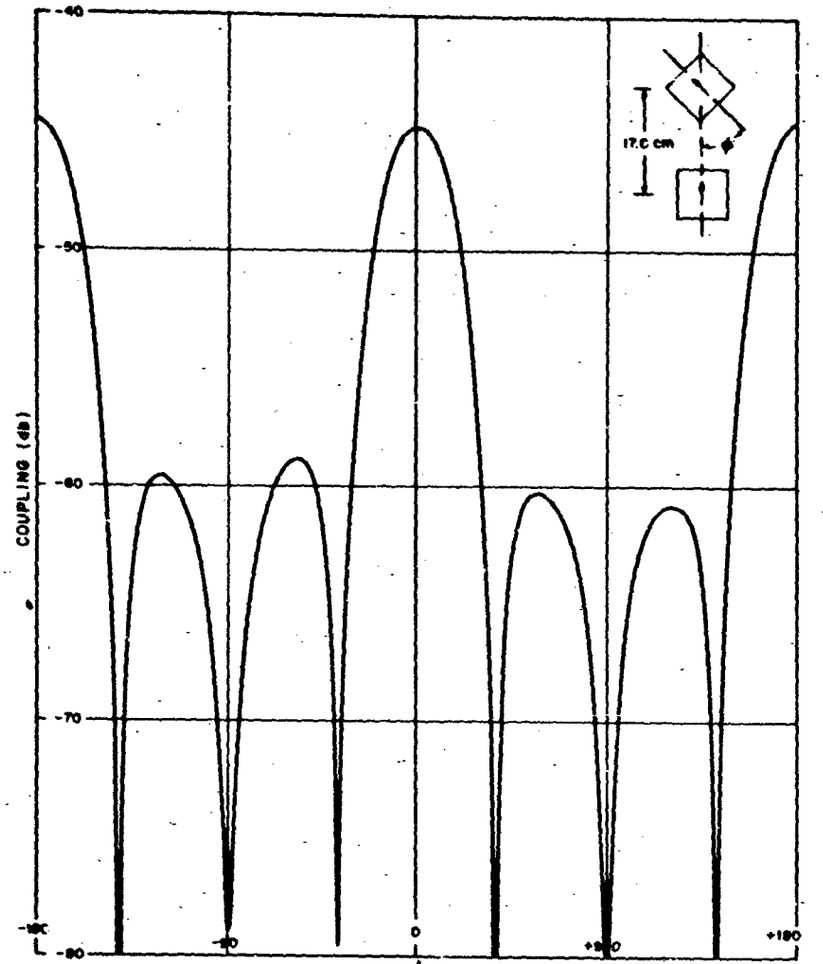

Fig. 7a

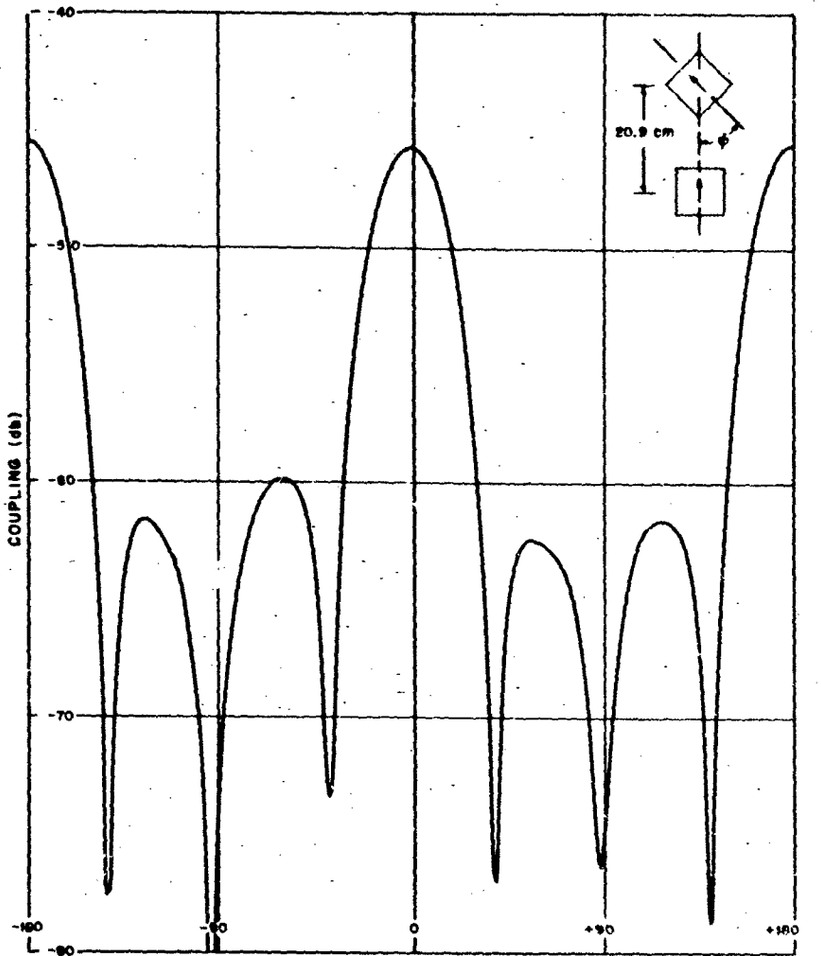

Fig. 7b

COUPLING BETWEEN TWO PYRAMIDAL HORNS

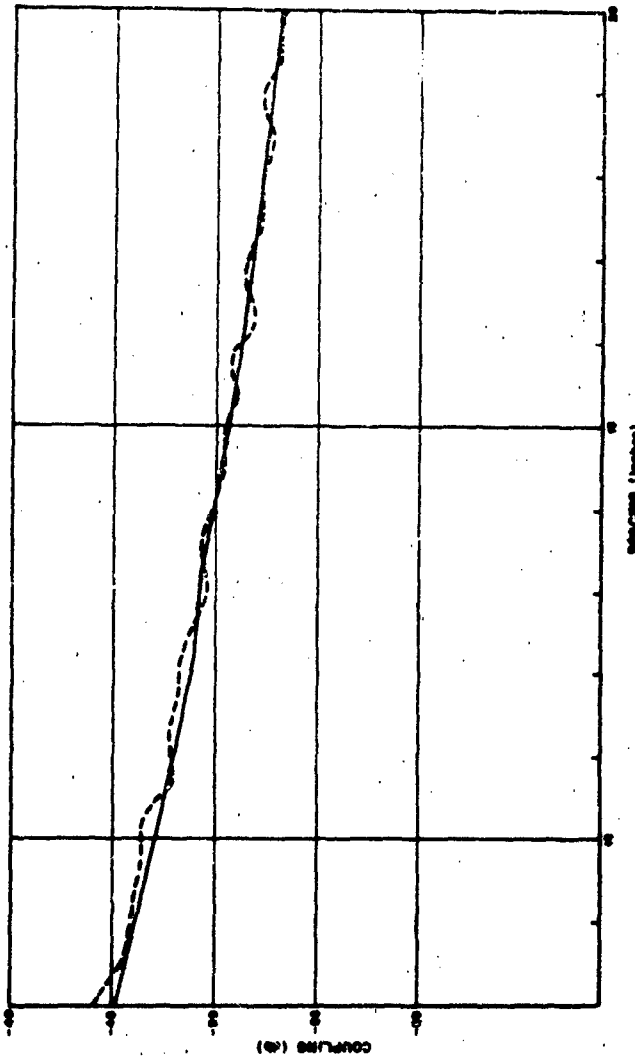

Fig. 7V COUPLING BETWEEN TWO PYRAMIDAL HORNS

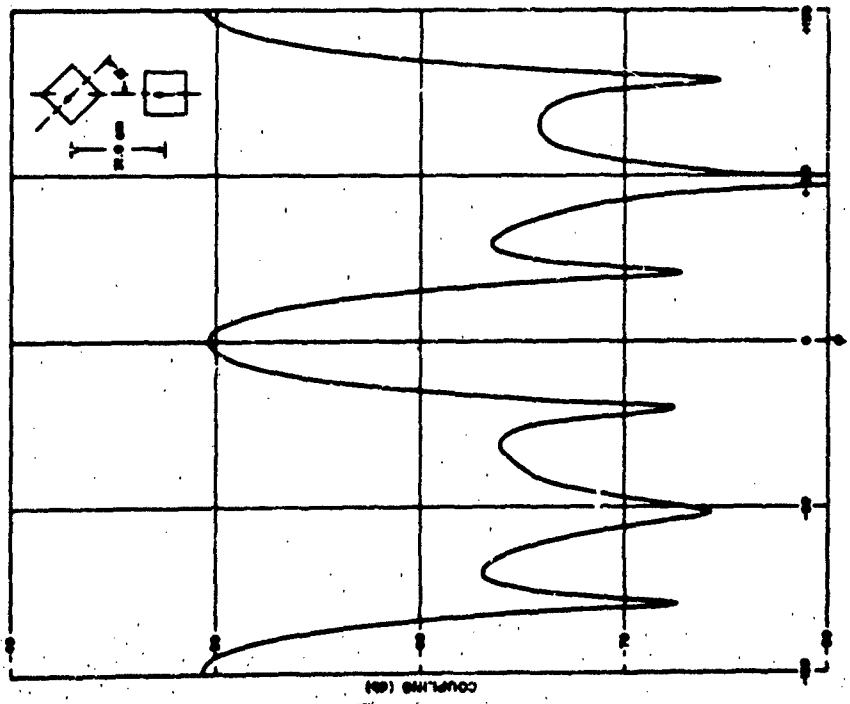

Fig. 7W COUPLING BETWEEN TWO PYRAMIDAL HORNS

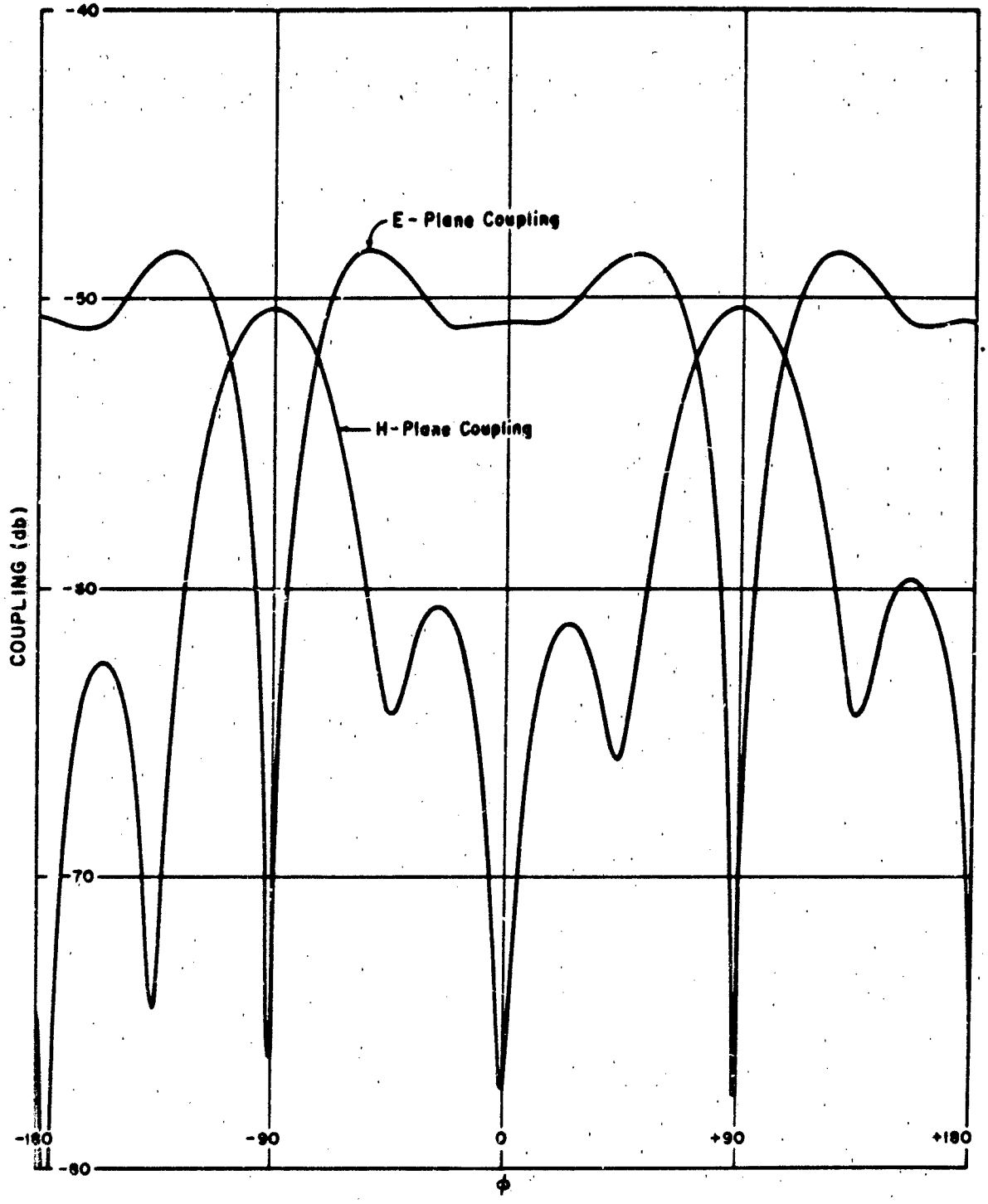

Fig. 8 COUPLING BETWEEN TWO E-PLANE HORNS

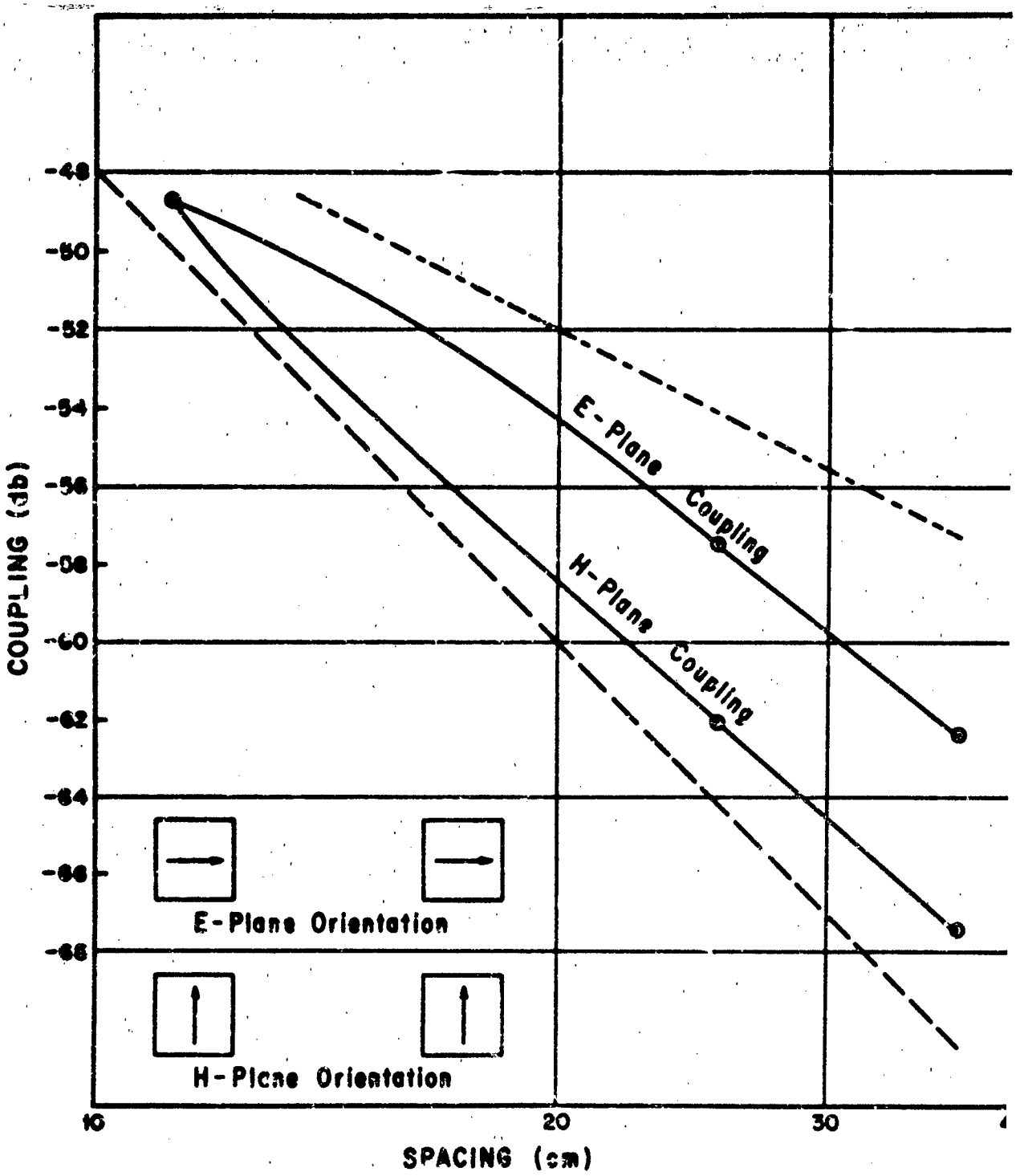

Fig. 9 COUPLING BETWEEN TWO E-PLANE HORNS

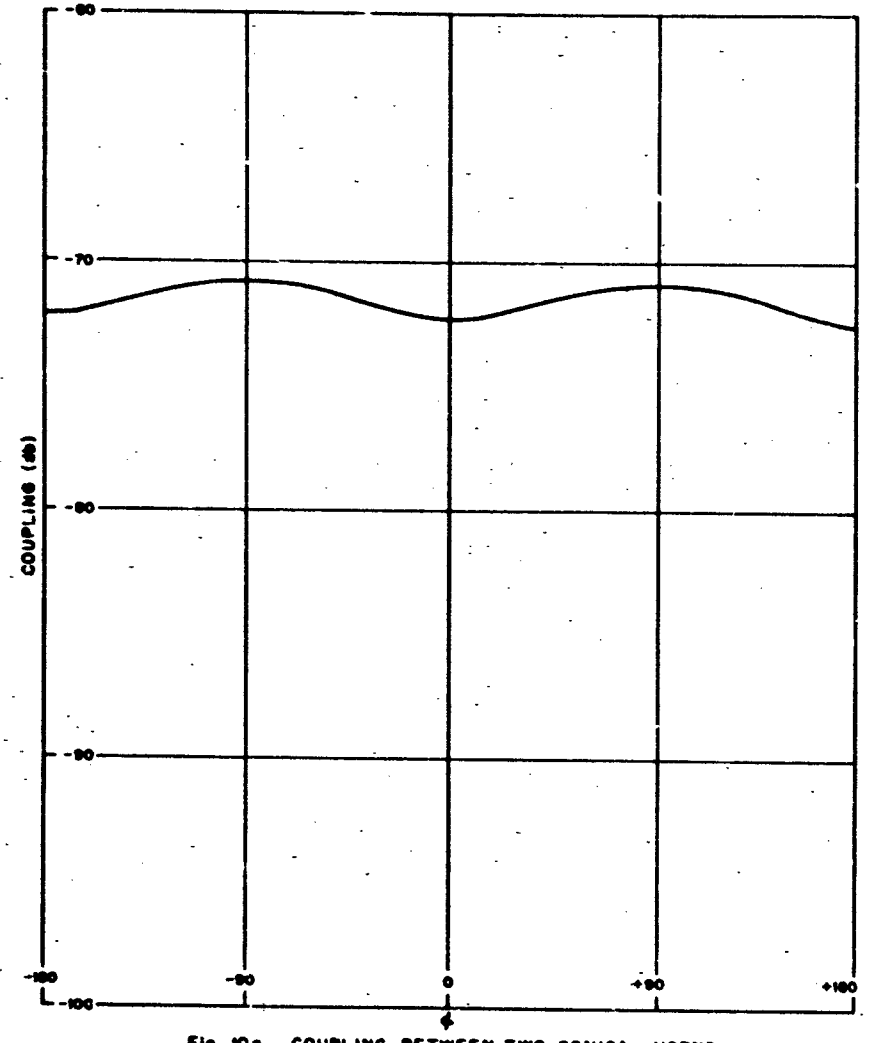

Fig. 10a COUPLING BETWEEN TWO CONICAL HORNS

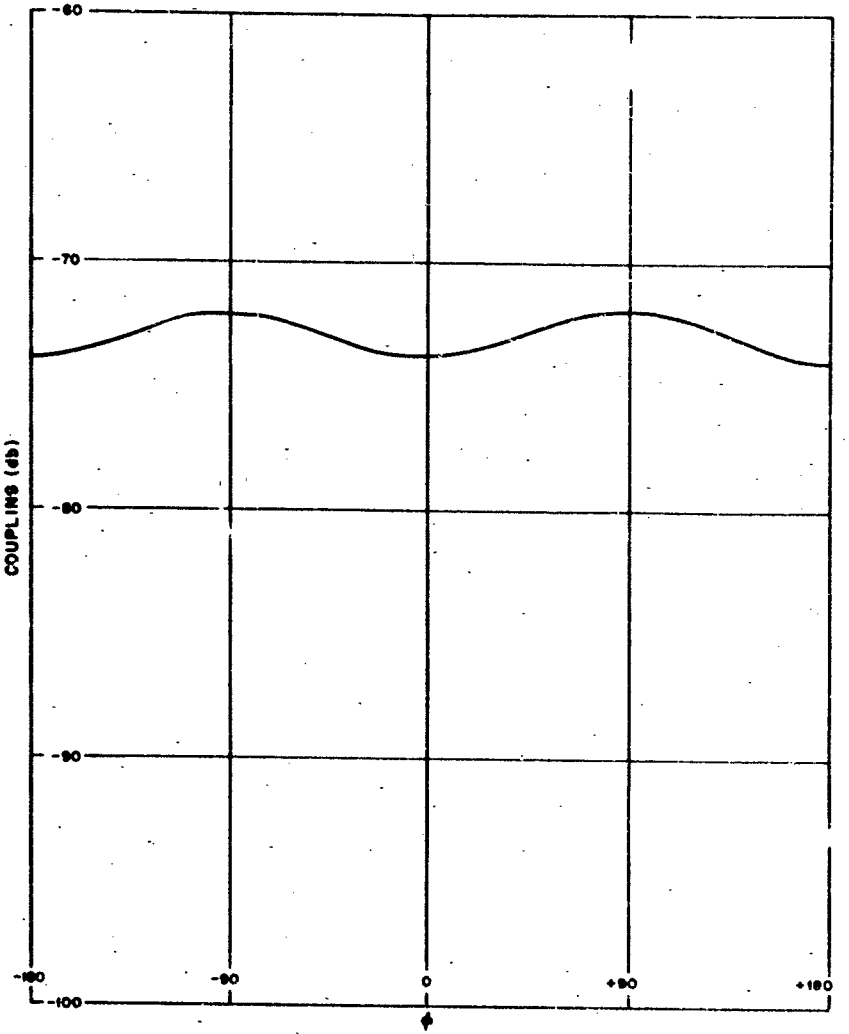

Fig. 10b COUPLING BETWEEN TWO CONICAL HORNS

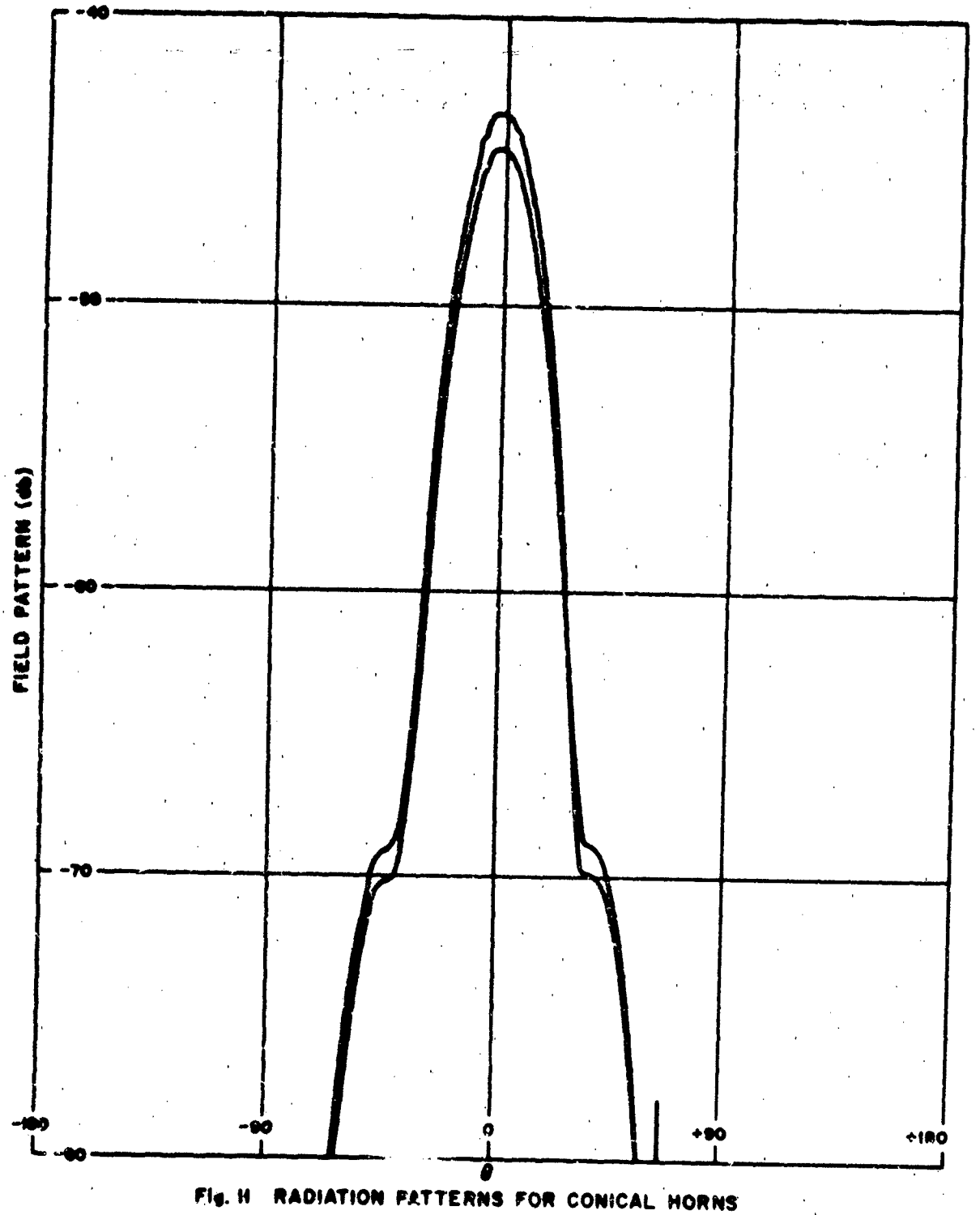

Fig. 11 RADIATION PATTERNS FOR CONICAL HORNS

APPENDIX A

RELATION BETWEEN COUPLING AND MUTUAL IMPEDANCE

Consider the general linear two-port network depicted in Fig. 12.

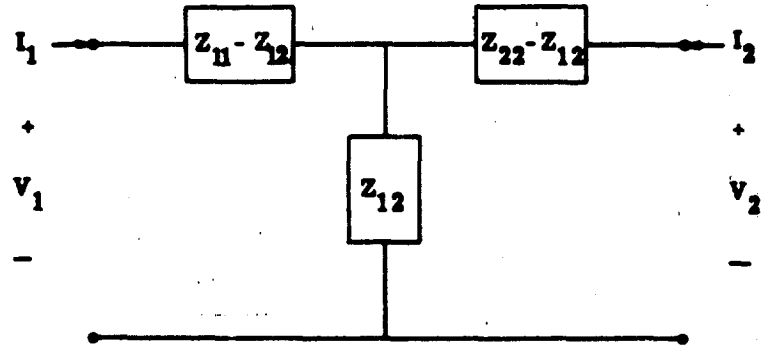

Fig. 12. Two-port network.

The network equations are:

$$V_1 = Z_{11} I_1 + Z_{12} I_2$$
$$V_2 = Z_{21} I_1 + Z_{22} I_2 \,. \tag{A.1}$$

Since antenna pairs are generally linear and reciprocal,

$$Z_{12} = Z_{21} \quad \text{(mutual impedance)} \,. \tag{A.2}$$

Furthermore, for far-field coupling, we see that

$$|Z_{12}| << |Z_{11}|$$
$$|Z_{12}| << |Z_{22}| \,.$$

The power transmitted is:

$$W_t = I_1^2 \, \mathrm{Re}\,(Z_{11}) \, .$$

The power received by a matched load is:

$$W_r = I_2^2 \, \mathrm{Re}\,(Z_{22}) = \frac{I_1^2 \, |Z_{12}|^2}{4 \, \mathrm{Re}\,(Z_{22})} \, .$$

Thus the far-field coupling is:

$$C = \frac{W_r}{W_t} = \frac{|Z_{12}|^2}{4 R_{11} R_{22}} \tag{A.3}$$

where

$$R_{11} = \mathrm{Re}\,(Z_{11})$$
$$R_{22} = \mathrm{Re}\,(Z_{22}) \, .$$

Mutual impedance is obtained from an open-circuit measurement, whereas coupling is obtained from a tuned measurement.

$$Z_{12} = \left. \frac{V_2}{I_1} \right|_{\substack{\text{receiver} \\ \text{open-circuited}}} \tag{A.4}$$

The loading that occurs in near-field situations will alter the relation given by Eq. A.4.

APPENDIX B

DERIVATION OF SQUARE SPIRAL FIELDS

In this section the radiation fields of the square spiral antenna are derived. The antenna is assumed to be made up of a series of linear wire elements arranged in a configuration similar to that of the square spiral (see Fig. 14). Each wire carries a traveling wave of current. The phase of each current is the same as the phase of the corresponding current on the spiral. The magnitude of the current on each wire element is held constant, and attenuation, due to radiation, is depicted by reducing the current magnitude on successive wire elements in each leg of the spiral. If one assumes a constant magnitude current on each wire element, the vector potential may be calculated.

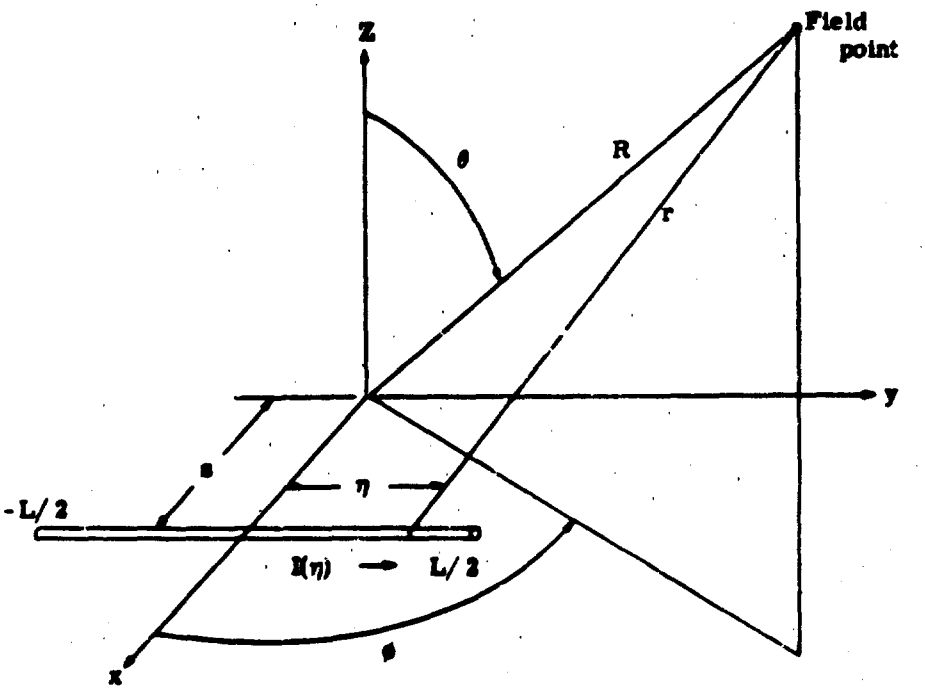

Fig. 13. Geometry for square spiral analysis.

The vector potential due to a traveling wave of current on a linear wire element displaced a distance s from the origin is found as follows. For a y-directed wire (Fig. 13), the vector potential at a large distance r from the wire is given by

$$A_y = \frac{1}{4\pi R} \int_{-\frac{L}{2}}^{\frac{L}{2}} I(\eta)\, e^{-jkr}\, d\eta' . \qquad \text{(B.1)}$$

If R is large compared to a wavelength, r is given approximately by

$$r = R - \eta \sin\phi \sin\theta - s \cos\phi \sin\theta ,$$

The current is assumed to have the form

$$I(\eta) = I_o\, e^{-j\beta(\eta + \ell)} \qquad \text{(B.2)}$$

where the factor $-j\beta\ell$ will be used later to adjust the relative phase between currents on different wires.

Equation B.1 now becomes

$$A_y = \frac{e^{-jkR}}{4\pi R} \int_{-\frac{L}{2}}^{\frac{L}{2}} I_o\, e^{-j\beta(\eta+\ell)}\, e^{jk(\eta \sin\phi \sin\theta + s\cos\phi \sin\theta)}\, d\eta$$

or

$$A_y = \frac{I_o\, e^{-j(kR + \beta\ell - ks\cos\phi \sin\theta)}}{4\pi R} \int_{-\frac{L}{2}}^{\frac{L}{2}} e^{j(k\sin\theta\sin\phi - \beta)\eta}\, d\eta .$$

After integrating and combining the two resulting exponentials into a sine term, one obtains

$$A_y = \frac{I_o\, e^{-j(kR + \beta\ell - ks\cos\phi \sin\theta)}}{2\pi R\,[\beta - k \sin\theta \sin\phi]} \sin\frac{L}{2}\,[\beta - k \sin\theta \sin\phi] \qquad \text{(B.3)}$$

where

s = the distance the element is displaced from the origin

L = the length of the element

β = propagation factor for current wave

k = propagation factor for waves in free space.

In a similar manner, the vector potential due to a traveling wave of current on an x-directed wire is given by

$$A_x = \frac{I_o e^{-j(kR + \beta\ell - ks\cos\phi\sin\theta)}}{2\pi R[\beta - k\sin\theta\cos\phi]} \sin\frac{L}{2}[\beta - k\sin\theta\cos\phi] . \qquad (B.4)$$

In order to apply these results to the case of the square spiral, an approximation to the square spiral geometry must be made. It may be seen, in Fig. 14(a), that the geometry of the square spiral can be divided into four triangular regions and one small square region by drawing four lines which pass through the corners of the wires. If the four triangular regions are now translated so that the vertices of the triangles (points a_1, a_2, a_3, and a_4) are positioned at the same point "a" in space, the geometry of Fig. 14(b) results.

Note that this translation has eliminated the small square region at the center of the spiral. The relative translation between diametrically opposite triangles is equal to the length of the diagonal of this small square region. Since the diagonal length is equal to the spacing between the spiral wires, the translation will be small if the wires are spaced very closely together.

The geometry in Fig. 14(b) is more easily analyzed since each wire element is geometrically symmetric with respect to the axis it crosses. The current on each element in Fig. 14(b) will be assumed to be the same as on the corresponding element in Fig. 14(a).

The total vector potential for the spiral antenna may now be found by summing the contributions due to each wire element. Equations B.3 and B.4 will be altered for use in these summations.

Performance of these summations requires consideration of the direction of propagation of the current wave on each wire element. In Fig. 14(b), the current waves on

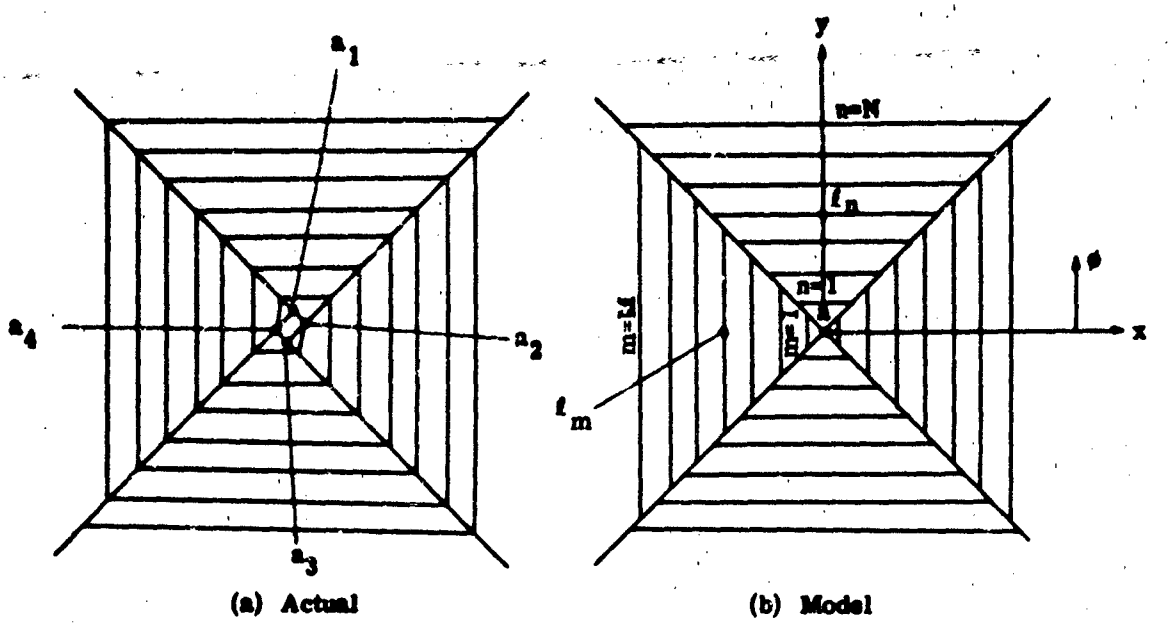

Fig. 14. Square spiral configuration.

the y-directed elements crossing the positive x-axis travel in the negative y-direction (downward). However, the waves on the elements crossing the negative x-axis travel in the positive y-direction (upward). This difference in the directions of wave propagation on y-directed elements may be considered in the y-component of the total vector potential by changing the sign of β (except in the exponential term) in Eq. B.3 when it is used for components crossing the negative x-axis. Similar considerations must be made in Eq. B.4.

The relative phase between currents on all elements must also be considered in performing the summation, hence, the factor $-j\beta\ell$. This factor may be used to adjust the phase of the current at the center of the wire element being considered. It is easily seen from Eq. B.2 that if the phase of the current at the center of the wire ($\eta = 0$) is correctly chosen, then the phase of the current at other positions along the wire ($|\eta| > 0$) will also be correct. The factor $-j\beta\ell$ will give the correct phase at the center of each wire element if ℓ is defined as the length of the spiral leg from its beginning at the center of the spiral out to the center of the element being considered. With ℓ defined in this manner, the current at the center of the mth y-directed wire element is given by

$$I_m = (-1)^{m+1} |I_m| e^{-j\beta\ell_m} ,$$

where m = 1 designates the first y-directed wire element to the right (or left) of the origin and m = M designates the y-directed element farthest to the right (or left) of the origin (see Fig. 14(b). The factor $(-1)^{m+1}$ accounts for the out-of-phase feed at the center of the spiral. Similarly, for x-directed elements, the current at the center of the nth element is

$$I_n = (-1)^{n+1} |I_n| e^{-j\beta\ell_n}$$

The only remaining alteration of Eqs. B.3 and B.4 needed to make them applicable to the spiral antenna is to change the sign of "s" (element displacement from origin) for elements crossing negative axes.

With the above alterations of Eqs. B.3 and B.4 taken into account, expressions for the total vector potentials in the x and y directions, respectively, may be formulated and are given by:

$$A_x = \sum_{n=1}^{N} (-1)^{n+1} \frac{I_n e^{-j(kR + \beta\ell_n - ks_n \sin\theta \sin\phi)}}{2\pi R(\beta - k \sin\theta \cos\phi)} \sin\frac{L_n}{2}(\beta - k \sin\theta \cos\phi)$$

$$+ \sum_{n=1}^{N} (-1)^{n+1} \frac{I_n e^{-j(kR + \beta\ell_n - ks_n \sin\theta \sin\phi)}}{2\pi R(\beta + k \sin\theta \cos\phi)} \sin\frac{L_n}{2}(\beta + k \sin\theta \cos\phi) \quad \text{(B.5)}$$

and

$$A_y = -\sum_{m=1}^{M} (-1)^{m+1} \frac{I_m e^{-j(kR + \beta\ell_m - ks_m \cos\phi \sin\theta)}}{2\pi R(\beta + k \sin\theta \sin\phi)} \sin\frac{L_m}{2}(\beta + k \sin\theta \sin\phi)$$

$$- \sum_{m=1}^{M} (-1)^{m+1} \frac{I_m e^{-j(kR + \beta\ell_m - ks_m \sin\theta \sin\phi)}}{2\pi R(\beta - k \sin\theta \sin\phi)} \sin\frac{L_m}{2}(\beta - k \sin\theta \sin\phi) \quad \text{(B.6)}$$

where

I_m = magnitude of the current on the mth element,

s_m = displacement of the mth element from the origin,

L_m = length of the mth element.

The total vector potential due to all currents on the spiral is then given by

$$\bar{A} = A_x \hat{x} + A_y \hat{y} \ . \tag{B.7}$$

$\bar{A}$ may be expressed in terms of spherical coordinates as follows:

$$\bar{A} = A_\theta \hat{\theta} + A_\phi \hat{\phi}$$

where

$$A_\theta = A_x \cos\phi \cos\theta + A_y \sin\phi \sin\theta \tag{B.8}$$

$$A_\phi = -A_x \sin\phi + A_y \cos\phi \ . \tag{B.9}$$

The electric fields are then given by:

$$E_\theta = -j\omega\mu A_\theta \tag{B.10}$$

$$E_\phi = -j\omega\mu A_\phi \ . \tag{B.11}$$

Performing the indicated operations produces the following expressions for E_θ and E_ϕ:

$$\begin{aligned} E_\theta = \frac{-j\omega\mu e^{-jkR}}{2\pi R} \Bigg[& \cos\phi\cos\theta \sum_{n=1}^{N} (-1)^{n+1} \frac{I_n e^{-j(\beta\ell_n - ks_n \sin\phi \sin\theta)}}{(\beta - k\sin\theta\cos\phi)} \sin\frac{L_n}{2}(\beta - k\sin\theta\cos\phi) \\ & + \cos\phi\cos\theta \sum_{n=1}^{N} (-1)^{n+1} \frac{I_n e^{-j(\beta\ell_n + ks_n \sin\theta \sin\phi)}}{(\beta + k\sin\theta\cos\phi)} \sin\frac{L_n}{2}(\beta + k\sin\theta\cos\phi) \\ & - \sin\phi\cos\theta \sum_{m=1}^{M} (-1)^{m+1} \frac{I_m e^{-j(\beta\ell_m - ks_m \cos\phi \sin\theta)}}{(\beta + k\sin\theta\sin\phi)} \sin\frac{L_m}{2}(\beta + k\sin\theta\sin\phi) \\ & - \sin\phi\cos\theta \sum_{m=1}^{M} (-1)^{m+1} \frac{I_m e^{-j(\beta\ell_m + ks_m \cos\phi \sin\theta)}}{(\beta - k\sin\theta\sin\phi)} \sin\frac{L_m}{2}(\beta - k\sin\theta\sin\phi) \Bigg] \end{aligned} \tag{B.12}$$

$$E_\phi = \frac{j\omega\mu e^{-jkR}}{2\pi R}\left[\sin\phi \sum_{n=1}^{N}(-1)^{n+1}\frac{I_n e^{-j(\beta\ell_n - ks_n \sin\phi \sin\theta)}}{(\beta - k\sin\theta\cos\phi)}\sin\frac{L_n}{2}(\beta - k\sin\theta\cos\phi)\right.$$

$$+ \sin\phi \sum_{n=1}^{N}(-1)^{n+1}\frac{I_n e^{-j(\beta\ell_n + ks_n \sin\theta \sin\phi)}}{(\beta + k\sin\theta\cos\phi)}\sin\frac{L_n}{2}(\beta + k\sin\theta\cos\phi)$$

$$+ \cos\phi \sum_{m=1}^{M}(-1)^{m+1}\frac{I_m e^{-j(\beta\ell_m - ks_m \cos\phi \sin\theta)}}{(\beta + k\sin\theta\sin\phi)}\sin\frac{L_m}{2}(\beta + k\sin\theta\sin\phi)$$

$$\left.+ \cos\phi \sum_{m=1}^{M}(-1)^{m+1}\frac{I_m e^{-j(\beta\ell_m + ks_m \cos\phi \sin\theta)}}{(\beta - k\sin\theta\sin\phi)}\sin\frac{L_m}{2}(\beta - k\sin\theta\sin\phi)\right] \quad \text{(P.13)}$$

It should be noted that throughout this analysis no restriction has been placed on the magnitude of the current on the spiral (I_n and I_m) except that it must be constant over the length of any individual wire element. Magnitude adjustments may be made between successive wire elements, however, and these adjustments may follow a certain mathematical relationship. A logical choice for this relationship would be a current magnitude which attenuates only slightly until the "radiation region" of the spiral is reached, and thereafter, attenuates at a greater rate. The expression

$$\left|I_m\right| = \frac{I_o}{1 + e^{-a(\ell - \ell_m)}}$$

has these characteristics and was used in computing field patterns.

THE EQUIVALENT RADIUS OF ARBITRARILY SHAPED ANTENNAS

By
Charles W. Su
Northrop Corporation
Norair Division
Hawthorne, California

Presented at the Fourteenth Annual Symposium on Antenna Research and Development
at
Monticello Facility
University of Illinois
6-8 October 1964

INTRODUCTION

General procedures for determining the equivalent radius of uniform antennas with arbitrary cross-sections are described. Once the equivalent radius is known, it is possible to make use of the published literature for cylindrical antennas to determine the input impedance.

The equivalent radius of a uniform antenna with non-circular cross-section was suggested by Eric Hallén [1]. Hallén stated that antennas with non-circular cross-sections could be examined mathematically by considering them to be cylindrical in shape and to have an equivalent radius. Once the equivalent radius is known, it is possible to make use of the published literature for cylindrical antennas to determine the input impedance. Hallén advanced the theory that the equivalent radius of an antenna with non-circular cross-section was equal to the radius of a circular antenna, which in conjunction with a larger concentric circular cylinder had the same capacitance.

However, Hallén's technique becomes difficult to apply when the shape is not conformably mapable to a circle, which is possible only for a limited number of classical configurations. Shintaro Uda and Yasuto Mushiake [2] used a different theory from that of Hallén and derived an approximate expression for the equivalent radius given by:

$$\log_e \rho \cong \frac{1}{a^2} \oint_c \oint_c \log_e d(s, s_1)\, ds_1 ds$$

where: ρ = equivalent radius

$d(s, s_1)$ = direct distance between two points s and s_1, taken on the closed periphery c of the cross-section.

a = length of the closed curve c.

The equivalent radius as derived by the approximate expression of Uda and Mushiake has been compared analytically and numerically with the equivalent radius found using Hallén's method on a few arbitrary shapes. These two methods give equivalent radii which differ by approximately 0.15 to 5.0 percent in the cases investigated.

Measurements have been made on the arbitrary shapes presented in this paper (Figures 4, 5, 6) and reasonably good agreement has been found between the input impedance of the noncircular antenna and the cylindrical antenna of the equivalent radius over a frequency range from below the first resonance to above the second resonance.

EQUIVALENT RADIUS OF ELLIPTICAL CONDUCTOR

Hallén's method will be used as an example for the derivation of the equivalent radius of an elliptical conductor.

Consider an elliptical conductor of major axis a and minor axis b with zero potential concentric with a circular cylinder of radius R with potential ϕ_0 as shown in Figure 1. The equation for the ellipse is:

$$\frac{x'^2}{\left(\frac{a^2}{c^2}\right)} + \frac{y'^2}{\left(\frac{b^2}{c^2}\right)} = 1 \qquad (1)$$

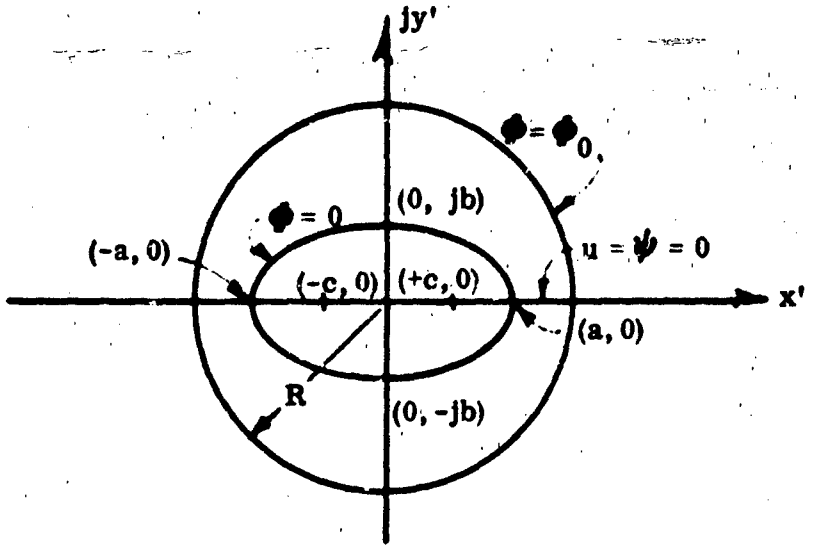

Figure 1 - Elliptical Conductor Concentric with a Circular Cylinder

Let $\cosh^2 v = \frac{a^2}{c^2}$ and $\sinh^2 v = \frac{b^2}{c^2}$

Equation (1) approaches a circle as v approaches π. Let v be $\frac{\pi}{n}$, where n is a number larg 1, then

$$\frac{\pi}{n} = \tanh^{-1} \frac{b}{a} .$$

From inverse cosine transformation and the boundary conditions, we obtain

$$\phi_o = C_1 \pi + C_{2i} ,$$

where

$$C_1 = n \phi_o / \pi (n - 1)$$

and

$$C_{2i} = \phi_o / (n - 1)$$

It follows then:

$$\left.\begin{aligned} x' &= c \cos\left[\frac{\pi (n-1)}{n \phi_o} u'\right] \cosh\left[\frac{\pi (n-1)}{n \phi_o} \left(\frac{\phi_o}{n-1} + v'\right)\right] \\ y' &= -c \sin\left[\frac{\pi (n-1)}{n \phi_o} u'\right] \sinh\left[\frac{\pi (n-1)}{n \phi_o} \left(\frac{\phi_o}{n-1} + v'\right)\right] \end{aligned}\right\} \quad (2)$$

or

$$\frac{x'^2}{c^2 \cosh^2\left[\frac{\pi(n-1)}{n\phi_o}\left(\frac{\phi_o}{n-1}+v'\right)\right]}+\frac{y'^2}{c^2 \sinh^2\left[\frac{\pi(n-1)}{n\phi_o}\left(\frac{\phi_o}{n-1}+v'\right)\right]}=1.$$

When

$$\frac{\pi(n-1)}{n\phi_o}\left(\frac{\phi_o}{n-1}+v'\right)=\frac{\pi}{n}\left[1+\frac{(n-1)\,v'}{\phi_o}\right]\gg 1,$$

$$c^2 \cosh^2\frac{\pi}{n}\left[1+\frac{(n-1)\,v'}{\phi_o}\right]\approx c^2 \sinh^2\frac{\pi}{n}\left[1+\frac{(n-1)\,v'}{\phi_o}\right]. \quad (3)$$

For this case, equation (3) is equal to R^2 as $v' = \phi_o$.

Therefore

$$R = c \cosh\frac{\pi}{n}\left[1+\frac{(n-1)\phi_o}{\phi_o}\right] = c \cosh \pi . \quad (4)$$

The total flux between the two conductors is

$$Q = 2\pi\epsilon C_1 = \frac{2\pi\epsilon n\phi_o}{\pi(n-1)} = \frac{2n\epsilon\phi_o}{n-1} . \quad (5)$$

an

The capacitance between the two conductors is then:

$$\text{Capacitance} = \frac{Q}{\phi_o} = \frac{2n\epsilon}{n-1} . \quad (6)$$

The capacitance for coaxial cylinders of radii ρ and R is:

$$\text{Capacitance of coax.} = \frac{2\pi\epsilon}{\log_e \frac{R}{\rho}} . \quad (7)$$

The equivalent radius of an antenna with noncircular cross-section is equal to the radius of a circular antenna, which in conjunction with a larger concentric circular cylinder, has the same capacitance. So equating (6) and (7), ρ will be the equivalent radius of the elliptical conductor:

$$\rho = c(\cosh \pi) \Big/ e^{\left(\frac{\pi(n-1)}{n}\right)} \quad (8)$$

Substituting

$$n = \pi \Big/ \tanh^{-1}\left(\frac{b}{a}\right) ,$$

we obtain

$$\rho = \frac{\cosh \pi}{e^{\pi}}\, c e^{\tanh^{-1}\left(\frac{b}{a}\right)} . \quad (9)$$

But when $x > 3$, $\cosh x = \frac{1}{2} e^x$ correct to three significant figures.

Therefore

$$\rho = \frac{c}{2} e^{\tanh^{-1} \frac{b}{a}} \qquad (10)$$

Applying the definition of hyperbolic tangent

$$\tanh x = (e^{x} - e^{-x}) / (e^{x} + e^{-x})$$

equation (10) becomes:

$$\rho = \frac{a + b}{2} . \qquad (11)$$

Equation (11) is the expression for the equivalent radius of an elliptical conductor with major ax. and minor axis b.

When either the major axis or the minor axis of the elliptical conductor shrinks to zero, th elliptical conductor will become a thin flat strip. If the minor axis shrinks to zero, equation (11) becomes:

$$\rho = \frac{a}{2} , \quad \text{or} \quad \rho = 0.25 \text{ (width)} \qquad (12)$$

This is the equivalent radius of a thin flat strip. The result is in agreement with a previous inv gation [3]. If a = b = r, the ellipse will then become a circle with radius r. From equation (11) a = b = r:

$$\rho = \frac{2r}{2} = r$$

It is observed that the equivalent radius is equal to the radius of the circle.

ARBITRARY GEOMETRIES

For those geometries which are not easily conformably mapable Hallén's method becomes difficult to apply and other techniques must be employed. In the shapes which follow, the expres of Uda and Mushiake has been used. The integral can be evaluated analytically for cross-sectio of straight line elements. A few examples are shown below.

Antenna With L-Shaped Cross-Section (Figure 2a)

$$\rho \cong a e^{\mu(\eta)}$$

$$\mu(\eta) = \frac{1}{(1+\eta)^2} \left[-\frac{3}{2} (1+\eta)^2 + \eta^2 \log_e(\eta) + \eta \log_e(1+\eta^2) + \tan^{-1}(\eta) + \eta^2 \tan^{-1}\left(\frac{1}{\eta}\right) \right] .$$

Antenna With T-Shaped Cross-Section (Figure 2b)

$$\rho \cong a^{4p} b^{p} \eta^2 (a^2 + b^2)^{2p\eta} e^{\mu(\eta)} .$$

$$p = 1/(2+\eta)^2$$

$$\mu(\eta) = \frac{1}{(2+\eta)2}\left[\tan^{-1}(\eta) + \eta^2 \tan^{-1}\left(\frac{1}{\eta}\right) - 6 - \frac{3}{2}\eta^2 - 6\eta + 4\log_e(2)\right].$$

Antenna With Cross-Shaped Cross-Section (Figure 2c)

$$\rho \cong a^p b^{p\eta^2} (a^2 + b^2)^{p\eta} e^{\mu(\eta)}$$

$$p = 1/(1+\eta)^2$$

$$\mu(\eta) = \frac{1}{2(1+\eta)^2}\left[2(1+\eta^2)\log_e(2) + 2\tan^{-1}(\eta) + 2\eta^2 \tan^{-1}\left(\frac{1}{\eta}\right) - 3(1+\eta)^2\right].$$

Antenna With U-Shaped Cross-Section (Figure 2d)

$$\rho \cong a^p b^{2p\eta^2} (a^2 + b^2)^{p\eta(\eta+2)} e^{\mu(\eta)}$$

$$p = 1/(1+2\eta)^2$$

$$\mu(\eta) = \frac{1}{2(1+2\eta)^2}\left[4\tan^{-1}(\eta) + 8\eta\tan^{-1}(\eta) + 4\eta^2 \tan^{-1}\left(\frac{1}{\eta}\right) - 3(1+2\eta)^2\right].$$

Antenna With H-Shaped Cross-Section (Figure 2e)

$$\rho \cong a^p b^{8p\eta^2} (a^2 + b^2)^{4p\eta} (a^2 + 4b^2)^{4p\eta^2} e^{\mu(\eta)}$$

$$p = 1/(1+4\eta)^2$$

$$\mu(\eta) = \frac{1}{2(1+4\eta)^2}\left[16\eta\tan^{-1}(2\eta) + 8\eta^2 \tan^{-1}\left(\frac{1}{\eta}\right) + 8\tan^{-1}(\eta) - 3(1+4\eta)^2 + 8\eta^2\log_e(4)\right].$$

Antenna With Hat-Shaped Cross-Section (Figure 2f)

$$\rho \cong e^{\mu}$$

$$\mu = \frac{1}{16(a+b+c)^2}\left\{-24a^2 - 24b^2 - 24c^2 + 4a^2\log_e(a^2) - 48ab - (8b^2 - 16c^2)\log_e(4c^2 + b^2) + 32bc\tan^{-1}\left(\frac{b}{2c}\right) - 48ac + 8a^2\tan^{-1}\left(\frac{b}{a}\right) + (8ab + 4b^2 - 4a^2)\log_e(a^2 + b^2) - 48bc\right.$$

$$+ (8b^2 - 16ab) \tan^{-1} \left(\frac{a}{b}\right) - 32bc \tan^{-1} \left(\frac{2c}{b}\right) + 16c^2 \log_e (4c^2)$$

$$+ (16a^2 + 32ac + 16c^2) \log_e (2a + 2c) + 8 (2c + a)^2 \tan^{-1} \left(\frac{b}{2c + a}\right)$$

$$- (32c^2 + 32ac + 8a^2) \log_e (2c + a) + 8b (a + 2c) \log_e \left[b^2 + (a + 2c)^2 \right]$$

$$+ (16ac + 16c^2 + 4a^2 - 4b^2) \log_e \left[b^2 + (a + 2c)^2 \right] + 16ab \tan^{-1} \left(\frac{a + 2c}{b}\right)$$

$$+ (32bc + 8b^2) \tan^{-1} \left(\frac{a + 2c}{b}\right) \Bigg] .$$

Antenna With Rectangular Cross-Section (Figure 2g)

$$\rho \cong a^p b^{p\eta^2} (a^2 + b^2)^{\left(\frac{1}{4} + p\eta\right)} e^{\mu(\eta)}$$

$$p = 1/2(1 + \eta)^2$$

$$\mu(\eta) = \frac{1}{4(1 + \eta)^2} \left[4 \tan^{-1} (\eta) + 4\eta^2 \tan^{-1} \left(\frac{1}{\eta}\right) + 2\pi\eta - 6 (1 + \eta)^2 \right] .$$

Antenna Made From Two Circular Cylinders in Parallel (Figure 2h)

$$\rho \cong R^{\left[\frac{1 + \eta^2}{(1 + \eta)^2}\right]} \eta^{\left[\frac{\eta 2}{(1 + \eta)^2}\right]} D^{\left[\frac{2\eta}{(1 + \eta)^2}\right]}$$

Antenna Made From Two Flat Strips in Parallel (Figure 2i)

$$\rho \cong e^{\mu} .$$

$$\mu = \frac{1}{16b^2} \left[- 24b^2 + 4b^2 \log_e (b^2) + 4b^2 \log_e (4c^2 + b^2) \right.$$

$$\left. + 32bc \tan^{-1} \left(\frac{b}{2c}\right) \right] .$$

or

$$\mu = \frac{1}{16a^2} \left[- 24a^2 + 4a^2 \log_e (a^2) + 16c^2 \log_e (2c) \right.$$

$$+ (16a^2 + 32ac + 16c^2) \log_e (2a + 2c) - 32c^2 \log_e (2c + a)$$

$$\left. - (32ac + 8a^2) \log_e (2c + a) \right] .$$

Antenna Made From Two Angle Strips in Parallel (Figure 2j)

$$\rho \cong e^{\mu}$$

$$\mu = \frac{1}{16(a+b)^2}\Big\{ -24a^2 + 4a^2 \log_e (a^2) + 16c^2 \log_e (2c)$$

$$+ (16a^2 + 32ac + 16c^2) \log_e \left[2 (a + c)\right] - 24b^2 - 48ab$$

$$- (32c^2 + 32ac + 8a^2) \log_e (2c + a) + 4b^2 \log_e (b^2)$$

$$+ 4b^2 \log_e (4c^2 + b^2) + 32bc \tan^{-1} (\tfrac{b}{2c}) - 32c^2 \tan^{-1} (\tfrac{b}{2c})$$

$$+ 8ab \log_e (a^2 + b^2) + 8a^2 \tan^{-1} (\tfrac{b}{a}) + 8b^2 \tan^{-1} (\tfrac{a}{b})$$

$$- 8b^2 \tan^{-1} (\tfrac{2c}{b}) - 16bc \log_e (4c^2 + b^2) + 8ab \log_e \left[(2c + a)^2\right.$$

$$\left. + b^2\right] + 16bc \log_e \left[(2c + a)^2 + b^2\right] + 8 (2c + a)^2 \tan^{-1} (\tfrac{b}{2c + a})$$

$$+ 8b^2 \tan^{-1} (a + 2c)/b \Big\} .$$

Antenna Made From Three Circular Cylinders in Parallel (Figure 2k)

$$\rho \cong e^{\mu}$$

$$\mu = \frac{1}{(1 + \eta_2 + \eta_3)^2}\Big[\log_e R + \eta_2^2 \log_e (\eta_2 R) + \eta_3^2 \log_e (\eta_3 R)$$

$$+ 2\eta_2 \log_e (D_{12}) + 2\eta_2\eta_3 \log_e (D_{23}) + 2\eta_3 \log_e (D_{31}) \Big] .$$

If

$$D_{12} = D_{23} = D_{31} = D$$

$$\rho \cong \eta_2 \left[\frac{\eta_2^2}{(1 + \eta_2 + \eta_3)^2}\right]_{\eta_3} \left[\frac{\eta_3^2}{(1 + \eta_2 + \eta_3)^2}\right] \times$$

$$D\left[\frac{2(\eta_2 + \eta_3 + \eta_2\eta_3)}{(1 + \eta_2 + \eta_3)^2}\right]_R \left[\frac{1 + \eta_2^2 + \eta_3^2}{(1 + \eta_2 + \eta_3)^2}\right] .$$

when $\eta_2 = 1$, $\eta_3 = \eta$

$$\rho \cong \eta^{\left[\frac{\eta^2}{(2+\eta)^2}\right]_D \left[\frac{2(1+2\eta)}{(2+\eta)^2}\right]_R \left[\frac{2+\eta^2}{(2+\eta)^2}\right]} .$$

When $r_1 = r_2 = r_3 = R$, $D_{12} = D_{23} = D_{31} = D$

$$\rho \cong (D^2 R)^{\frac{1}{3}}$$

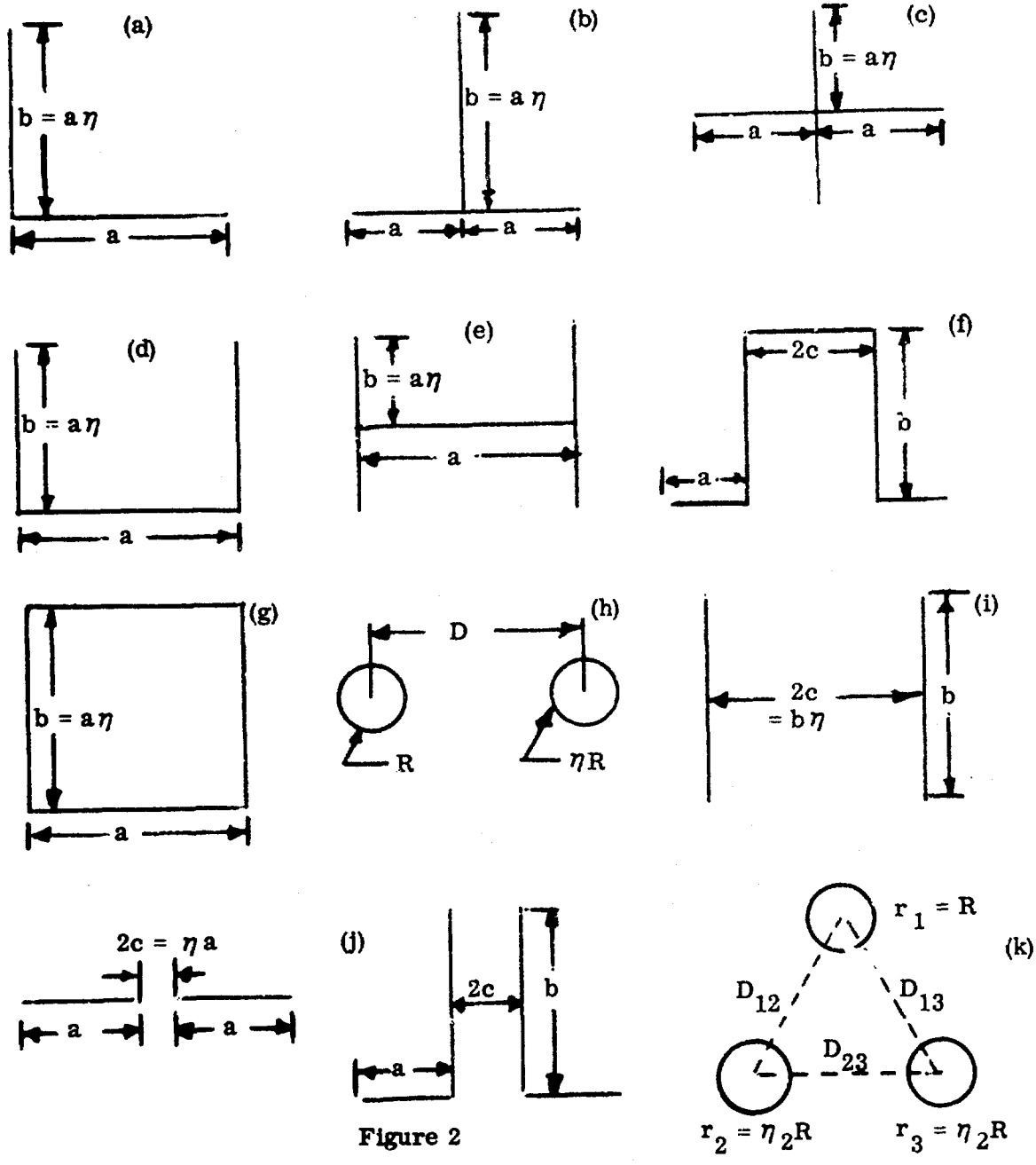

Figure 2

Antennas With Arbitrary Cross-Section

By applying numerical analysis techniques, Uda's method has been extended to geometrical cross-sections of arbitrary shapes. For the airfoil section shown in Figure 3, $\rho = 1.29$.

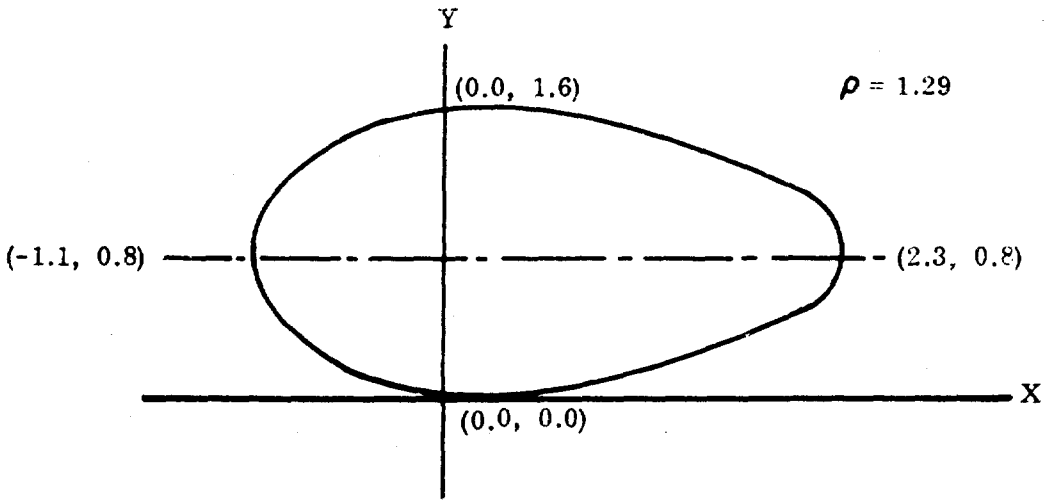

X	0.0	0.8	1.08	0.5	-0.32	-1.11	-1.87	-2.16	-1.42	-0.64
Y	0.0	0.25	0.96	1.5	1.6	1.43	1.15	0.63	0.3	0.07

Figure 3 Air Foil Cross-Section

EXPERIMENTAL MEASUREMENTS

Experimental results obtained for three of the cross-sectional shapes of Figure 2 are shown in Figures 4, 5 and 6, along with measurements on cylinders of the same equivalent radius. The agreement is good.

REFERENCES

1. Eric Hallén, "Theoretical Investigation into the Transmitting and Receiving Qualities of Antennas", Nova Acta Regiae Soc. Sci. Upsaliensis, Ser. IV, 11, No. 4. 1-44, 1938.

2. Shintaro Uda and Yasuto Mushiake, "Yagi-Uda Antenna", Sasaki Printing and Publishing Company, Ltd., Sendai, Japan, 1955.

3. John D. Kraus, "Antennas", McGraw-Hill Book Company, Inc., 1950, p. 238.

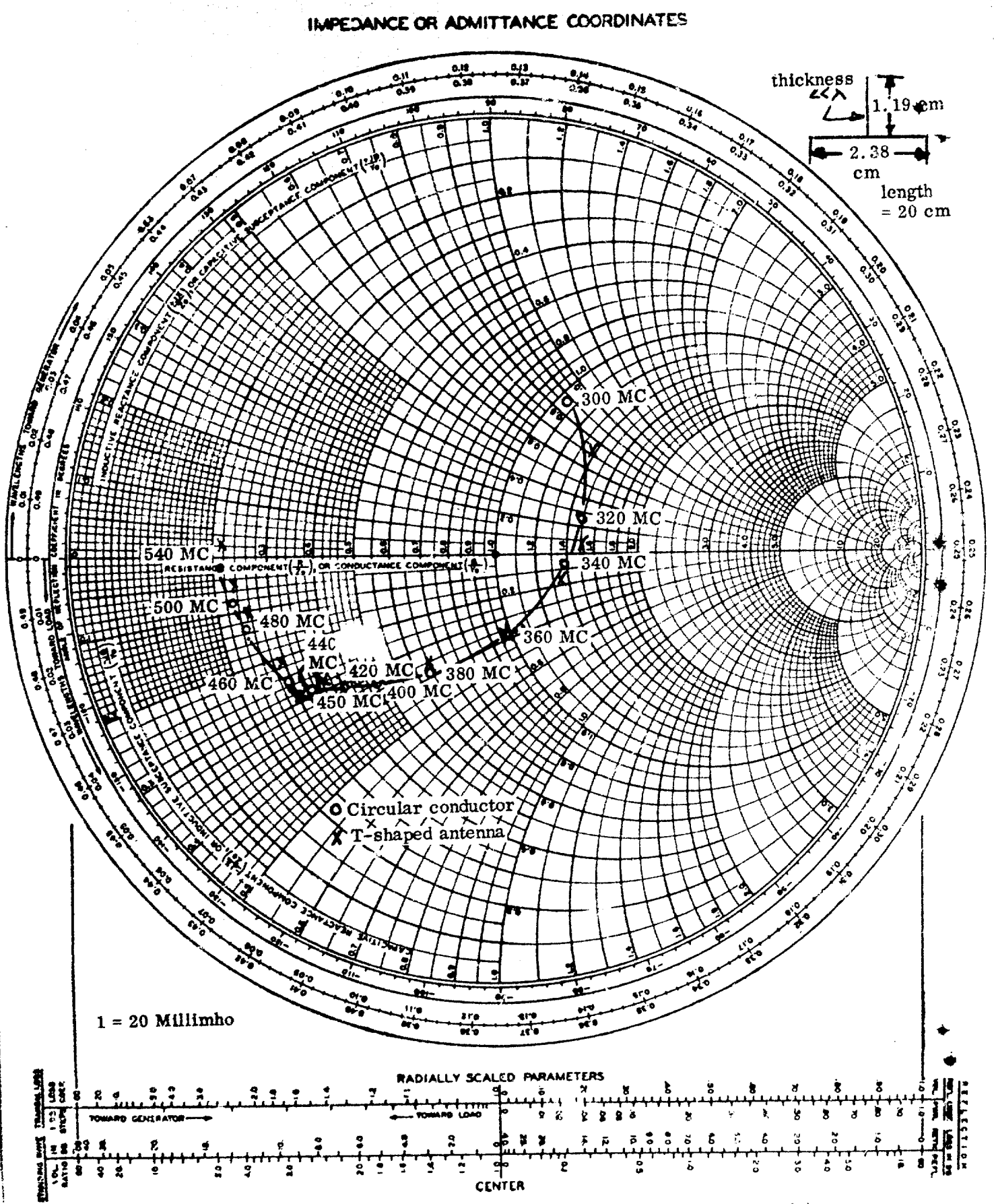

Figure 4. Measured Feed Point Admittance of Circular Conductor and T-shaped Antenna

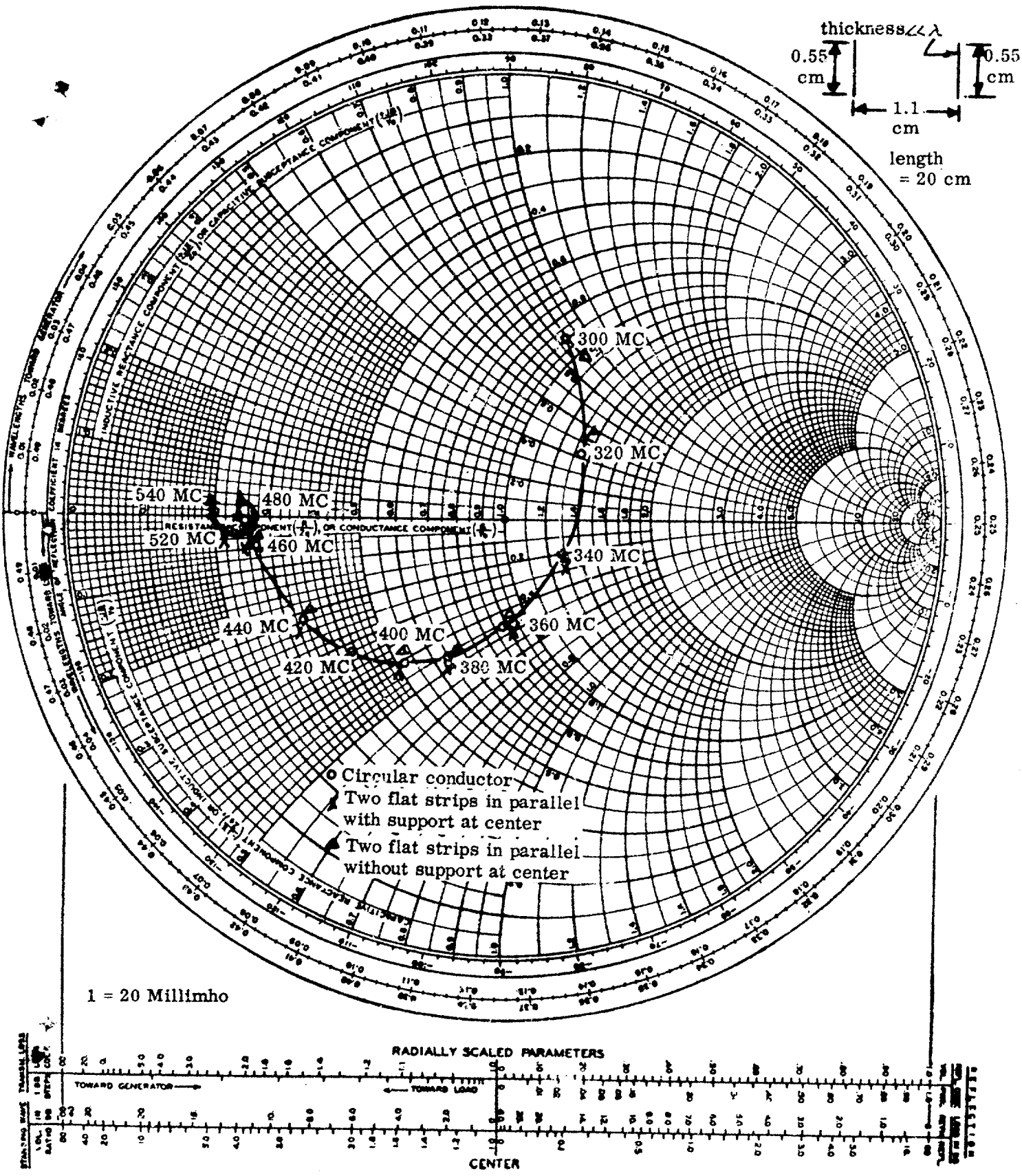

Figure 5. Measured Feed Point Admittance of Circular Conductor and Two Flat Strips in Parallel.

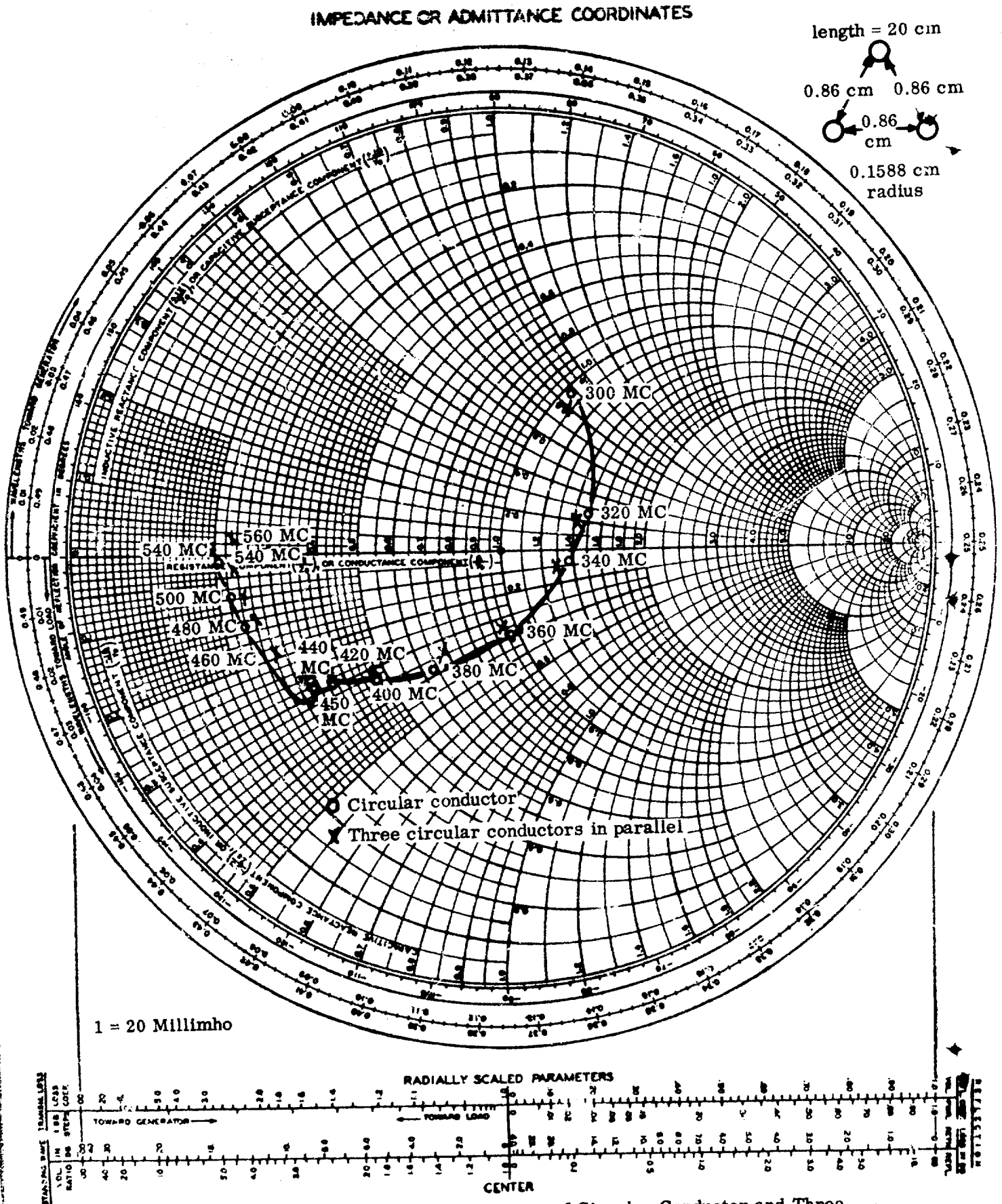

Figure 6. Measured Feed Point Admittance of Circular Conductor and Three Circular Conductors in Parallel.

TRANSVERSE FOCAL REGION PROPERTIES OF A SPHERICAL REFLECTOR

Geoffrey Hyde

Radio Corporation of America
Defense Electronic Products
Moorestown, New Jersey

TRANSVERSE FOCAL REGION PROPERTIES OF A SPHERICAL REFLECTOR

Geoffrey Hyde

Radio Corporation of America
Defense Electronic Products
Moorestown, New Jersey

Introduction

This paper is concerned with the possibilities of feeding large spherical reflectors with a feed system transverse to the axis of the antenna, in situations requiring limited electronic scanning. The work has largely been supported by the Air Force Cambridge Research Laboratories under AF19(628)2758, "Transverse Antenna Feeds". Support has also come from RCA in connection with research for an antenna for multiple target radar systems (MUTAR). It is the purpose of this work to develop a transverse feed system that corrects for aberrations and permits scanning.

Research on spherical reflectors has been going on for some time [1,2]. This effort arose from ideas put forward by Carl Sletten [3], Chief of the Microwave Physics Laboratory, AFCRL, and was supervised in its first year by Roy C. Spencer who has contributed heavily to the program, especially the geometric optics analysis. The study to date has completed work on geometric optics, [4,5] and polarization [6]. Evaluation of focal region fields and the feed problem are the present areas of endeavor.

Geometric Optics

The sphere is the simplest of all three-dimensional surfaces because its radius of curvature is constant. Consequently, it has no preferential direction as do the paraboloid and the ellipsoid and every radius (or normal) passes through its center and is an axis of symmetry. This is the property that attracts our attention in scanning applications.

Consider a parallel pencil of rays incident on the concave side of a spherical cap as in Figure 1. Let the ray through the center 0 of the sphere, the central ray, be the axis. For any incident ray, the law of reflection states, (a) that the reflected ray lies in the plane of incidence (the plane containing the normal to the surface, OB and the incident ray AB), and (b) that the angle of reflection equals the angle of incidence. The plane of incidence therefore contains the center, which lies on the normal as well as the axis, and intersects the sphere in a great circle. It follows that (a) all problems of reflection of a single ray reduce to that of reflection from a circle; and (b) all reflected rays intersect the axis. There can therefore be no skew rays (rays that miss the axis), as there are in the off-axis illumination of the paraboloid. It further follows that all incoming linearly polarized waves are treated alike.

Incoming rays parallel to and very near the ray passing through the center of the sphere pass through a focus F called the paraxial focus located half-way from the

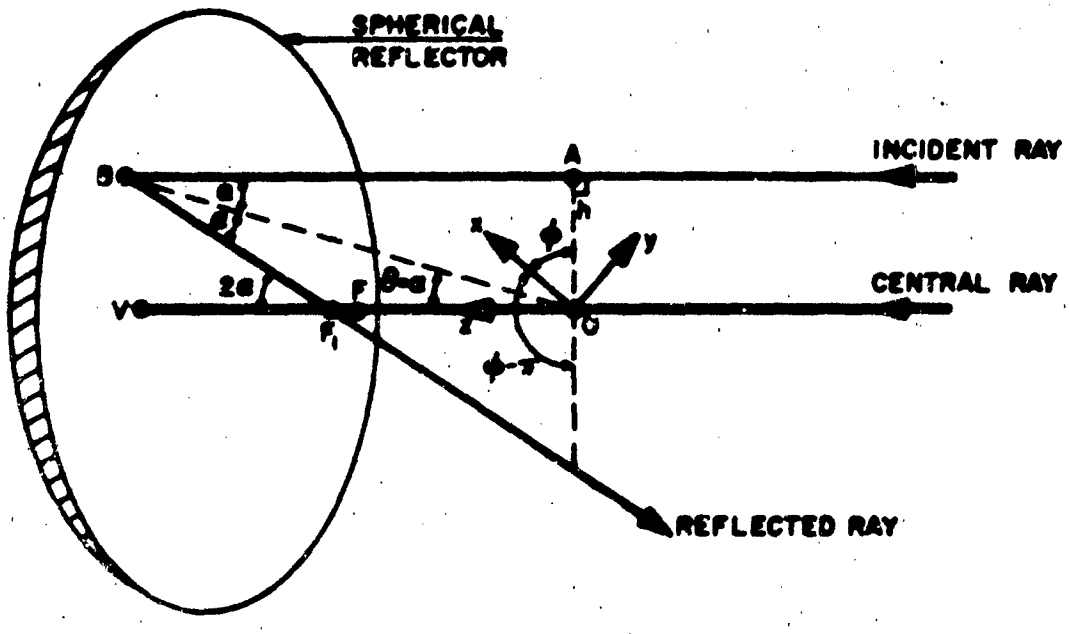

Figure 1. Spherical Cap and Incident and Reflected Ray

center of curvature to the spherical reflector. In general, for any doubly curved reflector all reflected rays are tangent to two caustic surfaces. A caustic is defined as the envelope of reflected (or refracted) rays as the position of the point of incidence is varied. A sphere has two caustics, the axial caustic lying along the central ray, and the caustic surface discussed below.

Let us now consider a family of parallel rays, i.e., a bundle of rays, traced through reflection from a spherical reflector. A plane section is shown in Figure 2. It is evident that the reflected rays fold into a sort of a fan whose envelope is densely populated by rays. This is the caustic curve. It is formed by the crossing of adjacent rays in a plane. In Figure 3, we have drawn a spherical reflector with three rays incident on it. These are the central ray or axial ray, and the edge rays or marginal rays. For our purposes the marginal ray is the outermost ray that is properly reflected. It is characterized by the maximum allowable value of h, h_{max} and the maximum angle of incidence $\alpha_{max} = \theta_{max}$. The axial caustic, the caustic surface and the paraxial focus are all indicated and have been previously discussed. Every ray is tangent to the caustic surface. In particular the marginal rays are tangent at the points M_1. $M_1 M_1$ is termed the marginal focus. The marginal rays intersect on the axis at F_1 and then intersect the caustic surface a second time at the points C_1. The circle of diameter $C_1 C_1$, "the circle of least confusion", is the smallest circle that contains all the rays. For our purposes the region lying between the caustic surfaces and between the paraxial focus and the marginal focus is the focal region, and it is here that we must concentrate our efforts.

Of the properties of rays of interest in this study, perhaps the decisive one is optical path-length. Path-length enters into the expressions of wave theory as phase, and thus into the evaluation of that theory. Figure 4 shows portions of concentric spherical surfaces of radii R and r_p. A ray AB parallel to the axis OV is reflected

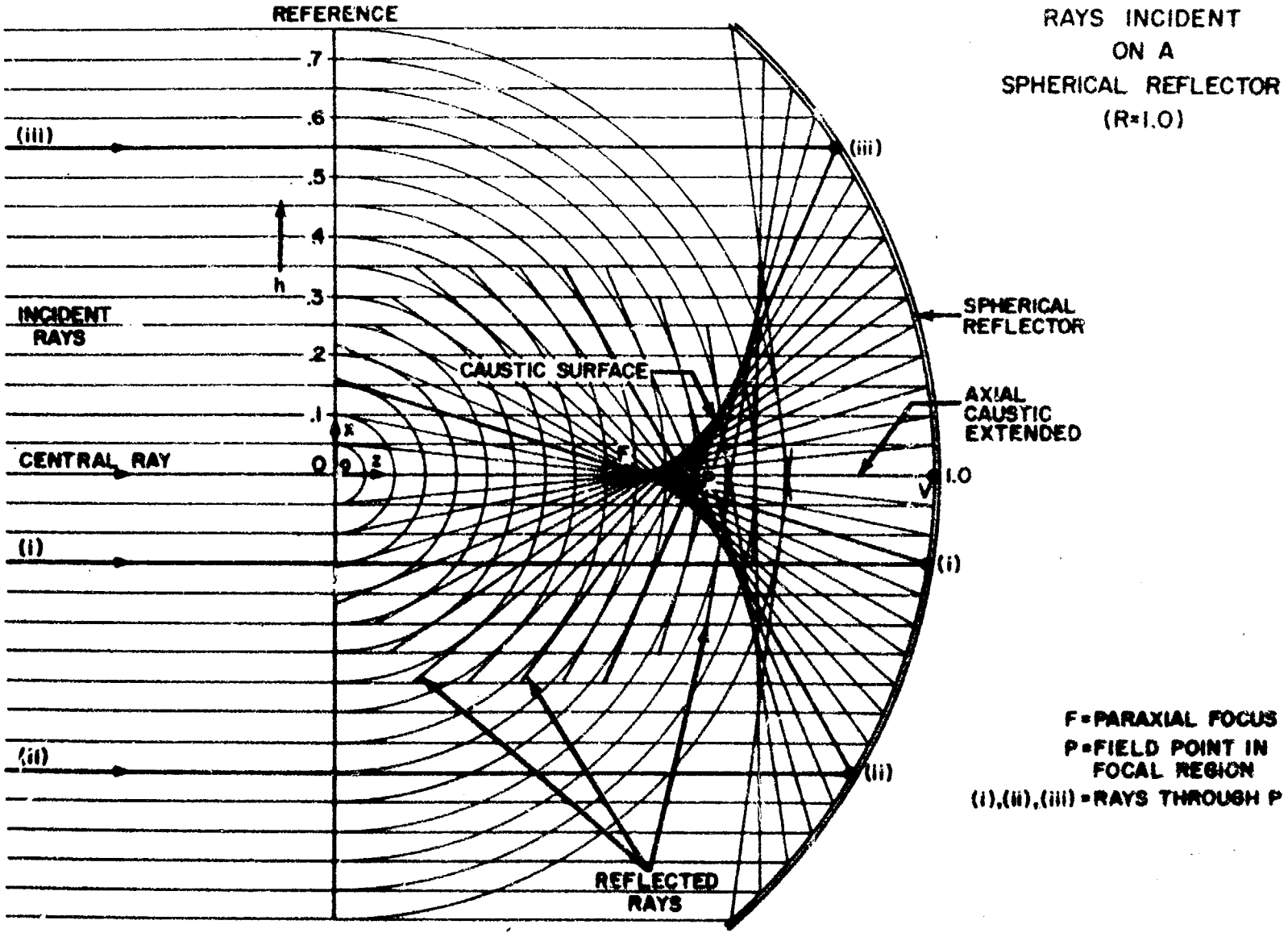

Figure 2. Caustic by Geometric Ray Tracing

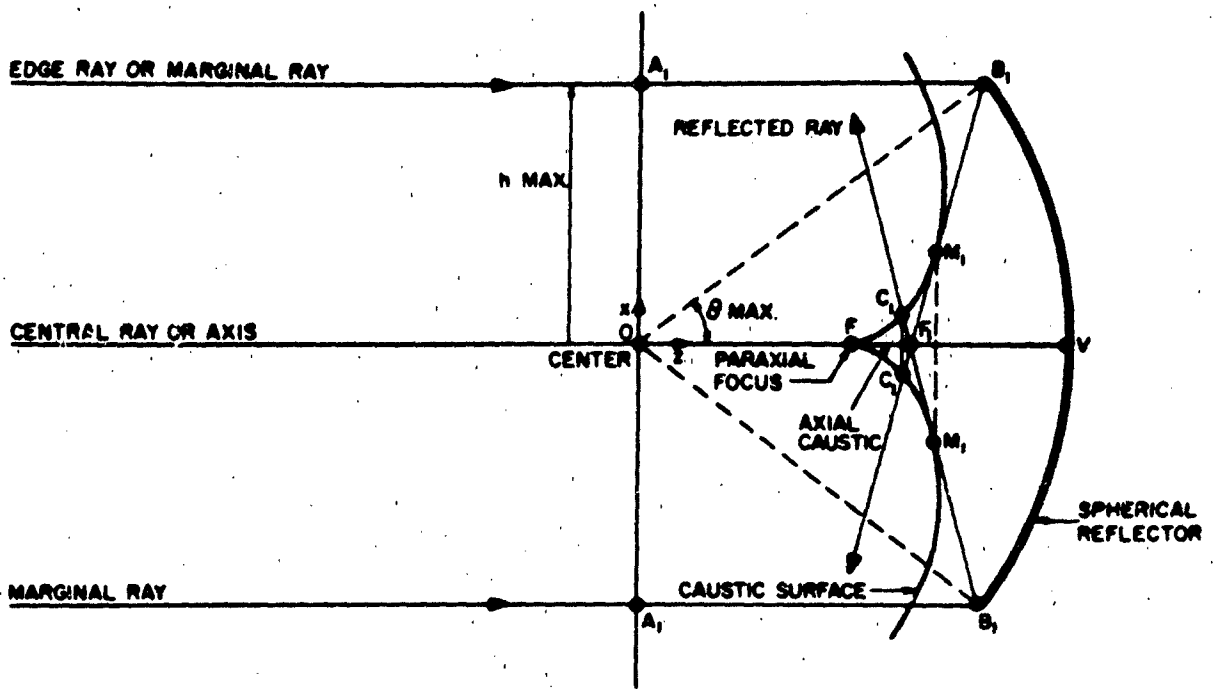

Figure 3. Focal Region of a Sphere

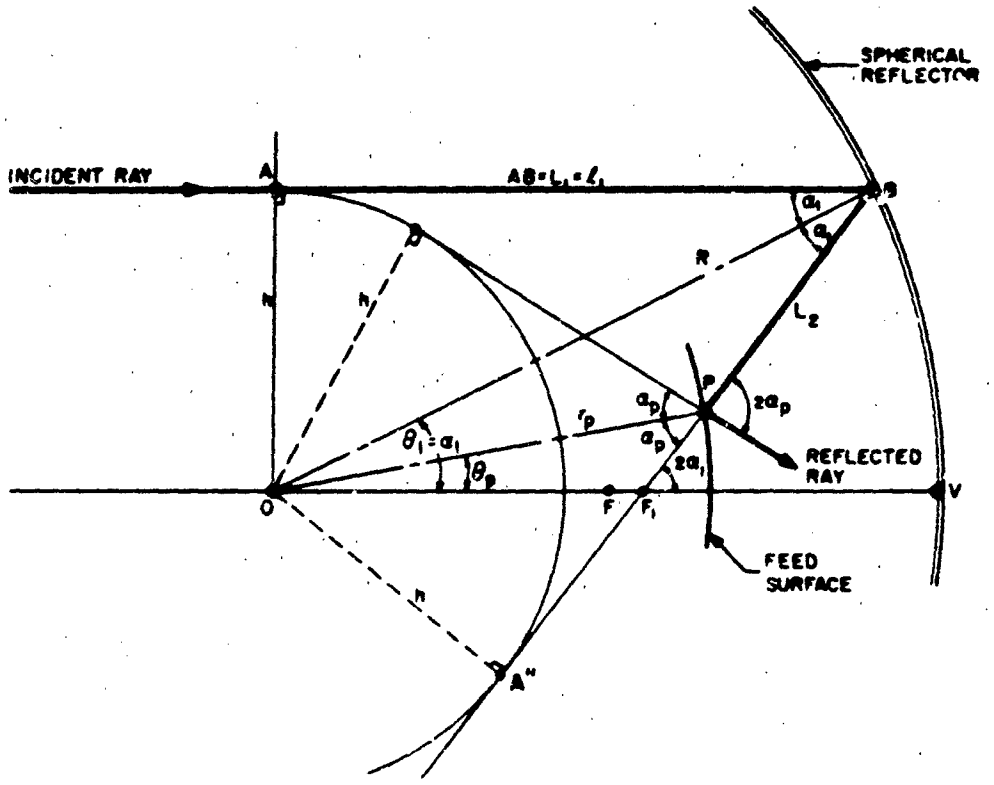

Figure 4. Reflection from Two Concentric Spheres

at B on the spherical reflector and is incident at P on the second surface. Computationally, it proves useful to normalize all lengths with respect to R. Thus the computations done for the single reflector feed surface case were made using the formulas below, all of which may be derived from Figure 4.

$$L = 2\ell_1 - \ell_p$$

$$\theta = 2\sin^{-1} h - \sin^{-1}\frac{h}{r_p}$$

where

$$\ell_1 = (1-h^2)^{1/2}$$

$$\ell_p = (r_p^2 - h^2)^{1/2}$$

The plot of L against h (Figure 5) has even symmetry about $h=0$, and the slope of the curves is always zero at $h=0$, the axial caustic, but has other stationary values only for $r_p > 0.50$ which mark the locus of the caustic surface. Figure 6 shows the graphs of θ vs h, which have odd symmetry. This means that there are up to three rays which pass through some field points (r_p, θ_p). The stationary points denote the caustic surface. Curves for L vs θ_p were plotted (Figure 7). Almost all the properties seen in the other curves are to be found in these "fish tails". The cusps of the "fish tail" mark the caustic surface. A line of constant θ_p has up to three intersections with a curve for constant r_p, denoting the three rays through a field point. Note that for reflectors of radii 150 to 300 wavelengths, a change of 0.01 in L on the graphs may be a change 1.5 to 3 wavelengths, or 500° to 1000° of phase. If one considers 90° to be important, changes in the fourth significant figure of normalized path-length are worthy of note.

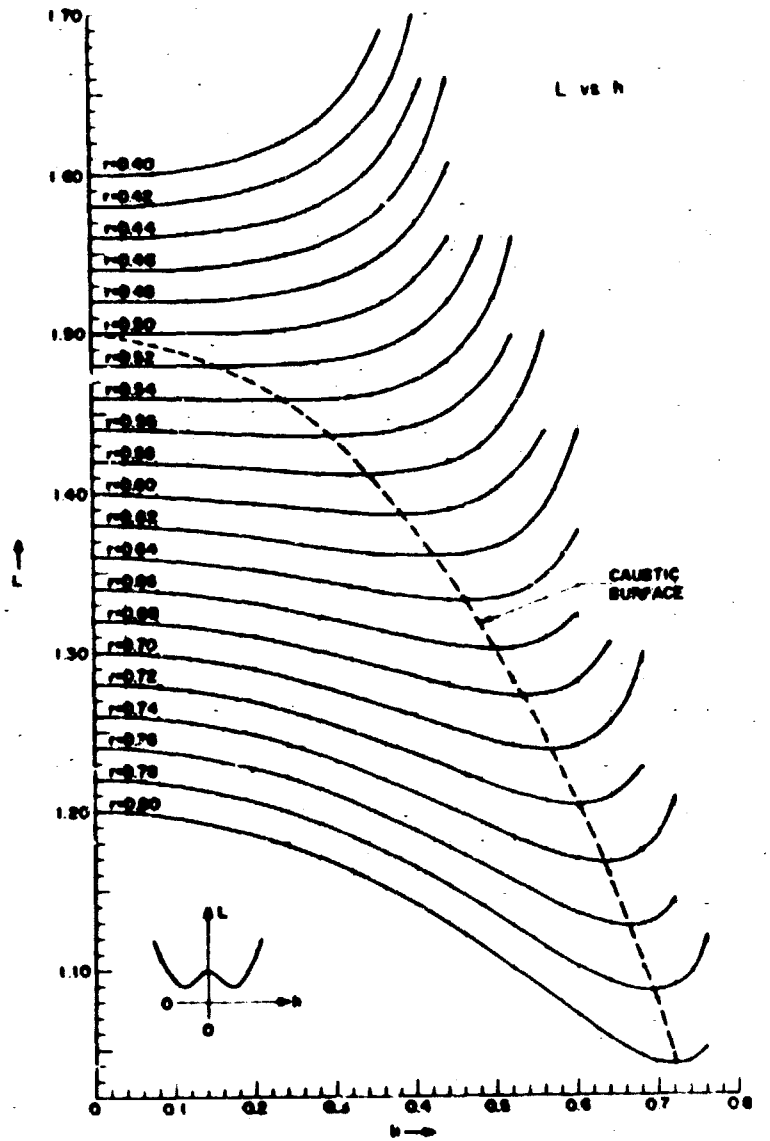

Figure 5. Path-Length versus h

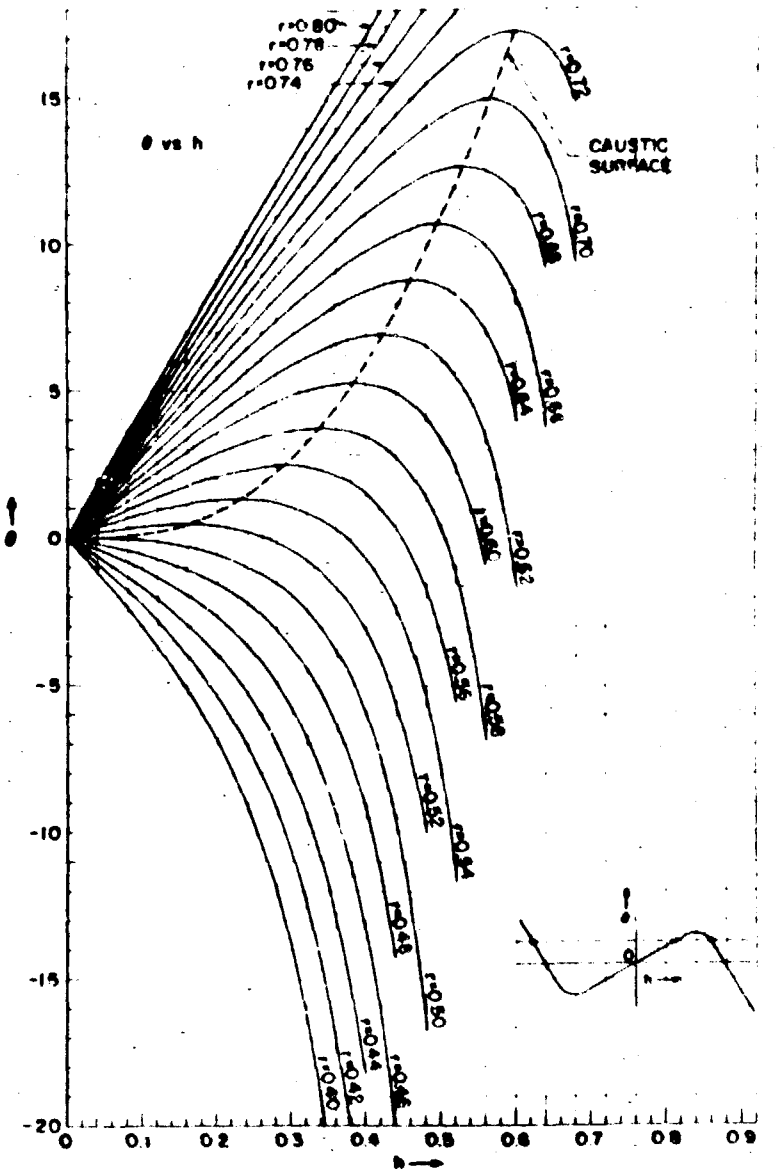

Figure 6. θ versus h

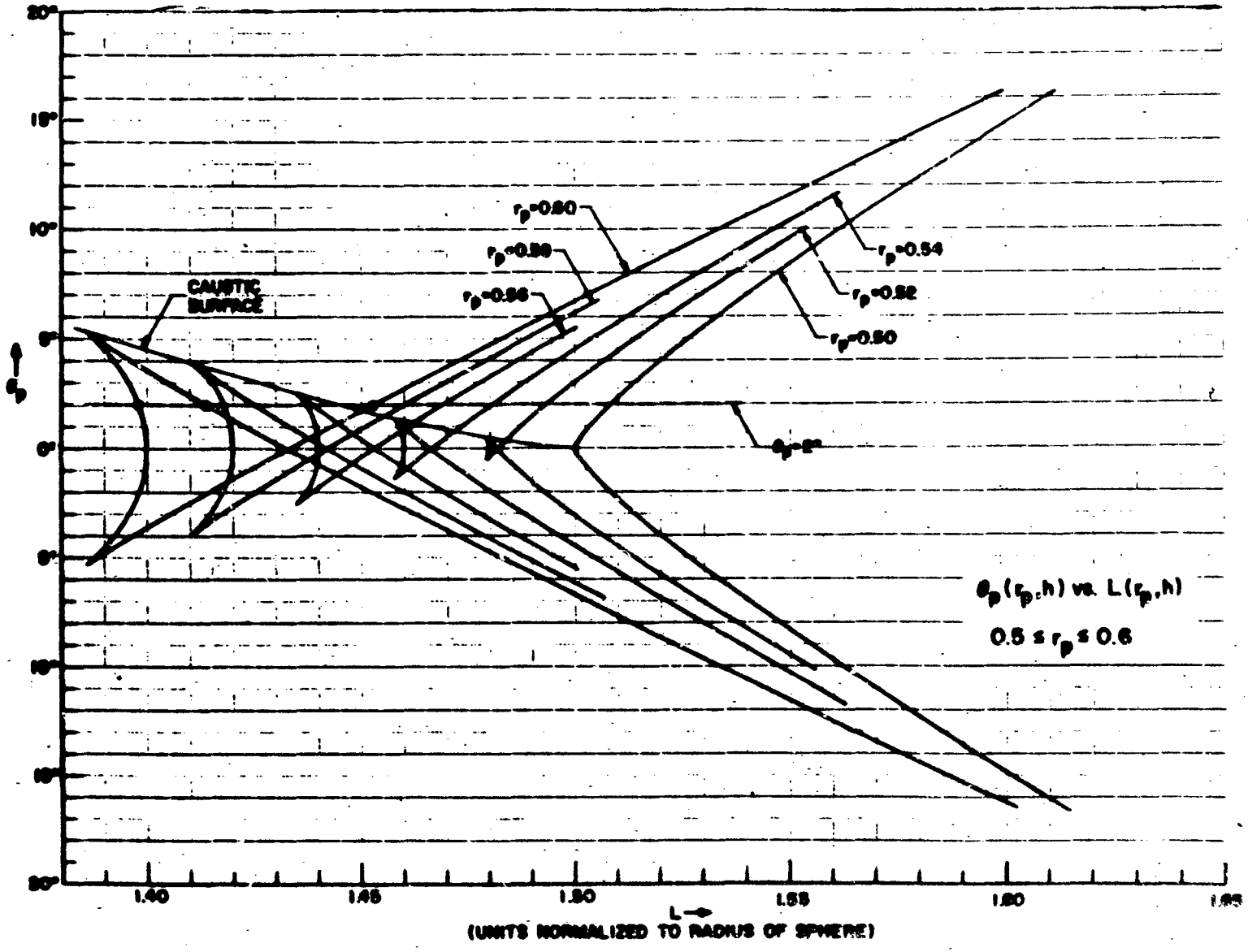

Figure 7. θ versus Path-Length

Polarization:

The spherical reflectors under study subtend angles at the center of curvature of the order of 60°. The resulting wide angles of incidence preclude the neglect of polarization effects, as substantial contributions of cross-polarized fields can arise.[6] If one considers a linearly polarized plane wave incident on a spherical reflector, applying the current distribution method[7] one quickly obtains for the current on the reflector, $\overline{K}$, using the notation of Figure 8,

$$\overline{K} = 2H_1 \hat{n}_s x (\hat{n}_1 x \hat{e}_1)$$

If $\hat{n}_2$ is the unit vector in any direction 2, the component of current radiating in this direction is:

$$\overline{K}_{2\perp} = \overline{K} - (\overline{K} \cdot \hat{n}_2)\hat{n}_2$$

For an incoming $\hat{i}$ polarized wave, if z is the direction of propagation

$$\hat{e}_1 = \hat{i} \; ; \hat{n}_1 = \hat{k}$$

and thus:

$$\overline{K} = 2H_1 \hat{n}_s x \hat{j}$$

To a good approximation, for spherical reflectors of the size and shape contemplated, the polarization is essentially that of the specularly reflected ray. This is evidenced by the fact that the circle of least confusion subtends less than 7° at any point of incidence in a spherical reflector subtending 60° at the center as shown in Figure 9. This type of assumption concerning the specularly reflected ray is also inherent in the stationary phase approximation.

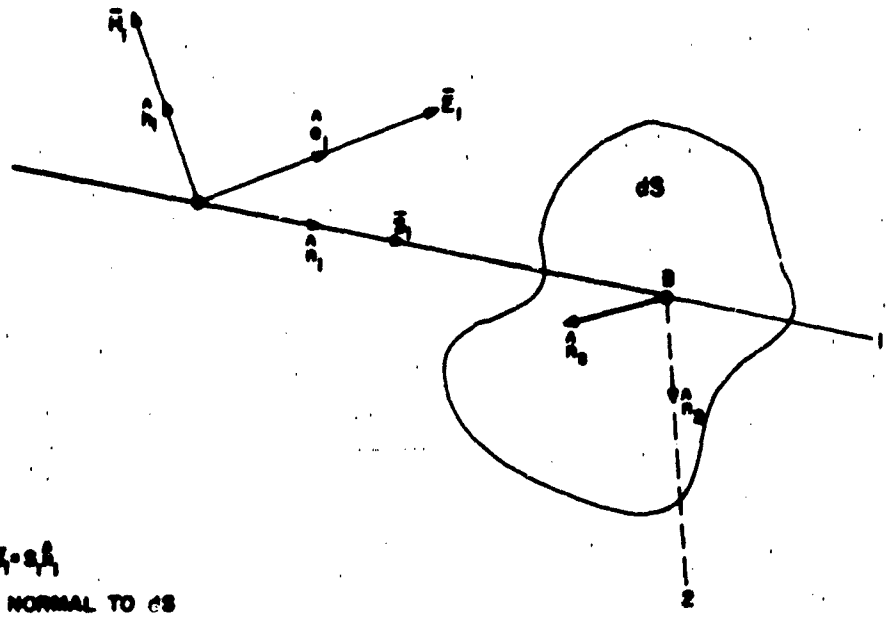

$\bar{E}_1 = E_1 \hat{a}_1$

$\bar{H}_1 = H_1 \hat{a}_1$

$\bar{E}_1 \times \bar{H}_1 = S_1 \hat{a}_1$

$\hat{n}_0$ = UNIT NORMAL TO dS

$\hat{a}_2$ = UNIT VECTOR IN DIRECTION 2

$\hat{a}_1$ = UNIT VECTOR IN DIRECTION 1

Figure 8. Plane Wave Incident on Curved Surface

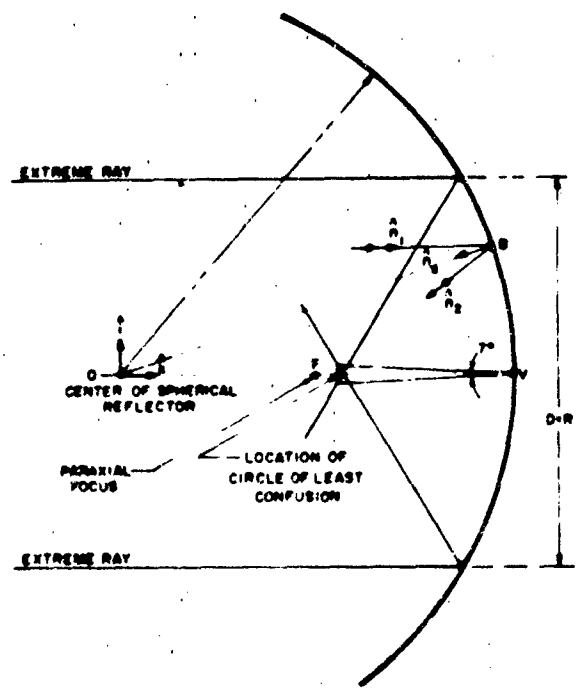

Figure 9. Optics of a Spherical Reflector

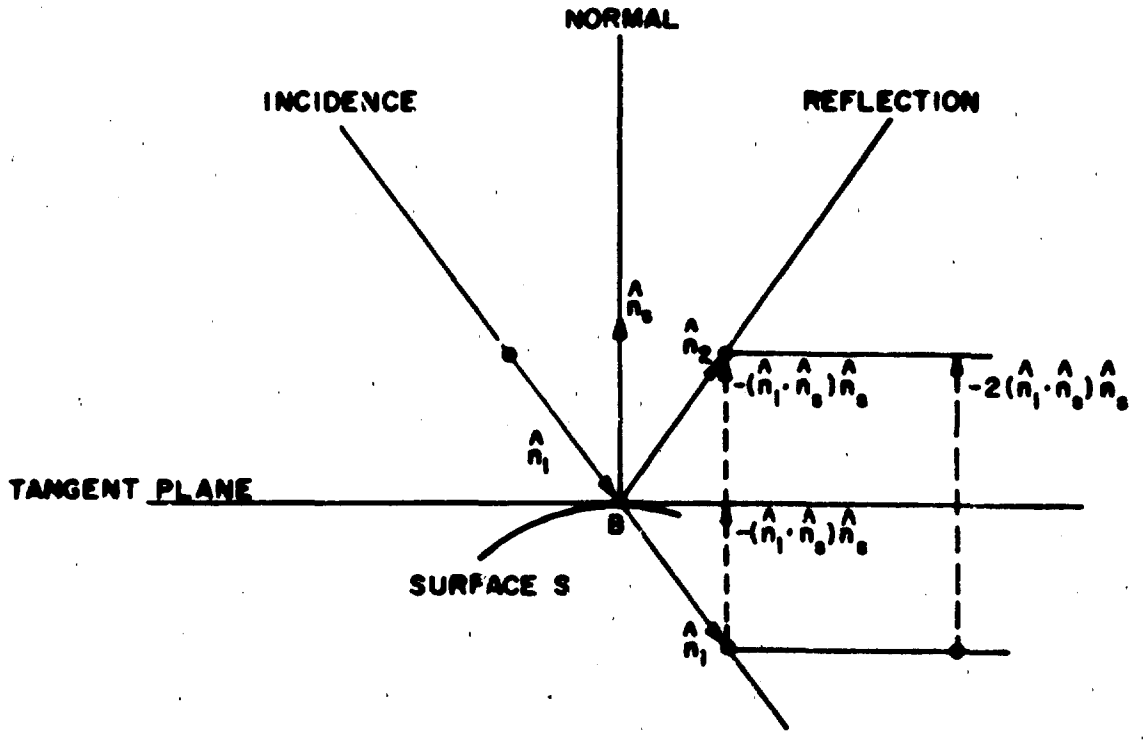

Figure 10. Specular Reflection from a Curved Surface

For the specular ray (see Figure 10)

$$\hat{n}_2 = \hat{n}_1 - 2(\hat{n}_1 \cdot \hat{n}_s)\,\hat{n}_s$$

hence

$$\hat{n}_2 = \hat{k} - 2(\hat{k} \cdot \hat{n}_s)\hat{n}_s$$

nd

$$\overline{K}_{2\perp} = 2H_1 \left[\hat{n}_s \times \hat{j} - (\hat{i} \cdot \hat{n}_s)(\hat{k} - 2\,(\hat{n}_s \cdot \hat{k})\hat{n}_s) \right]$$

If the center of the spherical reflector is chosen as the origin of coordinates, one an write in spherical coordinates.

$$\hat{n}_s = -\frac{\overline{OB}}{\overline{OB}}$$

$$= -\hat{\rho} = -(\hat{i} \sin\theta \cos\varphi + \hat{j} \sin\theta \sin\varphi + \hat{k} \cos\theta)$$

whence

$$\bar{K} = 2H_1 \left[\hat{i} \cos\theta - \hat{k} \sin\theta \cos\varphi\right]$$

and

$$\hat{n}_2 = -(\hat{i} \sin 2\theta \cos\varphi + \hat{j} \sin 2\theta \sin\varphi + \hat{k} \cos 2\theta)$$

and finally

$$\begin{aligned}\bar{K}_{2\perp} = H_1 \big[&\hat{i}\, 2(\cos\theta - \sin\theta \sin 2\theta \cos^2\varphi) \\ &- \hat{j} \sin\theta \sin 2\theta \sin 2\varphi \\ &- \hat{k}\, 2 \cos\theta \sin 2\theta \cos\varphi\big]\end{aligned}$$

Using spherical unit vectors, which are readily identifiable on the spherical reflector surface,

$$\bar{K} = 2H_1 (\hat{\theta} \cos\theta - \hat{\varphi} \cos\theta \sin\varphi)$$

$$\hat{n}_2 = -(\hat{\rho} \cos\theta + \hat{\theta} \sin\theta)$$

and

$$\begin{aligned}\bar{K}_{2\perp} = 2H_1 \big[&\hat{\rho} \cos\theta \sin\theta \cos\varphi \\ &+ \hat{\theta} \cos\varphi (1+\sin^2\theta) \\ &- \hat{\varphi} \cos\theta \sin\varphi\big]\end{aligned}$$

For an incident $\hat{j}$ - polarized wave one can show that:

$$\begin{aligned}\bar{K}_{2\perp} = H_1 \big[&-\hat{i} \sin\theta \sin 2\theta \sin 2\varphi \\ &+ \hat{j}\, 2(\cos\theta - \sin\theta \sin 2\theta \sin^2\varphi) \\ &- \hat{k} \sin 2\theta \cos\theta \sin\varphi\big]\end{aligned}$$

as one might expect, with $\hat{i}$ and $\hat{j}$, $\sin\varphi$ and $\cos\varphi$ interchanging their roles.

Figures 11, 12, and 13 are polar plots of the $\hat{i}$, $\hat{j}$, $\hat{k}$ components respectively of effective surface current density as they would appear on the surface of the spherical reflector if one were looking down the central ray at the reflector. The values shown are valid perhaps for $\theta \leq 35°$, but are shown out to 90° as a point of interest. The

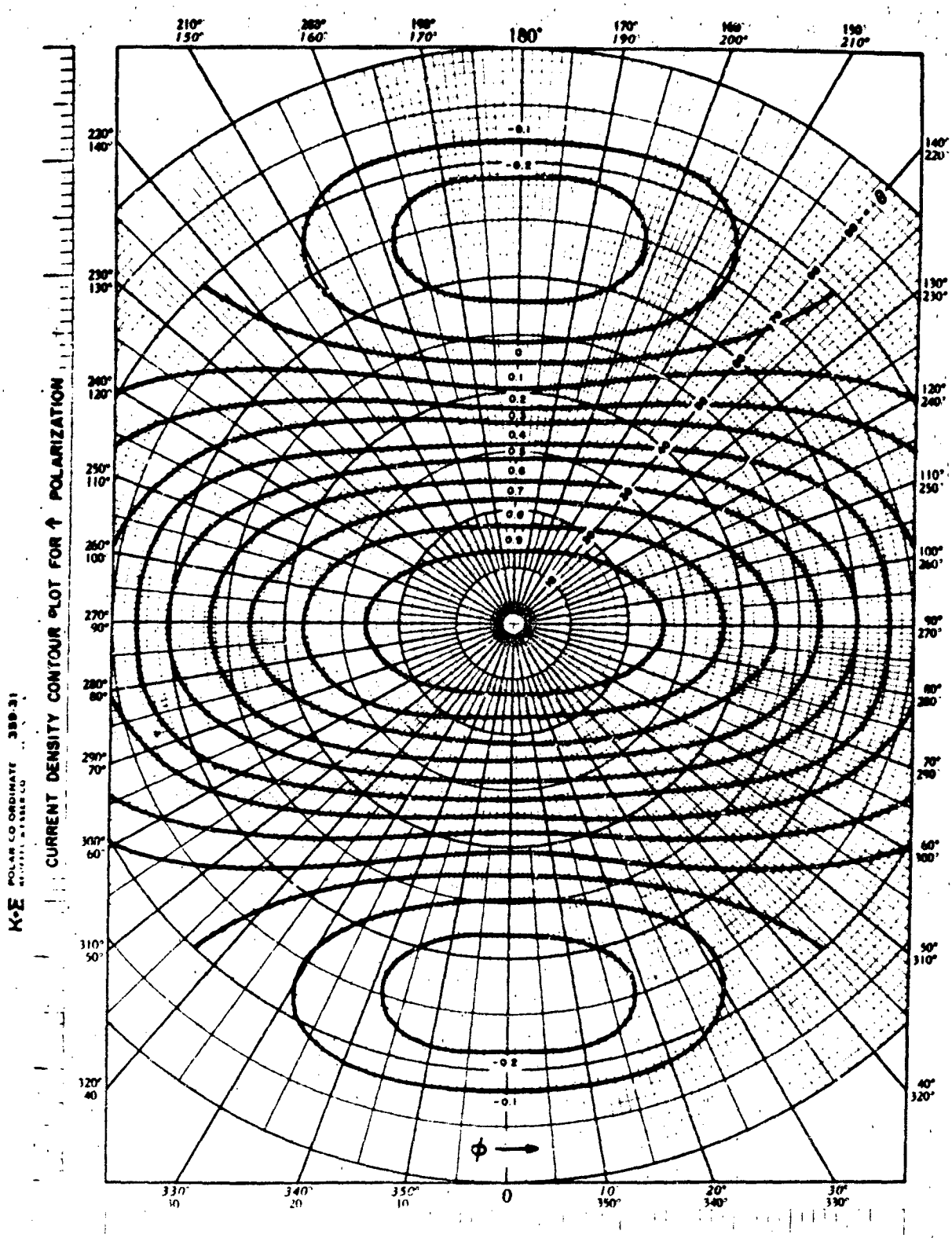

Figure 11. Effective Surface Current Density Contour Plot for $\hat{i}$-Polarization

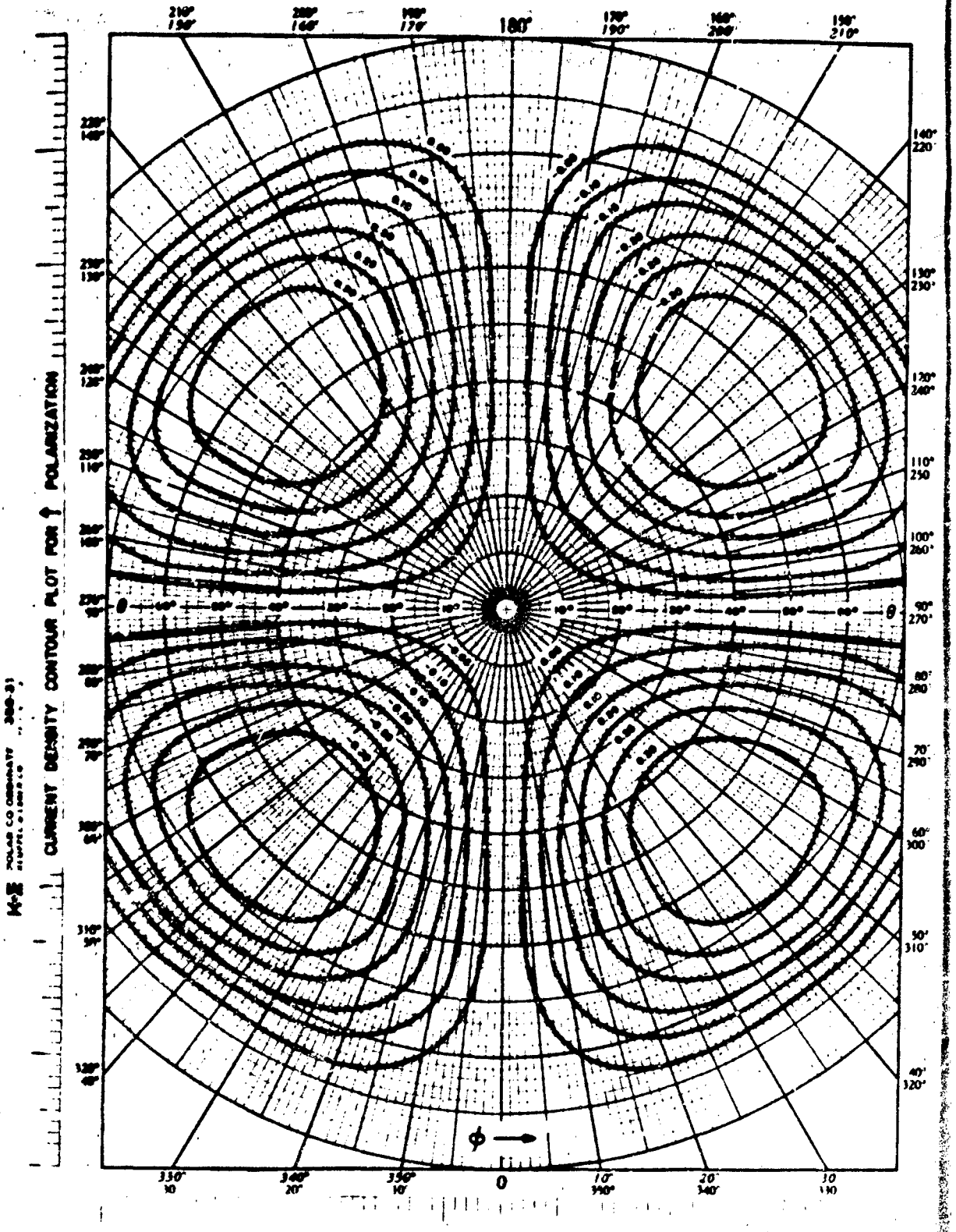

Figure 12. Effective Surface Current Density Contour Plot for $\hat{j}$-Polarization

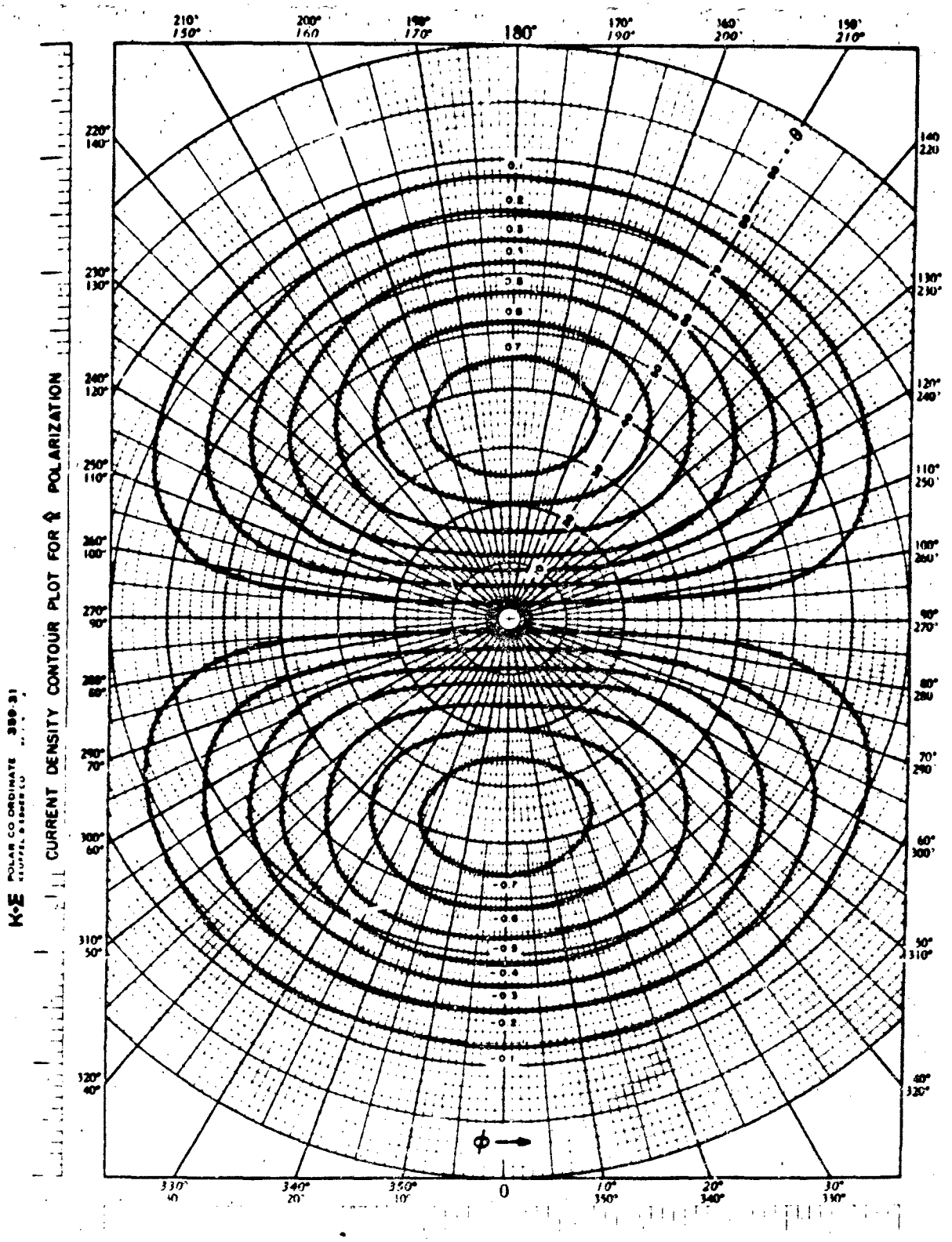

Figure 13. Effective Surface Current Density Contour Plot for $\hat{k}$-Polarization

$\hat{j}$-component has the familiar four-lobed cross-polarized pattern, and also is suppressed more strongly than the $\hat{k}$-component as θ approaches 0°. Note the band of zeros for the $\hat{i}$ component for $\theta \geq 45°$, which seems to be the cause of the squashed-down elliptical contours for smaller values of θ.

Focal Region Fields

It is evident from the foregoing that any point in the focal region not on the axial caustic receives field contributions from as many as three rays, i.e. three regions on the reflector. If one were to sum up the field contributions from the reflector at a general point in the focal region, one would expect to find that everything cancels except that arising from these three regions and the effects of discontinuities in the current distribution such as are caused by edges, aperture blocking, etc. Let us neglect discontinuities in the current distribution. Since the surface current and charge obey the continuity equation, only the current distribution need by considered. If, further, it is assumed that the focal region is in the far field of the contributing regions of the reflector, for an incident uniform $\hat{i}$ polarized plane wave, we can write for the field at a point P,

$$\frac{\overline{E}_P}{C_1} = I = \int_{\text{Reflector}} [\overline{K} - (\overline{K} \cdot \hat{n}_2)\hat{n}_2] \frac{e^{j\frac{2\pi}{\lambda}(L_1 + L_2)}}{L_2} dS$$

where L_1, L_2, are path-lengths from Figure 4, and $C_1 = -j\frac{\omega\mu}{2\pi}$. Then it can be shown that

$$I = 2H_1 \iint \left[\hat{i}\,(\cos\theta - \sin\theta \sin 2\theta \cos^2\phi) - \hat{j} \sin\theta \sin 2\theta \sin\phi \cos\phi - \hat{k} \cos\theta \sin 2\theta \cos\phi\right]$$

$$\times \left[\frac{e^{j\frac{2\pi}{\lambda}\left[R\cos\theta + \left(R^2 + r_p^2 - 2r_pR\left[\sin\theta_p \sin\theta \cos(\phi-\phi_p) + \cos\theta_p \cos\theta\right]\right)\right]^{1/2}}}{\left(R^2 + r_p^2 - 2r_pR\left[\sin\theta_p \sin\theta \cos(\phi-\phi_p) + \cos\theta_p \cos\theta\right]\right)^{1/2}}\right]$$

$$\times \left[R^2 \sin\theta d\theta d\phi\right]$$

The processes which led to this integral lead inevitably to the method of stationary phase in its evaluation. Stationary phase is an asymptotic method[8,9,10] mathematically related to the method of steepest decent, but resting on a somewhat weaker mathematical foundation. It has, however, a strong physical relationship to wave motion problems. Basically, it says that if contributions at a field point remote from an equiphase surface are added, they tend to cancel except for the contributions from regions where the phase has a stationary value, i.e., its partial derivatives are zero. And it can be shown that this approximation is quite accurate subject to certain limitations. The most important of these boils down to the requirement for our case that $\frac{2\pi}{\lambda}R$ is a very large number. For $R \geq 170$, $\frac{2\pi}{\lambda}R > 1000$. The method can be shown to break down at foci and caustics, in the simple form discussed here. Basically, what we have achieved is an extension of the geometric optics model to give us some evaluation of the field, including interference and polarization effects, at points in the focal region which are not on or very near the axial caustic and the caustic surface. For the relatively large feed surfaces we contemplate, this is a significant portion of the transverse focal region.

The stationary phase conditions are

$$\frac{\partial L}{\partial \phi} = 0; \quad \frac{\partial L}{\partial \theta} = 0;$$

which lead to the relationships

$$\phi - \phi_p = \begin{cases} 0 \\ \pi \end{cases}$$

and

$$\frac{\sin \theta}{r_p} = \frac{\sin (\theta \pm \theta_p)}{L_2}$$

The first relationship simply says that stationary points lie in the plane of incidence containing the field point P. The second is simply the sine law for triangle OPB of Figure 4. Both of these conditions arise in the geometric optics treatment and show the strong relationship between this stationary phase evaluation and the geometric optics model. Finally then, we can show that at the points of concern, so-called field points of the first kind,

$$\frac{\mathbf{E}_p}{C_1} = C_2 \Big[\hat{i} (U_1 P_{i1} + U_2 P_{i2} + U_3 P_{i3}) + \hat{j} (U_1 P_{j1} + U_2 P_{j2} + U_3 P_{k3}) + \hat{k} (U_1 P_{k1} + U_2 P_{k2} + U_3 P_{k3}) \Big]$$

where the subscripts 1, 2, 3, refer to the values θ_1, θ_2 and θ_3 which can contribute at $P = P(r_p, \theta_p, \phi_p)$, and subscripts i, j, k refer to components of polarization $(\overline{K} - (\overline{K} \cdot \hat{n}_2)\hat{n}_2)$. Thus P_{j2} is the j component of polarization evaluated for θ_2, if θ_2 exists. And U_3 is the stationary phase factor evaluated for θ_3, if θ_3 exists.

where

$$U = \frac{e^{j\frac{2\pi}{\lambda}L}}{L_2} \quad \frac{\epsilon_{\theta\theta}\,\epsilon_{\phi\phi}}{|L_{\theta\theta}\,L_{\phi\phi}|}\,1/2$$

where $L_{\theta\theta}$, $L_{\phi\phi}$ are the second partial derivatives of L with respect to θ and ϕ respectively, and $\epsilon_{\theta\theta}$, $\epsilon_{\phi\phi} = e^{\pm j\pi/4}$, with the ± sign chosen the same as the sign of $L_{\theta\theta}$, $L_{\phi\phi}$ respectively, and account for the so-called anomalous phase change when passing a caustic. Results have been computed for points on concentric spherical surfaces, (r_p = constant), for R = 170 λ, 400 λ. Typical results are shown in Figures 14 to 20, for the values of parameters r_p, θ_p, ϕ_p shown.

Experimental Work

The experimental model being used at the time this paper was written was a pillbox with a circular cylinder back wall operating in the TEM mode. This is a two-dimensional analog to the spherical reflector. While it suffers from some defects, to whit - only one polarization is supported and there is no convergence to an axial caustic, it does have a caustic similar to the caustic surface and permits the development of measurement techniques. Amplitude and phase distributions in the focal region are being measured.

The experimental model consists of two parallel plates 9' x 5' separated by 1/4". The leading edge is straight and slightly flared in the transverse plane. The back wall is a cylinder with a 7' radius of curvature. The measurements are being made at 24Kmc/s, that is, for a wavelength of about 1/2". The pillbox is being illuminated from a distant source. The resultant internal fields are being sampled by a capacitive probe which can be moved throughout the region of interest. A major advantage of the pillbox is that the parallel plates permit ready access to the focal region, as compared to the full sphere. After the completion of these measurements, experiments on a

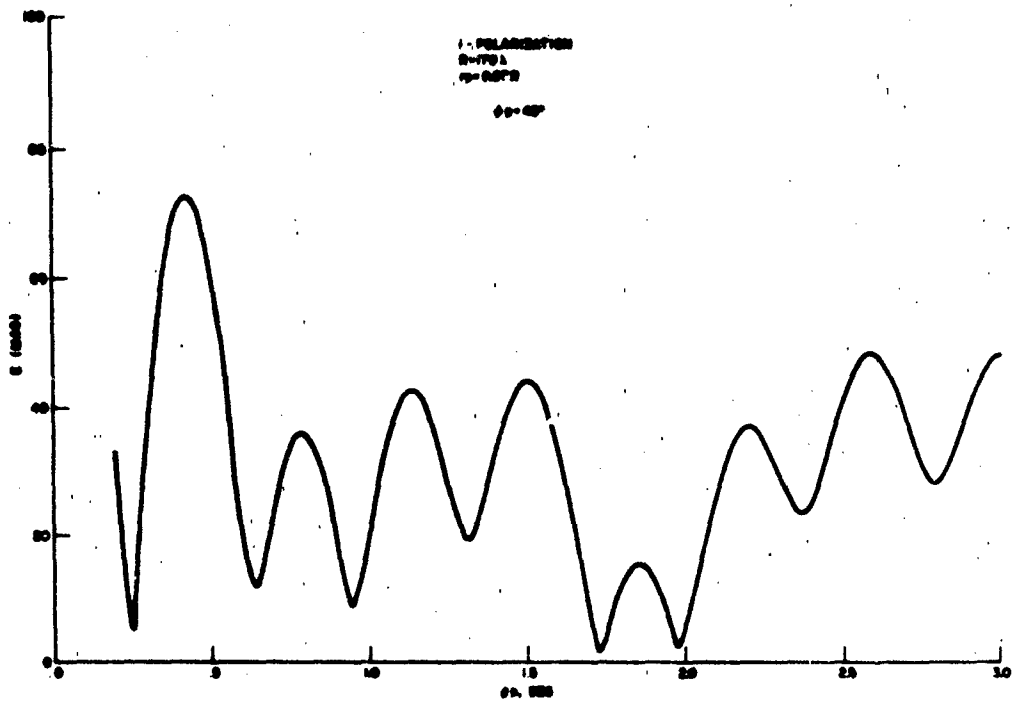

Figure 14. Focal Region Fields

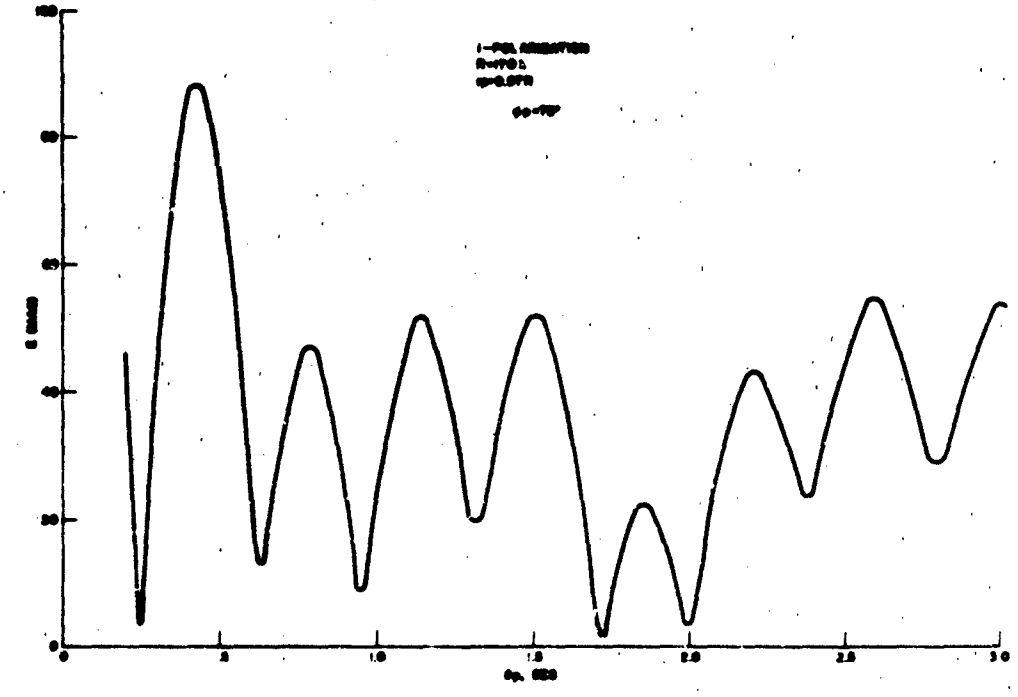

Figure 15. Focal Region Fields

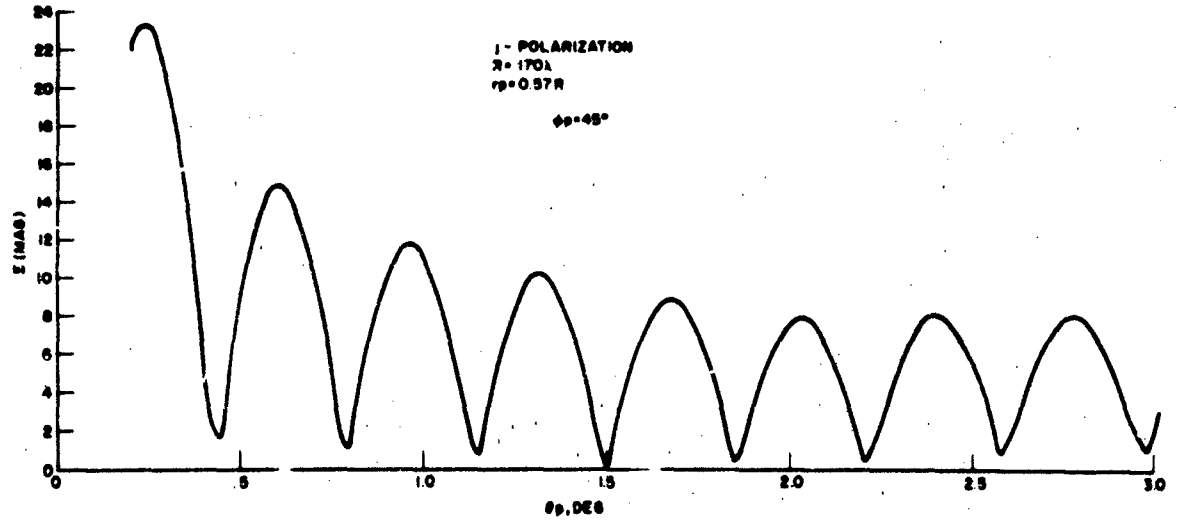

Figure 16. Focal Region Fields

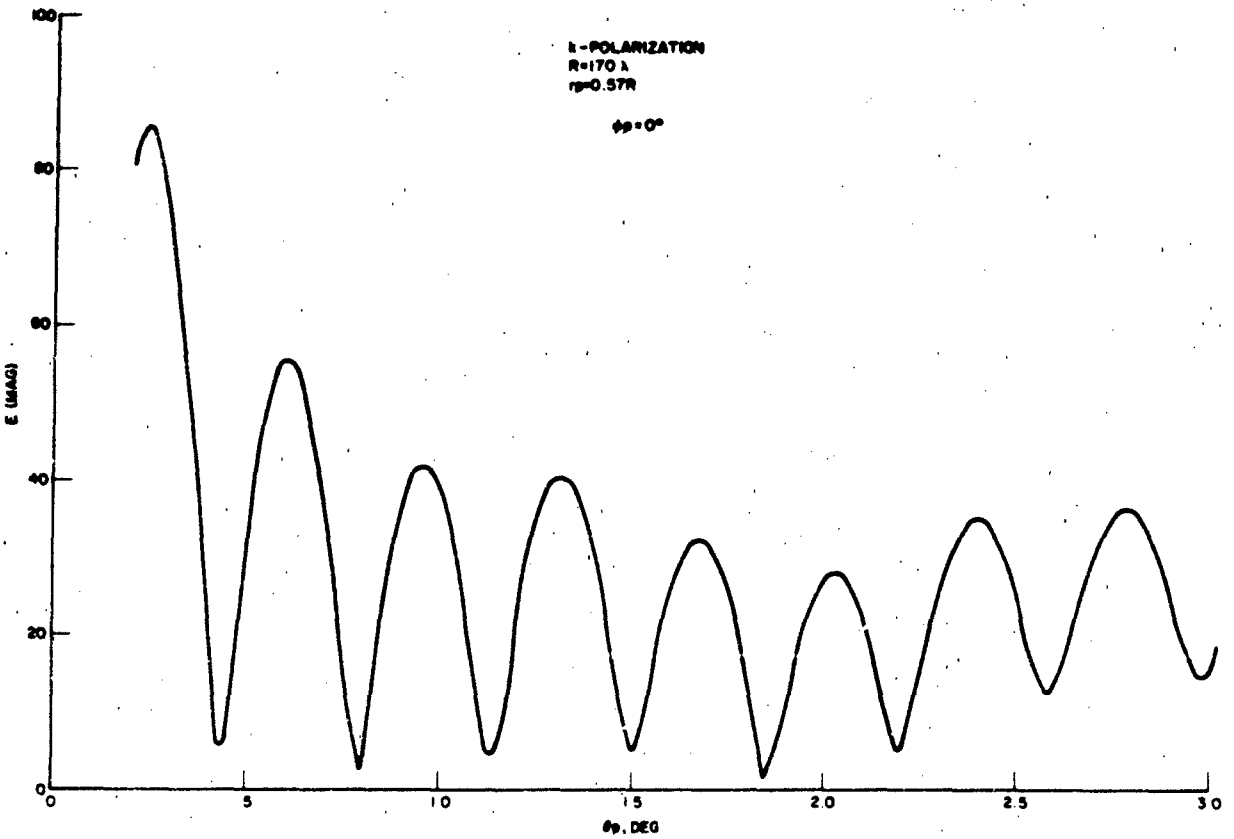

Figure 17. Focal Region Fields

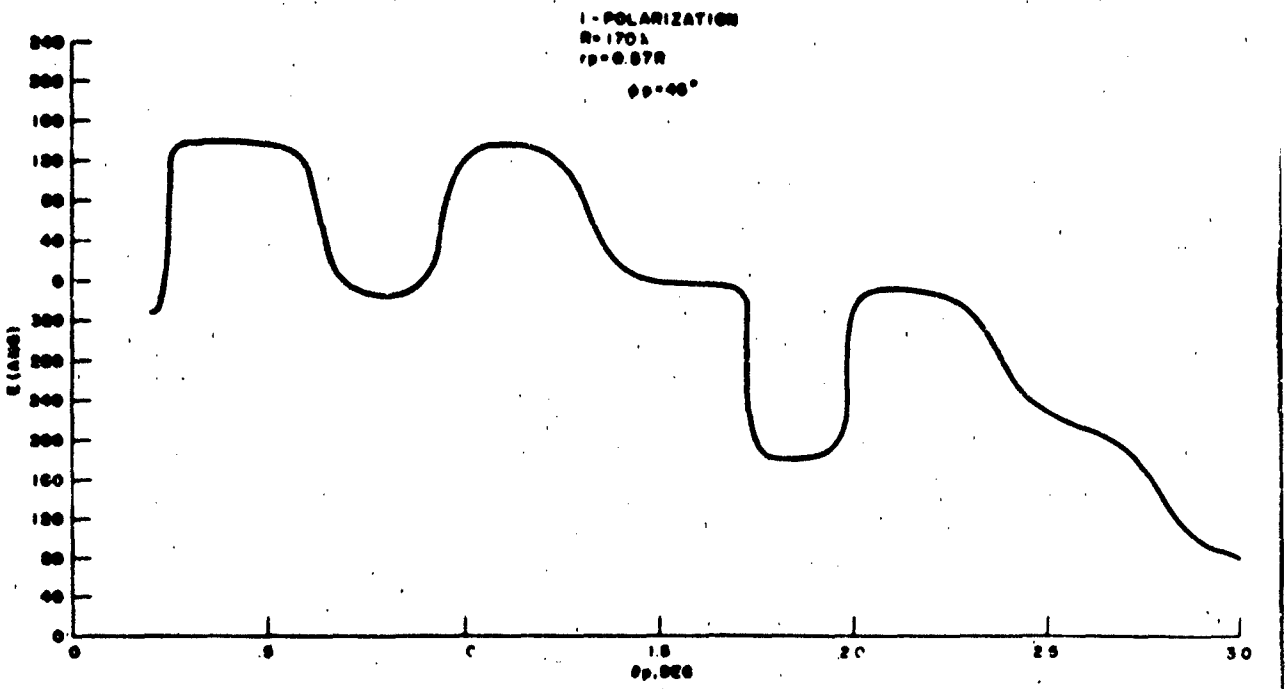

Figure 18. Focal Region Fields

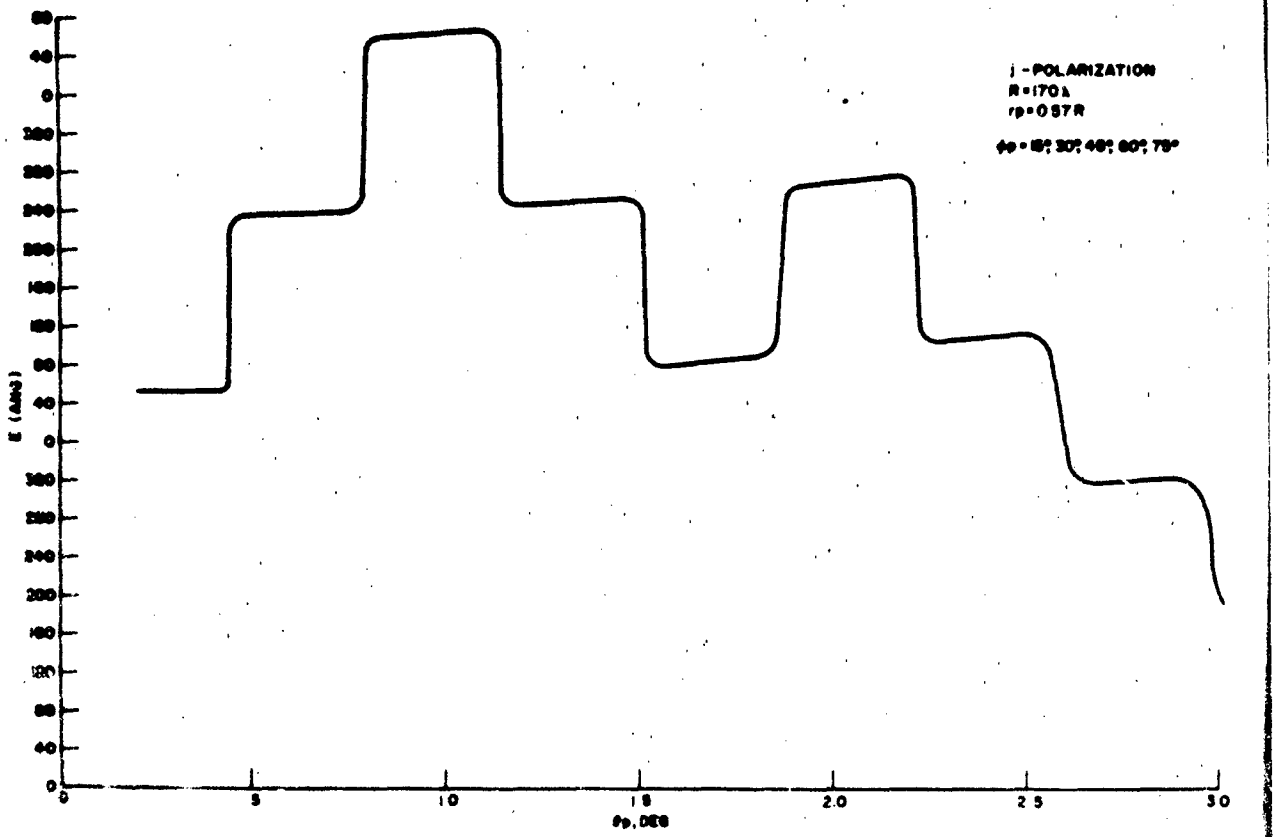

Figure 19. Focal Region Fields

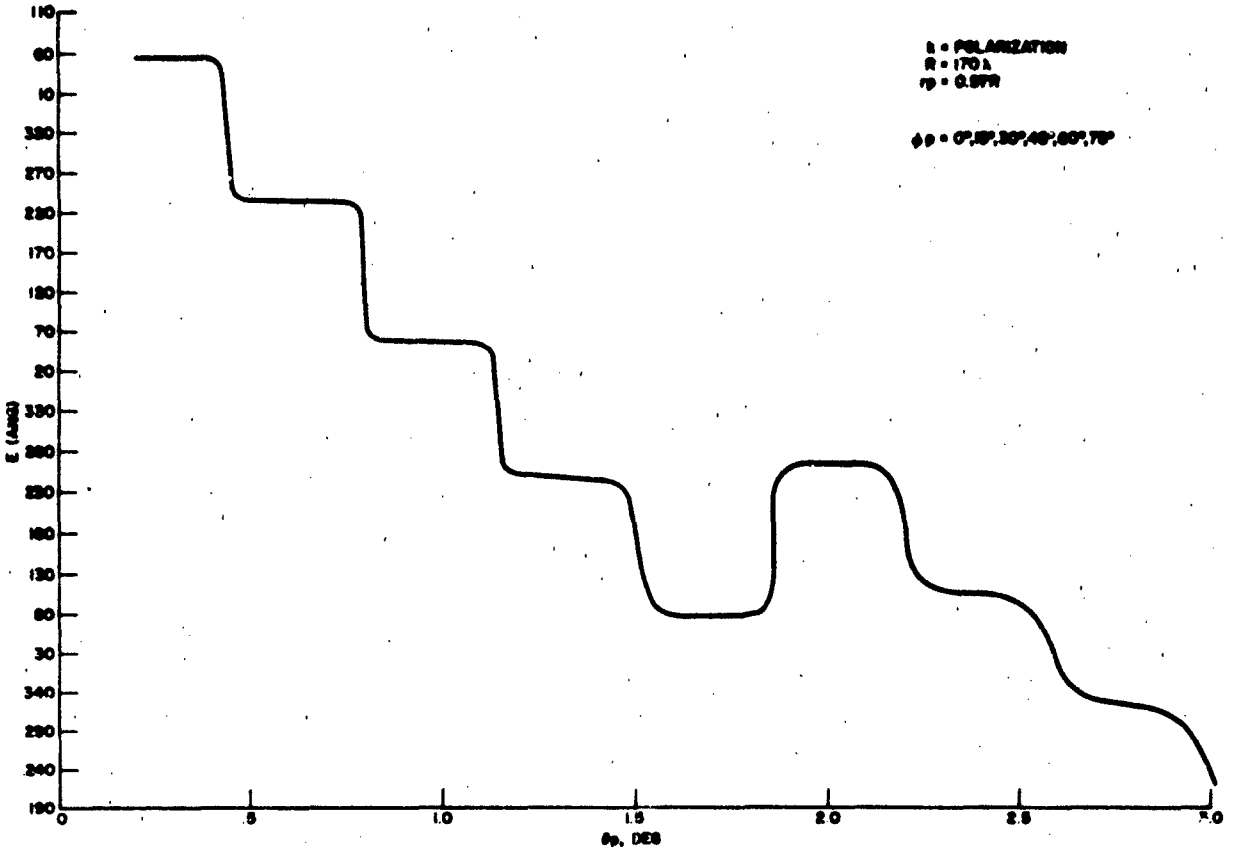

Figure 20. Focal Region Fields

spherical reflector will begin. These will stress the proper feeding of the reflector as well as probing the focal region. Present investigations into the feed problem and past experience in related work indicate that while analysis will provide guidelines, a large lacing of empirical optimization will ultimately be required.

REFERENCES

1. "Correction of Spherical Aberration by a Phased Line Source"
   Roy C. Spencer, C. J. Sletten and J. E. Walsh,
   AFCRC Report E5069, May 1951

2. "Theoretical Analysis of the Effect of Spherical Aberration on Gain"
   Roy C. Spencer,
   AFCRC Report E5062, Dec. 1951.

3. "Modern Antennas for Space Communication"
   C. J. Sletten,
   AFCRL-63-51, Feb. 1963 - see Section 4.

4. "Transverse Focal Region of a Spherical Reflector - Part 1: Geometric Optics"
   Roy C. Spencer and Geoffrey Hyde
   AFCRL-64-292

5. "Optics of the Focal Region of a Spherical Reflector"
   Roy C. Spencer and Geoffrey Hyde, paper presented at American
   Optical Society meeting in New York City, Oct. 1964.

6. "Transverse Focal Region of a Spherical Reflector - Part 2: Polarization"
   Geofrey Hyde and Roy C. Spencer, to be published

7. "Microwave Antenna Theory and Design"
   S. Silver, Vol. 12
   Rad. Lab. Series, McGraw-Hill, 1949, section 5.7

8. "Principles of Optics"
   M. Born and E. Wolf, Pergamon Press 1959, Appendix III

9. "Methods of Mathematical Physics"
   Jeffreys and Jeffreys
   Cambridge, 1946, chapter 17

10. "Asymptotic Methods in Analysis"
    N. deBruijn, North-Holland, 1958, chapter 4 and 5

DUAL MODE PATTERN AND RECIPROCITY STUDIES WITH A SIMPLE WAVEGUIDE FEED AND REFLECTOR ANTENNA

by

M. W. Scheldorf

Antenna Research Facility
IITRI, Geneva, Illinois

GENERAL

A multimode antenna behavior measurement program is being conducted as a part of a general RFI prediction and minimization project undertaken by the Antenna Research Facility of IIT Research Institute for the U. S. Army Signal Corps. A preliminary study is finished, determining the dual mode behavior of a simple antenna arrangement. A complete and essential reference for the general theory of dual mode behavior of a rectangular waveguide is found in the 1962 IRE Wescon Convention Record TP-1, Paper 12-4, "Antenna Beam Shifting by Dual Modes", Kitsuregawa and Tachikawa. This paper discusses the changes in primary and secondary radiation patterns for different amplitude ratios and phase difference between TE_{10} and TE_{20} modes.

In the experimental work, a 4.28 KMC signal frequency is used for a number of tests with a 3" x 1 1/2" waveguide. The modes are restricted to the dominant with a wavelength of 3.153" and the first higher order mode with a wavelength of 11.49". These wavelengths are sufficiently well separated to permit excitation of either or both modes with ease.

A parabolic cylinder feed unit is constructed. It is shown

in Photo 1-A. A 24" length of 3" x 1 1/2" rectangular waveguide is fitted with three removable probes; one at the center of the wide face (or the back side of the view shown), for TE_{10} excitatio and two probes located in the wide faces on opposite sides, halfway between the center and the narrow sides, for TE_{20} excitation. The photo shows one of the TE_{20} probes. A series of holes spaced 0.1" are located on the top wide face, in a transverse location such that equal TE_{10} and TE_{20} fields will be measured for equal maximum amplitudes. A movable plunger 1-B is provided and the probe longitudinal positions so chosen that at one location the short-circuit face of the plunger will produce a quarter wavelengt spacing to the corresponding probes, at both operating modes. The long section shown omits two horn flaps at the left end, held on by machine screws (the tapped holes are visible).

After some preliminary field pattern tests, the following arrangements are chosen to excite the waveguide with TE_{10} only, TE_{20} only and a mixture of TE_{10} and TE_{20}.

TE_{10} only: The centrally located probe is excited by itself.

TE_{20} only: The TE_{20} probes are fed in parallel with a phase shifter added to one cable, to obtain the deserved phasing.

TE_{10} plus TE_{20}: One TE_{20} probe is excited by itself and a parasitic probe is placed near it by means of a short-circuited wire stub projecting into a hole in the waveguide wall between the feed probe and the open end of the waveguide.

The setup including horn flaps, attached to the open end of the waveguide is seen in Photo 2. Measurements of field distributi

at 0.1" intervals are made as indicated by the curves of Figure 1. These measurements include holes between the probes and the plunger. This accounts for the irregular and rapid variations at the left end of each curve.

The TE_{10} distribution is excellent. There is only one oscillation, which proves the absence of the TE_{20} component.

The TE_{20} distribution is not as successful. There is a variation in both the length of the period and its amplitude. This indicates a lack of balance in the excitation of the two probes.

The TE_{10} and TE_{20} combination is similar to the TE_{20} distribution but does demonstrate the presence of additional TE_{10} component by virtue of the greater amplitude and period length variation.

PRIMARY PATTERNS

Radiation patterns of the waveguide section as a primary feed for a reflector are taken as shown in Figure 2. The experimental patterns agree with the theory of the Kitsuregawa and Tachikawa paper. For a simple TE_{10} mode, the primary radiation pattern has a single beam directed along the axis of the waveguide. For the simple TE_{20} mode, there are two beams, with the null along the waveguide axis. When both modes are present there are two beams of unequal amplitude and the null is not along the waveguide axis.

SECONDARY PATTERNS

The measurement of secondary patterns requires a special reflector arrangement. Normally one would expect to place the horn of the feed waveguide at the focus of a paraboloid. In the

present case this is undesirable because the waveguide structure is extensive and in one case employs two cables connected to the wide sides of the section. The resultant aperture blocking can result in considerable distortion of the secondary pattern.

A parabolic cylinder is used in its place. This enables the feed to be directed into the cylinder at an angle so that the major portion of the reflected energy will miss the feed structure. See Photo 5. This shows the feed, the parabolic cylinder and the elevation positioner used to rotate the antenna assembly on a horizontal axis.

Photo 3 shows the pattern range, including the horn antenna for a remote unit. Photo 4 shows a better view of the parabolic cylinder as seen from the roof of the penthouse used to mount the remote antenna. This photograph includes the power supply and klystron unit under the condition where the multimode antenna is used as a transmitting source.

The parabolic cylinder is designed on the basis of a 10 db edge illumination from a roughly calculated primary pattern shape. As a result of the experimental curves of Figure 2, it is anticipated that the calculated parabolic aperture may be too large. For this reason the aperature is reduced the appropriate degree by covering a portion of the extreme edge, on both sides, with a 30 db absorber pad.

Figure 3 shows the measured secondary patterns for the TE_{10} mode alone. One curve is for the entire parabolic cylinder (wide reflector). The other curve is for the condition with part of

the surface covered (narrow reflector). Both curves indicate the usual narrow beam and quite low side lobes. The narrow reflector exhibits a wider main beam and poorer side lobes as it should.

Figure 4 shows the measured secondary patterns for the TE_{20} mode alone. Again measurements are made with both sizes of reflector. These patterns exhibit the double-beam shape that should be expected, except that the null is not as deep as anticipated. A subsequent pattern will demonstrate this more clearly. Otherwise the comments for the TE_{10} mode apply here also.

Figure 5 shows the measured secondary patterns for the condition where both TE_{10} and TE_{20} modes are present. The pattern is what might be expected from a consideration of the primary and secondary patterns of the TE_{10} and TE_{20} cases.

In this instance, since both modes are contributing to the radiation, it is appropriate to test for pattern reciprocity. For this reason, power is fed into the dual mode waveguide in one case and into the remote horn antenna for the other case. The agreement is quite satisfactory.

ADDITIONAL RECIPROCITY TESTS

It is desireable to extend the reciprocity tests with some more arrangements than can be more convincing. The first tests are made with the secondary patterns. The waveguide section is fed thru a coaxial cable which is matched to give the maximum signal as a transmitter by means of a double stub tuner. Then the transmitter source and crystal detector receiver are interchanged, detuning the double stub tuner until the lower portion of the pattern

enters the noise level region of the recording system. With these secondary pattern tests, the detuning necessary is not a large amount, because of the circuit gain loss introduced by the use of the parabolic cylinder reflector.

Two conditions are tried. In the first case, the waveguide section is excited by the TE_{10} probe and one TE_{20} probe, with a phase shifter in the cable to the TE_{20} probe. The comparison curves are shown in Figure 6. Again the agreement is quite satisfactory. In the second case, both TE_{20} probes are fed and the TE_{10} probe used as a parasitic element, connecting its output to a short-circuited second double stub tuner. These comparisons are shown in Figure 7. The results again confirm reciprocity.

Additional reciprocity tests are also performed with the primary patterns. In this case it is possible to start with a much higher signal level at the receiver in the first step and then use much more detuning when the waveguide section is used as a receiver. Two wide divergent are made and the comparisons are shown in Figures 8 and 9. Again the validity of reciprocity seems to be indicated.

A final test for reciprocity is made by means of the feed distributions in the waveguide section. In this case a rather unusual characteristic is disclosed. A complete description will be undertaken following a note on a final set of pattern tests.

The TE_{20} mode primary and secondary patterns are repeated. The TE_{20} probes are fed by two carefully made equal length cables. The balance is verified by means of transverse field distribution

tests. These distribution characteristics will be discussed at some length later. The results are indicated in Figure 10. Note that the primary pattern has a very sharp deep null and that the secondary pattern has a similar very sharp deep null. The principal interest in these curves is to confirm experimentally what is expected from theoretical considerations.

MODAL VARIATIONS WITH RECEIVED SIGNAL

As indicated above, tests to prove reciprocity in the waveguide longitudinal field distribution produce a rather unusual result. The general observation is made that this field distribution during reception of a signal varies widely with the angle of arrival and with the reflection of the individual modes at a constant arrival angle. With respect to the angle of arrival, it is found that in the direction of the waveguide axis, only TE_{10} excitation is produced. This is quite natural when it is observed that the TE_{20} mode cannot be excited from a plane wave impinging on the waveguide mouth at this angle.

As the angle from the axis is regularly increased, there is a progressive improvement in the ability to excite the TE_{20} mode. That is, as the angle increases, the ratio of TE_{20} to TE_{10} increases. One might suspect that this ratio could be a simple function so that at a given angle the relative mode levels would be a constant value. In an attempt to discover this simple relationship it is found that the reflection of each mode makes this relationship fail. It is a matter of the wave impedance presented at the mouth of the waveguide for the component modes. Some experimental evidence will

clarify both types of field distribution variation.

Figure 11 indicates both types of variation. The waveguide section is terminated in a short circuit plunger, because this provides the only reflection coefficient that can be introduced with certainty and which will therefore permit a comparison with calculated results. In order to assure a complete reflection fro the plunger, all the probes are removed. The signal source is a simple open-ended waveguide mounted on a vertical shaft fitted wi a dial plate. The physical arrangement is shown in Photo 2.

Figure 11B is the case where the reflections are kept fixed and the arrival angle is varied. Note that there is a steady progression from a pure TE_{10} mode condition to more and more TE_{20} mode content.

Figure 11A is the case where the arrival angle is kept constant at 20° and the short circuit plunger is varied in position. This produces different wave impedances for the two modes at the mouth of the waveguide and also varies their time phase. There is no particular trend because the steps are very large, but a great variety of forms is produced. It is highly desirable that these curve shapes be correlated with calculated results in order to justify the origin of the variations.

For the correlation refer to Figure 12. Here are plotted curves for longitudinal feed distributions for four time phases, 0°, 30°, 60° and 90° and for nine relative amounts of TE_{10} and TE_{2} field. The curves of Figure 11B are found to correspond to a constant time phase of 0° and with relative field values as follows:

0° angle corresponds to TE_{20}/TE_{10}=0.0, 10° angle corresponds to TE_{20}/TE_{10}=0.75; 20° angle corresponds to TE_{10}/TE_{20}=0.25; 35° angle corresponds to halfway between TE_{10}/TE_{20}=0.5 and 0.25 and 90° angle corresponds to TE_{10}/TE_{20}=0.25.

The curves of 11A do not follow a constant time phase. 3/4" shorter corresponds to 90° phase and TE_{10}/TE_{20}=0.75; normal corresponds to 60° phase and TE_{10}/TE_{20}=0.75; 1 1/2" longer corresponds to 30° phase and TE_{10}/TE_{20}=0.5; and 2 1/4 longer corresponds to 0° phase and TE_{10}=TE_{20}. It is entirely possible that more careful measurements would show that the relative amounts of TE_{10} and TE_{20} is constant, with a variation only in time phase.

TRANSVERSE DISTRIBUTION STUDIES

Transverse field distribution measurements are another way of determining the relationship between the TE_{10} and TE_{20} modes. A series of calculated curves similar those for the longitudinal distribution are shown in Figure 13. The abscissa values are purposely chosen to agree with specific hole positions in the waveguide for the experimental data which follows.

Experimental measurements are made with the short waveguide section of Photo 1C. This section has a grid of holes spaced 0.2" with thirteen holes across the wide face of the waveguide and with thirty-five of these rows. Two rows of the holes have spacings of 0.1" in order to get better resolution at distances from the mouth periodically related to the two waveguide wavelengths. The experimental results are given in Figure 14. The shifting back and forth of the general slope of the curve is due to the slow

change in phase of the TE_{20} component which makes it add on one side and subtract on the other with a progressive change along the waveguide length. The notches at the center correspond to those rows where the TE_{10} standing wave component is low. At row 19 and 20 there is a low level contribution from both modes. This is coordinated with a deep notch in the longitudinal field distribution. It is not possible to solve for any particular value of relative TE_{10} and TE_{20} fields, but the presentations intend to familiarize the reader with the behavior of mode distribution variations.

CONCLUSIONS

Two distinct conclusions may be drawn from the results of the antenna study.

1. Reciprocity in antenna radiation patterns, while not exactly proven, is a quite well established fact.

2. The variation of modal content in reception, dependent on the angle of arrival and on the nature of the receiving end reflection, is clearly shown.

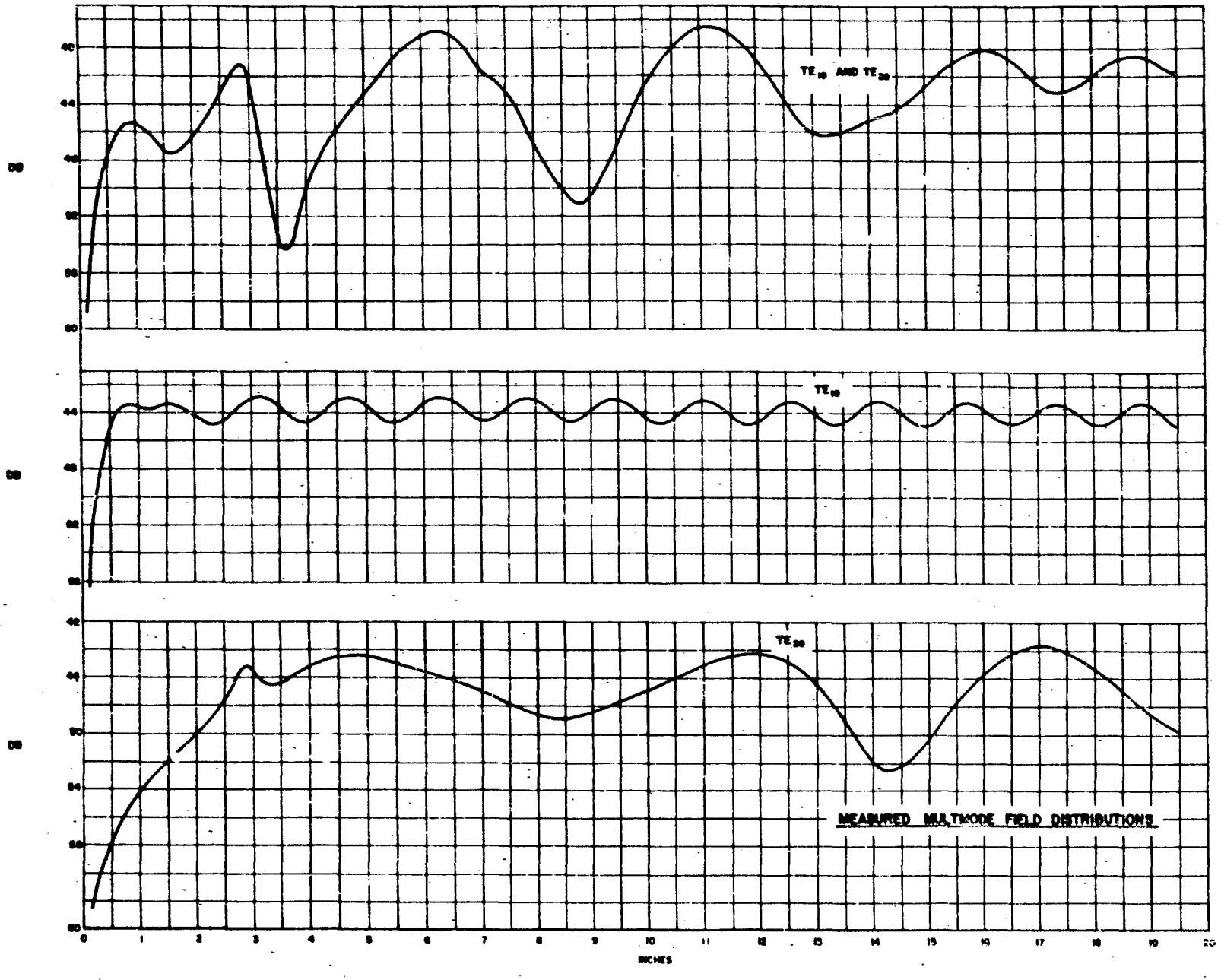

MEASURED MULTIMODE FIELD DISTRIBUTIONS

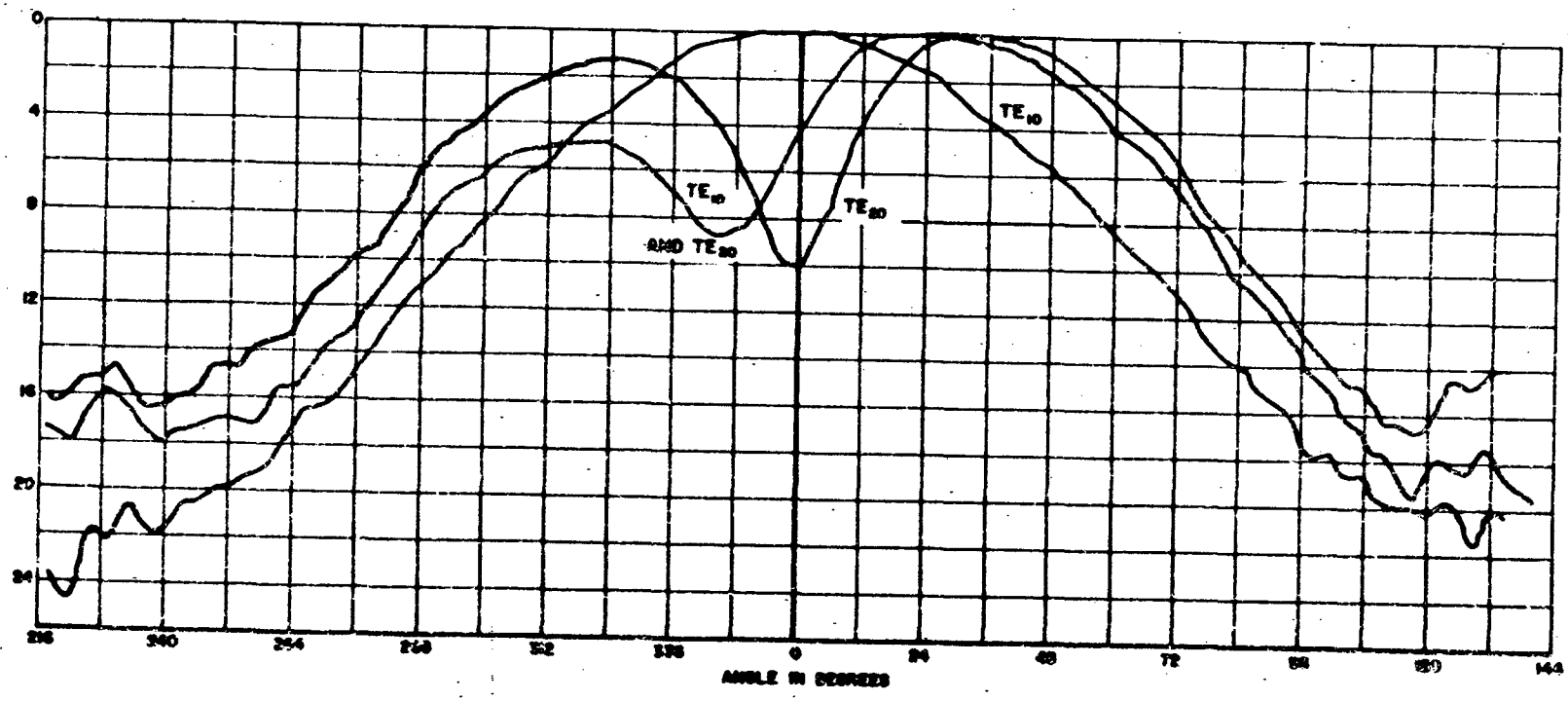

PRIMARY RADIATION PATTERNS

H-PLANE

FIG. 2

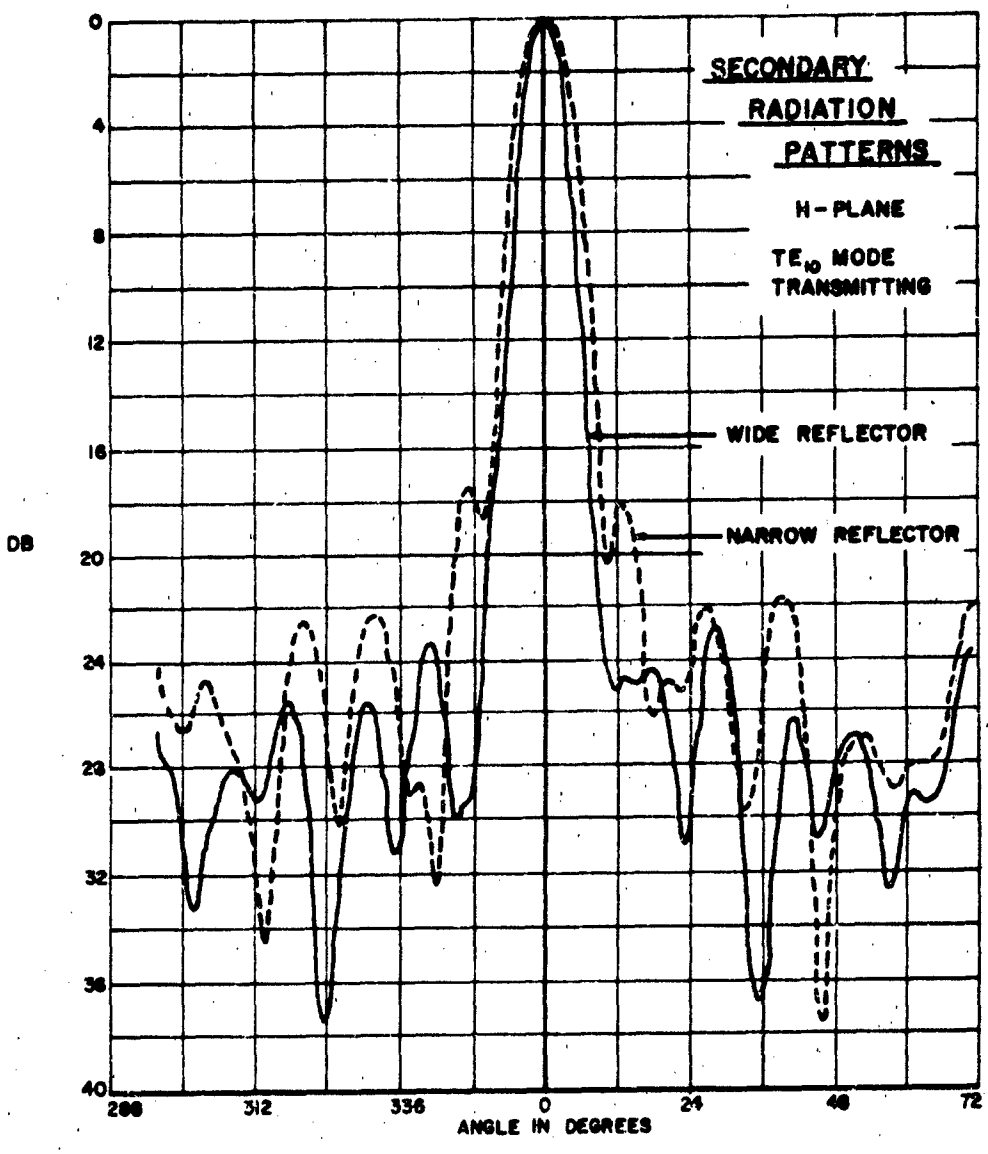
SECONDARY
RADIATION
PATTERNS
H-PLANE
TE10 MODE
TRANSMITTING
WIDE REFLECTOR
NARROW REFLECTOR
DB
0
4
8
12
16
20
24
28
32
36
40
288
312
336
0
24
48
72
ANGLE IN DEGREES

FIG. 3

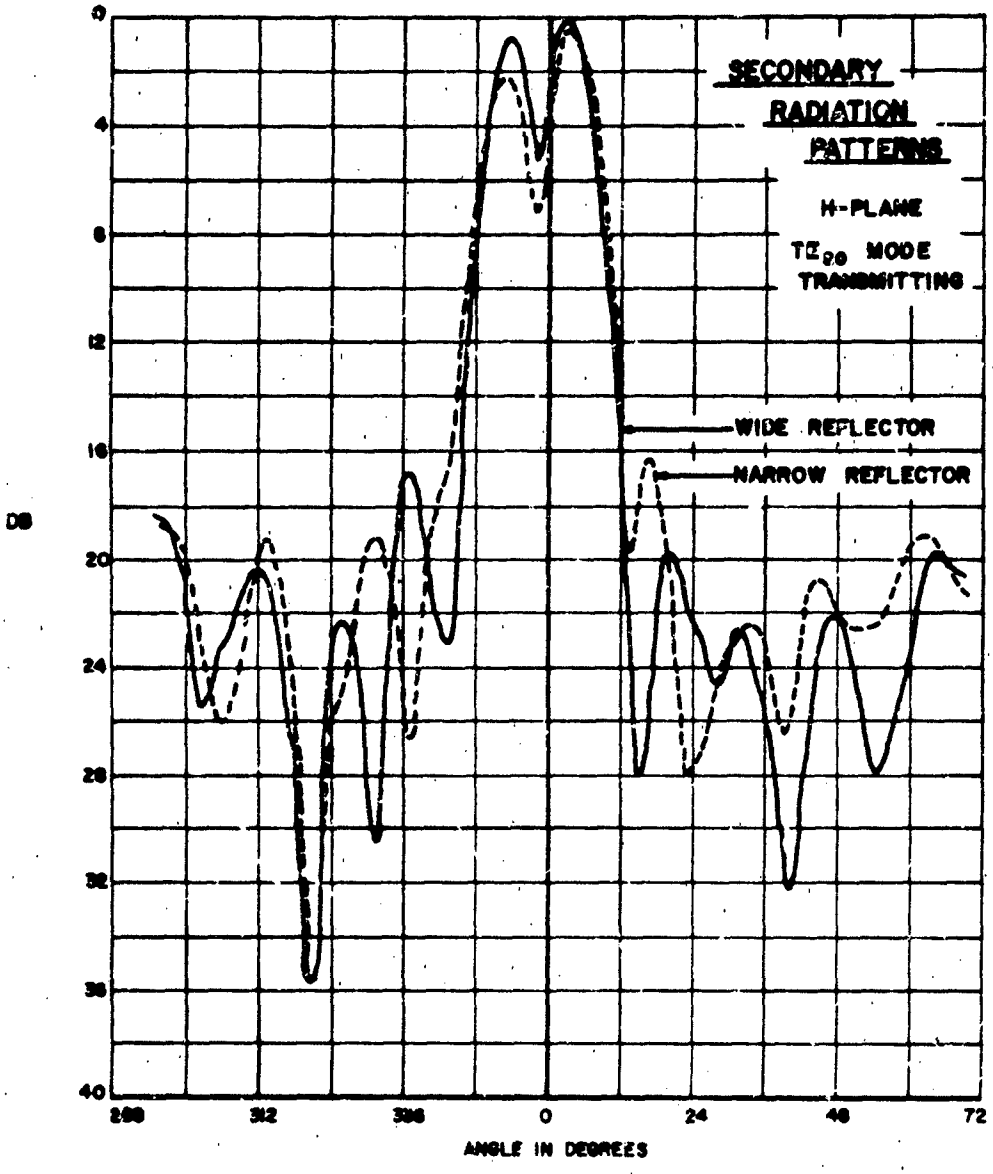
SECONDARY
RADIATION
PATTERNS
H-PLANE
TE20 MODE
TRANSMITTING
WIDE REFLECTOR
NARROW REFLECTOR
DB
0
4
8
12
16
20
24
28
32
36
40
288
312
336
0
24
48
72
ANGLE IN DEGREES

FIG. 4

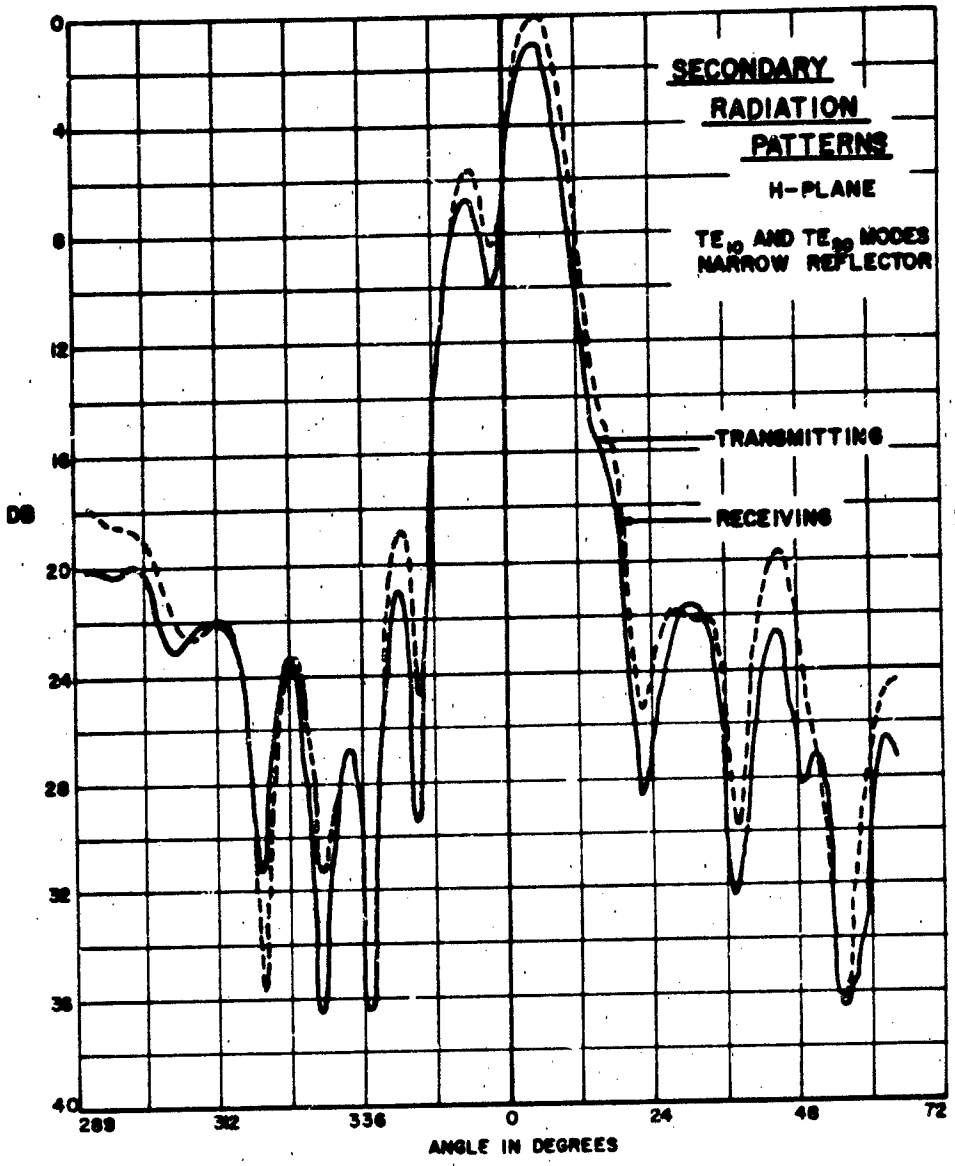
SECONDARY
RADIATION
PATTERNS
H-PLANE
TE10 AND TE20 MODES
NARROW REFLECTOR
TRANSMITTING
RECEIVING
DB
0
4
8
12
16
20
24
28
32
36
40
288
312
336
0
24
48
72
ANGLE IN DEGREES

FIG. 5

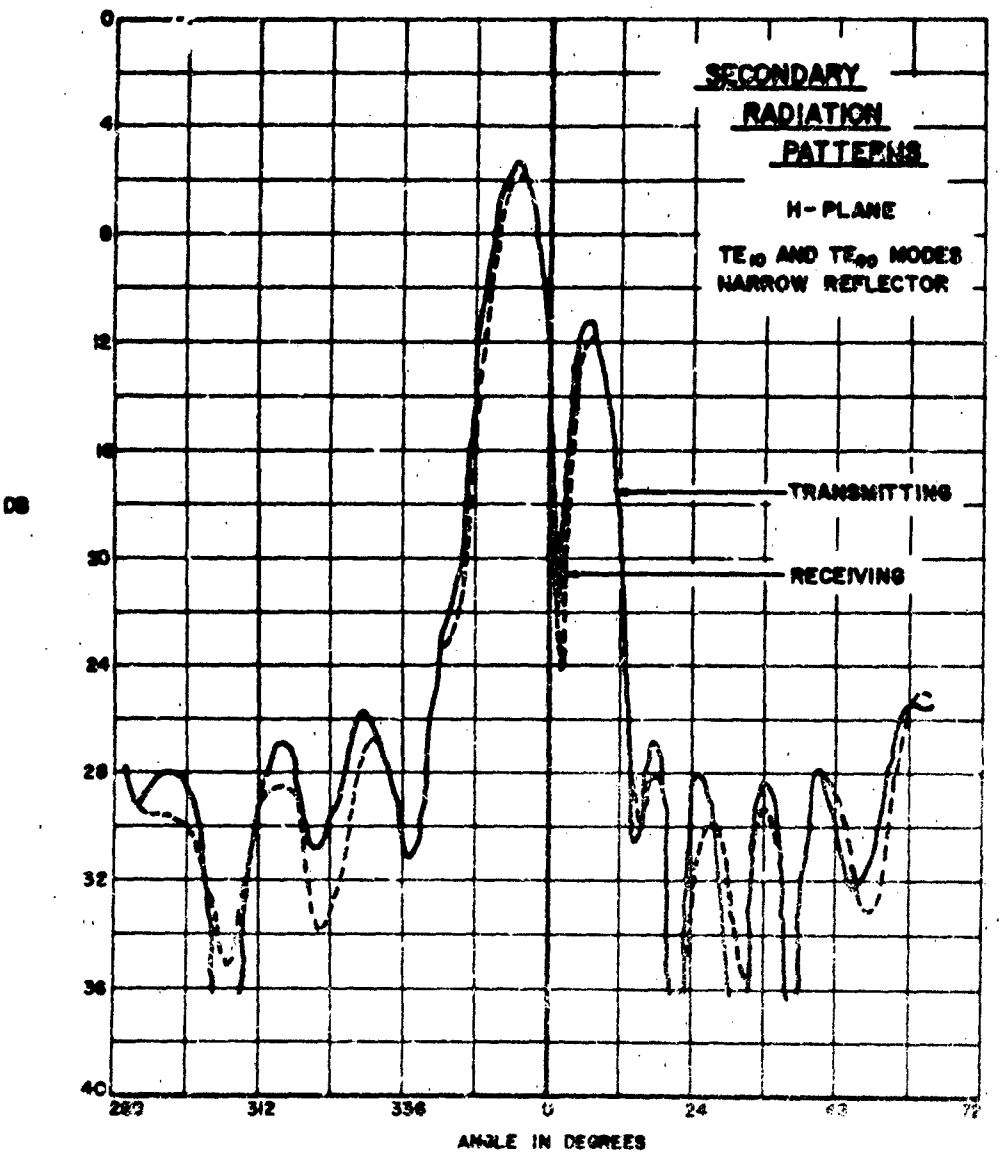
SECONDARY
RADIATION
PATTERNS
H-PLANE
TE10 AND TE00 MODES
NARROW REFLECTOR
TRANSMITTING
RECEIVING
DB
0
4
8
12
16
20
24
28
32
36
40
288
312
336
0
24
48
72
ANGLE IN DEGREES

FIG

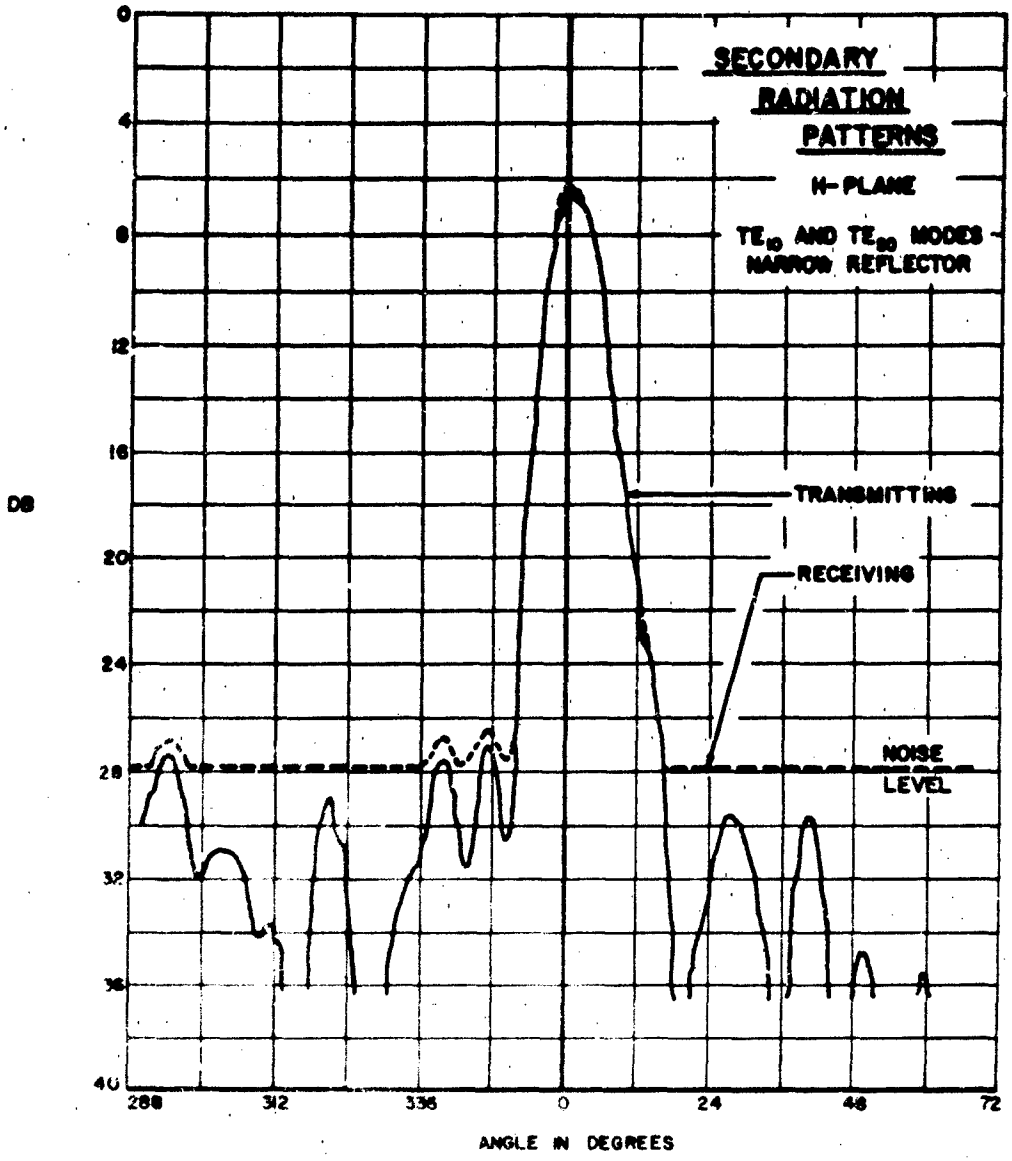
SECONDARY
RADIATION
PATTERNS
H-PLANE
TE_{10} AND TE_{20} MODES
NARROW REFLECTOR
TRANSMITTING
RECEIVING
NOISE
LEVEL
DB
0
4
8
12
16
20
24
28
32
36
40
288
312
336
0
24
48
72
ANGLE IN DEGREES

FIG. 7

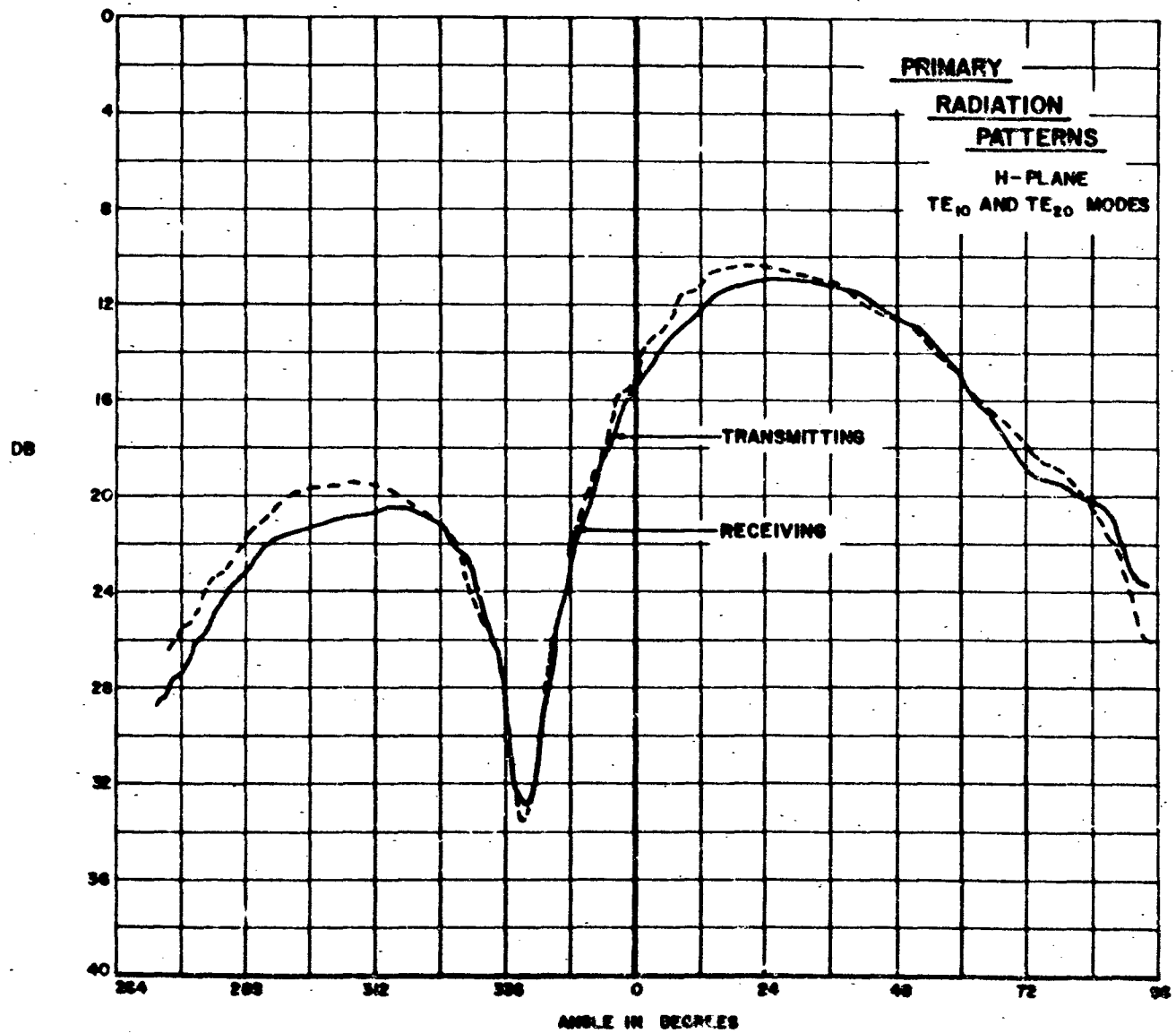
PRIMARY
RADIATION
PATTERNS
H-PLANE
TE10 AND TE20 MODES
TRANSMITTING
RECEIVING
DB
0
4
8
12
16
20
24
28
32
36
40
264
288
312
336
0
24
48
72
96
ANGLE IN DEGREES

FIG. 8

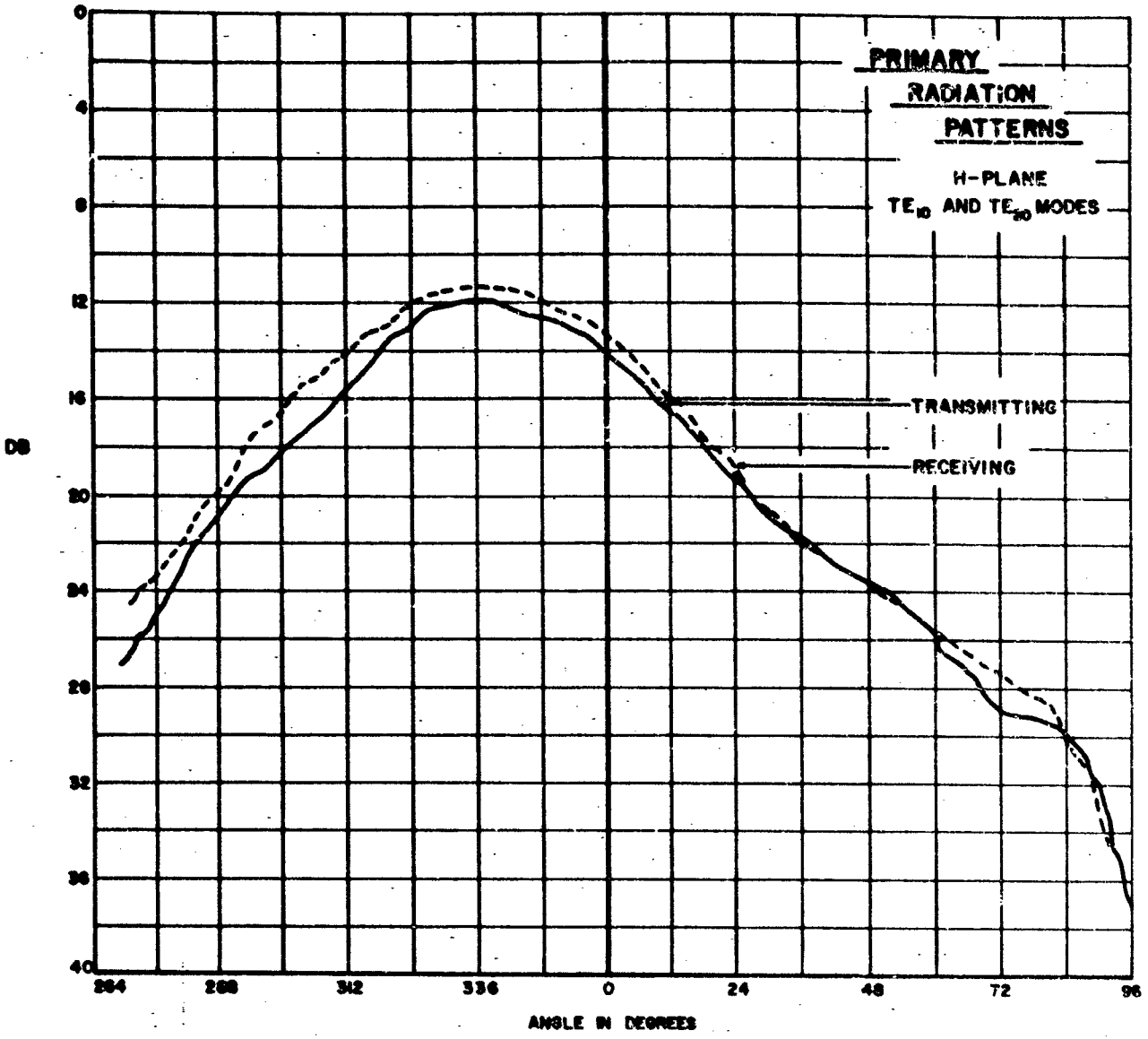
PRIMARY
RADIATION
PATTERNS
H-PLANE
TE10 AND TE20 MODES
TRANSMITTING
RECEIVING
DB
0
4
8
12
16
20
24
28
32
36
40
264
288
312
336
0
24
48
72
96
ANGLE IN DEGREES

FIG. 9

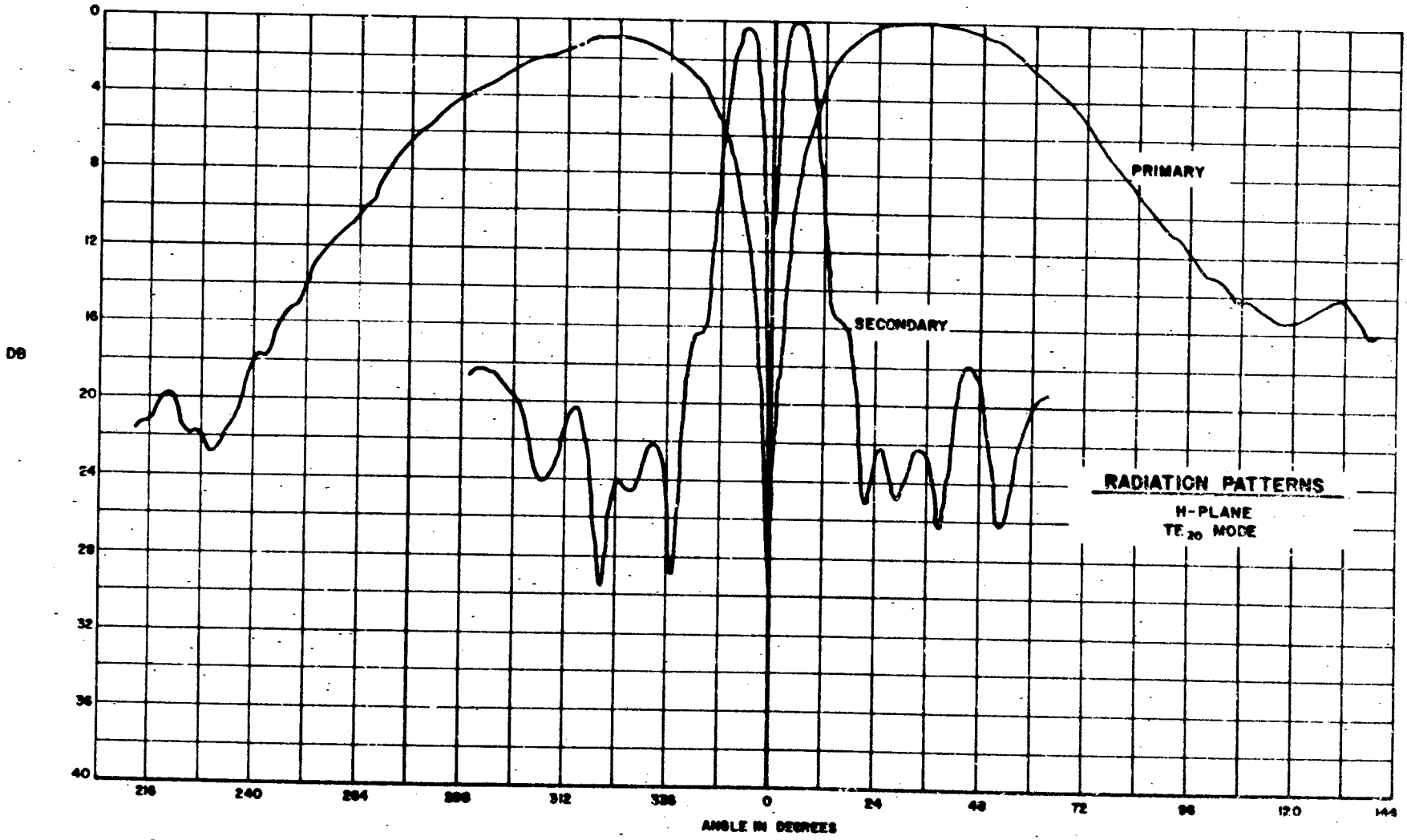
0
4
8
12
16
20
24
28
32
36
40
DB
216
240
264
288
312
336
0
24
48
72
96
120
144
ANGLE IN DEGREES
PRIMARY
SECONDARY
RADIATION PATTERNS
H-PLANE
TE20 MODE

FIG. 10

LONGITUDINAL FIELD DISTRIBUTIONS

RECEPTION OF A PLANE WAVE
4.28 KMC

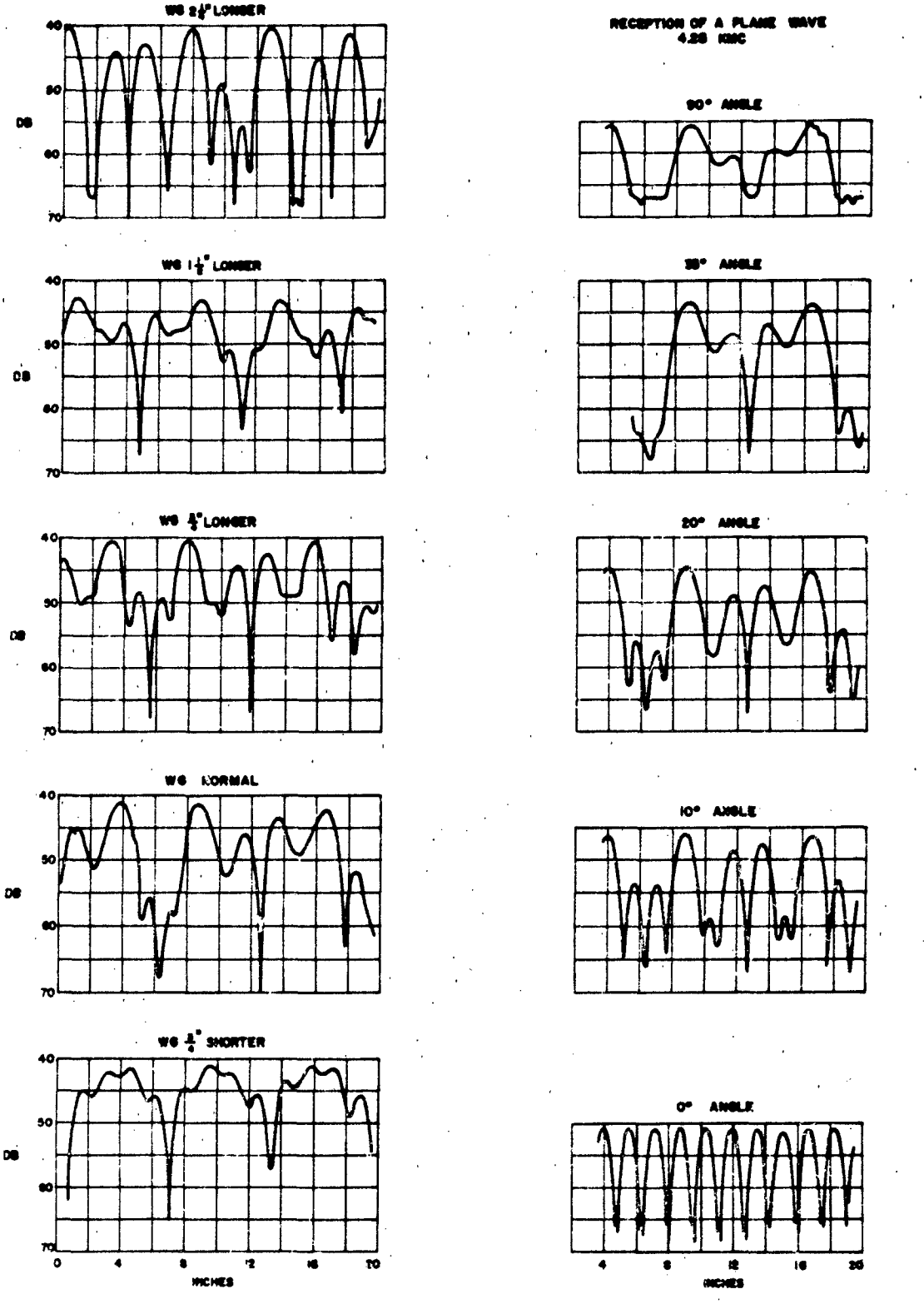

A 20° ANGLE

B PLUNGER NORMAL

FIG. 11

CALCULATED LONGITUDINAL
FIELD DISTRIBUTIONS

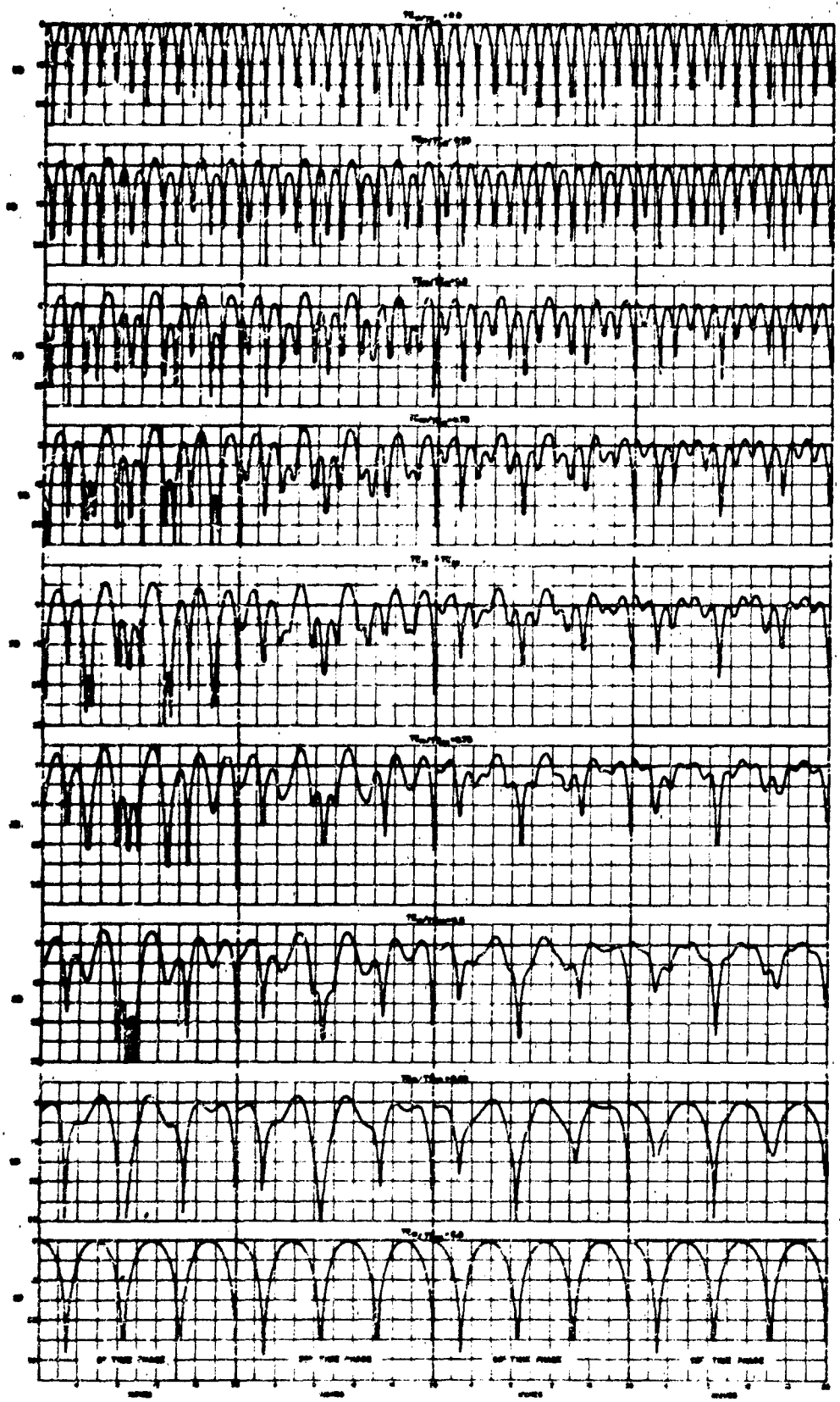

CALCULATED TRANSVERSE FIELD DISTRIBUTIONS

GENERAL TE_{on} - TE_{on} CASE

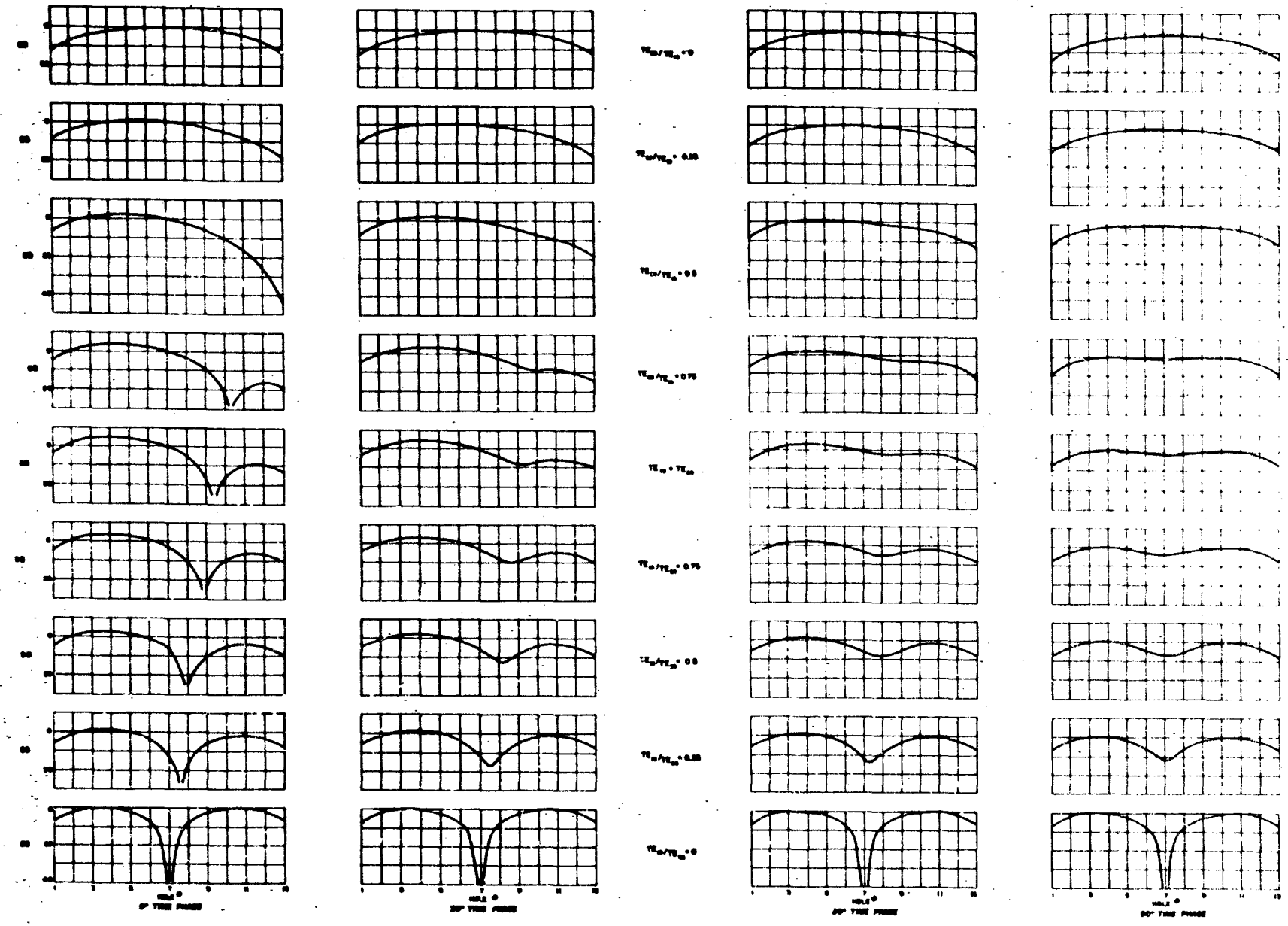

FIG 13

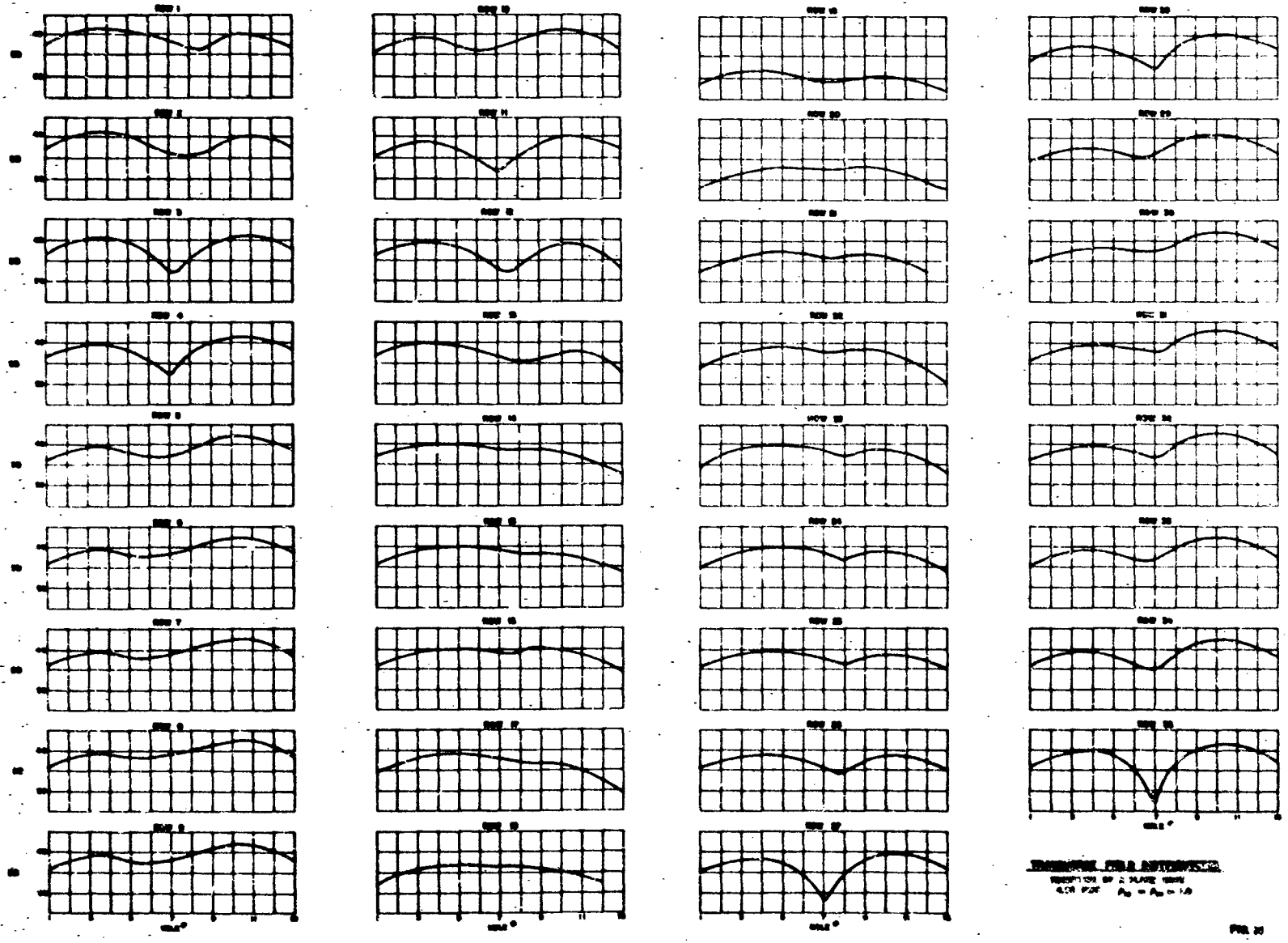

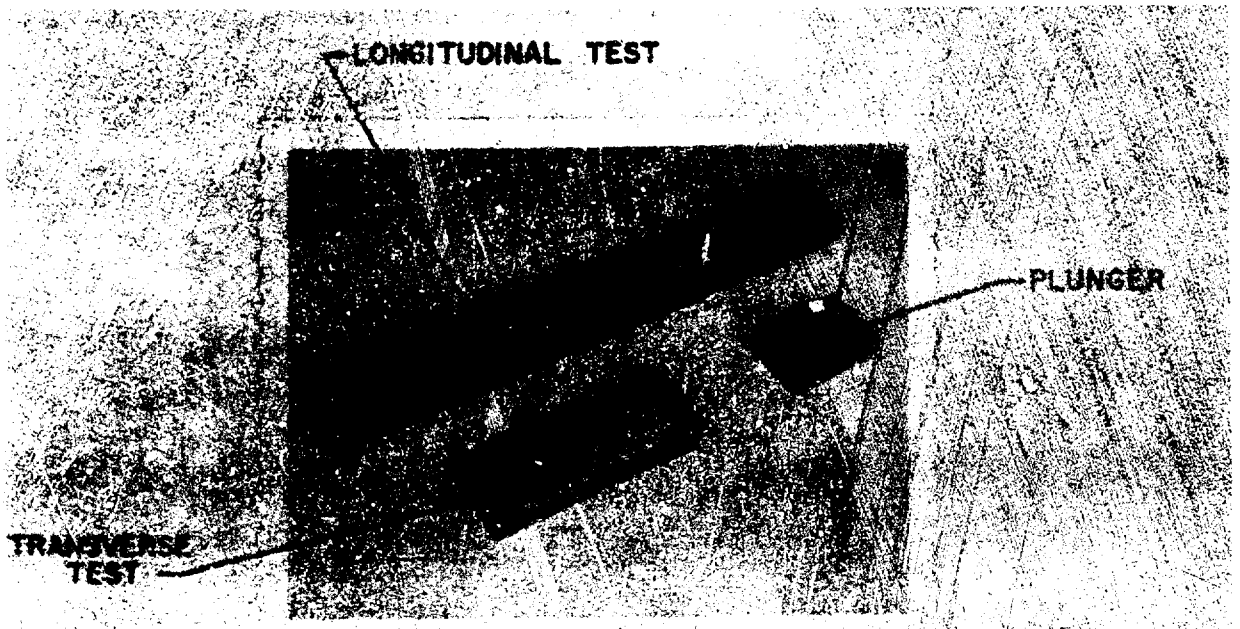

PHOTOGRAPH - 1
WAVEGUIDE SECTIONS WITH HOLES



PHOTOGRAPH - 2
CONTROL OF ANGLE OF
ARRIVAL IN RECEPTION

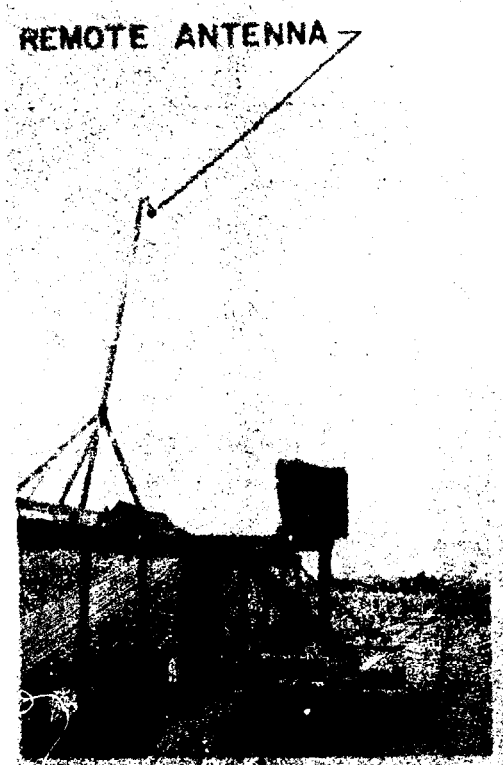

PHOTOGRAPH-3

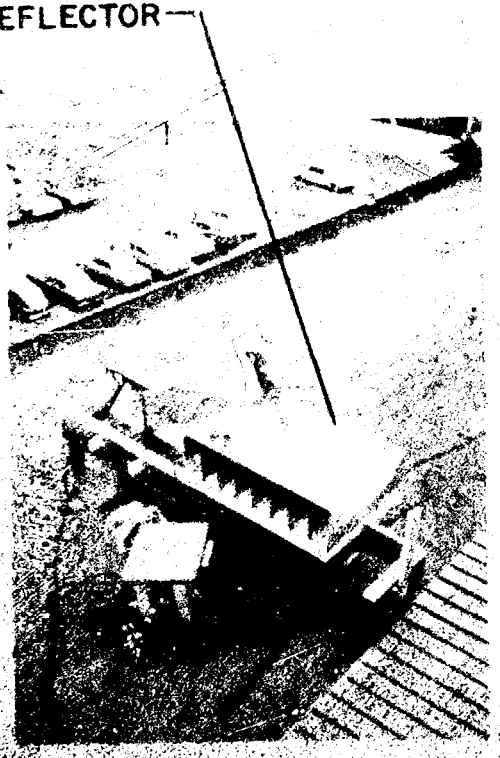

PHOTOGRAPH-4
POSITIONER AND
MOUNTING DETAIL

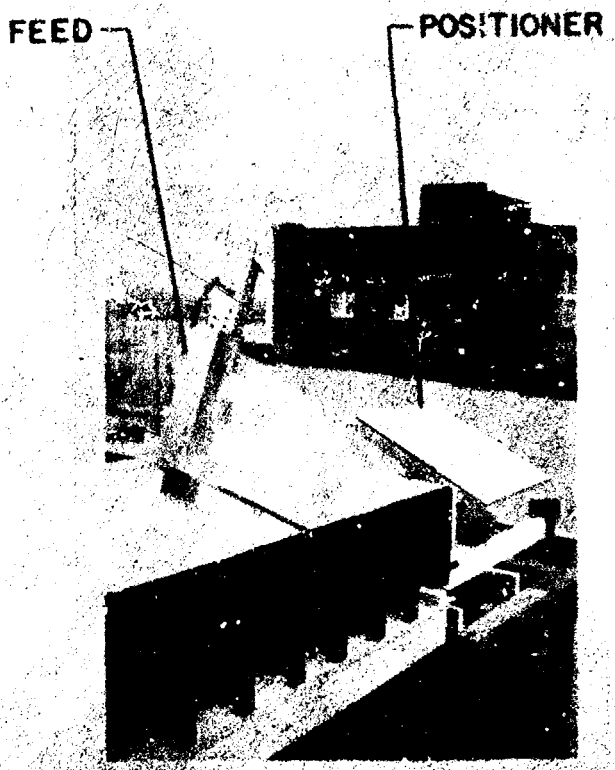

PHOTOGRAPH-5
FEED AND
REFLECTOR

SOME GEODESIC LENSES AND THEIR APPLICATIONS

September 1964

Prepared By

J. L. McFarland

Prepared for presentation to the 14th Annual
Symposium on USAF Antenna
Research and Development
Monticello, Illinois
6-8 October 1964

NORTH AMERICAN AVIATION / Autonetics
Anaheim, California

ABSTRACT

A perfectly focussing parallel plate catenary geodesic lens will be derived. Measured Antenna Patterns will be presented to illustrate the broad-band, perfectly focussing, low sidelobe characteristics of the catenary lens. This lens is capable of producing a phased line source, or it can radiate directly from the catenary curve. In the latter case, the beamwidth of the radiated antenna pattern is determined by the broadside projected aperture in one plane and the end-fire projected aperture in the other.

Some applications of the lens will be discussed; e.g., it lends itself to $\csc^2 \theta$ shaping in one plane and a narrow beam in the other plane. One may also take advantage of the natural catenary shape of suspended cables to implement a very narrow beam lens.

A perfectly focussing parallel plate geodesic lens that radiates from a generalized convexed cylinder will be derived and discussed. This particular lens is useful where flush mounting is required on a cylindrical vehicle and where radiation is desirable directly from the lens (that is, no transmission lines or array elements are used).

A wide angle geodesic lens used in conjunction with a serpentine delay line will be discussed. The application here is to form a multiple band-pass output high Q filter. This particular combination can also be used for a chirping - dechirping network, pseudo-noise coding of waveforms, etc.

CONTENTS

	Page
Abstract	iii
I. Family of Catenary Geodesic Lenses	1
Experimental Results	3
II. Perfectly Focussing Conformal Geodesic Lenses Radiating From Curved Surfaces	11
III. Optical Filter	17

ILLUSTRATIONS

Figure		Page
1.	Cylinder-Plane Geometry Defining Symbols Used in Derivation	1
2.	Geometry of the Developed Lens	2
3.	Feed Pattern to Aperture Distribution Transformation Functions for Perfectly Focussing Catenary Geodesic Antennas	4
4.	Catenary Lens Radiating From the Cylinder-Plane Intersection	5
5.	Equations Used in the Derivation of the Catenary Lens	6
6.	Experimental Model of the Right-Angle Catenary Geodesic Lens	7
7.	Sum and Difference Patterns of Experimental Model	8
8.	Antenna Patterns Illustrating Broadband Capability of Experimental Model	9
9.	Flush Mounted Antenna on a Cylindrical Vehicle	11
10.	The Arc $\overline{PQ}$ From Which Radiation is to Occur	12
11.	Geometry Defining Symbols Used in Lens Derivation	13
12.	Geometry of Lens Using a Circular Cylinder as an Example	16
13.	Schematic of the Optical Filter	18
14.	Geometry of the Filter	19

I. FAMILY OF CATENARY GEODESIC LENSES

Perfectly focussing true time delay parallel plate geodesic lenses find application in many areas; e.g., modern radar systems, IFF antennas, etc. Of particular interest are those lenses that are developable whose output lies along a straight line so that radiation may take place directly from the lens. The folded parallel plate pillbox is an example of such a lens. This paper describes an infinite family of geodesic lenses, all of which have the mentioned properties. The folded parabolic pillbox will be shown to be a special case of a general class of "catenary geodesic lenses." All of the members of the family are parallel plate lenses whose mean surface is formed by the intersection of a catenary cylinder and a plane.

Consider Figure 1. $y = f(x)$ expresses an arbitrary right cylinder. $z = y \tan \phi$ expresses a plane independent of x and going through the origin (although there is no loss in generality in having it go through the origin) that cuts the cylinder as shown. Point "P" is the feed point located at (0, 0, f). The y_2 axis is defined as being in the plane of the planar cut.

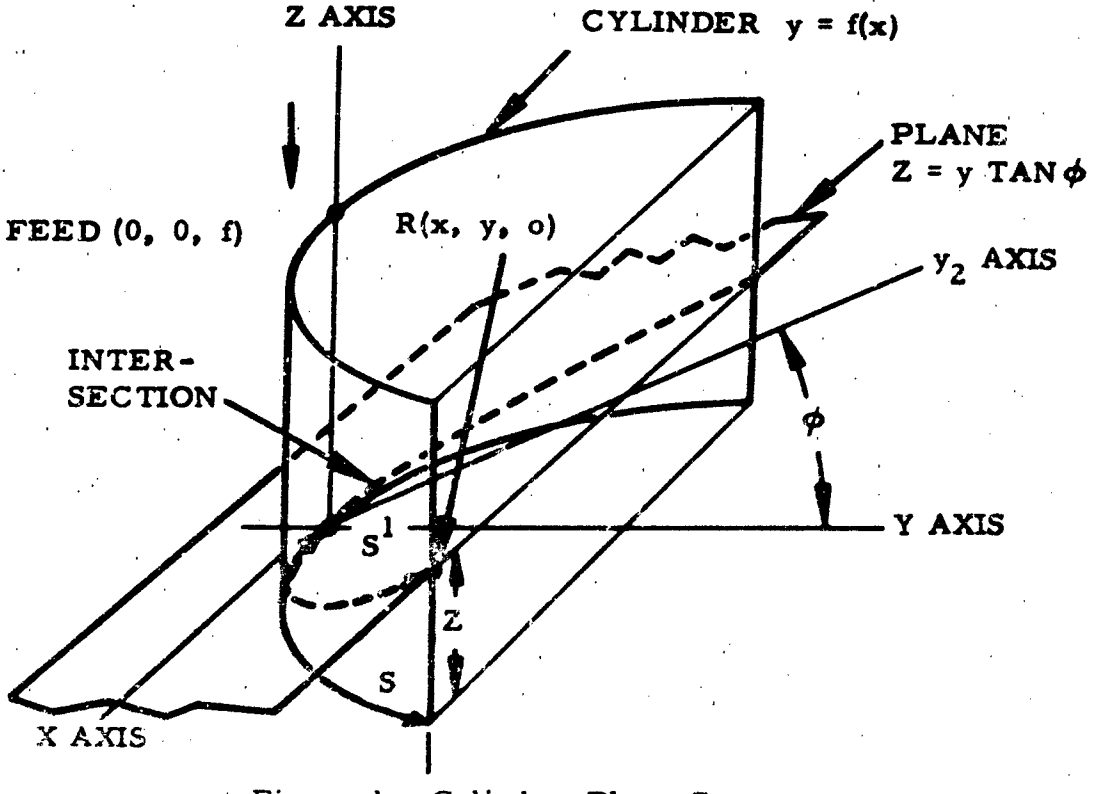

Figure 1. Cylinder-Plane Geometry
Defining Symbols Used in Derivation

From Figure 1, equations 1 through 4 are evident. (For equations, see Figure 5). Since the cylinder is singly curved (developable), consider the lens to be developed, yielding the geometry as shown in Figure 2. In the developed case, all geodesics become straight lines, thereby making analysis simple.

From Fermat's principle, the total path length of any ray from the feed point "P" to the aperture (at $y_2 = y_{2_o}$ is a constant, for perfect focussing. Equations 5 and 6 are easily seen from Figure 2; hence, equation 7 follows from Fermat's principle and equations 5 and 6.

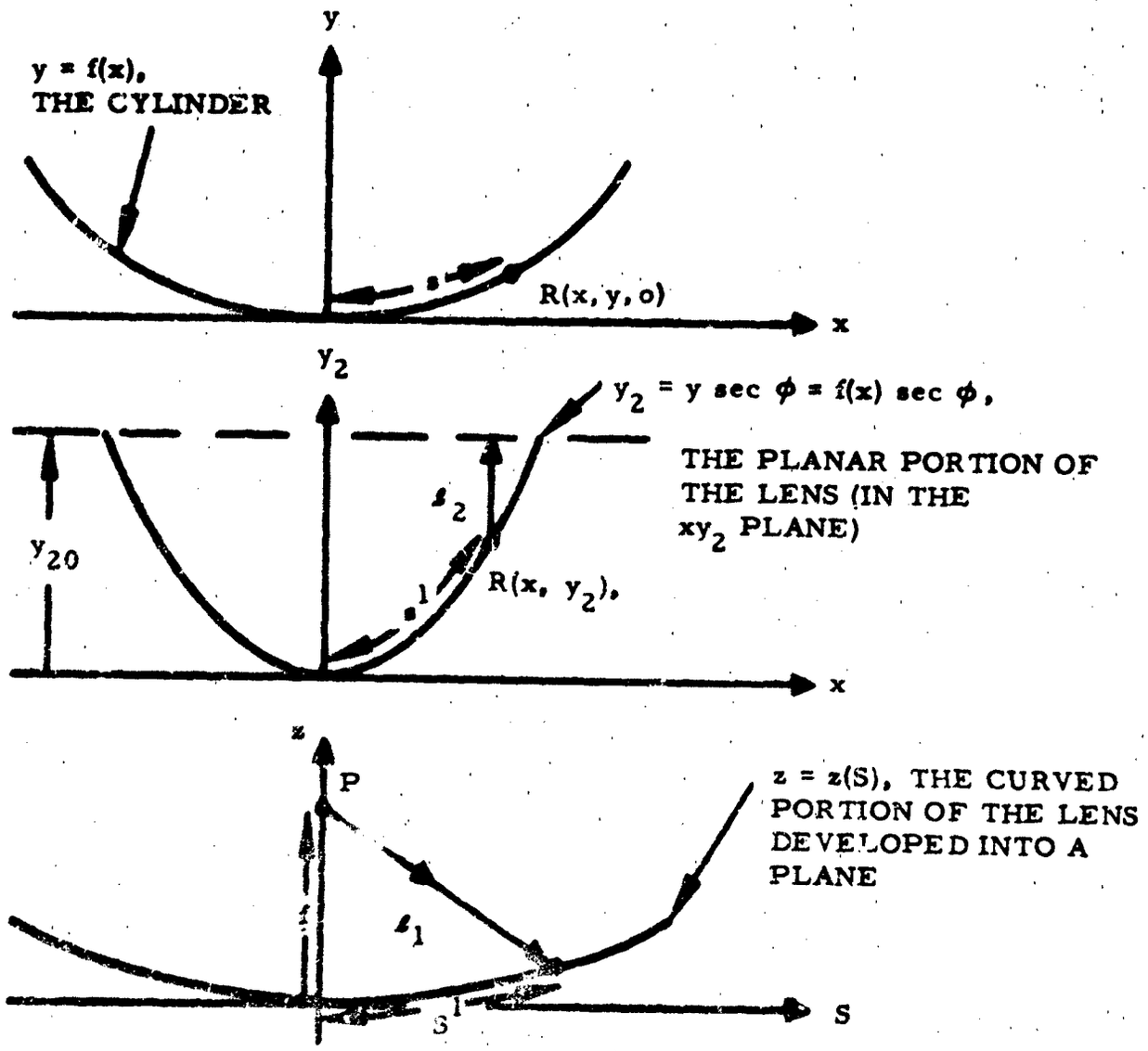

Figure 2. Geometry of the Developed Lens

The constant in equation 7 is obviously $f + y_{2_o}$. Equation 8 then follows. Differentiation of equation 8 with respect to x gives equation 9. Equation 10 follows from differentiation of equation 3. Equating equations 9 and 10 and using equations 1 and 2 yield equation 11. Integrating equation 11 and conditioning the solution to pass through the origin gives the solution of the cylinder (equation 13). z(s) then becomes the hyperbola by substitution (equation 16).

Thus, for every δ (or ϕ), there is a catenary cylinder yielding a perfectly focussing lens. The folded parabolic pillbox is the end-point special case solution corresponding to $\phi = \pi/2$, or $\delta = \infty$. By taking the limit of the solution as $\delta \rightarrow \infty$ one obtains the results given by equations 14 and 15. In this case the developed and planar portion of the lens approach one in the same parabola, and the lens folds back upon itself, giving the folded parabolic pillbox as a special case.

Figure 3 shows a graph illustrating the amplitude transformation functions of the family; e.g., $p(x) = p(\theta)\, d\theta/dx$, where $p(\theta)$ is the power pattern of the feed and x is the aperture variable. The curves show a pronounced inflection point and pedestal effect that may be desirable for low sidelobe distributions.

It should be noted that radiation could occur at essentially the intersection, if one chooses. This would give the same antenna pattern in the xy_2 plane, but would narrow the beamwidth in the yz plane in accordance with the end-fire law. Figure 4 shows a sketch of this configuration with extraneous tin removed and inverted relative to Figure 1. It is perhaps worthwhile mentioning that, in general, the catenary more closely resembles a circle than does a parabola; therefore, one would expect the catenary lens to be capable of slightly more scan than the parabola. The degree of difference in scan capability has not been established.

EXPERIMENTAL RESULTS

The catenary lens corresponding to the $\phi = 0$ solution was built and tested. The f/D ratio was .5, the aperture 5 feet, and the frequency X band. Figure 6 shows a photograph of this model. Figure 7 shows the sum and difference patterns at 9 kmc. The sum pattern was scanned $\pm$ 2.5 beamwidths from broadside without appreciable degradation. No attempt was made to scan beyond this value. Figure 8 shows a frequency run using a less directive feed (standard width X band waveguide). These patterns illustrate the broad band capability of the family of lenses.

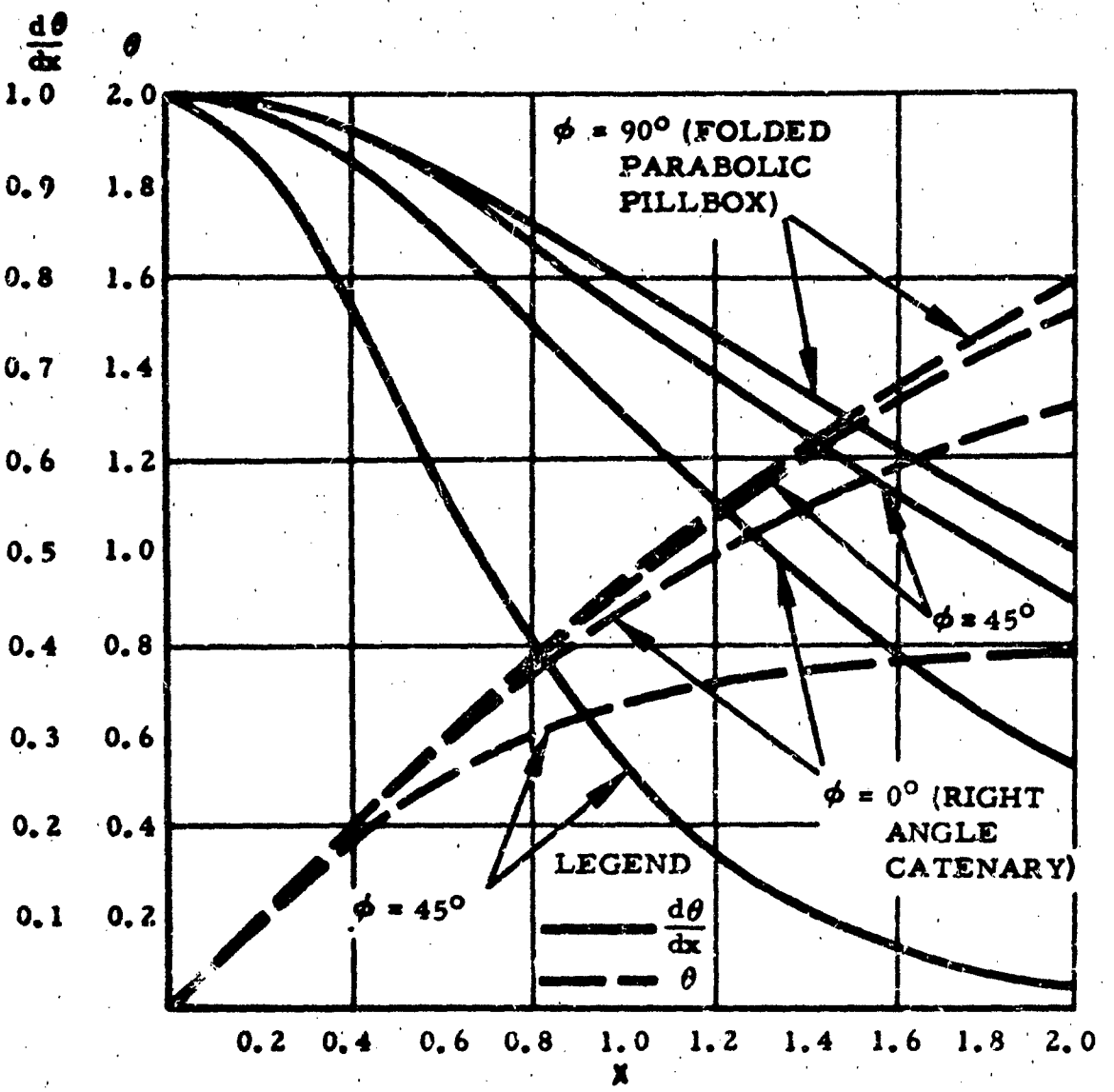

Figure 3. Feed Pattern to Aperture Distribution Transformation Functions for Perfectly Focussing Catenary Geodesic Antennas

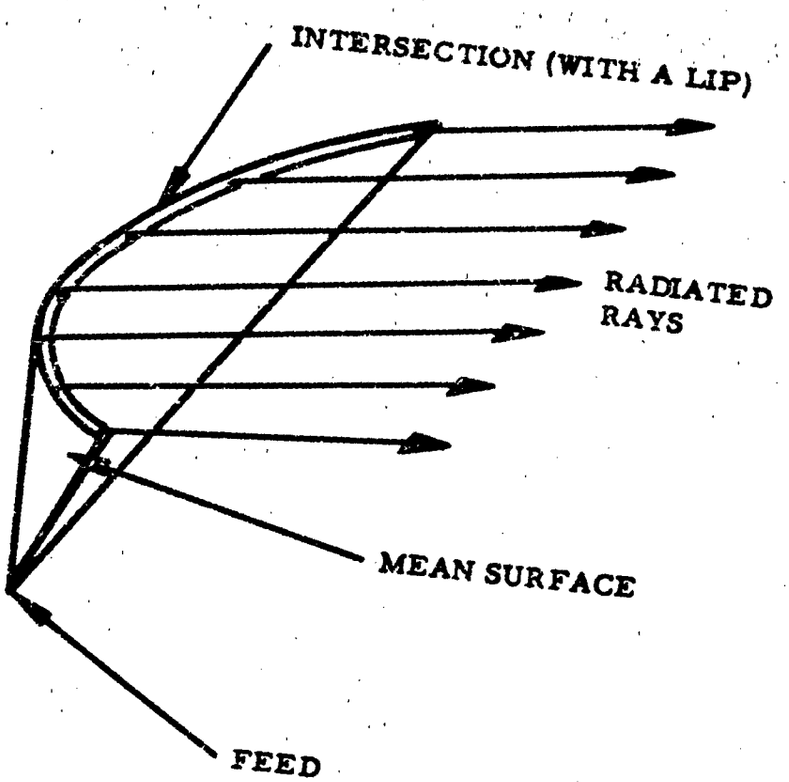

Figure 4. Catenary Lens Radiating From The Cylinder-Plane Intersection

(1) $y_2 = y \sec \phi$

(2) $z = y \tan \phi$

(3) $s = \int_0^x \sqrt{1 + \left(\frac{dy}{dx}\right)^2}\, dx$

(4) $s' = \int_0^x \sqrt{1 + \left(\frac{dy_2}{dx}\right)^2}\, dx$

(5) $\ell_1 = \sqrt{s^2 + (f - z)^2}$

(6) $\ell_2 = y_{2_0} - y_2$

(7) $\ell_1 + \ell_2 = \sqrt{s^2 + (f - z)^2} + y_{2_0} - y_2 = \text{constant}$

(8) $s = \sqrt{(f + y_2)^2 - (f - z)^2}$

(9) $\frac{ds}{dx} = \frac{(f + y_2)\frac{dy_2}{dx} + (f - z)\frac{dz}{dx}}{\sqrt{(f + y_2)^2 - (f - z)^2}}$

(10) $\frac{ds}{dx} = \sqrt{1 + \left(\frac{dy}{dx}\right)^2}$

(11) $x = \delta \int \frac{dy}{\sqrt{y^2 + 2\delta y}}$

(12) $\delta \equiv f(\sec \phi + \tan \phi)$

(13) $\frac{y}{\delta} = \cosh \frac{x}{\delta} - 1$

(14) $\lim_{\delta \to \infty} y_2(x, \delta) = \frac{x^2}{4f}$, a parabola

(15) $\lim_{\delta \to \infty} z(s, \delta) = \frac{s^2}{4f}$, a parabola

(16) $\left(\frac{z}{\delta \tan \phi} + 1\right)^2 - \left(\frac{s}{\delta}\right)^2 = 1$

Figure 5. Equations Used in the Derivation of the Catenary Lens

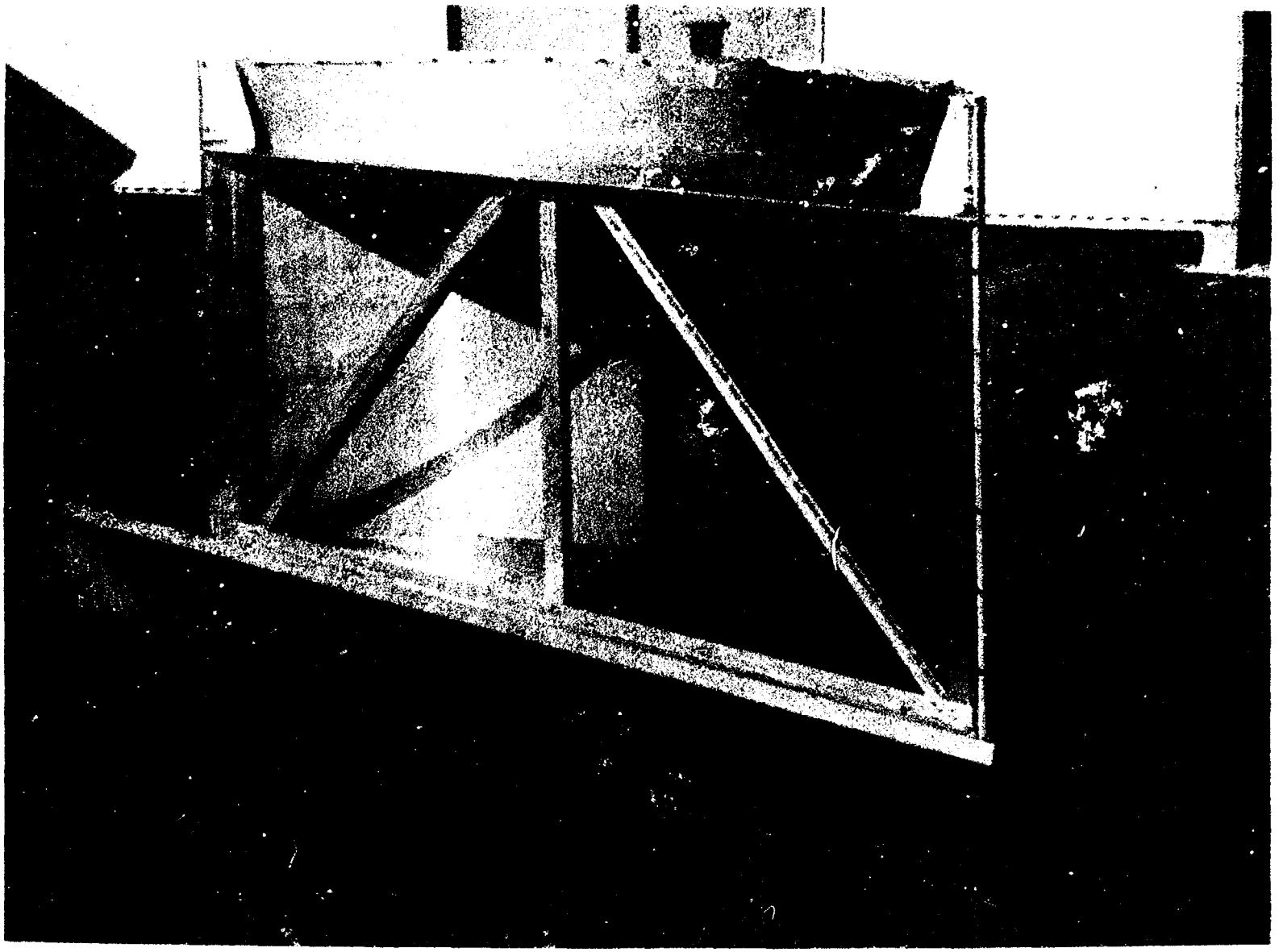

Figure 6. Experimental Mooel of the Right-Angle Catenary Geodesic Lens

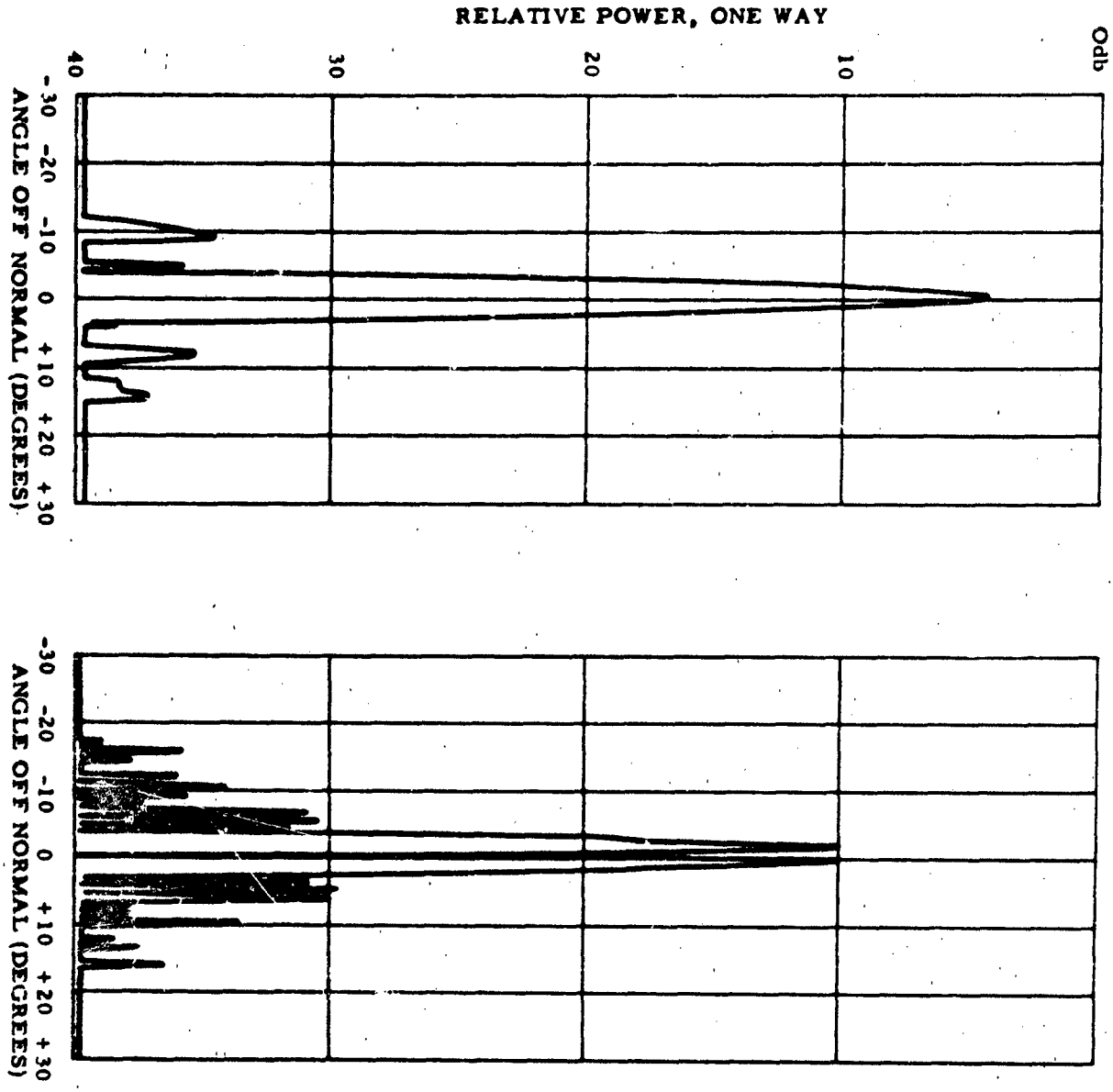

Figure 7. Sum and Difference Patterns of Experimental Model

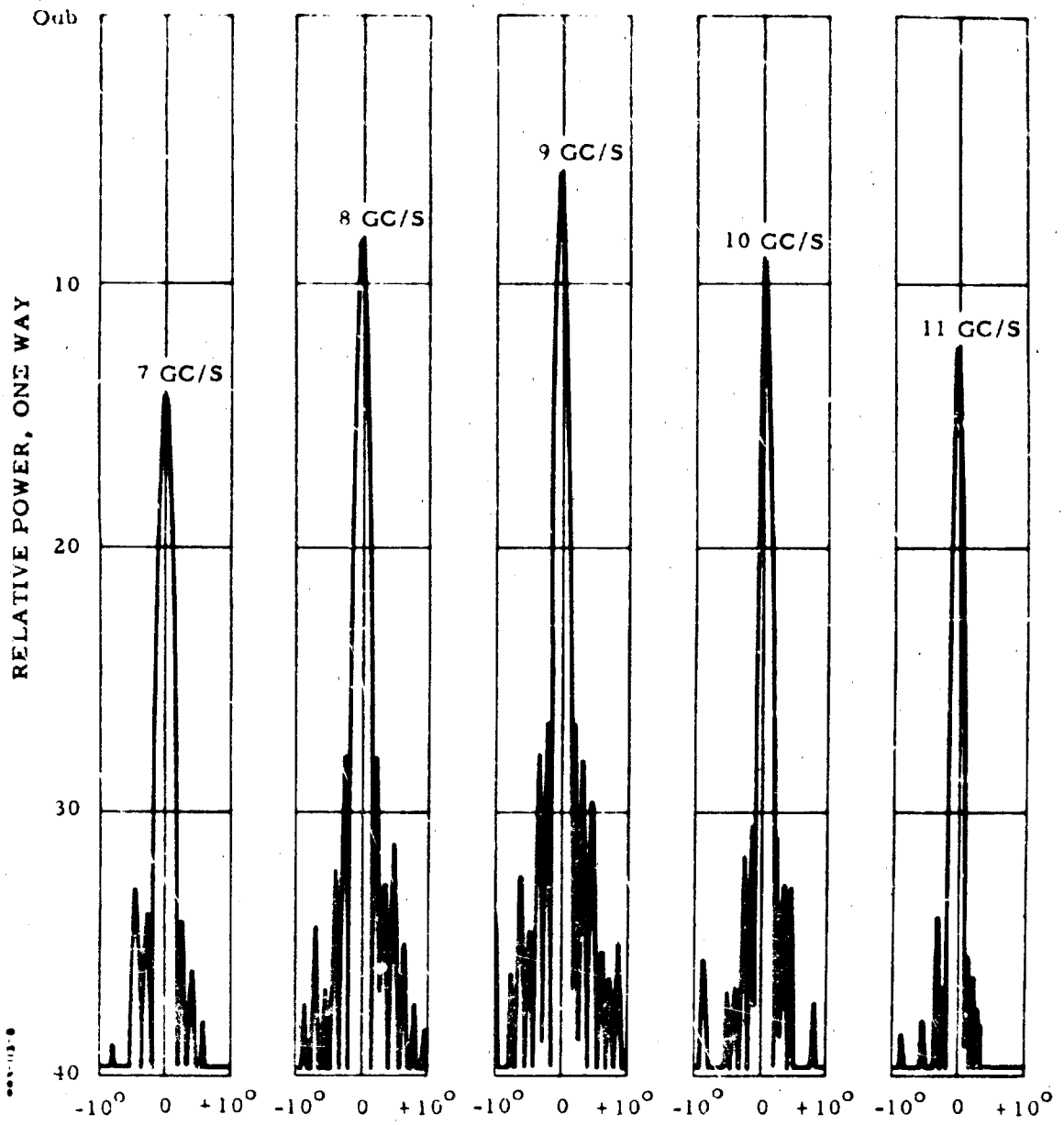

Figure 8. Antenna Patterns Illustrating Broadband Capability of Experimental Model

II. PERFECTLY FOCUSSING CONFORMAL GEODESIC LENSES RADIATING FROM CURVED SURFACES

There are some applications where it is necessary to radiate or receive electromagnetic energy from a curved surface, where the antenna must conform to some particular shape, i.e., it must be flush mounted. The reasons for requiring this may be aerodynamic, minimum volume, etc. The shape of the mounting structure may be cylindrical, conical, etc.

It is the purpose of this paper to derive and describe a parallel plate geodesic lens where radiation occurs from a generalized curved surface. The technique holds for almost any surface of interest, provided the surface is developable. However, the case given here applies only to cylinders.

Consider Figure 9 to represent a portion of a generalized curved surface (such as a vehicle surface, for example) and let the arc PQ represent the desired arc from which radiation occurs. It is assumed that radiation occurs normal to the axis of the cylinder.

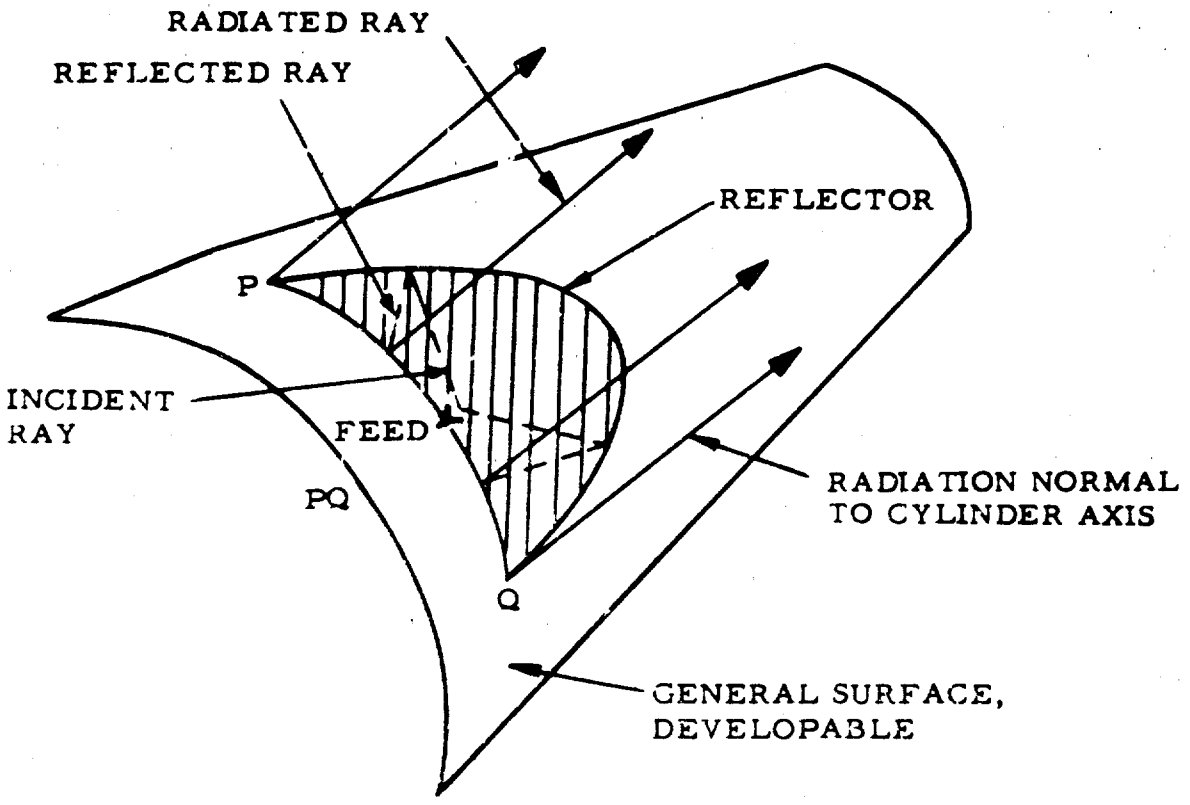

Figure 9. Flush Mounted Antenna on a Cylindrical Vehicle

Shown cross hatched is the mean surface of a flush mounted parallel plate geodesic lens. The lens uses both a reflector and the curvature of the arc $\overline{PQ}$ in order to form an in-phase condition in the direction of the desired main beam. The lens may folded or not folded, depending upon feed blockage criteria. The lens to be derived is perfectly focussing; however, scanning may be performed to some extent by feed movement. Monopulse may be achieved by using two feeds.

Let the arc $\overline{PQ}$ be given, and defined by

$$S = S(\alpha) \quad \text{(See Figure 10)} \tag{17}$$

where S = arc length and α is the angle that the normal makes with the vertical as shown.

Let the lens be developed or flattened out as shown in Figure 11.

The path of a typical ray leaving a feed at point F is shown as FRAA'. "R" is the point on the reflector. Points A and A' will become common when the lens is not developed; i.e., points A and A' will touch.

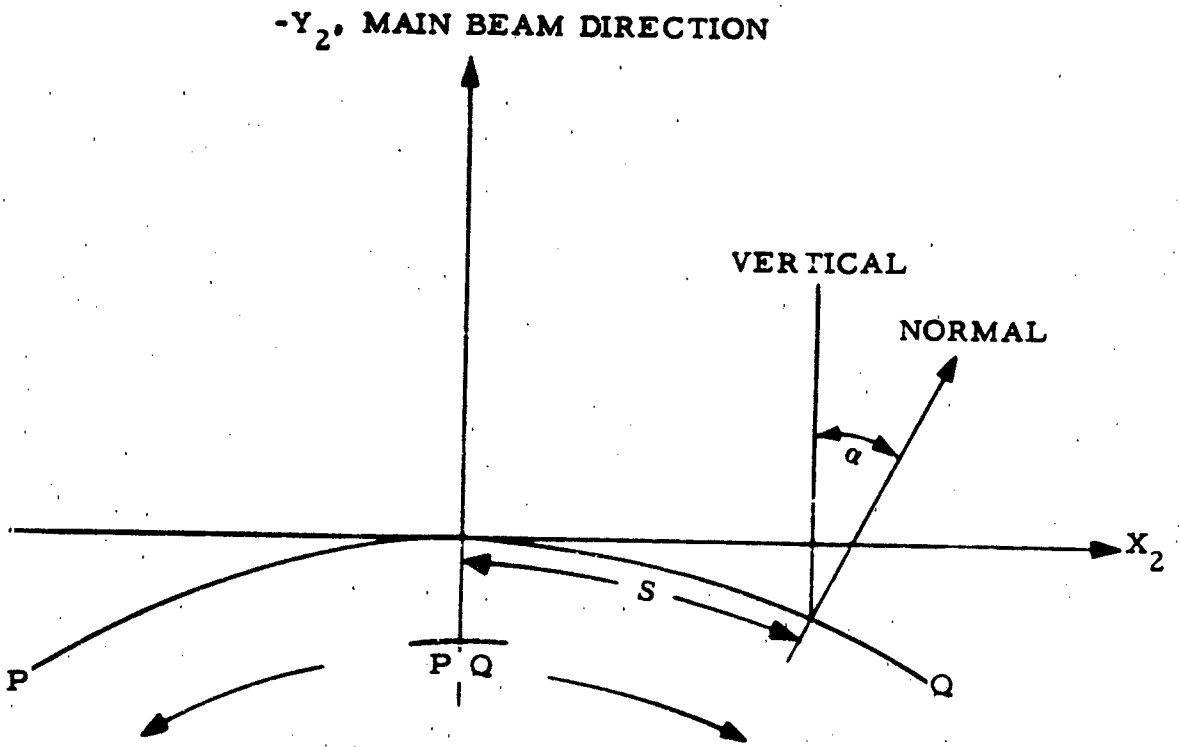

Figure 10. The Arc $\overline{PQ}$ From Which Radiation is to Occur

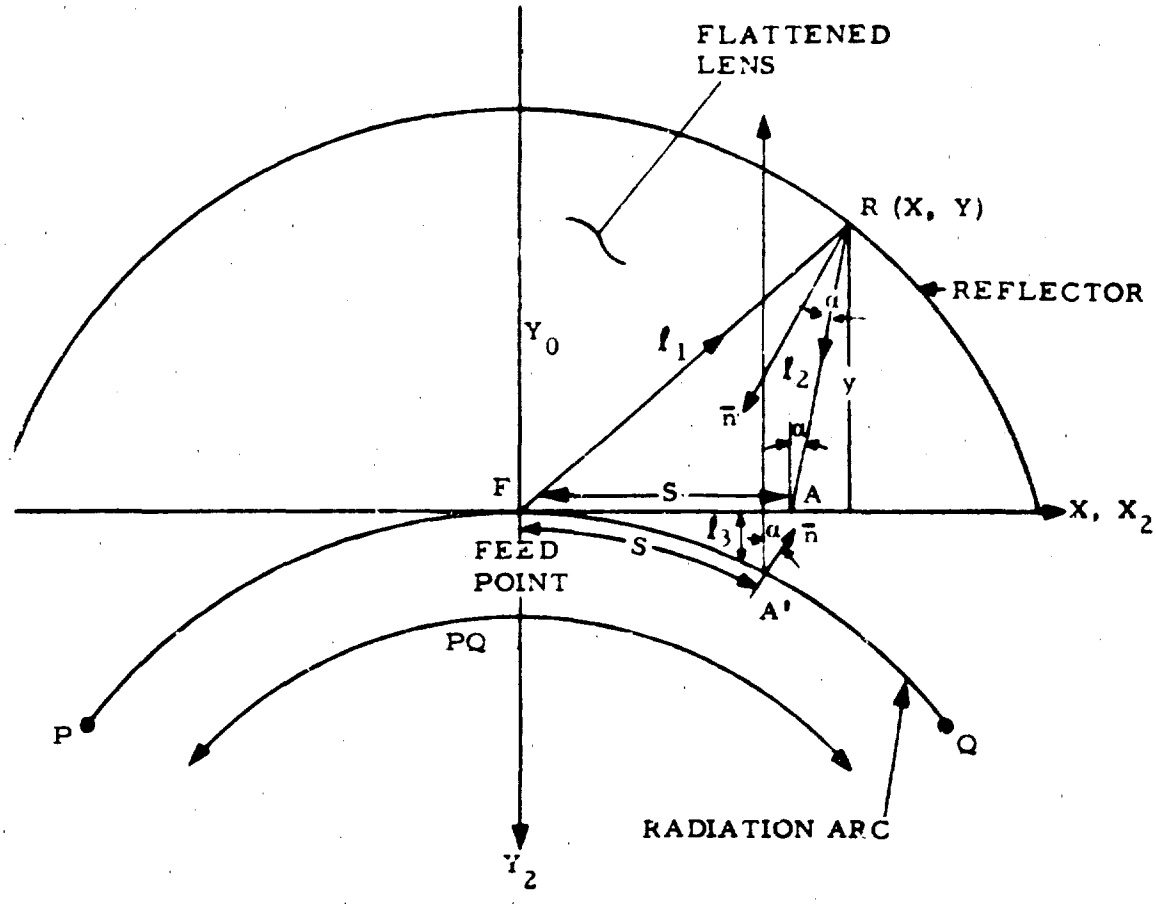

Figure 11. Geometry Defining Symbols Used in Lens Derivation

From Figure 11 it can be seen that (18) follows:

$$S(\alpha) = x(\alpha) - y(\alpha) \tan\alpha \tag{18}$$

Now, the condition for perfect focusing is conditioned by (19)

$$\ell_1 + \ell_2 + \ell_3 = \text{constant} \tag{19}$$

The following relations can be easily obtained:

$$\ell_1 = \sqrt{x^2(\alpha) + y^2(\alpha)} \tag{20}$$

$$\ell_2 = y(\alpha) \sec\alpha \tag{21}$$

The constant in equation (19) is easily seen to be $2y_o$. (The path via the vertex of the reflector is used to arrive at this constant.)

Let the arc $\overline{PQ}$ be expressed in terms of $y_2 = y_2(x_2)$. Then it follows that:

$$S = \int_0^{\ell_3} \sqrt{1 + \left(\frac{dx_2}{dy_2}\right)^2}\, dy_2 \tag{22}$$

but $\frac{dy_2}{dx_2}$ can be seen to be:

$$\frac{dy_2}{dx_2} = \tan \alpha \tag{23}$$

Hence (22) becomes, by substitution of (23):

$$S = \int_0^{\ell_3} \csc \alpha \, dy_2 \tag{24}$$

Differentiating (24) with respect to the upper limit ℓ_3 yields:

$$\frac{dS}{d\ell_3} = \csc \alpha \tag{25}$$

Hence,

$$\ell_3 = \int_0^{S(\alpha)} \sin \alpha \, dS(\alpha) \tag{26}$$

Equation (19) now becomes, by substituting (20), (21), and (26):

$$\sqrt{x^2(\alpha) + y^2(\alpha)} + y(\alpha) \sec \alpha + \int_0^{S(\alpha)} \sin \alpha \, dS(\alpha) = 2y_0 \tag{27}$$

Now solving (18) for $x(\alpha)$ and substituting this into (27) gives an equation that can be explicitly solved for $y(\alpha)$. Then, substituting this explicit form of $y(\alpha)$ into (18) gives an equation that is explicitly soluble for $x(\alpha)$. Hence, the reflector shape is known in parametric form, $x(\alpha)$ and $y(\alpha)$.

An example will now be given to illustrate the technique. Suppose that the radiating arc PQ is circular. Then

$$S(\alpha) = R\alpha \tag{28}$$

where R is the radius of curvature.

Then $dS(\alpha) = R\,d\alpha$ (29)

ℓ_3 will then become

$$\ell_3 = R \int_0^{\alpha} \sin\alpha \, d\alpha = R(1-\cos\alpha) \tag{30}$$

(27) then becomes:

$$\sqrt{x^2 + y^2} + y\sec\alpha + R(1-\cos\alpha) = 2y_0 \tag{31}$$

Equation (18) becomes (32):

$$x - y\tan\alpha = R\alpha \tag{32}$$

(31) and (32) will give for $y(\alpha)$ the following:

$$y(\alpha) = \frac{(\gamma + R\cos\alpha)^2 - (R\alpha)^2}{2R(1 + \alpha\tan\alpha) + 2\gamma\sec\alpha} \tag{33}$$

where $\gamma = 2y_0 - R$

By use of (18), (33) will give an explict relationship for $x(\alpha)$:

$$x(\alpha) = R\alpha + \tan\alpha \frac{(\gamma + R\cos\alpha)^2 - (R\alpha)^2}{2R(1 + \alpha\tan\alpha) + 2\gamma\sec\alpha} \tag{34}$$

(33) and (34) represent the shape of the developed reflector.

Figure 12 shows a plot of the results in the developed form.

If radiation were desired from the concaved side (rather than the convexed side) the same technique for deriving the reflector shape can be used.

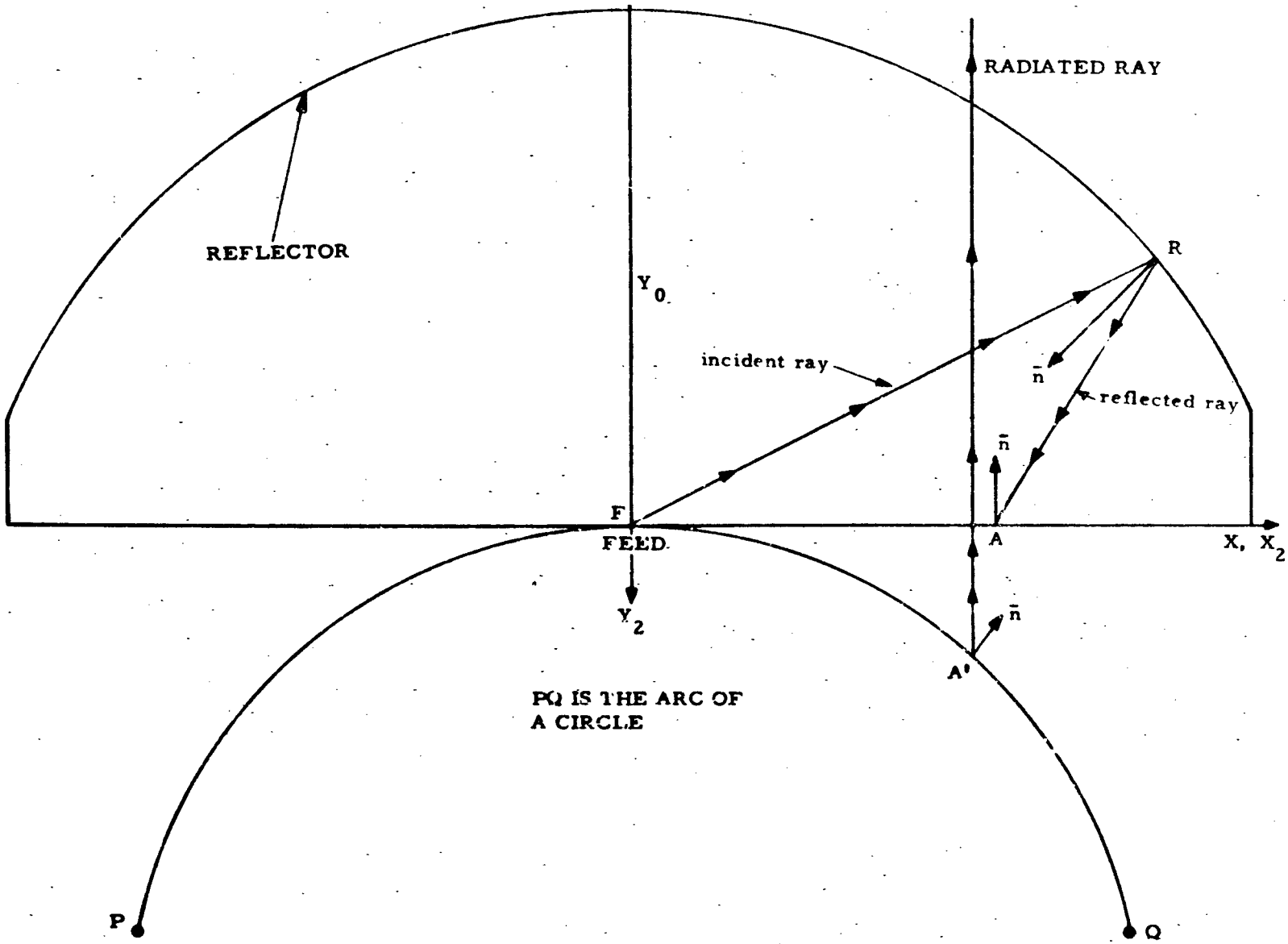

Figure 12. Geometry of Lens Using a Circular Cylinder as an Example

III. OPTICAL FILTER

The following is a brief description of an optical filter that is extremely simple in design and has some advantages over filters now available as shelf items. These advantages will be discussed after a description of the optical filter.

Consider any multiple beam forming true-time-delay device that has a fixed straight line aperture whose amplitude distribution at its aperture remains an even function (about the aperture center) for all beam positions. There are many such devices that fit in this category. To list a few: the Myers-Chu Figure of revolution geodesic parallel plate lens with multiple feeds, the circular folded pillbox with multiple feeds, a flat parallel plate lens using a semicircular dielectric between plates with multiple feeds, and the Maxson tilt end-fed traveling wave array operating in the TEM mode (the velocity of propagation in the TEM mode is not a function of frequency) . Now consider an end-fed frequency-scanning line source to be placed at the straight line output aperture of the multiple-beam-forming device. (Again, there are many ways in which an end-fed frequency-scanning line source can be implemented; e.g., a serpentine stripline, coax, or waveguide, a helix operating in the TEM or TE_{10} mode, etc. Couplers do not have to be directional in principle; however, for the purposes of this analysis, it will be assumed that the couplers are directional). Schematically, the filter under discussion is shown in Figure 13.

The device operates as follows: The input signal contains a wide band of frequencies. The frequency-scanning delay line produces different phase gradients at the elements for different frequency components. Each frequency is focused to a different place along the feed locus of the muitiple beam device; hence, each multiple feed along the feed locus will pick up a narrow band of frequencies and reject others.

The simplest way to analyze the device is to derive the transfer function between the nth feed (a typical feed) and the input - then by the reciprocity theorem, this will also represent the transfer function between the input and the nth feed. If a Dirac delta function $\delta(t)$ is transmitted out of the nth feed, the Fourier Transform of the response at the "input" represents the transfer function, $F_i^n(j\omega)$, between the input and the nth feed. Assume that the multiple beam forming device is perfectly focusing; i.e., it produces a tilted plane wave (the angle of

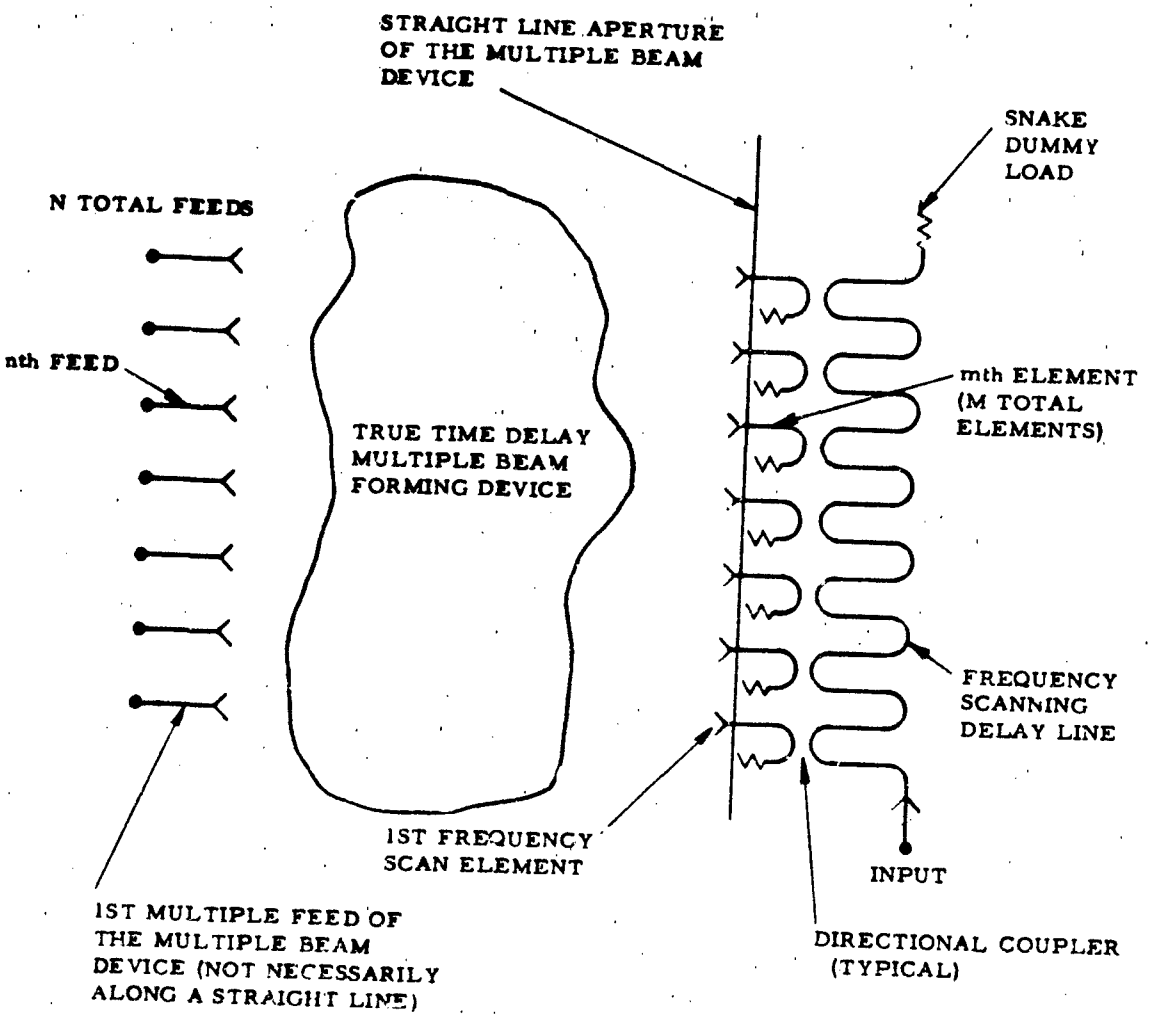

Figure 13. Schematic of the Optical Filter

tilt, θ, of the plane wave is dependent upon which feed, of the N total feeds, is under consideration) at the frequency-scanning aperture. Schematically this situation is shown in Figure 14.

Now, the power pattern produced by the nth feed $p(\theta)$ produces an amplitude distribution at the frequency-scanning aperture. Define the amplitude distribution produced by the nth feed at the frequency scanning aperture as A_m^n. The conductance distribution of the serpentine feed also produces an amplitude distribution; define this amplitude distribution as B_m. Hence, the response at the "input" terminal, $f_i^n(t)$, to the $\delta(t)$ from the nth feed may be written:*

$$f_i^n(t) = \sum_{m=1}^{M} A_m^n B_m \, \delta \left[t - t_o - \frac{(M-m)d\sin\theta}{v_1} - \frac{ms}{v_2} \right]$$

*Rigorously speaking, the results apply exactly only if a TEM delay line (snake) is used; however, for practical purposes, the results apply also to NON-TEM mode delay lines.

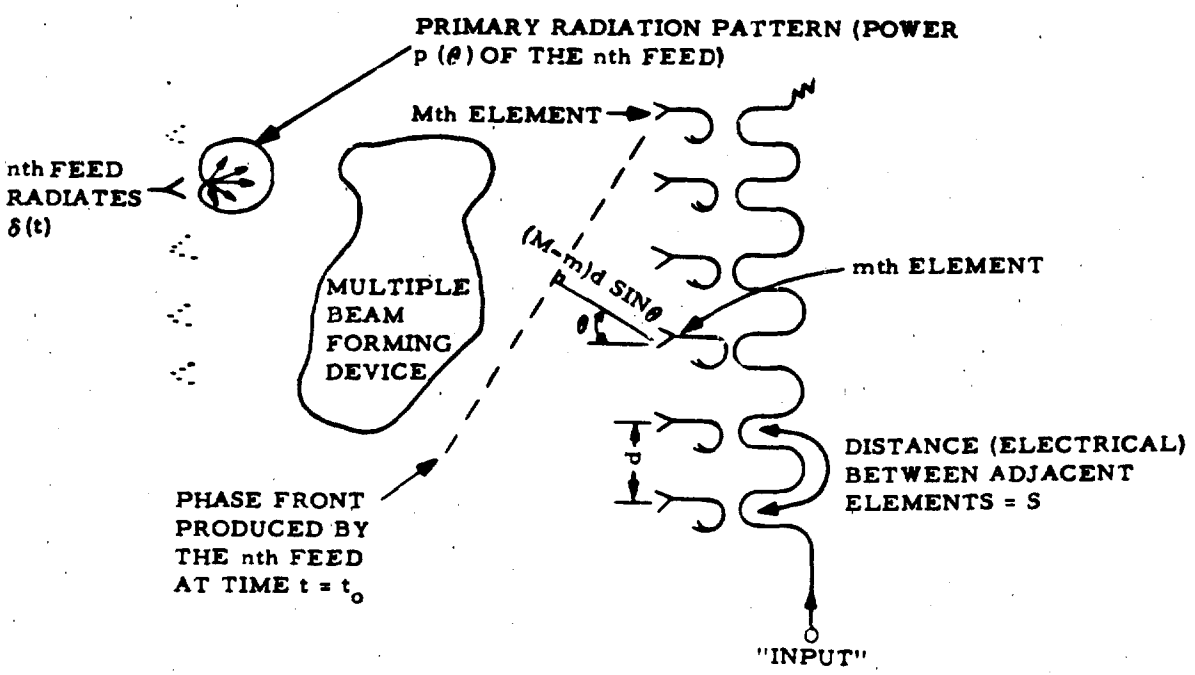

Figure 14. Geometry of the Filter

where

d = interelement spacing of serpentine elements

θ = angle measured from the serpentine array normal positive toward the load end

v_1 = phase velocity of the propagated wave from the feeds to the serpentine delay line

v_2 = phase velocity of the serpentine delay line

s = distance between elements on the serpentine delay line via the snake path

t_o = time required for a ray to propagate from the nth feed to the Mth element on the snake

Hence, the transfer function between the nth feed and the "input" is as follows:

$$F_i^n(j\omega) = \sum_{m=1}^{M} A_m^n B_m e^{-j\omega\left(t_o + \frac{M d \sin\theta}{v_1} + \frac{ms}{v_2} - \frac{md\sin\theta}{v_1}\right)}$$

$$\text{or } F_i^n(j\omega) = e^{-j\omega\left(t_o + \frac{M d\sin\theta}{v_1}\right)} \sum_{m=1}^{M} A_m^n B_m e^{jm\omega\left(\frac{d\sin\theta}{v_1} - \frac{s}{v_2}\right)}$$

The phase term $e^{-j\omega\left(t_o + \frac{M d\sin\theta}{v_1}\right)}$ will be dropped, leaving:

$$F_i^n(j\omega) = \sum_{m=1}^{M} A_m^n B_m e^{jm\omega\left(\frac{d\sin\theta}{v_1} - \frac{s}{v_2}\right)}$$

or in another form

$$F_i^n(k) = \sum_{m=1}^{M} A_m^n B_m e^{jm(k_1 d\sin\theta - k_2 s)}$$

where

$k_1 = \frac{\omega}{v_1}$, the propagation constant in the multiple beam-forming device

$k_2 = \frac{\omega}{v_2}$, the propagation constant in the serpentine delay line.

$F_i^n(k)$ can be recognized as the expression for the far field pattern of the serpentine snake with an amplitude distribution of $A_m^n B_m$ (rather than B_m) at an angular frequency ω and using a "wrap-up factor of $\frac{s}{d}$"; however, the variable of interest in our case is ω, not sin θ. So the transfer function $F_i^n(j\omega)$ | that is, the amplitude response vs. frequency | resembles the previously mentioned antenna pattern closely. As a matter of fact, in the case where k_2 is proportional to k_1 the shape of the transfer function is the same as the shape of the antenna pattern mentioned. In the case where k_2 is not proportional to k_1 (as is the case when a TEM mode multiple beam forming device is used in conjunction with a non-TEM mode delay line) the analogy is not quite so simple. Even in this case, however, the antenna pattern mentioned will closely resemble the transfer function.

It is of interest to note that all M elements of the serpentine delay line are used simultaneously for all N output ports of the filter; thus, the "Q" of filter is high for all output ports. This is one advantage of this filter technique. Low side-lobes can be achieved in the transfer function by designing the product $A_m^n B_m$ to be tapered. The taper of the factor A_m^n can be increased by using a more directive feed at the nth port. The taper of the factor B_m can be controlled by appropriate conductance design in the snake delay line. Another point of interest is the fact that the product $A_m^n B_m$ can be made virtually independent of n; that is, the shape of the transfer function can be made to be the same for all output ports of the filter; however, the bandwidth increases and the gain decreases for output ports away from the broadside case (in such a fashion that the gain-bandwidth product remains constant). The way in which one can implement the independence of $A_m^n B_m$ on n is to increase (in a secθ fashion) the output feed sizes as the port progresses from the broadside case to the extreme scan case. Since the gain-bandwidth product remains constant for all output ports (it is assumed that losses incurred are not dependent upon n) it can be seen that, in order to make $A_m^n B_m$ independent of n, the gain will decrease as cosθ, hence, the bandwidth will increase as secθ.

If a constant bandwidth is desired from all output ports, a constand gai.. will also exist at all ports. This can be achieved only if the gain factor for the amplitude distribution $A_m^n B_m$ increases as sec θ (θ is a function of n). This condition can be met, or at least approximated by decreasing the feed sizes away from broadside. Of course, the side lobe levels of the transfer function will increase as the port is farther removed from broadside.

An experimental model is presently being built; however, measured results are not yet available.

HI GAIN ANTENNAS

A SURVEY OF SIDE LOBE OPTIMIZATION, SUPPRESSION AND CANCELLATION TECHNIQUES

By

John B. Damonte
Dalmo Victor Company, Belmont, California

1.0 INTRODUCTION

The purpose of this paper is to describe some of the techniques that are available for designing low side lobe antennas. The term "low side lobes" is a relative term without much meaning unless it is particularized. For the sake of clarity, the discussion that follows will be in terms of an equally spaced, ten element, linear array of identical elements. For half wavelength element spacing, and broadside operation, the absolute gain of such an array is of the order of 10 db and "low side lobes" are defined to be of the order of -30 db relative to the main lobe peak.

Our goal will be to develop designs that optimize the side lobe performance without unduly compromising the absolute gain or the beamwidth. Given the ten element array described above, there are three basic approaches that one can take in designing a low side lobe antenna system:

1. Side lobe optimization
2. Side lobe suppression
3. Side lobe cancellation

Side lobe optimization defines the approach which utilizes conventional design techniques to extract a low side lobe design consistent with good gain and beamwidth performance. It implies the best or most favorable tradeoff between side lobe level, gain and beamwidth. These techniques are briefly described in Section 2.0.

Side lobe suppression defines an approach which starts with an "optimized design" and applies unconventional design techniques to further reduce the apparent side lobe level. It implies an antenna system that forces the inherent side lobe level to appear as a lower side lobe level or suppresses side lobes at the antenna terminals. These techniques are discussed in Section 3.0.

Side lobe cancellation defines an approach which utilizes an antenna whose side lobes have been optimized and suppressed to the extent that is possible, and then applies various means to the system to cancel, nullify or compensate for the effects of the side lobes. These techniques are discussed in Section 4.0.

On the basis of these assumptions and definitions, let us now review these approaches in detail to see what sort of latitude they offer the antenna designer.

2.0 SIDE LOBE OPTIMIZATION

We have defined side lobe optimization to mean the most favorable tradeoff between side lobes, gain and beamwidth. For any particu design, there are a limited number of parameters available to the designer to optimize the pattern performance. For an equally spaced, ten element, linear array of identical elements with $\lambda_o/2$ spacing, the general expression [1, 2] for the voltage radiation pattern may be written as:

$$E(\theta\phi) = \sum_{i=0}^{n-1} \bar{a}_i \, E_{oi}(\theta\phi) \, e^{ji\psi}$$

where $\bar{a}_i$ = complex feeding coefficient of the ith element

E_{oi} = element pattern of the ith element

n = total number of elements

$\psi = \frac{2\pi s}{\lambda_o} \cos\theta$

s = element spacing

θ & ϕ = usual polar and equatorial pattern angles

For this particular array, equation (2.1) can be written as:

$$E(\theta\phi) = E_o(\theta\phi) \sum_{i=0}^{9} \bar{a}_i \, e^{ji\pi\cos\theta}$$

For the moment we will assume that the element patterns $E_o(\theta\phi)$ are isotropic and that the element spacing s and the wavelength λ_o have been predetermined and are fixed. This leaves only the feeding coefficients $\bar{a}_i$ as design variables.

The feeding coefficients $\bar{a}_i$ define the amplitude and phase of the energy fed to each of the array elements. Generally, the phase is held constant from element to element since such a phase distribution provides a pattern with the highest gain and the narrowest beamwidth for a given amplitude distribution. The choice of array amplitude distribution is a tradeoff between beamwidth, gain and side lobe level. Two "optimum" amplitude distributions for arrays

are the Dolph-Tchebyscheff [3-7] and the Taylor [8-10] distributions. The Dolph-Tchebyscheff distribution will be applied to this array. It provides the narrowest null beamwidth for a given level of equal side lobes. Curves showing how the gain and beamwidth vary as a function of side lobe level are presented in Figures 2.1 and 2.2. Using these curves and the feeding coefficient tables [6], the designer can quickly develop a design which is optimum for his particular needs in terms of side lobes, beamwidth and gain.

Although it is possible to design an antenna for very low side lobes, realizing such performance may be quite another story. As the design side lobe level becomes very small, the requirement on tolerances becomes prohibitive. Analyses [11-13] and measurements over the years indicate that with reasonable - but not excessive - care, one may realize the side lobe performance shown in Table I.

TABLE I - DESIGN VS MEASURED SIDE LOBE LEVEL

D-T Design Side Lobe Level	Measured Side Lobe Level	Difference
-20 db	-19 db	1 db
-30 db	-26 db	4 db
-40 db	-32 db	8 db

In addition to the tolerances on the feeding coefficients, dielectric and metallic obstructions in the vicinity of the radiators tend to distort the ideal distributions so that the design performance is not realized.

In an actual design, the array elements will consist of horns, dipoles, endfire arrays, etc. Although the element patterns are assumed to be identical, they often are not - due to mechanical arrangement and mutual coupling. Referring to equation (2.1), it can be seen that this has the effect of modifying the feeding coefficient and therefore the array distribution as a function of the pattern angle. In some cases, this effect can actually be used to advantage to develop an antenna with very low side lobes. Consider, for example, a 10 element array of horns whose outboard elements have patterns that are narrower than the central elements for angles near the main lobe and patterns that are

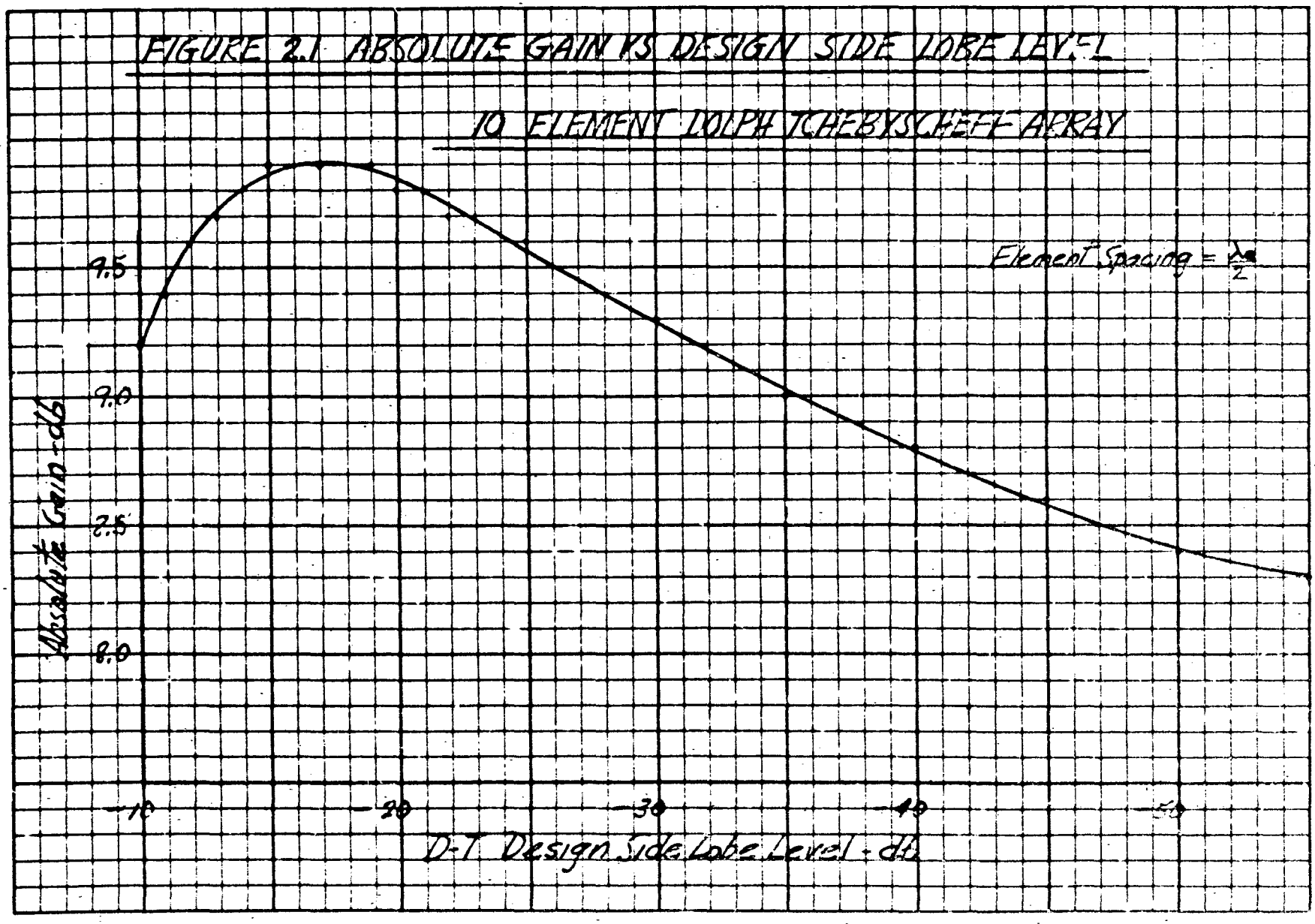
FIGURE 2.1 ABSOLUTE GAIN VS DESIGN SIDE LOBE LEVEL
10 ELEMENT DOLPH TCHEBYSCHEFF ARRAY
Element Spacing = λ/2
Absolute Gain - dB
9.5
9.0
8.5
8.0
-10
-20
-30
-40
-50
D-T Design Side Lobe Level - dB

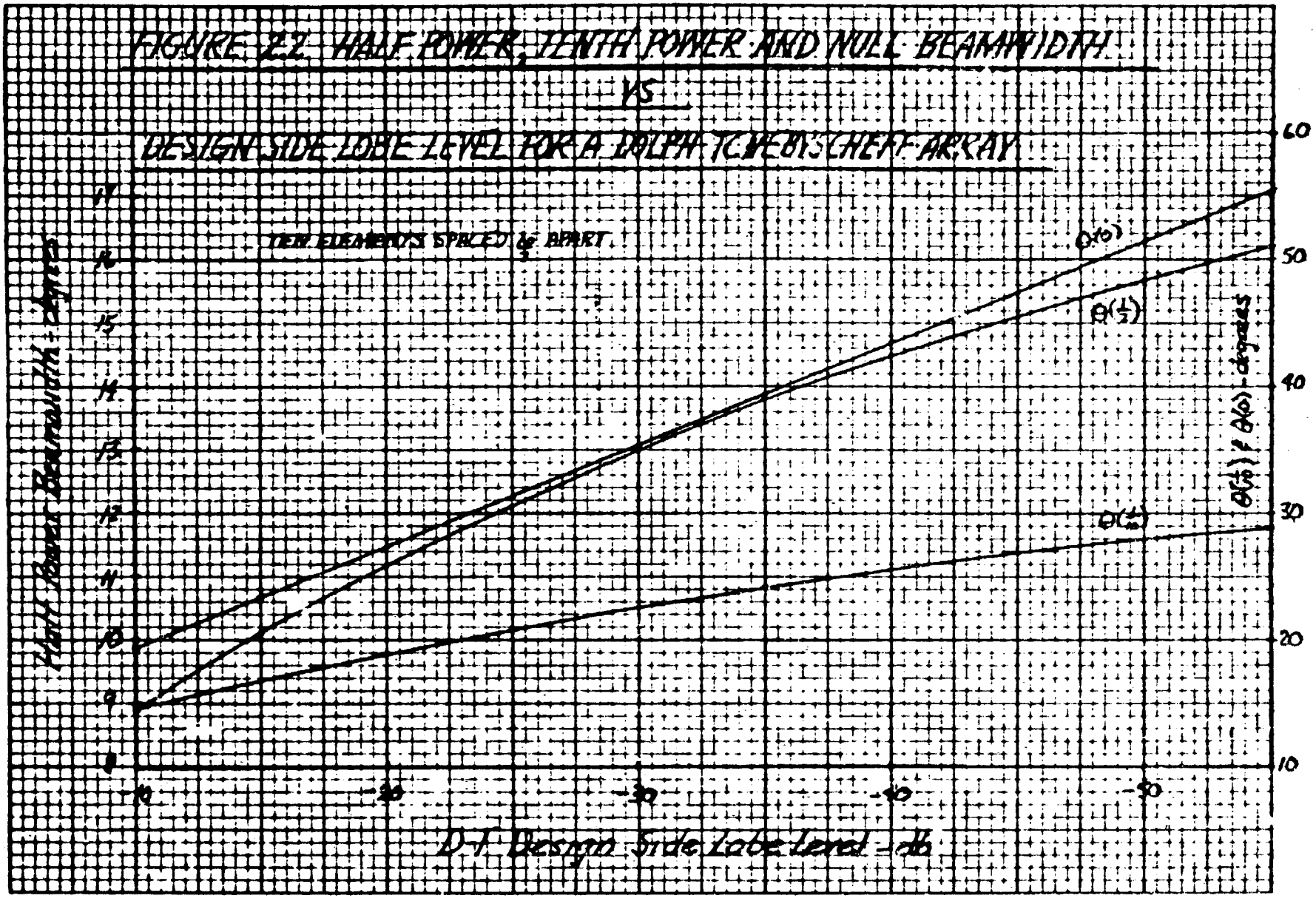
FIGURE 22. HALF POWER, TENTH POWER AND NULL BEAMWIDTH
VS
DESIGN SIDE LOBE LEVEL FOR A DOLPH TCHEBYSCHEFF ARRAY
TEN ELEMENTS SPACED ½ APART
θ(1)
θ(½)
θ(⅒)
θ(½) & θ(1) - degrees
Half Power Beamwidth - Degrees
D-T Design Side Lobe Level - db
60
50
40
30
20
10
-10
-20
-30
-40
-50

broader for large angles, as shown in Figure 2.3. If the array feeding coefficients are initially adjusted for an ideal Dolph-Tchebyscheff distribution at broadside, the "near-in" side lobes will be generated by an array with greater than the "design" amplitude taper. The "far-out" side lobes will be generated by an array with less than the design taper -- however, at these angles the element pattern directivity tends to reduce the side lobes below the array design level. To optimize this design approach, t elements should be chosen to meet the condition that:

Desired Side Lobe Level = Modified "Design" Level
+ Drop in Element Gain

Although the element spacing chosen for our array ($\lambda_o/2$) will not give rise to grating lobes, it is not uncommon to use element spacings of approximately one wavelength where grating lobes do become a problem in low side lobe arrays. Depending on the element spacing and the design side lobe level, it can be shown tha grating lobes can be reduced to reasonable levels without material affecting gain or beamwidth by slightly perturbing [14] the element spacing so that the array becomes an unequally spaced array. In addition to reducing the effects of grating lobes, unequal element spacing can be used as a form of amplitude tapering - called space tapering [15] - to realize excellent side lobe performance for electronic scanning applications.

3.0 SIDE LOBE SUPPRESSION

3.1 The Mattingly Approach

Having optimized the side lobes by conventional means, one now asks " what can be done to suppress the side lobes?". Mattingly [1] recently pointed out the Dolph-Tchebyscheff design of linear array is optimum only for one way patterns. Recall that for an array of (n + 1) elements, the Dolph-Tchebyscheff design sets the voltage array factor $E(\theta)$ equal to the Tchebyscheff polynomial of degree

$$E(\theta) = T_n$$

For the radar case where the same antenna is used for transmissi and reception, the round trip pattern $E_{RT}(\theta)$ is given by

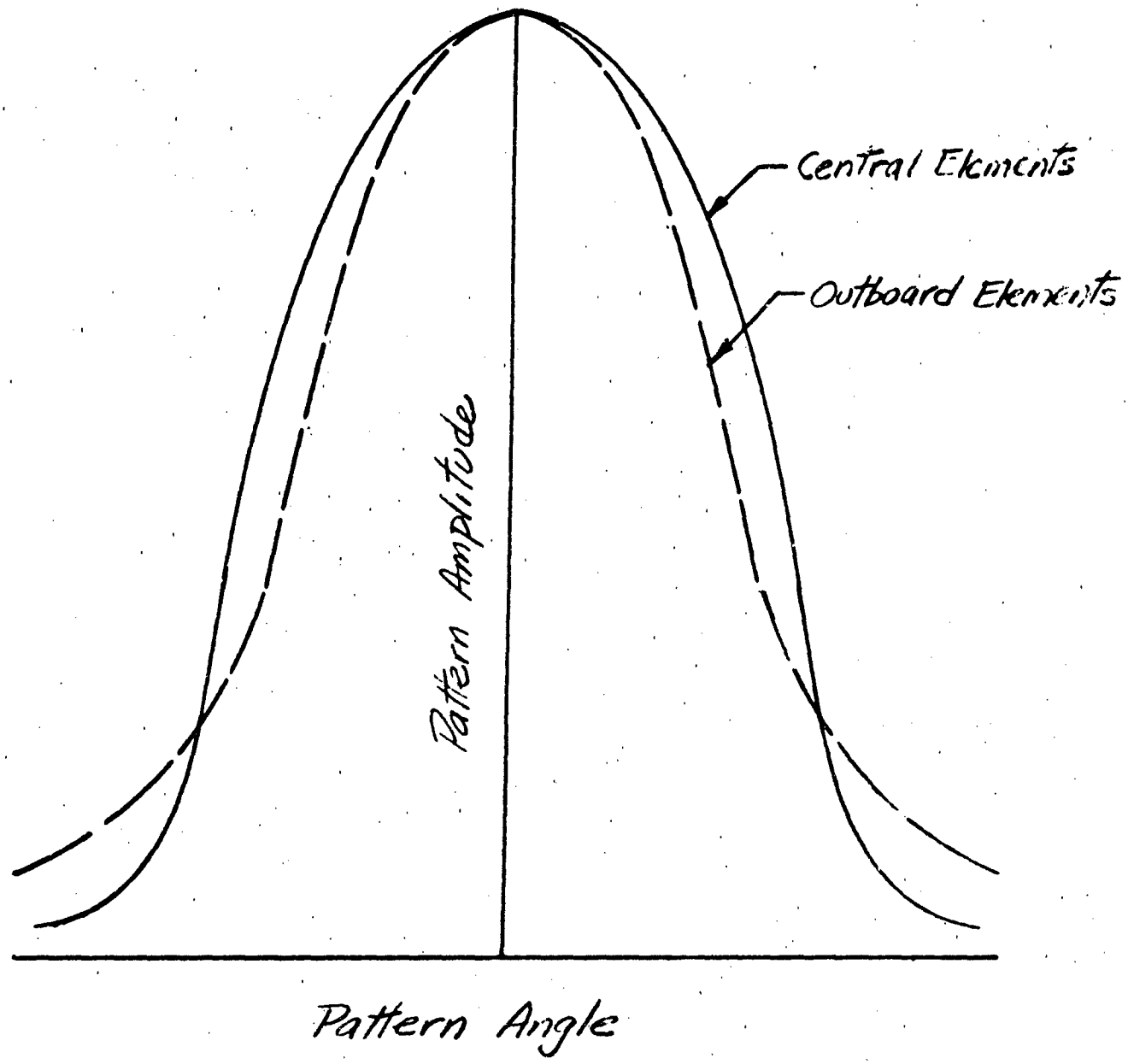

FIGURE 2.3 ARRAY ELEMENT PATTERNS

$$E_{RT}(\theta) = E_T(\theta) \cdot E_R(\theta) = (T_n)^2$$

$(T_n)^2$ is a polynomial of degree $2n$, but note that it is not equal to a Tchebyscheff polynomial of the same degree (T_{2n}).

$$(T_n)^2 \neq T_{2n}$$

Therefore, the round trip pattern of such an antenna does not represent the optimum relationship between null beamwidth and equal level side lobes. Fortunately, (T_{2n}) can be expressed in terms of $(T_n)^2$ as follows:

$$T_{2n} = 2(T_n)^2 - 1$$

and

$$T_{2n} = 2\left[T_n + \frac{\sqrt{2}}{2}\right] \cdot \left[T_n - \frac{\sqrt{2}}{2}\right]$$

The round trip pattern can now be expressed as

$$E_{RT}(\theta) = 2\left[T_n + \frac{\sqrt{2}}{2}\right] \cdot \left[T_n - \frac{\sqrt{2}}{2}\right] = T_{2n}$$

Comparing equation (3.6) with (3.2) we can define transmit and receive patterns as follows:

$$E_T(\theta) = \sqrt{2}\left[T_n + \frac{\sqrt{2}}{2}\right]$$

$$E_R(\theta) = \sqrt{2}\left[T_n - \frac{\sqrt{2}}{2}\right]$$

In order to realize a round trip pattern that is a Tchebyscheff polynomial of degree $2n$ we must use different patterns for trar mit and receive. Equations (3.7) and (3.8) indicate that the new antenna is simply the original Dolph-Tchebyscheff array, whose pattern is given by T_n, plus an omnidirectional antenna with a relative pattern level of 0.707. The omnidirectional antenna is combined with the main antenna in phase addition on transmissio and in phase opposition on reception. A schematic of such a system is shown in Figure 3.1. For an array with an odd numbe

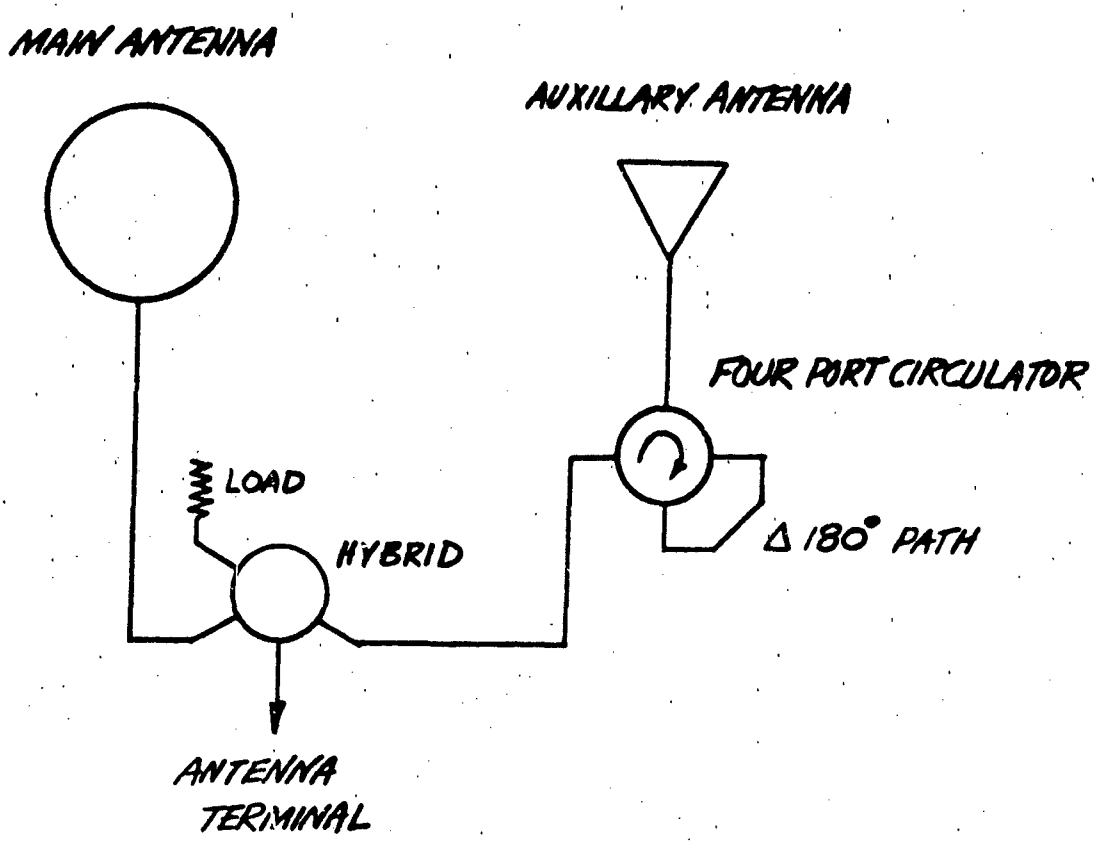

FIGURE 3.1 SIDE LOBE SUPPRESSION SCHEMATIC

of elements, the auxiliary antenna can be combined with the center element.

For a ten element array with $\lambda_o/2$ element spacing and T_n designed for -27 db side lobes, Figure 3.2 shows a plot of voltage pattern T_n together with the omnidirectional patterns +0.707 and -0.707. The combined Dolph-Tchebyscheff and omni patterns for transmit and receive are shown in Figure 3.3. The transmit and receive patterns are then combined to yield the round trip pattern T_{2n} as shown in Figure 3.4. Also shown in this plot is the unoptimized pattern $(T_n)^2$. The major differences between the two patterns are:

a. (T_{2n}) has side lobes 6 db lower than $(T_n)^2$

b. (T_{2n}) has a null beamwidth approximately 10% narrower than $(T_n)^2$

c. (T_{2n}) has twice as many side lobes as $(T_n)^2$

d. The one way side lobes associated with (T_{2n}) are 3 db higher than (T_n)

The fact that (T_{2n}) has twice as many nulls as $(T_n)^2$ is evident when one studies Figure 3.3. The purpose of the auxiliary antenna is to bias the (T_n) pattern plus and minus so as to double the number of nulls and to position the nulls so that on pattern multiplication $\left[E_T(\theta) \cdot E_R(\theta)\right]$ the resulting side lobes will be suppressed. This is really the key to how this suppression scheme operates. It should be obvious that this approach works equally well with other than Dolph-Tchebyscheff arrays. For antennas with tapered side lobe distributions, one simply employs an auxiliary antenna with a tapered pattern.

There is still a question of absolute gain to be answered. For the ten element array described above, the one way absolute gain was computed for each of the three patterns as follows:

$$E(\theta) = T_n \qquad G_{m_1} = \frac{G_o}{(n+1)} \frac{\left[\sum_{k=0}^{n} A_k\right]^2}{\left[\sum_{k=0}^{n} A^2{}_k\right]} \qquad (3$$

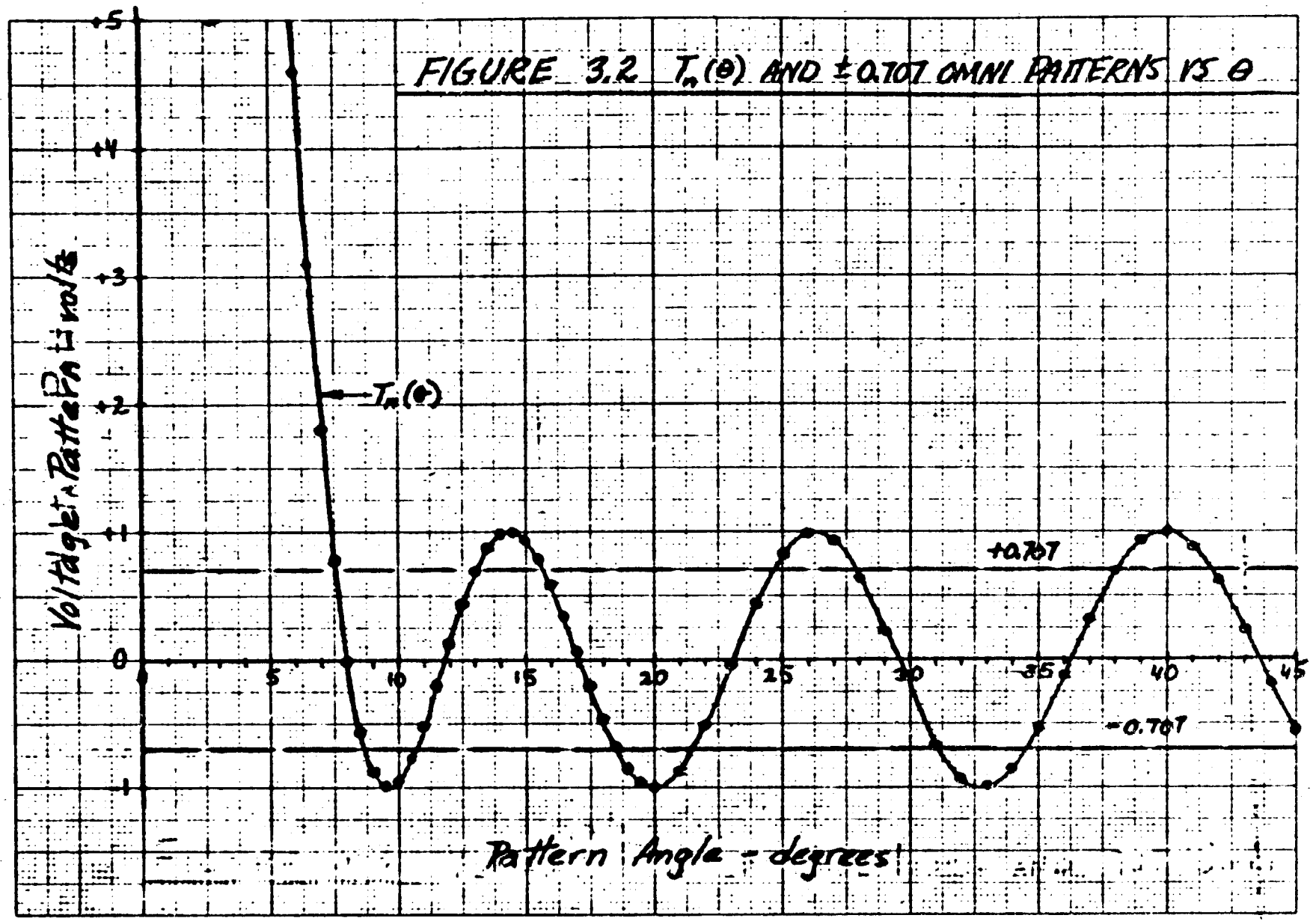
FIGURE 3.2 $T_n(\theta)$ AND ±0.707 OMNI PATTERNS VS θ
Voltage Pattern ratio
+5
+4
+3
+2
+1
0
-1
$T_n(\theta)$
+0.707
-0.707
5
10
15
20
25
30
35
40
45
Pattern Angle - degrees

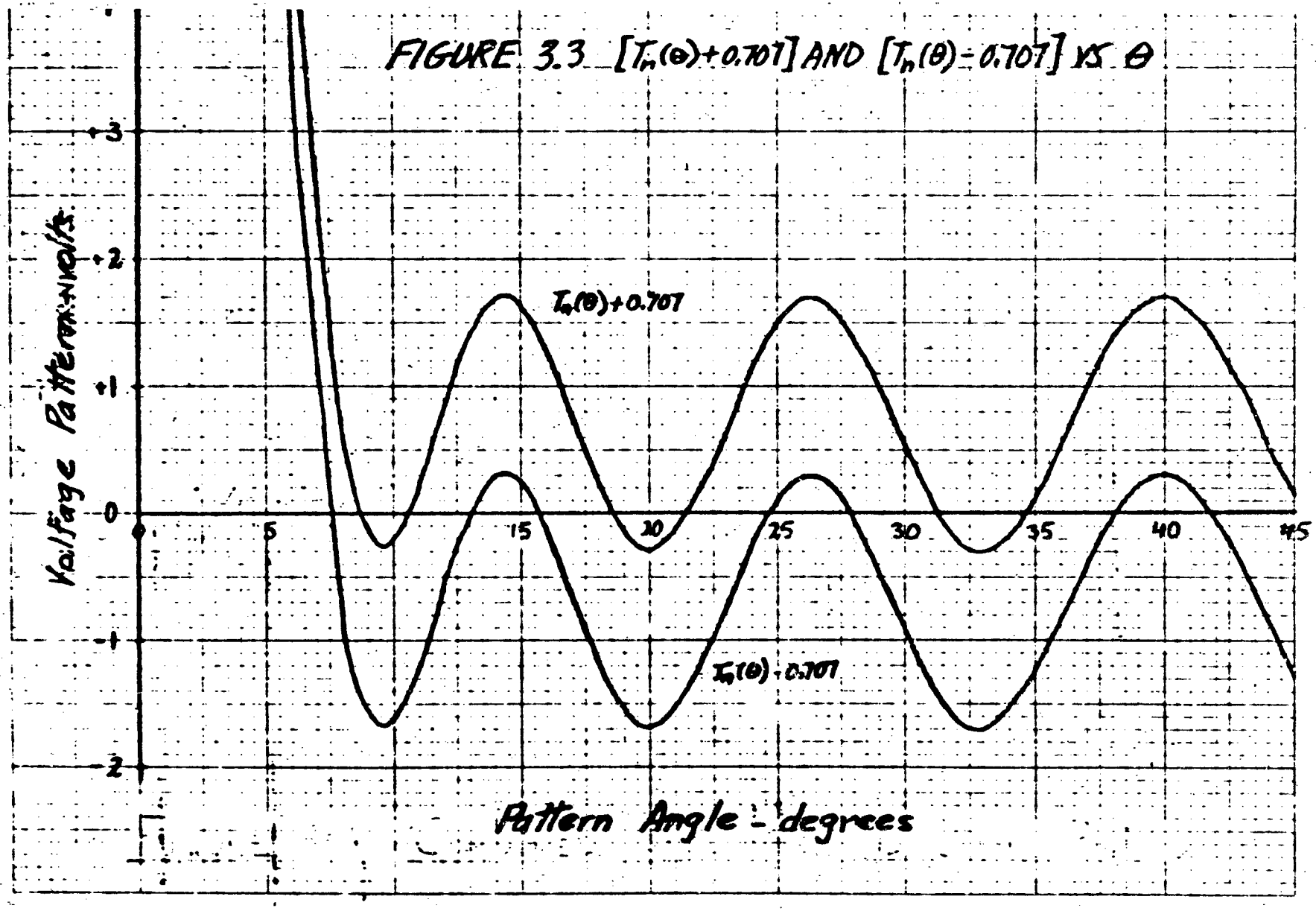
FIGURE 3.3 [T_n(θ)+0.707] AND [T_n(θ)-0.707] VS θ
Voltage Patterns-Volts
3
2
1
0
-1
-2
0
5
15
20
25
30
35
40
45
T_n(θ)+0.707
T_n(θ)-0.707
Pattern Angle - degrees

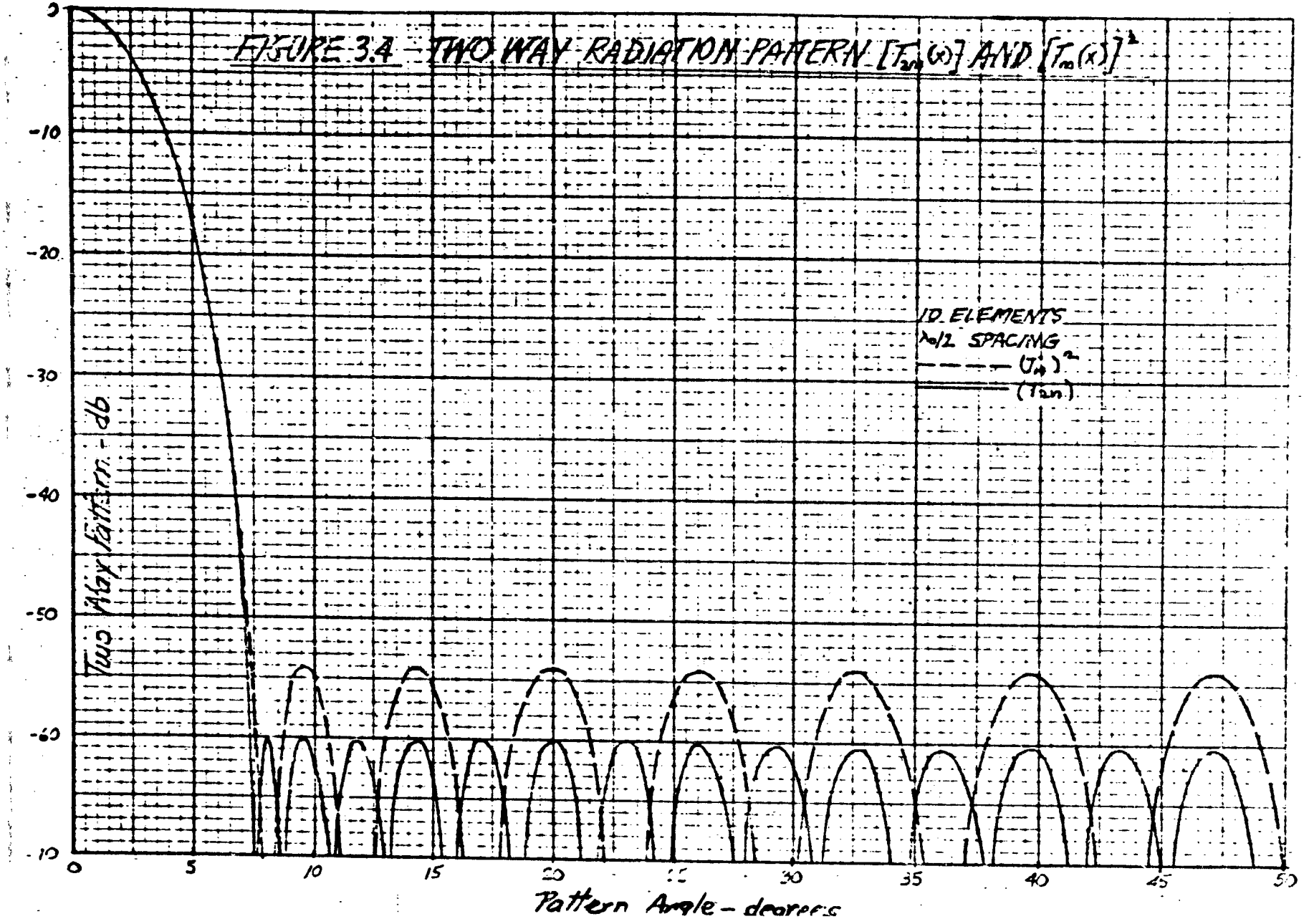
FIGURE 3.4 - TWO WAY RADIATION PATTERN $[T_{2n}(x)]$ AND $[T_{2n}(x)]^2$
0
-10
-20
-30
-40
-50
-60
-70
Two Way Pattern - db
0
5
10
15
20
25
30
35
40
45
50
Pattern Angle - degrees
10 ELEMENTS
λ/2 SPACING
$(T_{2n})^2$
(T_{2n})

$$E(\theta) = T_n + 0.707 \qquad G_{m_2} = \frac{G_o}{(n+1)} \frac{\left[\left(\sum_{k=0}^{n} A_k\right) + (0.707)\right]^2}{\left[\left(\sum_{k=0}^{n} A^2{}_k\right) + (0.707)^2\right]}$$

$$E(\theta) = T_n - 0.707 \qquad G_{m_3} = \frac{G_o}{(n+1)} \frac{\left[\left(\sum_{k=0}^{n} A_k\right) - (0.707)\right]^2}{\left[\left(\sum_{k=0}^{n} A^2{}_k\right) - (0.707)^2\right]}$$

Curves showing how these figures vary as a function of the desig side lobe level of T_n are plotted in Figure 3.5. Also plotted in this figure ars the two-way gains for $(T_n)^2$ and (T_{2n}) computed as follows:

$$E_{RT}(\theta) = (T_n)^2 \qquad G_m = \left[G_{m_1} \right]^2$$

$$E_{RT}(\theta) = (T_{2n}) \qquad G_m = G_{m_2} \cdot G_{m_3}$$

For a design side lobe level of -25 db, the two way gain for $(T_n)^2$ is 0.1 db higher than that for T_{2n}. For higher values of design side lobes, the gain for the two systems is essentially the same. The division of power between the main antenna P_M and the auxiliary antenna P_A can be determined by pattern integration.

There are several variations of this approach which are worth cor sidering. In the process of optimizing the two-way pattern, the null beamwidth of (T_{2n}) can be set equal to that of $(T_n)^2$. In this case the round trip side lobe improvement is 9 - 13 db rather than 6 db depending on the original design side lobe level, as show in Figure 3.6. This is due to the fact that the initial (T_n) can ha a slightly broader null beamwidth ---- and thus a lower initial side lobe level. In this process, the 3 db and 10 db beamwidths of this new (T_{2n}) may be slightly broader than the original $(T_n)^2$ depending on the side lobe level.

Another variation would utilize an auxiliary antenna whose relative voltage level is something other than 0.707. The plot in Figure 3. indicates that, for the initial type of optimization, a maximum side lobe suppression of 6 db is realized for an auxiliary antenna level

FIGURE 3.5 ABSOLUTE GAIN VS DESIGN SIDE LOBE LEVEL FOR ARRAYS WITH $[T_M(x)]^2$ AND $T_{2m}(x)$ PATTERNS

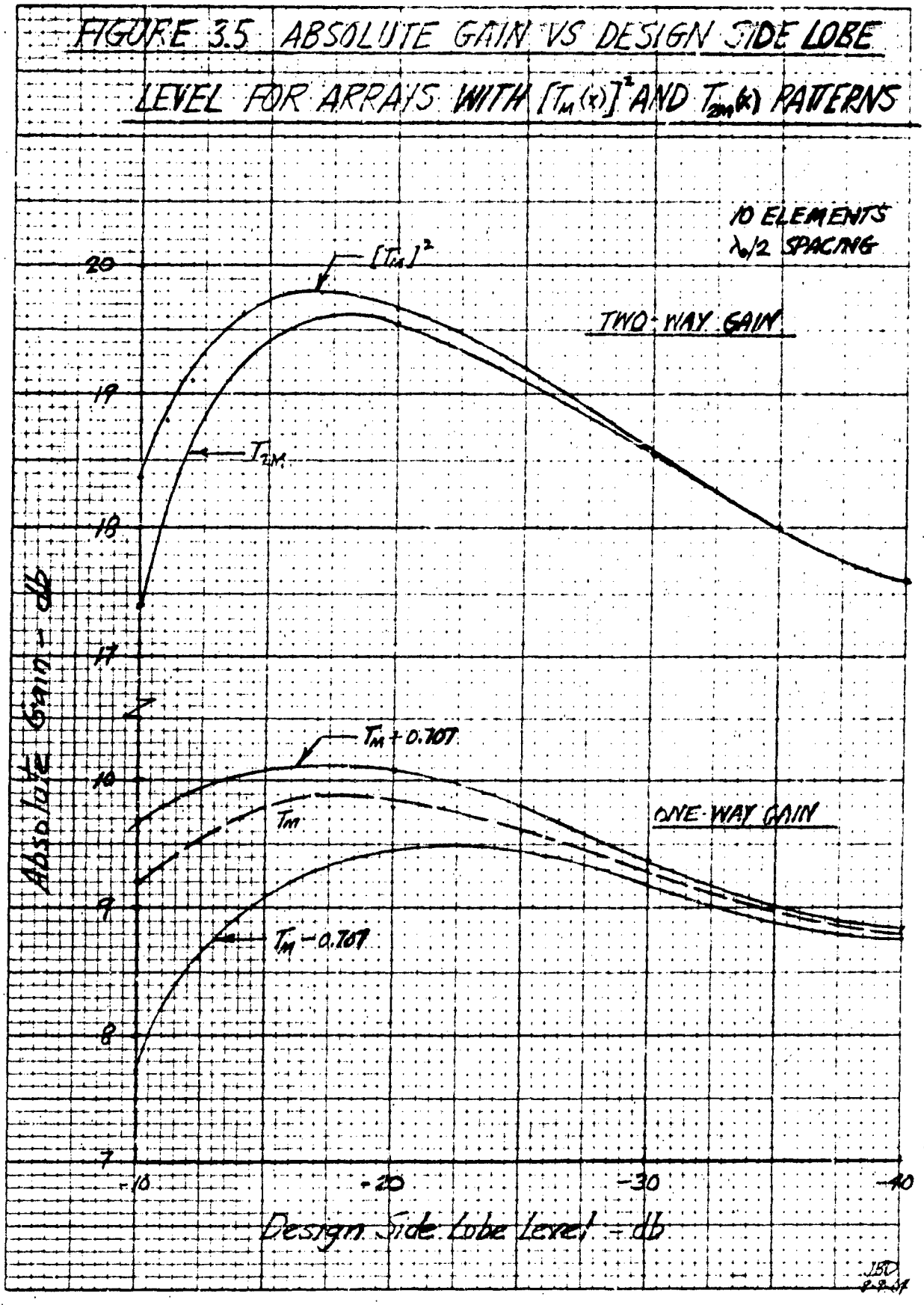

FIGURE 3.6 SIDE LOBE SUPPRESSION PERFORMANCE FOR MATTINGLY AND MAC PHIE APPROACHES

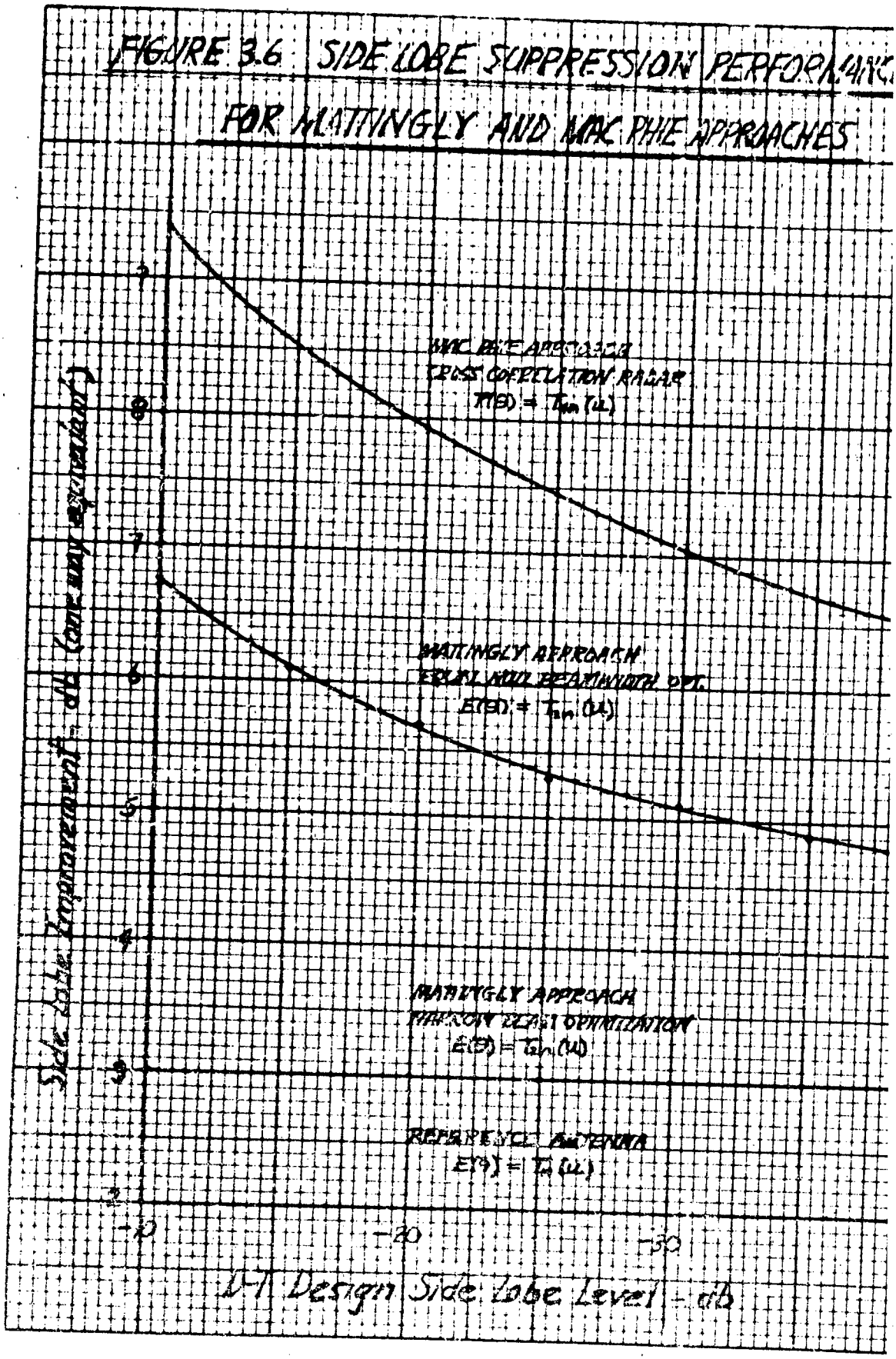

FIGURE 3.7 ROUND TRIP SIDE LOBE SUPPRESSION VS AUXILIARY ANTENNA BIAS LEVEL

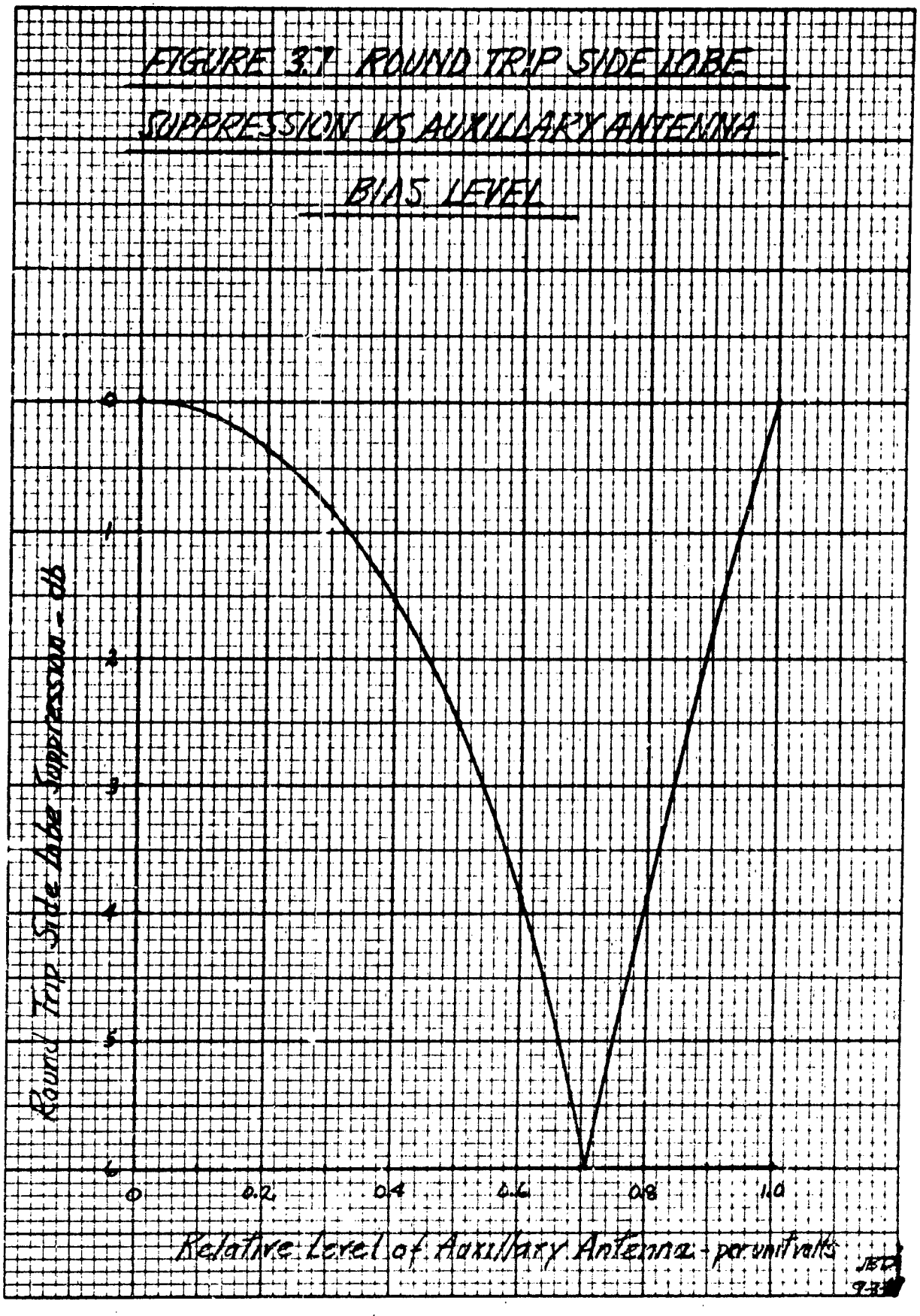

of 0.707, falling off as this value increases or decreases from 0.707. This curve can be used to estimate the effects of main antenna and auxiliary antenna pattern deviations from the ideal.

Although the Mattingly system offers a side lobe suppression of 6 - 10 db round trip, there are several questions that need answ

1. What happens to the side lobe suppression capabilit if the relative phase between the main and auxiliary antennas is something other than 0 and π ?

2. What is the best way of implementing the auxiliary antenna?

The answers to both of the questions depend on the particular design and application.

3.2 The MacPhie Approach

In reviewing Mattingly's work [16], MacPhie [18] indicated that ever though the terminal voltage of the antenna is of the form

$$V_{RT} = K_1 T_{2n}$$

The square-law detector employed with many receiving systems generates a system output of the form

$$P_{RT} = K_2 (T_{2n})^2 \qquad (2$$

This is a polynomial of degree 4n but it is not the Tchebyscheff polynomial of degree 4n

$$(T_{2n})^2 \neq T_{4n} \qquad (2$$

The ideal system output should have the form

$$P_{RT} = K_3 \quad n \qquad (2$$

MacPhie describes a two-frequency, cross correlation type of radar system which develops this optimum system output. In essence, two patterns are transmitted simultaneously, each at a different frequency. Two slightly different patterns are used on reception a la Mattingly. The resulting system output is of the form

$$P_{RT} = K_4 \, Re\left[A_1(u) \, A_2^{*}(u) \, B_1(u) \, B_2^{*}(u) \right] \qquad (3$$

where Re means "the real part of"

* indicates the complex conjugate

The transmit patterns $A_1(u)$, $A_2(u)$ and the receive patterns $B_1(u)$, $B_2(u)$ are related to the original Dolph-Tchebyscheff distribution T_n as follows:

$$A_1(u) = T_n(u) + 0.9240 \quad (3.19)$$

$$A_2(u) = T_n(u) + 0.3828 \quad (3.20)$$

$$B_1(u) = T_n(u) - 0.9240 \quad (3.21)$$

$$B_2(u) = T_n(u) - 0.3828 \quad (3.22)$$

This optimized pattern (T_{4n}) is compared on an equal null beam width basis with (T_{2n}) and (T_n) in Figure 3.6. It indicates a side lobe suppression improvement of approximately 2 db (one-way equivalent) over the Mattingly approach The cost of this improved performance is the complexity that goes with a two-frequency, cross-correlation radar system.

3.3 The Price Approach

The Mattingly and MacPhie approaches described above involve a pattern multiplication of the transmitted and received patterns. For a "receive only" system, Price[19] has shown that one can get the equivalent of (T_{2n}) and (T_{4n}) operation if one is willing to accept the complexity of a non-linear data processing scheme. Starting with an array whose pattern is optimized for (T_n), (T_{2n}) performance is achieved by generating the appropriate terms in equation (3.5) in parallel receive channels and then multiplying them together as shown in Figure 3.8. Ksienski[20] suggests that it might be simpler to carry out the operation given by equation (3.4) --i.e., square the array output and subtract the auxiliary antenna or a sample of the center element. The side lobe suppression possible with this system is essentially the same as the Mattingly and MacPhie systems.

3.4 Time Modulation Approach[21]

If it were possible to vary the position of the side lobes as a function of time without affecting the shape or position of the main lobe,

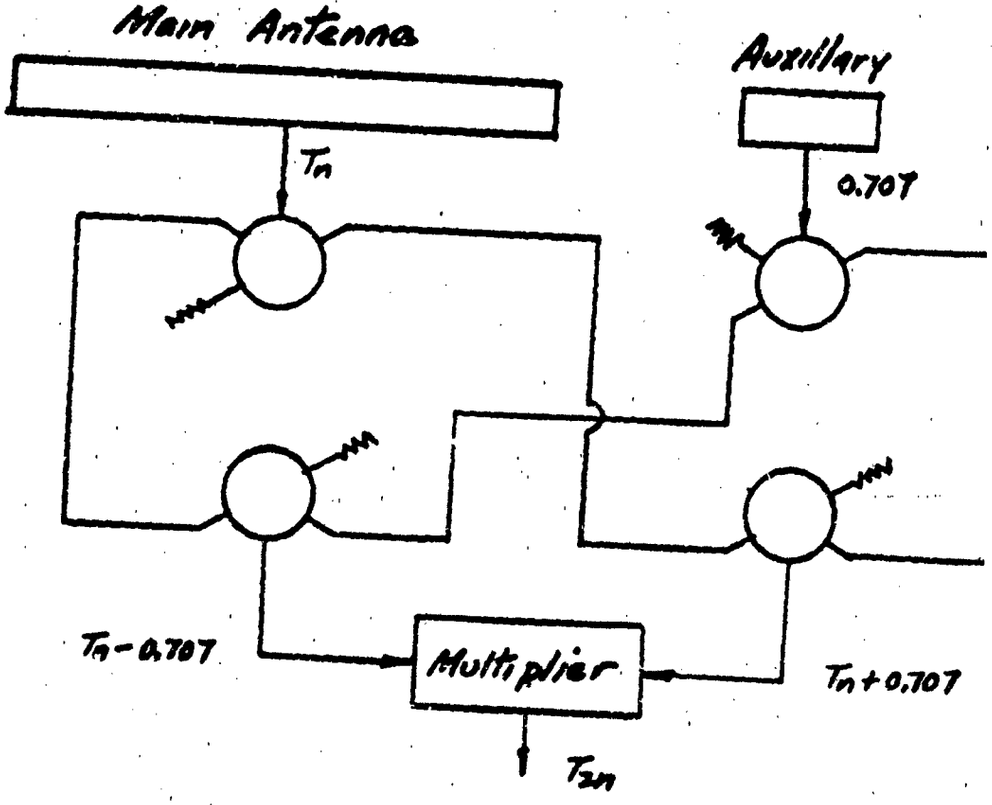

a. Price Receive Only Approach

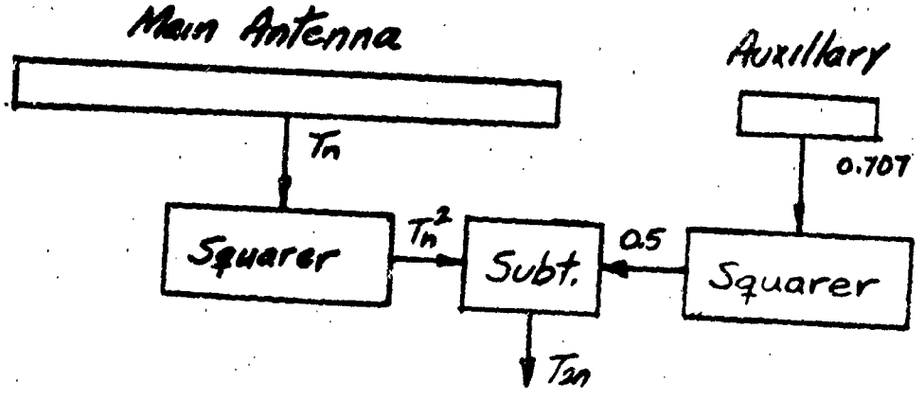

b. Ksienski' Receive Only Approach

Figure 3.8 Side Lobe Suppression Schematic

then averaging the output of the array before detection would result in a pattern with reduced side lobes. It is necessary to do the averaging before detection to take advantage of the destructive phase interference that takes place between adjacent side lobes at the r.f. frequency. From our study of array theory, we know that one way to shift the side lobe positions is to vary the length of the array without changing its relative aperture distribution.

Suppose we were dealing with a uniformly illuminated array of length L as shown in Figure 3.9. If we now modulate the length L by an amount L^1 where

$$L^1 = p L f(t) \tag{3.23}$$

p = fraction of L added and subtracted

f(t) = modulation function of t

The resulting far zone voltage pattern will have the form

$$E(\theta, t) = C \frac{\sin\left\{\frac{2\pi L}{\lambda_o}\left[1 + p f(t)\right]\cos\theta\right\}}{\sin\left\{\frac{2\pi L}{\lambda_o n}\cos\theta\right\}} \tag{3.24}$$

where C = constant - terms not dependent on t

n = number of elements

If we now filter out the "carrier" frequency or "dc term" of the modulation, we will have carried out a phase coherent averaging operation and the resulting output will be:

$$b_o(\theta) = C \frac{\sin\left\{\frac{2\pi L}{\lambda_o}\cos\theta\right\}}{\sin\left\{\frac{2\pi L}{\lambda_o n}\cos\theta\right\}} \cos\left(\frac{2\pi L p}{\lambda_o}\cos\theta\right) \tag{3.25}$$

where f(t) is assumed to be a square wave with a fractional "on" period p.

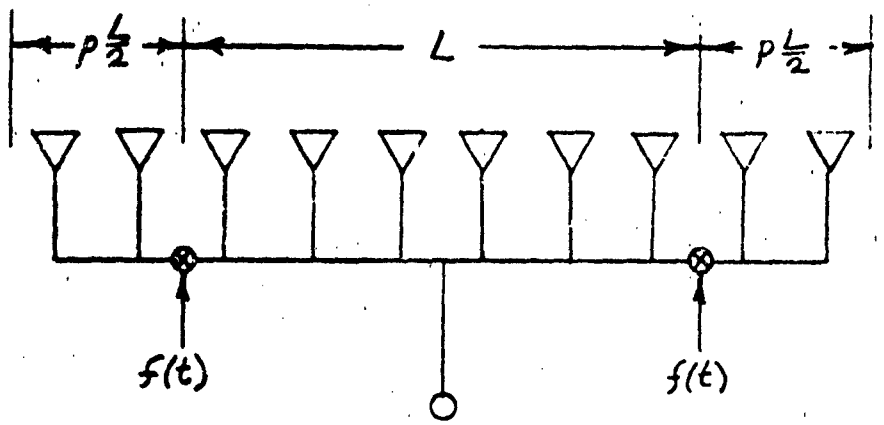

a. Switched Uniform Array

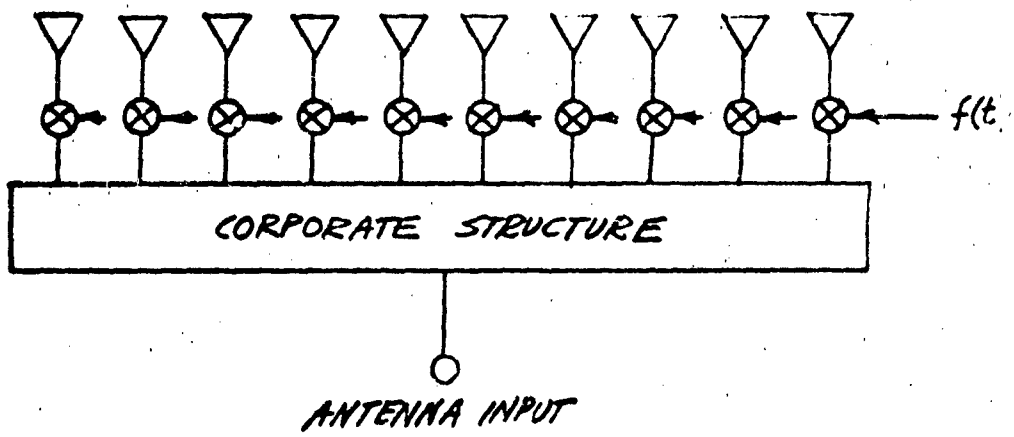

b. Switched Tapered Array

FIGURE 3.9 TIME MODUATION SCHEMATICS

The pattern described by equation (3.25) is that of a uniformly illuminated array but with a superimposed cosine term that suppresses the side lobes. This was accomplished by adding and subtracting part of the array as shown in Figure 3.9. The optimum value of p is 0.25 and with this value of p, the first side lobe is suppressed from the usual -13-1/4 db to -23 db -- a net improvement of approximately 10 db!

It sounds a little bit like we are getting something for nothing! However, an analysis of what happens to absolute gain quickly shows the price we pay. Kummer [22] has made such an analysis and he shows that the loss in gain due to time modulation compared to the static or standard array with the same aperture size and receiving pattern is:

$$\Delta G = \frac{G_{TM}}{G_o} = \frac{\sum_{i=0}^{n-1} \left| A_i \left(\frac{\tau_i}{T} \right) \right|^2}{\sum_{i=0}^{n-1} |A_i|^2} \qquad (3.26)$$

where A_i = ith feeding coefficient for the static array

τ_i = "on" time for the ith element

T = modulation period

n = total number of array elements

For uniform array switched -13-1/4 db side lobes to -40 db side lobes, the time modulated antenna had 3.53 db less gain than a static antenna with the equivalent amplitude taper that delivered -40 db side lobes. For an array with -30 db side lobes time modulated to -40 db side lobes, the loss in gain was only 0.51 db.

These results indicate that in order to reduce the loss in gain due to time modulation, the array ought to be designed for the lowest possible side lobes by conventional techniques. Time modulation then becomes useful in further suppressing the side lobe level.

It is interesting to note that very low side lobe arrays -- whether static or time modulated, become increasingly stringent on the tolerance to which the A_i are controlled. For the static case, once the power dividers in the corporate structure are set, nothing further can be done. For the time modulated case, τ_i can be programmed to optimize side lobe performance.

3.5 Summary

The side lobe suppression approaches described above uti time modulation, non reciprocal antennas and/or non line data processing to achieve a substantial improvement in s lobe performance. The use of an auxiliary antenna may i additional noise, thereby reducing the signal to noise rati of the system. Whether this will have a deteriorating effe the overall system will depend on the initial value of S/N the type of system being employed.

4.0 SIDE LOBE CANCELLATION

Having optimized and suppressed the side lobes to the exte it is reasonable, one asks, "what can I do to cancel or at reduce the effect of the side lobes on the system?".

4.1 Logical Switching Techniques

The basic approach used in logic switching systems is to d whether a signal is being received via the side lobes and, to turn off the presentation. A typical schematic of such a is shown in Figure 4.1a to consist of a main antenna, an a antenna and a logic block. Given a main antenna whose ra pattern $P_M(\theta)$ is of the form shown in Figure 4.1b, the a antenna is chosen so that its pattern, $P_A(\theta)$, acts as an en for the side lobe structure. These two signals are detecte fed to the logic block where their amplitudes are compared each range cell. For any particular range cell, if $P_M(\theta_1$ the switch is closed and the system works like a normal ra system. If $P_M(\theta_1) \leq P_A(\theta_1)$, the switch is open and the p tation for that range cell and that angle of look θ_1 is blank This occurs when an undesireable signal is being received side lobes. It should be noted that in blanking the presenta this resolution cell, a desireable signal on the main lobe w be blanked.

In an area with large prominent targets, this behavior coul to presentation blanking for appreciable periods of time wh could result in poor detection capability of desired target s. Obviously such a system is vulnerable to intentional jammi however, there are techniques that allow one to minimize t of such jamming.

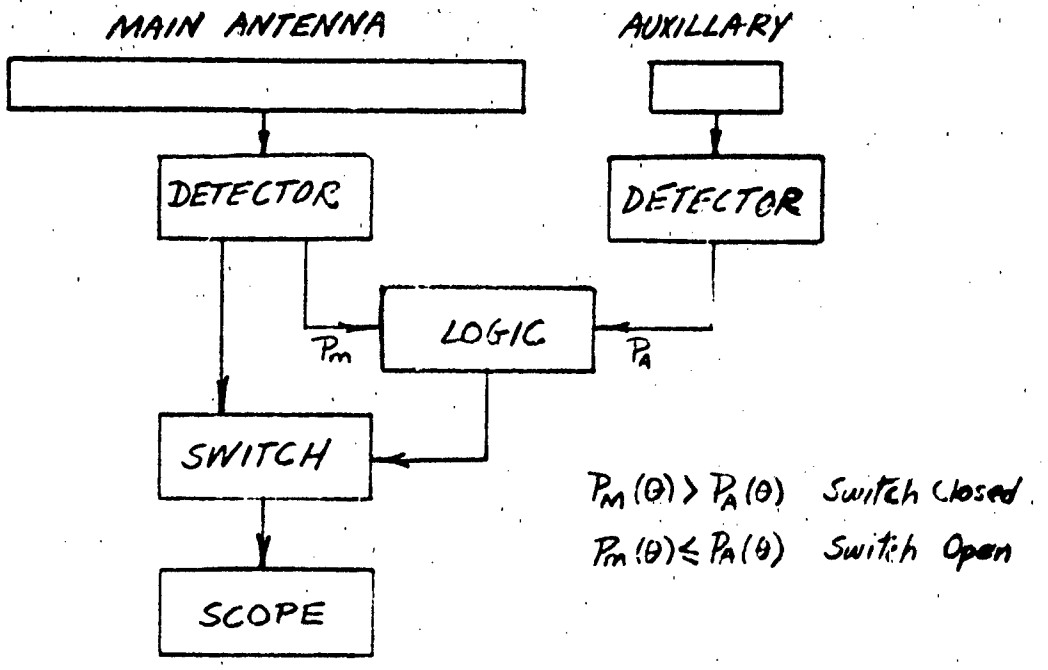

a. Logical Switching System Schematic

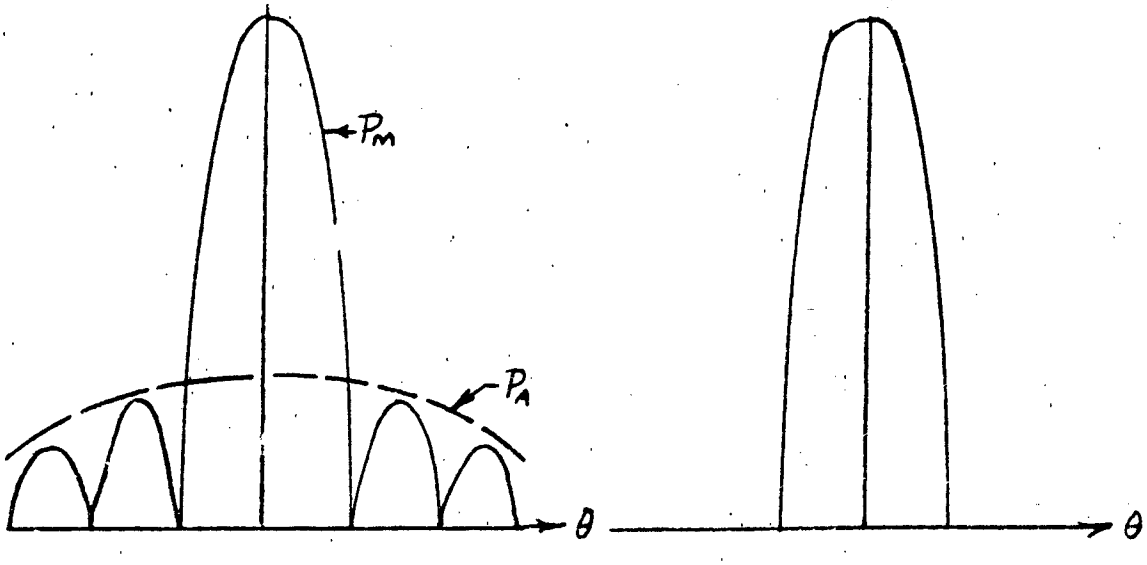

b. Unswitched Patterns

c. Switched Output

FIGURE 4.1 LOGICAL SWITCHING SYSTEM

The logic system makes an "on-off" decision on a resolution ce by resolution cell basis. That is, it is a single pulse detection and comparison system. Since detection takes place before sig integration - usually the presentation scope -- the system suff an appreciable loss in sensitivity. To first order approximatio the loss in sensitivity for such a post detection integrating syst is:

$$\text{Loss in S/N} = 5 \log_{10} n$$

where S/N = signal to noise ratio

n = number of pulses integrated per resolution cell without logical switching

For a typical system which integrates 50 pulses in sequence pe resolution cell, this is a loss of 8-1/2 db in S/N, which reduce the radar detection range to 35%. This is a serious penalty and may be prohibitive for most radar applications where target ec signals are small. For certain "receive only" applications whe one is looking at "beacons" with large S/N, the losses of logica switching are quite acceptable. The pattern [23] that results fro the logical switching approach is shown in Figure 4.1c. Since t switching or cancelling occurs at video levels, these systems a often called video cancellers.

To increase the sensitivity of the system in the region of the ma lobe, the pattern of the auxiliary antenna can be chosen to be a cardioid with its null on-axis.

4.2 Side Lobe Modulation

It is possible to suppress the side lobe level without materially affecting gain or beamwidth by using a periodically variable antenna that acts to "tag" or modulate the energy received via the side lobes so that it can be filtered and eliminated. There are several ways of doing this. Two of the schemes in current favor employ

1. Phase modulation
2. Frequency modulation

The phase modulation scheme involves the use of a low gain auxiliary antenna whose pattern $f(\theta)$ forms an envelope for the main antenna pattern $F(\theta)$ as shown in Figure 4.2a. The auxiliary antenna is used on reception only and is alternately connected "in phase" and "out of phase" with the main antenna at some predetermined modulation rate, f_m, as shown schematically in Figure 4.2b. The resulting voltage pattern $E(\theta)$ alternates between:

$$E_o(\theta) = \left[F(\theta) + f(\theta) \right] \qquad (4.2a)$$

$$E_\pi(\theta) = \left[F(\theta) - f(\theta) \right] \qquad (4.2b)$$

where $F(\theta)$ = voltage pattern of the main antenna

$f(\theta)$ = voltage pattern of the auxiliary antenna

$E_o(\theta)$ and $E_\pi(\theta)$ are plotted in Figure 4.3. Note that signals arriving via the side lobes are modulated 100% while those arriving via the main lobe are practically unaffected. This can be described mathematically as follows:

$$\% \text{ modulation} = \left[\frac{E_o(\theta) - E_\pi(\theta)}{E_o(\theta) + E_\pi(\theta)} \right] \times 100\% \qquad (4.3)$$

Substituting from equation (4.2)

$$\% \text{ modulation} = \frac{f(\theta)}{F(\theta)} \times 100\% \qquad (4.4)$$

Note that for large side lobes, $f(\theta)$ must be large if % modulation is to be large (50 - 100%). Large values of $f(\theta)$ can sometimes adversely affect the main lobe as shown in Figure 4.4. To reduce this effect, the auxiliary pattern, $f(\theta)$, is chosen to resemble a cardioid pattern.

Although the net effect of this system is to suppress signals received via the side lobes, it should be noted that the auxiliary antenna introduces additional noise due to its broad pattern. This means that the overall signal to noise ratio will be degraded.

The second approach to modulating the side lobe signals received via the side lobes involved frequency modulation. It is a well known fact that the angular location of the side lobes depends not

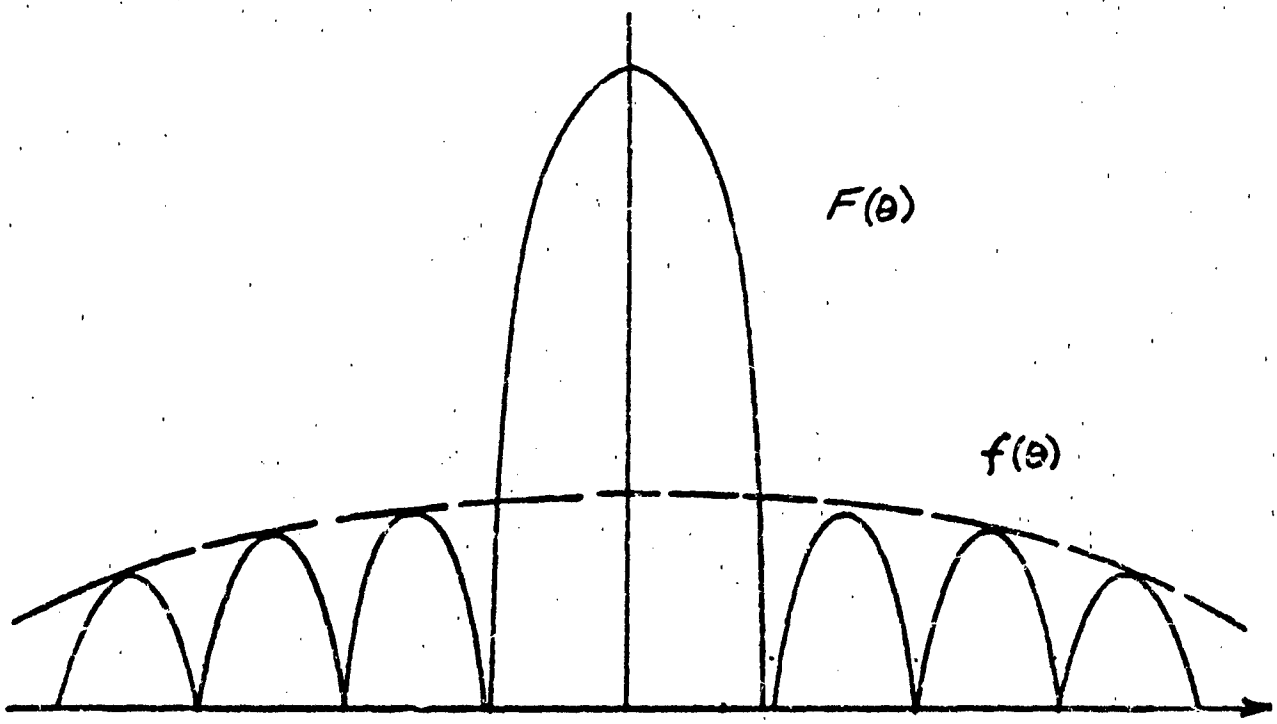

a. Main Antenna and Auxillary Antenna Patterns

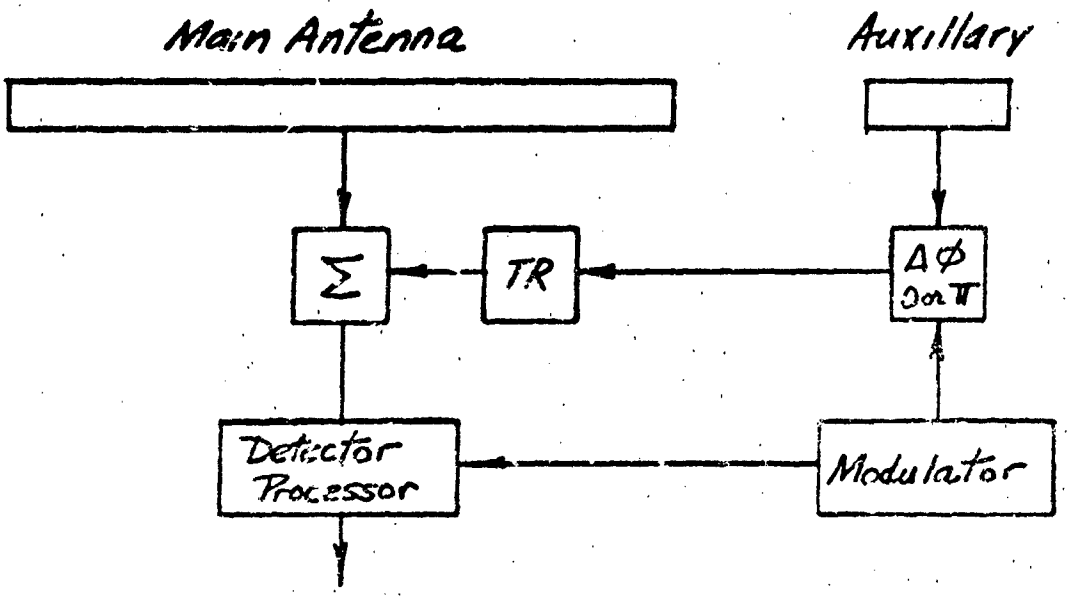

b Phase Modulation Schematic

FIGURE 42 PHASE MODULATION SYSTEM

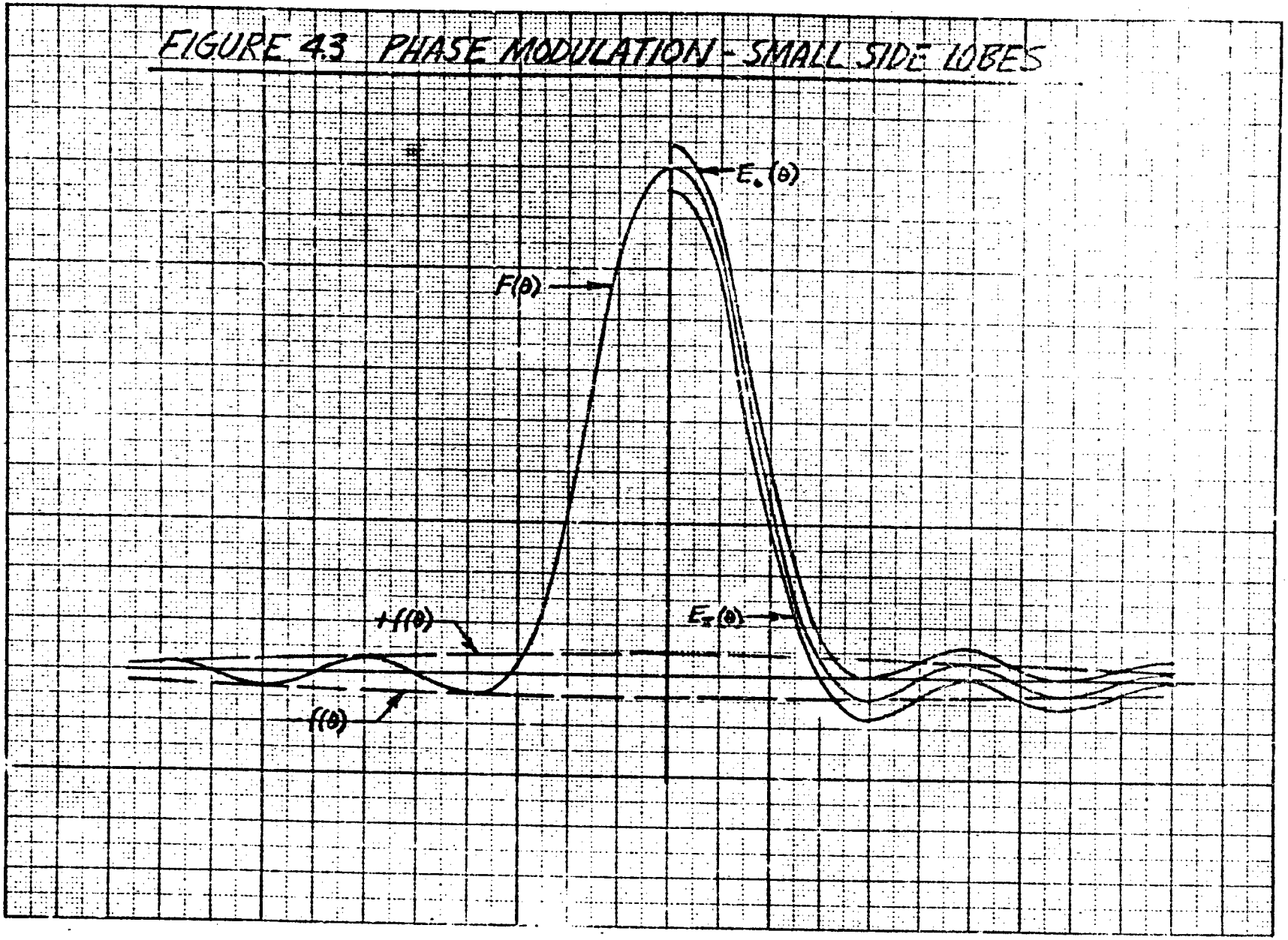
FIGURE 43 PHASE MODULATION - SMALL SIDE LOBES
E₀(θ)
F(θ)
+f(θ)
E₂(θ)
f(θ)

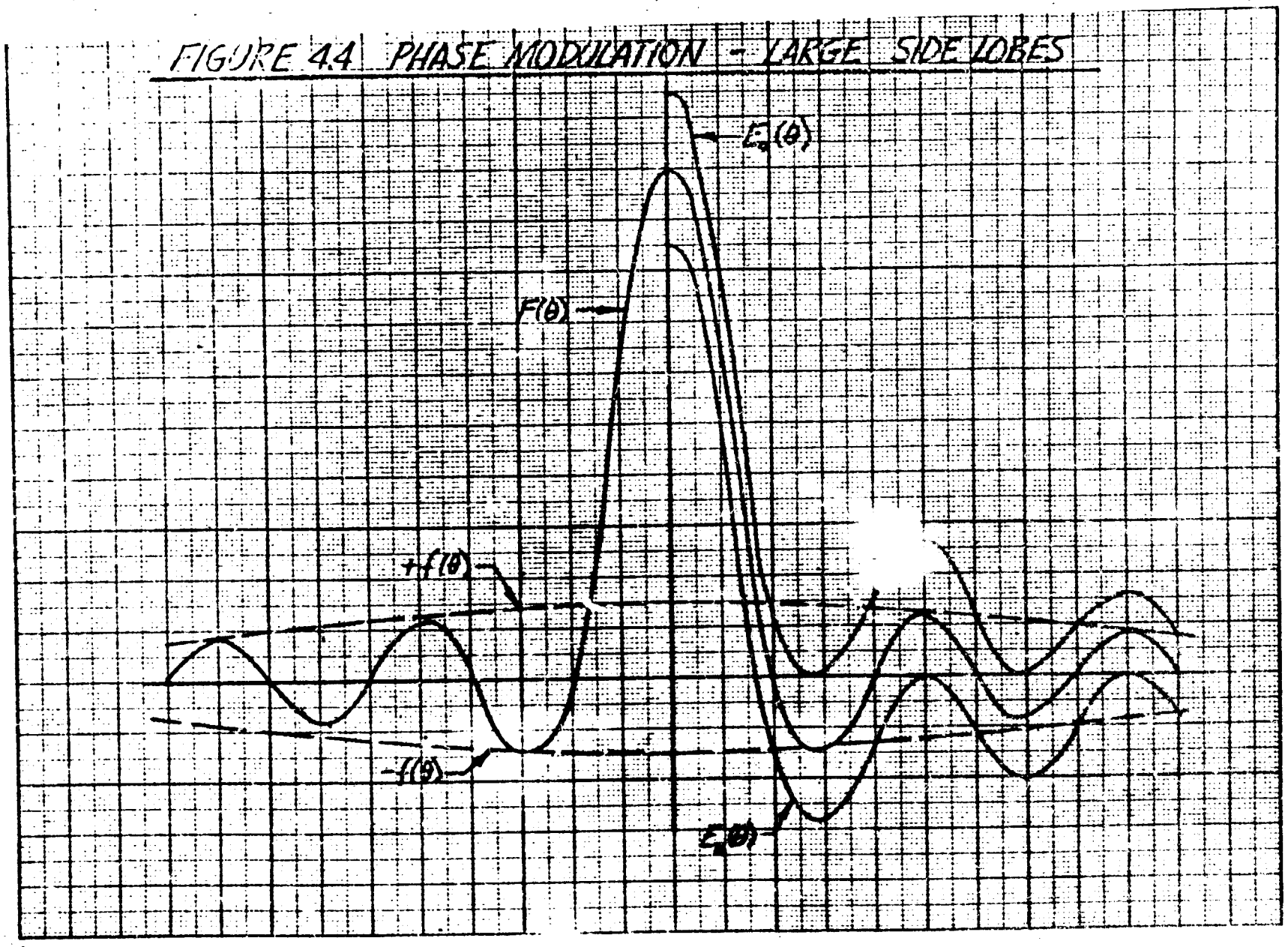
FIGURE 4.4 PHASE MODULATION - LARGE SIDE LOBES
$E_0(\theta)$
$F(\theta)$
$+f(\theta)$
$-f(\theta)$
$E_0(\theta)$

only on the antenna parameters but on frequency (or wavelength). For a uniformly illuminated aperture the pattern is given by:

$$F(\theta) = \frac{\sin\left(\frac{\pi D}{\lambda_o}\cos\theta\right)}{\left(\frac{\pi D}{\lambda_o}\cos\theta\right)} \qquad (4.5)$$

For a uniformly illuminated array, the pattern is given by:

$$F(\theta) = \frac{1}{n}\,\frac{\sin\left(\frac{n\pi s}{\lambda_o}\cos\theta\right)}{\sin\left(\frac{\pi s}{\lambda_o}\cos\theta\right)} \qquad (4.6)$$

If the radar system transmits alternate pulses at frequencies f_1 and f_2 where f_1 and f_2 are sufficiently separated, the resulting radiation patterns have pencil beams that lie one atop the other but side lobes that straddle one another as shown in Figure 4.5. Signals arriving via the side lobes tend to be modulated whereas signals arriving via the main lobe are unmodulated. Obviously, the modulation and therefore the side lobe suppression varies with pattern angle and may not be as good as that possible with phase modulation. This approach has the advantage that no auxiliary antenna is necessary. On the other hand, suppression of the first few side lobes requires that f_1 and f_2 be widely spaced. This means we must have a wide band system which may complicate the design.

Although it is possible to modulate signals arriving via the side lobes and thus filter and eliminate them, it must be remembered that real targets on the main lobe are not fixed in amplitude but fluctuate. This fluctuation or scintillation may have a broad spectrum depending on the target, and may include the modulation frequency. This means that a desired scintillation target on the main lobe could be mistaken for a modulated signal arriving via the side lobes and thus be filtered and eliminated from the radar presentation.

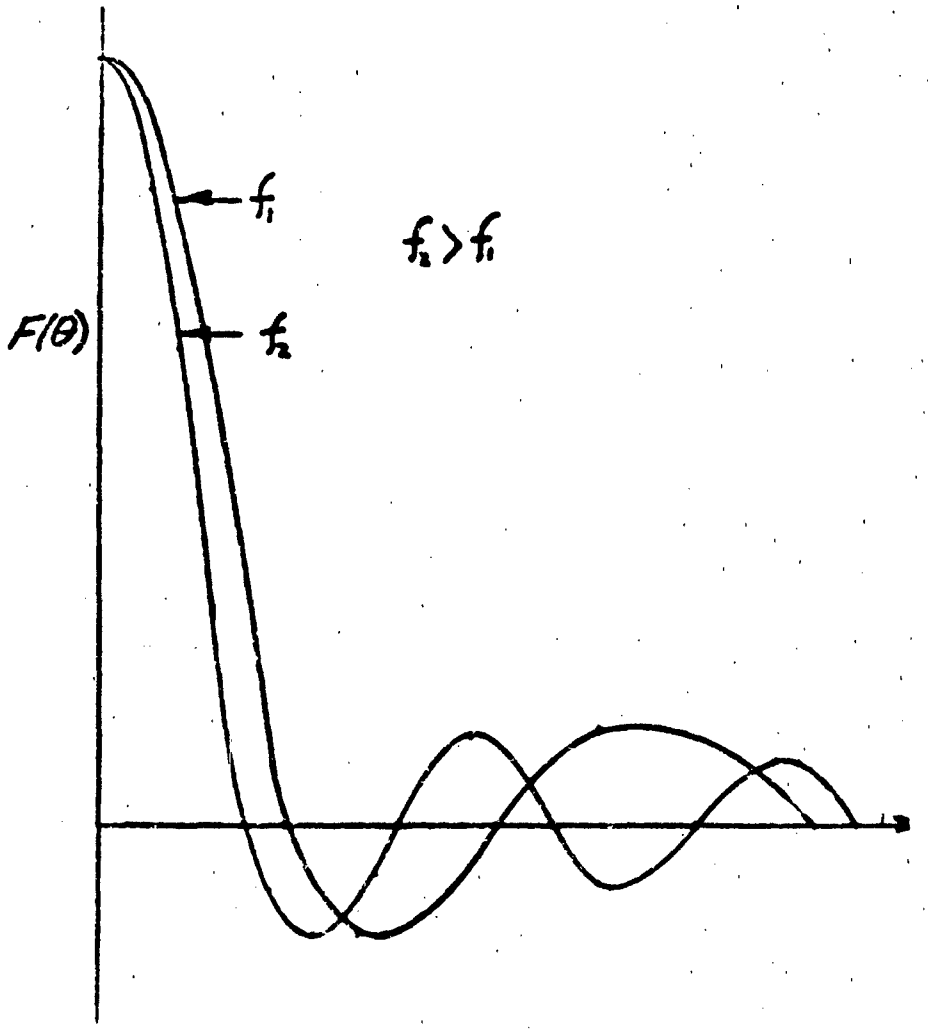

FIGURE 4.5 FREQUENCY MODULATION PATTERNS

5.0 CONCLUSIONS

In our quest for design approaches that optimize side lobe performance without unduly compromising gain and beamwidth, we have discussed three general approaches:

1. Side lobe optimization - the thoughtful application of conventional design techniques to generate an exceptionally good design,

2. Side lobe suppression - the application of unconventional techniques such as time modulation, non-reciprocal antennas and non-linear data processing to suppress the inherent side lobe level to a lower level, and

3. Side lobe cancellation - a last resort in which one attempts to compensate the system for the effects of the side lobes that cannot be reduced.

In attempting to form a basic design policy with regard to side lobe performance, the words of Angelique Arnauld are most appropriate:

"Perfection consists not in doing extraordinary things, but in doing ordinary things extraordinarily well."

For most design situations, there is more to be gained in side lobe optimization than in either of the other two approaches. For special applications, certain of the side lobe suppression techniques appear promising but require a good deal of additional development. Except for certain "receive only" applications, where S/N is not a consideration, present day side lobe cancellation techniques do not appear to be particularly attractive.

REFERENCES

1. S. Schelkunoff, "A Mathematical Theory of Linear Arrays", Bell System Technical Journal, Vol. 22, No. 1, pp 80-107; January 1943

2. Samuel Silver, "Microwave Antenna Theory and Design", MIT Radiation Laboratory Series, Vol. 12, McGraw Hill Book Co., pp 257 - 284; 1949

3. C. L. Dolph, " A Current Distribution for Broadside Arrays Which Optimize the Relationship Between Beamwidth and Side Lobe Level", Proceedings of the IRE, Vol. 34, pp 335 - 348; June 1946

4. H. J. Riblet, "Note on Dolph's Paper", Proceedings of the IRE, Vol. 35, pp 489-492; May 1947

5. Robert J. Stegen, "Exciation Coefficients and Beamwidths of Tchebyscheff Arrays", Proceedings of the IRE, Vol. 41, No. 11, pp 1671-1674; November 1953

6. L. B. Brown and G. A. Scharp, "Tchebyscheff Antenna Distributio Beamwidth and Gain Tables", Naval Ordnance Laboratory, Corona, California, NOLC Report No. 383; February 1958

7. Robert J. Stegen, "Gain of Tchebyscheff Arrays", Transactions of PGAP, Vol. AP-8, No. 6, pp 629-631; November 1960

8. T. T. Taylor, "Design of Line Source Antennas for Narrow Beamwidth and Low Side Lobes," Transactions of PGAP, Vol. AP-3, pp 16-28; January 1955

9. T. T. Taylor, "Design of Circular Apertures for Narrow Beamwidth and Low Side Lobes", Transactions of PGAP, Vol. AP-8, pp 17-22; January 1960

10. R. C. Hansen, "Tables of Taylor Distributions for Circular Aperture Antennas", Transactions of PGAP, Vol. AP-8, pp 23-26; January 1960

11. Baillin and Ehrlich, "Factors Affecting the Performance of Linear Arrays", IRE Transactions of PGAP, Vol. AP-1, pp 85-101; February 1952

12. D. Ashmead, "Optimum Design of Linear Arrays in the Presence of Random Errors", Transactions of PGAP, Vol. AP-4, pp 81-92; December 1952

REFERENCES (Cont'd)

13. O'Neill and Bailin, "Further Effects of Manufacturing Tolerances on the Performance of Linear Shunt Slot Arrays", Transactions of PGAP, Vol. AP-4, pp 93-102; December 1952

14. Roger F. Harrington, "Side Lobe Reduction by Non-Uniform Element Spacing", Transactions of PGAP, Vol. AP-9, pp 187-192; March 1961

15. Robert E. Wiley, "Space Tapering of Linear and Planar Arrays", Transactions of PGAP, Vol. AP-10, pp 369-377; July 1962

16. R. L. Mattingly, "Non-Reciprocal Radar Antennas", Proceedings of the IRE, Vol. 48, pp 795-796; April 1960

17. R. L. Mattingly, "Directive Antenna Systems", U.S. Patent No. 3,028,581; April 3 1962

18. Robert H, MacPhie, "Optimum Cross Correlation Radar System", Proceedings of the IRE, Vol. 50, pp 2508-2509; December 1962

19. Oliver R. Price, "Reduction of Side Lobe Level and Beamwidth for Receiving Antennas", Proceedings of the IRE, Vol. 48, pp 1177-1178; June 1960

20. A. Ksienski, " Signal Processing Antennas", Microwave Journal, Vol. 4, pp 83-84; October 1961

21. Kummer et al, "Ultra-Low Side Lobes from Time-Modulated Arrays", Transactions on Antennas and Propagation, Vol. AP-11, pp633 -639; November 1963

22. Kummer et al, loc. cit., pp 638-639.

23. Gustafson et al, "New Concepts in Antenna Research", Electronic Design, p 177; February 15 1961

LIGHTWEIGHT LARGE-APERTURE ARRAYS FOR AIRBORNE APPLICATIONS

B. M. Bowman, W. O. Klever, A. E. Marble
Goodyear Aerospace Corporation. Akron 15, Ohio

INTRODUCTION

This paper describes design and fabrication techniques that Goodyear Aerospace Corporation has found useful in the development and production of large-aperture airborne arrays. Two such arrays are shown in Figures 1 and 2. Design emphasis has been placed necessarily on minimizing size and weight without sacrificing performance or reliability. The particular antennas discussed are of the resonant, edge-slotted, wave-guide type. However, most of the features discussed are useful with other types of arrays.



Figure 1 - X-Band Shaped-Beam Wave-Guide Array

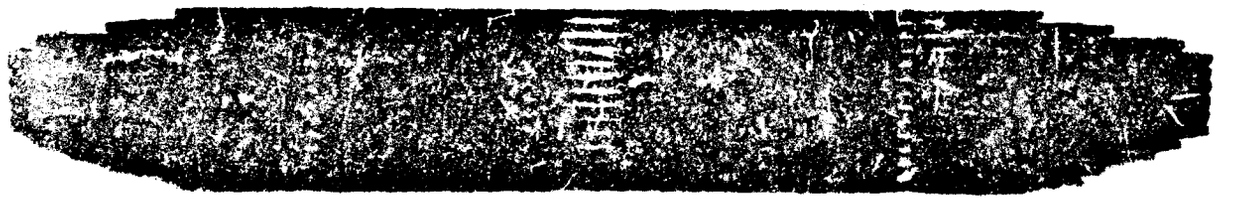

Figure 2 - X-Band Fan-Beam Array

SHAPED BEAM SYNTHESIS

Where vertical aperture must be minimized and where the phase of the field pattern is not specified, the unit circle representation of the Schelknnoff[1a] array polynomial has proved to be a powerful tool for shaped-beam synthesis. The theory and application of this technique have been described adequately in the literature.[2, 3, 4, 5] Not apparent from these references, however, is the simplicity of the method and the rapidity with which the designer can become skilled in the manipulations required for beam shaping.

The method, very briefly, is as follows. Schelkunoff showed that the magnitude of the array factor of an n element linear array is

$$|E(\psi)| = \left|a_o + a_1 Z + a_2 Z^2 + \ldots a_{n-2} Z^{n-2} - Z^{n-1}\right| \qquad (1)$$

where $Z = e^{j\psi}$, $\psi = 2\pi d/\lambda \sin \phi$, a_m is the complex current element excitation of the mth element, d is the separation between elements, and ϕ is the angle from a normal to the array. The polynomial can be factored into (n - 1) binomials so that Equation 1 can be written

$$|E(\psi)| = \left|(Z - r_1)(Z - r_2) \ldots (Z - r_{n-2})(Z - r_{n-1})\right| . \qquad (2)$$

The r's are the complex roots of the polynomial. Z is a unit vector and hence moves on the circumference of a unity radius circle as the value of ψ changes. If the roots are plotted on the same coordinates as the unit circle, as in Figure 3, each quantity $(Z - r_m)$ can be represented graphically as a vector from Z to a point r_m. Thus the value of $|E|$ for any value of ψ is obtained readily either by graphical measurement or by direct computation of the product of the distances between the corresponding location of Z and each of the roots.

Taylor and Whinnery[2] developed an analog computer that permits direct observation of $|E(\psi)|$ as the root locations are manipulated. Such a machine has the obvious advantages of speed and convenience. However, the graphical solution is capable of reasonable speed and accuracy if the number of roots is not too large and the measured values of $(Z - r_m)$ are recorded in tabular form for subsequent multiplication.

A simple uniform array representation is shown in Figure 3. Note that a zero or null in $|E|$ occurs wherever a root falls on the unit circle. As a very simple example of pattern shaping, Figure 4 shows the effect of moving one of the roots off the circle. Several effects are noted.

1. The null at +90 deg has disappeared.
2. The peak of the beam has shifted slightly in angle (and in absolute magnitude if directivity were to be computed).
3. The excitation currents are all different as can be seen from the polynomial coefficients.

The designer soon develops a facility for array factor shaping as experience in root manipulation is gained. Obviously more roots are required as shaping requirements are increased. An example of an eight-element shaped array factor is shown in Figure 5.

---

[a] Superior numbers in the text refer to items in the List of References.

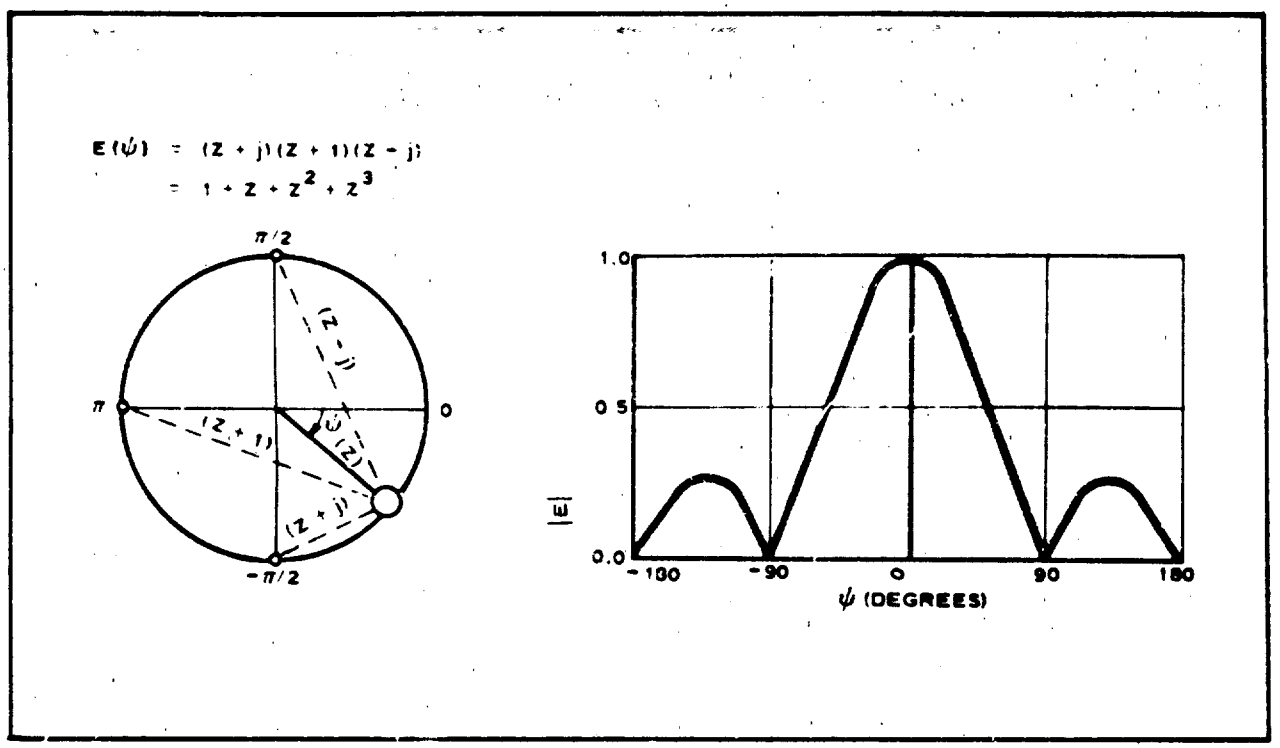

Figure 3 - Unit Circle Representation of Four-Element Uniform Array

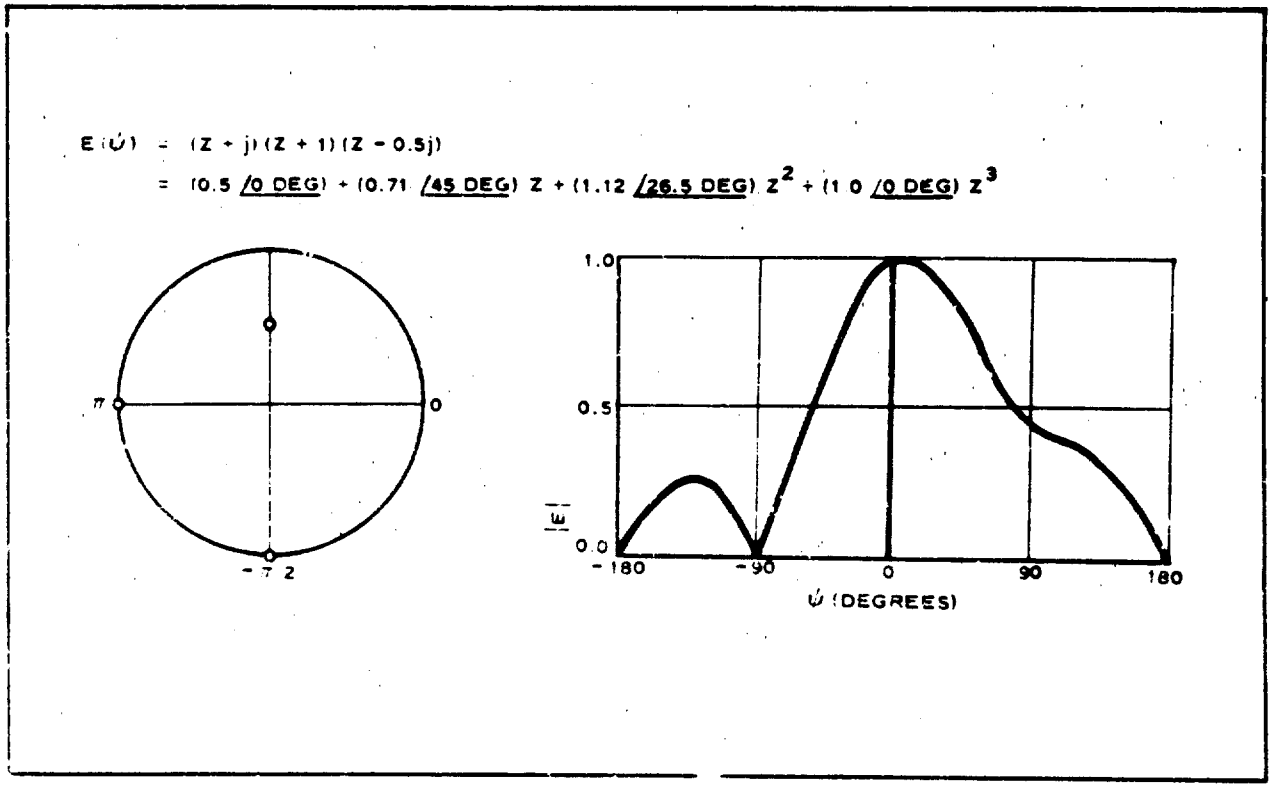

Figure 4 - Unit Circle Representation of Four-Element Nonuniform Array

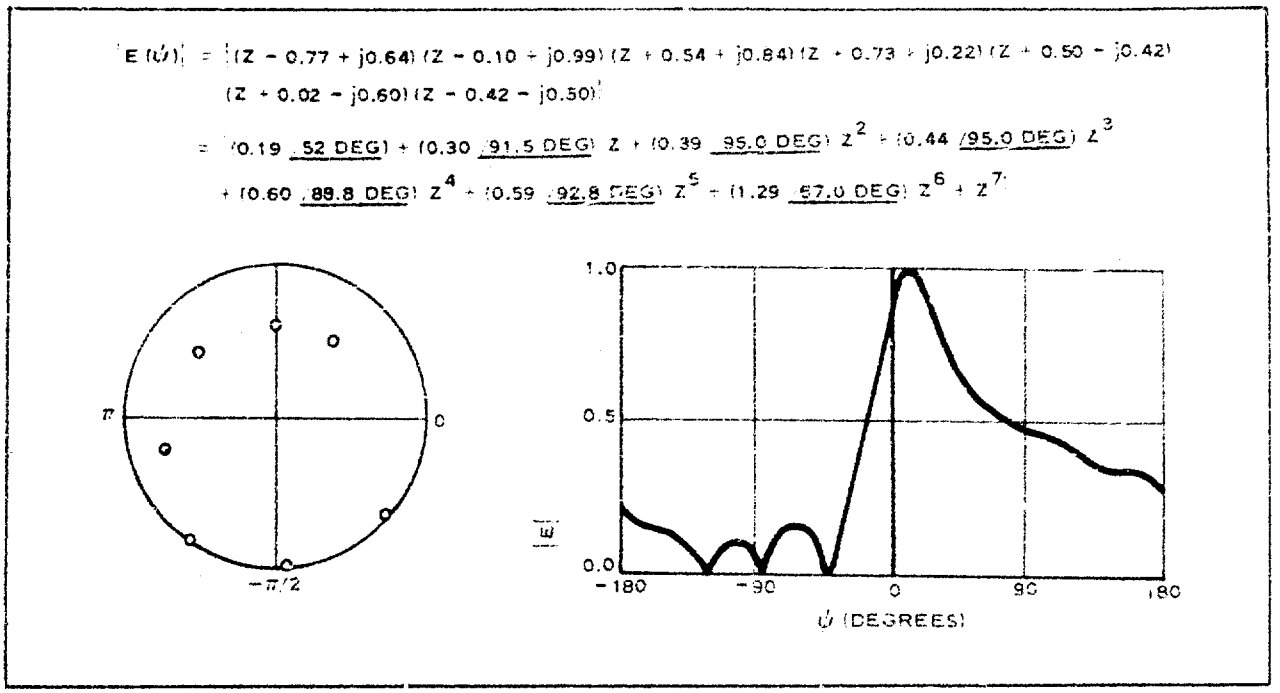

Figure 5 - Unit Circle Representation of Eight-Element Nonuniform Array

An interesting and useful aspect of the method arises from the fact that a non-unity root can be replaced by its inverse conjugate value without changing $|E(\psi)|$. Thus it can be shown that $2^N/2$ different sets of driving currents (where N is the number of non-unit roots) will produce identical power patterns. This feature has been found useful in series wave guide power dividers where the lowest possible ratio of driving current magnitudes is dictated by the limited practical range of slot coupling coefficients. In this case the set of driving currents with the lowest ratio of maximum to minimum value would be selected.

The graphical pattern computation is accurate to a few tenths of a decibel if done with care. However, two digital computer programs are desirable:

1. Computation of normalized power pattern $|E(\psi)|$ from root locations
2. Computation of all the $2^N/2$ sets of polynomial coefficients from a single set of input roots

The first program can be used in place of the graphical solution if it is more convenient, or as a final accurate computation. The second program avoids the tedious expansion of the complex roots into the polynomials.

The unit circle synthesis has also been found useful in compensating for pattern distortions resulting from mutual coupling. The procedure consists of comparing measured to computed patterns, which assume no coupling, and modifying the array factor accordingly. This iterative process appears to converge quite rapidly if initial coupling effects are not severe.

POWER DIVIDER

The center-feeding power divider, shown in the array of Figure 1, was selected on the basis of simplicity of design, ease of reproducibility, and ease of integration into the over-all antenna package. E-plane bifurcations were considered

and were rejected because they did not meet any of these requirements. The power divider is the resonant type with inclined slots in both narrow walls of a standard WR 90 wave-guide section. Although power dividers of this type have been built with slots in one edge, the literature shows no data for this doubly slotted configuration.

Measurements on several test units indicate that the presence of a companion slot has no noticeable effect on the coupling of the original slot. When a pair of opposing slots is terminated in a single section of wave guide, as in Figure 6, there is very little coupling (<40 db) between the two sides, due perhaps, to the section of transmission line between them which is below cut-off.

To design a usable unit it is necessary to know the relationship between the slot conductance g, the slot angle θ, and the slot depth D. Test units were made with single slots in each side of a wave guide, the slots having the same angle and same longitudinal center line position. Input admittance measurements were made with reference to the slot center line with slot depths increased by small increments until pure conductance was measured. The slot conductance was then determined by the input admittance, and checked by output arm coupling measurements. Several 16-output power dividers were then made based on the original data and the coupling values rechecked. The results of these tests indicate that the conductance is related to the slot angle in accordance with $g = K \tan^2 \theta$, where K is a constant dependent on frequency and geometry. The measured conductance data are shown in Figure 7.

The maximum usable angle is of the order of 25 deg because the proximity of the slot edge to the coupled guide seems to yield erratic data above this angle. Due to the variation in wall thickness and inability to separate centerline spacing errors from slot-depth changes, an exact relationship was not determined between slot depth and slot angle. However, the outside centerline distance is of the order of a half guide wave length. The latter relationship and the slot depth versus θ curves are shown in Figure 7.

Although an exact equivalent circuit for the power divider has not been determined, a workable model, at resonance, is shown in Figure 8. With matched loads on all coupled arms it is seen that the input conductance is simply the sum of the individual conductances because the slot spacing is one-half wave length. Power divider design requires that these conductances total 1.0. The power coupled out any slot is then $P_s = gP_{in}$, where

P_s = power coupled out slot s,

P_{in} = power at power divider input flange,

g = conductance of slot.

Off resonance there is a susceptance contribution from the slots which, in conjunction with the deviation from half wave-length spacing, causes some mismatch and hence changes in the power division.

The results of high-power tests on a 24-slot power divider are shown in Figure 9. As indicated, this power divider would handle 200 kw at 15 psia internal pressure. Although no external radiation source was used, each test condition was held for two hours or until breakdown occurred.

PHASING TECHNIQUE FOR VERTICAL PATTERN

The resonant slotted wave guide feed systems described above cannot readily

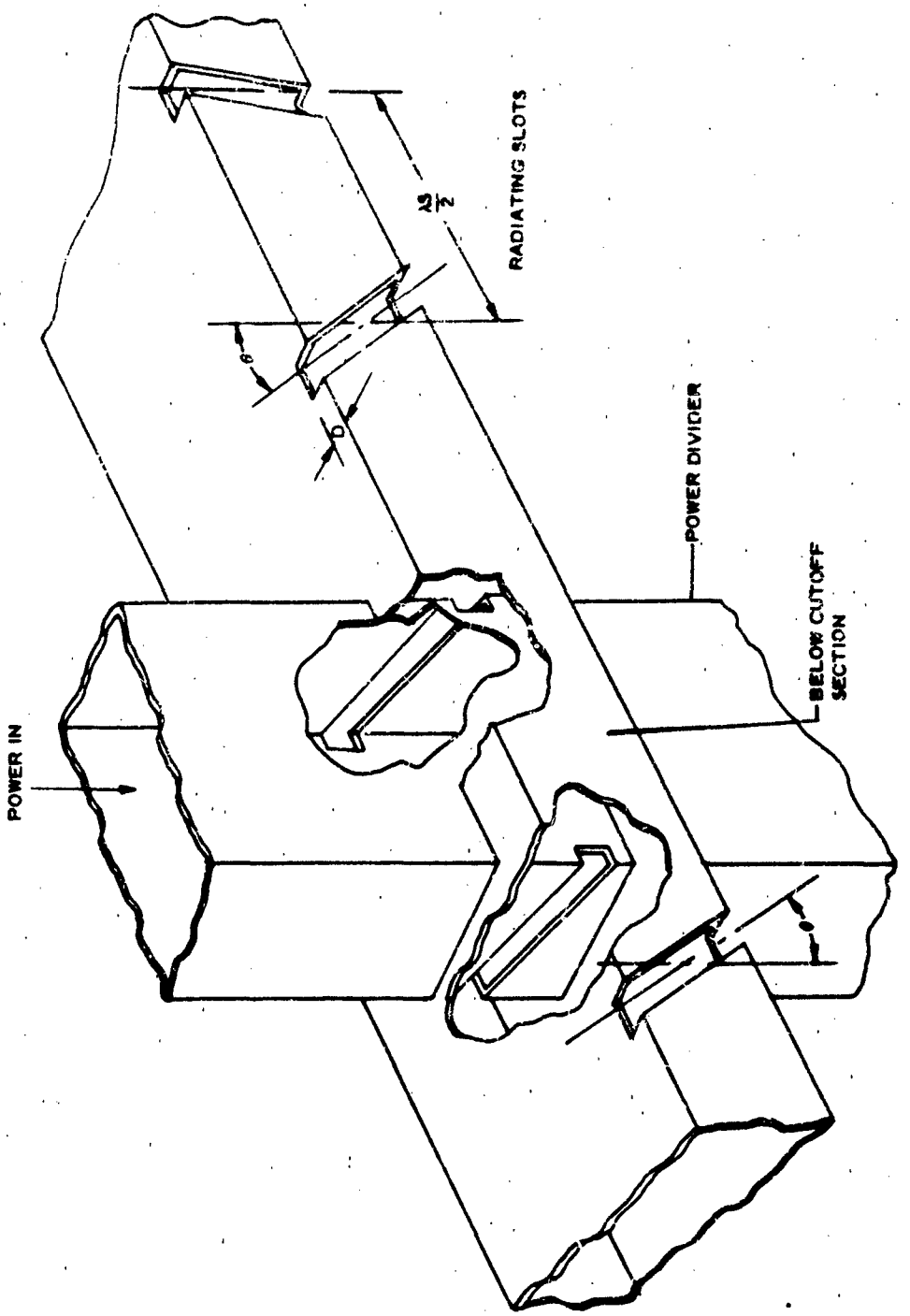

Figure 6 - Configuration of Power Divider Junction

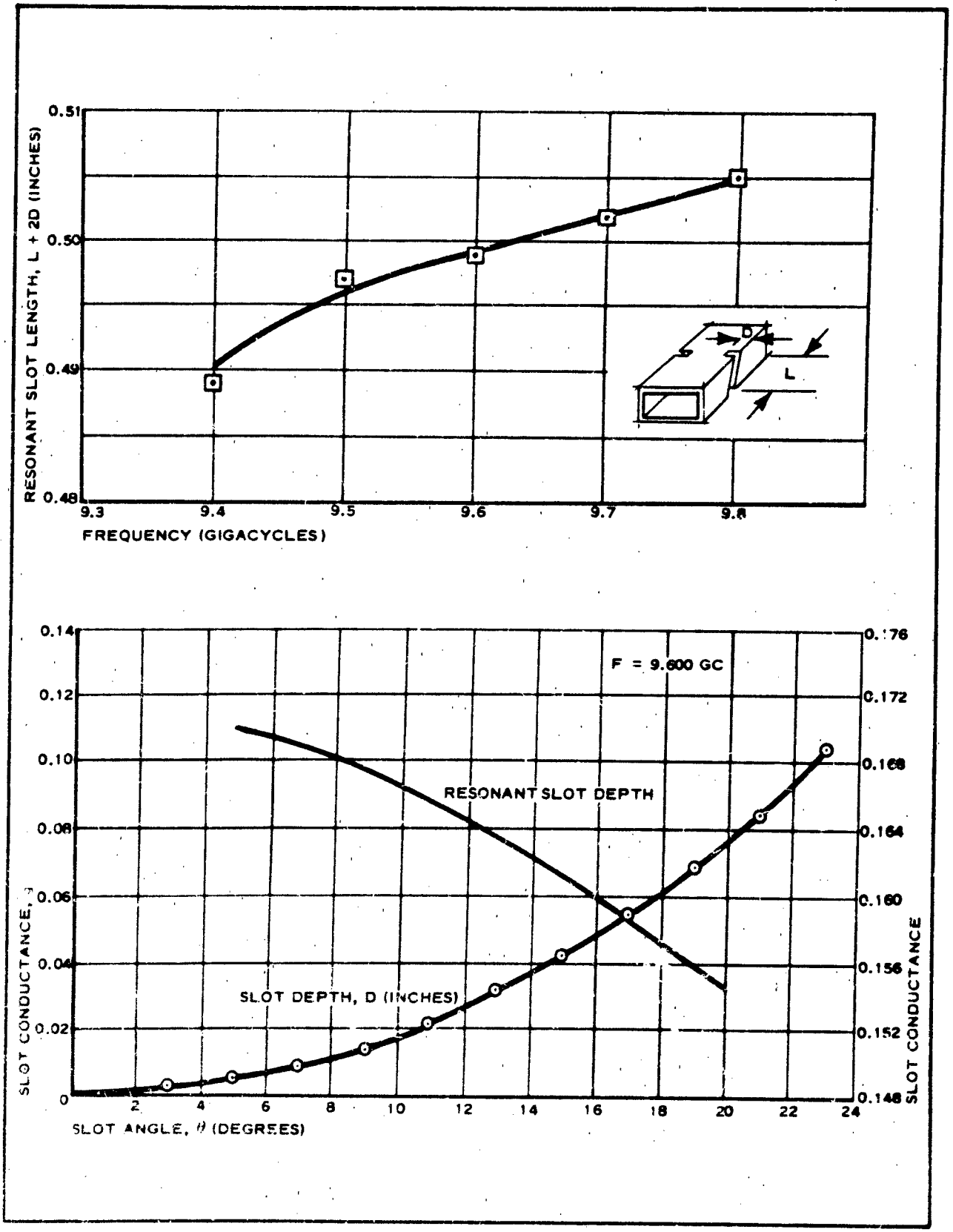

Figure 7 - Power Divider Design Data for 0.062-in.-Wide Slots, WR-90 Wave Guide

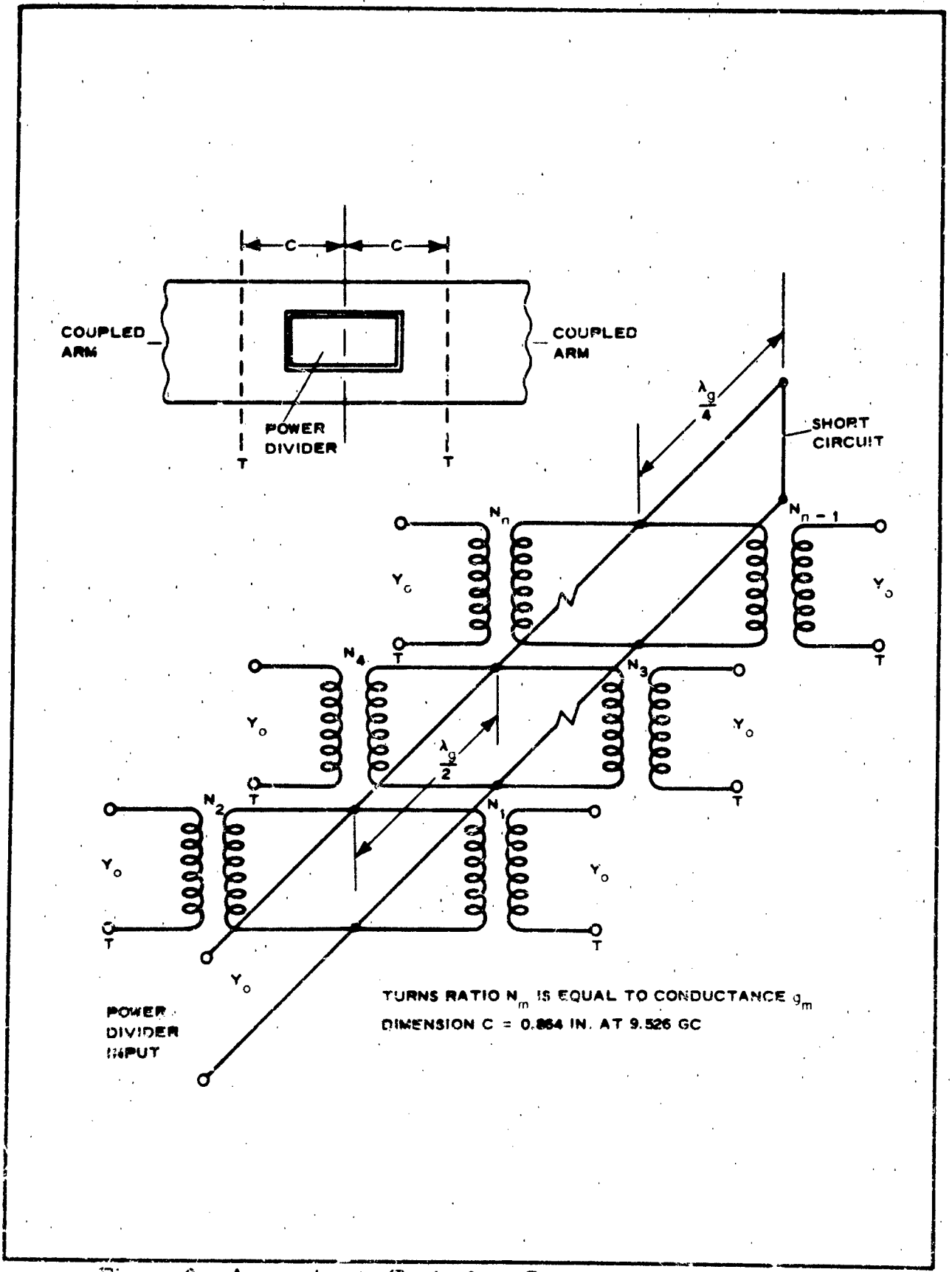

Figure 8 - Approximate Equivalent Circuit for Power Divider

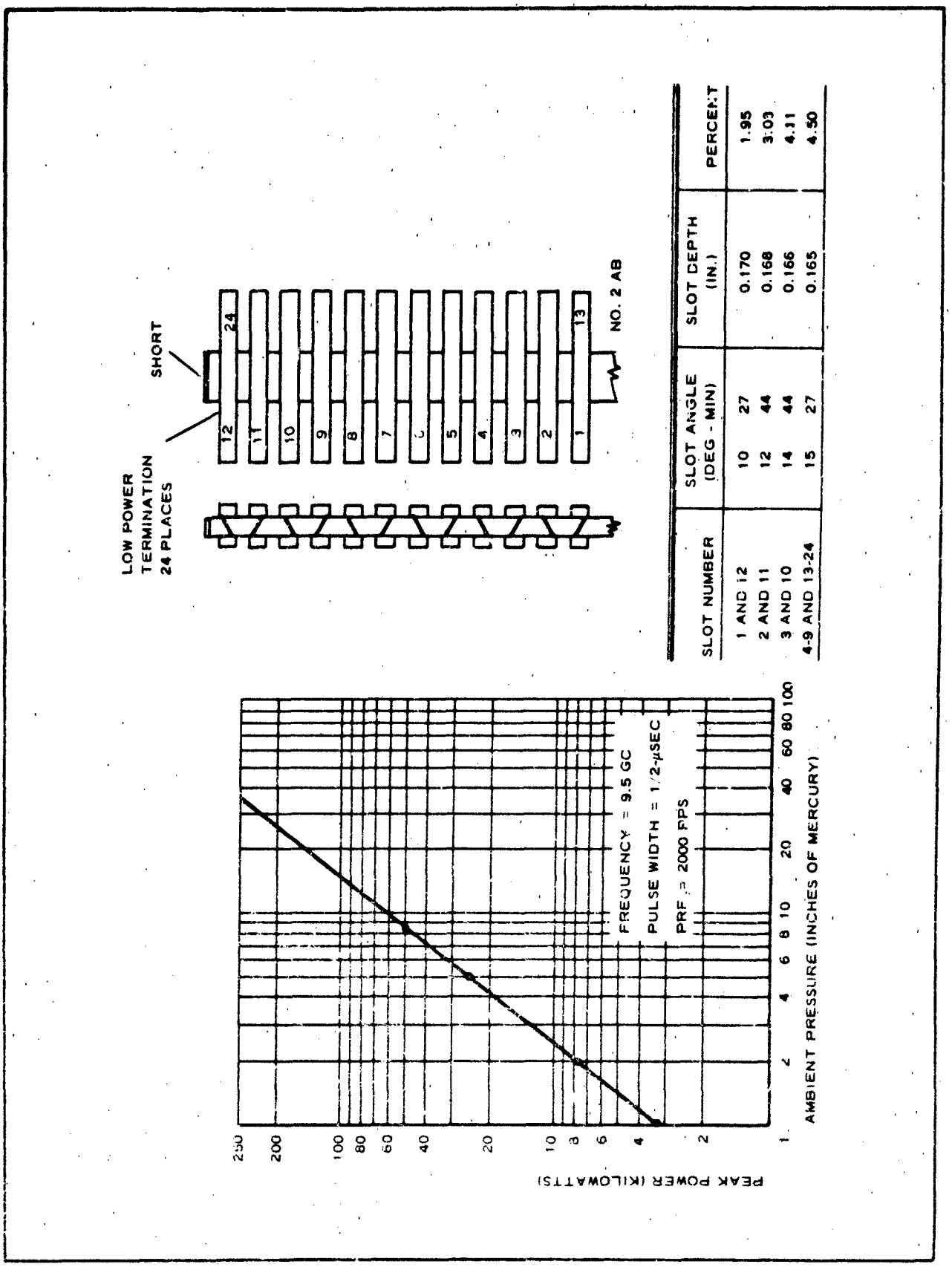

SLOT NUMBER	SLOT ANGLE (DEG - MIN)	SLOT DEPTH (IN.)	PERCENT
1 AND 12	10 27	0.170	1.95
2 AND 11	12 44	0.168	3.03
3 AND 10	14 44	0.166	4.11
4-9 AND 13-24	15 27	0.165	4.50

Figure 9 - Breakdown of 24-Slot Power Divider

be designed to control excitation phase as well as amplitude. The most comm phasing technique utilizes dielectric phase shifters in each branch guide. Su phase shifters usually add cost to development and fabrication, add weight, i terfere with radiating element placement (and hence degrade the patterns), a might result in design problems for a broad operating temperature range. A simple alternative technique is illustrated by the array of Figure 1. The pha of each element in the vertical direction is determined by the distance betwe the power divider and the first edge slot in the resonant slot pattern of each element. This means that each horizontal element is slightly different, henc the azimuth patterns of each element are also slightly different. However, these differences are too small, in an array of the size shown, to be of prac tical consequence. The composite azimuth pattern is found to correspond ve closely to that of a single element having an average distance between the po divider and the first slot.

The phase shifter employed is, then, a length of wave guide corresponding t the desired phase. It need never exceed a half-guide wave length because either the power divider slot or radiating slot angles can be reversed to obta a 180-deg phase shift. The desired phase shift is easily predicted and is co paratively economical and reliable. It does require, for the design shown ir Figure 1, that each of the elements be different. However, the production methods are such that the resulting added cost is very small.

SIDE LOBE REDUCTION

The array of Figure 1 is unconventional in the method utilized for side-lobe control as well as for phasing. For simplicity of manufacture it was desire that all slot angles be the same (except for reversals), resulting in an essen tially uniform array. However, because of a specified maximum azimuth si lobe level of 13.0 db, some means of side-lobe suppression was deemed nec sary to provide margin for center blocking (due to the power divider and pha ing spaces) and for manufacturing tolerance effects.

The required suppression was obtained simply by eliminating certain slots f the otherwise uniform slot pattern in each of the horizontal elements. Wher properly designed, such missing slots create an interferometer type of sub- traction pattern of such magnitude and phase that the near-in side lobes are duced at the expense of an increase in other side lobes. An example is give in Figure 10 for a computed array factor with and without two missing slots near each end. As can be seen, the maximum side-lobe level has been redu at the expense of a general increase in other side lobes and a slight beam bi ening. Not shown by the normalized curves is a gain reduction of 0.3 db.

No straightforward design procedure has been devised. However, with a ra simple digital computer program, it is possible to examine quickly a range numbers and locations of missing slots from which the optimum slot pattern be selected. Figure 11 shows typical variations in first side-lobe level and beam width for a limited range of missing element locations.

The above technique is not proposed as a substitute for more sophisticated s lobe reduction techniques. However, it might be a suitable alternative whe simplicity is advantageous and the slightly reduced performance (as compar to smooth tapering) can be tolerated.

PRESSURE SEAL

To utilize fully the weight and volume advantages of a wave-guide array, th

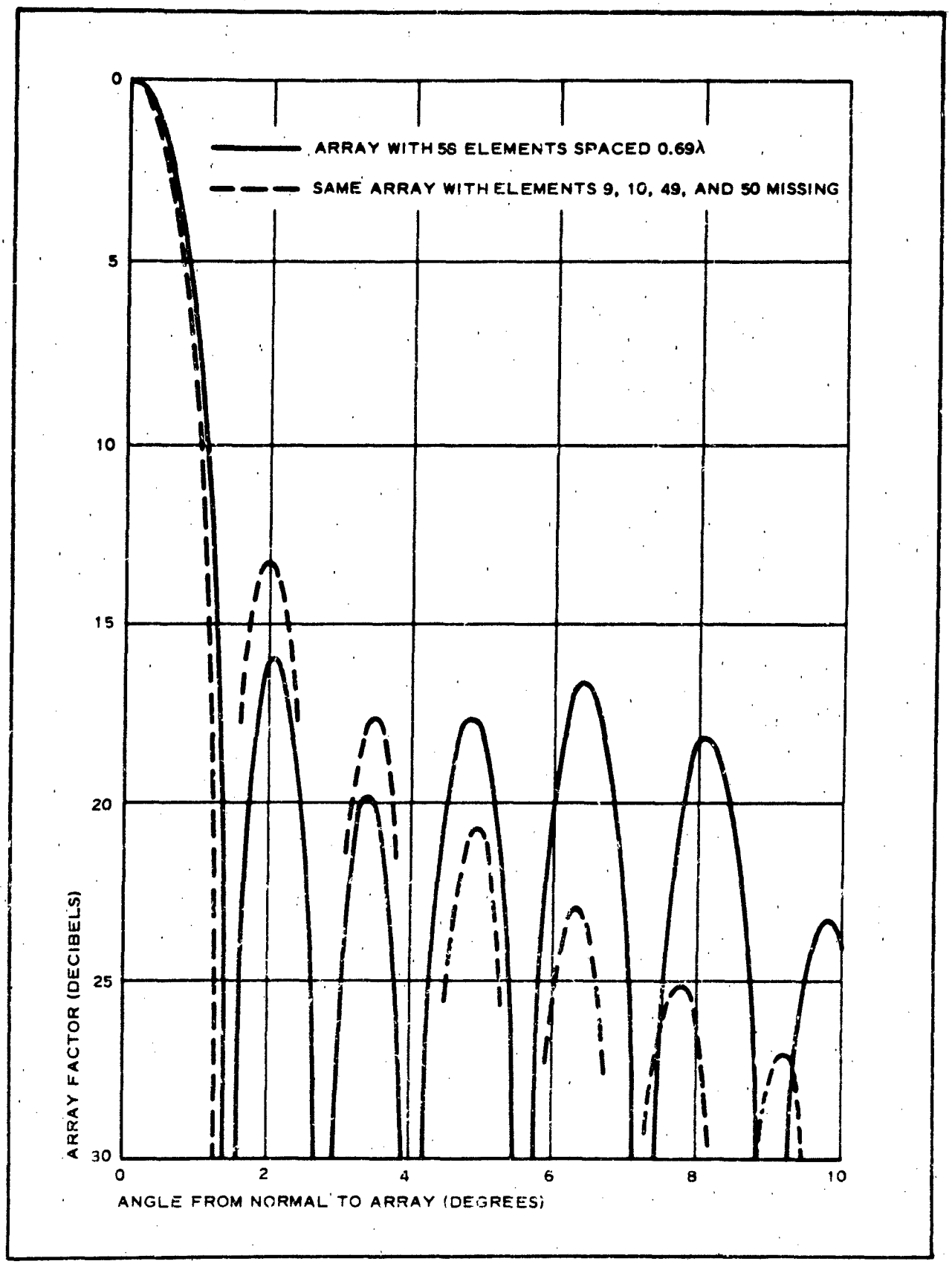

Figure 10 - Example of Effect of Missing Slots on Side Lobes

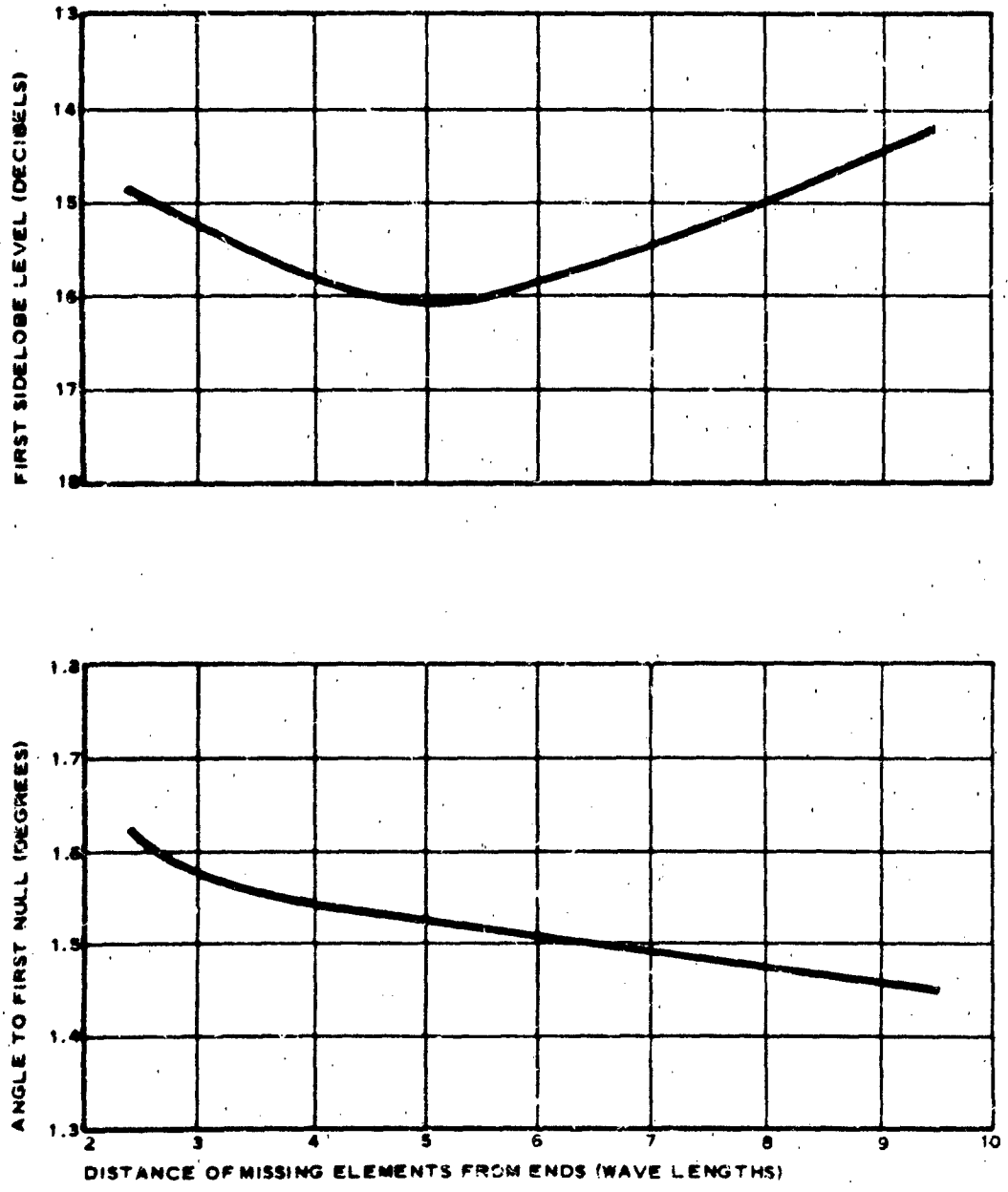

Figure 11 - Effect of Missing Element Location on First Side-Lobe Levels and Beam Width

pressure seal must add negligible weight to the array. Thin dielectric films bonded directly to the wave-guide elements have been used successfully to meet the pressure-seal requirements very well. Several sealing systems for RG-67/U wave guide are listed in Table I together with their temperature and pressure limits.

TABLE I - WAVE GUIDE SEALING SYSTEM CHARACTERISTICS

Pressure cover	Maximum service condition (F)	Test pressure (psig)
0.002-in. Mylar with polyester adhesive	250	30
0.010-in. Teflon with high-temperature adhesive	500	30
3M No. 57 thermo-setting electrical tape	200	20

Placing the dielectric film in intimate contact with the radiating slots causes the slot to appear longer than it is. This loading effect is shown for different films in Figure 12. The locus of admittances for various thicknesses of film coincides with the locus of admittances for various slot depths. This fact is very useful in determining resonant depths.

Power breakdown at high altitudes can occur at peak power levels that normally are encountered in airborne applications. In pressurized slotted arrays this breakdown occurs normally immediately outside the slot and will erode the pressure cover and eventually cause failure. The peak-power breakdown limits of the edge slots covered with Teflon are shown in Figure 13. Additional power handling capacity can be obtained by making the slots wider or by removing the dielectric cover from the immediate vacinity of the slots.

PRODUCTION TECHNIQUES

Theoretical tolerance studies and subsequent experience have shown that many of the dimensions of X-band resonant arrays require accuracies approaching those obtainable only with jig boring mills. However, special techniques have been developed to permit the use of more conventional equipment. Most of these techniques require a very high precision wave guide and tight inspection during processing. In the array of Figure 1 all slots in the element guides have the same angle. Thirteen slots of the same inclination are cut on the specially designed gang mill shown in Figure 14. This process maintains tolerances of ±0.001 in. on slot centerline location and slot depth. In cases where slot angles vary, such as in the power divider, tooling costs can be high and the use of a jig borer appears to be the most economical method of production.

Bulky mechanical fastening methods and conventional brazing processes cannot provide the lightweight and high accuracies necessary for airborne arrays. Resin bonding methods therefore have been used extensively for assembly. Preimpregnated film adhesive systems have been developed which give high strength aluminum-to-aluminum bonding at service temperatures up to 500 F. Glue-line thicknesses can be controlled to within 0.001 in. when assembly is

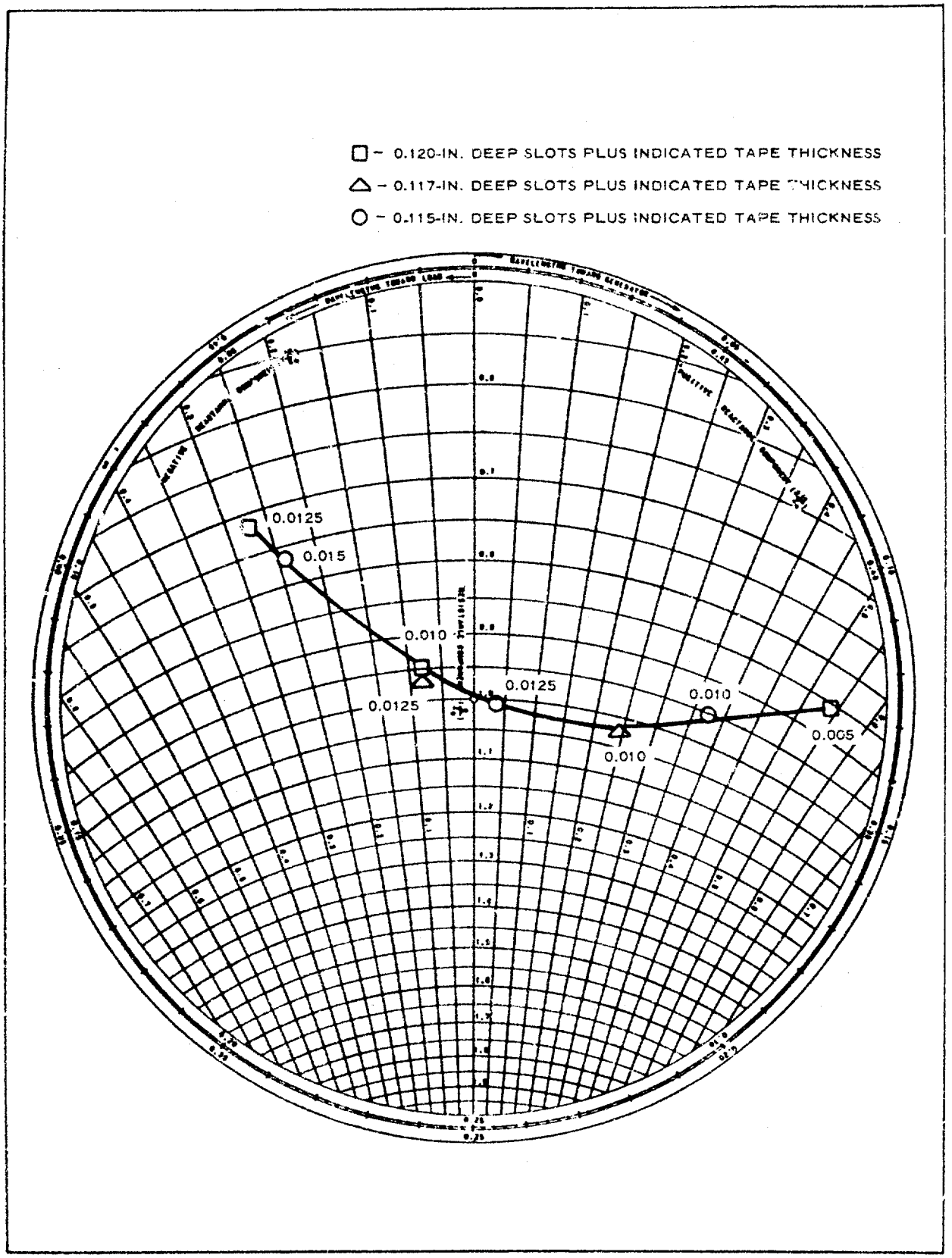

Figure 12 - Input Admittance of Element Guide as a Function of Dielectric Film Thickness and Slot Depth

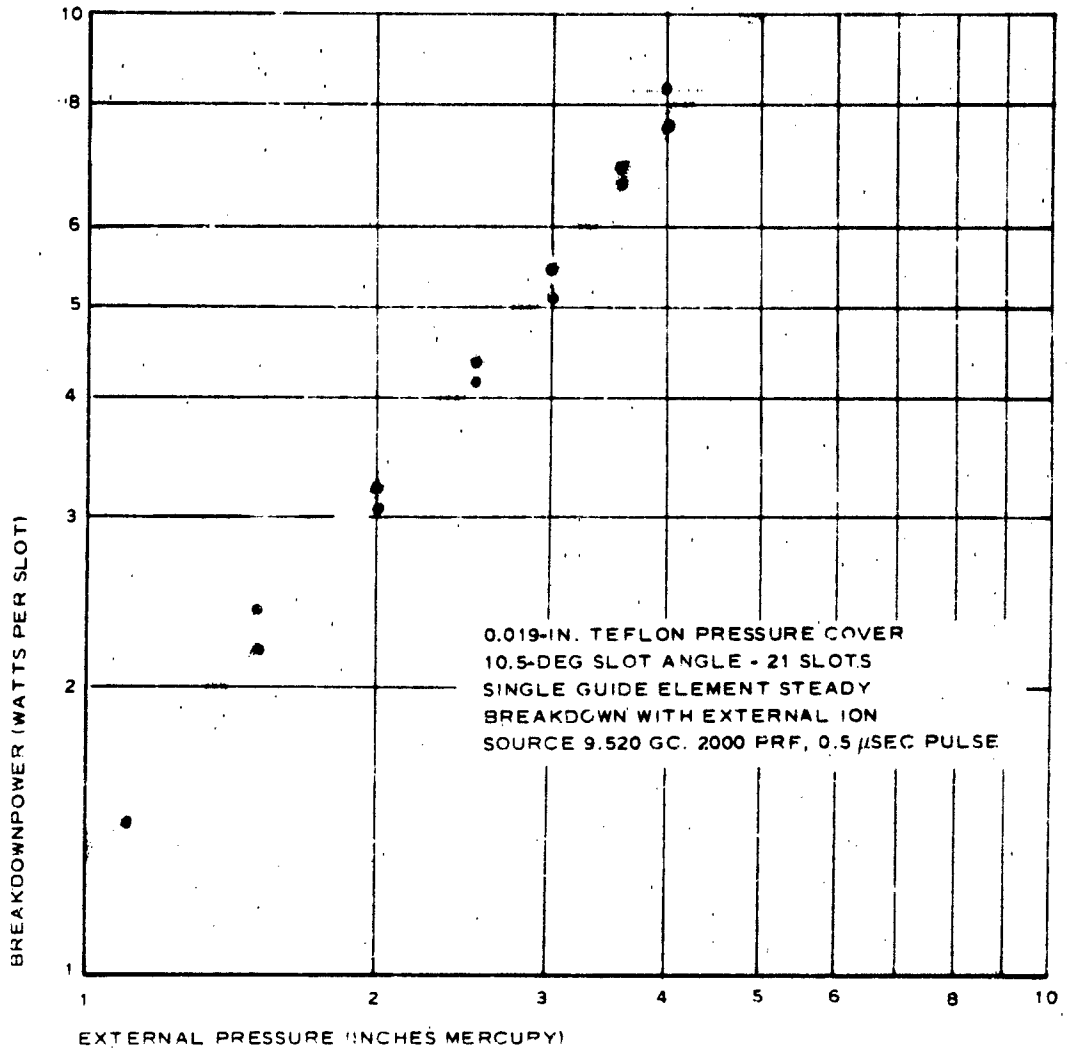

Figure 13 - Power Handling Capacity of Teflon Covered Slot, 0.062-In. Wide, versus External Pressure

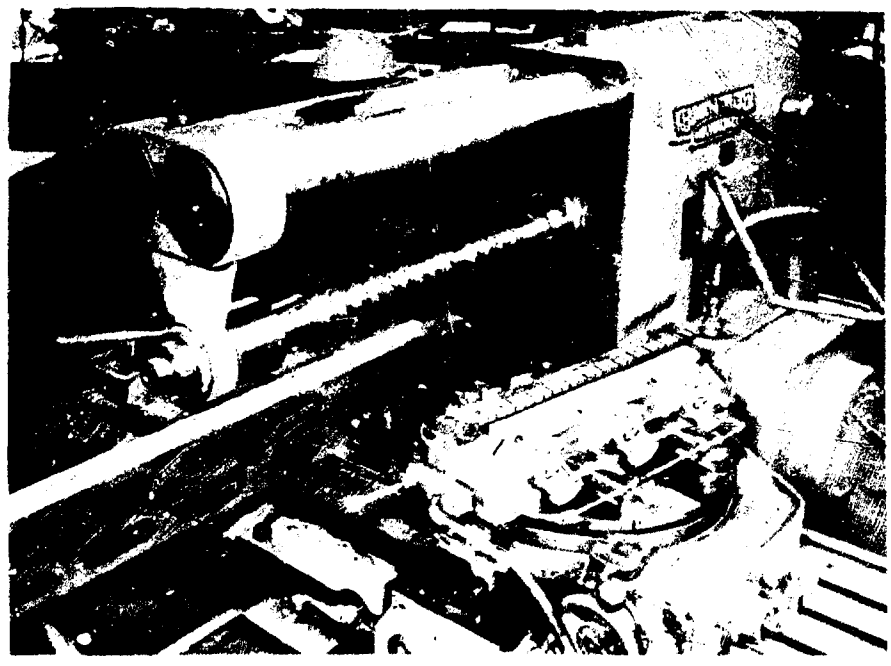

Figure 14 - Slotting Facility for Element Wave Guides

done in a properly designed holding fixture.

SUMMARY

The above discussions touch briefly on several techniques that have been employed successfully in array development but which have not received extensive coverage in the literature. The material has been drawn from several programs conducted at both the Akron, Ohio and the Litchfield Park, Arizona plants of Goodyear Aerospace. The paper should be considered as a compendium of solutions to specialized problems rather than as a treatise on array design.

LIST OF REFERENCES

1. Schelknnoff, S. A.: A Mathematical Theory of Linear Arrays. Bell System Technical Journal, pp 80-107, January 1943.
2. Taylor, T. T. and Whinnery, J. R.: Applications of Potential Theory to the Design of Linear Arrays. Journal of Applied Physics, pp 19-29, January 1951.
3. Kaminow, I. P. and Stegen, R. J.: Waveguide Slot Array Design. Hughes Aircraft Co. Technical Memorandum No. 348, pp 55-57, 1 July 1954.
4. Silver, S. et al.: Microwave Antenna Theory and Design. Vol 12, Radiation Laboratory Series, New York, McGraw-Hill Book Co., 1949.
5. Woody, W. C.: Two-Dimensional Array Synthesis. The University of Michigan Ninth Annual Radar Symposium, Fort Monmouth, N. J., June 1963 (GERA-904).

ANTENNA RANGE EVALUATION FOR MEASUREMENTS OF GEMINI TRACK RADAR

By J. H. Diel*

ABSTRACT

The accuracy in direction measurement required for success of the rendezvous mission of Project GEMINI has brought about the necessity for improvement in antenna measurement facilities. In order to adequately evaluate the performance of the radio direction finding device both the electrical and the mechanical characteristics of the antenna range must be excellent.

This paper describes the techniques used to set up and evaluate an outdoor free space type antenna range for measurement of the pointing accuracy of the GEMINI Track Radar. Since the anticipated accuracy of the radar is a few milliradians it is desirable to attain an overall measurement accuracy of less than one milliradian. In order to obtain this measurement accuracy it is necessary to hold the signal level of all extraneous signals, both reflected and externally generated, to -51 db over a four foot by six foot test aperture at the measurement frequency of about 1400 Mc/sec. This condition is sufficient when the mechanical errors in pointing the radar are held to negligible size (i.e., about 0.1 mr).

The method used to obtain this accuracy in the standing wave field consisted of the placement of radio frequency absorbing material at various places on the antenna range tower holding the measured antenna, and the use of a suitable antenna to illuminate the test antenna. The evaluation procedures included measurements of the standing wave field using the off peak amplitude measurement method, and an on peak phase measurement method using the interferometer techniques. The mechanical accuracy was maintained by use of a theodolite for boresighting and a redundant closed circuit television system and synchro system for measurement of the test direction.

* PHYSICAL SCIENCE LABORATORY
NEW MEXICO STATE UNIVERSITY
Box 548
University Park, New Mexico
Contract: McDonnell Aircraft Co., P.O. Y30412R

1.0 INTRODUCTION

The following paper is a discussion of measurements made for the purpose of evaluating the track radar on the GEMINI Spacecraft. This work was done under the sponsorship of McDonnell Aircraft Corporation, St. Louis, Missouri.

The objective of the study is to obtain a facility capable of measuring the accuracy of a radar at about 1400 Mc sec with a few milliradians accuracy. This radar and the attached mockup require a test aperture four feet high by six feet wide.

The antenna range to be used for this measurement is situated at the Physical Science Laboratory of New Mexico State University. This is an outdoor free space type range with the portion of this range used consisting of two wooden towers 375 feet apart and constructed such that the antennas being tested are positioned at a height of 86 feet above the ground. The physical layout of this range is shown in Fig. 1.

The desired accuracy of the measurement is a one milliradian angular accuracy . The steps necessary to obtain and prove this field are:

1.1 Determine field characteristics required for this accuracy.

1.2 Make a study of the environment to determine the level of any externally generated interfering signals.

1.3 Study the illuminating antenna and its compatability with the range configuration.

1.4 Make experimental measurements based on this study to obtain the desired standing wave field.

1.5 Measure the phase front configuration to confirm that the desired accuracy has been achieved.

1.6 Verify the mechanical angle accuracy of the measurement system.

2.0 DETERMINATION OF ACCURACY DESIRED

The radar whose accuracy is to be measured is basically two orthogonal circularly polarized interferometers with spacings of 0.824 wavelengths.

In order to determine the phase front variation allowable to obtain a measurement accuracy of one milliradian it is necessary to use the

interferometer equation:

$$\chi = \frac{2\pi d \sin\theta}{\lambda}$$

where χ is the phase angle difference between the two antennas, θ is the angle of incidence of the incoming wave and d is the separation distance of the elements of the interferometer. Since the largest angle to be measured (θ) is approximately 25° this equation yields an allowable error in χ of 15.85 minutes for an error in θ of one milliradian (3.43 minutes). For angles near θ = 0°, the allowable error in the phase front is 17.8 minutes.

Since amplitude measurements of the standing wave field are easier to make, it is desirable to use this type of measurement for any preliminary measurements required to determine the configuration of the range necessary to obtain the desired accuracy. In order to use amplitude measurements, it is necessary to determine the reflected signal level or standing wave field necessary to obtain a given accuracy of the phase front or pointing angle.

It can be shown by use of geometric considerations and propagation equations that the minimum extraneous coherent signal level required to give an error in pointing direction of an interferometer of one milliradian is given by

$$P = 20 \log_{10}\left[\tfrac{1}{2}\tan(2\pi d \sin\delta)\right]$$

where P is the extraneous signal level in decibels, δ is the angular pointing error, and d is the antenna spacing in wavelengths. Thus if a reflected signal level of -51.8 db is maintained the angular error will be no longer than one milliradian.

3.0 RADIO FREQUENCY INTERFERENCE TEST

A radio frequency interference test was made to determine if the test site environment was suitable. This was made by recording all signals received at a test antenna over a period of at least 24 hours for the test frequency and for this frequency ± the receiver I.F. frequency. The antenna used was a hybrid stub with hemispherical coverage and mixed polarization as a function of direction. Throughout the test periods the antenna was rotated slowly to achieve optimum reception of any incoming signal. With a receiver sensitivity of -80 dbm no signals were received during any of these tests. This R.F.I. signal level is adequate for the measurements.

4.0 ILLUMINATING ANTENNA STUDY

The illuminating antenna used was a 10 foot parabola fed with an eight turn helix to minimize edge illumination. Radiation patterns were taken of this antenna to determine the optimum feed position. The parameter optimized was the sidelobe level under the restrictive conditions of a polarization axial ratio of less than 1.0 db and a signal taper over the aperture of less than 0.5 db. This optimum pattern is shown in Fig. 1.

It can be seen from Fig. 1 that if spectral reflection from the ground is assumed there are two reflections from the ground to the test region. These occur at angles of approximately 17° and 32° with respect to the illuminating antenna coordinates. At these angles signal levels of approximately -37 db and -40 db occur on the pattern. If space loss differences due to different path lengths and reflection losses at the ground surface due to a wave hitting a dielectric surface with an assumed dielectric constant to 2.6 (dry sand) at an oblique angle of incidence are taken into account, the maximum reflected signal level which could result from ground scatter is 42 db down from the main signal.

5.0 EXPERIMENTAL ADJUSTMENTS OF THE STANDING WAVE FIELD

In spite of the low ground reflection levels, it was found by measurement that the standing wave field in the test region was still high. This was caused by the presence of reflecting elements in the vicinity of the test region such as the protective railing around the top of the tower, the antenna rotator, the antenna support pole and other such necessary objects. In order to rid the field of these objects as many as possible were covered with rf absorbing material. Using this technique, the amplitude of the measured extraneous signals was reduced to a maximum value of -44.6 db and an average value of -48.3 db.

6.0 PHASE FRONT MEASUREMENTS

The variation in the phase front across the aperture is the parameter which will ultimately determine the accuracy of the measurement of the radar angle. This variation was therefore measured as a final proof of the test region. This was done using an interferometer composed of two left circularly polarized spirals 0.965 wavelengths (8 inches) apart. The interferometer was set up so that a null appeared at a reference zero position. This null was frequently rechecked during the test periods. The zero null position was determined using a theodolite to position the ground plane of the interferometer perpendicular to the direction from the phase center of the illuminating antenna to the phase center of the interferometer. An autocolimating technique utilizing an optically flat mirror fastened to the ground plane of the interferometer was the method used to measure this perpendicularity. In

order to recheck this boresight during the tests a closed circuit TV with a 15-inch Wolensak lens and internal reticle calibrated in milliradians was affixed to the interferometer. For scanning in the horizonal direction this interferometer was mounted on a remotely controlled cart which ran back and forth on a track composed of an aluminum I-beam with an adjustable track affixed to it. For scanning in the vertical the interferometer cart system is mounted on an adjustable height fiber glass column passing through the center of the azimuth rotator. The calibration of this system resulted in a most probable measurement error for the total system of ±58.2 seconds in pointing direction or ±5.90 minutes in phase front. Using this instrumentation the phase front was measured over a four foot high by six foot wide aperture in four inch increments vertically and four inch increments horizonally. The data was taken by moving the cart to a particular position in the field and rotating the cart until the interferometer null appeared at the detector. The angle at which this occurred was measured using a synchro system with an accuracy of ±25.1 seconds (included in the cart accuracy of ±58.2 seconds) and compared to the predicted value of rotation necessary to obtain a spherical phase front with its origin at the calculated phase center of the illuminating antenna. These data were then reduced to a form which gives the phase front error as a function of position. A contour plot representation of this phase front is shown in Fig. 2. It was found that the phase front has a maximum error in any one measurement (i.e., for any particular position of the cart which would correspond roughly to any particular position of the radar being measured) of 34.4 minutes in the phase front or 1.93 milliradians in radar pointing direction. The most probably error in pointing direction for the phase front is 12.2 minutes or 0.69 milliradians.

7.0 MECHANICAL ANGLE ACCURACY

The mechanical angle accuracy for the radar measurement included the necessity of maintaining that accuracy in conjunction with the capability of rolling the spacecraft mockup containing the radar in 10° increments about its roll axis. A roll bearing was fabricated for this purpose and was constructed to maintain an angular accuracy in the pointing direction of the radar of ±42.4 seconds or 0.205 milliradians. The angular orientation of the radar for the various directions for which data were taken was measured using the same synchro system as for the phase measurements with the closed circuit TV system used for a backup. For all axis angles the TV system used targets positioned by the theodolite to an accuracy of ±14.2 seconds.

8.0 CONCLUSIONS

Using an outdoor free space type of antenna range, the measurement system which has been obtained for measurement of the pointing angle of an interferometer type radar has an overall angular accuracy characterized

by a most probable error of 0.648 milliradians. This figure includes an overall mechanical accuracy of ±42.4 seconds and a phase front error of ±12.2 minutes (most probable errors).

The configuration of the radar tested mounted on the front section of a GEMINI mockup is shown in Fig. 3.

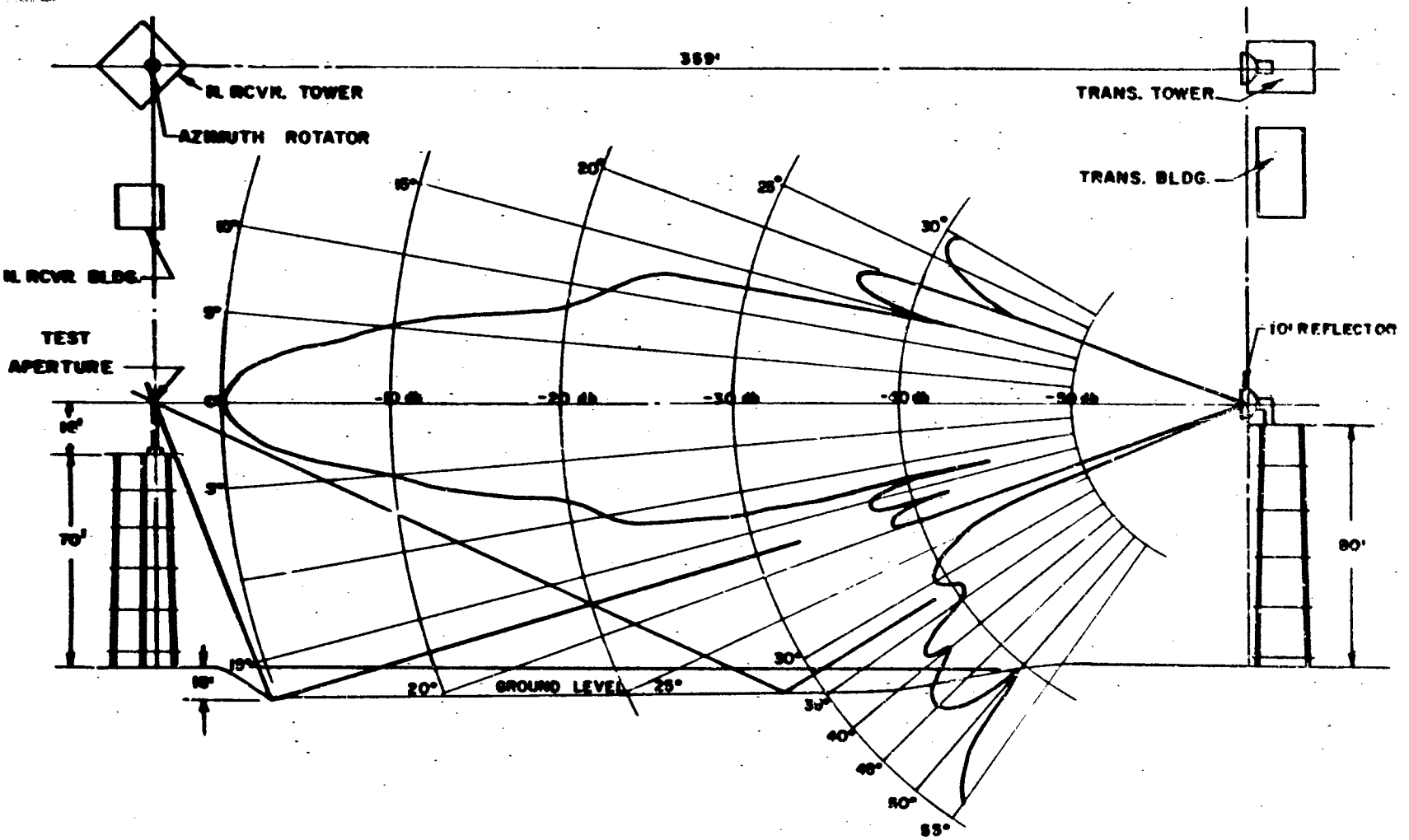

FIG. 1 - ARRANGEMENT AND DISTANCES FOR PSL NORTH RANGE

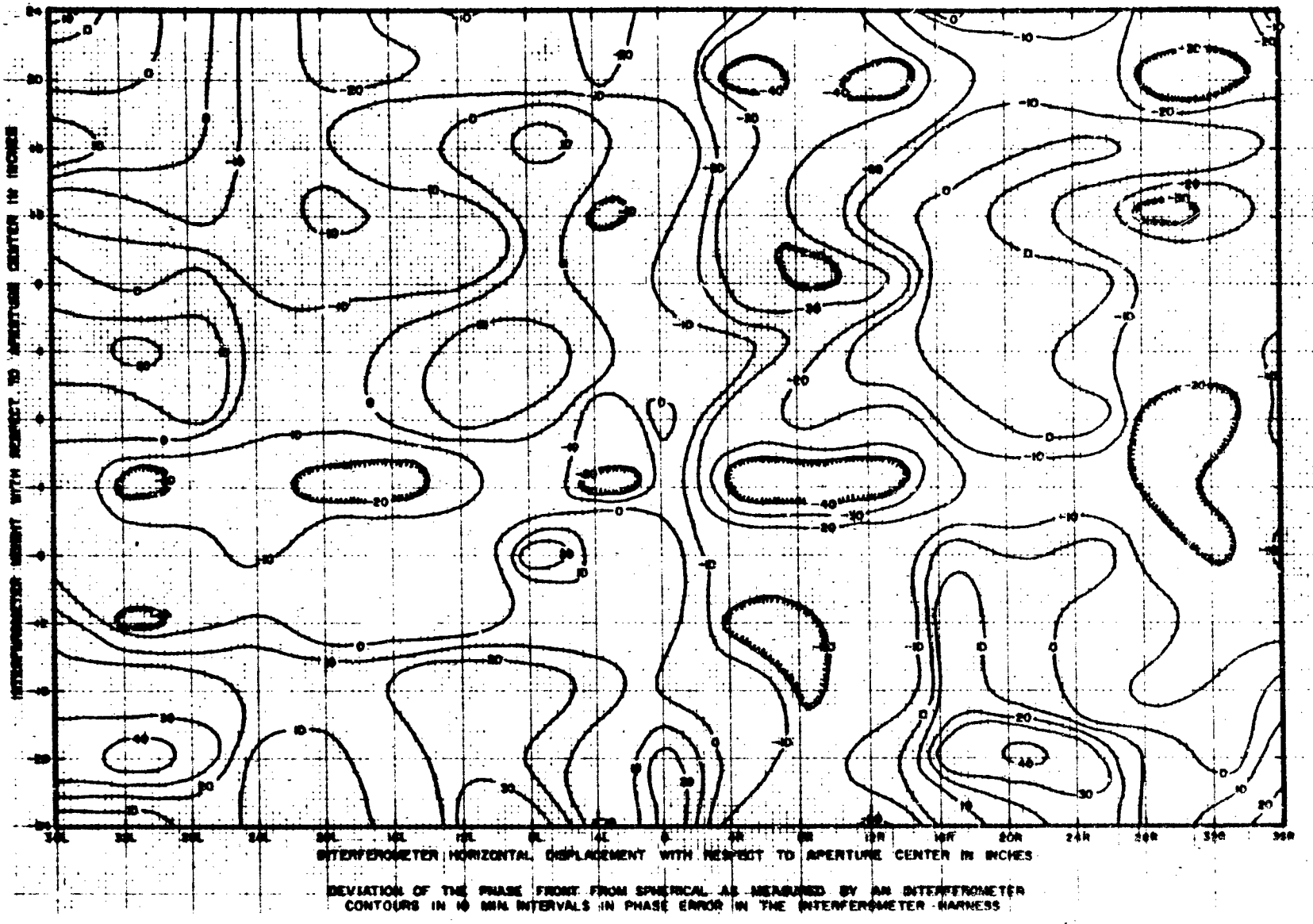

FIG. 2 - PHASE CONTOURS VERSUS AN IDEALLY PERFECT SPHERICAL PHASE FRONT OVER A FOUR BY SIX FOOT APERTURE



FIG. 3 - GEMINI RADAR FLIGHT CONFIGURATION

DESIGN AND EVALUATION OF ANTENNAS FOR USE IN A THERMAL ENVIRONMENT OF 2000°F

Godfrey F. Buranich
Cornell Aeronautical Laboratory, Inc.
Buffalo, New York

This paper presents information to aid in the selection of materials for ennas operating at high temperatures. Experimental helical antennas have n designed and fabricated using a variety of these materials and the ctrical performance of these assemblies have been measured at room ıperature and at elevated temperatures. No significant degradation has n noted due to the reduced electrical conductivity of the metals used or to thermal environment. Experimental data is presented in support of these clusions. Other antenna models are being fabricated for evaluation of itional designs. The paper also outlines the oxidation resistance properties ıigh temperature materials and the performance of present-day protective tings.

Experimental data compiled in an investigation of temperature effects :he power handling capability of microwave devices is also presented.

A review of the reentry environment to be experienced by various icles requiring hot antennas is presented and an outline of applicable ablati n radiation heat protection methods is given.

The purpose of this investigation is to compile handbook information ful for the design, fabrication and evaluation of high temperature antennas.

HIGH TEMPERATURE METALS

Metals for use at high temperatures can be categorized into four gener groups. These are steels, titanium alloys, super alloys, and refractory meta alloys. Steels and titaniu~ alloys lose much of their strength at temperature less than 1000°F, while)er alloys may be considered for applications requiring strength at 2000°F. Refractory metals can be used in thermal envir ments up to about 4500°F and are generally stronger than super alloys at 1800 The upper temperature limit of each of these materials is dictated by the strer requirements in the proposed application, by other characteristics which inclu fabricability, oxidation resistance, cost and weight, and by the peak value and duration of the high temperature enviro nment . Figure 1 shows curves of the strength/temperature relationships of the above groups of metals. The superiority of the super alloys at temperatures above 1000°F is clearly eviden as is the superiority of the refractory metals above 2000°F.

The choice of materials for use at about 2000°F is more complex since inherently oxidation-resistant super alloys, which are also attractive becaus e they can be fabricated readily using conventional methods, have inferior strength characteristics compared to the refractory metals. Refractory metal however, require controlled-atmosphere chambers for welding operations and must be provided with protective coatings to prevent catastrophic oxidation at high temperatures.

Figure 1 shows the increased strength and elevated temperature capabil alloyed metals as compared to the pure metals. Generally alloys lose signifi- cant strength at a temperature of about 50% of their melting point. It is to be noted that new alloys are being continuously developed for increased strength at elevated temperature but such extensions are generally made at the expense of the ease of fabrication and ductility of the metal. The competing strength-de characteristics of representative metals useful at 2000°F is shown in Figure 2. The nickel alloys such as Rene 41 and Haynes 25, which contain refractory met elements, retain strength to higher temperatures than those without these elem such as the Inconel alloys. Inconel metals lose most of their strength at 1500- 1800°F.

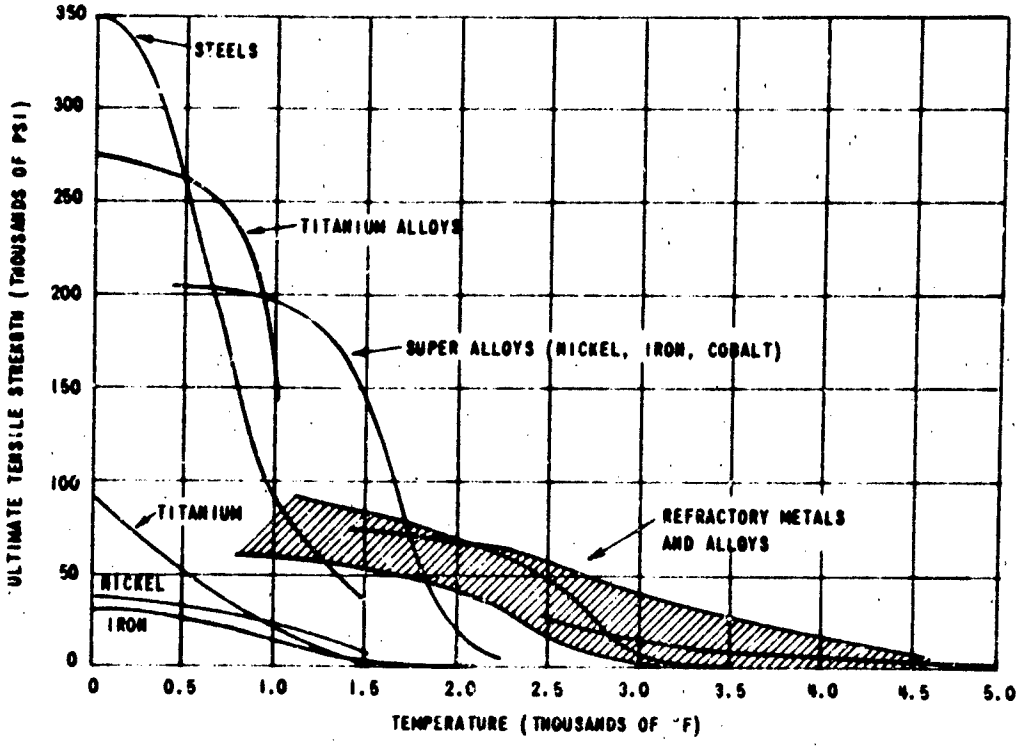

Figure 1 TENSILE STRENGTHS OF METALS AND METAL ALLOYS

Courtesy Johns Hopkins University

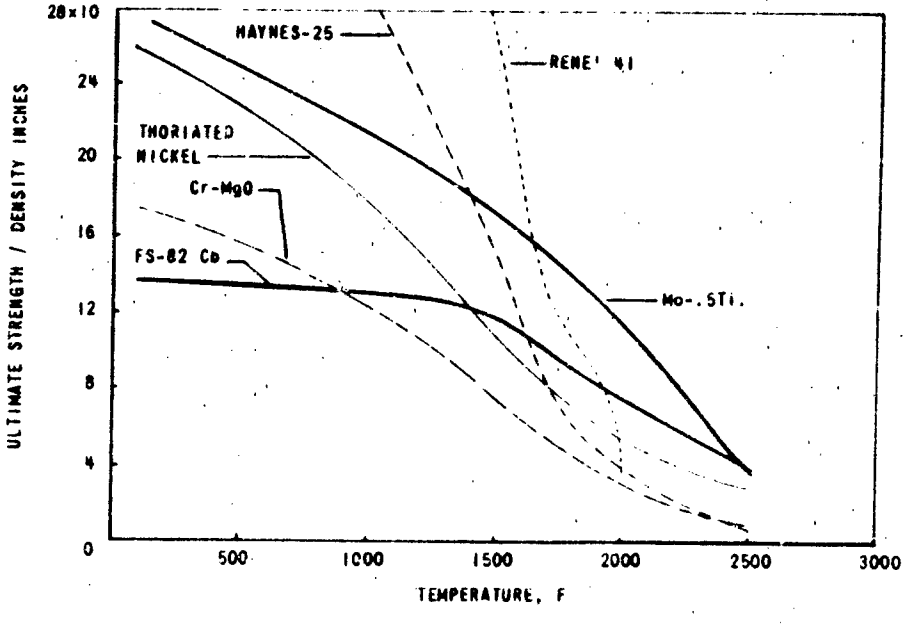

Figure 2 COMPARISON OF SUPERALLOYS, REFRACTORY-METAL ALLOYS, AND COMPOSITES

In the selection of metals for high temperature use it is therefore necessary to use refractory metals above 2000°F if high strength is required. Tantalum and columbium refractory metals are preferred because they are ductile at room temperature and use conventional machining operations, although brazing and welding must be done in a nonoxidizing atmosphere. Protective coatings usable to 3000°F for short times have been developed. Molybdenum has been investigated to a great extent, but this material requires special facilities and techniques for machining and fabrication operations because it is brittle at room temperature. Protective coatings have been developed for molybdenum for use to 3000°F.

At temperatures below 2000°F the super alloys have adequate strength and inherently good oxidation resistance. However, those super alloys having the highest strength at elevated temperatures are often precision cast into parts because of fabricability problems.

Composite Materials

Composite materials are mixtures of high strength materials (usually oxides or refractory metals) and metals with low melting points. A composite material is of interest because it retains strength to a temperature which approaches 80% of the melting point of its metal matrix. Composite techniques have extended the useful temperature range of oxidation resistant metals. Typical of composite materials are: TD nickel, which consists of sub-micron-sized particles of thoria in a nickel matrix; a silver composite, which uses whiskers of alumina in a silver matrix; and a chromium matrix with dispersed magnesium oxide. Of these three, TD nickel is the most useful and available to date. Its continued development by the DuPont Corporation has resulted in a compilation of considerable data regarding its strength, oxidation resistance and fabrication methods. NASA has also conducted an evaluation program* on this material because of its usefulness at 1800 to 2400°F. TD nickel has strength which exceeds that of the super alloys above 2000°F, and it retains good strength at 2400°F which is about 90% of the melting point of nickel. The dispersed

*NASA TN D-1944

thoria is radioactive but if ingestion is avoided (this hazard is particularly likely in dry-grinding operations), no personnel exposure hazard exists.

Investigations of a composite consisting of alumina whiskers in a silver matrix have shown that this material retains much of its strength to 1400°F even though silver has a melting point of 1760°F. Investigations are continuing to combine alumina whiskers with a nickel alloy matrix as a composite material superior to TD nickel, which will retain strength (and oxidation resistance) to a temperature approaching the melting point of nickel (2650°F). Growing of the whiskers and proper wetting of the whiskers by the matrix are two current problems which are impeding progress in this program.

A chromium matrix containing magnesium oxide particles is a composite material having good oxidation resistance and a high melting point (2700°F). Tests by NASA,* however, have found it to be non-competitive with other materials on a strength basis, its oxidation was rapid above 2200°F, and the oxide coating spalled upon cooling.

PROTECTIVE COATINGS

Oxidation resistance is that characteristic of a material which enables it to retain a uniform (or slowly varying) weight while exposed to oxygen at high temperature. Oxidation is a process which causes a material to produce an oxide powder or film on its surface. As a result there occurs a thinning of the base material and an obvious reduction of strength. In an extreme case this process of oxidation is similar to combustion. Such catastrophic failure of a structural member of a vehicle can occur after damage to its oxidation-resistant protective coating. For this reason materials having at least limited oxidation resistance are strongly preferred for use at high temperatures in place of those which depend wholly on a protective coat.

Initial oxidation of a clean material is relatively rapid until an oxide film is formed. This film then forms a partially protective coating and subsequent

*NASA TN D-1785

oxidation proceeds much more slowly and may eventually become nil. At temperatures which are beyond the oxidation resistance capability of a material, this reduced oxidation rate and the attainment of a constant weight is not reached. The material in such an environment continues to oxidize (rapidly) until it is entirely consumed.

Figure 3 shows the relative oxidation resistance of representative super alloys at 2000°F based on a weight gain. The depth of oxide penetratio into the metal is sometimes used as a measure of oxidation. Oxidation resistance of representative Inconel metals based on oxidation penetration is shown in Figure 4. The initial oxide penetration into these metals is show to remain essentially constant for various temperatures which are greatly in excess of the temperatures at which Inconel retains useful strength.

Oxidation protection may be provided for assemblies using nonoxidatic resistant materials by spraying on a protective coat of alumina. Alumina has attractive high-temperature features for this purpose but it has porosity, and oxidation of the underlying metal will occur, although at a slow rate. Such a reduced rate of oxidation may be acceptable for some applications. In fact flame spraying technology has been developed to such an extent that almost an material can be processed. Current investigations are being made of this technology for the protection of a base metal against oxidation at high temperatures. Spalling and peeling occur between materials having grossly unmatc thermal expansions. Application of a protective coating with a spraying proce has the additional advantage that large assemblies can be coated, and that repairs of damaged items can be made.

The use of nonoxidizing precious metals, such as gold or platinum, as a plating or cladding on high strength materials provides only limited protectio because of the diffusion of such coatings into the base metal with time and temperatures. Unmatched thermal coefficients of expansion between metals become a problem if extreme temperature ranges are encountered. Quantita data on the performance of such coatings (and coatings of palladium and rhodi have not been found. Platinum coatings may yet however prove to be useful.

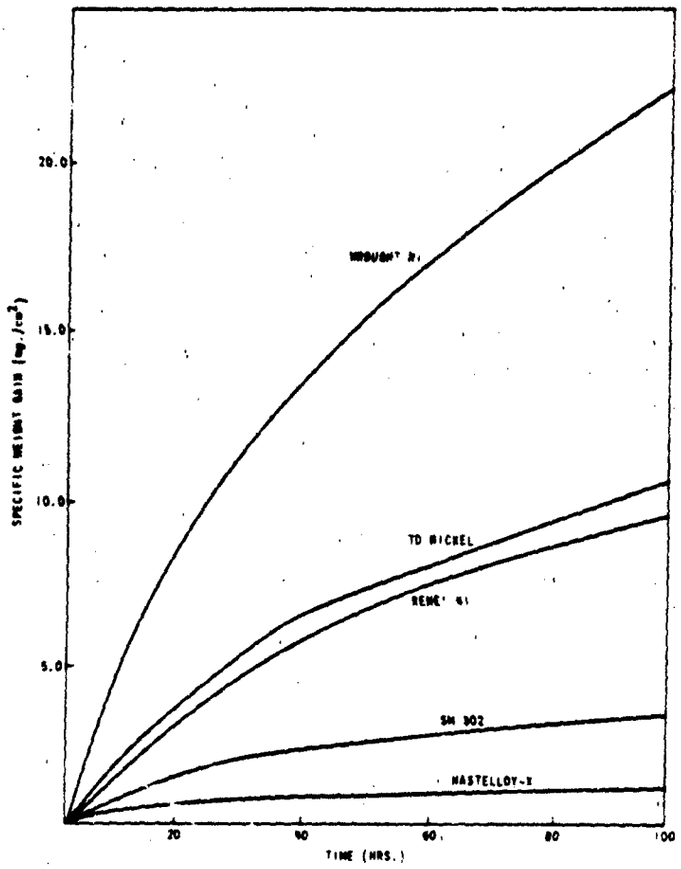

Figure 3 OXIDATION RESISTANCE - 2000°F

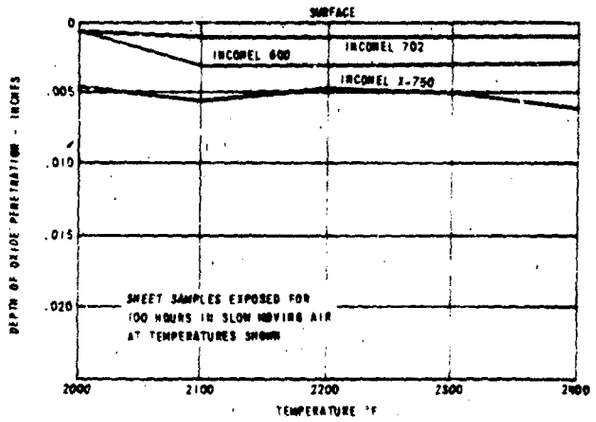

Figure 4 OXIDATION RESISTANCE OF INCONEL

The increasingly more rapid weight gain of a material exposed temperatures above its oxidation-resistant capability is shown in Figur for selected refractory metals. (Volatility of oxidation products of so materials will cause a correspondingly rapid decrease of weight).

The application of protective coatings to refractory metals requ special facilities. The material to be coated must be subjected to a hig temperature, and sometimes, simultaneously to a vacuum. Most facil: can accommodate only small items. Several types of coatings have bee developed and provide oxidation resistance without undue degradation of physical properties of the base metal.* Of these, the most promising the chrome-titanium-silicide coating of Thompson Ramo Wooldridge for columbium, and the tin-aluminum coating of General Telephone and Ele for tantalum.** A peculiarity of most of the coatings requires that the evaluated at various pressures and temperatures to insure that no degra performance exists within the entire environmental range which may be encountered in an application. Experience to date has shown that some provide protection for extended periods of time at temperatures in exce: 2500°F, but provide little protection at 1800°F. Other coatings have be to vaporize in a low-pressure environment, and therefore have short lif elevated temperatures at such pressures. Figure 6 shows the protectiv a typical coating as a function of temperature.

The coating of threaded fasteners remains a problem because coa build up in nonuniform fashion on various parts of the thread.

*DMIC Report 195

**DMIC Memorandum 183

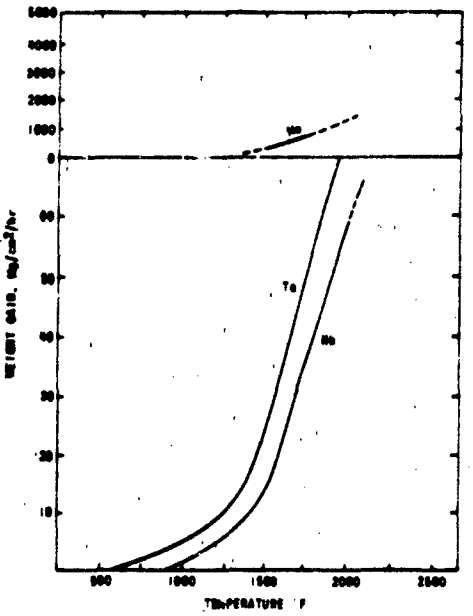

Figure 5 OXIDATION OF REFRACTORY METALS

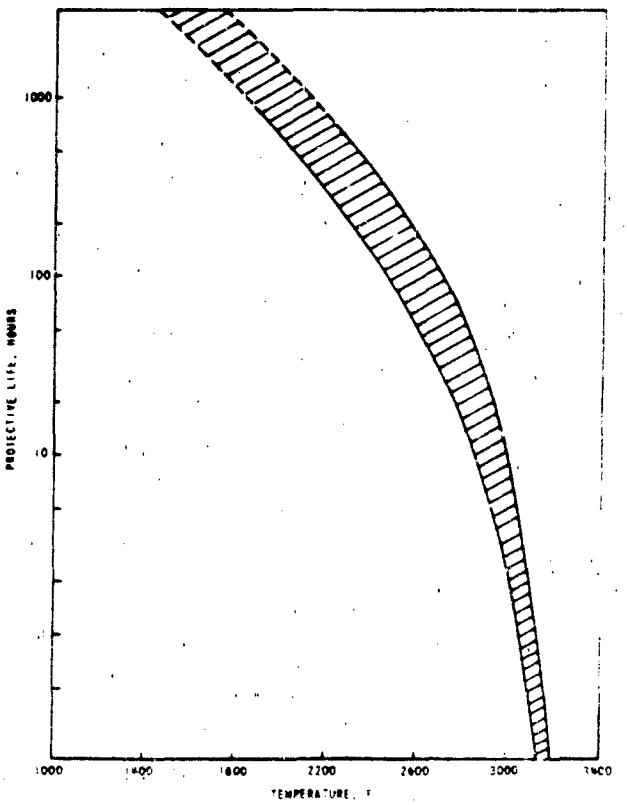

Figure 6 PROTECTIVE LIFE OF Cr-Ti-Si COATING ON COLUMBIUM

METAL TO DIELECTRIC SEALS

High-altitude operation of high-power antenna systems requires the use of metal/dielectric seals. The thermal expansion of materials is of importance in glass- and ceramic-to-metal seals. Seals of these types are made with a chemical bond which is produced when the materials are placed in contact and heated to a high temperature. If the thermal expansion of the materials is matched, no stresses will be created at the joint during cooling. If an unequal thermal expansion does exist, a tensile or compressive stress exist and may result in the rupture of the weaker material. Since ceramics have much greater strength in compression than they do in tension, an external seal, i.e., ceramic surrounded by metal, is a preferred type of seal. Metal having a greater thermal expansion coefficient than ceramics will, upon cooling, place the ceramic into compression in such an assembly. The thermal expansion coefficient mismatch which can be accommodated is limited to the stresses which such materials can survive. Large differential expansions can be accommodated only by allowing the metal to deform.

Figure 7 shows the thermal expansion of representative high-temperature metals and common ceramics. Columbium, beryllia and alumina have closely matched thermal expansion properties. Mullite and molybdenum are also closely matched. Generally, the published information on the thermal expansion of ceramics is an average value from which considerable deviation can be expected. Figure 8, for example, shows the spread of values obtained in comparing data gathered by various investigators on materials supplied by a number of organizations.

The initial process in producing a ceramic-to-metal seal requires metallizing of the ceramic. The most common method is the molymanganese process, which consists of painting a ceramic surface with a mixture of molybdenum and manganese. Subsequent firing bonds this metal to the ceramic. On pure alumina this bond will survive temperatures of 2600° to 3000°F in a non oxidizing atmosphere. The conventional brazing operation which joins this metallized ceramic to a metal uses brazing materials of low melting points, this is the reason that present-day widely used seals are limited to about 170 Brazes with higher melting points have been developed and some seals are now capable of withstanding temperatures to 2700°F. This high-temperature seal employs a palladium metal braze to join columbium to a tungsten metallized alumina ceramic.

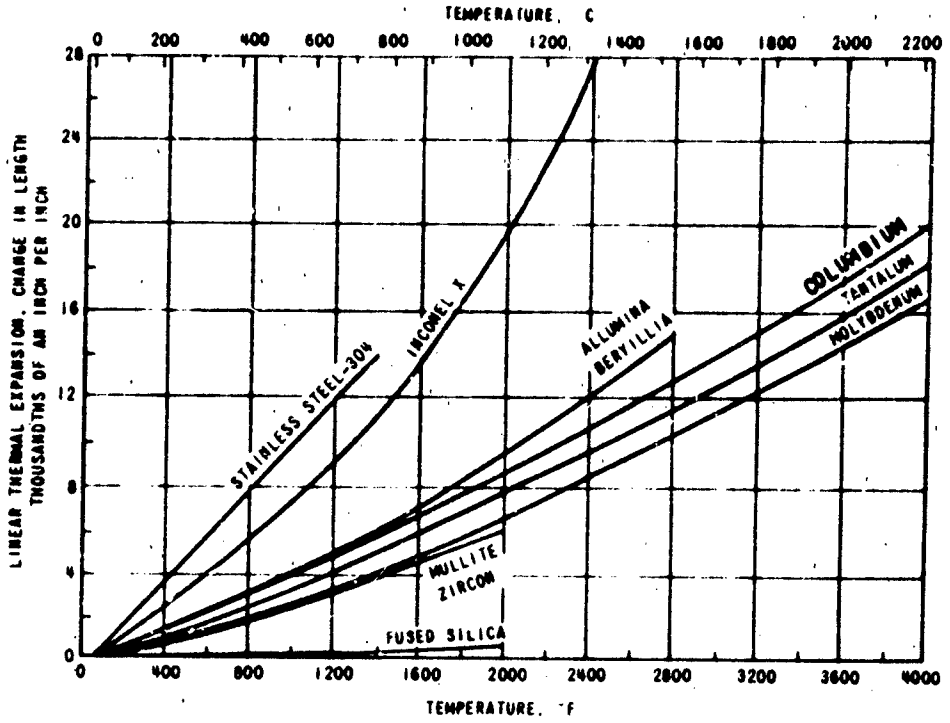

Figure 7 THERMAL EXPANSION OF MATERIALS

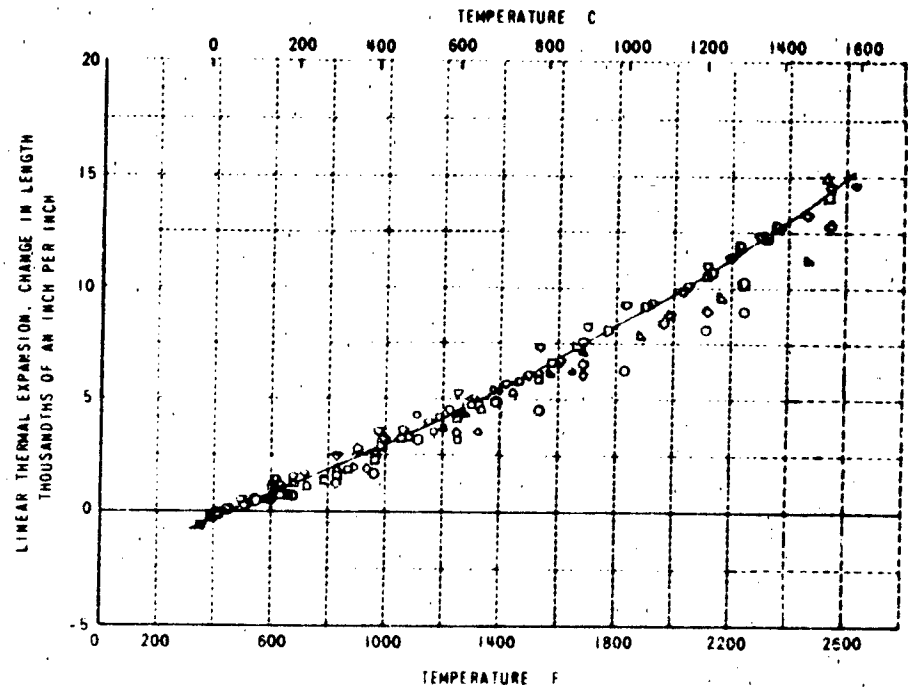

Figure 8 THERMAL EXPANSION OF ALUMINA - SPREAD OF VALUES

ELECTRICAL PROPERTIES

The electrical properties of materials which are of importance in the design of microwave antennas are the conductivity of metals, and the dielectric constant and loss factor of dielectrics. Figure 9 shows the resistivity and its variation with temperature of representative metals and compounds. Figure 9 also shows the theoretical attenuation of S-band wave-guide which is made of metals of various resistivities. Since the microwave attenuation occurs in the skin layer of conductors, the protective coating (three to seven mils thick) applied to refractory metals is a more important factor than the base metal. Molybdenum disilicide is one such material for which (contradictory) data is available. (High-temperature resistivity values range from 80 to 250 microhm-cm). It has good oxidation resistance to 3000°F. It is to be noted that the resistivities listed are DC values and that the microwave values may be appreciably different especially for materials which employ powder-metallurgy fabrication techniques. Among these is a new material, Carborundum's Boride Z, which is 10% molybdenum disilicide and 90% zirconium diboride, and which has oxidation resistance to 3600°F, making it suitable for possible use on hypersonic vehicles. It has a room temperature resistivity similar to the refractory metals.

In view of the small electrical loss introduced by metals having relatively large resistivities, the use of high-temperature metals for antennas will not seriously affect their electrical performance.

Figure 10 presents the temperature characteristics of the electrical properties of high-purity alumina and fused quartz. The increasing dielectric constant and the rapid increase of the loss factor occur for all the common ceramics, with the degree of slope varying among materials having different purities. A loss tangent of 0.01, which is the high-temperature value of typical ceramics, is the same value which plastic radome materials have at room temperature. Little importance is therefore attached to the increased loss tangent of ceramics at high temperature. The significant increase in the value of dielectric constant with temperature more critically effects the electrical performance of antennas. An antenna using a ceramic window normally incorporates matching devices to compensate for it. The change of dielectric constant will therefore change the VSWR of the assembly.

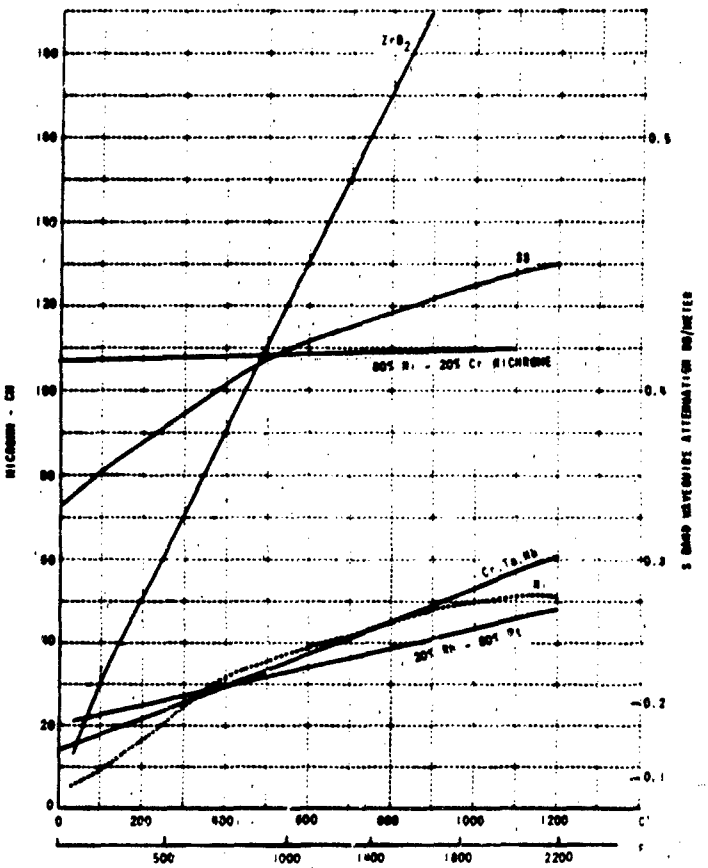

Figure 9 RESISTIVITY vs TEMPERATURE

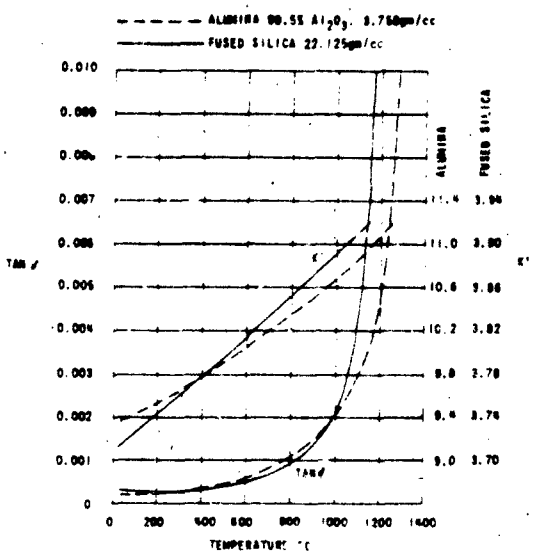

Figure 10 HIGH TEMPERATURE PROPERTIES OF DIELECTRICS

ANTENNA DESIGN AND TEST

The antenna range at the Wright-Patterson Air Force Base was used to compare the electrical performance of helical antennas made of conventional and high-temperature materials. Specific measurements were made to compar the radiation efficiencies of identical antennas made of different metals. Additional tests were made on nichrome and tantalum antennas to determine any changes in electrical performance produced by a 2000°F thermal environment.

The thermal test environment is produced by silicon-carbide heating elements inserted into a concrete or brick radome containing the antenna under test. Two types of thermal radomes have been used. One was made of castable concrete which was formed in matched molds. A second model was machined from fire brick. Both had a wall thickness of 1.5 inches. Figure 11 shows the fire-brick radome/silicon-carbide heating element combination. The advantage of the concrete or brick radomes lies in the fact that little heat escapes from the enclosure and therefore a few kilowatts of electrical power are sufficient to attain and maintain a 2000°F environment. The globar elements distort the radiation pattern of the test antenna and the radome introduces loss which varies with temperature. These modifying influences, however, can be readily separated from the effects produced by temperature on the electrical performance of the antennas.

Helical antennas characteristically have an elliptical polarization. In order to compare the efficiences of such antennas, radiation patterns were plotted automatically for two orthogonal polarizations for each of two mutually perpendicular elevation planes. The total area enclosed within these four radiation patterns is proportional to the antenna efficiency. A comparison of the total area of each of the helical antennas therefore was used as a measure of the relative efficiency of antennas made of different materials. Figure 12 shows the type of helical antenna used in these tests.

Table 1 lists the total areas enclosed by the radiation patterns of antennas made of copper, stainless steel, nichrome and tantalum. The tantalum

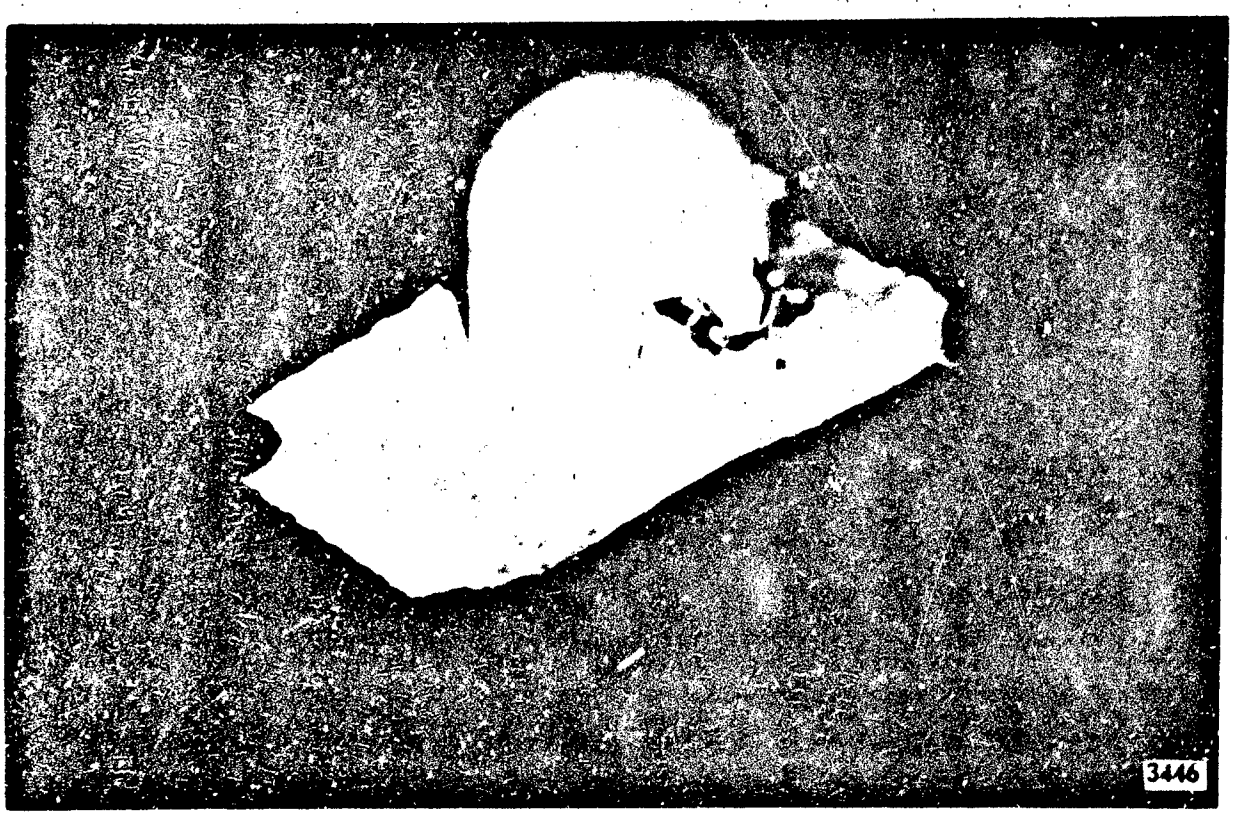

Figure 11 BRICK RADOME

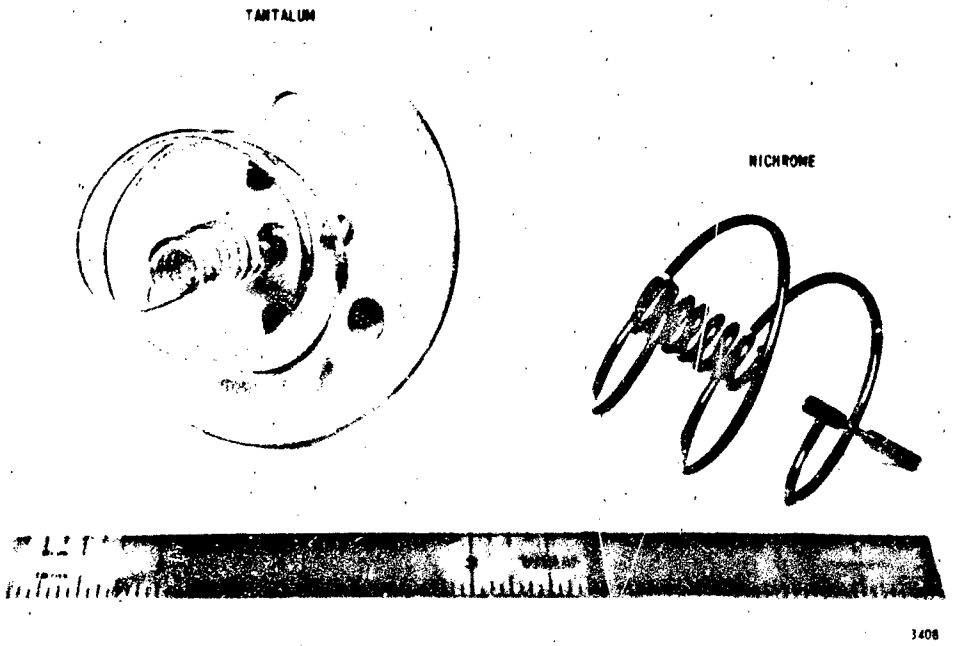

Figure 12 HELICAL ANTENNAS

antenna had a tin-aluminide high-temperature protective coating. The metals have room temperature resistivities of 2, 70, 120, and 20 microhm-cm, respectively. The resistivity of the protective tin-aluminide coating (approximately 3 mils thick) is not known. An inspection of the data shows that a metal having a resistivity as high as 120 microhm-cm has no noticeable effect on the performance of these antennas, and this finding is in agreement with a theoretical analysis developed by Ramo and Whinnery. (The low efficiency of the coated tantalum antenna is attributed to mechanical difficulties with the connector.)

TABLE I

Comparison of Radiation Pattern Areas

Antenna Material	Area
Copper	25
Stainless Steel	24.4
Nichrome	25.4
Tantalum (Coated)	20.8

A simple method used to determine the effect of temperature on the electrical performance of antenna consisted of mounting the radome and the heating element on a ground plane, with an opening for inserting the antenna accessible from under neath. The heating elements in the radome are turned on until the assembly stabilizes at the test temperature of 2000°F, and a remote pickup horn is positione above the housing (for testing an endfire broadbeamed antenna). The signal strength is recorded as a function of time after insertion of the cold antenna into the hot housing. A small metal assembly, such as helical antenna, will rapidly (perhaps in one minute) reach the temperature maintained in the thermal enclosur Thus, any signal strength variation detected during this short interval of time can be considered a thermal effect on the antenna performance. Tests made in this fashion on a nichrome and a coated tantalum antenna showed no significant therma effects on antenna performance at 2000°F.

VSWR measurements using this same technique of noting electrical performance as a function of time after insertion of a cold antenna into a hot radome are yet to be made. Monitoring the incident and reflected energy in the antenna feed line appears to be a method which can be readily instrumented. The use of a swept-frequency reflectometer is particularly appropriate for this use.

Several other types of antennas are being fabricated and will be evaluated in a thermal environment up to 2000 F. One of these is an open-ended columbium waveguide sealed with an alumina window. This assembly will serve to provide experimental data useful for documenting the selection of materials, sealing procedures and the compatibility of fabrication methods with assemblies requiring ceramic-to-metal seals and a protective coating. Relatively limited performance of this assembly in thermal shock is one problem becoming evident. A flexible seal using a fused silica window will be investigated further.

A planar spiral antenna is being fabricated using alumina dielectric as a substrate with copper plating for conductors. The copper will be overplated with gold for oxidation protection. This combination is expected to be useful to 1700°F. Fired-on-platinum paste conductors on alumina will extend this range to 2300°F. Flame-sprayed alumina will be evaluated for enhancement of the power handling capability of the spiral antenna. Present experiments are using silk screening of platinum paste on fused silica which is useful to 1700-1800°F. The use of this material will also shed light on the importance of loss in the substrate material. There is reason to believe that very low-loss material such as fused quartz will result in VSWR fluctuations because of unattenuated reflections from the ends of the spiral. It is agreed that conventional low-loss plastics have sufficiently greater loss compared to fused quartz that such reflections are decreased and do not affect the VSWR.

POWER HANDLING CAPABILITIES

The possible degradation of the power handling capability of an antenna in a hot thermal environment, as a function of temperature and the material from which the antenna is fabricated, is being experimentally determined. Power breakdown tests are being performed in a waveguide assembly in which samples of selected materials are heated to a temperature of 2000°F. Power handling tests of materials are being performed in this manner in order to avoid the modifying influence of dielectric supports, feeds and other physical peculiarities of antenna assemblies, and to also avoid the added complexity of having to design a suitable chamber for maintaining the antenna at 2000°F while it is simultaneously contained in a vacuum.

Figure 13 shows the experimental set-up used for the breakdown tests. S-band microwave power of about 1 kw peak is coupled to the test section enclosed by fire bricks. Silicon-carbide heating elements inserted into the brick structure provide the necessary heat using a 60-cycle power input of 3 to 4 kw. A chromel-alumel thermocouple is used for temperature measurements and it also provides an input to circuitry which automatically controls the heating current to maintain a selected temperature at the test point. The thermal drop along the test section (a 12-inch long tantalum waveguide suitably coated for use at 3000°F) is rapid enough to allow the use of copper waveguides for adjacent sections. Cooling coils are soldered on these copper waveguides to insure the existence of suitable low temperatures at the conventional waveguide windows located at the next flange assembly. A one-millicurie Cobalt-60 radioactive source is positioned on the test waveguide during breakdown measurements to give repeatability to the measurements. It is usually argued that breakdown occurs when a suitable ionizing particle (from background ionization present in the laboratory) enters the waveguide during the presence of the pulsed microwave energy. Since such coincidence occurs very infrequently, the experimental procedure of slowly increasing the microwave power until breakdown occurs results in impressing power above the breakdown threshold before this coincidence occurs. A spread of breakdown values is obtained in repeated tests. Investigators have shown that a given power setting may have to be maintained for an hour or more before readjusting it to a higher

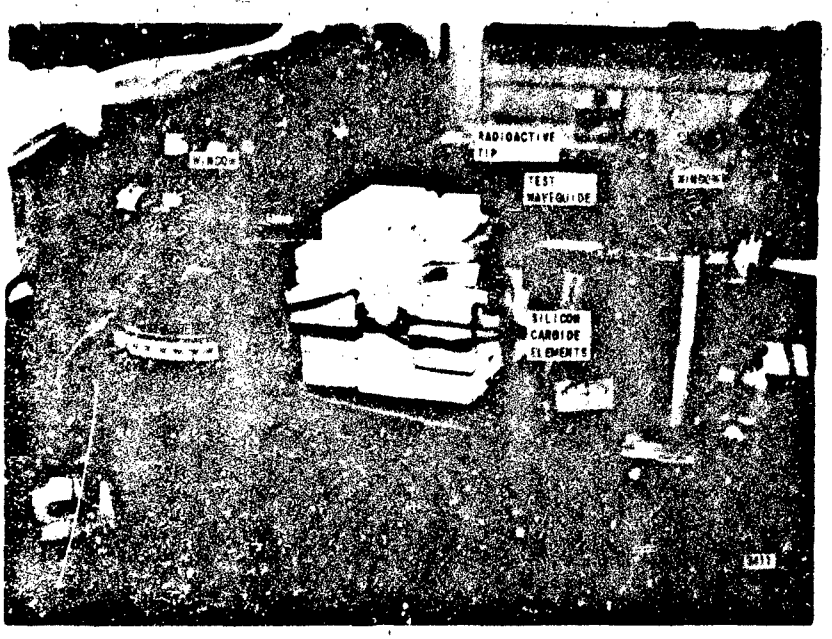

Figure 13 POWER HANDLING TESTS

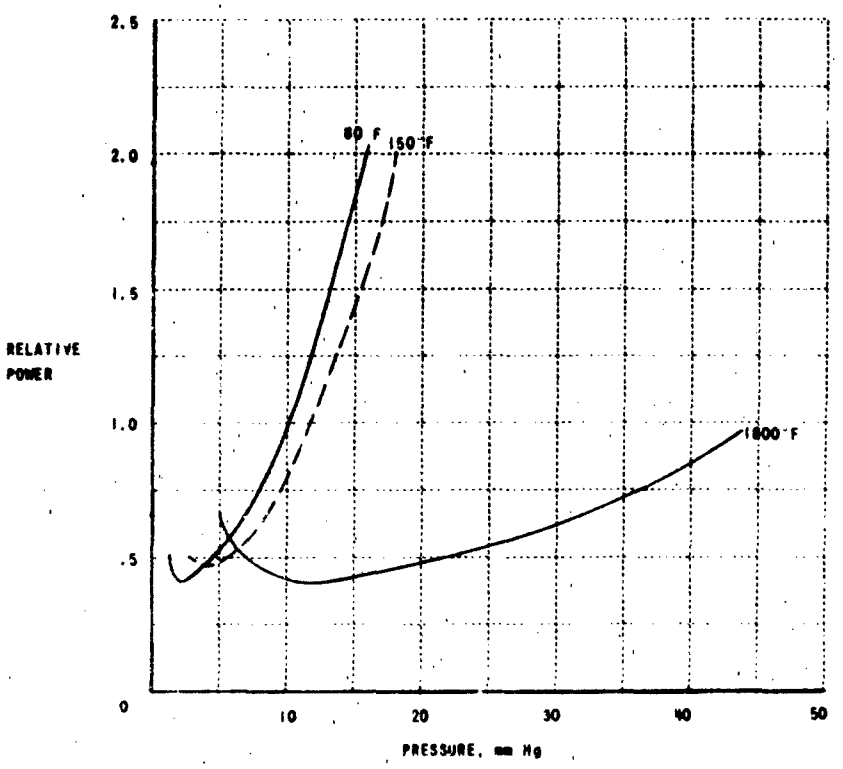

Figure 14 BREAKDOWN OF COPPER HEMISPHERES

level to insure that the inherent power-handling capability of a device is not being exceeded. If a radioactive source is used, the frequency of background ionizing events is greater and repeatable breakdown readings may be taken at intervals of less than one minute.

Breakdown tests were run on a waveguide in which two hemispheres 0.335 inches in radius were located on the centerline of the broad wall and spaced to produce an electrical match. Copper hemispheres at room temperature had a power-handling versus pressure characteristic as shown in Figure Minimum power handling occurs at a pressure of about 2 mm Hg and the power handling capability rapidly increases with increasing pressure. The figure also shows that at higher temperatures, approximately the same minimum power-handling capability is noted except that it occurs at higher pressures. This characteristic is in agreement with theory which states that power handling is a function of gas density. The density which exists at a selected pressure at room temperature can be reached at high temperature only by increasing the pressure. This cold- (26°C) to-hot pressure ratio is proportional to 293/T where T is the hot temperature in degrees Kelvin. A curve is shown for the assembly after cooling to 150°F to indicate the degree of experimental stability which existed over the testing interval. Considerable warping of the test section occurred during the heating operation and may explain the discrepancy noted. Hemispheres made of TD nickel produced similar performan with temperature.

RE-ENTRY ENVIRONMENT

The hot thermal environment experienced by antennas on re-entry vehicles varies appreciably among vehicles, trajectories and with location on the vehicle. The generated heat is the result of the decreased kinetic energy of a vehicle as it decelerates during atmospheric entry. A lunar re-entry vehicle (having a velocity of 36,000 ft/sec) has an energy content of 26,000 BTU/lb, and an ICBM has an energy content of 10,000 BTU/lb. The efficiency of conversion of kinetic energy into re-entry body heating is relatively efficient (80%) at altitudes above 300,000 feet and is relatively inefficient (1%) at an altitude of 150,000 feet. Because little kinetic energy is lost at high altitudes, most of the heating occurs at an inefficient rate. The extremely rapid atmospheric entry of an ICBM results in a relatively low total heat input into the body, but such a vehicle encounters very large decelerations and extremely high heating rates. The manned re-entry vehicle must be designed to limit re-entry deceleration within the tolerance of the human occupant. Heating time in such a trajectory is at a low rate but long and the total heat input is higher than would have been experienced in a faster re-entry. The highest heating rates are at the stagnation point of the vehicle with as little as 1% of this value existing at the back of the vehicle, which is shielded from the oncoming flow by other sections of the body. It is estimated that 5×10^6 BTU are transferred to a blunt re-entry vehicle. Radiative and ablative techniques are used to protect the vehicle from excessive heating. The radiative system is capable of re-radiating an unlimited amount of heat, but metals cannot withstand heating rates in excess of about 90 BTU/ft^2-sec. Since heating rates an order of magnitude higher than this exist on portions of a re-entry vehicle, ablative coatings must be used. Various types of plastics and quartz are used for this purpose. These materials dissipate several thousand BTU per pound and can withstand all expected heating rates. Since there is a practical limit on the weight of ablators which can be carried on space vehicles, sufficient ablation material is used only to protect the areas of vehicles which undergo high heating rates. A combination of ablators and high-temperature materials, i.e., refractory metals, super alloys and ceramics, has been found to produce the most lightweight heat-protection system.

Figure 15 shows the temperature distribution expected on the ASSET vehicl and indicates the environment which will be encountered by antennas as a function of their location on such a vehicle. If ablation protection is requir the antenna will be required to transmit through a "radome" whose thickne will vary with time during re-entry.

Thermal shock is a problem encountered by antenna windows. The thermal shock to be expected is of such a severe nature that beryllia - a material exhibiting good thermal shock characteristics due to its high thermal conductivity -- will probably fracture. Recent studies have shown that low thermal expansion, a unique characteristic of fused quartz, may b a necessary characteristic for extreme-thermal-shock survival.*

Figure 16 represents the thermal loads experienced by an Apollo ty re-entry vehicle. The short time of high flux input emphasizes the suitabil ablation protection for the period of time during which the re-radiation cap of metals is exceeded.

The X-15A-2 is made largely of Inconel metal, and an upper tempera limit of 1200°F is being provided through the use of ablation coatings. Thi coating (T-500) is applied in varying thicknesses up to 0.6 inches. Unprote skin temperature would approach 2000°F or higher over much of the forwar fuselage.

*OSU-RTD Symposium on Electromagnetic Windows, June 1964.

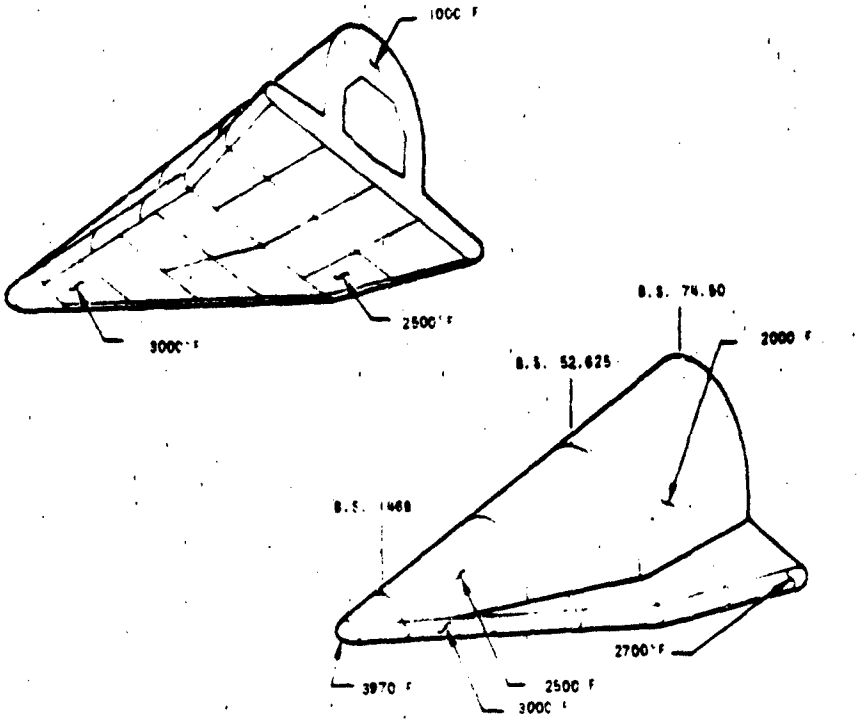

Figure 15 MAXIMUM DESIGN TEMPERATURES - ASSET

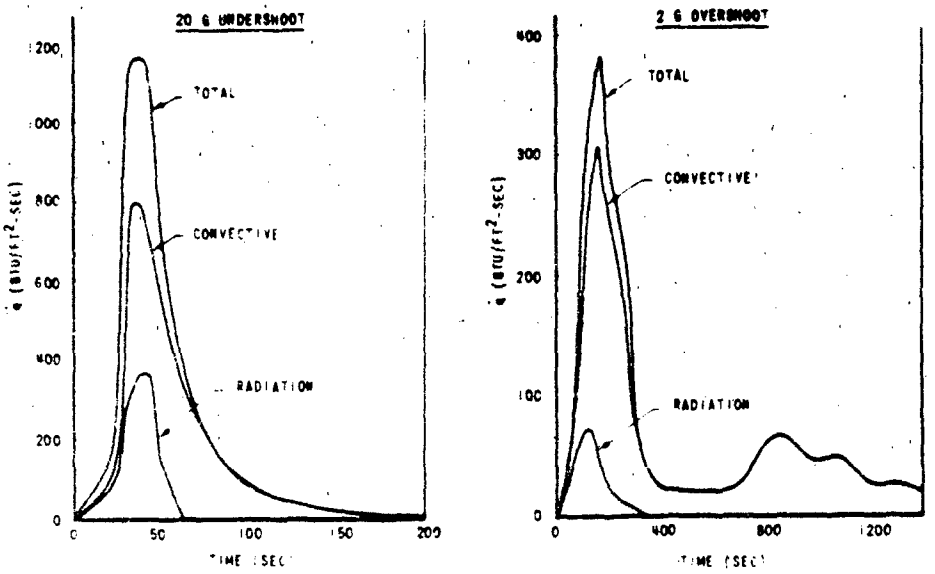

Figure 16 PEAK HEATING RATES

REFERENCES

Information contained in this report has been obtained from a large number of sources and used directly or combined with others to present relationships illustrating various characteristics of interest to this investigation. Sources from which much related data has been abstracted are:

The Current Status and 1960 Potential of Selected Defense Metals. DMIC Memorandum 183, October 1963, Battelle Memorial Institute, Columbus, Ohio

An Investigation of a New Nickel Alloy Strengthened by Dispersed Thoria. TND-1944, July 1963, National Aeronautics and Space Administration

Summary of the Seventh Meeting of the Refractory Composites Working Group. DMIC Memorandum 184, May 1963, Battelle Memorial Institute, Columbus, Ohio

Recommendations and Evaluations of Materials - Research Areas of Importance to Missile and Space Vehicle Structures. TN D-2125, October 1963, National Aeronautics and Space Administration

An Analytical Investigation of the Loads, Temperatures and Ranges Obtained during the Recovery of Rocket Boosters by Means of a Parawing. TN D-1003, February 1962, National Aeronautics and Space Administration

A Review of the Refractory Metals. LR-358, November 1962, National Aeronautics Establishment, Ottawa, Canada

Properties of Coated Refractory Metals, DMIC Report 195, January 1964, Battelle Memorial Institute

Temperature Effects on Material Characteristics. CoA Report No. 135, August 1960, The College of Aeronautics, Cranfield, England.

Thermophysical Properties of Solid Materials. Report No. 58-476. November 1960, Wright Air Development Division.

Much helpful information was also obtained from technical literature of the DuPont Company, the International Nickel Company and others.

DESIGN, EVALUATION AND PERFORMANCE OF MODERN MICROWAVE ANECHOIC CHAMBERS FOR ANTENNA MEASUREMENTS *

Elery F. Buckley
Emerson & Cuming, Inc.

Microwave anechoic chambers are currently in use for a great variety of indoor measurements on antennas, antenna systems, and associated radomes as well as for the study of the radar cross-section of a host of materials and targets. There are three distinct types of measurement performed routinely. As discussed in some detail in Reference 1, these are

1) Antenna pattern measurements
2) Radar cross-section measurements of passive or active targets
3) Antenna-impedance, antenna-coupling or antenna-RFI-compatibility measurements.

Antenna-pattern, boresight and radome work involve operation of the chamber with one-way energy propagation only. The prime requirement is that an appropriate transmitting antenna at one location within the chamber set up an essentially plane-wave field throughout another volume of the chamber of dimensions sufficient to encompass the antenna or array whose characteristics are to be measured. This volume is frequently referred to as the quiet zone, and its "quietness" or reflectivity level is evaluated by one of several methods outlined below. All of these methods involve determination of the ratio of reflected field intensity to direct transmitted field intensity at points of interest with specific antennas and antenna orientations.

Major emphasis is placed upon the functioning of anechoic chambers with one-way energy propagation as is appropriate to most antenna-pattern work. Radar-cross-section and antenna-impedance measurements require energy propagation both from and to the vicinity of the transmitting antenna. Some differences in chamber design may be involved and evaluation procedures are quite different for two-way energy propagation. No discussion of these procedures is included here but the reader is referred to References 2 and 3 for information on radar-cross-section performance and evaluation of anechoic chambers.

* This paper is an abridgment of material prepared for inclusion in the forthcoming revision of the Radome Handbook. Step-by-step details of test procedures have been omitted to make this presentation primarily a tutorial review and a summary of the state-of-the-art.

1. Design of Microwave Anechoic Chambers

The achievement of the lowest possible level of reflected energy in an anechoic chamber depends upon the proper manipulation of two variables:

- the characteristics of the absorbing materials used to cover the internal chamber surfaces
- the shaping of the chamber to direct residual reflected energy away from the quiet zone or working volume.

Hiatt, et al of the University of Michigan (Reference 4) have considered many of the important aspects of chamber design and of absorber and chamber evaluation. The reader is referred to this report as a general reference and bibliography to supplement the information given here.

Since experimentation with a large anechoic chamber is prohibitively expensive, and since several proven chamber configurations and absorber arrangements are available, the design of anechoic chambers is usually best left to experienced designers. The following discussions summarize various factors which should be considered in any design effort.

1a.) Characteristics of Absorbing Materials

Currently available premium-quality absorbing materials exhibit reflectivities of -40 to -50 db at normal incidence and also under conditions of specular reflection at equal incidence and reflection angles up to as much as 60°. This means that the energy reflected in the direction of the receiving test antenna is 40 to 50 db below that reflected in the same direction by a highly conducting flat plate, but does not mean by any stretch of the imagination that the remaining major portion of the incident energy is totally absorbed by the material. Particularly when absorbing materials are shaped in the form of pyramids or cones which are relatively large with respect to incident wavelength, there is somewhat diffuse scattering of unabsorbed incident energy in essentially all directions.

For argument's sake, we might assume that true absorption occurs for 99% of incident energy and that zero through-transmission results because of a metallic mounting surface. Therefor the remaining 1% of the energy is reflected, corresponding to a "total" power reflection coefficient of -20 db. Conceivably, scattering may be such that in any sm solid angular increment subtended by a distant test antenna,

including that increment in the specular direction, the energy reflected is 50 db below that which would be specularly reflected by a flat conducting surface. For any given application, therefor, the best "absorber" is that which reflects least in those directions of maximum interest. In a flat-wall rectangular-box antenna-pattern or boresight range the forward specular direction at areas midway between transmitter and receiver is most critical, whereas in a cross-section range, straight backscatter into the region of the transmitting antenna may be equally important for the absorbing material located in heavily illuminated areas.

In flat-wall rectangular-box chambers suitable for pattern and boresight tests, it appears to be usual practice to employ scattering absorber materials of long pyramidal or conical configuration over large areas midway between transmitter and receiver as well as behind the receiver, and frequently to use less expensive materials in other regions where the usually stronger specular reflection from these materials will not be directed into the vicinity of the receiver.

Even with physically tapered absorbing materials which are characterized by a strong tendency to scatter incident energy in many directions at the higher frequencies, there is usually a relatively strong specular component which becomes more and more predominant as frequency decreases because the taper dimensions become less in terms of wavelength and the material appears as a "smoother" reflecting surface. Shaping of the internal surfaces of the chamber then offers advantages in directing the more predominant specular-reflection component away from the working volume.

1b.) Shaping of the Anechoic Chamber

The simplest configuration of an anechoic chamber is, of course, a rectangular room with flat internal surfaces covered with absorbing material. The obvious and experimentally well established limitation of such a structure is first-bounce specular reflection of energy from areas on side walls, floor and ceiling midway between transmitting and receiving antennas. This assumes of course that the line-of-sight of the transmitting antenna is essentially parallel to these surfaces. While it may be possible for short-range work to transmit more or less diagonally in a horizontal plane to minimize side-wall effects, one is economically obliged for long-range operations to transmit approximately along the axis of an enclosure whose length is substantially greater than its width and height.

Several alternative steps can be taken to minimize the limiting first-bounce reflections of a rectangular flat-wall chamber. Operationally, antennas of minimum side-lobe lev and minimum possible beamwidth consistent with far-field ar other experimental requirements will reduce the illuminatior level of offending areas by the transmitter and the sensitivity of the receiver to reflections from the offending areas. Similar improvement is possible by making the chamber widt and height as large as possible with respect to transmission length, but economic limitations may not permit sufficient increase in these dimensions when transmission length exceeds 50 feet or so.

As mentioned above, a strongly scattering absorber ma be used on flat chamber surfaces to minimize specularly reflected energy in the frequency range where the absorber is an effectively "rough" reflecting surface. Nevertheless, the specular component continues to predominate at lower frequencies, and there appears to be a trend toward the use of very thick absorbers to keep this low-frequency region well below the range when maximum performance is required 18-inch pyramidal absorbers have been used for S- and X-ban operation. This approach is expensive and subject to rapidly diminishing returns.

After maximum advantage has been gained by the use of directive antennas and scattering absorbing materials, further reduction of chamber reflectivity (or equivalent reflectivity at reduced cost) is frequently possible by the addition of one of several varieties of baffles or by other modifications of chamber shape.

There is considerable controversy concerning the effectiveness of baffles and other modifications in the shape of anechoic chambers in improving performance, much of which arises from proprietary or patent-encouraged positions of commercial manufacturers. Independent studies by Hiatt, et al (Reference 4, page 60) and Ferris, et al (Reference 5) of the University of Michigan have concluded that appropriate baffles can improve chamber performance when dimensions are "large in terms of wavelength".

Historically, there is ample evidence of the necessity for greatly reducing the magnitude of half-way reflections from flat surfaces parallel to the direction of propagation in anechoic chambers as well as in outdoor antenna test ranges. These reflections in chambers were particularly severe in the days when the best absorbers exhibited

reflectivity of only -20 db or so and were characterized by maximum reflection in the specular direction. During this period most of the common baffle configurations were developed.

Outdoor test ranges were equipped with transverse "fences" to prevent illumination of the areas half-way between transmitter and receiver, and diffraction effects from the top edge of the fence were much more easily tolerable than the ground reflections which they replaced. The idea of the transverse fence was applied to anechoic chambers in the form of a shallow transverse absorber-covered baffle projecting normally from side-walls, floor and ceiling approximately midway between transmitting and receiving stations. The idea was soon extended to a series of transverse baffles to take care of different transmission lengths in the same chamber. Rather elaborate shaping of transverse baffles was used in an effort to entrap reflected energy and/or to insure that all but direct-ray energy to the quiet zone suffered two, three or even more reflections. (See References 6 and 7.)

The performance limitation in a chamber with many transverse baffles is imposed by edge-diffracted energy from peaks of the baffles. Such energy has a sizable forward-scattered component over which very little control can be exercised by choice of absorbing material. These considerations prompted the "aperture-type" chamber in which the basic element is a single transverse baffle in a preferably funnel-shaped chamber, the aperture in general being relatively close to the transmitting end of the chamber, with an opening sufficiently small that no direct illumination of side, floor and ceiling surfaces on the receiving side of the aperture is possible. This design was developed by Buckley at Emerson & Cuming, Inc. (See Reference 8.)

Figure 1 illustrates the evolution (from a rectangular box) of the aperture-type chamber and, more recently, the funnel- or horn-type. In Fig. 1(a), energy reflected from regions midway between transmitter and receiver appears to proceed toward the receiver from the image points shown. In addition to phase shifts occurring at the reflection points, the considerable difference in path-length to the receiver along the direct-ray path from the transmitter and along the reflected-ray paths from the images generates a pronounced interference pattern between direct and reflected rays as a function of receiver position. The path-length difference also permits substantial changes in the interference pattern with changes in frequency.

In Fig. 1(b) the aperture edges constitute the major reflection points and, since these points are closer to the direct-ray path than those in Fig. 1(a), the transmitter images approach the transmitter. The differences between direct-ray and reflected-ray path-lengths are much less in the aperture chamber and the cycles of the interference pattern are physically much longer. This effect, coupled with the reduced magnitude of reflected energy at the aperture edges, results in much more nearly uniform illumination of the chamber in the vicinity of the receiver, and therefore much lower chamber reflectivity.

The aperture-type chamber, in addition to exhibiting lower reflectivity than the rectangular-box type, can have much reduced width and height at the transmitting end, as shown in Fig. 1(b), and is therefor more economical. Aperture-type chambers have recently been reported as very successful pulsed back-scatter ranges at Cornell Aeronautical Laboratory. (See Reference 9)

As the aperture is moved closer and closer to the transmitter the dimensions of the transmitting end of the chamber can be correspondingly reduced. The funnel of Fig. 1(c) appears as the limiting case in which the aperture edges coincide with the physical extremities of the transmitting antenna, and the longitudinal chamber surfaces are defined by lines joining the transmitting-antenna extremities to a suitable limiting contour on the receiver-end wall. Under these conditions, the transmitter and its images essentially coincide and the troublesome path-length differences noted above essentially disappear. The validity of this argument becomes nebulous, of course, in the frequency range where a scattering-type absorber on the funnel generates diffuse-reflection components comparable in magnitude to specular components.

There are two clear disadvantages to the limiting funnel chamber configuration of Fig. 1(c). First, the quiet zone must be within the flaring portion of the funnel for minimum reflectivity rather than within a rectangular extension of the large end of the flared section, for example, as might be desirable for a long quiet zone. Secondly, bi-static reflectivity measurements of a target in the quiet zone are not feasible since separate transmitting and receiving antennas cannot be spaced apart as required in the throat of the funnel. Additionally, at microwave frequencies, physical alignment and fitting of the transmitting antenna in the throat of the funnel may be critical. A few funnel-type

chambers have been proposed or constructed by The B. F. Goodrich Co. Performance data and test procedures have not become generally available as of this writing.

The most widely used type of shaped anechoic chamber is the longitudinal-baffle variety designed to avoid the multiple edge-diffraction effects of many transverse baffles in a chamber where the transmission length must be variable. Ray tracing is used to determine a configuration which directs specularly reflected energy away from a central cylindrical quiet zone which extends essentially the full length of the chamber. Figure 1-2 illustrates a typical configuration. This design was developed by Buckley at Emerson & Cuming, Inc. (Reference 10). Baffles of this type are undoubtedly effective in controlling the specular component of energy reflected from side walls, floor and ceiling of a chamber throughout the frequency range where the slant surfaces of the baffles extend at least several wavelengths in the dimension normal to the line of the peak.

An investigation by Kay of TRG (See Reference 11) has compared the performance of a single transverse metallic fence with that of a metallic longitudinal baffle in reducing ground scatter on an outdoor range. The conclusion is drawn that a properly designed single transverse half-way fence is preferable to the optimum longitudinal baffle. No investigation was reported of the effects of multiple fences to accommodate different transmitter-receiver distances.

Paved longitudinal baffles are reported by Honer and Fortner of Micronetics (See Reference 12) to offer effective minimization of ground reflection effects in 600-foot and 1000-foot outdoor pulsed reflectivity ranges.

The end wall of an anechoic chamber behind the receiving antenna is usually in the form of a vertical wedge or cylinder, or at least a slanted flat surface, so that specular reflections are directed away from the receiver. A flat wall behind the transmitting antenna is adequate in general unless high-level backlobes or dipole-type patterns, for example, must be tolerated in the transmitting antenna. In the latter instances, baffling or shaping of the transmitting-end wall should be employed to avoid specular reflections directly down-range.

Reference 13 describes and illustrates several flat-wall and baffled anechoic chambers, as well as outdoor test ranges. The emphasis in this reference is on use of

these facilities as radar cross-section ranges, but many of them are obviously suitable for antenna-pattern and boresighting work.

2. Evaluation of Microwave Anechoic Chambers as Antenna-Pattern and Boresight Ranges

Many procedures for evaluating the reflectivity of anechoic chambers have been employed. These range from simple comparison of antenna patterns recorded in a chamber with those obtained for the same antenna on a proven outdoor range, to much more elaborate techniques such as described below. Hiatt, et al (Reference 4, pp. 34-41) have referenced and summarized most of these procedures. For modern low-reflectivity chambers only a few techniques appear to be satisfactorily comprehensive -- a) the "antenna-pattern comparison" procedures introduced and widely used by Emerson & Cuming, Inc., b) the "free-space VSWR" technique, championed by The B. F. Goodrich Co., and c) a thorough field probe found valuable by several laboratories, particularly at VHF and lower UHF frequencies where methods a) and b) may be difficult to use. Each of the above methods has certain features which make it attractive for specific purposes.

All the procedures to be described attempt to relate the level of reflected field intensity to direct transmitted field intensity under the conditions of interest. In all cases, the measured level of reflected energy is dependent upon the directivity of the antennas used in measuring the quantities. The purist would undoubtedly be happier with defined characteristics which apply strictly to the chamber or test range itself under illumination by a truly isotropic radiator. While such quantities can certainly be defined, their adequate measurement would likely be difficult, if not impossible, and their practical utility in predicting chamber performance with typically directive antennas would be limited. Therefore, it seems preferable to recognize at the outset that the errors in a recorded antenna pattern, for example, due to reflected energy, depend not only upon the distribution of illuminating energy (i.e., upon the directivity of the transmitting antenna), but upon the reflected energy accepted by the receiver (i.e., upon the directivity of the receiving antenna).

The methods described here are applicable equally to evaluation of the performance of any antenna pattern range, whether it be an open range, outdoors, or a fully enclosed microwave anechoic chamber.

Evaluation of the performance of a microwave anechoic chamber where the magnitude of the reflected field within the design quiet zone is required to be below that of the direct field by a specific number of

decibels, frequently 50 db or more in today's designs, requires precise measurement of extremely minute variations in total received-signal strength, corresponding to in-phase and out-of-phase addition of direct-ray and reflected-field components. For example, a 0.055-db total excursion in the peak value of the main lobe of a probe-antenna pattern indicates -50 db quiet-zone reflectivity.

The accurate detection and read-out of such a small change in peak response cannot be accomplished without relatively elaborate precision circuitry. Therefore, most chamber-evaluation procedures depend on various "off-peak" detection methods in which the probe antenna is oriented so that its response to "direct-ray" is greatly reduced and the minute effects of reflected energy are observed as now relatively much larger variations. For example, if the main lobe of the probe antenna is aimed so that the direct ray causes a response 20 db below the peak value, the maximum excursion corresponding to quiet-zone reflectivity of -50 db is now 0.55 db and is clearly observable with standard pattern-recording instruments.

2a.) The Pattern-Comparison Evaluation Method

The pattern-comparison technique is one of the most widely accepted and versatile of the several "off-peak" techniques which have been used for evaluating the quiet-zone reflectivity of a microwave anechoic chamber. The recording of a series of antenna patterns has the distinct advantage that it provides an antenna engineer with an intuitive "feel" for the quality of his range by displaying the very small pattern perturbations that can result from even extremely low-level residual reflections.

The details of the technique are specifically as follows. The chamber is illuminated by a transmitting antenna located and oriented in the manner for which the chamber was designed. Usually the design calls for this antenna to be aimed approximately along the major axis of the chamber from a point at or near one end. For evaluation purposes the receiving antenna is mounted upon an azimuth and/or elevation rotator within the design quiet zone and in a transverse vertical plane at a typical distance from the transmitting antenna. Sets of patterns are then recorded at closely adjacent test points along various radii of the quiet zone. One pattern of each set, usually the one recorded with the receiving antenna on the axis of the chamber, is chosen as a reference. The remaining patterns of that set are superimposed upon this reference one by one, with the peaks of the main lobes coinciding (see Figure 2 for representative patterns), and the deviations of each pattern

from the reference are tabulated at the -10, -15, -20, -25 and -30 db levels on each side of the reference.

The deviations at each reference-pattern level are then plotted versus the radial distance between the chamber axis and the test point, as in Figure 4, and the cyclic variation of the deviation with distance from the axis displays the constructive and destructive interference between the direct-ray electric vector from the transmitter and the resultant electric vector arising from energy reflections to which the test antenna is sensitive. If, for example, it is found that at the angle corresponding to -25 db on one side of the reference pattern, the peak-to-peak magnitude of one cycle of the deviation curve is 0.6 db, it is readily shown that the resultant reflected energy level is -55 db in the region of the test points corresponding to that cycle. The graphs of Figure 3 plot on the ordinate scale the quantity

$$20 \log_{10} \left[\frac{x + y}{x - y} \right] \qquad (1)$$

which represents the peak-to-peak variation in decibels of the total electric-field magnitude resulting from interference between the direct-ray electric vector x (abscissa scale) and the reflected electric vector y (parameter of family of curves) over the decibel ranges of x and y commonly encountered in this evaluation procedure.* In the numerical example immediately above, Figure 3 may be entered at 0.6 db ordinate and -25 db abscissa to read out -55 db reflectivity.

Each cycle of each deviation curve of Figure 4 along each traverse line yields a value of reflectivity for the corresponding region of the quiet zone. The several reflected-energy values along the various radial traverse lines are usually averaged, or otherwise statistically analyzed, to yield a number or numbers to characterize the performance of the chamber. An example is given at the lower right of Figure 4.

* While the curves of Figure 3 are plotted as straight lines, they are actually very slightly concave upward. They may be extrapolated as straight lines to the left and downward as far as may be desired, but should not be extended upward and to the right without additional calculations. For example, the curve for -20 db reflectivity should intersect the -15 db abscissa at 11.05 db, and all other curves should be parallel to this one. All lines are correct as plotted at the 5.7-db ordinate value.

The transverse vertical plane containing the many points at which patterns are recorded is preferably that plane located at the maximum design distance from the nominal transmitting-antenna position. The test then reveals the minimum performance of the chamber, since quiet-zone performance, under all usual test conditions, improves as the transmitting and receiving antennas are brought closer together.

A very substantial collection of experimental data of this type shows that one horizontal and one vertical radial traverse of the quiet zone with one polarization, and with either azimuth or elevation patterns, is sufficient to characterize initially the performance of an anechoic chamber at any frequency of interest.

At frequencies of 200 Mc or so, or whenever chamber cross-sectional dimensions are comparable to wavelength, even as much as one half-cycle of the deviation curves of Figure 4 may not exist within the design quiet zone, and the Field Probe Evaluation Method described below may be a more appropriate test procedure.

2b.) The Free-Space VSWR Evaluation Method

Since there does not appear to be any readily available reference which describes this technique in detail, the following excerpts from Hiatt, et al (Reference 4, pp. 38-40) must serve as a summary.

". . . . . Transmitting and receiving horns are set up as they would be for an antenna pattern test . . . . . Room reflectivity data is obtained as a function of the aspect ϕ of the receiving horn, with ϕ varied in discreet steps (for example, 10°) from $\phi = 0°$ (looking at the transmitter) to $\phi = 180°$. At each aspect, the horn is moved back and forth along its axis to produce a change in the received signal from a maximum to a minimum. It is assumed that this results from the in-and out-of-phase addition of the direct signal E_1 and the reflected signal E_2, the ratio of which can be obtained from the maximum to minimum ratio R using equation 2.

$$E_2 = E_1 \left[\frac{R - 1}{R + 1} \right] \qquad (2)$$

The value used for E_1 depends on the orientation of the horn, and is found from the average signal received as the horn is moved along its axis by normalizing this relative to the peak value observed when $\phi = 0°$."

" . . . . . (this) B. F. Goodrich method provides the ratio for one antenna location as a function of the receiver orientation . . . . . The measurement would be repeated for the desired number of locations within the quiet zone to give a complete picture of the room performance."

2c.) The Field Probe Evaluation Method

Neither the pattern-comparison procedure nor the free-space VSWR technique, as described above, extract detailed information about the uniformity of the total illuminating field over wide areas. For strictly pattern work, when the shape of an antenna pattern is the characteristic under study, relatively large variations in illumination level within the quiet zone are tolerable if the antenna aperture is small with respect to the dimensions of the quiet zone. Under such circumstances, the pattern-comparison procedure is highly instructive since it gives range performance in terms of small changes in pattern shape.

Where accurate measurements of antenna gain must be made, and when the aperture of the gain standard antenna is significantly different in shape or size from the aperture of the antenna under test, uniformity of illuminating field is of greater importance than in the above application. If it can be assumed that transmitter power and receiver sensitivity remain constant, then the variations of the on-peak or zero-aspect response of the test antenna observed as a function of antenna position in either the pattern-comparison or free-space VSWR technique constitute a partial map of the illuminating-field magnitude. A survey much more nearly complete than provided by the above techniques may be required when field-intensity variations throughout a sizable volume must be known.

Probing and mapping of illuminating field intensity can be automated by driving a probe receiving antenna along a straight-line path by means of a lead screw or other device while a strip-chart recorder plots antenna response versus antenna position. Care must be taken to prevent interfering reflections from moving parts. Off-peak orientation of the probe antenna can be used both to relax the required precision of recording and to obtain additional information about chamber performance.

When variations of field intensity of less than about 0.1 db are to be measured accurately, ordinarily available equipment stability is insufficient, and instrumentation

becomes more elaborate. From Figure 3, 0.1 db peak-to-peak perturbation of on-peak (x = 0) level corresponds to reflectivity of -45 db. Buckley (Reference 14) has described a null-balance technique for point-to-point measurement of field intensity variations down to 0.01 db. A two-channel comparison system uses

a) a moving receiving antenna, oriented for maximum output, to probe the field as required,
b) a stationary pick-up antenna or other means of sampling transmitter output to provide a reference energy level, and
c) an accurate amplitude-sensitive null detector capable of measuring minute differences between the response of the moving antenna and the reference signal (e.g. Weinschel Dual Channel Insertion Loss Test Set).

In any case, curves of the response of the receiving antenna versus its transverse off-center position show cyclic variations very similar to the deviation curves of Figure 4, and chamber reflectivity may be derived as in the pattern-comparison procedure by entering Figure 3 at the appropriate pattern level x with the values of db spread measured from the curves.

If the volume explored by the probe antenna is very large or three-dimensional, inverse-square corrections for the varying distance between transmitter and probe must be included unless they are very much smaller than the observed variations of probe output.

2d.) Comparison of Evaluation Methods and their Applicability to Boresight Ranges

The field probe evaluation technique is by far the most rigorous of the test procedures described above. It is required for a typical pattern range only when detailed information about field uniformity is needed for ensuring accuracy of absolute gain measurements. One of the other procedures is entirely adequate in almost all cases where accuracy of pattern shape is the antenna characteristic of major interest. Nevertheless, when the field-probe method is automated to the extent that curves similar to those of Figure 4 can be recorded directly without the necessity of recording and comparing patterns, this appears to be a relatively rapid test procedure.

The reflectivity levels measured by the methods described can be related to accuracy of boresight measurements when detailed knowledge of the patterns of antennas to be tested is at hand. Figure 3 permits readout of the peak-to-peak variation at any pattern level due to measured reflectivity, and the corresponding angular variations are evident immediately from the known pattern. When using the pattern-comparison procedure for evaluation of a boresight range it may be sufficient to compare patterns, for example, near the level corresponding to pattern cross-over in a monopulse system in order to obtain a direct indication of the angular resolution permitted by range reflections.

The VSWR evaluation method should also be capable of indicating boresight resolution directly when the antenna to be boresighted is used as the probe and is oriented at the cross-over angle, for example. Motion of the antenna in a direction at right angles to the transmitter line-of-sight is equally as important as motion along the probe axis.

When a beam-seeker or null-seeker such as the Carco Electronics or California Technical Industries boresight-error measuring system is employed, a field probe in the transverse plane by an antenna oriented for peak response on axis should yield data which is easily interpreted in terms of angular resolution.

3. Performance of Microwave Anechoic Chambers as Antenna-Pattern and Boresight Ranges

The measured performance of several anechoic chambers which were designed specifically as antenna pattern and boresighting ranges is summarized below.

Eccosorb Anechoic Chamber No. 225, of the aperture type, is located at Warner Robins Air Force Base, Georgia. Chamber dimensions are approximately 31 feet wide, 25 feet high and 102 feet long. An elliptical aperture of maximum width 12 feet and maximum height of 8 feet is centered in a transverse wall about 32 feet from the transmitting antennas. The chamber was evaluated at 13.5 Gc by the null-balance technique of probing the field in the vicinity of the receiving antennas. In this case the probe antenna was one of the 22-db pyramidal horns which are used in the California Technical Industries Beam Seeker installed as part of the boresight test facility. The probe was traversed $\pm$ 35 inches horizontally with respect to chamber axis, and $\pm$ 21 inches vertically, in a plane normal to the chamber axis at a distance of

1160 inches from the location of the transmitting antennas being boresighted. Average reflectivity varied from -52 db to -55 db depending upon the beamwidth of the parabolic orange-peel antennas under test. These reflectivity levels correspond to peak-to-peak variations of 0.03 to 0.045 db in the illuminating field strength.

Eccosorb Anechoic Chamber No. 250 is a longitudinally baffled chamber installed at Canadian Westinghouse Company, Ltd., Hamilton, Canada, for boresight testing of X-band monopulse antenna systems. This chamber, of dimensions approximately 30' x 30' x 98', was evaluated by both the null-balance and pattern-comparison methods at 9.375 Gc with a separation of 900 to 1000 inches between transmitting and receiving antennas. A 20-db-gain transmitting antenna was used in both tests. In the field-probe test, 6-foot-long traverses of a 15-db probe antenna were executed along horizontal, vertical and 45° diameters of the quiet zone at the receiving end, and the measured average reflectivity was -41 db corresponding to an average peak-to-peak variation of approximately 0.16 db in illuminating field strength. In the pattern-comparison tests, patterns of a 20-db receiving horn antenna were recorded at 1-inch increments along vertical and horizontal radii of the 6-foot diameter quiet zone, and average reflectivity of -54 db was computed. The difference between this value of -54 db and the value of -41 db indicated by the field-probe technique is due to two factors:

a) Directivity of the receiving antenna was 5 db greater in the pattern-comparison test, and
b) Normalization of pattern peaks was used in the pattern-comparison data reduction, so that computed reflectivity is based upon the shape only of the recorded patterns rather than upon small variations in peak-of-pattern level.

A chamber installed at N. V. Hollandse Signaalapparaten in The Netherlands is essentially identical with the Canadian Westinghouse facility and was evaluated by a slightly modified pattern-comparison procedure. The measured reflectivity of -53 db compares very favorably with -54 db in the Canadian chamber.

Eccosorb Anechoic Chamber No. 423 is a smaller longitudinally baffled anechoic chamber (16' x 16' x 28') in use at Motorola Inc., Scottsdale, Arizona for production boresight testing of small missile seeker antennas. Evaluation of this chamber was by the pattern-comparison procedure at 9 Gc using vertically polarized 20 db horn transmitter and receiver at a separation of approximately 20 feet. The patterns recorded at 1-inch increments along 36-inch horizontal and 18-inch vertical traverses showed no deviations within $\pm$ 72° which were sufficient to indicate reflectivity greater

than -65 db. Similar tests using as receiver the circularly polarized Motorola antenna to be boresighted showed no detectable deviation at any pattern level down to 30 db below peak. At the critical -3 db pattern points on this antenna, reflectivity of -65 db corresponds to a peak-to-peak perturbation of 0.013 db and to an angular resolution of $\pm$ 0.01 degree.

4. References

1. Buckley, E. F., "Outline of Evaluation Procedures for Microwave Anechoic Chambers", Microwave Journal, August 1963, pp. 69-75.

2. "Evaluation of Radar-Cross-Section Ranges for Continuous-Wave Operation", Emerson & Cuming, Inc., March 1964.

3. Emerson, W H. and Browneil, F. P., "State-of-the-Art Anechoic Backscatter Ranges", M. I. T. Lincoln Laboratory Radar Reflectivity Measurements Symposium, June 1964, Advance Record published as Rome Air Development Center Technical Documentary Report No. RADC-TDR-64-25, Vol. 1, April 1964, pp. 50-65.

4. Hiatt, R. E., Knott, E. F., Senior, T. B. A., "A Study of VHF Absorbers and Anechoic Rooms", The University of Michigan Report No. 5391-1-F, February 1963.

5. Ferris, J. E., Hiatt, R. E., Senior, T. B. A., and Shamp, D. J. "On the Design of a NASA-MSC Antenna Facility", The University of Michigan Report No. 05921-1-F, August 1963, pp. 68-69.

6. Ibly, Frank J., "Anechoic Chamber-Design, Construction and Test of Model, Using Light Beams to Simulate Microwave Energy", Lockheed Aircraft Corporation, Missile Systems Division, Palo Alto, California, Report MSD 2112, 15 March 1957.

7. Smith, Chester L. and Gargaro, Dolores T., "Design of Two Anechoic Chambers", Raytheon Manufacturing Company, Missile Systems Division, Bedford, Massachusetts, Proc. OSU-WADC Symp. Vol. 1, WADC-TR-58-272 (June 1958)

8. U. S. Patent No. 3,113,271, E. F. Buckley, Emerson & Cuming, Inc., Canton, Massachusetts.

9. Wohlers, R. J., "Indoor Range Design", Rome Air Development Center Technical Documentary Report No. RADC-TDR-64-25, Vol. 1, April 1964, pp. 257-286.

10. U.S. Patent No. 3,120,641, E. F. Buckley, Emerson & Cuming, Inc., Canton, Massachusetts.

11. Kay, A. F., "A Comparison between Longitudinal Baffling and Transverse Fence for Reducing Range Ground Scattering". Rome Air Development Center Technical Documentary Report No. RADC-TDR-64-25, Vol. 1, pp. 110-126.

12. Homer, R. E., and Fortner, W. D., "Outdoor Pulsed Radar Reflectivity Range", Rome Air Development Center Technical Documentary Report No. RADC-TDR-64-25, Vol. 2, pp. 274-285.

13. Radar Reflectivity Measurements Symposium, Rome Air Development Center Technical Documentary Report No. RADC-TDR-64-25, Vol. 2, Section VII, Range Descriptions, pp. 197-372.

14. Buckley, E. F., "The Design and Evaluation of Microwave Anechoic Chambers", Paper presented at Joint Meeting of IRE-PGME, PGMTT and PGAP, Chicago, Illinois, April 8, 1960, pp. 14-16 (Paper available from Emerson & Cuming, Inc., Canton, Massachusetts).

September 1, 1964

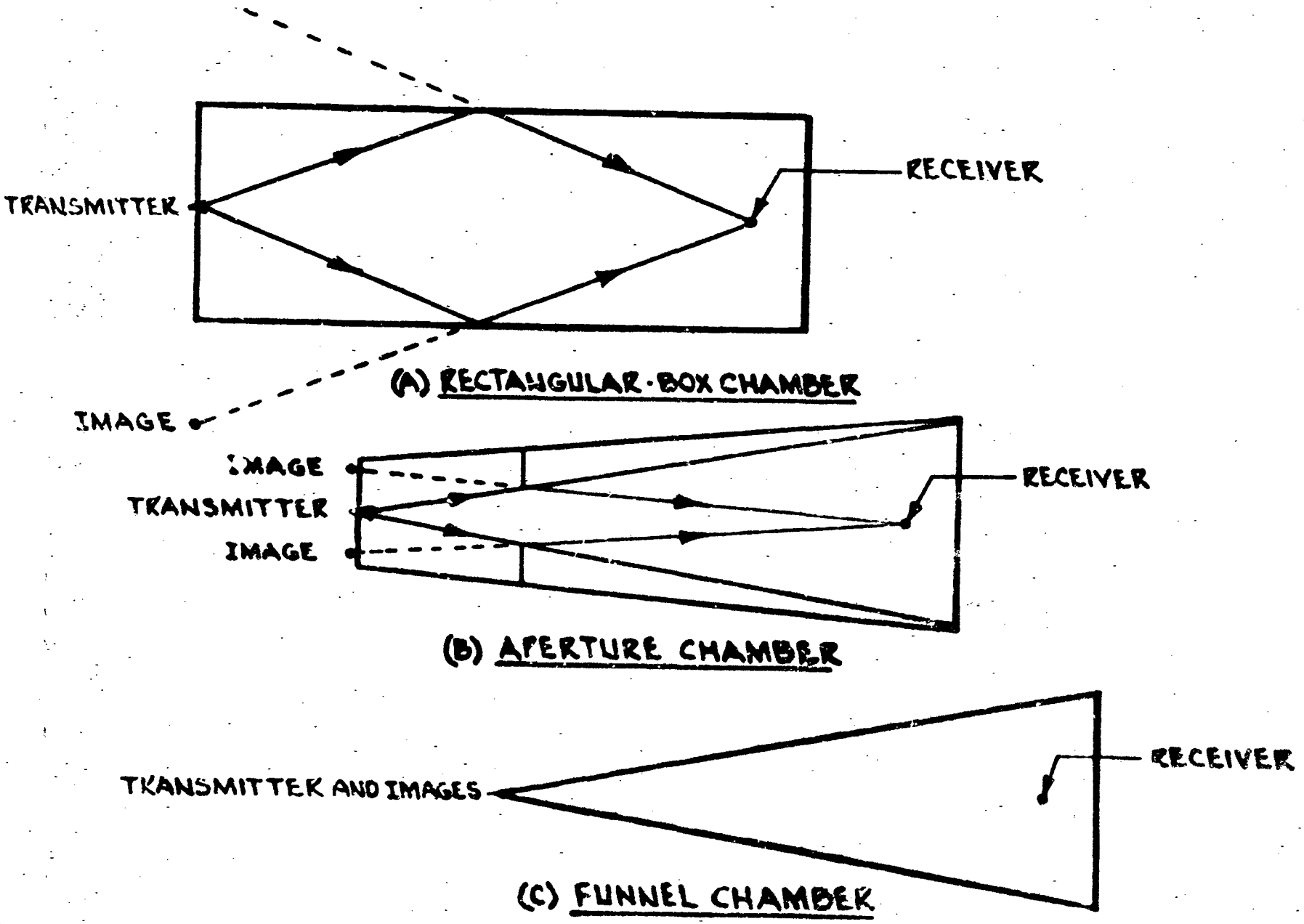

FIGURE-1 EVOLUTION OF APERTURE AND FUNNEL ANECHOIC CHAMBERS

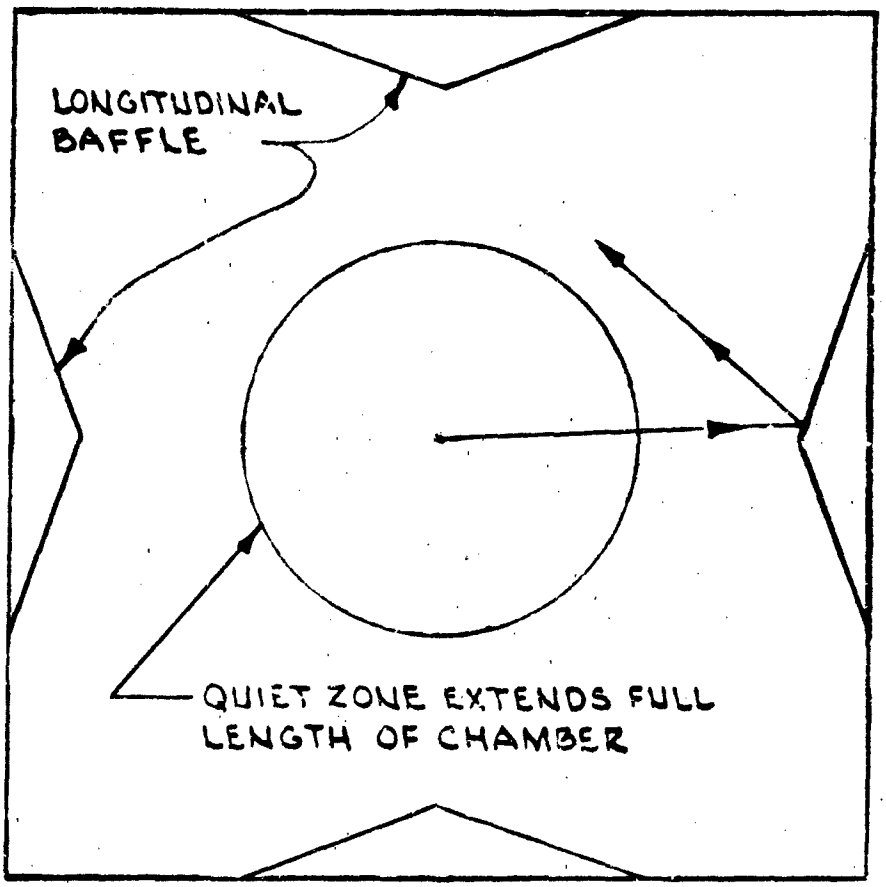

FIGURE 1·2

VERTICAL TRANSVERSE SECTION THROUGH TYPICAL LONGITUDINAL BAFFLE CHAMBER CONFIGURATION

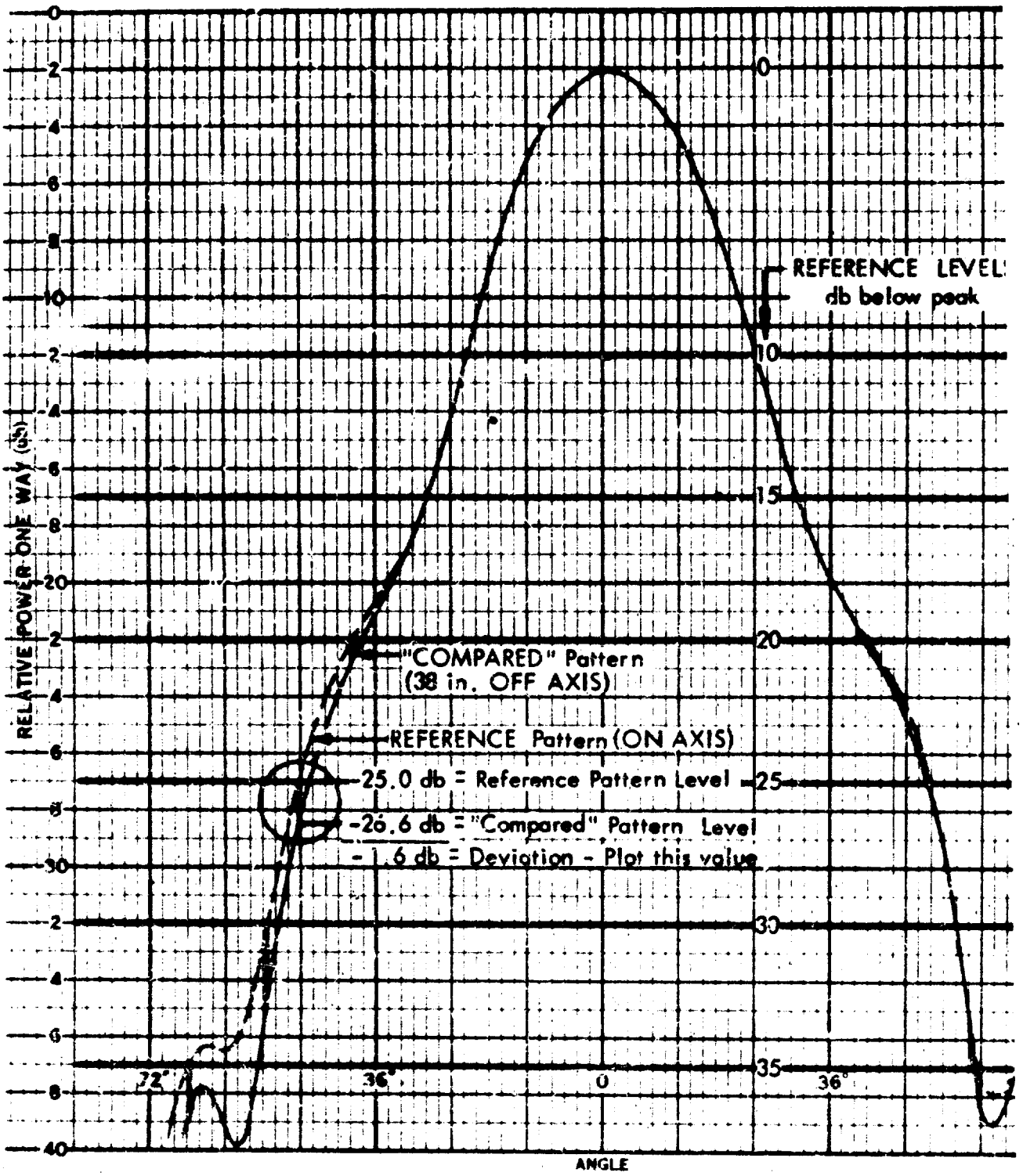

Figure 2

Method of
COMPARING PATTERN

Pattern - Comparison Evaluation
ECCOSORB® ANECHOIC CHAMBER No. 385
Fort Monmouth, New Jersey
December, 1962

2.6 Cc, 20 db Horns
Vertical Polarization
65 ft. Transmission Distan
Azimuth Patterns
Traverse: Lower Vertical
Radius of Quiet Zon

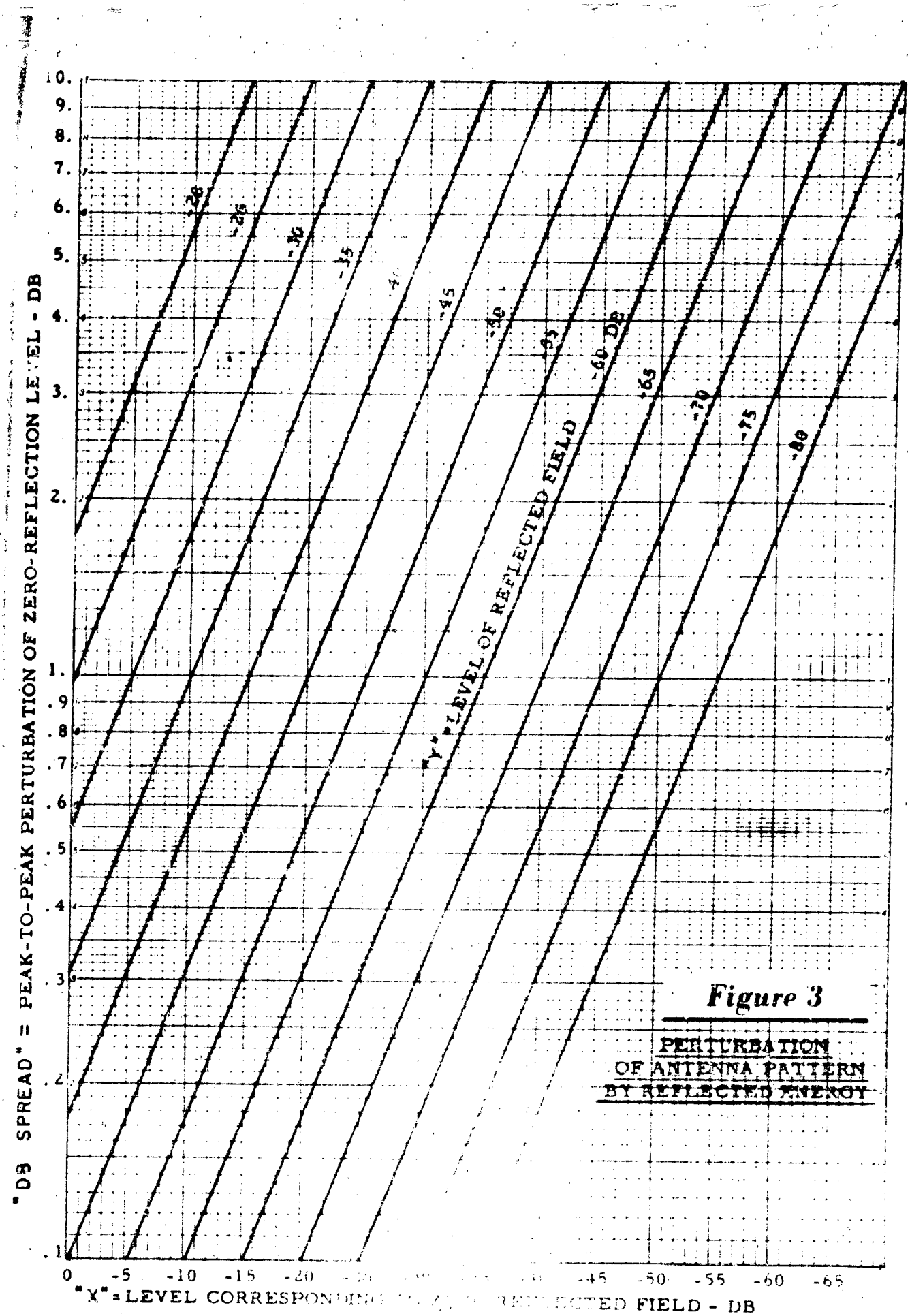

Figure 3

PERTURBATION OF ANTENNA PATTERN BY REFLECTED ENERGY

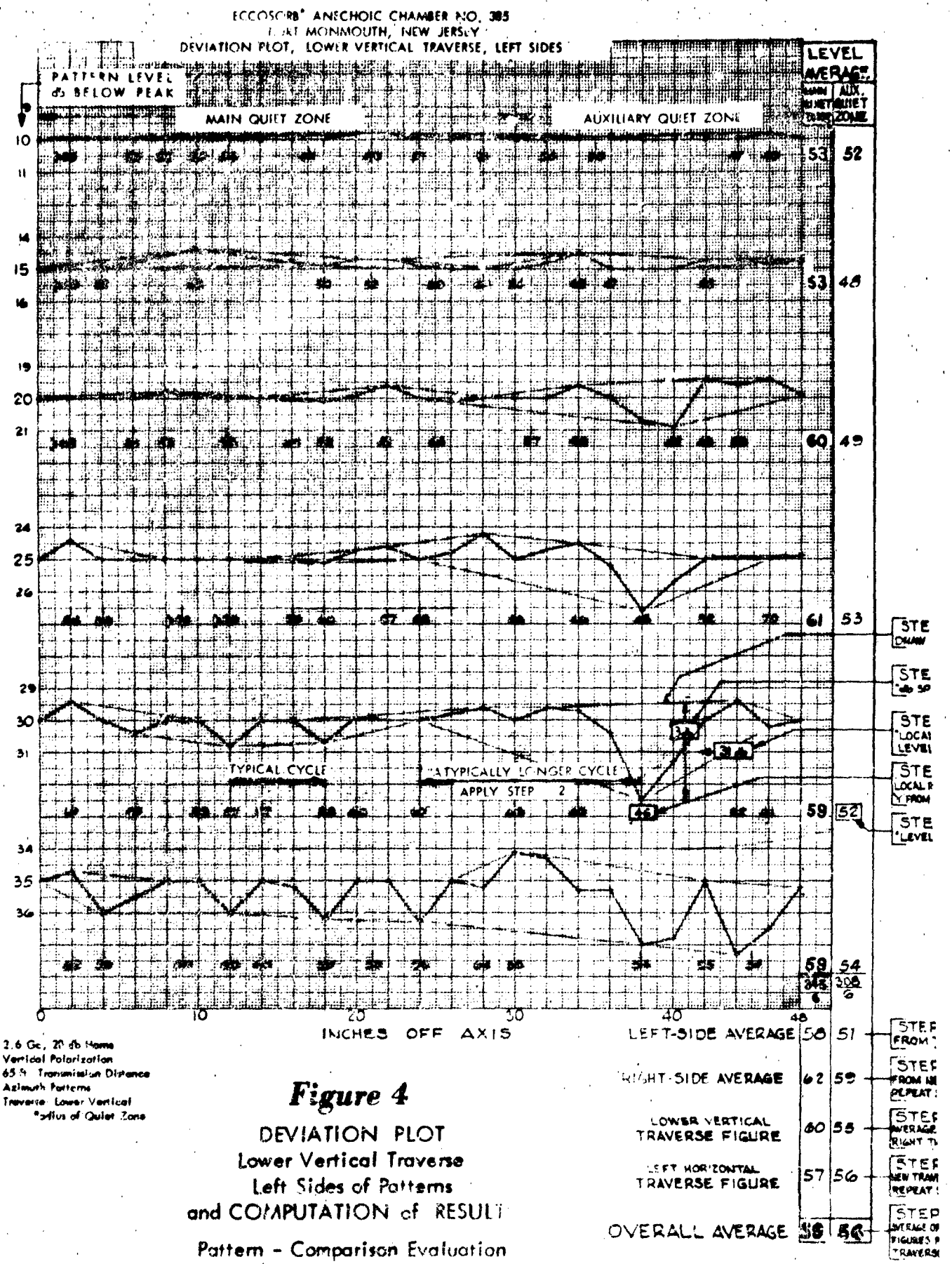

Figure 4

DEVIATION PLOT
Lower Vertical Traverse
Left Sides of Patterns
and COMPUTATION of RESULT

Pattern - Comparison Evaluation
ECCOSORB® ANECHOIC CHAMBER No. 385
Fort Monmouth, New Jersey
December, 1962

R.F. CORONA ON TITANIUM SURFACES AT ELEVATED TEMPERATURE

by Paul F. Stang

Presented at the Fourteenth Annual Symposium
on USAF Antenna Research
and Development
University of Illinois
6-7-8 October 1964

Lockheed-California Company
A Division of Lockheed Aircraft Corporation
Burbank, California

Summary:

Lack of information in published literature concerning the effect of elevated temperature at low air pressure on corona and breakdown, particularly for titanium surfaces, prompted a research study by Lockheed-California Company. The studies were conducted in view of increasing speeds and penetration into the upper atmosphere by supersonic air vehicles which use titanium as structural metal. The skin temperature of a high speed airborne vehicle rises with increasing velocity due to air friction. Titanium when heated to temperature above 400°F temperature, shows a decreasing voltage potential for corona discharge as the surface temperature of titanium increases the evaporation of electrons commonly called thermionic emission depends on the metal used and applied temperature, and titanium turns out to be a good emitter. Electrons within the metal surface will be freed by thermal energy with increasing probability that the electrons escape from the metal surface. The effectiveness of electron emission from titanium is studied and its results on the occurrence of H.F. corona discharges is presented in graphs and color slides. An 8" diameter, circular titanium heated surface was used for the investigations. The tests were conducted at low air pressures to simulate operational altitudes between 50,000 and 200,000 feet. The applied R.F. frequency was 2 Mc, and electrode separations up to 10 inches were studied.

Introduction:

This paper presents experimental results on corona or glow discharges at low air pressure corresponding to altitudes from 50,000 feet to 200,000 feet in the H.F. range at 2.0 Mc. Investigations of corona or glow discharges were made as a function of temperature. These tests were conducted to investigate particularly titanium as structural metal at temperatures up to 700°F

of the MC range. The results obtained indicate that at higher temperature a lower voltage potential applied initiates the corona process. At ambient or room temperature approximately a 20 percent higher voltage potential is necessary to obtain the same effect to start corona or glow discharge.

No references were found in current literature treating the subject. The influence of elevated temperature on titanium at low air pressures corresponding to the upper atmosphere with R.F. corona phenomena at high frequency (2 Mc) shows an analogue to the vacuum tube. A tube is evacuated to an air pressure of 1 micron. The cathode is an emitter like tungsten or oxides, not unlike titanium which, when heated, shows the characteristic discoloration of a heat cycle and is coated with a thin layer of titanium oxide. The applied plate voltage makes the emitted free electrons move rapidly to the anode. The electrode configuration of a capacitive type antenna at R.F. frequency is an analogue. However, the electron being negative ions oscillate with the applied frequency.

Experimental Procedure:

The experimental set up used for the test is shown in Fig. 1. The R.F. power source was a surplus Navy TDE 2 transmitter. An autotransformer was designed and built to boost the R.F. output voltage to a maximum of 13000 volt at 2 Mc. The Pyrex glass discharge chamber is 12.0 inches in diameter and 36.0 inches in length and mounted vertically. An 8.0" diameter circular titanium structure was built and a heater element inserted. This structure was located inside the Pyrex glass chamber. The circuit used is schematically shown in Fig. No. 2. By regulating the applied 60 cycle a-c voltage on the heater element with a variac the temperature on the titanium surface was controlled and calibrated as function of heating time and applied voltage potential - see Fig. No. 3. To prevent heat radiation to the Pyrex glass chamber an asbestos collar was built around the circular titanium structure. The tests were made in steps of 100°F up to 700°F. The measurements were conducted with the following electrode configurations.

1.) 1.0" sphere to 8" dia. circular titanium plate
3.0" cylindrical stub to 8" dia. circular titanium plate
1.0" cylindrical stub to 8" dia. circular titanium plate
0.5" cylindrical stub to 8" dia. circular titanium plate

The electrodes were mounted on the vertical axis of the cylindrical test chamber with the lower heated electrode grounded. The tests were conducted with spark gaps of 5.0 and 10.0 inches distance, and simulated altitudes from 50,000 feet to 200,000 feet.

Evaporation of Electrons from Metal:

The phenomenon of evaporation of electrons, commonly called thermionic emission depends on the metal used and its temperature. At ambient temperature few electrons are able to leave the metal surface, but electrons within the metal will be freed by heat, which imparts to the electrons the energy to move out of the metal surface. To determine the amount of electrons which escape from the surface per unit in one second, we must know the velocity distribution and density of the electrons inside the metal at various temperatures, and the

difference in potential energy between an electron at rest inside and outside the metal. The work that must be done to take an electron at rest within the metal and transport it across the surface to a distance at which the surface force is negligible is called work function. The work function depends on the metal used, and is measured in electron Volts (eV) necessary to remove a unit charge from the surface. It is known from the literature [1] that electropositive metals have small work functions and, therefore, emit much larger electron currents at a given temperature than electronegative metals. Titanium belongs to the electropositive metals,[2] and it can be expected that titanium acts as a good emitter. Work function of the elements is plotted in graph No. 4. The work function of titanium is 4.09 eV[3], tungsten has 4.52 eV, and thorium 3.41 eV. The work function of titanium is approximately between tungsten and thorium. Thorium and tungsten are good emitters and are used for filaments in vacuum tubes.

Experimental Results:

Measurements are made with the 1.0" diameter sphere to 8" diameter circular heated titanium plate for gap distances of 5, and 10 inches. Results of these tests are plotted in Fig. No. 5 and No. 6.

It is apparent that temperature has a strong influence on the corona or glow discharges process in the lower altitude region but ceases to be a significant factor above 100,000 feet. This effect indicates that at altitudes above 100,000 feet or so, free ions resulting from collision alone are in sufficient numbers to initiate the breakdown process because of the longer mean free paths of electrons. At lower altitudes below 100,000 feet, the mean free paths of the electrons becomes shorter and at higher temperature thermal ionization is more effective. Other measurements were made with

(Aluminum) 3.0" cylindrical stub to 8.0" die heated titanium plate
(Brass) 1.0" cylindrical stub to 8.0" die heated titanium plate
(Brass) 0.5" cylindrical stub to 8.0" die heated titanium plate

The results are plotted in Fig. No. 7
8
9
10
11
12

1) Gaseous Conductors by Cobine, page 111
2) Handbook of Physics by Smekal (printed in German)
3) Reference Data for Radio Engineers

Conclusion:

It can be seen that in all the tested electrode configuration the influenc of temperature is more pronounced at lower altitudes. The thermionic emission of electrons on titanium surfaces or its oxides is, therefore, another factor which must be observed in design and development of H.F. antennas for the high temperature airframe when titanium is its structural metal.

Block Diagram of Test Set up

Fig. No. 1

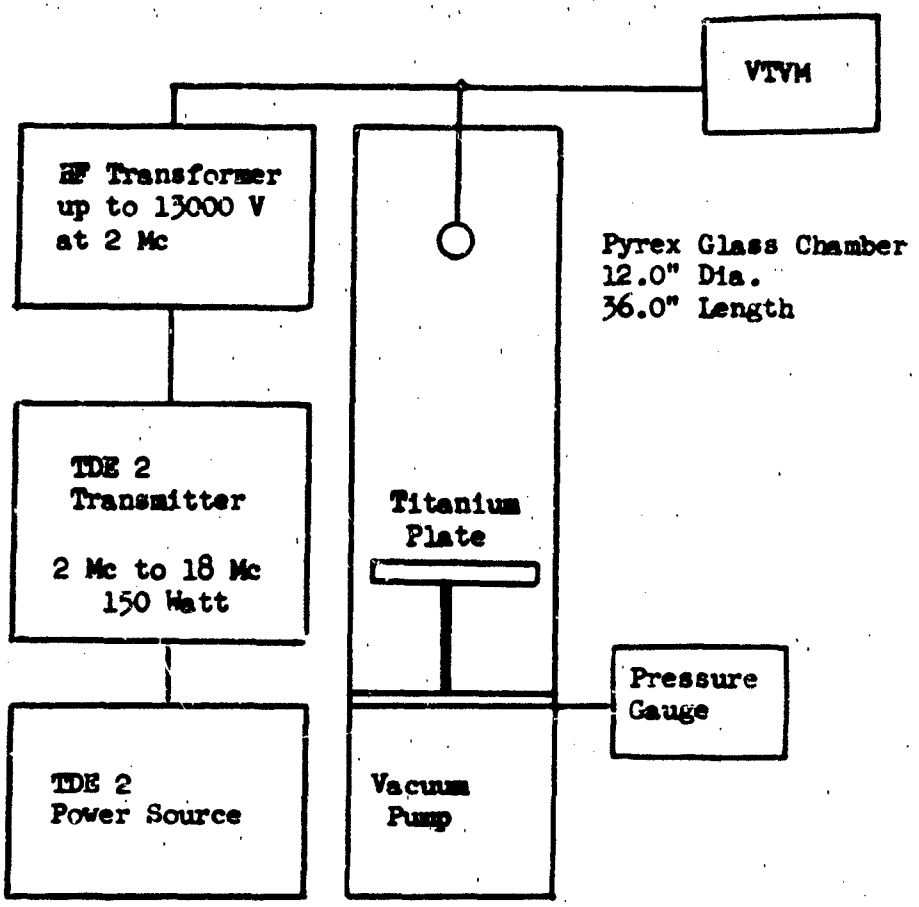

Fig. No. 2

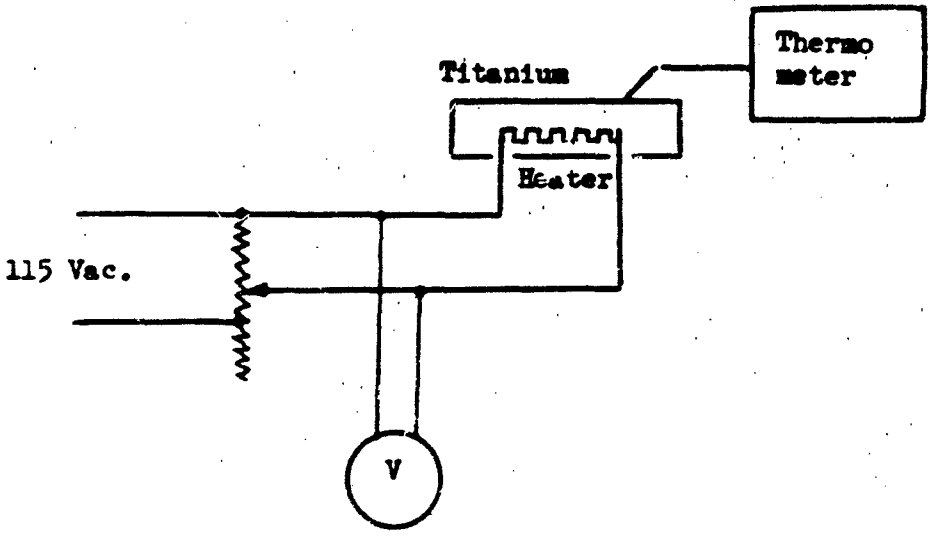

Fig. No. 3

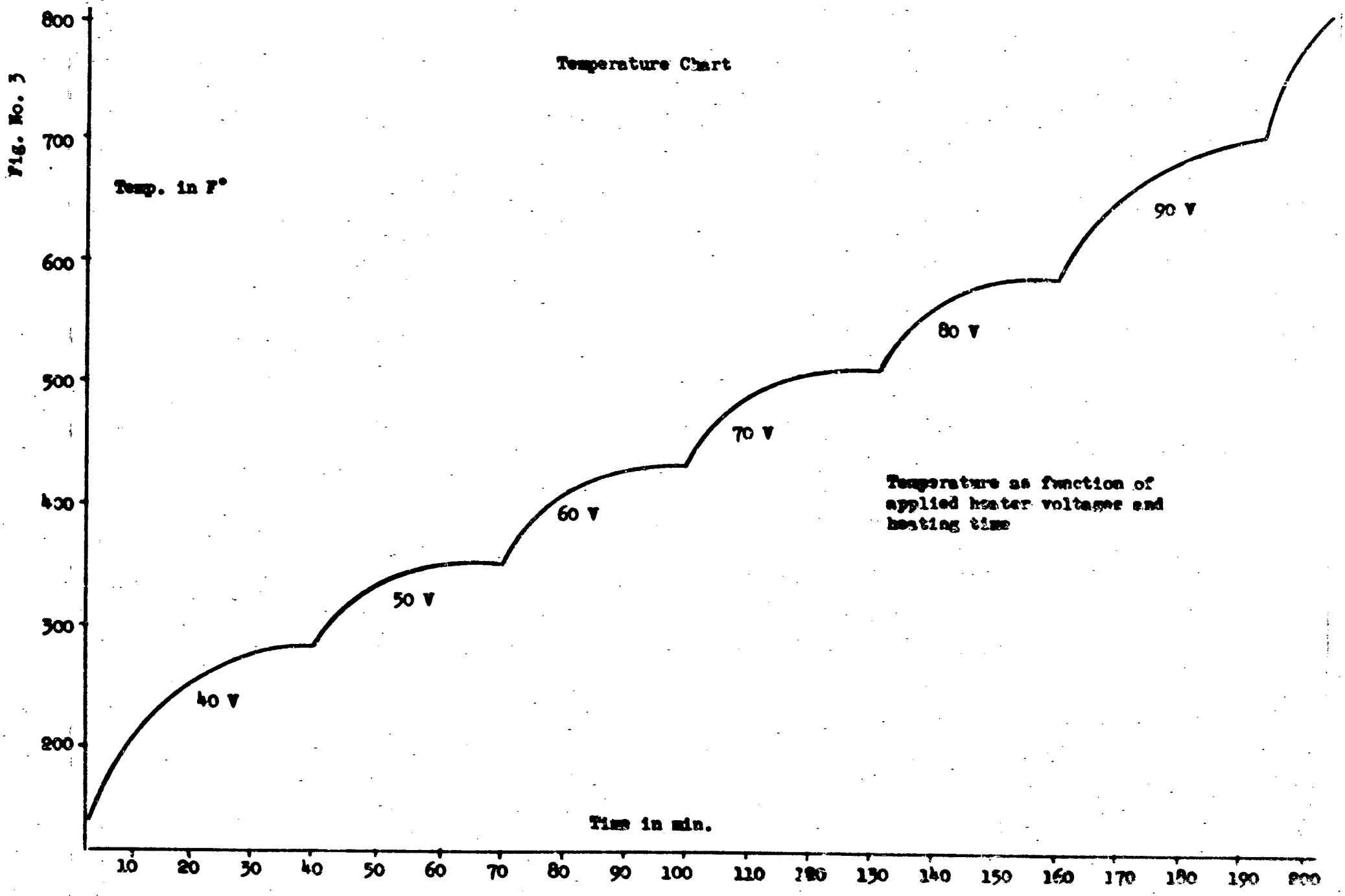
Temperature Chart
Temp. in F°
800
700
600
500
400
300
200
40 V
50 V
60 V
70 V
80 V
90 V
Temperature as function of applied heater voltages and heating time
Time in min.
10 20 30 40 50 60 70 80 90 100 110 120 130 140 150 160 170 180 190 200

Fig. No. 4

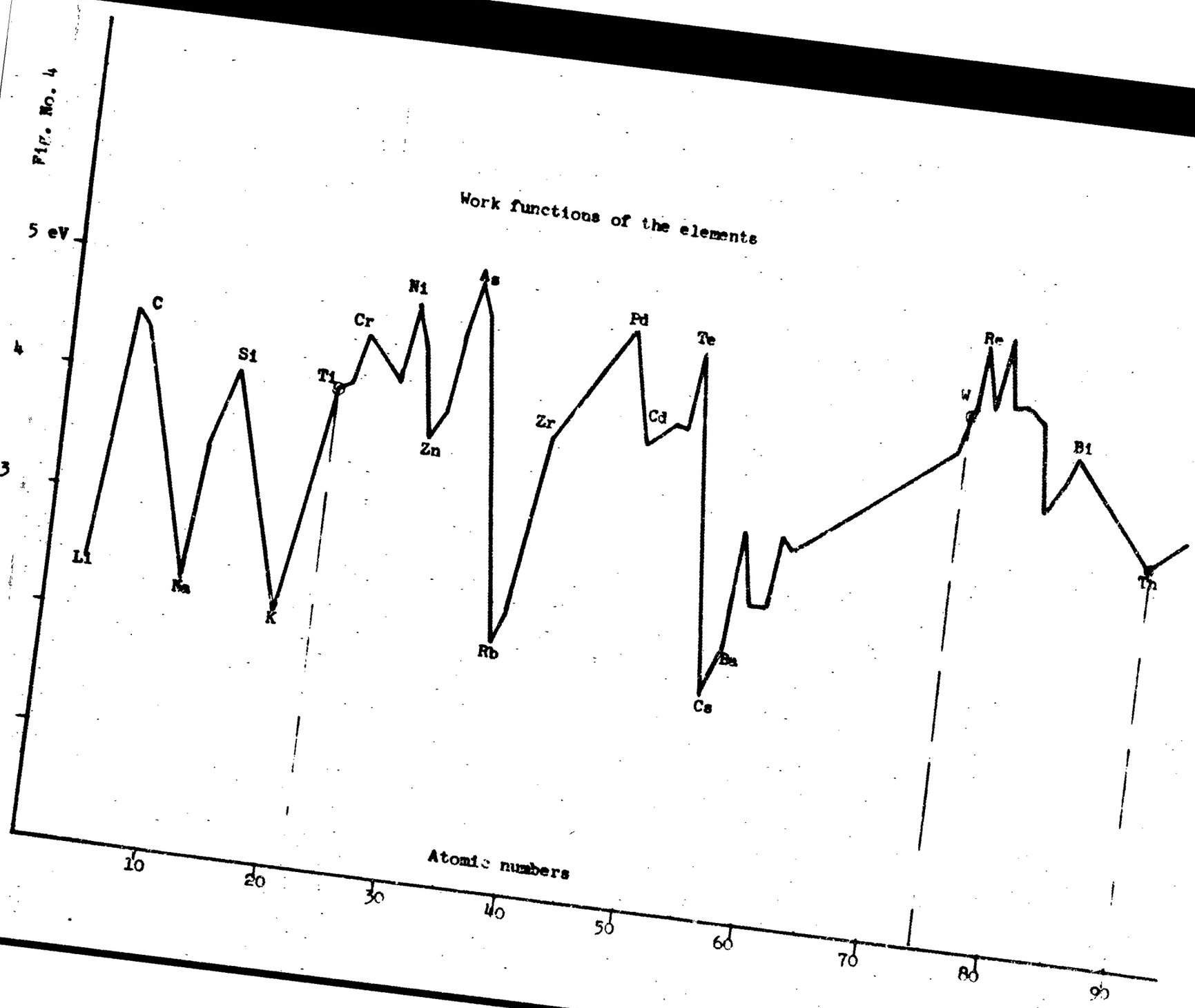
Work functions of the elements
5 eV
4
3
2
1
Li
C
Na
Si
K
Ti
Cr
Ni
Zn
As
Rb
Zr
Pd
Cd
Te
Cs
Ba
W
Re
Bi
Th
10
20
30
40
50
60
70
80
90
Atomic numbers

Fig. No. 5

H.F. Corona start voltage as a function of temperature

5.0" gap f = 2.0 Mc

contacts: 1.0" sphere - 8.0" dia.

heated titanium plate

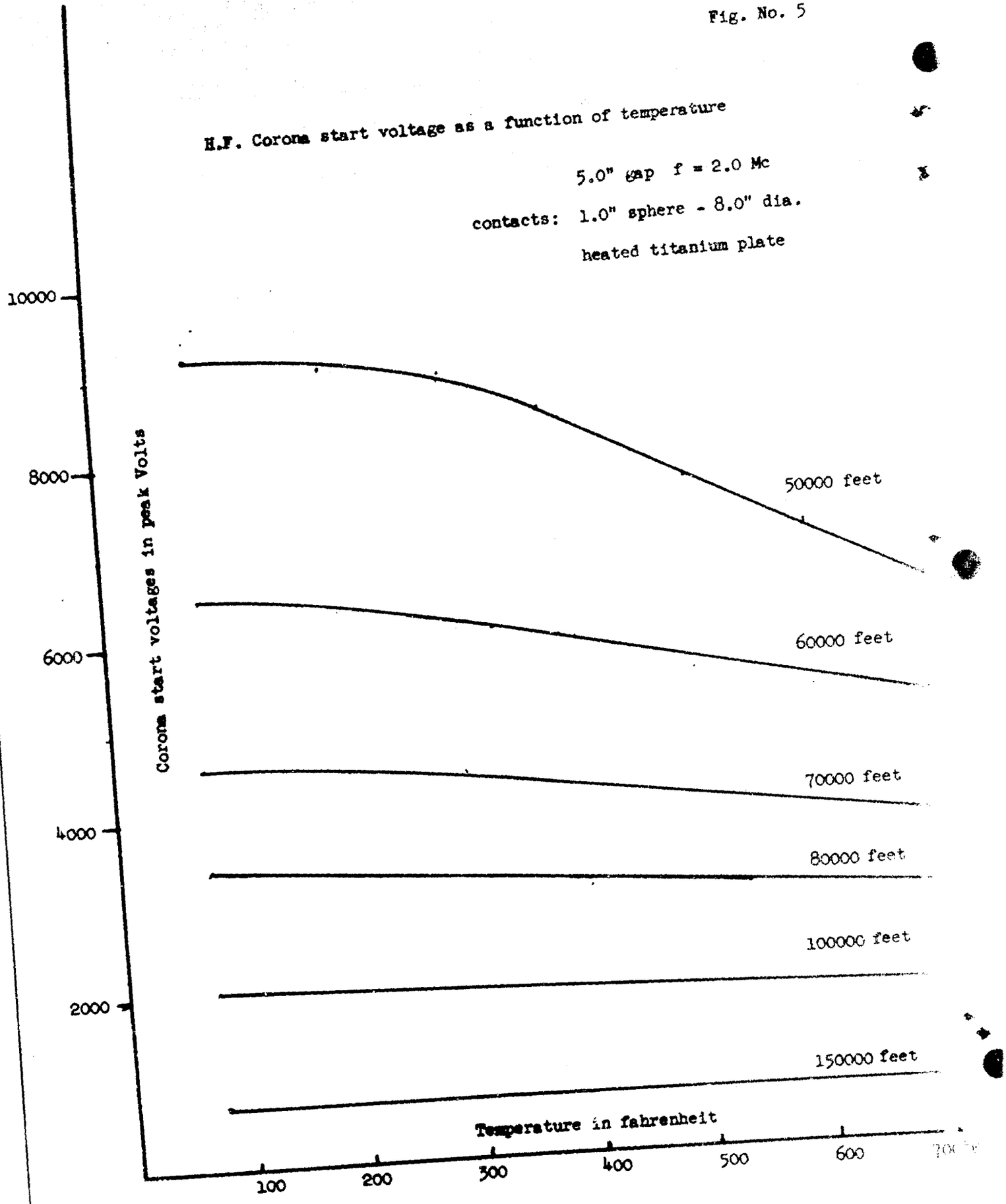

Fig. No. 6

Corona start voltages as a function of temperature

10 inch gap

f = 2 Mc

1.0" sphere - 8" plate

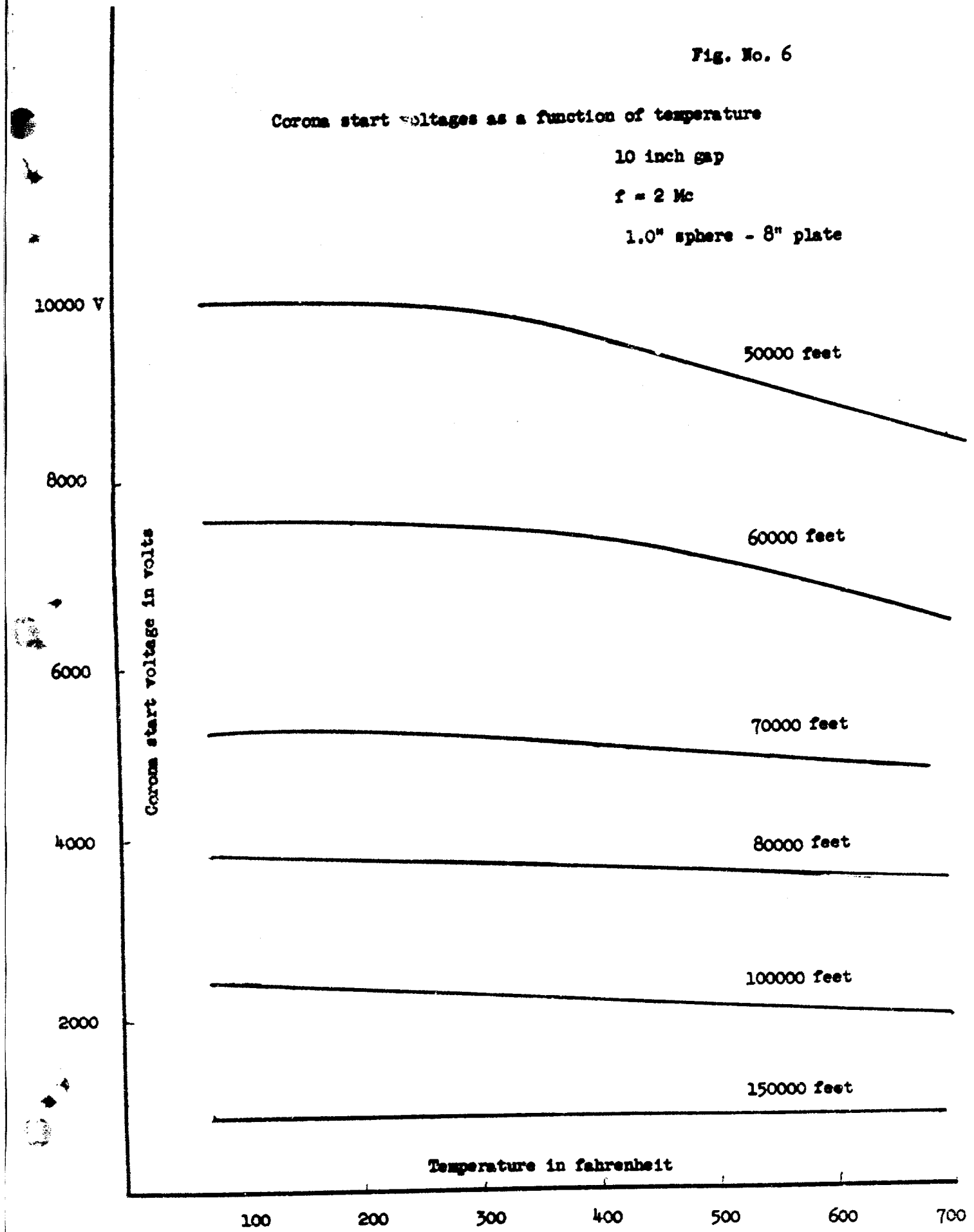

Fig. No. 7

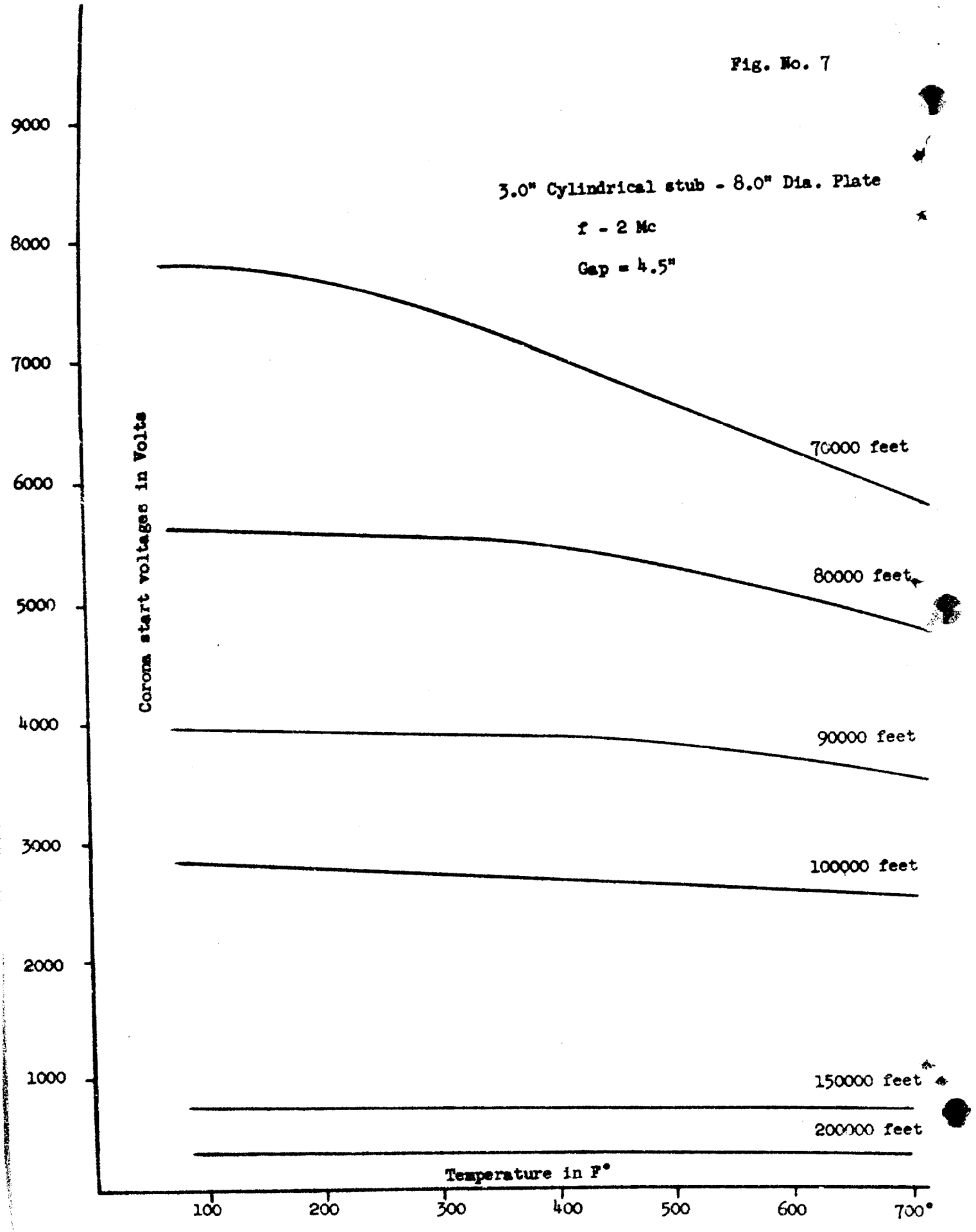
3.0" Cylindrical stub - 8.0" Dia. Plate
f - 2 Mc
Gap = 4.5"
Corona start voltages in Volts
9000
8000
7000
6000
5000
4000
3000
2000
1000
70000 feet
80000 feet
90000 feet
100000 feet
150000 feet
200000 feet
Temperature in F°
100
200
300
400
500
600
700°

Fig. No. 8

Corona start voltage as a function of altitude and temperature

I = 70°F
II = 700°F
f = 2.0 Mc
Contacts: 3.0" Cylindrical stub - 8.0" Dia. (Titanium) heated plate.
Gap = 4.5"

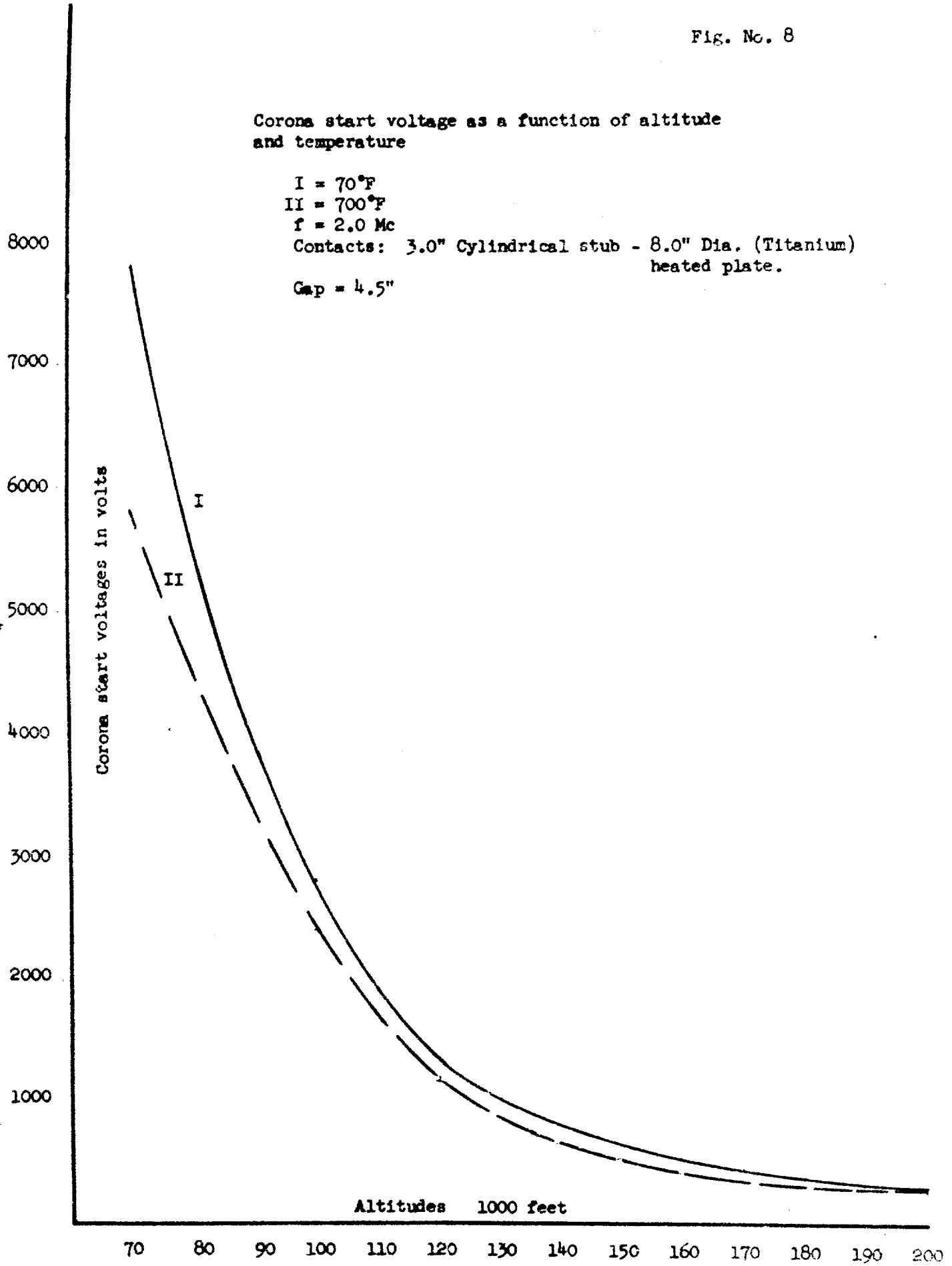

Fig. No. 9

Corona start voltages as a function of temperature

f = 2 Mc gap = 10.0"

contacts: 1.0" cylindrical stub (Brass) - 8.0" Dia. heated titanium plate.

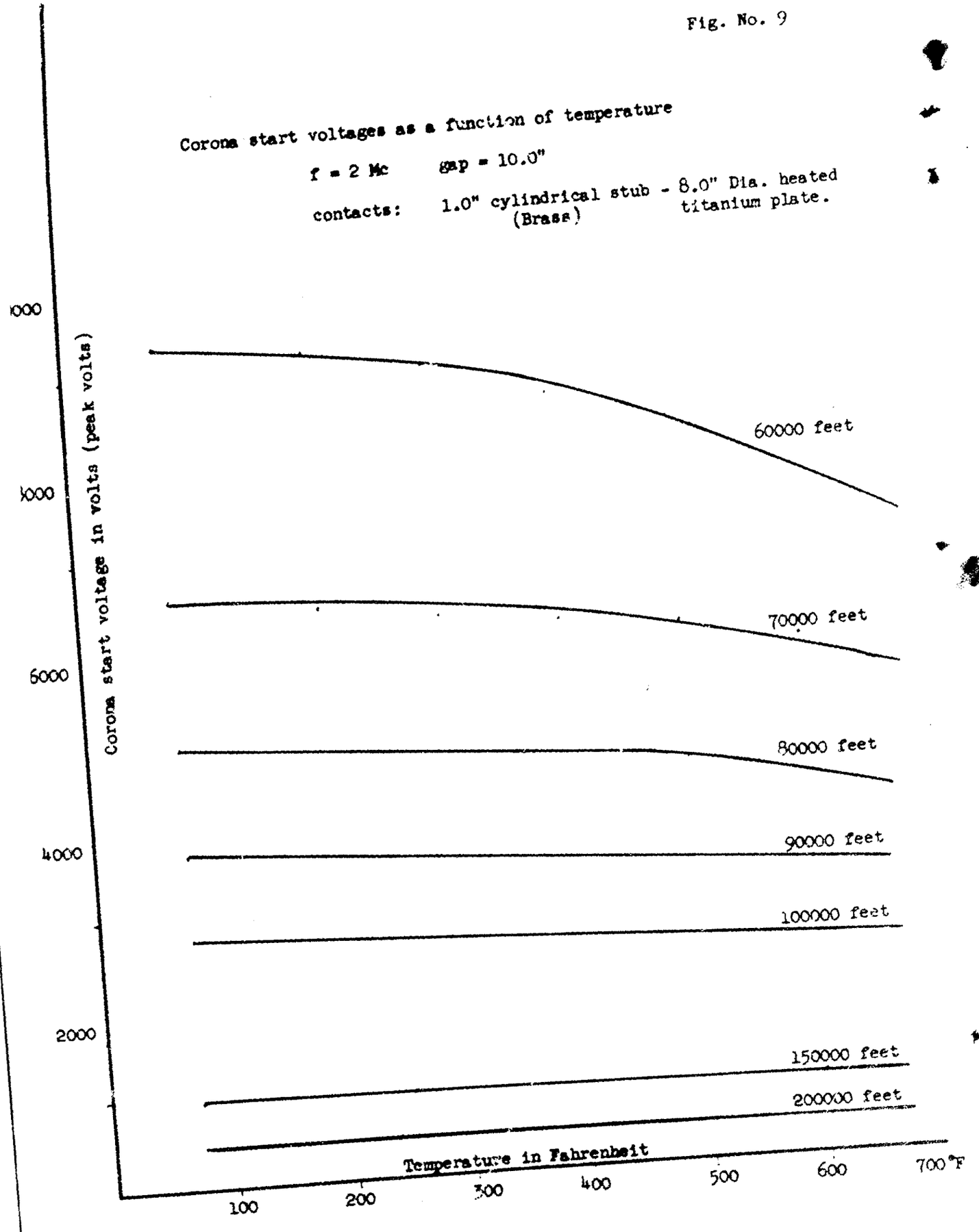

Fig. No. 10

Corona start voltages as a function of altitudes and temperature

I = 70°F gap = 10.0"

II = 600°F

contacts: 1.0" cylindrical stub
to 8.0" Dia. heated Titanium plate

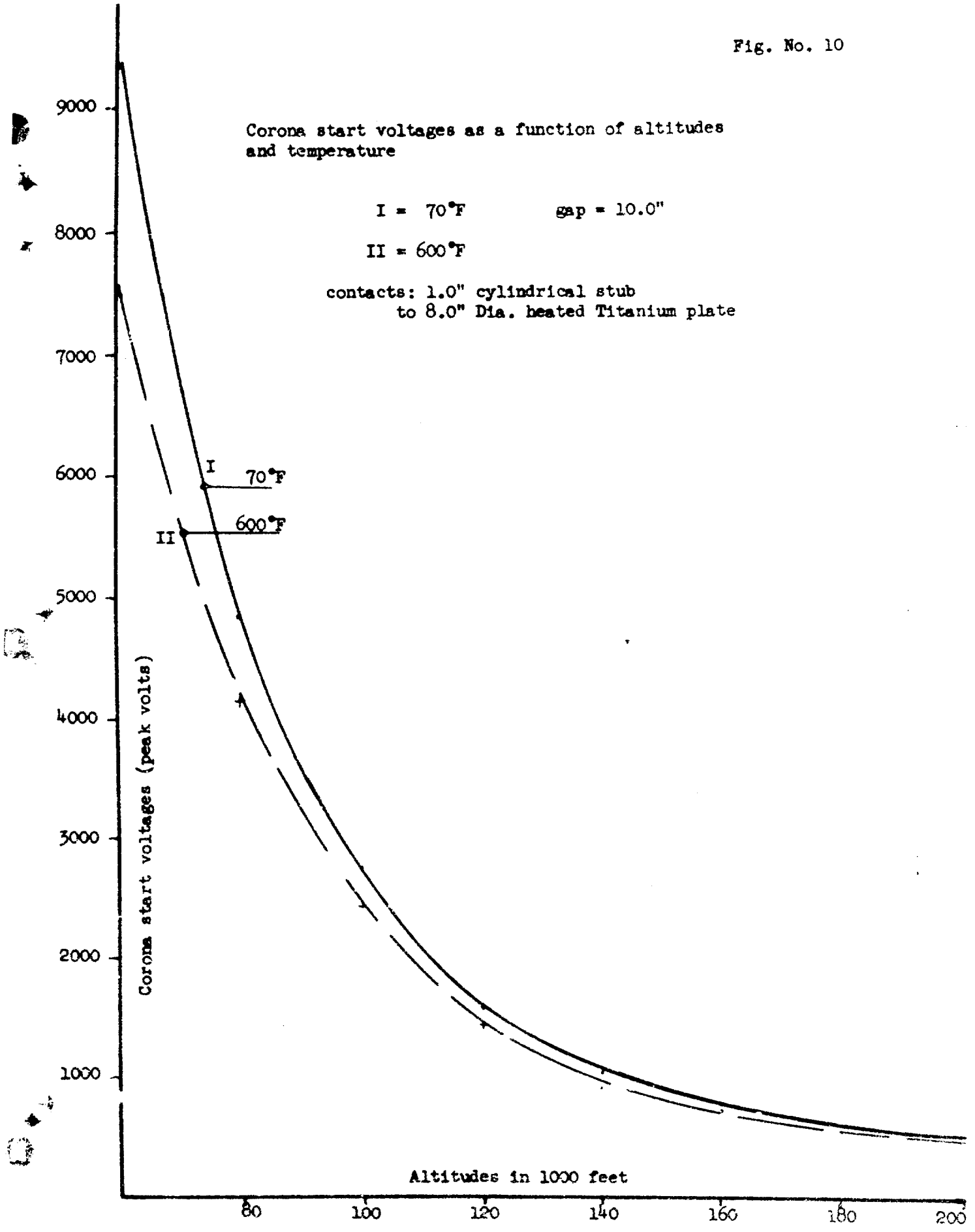

Fig. No. 12

H.F. Corona start voltages as a function of altitudes

f = 2.0 Mc

Gap = 12.0"

contacts: 0.5 cylindrical stub - 8.0" Dia. heated titanium plate

I = 70°F

II = 600°F

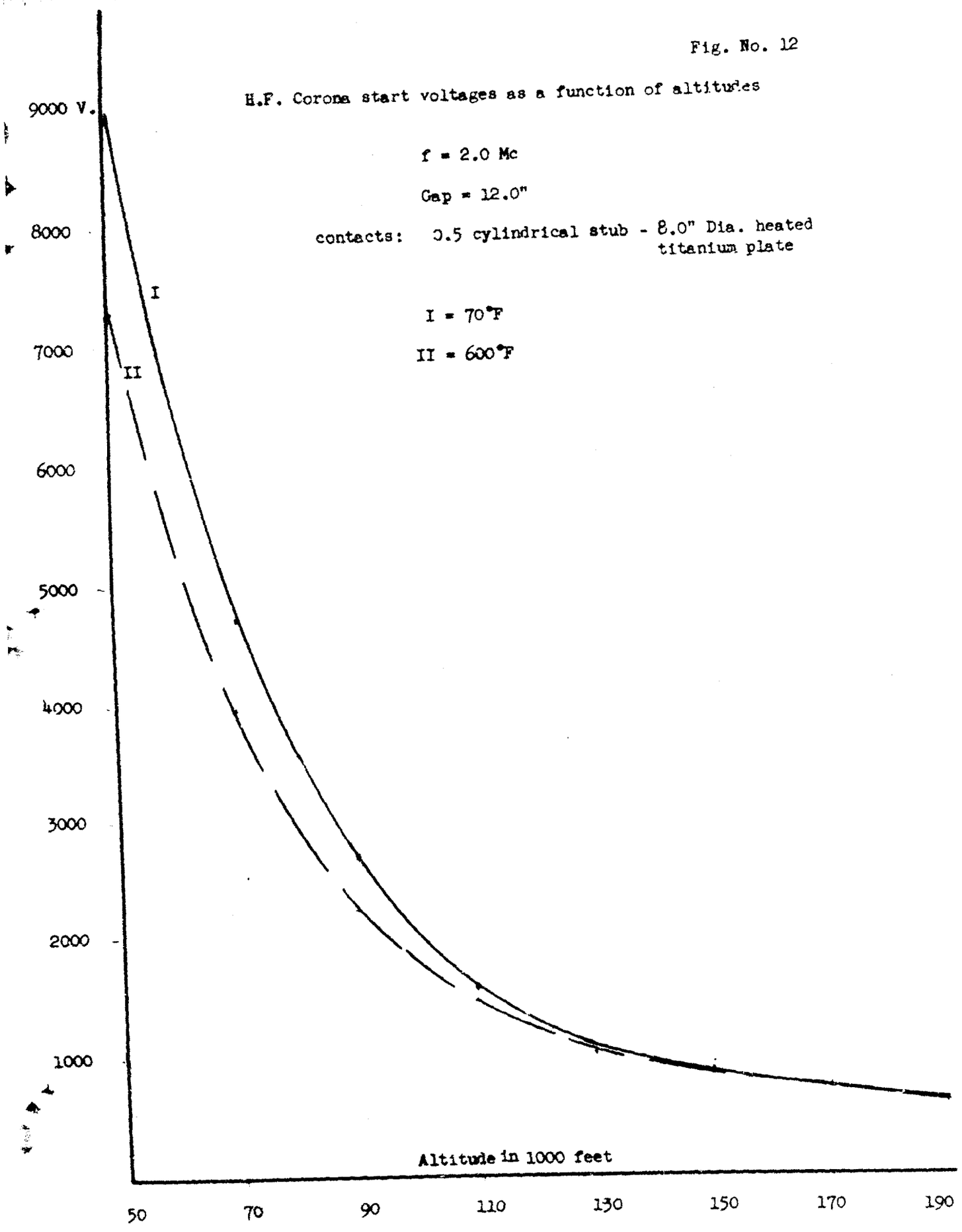

Preceding Page Blank

A PRECISION GROUND-REFLECTION ANTENNA BORESIGHT TEST RANGE

by

J. S. Hollis
Principal Engineer, Scientific-Atlanta, Inc.

R. E. Pidgeon, Jr.
Senior Electronic Engineer, Scientific-Atlanta, Inc.

and

R. M. Schutz
Design Engineer, McDonnell Aircraft Corporation

Prepared for Presentation at

Fourteenth Annual Symposium on
USAF Antenna Research and Development
University of Illinois
6-8 October 1964

A PRECISION GROUND-REFLECTION ANTENNA BORESIGHT TEST RANGE

J. S. Hollis*, R. E. Pidgeon, Jr.†, and R. M. Schutz‡

1. INTRODUCTION

The purpose of this paper is to describe the NASA-MSC-FO-MILA** antenna test facility and the results of measurements of the range characteristics. This antenna range, which is shown in Figure 1.1 and in the plan view of Figure 1.2, was designed specifically for making boresight-accuracy and calibration tests of the 1428-Mc Gemini Rendezvous Radar and secondarily as a general purpose antenna test facility.

The range has the dual capability of operating as a ground-reflection range and as a conventional elevated range. As can be seen from Figure 1.2, the surface of the range is graded plane. In the ground-reflection mode of operation the antenna under test, assuming that it is operated on reception, is illuminated by direct-path energy from the source antenna and by energy which is specularly reflected from the smooth range surface. In this manner reflections from the earth are used to advantage rather than being allowed to contribute to the received field in a random fashion. The ground-reflection mode of operation is the subject of this paper.

In the elevated mode, discrimination against extraneous reflections is achieved by the directional characteristics of both the transmitting antenna and the antenna under test and by the use of diffracting or absorbing materials. While the performance of the range has not been tested for the elevated mode, the planar range surface is advantageous for this mode because the location and size of the region of specular reflection can be calculated.

For the rendezvous radar boresight application the radar is tested in a full-scale mockup of the Gemini Spacecraft, shown in Figure 1.3. The mockup is mounted on a precision, multi-axis positioner on top of the range control building. To aid in suppressing reflections from the support structure, the building is oriented such that its sides make angles of 45 degrees with the axis of the range, and the two illuminated sides of the building are covered with weatherproof, high performance, microwave absorbing material.

---

*Principal Engineer, Scientific-Atlanta, Inc.

†Senior Electronic Engineer, Scientific-Atlanta, Inc.

‡Design Engineer, McDonnell Aircraft Corporation.

**National Aeronautics and Space Administration--Manned Spacecraft Center--Florida Operations--Merritt Island Launch Area. In this paper the range will be called the Gemini Rendezvous Radar Boresight Test Range or appropriate contractions.

T[illegible] range was designed and validated for NASA as a co-operative effort between Scientific-Atlanta and McDonnell Aircraft Corporation, the prime contractor for the Gemini Spacecraft, and is instrumented with Scientific-Atlanta equipment. Architects were John J. Harte Associates, Architects and Engineers, and the facilities contractor was Williams Development Corporation. Equipment for making pre-installation acceptance tests of the radar was designed and fabricated by Westinghouse Aerospace Division, Baltimore, Maryland, the subcontractor for the radar.



Figure 1.1: Aerial View of Radar Boresight Range

The spacecraft mockup is shown mounted on the control building at the left. The source tower is at the right between two floodlight towers. This photograph was made before the grass cover was established. The sprinklers shown in the dark areas on the range are removed during range operation.

Preceding Page Blank

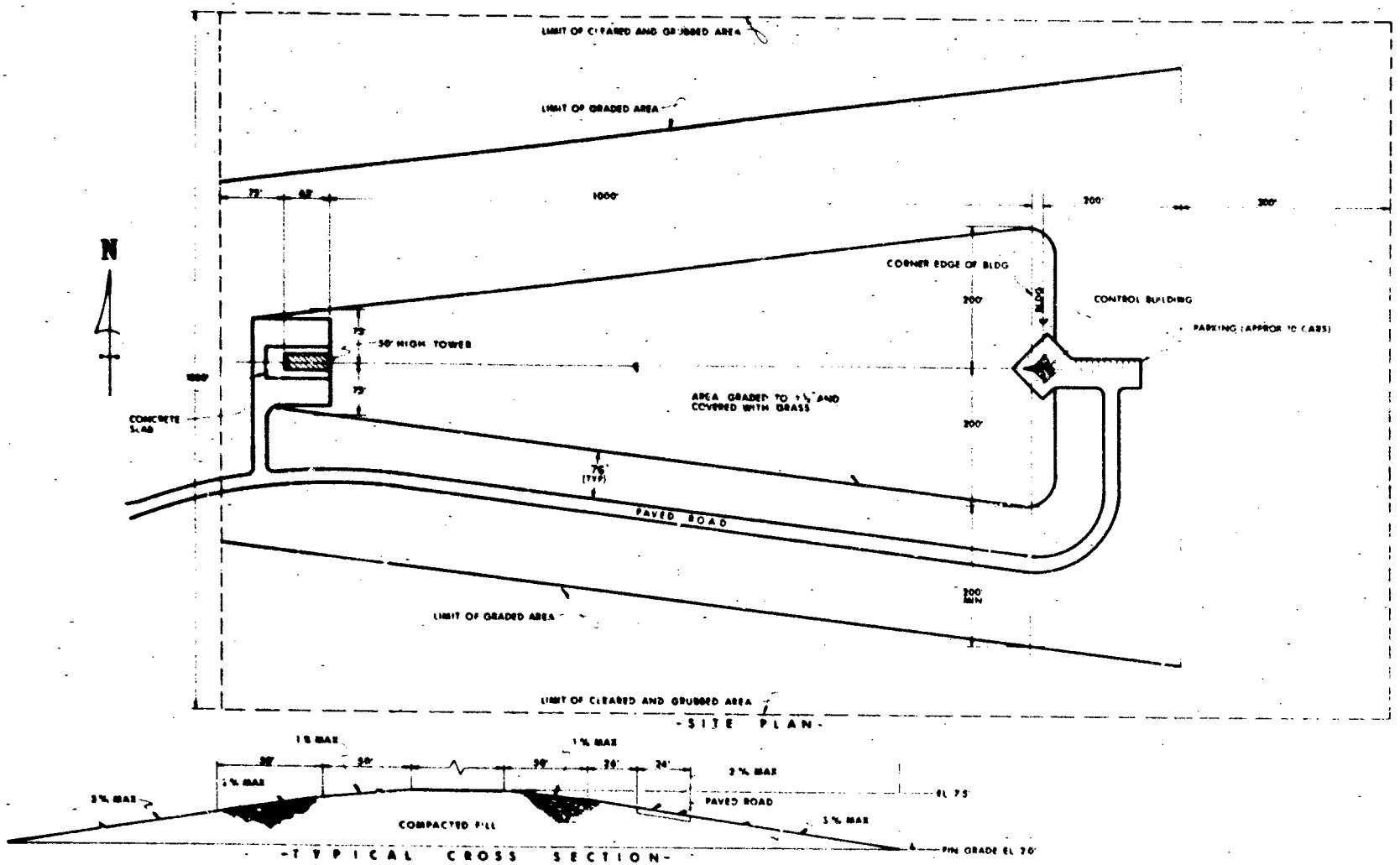

Figure 1.2. Plan View of Radar Boresight Range

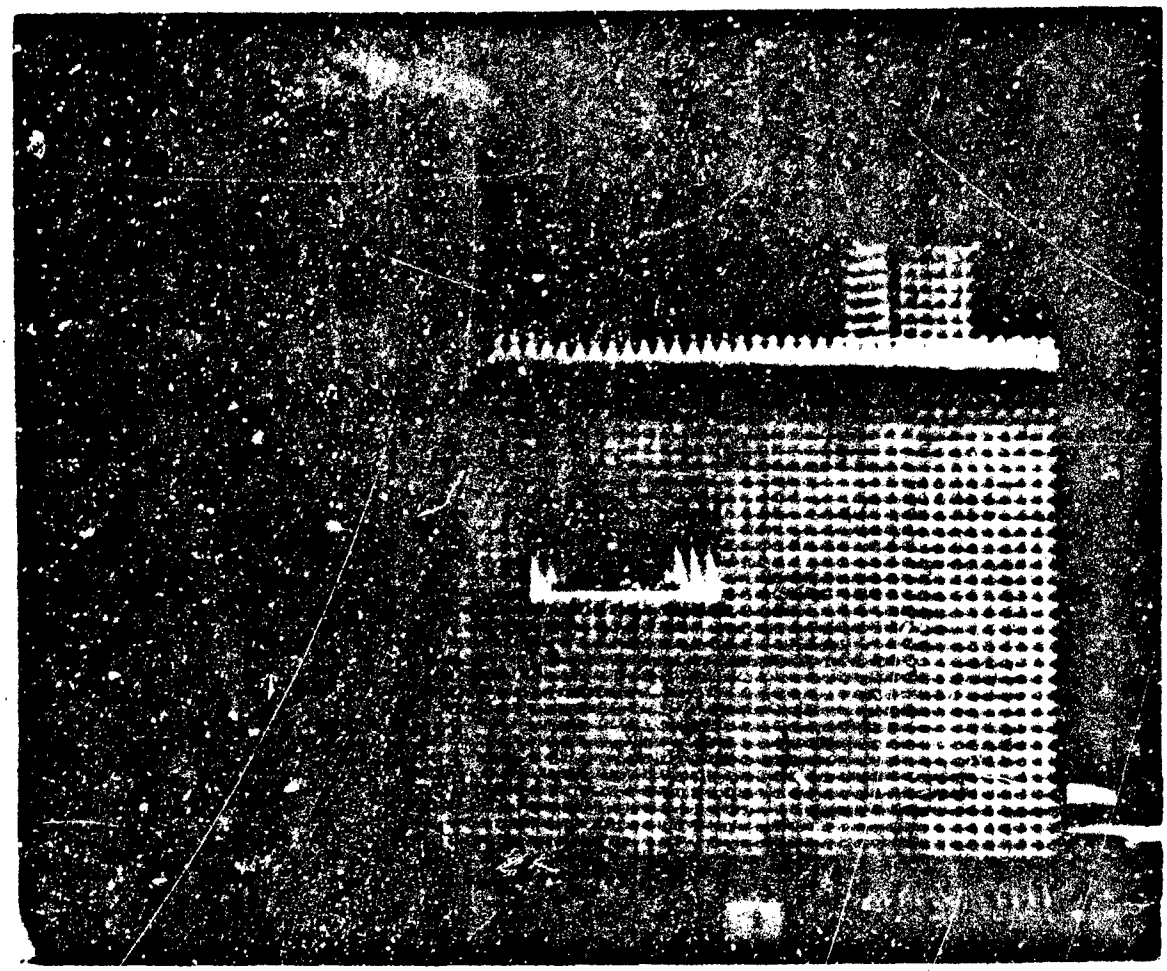

Figure 1.3. Gemini Spacecraft Mockup On Control Building

Absorber panels (B. F. Goodrich type VHP-18) on the control building can be removed in case of high winds. An absorber insert (not shown) is provided for the control building window. The small, absorber-covered structure on the roof to the right is a work stand for servicing the radar.

2. THE GEMINI RENDEZVOUS RADAR

A brief description of the Gemini rendezvous radar is given to provide an understanding of some of the major problems associated with establishing the specifications for the boresight test range.

The purpose of the rendezvous radar[1] is to measure the range and relative bearing from the Gemini spacecraft to the unmanned Agena target vehicle during the rendezvous of the two satellites in space.* A co-operative radar system is employed in which an RF pulse is transmitted from the Gemini radar, received by a transponder in the target vehicle, and re-transmitted after a short delay at a different frequency. The range to the target vehicle is determined from the measured delay between transmission and reception of the signals. Readouts are provided for range, range rate, and direction to the Agena vehicle, and an on-board digital computer calculates the orbital corrections which are necessary to effect rendezvous.

The Gemini rendezvous radar operates as a two-channel phase-monopulse radar or interferometer to measure the direction of arrival of the received signal. Three antennas are incorporated in the interferometer with one antenna common to both channels. A fourth antenna is used as the transmitting antenna. The antennas are located on the spacecraft as shown in Figure 2.1.

The phase differences between the signals received by the two orthogonal pairs of antennas are measured by the radar. The electrical phase differences ϕ_1 and ϕ_2 are related to the space direction angles α and β as illustrated in Figure 2.2 by the equations

$$\phi_1 = \frac{2\pi d}{\lambda} \cos \alpha; \qquad \phi_2 = \frac{2\pi d}{\lambda} \cos \beta \tag{1}$$

where d is the spacing between the phase centers of each antenna pair, λ is the wavelength, and α and β are measured from the yaw and pitch axes of the spacecraft, respectively. These angles are limited by the radar to the intervals of 90 degrees ±25 degrees. The radar provides coverage for yaw and pitch angles up to ±25 degrees.

Each channel of the interferometer locates the source of radiation on the surface of a cone. The spacing between the antennas is less than λ; thus a unique cone is defined for each channel of the interferometer. The direction to the source of radiation is

---

[1] Vester, B. H., "Gemini Rendezvous Radar," The Westinghouse Engineer, Volume 24, Number 1; January 1964.

*In the rendezvous mission the two-man Gemini spacecraft will be launched into an orbit which is approximately co-planar with that of an unmanned Agena target vehicle launched earlier. With the aid of guidance information furnished by the rendezvous radar, corrections will be made to the orbit of the Gemini vehicle to bring it into contact with the Agena vehicle.

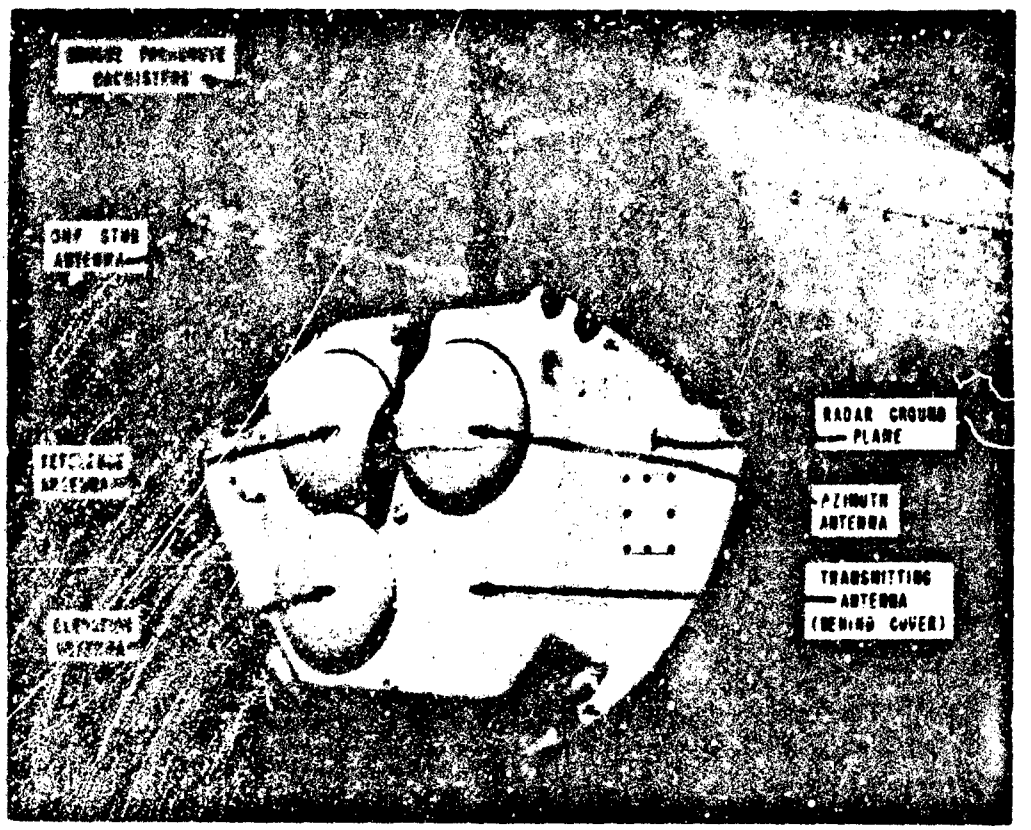

Figure 2.1. Rendezvous Radar Installed in Spacecraft Mockup

given by the intersection in space of these two cones as illustrated in Figure 2.3. Ambiguity results from the two lines of intersection of the cones, one in the hemisphere forward of the spacecraft and the other in the hemisphere to the rear of the spacecraft. The null in the rear hemisphere is discriminated against by the directivity of the radar antennas.

The circularly polarized radar antennas are printed-circuit Archimedian spirals located over a ground plane. The beamwidth of the interferometer antennas is approximately 70 degrees measured between the 3-db points on the pattern. Measurement of the phase differences between the antennas is achieved by rotating the antennas about their axes with servos to obtain nulls and measuring the angles of

rotation with shaft-position encoders. The phase delay thus introduced in each antenna is very nearly proportional to rotation of the antenna for small ellipticity ratios.

This paper is concerned with techniques and equipment employed for measuring the accuracy with which the radar determines the direction to the Agena, defined as the boresight accuracy. Equipment designed by Westinghouse and referred to previously is employed to measure the radar range accuracy.

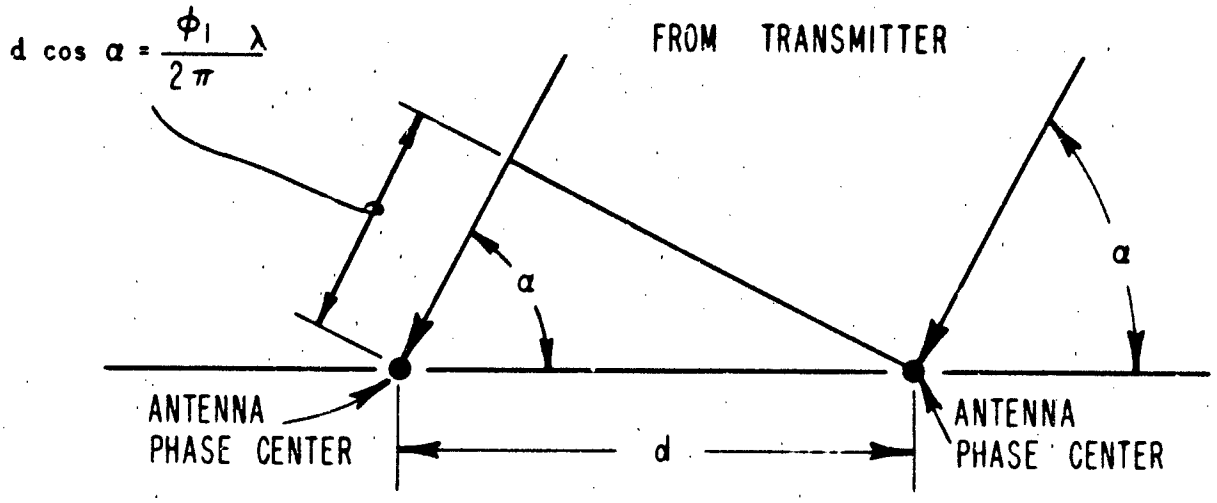

Figure 2.2. Illustration of Relationship Between Electrical Phase and Space Angle in Interferometer

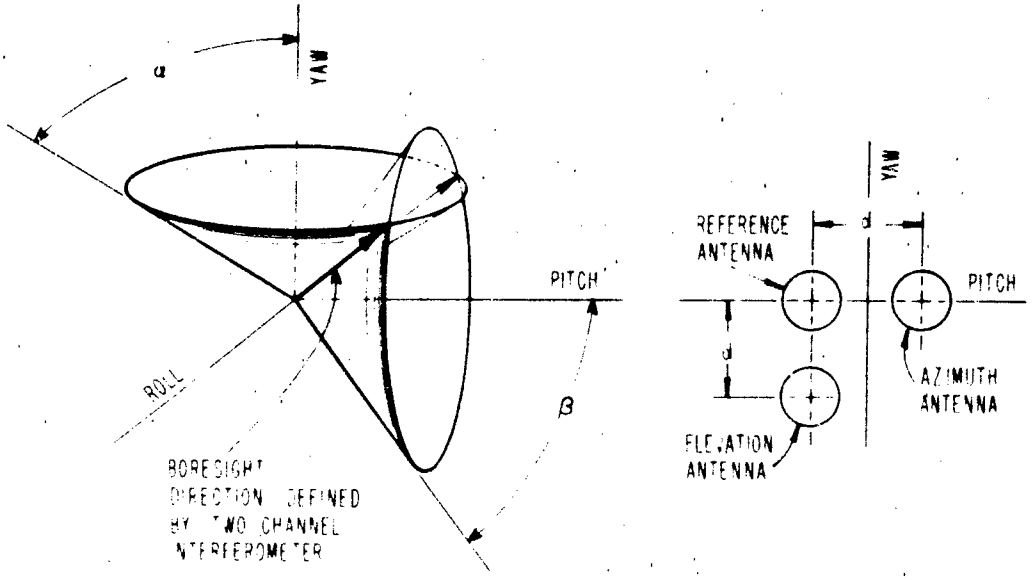

Figure 2.3. Determination of Boresight Direction by Intersection of Cones of Constant Phase Delay

3. THE RENDEZVOUS RADAR BORESIGHT MEASUREMENT PROBLEM

The Gemini rendezvous radar must function in a space environment of zero atmospheric pressure, increased solar radiation levels, and zero gravity. In establishing criteria for the acceptance tests of the boresight accuracy, it was considered impracticable to attempt to simulate a zero-pressure environment or to take into account in the measurements the effects of the increased level of solar radiation. The effect of gravity on the boresight directions measured by the radar was investigated in the manner described in Section 6.

The boresight-measurement problem can be divided into the following categories:

(a) Establishment of an incident 1428-megacycle, circularly polarized field over the active aperture of the radar antennas which would adequately simulate an incident plane wave of constant amplitude,

(b) Provision for supporting, positioning, and indicating the orientation of the radar,

(c) Establishment of a frame of reference in which the measurements could be made,

(d) Determination of the location of the source of radiation, and

(e) Establishment of an optical line of sight from the source of radiation to the radar to permit its comparison with the line of sight indicated by the radar.

We will not dwell on a discussion of the various range configurations[2] that might have been employed for testing the rendezvous radar. The ground-reflection range was selected because of the high suppression required of extraneous signals, the low directivity of the radar antennas, and because this type of range is in keeping with the flat terrain which exists at Merritt Island.

A discussion of some of the basic problems involved in the establishment of the incident field over the test aperture and which influenced the selection of the range configuration is given in the following paragraphs.

---

[2] Hollis, J. S., and R. E. Moseley, "Siting Considerations in Microwave Antenna Measurements," Essay No. 3, Scientific-Atlanta, Inc.; August 1961.
Cumming, W. A., "Radiation Measurements at Radio Frequencies: A Survey of Current Techniques," Proc. IRE, Volume 47, No. 5, pp. 703-735; May 1959.

3.1 Suppression of Extraneous Reflections

The radar-boresight error specification for which the range was designed was 3 milliradians. In a typical measurement problem of this type it is customary to require that the measurement system error be an order of magnitude smaller than the tolerance of the quantity being measured. This criterion would have resulted in a measurement system overall accuracy of 0.3 milliradian and would have limited the error caused by extraneous reflections to the order of 0.1 milliradian.

Calculations showed, however, that this degree of accuracy would have demanded suppression of range reflections and tolerances on other measurement errors which were not considered practicable. A more realistic range accuracy goal appeared to be 1 milliradian with a maximum allowable contribution from extraneous reflections of 0.3 to 0.5 milliradian.

The required suppression of range reflections can be determined by considering the relationship of the radar electrical phase error to boresight error. Differentiation of equations (1) gives

$$\frac{d\phi_1}{d\alpha} = -\frac{2\pi d}{\lambda} \sin \alpha;$$

$$\frac{d\phi_2}{d\beta} = -\frac{2\pi d}{\lambda} \sin \beta . \qquad (2)$$

The mechanical spacing d between antenna centers is 6.80 inches. Evaluation of equations (2) for the range of the variables α and β gives the approximate relationship

$$d\phi_1 = 5d\alpha ;$$

$$d\phi_2 = 5d\beta . \qquad (3)$$

Referring to Figure 3.1, let A be the amplitude of the phasor at the difference terminals of one of the interferometer summation networks caused by a direct-path signal impinging upon the antenna. If B is the amplitude of the phasor produced by an extraneous signal entering the same antenna, the maximum electrical phase deviation will occur when the two phasors are in quadrature. The error ϵ will be $(B/A)\times 10^3$ milliradians if $B \ll A$. For the worst-case condition, if equal and oppositely phased extraneous signals exist in each channel of an interferometer pair, the phase error will be $2(B/A)\times 10^3$ milliradians, corresponding to a boresight error contribution of about $0.4(B/A)\times 10^3$ milliradians in accordance with equations (3).

If the contribution of extraneous signals is to be, say, 0.4 milliradian, we must let

$$0.4(B/A)\times 10^3 \text{ mr} = 0.4 \text{ mr} , \tag{4}$$

giving

$$B/A = 10^{-3} . \tag{5}$$

These calculations indicate that the maximum level of the sum of all extraneous signals should be held to the order of 60 decibels below the level of the direct-path signal to meet the above criterion. It should be noted that the calculations give the maximum error contribution from one interferometer channel. The magnitude of the total boresight error is given by the rms sum of the errors in the two channels.

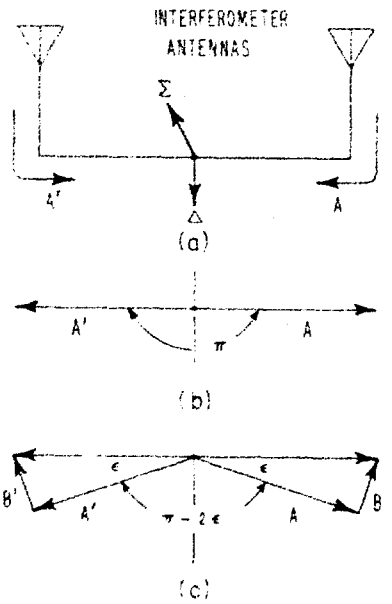

(a) FUNCTIONAL DIAGRAM OF ONE CHANNEL OF INTERFEROMETER.

(b) IDEALIZED PHASOR DIAGRAM SHOWING SUMMATION OF DIRECT PATH SIGNALS IN DIFFERENCE CHANNEL.

(c) PHASOR DIAGRAM SHOWING EFFECT OF EXTRANEOUS SIGNALS.

Figure 3.1. Illustration of the Effect of Extraneous Reflections on Boresight Accuracy (A=A'; B=B')

3.2 Range Length

In order to establish the range length it was necessary to determine the extent of the active aperture of the radar antennas, that is, over how much of the spacecraft quasi constant-amplitude, constant-phase conditions must be provided. Upon consideration of the problem and after consultation with leading antenna authorities, it was concluded that one could not predict to any degree of certainty the contributions of currents flowing over the surface of the spacecraft to the indicated boresight angle. However, one can show easily that the contribution may be significant.* It was therefore decided that the entire spacecraft would be mocked-up and that the phase error would be limited to less than $\lambda/16$ over the aperture represented by the maximum projection of the spacecraft normal to the direction of incidence. This would have resulted in a range length of about 700 feet. The range length was set at 1000 feet because this length resulted in a lower grazing angle for the ground-reflection range configuration and at the same time provided a more desirable phase-variation limit.

3.3 Gain of the Source Antenna

The maximum gain of the source antenna (actually the directivity rather than gain) is limited because of one of two factors: (a) the requirement for a nearly constant field over the test aperture[3] and (b) the requirement for control of the circularity of the incident field at the test aperture. To adequately simulate far-zone conditions, a criterion was established that the taper of the field over the test aperture should not vary more than approximately 0.25 decibel.

The maximum projection of the spacecraft is 10 feet at nose-on incidence, but the horizontal projection increases to approximately 19 feet as the spacecraft is rotated in azimuth. The variation of the field in the vertical plane is determined by the ground-reflection range configuration discussed in Section 4. The variation of the field horizontally is determined directly by the directivity pattern of the source antenna. However, it became evident that the ground-reflection range configuration was the major factor in deciding the beamwidth since the maximum allowable height of the center of the source antenna was about five feet. An 8-foot diameter antenna was employed giving a beamwidth of about 5 degrees and a directivity of about 30 decibels.** Estimates of the cross-polarization characteristics of a paraboloidal reflector with an axial ratio of 0.373 indicated that the change in circularity should not be excessive over the 19-foot test aperture. Aperture amplitude and polarization patterns are presented in Section 6.

[3] Chastain et al, Investigation of Precision Antenna Pattern Recording and Display Techniques, Final Report, Contract AF 30(602)-2737, Scientific-Atlanta, Inc., April 1963, AD415912.

*Subsequent measurements have shown that currents on the spacecraft do contribute significantly to the boresight direction.

**In the ground-reflection range this directivity is increased by about 5 decibels by the in-phase interference from the ground-reflected wave.

4. CONSIDERATION OF THE GROUND-REFLECTION* ANTENNA TEST RANGE

The ground-reflection antenna test range has been employed for a number of years and has been described in the literature.[4] A rigorous description of the theory of operation is exceedingly complex; however, its principle of operation can be explained in an elementary manner by the method of images of geometrical optics and by use of Rayleigh's criterion of roughness[5] of physical optics.

The range geometry is given by Figure 4.1. The range is plane and smooth within Rayleigh's criterion to provide for specular reflection of the incident energy. At frequencies above about 100 megacycles for nearly grazing angles of incidence and for both horizontal and vertical polarizations, the phase of the reflection coefficient for a plane incident wave is virtually 180 degrees.[6] Under this set of assumptions an image of the transmitting antenna appears to lie below the range surface, equidistant from the antenna, thus maintaining the angle of incidence i equal to the angle of reflection r at the range surface. It has been shown that for a unity reflection coefficient and, neglecting the vertical directivity pattern of the transmitting antenna, the field variation with height at the test antenna is approximated by

$$E = 2E_o \sin \frac{2\pi h_1 h_2}{\lambda R} . \qquad (6)$$

where E_o is the field produced by direct-path transmission.[7] E thus has a sinusoidal variation with height, with a value of zero for $h_2 = 0$ and a first maximum for

$$\frac{2\pi h_1 h_2}{\lambda R} = \frac{\pi}{2} . \qquad (7)$$

*This type of range has been described by the terms ground-level and ground-plane. The term ground-reflection more specifically describes the principle of operation than do the alternate designations.

[4]Cutler, C. C., A. P. King, and W. E. Kock, "Microwave Antenna Measurements," Proc. IRE, Volume 35, No. 12, pp. 1462-1471; December 1947.
Hollis and Moseley, op cit.
Cohen, A., and A. W. Maltese, "The Lincoln Laboratory Antenna Test Range," The Microwave Journal, April 1961.
Campanella, A. J., C. F. Douds, and R. E. Wolfe, Feasibility Study of a High Performance Antenna Test Range (U), HRB Singer, Inc., Contract AF 30(602)-2445, Report No. RADC-TDR-62-301; 19 October 1962.
Christie, R. A., Antenna Testing Facilities, Bell Telephone Laboratories, Inc., Whippany, New Jersey.
Communications with Mr. George Dale, Bell Telephone Laboratories, Inc., Whippany, New Jersey.

[5]Kerr, D. E., Propagation of Short Radio Waves, Radiation Laboratory Series, Volume 13, McGraw-Hill; equation 19 and footnote page 16.

[6]Jordan, E. C., Electromagnetic Waves and Radiating Systems, Prentice-Hall, Inc., New York, p. 613; 1961.

[7]Cutler et al, op cit.

or

$$h_2 = \frac{\lambda R}{4h_1} \quad . \tag{8}$$

In consideration of the geometry of Figure 4.1, it is evident that, in the ground-reflection antenna test range, the incident wave produced by the transmitting antenna is not plane. Further, the antenna usually has a significant change in directivity with elevation angle. Experimental measurements have shown, however, that equation (6) predicts the field variation with height quite well near the region of the maximum. Although the field may depart from the predicted value in the vicinity of the nulls, this is of no consequence since the vertical aperture of the antenna under test must be limited to a height d such that the field variation predicted by equation (6) is small. A generally accepted criterion for the total variation is 0.25 decibel.

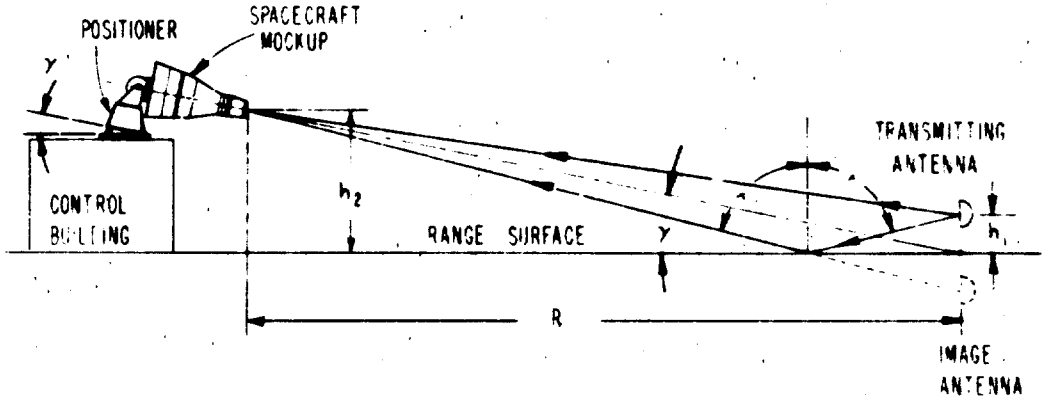

Figure 4.1 Illustration of the Principle of the Ground-Reflection Range

Figure 4.2 shows the limits of the field variation in decibels as a function of the normalized aperture height d/h_2. Here, h_2 is the height of the center of the test aperture, which is assumed coincident with the maximum given by equation (8). The height h_1 is predicted by equation (8) to be 5.75 feet for a range length of 1000 feet and height h_2 of 30 feet, the nominal values for the rendezvous measurement problem.

4.1 Height of the Apparent Source of Radiation

The apparent source of radiation for the ground-reflection range can be defined as the center of phase of the array formed by the transmitting antenna and its image in the reflecting surface of the range. Although it has been shown that a unique center of phase usually does not exist except over a small region of solid angle of the

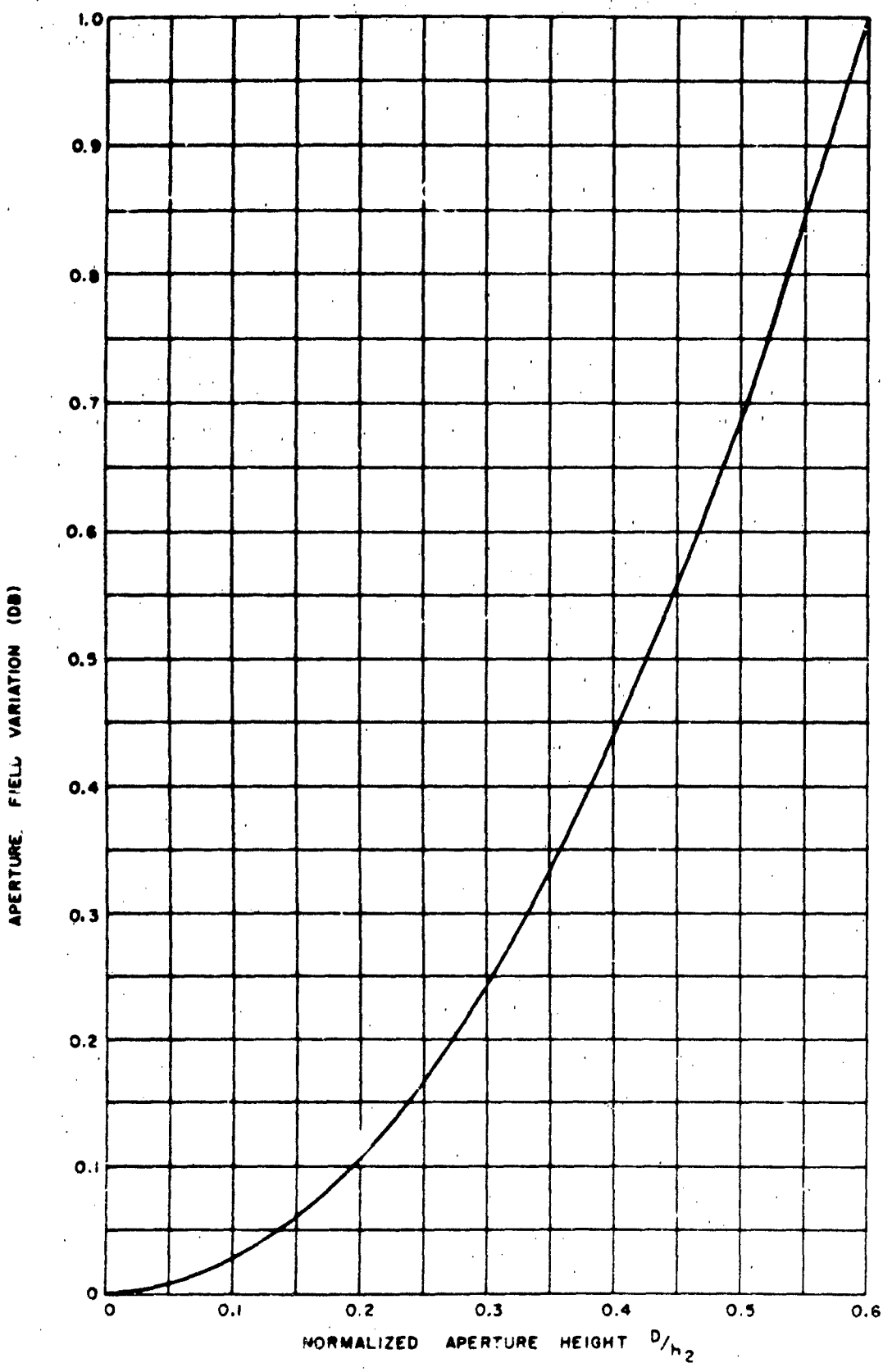

Figure 4.2. Limits of Field Variation with Height Over the Test Aperture of a Ground-Reflection Antenna

far-zone pattern of a directional antenna[8], such a center of phase can be defined as it exists at the center of the test aperture. By the method of images it can be shown that the height of this center of phase is approximated by

$$h = \frac{1-R}{1+R} h_1 , \qquad (9)$$

where R is the amplitude ratio of the specularly reflected wave to the direct-path wave. This approximation is based on 180-degree phase reversal of the incident wave at the range surface and constant phase of the transmitting antenna far-zone field with elevation.

In typical ground-reflection antenna range applications the phase center (hence the apparent source) is often assumed to be located at the intersection of the range surface with the vertical line joining the centers of the antenna and its image. While this assumption is satisfactory for many applications, the height of the apparent source can vary significantly; therefore it was necessary to determine its location. For example, a radar accuracy specification of 3 milliradians is represented by a circle which is 3 feet in radius at the test range of 1000 feet. It was necessary to determine that the location of the apparent source could be predicted with small error compared with this radar error specification. It was further required that a direction be assigned for the mean location of the apparent source, which would be used as a comparison standard in making the boresight measurements. The method employed to accomplish this and the results are described in paragraph 6.3.

4.2 Range Surface

The primary requirements for the range surface are that it be graded smooth within Rayleigh's criterion and have a shape which produces a unique image of the transmitting antenna in the range surface for all orientations of the spacecraft mockup. These requirements are met by a plane surface over the major area of illumination, which is graded to the tolerances shown in the plan view of Figure 1.2.

Most of the reflected energy comes from within the first few Fresnel zones on the range surface[9]. These zones are bounded by ellipses for a plane range surface and a point source transmitting antenna. For the range constants at L-band, the first Fresnel zone has major and minor axes of approximately 495 feet and 22 feet and is centered 280 feet in front of the source antenna. The tenth Fresnel zone has major and minor diameters of 888 and 80 feet and is centered 447 feet from the source antenna.

[8] Tetsu Morita, Determination of Phase Centers and Amplitude Characteristics of Radiating Structures, Technical Report No. 1, SR 1, Proj. 898, Stanford Res. Inst., Menlo Park, California, Contract DA04-200-ORD-273, AD68240; March 1955.

[9] Campanella et al, op cit.

The range surface is controlled over the area indicated in Figure 1.2 in addition to the region of specular reflection to reduce errors from diffuse reflection.

The Rayleigh criterion[10] is given by

$$\eta \sin \psi < \lambda/k , \qquad (10)$$

where η is the height of a surface irregularity, ψ is the grazing angle and k is usually set between 8 and 32, the constant 32 defining a very smooth surface.

Letting $\lambda = 8$ inches ($f \sim 1428$ Mc), and $\psi \sim 2°$, the constants for the current problem, and letting $k = 32$, gives $\eta < 7$ inches or ± 3.5 inches. However, because of the extreme accuracy requirements of the problem and because the antenna range is to be employed in higher frequency applications later, the surface was graded to a tolerance of ± 1 inch. Surveys of the range have since led to the conclusion that the graded surface probably has a $\pm 1/2$-inch tolerance exclusive of the Bermuda grass cover.

The question of the type of surface which would be employed was of some concern. Gravel in the form of graded, crushed aggregate would be a good choice, because it would allow rainwater to leach into the surface and yet would resist wind erosion. It was decided against, however, because of the cost.

Asphalt and concrete were considered but were discarded because of the cost and the drainage problem caused by their lack of perviousness. The cost of asphalt or concrete could have been reduced by use of a narrow strip of either material down the center of the range with grass on both sides. While this technique can be employed, it was rejected because of the high angular-accuracy requirement of the measurement problem, the consequent desire to have no linear discontinuities along the length of the range, and because of the drainage problem.

Grass has been criticized as a range surface because the blades can fill with water, which has a high dielectric constant, resulting in changes in the reflecting characteristics. However, grass was chosen because of the low initial cost, but with the specification that it be maintained closely mowed. In measurements which have been made to date the effect of moisture on the grass or of the moisture content of the range surface has been found to be insignificant. Specifically, polarization measurements have been made immediately before, during, and after a severe thunderstorm with a circularity change of less than 0.1 decibel from an axial ratio of 0.5 decibel. The measurement after the rain was made with large puddles of water on the range. Measurements have not been made at frequencies other than L-band, nor has it been possible to make precisely controlled measurements of the height of the apparent source immediately before and after a rain for comparison purposes.

[10] Kerr, op cit, equation (19) and footnote, page 416.

5. RANGE INSTRUMENTATION

Primary considerations in the design of the instrumentation system were accuracy of the boresight measurements, rapidity and ease of acquiring data, and flexibility of operation. The range can be used for making general antenna measurements as well as boresight measurements, and equipment is provided which makes possible detailed study of the characteristics of the range itself.

Operation of the range is conducted from the centralized console shown in Figure 5.1. Major items of equipment are identified, indicating the degree of control provided. Most of the units shown are standard items of range instrumentation and are not discussed in detail. The positioning system and other special items are described in the following paragraphs. Plans are currently being considered for incorporating the additional equipment necessary to extend the full capability of the range for operation through X-band.

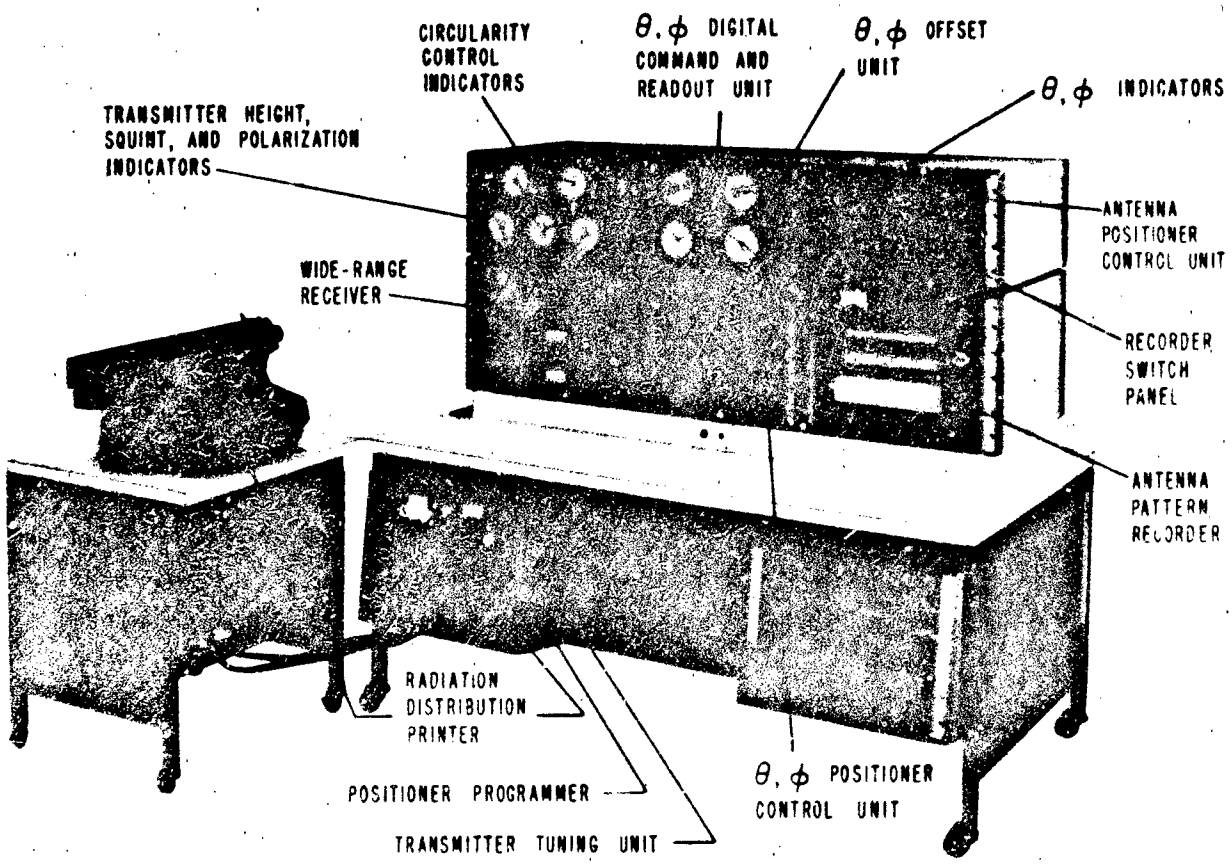

Figure 5.1. Range Operating Console. A polar recorder not shown is mounted on a removable wing normally located at the right of the console.

5.1 Spacecraft Mockup

The spacecraft mockup is a full-scale RF model of the Gemini Spacecraft in which the major details forward of the rear mounting structure are retained.* Windows and large protuberances are included, but minor details, such as skin corrugations, are omitted. A semi-monocoque design was chosen to provide high mechanical integrity. The inner skin, which provides nearly all of the structural strength, is thermally insulated from the outer skin, which serves to electrically simulate the skin of the actual spacecraft. To reduce structural deformations from stresses caused by non-uniform solar heating, the interior of the mockup is cooled by air supplied from the air-conditioned control building.

5.2 Positioning and Indicating Equipment

The accuracy requirements of the Gemini rendezvous radar plus the weight and size of the spacecraft mockup dictated that the positioner for supporting the mockup have unusual positioning capabilities and accuracies. This equipment, the coordinate system which is employed in the boresight problem, and the method of optically aligning the positioner and radar in the coordinate system are described in the following paragraphs.

5.2.1 Coordinate System

The coordinate system shown in Figure 5.2 relates the spacecraft coordinates (roll, pitch, and yaw), radar coordinates, and positioner axes to the location of the source

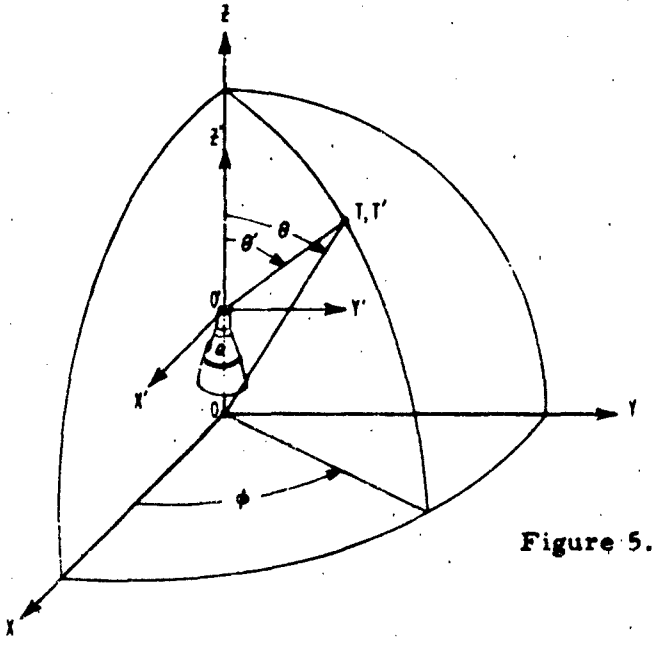

Figure 5.2. Spherical Coordinate System

*The spacecraft mockup was designed by McDonnell Aircraft Corporation and fabricated by the 6549th Maintenance Squadron, Patrick Air Force Base, Florida.

of radiation in a composite coordinate system. This system is in agreement with standards established by the Inter Range Instrumentation Group (IRIG) for testing space-vehicle antennas.[11] The spacecraft mockup is fixed with respect to the XYZ coordinate system, and the source of radiation, defined by the point T', moves over the surface of the sphere.*

The primed coordinate system is fixed relative to the radar; the X'Y' plane is located coincident with the phase centers of the radar antennas, assumed to be on the surface of the radar ground plane, and the Z' axis is adjusted coincident with the Z (roll) axis.

Figure 5.3 depicts the coordinate system as it is oriented in the test range, showing the relationship of the positioner axes to the spacecraft and radar coordinate system.

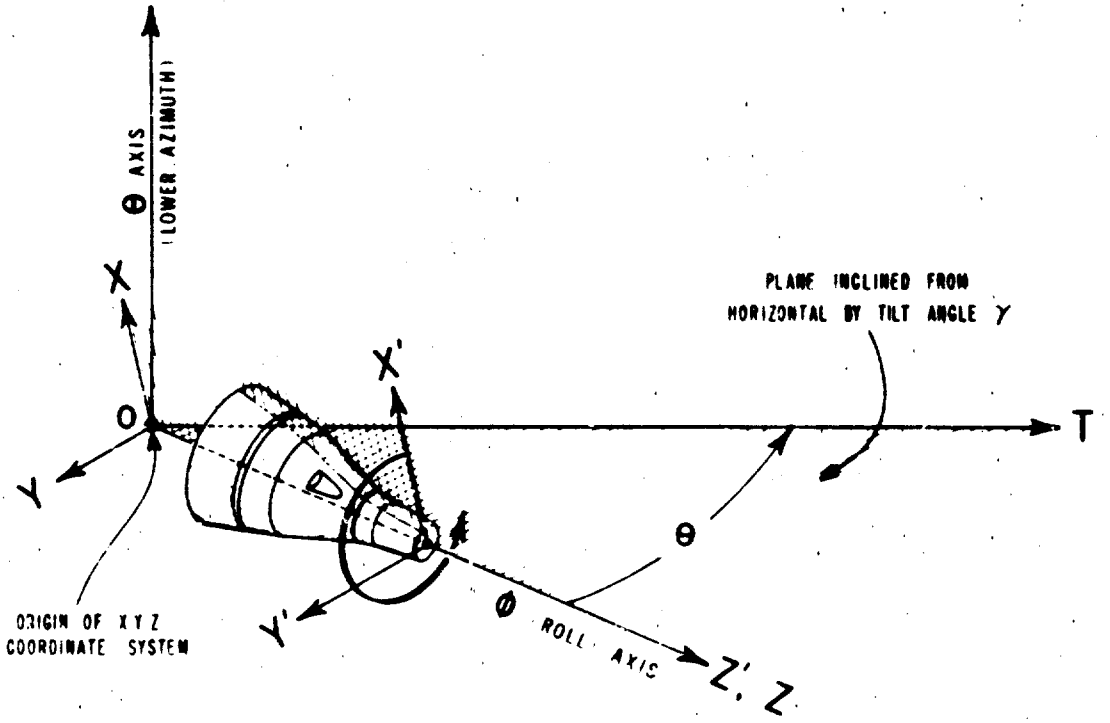

Figure 5.3. Spherical Coordinate System Shown in Relationship to Range Geometry. The spacecraft mockup is shown rotated clockwise in θ.

Parallax between the angles θ and θ' exists because the spacecraft mockup is cantilevered over the edge of the control building to reduce reflections into the radar antennas from the control building and positioner. This parallax is accounted for in

[11] "IRIG Standard Coordinate System and Data Format for Antenna Patterns," IRIG Document No. 102-61.

*Here, as in the usual antenna test range, the line OT' remains fixed relative to the earth. The coordinate system moves relative to the space-fixed line OT'.

computation of tables of the radar digital readout as a function of the θ, ϕ orientation of the mockup.*

5.2.2 Positioner

The multi-axis positioner shown in Figure 5.4 supports and orients the full-scale Gemini mockup. The positioner, which is used here in the same manner that a conventional model tower is used for supporting antenna models, is an azimuth-over-elevation-over-azimuth antenna positioner. The upper-azimuth axis is the ϕ (roll) axis, and the lower-azimuth axis is the θ axis. The elevation axis enables the ϕ and θ axes to be adjusted orthogonal, and permits the spacecraft mockup to be mounted in a vertical position for ease of installation.



Figure 5.4. Rear View of Spacecraft Mockup and Multi-Axis Positioner

In testing the Gemini radar, static measurements** are made in which the spacecraft mockup is oriented to successive positions, which are indicated to an accuracy of

*An uncertainty in the parallax calculations is theoretically caused by lack of knowledge of the location of the phase centers of the radar antennas. A similar error would be introduced by the uncertainty in axial location of the phase center of the source antenna, however this source of error can be eliminated by squinting the antenna to direct its beam axis toward the radar antennas, and, in any event, both parallax errors are small.

**A preliminary design study is being conducted to determine specifications for equipment modifications to permit dynamic accuracy measurements under conditions of controlled acceleration and velocity of the mockup.

0.01 degree, and the radar digital readout is compared with the calculated values. To facilitate making these measurements, the positioner is controlled by a high-performance two-channel servo system with independent operation of the θ and ϕ axes.

Two modes of operation of the servo system are provided, a rate mode and a position mode. In the rate mode of operation, the θ and ϕ axes of the positioner are driven at constant rates as set by individual rate controls. Antenna patterns may be recorded in the conventional manner in this mode. In the position mode of operation, the positioner is servo-driven to manually set angles of orientation. The θ, ϕ command angles and the digital readout of positioner orientation are displayed on direct-reading counters having a resolution of 0.002 degree. The high resolution of the positioning servo system makes it possible to position the spacecraft mockup smoothly to within a few thousandths of a degree.

In addition to the manual control capabilities, the positioner can be program-controlled to automatically generate a series of ϕ cuts for examining the characteristics of an antenna over the sphere of radiation.

5.2.3 Alignment of Coordinate Systems

The Z and Z' axes* are brought to within 0.1 milliradian of coincidence by means of a precision clinometer. The coordinate system is defined to measure θ from the Z axis to the line OT. The line OT is defined as the line joining the origin O with a surveyed point T on the range surface directly beneath the center of the source antenna. The θ-readout counter is set to zero when the Z-axis is aligned with OT. Alignment of the Z-axis and the line OT is accomplished by the optical reflection procedure illustrated in Figure 5.5. The line OT is referred to as the optical boresight.

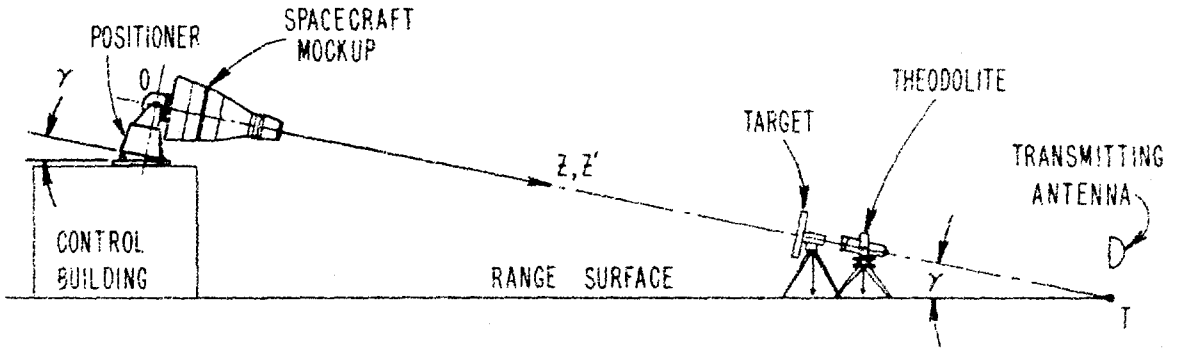

Figure 5.5. Illustration of the Optical Reflection Technique for Aligning the Z and Z' Axes with the Line OT

*The Z' axis is defined by a line passing through a reference point on the radar ground plane and normal to a plane which is defined by three flats on the ground plane.

In this procedure, an optically flat 4-inch diameter mirror is mounted on a fixture in front of the radar with the surface of the mirror parallel to the surface of the radar ground plane. A theodolite and target are located at surveyed bench marks such that the optical axis of these instruments is aligned with OT'. The distance from the origin O to the target is approximately 858 feet; this distance places the target and theodolite at a convenient eye level.

The positioner is oriented to center the target in the mirror, and the spacecraft mockup is then rolled to detect any misalignment of the Z and Z' axes. If required, the positioner can be reoriented slightly so that the center of the target rotates about the center of the mirror as the mockup is rolled. This procedure precisely aligns the Z axis with the line OT.

The direction to the source of radiation is defined by the line OT'. It is necessary to bring OT and OT' into coincidence, since T' is not necessarily located on the range surface but at a height h, approximated by equation (9). Because of extraneous reflections and other measurement errors, the location of T' cannot be determined as a unique point, but as the center of a small region of uncertainty. The direction OT' is measured by the interferometer procedure* using the interferometer which has a resolution of about 0.1 milliradian, or the radar, which has a resolution of approximately 0.8 milliradian. The line OT' thus defined is aligned with OT either by moving OT' into coincidence with OT or by moving the Z axis into coincidence with OT' with the 0 readout counters set to zero. OT can be changed by varying the elevation squint angle of the transmitting antenna; the Z axis can be changed by tilting the positioner with the mechanism provided for this purpose.

It is planned to supplement the optical boresight alignment system with one in which a television camera with a telescopic lens is mounted in the front of the spacecraft mockup and aligned optically with the surveyed point T, using the previously described optical boresight procedure to establish an accurate reference. This system will provide a convenient monitoring capability for frequent checks of the boresight reference.

5.3 Transmitting Equipment

The transmitting equipment furnished for the radar boresight range includes signal sources, antennas, and associated equipment, antenna positioning equipment, and equipment for making polarization adjustments. All of the transmitting equipment is controlled remotely from the operating console.

The wooden source tower shown in Figure 1.1 was designed to permit antenna impedance, radio interference, and Gemini and Agena RF compatibility measurements to be made. The antenna positioner, shown in Figure 5.6, is raised by means of a hoist

*See paragraph 6.3.

controlled from the operating console to the proper height for ground-reflection range operation, or to the top of the tower for operation of the range as an elevated range. The antenna positioner provides for ±4.5 degrees of azimuth and elevation motion of the transmitting antenna and for rotation about the axis of the antenna.

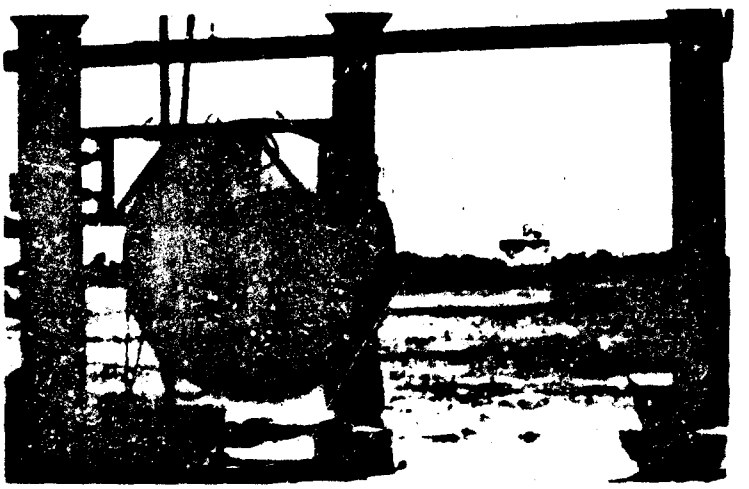

Figure 5.6. Transmitting Antenna, Positioner, and Hoist Viewed Looking Toward the Control Building

The circularity of the received field is adjusted remotely by varying the relative amplitude and phase of the orthogonal components of the transmitted field. This capability makes it convenient to obtain polarization data on the range characteristics or the system under test. For example, the circularity of the received field can be changed to determine the sensitivity of the rendezvous radar to polarization changes.

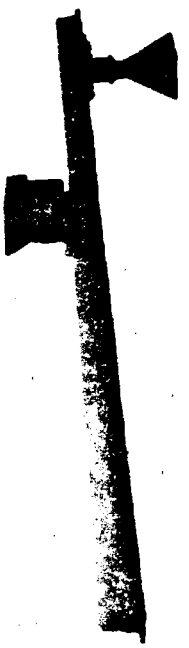

5.4 Receiving and Recording Equipment

Antenna-range receiving and recording instruments include a 20-Mc to 100-Gc wide-range receiver, rectangular- and polar-coordinate antenna pattern recorders, and a radiation distribution printer.*

Field probes are provided for sampling the incident RF field in front of the spacecraft mockup. The aperture field probe is shown in Figure 5.7; the horn antenna is mounted on a small remotely controlled carriage. With this device mounted on the front of the spacecraft mockup, the field amplitude distribution can be determined over a 16-foot diameter aperture.

Figure 5.7. Aperture Field Probe with Horn Antenna Mounted on Carriage

*An instrument for numerically recording the relative antenna gain in decibels as sampled at discrete angular increments in θ and ϕ. See L. Clayton and J. S. Hollis, Polarization Analysis by Measurement of Multiple Components, 13th Annual Symposium. USAF Antenna Research and Development Program; October 14-18, 1963.

The polarisation probe is shown in Figure 5.8 mounted on the front section of the spacecraft mockup. The polarization positioner can be mounted on the aperture field probe as shown in Figure 5.9 to permit measurements of polarization over the test aperture.



Figure 5.8. Polarization Probe Mounted on Spacecraft Mockup. The rendezvous radar is not shown in this photo.

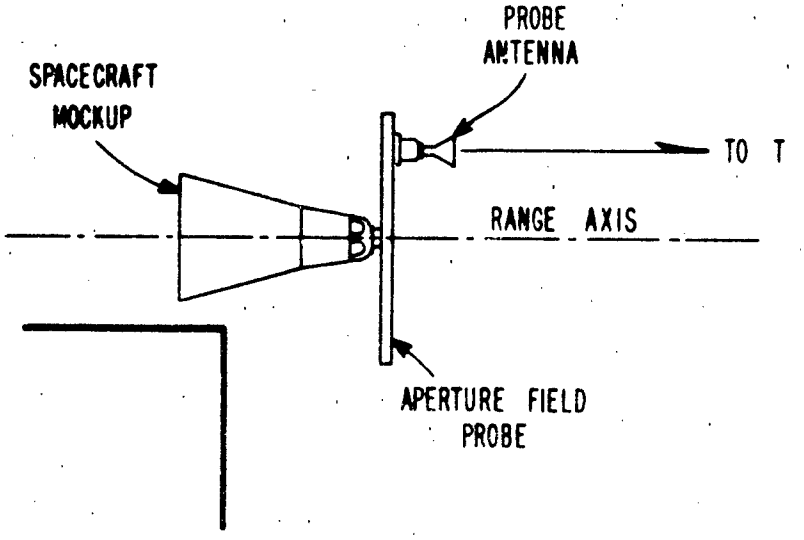

Figure 5.9. Illustration of the Use of the Polarization Probe to Obtain Polarization Patterns as a Function of Position in Test Aperture

6. MEASUREMENTS

6.1 Introduction

A field trip was made to validate the range in the ground-reflection mode for making acceptance measurements of the rendezvous radar boresight accuracy. To determine the performance of the range measurements were made (1) of the amplitude and polarization of the incident field over the test aperture, and (2) of the specific capability of the range for making boresight measurements. Samples of the data are presented in the following paragraphs.

While indicative of the performance of the range at L-band, the measurements are in no sense comprehensive and, in fact, raise many questions concerning the detailed mechanism of the range operation which are worthy of investigation and for which the instrumentation is already provided. Because the measurements to determine the boresight capability of the range are somewhat unusual, the procedure used in making the measurements is described in some detail.

6.2 Aperture-Field Measurements

6.2.1 Amplitude

Field patterns were recorded over a 16-foot diameter aperture in front of the spacecraft mockup employing the aperture probe shown in Figure 5.7. The probe was mounted to the front of the mockup and parallel with the pitch axis. Measurements were made with the mockup oriented at zero degrees in θ; the mockup was rolled to successive ϕ angles, and the field was explored by moving the sampling antenna radially across the center of the aperture.

A linearly polarized horn antenna with a gain of about 15 decibels and with 30-degree beamwidths was mounted to the probe carriage. The purpose of using a relatively high-directivity antenna was to minimize the effect of reflections from the probe-support structure and spacecraft mockup to give a measure of the incident field. The relative position of the horn on the carriage was adjusted for each ϕ angle to obtain patterns of the vertical and horizontal polarization components as a function of radial distance from the roll axis. Aperture field patterns are given in Figure 6.1.

Figures 6.1(a) and 6.1(b) are patterns of the vertical and horizontal polarization components as a function of vertical position in the aperture. From equation (8), the calculated height h_1 of the transmitting antenna which produces an interference maximum at the center of the receiving aperture is 5.75 feet. The corresponding

height of the transmitting antenna was determined experimentally to be approximately 5.1 feet. For these patterns the elevation squint angle of the transmitting antenna was −0.5 degree (down). It was found that the height of the interference maximum does not vary appreciably with small changes in elevation squint angle, indicating that the phase of the far-zone pattern of the transmitting antenna is relatively constant with elevation angle. Additional measurements are required to explain the difference between the height h_1 calculated by the simplified theory leading to equation (8) and that determined experimentally.

It is seen that the peak of the interference pattern for the horizontal component is approximately 1 foot lower than that of the vertical component. The height of the transmitting antenna could be readjusted for a best compromise for the two polarizations, although from a practical viewpoint this is a finer adjustment than is likely to be necessary.

The shapes of the vertical patterns are in virtual agreement with those predicted by equation (6) and Figure 4.2. The vertical taper of the field is approximately 0.25 decibel in 10 feet, which is the maximum diameter of the spacecraft. Because of the small difference in the height of the horizontal and vertical polarization maxima, the total vertical taper is approximately 0.35 decibel.

Figures 6.1(c) and 6.1(d) are patterns of the vertical and horizontal polarization components as a function of horizontal position in the aperture. The amplitude taper in the horizontal plane is a function of the beamwidth of the transmitting antenna. The horizontal dimension of the aperture represented by the mockup is 10 feet when the mockup is oriented to zero degrees in θ and increases to approximately 19 feet as the mockup is positioned to the specified limits in θ. Under these conditions the transmitting antenna beamwidth is sufficient to provide an illumination taper of less than about 0.25 decibel.

The vertical and horizontal field patterns provide an indication of the proper adjustment of the height and squint angles of the transmitting antenna, and confirm that the range operates in general accordance with the theory discussed in Section 4. The smoothness of the patterns indicates virtual freedom of interference from objects which are within the directivity pattern of the probe horn. The high degree of suppression of extraneous reflections required for the boresight measurement problem dictates a measurement technique of greater sensitivity and accuracy, as discussed in paragraph 6.2, to determine the range capabilities for this application.

6.2.2 Polarization

Polarization patterns of the incident field were made with the polarization probe shown in Figure 5.7. The linearly polarized probe antenna shown in this photograph

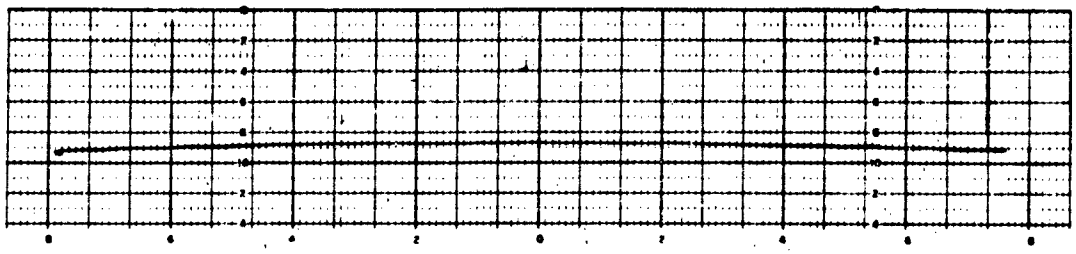

(a) Vertical Pattern, Vertical Polarization

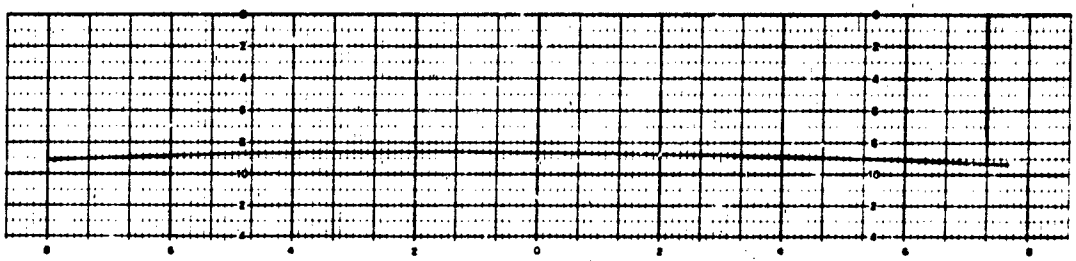

(b) Vertical Pattern, Horizontal Polarization

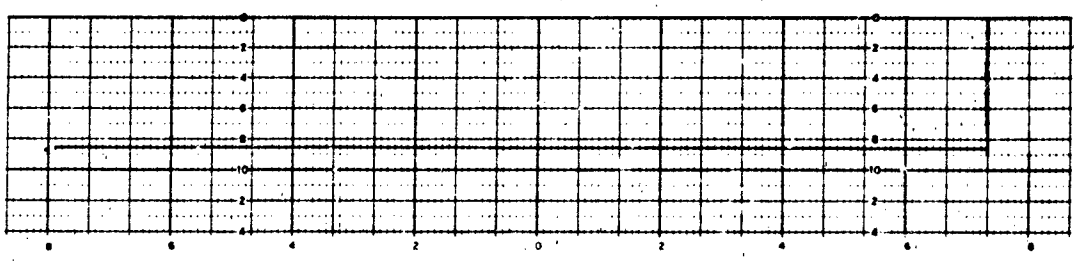

(c) Horizontal Pattern, Vertical Polarization

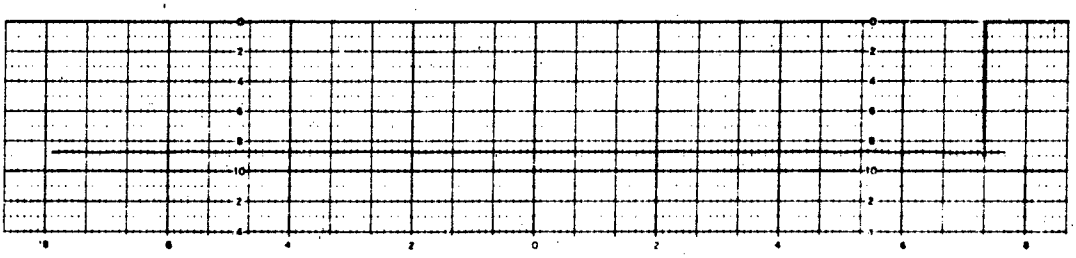

(d) Horizontal Pattern, Horizontal Polarization

DISTANCE FROM CENTER OF APERTURE (FEET)
(DOWN, LEFT) (UP, RIGHT)

Figure 6.1. Aperture Field Patterns

was employed for these measurements. The circularity of the incident field at the center of the test aperture was adjusted from the operating console by varying the relative amplitude and phase of the vertical and horizontal field components of the source antenna. This adjustment capability permits compensation for the difference in reflection coefficient of the range surface for the horizontal and vertical field components and permits measurements to be made of the sensitivity of the measured boresight direction to the polarization of the incident field. The polarization pattern shown in Figure 6.2 illustrates that the axial ratio can be adjusted to less than 0.1 decibel at a given position in the test aperture.

Figures 6.3 and 6.4 indicate the range of adjustment provided by the circularity control unit. Figure 6.3 is a family of polarization patterns with relative amplitude as a parameter. The relative phase between the orthogonal components is approximately 90 degrees.

Figures 6.4(a) and 6.4(b) are polarization patterns recorded as a function of the relative phase angle between orthogonal field components. Figure 6.4(a) is recorded in decibels; Figure 6.4(b) is a linear voltage recording for approximately the same phase variations.

The circularity control unit may be employed to obtain precise linear polarization of the incident field after insertion of a fixed phase delay to increase the range of adjustment. The patterns of Figure 6.4 degenerate into the linearly polarized patterns shown in Figure 6.5 with a tilt angle of 45 degrees as the relative phase goes to zero. The linear-voltage pattern of Figure 6.5(b) has the predicted classic shape of two tangent circles. The tilt angle of the incident field can be set by rolling the transmitting antenna about the axis of the beam.

The axial ratio of the incident field at the center of the test aperture as a function of frequency is given in the graph of Figure 6.6. The change in axial ratio is probably caused by amplitude and phase changes in the circularity control circuits of the transmitting antenna. The change is negligible over the operating range of the Gemini rendezvous radar.

Polarization patterns as a function of position in the receiving aperture were recorded by mounting the polarization probe on the aperture field probe as illustrated in Figure 5.9. Axial ratio as a function of vertical and horizontal position in the aperture is given in Figure 6.7. These patterns were recorded after adjustment of the circularity at the center of the test aperture and without changing the transmitting antenna squint angles.

The variation in axial ratio with horizontal position in the test aperture is largely caused by the off-axis depolarization characteristics inherent in the paraboloidal

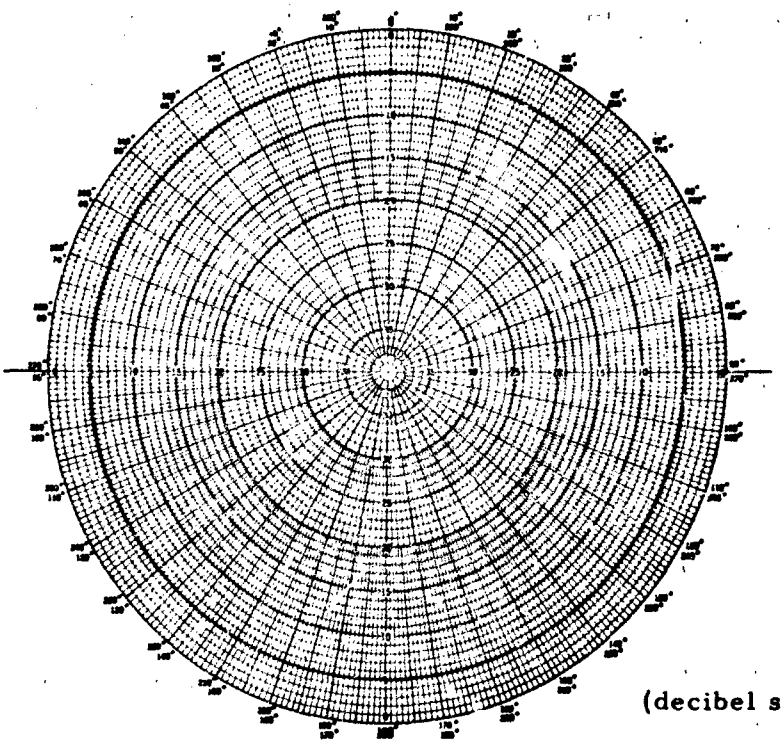

Figure 6.2. Polarization Pattern Measured at Center of Test Aperture

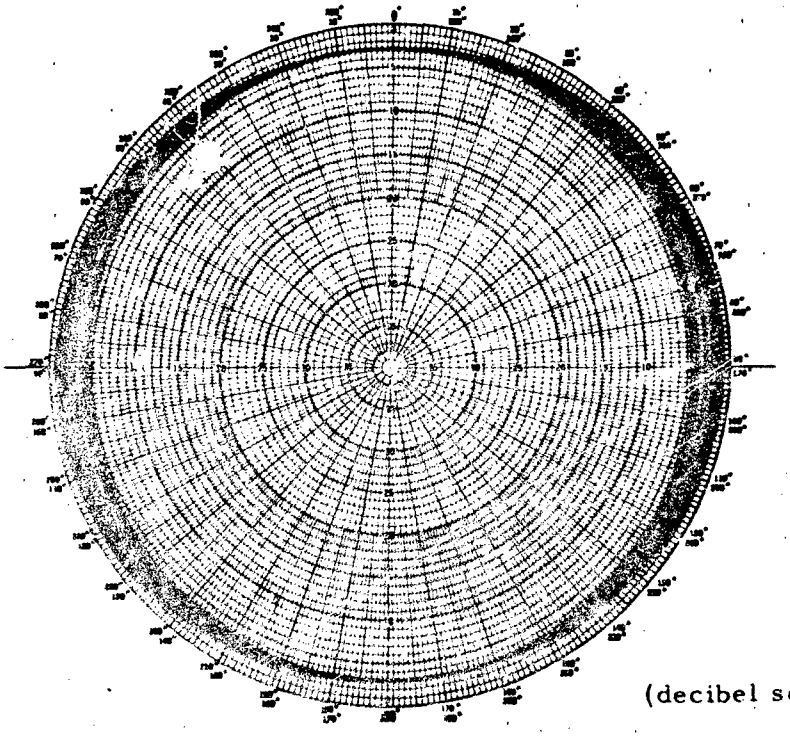

Figure 6.3. Family of Polarization Patterns as a Function of Relative Amplitude of Orthogonal Field Components

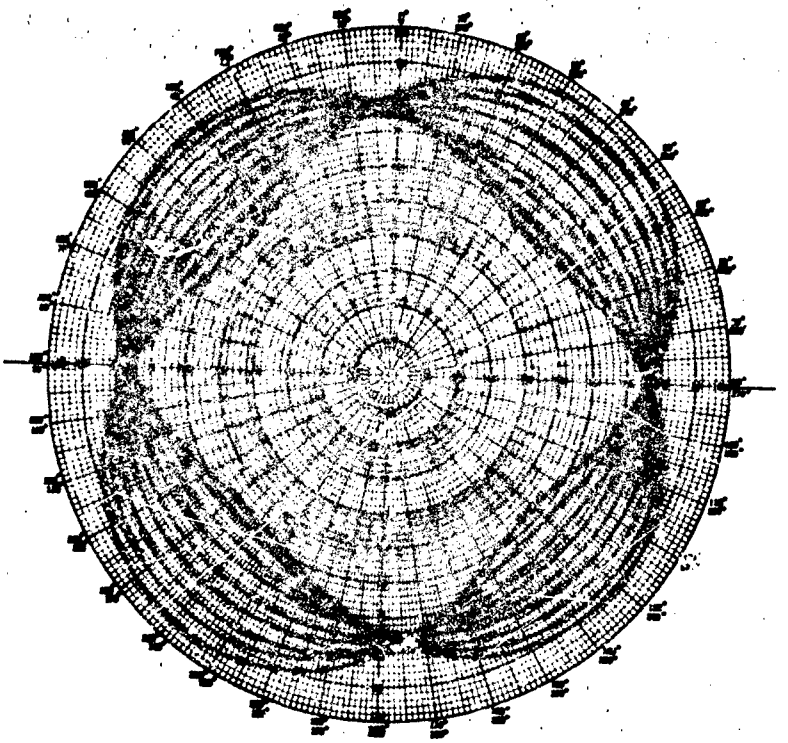

(a) Decibel Scale

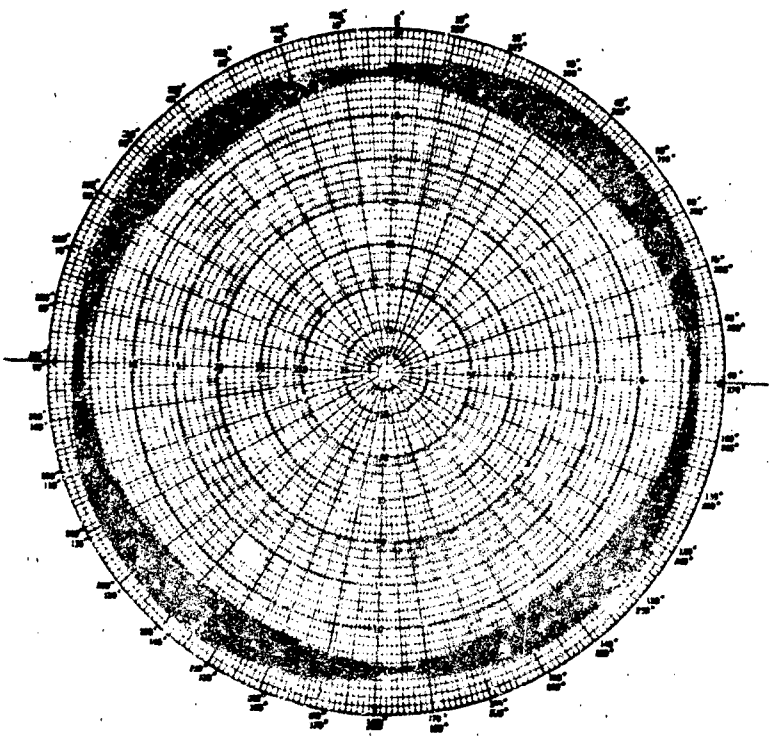

(b) Linear-Voltage Scale

Figure 6.4. Family of Polarization Patterns as a Function of Relative Phase Between Orthogonal Field Components

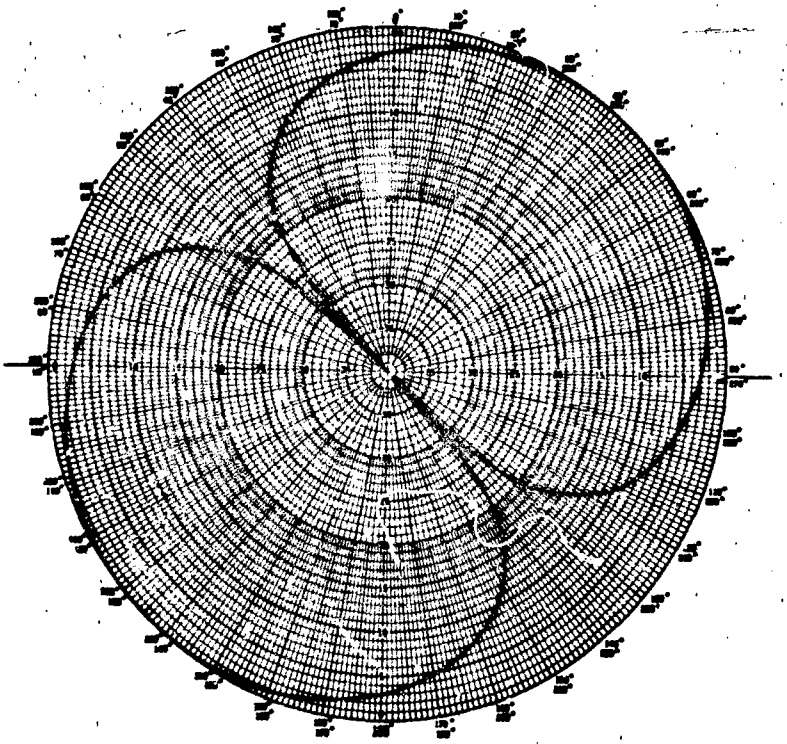

(a) Decibel Scale

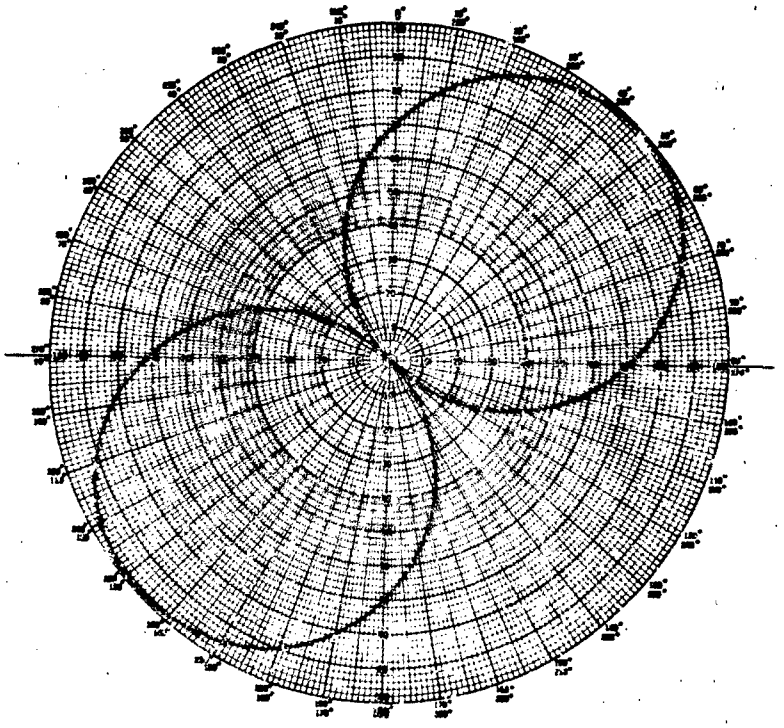

(b) Linear-Voltage Scale

Figure 6.5. Polarization Pattern of Linearly Polarized Field

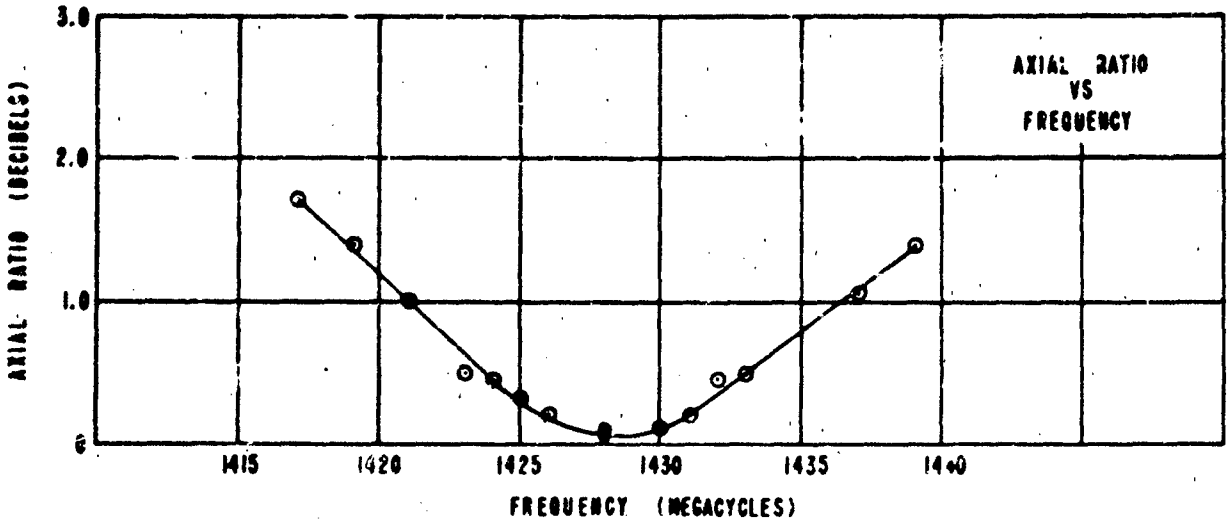

Figure 6.6. Axial Ratio as a Function of Frequency

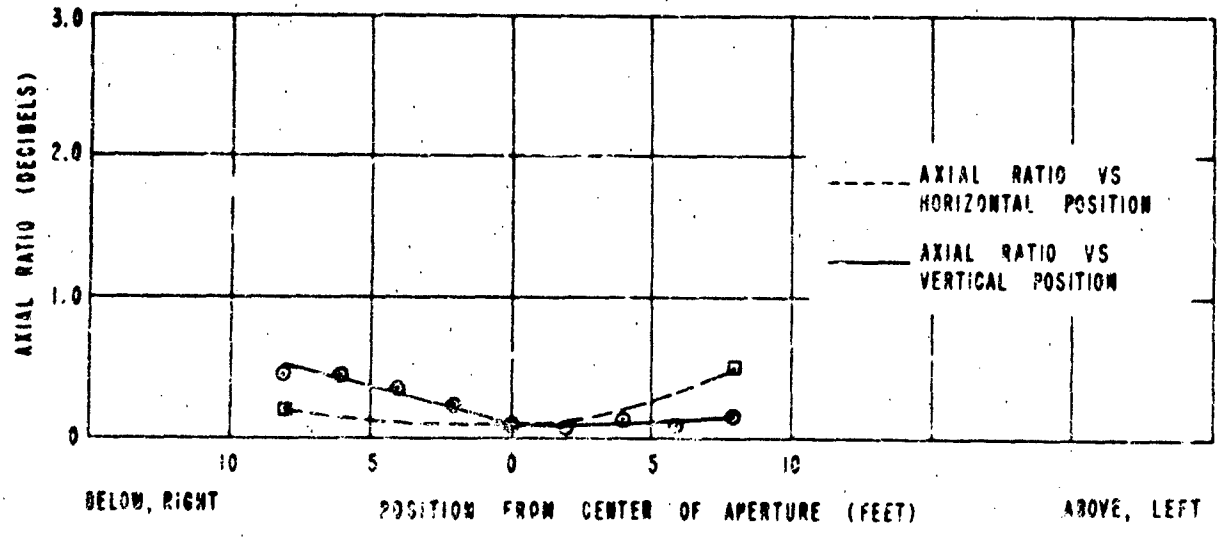

Figure 6.7. Axial Ratio as a Function of Position in the Aperture

transmitting antenna. A less directive transmitting antenna would result in both a smaller variation in axial ratio and a smaller taper of the field amplitude with horizontal position, but would increase the susceptibility to extraneous reflections. The directivity employed appears to be a reasonable compromise.

6.3 Boresight Measurements

6.3.1 Discussion of the Measurement Problem

To determine the boresight measurement capability of the range, it is necessary to measure the direction of arrival and purity of the phase front of the incident field. The measurements must be made either with a device that does not perturb the incident field or with a measuring technique that is not affected by reflections from the test device. Furthermore, these measurements must be made under conditions that simulate the specific boresight measurement problem. High-directivity antennas cannot be employed in the measuring device because their directivity would discriminate against wide-angle reflections to which the radar is sensitive.

Direct measurement of incident-field phase over the aperture to the required accuracy was considered impractical because of probe-structure reflections and mechanical limitations. It was decided to employ an interferometer with radiation characteristics similar to those of the radar to determine the direction to the apparent source in a manner that cancels errors caused by reflection of energy from the probe-support structure. The spacecraft mockup was employed to support the interferometer so that double-bounce reflections between the support structure and fixed objects would be taken into account, and so that the same degree of shielding of the test positioner which exists during radar boresight measurements would be provided.

6.3.2 Principle of Operation of the Interferometer

The interferometer functions in the manner of the Gemini rendezvous radar to produce nulls in the two interferometer channels which are determined by

(a) the angles of rotation of the azimuth and elevation spirals relative to the reference spiral,

(b) the circuit phase delays of the azimuth and elevation channels, and

(c) the direction to the source of radiation.

A block diagram of the interferometer is given in Figure 6.8. The ground plane and spiral antennas are identical with those of the Gemini rendezvous radar. Rotation of the azimuth and elevation antennas and control of the variable attenuators is

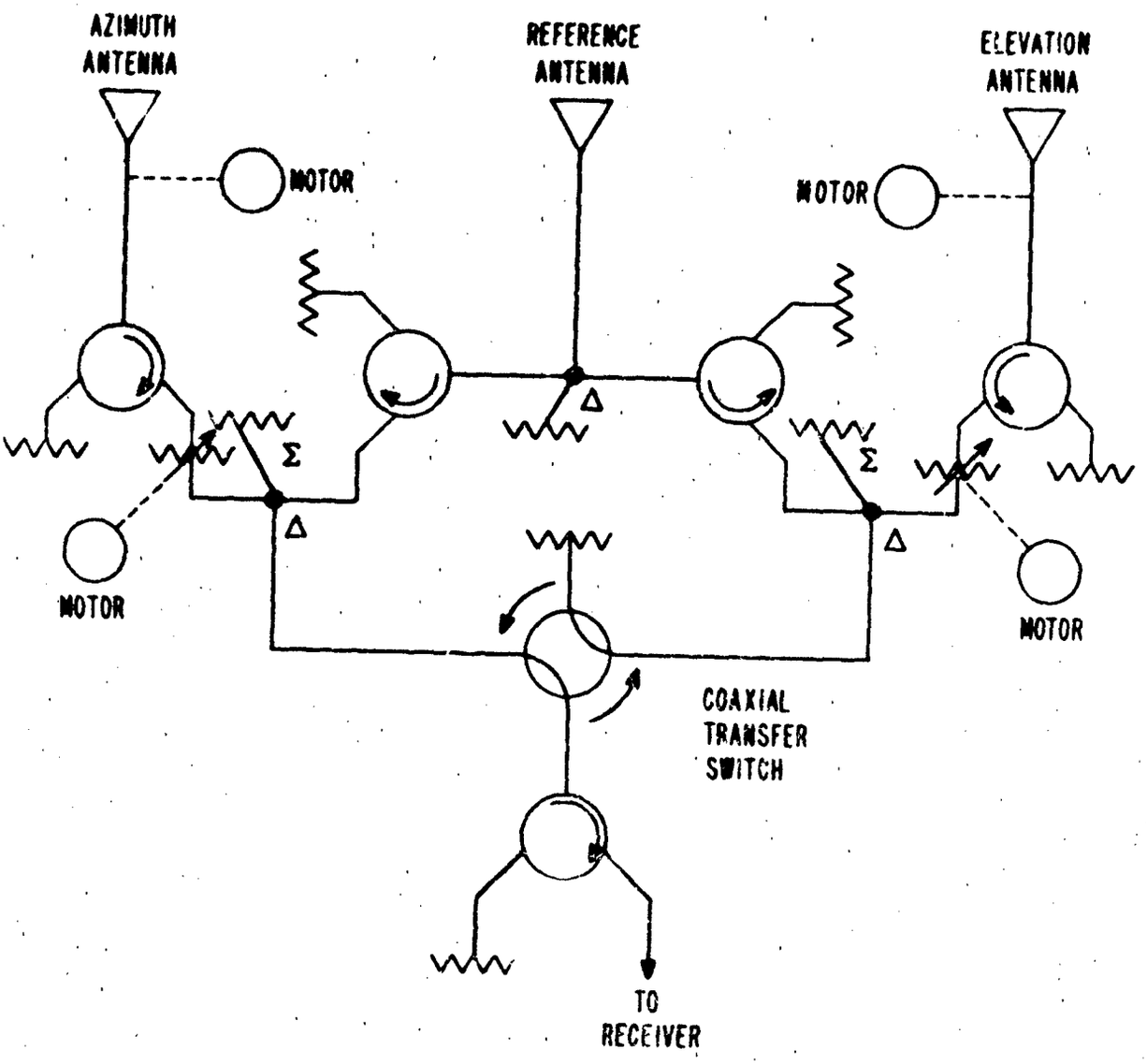

Figure 6.8. Block Diagram of Interferometer

effected from the operating con. ' to obtain a null in each channel. Readout of the rotation of the spiral antennas is not provided; instead, the direction of arrival of the incident field is determined by the following procedure.

(a) From Figures 5.3 and 6.9 it is seen that the line OT is identically located relative to the spececraft under two sets of conditions: (1) with the spacecraft mockup rotated clockwise about the θ axis to a position θ, ϕ, and (2) with the mockup rotated counterclockwise about the θ axis and rolled 180 degrees in ϕ to the same position θ, ϕ. The position in the latter case is identified by the underscored symbols $\underline{\theta}, \underline{\phi}$.

(b) The relationship of the line OT to the mockup is unchanged under the two conditions described in (a), but the mockup is inverted and changed in position relative to earth-fixed objects. The source of radiation T' is earth-fixed relative to T and therefore moves in the space-fixed coordinate system to the position $\underline{T'}$ as illustrated when the positioner is rotated to $\underline{\theta}, \underline{\phi}$.

(c) If T' is located at T, and if the interferometer is nulled with the mockup positioned to a given θ, ϕ orientation, a null will also exist when the mockup is rotated counterclockwise about the θ axis to the identical $\underline{\theta}, \underline{\phi}$ orientation.

(d) If T' is not coincident with T, the location of T' can be determined by nulling the interferometer at a given θ, ϕ orientation and, without changing the electrical adjustment, positioning the mockup to a direction $\underline{\theta}, \underline{\phi}$ which nulls both channels. This procedure moves $\underline{T'}$ to its original location T' in the space-fixed coordinate system. The location of T' relative to T can be calculated from the measured θ, ϕ and $\underline{\theta}, \underline{\phi}$ angles.

Reflections from the spacecraft mockup do not introduce measurement errors because the spacecraft illumination is identical for the two null conditions. In addition, the interferometer absolute accuracy is not a factor because the interferometer adjustment is unchanged during the course of a measurement.

The interferometer method described measures the direction of OT' but does not provide information concerning the distance OT'. The direction OT' is defined by the mirror symmetry of the incident field for the clockwise and counterclockwise θ orientations. Discussions referring to the location of the apparent source are made on the assumption that the center of phase lies in the plane of the source antenna.

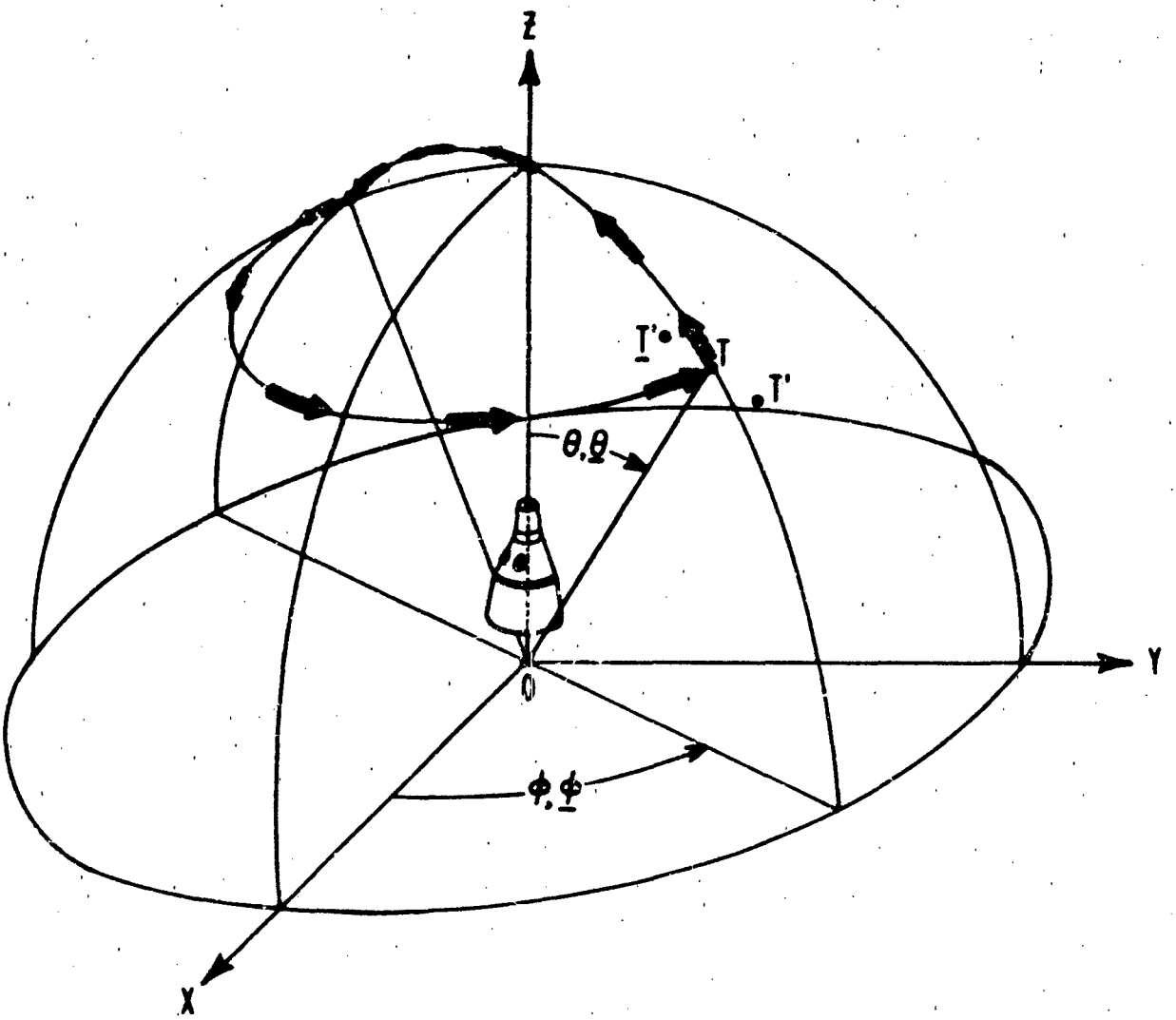

Figure 6. 9. Illustration of the Method Employed for Positioning the Spacecraft to Obtain Two Identical Orientations of the Spacecraft Relative to OT

6.3.3 Practical Considerations

The process of positioning the mockup to obtain nulls in both interferometer channels simultaneously as described in paragraph 6.3.2 is time-consuming. Therefore, the procedure illustrated by Figure 6.10 was employed in which the two interferometer channels are nulled independently. The spacecraft mockup is positioned about the roll axis to orient the antennas horizontally and vertically.

One interferometer channel is employed for azimuth measurements and the other for elevation measurements. The interferometer is nulled for the direction OT' for the clockwise orientation of the θ axis as in paragraph 6.3.2. For the counter-clockwise orientation, azimuth nulls are obtained by rotation through $\Delta\theta$; elevation nulls are obtained by rotation in elevation through ΔE by means of the elevation axis of the positioner, indicated in Figure 6.10. It is seen that OT' is located relative to OT by azimuth and elevation angles $(\Delta\theta)/2$ and $(\Delta E \cos\theta)/2$, respectively.

The effect of extraneous reflections from sources external to the spacecraft mockup is to cause scattering of the measured location of the apparent source as test conditions such as the position of the spacecraft are changed. The magnitude of the effect of extraneous reflections on the measured boresight direction is discussed in paragraph 3.1. It should be noted that the interferometer measurement method is sensitive to at least the following error sources in addition to errors from extraneous reflections.

(a) spacecraft positioner and angle-readout errors,

(b) coordinate system misalignment,

(c) frequency drift,

(d) amplitude and polarization variations of the incident field,

(e) RF leakage into the interferometer circuits, and

(f) interferometer changes caused by gravity.

The measurement procedure requires that the mockup be rolled 180 degrees in moving from θ, ϕ to $\underline{\theta}, \underline{\phi}$, and, therefore, the measurements are sensitive to effects of gravity. For example, loose cables behind the interferometer panel which can change in position as the mockup is rolled can cause large errors by introducing a different field perturbation for the two opposite orientations of the interferometer. Furthermore, the interferometer-measurement procedure provides a means for testing the radar for errors caused by rolling the mockup. It was found during range tests that an error of a few tenths of a milliradian was introduced by the deflection of shock mounts on which the interferometer was mounted.

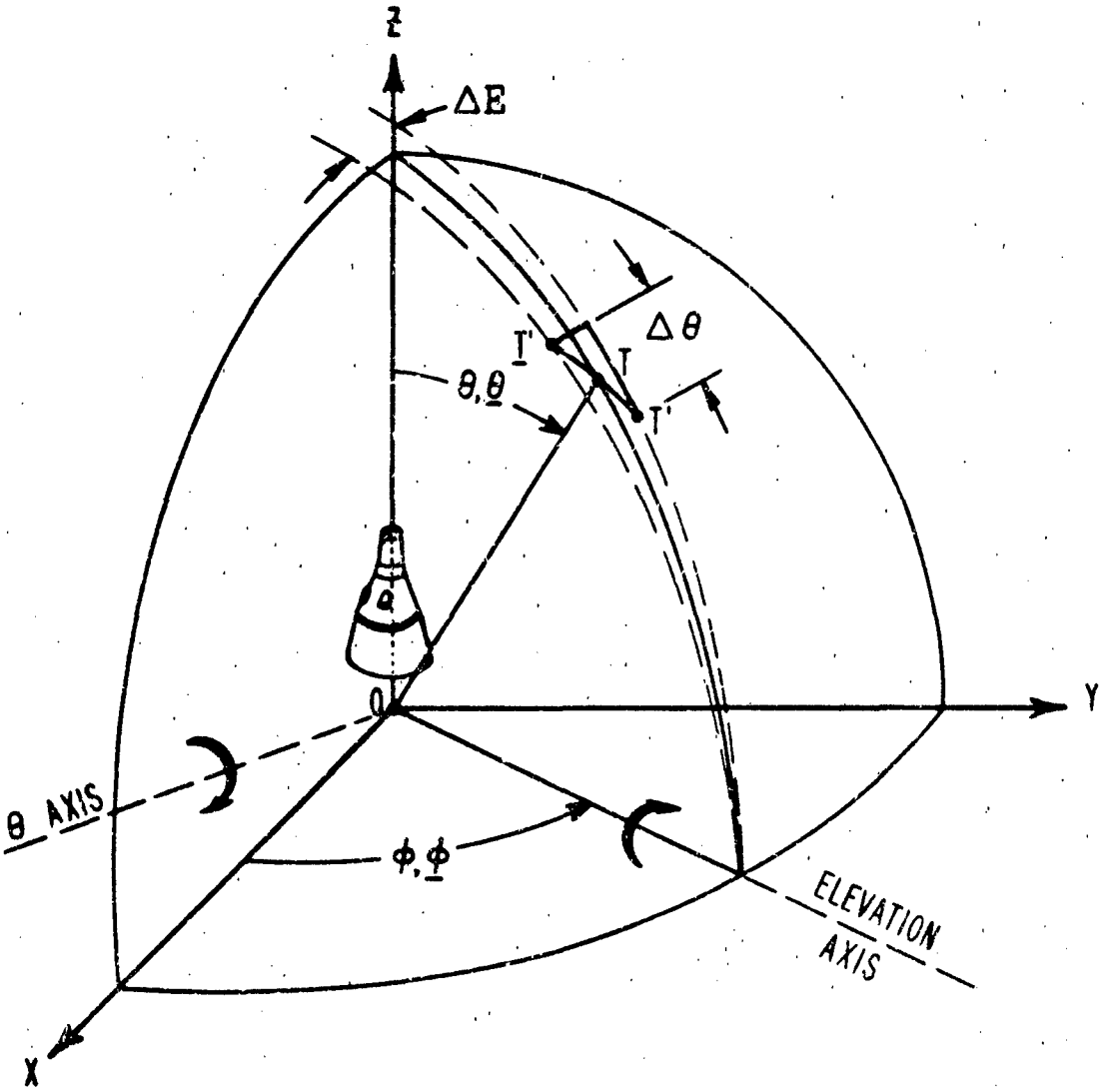

Figure 6.10. Illustration of the Method Employed for Positioning the Spacecraft Mockup to Make T' Coincident with T'

In making the measurements which are presented in the following paragraphs, it was necessary to exercise extreme care in each of the items listed above.

6.3.4 Interferometer Test Results

Figure 6.11 is a scatter plot of the measured azimuth of the apparent source of radiation as a function of θ over the range of 0 to 25 degrees. The data were taken over a period of several days and were made in conjunction with apparent-height measurements.

The measured data show a counterclockwise bias of about 0.35 milliradian and a total scatter of about 0.55 milliradian from the mean. The indicated bias is probably a result of an initial optical boresight error which occurred prior to refinement of the optical boresight procedure. The azimuth error appears to be independent of θ.

Figure 6.12 shows curves of the measured height of the apparent source as a function of θ for an elevation squint angle of −0.5 degree. The measurements were made under a number of different conditions and over a period of several days. After curve (1) was made the coordinate system alignment was checked and the optical boresight tests were repeated before taking the data represented by the remaining curves.

From the data presented, the mean elevation of the apparent source is 0.35 milliradian above the range surface and the maximum error from the mean is 1.17 milliradian. However, it is felt that curve (1) is not representative of the range capabilities because of misalignment errors and, excluding curve (1), the data indicate a mean elevation of 0.25 milliradian above the range surface and a maximum error of 0.55 milliradian from the mean.

The interferometer elevation channel was employed for curves (1) and (2) and the azimuth channel was employed for the remainder of the curves by rolling the spacecraft mockup 90 degrees in ϕ.

For curves (5) and (6) the transmitting antenna was squinted in azimuth to direct the axis of the beam toward the interferometer. From these curves there appears to be a slight improvement from squinting the source antenna, although the effect was not noticed in the azimuth tests.

Figure 6.13 is a graph of the measured height of the apparent source as a function of the elevation squint angle of the source antenna. The dashed curve was calculated from equation (9) on the assumption of a $(\sin x)/x$ radiation pattern with a 3-decibel elevation beamwidth of 5 degrees and unity reflection coefficient at the range surface. It is seen that the measured data are in general agreement with the calculated data.

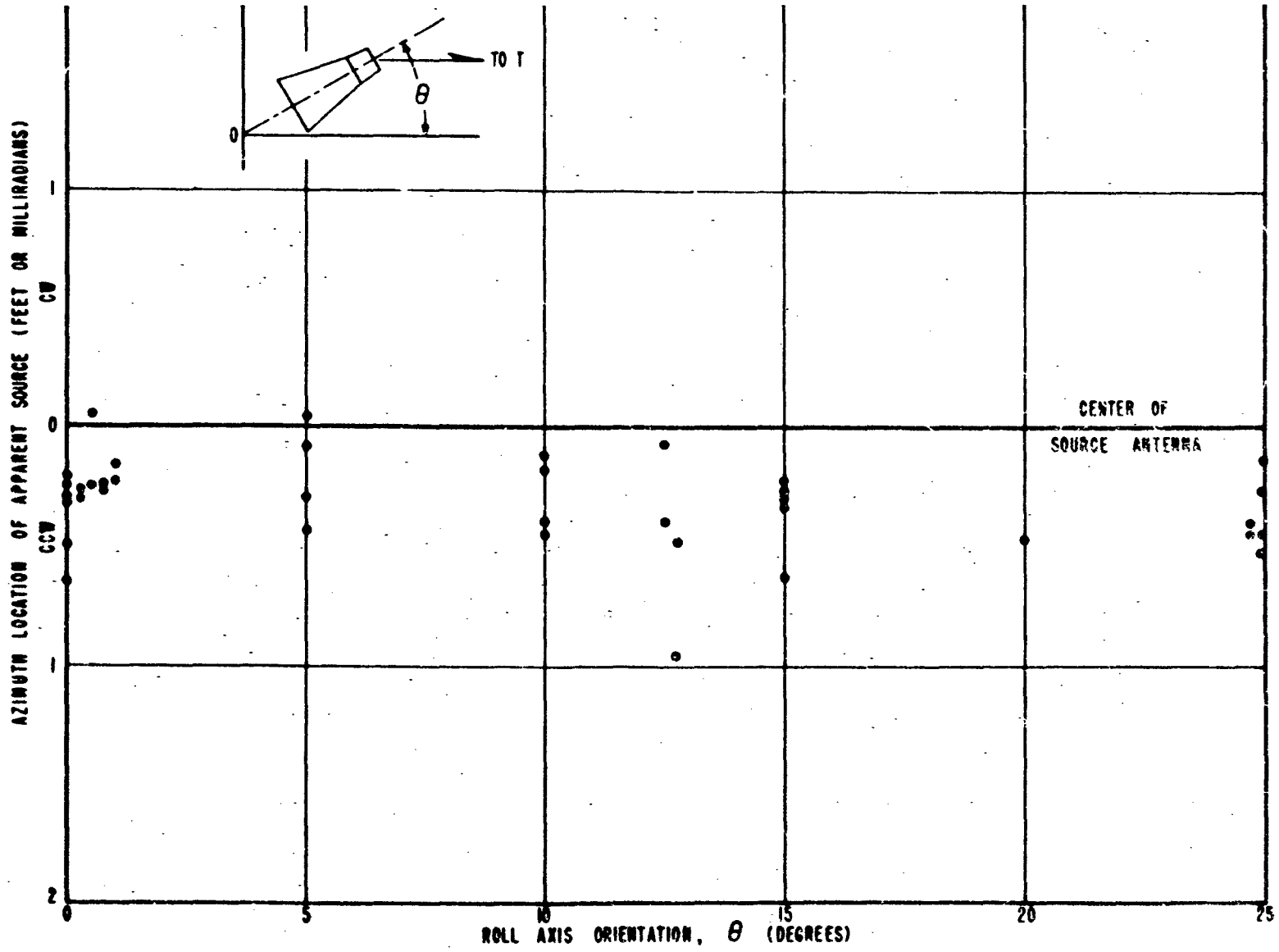

Figure 6.11. Measured Azimuth of the Apparent Source Versus θ at L-Band

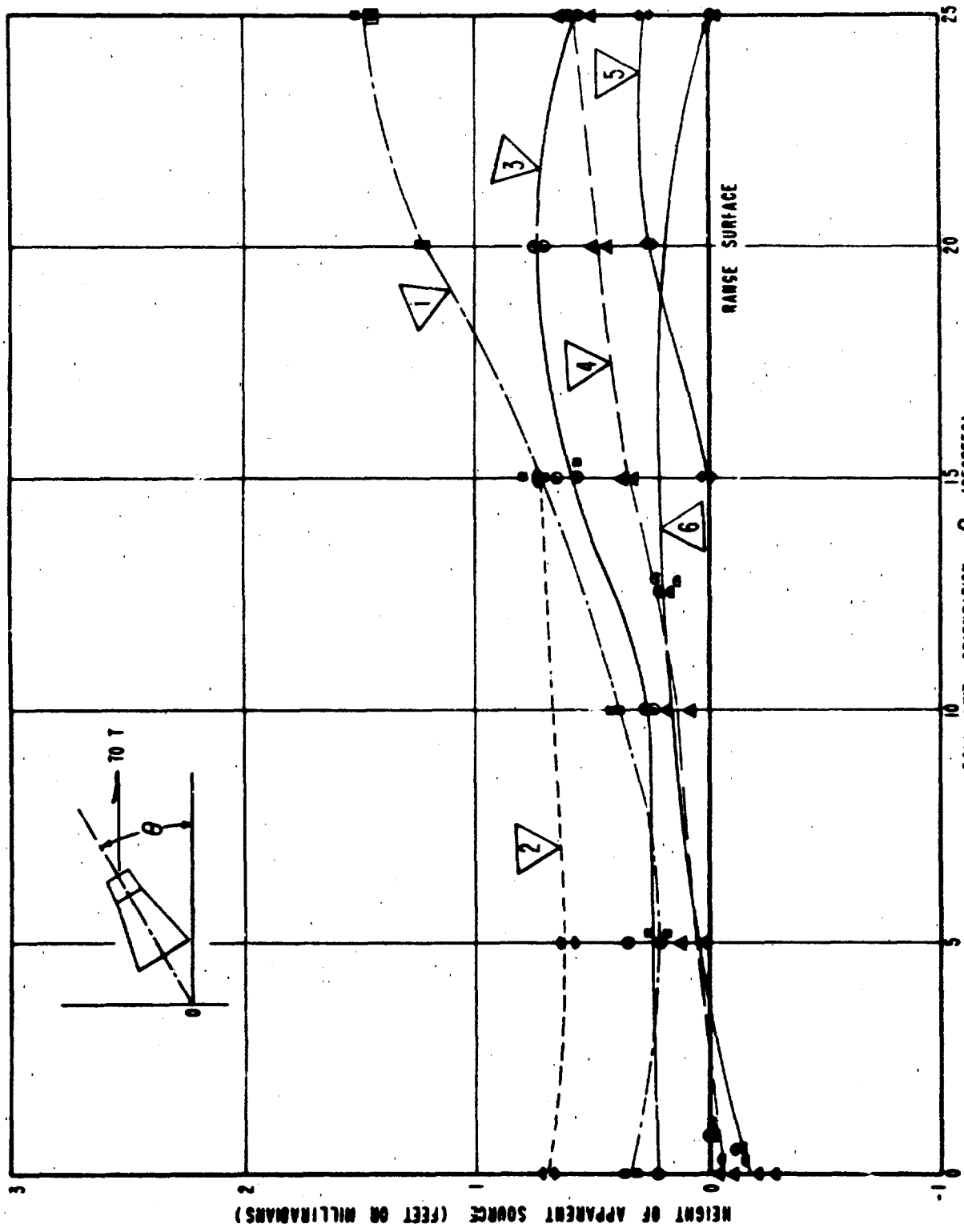

Figure 6.12. Measured Height of the Apparent Source Versus θ at L-Band
The transmitter elevation squint angle is −0.5 degree.

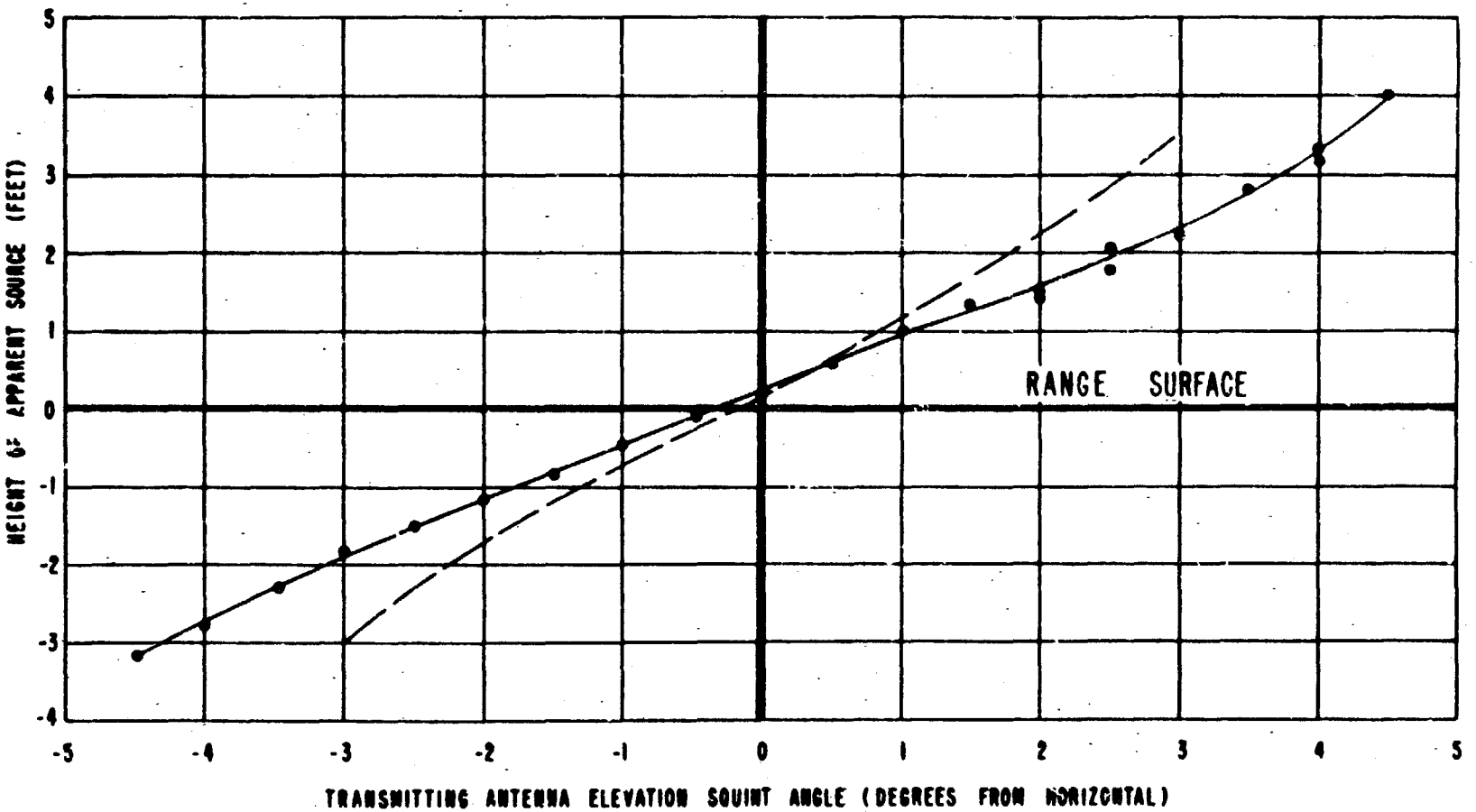

Figure 6.13. Height of Apparent Source as a Function of Transmitting Antenna Squint Angle. The dashed curve was calculated from equation (9).

Furthermore, the smoothness of the experimental curve indicates the high accuracy capability of the interferometer technique.

7. SUMMARY

Measurement of the Gemini radar boresight accuracy required development of a test range with suppression of extraneous signals on the order of 60 decibels, establishment of a circularly polarized incident field with low axial ratio and amplitude taper over the active aperture of the spacecraft mockup, and provision for precise positioning of the mockup. Careful design and construction of the ground-reflection range resulted in a low level of extraneous reflections. Aperture amplitude and polarization test probes provide an indication of the proper adjustment of the incident field. A precision multi-axis positioner, controlled by a high-performance servo system, supports and positions the spacecraft mockup with positioning and readout accuracies of 0.01 degree. The accuracy of the optical boresight technique developed for aligning the coordinate system is 0.1 milliradian.

A two-channel interferometer was employed in the L-band range-validation tests to measure the direction to the apparent source and the purity of the phase front by a method which is insensitive to reflections from the probe-support structure. Tests indicate that the measurement accuracy of the interferometer is a few tenths of a milliradian. The measured scatter in the location of the apparent source was within approximately 0.55 milliradian of the mean in azimuth and elevation. The height of the apparent source measured as a function of elevation squint angle of the transmitting antenna is in general agreement with that calculated on the basis of a point source and a plane reflecting surface.

In measurements made to date, the effect of moisture on the range surface has been found to be insignificant at L-band. It is anticipated that the range will be evaluated at higher frequencies, both as an elevated range and as a ground-reflection range, and at lower frequencies as a ground-reflection range.

Experience gained in the operation of the range for preliminary tests of the Gemini rendezvous radar confirms that the range meets the design objectives and has additional merit in the rapidity with which measurements can be made and in the flexibility provided for controlled experiments.

ACKNOWLEDGEMENTS

The efforts of a number of people are gratefully acknowledged in contributing to the work described. Especially significant were the technical contributions of Dr. Lorimer Clayton and Mr. S. F. Hutchins of Scientific-Atlanta, Inc. throughout the program and the assistance of Mr. Bernard J. Geolat of McDonnell Aircraft Corp. in making the measurements.

EFFECT OF AMBIENT PLASMA ON ANTENNA BREAKDOWN AND RADIATION CHARACTERISTIC* (U)

John B. Chown** and David E. Weissman**

Most of the treatments of the attenuation experienced during reentry consider only the low-signal-level case, where the power is such that the plasma is undisturbed by the field. The purpose of this presentation, however, is to explore the nonlinear plasma effects that occur at higher power levels and ultimately limit the amount of power that can be radiated from a given antenna.

The breakdown of antennas at low pressure has been studied in the past by various investigators.[1-5] The equation that describes the breakdown mechanism for CW is:

$$\frac{\nu_i}{P} = \frac{\nu_a}{P} + \frac{DP}{(P\Lambda)^2}$$

where ν_i is the frequency of ionization per electron, ν_a is the frequency of attachment per electron, D is the diffusion coefficient, Λ is the diffusion length for the particular geometry and conditions considered. The above equation is normalized to pressure assuming $T = 273^{\circ}K$. The pressure, P, is included here as a measure of the collision frequency. The data to be presented later are given in terms of ν, the collision frequency.+

* The work described herein was supported by Sperry Gyroscope Company under BSD prime Contract AF 04(694)-330.

** Stanford Research Institute, Menlo Park, California.

+ ν for elevated-temperature air is assumed to be $4 \times 10^{10} \sqrt{T}$.

The right side of the above equation represents the loss of electrons by attachment and diffusion respectively, while the left side is the production rate of electrons due to the presence of the RF field.

A series of measurements has been made using a low-pressure flame to determine the effect of incident power level on the power radiated from a slot antenna submerged in an ionized medium. Data were obtained at several different collision and plasma frequencies.* The *L*-band slot antenna used in the tests is shown in the low-pressure vessel (Fig. 1). The slot-backing cavity was filled with Teflon and a thin alumina window used as a pressure seal. A thin plasma layer of thickness (d) was produced over the slot surface, using a potassium-seeded ethylene-oxygen flame. The carbon burning chamber and thin slit through which the thermally ionized gas passes is visible below the antenna. The plasma thickness was such that $d \ll \lambda$, a condition that is similar to the plasmas existing about slender re-entry bodies. Visible also in the low-pressure chamber is a movable unbalanced ion probe, used to obtain the plasma-density profiles.

Figure 2 presents the power required for breakdown as a function of collision frequency ν. The top curve indicates the breakdown power level for free diffusion D_f and the lower curve for ambipolar diffusion (ν_a).** In the breakdown process, the diffusion loss mechanism dominates below the minimum breakdown power point.

---

* Plasma frequency $\omega_p \approx 2\pi \times 10^4 \sqrt{N_e}$, where N_e is the electron density per cubic centimeter.

** (1) Ambipolar diffusion is applicable when the Debye length, $\lambda_D < \Lambda$, the diffusion length.

(2) Loss of electrons via ambipolar diffusion is approximately 1/40 that of the rate when free diffusion is assumed.

In an un-ionized gas or one of very low degree of ionization, the free diffusion coefficient is used to determine the breakdown field strength. When an antenna is immersed in a plasma, however, the diffusion process may be ambipolar. Under this condition, the electrons remain in the region of high electric fields for longer periods of time than under free-diffusion conditions. Thus, their probability of gaining ionizing energy is increased and the breakdown field strength (and consequently power level) is reduced.

In Fig. 3 the power radiated normal to the L-band slot antenna is given for various ratios of ω_p/ω. The collision frequency corresponds to the minimum power handling point in Fig. 2. Where high fields are present and breakdown considerations are important, the plasma becomes nonlinear in the sense that as the power delivered to the antenna is increased the characteristics of the medium are altered. As can be seen in Fig. 3, when the plasma is such that $\omega_p \ll \omega$ and free diffusion is applicable, the change in the plasma is abrupt and the power radiated typically decreases by an order of magnitude. When $\omega_p \leq \omega$ and the diffusion is ambipolar, the decrease in the radiated power is only a few decibels, since the initial breakdown level has now decreased. In the case where $\omega_p > \omega$, the transition to the nonlinear plasma condition is gradual, with no abrupt change in signal level. Once breakdown has been sustained, however, the radiated signal level is essentially the same, irrespective of the initial conditions.

As the power is increased (Fig. 3) beyond the breakdown level, the additional power is absorbed in the plasma, which grows in extent and density. Figure 4, which is the plasma-density profile normal to the slot obtained with the probe, indicates this point clearly. Even though the ambient electron density levels differ by an order of magnitude, once the RF power is applied and breakdown occurs, the density profiles are essentially the same. It can thus be seen that for thin plasmas, which are considered here, once breakdown exists, the power radiated is ostensibly independent of the initial conditions and the low-signal-level attenuation as well.

Conclusions

(1) Once the RF field magnitude is such that the plasma becomes nonlinear, increasing the power delivered to the antenna does not increase the radiated power, but merely increases the temperature and extent of the plasma.

(2) The tests indicate that the maximum power radiated by an antenna is essentially determined by the breakdown power level measured under ambipolar diffusion conditions. For example, this may be accomplished in the CW case by measuring the power radiated by the antenna under breakdown condition just prior to extinction of the glow discharge, over the collision frequency range of interest. This test may be performed without the necessity of supplying an ambient density in the vicinity of the antenna.

(3) When one is interested in radiating as much power as possible, there is little or no advantage in reducing the incident power delivered to the antenna so long as the ambient electron density in the vicinity of the antenna is such that the diffusion is ambipolar.

REFERENCES

1. J. Gould and L. W. Robert, "Breakdown of Air At Microwave Frequencies," J. Appl. Phys., 27, No. 10, pp. 1162-1170 (October 1956).

2. A. D. MacDonald, "High-Frequency Breakdown of Air At High Altitudes," Proc. IRE, 27, No. 3, p. 436 (March 1959).

3. S. C. Brown, "High Frequency Gas Discharge Breakdown," Proc. IRE, 39, No. 12, pp. 1493-1501 (December 1951).

4. W. E. Scharfman and T. Morita, "Voltage Breakdown of Antennas at High Altitudes," Tech. Report 69, SRI Project 2494, Contract AF 19(604)-3458, Stanford Research Institute, Menlo Park, California (April 1960).

5. J. B. Chown, "Study of Plasma-Induced Voltage Breakdown at Low Pressure," Final Report, SRI Project 3369, Contract AF 33(600)-41517, Stanford Research Institute, Menlo Park, California (July 1961).

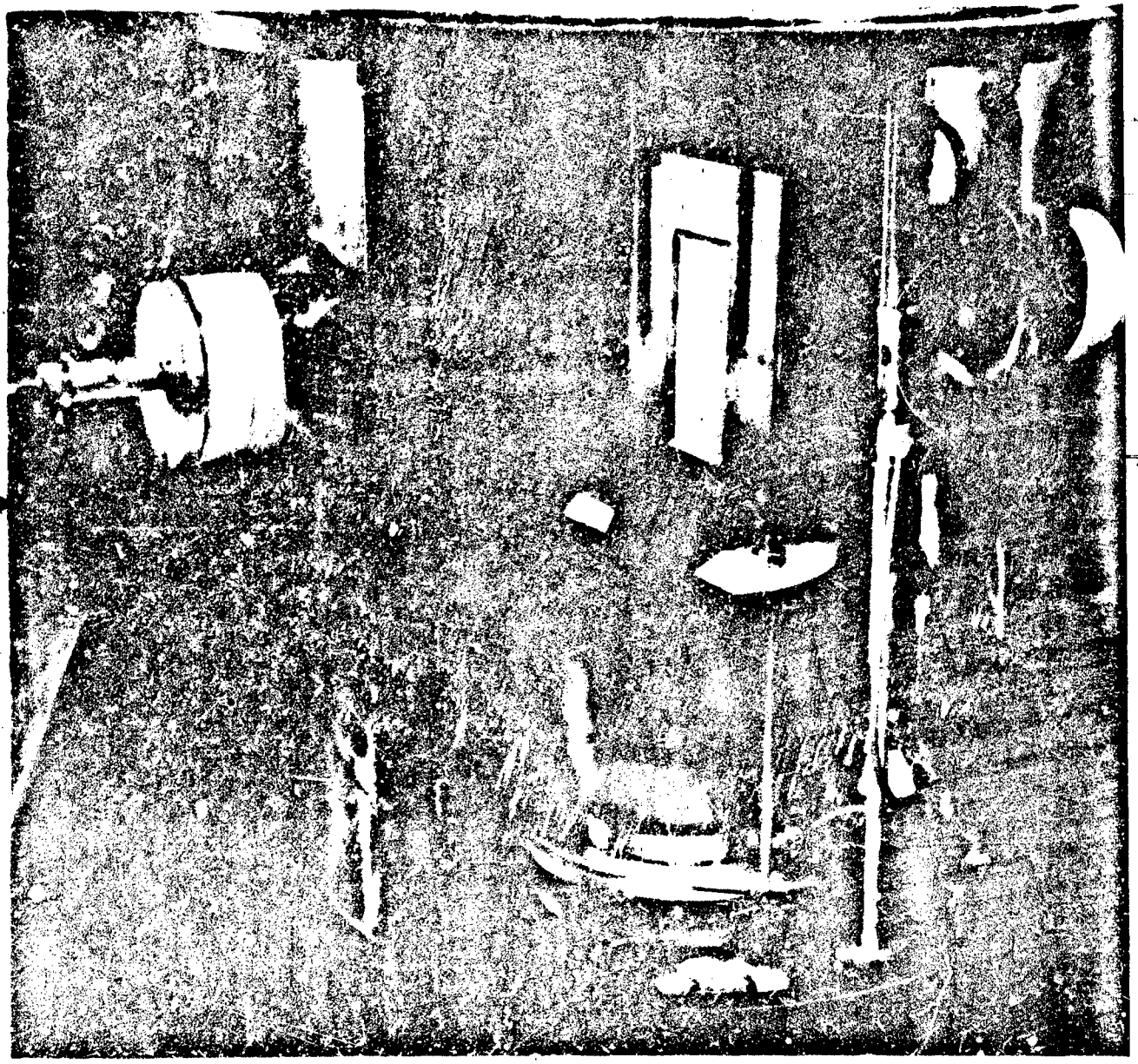

FIG. 1 Experimental Setup

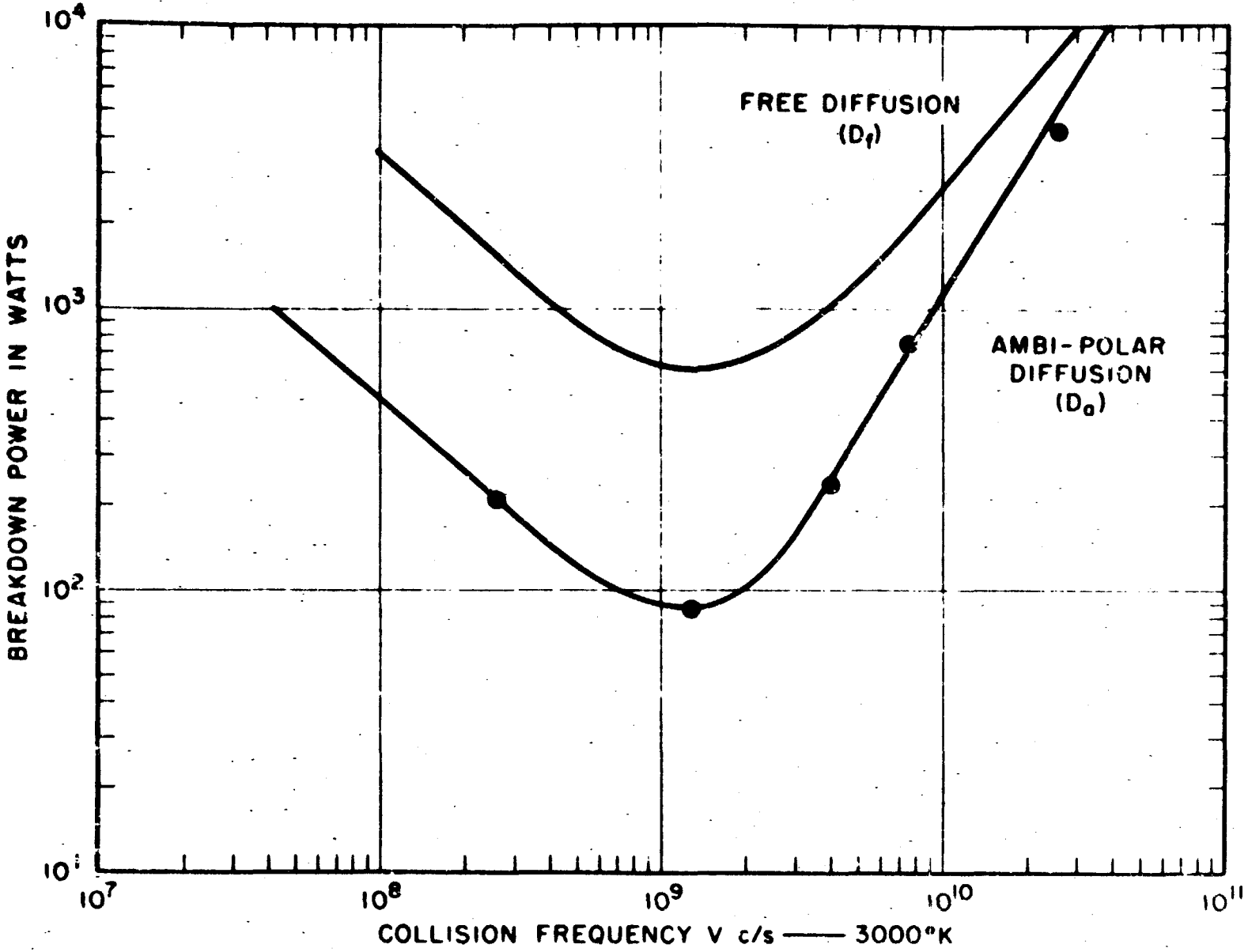

FIG. 2 Breakdown Characteristics of 2-Inch L-Band Slot Antenna

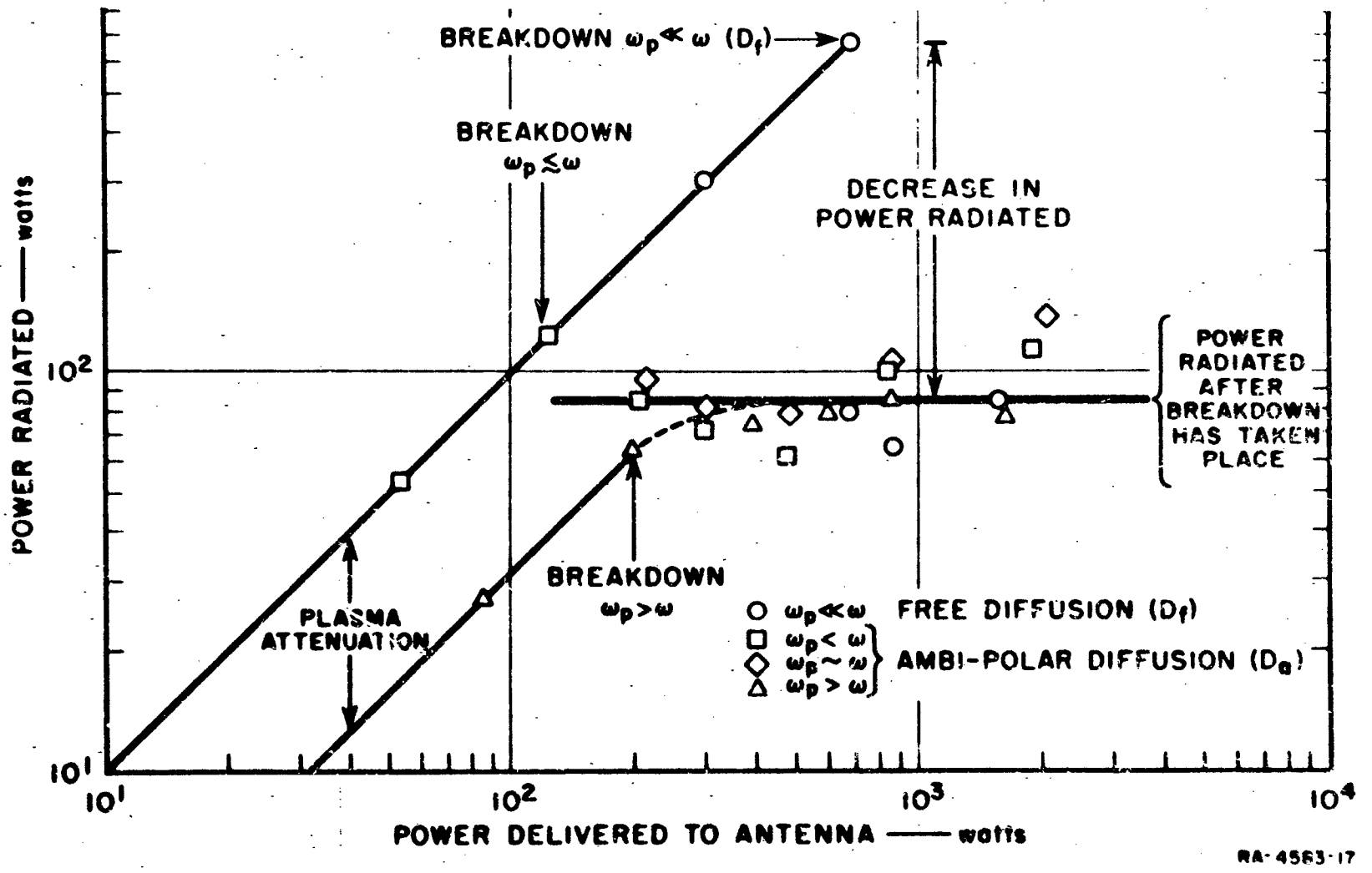

FIG. 3 Power Radiated Normal To An L-Band Slot Antenna At $\nu = 1.3 \times 10^9$ For Various Ratios of ω_p/ω .

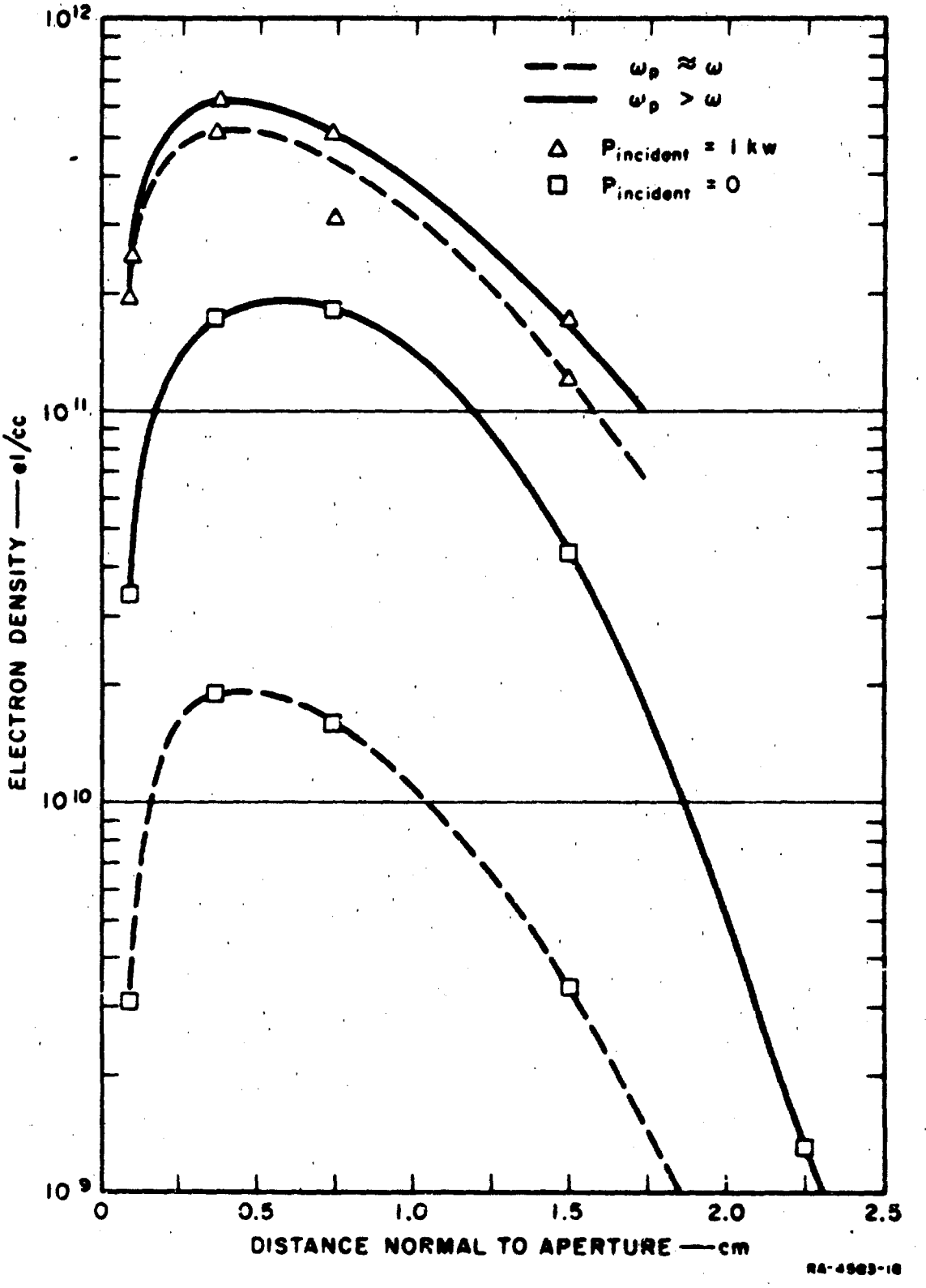

FIG. 4 Effect of RF Field On Plasma Density Over L-Band Slot Antenna At $\nu = 1.3 \times 10^9$.

RF BREAKDOWN IN A SPACE ENVIRONMENT*

E. F. Vance and J. E. Naneviez

Stanford Research Institute
Menlo Park, California

Under high-vacuum conditions, such as those that exist in space, electron mean-free-path is generally large compared to the dimensions of RF equipment, so that ordinary gas discharges are not normally a problem. Under such conditions, however, multipactor (or electron resonance) discharges can occur on RF equipment. RF breakdown voltage for parallel plates is illustrated in Fig. 1 for pressures ranging from a few hundred microns Hg, where gas processes predominate, to a fraction of a micron Hg, where secondary emission processes predominate.

The multipactor discharge is dependent upon secondary electrons produced at one electrode being accelerated across the electronde gap in a half period (or an odd multiple of a half period) of the RF wave, whereupon they strike the electrode and produce new secondary electrons to be accelerated back across the gap during the next half period.[1] Since a dc field in the electrode gap will tend to upset the synchronism between the electron transits and the RF field, or cause most of the electrons in the gap to be collected by the positive electrode, the application of a dc bias may be considered an appropriate means of preventing multipactor discharges. As the theoretical[2] and experimental

* The work described herein was supported by the Air Force Cambridge Research Laboratories under Contract AF 19(628)-325.

data of Fig. 2 indicate, the gap can be biased until the discharge fails to occur, but bias voltages of the order of the upper RF breakdown voltage are required. Furthermore, below cutoff the bias voltage serves merely to establish a new one-sided multipactor discharge mode at the positive electrode.[3,4]

In electrode structures such that the electric field is non-uniform, electron motion between the electrodes tends to be asynchronous. However, multipactor discharges occur in certain non-uniform field structures just as they occur under the asynchronous condition imposed by bias on a uniform field gap. Thus coaxial cylinders such as transmission lines and cavities support multipactor discharges over a wide range of RF and bias voltages, as illustrated in Fig. 3, where rms breakdown voltage is plotted as a function of bias voltage for several center conductor diameters.

Experiments have also been conducted with electrically small discone antenna configurations. Figure 4 shows contours of multipactor discharge initiation voltage (rms volts) at 57 Mc for cone angles ranging from 90° (top-loaded monopole) to 60°. For angles less than 60°, the discharge voltages were so eratic that smooth contours could not be obtained, and for cone angles less than 30° no discharges were observed. However, when ambient ionization was introduced by producing a small auxilliary discharge at VHF in the vacuum chamber, multipactor discharges occurred for all cone angles of 15° or greater, and the discone discharge continued even after the VHF discharge was stopped. After the VHF discharge had been extinguished, the discone voltage was reduced until the discone

discharge became extinguished. The rms voltages at which the discone discharges extinguish are shown in Fig. 5. These extinguish voltages may be taken as an indication of the voltage at which multipactor discharge occurs in the presence of ambient ionization, since once established, the discharge provides its own ionization.

Since most of the energy the electron gains from the RF field during its transit across the electrode gap is dissipated when it strikes the electrode, the power absorbed by the discharge increases with the RF frequency of the discharge (i.e., the number of electron impacts per second). Power loss to the multipactor discharge is thus most severe at the higher frequencies.

It is concluded, therefore, that the possibility of multipactor discharge should be considered in the design of RF transmission lines, cavities, and antennas for use on space vehicles. Particular care is required for vehicles operating in ambient ionization such as exists in the earth's ionosphere.

REFERENCES

1. Hatch, A. J and Williams, H. B., J. Appl. Phys. 25, 4, pp. 417-23 (1954).

2. Milazzo, C., "Study of Multipactor Discharge In The Presence of A dc Bias," Tech. Memo TM G1-15, General Electric Co., Palo Alto, California (13 March 1961).

3. Vance, E. F., J. Appl. Phys. 34, 11, pp. 3237-3242 (1963).

4. Vance, E. F., and Nanevicz, J. E., "One-Sided Multipactor Discharge Modes," Tech. Report 77, SRI Project 3977, Contract AF 19(628)-325, Stanford Research Institute, Menlo Park, California (April 1963).

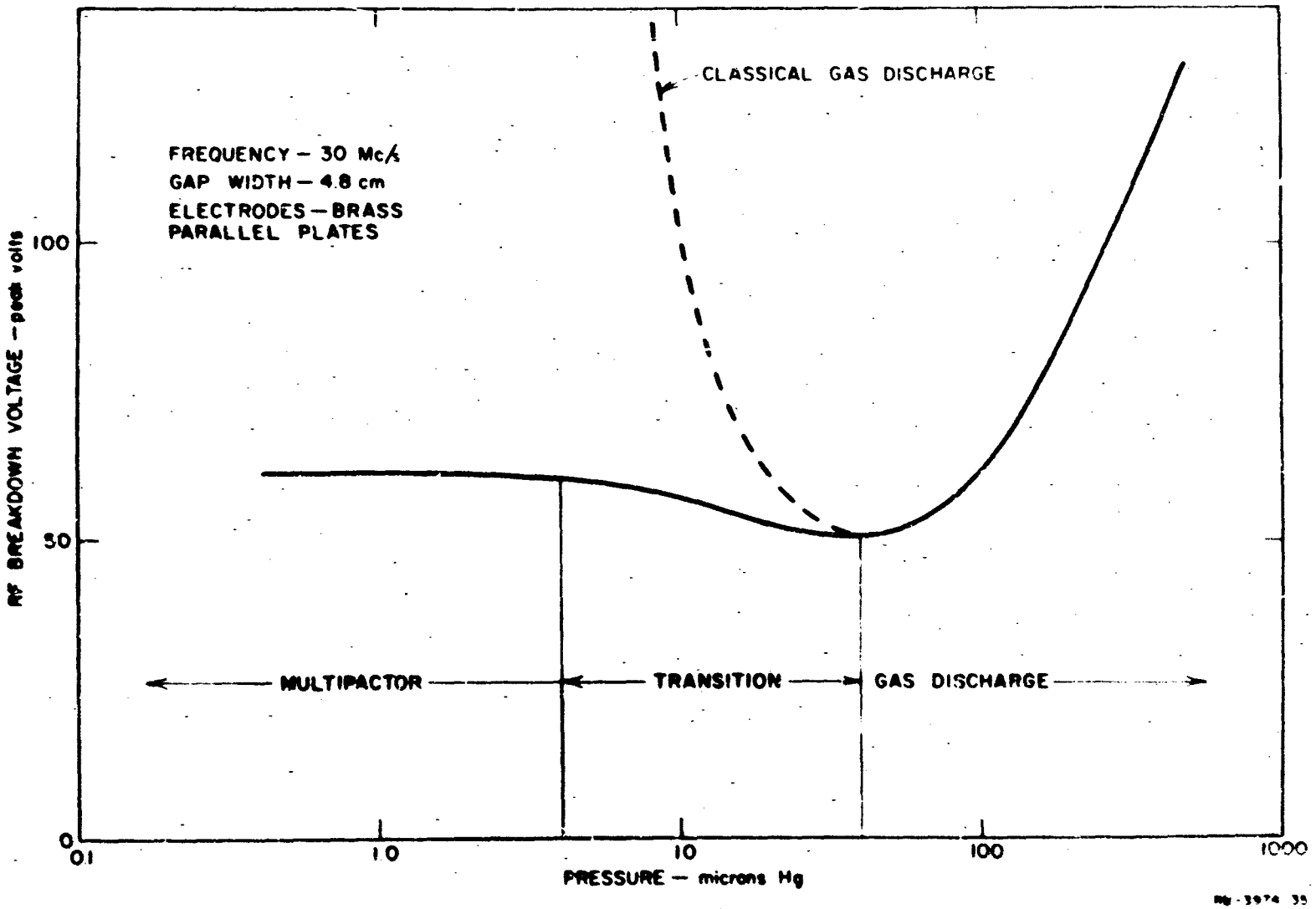

FIG. 1 VARIATION OF RF BREAKDOWN VOLTAGE WITH PRESSURE

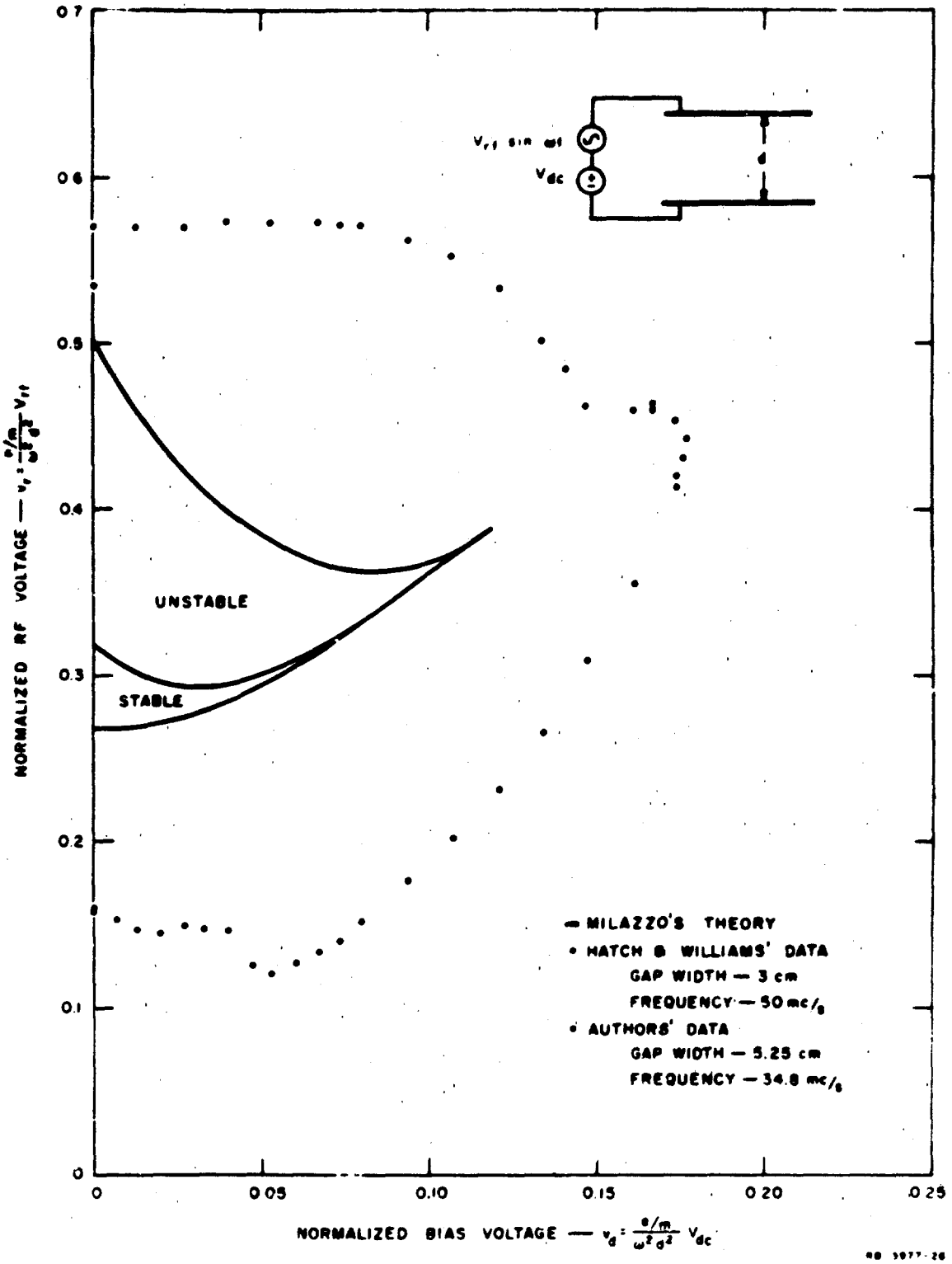

FIG. 2 THEORETICAL AND EXPERIMENTAL REGIONS OF BIASED MULTIPACTOR DISCHARGE

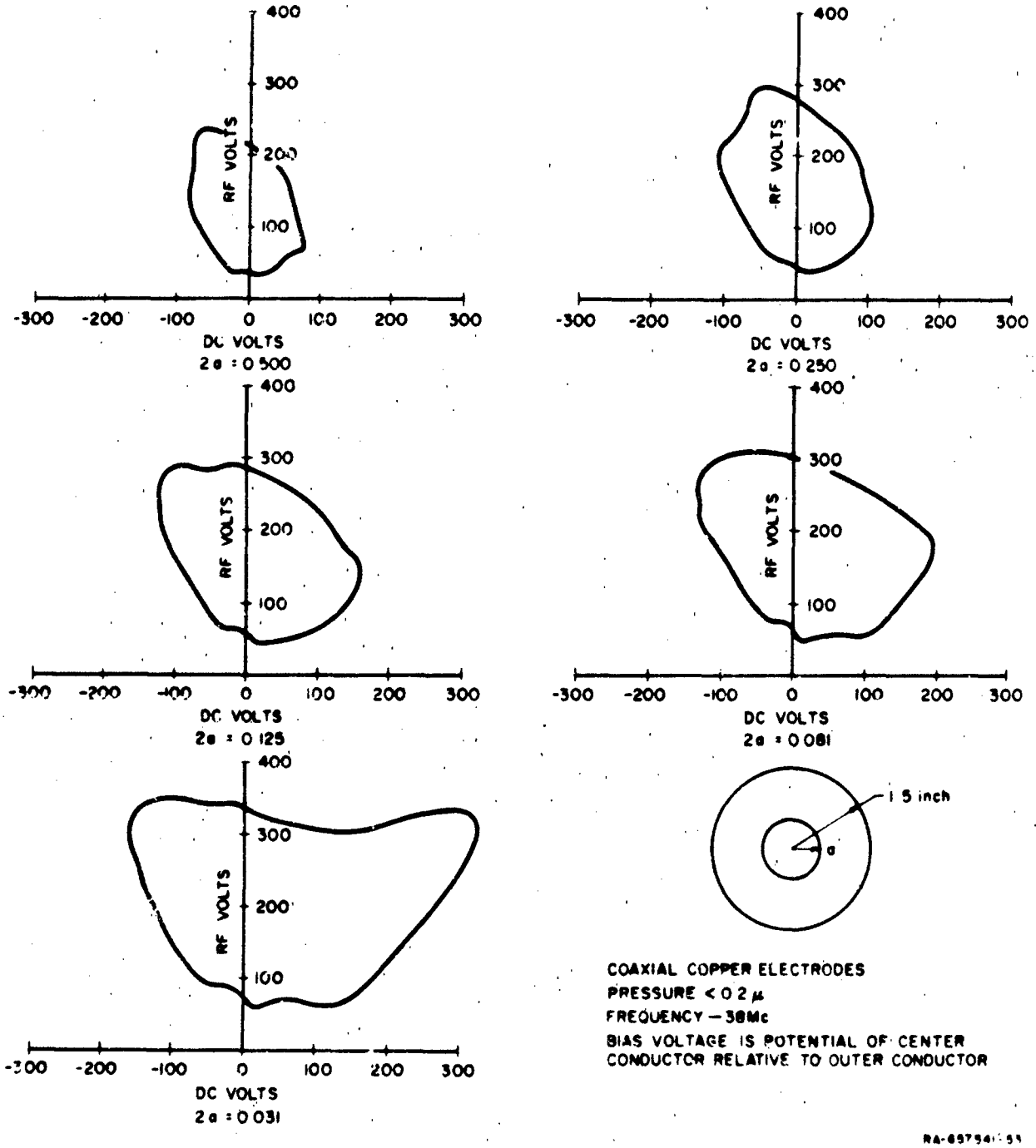

FIG. 3 REGIONS OF MULTIPACTOR DISCHARGE IN A COAXIAL GEOMETRY

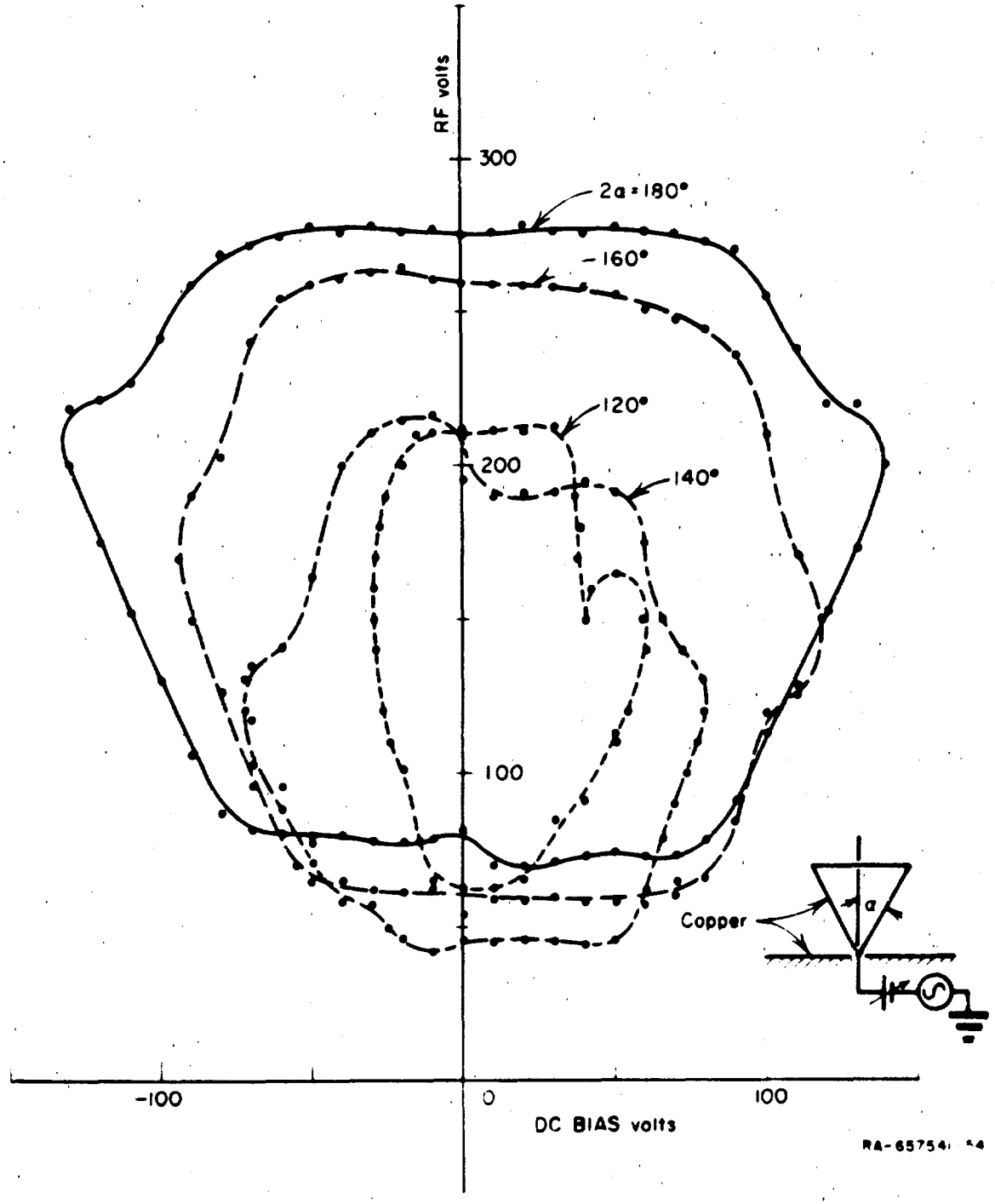

FIG. 4 REGIONS OF MULTIPACTOR DISCHARGE FOR SMALL DISCONE ANTENNAS

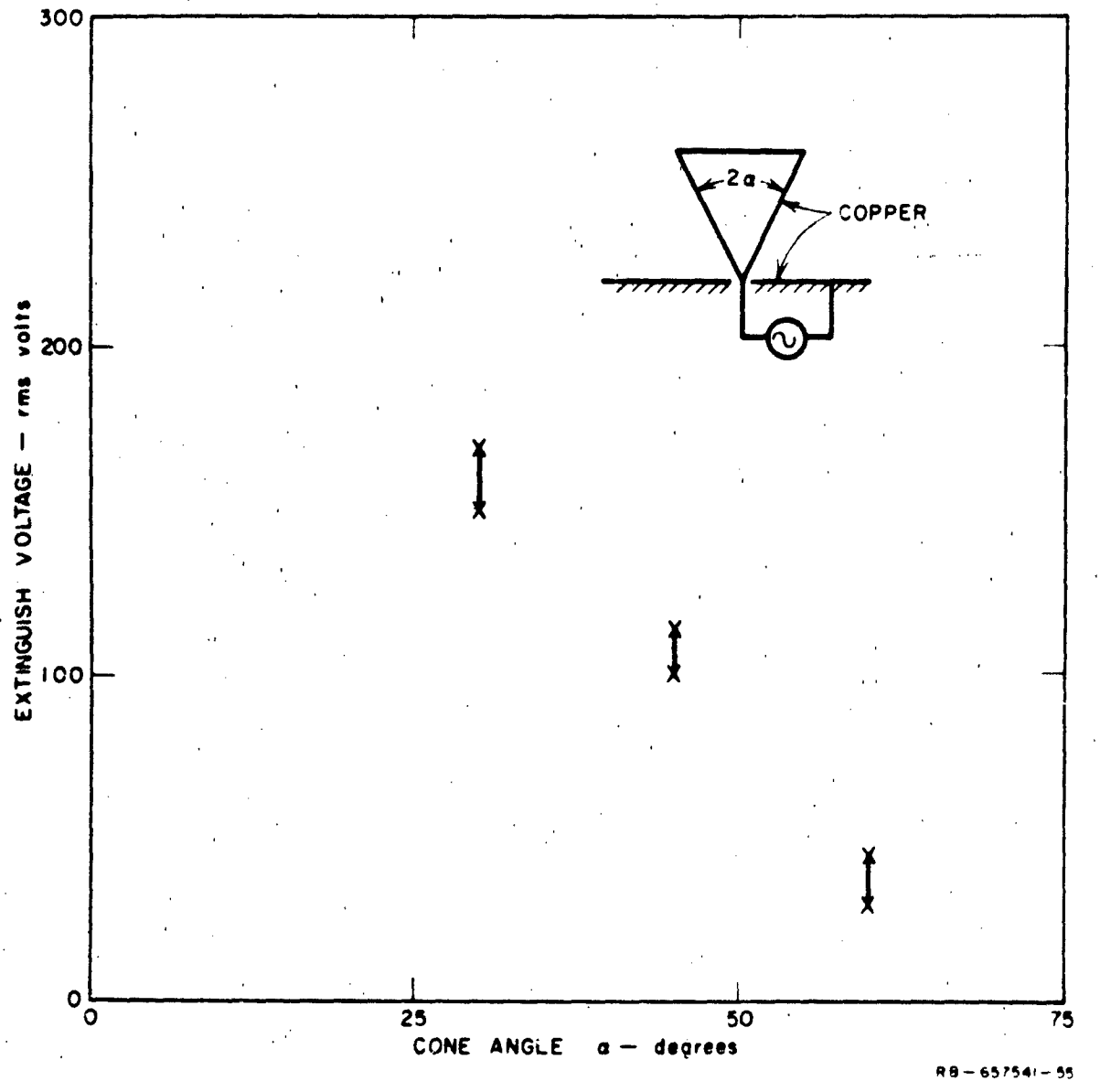

FIG. 5 DISCHARGE EXTINGUISH VOLTAGE FOR SMALL DISCONE ANTENNAS

INTEGRATED LOW PROFILE ANTENNAS*

By

Earl R. Murphy

Donald R. Wehner

*The work reported here was sponsored in part by the Air Force Systems Command, Research and Technology Division, Rome Air Development Center, Griffiss Air Force Base, New York, 13442.



MOTOROLA INC.
WESTERN CENTER
Military Electronics Division
8201 EAST McDOWELL ROAD SCOTTSDALE ARIZONA

Introduction

A class of low profile transmission line antennas[1] has been developed for compact, portable communications systems where a low silhouette antenna is desirable. The spatial patterns of these antennas are comparable to those of a quarter wavelength monopole above a ground plane although the antenna height is reduced by a factor of 30. Maximum performance of these radiating structures has been obtained by the application of integrated antenna techniques in their design. These techniques avoid the losses associated with a transmission line and coupling networks normally used between the RF source and the antenna by integrating the solid state amplifier or oscillator directly into the antenna structure. This technique is particularly desirable for radiators with low radiation resistance such as the transmission line antennas since the transmission line and coupling network losses greatly affect the transmission efficiency. The two integrated devices discussed in this paper are a transmission line antenna-transistor amplifier, or antennafier, and a transmission line antenna-transistor oscillator, or antennamitter.

TECHNICAL DISCUSSION

Transmission Line Antenna

The integrated low profile antenna is a transmission line antenna excited by a UHF power transistor connected to the antenna structure. The transmission line antenna consists of a quarter wavelength of wire formed into a Figure 8 and mounted parallel to and typically 2.5 electrical degrees above a small ground plane. Each end of the transmission line is RF shorted to the ground plane. This quarter wavelength transmission line antenna is tuned to half wave resonance by means of the capacitive reactance of a transmission line stub connected to the midpoint of the antenna as shown in Figure 1. Tuning is accomplished by adjusting the length of this stub. Impedance matching of the UHF power

transistor is accomplished simply by moving along the transmission line from either grounded end until the proper input impedance is found. The impedance everywhere along the line is real at the half-wave resonance frequency and rises rapidly along the line when moving away from either grounded end.[2,3] The 50 ohm point, for example, is approximately 2 degrees ($\lambda/180$) away from the grounded end.

The equivalent circuit of the antenna is a sharply tuned parallel resonant circuit. A Q of 100 is typical. The Q can be adjusted by varying the spacing above the grounded plane. The radiation resistance referred to the maximum current point along the antenna is proportional to the square of distance above the ground plane.[4] As the radiation resistance increases the Q decreases. This high Q provides an advantage in that the antenna can serve as a tank circuit thus lending itself readily to integrated antenna techniques.

The Figure 8 transmission line antenna efficiency is about 1 to 2 db less than a quarter wave monopole mounted above the same size ground plane and spatial patterns are very similar.

Antennamitter

In a 300 mc oscillator-antenna circuit, or antennamitter, the antenna becomes the oscillator tank circuit and feedback is achieved by coupling power from the antennamitter output into the emitter of the UHF power transistor in the common emitter circuit. This is accomplished by means of a variable capacitor from collector to emitter. The circuit is shown in Figure 2. Feedback is adjusted for maximum radiated power output. The transistor is mounted directly on the ground plane. This provides both a good heat sink and direct connections to the antenna and ground points.

Antennafier

For a 300 mc RF amplifier-antenna circuit or antennafier, the antenna serves as the output tank circuit. The input power to be amplified and radiated is matched to the base circuit of the UHF

power transistor by means of a π network. This is shown in Figure 3. In contrast to the antennamitter, feedback from the radiated output power to the input circuitry must be prevented. This is readily accomplished with the Figure 8 antenna design by mounting the π network input circuit on the opposite side of the ground plane from the antenna. In a practical portable communications system application the antennafier would be the RF output section to be driven by a crystal controlled RF source. This could be a relatively low powered source since the antennamitter provides gain.

Measurements and Observations

A radiated power of $1\frac{1}{2}$ watts at 300 mc has been measured from the antennamitter. The over-all efficiency, that is, the ratio of radiated power to prime power input, exceeded 50 percent. The spatial radiation pattern is comparable to that of a quarter wavelength monopole over an equivalent size ground plan and variations in the pattern in the azimuth plane were less than $\pm$ 1 db. Somewhat less radiated power has been observed from the antennafier, however this was the result of insufficient available drive power rather than a basic limitation of the device. Integration of the transistor amplifier into the transmission line antenna resulted in 6 to 8 db more radiated power than from the equivalent non-integrated antenna. The power input to both devices was the same. The available radiated power for both devices is limited only by the state of the art of transistor design. Both devices demonstrated a high tolerance to perturbations in the immediate environment. Various objects, including half and quarter wavelength rods, were brought within one inch of the integrated antennas and no appreciable detuning was observed.

Conclusions

The low profile transmission line antenna when integrated with a solid state RF power source provides a compact, efficient, low

silhouette, omni-directional radiating device. This technique has been demonstrated at 300 mc and can be extended to higher frequencies and higher power levels as better high frequency transistors become available.

Integrated antenna techniques allow the maximum efficiency to be realized from high Q, low radiation resistance antennas such as the transmission line antenna discussed above. The ratio of radiation resistance to ohmic resistance is optimized by integrating the RF source directly into the radiating structure thus avoiding transmission line and coupling network losses.

[1] King, Ronald, Harrison, C.W. Jr., and Denton, D.H. Jr. "Transmission-Line Missile Antennas," IRE Transactions on Antennas and Propagation, pp 88-90, January, 1960.

[2] Starer, James E. and King, Ronald, "Radiation Resistance of a Two Wire Line", Proceedings of the IRE, pp 1408-1412, November, 1963.

[3] King, R.W.P, "Transmission-Line Theory," McGraw-Hill Book Co., Inc., New York, N.Y., 1955.

[4] Burton, Robert W. and King, Ronald W., "Theoretical Considerations and Experimental Results for the Hula-Hoop Antenna," The Microwave Journal, pp 89,90, November, 1963.

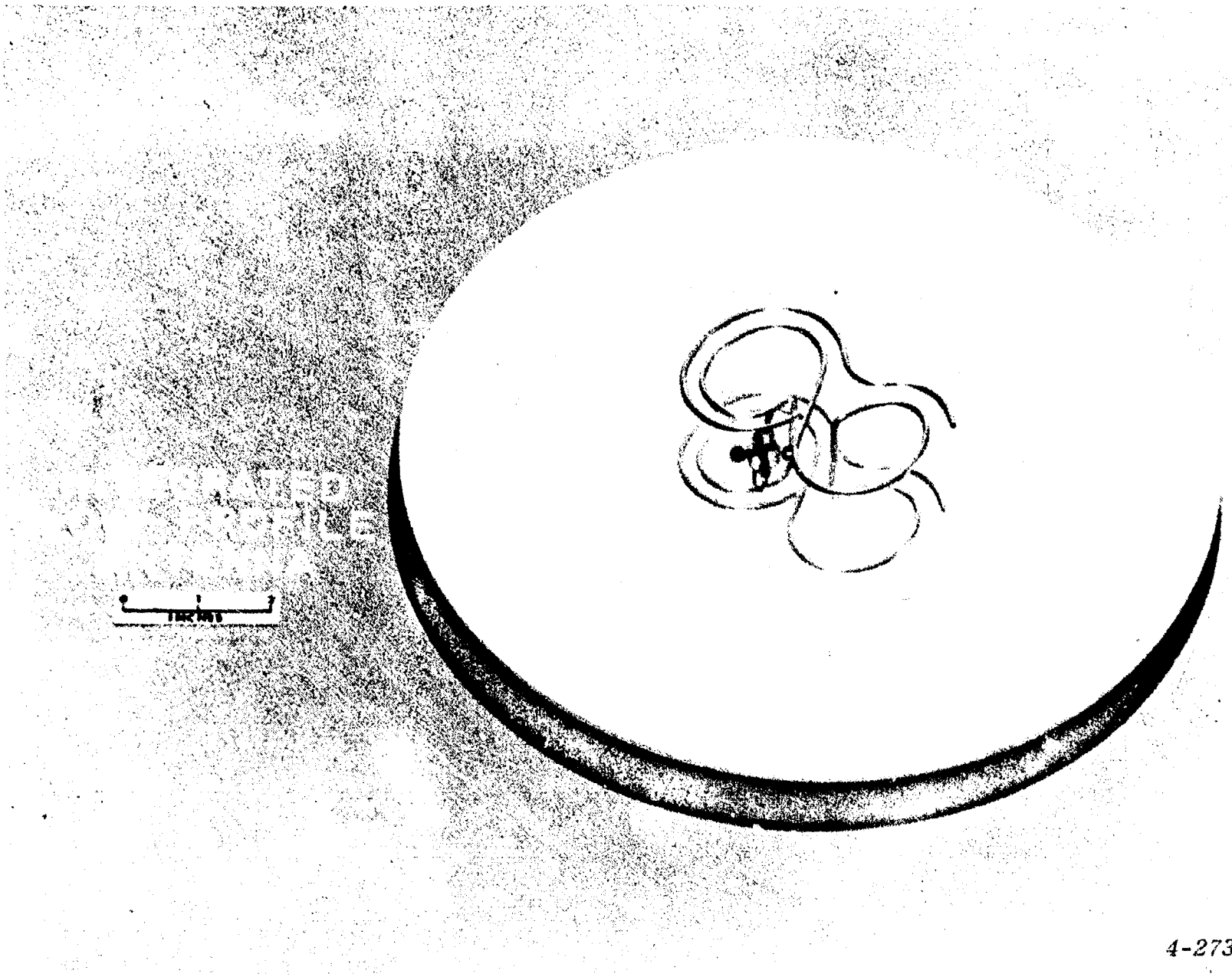

Figure 1. 300 Mc Integrated Low Profile Antenna

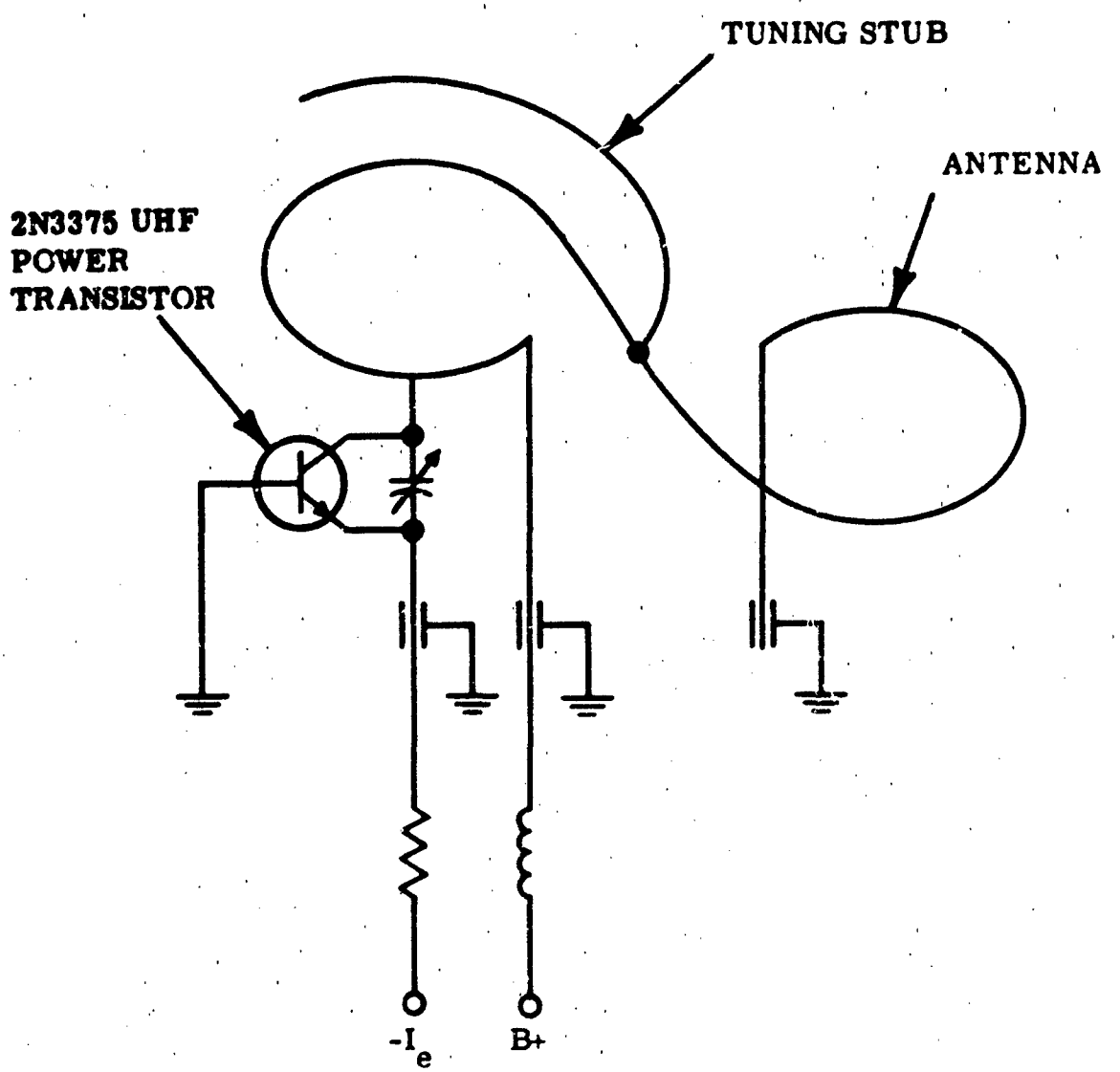

Figure 2. 300 Mc Antennamitter

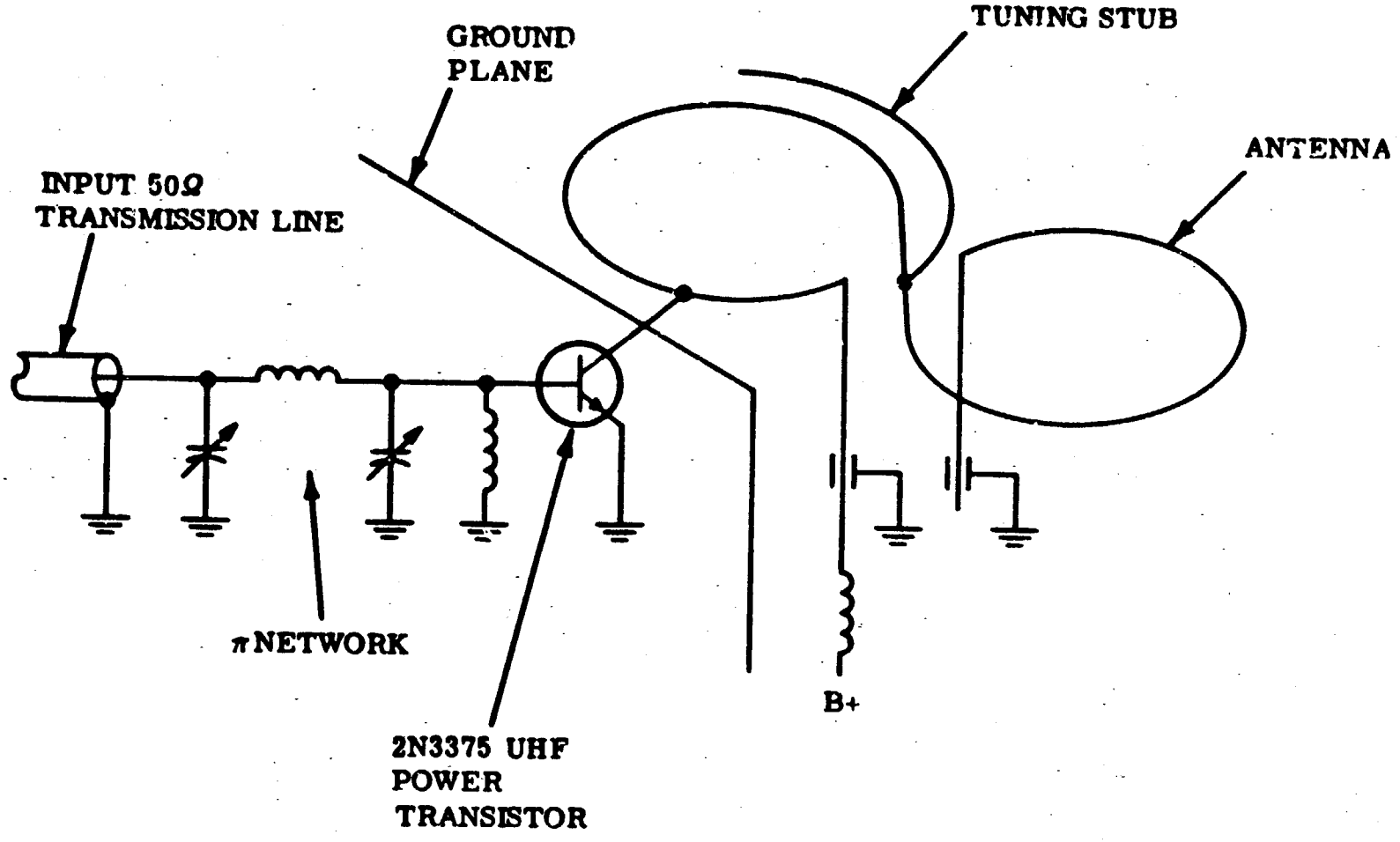

Figure 3. 300 Mc Antennafier

A HIGH TEMPERATURE C-BAND ANNULAR SLOT ANTENNA

By

Charles R. Bitter
Jack W. Pool
William E. Porteous

MOTOROLA INC.
Military Electronics Division
WESTERN CENTER
8201 EAST McDOWELL ROAD SCOTTSDALE, ARIZONA

INTRODUCTION

The advent of the high performance supersonic aircraft having airframe skin temperatures in excess of 650 degrees Fahrenheit for long durations has brought about requirements for rugged heat resistant antenna structures.

This paper describes the development of one such cavity backed annular slot antenna designed to efficiently and reliably operate with a C-band beacon transponder. Several units have been built for use by the Air Force Flight Test Center, Edwards Air Force Base, California.

The pattern requirements for the delivered antennas are that they be similar to that of a vertical monopole over a ground plane as installed on the belly of a large airframe. In order to operate with the matching transponder a maximum VSWR of 1.5:1, over a ten per cent bandwidth is required. A 50 ohm coaxial transmission line is used. Installation is to be flush with the airframe mold line.

ELECTRICAL DESIGN CONSIDERATIONS

It has been shown for an annular slot antenna, in an infinite ground plane, having an outer diameter of 2b and an inner diameter of 2a that if

$$\beta a < 2, \text{ where } \beta = \frac{2\pi}{\lambda},$$

the resulting radiation pattern will be very similar to that of a short monopole fed over a ground screen.[1] Further, by adjusting the ratio of the slot outer diameter to the slot inner diameter, the antenna may be designed to have a low VSWR over nominal bandwidths.

Noting these two effects a cavity backed, annular slot antenna was designed utilizing a conic tapered center conductor to match the antenna aperture to the transmission line. As a first step in arriving at a final design a βa of 0.6 and an outside diameter to inside diameter ratio of 5:1 were chosen as parameters for the slot aperture. An air dielectric cavity of depth $\frac{\lambda}{8}$ was then constructed. This gave an initial breadboard antenna which had a measured VSWR of less than 1.6:1 across an eleven per cent frequency bandwidth at C-band. No auxiliary impedance matching was necessary.

Since the annular slot antenna is required to operate on high performance, supersonic aircraft in high heat thermal environments it was then necessary to fill the cavity void with a high temperature resistant, low loss dielectric material. This required the free space air dielectric breadboard version of the antenna to be scaled proportional to the dielectric constant of the material. The dielectric constant, ϵ, of the selected material was 7.0. However measured data taken using a scaled version of the initial

---

[1] Jasik, H., Antenna Engineers Handbook, Chapter 8, pp 8-1 through 8-16, McGraw-Hill Book Company, Inc. 1961.

air dielectric breadboard model with a scale factor of $\frac{1}{\sqrt{\epsilon}}$ indicated that, for this particular design application there existed an effective dielectric constant, ϵ_{eff}. ϵ_{eff} was computed using measured impedance versus frequency data to be about 2.1. Then using the corrected scale factor of $\frac{1}{\sqrt{\epsilon_{eff}}}$ the final prototype antenna dimensions were computed and a model fabricated. The measured VSWR of this model was less than 6:1 over an eleven per cent bandwidth at C-band. Using a quarter wavelength transformer properly placed at the terminals of the antenna, the final dielectric filled annular slot antenna was matched to a 50 ohm line with a VSWR of less than 1.5:1 over a ten per cent bandwidth at C-band.

The measured radiation patterns of the final model mounted on a 9 x 9 wavelength ground plane are shown in Figure 1 and Figure 2. Figure 1 shows the azimuth pattern to be omnidirectional and have a ± 0.5 db maximum ripple. Figure 2 shows the elevation pattern to be similar to that of a vertical stub over a ground plane. The elevation half-power beamwidth is 53 degrees and the measured gain is about 3.0 db above an isotropic reference.

MECHANICAL DESCRIPTION

Figure 3 is a photograph of the C-band high temperature annular slot antenna, and Figure 4 is a cross section of the antenna showing the basic construction features.

The antenna dimensions are as follows: The ratio of outer diameter to inner diameter of the slot at the surface of the antenna is 6.5:1, and the inner conductor diameter at that point is 0.284 inches. The over-all diameter of the antenna, including the mounting flange is 3.5 inches, while the over-all mounting depth is 1.71 inches. Figure 5 shows a component parts layout of the assembly.

Four main parts constitute this assembly: (1) the cylindrical cavity, (2) the cavity dielectric filler, (3) the conic center conductor, and (4) the connector-impedance matching section. All metal parts are made of stainless steel. Fabrication and assembly is accomplished without the use of soldered or brazed joints. The center conductor is assembled by threading and tapping several of the stainless steel sections. This allows easy assembly with the dielectric filler.

A high temperature epoxide based adhesive provides a moisture seal between the impervious dielectric filler, cavity, and center conductor. The adhesive bond also adds structural integrity to the center conductor assembly. In addition a retainer ring provides a positive mechanical attachment of the filler to the cavity. The entire antenna assembly mounts from the inside of the airframe such that the slot aperture is flush with the skin mold line. A high temperature asbestos gasket is used between the antenna flange and the airframe mounting surface to provide a positive moisture barrier at the airframe skin.

Materials Consideration:

In order to sustain temperatures in excess of 650 degrees Fahrenheit for extended time periods the structural materials

for the annular slot antenna had to be selected carefully. Particular attention was given to the electrical properties of the dielectric materials, and to the assembly techniques of the conducting elements. Obviously, conventional antenna materials such as aluminum, soft or hard solder, and phenolic plastics are not able to survive long-term exposures to temperatures in excess of 650 degrees Fahrenheit. Because of its excellent durability, availability, and coefficient of thermal expansion stainless steel, AISI No. 303, was selected as the material from which to fabricate the metallic structural parts. Stainless steel's compatibility with the titanium mounting surfaces in a high temperature airframe is excellent, since the coefficients of thermal expansion match more closely than with those of the aluminum alloys. Table I summarizes the coefficients of thermal expansion of these materials.

TABLE I

Coefficients of Thermal Expansion

Metallic Materials

Aluminum	2024 alloy	$12.9\ (10)^{-6}/^{o}F$
	6061 alloy	$13.0\ (10)^{-6}/^{o}F$
Stainless Steel	AISI 303	$5.3\ (10)^{-6}/^{o}F$
	AISI 304	$5.3\ (10)^{-6}/^{o}F$
	AISI 416	$3.2\ (10)^{-6}/^{o}F$
Titanium		$4.7\ (10)^{-6}/^{o}F$

For the established antenna design the selection of a good cavity dielectric filler material involves giving consideration not only to the electrical properties, such as dielectric constant and loss tangent, but also the the thermal and mechanical properties of the material. Major thermal characteristics are maximum temperature endurance and thermal expansion coefficient.

Strength, erosion resistance, porosity, and handling characteristics of the material are the major mechanical properties. Based on past experience it was decided that ceramic compounds offer the best overall characteristics in the thermal environment to be encountered. Ceramic compounds can be made impervious to moisture, have reasonable electrical parameters, and may, in some cases, be machined.

Several ceramic materials were investigated, and based on the pertinent mechanical and electrical requirements an impervious, very hard, but precision machinable ceramoplastic was selected as the cavity filler. This material is the Mycalex Corporation's Supramica 500. The electrical properties of this material are adequate to allow reasonable antenna efficiencies. The dielectric constant is about 7.0 and the loss tangent is near 0.001. The physical and thermal properties of this material make it very suitable for use in the established antenna design. It has a Rockwell M hardness of 115 thus offering a high resistance to erosion and impact shock. The material has a maximum temperature endurance of over 700 degrees Fahrenheit and a coefficient of thermal expansion near that of stainless steel.

To adequately support the center conductor at the input connector terminal a low loss, low dielectric constant, ceramic foam was chosen having a coefficient of expansion matching the other materials used for the antenna. Emerson and Cuming Inc., Eccofoam LM-43A was the material selected. It is a porous ceramic. However, moisture is prevented from coming in contact with the Eccofoam by the Supramica dielectric material and the epoxy adhesive bond on one side and the environment proof mating connector on the other. This Eccofoam material is available in several values of dielectric constant. A value of 2.0 for the dielectric constant was chosen since this was compatible with conventional low temperature coaxial cable dielectrics. The companion dissipation factor is about 0.006. Table II indicates the coefficients of thermal expansion for the dielectric materials selected.

TABLE II

Coefficients of Thermal Expansion

Dielectric Materials

Supramica 500 (Mycalex Corp. of America) (Clifton, N. J.)	$6.2 \times 10^{-6}/^{o}F$
Eccofoam No. LM 43A (Emerson & Cuming, Inc.) (Canton, Mass.)	$4.0 \times 10^{-6}/^{o}F$

When Table II is compared with Table I it may be seen that the coefficients of thermal expansion closely match for all the materials selected. The temperature resistance and compatibility of these materials was born out by repeated heat cycling of the antenna assembly from -55 degrees Fahrenheit to over 650 degrees Fahrenheit. These temperature limits were maintained for extended periods of time, up to fifteen hours in some cases, and then rapidly changed to the other extreme such as to reach that extreme in a very short time. No degradation of electrical performance or mechanical integrity, especially moisture resistance, was noted. A slight discoloration of the stainless steel occurred but otherwise there were no visible effects to the antenna. The mechanical integrity of the assembly was further substantiated by repeated impact shocks of 65 g's for 6 milliseconds in all major planes. In addition successive vibration tests of from 5 cycles at 0.2 inch displacement to over 2000 cycles at 15 g's yielded results that showed no mechanical damage or electrical performance degradation.

CONCLUSION

The antenna design described above yielded a compact, rugged, high-temperature resistant radiator capable of flush mounting on a flat surface. Complete filling of the antenna cavity void and the use of stainless steel fabrication without solder type connections permit long term operation of the antenna when the device is completely immersed in a high-temperature, erosion causing, environment.

No appreciable design effort would be required to provide a flush mounted assembly in compound radius surfaces. The design techniques employed may be applied to many related antenna types and by appropriate scaling of dimensions and dielectric properti may be extended to other design frequencies.

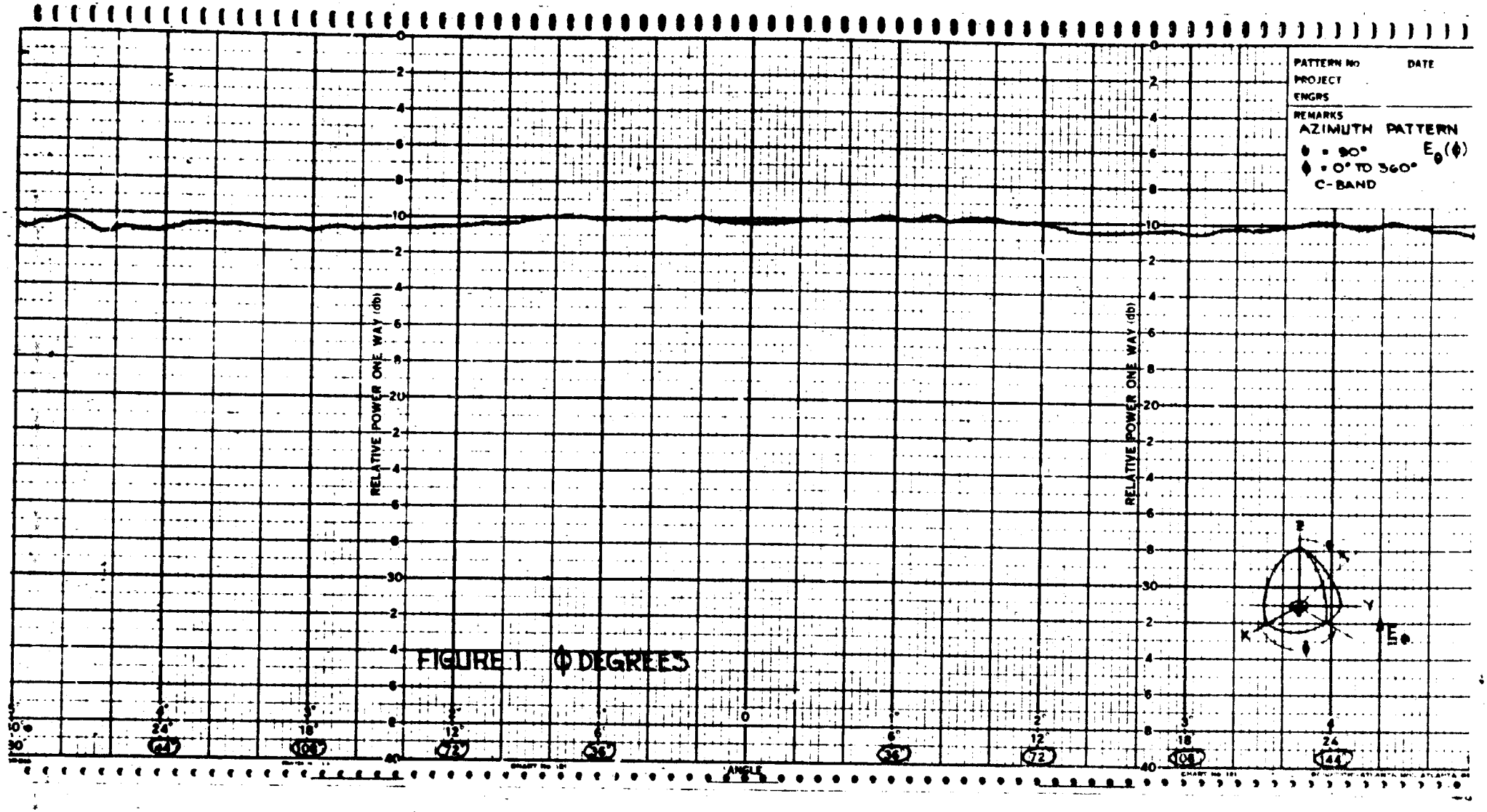

FIGURE 1 ϕ DEGREES

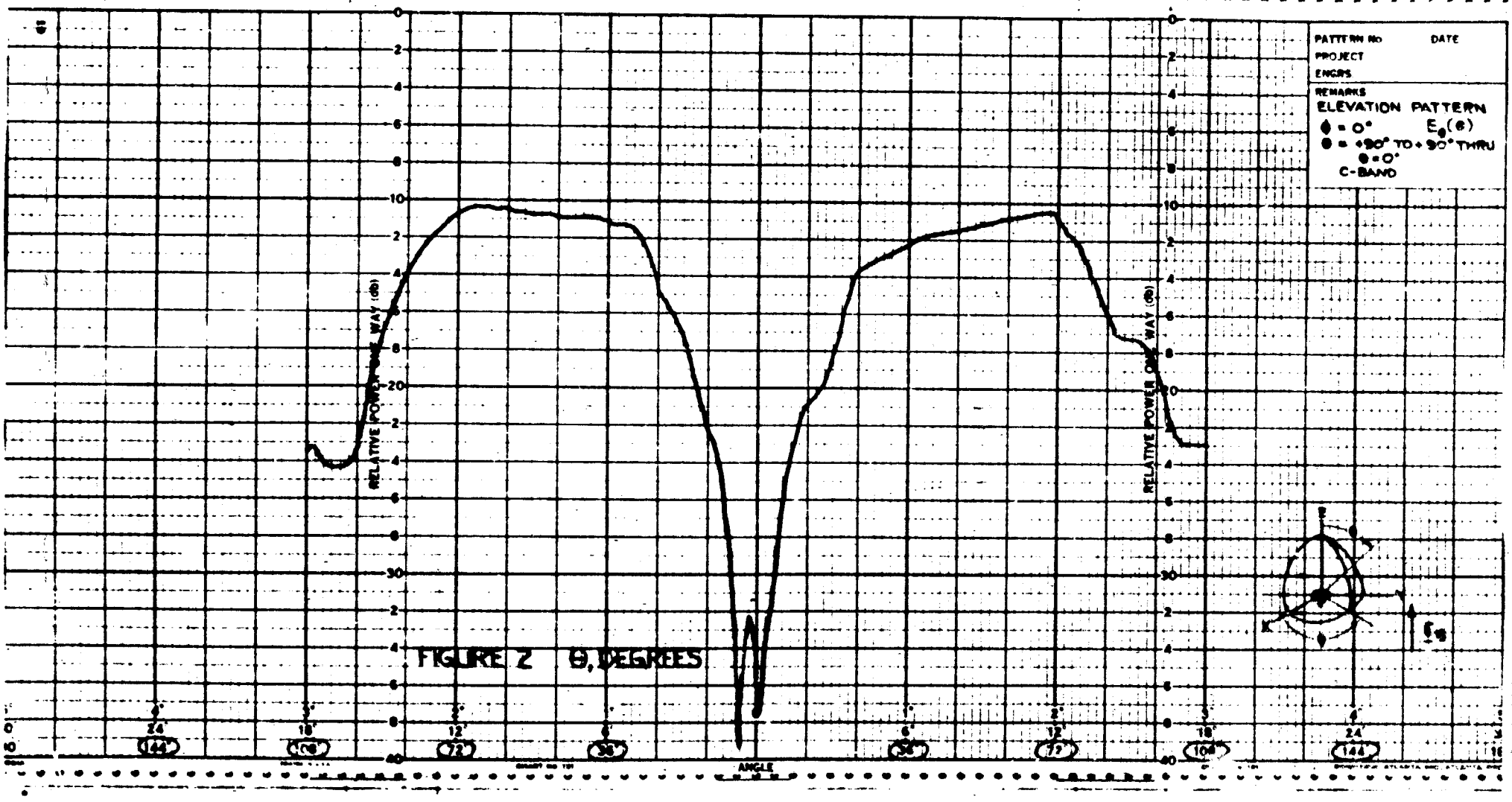

FIGURE 2 θ, DEGREES



Figure 3

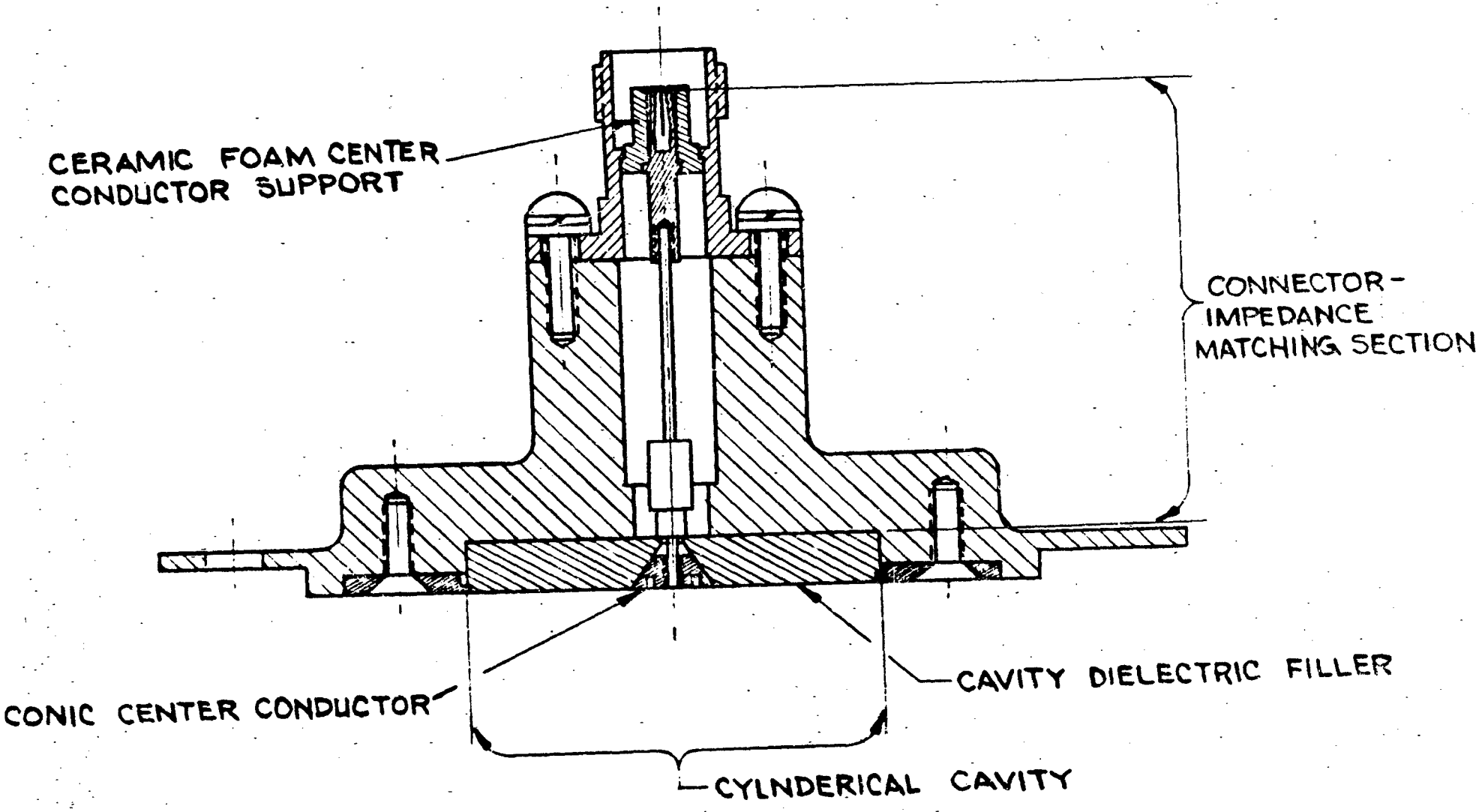

Figure 4. C-Band Annular Slot High Temp Antenna Cross Section

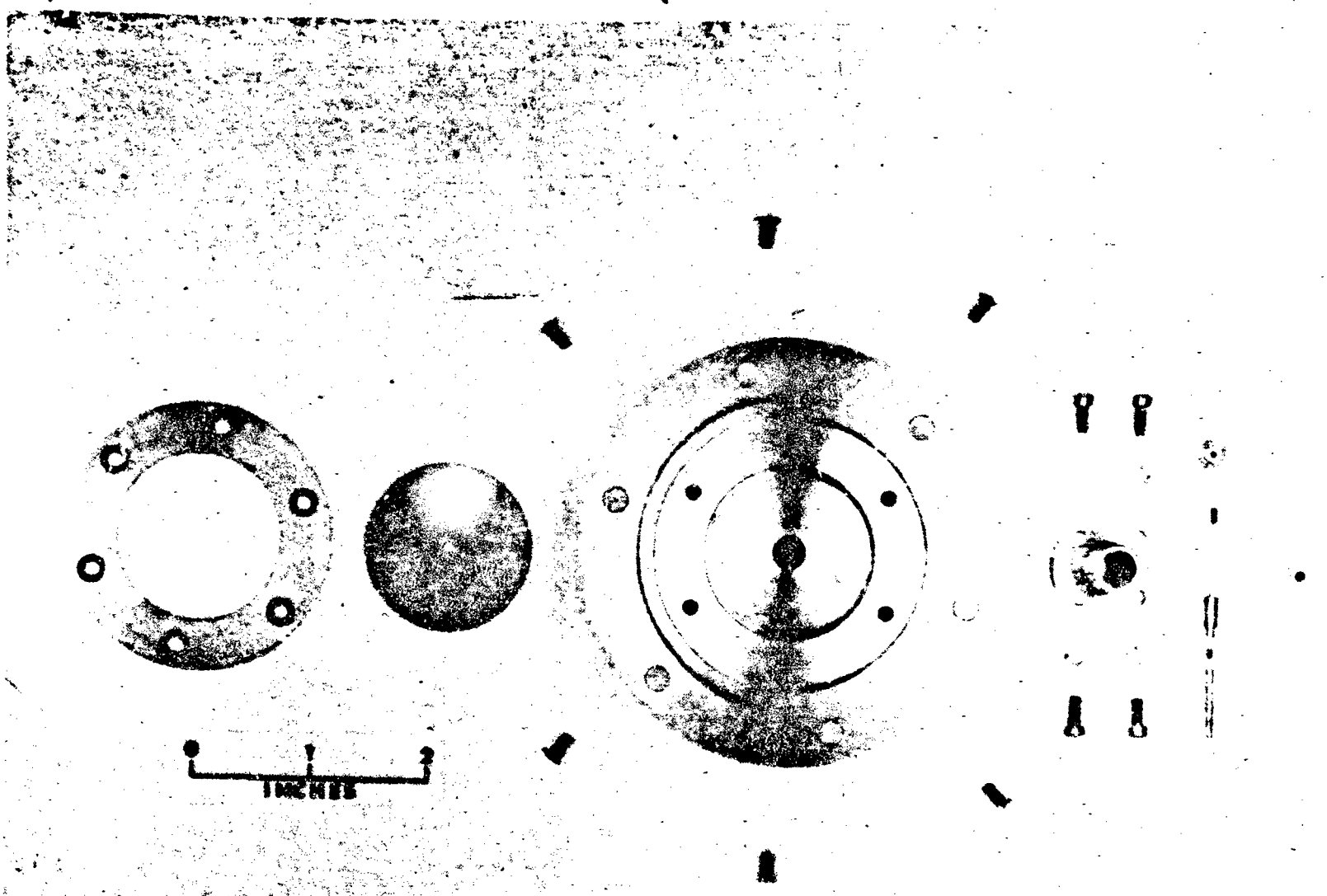

4-1945

Figure 5. Component Parts Layout

TITLE

THE USE OF STRIP-TRANSMISSION LINE TECHNIQUES AT X-BAND

by W. Bryant. D. Canady,
and G, Monser

ADVANCED DEVELOPMENT LABORATORIES, INC.
NASHUA. NEW HAMPSHIRE

Presented at 14th Annual Symposium on U S A F.
Antenna Research and Development
October 6 through 8, 1964

ACKNOWLEDGEMENT

This work was sponsored by the Antenna and Radome Section, Air Force Avionics Laboratory, RTD, under Mr. O. E. Horton, Project Engineer.

THE USE OF STRIP-TRANSMISSION LINE TECHNIQUES AT X-BAND

By: W. Bryant, D. Canady, and G. Monser

1.0 Introduction

Results are given on an Air Force R/D program sponsored by WADC which is directed toward the development of a broadband Butler matrix and array. An earlier paper by Mehron[1] has considered Butler matrices from a tutorial viewpoint. Here, we consider some of the design problems for providing matrices and arrays at X-band.

Early in the program we realized that before a suitable matrix could be made, it would be necessary to do some component design. In particular, we had to develop broadband phase shifters, couplers, and the associated feed-throughs and connectors for use in the matrix. Data on these matrix components is reported. Concurrent with the matrix effort, we have developed an array which would be serviced by this matrix. The array consists of 8 spiral radiators arranged in a linear array. Here again, effort was first directed in the individual element design. Data on the individual spirals used in the array is given. Also, available data on the array, which was undergoing evaluation at the time this paper was prepared, is included.

2.0 Factual Data

The two components which were to be designed were a broadband matrix to be operated from 7 to 11 Gc/s and a broadband eight element linear array to be serviced by this matrix.

2.1 Matrix Design

Before designing and building a broadband matrix for servicing the 8 element array, a 4 element narrow band matrix was

considered. Two different designs for this unit were built and tested. Figure 1 shows the center conductor layout for one of these designs. The basic components used in this narrow band matrix consisted of a high impedance Shimizu[1] coupler and a newly designed right angle transition from strip transmission line to type N coax. The required phase shifters were accomplished by means of differential line lengths in the matrix layout.

The average measured data from 7 to 11 Gc/s obtained from the matrix shown in Figure 1 is given below:

Mismatch: 1.38:1 all ports
Coupling from beam ports to antenna ports: 6.7 db
Isolation: 21.9 db (lowest value 14.0 db)
RMS phase error: @ 9.0 Gc/s (typical 2 beams) 3°

Since the ideal or no loss coupling from beam to antenna port is 6 db, the insertion loss of this matrix is 0.7 db. This loss is chiefly due to the copper and dielectric losses, variations in the outputs of the 3 db couplers, and mismatch losses.

Next, a layout of a narrow band eight element Butler matrix as shown in Figure 2 was made. The same basic components were used in this matrix as before. All interconnecting line lengths were accomplished in the same high impedance line as used in the coupled region of the 3 db directional coupler. Differential phase shifts were accomplished by means of varying line lengths. All beam and antenna ports utilized 50 ohm right angle connectors - thus requiring the tapered line length at each port.

Complete measured data was not available at this writing. However, the data available shows the amplitude distribution from

beam ports to antenna ports to average 10.5 db over the 7.0 to 11.0 Gc/s frequency band, with the highest readings at the high end of the frequency band. Average isolation data was greater than 20 db over the band.

In connection with the above development efforts, it was first necessary to seek adequate matrix component design. The principal elements under consideration are the directional couplers and phase shifters. However, connectors and feed-throughs are of nearly equal importance if an adequate design is to be provided.

In developing a 3 db directional coupler, many different techniques were investigated. These included the following designs: hybrid ring (rat race), broadband hybrid ring, asymmetrical 3 db coupler, and a Shimizu 3 db directional coupler . The major disadvantage for these designs was the low isolation. The final design which, we felt, gave near optimum results was a high impedance Shimizu coupler where the coupled region was designed for a higher than nominal (50 ohms) impedance. Typical specifications were: average VSWR 1.35:1, average isolation 20 db, coupling 3.4 ± .6 db. It is felt that the higher impedance coupler performed better because of the smaller electrical length of the miters and corners in the coupler region.

In the development of the broadband phase shifters, a type A, Schiffman[3] phase shifter was adapted to fit our needs. Table I (below) gives average performance data across the 7 to 11 Gc/s band.

TABLE I

Design Value	Measured Phase Shift	Deviation from Average	VSWR
22.5°	23°	+4° -3°	1.25:1
45.0°	45°	+5° -7°	1.25:1
67.5°	70°	+6° -4°	1.25:1

Before any strip transmission line components could be designed for X-band operation, well matched transitions had to be developed. We achieved a mismatch of less than 1.30:1 over the 7 to 11 Gc/s band for a pair of in-line type N connectors, which were connected in line with the center conductor of a short section of strip transmission line. Right angle connectors were also developed with a mismatch of less than 1.30 over most of the same frequency band.

In addition to the above development problems, dielectric and copper losses cause the insertion loss of strip transmission line circuits to increase with increasing frequency. At X-band the type of material being used in this program had an attenuation of about 0.4 db per foot measured at 9 Gc. One means for decreasing the dielectric loss is to increase the ground plane spacing. This reduction can be effected up to about 10 Gc. Above 10 Gc a cut-off wavelength may occur and a waveguide or non TEM mode of transmission may be energized. Other limitations caused by the increase in frequency are transitions from strip transmission line to either coaxial or waveguide; tighter tolerances; effects caused by bends and mitered corners; generation of parallel plate mode caused by slight air spacing in the circuit boards.

2.2 Array

The design of the array shown in the photograph (Figure 3) was predicated on the success obtained with an S-band array of similar

design. The S-band model had undergone considerable development and a near-optimum design, we felt, had been provided. With this in mind and in the interests of economy and time, we chose to scale this model.

The development effort consisted of designing and evaluating a suitable balun to feed the array elements, construction and evaluation of the array elements, and a final evaluation of the array configuration. Data given in this paper is chiefly on the array elements. At the time this paper was prepared the array configuration had not been fully evaluated.

Figures 4 through 8 give measured data on a single element in the array. In Figure 4, the average VSWR for the elements is plotted. The characteristic for the individual elements was similar to the displayed curve. The VSWR increased at 7 Gc and decreased at 11 Gc when put into the array environment when compared to a single isolated element.

Figure 5 shows the measured isolation at 7 Gc between the end element and successive elements of the array using an insertion loss technique for measuring the isolation. From this plot, it might be concluded that no dividing walls are necessary between the elements within the cavity structure. However, as will be shown later, there is some justification for using dividing walls.

Figure 6 shows the average measured axial ratio for the spiral elements as a function of frequency. From this plot it is seen that an acceptable ellipticity was obtained.

Figure 7 illustrates the average measured gain for the units as a function of frequency. In this figure directivity using the beam area method[4] is sketched and the return loss due to VSWR is

indicated. Reasonably good agreement between computed directivity and the measured value is noted. The difference is believed due to radiation inefficiencies.

Figure 8 shows typical element patterns across the band for vertical and horizontal polarized radiation. From this data it is seen that beam shape remains well defined across the band and that minor lobe response is below 10 db.

We now return to a further discussion of isolation between elements. As noted earlier, isolation data obtained using an insertion loss technique warranted a tentative conclusion that no dividers would be required to separate the element cavities. To assure this conclusion was valid, the test series shown in Figure 9 was performed. In this figure we see compared the radiation from a signle test dipole mounted in the cavity and the same test dipole set-off with dividers in the cavity. The effect upon the radiation pattern appeared significant. For comparison purposes free space and cavity-mounted spiral element response is also included. Based upon these tests we included dividing walls within the cavity between radiating elements.

3.0 Concluding Remarks

The purpose of this paper has been to provide information on the use of strip-transmission line techniques at X-band. The development effort was chiefly concerned with providing a broadband eight element matrix for servicing an eight element linear array of spiral radiators. The components required for the development of the broadband eight element matrix have been designed and evaluated with proven feasibility. Prototype matrices have been evaluated using these components.

Data has been presented on the individual spiral elements to be used in the eight element array. Limited isolation measurements for the spirals in the array have been given.

Strip-transmission line techniques can be successfully applied to the design of broadband matrix and array configurations at X-band.

REFERENCES

1. Mehron, M.E., "Octave Bandwidth Multiple Beam Array", 13th Annual Symposium USAF, University of Illinois, Oct. 1963.

2. Shimizu, J.K., "A Strip-Line 3 db Directional Coupler", SRI Project 1592, June 1957.

3. Schiffman, B.M., "ANew Class of Broad-Band Microwave 90 Degree Phase Shifters", IRE Trans. MTT, Apr. 58, pp 232-237

4. Kraus, J.D., "Antennas", McGraw-Hill Book Co., N.Y. 1950, p.

5. Reed and Wheeler, "A Method of Analysis of Symmetrical Four-Port Networks", PGMTT, Oct. 1956, p. 246.

6. McNaughton and McCarry, "A New Broadband Co-Axial Hybrid Ring", ASTIA AD 142-507, Nov. 1956, The General Electric Co. Ltd., England.

7. R. Levy, "General Synthesis of Asymmetric Multi-Element Coup Transmission-Line Directional Couplers", PTGMTT, July 63, p.

8. Blass, J. "Multidirectional Antenna - A New Approach to Stacked Beams", 1960 IRE Convention Record, Part 1, Pages 48-50.

9. Shelton, J. and Kelleher, K., "Multiple Beams from Linear Arrays", IRE Trans. on Antennas and Propagation, Vol AP-9, No. 2, Page 154, March 1961.

10. Butler, J. and Lowe, R., "Beam Forming Matrix Simplifies Desi of Electronically Scanned Antennas", Electronic Design, Pg. 170.

11. Delaney, W., "Steering Radar Antenna Beams with a Lossless RF Matrix", Electronics, Page 50, July 13, 1962.

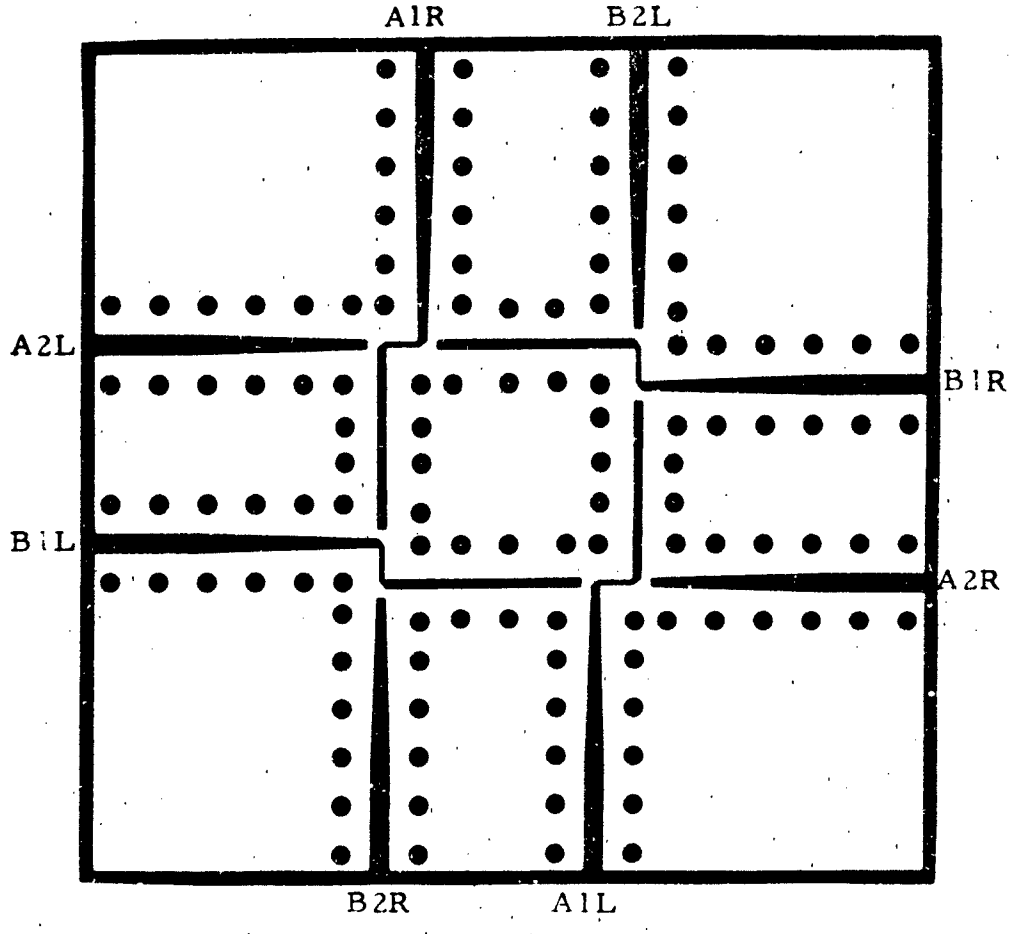

FOUR ELEMENT NARROW BAND BUTLER MATRIX

FIGURE 1.

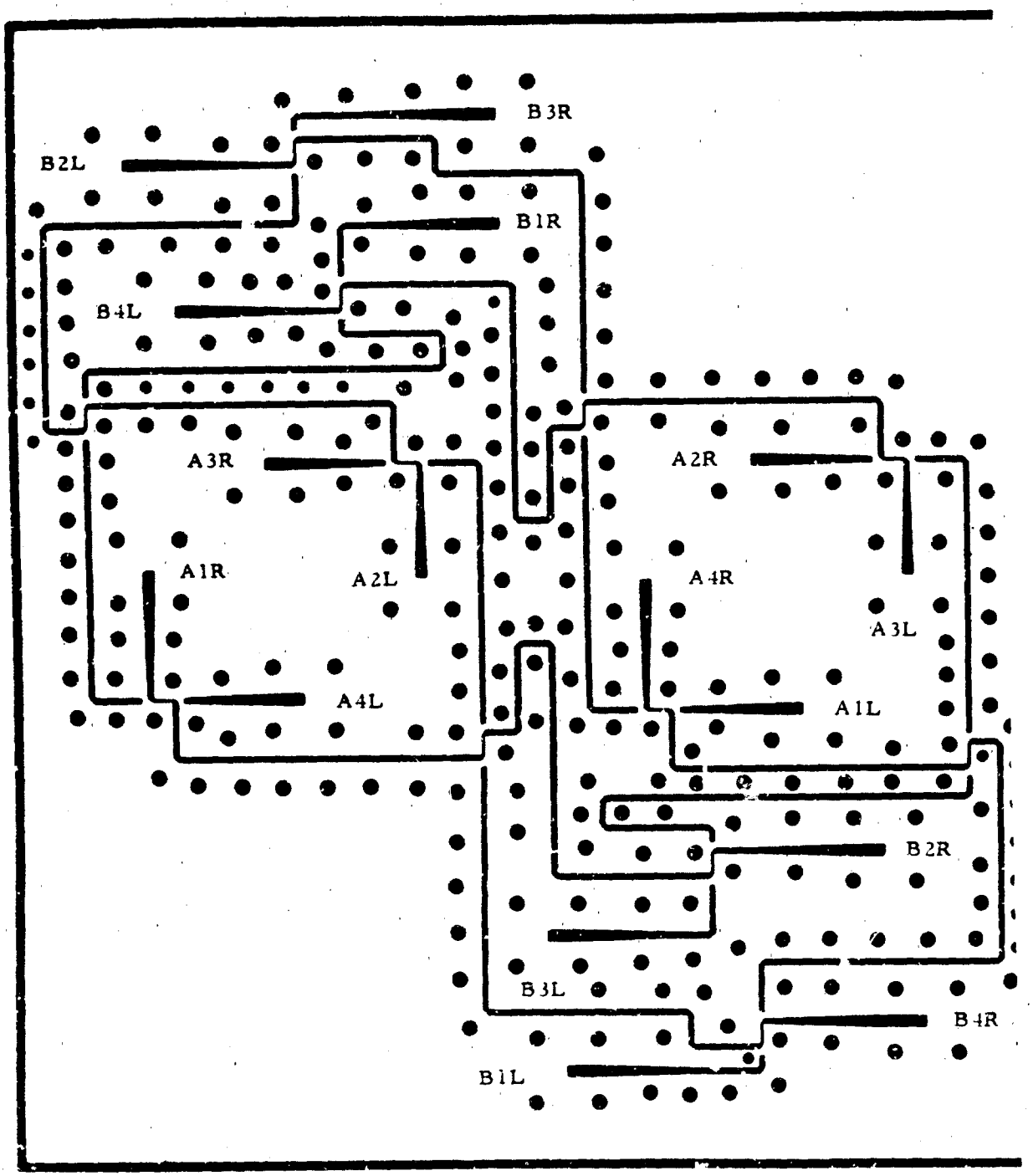

EIGHT ELEMENT NARROW BAND BUTLER MATRIX
FIGURE 2




1
2
3
4
5

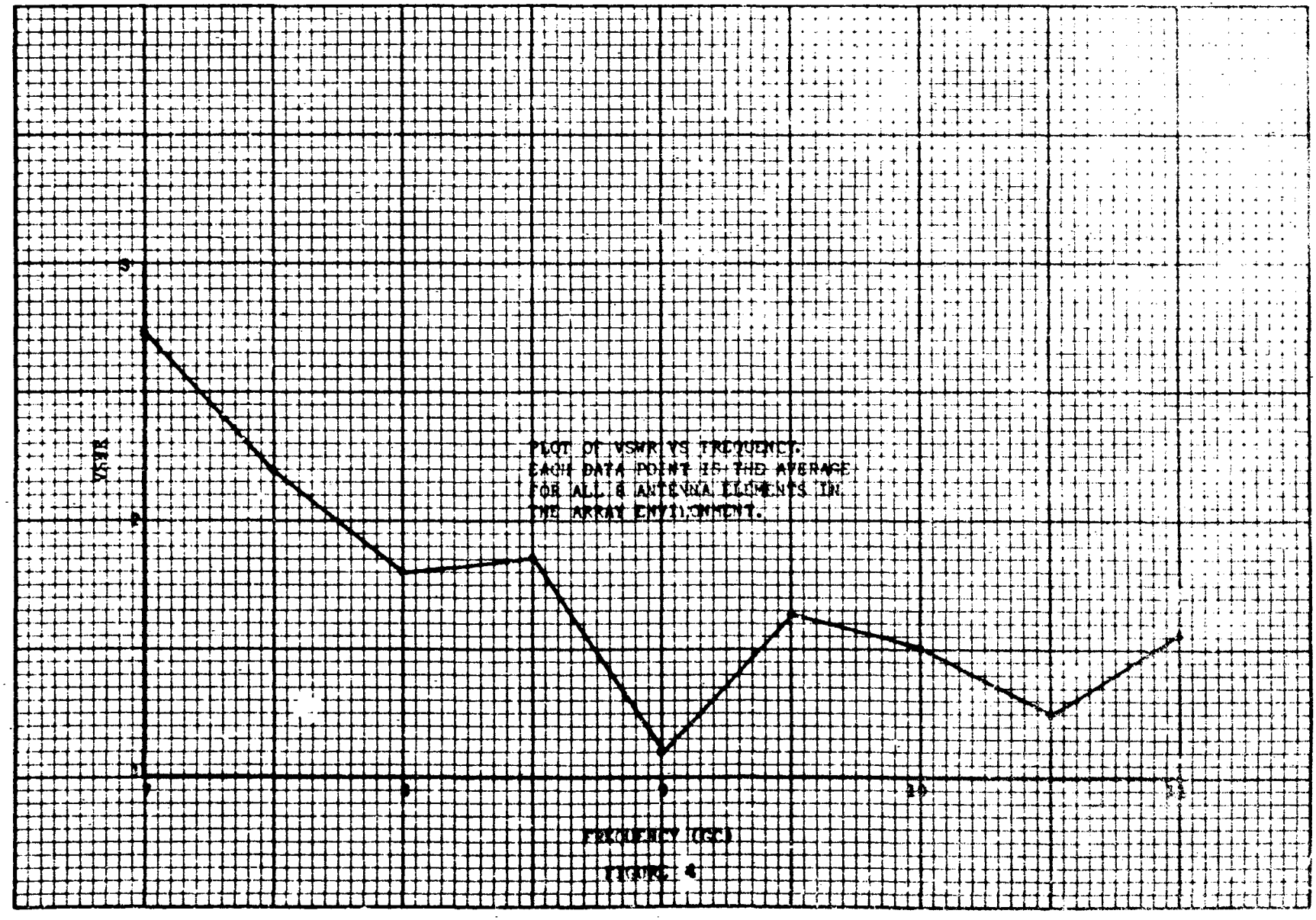
VSWR
PLOT OF VSWR VS FREQUENCY.
EACH DATA POINT IS THE AVERAGE
FOR ALL 8 ANTENNA ELEMENTS IN
THE ARRAY ENVIRONMENT.
FREQUENCY (GC)

FIGURE 4

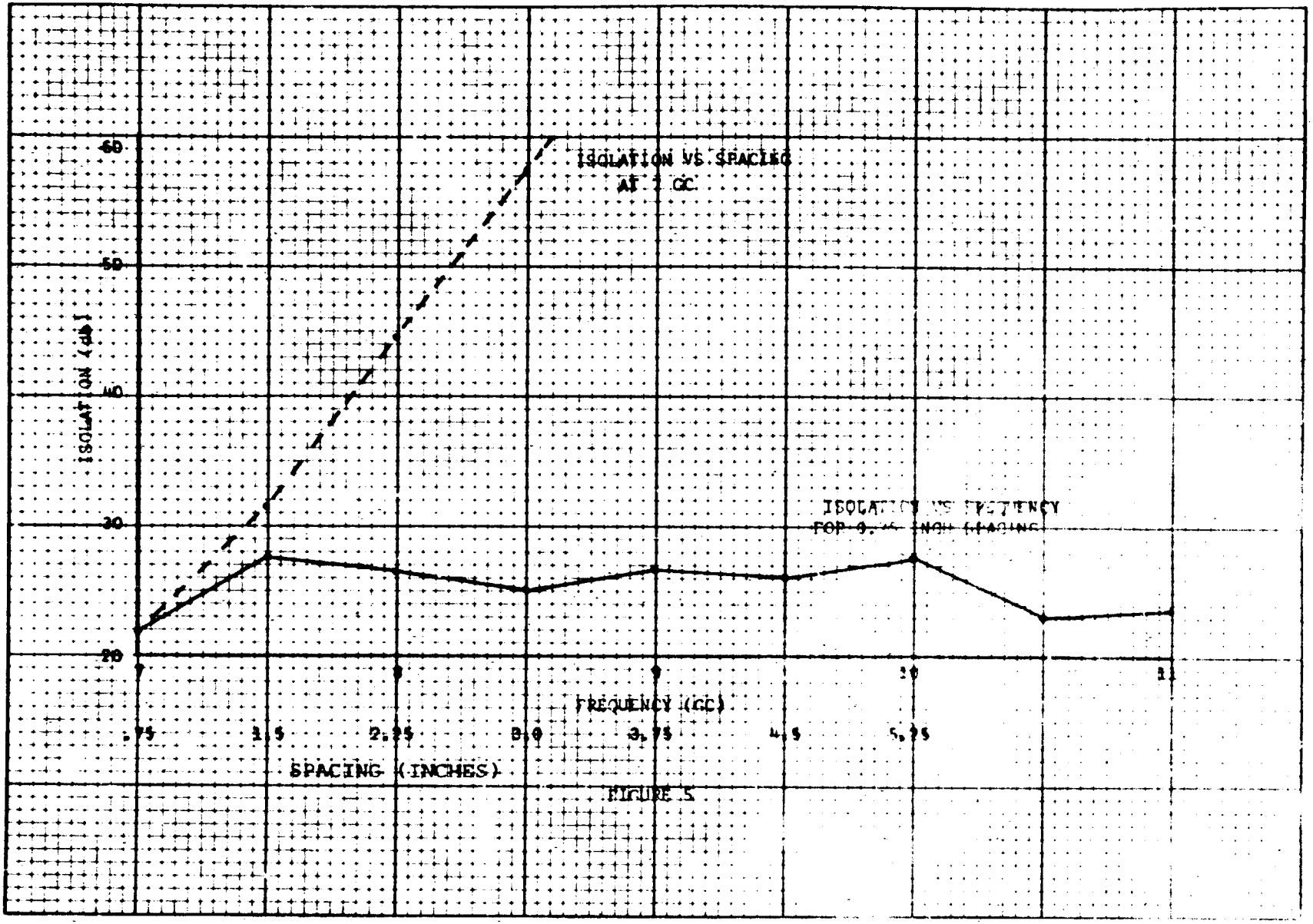
ISOLATION VS SPACING
AT GC
ISOLATION (dB)
60
50
40
30
20
ISOLATION VS FREQUENCY
FREQUENCY (GC)
.75
1.5
2.25
3.0
3.75
4.5
5.75
SPACING (INCHES)

FIGURE 5

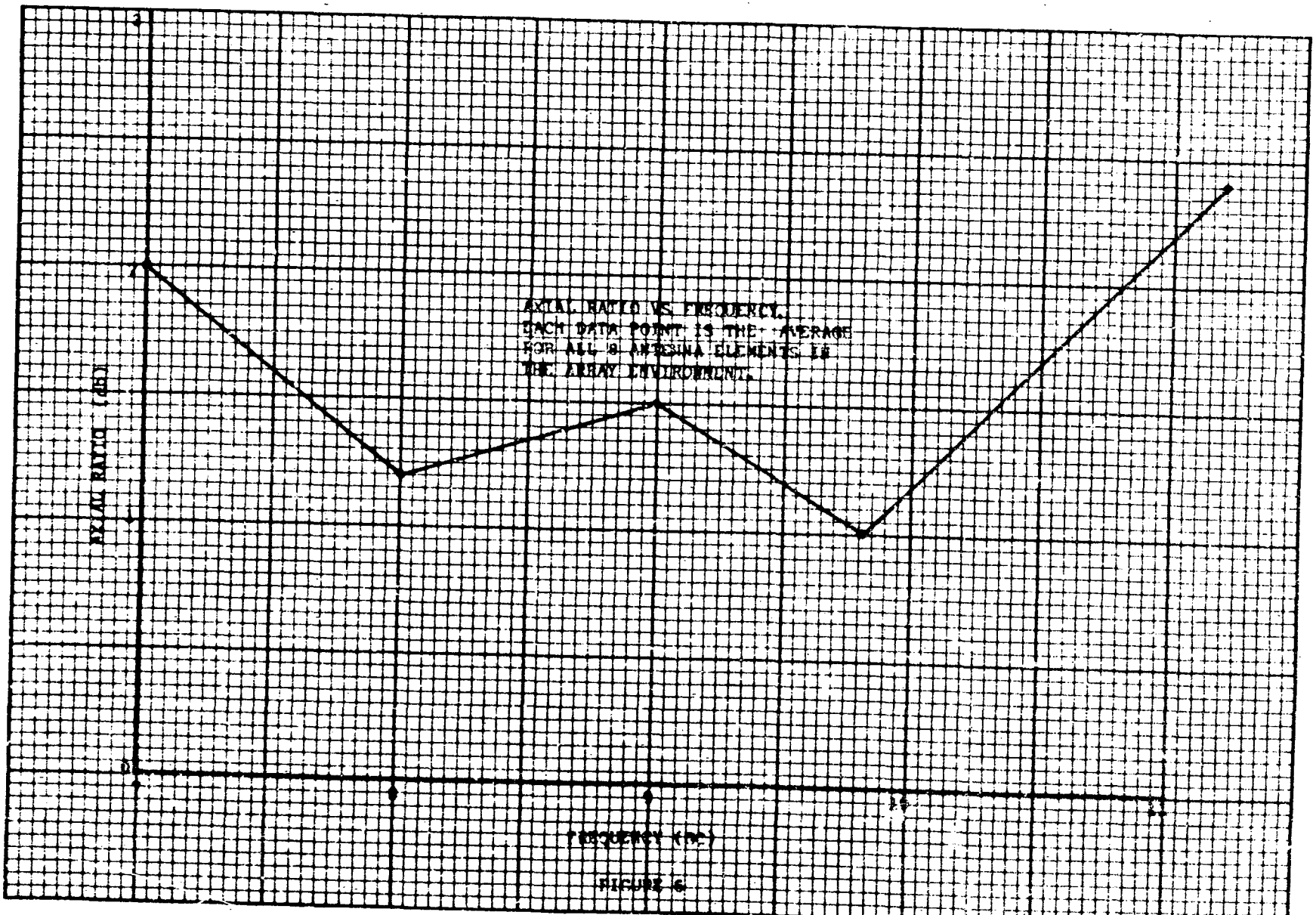
AXIAL RATIO VS. FREQUENCY.
EACH DATA POINT IS THE AVERAGE
FOR ALL 8 ARESINA ELEMENTS IN
THE ARRAY ENVIRONMENT.
AXIAL RATIO (dB)
FREQUENCY (Hz)

FIGURE 6.

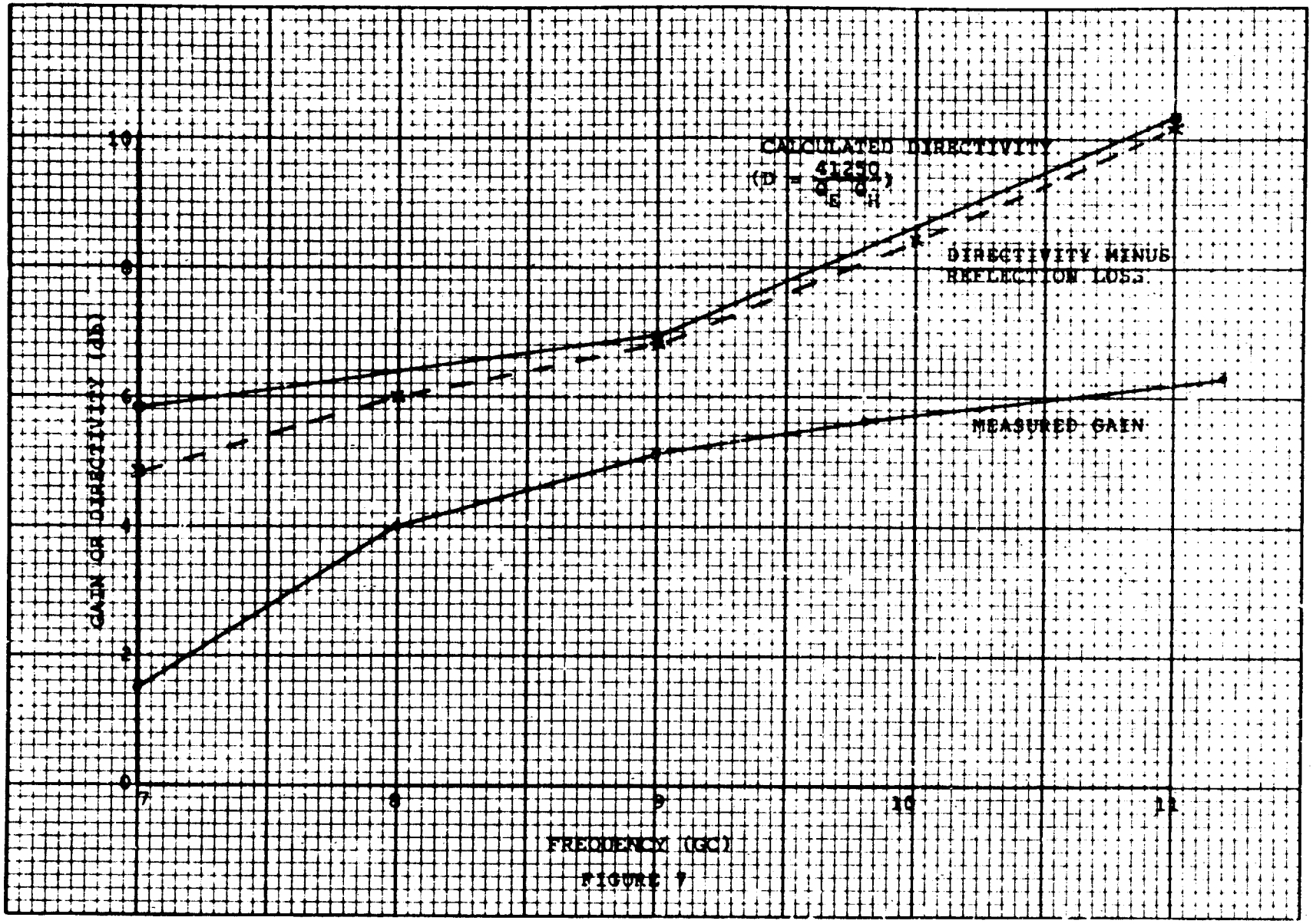
CALCULATED DIRECTIVITY
(D = 41250 / θE θH)
DIRECTIVITY MINUS
REFLECTION LOSS
MEASURED GAIN
GAIN OR DIRECTIVITY (DB)
FREQUENCY (GC)
0
2
4
6
8
10
7
8
9
10
11

FIGURE 7

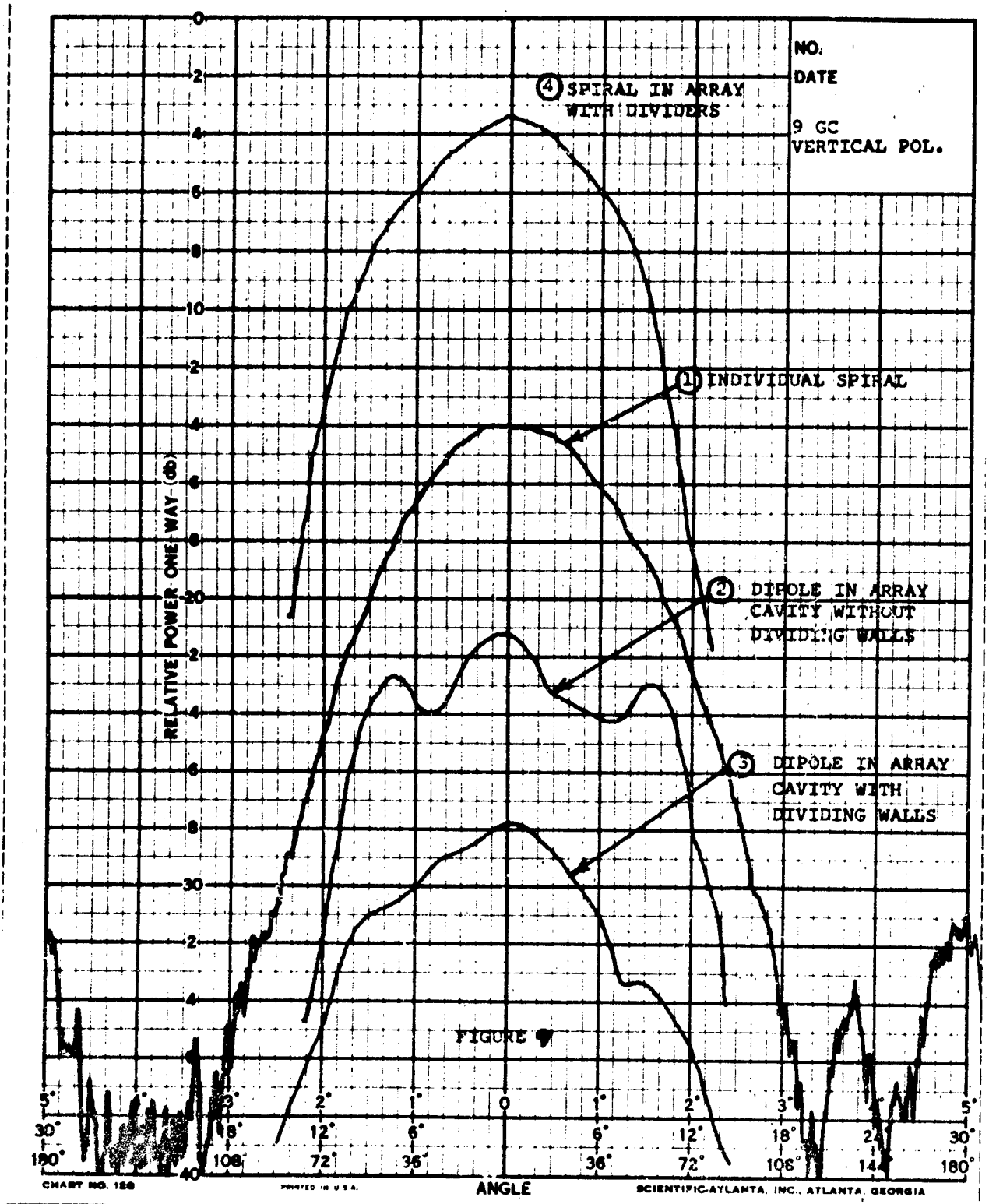
NO.
DATE
9 GC
VERTICAL POL.
4 SPIRAL IN ARRAY WITH DIVIDERS
1 INDIVIDUAL SPIRAL
2 DIPOLE IN ARRAY CAVITY WITHOUT DIVIDING WALLS
3 DIPOLE IN ARRAY CAVITY WITH DIVIDING WALLS
RELATIVE POWER ONE WAY (db)
0
2
4
6
8
10
20
30
40
5° 3° 2° 1° 0 1° 2° 3° 5°
30° 18° 12° 6° 0 6° 12° 18° 24° 30°
180° 108° 72° 36° 36° 72° 108° 144° 180°
ANGLE
CHART NO. 188
PRINTED IN U.S.A.
SCIENTIFIC-ATLANTA, INC., ATLANTA, GEORGIA

FIGURE 9

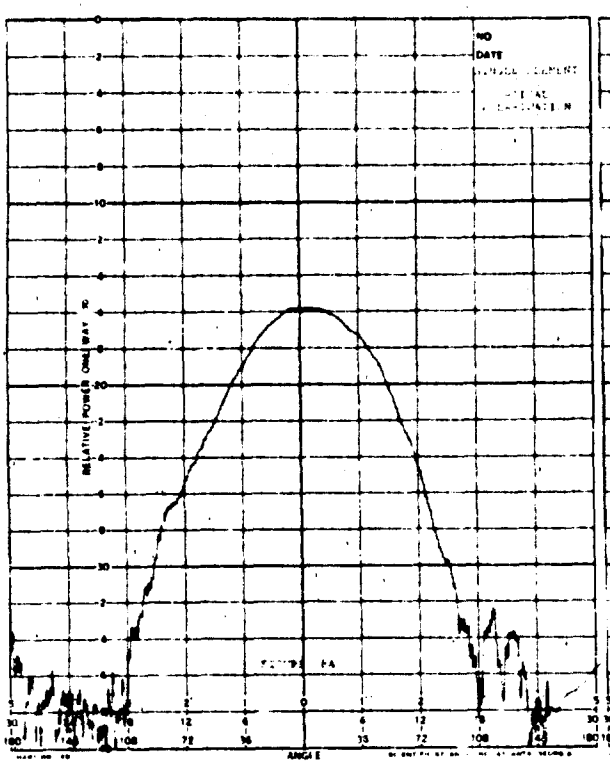
NO
DATE
RELATIVE POWER ONE WAY dB
ANGLE

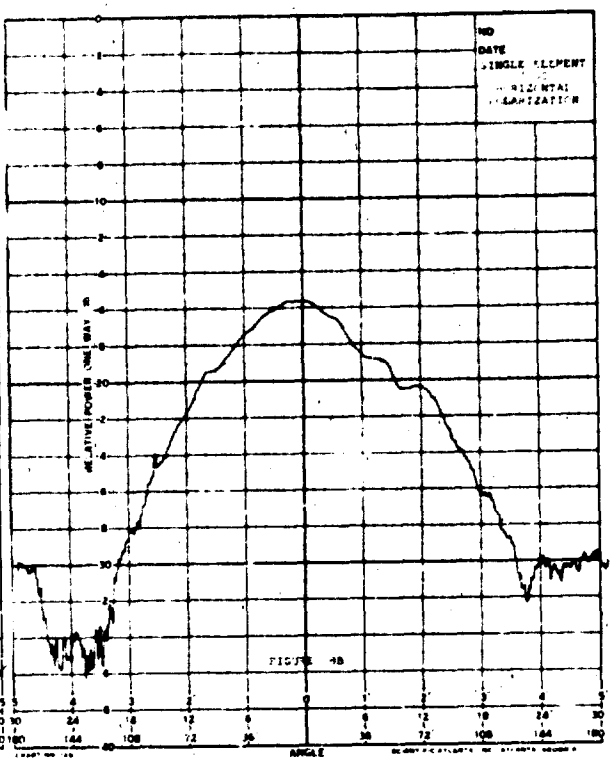
NO
DATE
RELATIVE POWER ONE WAY dB
ANGLE

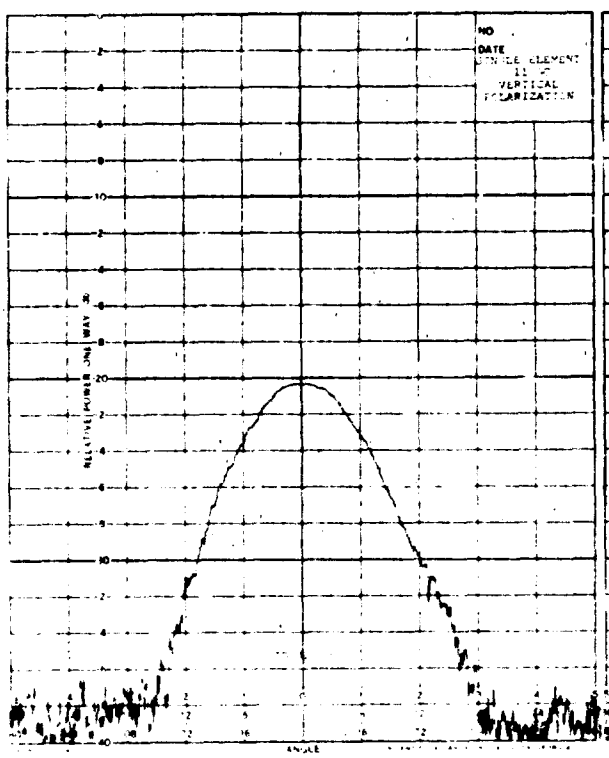
NO
DATE
VERTICAL
POLARIZATION
RELATIVE POWER ONE WAY dB
ANGLE

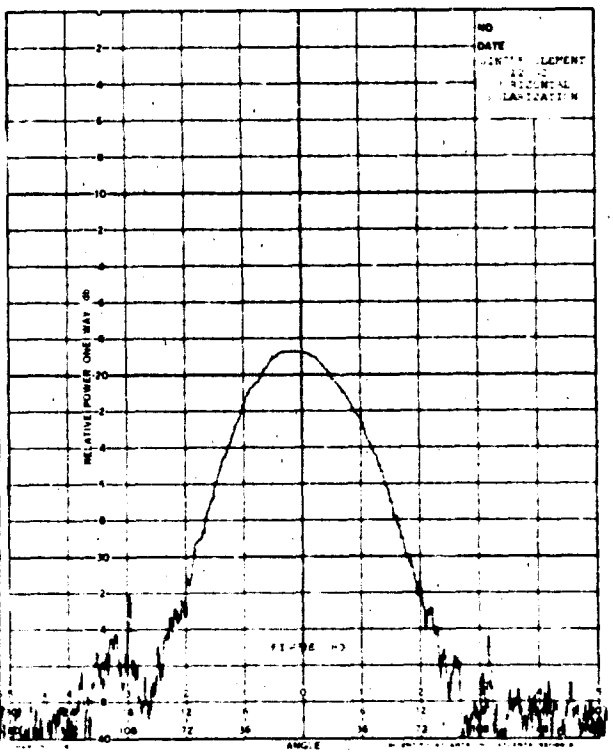
NO
DATE
RELATIVE POWER ONE WAY dB
ANGLE

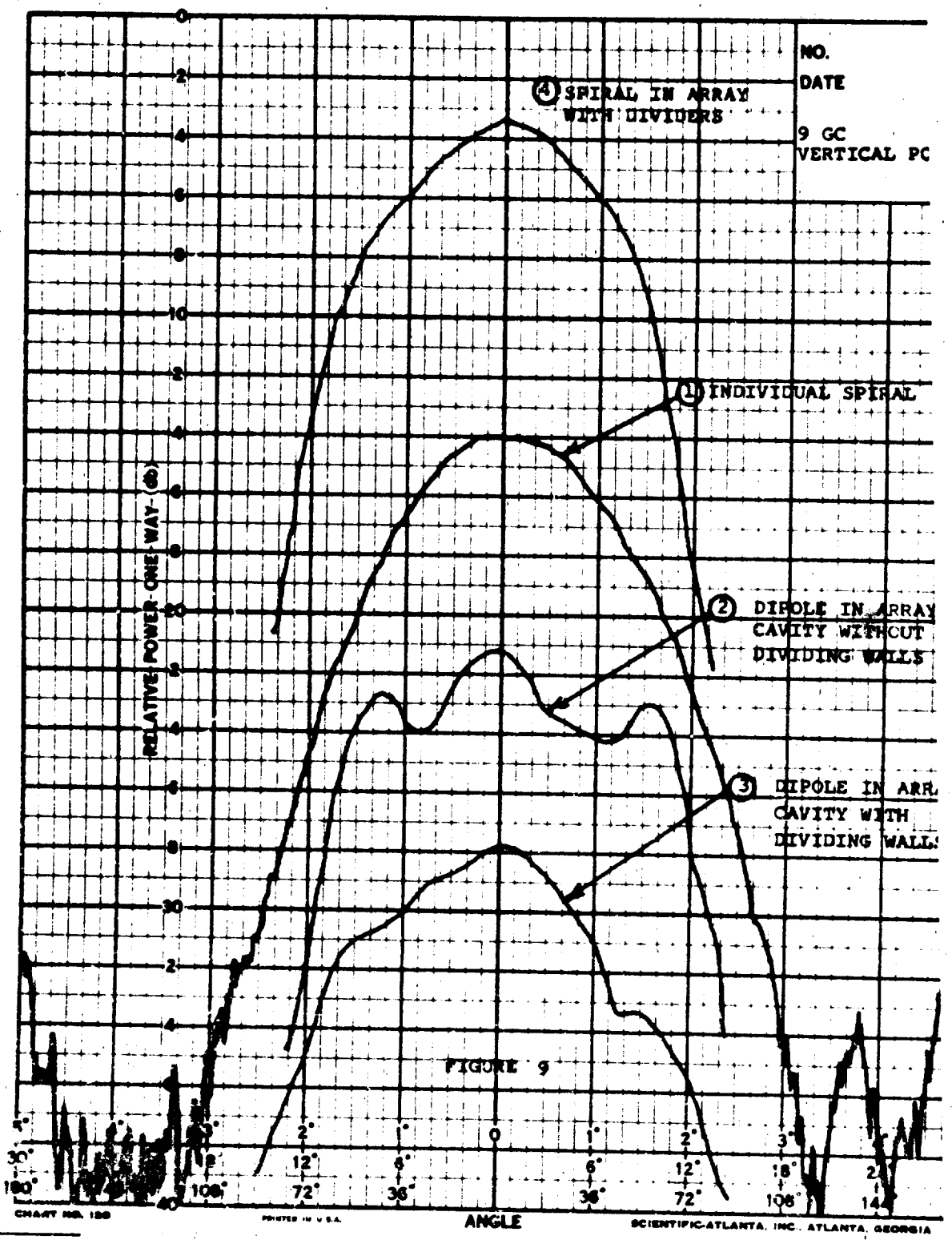
4 SPIRAL IN ARRAY WITH DIVIDERS
1 INDIVIDUAL SPIRAL
2 DIPOLE IN ARRAY CAVITY WITHOUT DIVIDING WALLS
3 DIPOLE IN ARR. CAVITY WITH DIVIDING WALL
NO.
DATE
9 GC
VERTICAL PC
RELATIVE POWER-ONE WAY-(dB)
ANGLE
SCIENTIFIC-ATLANTA, INC., ATLANTA, GEORGIA

FIGURE 9

HELIX FREQUENCY SCANNING FEED

by

G. H. Okubo

Presented at the USAF Antenna Symposium

Monticello Facility

University of Illinois

Hughes Aircraft Company
Ground Systems Group
Fullerton, California

14 September 1964
TP 64-14-38

This document contains proprietary information which shall not be reproduced or transferred to other documents or disclosed to others or used for manufacturing or any other purpose without prior written permission of Hughes Aircraft Company. Where related to a United States Government contract, such information may be disclosed as provided in such contract and may also be used by the United States Government for maintenance, servicing and repair purposes, or as otherwise provided by such prior written permission.

CONTENTS

		Page
I.	INTRODUCTION	1
II.	DESIGN CONSIDERATIONS OF THE HELIX PROPERTIES	1
	Propagation Characteristics	2
	Helix Impedance	3
	Helix Attenuation	4
	Helix Power Handling Characteristics	4
III.	DEVELOPMENT OF A PRACTICAL SHIELDED HELIX AT L-BAND	5
IV.	DEVELOPMENT OF THE POWER DISTRIBUTION COUPLERS	6
V.	COMBINATION HELIX-ANTENNA FREQUENCY-SCANNING SYSTEM	8
	CONCLUSION	9
	ACKNOWLEDGMENTS	9
	REFERENCES	27

ILLUSTRATIONS

Figure		Page
1	Propagation Characteristic for Helical Sheath, Pitch Angle = ψ, Radius = a	9
2	Helix Geometry	10
3	Propagation Characteristic for Unshielded Helix, $\psi = 10^{o}$, $\delta/o = 1/10\pi$, where δ is the Wire Diameter	11
4	Propagation Characteristics of a Tape Helix of Width δ and Radius a, in a Conducting Pipe of Radius b; b/a = 2.0, $\psi = 10^{o}$, $\delta/o = 1/10$	11
5	Impedance of an Unshielded Narrow Tape Helix, $\psi = 10^{o}$	12
6	Impedance of an Unshielded Tape Helix	13
7	Impedance of an Unshielded Round Wire Helix	14
8	Impedance of Round Wire Helix in a Conducting Pipe of Radius b, at the Limit of Zero Frequency	15
9	Shielded Helix Field Distributions, s = 0 and s = 0.5	16
10	Attenuation of an Unshielded Round Copper Wire Helix at 1.0 gc/s	17
11	Waveguide-to-Helix Transition	18
12	Helix-to-Waveguide Transition	18
13	Coupler Configuration	19
14	Coupling in db Versus Teflon Spacer Thickness	20
15	L-Band Dipole Plot for Helix Antenna	21
16	Helix Frequency Scanning Feed	22
17	Phase Versus Helix Coupler Output	23
18	Relative Amplitude Distribution for Helical Delay Line	24
19	Antenna Patterns Using Helical Line Feed	25

I. INTRODUCTION

In designing delay lines with conventional waveguides or coaxial lines at low frequencies (UHF), the problem of weight and size assumes increasing importance. Low frequency waveguide or rigid coaxial line, when used in the form of delay lines, is excessively bulky and massive. However, these problems of weight and size may be surmounted by using a helical conductor enclosed in a cylindrical shield. This type of feed line looks somewhat like an enlarged coaxial line with its center conductor formed into a helix. The light weight and compact features of the helical line offer great advantages when compared with the bulky waveguide configuration. In a VHF application investigation shows the helical line allows a weight saving of 20:1 over a conventional coaxial delay line.

This report will be concerned primarily with the development and test results of a lightweight, frequency-scanning, helical delay line. Preliminary efforts were directed toward investigating the feasibility of fabricating a practical frequency-scanning delay line in the form of a shielded helix. Having verified from experimental results that the shielded helical delay line is entirely practical from the standpoint of single mode operation and low loss at L-band frequencies, transition components associated with the helical line were developed. These components include waveguide-to-helical-line transition, helix load, power distribution couplers, etc. Finally, a linear array antenna was constructed with the objective of determining the frequency scanning capability of the helical feed line.

Throughout the course of the helical delay line program, Reference 3 has guided our experiments. The theoretical aspects of the helical line are treated in detail in references 2, 3, & 4, and will not be repeated in this report.

II. DESIGN CONSIDERATIONS OF THE HELIX PROPERTIES

In the design of helix frequency scanning delay line, it is necessary to consider the behavior of the following helix characteristics:

- Propagation constant (h)
- Helix impedance (Z)
- Attenuation constant (α)
- Peak power handling capacity (P_b).

To conduct an investigation most efficiently, it is desirable to predict and optimize the behavior of these properties in advance.

PROPAGATION CHARACTERISTICS

The sheath helix analysis shows many of the properties of the propagation characteristic of an actual helix.[1] The sheath model structure consists of a cylindrical conducting surface and of a current whose direction is taken at a helical angle, ψ, from the transverse plane. The propagation characteristic of a sheath helix is shown in Figure 1. The slow wave phenomenon is noted from the curve, as $\omega \to \infty$, $v/c \to \sin \psi$ where v is velocity of the wave in the axial direction.

Despite the fact that the analysis of the sheath model exhibits many properties of an actual helix, it is not complete in describing the propagation constant, especially, at high frequencies. An extensive analysis conducted by S. Sensiper for the open tape helix introduced the strong influence of the periodic nature in a helix.[2] Figure 2 is a sketch of an open tape helix. Analysis of the tape helix shows that the periodicity becomes evident when the wavelength of the operating frequency is equal to the length of a helix turn. Furthermore, because of the periodic nature of the structure, the solution of the open tape helix requires an infinite set of space harmonics to satisfy the boundary conditions.

Theoretical investigation of the open tape helix was extended to the case of a shielded helix by L. Stark[3] and later by C. M. Chu[4], who introduced the effects of discrete wire conductor in a helix.

The propagation characteristic of an open helix is shown in Figure 3 (after Sensiper) where:

$k = \frac{2\pi}{\lambda}$ = free space propagation constant.

h = axial propagation constant.

P = helix pitch.

ψ = helix pitch angle.

a = mean radius of the helix.

Reference 2 shows that there are certain values of propagation constant which are not permitted for normal slow wave operation. These values fall in the excluded regions of propagation shown in Figure 3. In the excluded regions, the velocities of the space harmonics travelling in the axial direction are greater than the speed of light, i.e., $|nm| < |k|$ for some m^{th} space harmonic. The result, an inefficient transmission line, is an abnormal mode radiating its power normal to the direction of propagation. The propagation constants of interest are bounded from the excluded region and are characterized by modes 1, 2, 3, 4, and 5.

Figure 4 shows the propagation characteristics of a shielded helix. Modes 1 and 4 are identical to that of the open helix. However in the shielded helix, the figure shows that modes can now exist in the excluded regions. These modes have cutoff frequencies and propagation characteristics similar to those that could exist in cylindrical waveguides. Reference 3 shows the properties of these modes are largely determined by the size of the outer pipe or the equivalent coaxial line, where the helix is replaced by a smooth cylinder.

For shielded helical transmission lines in general and delay lines in particular, it is desirable to operate along mode 4 in the second branch. As explained in detail in later sections, the efficiency of the helical line is increased when the frequency of operation is centered around ka = 1.5, corresponding to hp = 3π over that of operating at small values of ka. Operating along mode 4, it is possible to launch the pipe mode $e_{0,1}$. However, the cutoff frequency of this mode can be raised so that it can not propagate in the frequency band of interest. Reference 3 indicates that the cutoff frequency for mode $e_{0,1}$ is kb = 2.4 and for single mode operation b/a should be less than 1.6 (b = radius of conducting shield).

For a helical delay line the frequency-scan characteristic can be shown to be inversely proportional to the slope of the propagation characteristic. Consider the frequency scan equation (1).

$$kL \sin \theta = \phi - 2n\pi$$

where

θ = the angle of the main beam from the normal to the antenna.
L = free space distance between radiating elements.
k = free space propagation constant.
ϕ = total phase lag between adjacent elements.

For a shielded helix,

$$\phi = hL = kLR$$

where R is the retardation factor.

Inserting kLR for ϕ in equation (1) and differentiating with respect to k, it can be shown that in the region around broadside ($\theta = 0$),

$$\frac{\frac{d\theta}{dk}}{k} = R\,(0.573) = \frac{\text{change in scan angle in degree}}{\text{Percent change in frequency}} .$$

If the frequency of operation is in the normal helix modes, R can be approximated by csc ψ (the inverse of the slope shown in Figure 4).

HELIX IMPEDANCE

Knowledge of the helix impedance characteristics becomes useful when transitioning to other forms of transmission lines and in determining power handling capability. Impedance characteristics of a shielded and unshielded helix are shown in Figures 5, 6, 7, and 8.

The impedance curves shown in Figure 5 and Figure 6 are for an open tape helix. In Figure 5 the impedance is plotted versus frequency for the case where ψ is 10 degrees and the ratio of tape width to helix pitch (δ/p) is $1/10\pi^2$. Reference 2 explains how this curve was plotted from rigorous calculations. Calculations of helix impedance based on a developed helix is shown in Figure 6[4]. The curves show impedance characteristics with δ/p sec ψ taken as the variable. The s is equal to the number of turns per guide wavelength and is shown to be less than unity. However, s can be greater than unity; for this case, the largest integer of s is subtracted leaving s, as a rule, less than unity. To a close approximation, s = ka provided the helix is operated as a slow wave structure.

Both Figure 7 and Figure 8 show the variation of the helix impedance for a round wire helix. Figure 7 is the result of extending the impedance calculations of Figure 6 to a round wire. The impedance plot of Figure 8 is for a shielded helix at the limit of zero frequency[5], $s = 0$.

For a shielded helix operating in a slow wave mode ($s > 0$) Figures 5, 6, and 7 can be utilized in determining the impedance. The electric field configuration of the helix is shown in Figure 9 for $s = 0$ and $s = 0.5$.

HELIX ATTENUATION

Section II pointed out the benefits of operating on mode 4 rather than mode 1. By operating in the second branch, the pitch size can be increased, resulting in the use of larger diameter wire. The increase in wire diameter reduces the current concentration around the wire and, in general, improves attenuation.

Figure 10 shows the attenuation characteristic of an unshielded round copper wire helix at 1 gc/s from calculations in Reference 4. The curve shows that the attenuation increases as phase shift per turn increases, up to $s = 0.5$. Low attenuations at small values of s are the result of high impedance in this case. However, the phase change with frequency is also reduced at low s values. Therefore, best operation is close to $ka = 1.5$ or $s = 0.5$. The attenuation will be minimum for a broad range of wire diameter to helix pitch ratio. To determine attenuation at other frequency bands and for geometries scaled with the frequency, the attenuation constant goes as frequency to the three halves power.

The measured value of attenuation of the helical delay line reported here is shown in Table I. The loss appears comparable to a 50 ohm 1-5/8-inch coaxial transmission line. However, nearly half of the measured loss can be attributed to loss in the dielectric material. A substantial amount of dielectric material was used in the experimental helical line.

TABLE I. PROPERTIES OF A FABRICATED HELIX AT 1.35 gc/s

Mean Diameter = 3.047 inches
Pitch = 0.913 inch
Wire Diameter = 0.318 inch
Shield Diameter = 4.566 inches
Measured attenuation = 9.0 db/100 ft
Measured Peak Power Capacity > 1.5 megawatts[7]

Figure 10 can be used to determine the attenuation characteristics for a shielded helix operating in the delay line modes. For these modes the shield has little effect on the helix field configuration, as shown in Figure 9.

HELIX POWER HANDLING CHARACTERISTICS

In general, the helical delay line when used in a frequency scanning system must be able to transmit high pulsed power. The power handling capacity of the helix (equation 2) is as follows:[6]

$$P_b = \frac{2\epsilon}{\mu} (\pi r E_{max})^2 Z$$

where

r = radius of wire.
E_{max} = maximum E field.
Z = Helix impedance taken from Figure 7.

Equation (2) is derived with the assumption that the radial electric field has no variation around the wire. The approximation is most accurate in the region of minimum attenuation.

The influence of power breakdown due to wire diameter is shown in equation (2). For small conductor size the electric field intensity is increased and concentrated around the wire; hence voltage b eakdown is enhanced compared to a larger diameter wire. Here again, mode 4 operation appears desirable.

III. DEVELOPMENT OF A PRACTICAL SHIELDED HELIX AT L-BAND

For a frequency-scanning system, theory says that the helical delay line should operate on mode 4. The frequency corresponding to mode 4 operation centers at ka = 1.5. Furthermore, theory predicts that for minimum attenuation and peak power handling capability,

$$\frac{\text{wire diameter}}{\text{Helix pitch}} \approx 0.35$$

and for single mode operation,

$$\frac{b}{a} < 1.6 \ .$$

In order to experimentally verify the results obtained from theory, a helical main line section was fabricated to the dimensions shown in Table I.

$$\frac{\text{wire diameter}}{\text{Helix pitch (P)}} = \frac{0.318}{0.913} = 0.35$$

$$\frac{\text{radius of shield}}{\text{radius of helix}} = \frac{b}{a} = \frac{2.283}{1.523} = 1.5$$

The retardation factor $\csc \psi = 10.52$.

These parameters were selected to correspond to the optimum conditions predicted by theory. The operating frequency band was chosen to correspond to $1.1 < k'a < 1.3$. (The reason for not operating about ka = 1.5 was that theoretical study was not complete at the time of the experiment.) For $k'a = 1.1$ and 1.3 the frequencies are 1220 mc/s and 1520 mc/s, respectively. k' is modified to account for partial dielectric propagation.

To determine the propagation characteristics of the experimental helical line, a special cylindrical outer shield was constructed. The shield consists of a probe carriage which slides along a longitudinal slot and is similar to a coaxial slotted line. The helix termination was made of an annular cylinder of synthane and fitted between the helix and shield. VSWR of the termination is less than 1.1 over the frequency band. In conjunction with the helix slotted line, a phase measuring system was set up.

Measurements of phase versus axial distance showed good agreement with theory. As would be expected, the wavelength along the helix is shorter than the free space value due to the substantial amount of dielectric material used in supporting the helix conductor. Measurements show that the phase velocity parallel to the helix wire varies from 0.90 c at f = 1265 mc/s to 0.95 c at f = 1420 mc/s (c = velocity of light in free space).

At a frequency of 1350 mc/s, the insertion loss of the helix was measured as 0.092 db per foot. As mentioned earlier, loss in the dielectric material contributed to approximately half the measured insertion loss.

High power measurements have shown that the helical line is capable of withstanding more than 1.5 mw of transmitted power. The transmitter used for this test was the type AN/TPS-1 operating at a frequency of 1300 mc/s, PRF = 360 pps and a pulse width of 2 microseconds. The absolute power breakdown value of the main helix section was not determined. Power breakdown in the helix to waveguide transitions occurred prior to the main line helix.

Figures 11 and 12 show the type of helix to waveguide transitions used in the high power test. These transitions use the probe-type coupling technique and are not critically sensitive to dimensional variations. Over the frequency band 1260 mc/s to 1420 mc/s the VSWR is less than 1.1 for these transitions. Insertion loss of a single transition was measured as 0.022 db at 1350 mc/s.

IV. DEVELOPMENT OF THE POWER DISTRIBUTION COUPLERS

Directional couplers were developed to couple energy from the helix to the radiating elements. Design requirements were as follows:

- A large range of coupling values, -13 db to -30 db (required for low sidelobe antenna)
- These couplers should be highly directional in order to minimize reflection toward the input of the helix
- These couplers should not introduce high mismatch into the main line
- The power handling capability of the main line helix must not be degraded significantly by the introduction of the coupling wires inside the shield.

Two related types of coupling configurations were considered in satisfying these requirements. One is known as the coupled helix configuration[7]. This type of coupler consists of an auxiliary helix centered between the mainline helix and the shield. Models of this coupler for complete power transfer have been developed which exhibit extremely broadband directional coupling characteristics[8]. The second type of coupler is a short, fixed length of strip transmission line following the contour of the shield. The stripline is located between the shield and the mainline helix.

The first type of coupler, using coupled helices, has a natural coupling between parallel wire transmission lines; in particular, it is contra-directional in that the induced wave travels in the opposite direction to the inducing wave. If either the electric or magnetic coupling were eliminated, the coupling would be non-directional and if either were reversed,

the coupling would be co-directional. In lumped constant video directional couplers, the magnetic coupling can be reversed by reversing the winding sense of one coil. The same situation exists in the case of coupled helices.

Power transfer from the main helix to the coupling helix is accomplished in the following manner: Theory predicts that the power transfers back and forth from the main helix to the coupling helix along the axial distance to produce a "beat" or coupling wavelength. Therefore, it is possible to determine the tapping points (or length) of the coupling helix at which the required coupling value is desired. In this manner, complete or minimum power transfer can be accomplished by tapping at the peak or null of the "beat" wavelength.

Coupling coefficient can be controlled also by moving the coupling helix closer to the main helix or by varying the pitch and sense of winding the coupling helix. With tighter coupling the coupling coefficient is more constant over the frequency band. The directivity is affected by each of these variations and so a compromise must be made to maintain a desired value of constant coupling coefficient, constant transfer phase, and directivity over the frequency band. Coupling helices have been fabricated by winding a silver strip on a polyfoam core to fit over the main line. Beat pattern measurements were taken to verify theory.

The second type, the stripline coupler, is currently used in the helical delay line to achieve directional coupling by control of the impedance of the auxiliary line. The stripline coupler is similar in operation to the loop-type directional coupler used in some coaxial applications or stripline couplers. One advantage of this type of coupler is that the coupling stripline is much shorter than the coupled helices. Loop-type couplers (assuming proper construction) have intrinsic backward directivity; that is, the coupled energy in the secondary line travels in the opposite direction from that taken by the wave in the main transmission line or guide. Although loop-type directional couplers have found wide application in recent years in measurement systems, their design is largely one of "cut" and try.

The stripline coupling configuration developed for the helical line is shown in Figure 13. This coupler is simply a short section of helix (some $\lambda g/4$) with coaxial connectors attached at each end. A 7/8-inch coaxial line is used to increase the power handling capability of the coupler. Teflon dielectric spacers maintain a constant separation distance between the strip and the shield. Furthermore, these spacers ensure that the stripline follows the curvature of the shield, thus, promoting coupler repeatability, aid in matching the coupler, and increase power breakdown strength.

Various tests were conducted to determine the effect of changing the stripline parameters of the coupler. First, the distance (the thickness of the teflon spacers) between the shield and stripline was varied. The width of the stripline was also varied to maintain a reasonably good VSWR. A particular value of coupling coefficient was obtained for a specific teflon thickness. During preliminary testing no attempt was made to optimize the directivity; however, the objective was to obtain a directivity of greater than 20 decibels.

After the tests of varying the teflon thickness, angular variations of the stripline were introduced to observe the coupling effects. Using an 11-db coupler, angular variations along the helix pitch angle were tested. Test results showed that for minimum coupling variation versus frequency,

the optimum angle of the stripline was 9.37 degrees opposite the helix angle. Directivity measurement showed values of 17 decibels or greater. Further increase of stripline angle resulted in loss of directivity. The design information obtained from this test was extended to the 17-decibel coupler, and the result showed identical coupling variation.

For maximum directivity the width of the coupling strip was varied keeping the thickness of the teflon spacer constant. Maximum directivity is obtained when the ratio of the thickness of the teflon spacer to the width of the strip is 0.416 of an inch. The impedance of the coupled strip transmission line establishes the mismatch of the terminals relative to the transmission line. This impedance also affects the manner in which reflections from the two terminals of the coupler interact with each other. With a suitable choice of strip width for a given dielectric thickness, the coupled wave cancels at the directive arm and adds at the coupling arm.

Final design information for the power distribution coupler is shown in Figure 14. The ratio of the teflon thickness to the width was kept constant at 0.416 of an inch for all points along the curve.

V. COMBINATION HELIX-ANTENNA FREQUENCY-SCANNING SYSTEM

The linear array antenna used to determine the frequency-scanning capability of the helical delay line consisted of 10 dipoles placed collinearly along a corner reflector. Figure 15 shows a VSWR characteristic of a typical dipole. VSWR is equal to or less than 1.5 over the frequency range, 1320-1520 mc/s.

The helix-antenna components were assembled as a unit, as shown in Figure 16. The length of the main helix line was 48 inches long to provide for 10 couplers. The unit was designed with a retardation factor of 10.52 ($\csc\psi$) and to scan ±45 degrees over the frequency band of 1300 to 1500 mc/s. The spacing between couplers is 4.565 inches. From practical considerations and to obtain low sidelobes, a modified Taylor amplitude distribution was chosen for this type of an array. Coupling values ranged from -10 decibels to -26 decibels, producing a beamwidth of 13 degrees in the plane of scan.

Prior to testing the helix-antenna combination at the antenna pattern site, tests were conducted to determine the relative phase and amplitude at the outputs of the coupler. Relative phase measurements taken at the output of each coupler indicated that the curve of the phase error is similar for each frequency of interest. Correction of the phase error was accomplished by adjusting each of the coaxial cables attached to the couplers to an appropriate length. The curve depicting the corrected phase error in Figure 17 is the result of the phase measurement taken at the output of these adjusted coaxial lines. Amplitude measurement shows good agreement with the calculated values as shown in Figure 18.

Finally, the entire helix-antenna combination was taken to an antenna pattern site to determine its frequency scanning capability. The results of the test are plotted in Figure 19 over the frequency band 1250-1520 mc/s. The side lobes and beamwidth show good agreement with the calculated values.

CONCLUSION

The performance characteristics of the helix-antenna combination have been tested and, in the frequency band of interest, adhere closely to those predicted by theory. Thus, it was established that the shielded helical line is entirely capable of single mode operation, low loss, and high power capability at L-band frequencies and lower frequencies. Furthermore, it appears that this technique can be extended to the S-band region for wider beamwidths.

ACKNOWLEDGMENTS

The author wishes to expresa his appreciation to L. Stark for his instructive criticism during the course of this work, and to D. L. Thomas for his contribution toward the design of the necessary power distribution coupler.

45281-11

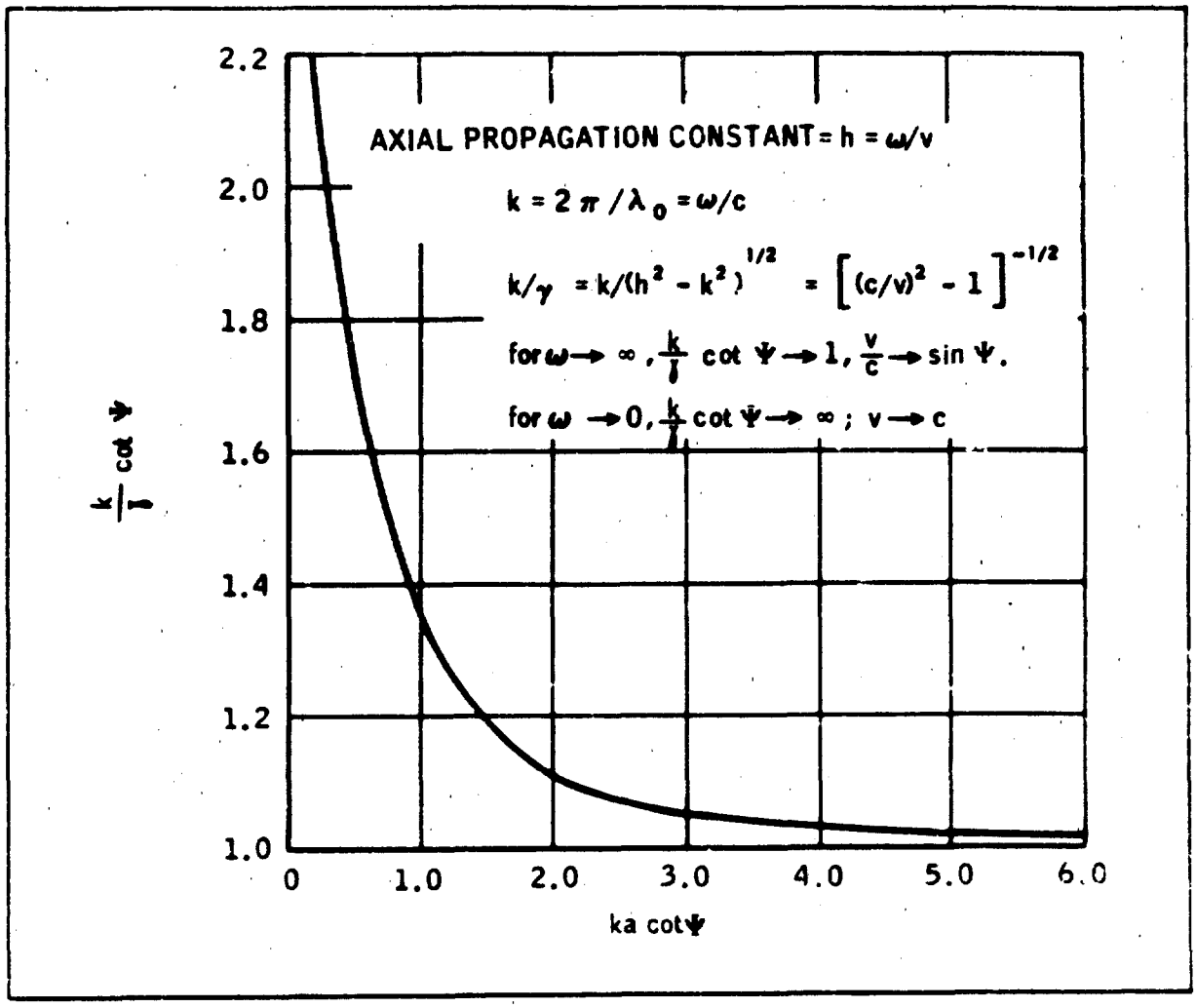

Figure 1. Propagation Characteristic for Helical Sheath, Pitch Angle = ψ, Radius = a

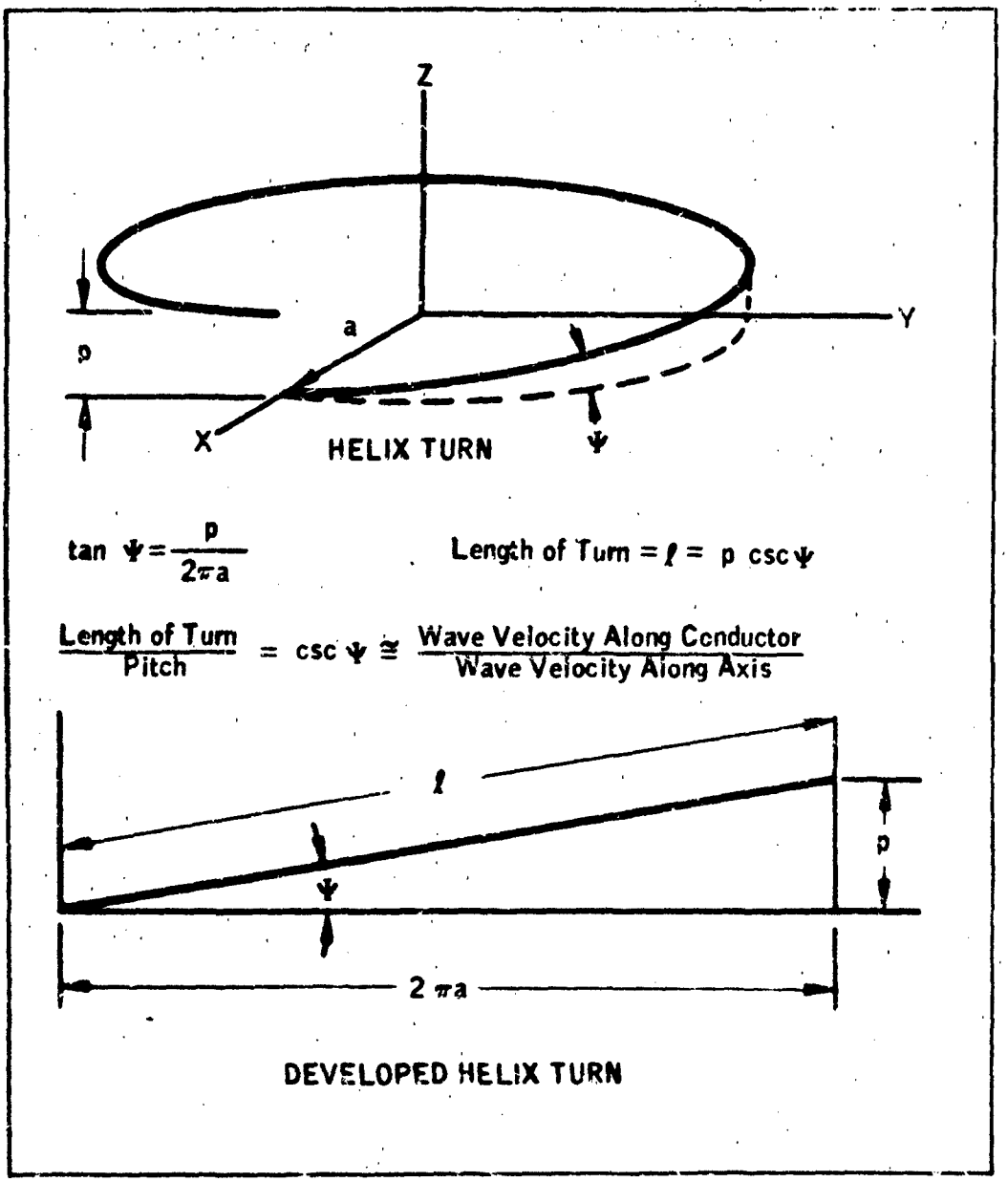

Figure 2. Helix Geometry

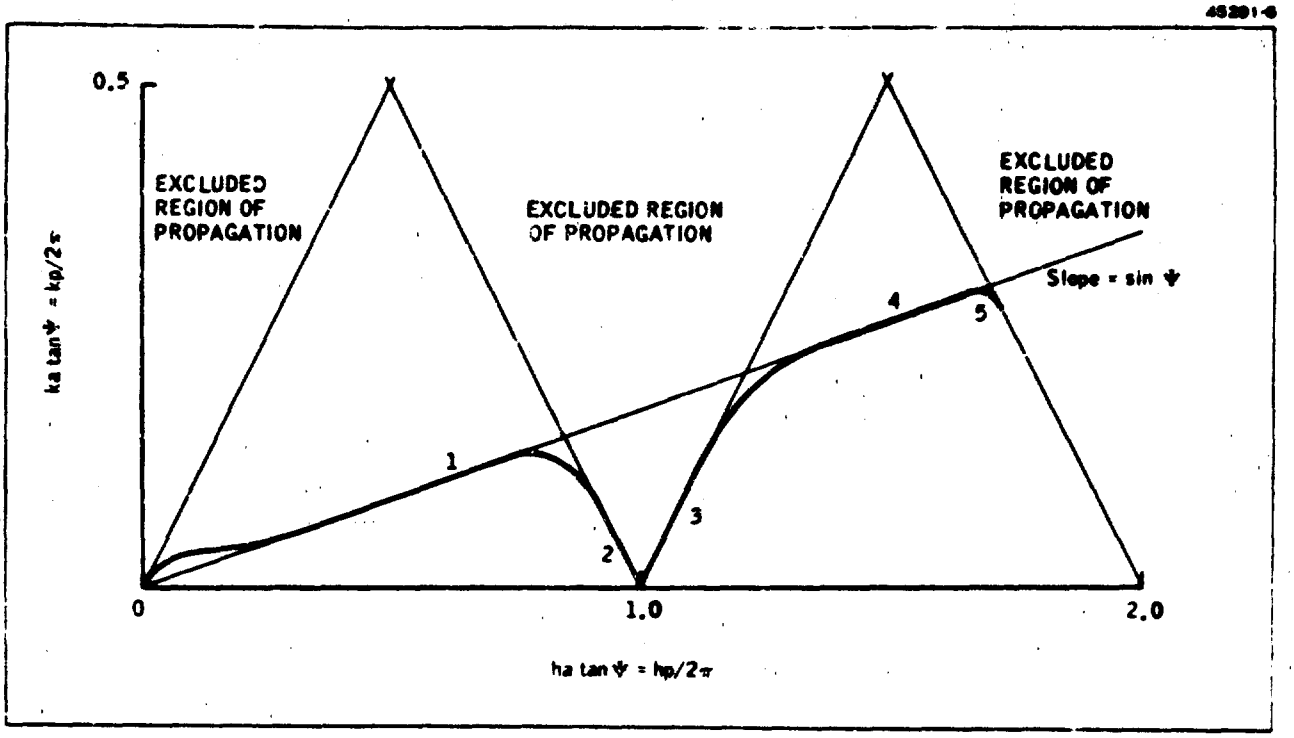

Figure 3. Propagation Characteristic for Unshielded Helix, ψ = 10°, δ/ρ = 1/10π, where δ is the Wire Diameter

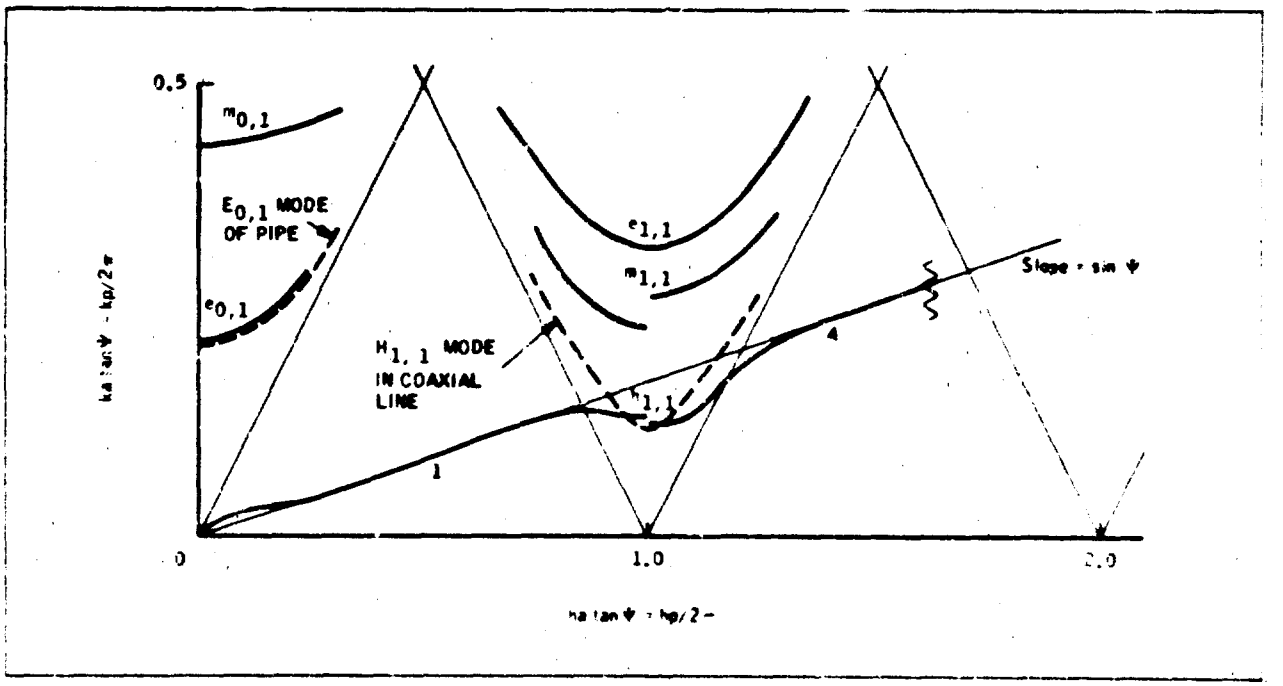

Figure 4. Propagation Characteristics of a Tape Helix of Width δ and Radius a, in a Conducting Pipe of Radius b; b/a = 2.0, ψ = 10°, δ/ρ = 1/10

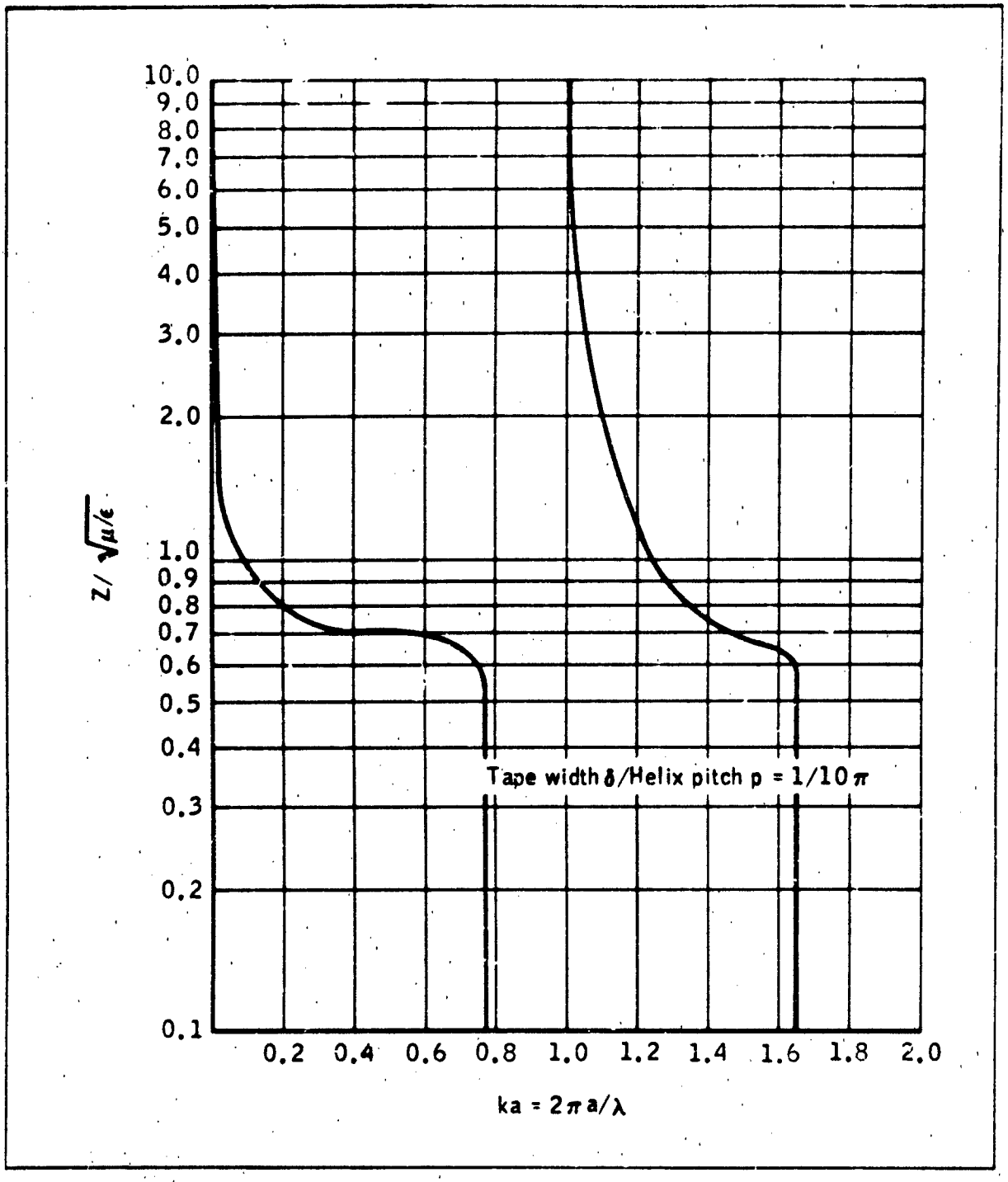

Figure 5. Impedance of an Unshielded Narrow Tape Helix, ψ = 10°

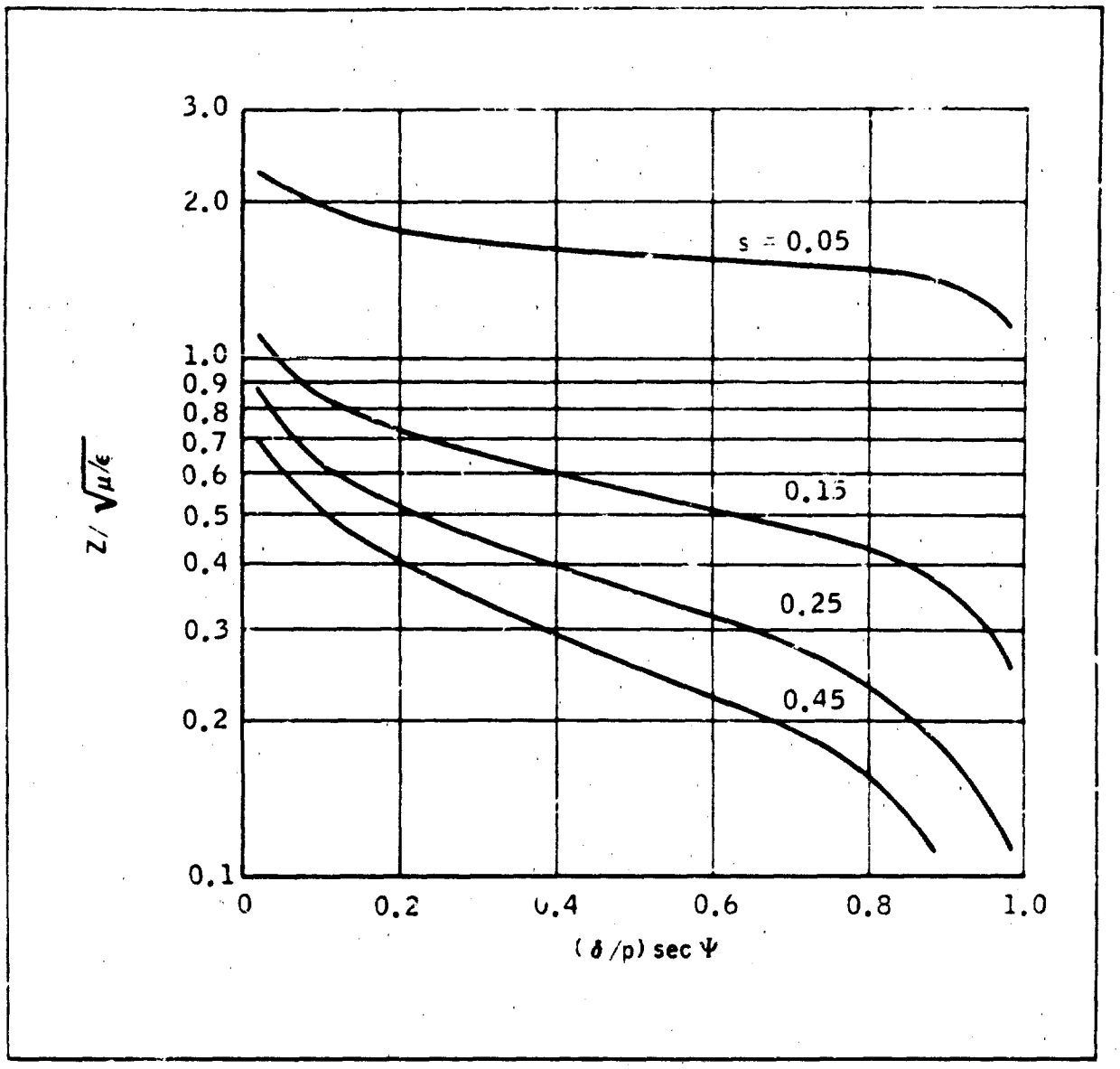

Figure 6. Impedance of an Unshielded Tape Helix

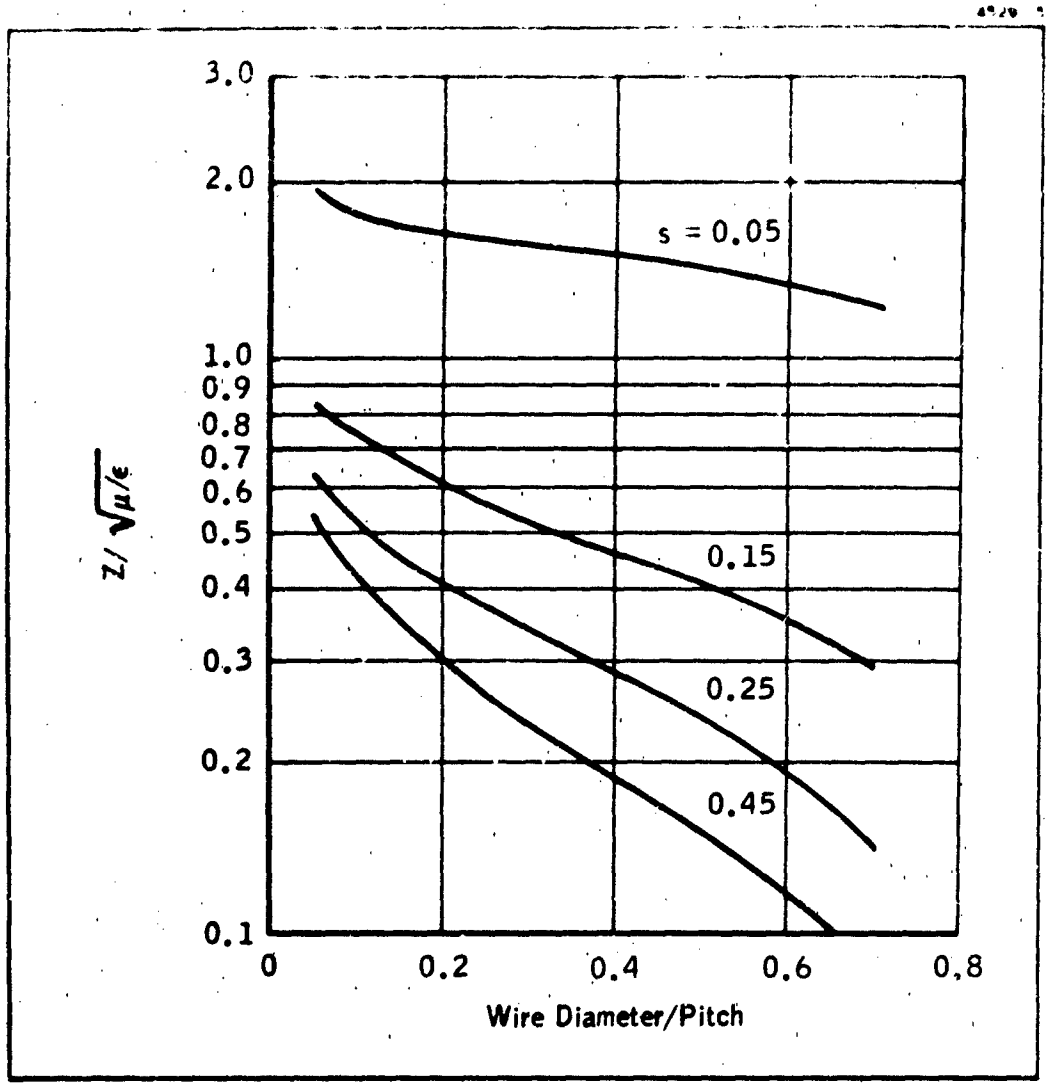

Figure 7. Impedance of an Unshielded Round Wire Helix

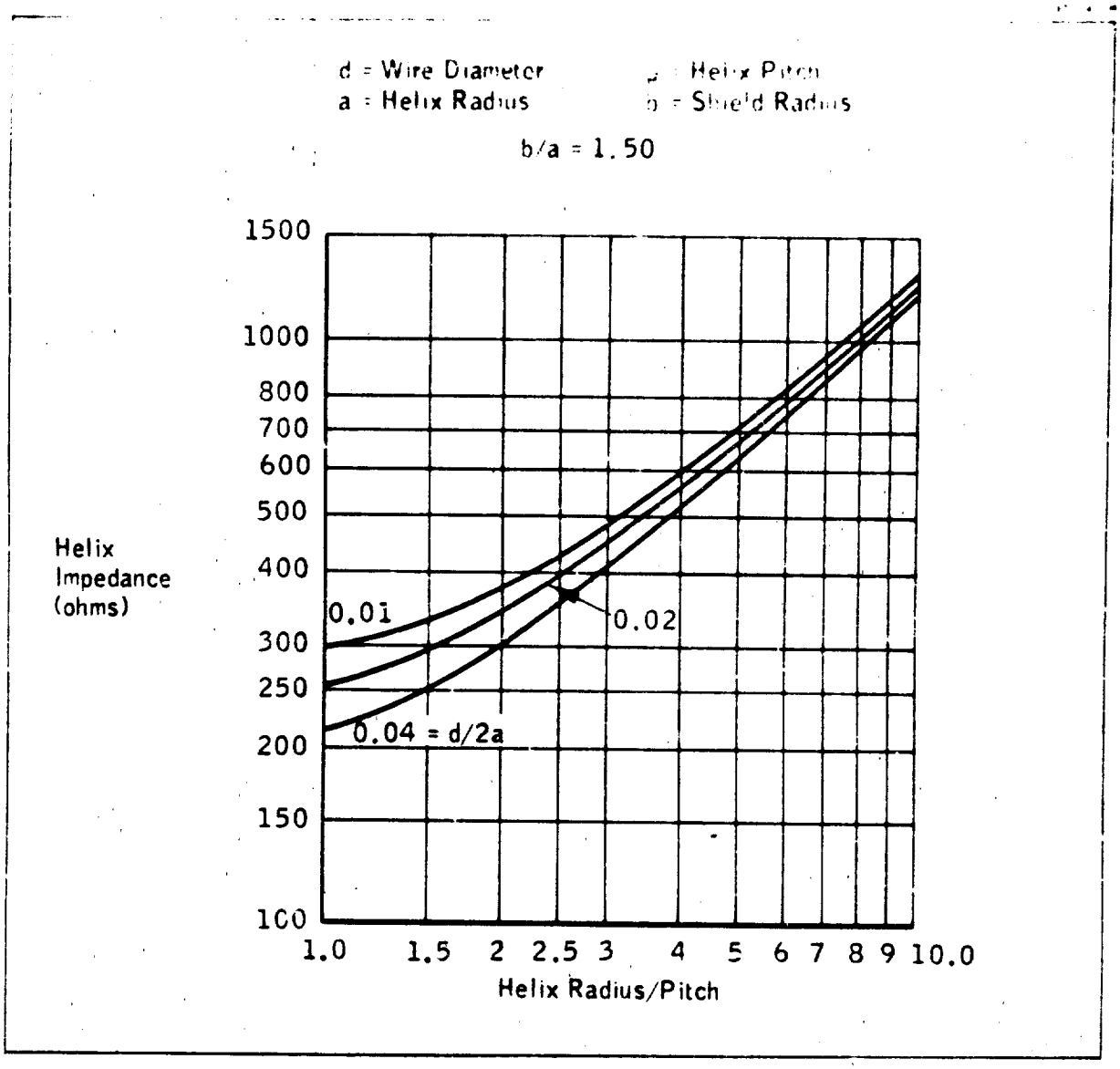

Figure 8. Impedance of Round Wire Helix in a Conducting Pipe of Radius b, at the Limit of Zero Frequency

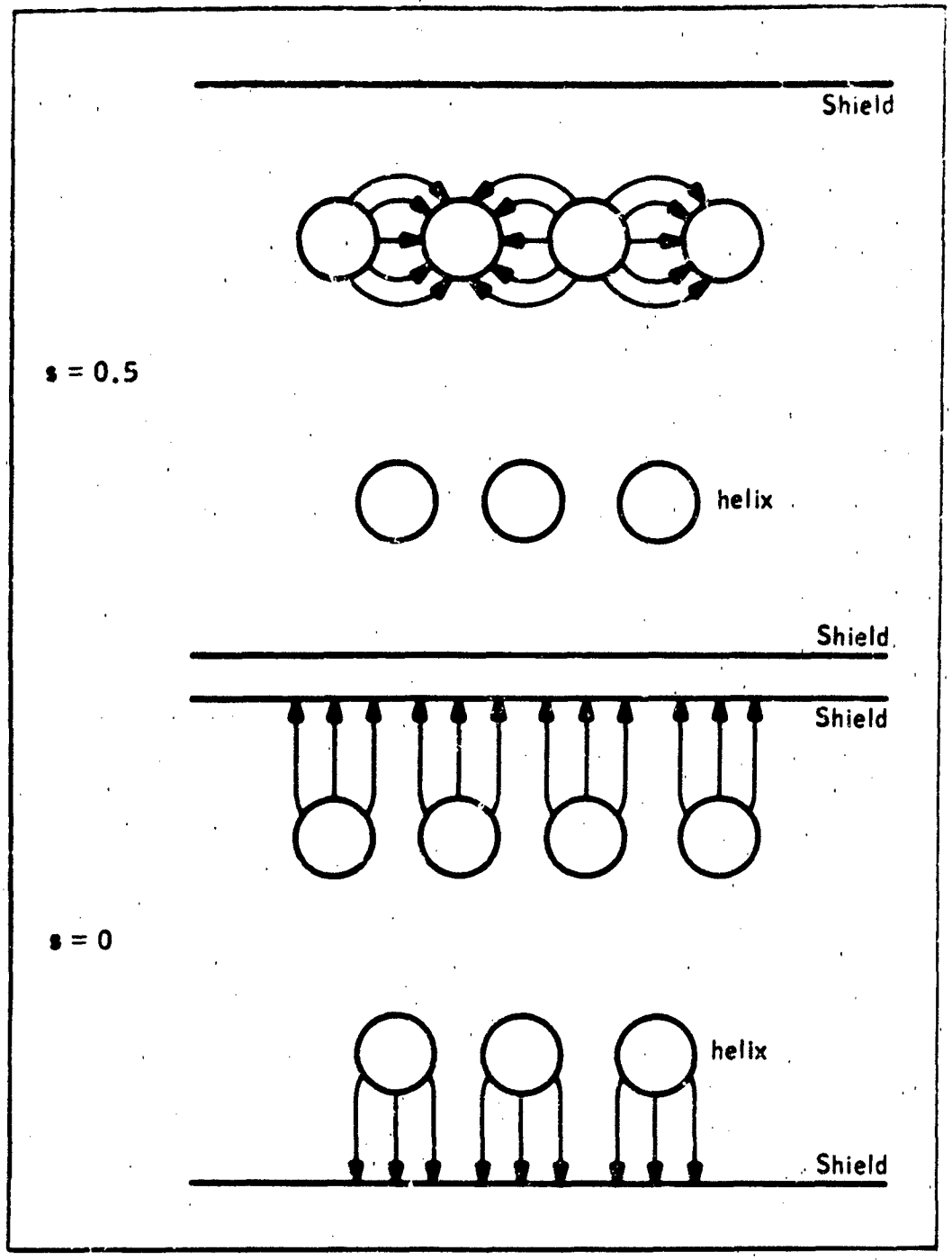

Figure 9. Shielded Helix Field Distributions, s = 0 and s = 0.5

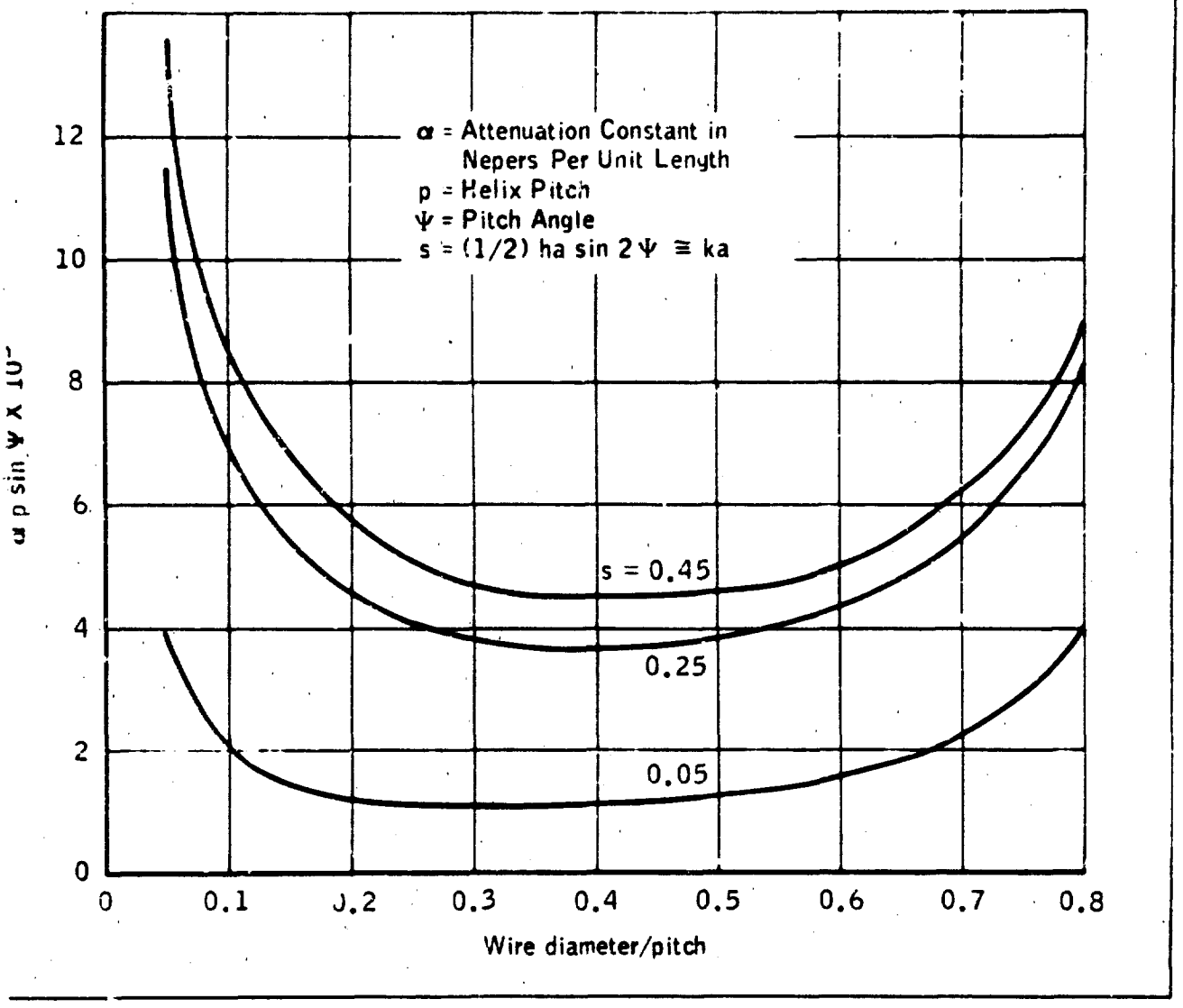

Figure 10. Attenuation of an Unshielded Round Copper Wire Helix at 1.0 gc/s

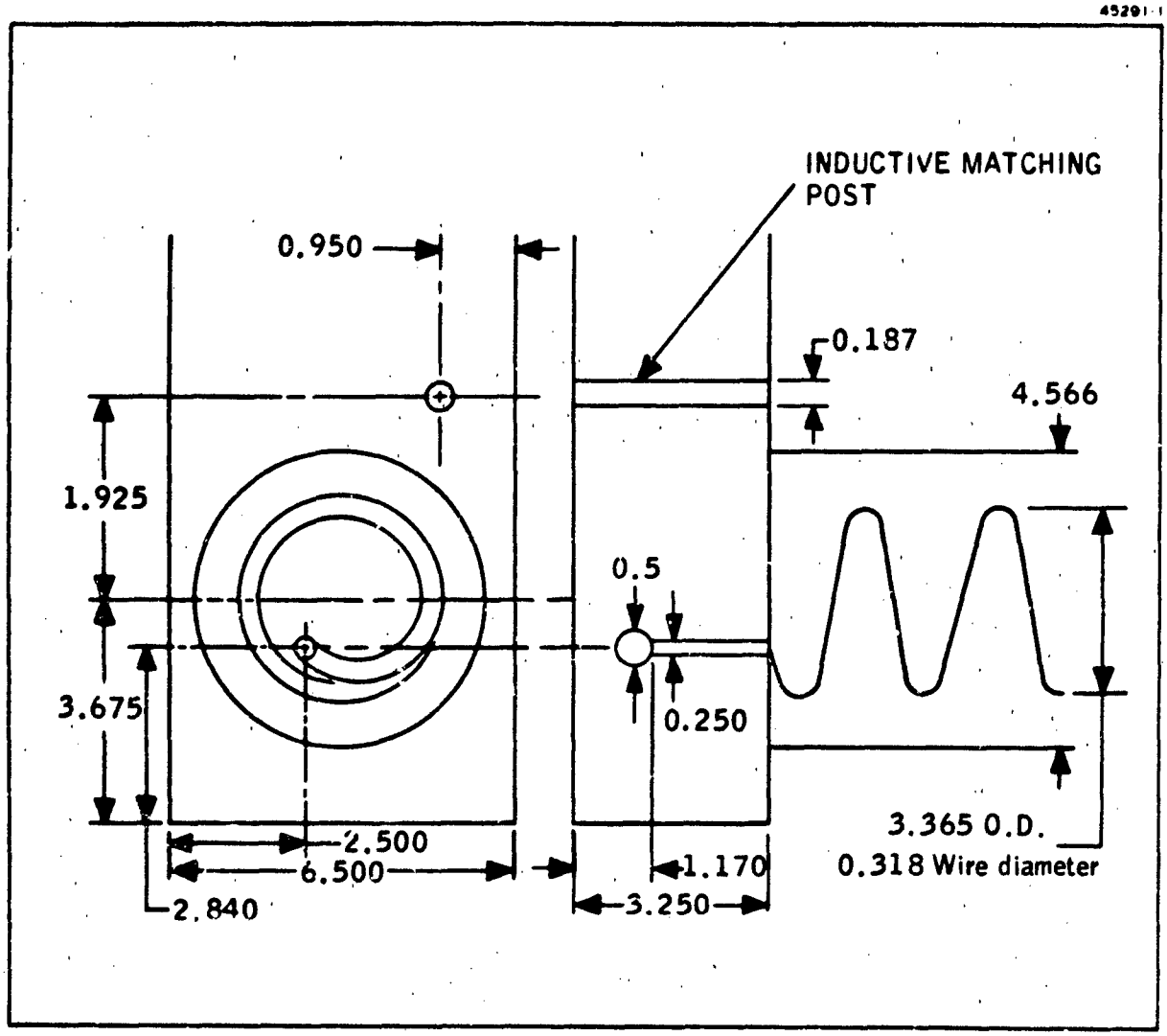

Figure 11. Waveguide-to-Helix Transition

62-08-055

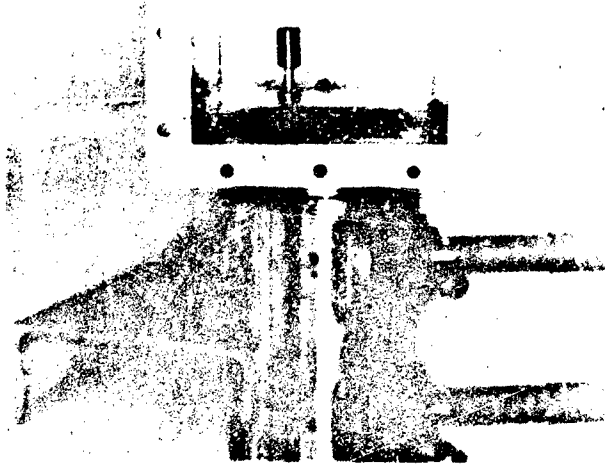

Figure 12. Helix-to-Waveguide Transition

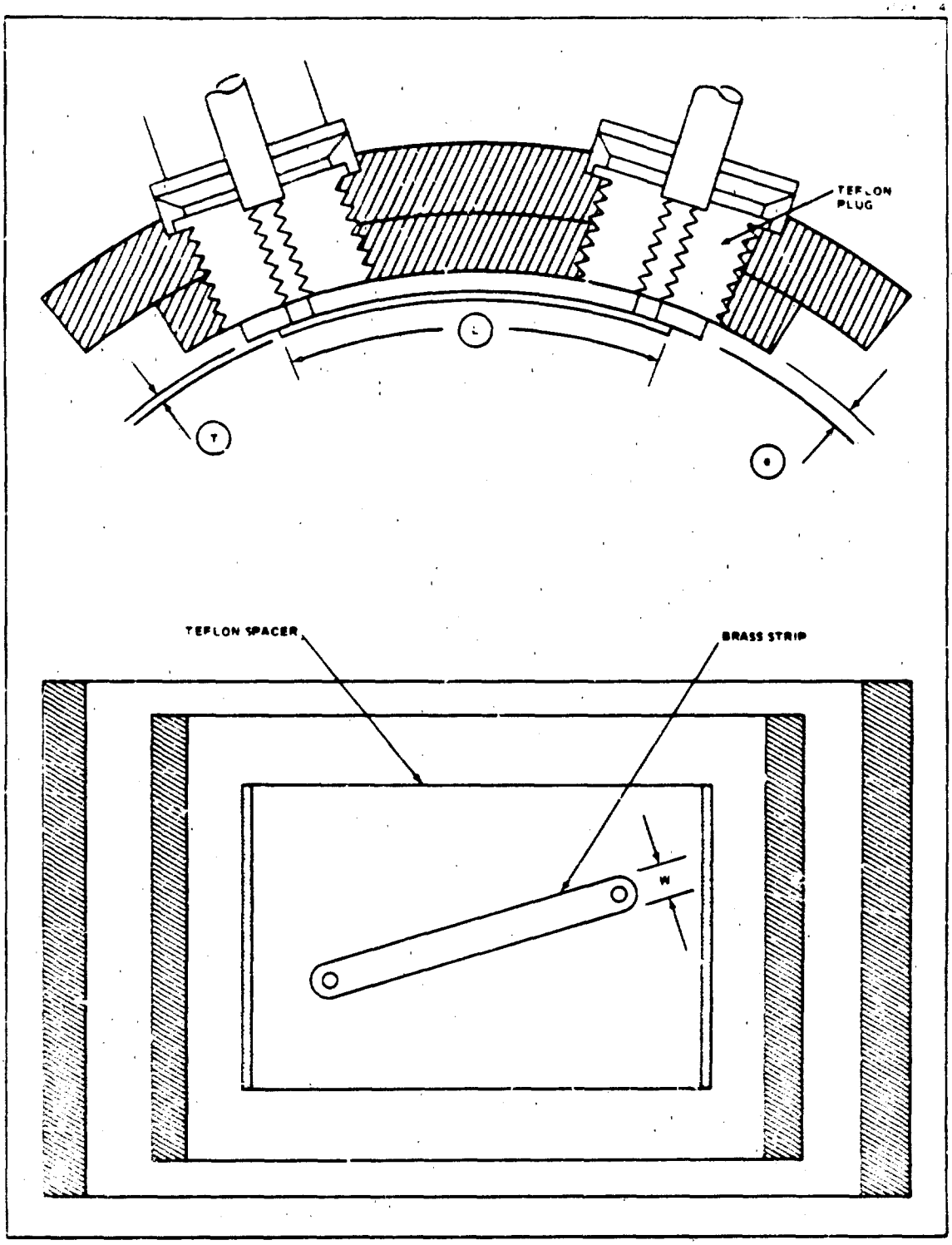

Figure 13. Coupler Configuration

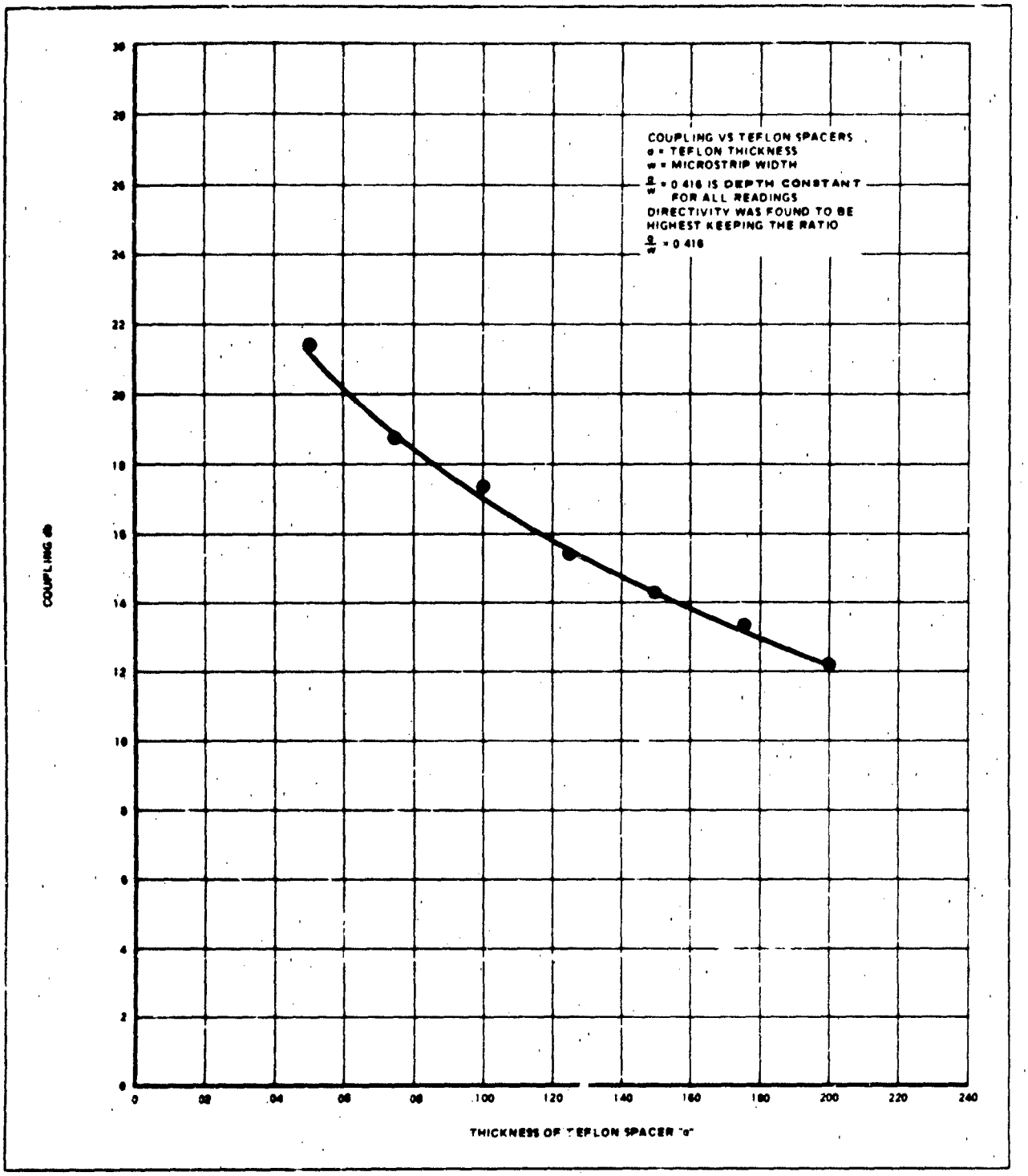

Figure 14. Coupling in db versus Teflon Spacer Thickness

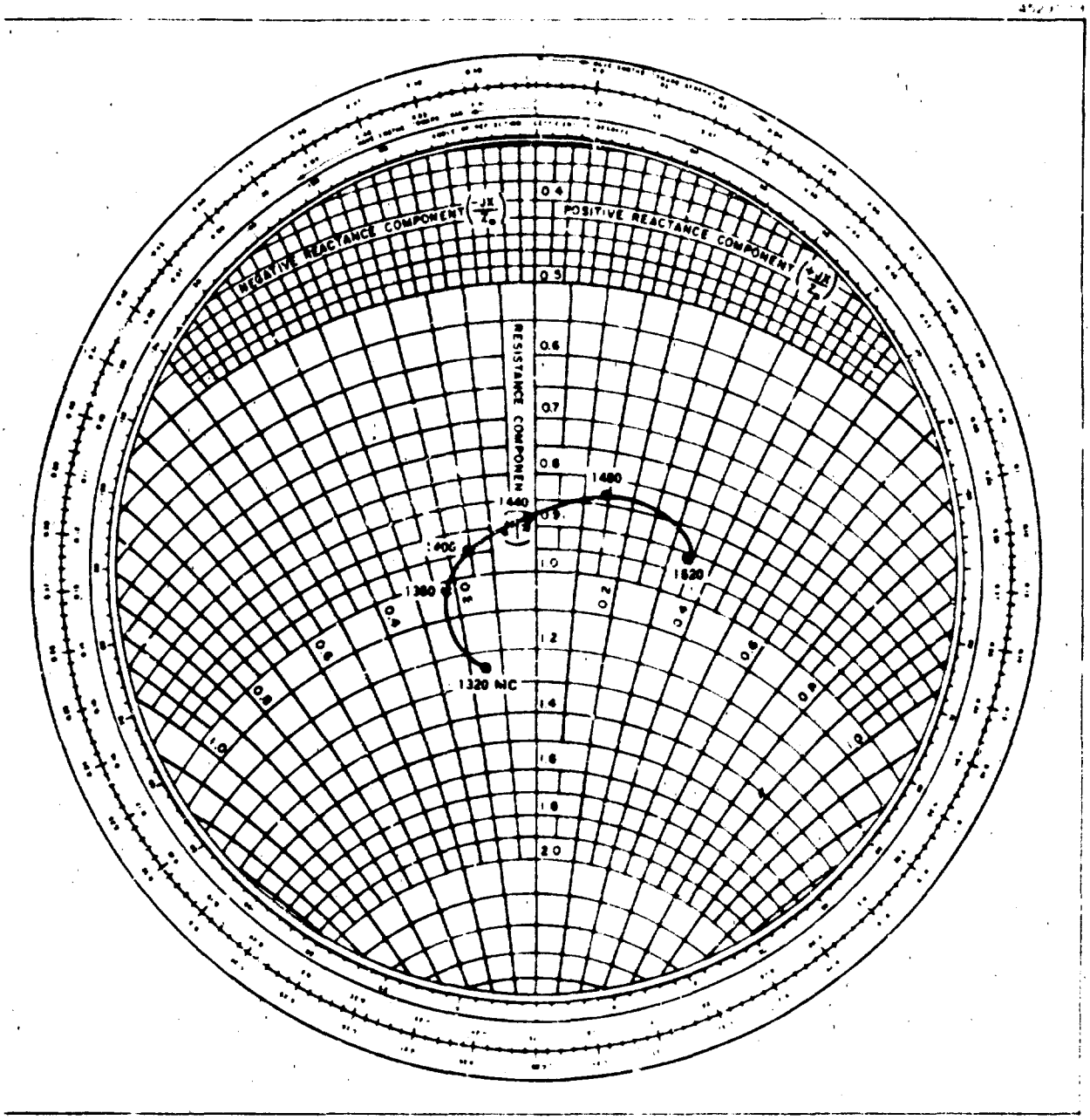

Figure 15 Typical Impedance Plot for Vivaldi Antenna

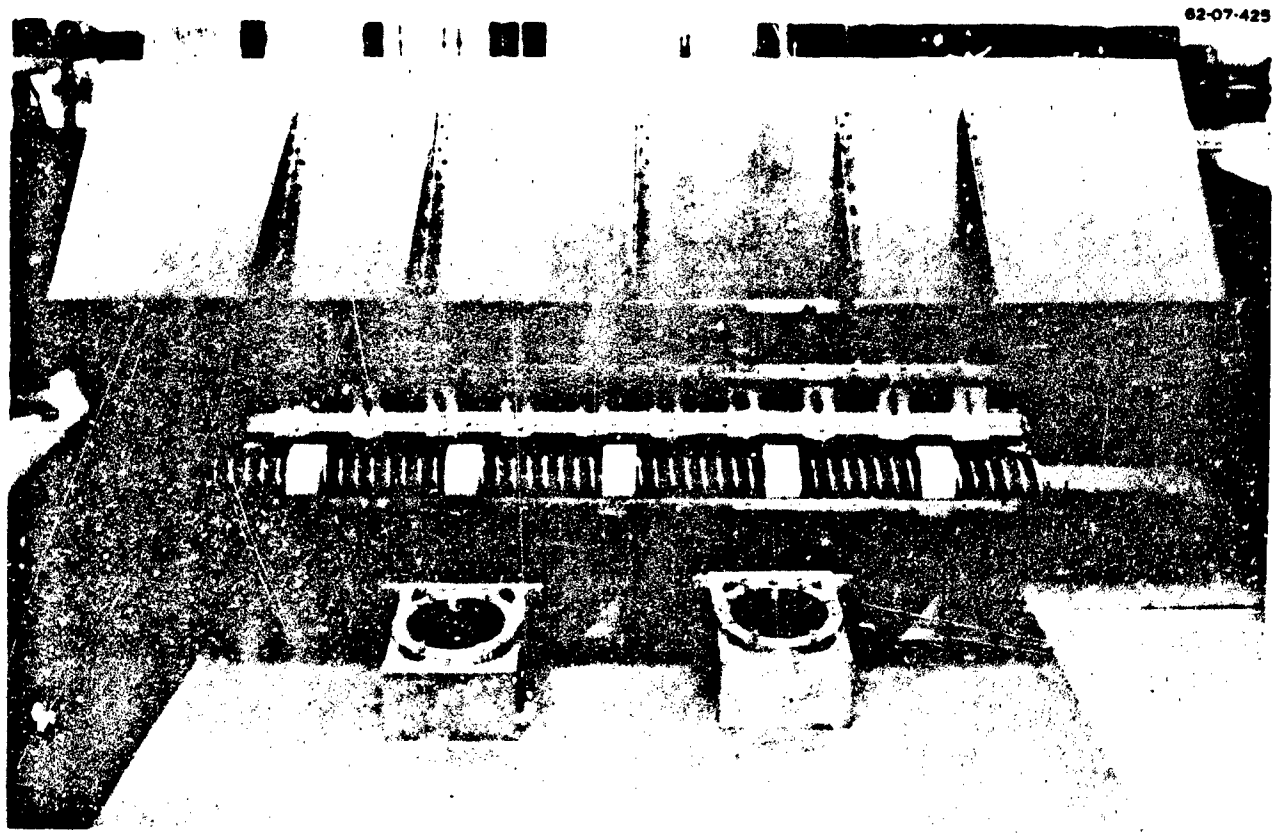

Figure 16. Helix Frequency Scanning Feed

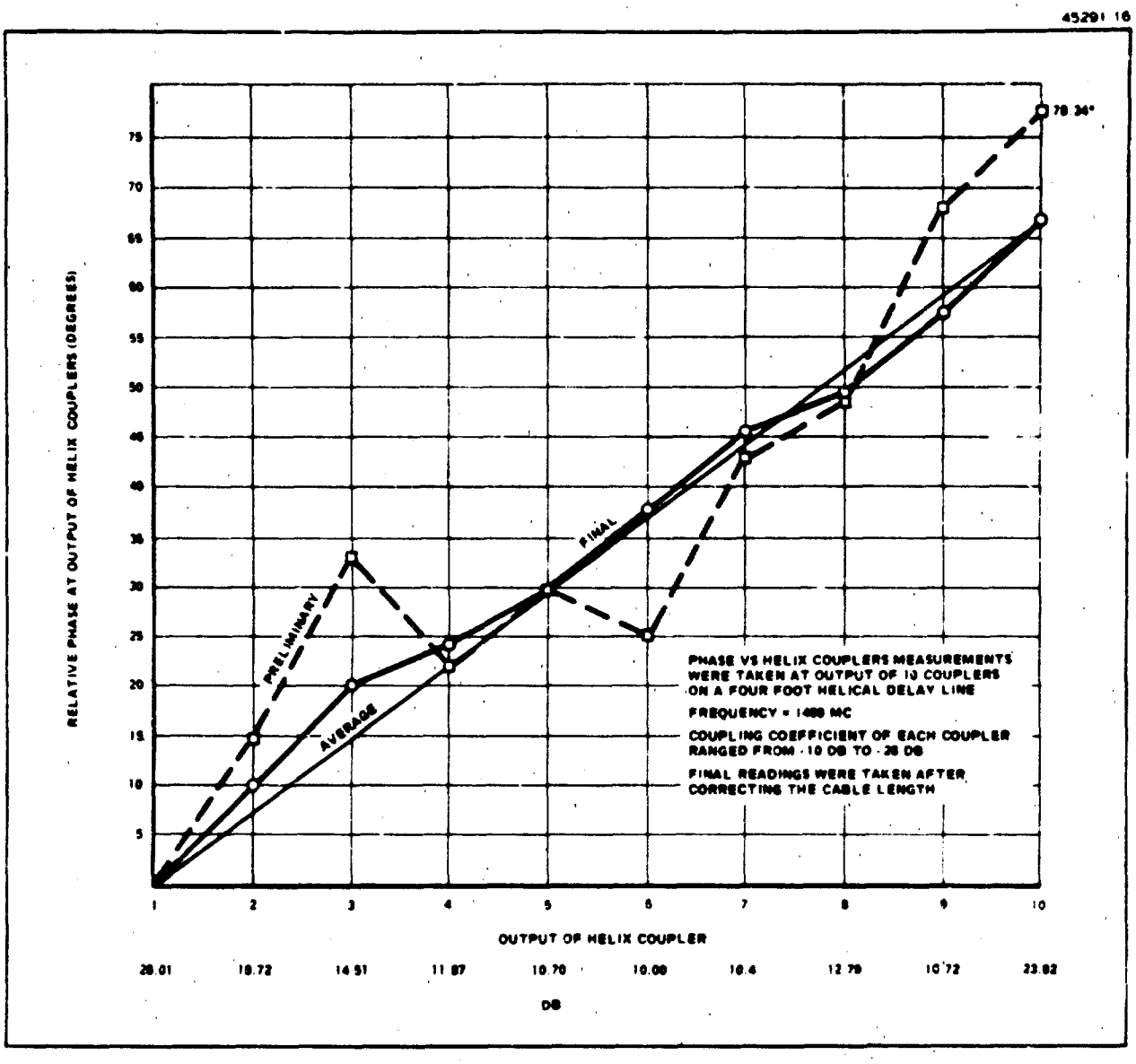

Figure 17. Phase Versus Helix Coupler Output

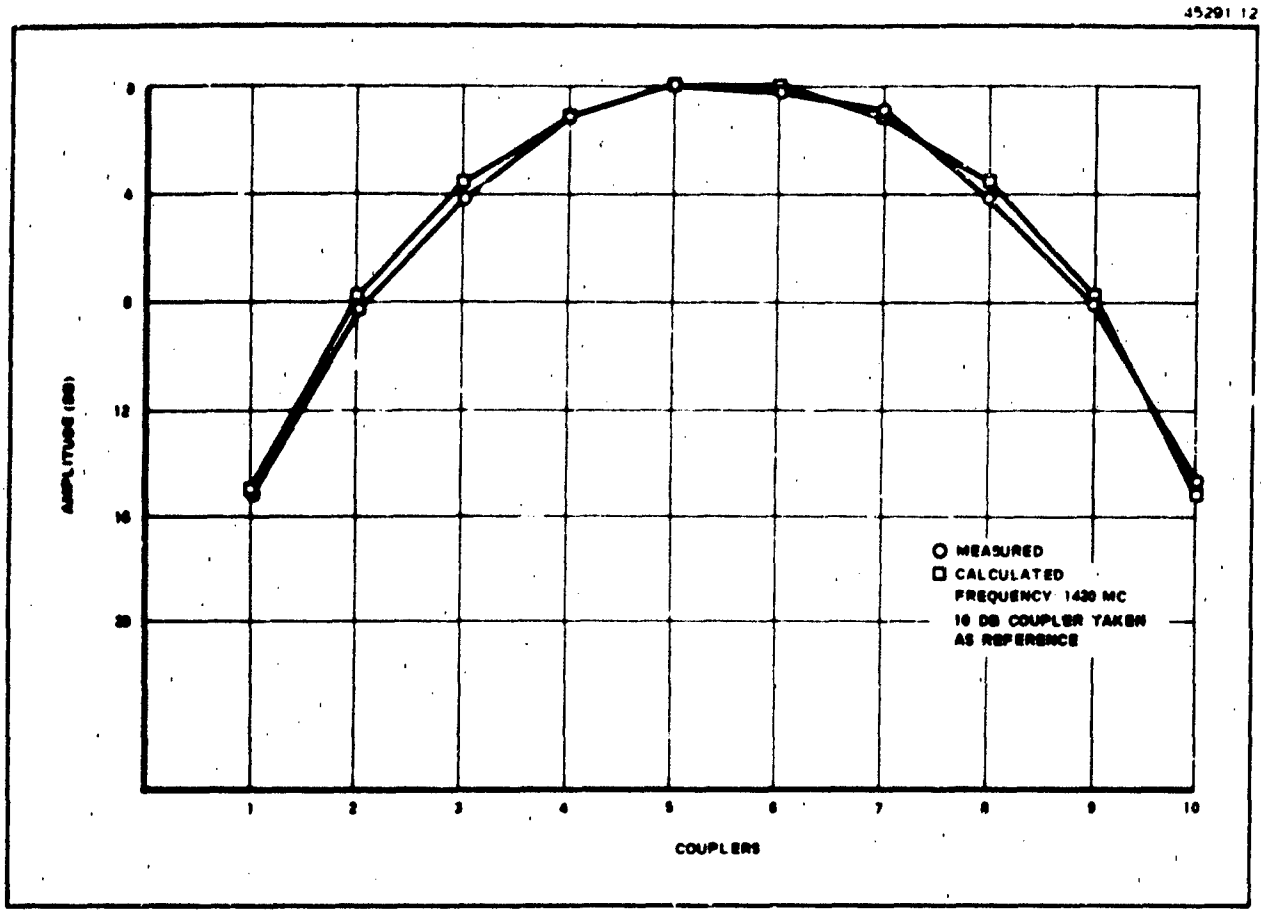

Figure 18. Relative Amplitude Distribution for Helical Delay Line

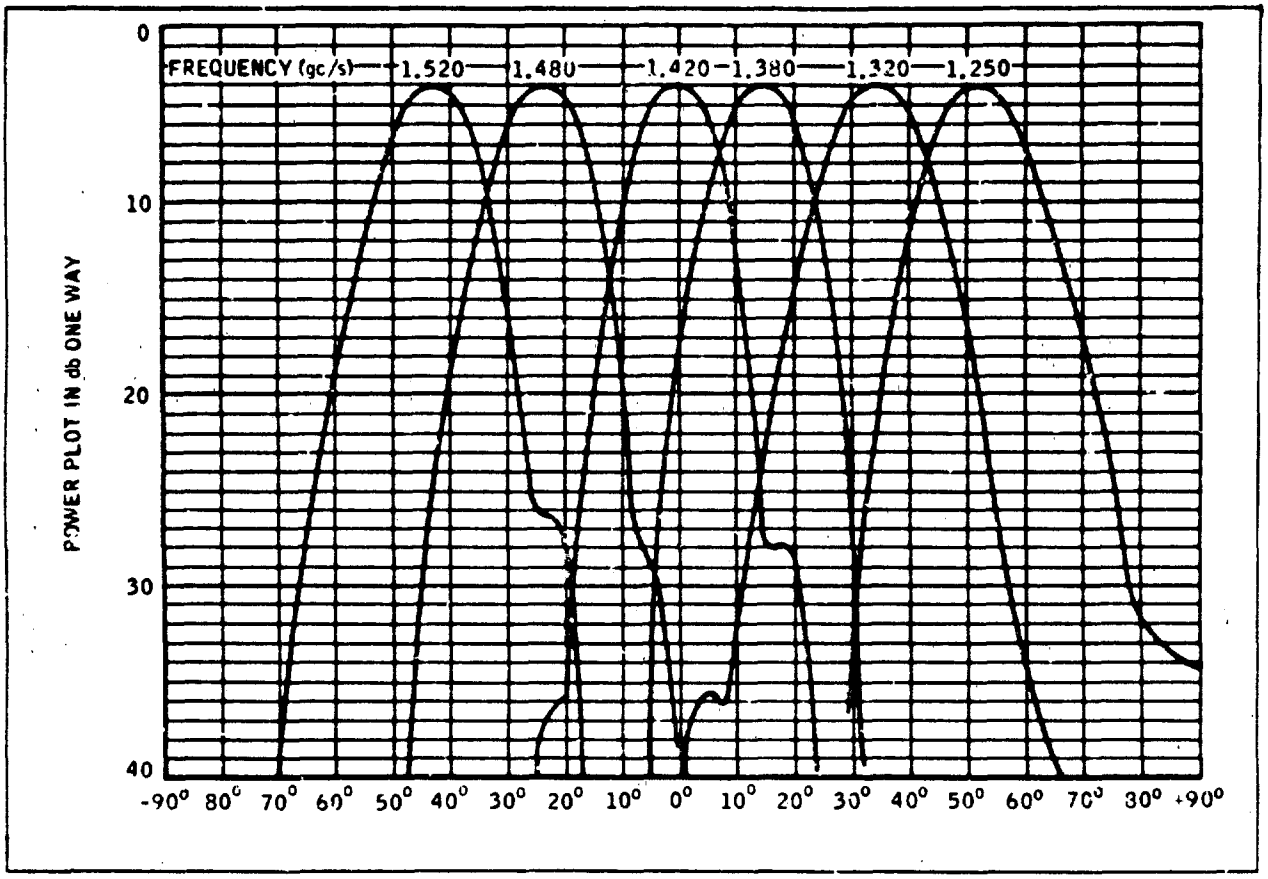

Figure 19. Antenna Patterns Using Helical Line Feed

REFERENCES

1. J. R. Pierce, "Traveling Wave Tubes" (D. Van Nostrand Co., Inc., New York, 1950).

2. S. Sensiper, "Electromagnetic Wave Propagation on Helical Conductors," Report No. 194, Research Laboratory of Electronics, M. I. T., May 1951.

3. L. Stark, "The Lower Modes of a Concentric Line Having a Helical Inner Conductor," Technical Report No. 26, Lincoln Laboratory, M. I. T., July 1953.

4. C. M. Chu, "Propagation of Waves in Helical Wave Guides," J. Appl. Phys., Vol. 29, No. 1, pp 88-99; January 1958.

5. H. S. Kirschbaum, "Characteristic Impedance and Phase Velocity of a Shielded Helical Transmission Line," Report C. I. T. 7, Carnegie Institute of Technology (No date).

6. Microwave Scanning Antennas, R. C. Hanson, Ed. New York Academic Press, Inc., Vol. II, Chap. 4; 1956.

7. Kompfner, R. et. al., "Coupled Helicies," Bell System Technical Journal, pp 127-178; January 1956.

8. L. Stark, "A Helical-Line Phase Shifter for Ultra-High Frequencies," Technical Report No. 59, Lincoln Laboratory, M. I. T., February 1954.

ABSTRACT

WIDE SCAN SHORT FOCUS MILLIMETER WAVE DIELECTRIC LENSES

By

A. Mayer

National Engineering Science Company
Pasadena, California

A foamed dielectric lens may be favored over a metal (egg-crate) lens - particularly in view of recent advances in plastics technology - for any of several reasons: its lower weight, smaller volume (by design such as in footnote 1), ease of fabrication, mechanical and thermal ruggedness, versatility or uniqueness (e.g., the practicability of good design having a ring focus), etc.....

This paper [1] is concerned with the design, performance and uses of dielectric lens antennas of the binormal or "two point corrected" type indicated in Figure 1.

Panel A represents in solid lines the cross-section of such a cylindrical lens and a focal line feed (at F), designed by geometric optics to produce a plane wave front emergent at design angle θ. (The lens surfaces are not portions of simple circular cylinders.) The focal line is parallel to but removed from the plane of lens symmetry. A feed at F', the mirror image of F, produces a second or alternate plane wave directed along $\theta' = -\theta$, shown in broken lines. The lens is designed for specified focal length f, diameter d, beam angle θ, operating wave length λ, and dielectric constant n; f, d and θ (but not λ) determine y_f, the feed offset from the plane of symmetry.

The lens material may be any suitable dielectric, we have successfully designed [1] and tested lenses of solid polystyrene and [2] of aluminum-loaded foamed

1. Based in part on "A Design Procedure for Dielectric Microwave Lenses of Large Aperture Ratio and Large Scanning Angle" by A. Mayer, Raytheon Report M/R 16-792, February 14, 1956. Mathematical details of design were presented in an article of same title, co-authored with F. S. Holt, in I.R.E. Trans. P.G.A.P., Vol. AP-5, No. 1, January 1957.
2. Cf. P.C. Fritsch, "Development of Light Weight Artificial Dielectrics," Raytheon Report M/R 16-540, January 1956.

epoxy resin.

Panel B shows a (two-) zoned version of the lens, stepped for lightness, reduction of transmission loss, and savings of material. The design of the parent lens (as in A) determines a family of interior binormal lenses all of which are optically exact for the stipulated design parameters, f, d, θ, n, and λ. Only a portion of each member lens goes to make up the final zoned lens (allowance for overlap).

Panel C shows that by rotating the cross-section in B about the x-axis we generate a spherically symmetric lens (whose surfaces are aspheric, quite aside from being stepped). This lens has a ring focus.

Some noteworthy features of these lenses are: (1) very short focal lengths (compactness) are achievable, (2) along with unusually low f/d ratios (≤ 0.35 compared to practical lower limits ~ 1.0 with metal lenses of egg-crate variety); (3) capability of large beam offset; and (4) room, by virtue of controlled axial offset, y_f, to accommodate many separate feeds or continuous feed structures on a ring focus.

Only the briefest comment on the design procedure is possible; see Ref. 1 for details. Figure 2 shows in solid line the upper half of a binormal lens which satisfies all the requirements of a stipulated design (f_o, $s_o = d/2$, θ, m, λ), the location of its intersection with the x-axis is not known. The interior intersection c_o is assumed to have the trial value c'. Starting from F, ray traces are made through c' to a conveniently chosen but arbitrary wave front W, then back to F, in a manner which satisfies (exactly) the optical requirement of the design. Alternate tracings are outward, toward W through the upper half of the interior surface then inward, toward F through the lower half of that surface. The collection of points (and associated slopes) determined by the ray tracings - e.g., the collection associated with trial value c' and identified by open circles and markings e_j, $\bar{e}_j$, i_j, $\bar{i}_j$ -- define a "ray lattice" it is relatively simple to determine a ray lattice which condenses as closely as desired to the knife-edge (at f_o, s_o) of the desired solution. When a ray lattice is found acceptable (good enough condensation at edge) polynominals are passed through the lattice points to determine the remaining surface coordinates. Although the calculation of ray lattices may be economically done on a desk calculator, it is desirable to determine the interpolation polynominals by computing machine. We have used fourth order polynominals (in y^2) and have

had excellent ray-trace checkouts for lenses of up to 48" diameter having f/d as low as 0.35 and θ as large as 60°, designed for K-band or x-band operation employing media of dielectric constant 2.54 or 1.6. The entire design mathematics are readily and economically programmed for computer.

Before citing specific performance data, we note some applications to illustrate the versatility of the binormal lens. The lens performs the functions[3] of scanning in one or two dimensions, when one or more feeds move on a scanning curve (for the cylinderical lens) or scanning surface (for the spherical lens). Experiments show that the antenna pattern does not deteriorate excessively for the motion of F on a "best scanning curve" (such as the broken line drawn through F and F' in Figure 1B) or on a "best" cap based on the focal ring (as shown in Figure 3). Figure 3 shows how simultaneous lobing or tracking may be achieved with stationary receivers (horns perhaps) at the points marked 1, 2, 3; corresponding beams are similarly numbered.

A similar arrangement, mounted in an airplane with x-axis perpendicular, can serve for (Doppler) navigation. Sequential switching orphasing of elements is of course possible: the ring feed easily becomes an array. As a passive or active beam transducer - a "repeater" with or without gain-it may accept signals from (say) direction 1 and relay such signals to any or all of directions 1, 2, 3 (incidence and return along 3 is a kind of corner reflector function). Applications to airport surveillance and beaconry are readily recognized.

The focal line or ring of the binormal lens leaves ample room for occupancy by passive and/or active primary radiators whose mutual coupling is controlled; e.g., horns, small depoles, slots, pill boxes with or without parametric and/or tunnel diode loadings. The use of binormal lenses in adaptive or data processing arrays is clearly possible. Their potential as a primary to feed a larger antenna - combined with low noise active element on the focal ring - is considerable.

As example of the performance obtainable with good but not best dielectric material, Figure 4 shows the contour of an unzoned K-band lens designed for $s_o = d/2 = 5.5"$, $f_o = 5.5"$, $\theta = 20°$, $\lambda = .9" = 2.3$ cm, $n = 1.5$, and Figures 5 and 6 show its test patterns. The patterns were measured with the lens fed 3. Most of these are readily suggested by Figure 1.

by small conical and pyramidal "optimum" horns designed for edge illustration 10 db down from the center. Comparison with a 55% efficient paraboloid of aperture $\pi s_o^2 \cos\theta$ is briefly tabulated:

	G(db) at design offset	G(db) on axis	$\theta_{E,3db}$	$\theta_{H,3db}$	Major SL (-db)	$\theta_{beam} - \theta_{SL}$	Scan Range
Parabola	-	28.5	6.5	-	17	9.2°	lmtd small
Foamed Dielectric Lens	26.0	26.5 feed on scan curve	5.6°	5.8°	13.5	8°	±20

The lower efficiency of this particular - and early-lens and feed combination is readily accounted for: by the extra thickness of the unzoned lens (loss and residual inhomogeneity in the loaded foamed epoxy); by the extreme simplicity of the feed horns used (these were not designed to compensate for astigmatism such as any aspheric lens processes, nor to have E- and H- plane phase centers coincident with those of the lens), etc. With zoning and improved lots of loaded-foam material, and especially with a very good microwave dielectric material like (unloaded) polystyrene, much better efficiencies were obtained. Even in this unelaborate preparation and testing, the scanning property and the relative uniformity of gain during scan is noteworthy.

If time permits, test results for other lenses will be discussed, e.g., for the lens of Figure 7. Designs for lenses of diameter considerably larger than those cited have been successfully carried out. These were mostly with $0.35 \leq f/d \leq 0.5$; the value 0.35 is not a lower range limit for the design parameter f/d.

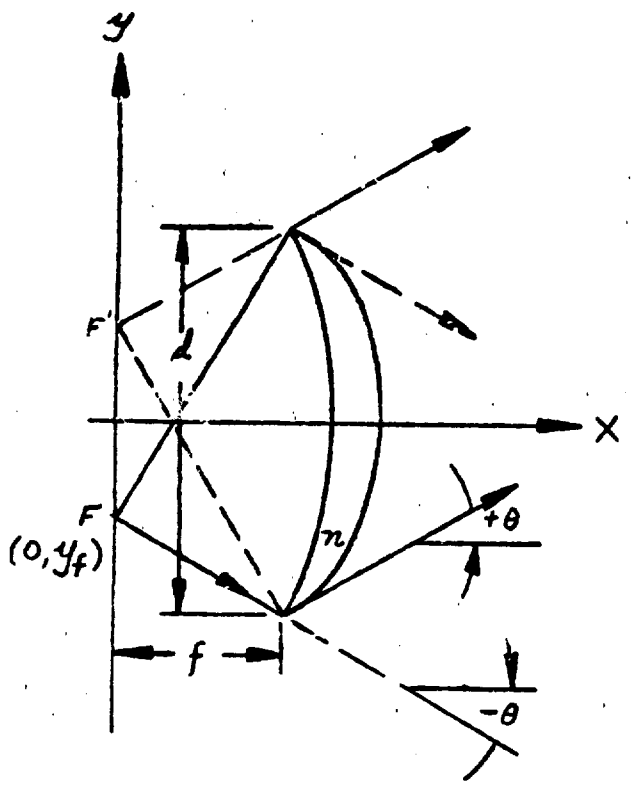

1A

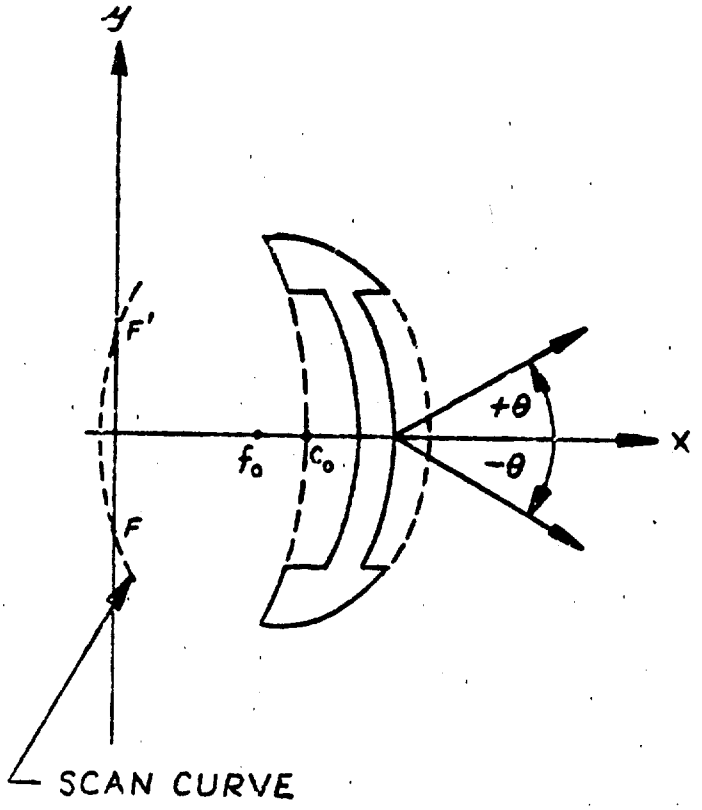

1B

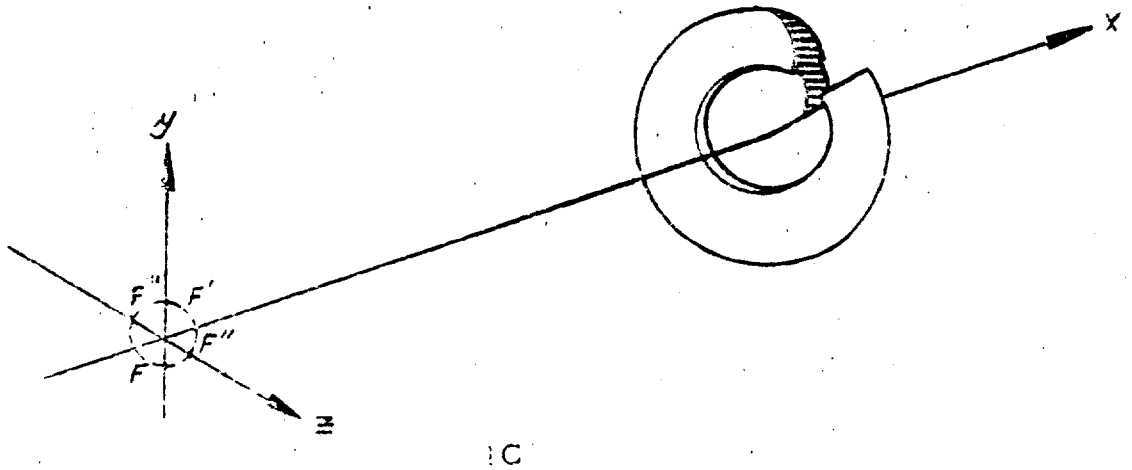

1C

FIGURE 1 (A) UNZONED BINORMAL LENS (B) SAME LENS ZONED (C) SPHERICAL LENS DERIVED FROM B. ALL CROSS-SECTIONS POSSESS MIRROR SYMMETRY.

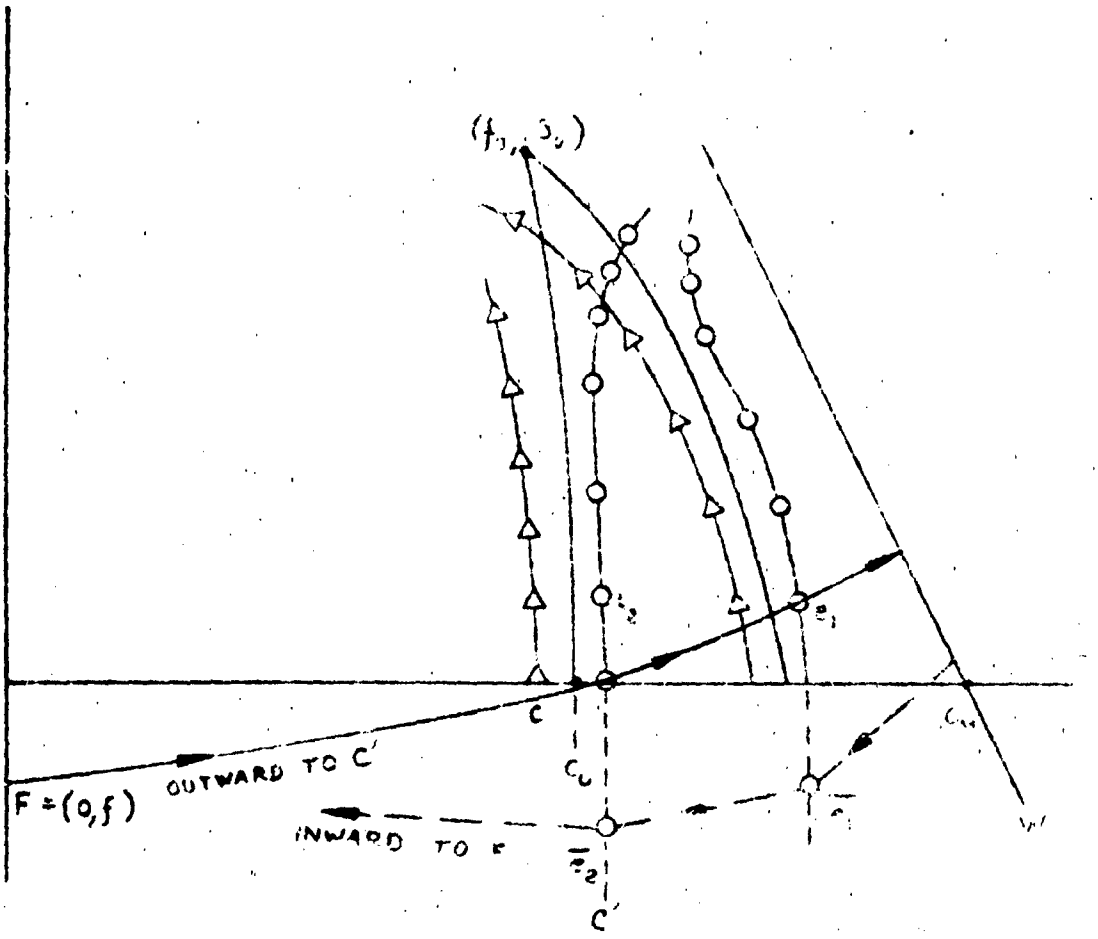

FIGURE 2 BENDING OF RAY LATTICES (UPPER HALF OF A SECTION THRU THE LENS

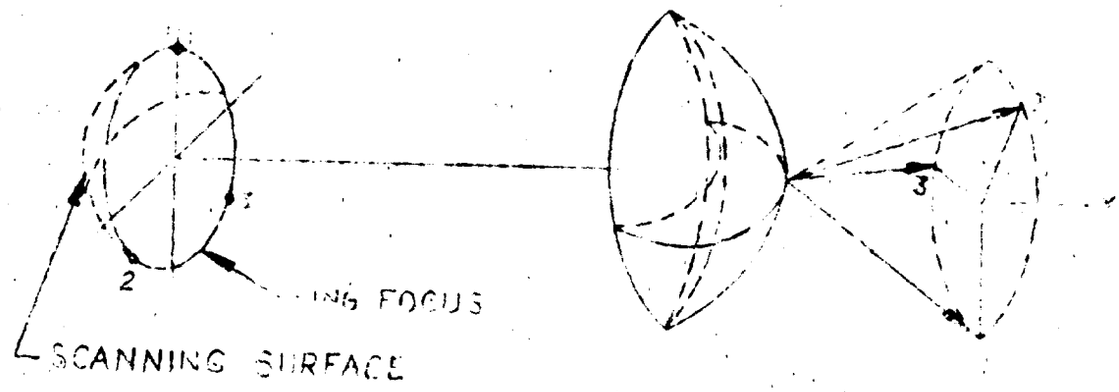

FIGURE 3 TRACKING 3 OR MORE BEAMS ON RING FOCUS

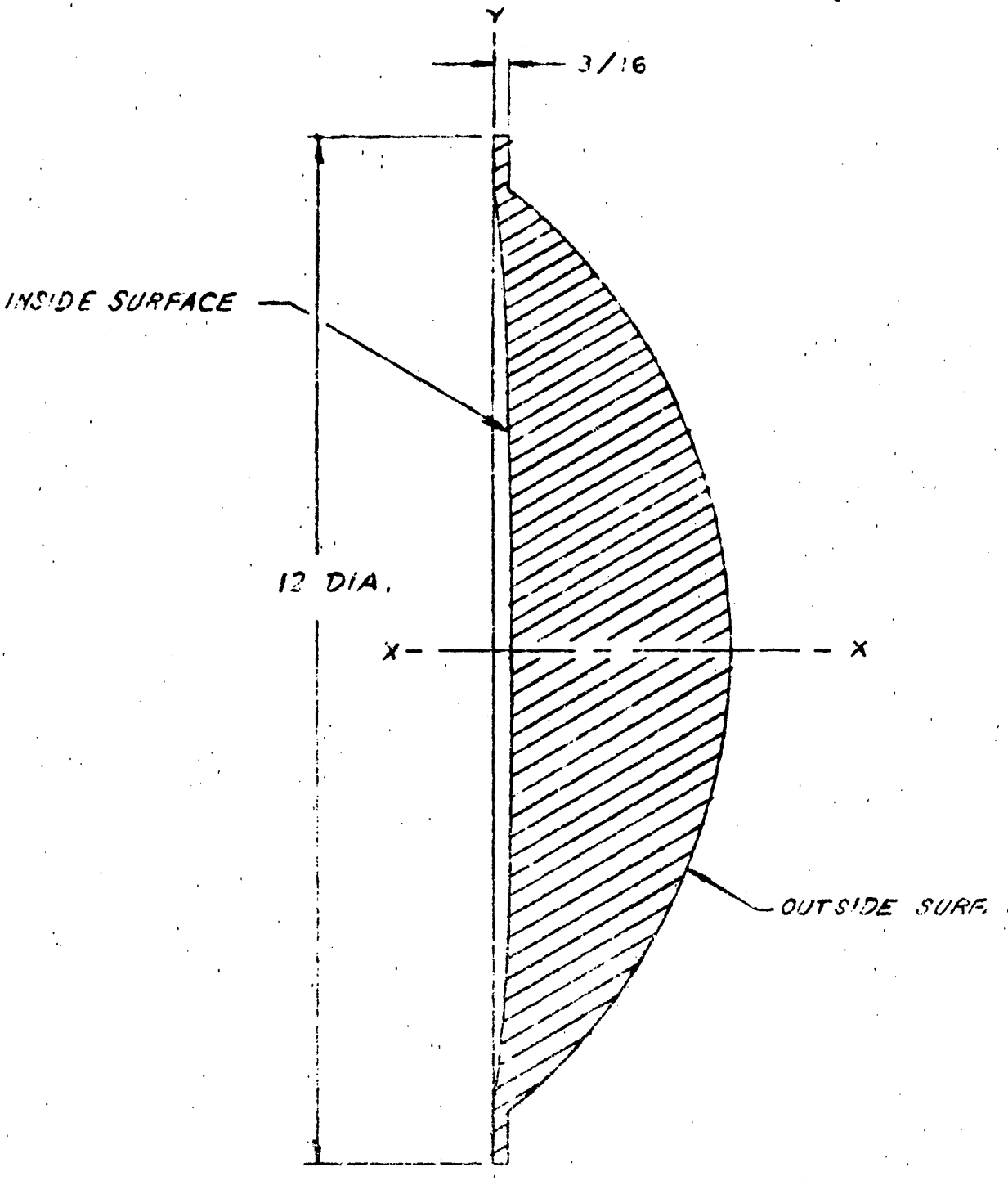

FIGURE 4 DIAMETER

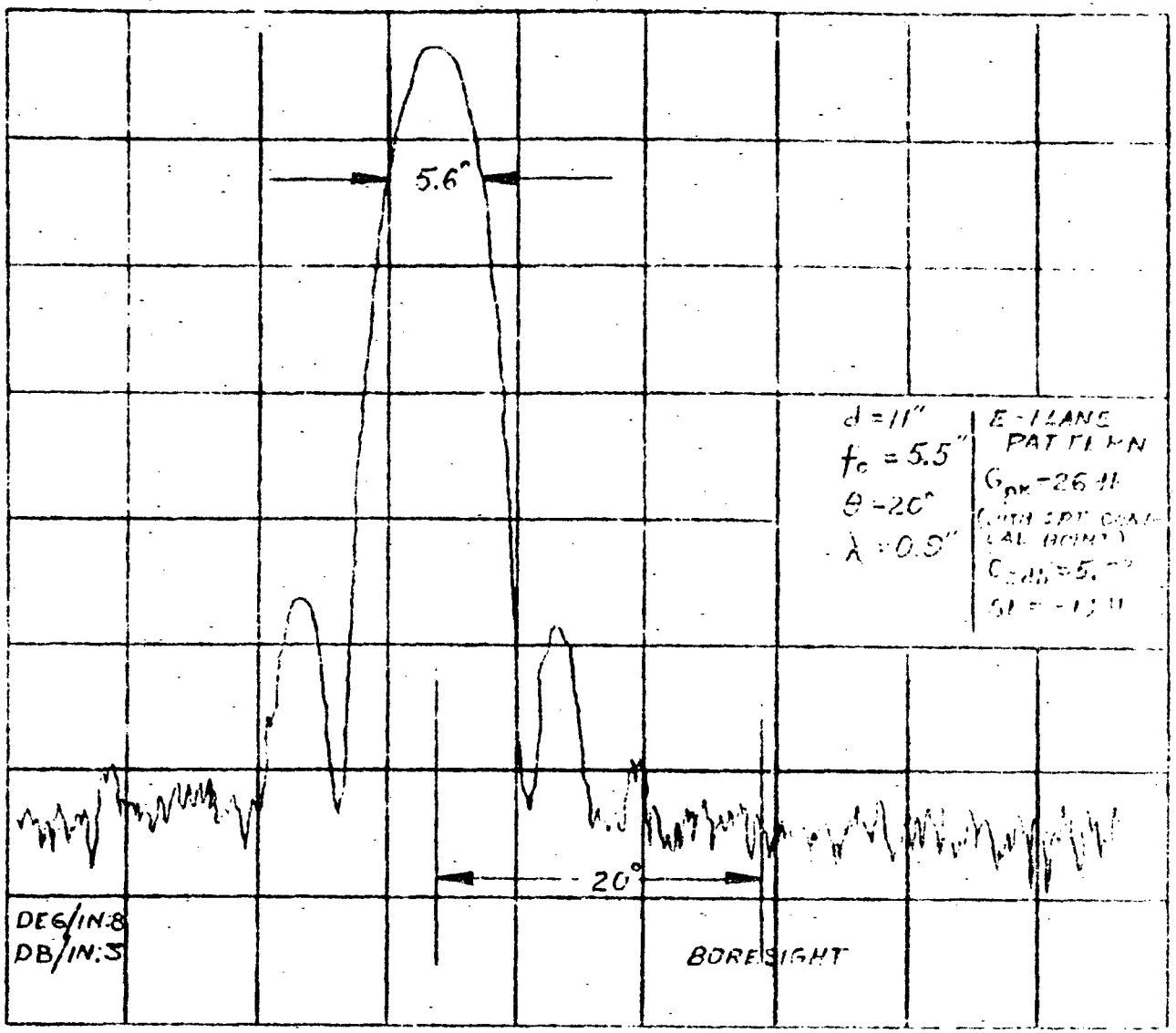

FIGURE 5 11" K-BAND LENS, E PLANE PATTERN

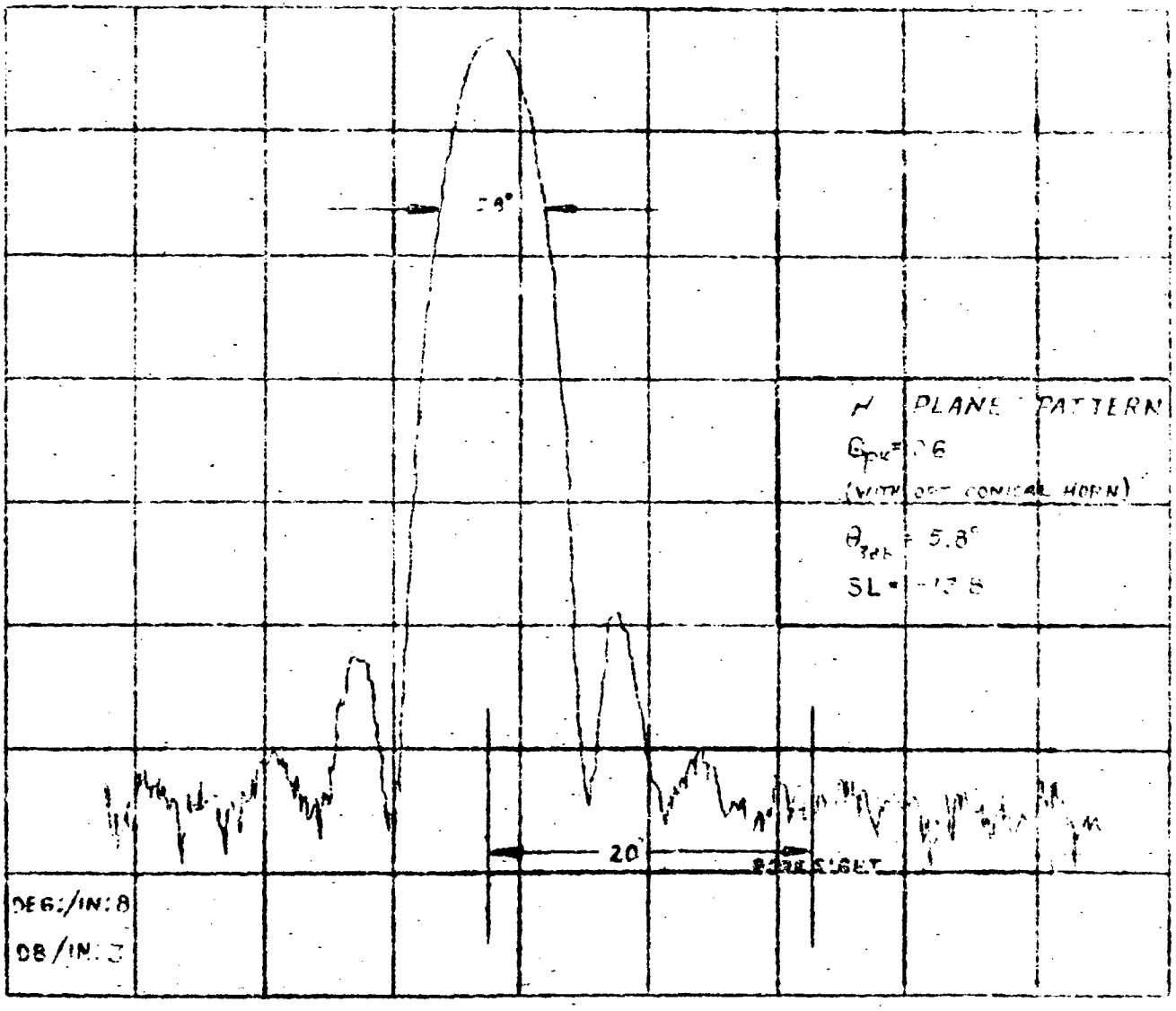

FIGURE 6 11" K-BAND LENS. H PLANE PATTERN

ANTENNAFIERS FOR BEAM-STEERING ARRAYS*

Jonathan D. Young
Antenna Laboratory
Department of Electrical Engineering
The Ohio State University
Columbus, Ohio 43212

ABSTRACT

An active steerable-beam array consisting of four transistorized dipole antennafiers has been constructed and evaluated. Beam control was accomplished by integrated gain and phase-shift circuitry in each dipole, coupled by an equal-amplitude corporate feed. Antenna patterns have been taken for different amplitude tapers with beam angles varying from broadside to endfire.

The antennafier element used was a gamma-matched half-wave dipole integrated with a T2028 transistor amplifier and a pi-section phase-shift and impedance transformation network with dual varactor control. Gain control was effected by adjusting base bias, while variable varactor bias in two legs of the pi-section was used to shift phase. Calibration curves of element control voltages vs. element gain and phase shift, and array control voltages vs. array beam characteristics have been obtained.

* The work reported in this paper was supported in part by Contract AF 33(657)-10386 between Research Technology Division, Wright-Patterson Air Force Base, Ohio and The Ohio State University Research Foundation.

ANTENNAFIERS FOR BEAM-STEERING ARRAYS*

Jonathan D. Young
Antenna Laboratory
Department of Electrical Engineering
The Ohio State University
Columbus, Ohio 43212

INTRODUCTION

Of the many beam-steering methods in use today and being evaluated for future use, one of the most promising developments is an array of antennas with integrated gain and phase-shift circuitry, called antennafiers, for electronic beam-steering. Electronic steering with antennafiers eliminates the need for heavy and complicated mechanical steering without paying the penalties incurred with mechanical or ferrite phase shifters.

The antennafier element can use relatively uncomplicated miniaturized circuitry which has simple control requirements, and thus can provide a saving of both space and cost.

Antennafier arrays may vary in number of elements, type of elements, and purpose; but all offer a relatively simple, compact, and inexpensive method for complete antenna beam control.

ANTENNAFIER ARRAY

A steerable-beam array has been built and tested using four identical $\lambda/2$ dipole antennafiers at 148 Mc. Fig. 1 shows a schematic diagram of one such element. The dipole antenna is connected by a gamma-match directly into the base of the T2028 VHF transistor. The

*The work reported in this paper was supported in part by Contract AF 33(657) - 10386 between Research Technology Division, Wright-Patterson Air Force Base, Ohio and The Ohio State University Research Foundation.

length of the gamma rod and resonating capacitance were adjusted for proper matching between the antenna and transistor. Gain adjustment was accomplished using Control Voltage A to vary the amount of forward bias between emitter and base.

A Pi network with reactive elements was chosen to couple the transistor to the transmission line because of its theoretical ability to transform the transistor output resistance to the characteristic impedance of the line while at the same time providing any desired phase-shift. Fig. 2 shows the required arm impedances vs. phase shift for a Pi network coupling the 12,000Ω output resistance of the T2028 transistor to a 50Ω transmission line. With fixed inductances L_B=.27 micro-henries and L_c = 1.0 micro-henries, the capacitances required to satisfy these impedance curves at 148 Mc are shown in Fig. 3.

The circuit chosen to approximate these requirements has a 2.2 pf fixed capacitor in arm A, and type PC 139 varactors in arms B and C. A bias variation of O to -45 volts for Control Voltages B and C gives a capacitance range of approximately 2 pf to 20 pf in arm C and approximately 4 pf to 40 pf in arm B. It was found that this circuit gives approximately a 180° phase-shift range with adequate matching.

Fig. 4 shows a curve of relative output signal amplitude of the Pi network vs. phase lag angle. As expected, the best matching occurs in the range where the network is most nearly able to satisfy the required arm impedances.

Comparisons of theoretical and experimental arm capacitance vs. phase angle for arms B and C are shown in Figs. 5 and 6. The discontinuities in the experimental curve of Fig. 5 occur when the limits of the obtainable capacitance range are reached. The lack of a "hump" in the

experimental characteristic of Fig. 6 results from using a fixed capacitor in arm A.

Four of the antennafier elements previously discussed, spaced a half wavelength apart, constitute the steerable-beam array as shown in Fig. 7. The elements are coupled by the feed structure shown in Fig. 8. This feed arrangement and the 180° element phase shift range theoretically provide a continuous range of beam angles from broadside to endfire in one quadrant.

The phase of the received signal at each element, with respect to the phase of element 1, vs. beam angle is shown in Fig. 9. Neglecting mutual coupling, the phase shifting circuits must compensate for this signal advance or delay, so that all element signals to the feed structure are added in phase at the desired beam angle. The reference base line, chosen as shown, modifies the phase shift requirements so that the continuous range of beam angles from broadside to endfire is obtainable from the phase shift circuitry which was used.

Fig. 10 shows the required circuit phase shift (with respect to the base line) vs. beam angle. The feed structure and phase shift circuitry satisfy the necessary requirements of the phase shift range for each element.

Experimental results show this to be a workable system for beam steering. Figs. 11-15, show calculated and measured antenna patterns for beam angles of 0°, 10°, 30°, 60°, and 90° off broadside respectively. The noticable assymmetry in the patterns near endfire is caused by the supporting structure. Discounting this, the patterns show a good agreement with the reference patterns calculated from point-source array theory.

The circuit phase shifts which produced these patterns are compared with theoretical predictions in TABLE 1. The difference

between calculated and experimental element phase, which is most acute for greater required phase shifts, is believed to be caused principally by coupling between the elements. For small beam angles from broadside the results seem within experimental error of the theoretical predictions.

SUMMARY

The antenna array described herein demonstrates the capability of rapid electronic beam steering. Good performance can be obtained over a continuous range of beam angles from broadside to endfire, using relatively inexpensive, lightweight, and uncomplicated antenna-fier elements.

Acknowledgements

The author gratefully acknowledges his colleagues J. R. Copeland, W. J. Robertson, and R. G. Verstraete for their assistance; also Dr. C.H. Walter for his advice and encouragement; and finally J. L. Kohli who performed many of the measurements.

TABLE I

Experimental and Theoretical Element Phase Shifts

Element Number	Predicted Phase	Experimental Phase
Broadside Pattern		
1	0°	$+12^\circ$
2	0°	-12°
3	0°	0°
4	0°	0°
30° Pattern		
1	-135°) 90°	98° (-146°
2	-45°) 90°	80° (-48°
3	$+45^\circ$) 90°	$+32^\circ$
4	$+135^\circ$) 90°	104° ($+136^\circ$
60° Pattern		
1	-78°) 156°	188° -104°
2	$+126^\circ$) 156°	192° $+84^\circ$
3	-126°) 156°	148° -84°
4	$+78^\circ$) 156°	$+64^\circ$
90° Pattern		
1	-90°) 180°	248° -170°
2	$+90^\circ$) 180°	264° $+122^\circ$
3	-90°) 180°	-142°
4	$+90^\circ$) 180°	228° $+170^\circ$

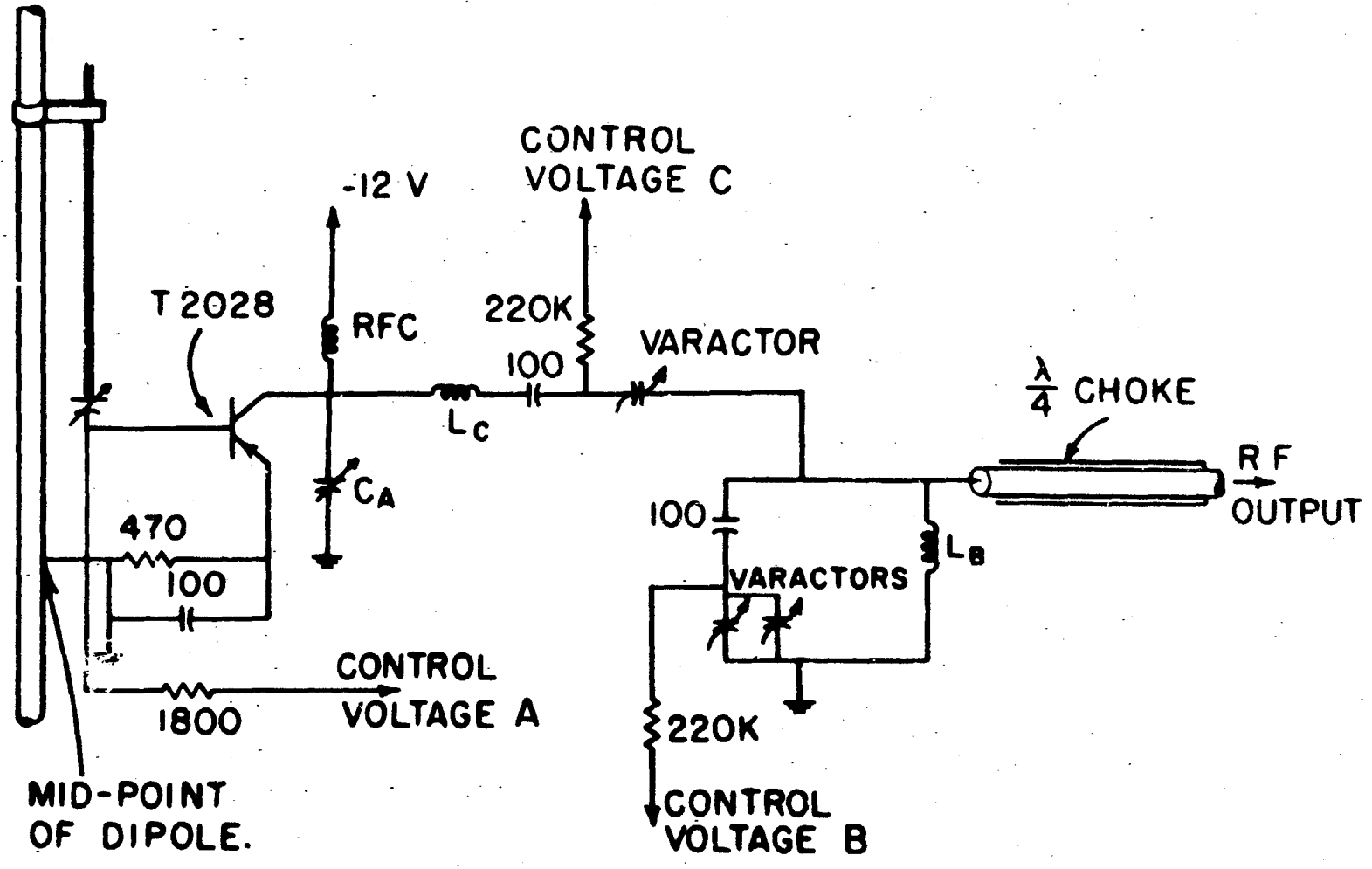

Fig. 1. Circuit of dipole antennafier with phase shifter.

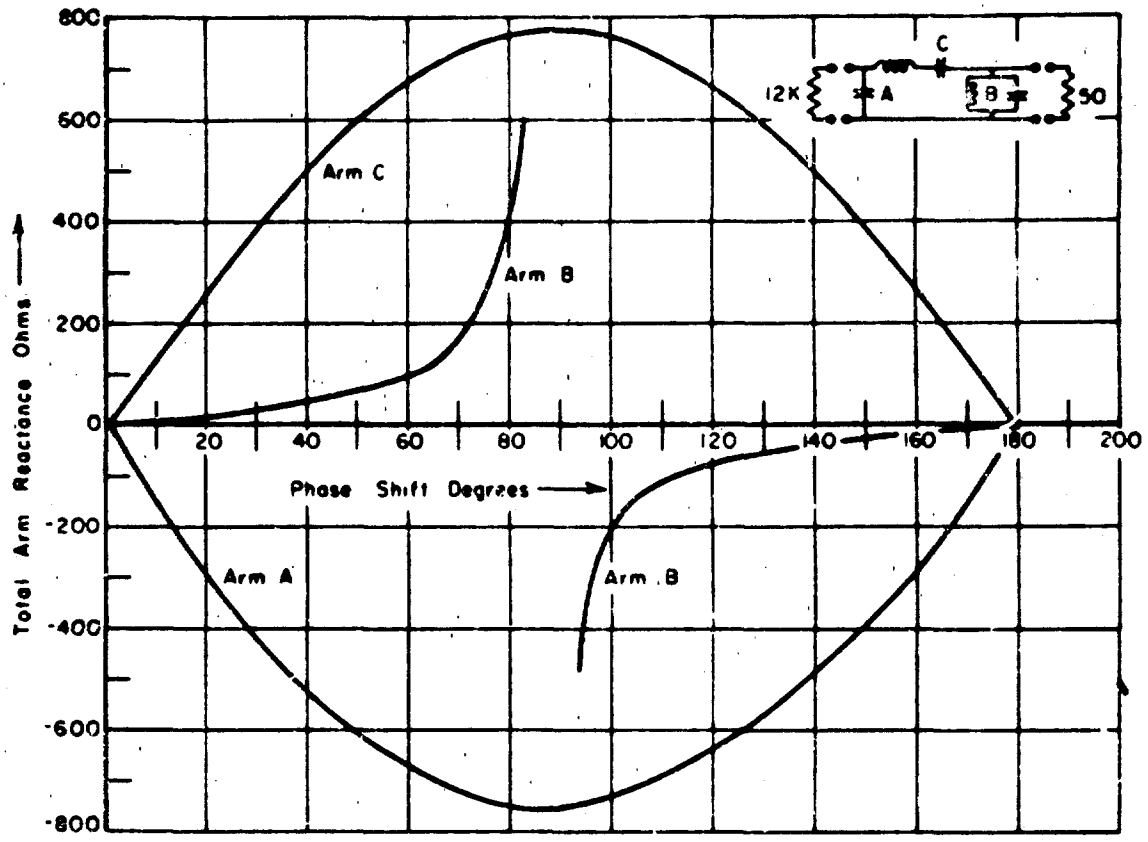

Fig. 2. Arm impedances of Pi-network versus phase shift for specified impedance transformation.

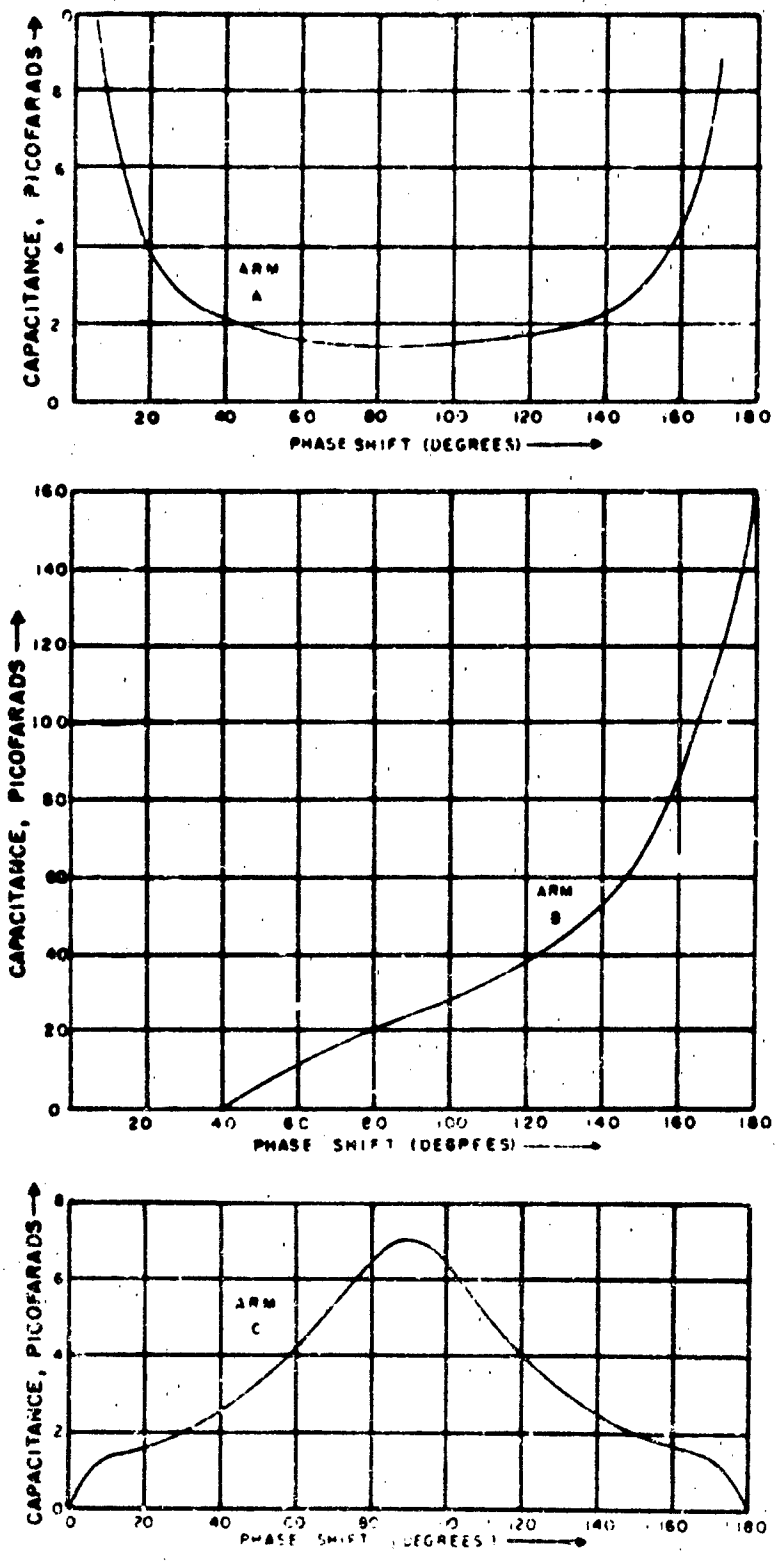

Fig. 3. Capacitances required versus phase shift for specified impedance transformation.

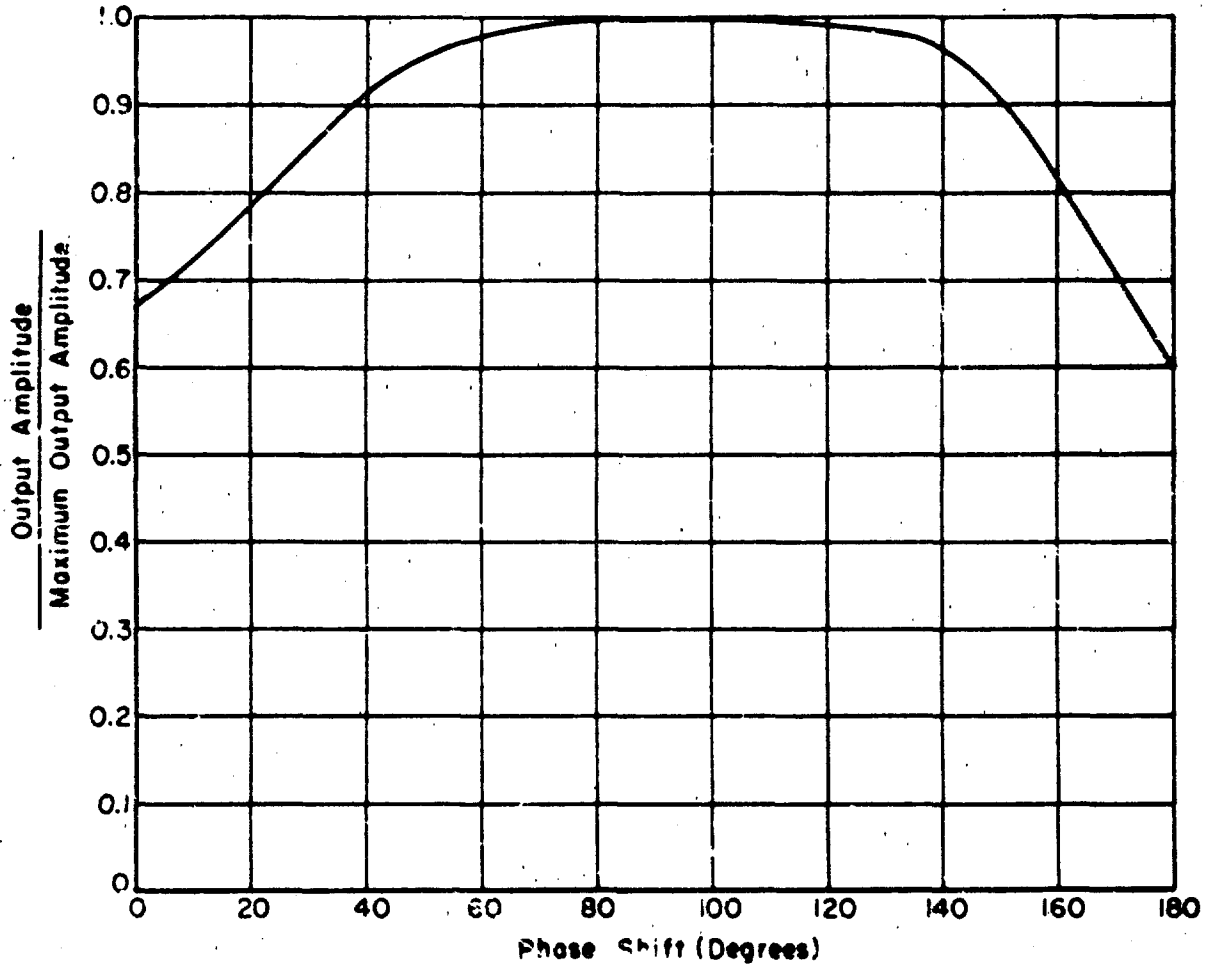

Fig. 4. Normalized antennafier output amplitude versus phase shift.

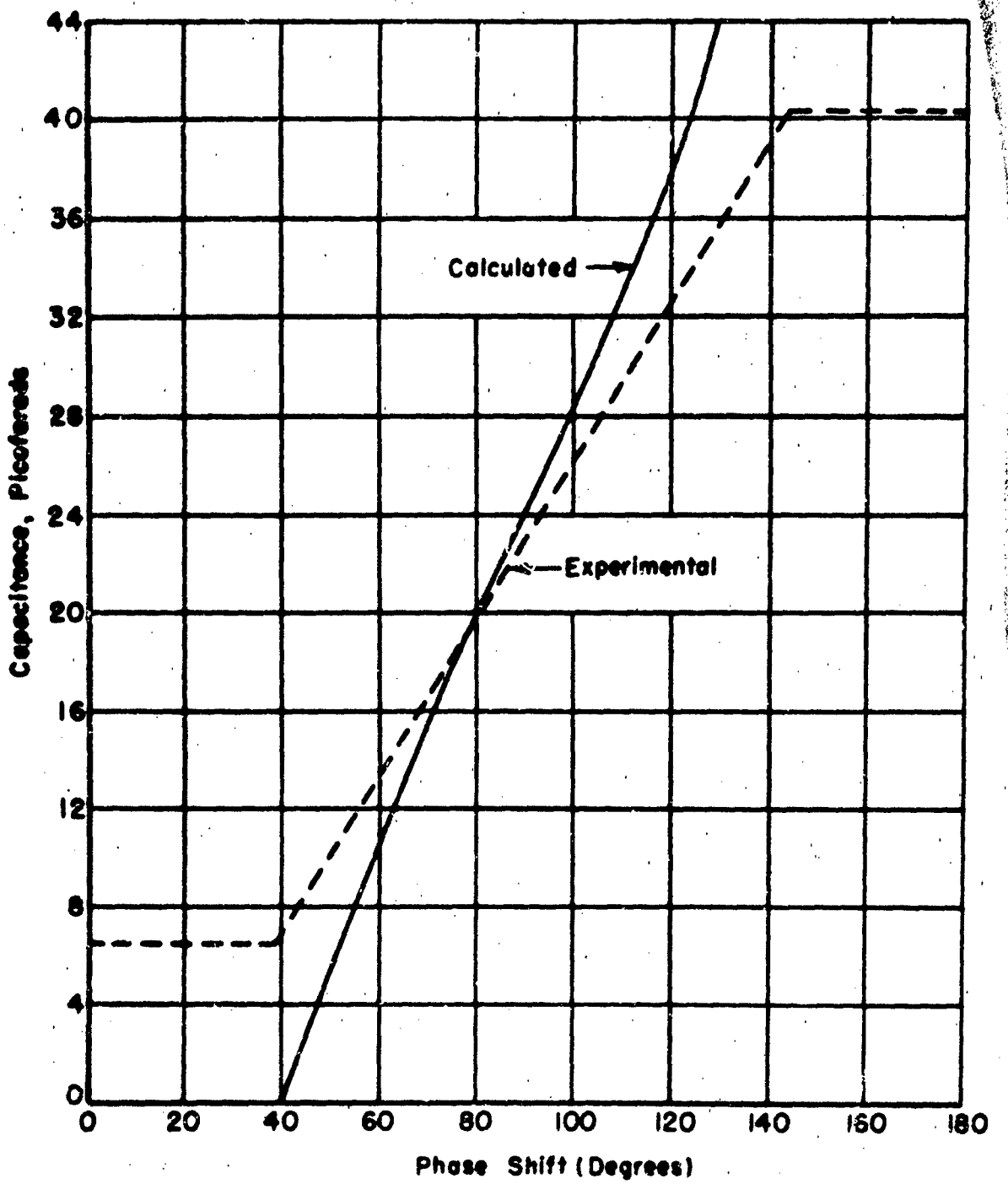

Fig. 5. Arm B capacitance versus phase shift

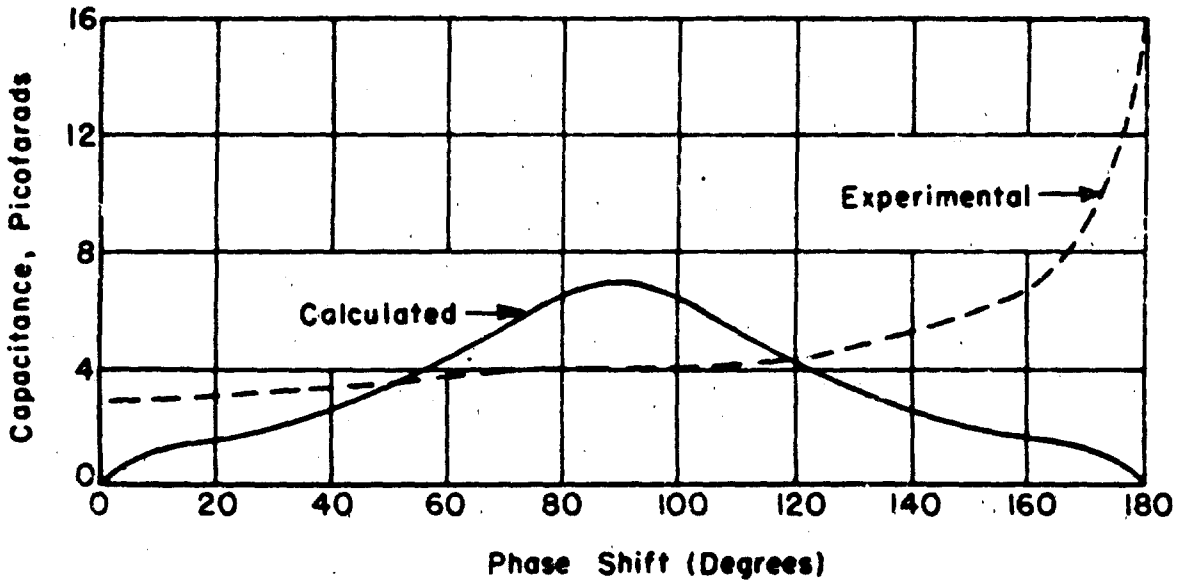

Fig. 6. Arm C capacitance versus phase shift.

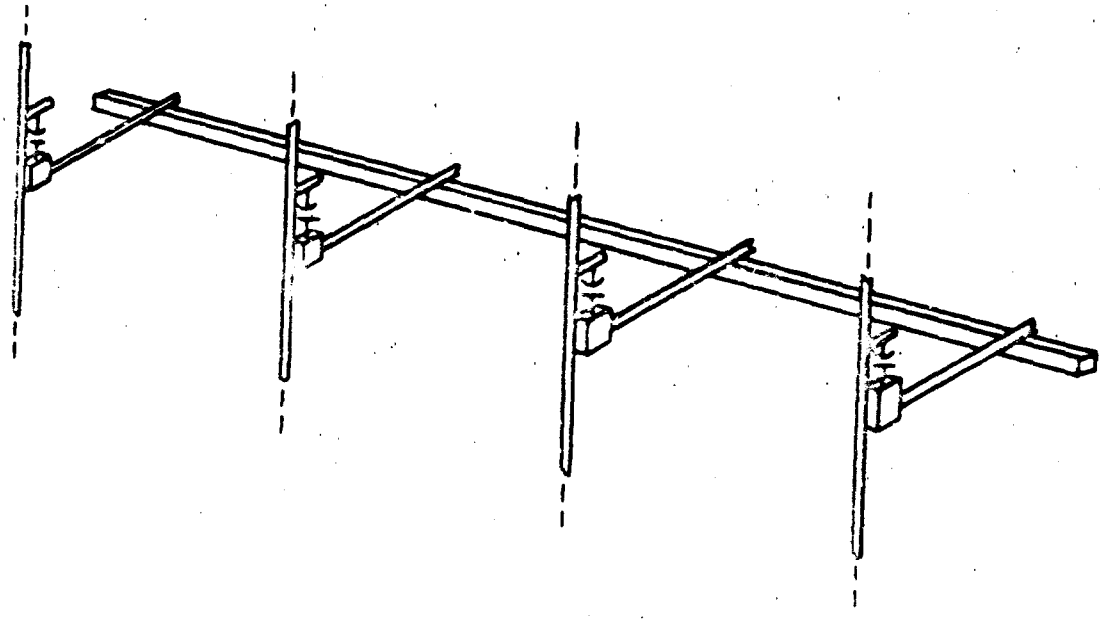

Fig. 7. Four-element antennafier array.

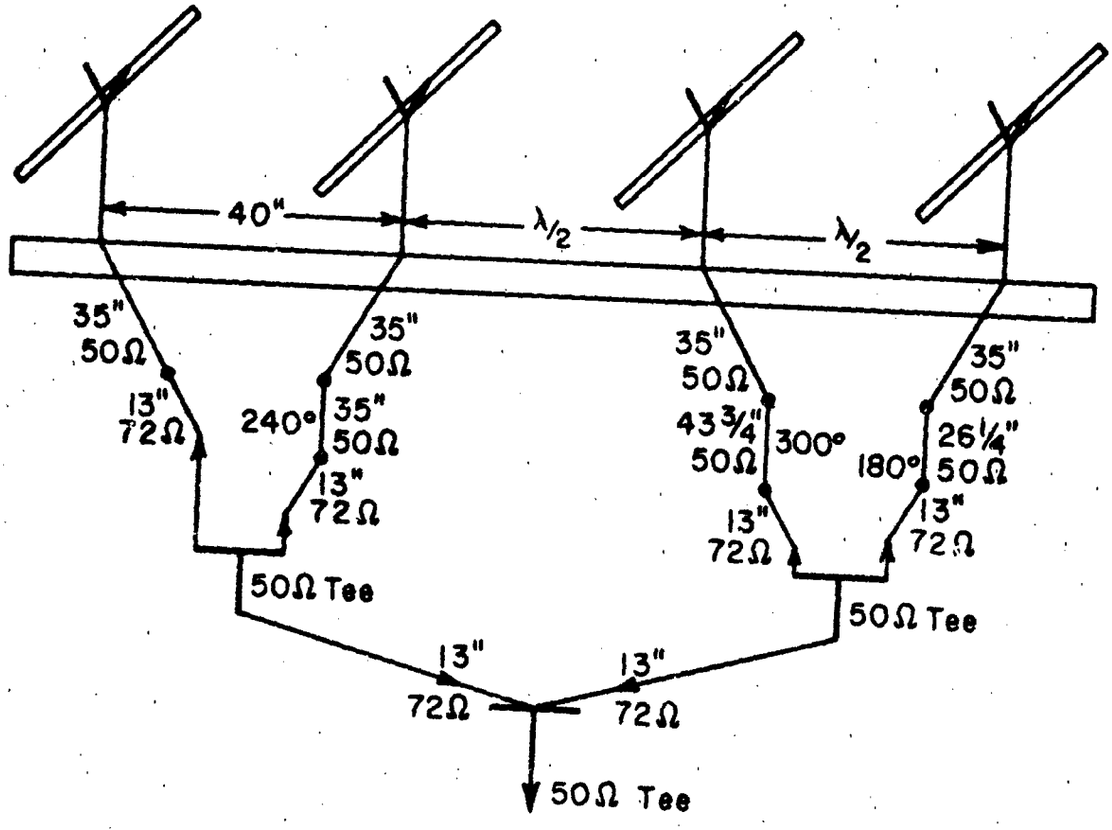

Fig. 8. Array feed system.

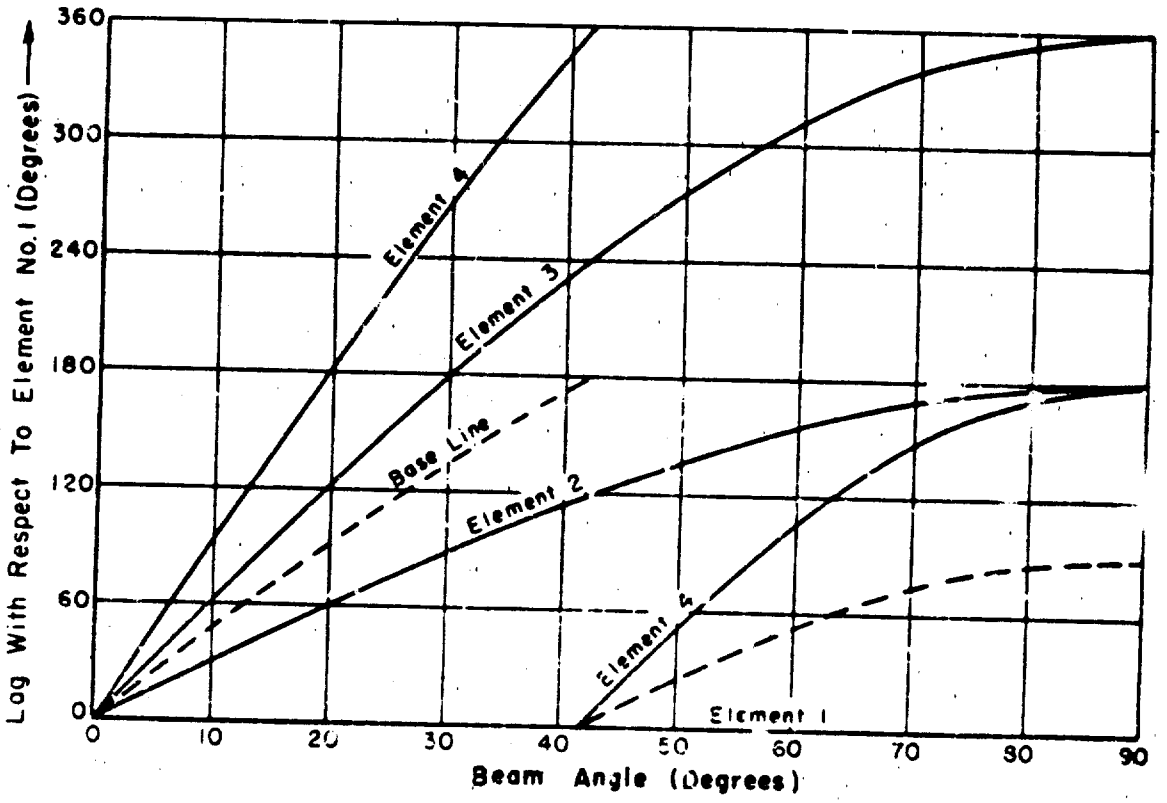

Fig. 9. Received signal phase versus beam angle.

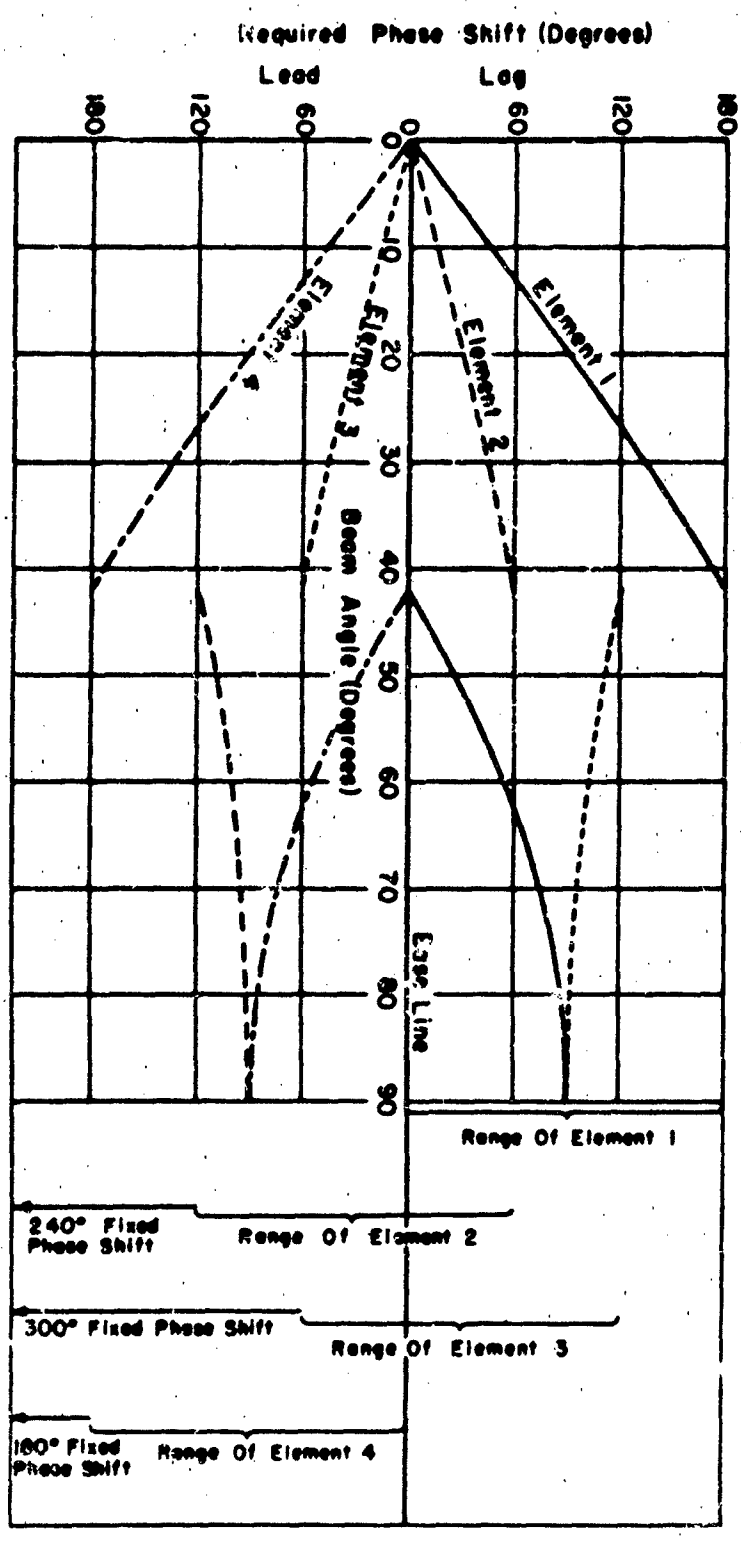

Fig. 10. Required phase shift versus beam angle.

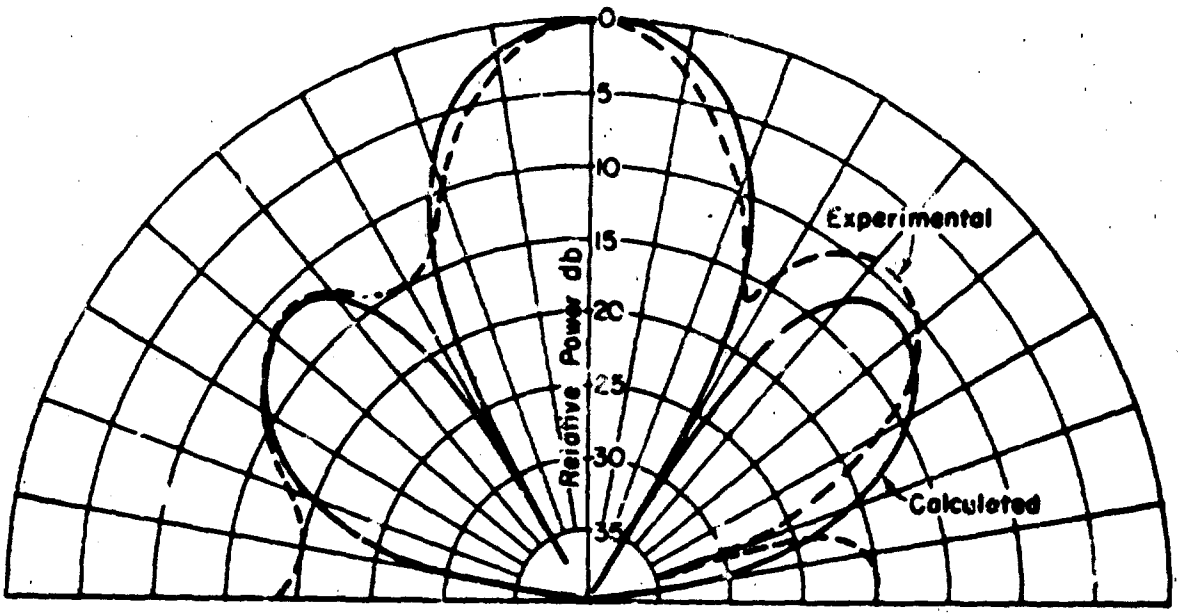

Fig. 11. Broadside array radiation pattern.

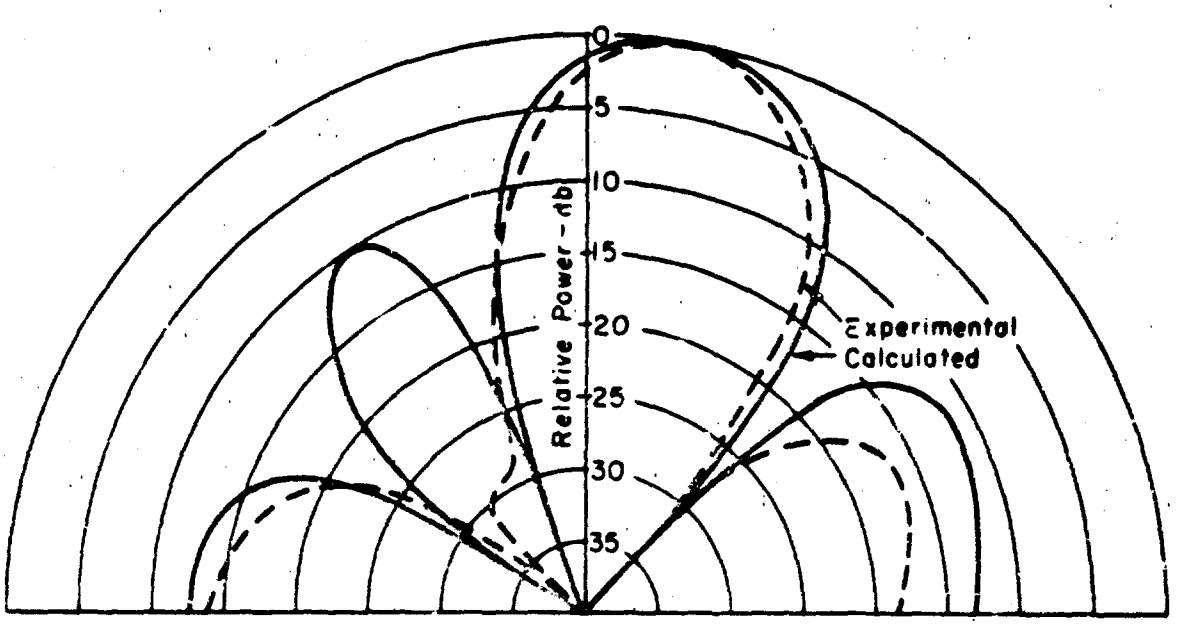

Fig. 12. Array radiation pattern for beam angle 10° off broadside.

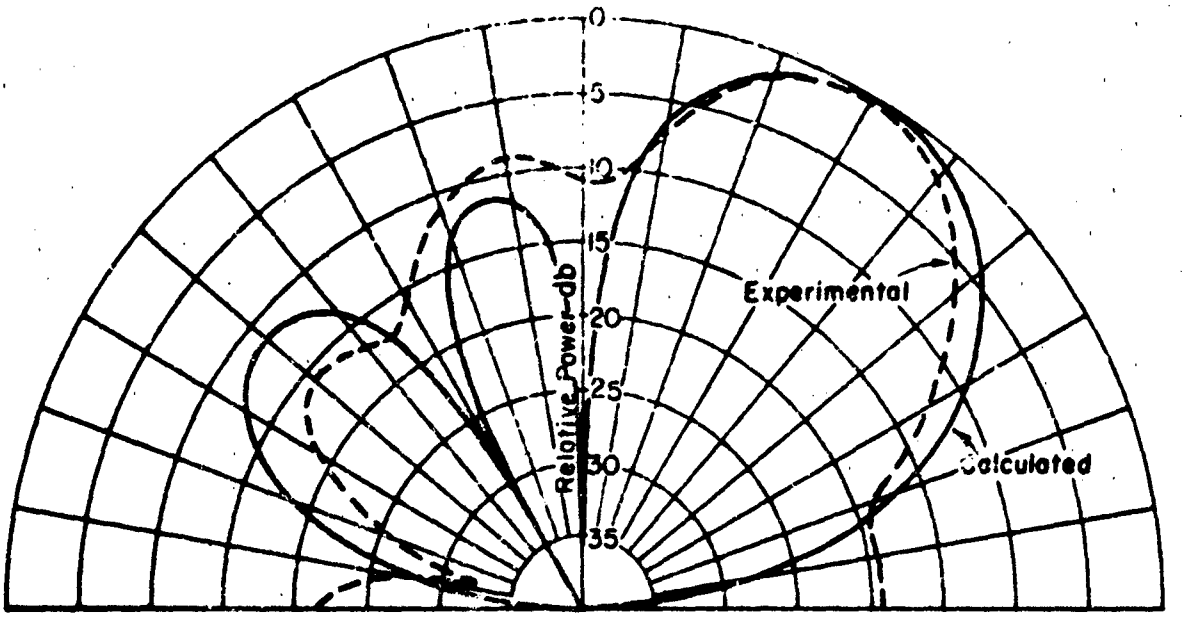

Fig. 13. Array radiation pattern for beam angle 30° off broadside.

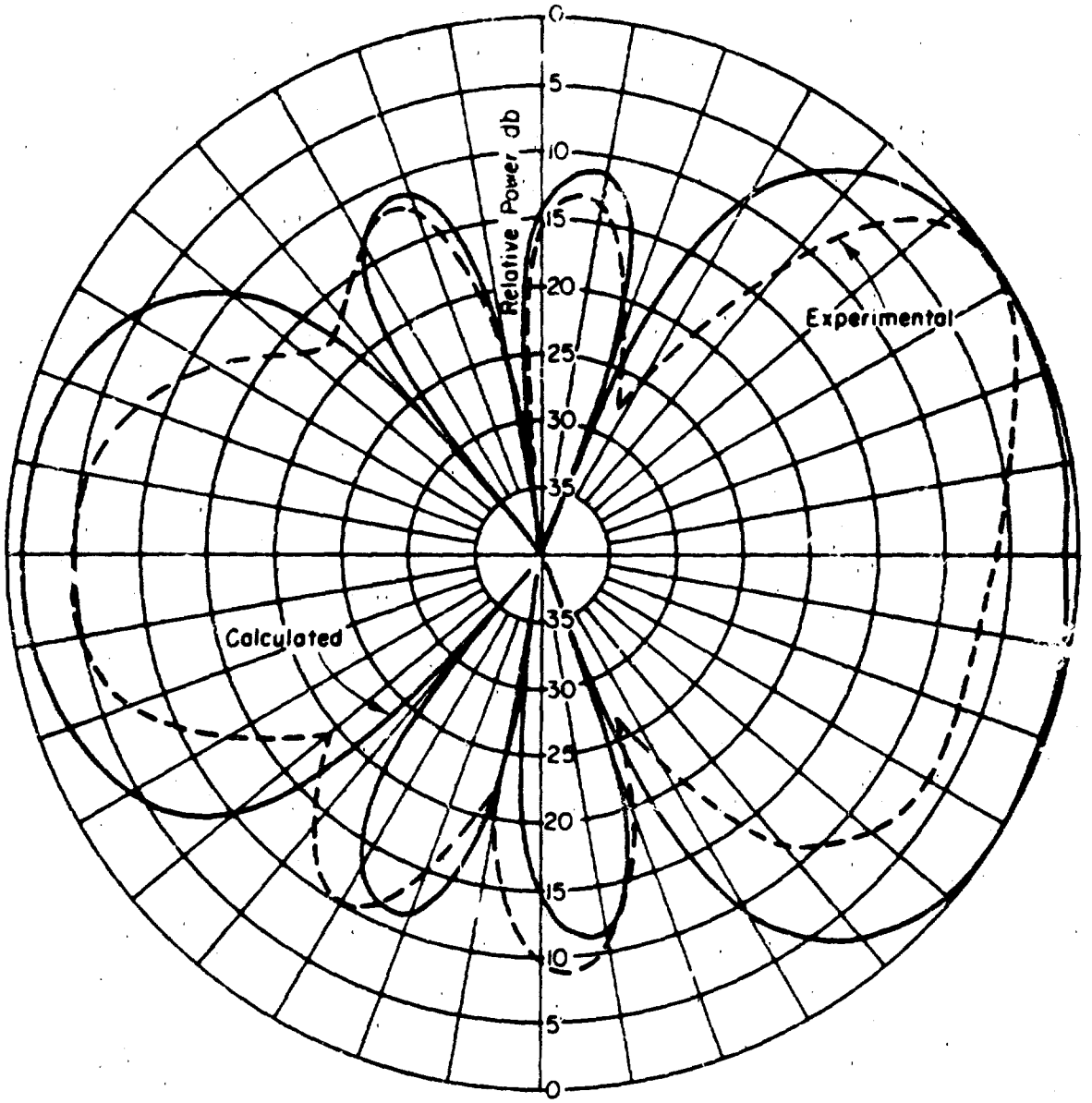

Fig. 14. Array radiation pattern for beam angle 60° off broadside.

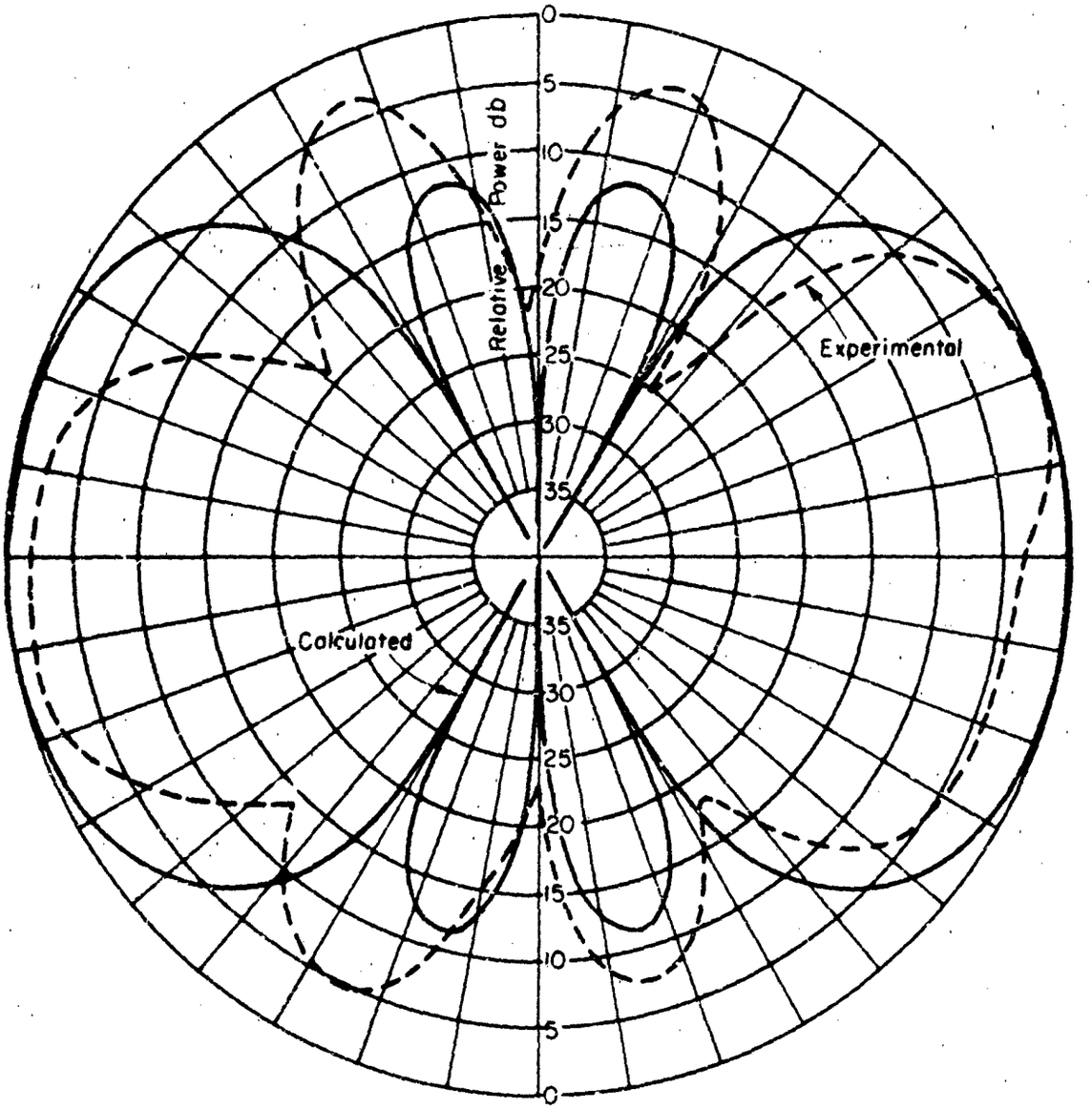

Fig. 15. Endfire (90°) array radiation pattern.

HIGH-POWER BEAM SWITCHING TECHNIQUES FOR MULTIBEAM ARRAY ANTENNAS

by

Helmut E. Schrank



Prepared for Presentation
at the

Fourteenth Annual Symposium
on USAF Antenna Research and Development

Monticello, Illinois

October 1964

Westinghouse Defense and Space Center
Surface Division
P. O. Box 1897 Baltimore 3, Md.

HIGH-POWER BEAM SWITCHING TECHNIQUES FOR MULTIBEAM ARRAY ANTENNAS

by
Helmut E. Schrank
Westinghouse Defense and Space Center
Surface Division
Baltimore, Maryland, 21203

INTRODUCTION

Many electronically controlled multiple-beam array systems presently under consideration require a means for rapidly switching microwave power from one beam to another, or from one array to another. In the present state of the microwave switch art, there are as yet no available components ideally suited for rapidly switching very high power levels. Ferrite RF switch power limitations are well below the power handling capability of the waveguide itself. High power gas plasma switches can be used in pairs in a balanced duplexer arrangement to form a 1:2 switch, but plasma devices suffer from the disadvantages of poor noise figure and slow recovery time.

This paper describes a technique for accomplishing multi-channel switching of high or low microwave power levels, using available state-of-the-art components. This technique operates on the basic principle of using binary hybrid power dividers to split the high power into lower-power parts, then digitally phase shifting these lower power levels, and recombining the parts into any one of a number of high power output channels.

The number of channels which can be switched is any binary number (i.e., $N = 2^n$), and the total power which can be switched is equal to N - times the power handling capability of the waveguide phase shifter components used. To introduce the technique a simple four-channel switch configuration will be discussed. This N = 4 configuration not only avoids excessive complexity in the discussion, but is a very practical configuration for the many array systems which use four planar arrays to achieve hemispheric coverage.

BUTLER-LOWE MATRIX SWITCH

The Butler matrix[1] is an arrangement of 3 db hybrids and fixed phase shifters which has been applied to multiple-beam array antennas. A four-element example is shown in figure 1 which has four input ports, four outputs, and is capable of producing four discrete

[1] This type of matrix was also developed independently by Willey (2) and Shelton (3). See references.

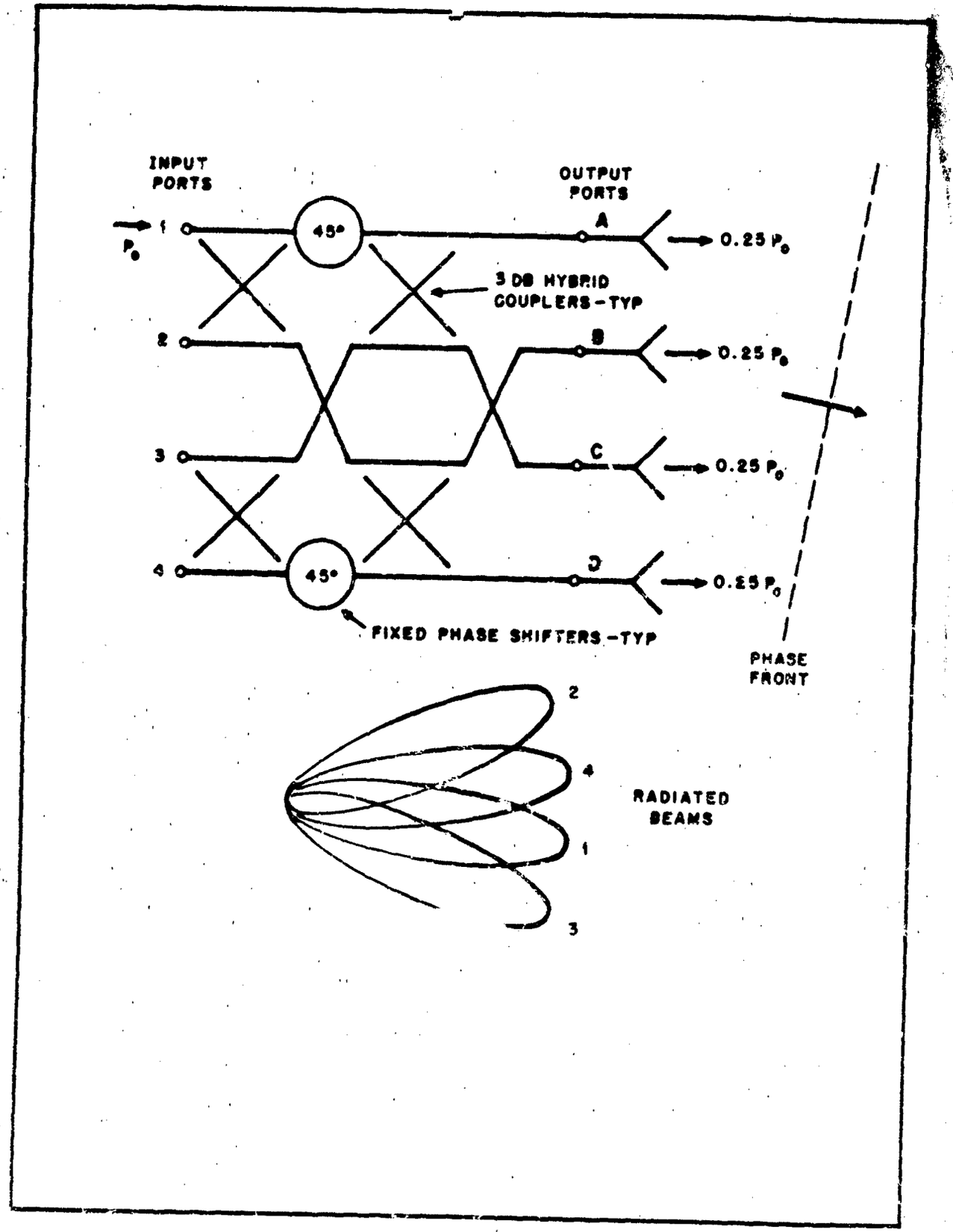

Figure 1. Four Beam Butler Array

beams as indicated. The device is inherently binary, and can be extended to produce 8, 16, or 2^n beams. Power introduced into any one of the input ports is divided equally among the output ports, but with various phase delays, as for example the values shown in table I.

Table I

Output Phases from 4-Port Butler Matrix
When Power Is Applied To Various Input Terminals

Input Terminal	1	2	3	4
A	-135°	-225°	-180°	-270°
B	-180°	- 90°	-315°	-225°
C	-255°	-315°	- 90°	-180°
D	-270°	-180°	-225°	-135°

When the output ports are connected to a linear array of antenna elements, a tilted beam is radiated. Higher order antennas of this type have been extensively studied and are well known (4), (5), and (6).

If instead of radiating the divided output power, we feed it into the ports of an identical Butler matrix, attached back-to-back, the power will be recombined in the second matrix and the total power will appear at a single terminal diagonally opposite the input port as shown in figure 2. If we now introduce variable phase shifters between the back-to-back Butler matrices as shown in figure 3, we can cause the power to recombine into any of the other terminals by properly adjusting the phase shifters.

For the four-port example shown, power into input terminal 1 can be recombined into output terminals 1, 2, 3, or 4 by providing the phase shift values A, B, C, and D given in table II.

Table II

Values of Phase Shift Required To
Switch Input 1 Into Four Outputs

Outputs	1	2	3	4
A	0	-180°	-180°	-270°
B	0	0	-270°	-180°
C	0	-180°	0	- 90°
D	0	0	- 90°	0

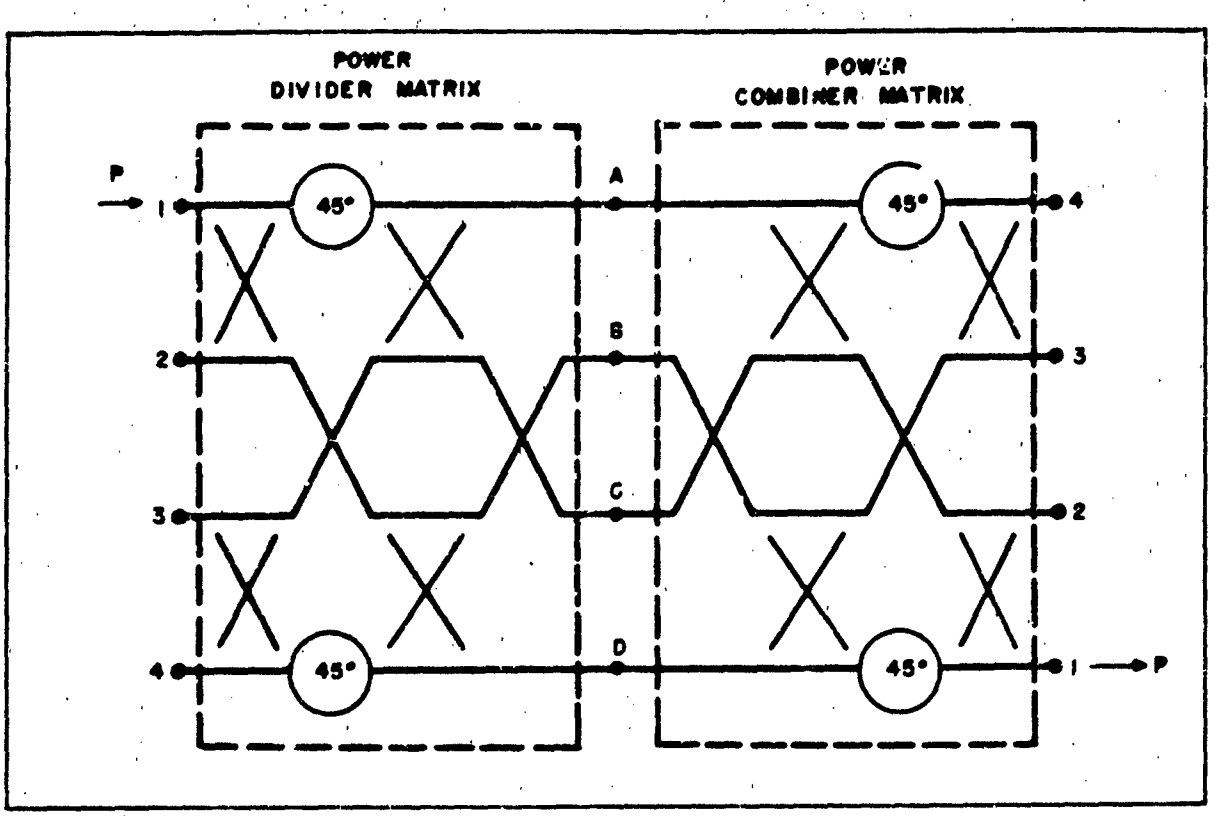

Figure 2. Back-To-Back Butler Matrices

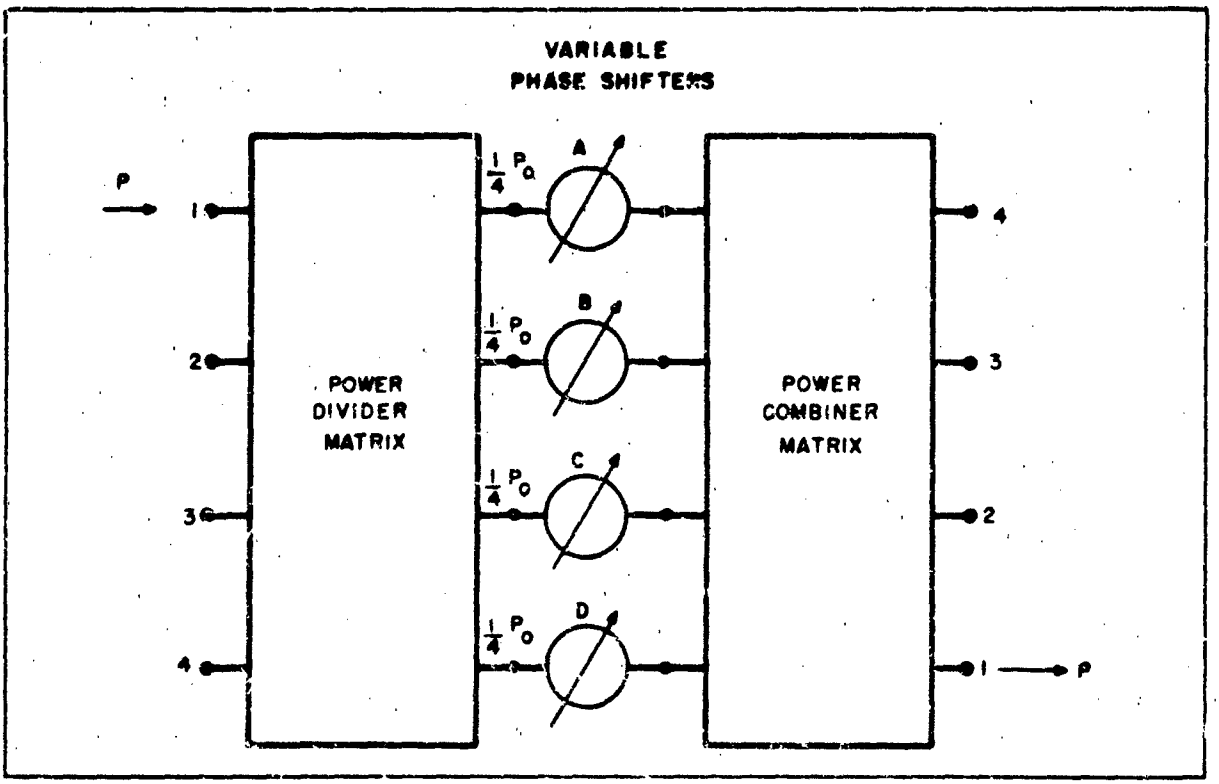

Figure 3. Four Channel Butler Matrix Switch

Notice that here all phase shifts are negative (i.e. additional delay) and are in discrete multiples of 90°, which conveniently allows the variable phase shifters to be digital rather than analog devices. Also note that each phase shifter is exposed to only one-fourth the total power being switched from input terminal 1 to any of four output terminals. By extending the principles illustrated here in this 4 port example to higher powers of 2, such as an N-port device, the total power which can be switched is N times the power-handling capability of the individual variable phase shifters. We can therefore use this technique for switching very high RF power levels by means of medium-power phase shifters, together with 3 db hybrids and fixed phase shifters which, of course, must be respectively capable of handling all or half of the total power being switched.

HYBRID-COUPLER MATRIX SWITCH

The Butler matrix includes fixed phase-shifters and some crossed lines which are necessary only for its original antenna application, but are not necessary for the switching application. A simpler matrix switch can be devised as illustrated in figure 4.

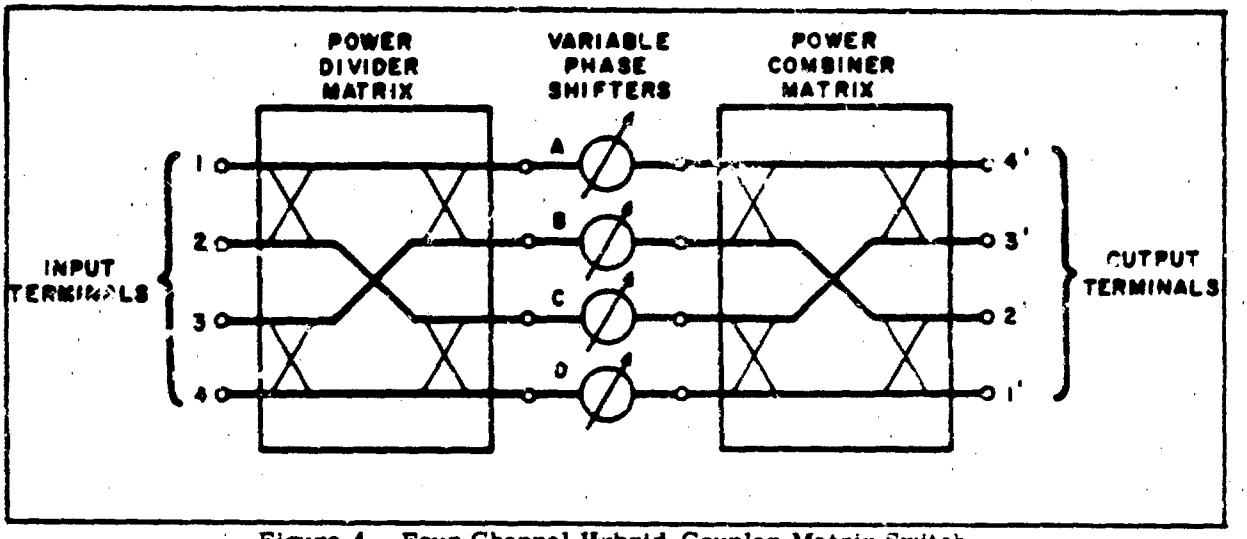

Figure 4. Four Channel Hybrid-Coupler Matrix Switch

Not only does this simpler arrangement eliminate the fixed phase shifters, but it can be shown that the variable phase shifters need to have only two values of phase shift, namely 0 and 180°, whereas up to three multiples of 90° are required in the Butler matrix configuration (see table II). The values of phase shift required in this simplified arrangement, and the corresponding switch paths established, are shown in table III. This hybrid-coupler matrix configuration can, of course, also be extended to higher orders, such that an N-terminal switch requires each of the phase shifters to handle only one N^{th} the input power. It can be made in either stripline or waveguide form, the latter being a natural choice for high power applications.

Table III

Phase Shift Requirements For A Four Channel Matrix Switch

Switch Paths Established	Phase Shift Values			
	ØA	ØB	ØC	ØD
1 ↔ 1', 2 ↔ 2', 3 ↔ 3', 4 ↔ 4'	0	0	0	0
1 ↔ 2', 2 ↔ 1', 3 ↔ 4', 4 ↔ 3'	0	0	-180°	-180°
1 ↔ 3', 2 ↔ 4', 3 ↔ 1', 4 ↔ 2'	0	-180°	0	-180°
1 ↔ 4', 2 ↔ 3', 3 ↔ 2', 4 ↔ 1'	-180°	0	0	-180°

COMBINATION SWITCH AND POWER AMPLIFIER ARRANGEMENTS

For systems requiring extremely high output power levels, the possibility of inserting N power amplifiers between the phase shifters and the combining matrix can be considered. The power amplifiers must have adequate phase and gain stability to provide good isolation of output power from the unswitched terminals.

Another variation of this technique which may have advantages in some systems is shown in figure 5, again in the form of a four-channel example. Here power amplifiers are used between the hybrid-coupler matrices and switching is done at the lower input power level. The multiple-throw switch can be a diode or ferrite device, depending on the power levels and switching speeds required. No variable phase shifters are involved, and the combined power of many power amplifiers can be rapidly switched to a single output terminal.

ANALYSIS OF IDEAL MATRIX SWITCHES

In analyzing the performance of hybrid-coupler matrix switches, the following phase properties (7) of 3 db hybrid couplers is used: a signal into one terminal of a coupler is split into two equal-amplitude components at the two opposite (output) terminals, with no coupling to the adjacent input terminal. The outputs are equal in amplitude but differ in phase by 90 degrees. The component at the in-line (primary) output terminal experiences a 45° delay relative to the phase of the signal which would exist at that terminal if there were zero coupling to the auxiliary (secondary) line. The other component experiences a 135° delay, which differs by -90° from the primary output. In other words, a signal which goes "straight" through a coupler comes out with a 45° delay, while a signal which goes "across" a coupler comes out with a 135° delay. It is assumed that all coupler matrix paths are made of equal electrical lengths, and therefore the above coupler phase delays are the only significant phase effects. With these "ground rules", the values of phases in table I can be verified, and the following simplified (but accurate) analysis method can be applied to various matrix switch configurations.

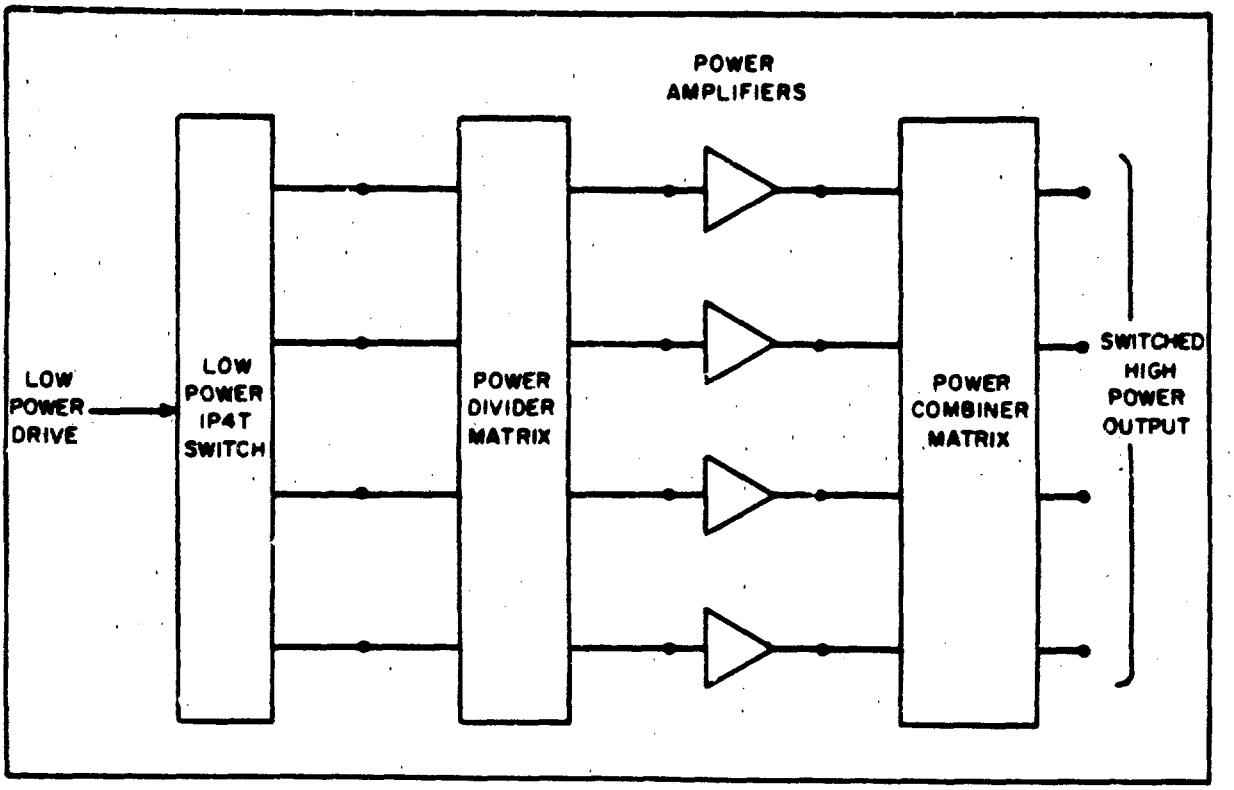

Figure 5. Four Channel Switch Amplifier Configuration

Consider the flow of signal components through a pair of back-to-back hybrid coupler matrices with no phase shifters as shown in figure 6. Power is fed into the divider matrix at input terminal 1. It splits into four equal amplitude components at intermediate terminals A, B, C, and D as shown. Component A is shown with a 90° phase lag with respect to the dotted reference phase. This 90° lag results from signal A having gone "straight" through two hybrid couplers, each contributing a 45° delay. Component B goes "straight" through the first coupler, and "across" the second, hence experiences 45° + 135° = 180° delay. The remaining components are easily derived in the same way.

Each of the four A, B, C, D components then enters the combining matrix and is further split into four equal-amplitude (but differing phase) outputs. These are represented by the four columns of four output signals shown to the right of the output terminals 1', 2', 3', and 4' in figure 6. Note how the components add up horizontally to a resultant output, which for this case is zero in all but output terminal 1', where all the power emerges if ideal lossless matrices are assumed for the moment. Later we will consider the effects of imperfect matrix components.

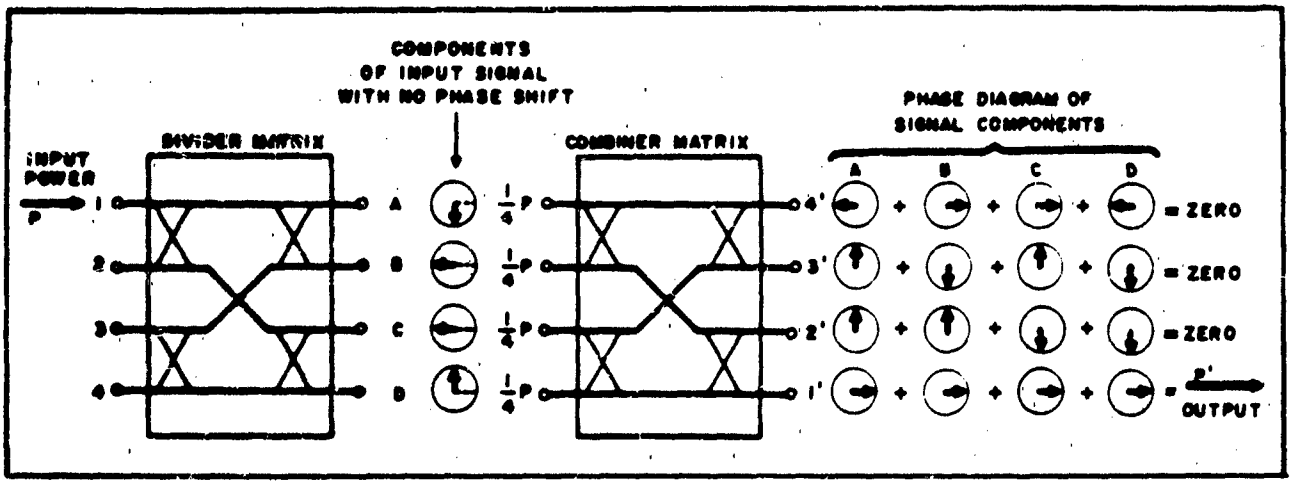

Figure 6. Phase Analysis of Matrix Switch

Using a similar analysis, it is simple to show how introducing 180° phase delays at terminals C and D will cause all the power coming into terminal 1 to be switched to output terminal 2'. Figure 7 is similar to figure 6 except for the introduction of the phase shifters. Note how output components in columns C and D are reversed in direction compared with figure 6, and how this results in complete power combination in terminal 2', with zero at the other terminals.

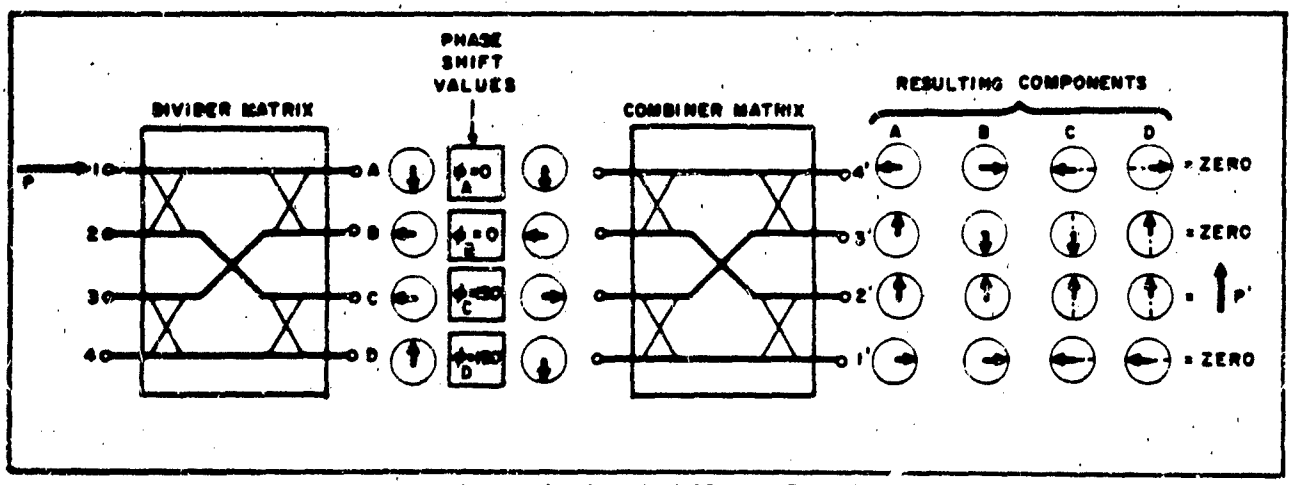

Figure 7. Phase Analysis of Matrix Switch

EFFECTS OF PHASE AND AMPLITUDE ERRORS

The analysis above dealt with ideal components in which perfect amplitude and phase shift values were assumed. For a practical matrix switch, it is necessary to examine the effects of imperfect components on the switch performance, to determine reasonable tolerances for the hybrid couplers and phase shifters.

First consider a four-channel switch with an amplitude error in one of the four paths. Let us assume, for example, that one of the four variable phase shifters has an insertion loss, such that its output amplitude is 0.5k (volts) where $k < 1$. The other three amplitudes are assumed to be 0.5 volts, resulting from a unit voltage at one of the switch input terminals.

Using the simple phasor diagram method of analysis on the switch condition of figure 7, the signals are now as shown in figure 8. A unit input voltage at terminal 1 produces 0.5 volt components at intermediate terminals A, B, C, and D. If one phase shifter, say ϕ_C, causes an amplitude error such that its output is only 0.5k volts, then all the output signal components in column C will have an amplitude of 0.25k. This results in imperfect cancellation in output channels 1', 3', and 4', such that a resultant voltage of $e = 0.25\ (1-k)$ appears. On the switched output channel 2', the resultant voltage will be $E = 0.25\ (3+k)$. Thus the signal in the desired channel is down by

$$A\ (db) = 20 \log_{10} \left[0.25\ (3+k)\right]$$

and the isolation (i.e., coupling into undesired channels) is given by

$$a\ (db) = -20 \log_{10} (E/e)$$

Assigning some numbers in this case results the following:

Voltage amplitude error k	0.944	0.891	0.795	0.707
Amplitude error in db	-0.5	-1.0	-2.0	-3.0
Loss in output A (db)	-0.12	-0.24	-0.46	-0.66
Isolation a (db)	-37	-33	-26	-23

It can be seen that the loss in the desired output due to a pure amplitude error in one path is roughly one-quarter of the amplitude error in db for a 4 channel switch. Thus it appears that

$$A\ (db) = 20 \log_{10} (k)/4$$

or $$A\ (db) = K\ (db)/4$$

For a higher number of channels, N, the output loss will be proportionately less, namely

$$A\ (db) = K\ (db)/N$$

The same analysis method can be extended to determine the effects of phase errors and amplitude errors in more than one channel, but then the question arises as to what assumptions to make for the various errors. This is best handled on the basis of statistics and random variables. Such an extension to the analysis is in process, and includes combinations of phase and amplitude errors.

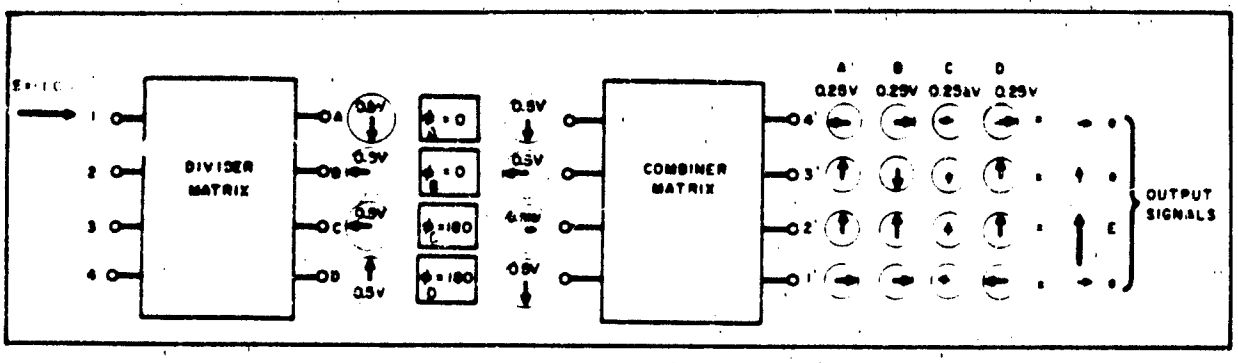

Figure 8. Amplitude Error Analysis

A similar analysis has been made on a hybrid matrix switch using magic-tee hybrids (8), but otherwise equivalent to the switch technique described above. In this analysis random amplitude and phase errors are assumed, such that they make equal contributions to the decoupling (isolation) of power to undesired output channels. Under these assumptions, the results indicate that for a 16 channel switch with better than -20 db of isolation, the overall amplitude and phase tolerances are 2.2 db and 16.0 degrees, respectively, while for -30 db isolation the values are 0.8 db and 5.2 degrees. Also, the tolerances become less stringent as the number of channels increases. These results are being confirmed and extended to less restrictive assumptions.

ACKNOWLEDGEMENTS

The author wishes to acknowledge the valuable contributions of Mr. Calvin C. Jones who conceived of the hybrid-coupler approach to this switching technique while the author independently took the back-to-back Butler matrix approach. The contributions of Richard S. Davis and Wendell P. Hooper are also gratefully acknowledged.

This study was initiated with Westinghouse support and is being continued under R. A. D. C. contract number AF-30(602)-3394-FSC-A082.

REFERENCES

(1) Butler and Lowe - "Beam Forming Matrix Simplifies Design of Electronically Scanned Antennas", Electronic Design, April 12, 1961, pp. 170-173

(2) Willey, R. E. - "Flat Array Antenna For A Doppler Navigation System", I. R. E. East Coast Conference on Aeronautical and Navigational Electronics, October 1959 Paper No. 5.1

(3) Shelton and Kelleher - "Multiple Beams from Linear Arrays", I. R. E. Transactions AP-9, No. 2, March 1961, pp. 154-161

(4) Delaney, W. P. - "An RF Multiple Beam Forming Technique", M. I. T. - Lincoln Lab. Report 41G-0012, Aug. 9, 1961; contract AF19(604)-7400

(5) Mehron, M. E. - "Octave Bandwidth Multiple Beam Array", Thirteenth Annual Symposium on USAF Antenna Research and Development, Univ. of Illinois Oct. 1963.

(6) Meads, S. K. - "A Fixed-Array, High-Data-Rate, Search and Height-Finding Radar", U. S. Naval Research Lab Report 5905, May 1963.

(7) Schrank and Grauling - "Phase Relationships in Short-Slot Hybrid Couplers", Proc. of the I. R. E., Nov. 1959, p. 2017

(8) Broussaud et Trevoux - "Un Commutateur D'Energie U. H. F. A Commande Electrique", Annales de Radioelectricite, XVI-No. 66, Oct. 1961, pp. 269-276.

THE DESIGN OF A BROADBAND ROTATING FEED FOR A LOW NOISE TEMPERATURE ANTENNA WITH AUTO-TRACK CAPABILITY

By D. G. Henry*

ABSTRACT

A feed is described that was designed to fit in a 19 foot parabolic reflector to give auto-track capability. The feed operates at 860, 900, 960, 1400, 1700, 2290 and 2800 Mc. The polarization is right circular from the reflector. The VSWR is 1.5:1.0 or better at the above frequencies. The peak-to-peak tracking modulation does not exceed 2.0 db at a rate not less than 20 cps. Maximum signal to noise ratio, rather than maximum gain, is desired from the reflector.

The feed described is a conical log-spiral with a spiral rate of 83 degrees, a cone angle of 20 degrees, a truncation diameter of 0.592 inch and a base diameter of 4.92 inches. The antenna is fed balanced by a broadband tapered balun. The half power beamwidth varies from 62 degrees at the lowest frequency to 97 degrees at the highest frequency. The beamwidth to first nulls varied from 160 to 175 degrees. The axial ratio of the conical log-spiral varies from 0.75 at 960 Mc (where it is the best) to 5.0 at 2800 Mc (where it is the worst).

The conical log-spiral feed is mounted in the dish and tilted at 15 degrees to give the auto-track mode. The half power beamwidth of the reflector and feed ranges from 4.4 to 1.5 degrees from the lowest to highest frequency. The tracking modulation level varies from 0.9 to 1.9 db from low end to high end. The front to back ratio is a minimum of 40 and a maximum of 48 db. The calculated noise temperatures range from 132 degrees Kelvin at 860 Mc to 37.5 degrees Kelvin at 2290 Mc, where it is a minimum. The noise temperature at 2800 Mc is 42.1 degrees Kelvin.

For final installation the conical log-spiral and broadband balun are potted in place and a pressurized protector is placed over the motor, reference generator, and rotary joint.

*PHYSICAL SCIENCE LABORATORY
NEW MEXICO STATE UNIVERSITY
Box 548
University Park, New Mexico
Contract NAS 10-48

1.0 INTRODUCTION

The National Aeronautics and Space Administration Launch Operations Directorate of the George C. Marshall Space Flight Center has requested the Physical Science Laboratory of New Mexico State University to provide a nutating feed or feeds for a 19 foot parabolic reflector, which offers a low noise temperature auto-track capability.

2.0 ELECTRICAL PARAMETERS

2.1 Operating Frequencies

The operating frequencies of interest are 860, 900, 960, 1400, 1700, 2290 and 2800 Mc/sec. The frequency of highest interest is 2290 with 960 and 1700 next and 2800 of least importance.

2.2 Polarization

Polarization diversity is desirable, but not required. If a single polarization is to be provided, right circular polarization is required.

2.3 VSWR Limits

The VSWR must be 1.3:1 or better at the critical frequencies (2290, 1700 and 960).

2.4 Noise Temperature

The feed shall provide for maximum signal to noise ratio rather than maximum gain. The noise temperature of the preamplifier is assumed 75° K.

2.5 Tracking Modulation

The peak-to-peak tracking modulation in db shall not exceed 2.0 ± .5 db.

2.6 Modulation Rate

The modulation rate shall not be less than 20 cps.

2.7 Reference Signal

A reference signal coherent with the modulation voltage must be provided. The reference level shall be a nominal 10 volts at 500 ohms.

3.0 MECHANICAL PARAMETERS

The feed shall be rigidly connected to the reflector and be mechanically balanced to preclude vibration. The feed must also be capable of all-weather operation and be impervious to moisture, rain and salt spray, and blowing sand for a period of three years

4.0 CONICAL SPIRAL

The conical log-spiral antenna is defined by a logrithmic equation. There are two arms to the spiral. The defining equation for the first arm is

$$\rho_1 = \rho_0 e^{b\phi} \qquad 4.1$$

where $b = \cot \beta \sin \alpha / \rho_0$ is determined from truncation. β and α are the spiral rate and cone angle respectively as shown in Fig. 1. The second arm is defined by

$$\rho_2 = \rho_1 e^{-b\pi} . \qquad 4.2$$

The diameters of the truncated portion of the cone and the base of the cone are determined by the extremes of frequency bandwidth desired. For this antenna, the diameter of the arms is a constant.

The first of this type of antenna tested had a spiral rate (β) of 73°, a cone angle (α) of 20°, a truncation diameter (d) of 0.592'', and a base diameter (D) of 4.92''. Since the antenna is a two armed structure and must be fed balanced, a broadband tapered balun[3] was constructed to excite and match the antenna. The radiation patterns were smooth, had no back radiation above -20 db, and with the exception of 2800 Mc/sec were essentially the same. The patterns were a great deal too broad to give the desired illumination in the 19 foot parabolic reflector. A summary of the pattern characteristics is given in Table I.

A change of the spiral rate (β) from 73° to 83° with all other parameters remaining the same was next studied. This antenna was much more critical in its impedance matching. The same type of broadband balun, as previously noted, was used to feed this antenna. The radiation patterns of the conical spiral were quite good at all frequencies with the possible exception of 2800 Mc/sec, although 2800 is quite good except for the axial ratio. This antenna will give very close to the desired illumination when placed in the 19 foot diameter parabolic reflector. The antenna is shown in Fig. 2. Table II gives a summary of the patterns shown in Figs. 4 through 24. The antenna coordinate system is shown in Fig. 3.

This antenna was the model with which all tests of the 19 foot parabolic reflector were run.

5.0 PRIMARY FEED TESTS IN REFLECTOR

5.1 Radiation Pattern Test Setup

The 19 foot diameter parabolic reflector was mounted on an elevator on a 30 foot tower. The 360° azimuth rotator is an integral part of this elevator. The 19 foot diameter parabolic reflector was used as a receiver in the radiation pattern measurement setup. The transmitter was located 3000 feet away (Fig. 25). A 10 foot diameter parabolic reflector with a linearly polarized feed, for the desired frequency, was used as a transmitting antenna.

The conical spiral antenna is shown mounted in the reflector for radiation pattern measurements in Fig. 26. The rf, a-c and modulation reference lines are run down the same tripod support leg.

5.2 Radiation Pattern Measurements

The conical spiral feed was mounted in the 19 foot diameter reflector with the axis of the cone coinciding with the axis of the reflector. The conical spiral was adjusted to give the best focus over the frequencies required. Radiation patterns at 960, 1700 and 2300 Mc/sec are shown in Figs. 28 to 33. These are the critical frequencies and also give a good representation of the entire group of operational frequencies. A coordinate system is shown in Fig. 27.

The average back radiation is down 47 to 50 db from the peak of the main lobe for all of the frequencies. The radiation patterns with the cone on axis were run so that a comparison of sidelobe and back radiation could be made when the cone is tilted off-axis to achieve the automatic track mode.

5.3 Modulation Level Tests

The conical spiral was tilted off-axis a number of different ways to determine the optimum position for a constant power modulation. This power modulation is the difference between the peak of the main lobe and the point where the beam crosses the axis of rotation.

The cone base was kept on-axis and the apex tipped off in the first series of tests. This configuration did not give a constant power modulation over the frequency range. The cone base was next moved off-axis and the apex kept on-axis. Various degrees of tilt were tried from 2.5° to 15°. The 15° tilt was found to give the most nearly constant power

modulation level over the frequency range. The modulation level at each frequency is shown in Figs. 34 through 40. The amplitude of the patterns is not relative but are only to show modulation level and beamwidth. As seen on the figures, only the first ten db of the pattern is plotted.

The front-to-back ratio when the feed is tilted does not differ appreciably from that when the feed is on axis. The first sidelobe is slightly higher due to feed tilt. A summary of the pattern characteristics is given in Table III. The VSWR and axial ratio are also included in this table. The measured and calculated gain are also shown on this table.

6.0 NOISE TEMPERATURE

The noise temperature of the 19 foot diameter reflector was calculated from the equation

$$T_A = 1/4\pi \int_0^{2\pi} \int_0^{\pi} T_B(\theta,\phi)\, G(\theta,\phi) \sin\theta \; d\theta \; d\phi \qquad 6.1$$

where T_A - antenna noise temperature
$T_B(\theta,\phi)$ - background temperature distribution
$G(\theta,\phi)$ - radiation pattern of the antenna.

Using the measured radiation pattern of the antenna, the measured value of the cosmic noise[1], and assuming that the earth has a noise temperature of 290° K, a noise temperature was calculated for each frequency. The results of these calculations are given in Table IV. The upper frequencies give the best noise temperature and are within the 75° K specification while the lower frequencies are somewhat higher than the 75° K desired.

The noise temperature of the dish at the upper frequencies is not as low as was expected. This is probably due to the fact that the screen hole size is an appreciable portion of a wavelength and allows leakage through the screen. Also the reflector surface has perturbations which give rise to sidelobes which tend to increase the noise temperature. These perturbations also cause a loss in gain as seen in Table III by comparing the measured with the calculated gain.

7.0 MECHANICAL CONSTRUCTION

7.1 Rotator Assembly

7.1.1 Motor-Generator Mount

The motor and generator are mounted such that they

form an integral part (Fig. 41). Pulleys, belt and bearing are mounted directly to this housing (Fig. 42). This complete unit can be removed from the tripod mounting plate.

7.1.2 Tripod Mounting Plate

The tripod mounting plate (Fig. 43) is used to support the motor-generator mount and feed antenna. Support studs are located at 120° on this plate. These studs are attached to the support arms attached to the dish. Next to one stud is located an rf connector, a-c plug and a reference generator output jack.

7.2 Tripod Assembly

7.2.1 Tripod Support Arms

The tripod support arms are made of fibercast pipe and are 10 feet long (Fig. 44). The pipe is 2.375" in diameter with a 0.210" wall. The pipe is made by FIBERCAST of Sand Springs, Oklahoma.

7.2.2 Adjustable Mounting Studs

Adjustable mounting studs are located on the ends of the support rods attached to the dish (Fig. 45). These studs can be adjusted a total of ± 1" linear travel. The studs will come marked for the proper position.

7.3 Radome

The radome (Fig. 46) is constructed of aluminum and is attached to the mounting plate by socket head cap screws from the reverse side of the plate. A stainless steel clamp is attached around the radome to help hold the o-ring in place. The radome is designed to be pressurized to 5 psi. The pressure is carried to the radome by means of 7/8" helix coaxial cable.

The radome is pressurized to protect the motor, generator and associated parts from condensation of moisture.

The radome should not be pressurized above the design pressure or serious damage could result.

7.4 Antenna Assembly

7.4.1 Counterweight and Ground Plane

The antenna has been dynamically balanced at 1200 rpm to minimize vibrations. The counterweight and ground plane have been bolted together to form a single unit (Fig. 47). Screws and bolts should not be removed from this assembly or the balance will be destroyed.

7.4.2 Conical Spiral Antenna

The conical spiral can be removed from the ground plane by removing the three (3) socket head cap screws on the underside of the ground plane. If this becomes necessary extreme care should be taken not to twist the rf connector at the base of the cone. The interior of the cone has been filled with a foam potting material and should not be disturbed. Failure to heed this warning can result in a destroyed balun and antenna.

7.4.3 Rotary Joint and RF Cable

The antenna counterweight and ground plane assembly can be removed by taking the rotary joint and rf connector off the end of the motor inside the radome. Set screws located at the base of the coupling shaft of the counterweight are then loosened and the entire assembly removed. Sealant and o-rings have been placed inside the motor shaft and should be removed with care.

The rotary joint is an RJ-3 (S/N 14) and is of advanced design as to long life at high speed and low noise. The rotary joint has been run a total of 10 hours and no noise has been detected.

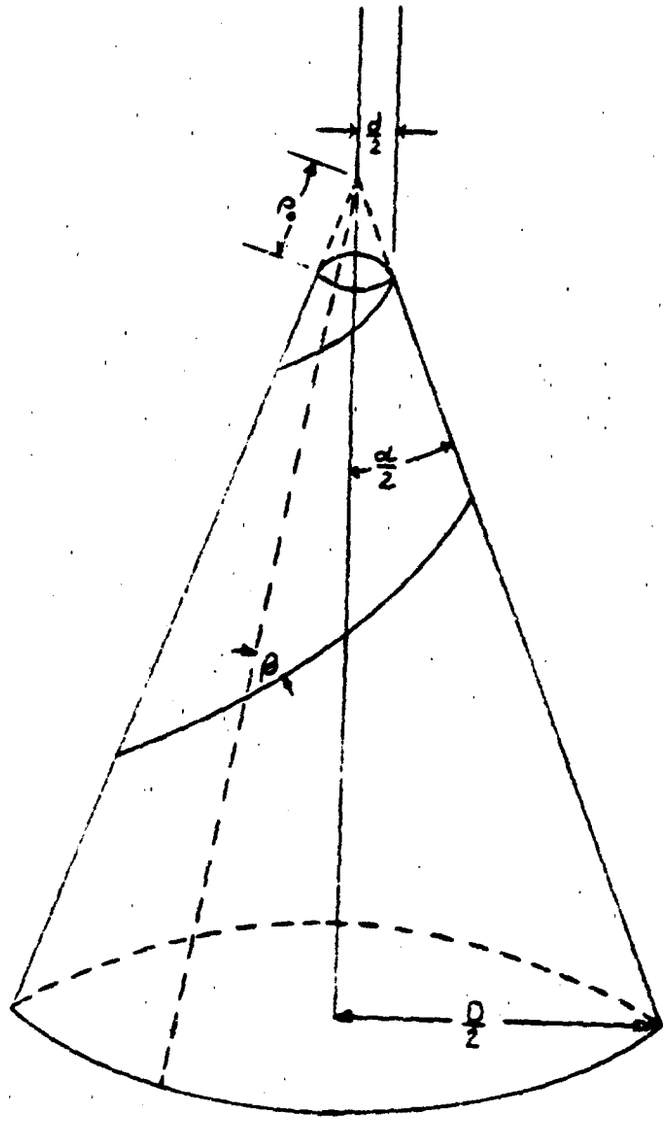

FIG. 1 - PARAMETERS OF THE CONICAL LOG-SPIRAL

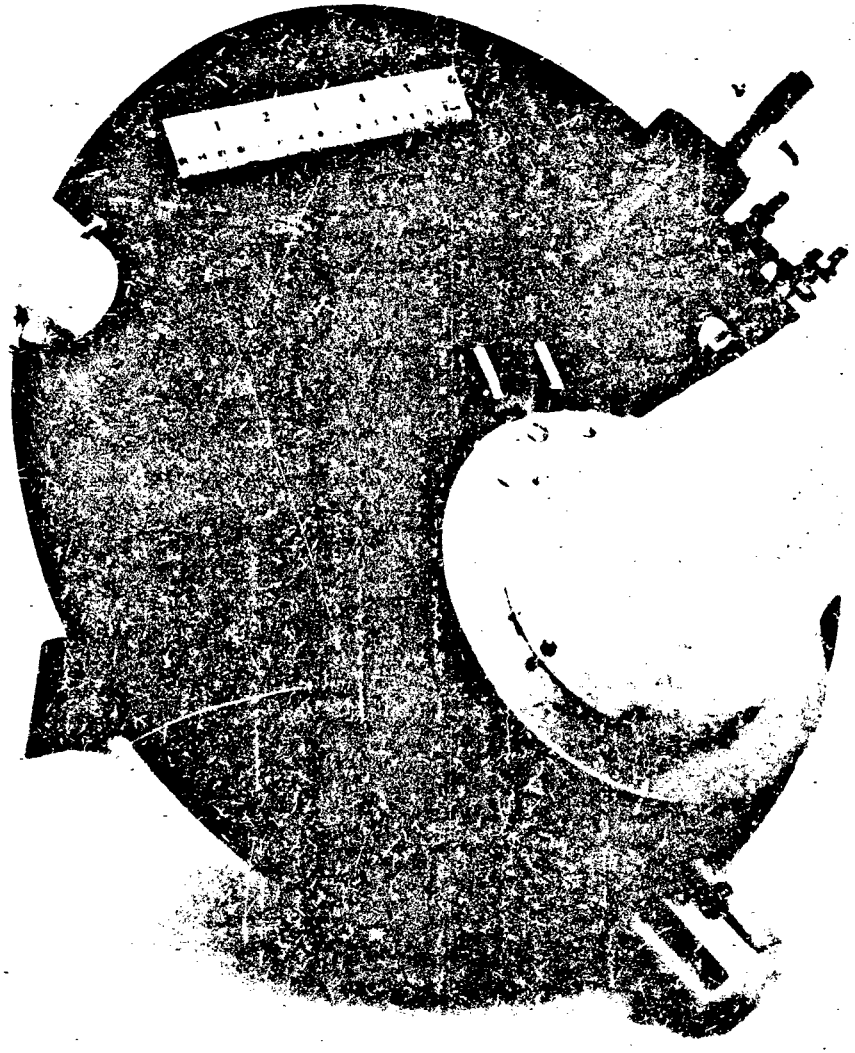

FIG. 2 - CONICAL SPIRAL, $\alpha = 20°$, $\beta = 83°$

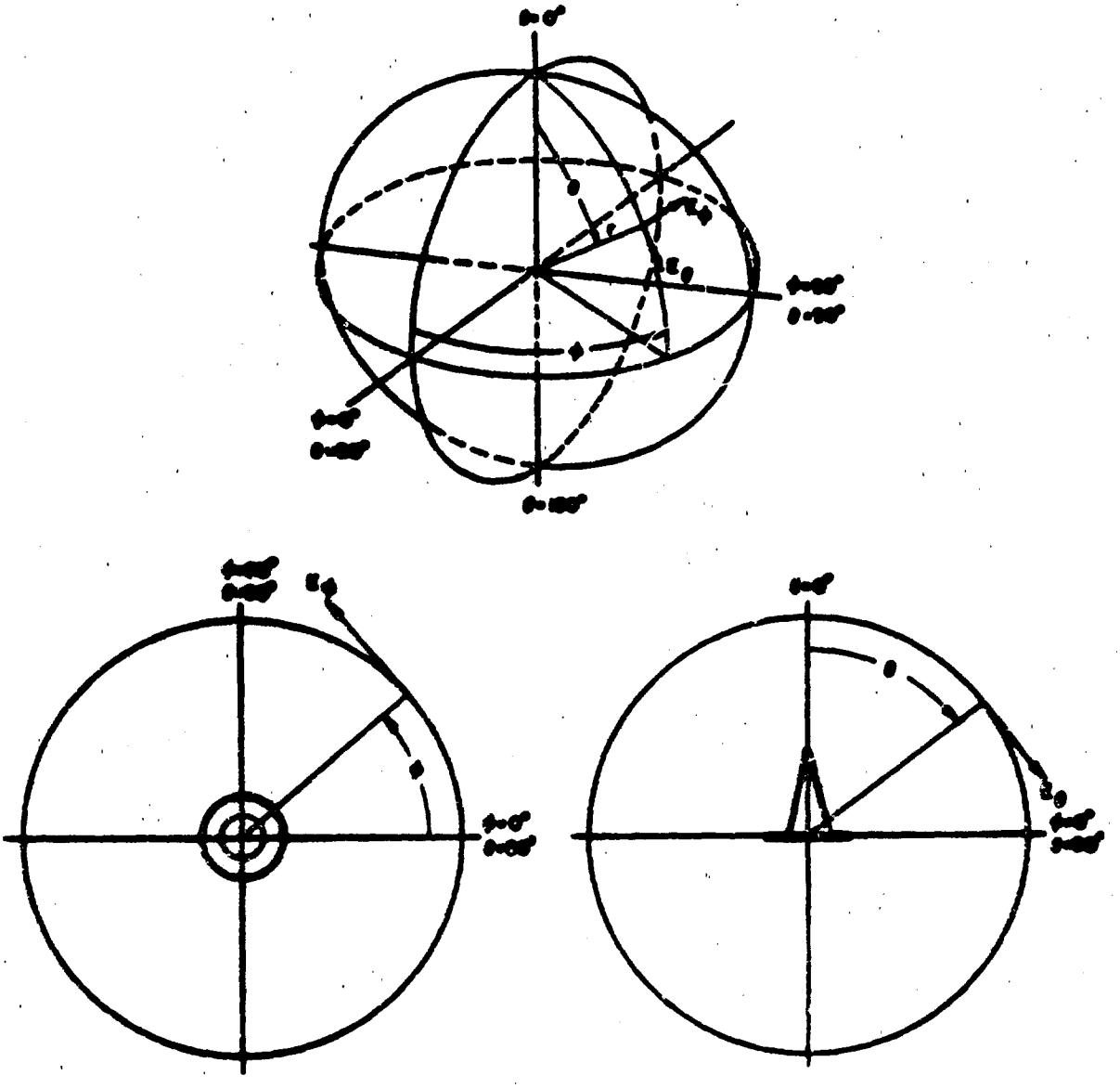

FIG. 3 - COORDINATE SYSTEM FOR CONICAL SPIRAL

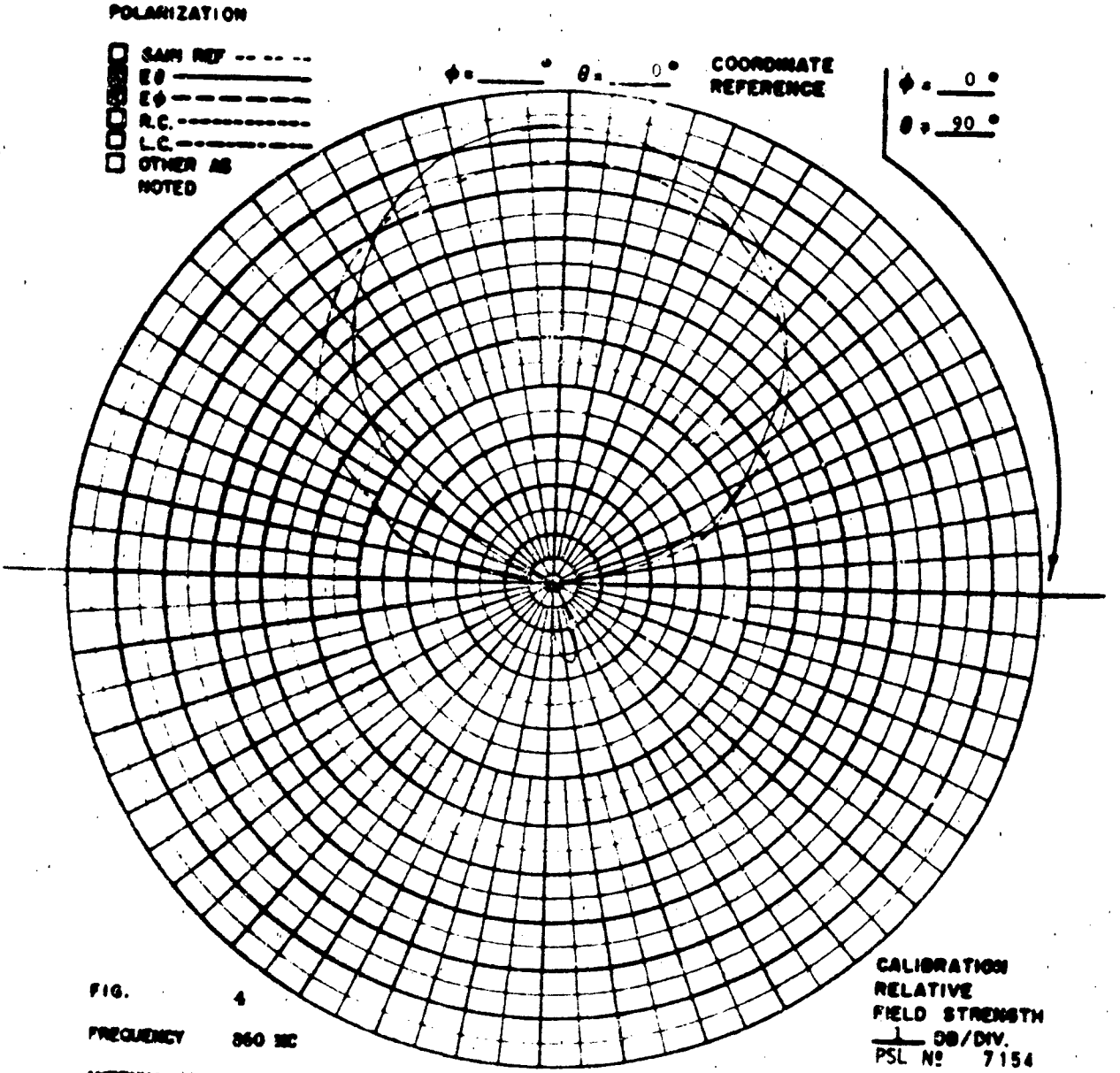

FIG. 4

FREQUENCY 860 MC

ANTENNA CONICAL LOG-SPIRAL.

REMARKS

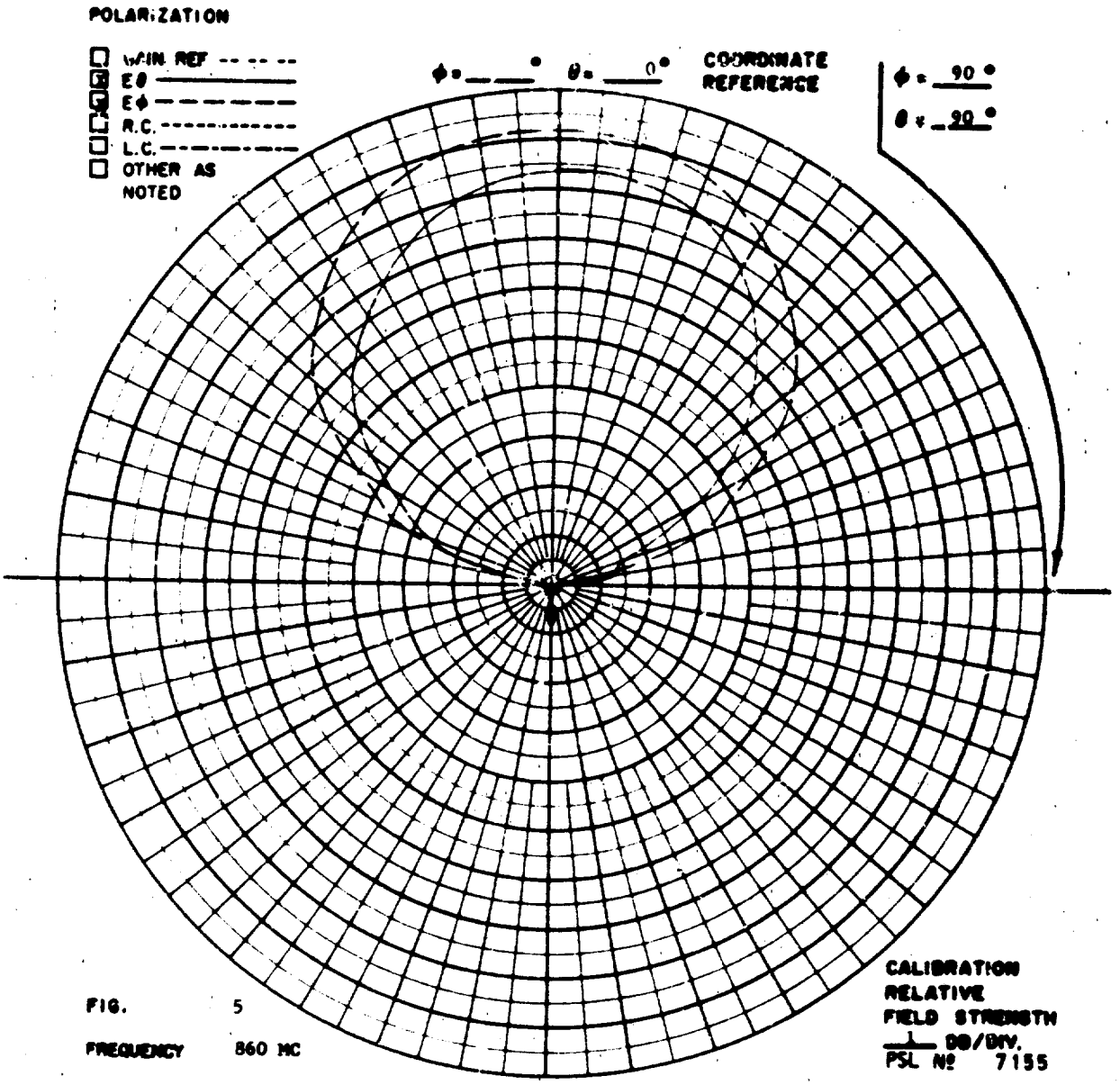

FIG. 5

FREQUENCY 860 MC

ANTENNA CONICAL LOG-SPIRAL.

REMARKS

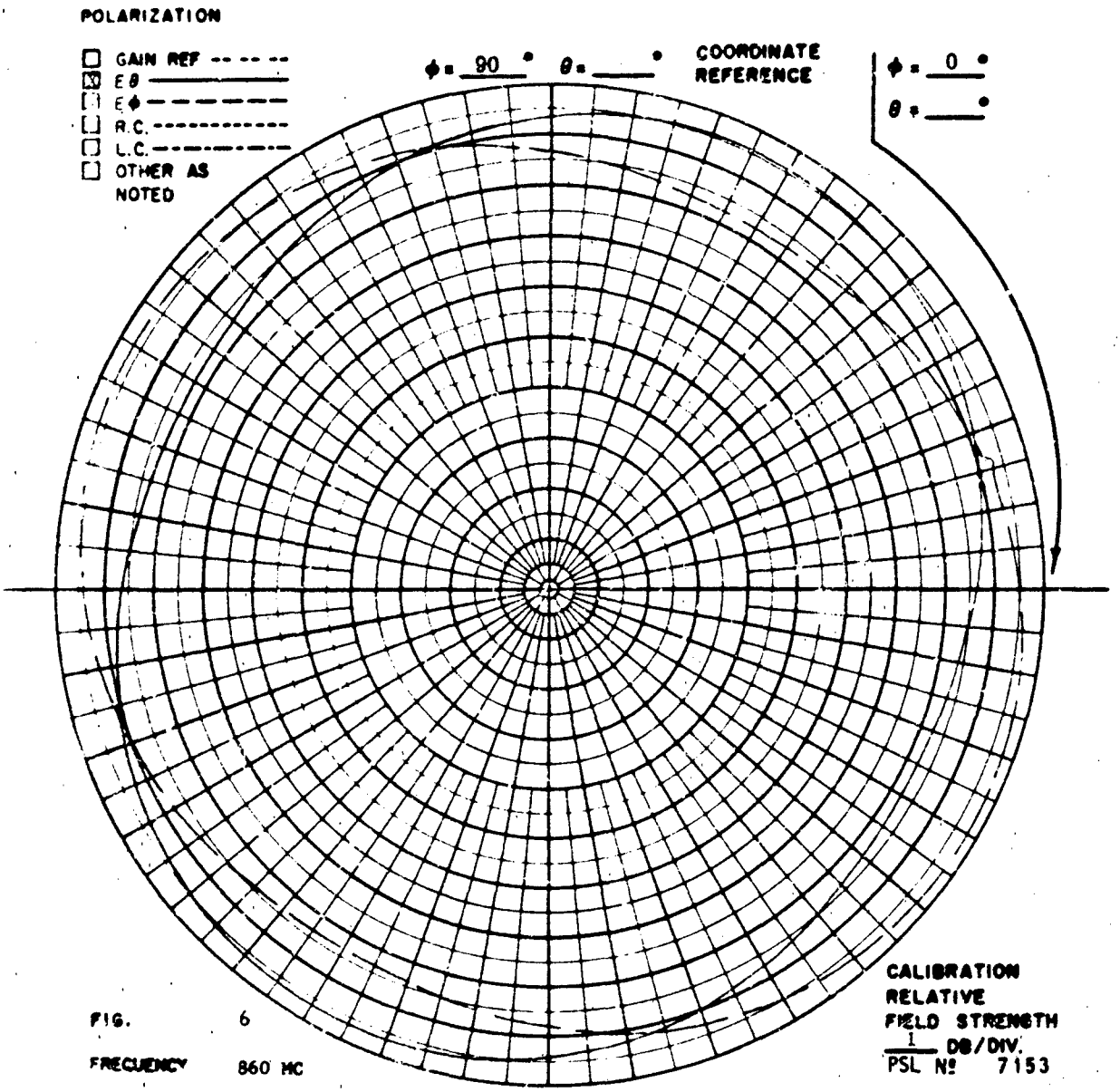

FIG. 6

FREQUENCY 860 MC

ANTENNA CONICAL LOG-SPIRAL.

REMARKS POLARIZATION ELLIPSE.

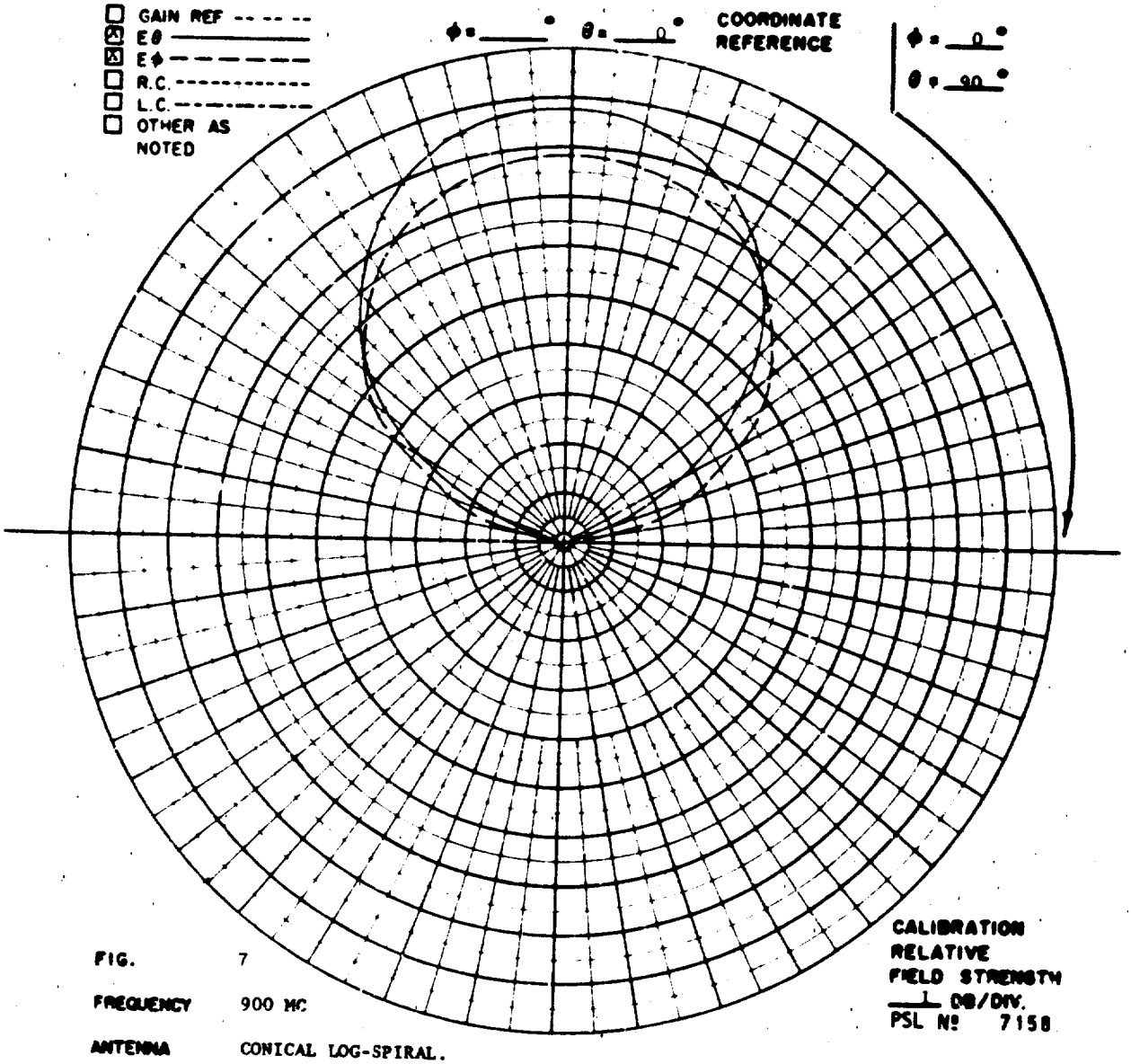

FIG. 7

FREQUENCY 900 MC

ANTENNA CONICAL LOG-SPIRAL.

REMARKS

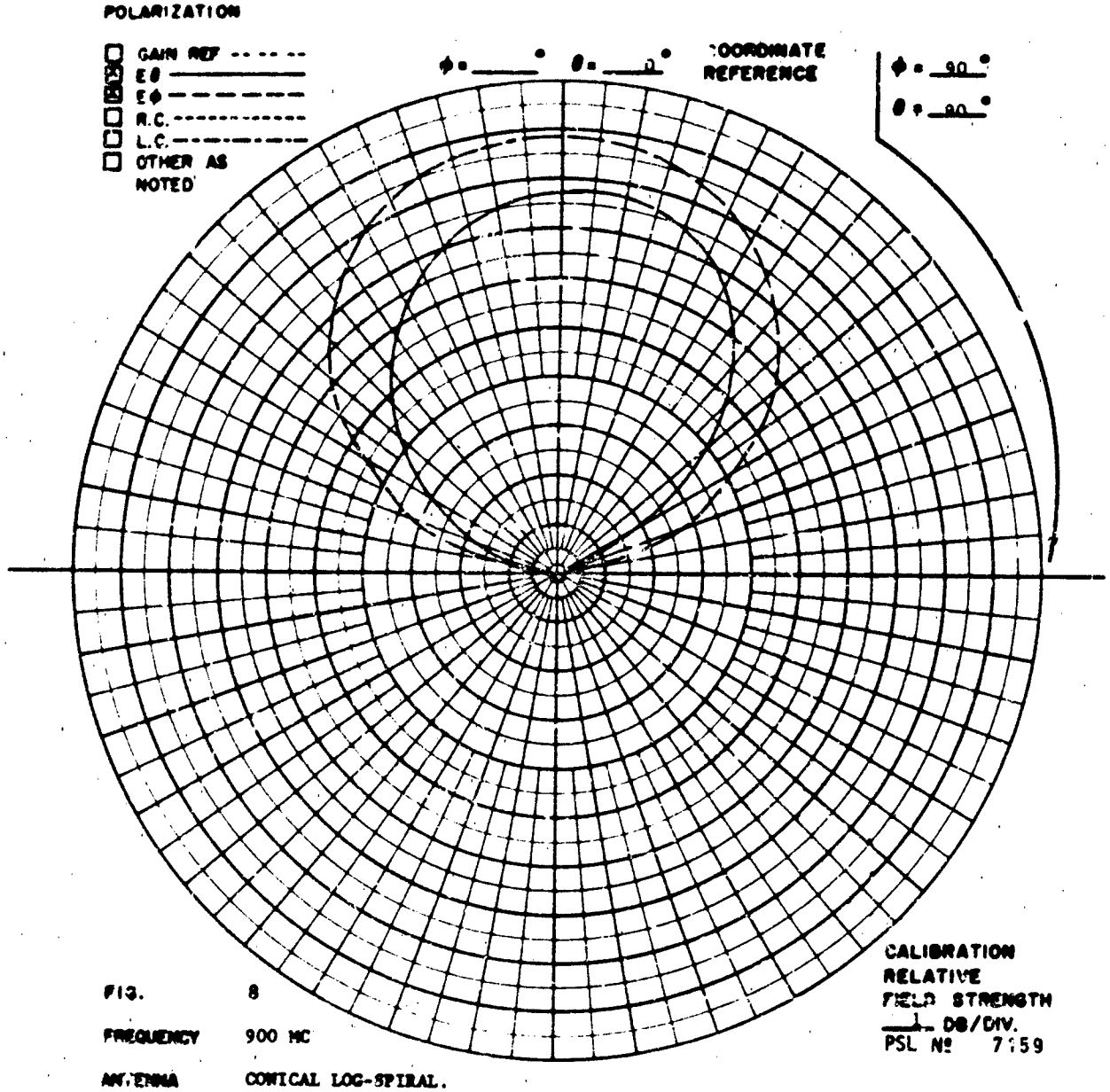

FIG. 8

FREQUENCY 900 MC

ANTENNA CONICAL LOG-SPIRAL.

REMARKS

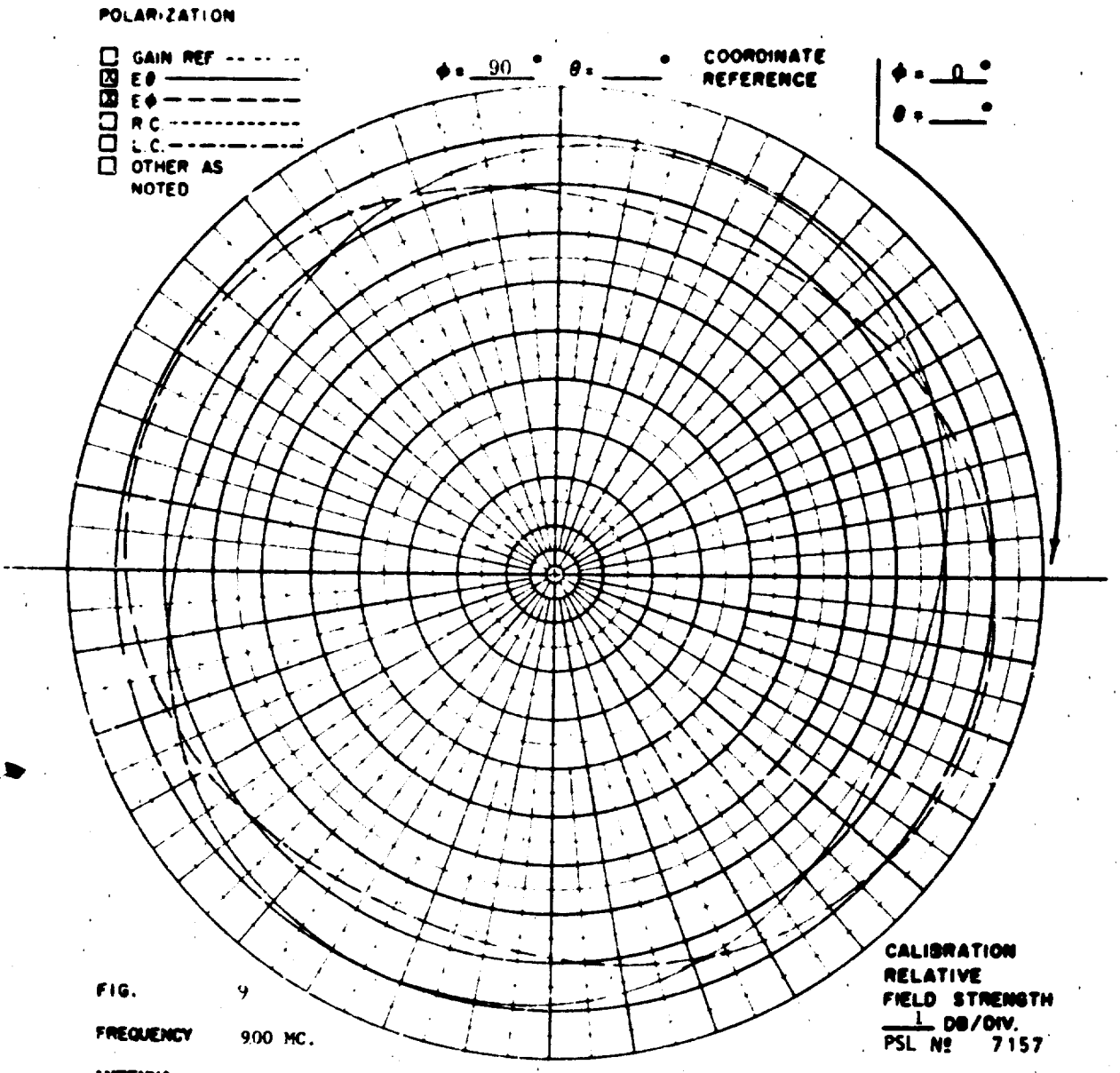

FIG. 9

FREQUENCY 900 MC.

ANTENNA CONICAL LOG-SPIRAL

REMARKS POLARIZATION ELLIPSE.

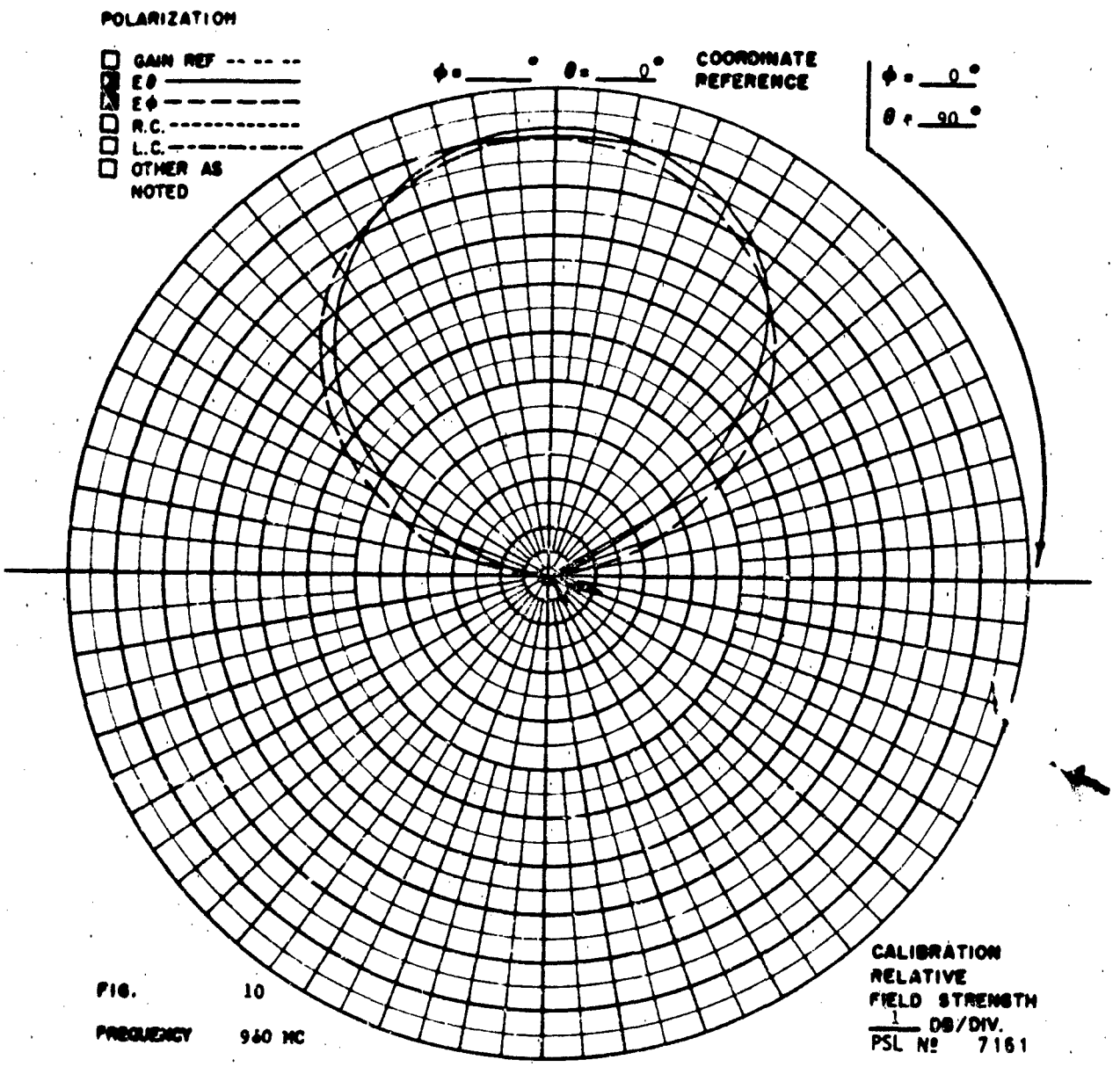

FIG. 10

FREQUENCY 960 MC

ANTENNA CONICAL LOG-SPIRAL.

REMARKS

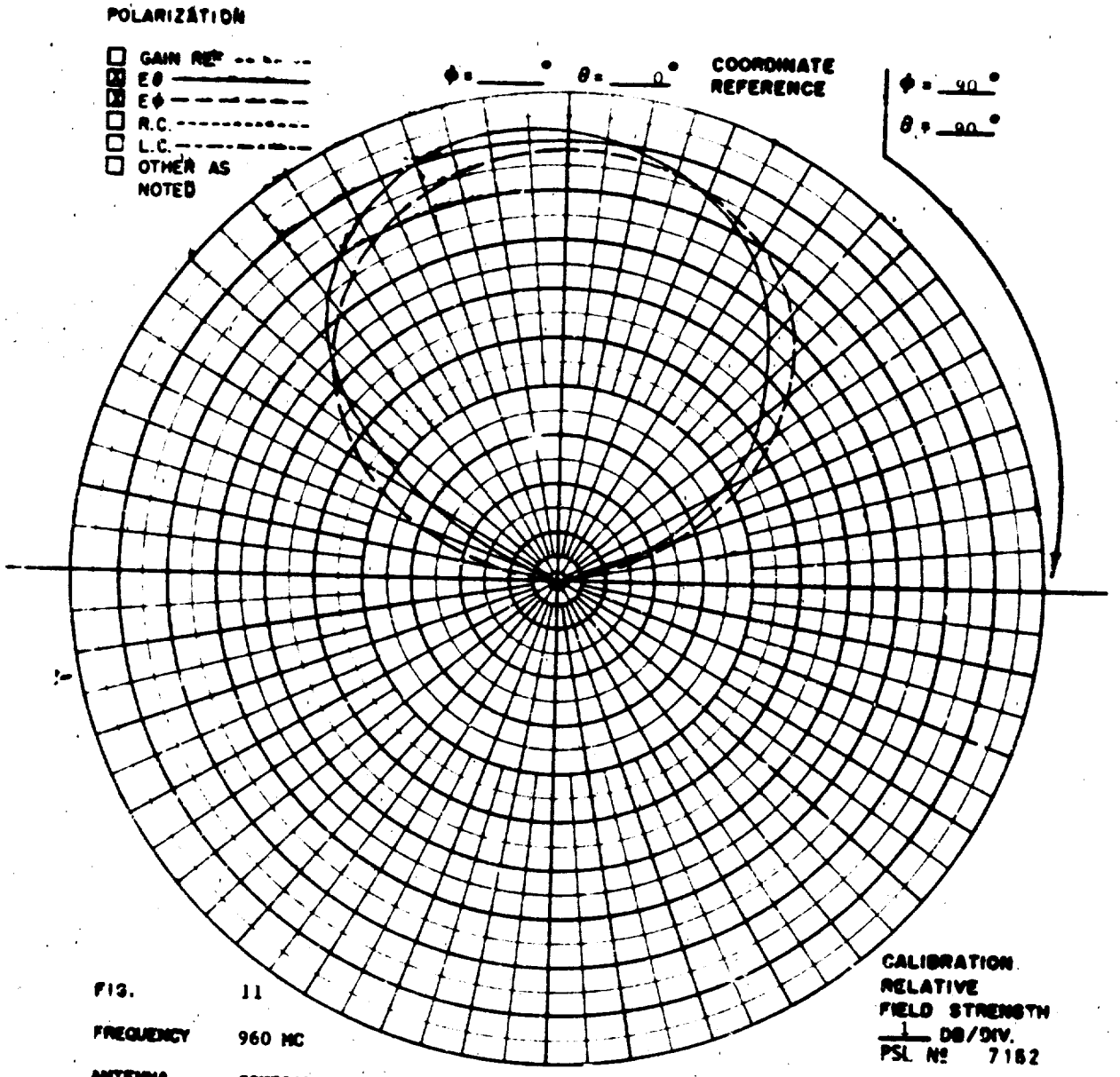

FIG. 11

FREQUENCY 960 MC

ANTENNA CONICAL LOG-SPIRAL.

REMARKS

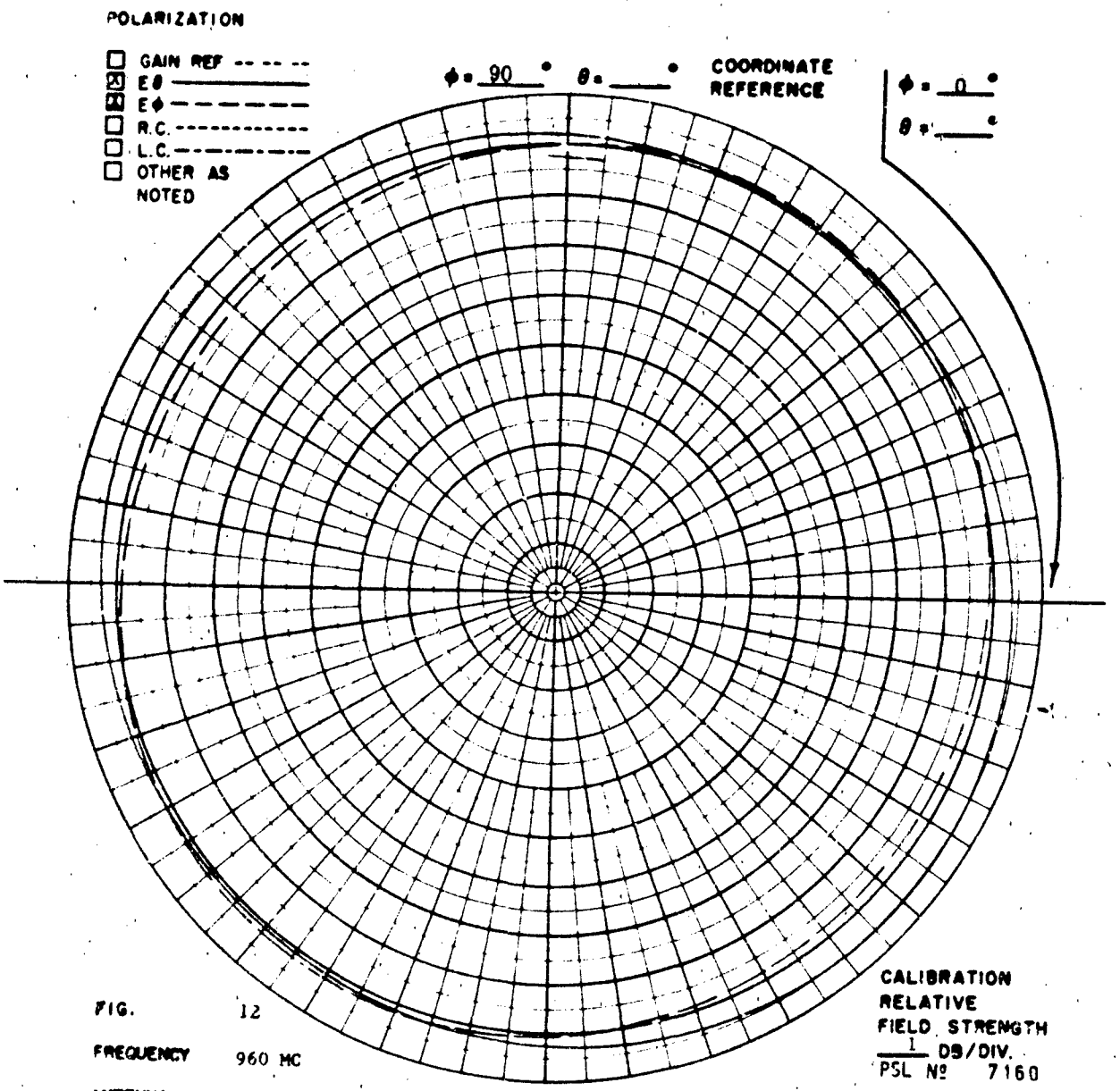

FIG. 12

FREQUENCY 960 MC

ANTENNA CONICAL LOG-SPIRAL

REMARKS POLARIZATION ELLIPSE.

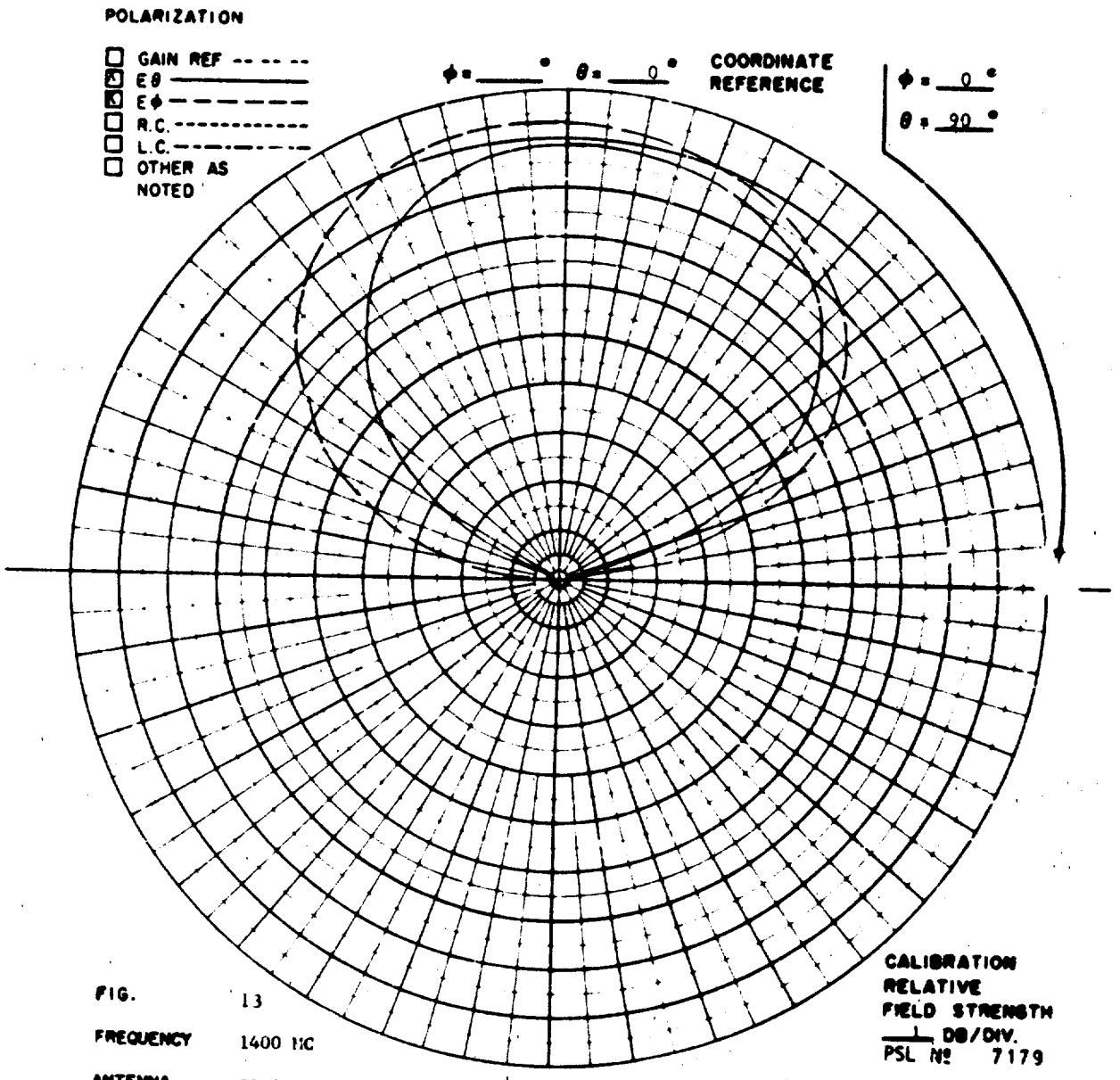

FIG. 13

FREQUENCY 1400 MC

ANTENNA CONICAL LOG-SPIRAL.

REMARKS

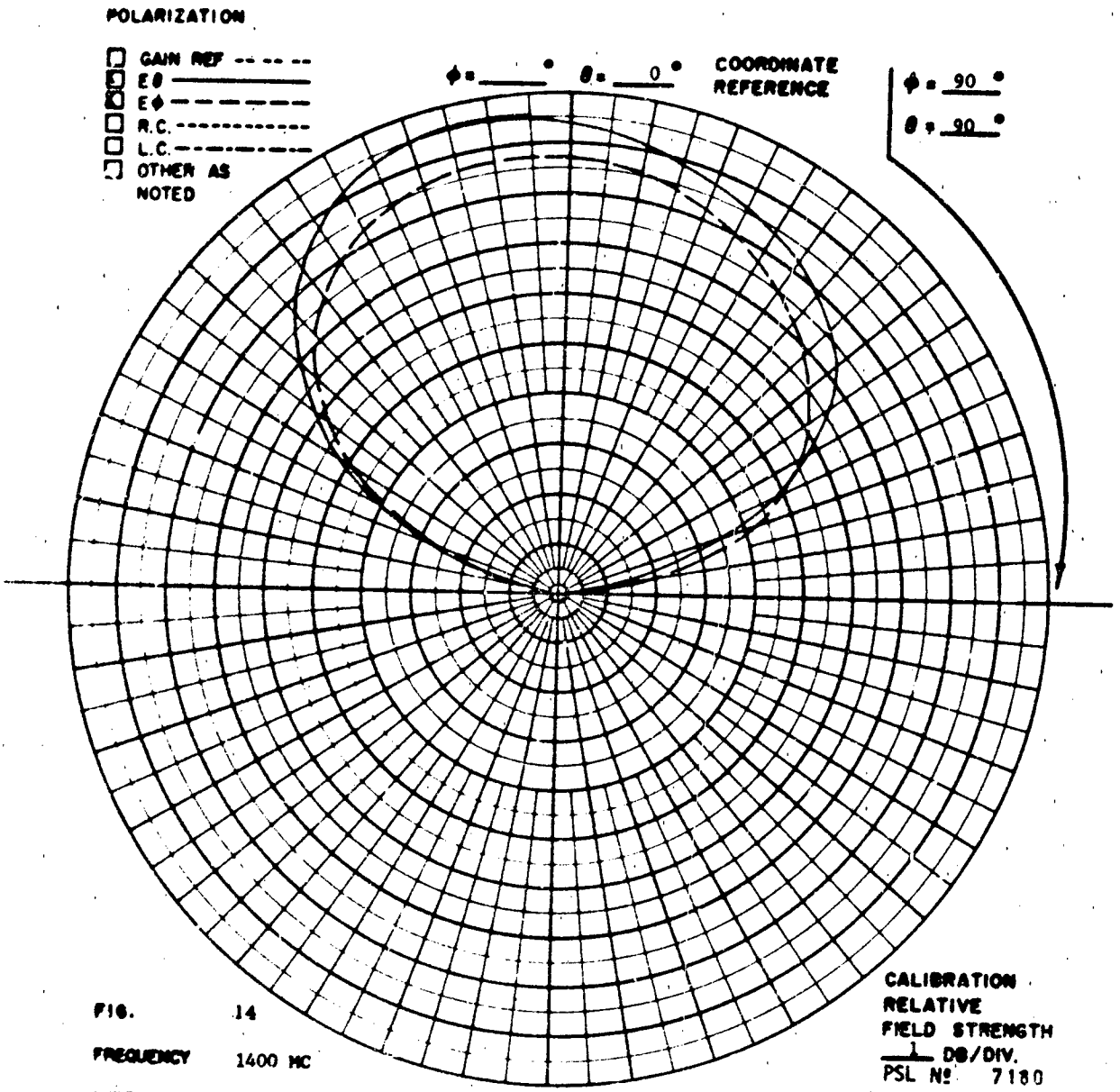

FIG. 14

FREQUENCY 1400 MC

ANTENNA CONICAL LOG-SPIRAL.

REMARKS

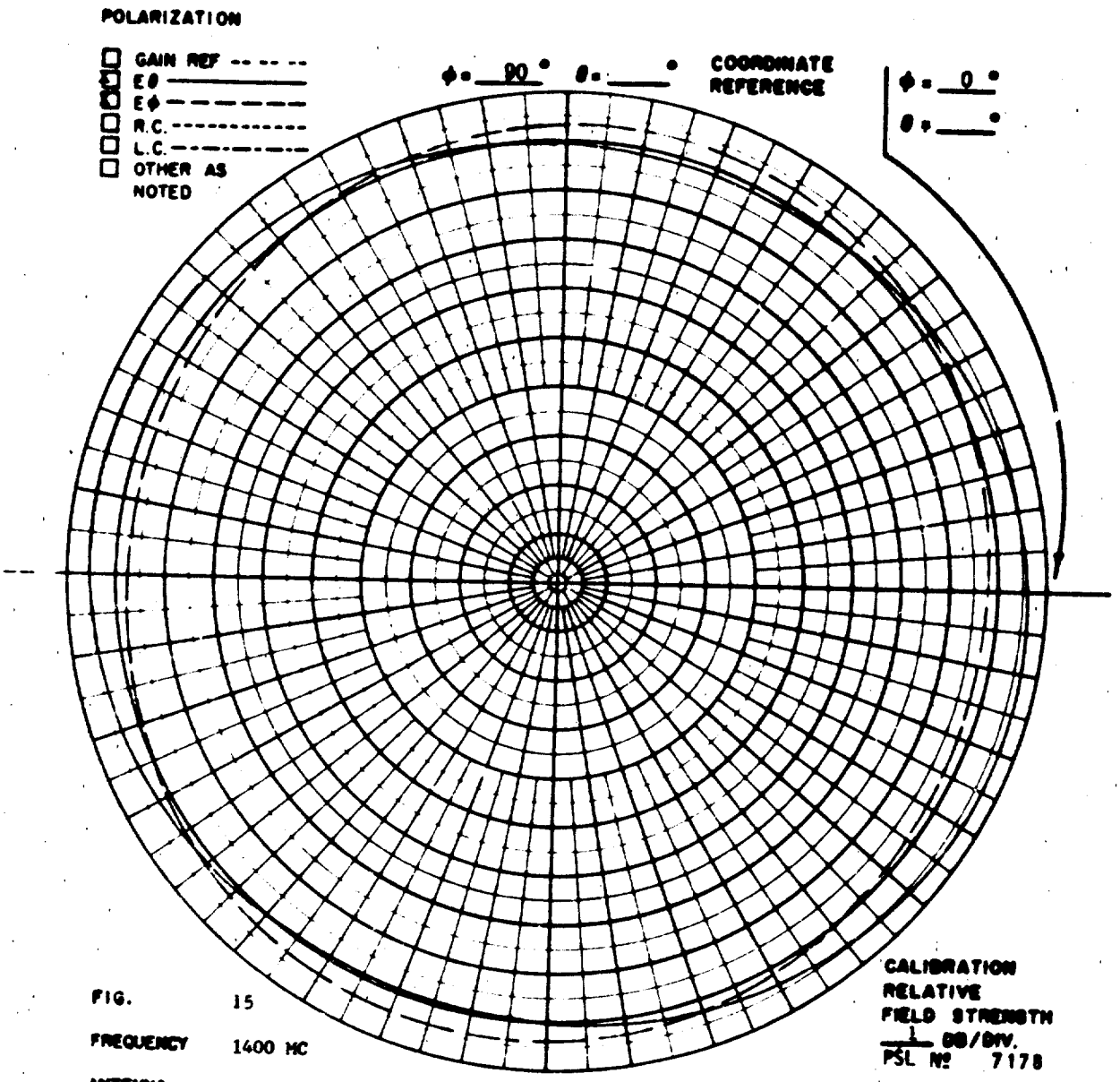

FIG. 15

FREQUENCY 1400 MC

ANTENNA CONICAL LOG-SPIRAL

REMARKS POLARIZATION ELLIPSE.

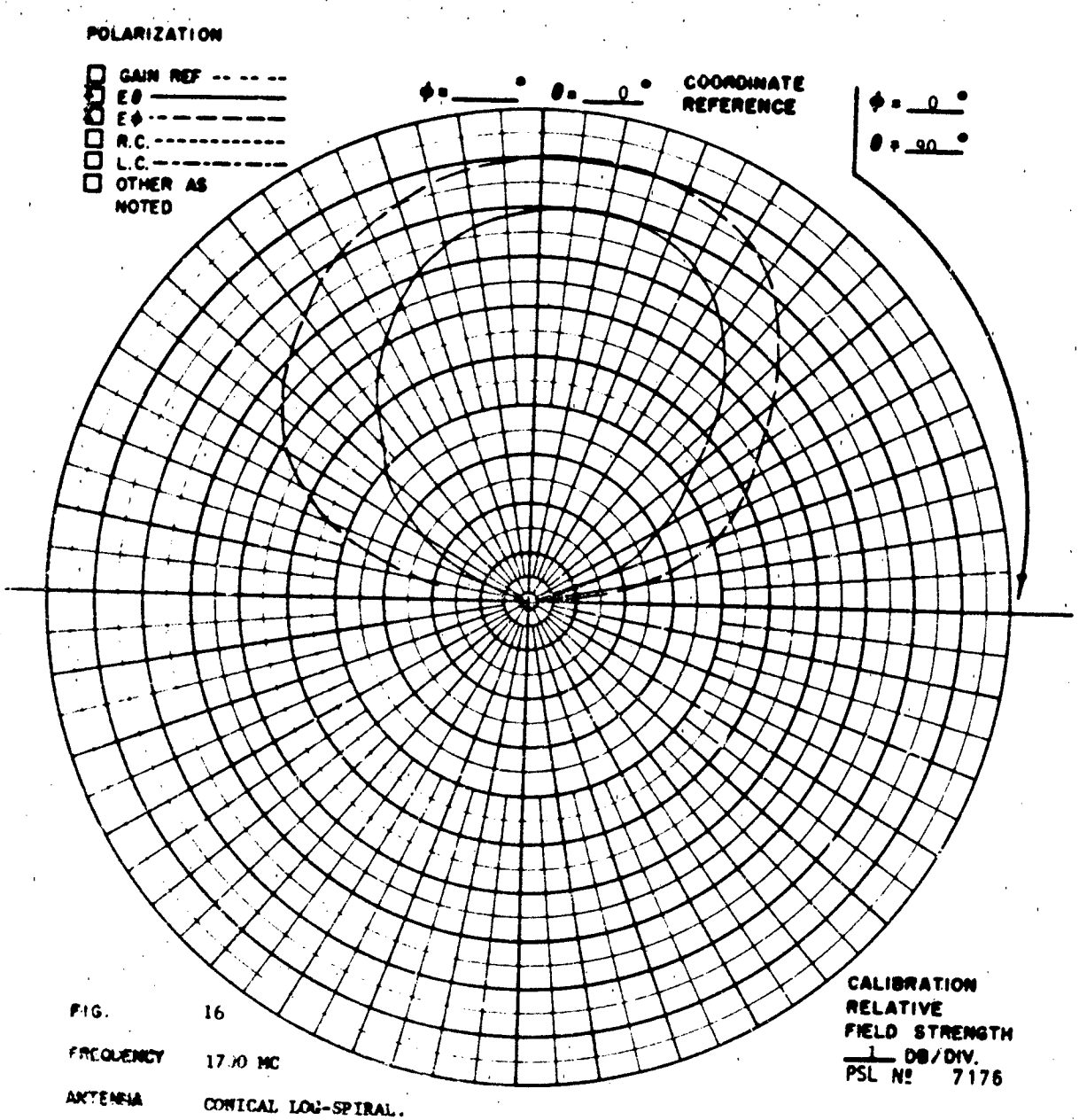
POLARIZATION
GAIN REF
Eθ
Eφ
R.C.
L.C.
OTHER AS NOTED
φ = ____ θ = 0
COORDINATE REFERENCE
φ = 0
θ = 90
CALIBRATION
RELATIVE
FIELD STRENGTH
1 DB/DIV.
PSL Nº 7176
FIG. 16
FREQUENCY 17.0 MC
ANTENNA CONICAL LOG-SPIRAL.
REMARKS

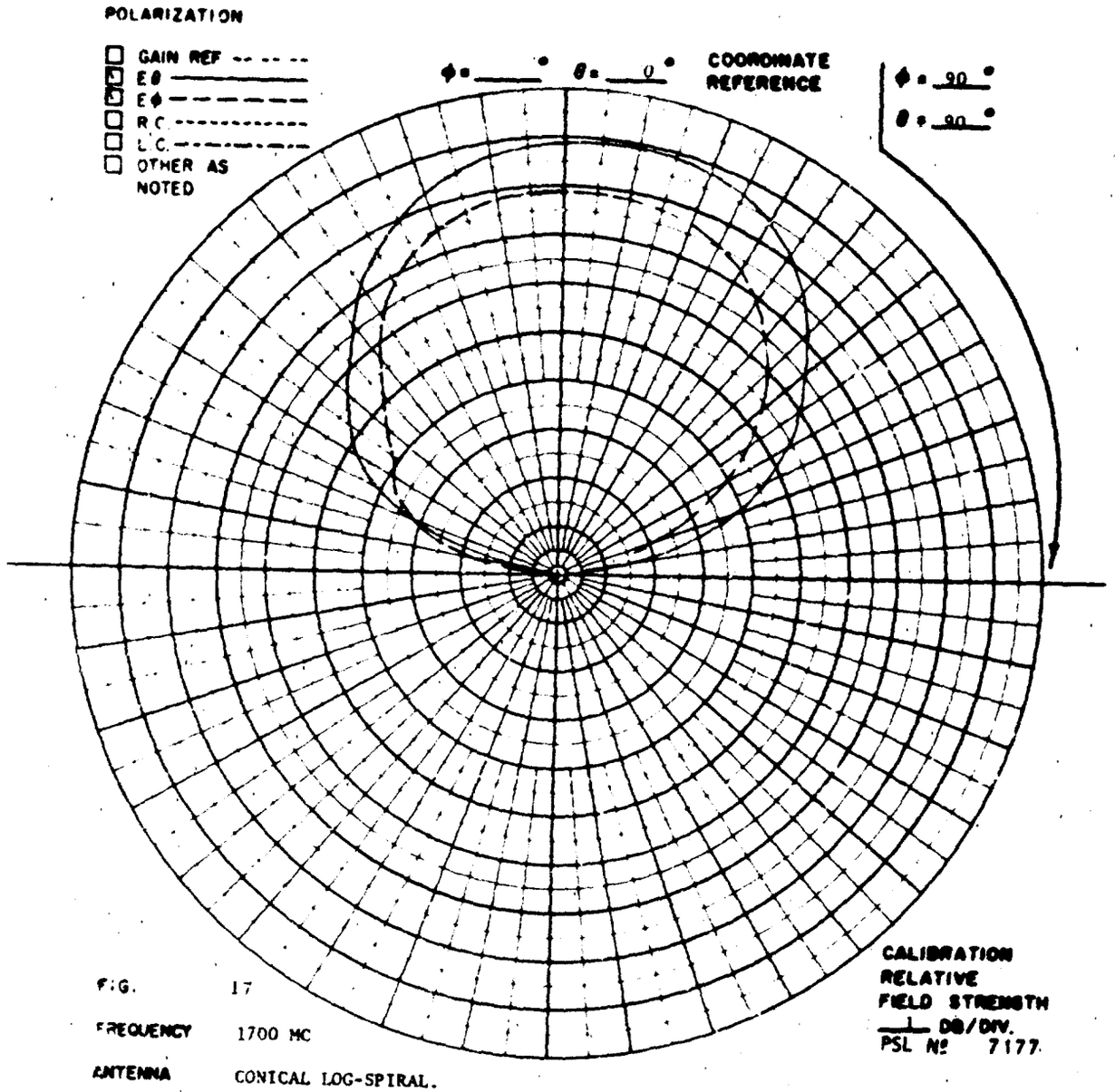

FIG. 17

FREQUENCY 1700 MC

ANTENNA CONICAL LOG-SPIRAL.

REMARKS

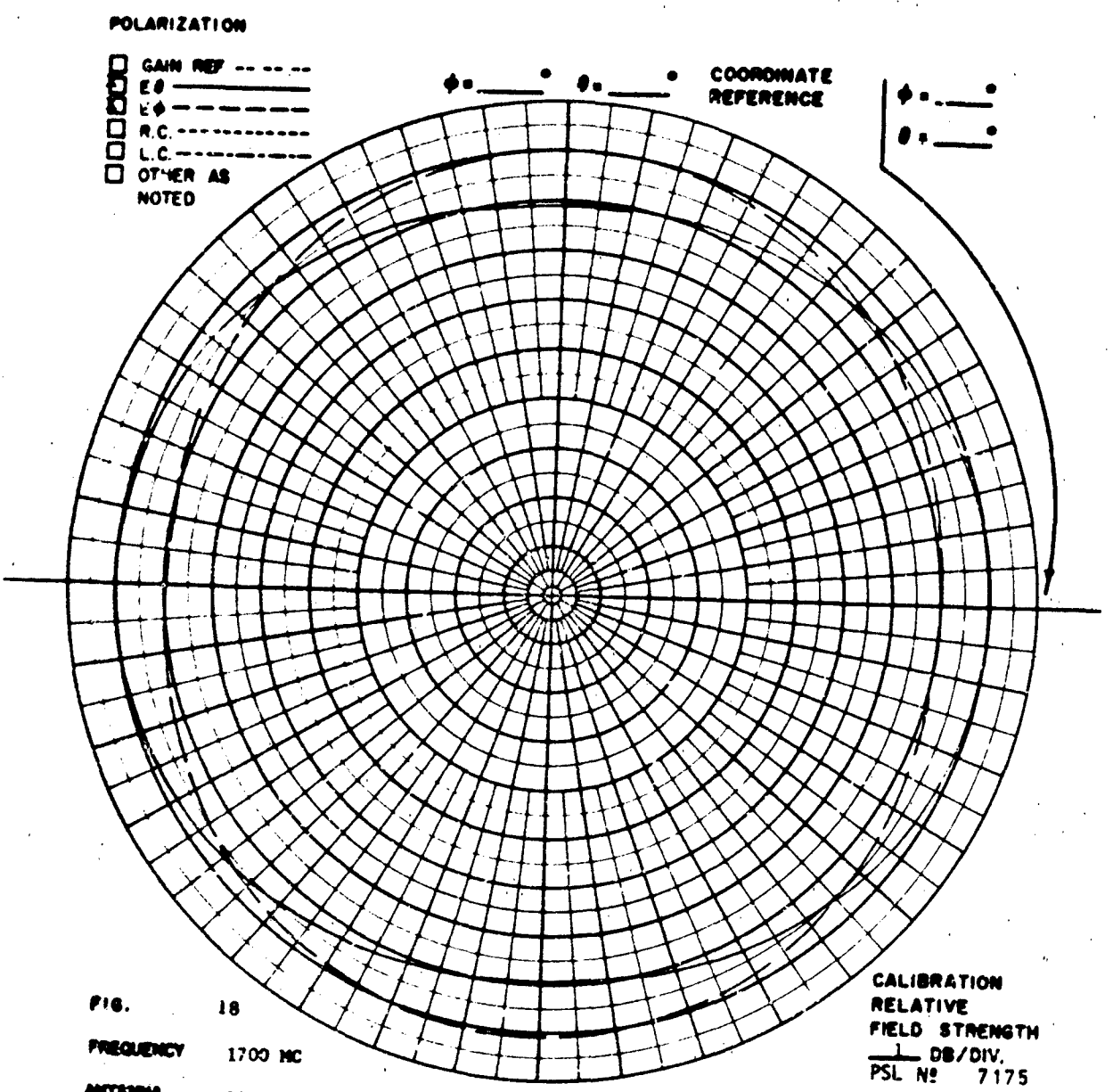

FIG. 18

FREQUENCY 1700 MC

ANT. CONICAL LOG-SPIRAL.

REMARKS POLARIZATION ELLIPSE.

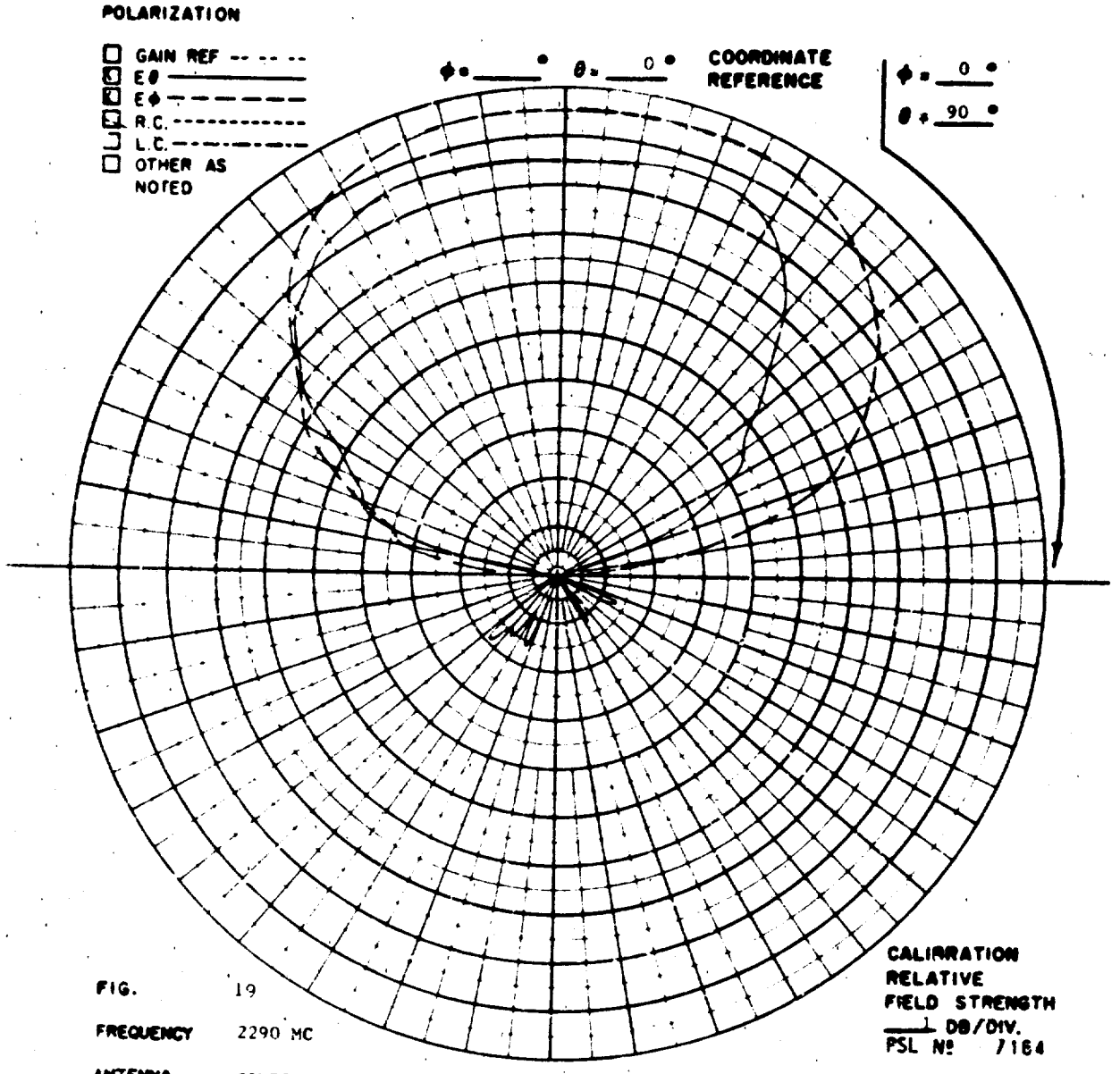

FIG. 19

FREQUENCY 2290 MC

ANTENNA CONICAL LOG-SPIRAL.

REMARKS

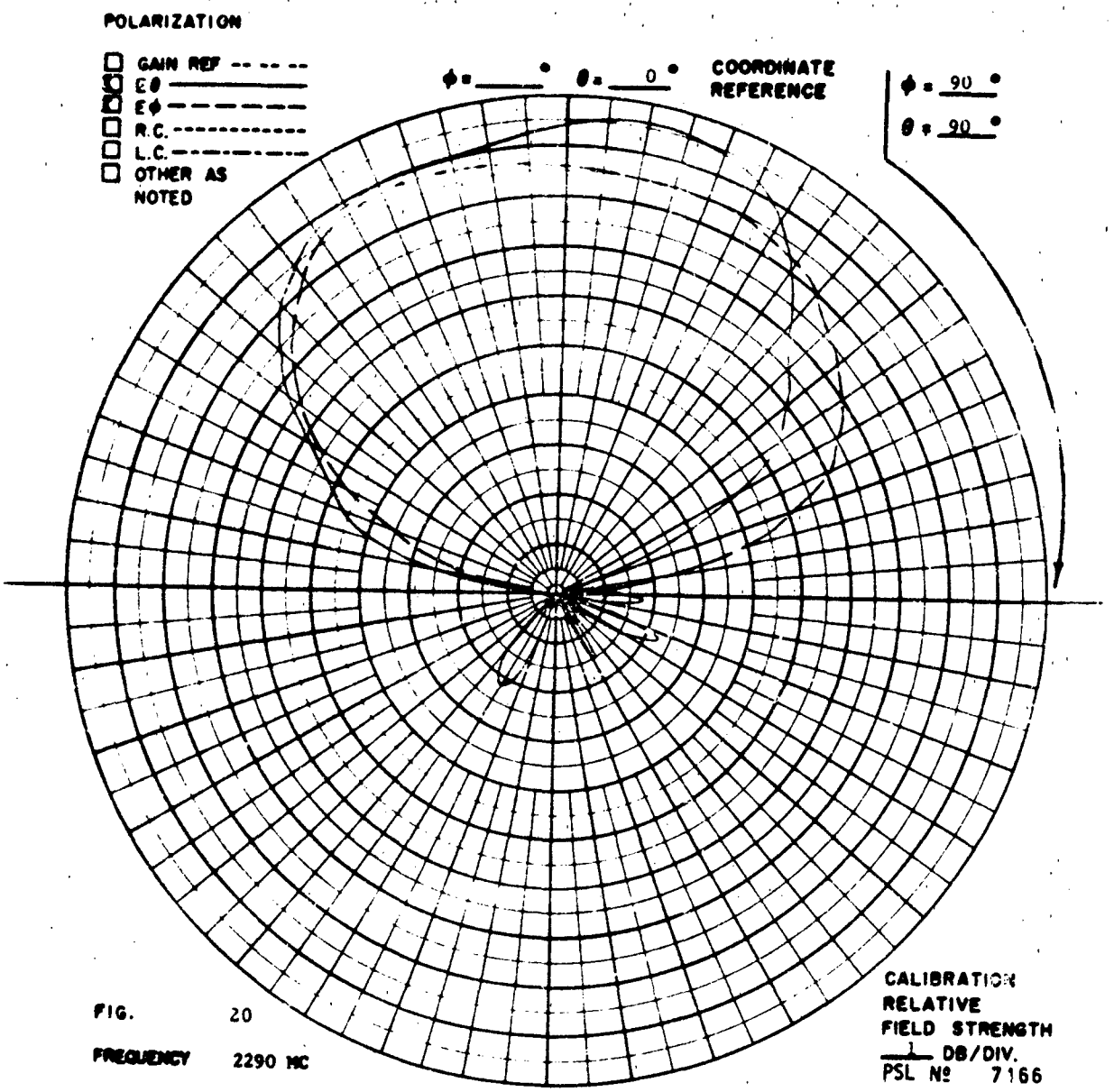

FIG. 20

FREQUENCY 2290 MC

ANTENNA CONICAL LOG-SPIRAL.

REMARKS

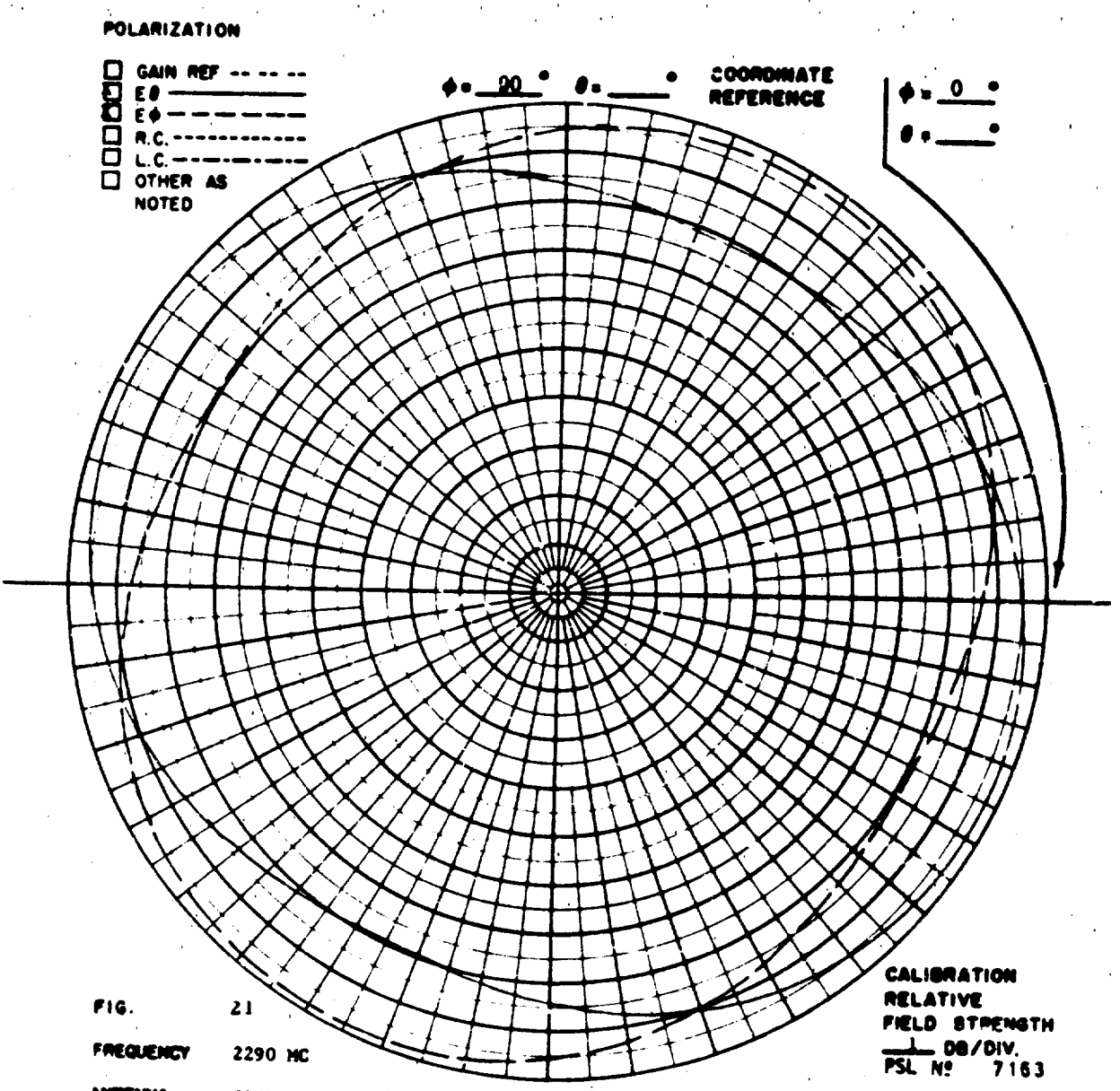

FIG. 21

FREQUENCY 2290 MC

ANTENNA CONICAL LOG-SPIRAL.

REMARKS POLARIZATION ELLIPSE.

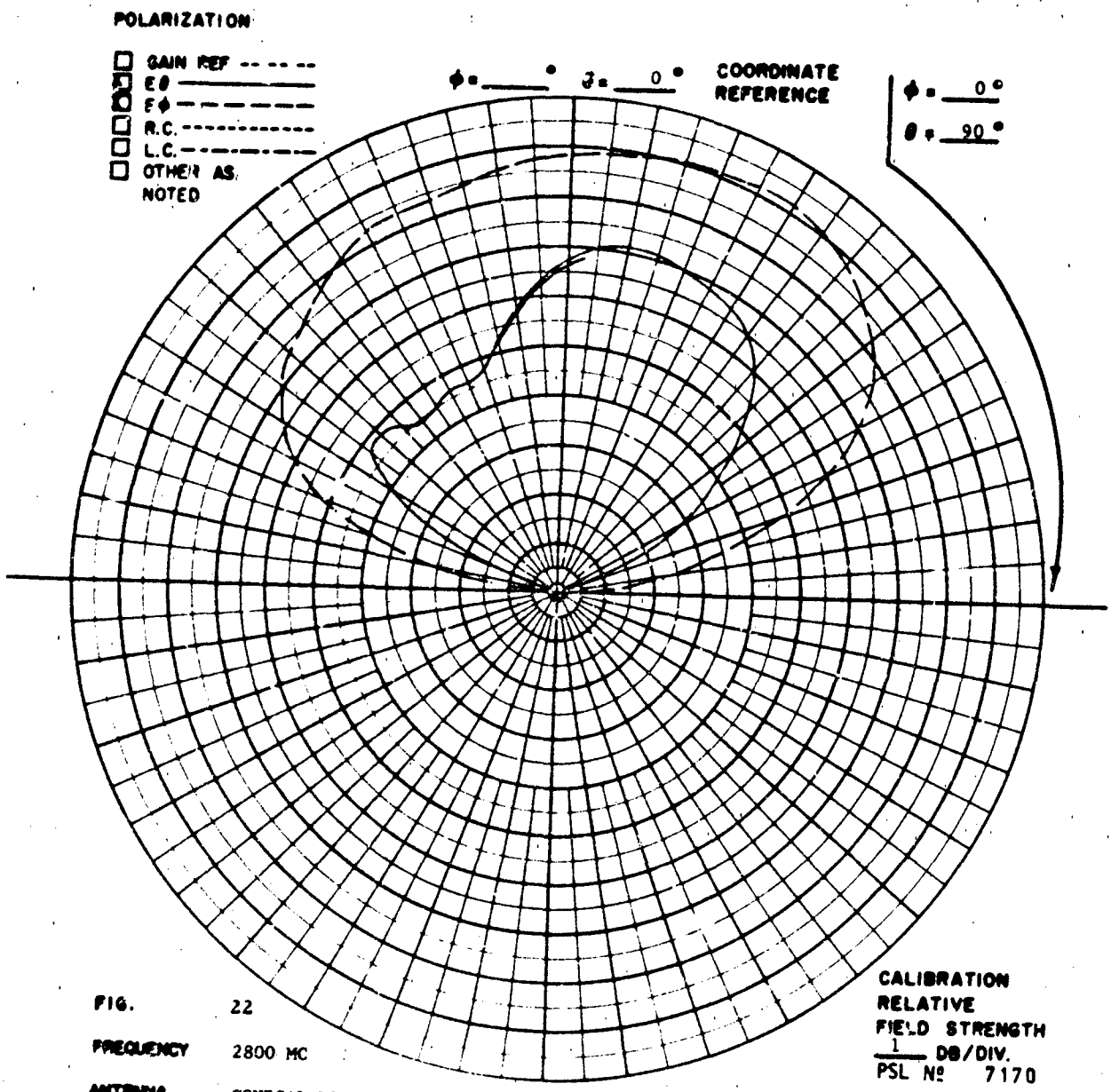

FIG. 22

FREQUENCY 2800 MC

ANTENNA CONICAL LOG-SPIRAL.

REMARKS

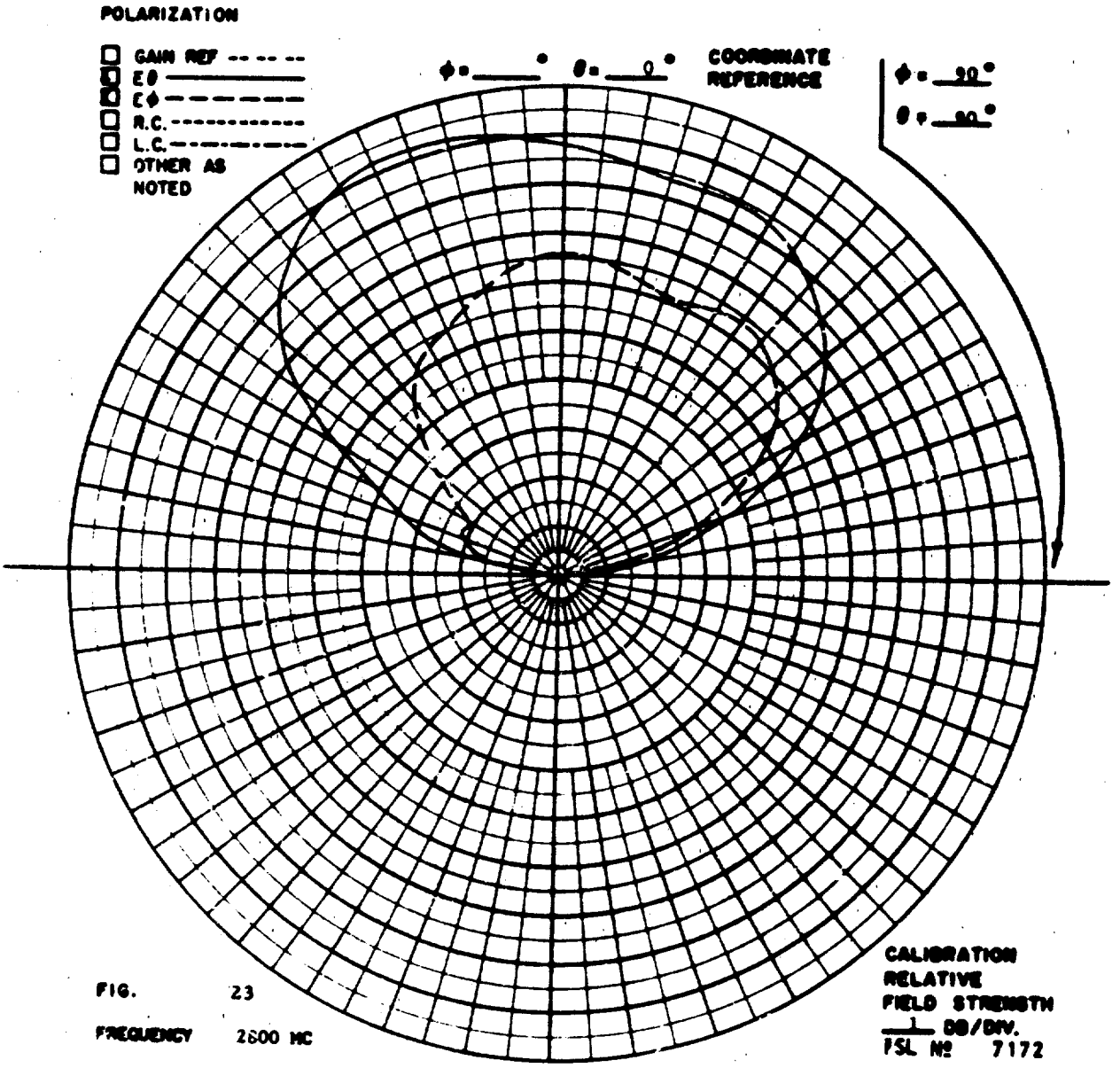

FIG. 23

FREQUENCY 2600 MC

ANTENNA CONICAL LOG-SPIRAL.

REMARKS

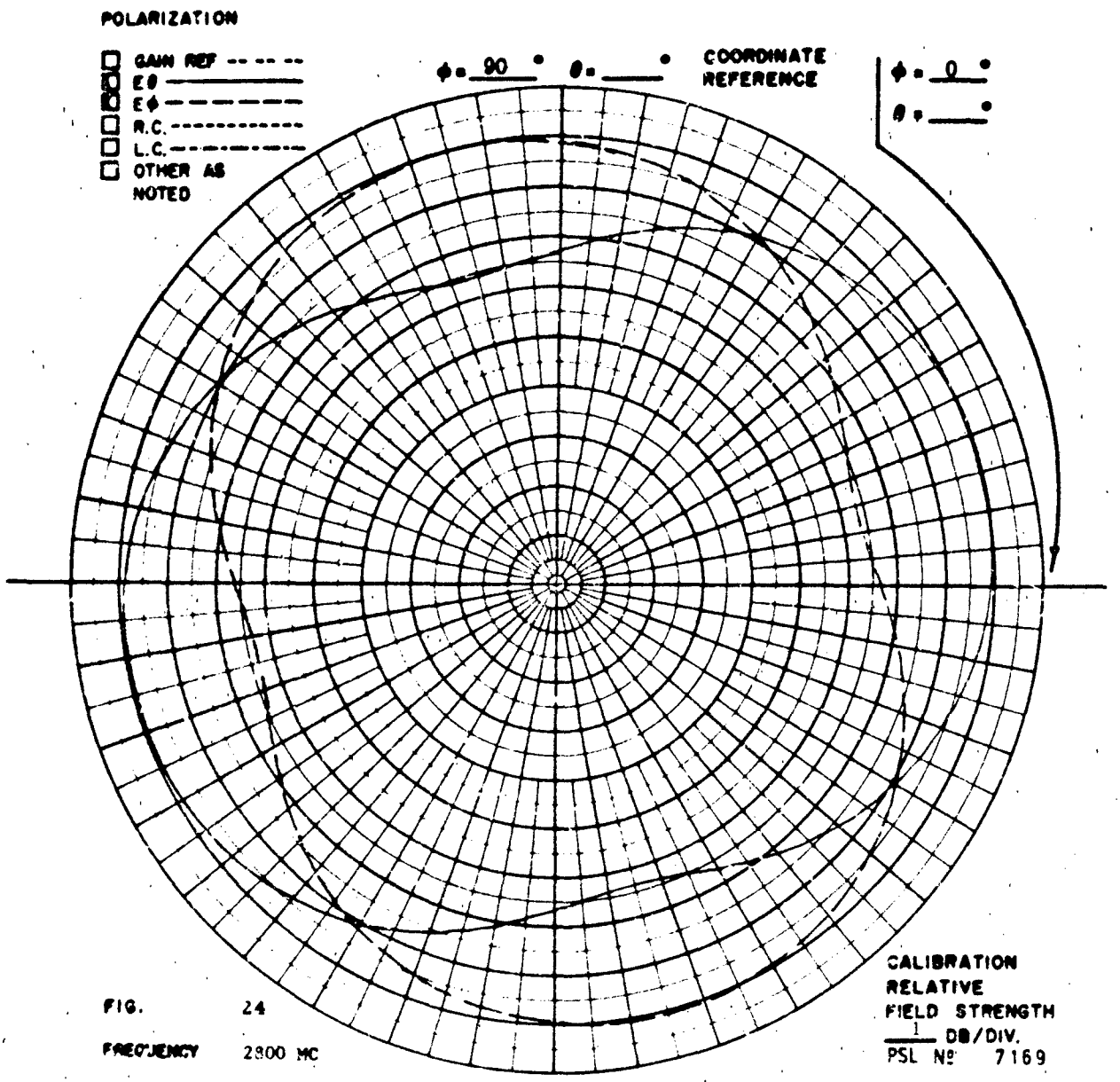

FIG. 24

FREQUENCY 2300 MC

ANTENNA CONICAL LOG-SPIRAL.

REMARKS POLARIZATION ELLIPSE.

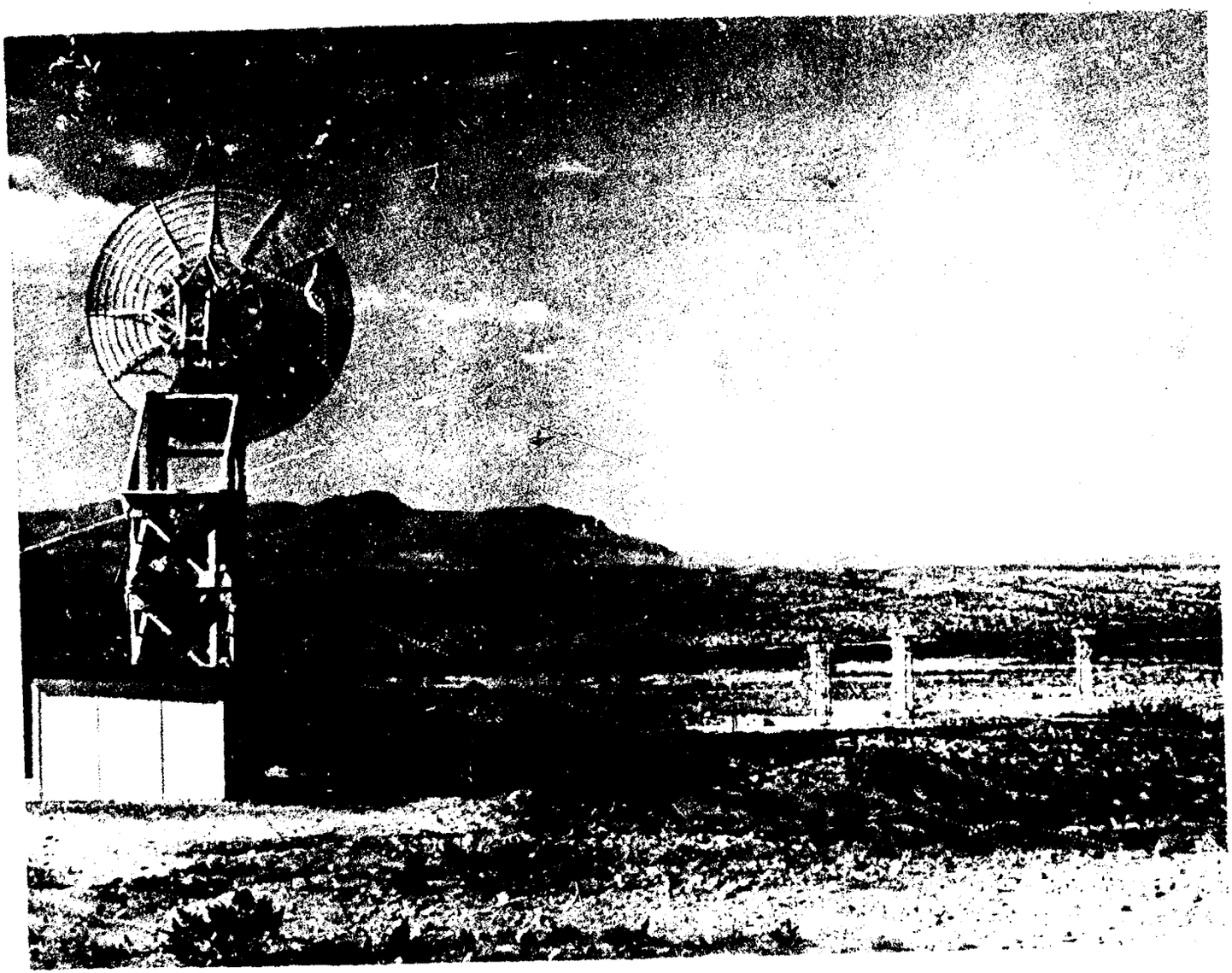

FIG. 25 - VIEW OF 3000 FOOT RANGE

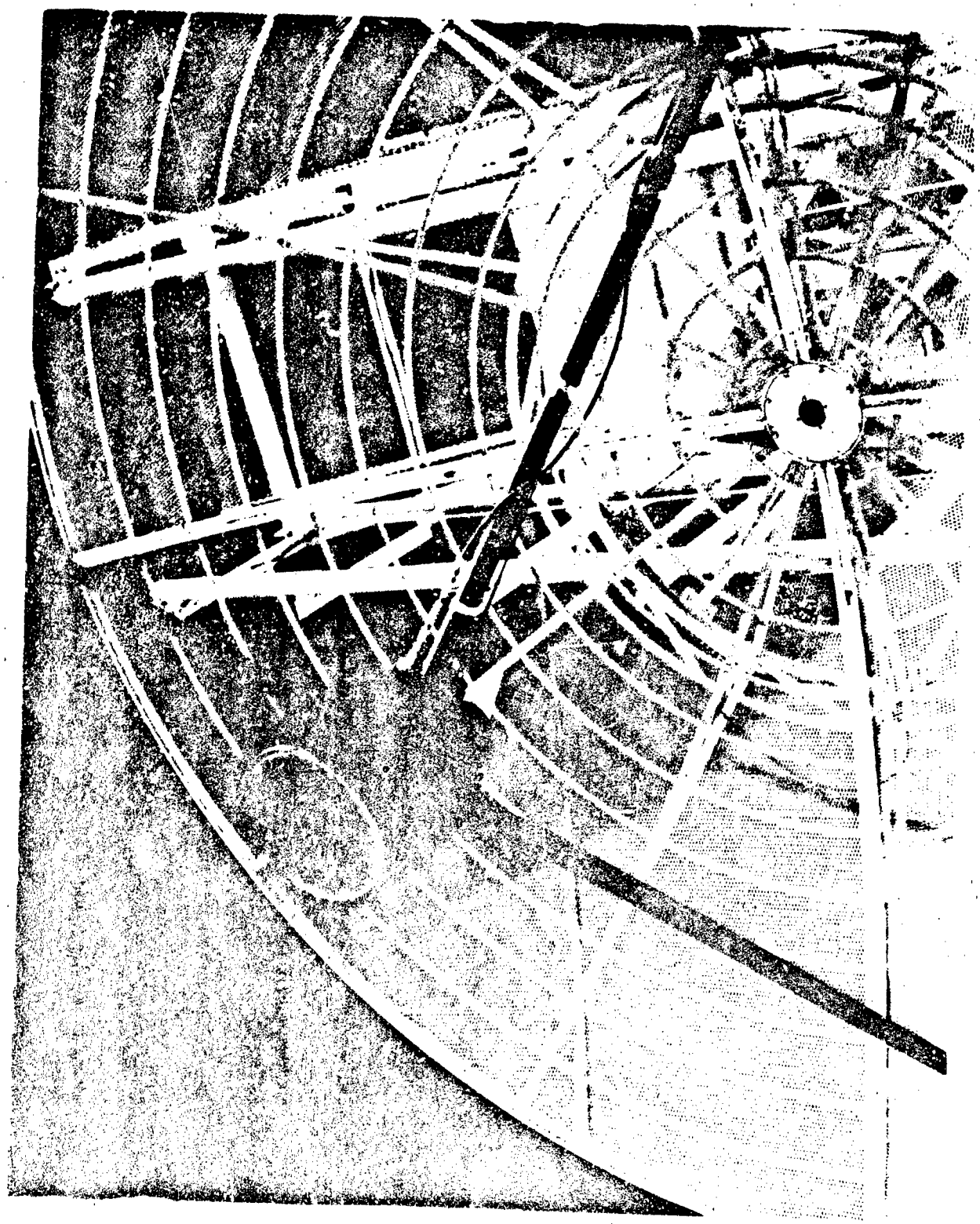

FIG. 26 - CONICAL SPIRAL MOUNTED IN REFLECTOR

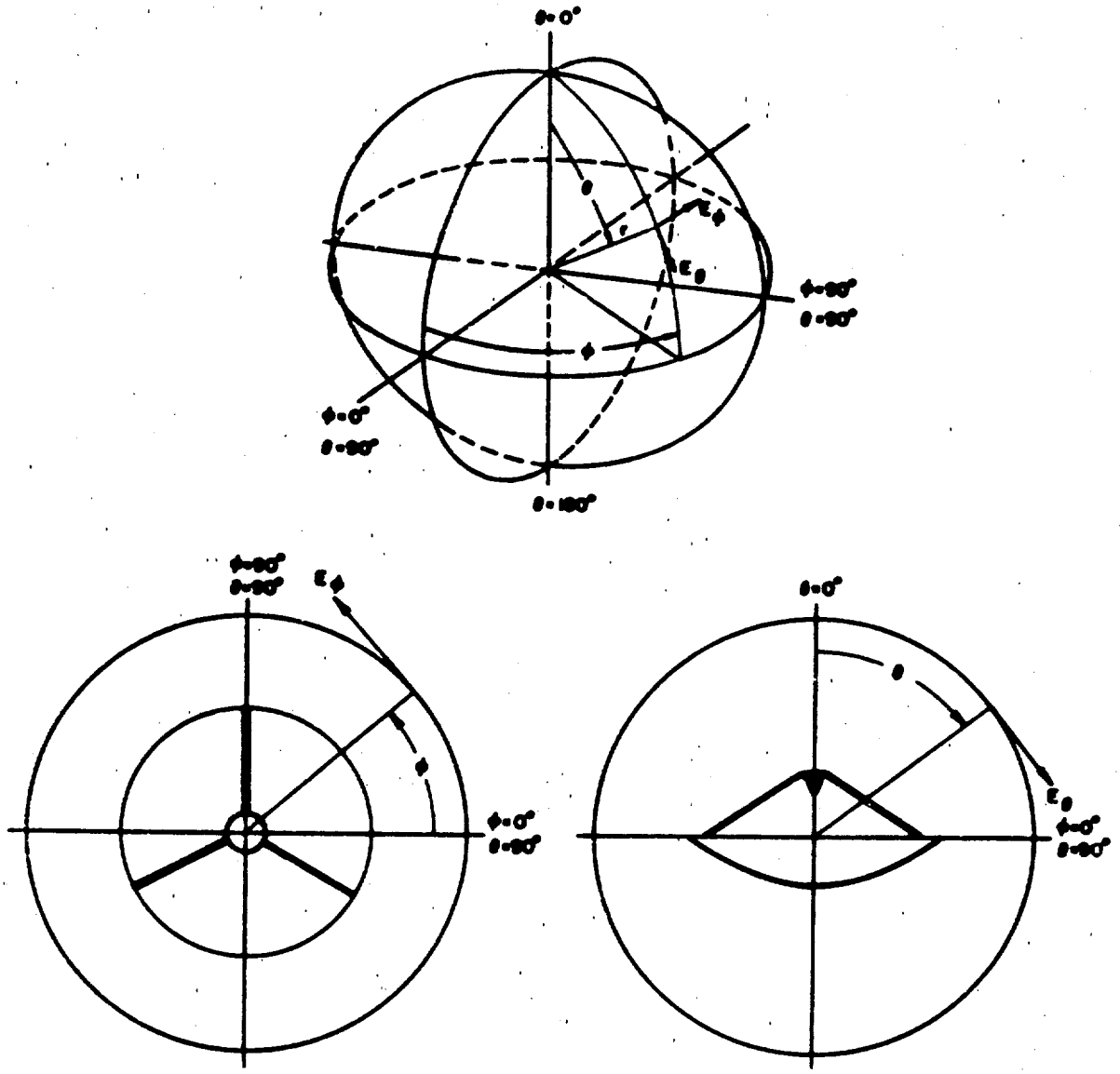

FIG. 27 - COORDINATE SYSTEM FOR 19 FOOT REFLECTOR

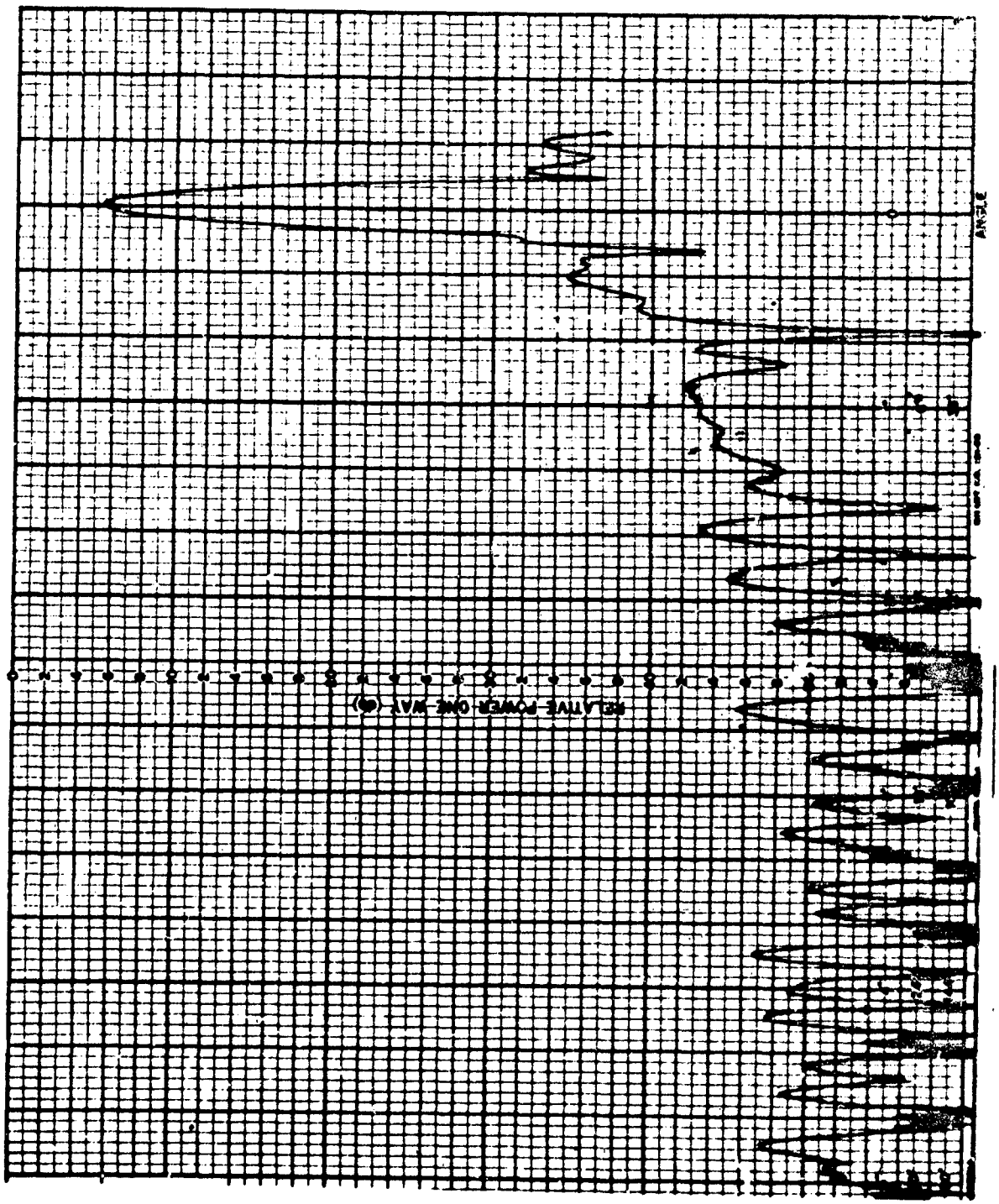

FIG. 28 - 960 MC, Eθ, FEED NOT TILTED

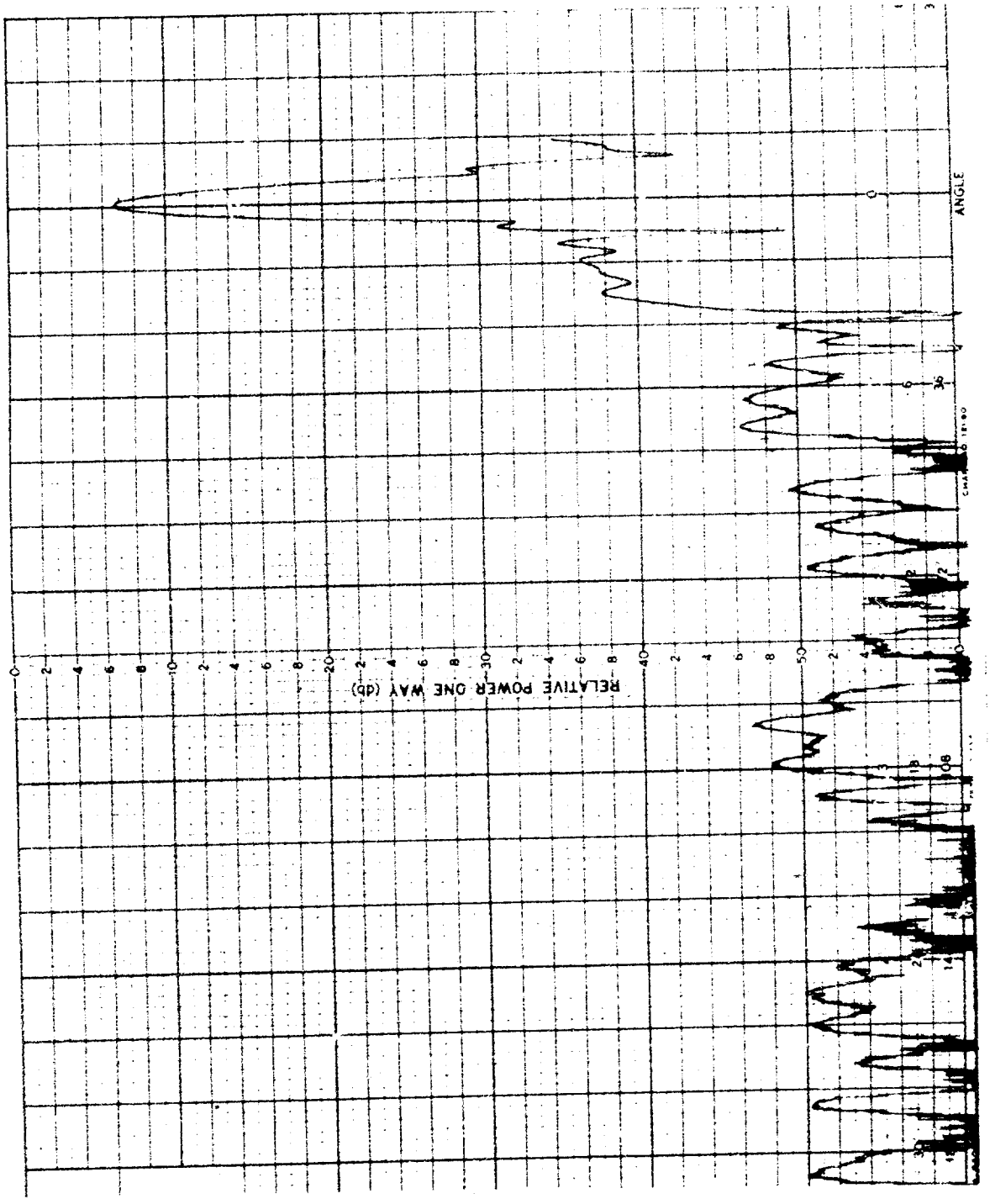

FIG. 29 - 960 MC, Eφ, FEED NOT TILTED

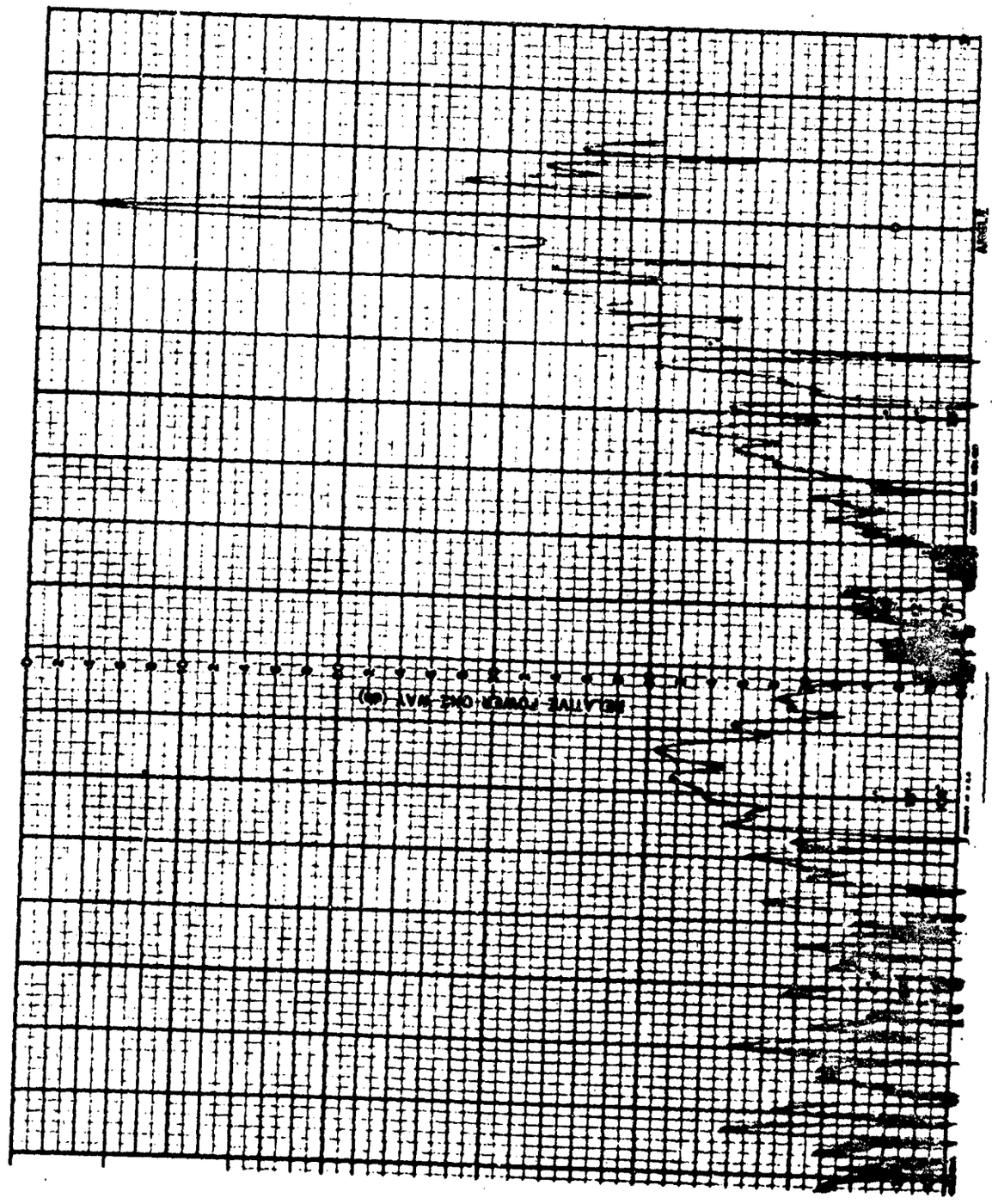

FIG. 30 - 1700 MC, $E\theta$, FEED NOT TILTED

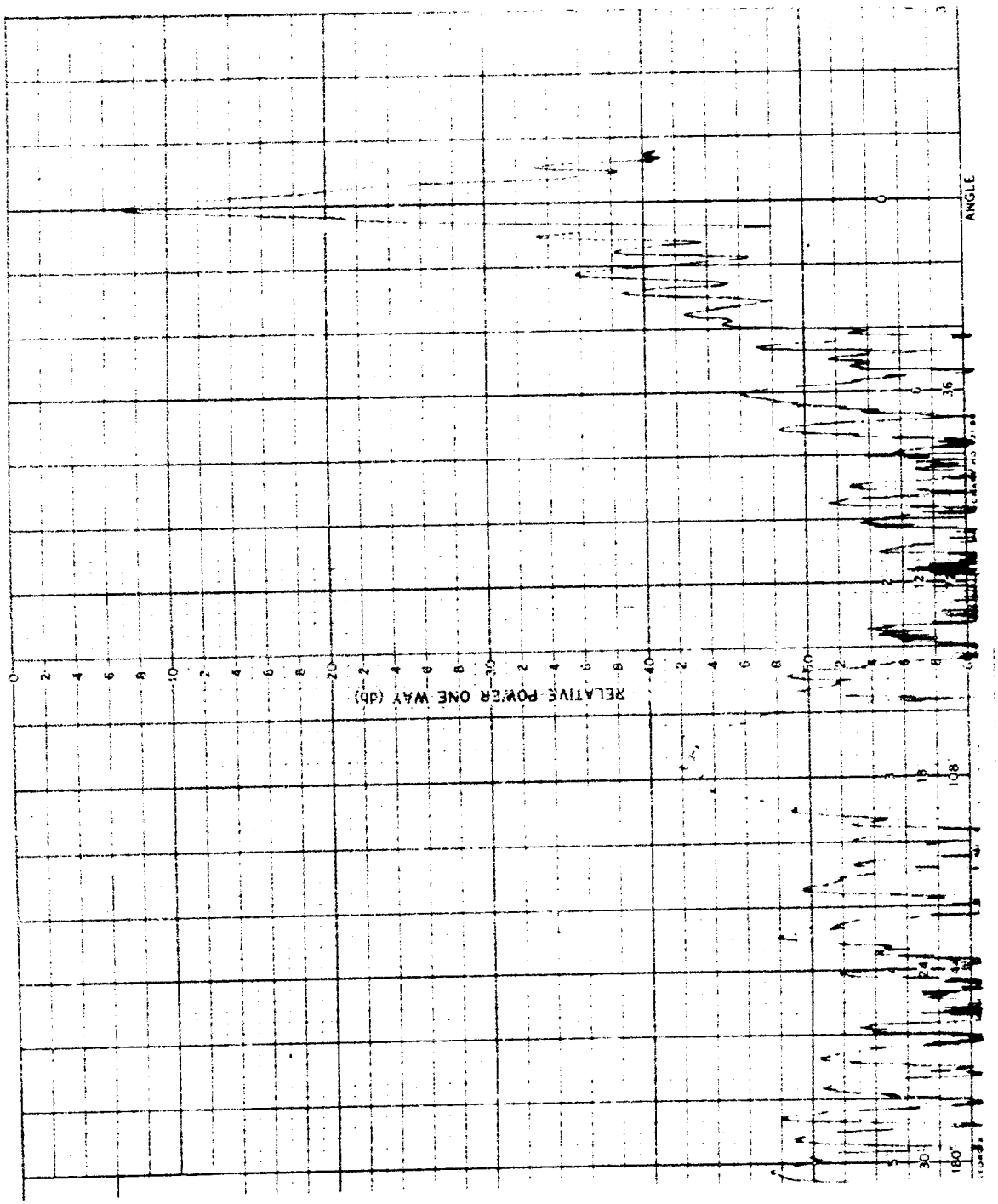

FIG. 31 - 1700 MC, $E\phi$, FEED NOT TILTED

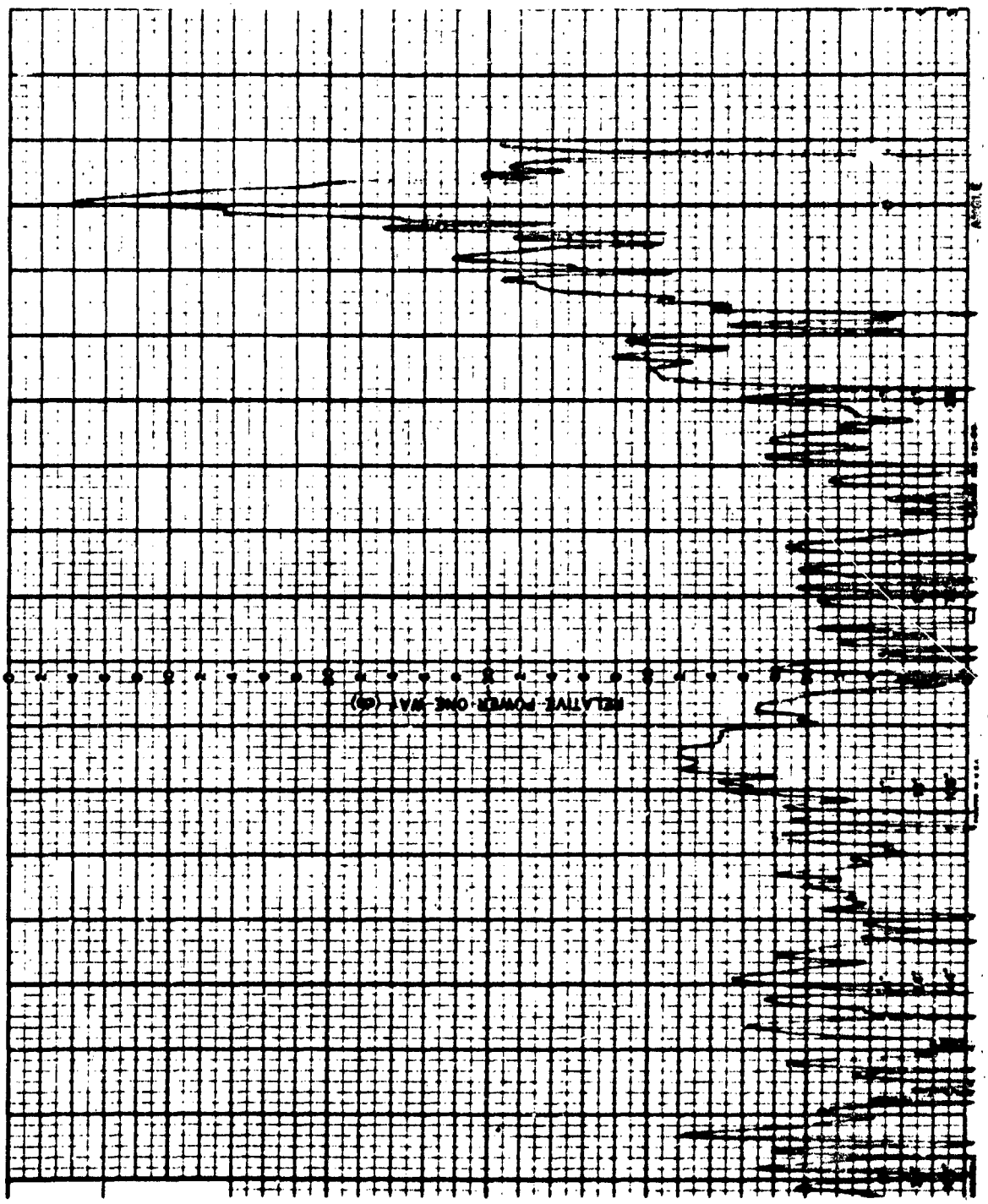

FIG. 32 - 2290 MC, Eθ, FEED NOT TILTED

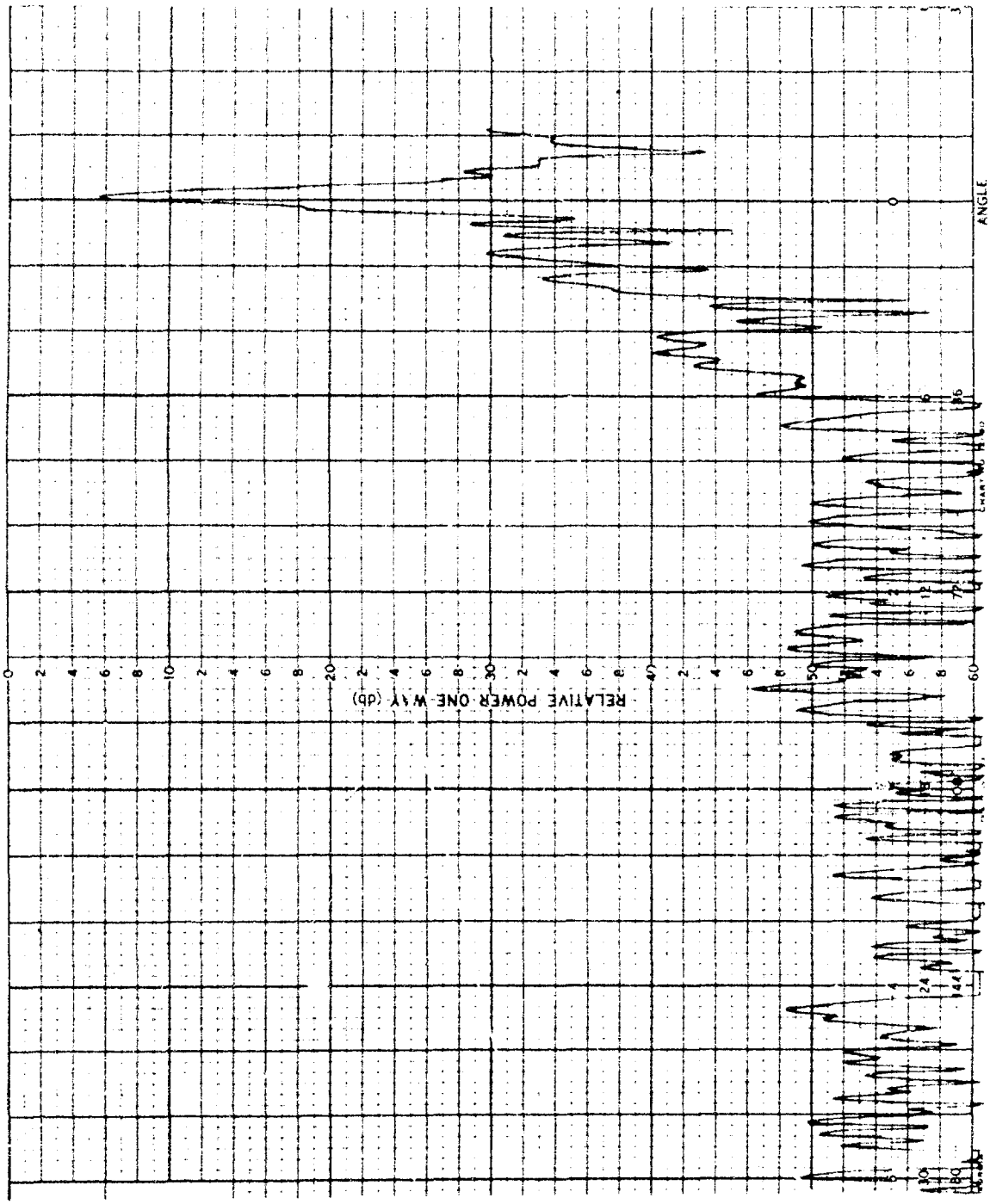

FIG. 33 - 2290 MC, E0, FEED NOT TILTED

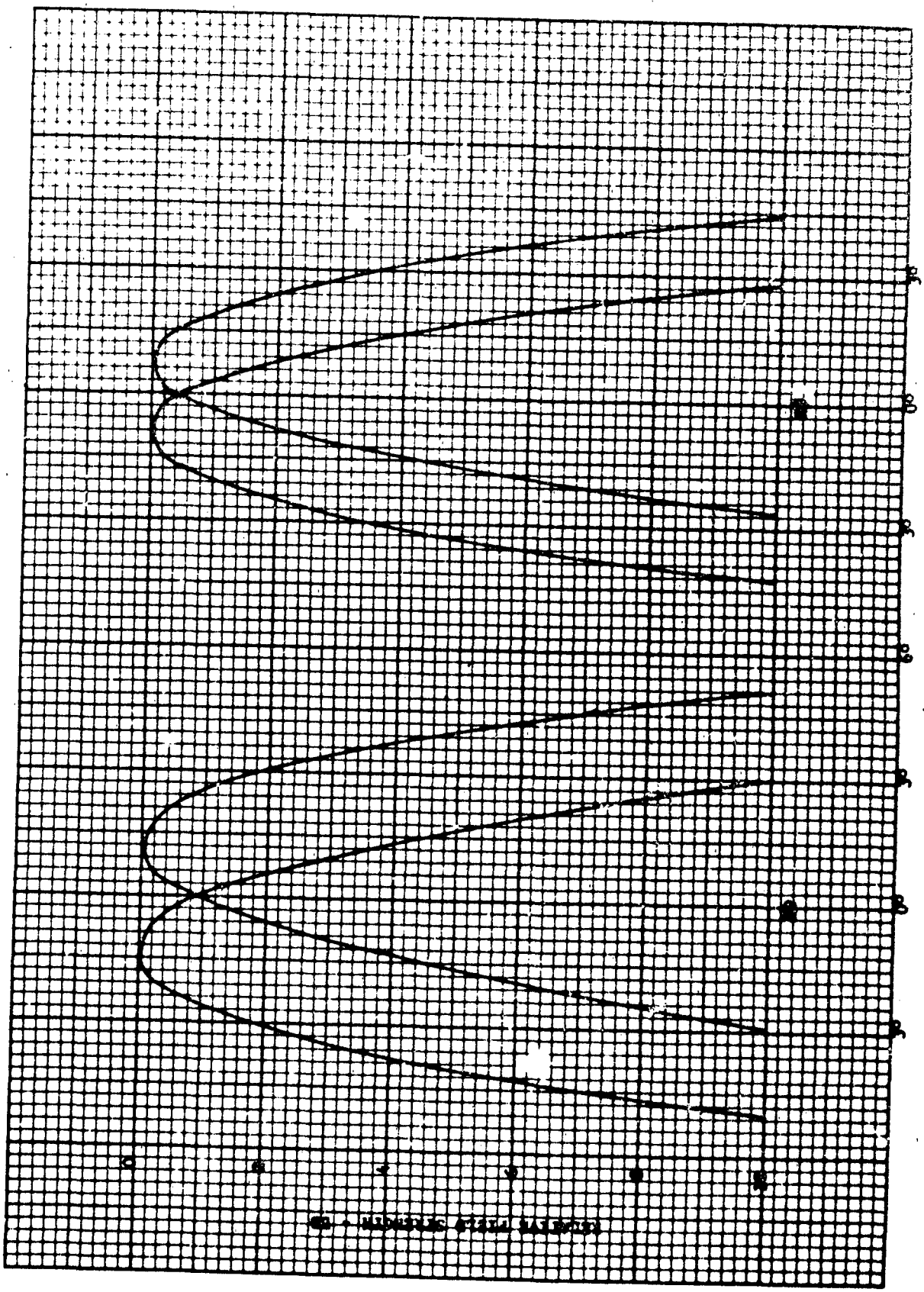

FIG. 34 - MODULATION LEVEL FOR 860 MC, 15° FEED TILT

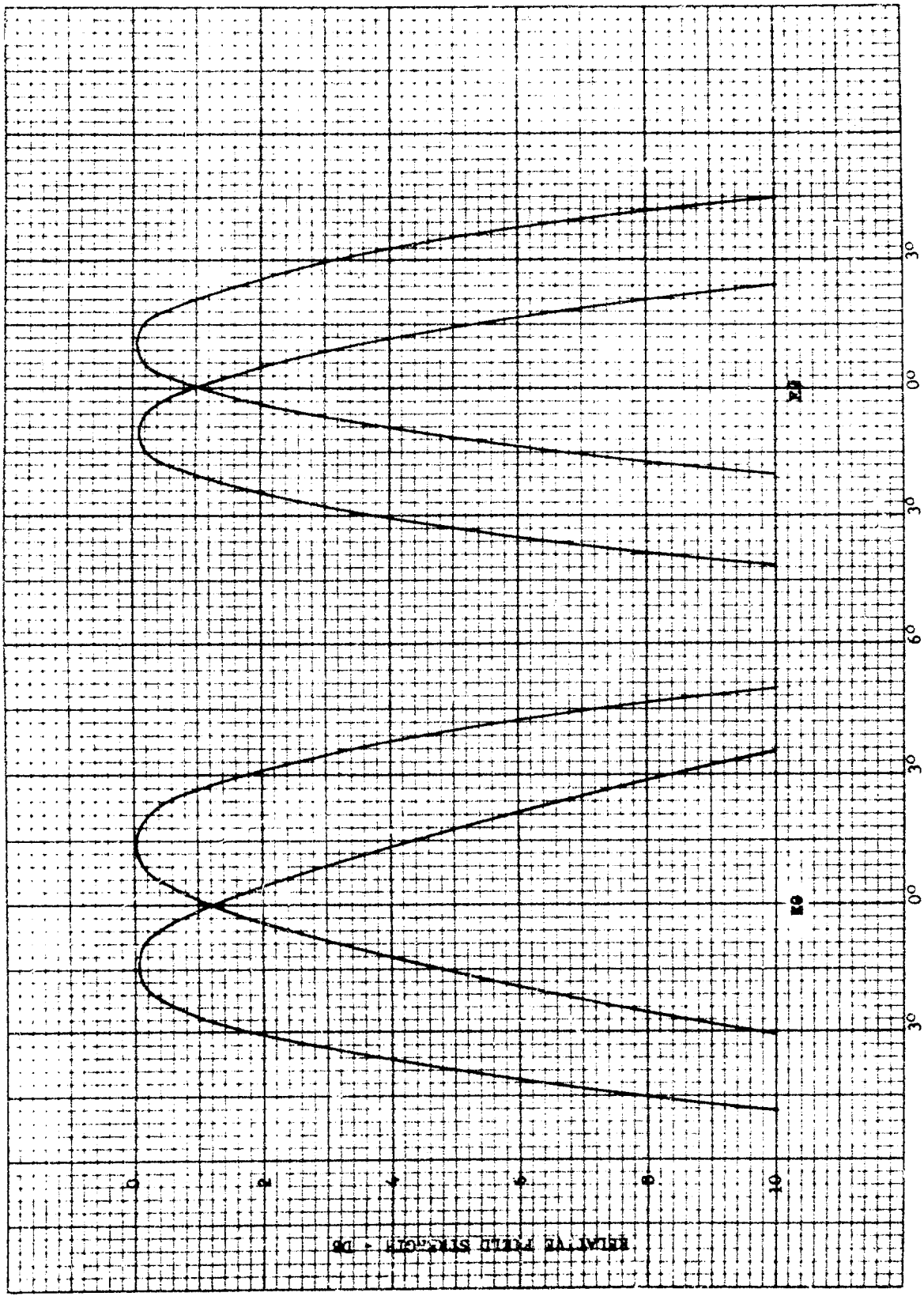

FIG. 35 - MODULATION LEVEL FOR 900 MC, 15° FEED TILT

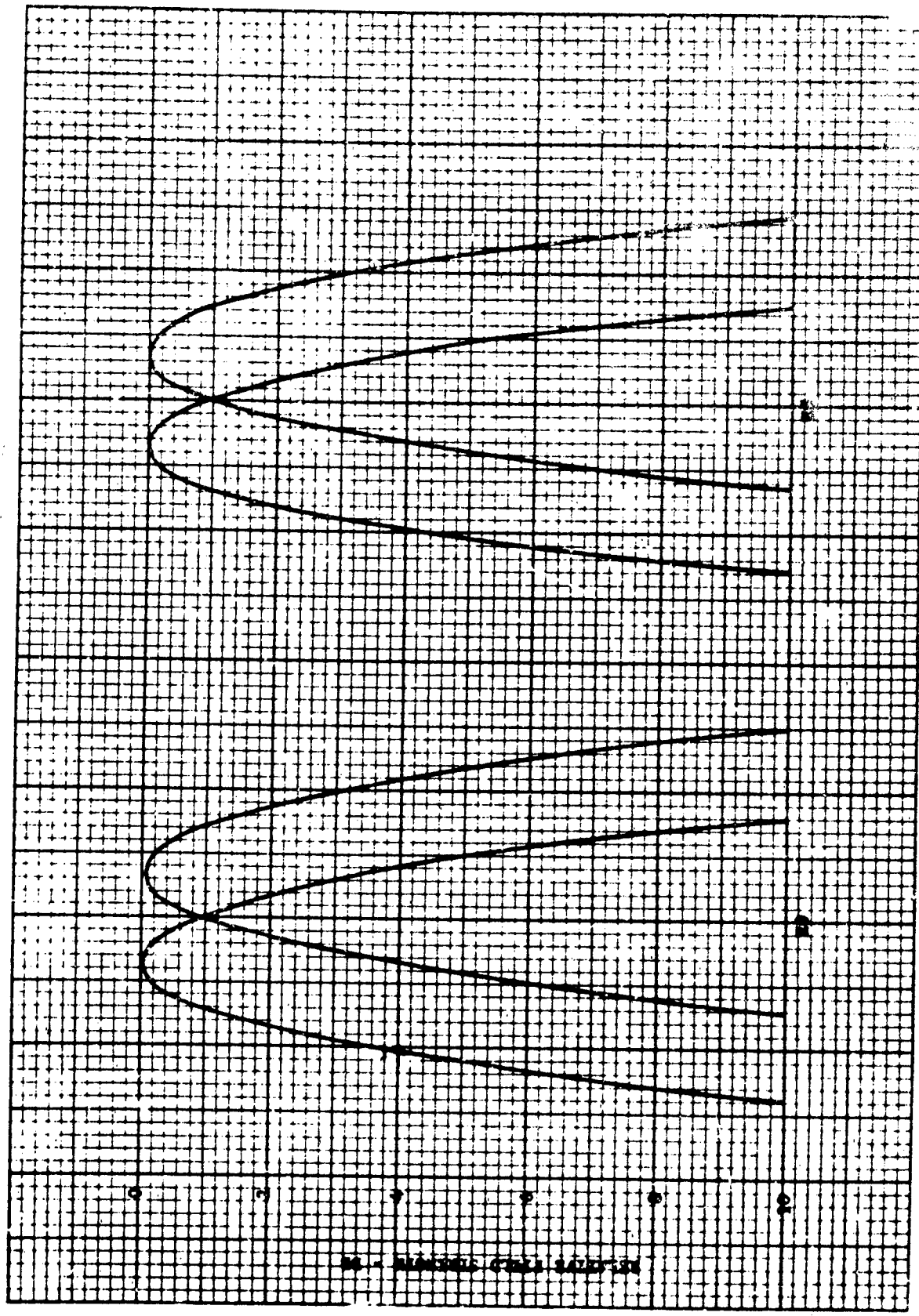

FIG. 36 - MODULATION LEVEL FOR 960 MC, 15° FEED TILT

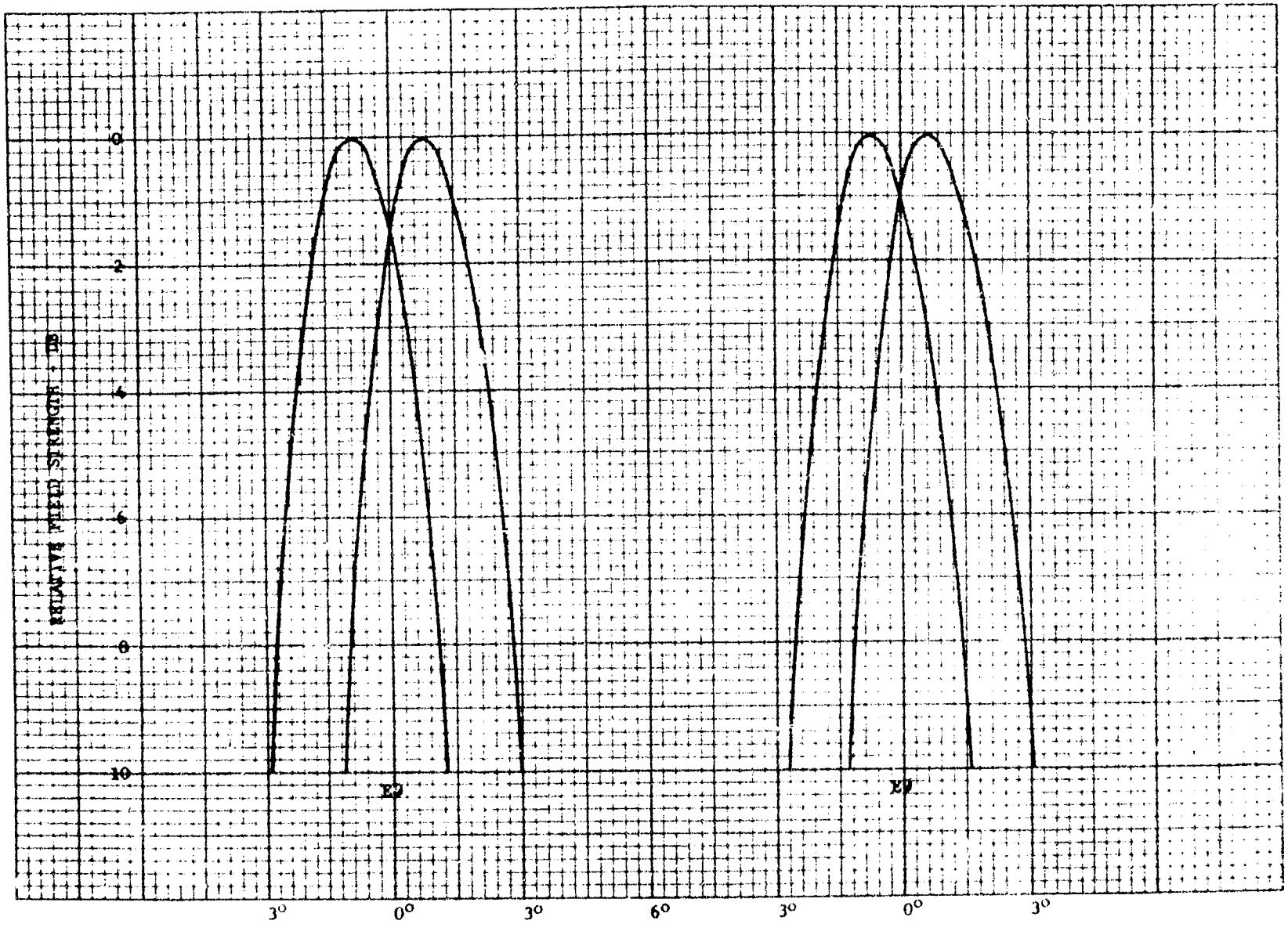

FIG. 37 - MODULATION LEVEL FOR 1400 MC, 15° FEED TILT

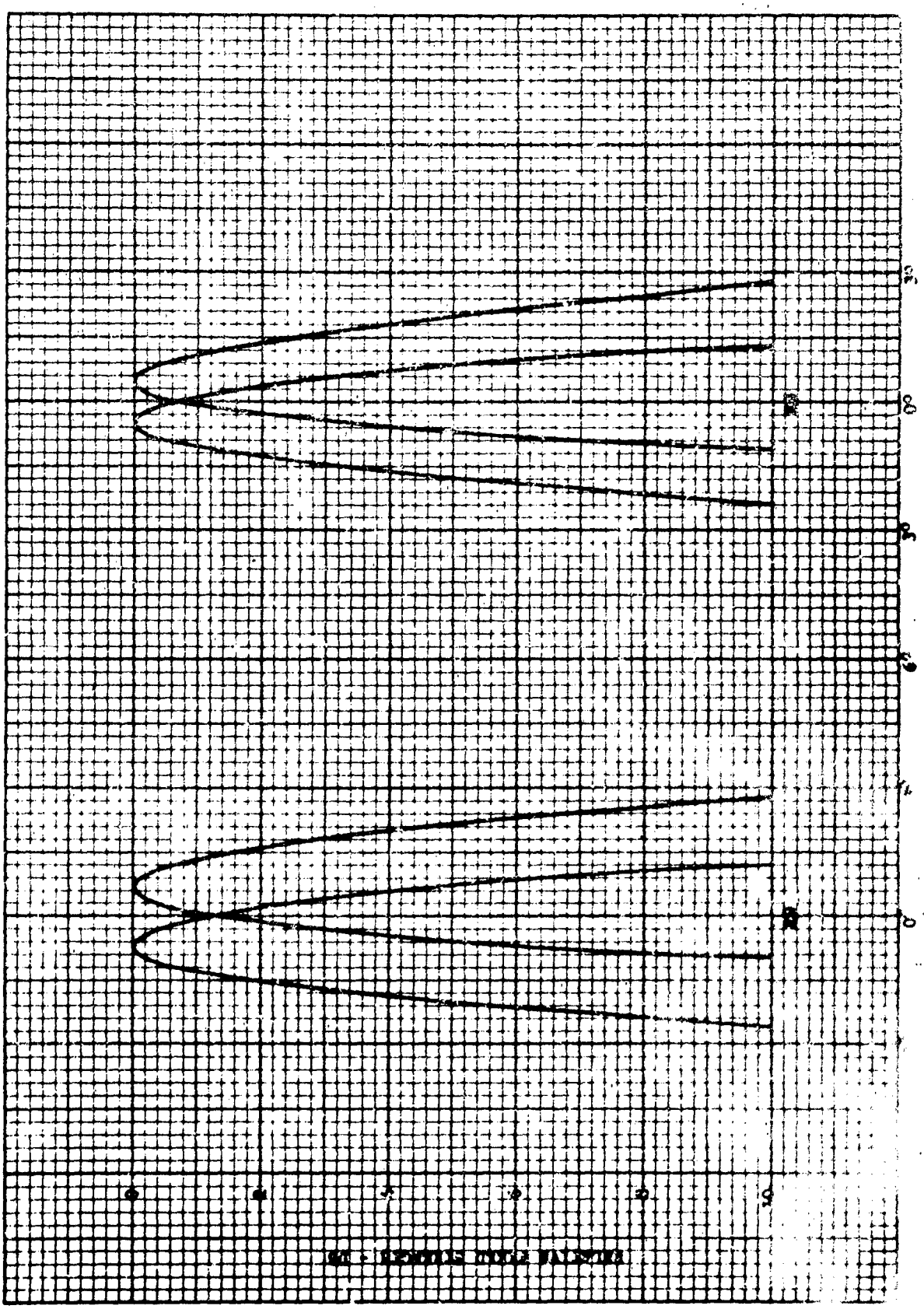

FIG. 38 - MODULATION LEVEL FOR 1700 MC, 15° FEED TILT

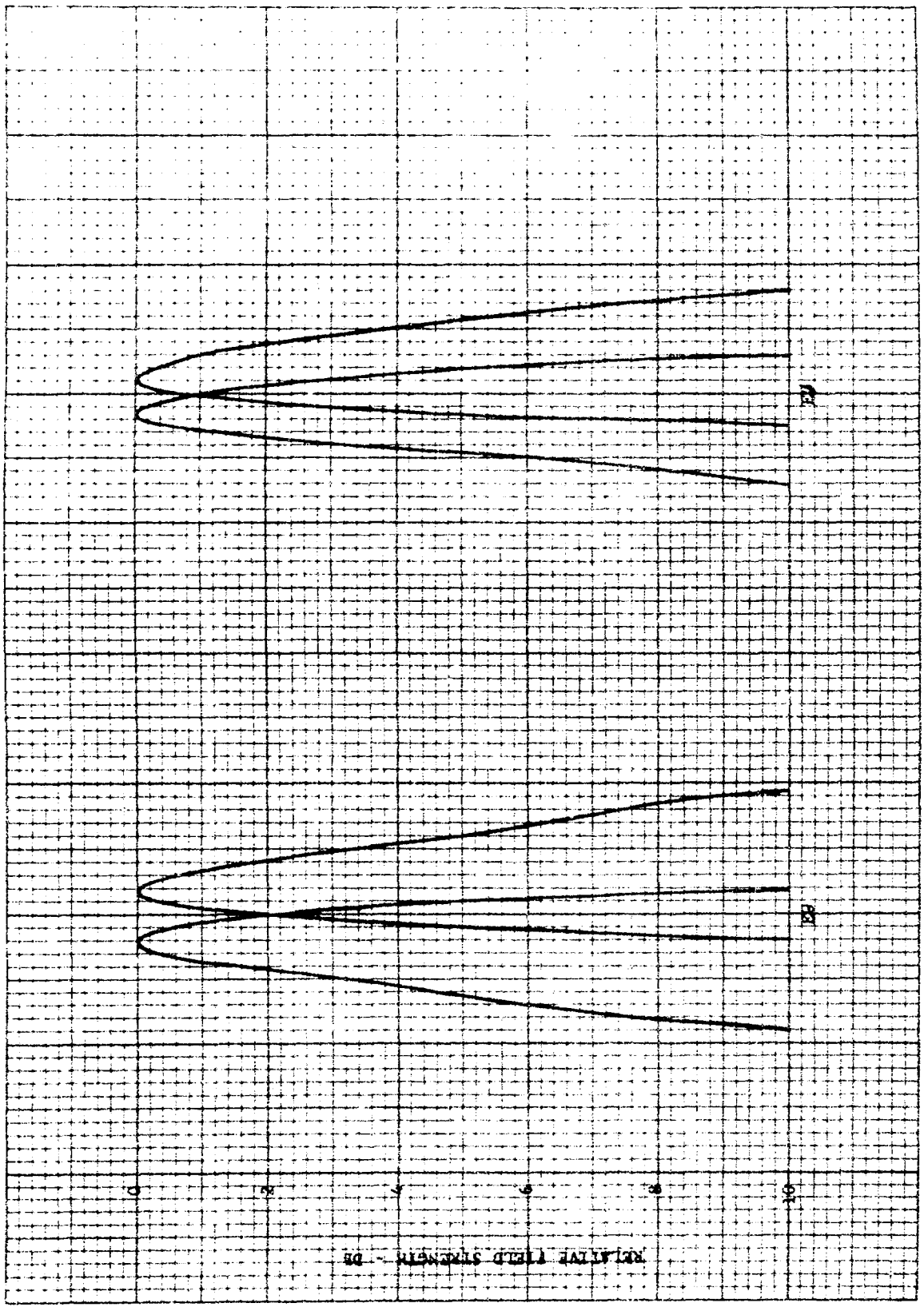

FIG. 39 - MODULATION LEVEL FOR 2290 MC, 15° FEED TILT

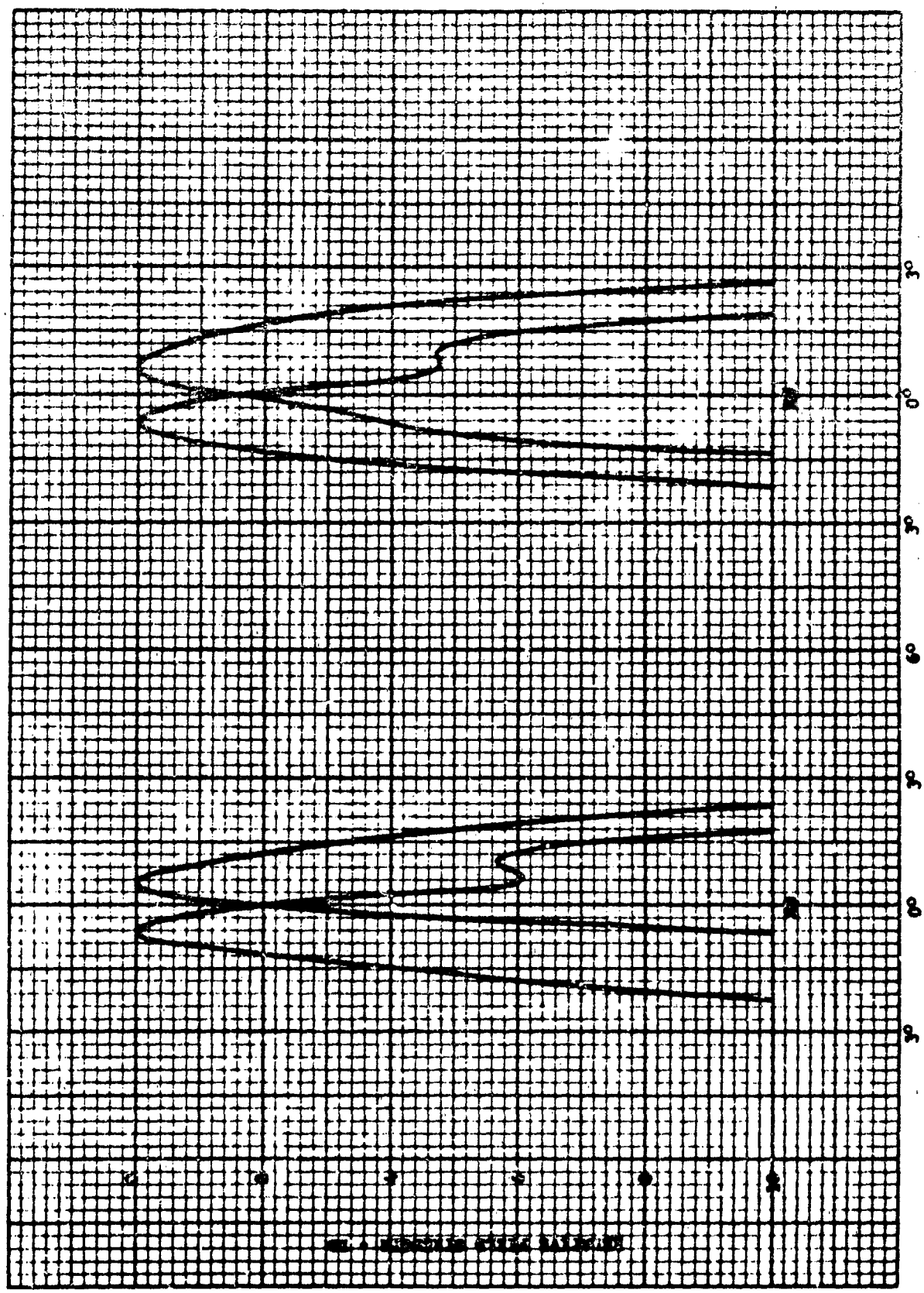

FIG. 40 - MODULATION LEVEL FOR 2800 MC, 15° FEED TILT

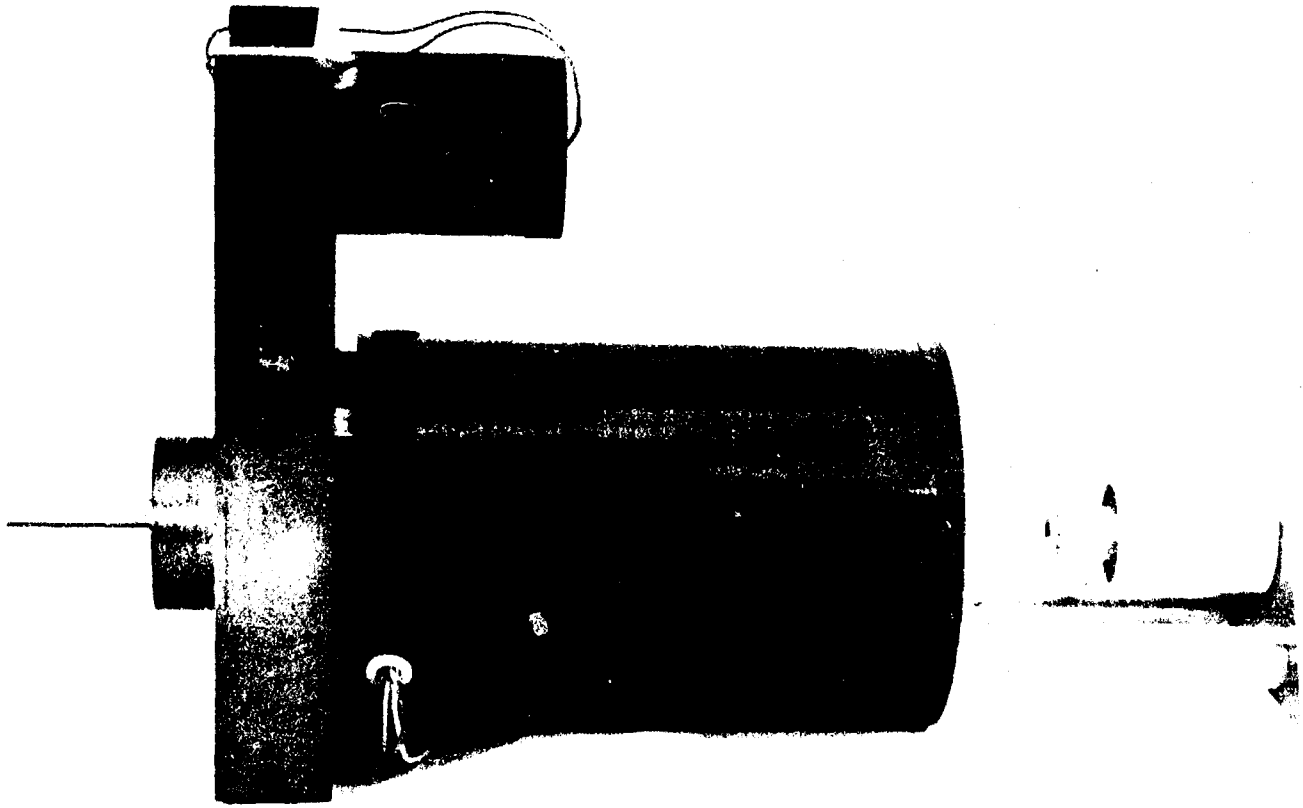

FIG. 41 - MOTOR-GENERATOR MOUNT

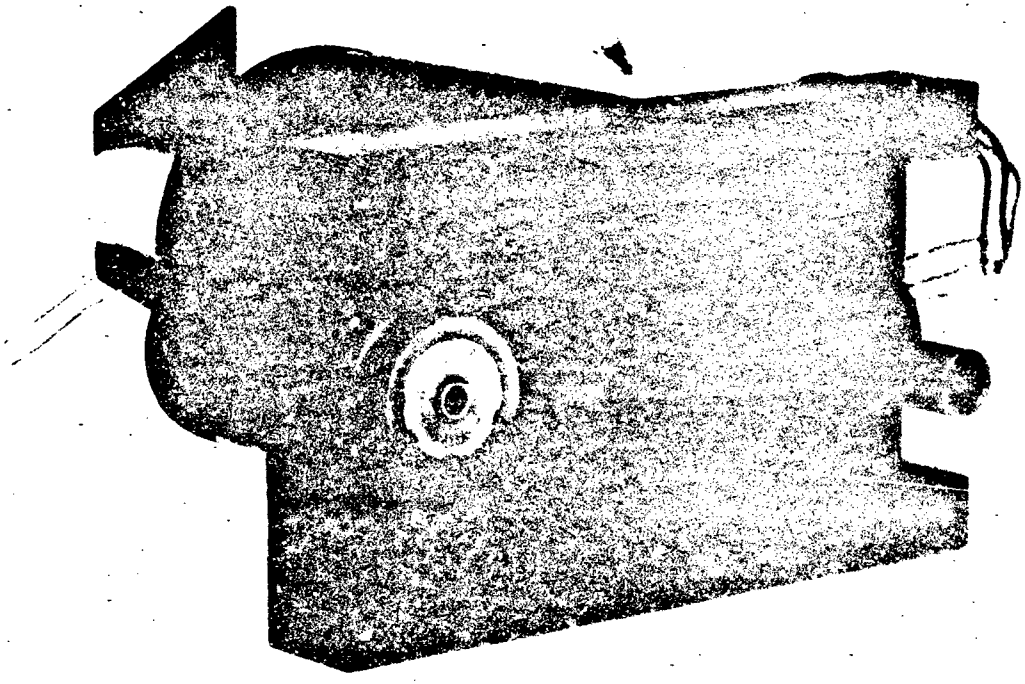

FIG. 42 - MOTOR-GENERATOR COUPLING

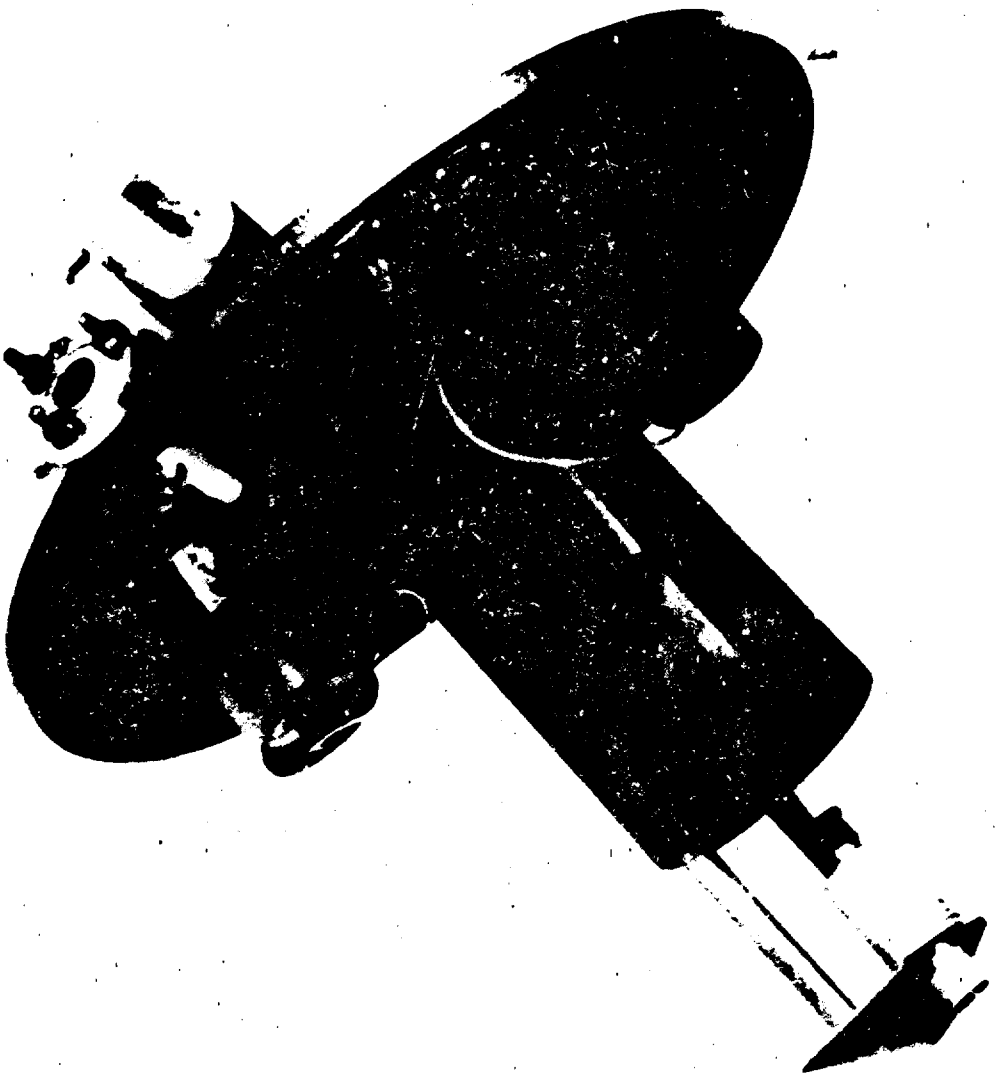

FIG. 43 - TRIPOD MOUNTING PLATE WITH MOTOR GENERATOR IN PLACE

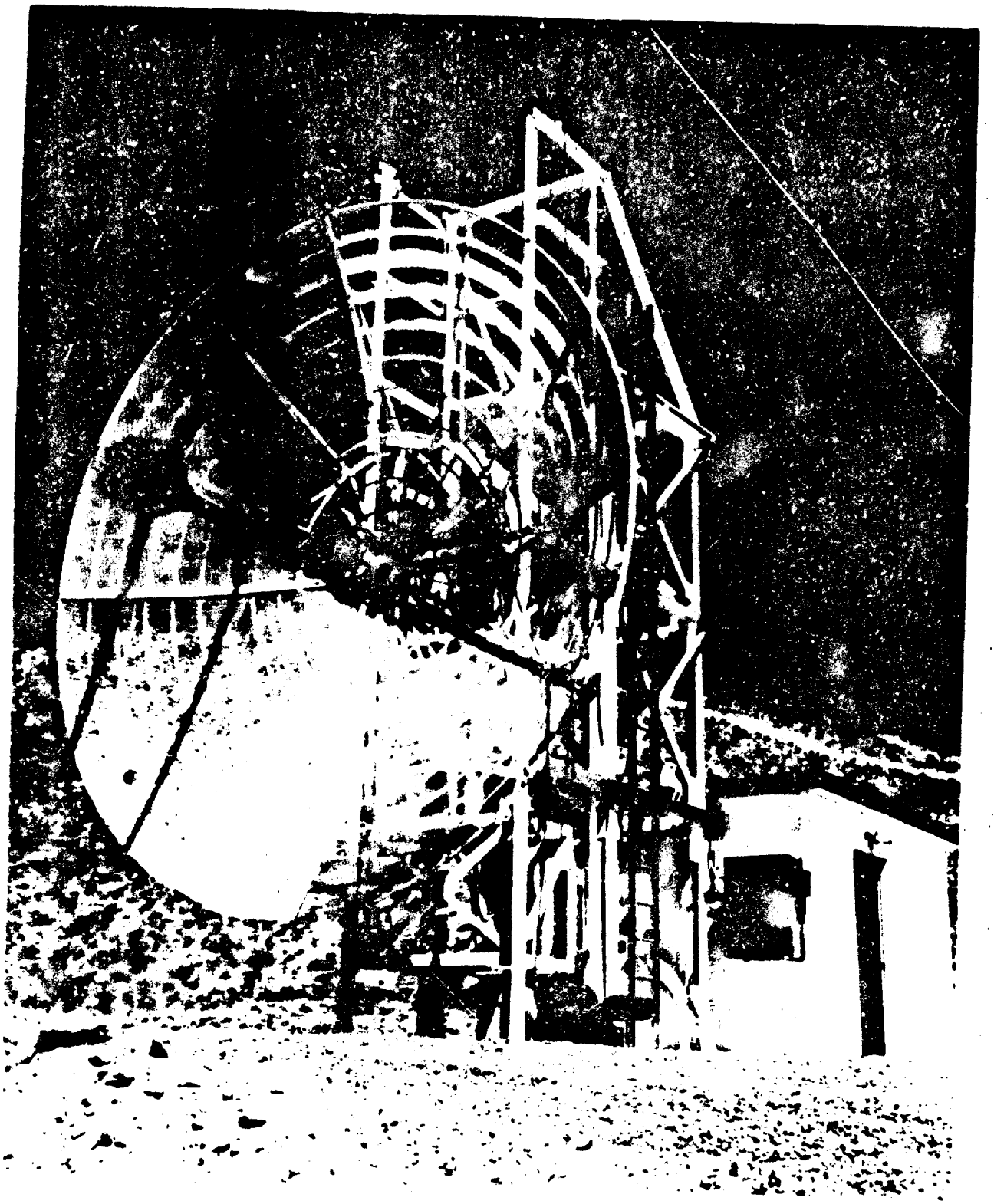

FIG. 44 - TRIPOD MOUNTED ON REFLECTOR

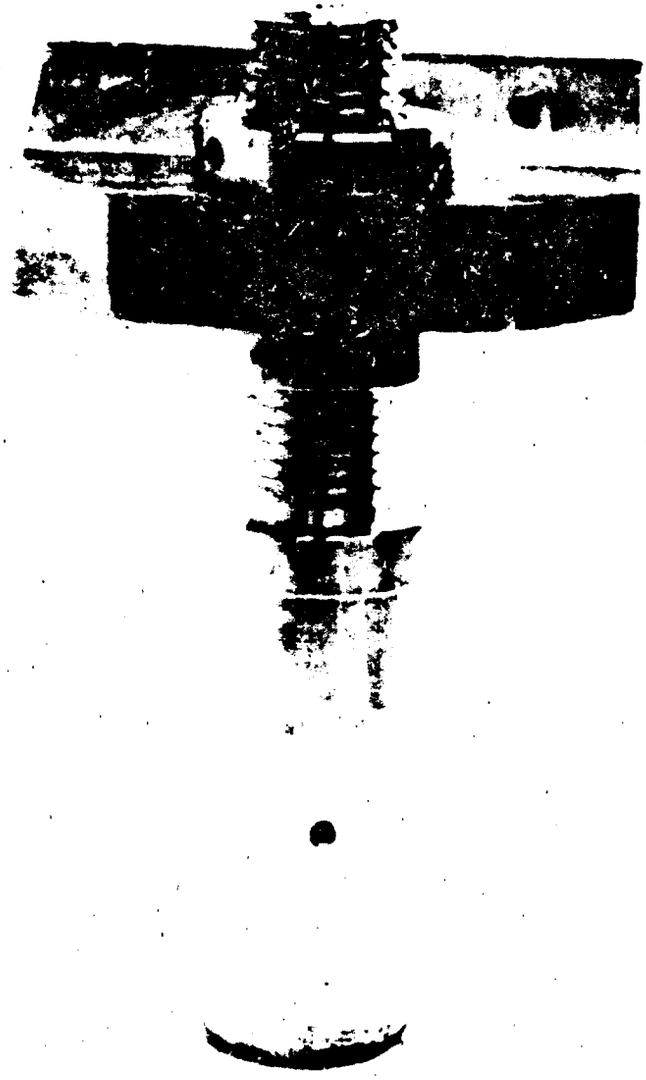

FIG. 45 - ADJUSTABLE TRIPOD MOUNTING STUDS

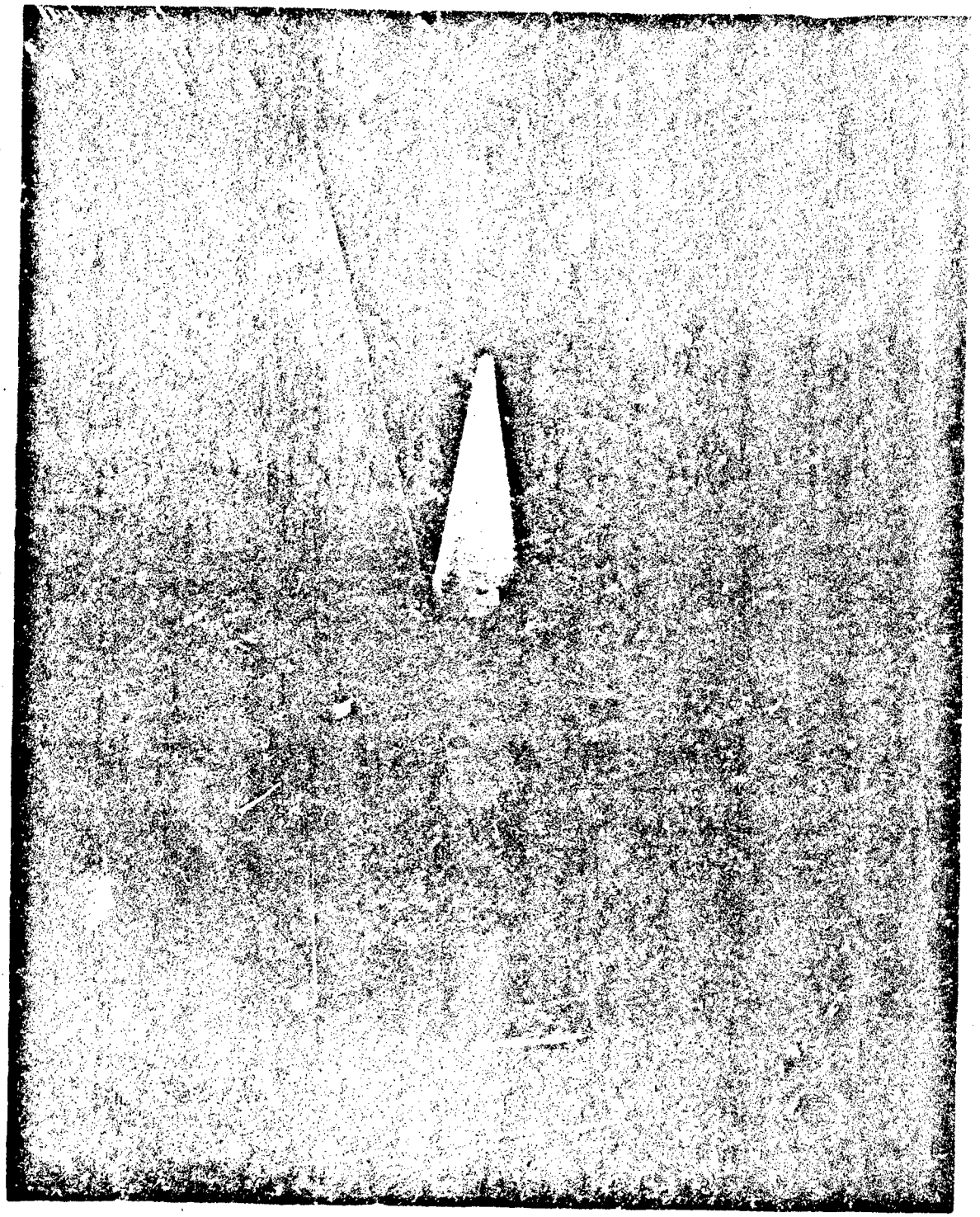

FIG. 46 - RADOME AND ANTENNA ON MOUNTING PLATE

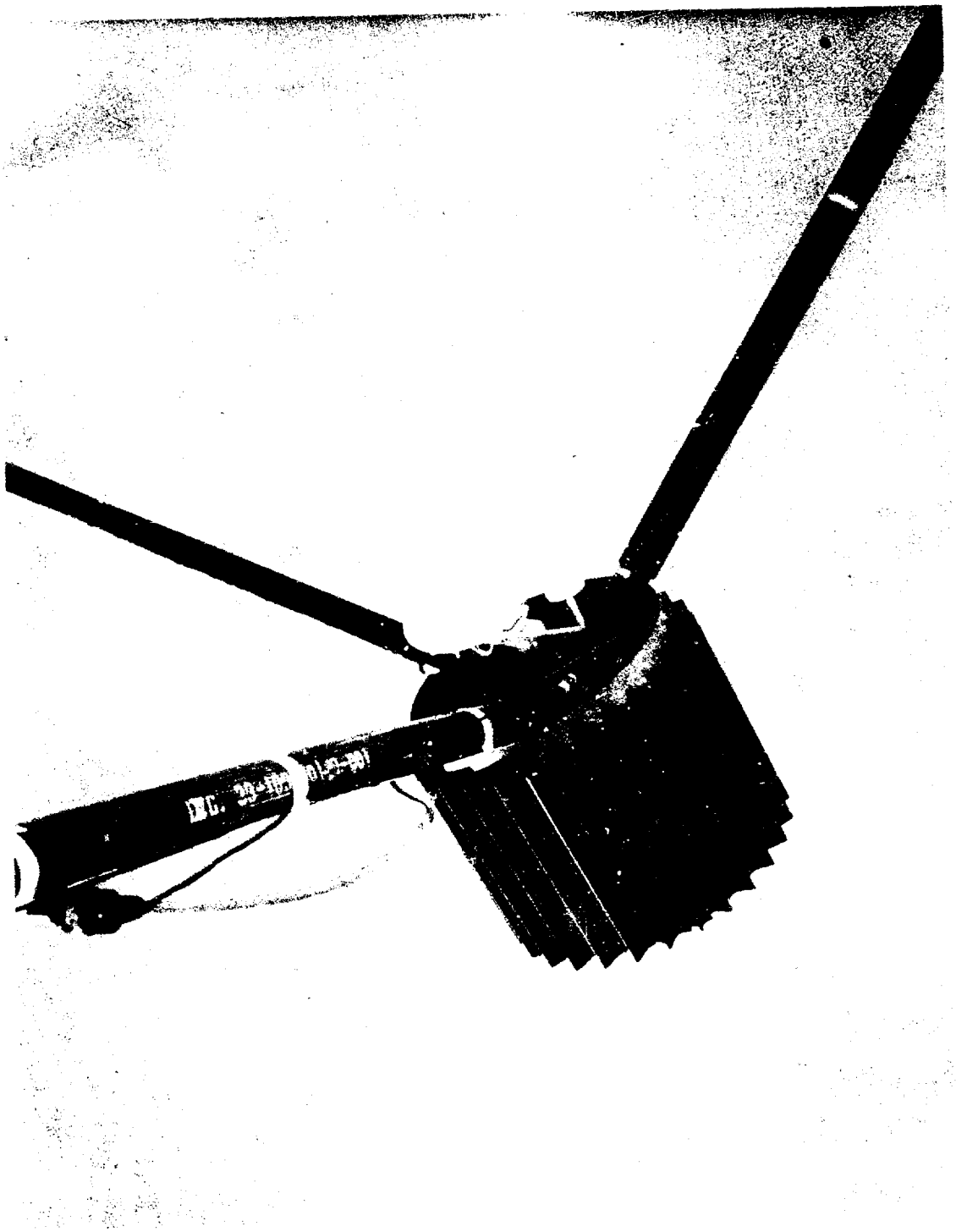

FIG. 47 - ANTENNA AND COUNTERWEIGHT

TABLE I

RADIATION PATTERN CHARACTERISTICS FOR CONICAL LOG-SPIRAL WITH $\beta = 73°$ AND $\alpha = 20°$.

Frequency	Axial Ratio	Half-Power Beamwidth	Beamwidth to First Nulls	VSWR
900	3.5 db	83°	207°	1.22
960	3.0	86°	198°	1.24
1400	1.75	90°	210°	1.45
2290	4.5	99°	227°	1.18
2800	5.25	93°	196°	1.40

TABLE II

RADIATION PATTERN SUMMARY FOR CONICAL LOG-SPIRAL WITH β=83° AND α=20°. PATTERNS ARE SHOWN IN FIG. 5 THROUGH FIG. 25.

Frequency	Axial Ratio	Half-Power Beamwidth	Beamwidth to First Nulls	VSWR
860	2.75 db	62°	160°	1.64
900	2.80	63°	160°	1.70
960	0.75	68°	165°	1.05
1400	1.30	80°	170°	1.38
1700	2.10	79°	170°	1.32
2290	3.5	95°	175°	1.33
2800	5.0	97°	175°	1.32

TABLE III

CHARACTERISTICS OF 19 FOOT PARABOLIC REFLECTOR WHEN FED BY A CONICAL SPIRAL WITH 15° TILT TO THE AXIS.

Frequency Mc/sec	Half-Power Beamwidth		Modulation Level (db)		Front-to-Back Ratio (db)	Axial Ratio (db)	Gain with Respect to Isotropic (db)		VSWR
	Eθ	Eφ	Eθ	Eφ			Measured	Calculated	
860	4.4°	4.1°	0.9	0.5	40	4.5	33.6	34.4	1.43
900	4.3°	4.1°	1.1	0.9	41	1.5	33.8	34.8	1.70
960	3.7°	3.7°	1.0	1.0	46	1.75	34.6	35.3	1.033
1400	2.3°	2.5°	1.4	1.0	47	2.25	37.5	38.6	1.48
1700	2.1°	2.1°	1.2	0.8	48	2.5	39.0	40.3	1.35
2290	1.5°	1.55°	1.8	1.2	48	4.5	40.7	42.9	1.12
2800	1.5°	1.4°	1.9	1.5	46	7.25	41.2	44.6	1.30

TABLE IV

NOISE TEMPERATURE OF 19 FOOT PARABOLIC REFLECTOR

Frequency	Cosmic Noise Temperature (°K)	Ground Noise Temperature (°K)	Antenna Noise Temperature (°K)
860	60°	290°	132°
900	50°	290°	97°
960	45°	290°	90°
1400	20°	290°	47°
1700	12°	290°	50°
2290	6°	290°	37.5°
2800	4°	290°	42.5°

BIBLIOGRAPHY

1. Henry, D. G., "Antenna Study for a High Accuracy Vehicle Tracking System," New Mexico State University, Physical Science Laboratory, Contract NAS 5-1032, November, 1961.

2. McClelland, O. L., "An Investigation of the Near Fields on the Conical Equiangular Spiral Antenna," Electrical Engineering Research Laboratory, University of Illinois, Contract AF 33(657)-8460, May 1962.

3. Duncan, J. W., Minerva, V. P., "100:1 Bandwidth Balun Transformer," Proceedings of the IRE, February, 1960.

A HIGH DIELECTRIC CONSTANT PHASING LENS FOR ELECTRONICALLY - SCANNED ANTENNA ARRAYS

By

R. Scott Brazil

MOTOROLA INC.
Military Electronics Division
WESTERN CENTER
8201 EAST McDOWELL ROAD, SCOTTSDALE, ARIZONA

1. INTRODUCTION

Since the advent of the electronically scanned antenna array there has existed a need for methods of developing relative phase and amplitude information without the complexity of a multitude of phase shifters and power dividers. The optical phasing lens can adequately satisfy this need. However, such lenses can assume dimensional proportions which render them unsatisfactory for airborne and space applications. To alleviate this problem, dielectric-filled lenses have been proposed. By this technique, lens dimensions are reduced by a factor inversely proportional to the square-root of the dielectric constant of the loading material.

The approach was pursued in an effort to radically reduce lens volume by a factor as great as 1000. Such reductions in size require the use of materials whose dielectric constants are on the order of 100 to 300.

This paper describes the results of a program to advance lens design and dielectric loading techniques. During the program dielectric plating methods were improved, materials were developed to conform to lens geometries, and electrical devices such as coupling elements, transmission lines and transition elements (coax to microstrip) were developed in very high dielectric constant materials. A demonstration model lens was designed, fabricated, and tested. The paper includes discussions of the modes of propagation in a dielectric lens, selection and processing of lens materials, and the development and testing of the experimental model lens.

2. MICROWAVE PHASING LENSES

For use in antenna and array scanning systems, microwave lenses are employed to develop the phase and amplitude of each array element. Geometric optics (ray tracing) is applied to develop the equations which describe the lenses' geometrical and electrical form. This design approach requires that equal electrical path lengths are developed throughout the lens unit, originating

from a point source (the lenses' focus), and culminating in an equi-phase front along a plane perpendicular to the lens body (the antenna aperture). Two basic lens types result from this technique:

1. "Normal" lenses, in which the electric field vector is in the plane of the lens media, and
2. "Constrained" lenses, in which the electric vector is normal to the lens media.

"Normal" lenses are designed using Snell's law. Thus, equal paths are developed through a lens by causing discrete "rays" to bend at prescribed dielectric interfaces. The classic Luneburg[1] lens is of this form.

"Constrained" lenses guide the rays along confined courses. Ray direction is not controlled by refraction. The Ruze[2] and Rotman[3] lenses are examples of the constrained lens design.

In each of the lens designs, a small microwave horn or similar radiator, is located at the lenses' focus. Energy is then "launched" into the lens media by means of this source. When the lens is being used as a phase computing device (rather than a direct radiating antenna), probes or similar type elements are placed along the contour opposite this focus. These "pick-off" elements serve to couple energy from the lens media to the antenna array.

The fundamental requirement of each type lens is that it develops equal path lengths from the focus to the antenna array. However, to properly perform this task, lenses, in general, must assume dimensions which result in their physical size becoming prohibitively large for many applications. The problem then becomes one of maintaining performance while reducing lens size. One means of accomplishing this task is to cause a uniform reduction in the velocity of propagation of the ray energy as it passes through the lens. This may be realized by uniformly increasing the lens media dielectric constant

over the value assumed during its initial design. This has been the approach used during the development of a High Dielectric Phasing Lens for Electronically Scanned Arrays.

3. HIGH DIELECTRIC LENS DESIGN

An earlier Motorola study had developed a microwave phasing lens assembly designed according to the methods reported by Rotman[3]. In this unit, multiple-beam scanning was achieved in one plane over ±50 degrees from a line source array. An S-band model having a 5-degree HPBW was built and tested. The model consisted of two parallel conducting plates separated by an air dielectric, spaced to support the TEM mode, and shaped to the calculated lens geometry. Figure 1 is a photograph of the completed model. Tests indicated the lens performed highly satisfactorily.

The ultimate objective of the development described by this report was to build an analogous unit in which the lens media is replaced by a high dielectric constant material. In so doing, electrical lengths are preserved while physical dimensions are reduced by a factor equal to the reciprocal of the index of refraction in the dielectric material.

3.1 Dielectric Material

Dielectric constant, loss and homogenuity are, of course, primary considerations in the selection of a dielectric material which is to be used in a microwave device. In this case, certain mechanical properties were also to be considered. Earlier work had shown that high dielectric constant bodies made up of many pieces of material which are cemented together to form a single unit are not satisfactory for use in a high performance lens system. This required that the selected material be supplied as a unit piece. In addition, to achieve the necessary lens contour geometry the material was to be machined to very close tolerances.

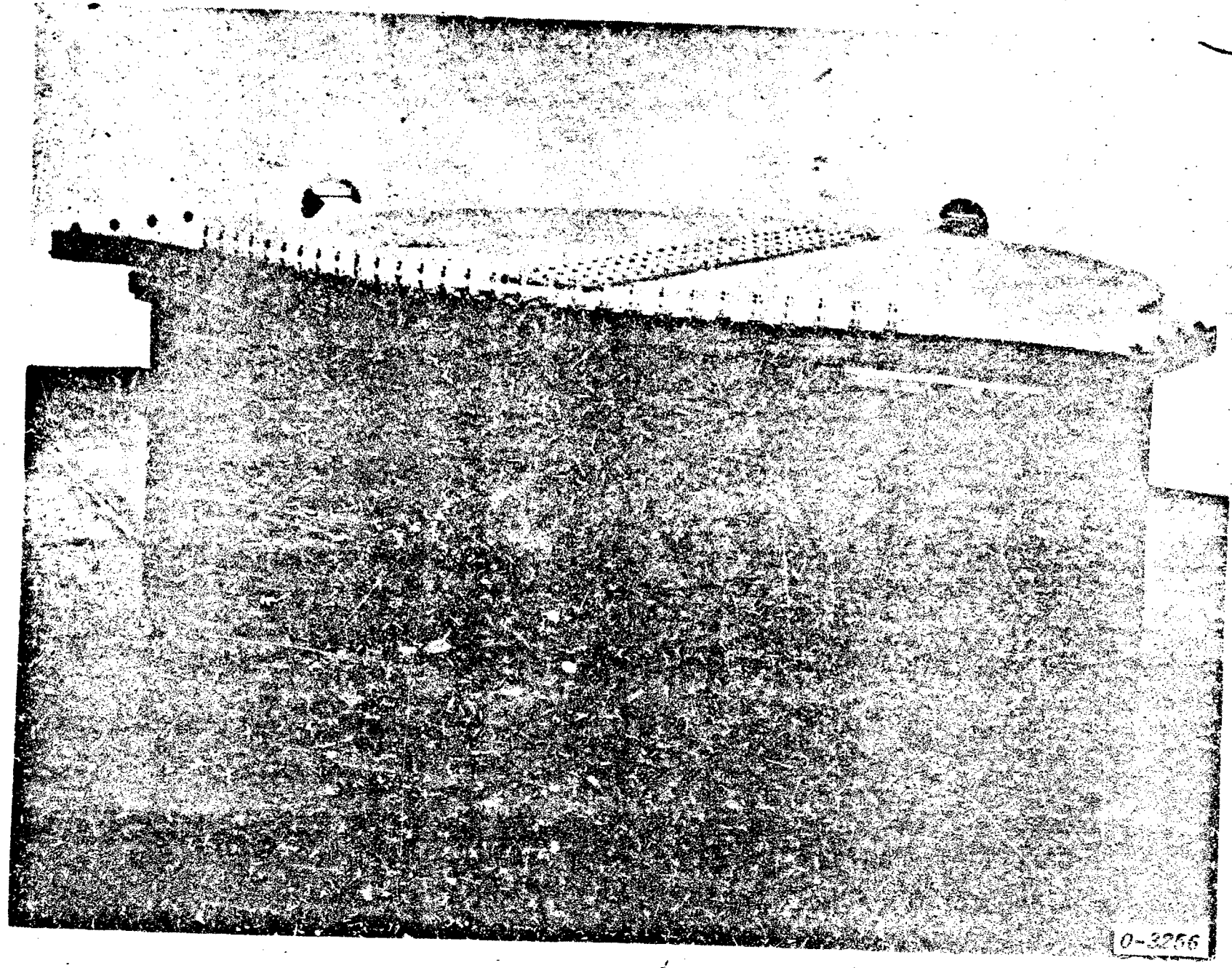

Figure 1. S-Band, Air Dielectric Parallel-Plate Phasing Lens for 5 Degree HPBW Line-Source Linear Array

Because of the extreme mismatch which results at an air interface in very high dielectric constant materials, a lens must be constructed with its coupling elements imbedded in the dielectric. Printed circuit techniques provide a relatively simple approach to this requirement, but their use requires that the shape, dielectric constant, and loss of the material are not altered by the plating and etching processes.

In order to achieve a significant size reduction, a material was sought having a dielectric constant in excess of 100. The required properties may be found in a newly developed low loss material produced by Motorola's Solid States Systems Division. This material is multicrystalline titanium dioxide, a homogeneous ceramic material having a dielectric constant of 110 and loss tangent $<.0003$.

3.2 Coupling Elements and Transitions

There are many factors which must be considered during the selection of the lens coupling elements. The antenna element's polarization, pattern shape, transmission line requirement, self and mutual impedance characteristic, aperture size, and fabrication technique must be compatible with each facet of the lens development. Following an extensive analytical and experimental study, the yagi and dipole antennas were selected to serve respectively as the dielectric lens launch and pick-off coupling elements.

Each of these antennas propagate a vertically polarized wave. The yagi exhibits a directive beamwidth and well controlled pattern shape, a stringent requirement for the lens launch element. The dipole has a very broad beamwidth; a desirable feature for the pick-off element. Each antenna can be fed with balanced, two conductor transmission lines. The combination of self and mutual impedance characteristics make each element a highly desirable selection. Half wavelength spacing of the pick-off elements is preferred for a

Tchebyscheff distribution of elements in the antenna array, thus, the dipole lends itself quite well to the resultant close proximity between adjacent pick-off elements. The proximity of beams from the multibeam array is determined, in the Rotman lens, by the relative spacing of the launch elements, thus, the half wavelength breadth of a yagi antenna allows for the placement of large numbers of fixed beams along the lenses' focal arc.

Finally, and perhaps of greatest significance, each of these antennas can be formed using printed circuit etching techniques. This is of utmost importance in this application due to the extremely miniature size the coupling elements assume when scaled down by the factor $1/\sqrt{\epsilon}$. (Typical dimensions of an S-band dipole imbedded in an $\epsilon = 110$ material are: line radii of .002 inch, element length of .190 inch, and transmission line separation of .035 inch.) Printed circuit-type methods are the obvious solution to the problems encountered in the fabrication of such elements.

Because of the very close physical spacing between adjacent elements, the transition from conventional sized system hardware to the dielectric-loaded lens coupling elements required the development of unique interconnection methods. The very miniature nature of the microstrip transmission lines also added to the complexity of the interconnection problem.

During an experimental evaluation of several approaches, the Microdot 31-50 receptical was modified to fit into the available space and also make the contact necessary for the electrical transition. Typical performance over a six-percent band of frequencies yielded an average mismatch of 1.5:1 and a coupling of 2.7 db below theoretical. (This performance was measured on a developmental model consisting of a set of yagi and dipole coupling elements, mounted on opposite ends of a 4-inch test bar of lens material. Modified Microdot transitions were used to make the necessary equipment interconnections.)

3.3 Lens Description

Having selected a lens design, the high dielectric constant material, and the lens coupling elements and transition method, an experimental model was designed, built and tested to demonstrate the feasibility of the technique. Since the dielectric-loaded lens was to be the electrical counterpart of the earlier S-band model (figure 1), it was necessary to validate the electrical equivalence of the two units. This was done by an analysis of their respective modes of propagation.

The literature [4, 5, 6, 7, 8, 9] describes propagation through dielectric materials in an environment of closely spaced ground planes. Barlow compares surface wave propagation to transmission line modes as a function of single and dual ground planes. Equations are derived for phase velocity through grounded and ungrounded dielectric sheets for each of TE, TM, and for TEM propagation. Richmond shows similar results and presents the data in graphical form for various ground plane and dielectric sheet spacings as a function of dielectric constant. Using these design criteria, it was shown that in the dielectric-filled lens model, the TM01 mode is supported. A surface wave is propagated along the dielectric interface with a velocity approximately $1/\sqrt{\mu\epsilon}$ that of the TEM mode in the air lens model. Thus, even though their mode of propagation is different, the two lens models exhibit equivalent electrical lengths to the ray paths through them. Therefore, where equal wavelength spacings exist in each unit, equivalent phase delay occurs.

The S-band air lens measured approximately 65-inches across. Multicrystalline titanium dioxide has a dielectric constant of 110. Thus, a reduction of $1/\sqrt{\epsilon}$, or .095 in the air lens dimensions was realized. This resulted in a volume reduction of 1160:1. The high dielectric-constant lens unit thus consisted of a 7.5-inch titanium dioxide disc supported over a ground plane.

Seven yagi antennas were placed about the focal arc and axially aligned, facing the center of the array of pick-off elements. They held beam positions of 0, ±20, ±30, and ±45 degrees relative to the center axis. Twenty-nine dipoles were placed at approximately half-wavelength intervals along the lenses' rear contour to serve as pick-off elements. These launch and pick-off elements are shown in figure 2.

3.4 Fabrication Techniques

In a high performance lens-array system, phase errors must be held to a minimum. When such errors occur, they appear at the array as deviations from a plane wavefront. Their presence causes degradation of the radiated pattern. The phase errors may be caused by many facets of the lens system: the basic lens design (geometry) is generally not perfect as the beam is scanned; the lens media is not homogeneous; the feed source is not located at the lens focus; and, loose mechanical tolerances alter the intended lens shape.

The lens design being used for this application exhibits negligible inherent phase errors with scan (theoretical maximum phase error for ±50 degrees of scan is 0.8 degrees while measured maximum error on the air lens model was 5 degrees). Homogeneity of the dielectric material can be controlled only during its manufacturing stage. Following delivery of the disc from the vendor its point-to-point dielectric constant cannot be altered. However, loose mechanical tolerances in the lens shape, or in the location of coupling elements can seriously impair a phasing lenses' performance. This is illustrated by observing the wavelength as measured in the dielectric. Free space wavelength at 2950 mc is 4.000 inches. This wavelength measured in the ϵ110 material is 0.330 inches. Thus, a one-mil dimensional tolerance represents 0.947 electrical degrees of phase error. For this reason, extreme care was taken in locating the lens coupling elements and in shaping the dielectric disc to the required lens shape.

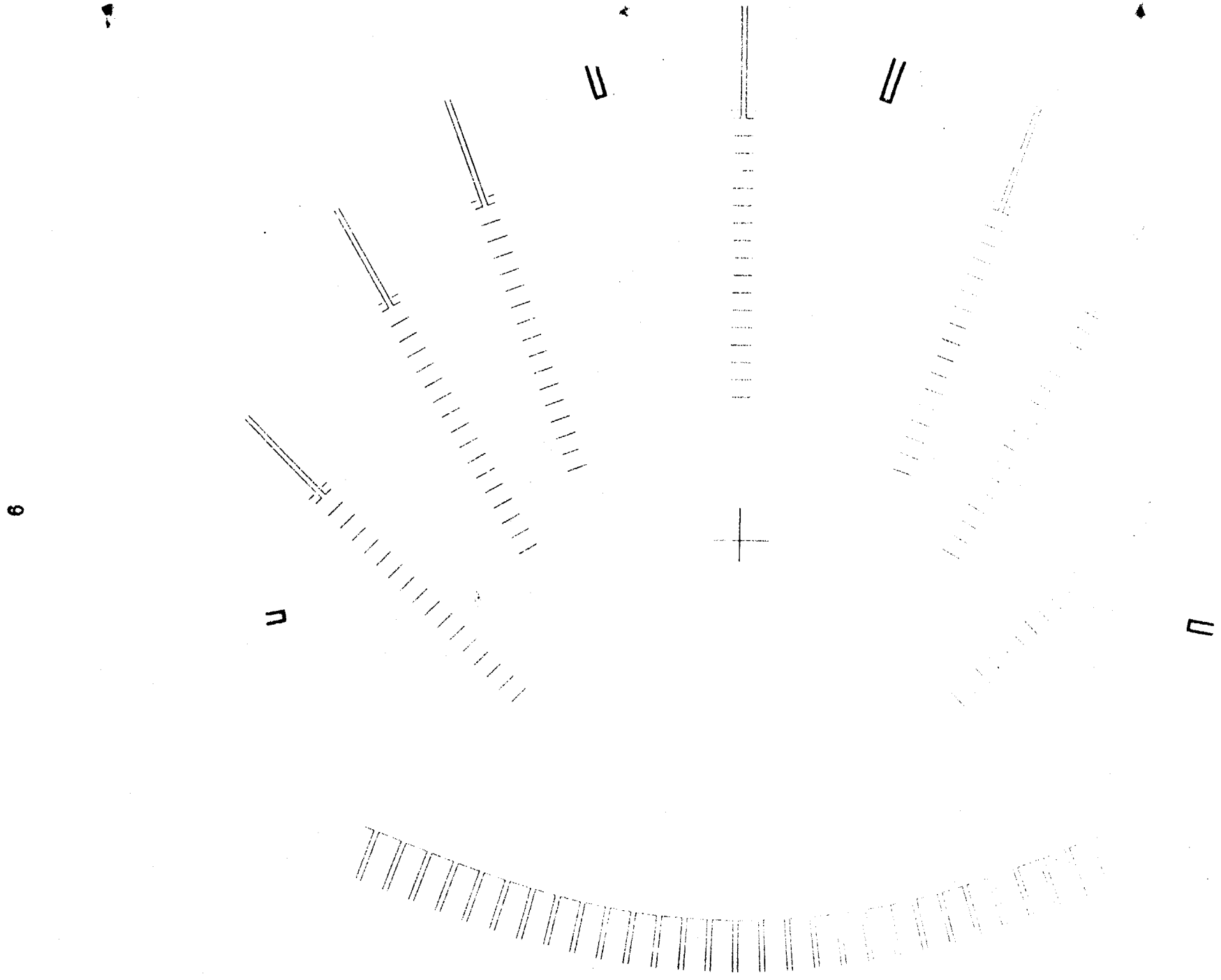

Figure 2. Titanium Dioxide Phasing Lens/Antenna Coupling Element Circuit Layout - Scale 1:1

3.4.1 Coupling Element Circuit

Artwork of the coupling elements was initially drawn to a 16:1 scale. Then, individual photographic negatives of each element in an 8:1 scale were accurately located in a phasing lens geometry, also placed on an 8:1 scale. The twenty-nine pick-off dipoles were positioned with their centers located on the rear contour. Location dowels were placed at four points along the perifery of the lens. These served to accurately align the finished negative to the dielectric plate during the photographic exposure process. The artwork was then reduced to photographic negatives on a 1:1 scale. Figure 2 is a print of the completed artwork.

3.4.2 Dielectric Lens Shaping

Reflections in a phasing lens can seriously degrade the lenses' performance. For this reason, if conditions are such that reflections are unavoidable, their phase must be controlled so as not to alter the desired phasing characteristic of the lens. A very large mismatch occurs at the lens edge, due to the high dielectric constant interface. The result is that energy is absorbed by the dipole pick-off elements both from an incident wave and from a wave reflected from the rear lens contour. These reflections can be tolerated only if their phase is equal for each pick-off element. To achieve this condition requires that the dielectric disc be shaped to the lens geometry with very close tolerances held along the rear face contour. Special tooling employed consisted of a "vertical floating-cam-follower" for the grinding operation. The device was made to support the ceramic disc vertically to a diamond-wheel grinder. The disc was keyed to a master cam which had been cut on a computer-programmed vertical mill to conform to the lens contour. The master cam and cam-follower permitted cutting slots for the "location" dowels which were to become an integral part of the lens assembly. These

dowels coincided in location to those placed on the coupling element artwork. Thus, the pick-off elements were automatically aligned to the reflective contour of the lens material.

3.4.3 Lens Plating and Etching

Following the grinding operation the lens disc was plated with 1-mil of copper on each side. A photo-sensitive spray-on film was applied and, following exposure through the artwork the coupling elements were etched onto the top surface. To insure a positive, reproducible method of accurately locating the coupling elements on the ceramic, a lens mounting base-plate was prepared with dowel pins corresponding in location to the dowel positions on the artwork and lens. This mounting plate was used for the photographic exposures, and assembly of the lens into a test assembly.

3.4.4 Lens Mounting Fixture and Circuit Connections

Because of the close proximity between pick-off elements, the microdot probes could not be aligned adjacent to one-another. To provide a uniform method of mounting, each probe was inclined at a 45-degree angle to the lens surface. A two-sided angle bracket was curved to the rear-face contour and suspended over the dipole transmission lines. Successive microdot probes were alternately placed in tapped holes on either side of the bracket as shown in figure 3.

Accurate location and pitch of the holes was necessary for the probe to align itself with the 2-mil-wide transmission line of the dipole. This difficult task was performed by first placing a 1:1 scaled-print of the lens coupling circuit onto the master cam which was used during the material grinding process. The circuit was accurately placed on the cam by means of the dowel locators, and, by photo-etching techniques. The cam was then placed on the

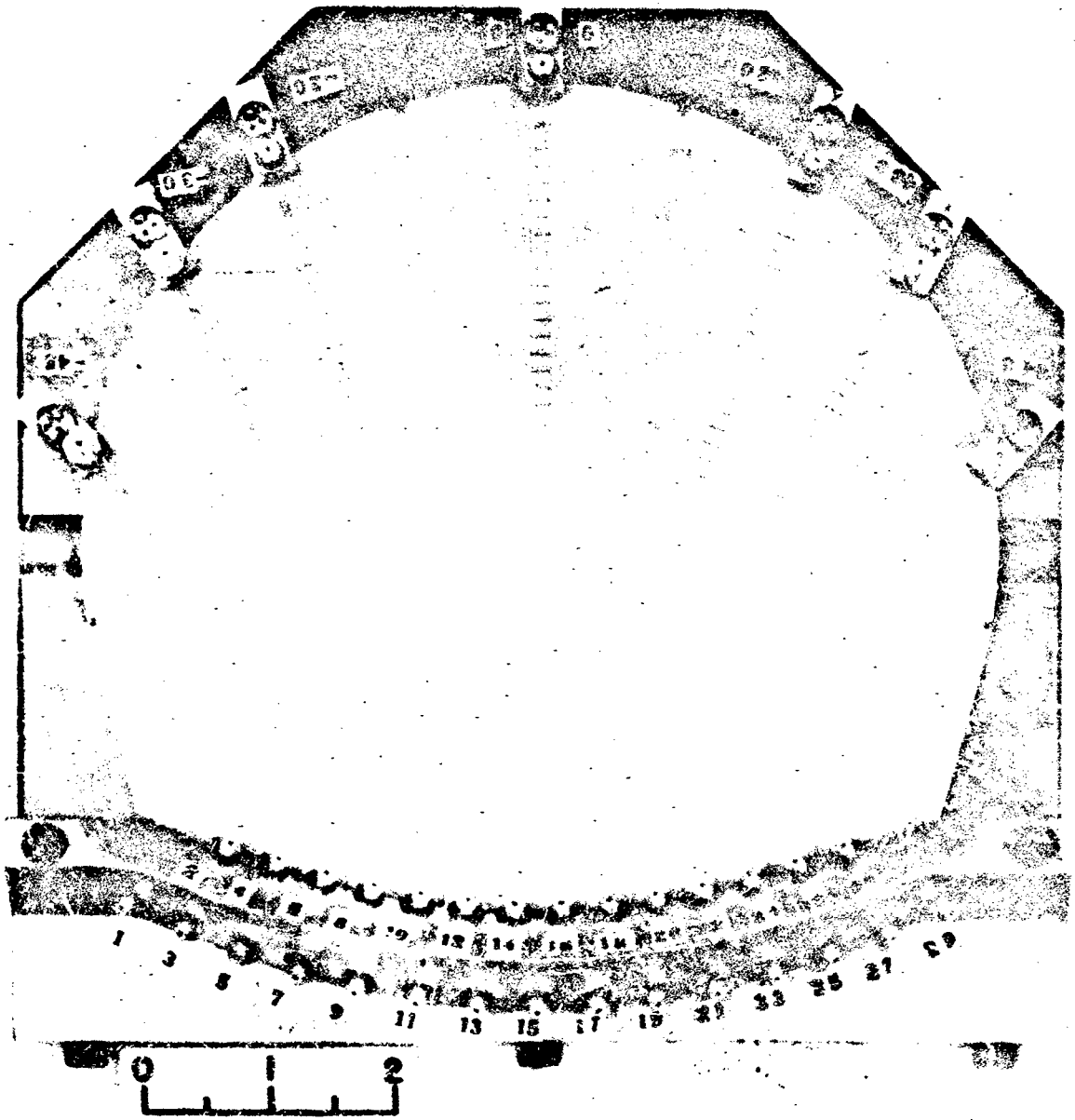

4-0121

Figure 3. Phasing Lens Mounting Fixture, Probe Connections and Titanium Dioxide Dielectric, Mounted with Coupling Elements

lens-mount base-plate and positioned to the base-plate dowels; thus the cam became a 1:1 dimensional counterpart of the dielectric lens. The entire fixture was then placed on an optically aligned, vertical jig-bore for drilling and tapping of the pick-off probe holes.

Each coupling probe was tapered to a sharp point on the bulkhead side (the microdot series 31-50 is basically a bulkhead receptical; it was modified with the taper for use on the lens fixture). Contact of the probe tip with the printed circuit transmission line was assured by spot-painting each connection with silver paint. The ground side of the transmission line was extended around the lens edge to the ground plane.

Elevated brackets were built which would allow locating a probe over each yagi transmission line. The probes and transmission lines were connected in the same manner as were the dipoles. Each yagi reflector element was bridged over the dual transmission lines with silver paint imbedded with gold wire. The reflector was isolated from the transmission line with 3-M mylar tape. All connections were tested for dc resistance. The ground lines had approximately 0.5 ohms; the high lines approximately 0.2 ohms; and the reflectors approximately 2.5 ohms. Following the resistance measurement each probe was bonded to the mounting case to prevent its movement.

Connection of the microdot probes to laboratory test equipment required a series of transitions. It was necessary to go from the miniature probe to a type 'N' coaxial connection. To do so in a minimum of space and signal-loss a special assembly was devised incorporating multiple transitions. Thirty-six of these transitions were made, each having an equivalent electrical length of 360 ±.4 degrees at 2950 mc. The average cable VSWR was found to be 1.97 at 2950 mc.

In order to prevent movement of the cables during phase measurements and to protect the dielectric lens from possible contamination and breakage, a supporting bulkhead was placed over the lens fixture. The transition assemblies were closely grouped in the support according to a pre-arranged connection scheme. Figure 4 shows the completed lens test assembly. Each yagi beam position was labeled as to its angular position, and each dipole coupling element was identified with a position number. The counterpart to figure 4 is figure 1 showing the identical lens design having an air dielectric.

3.5 Lens Test and Evaluation

3.5.1 Test Methods

Ideally, an evaluation of a phasing lens would consist of antenna pattern range tests performed with the array for which the lens was designed to operate. However, because of the complexity and expense involved, the array elements and coaxial members for this lens-array system were not assembled. In lieu of these tests, phase and amplitude coupling measurements were made. Energy was fed into the lens at each yagi position and detected at the pick-off probes. Additional measurements were made of the mutual coupling into neighboring lens elements; i.e., cross-coupling from feed point-to-feed point, and from dipole-to-dipole. The VSWR of each lens element was also determined.

The measurements were taken at the type 'N' connector of the transition assembly; 50-ohm terminations were placed on all probes and/or feed elements not actually being detected (except where otherwise specified). Tests were made with a 1 KC square wave modulated signal at 2750, 2950 and 3150 mc

A bridge technique incorporating a coaxial slotted line was used in making the phase measurements. Well-matched coaxial isolators were used to isolate

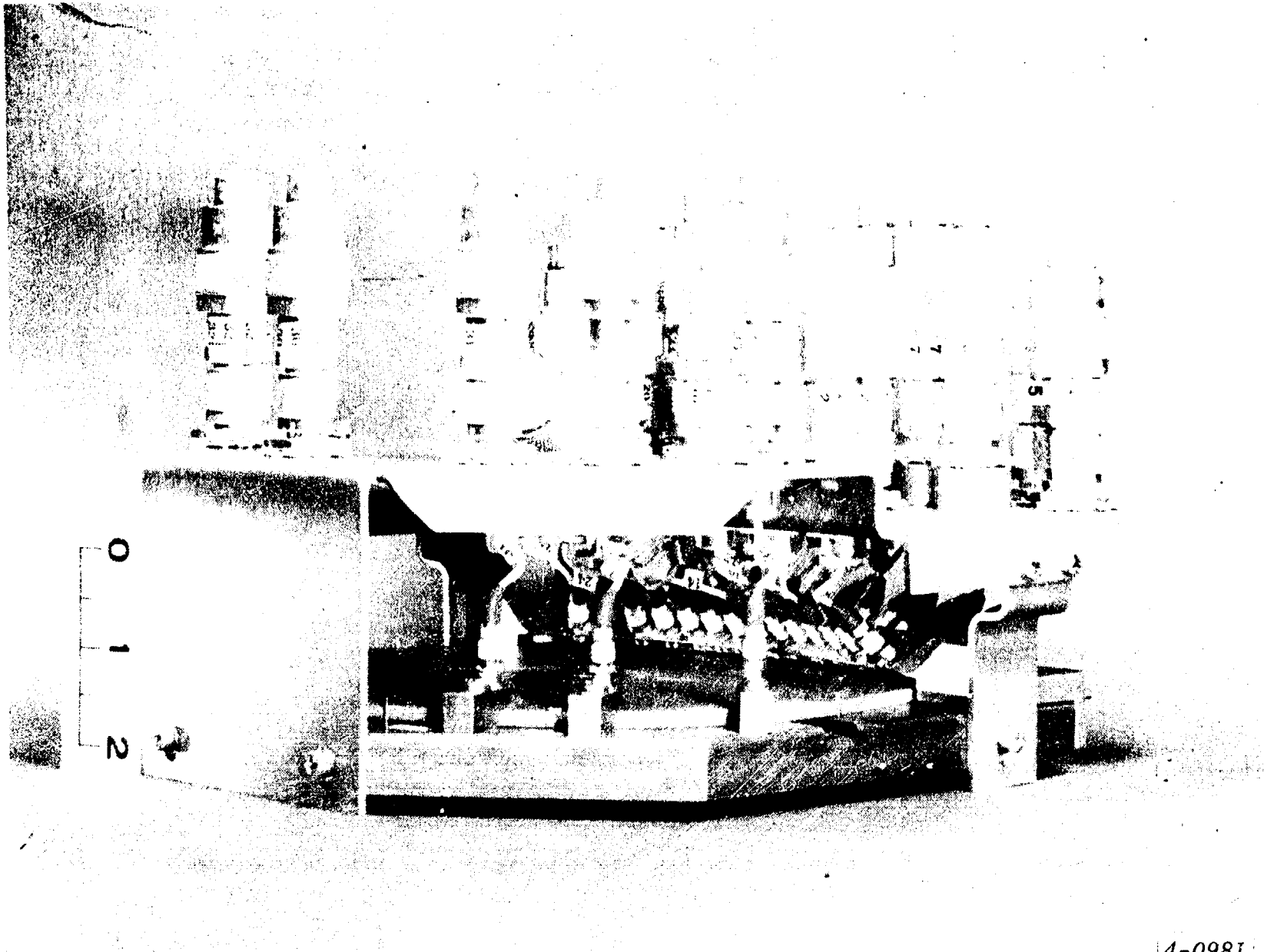

Figure 4. Dielectric Model (Titanium Dioxide ϵ = 110, Tan (.0003) of Parallel - Plate, Straight - Front Phasing Lens - Showing Mounting Fixture, connecting cables, and coaxial Terminations

the bridge system mismatches from the slotted line. Because the system was very sensitive to amplitude unbalances, care was taken to maintain a balanced bridge circuit at all times. Null depths on the order of 30 to 40 db were thus obtained. Using the center probe as a reference, changes in the null position were detected between adjacent probes along the rear-face contour. This null shift, Δ, was converted to degrees by the relation $\theta = \frac{360\ \Delta}{\lambda/2}$. These values were designated as the phase shift, from probe to probe, across the lens contour. A reflectometer set up was used during the VSWR and coupling measurements.

3.5.2 Test Results

Typical results of the dipole VSWR tests are presented in graphical form in figure 5. Pick-off probe positions are placed sequentially along the abscissa, the curves show the measured VSWR at the three test frequencies.

Typical coupling through the lens for the +30 degree beam position is given in figure 6. The graph shows the coupling, expressed in db, measured from the yagi input to each pick-off probe, plotted as before. Thus the data yields the amplitude distribution which would exist across an array fed by the lens.

Mutual coupling between the yagi beam positions and between arbitrarily selected dipole pick-off positions is given in tables I and II. The coupling, expressed in db, shows the energy level measured at various lens positions when power is fed into the specified lens element. Table III shows the same type of information as table I, for a condition of open circuits on all lens pick-off elements.

Data collected during the phase measurements required slight adjustment before it could be plotted. The phase delay attributed to each coaxial line

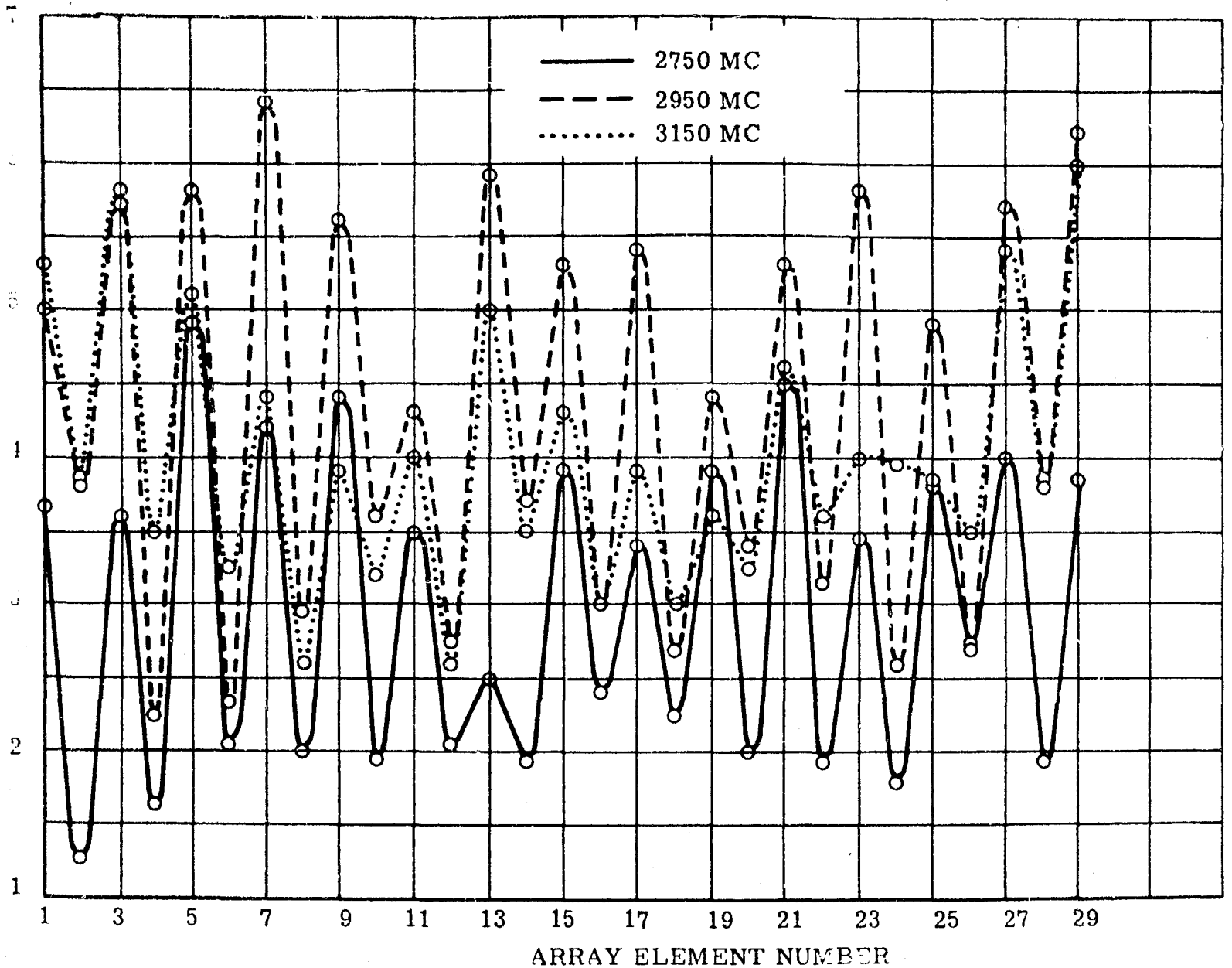

Figure 5. Measured Mismatch at Lens Pick-off Element Transition's

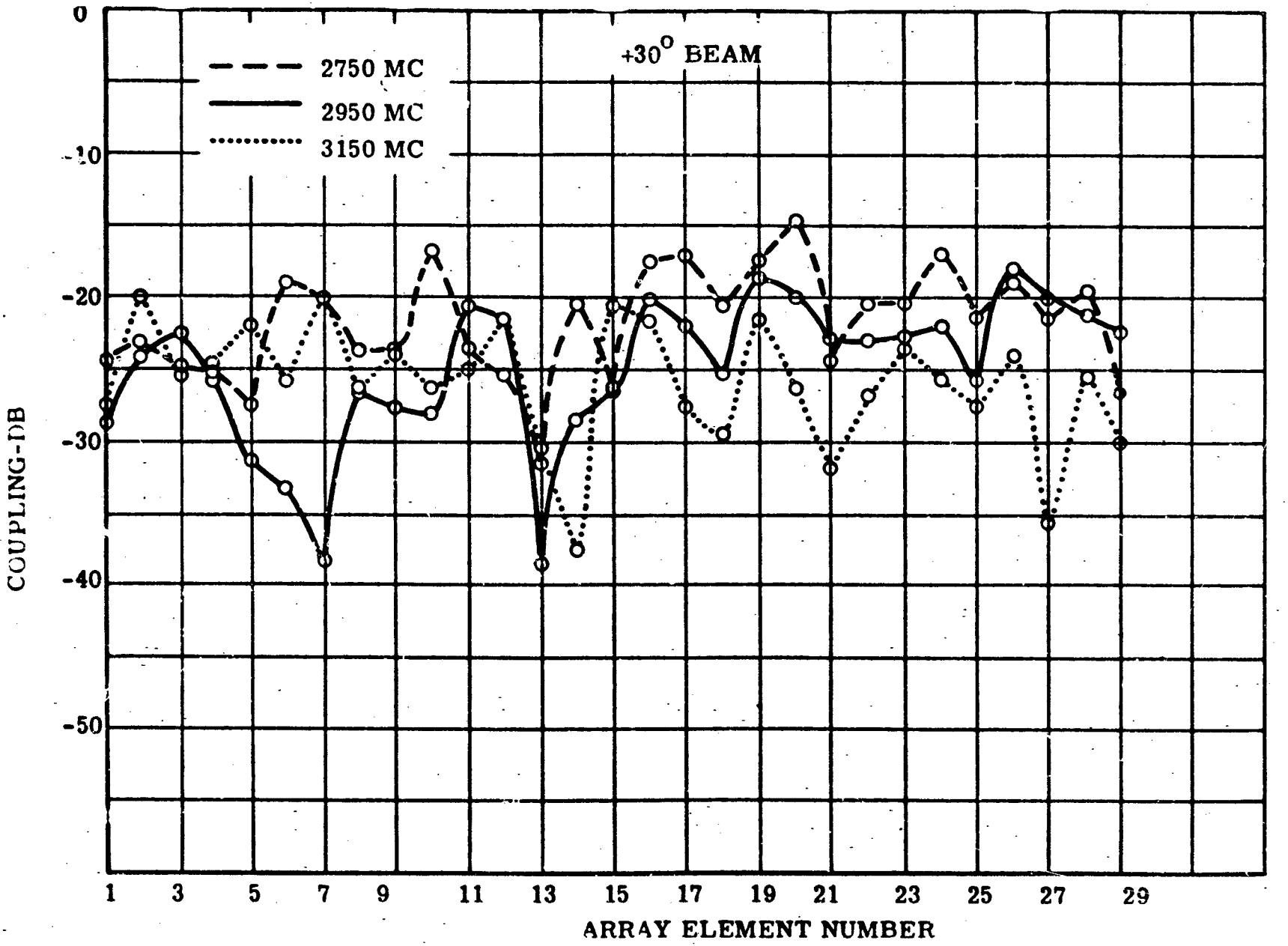

Figure 6. Measured Coupling Through Dielectric Lens at the Pick-off Elements: Input at the +30 Degree Beam Position

TITANIUM DIOXIDE

LENS MUTUAL COUPLING

TABLE I INPUT BEAM POSITION

Frequency (MC)	+45°	+30°	+20°	0°	-20°	-30°	-45°	DETECTED BEAM POSITION
2750		40	26.9	35.2	34.7	40	29.7	+45°
2950		29.8	28.7	40	32.4	30.1	31.1	
3150		30.6	40	30.7	38.7	40	40	
2750	40		31.6	31.4	33.0	18.1	30.5	+30°
2950	30.0		28.0	32.7	25.9	16.9	40	
3150	30.9		28.4	38.6	30.1	25.7	33.2	
2750	26.6	32.6		23.4	19.8	21.6	30.4	+20°
2950	28.3	25.8		26.6	21.1	24.5	40	
3150	40	27.4		29.0	18.6	34.0	35.7	
2750	35.3	32.0	23.5		27.3	27.6	34.3	0°
2950	40	33.0	27.2		33.7	40	37.0	
3150	30.8	36.8	28.2		28.3	34.8	40.0	
2750	33.5	30.0	20.3	26.6		25.8	33.8	-20°
2950	33.8	26.6	21.6	32.2		26.5	34.8	
3150	37.5	31.8	19.0	28.6		30.8	35.5	
2750	40	40	21.8	27.6	25.9		40	-30°
2950	30.1	40	25.3	40	26.9		38.7	
3150	40	26.8	34.6	36.6	33.9		31.1	
2750	29.5	30.6	30.7	32.9	29.6	37.8		-45°
2950	30.8	40	40	28.5	28.7	32.3		
3150	40	33.4	33.5	35.7	40	30.0		

TABLE II DETECTED PROBE NUMBERS

INPUT PROBE		Frequency (MC)	3	4	5	6	7	9	10	11	12	13
	#15	2750						27.9	26.1	26.0	31.6	19.9
		2950						31.7	25.8	40	28.2	21.0
		3150										
	#8	2750	31.9	14.0	28.7	33.2	15.2					
		2950	29.0	17.6	28.8	14.3	24.2					
		3150										

TABLE III INPUT BEAM POSITION

Frequency (MC)	+45°	+30°	+20°	0°	-20°	-30°	-45°	DETECTED BEAM POSITION
2750		32.6	30.5	31.0	25.9	40	23.6	
2950		24.1	33.9	39.8	29.6	34.5	27.6	+45°
3150		28.4	28.5	30.5	31.9	25.5	30.2	
2750	32.9		27.4	31.8	29.1	16.9	25.2	
2950	25.0		30.4	40	29.0	18.1	40	+30°
3150	27.9		36.0	31.7	29.8	19.0	40	
2750	30.4	27.5		25.8	15.1	24.0	28.1	
2950	34.3	30.9		29.0	21.8	27.0	30.5	+20°
3150	28.6	35.8		34.6	18.5	38.4	35.0	
2750	29.5	30.7	26.2		23.4	24.5	32.9	
2950	38.8	40	29.2		30.8	40	36.5	0°
3150	33.1	35.5	34.0		27.6	39.4	34.3	
2750	26.5	28.1	14.9	22.5		27.4	39.1	
2950	31.1	28.1	21.6	29.2		24.4	28.0	-20°
3150	32.2	29.5	19.5	26.9		40	33.7	
2750	40.0	17.0	24.4	23.8	29.6		40	
2950	33.1	17.7	27.0	39.8	24.5		29.0	-30°
3150	25.7	18.9	38.4	39.0	40		32.4	
2750	22.3	25.3	27.9	32.5	40	40		
2950	28.8	40	27.6	34.8	27.5	28.5		-45°
3150	30.4	40	32.3	34.2	33.6	32.1		

connecting the lens to an array was determined. Also, the amount of phase lead (or lag) resulting from an off-axis beam position was calculated for each array position. These values were added algebraically to the measured phase shift of each corresponding probe. The result was the predicted phase distribution at the aperture of a hypothetical array. Typical data are shown by the curves of figures 7 and 8. The solid straight line on the graphs represents the ideal phase distribution for scanning to the designated angle ($\pm 20^{\circ}$). The irregular curve is the phase distribution obtained after adjusting the measured phase shift through the lens. The data is plotted in degrees with the necessary phase lead or lag, relative to the array center element for each of the 29 lens output terminals.

4. CONCLUSIONS

From the results of studies made during this program, observations, conclusions, and recommendations can be made as follows:

1. Large, one-piece ceramic materials may be acquired having a dielectric constant in excess of 100 and dissipation factor less than 0.0003. These materials can be accurately shaped to a controlled geometry. Their surfaces can be plated with conductive materials without altering their dielectric properties. The materials can be etched with a multi-element antenna array of ultra-miniature circuits using photo-reduction, prin' i circuit techniques. Close tolerance dimensions can be obtained on line widths of approximately one-mil in close proximity to similar lines.

2. Inter-connection of conventional circuits to closely grouped circuits has been demonstrated. However, it is a problem area in which additional activity could greatly improve the present performance.

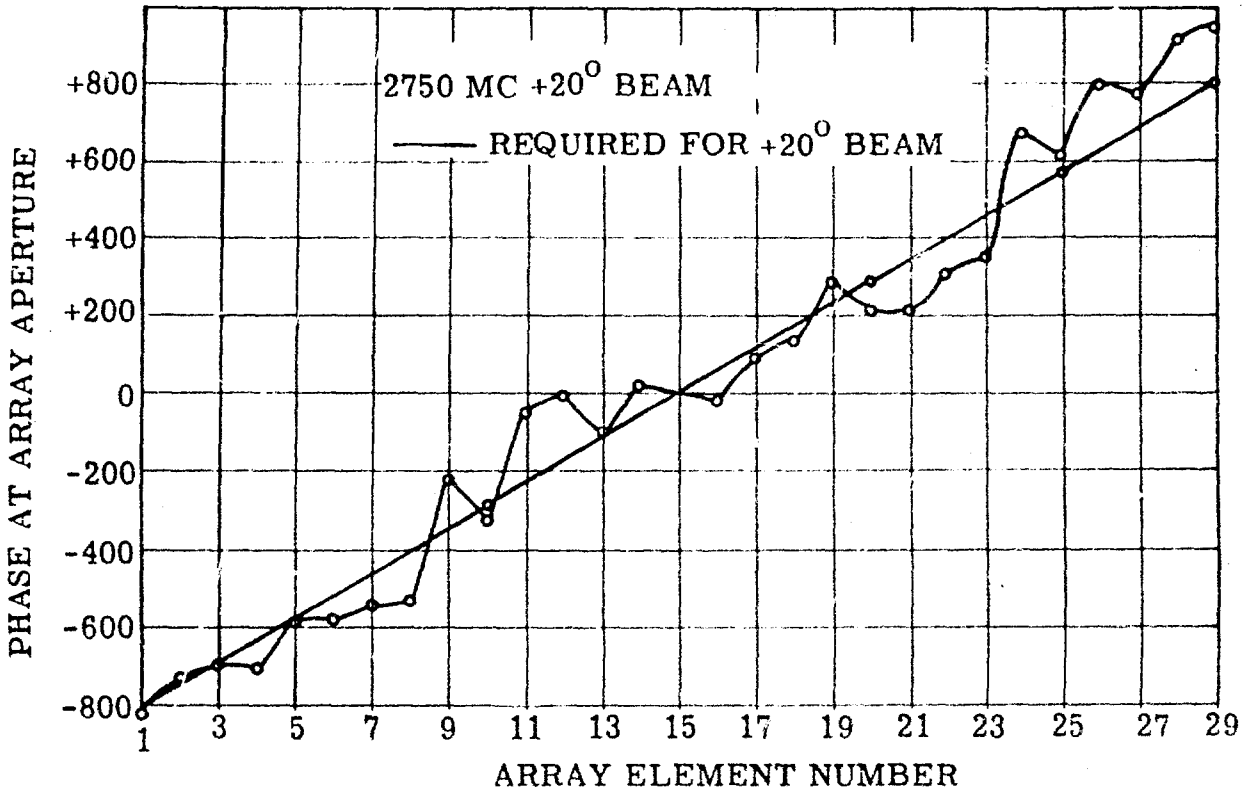

Figure 7. Titanuim Dioxide Lens Assembly Phase Distribution for the ±20 Degree Beam Position's

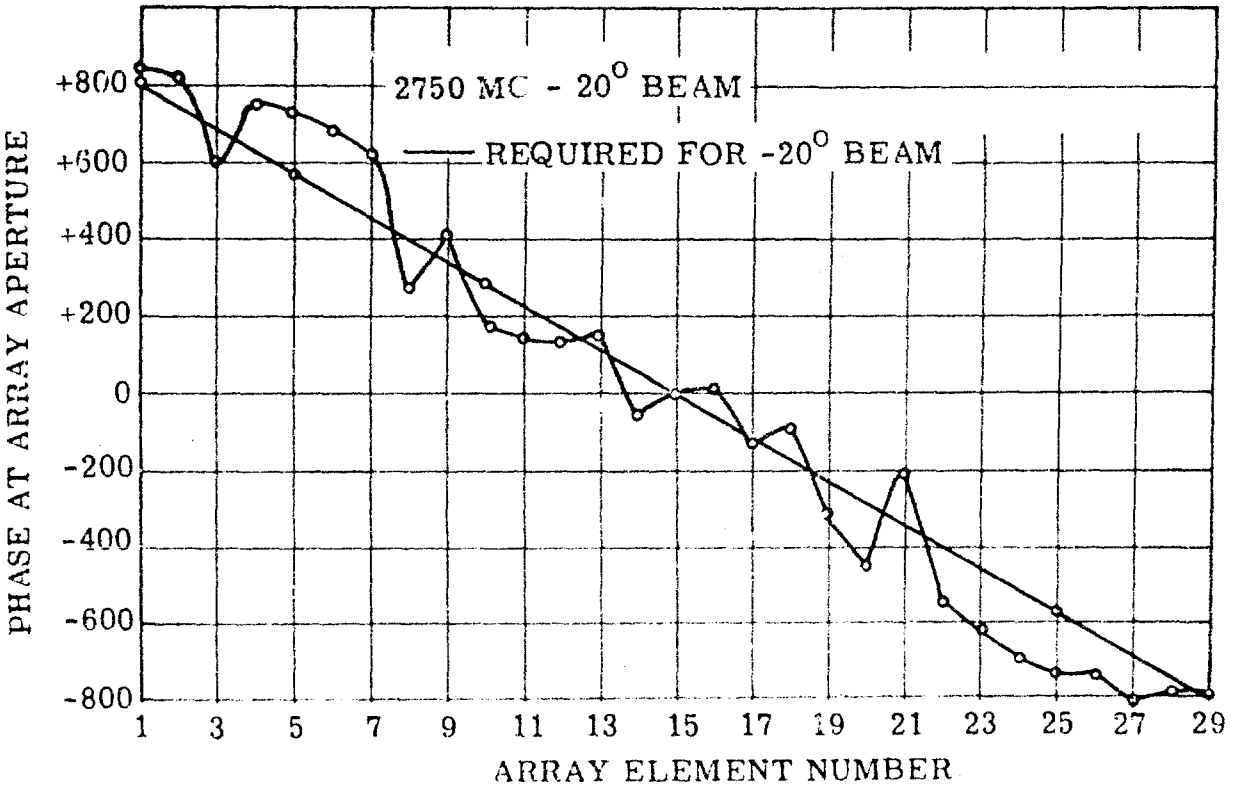

Figure 8. Titanuim Dioxide Lens Assembly Phase Distribution for the ±20 Degree Beam Position's

3. The narrow beam characteristics of the yagi launch elements were not demonstrated on the dielectric lens model. The measured average amplitude coupling across the lens equaled the predicted value (-23 db). However, amplitude levels across the lens aperture were of a random nature with values fluxuating ±5 db about the mean.

4. Phase distribution across the dielectric lens aperture did not meet the performance standard of its air lens counterpart. However the lens did exhibit the phasing characteristics of a wide scan-angle beam-culminating device. The phase distribution was not random; errors were not intolerable; beam positioning was vividly demonstrated; there was slight evidence of a pointing boresight-error, and of the primary source defocus.

5. With a demonstrated capability for coupling energy through very high dielectric-constant ceramics, the use of these materials in microwave devices becomes feasible. Such applications make possible volume reductions on the order of 1000:1 → 3500:1.

6. As a direct result of the development effort made during this study, a significant advance has been made in the state-of-the-art for microwave application of very high dielectric-constant materials.

5. ACKNOWLEDGEMENTS

The author wishes to express his appreciation for the many helpful suggestions given by N. Sakiotis, who conceived the high dielectric constant lens concept, Dr. T. Charlton, for his technical guidance, and R. Eckstein for his assistance in preparing the text.

REFERENCES

1. Luneberg, R. K., "Mathematical Theory of Optics," Brown University Press, Providence, R. I., 1944.

2. Ruze, John, "Wide Angle Metal-Plate Optics," Proceedings of the I.R.E., January, 1950, pp 53-59.

3. Rotman, W. and Turner, R. F., "Wide Angle Microwave Lens for Line Source Applications," AFCRC Report No. 62-18, January, 1962.

4. Barlow, H. M., and Cullen, A. J., "Surface Waves," Journal of Electronic Engr. Vol 100, November, 1953, pp 329-347.

5. Barlow, A. E., and Karbowick, A. E., "An Investigation of Cylindrical Surface Waves," Proceedings of the Institution of Electrical Engineers, November, 1953, pp 321-328.

6. Richmond, J. H., "Reciprocity Theorems and Plane Surface Waves," Engineering Experiment Station Bulletin, Ohio State University, July, 1959.

7. Angulo, Carlos M., "Diffraction of Surface Waves by a Semi-Infinite Dielectric Slab," I.R.E. Trans on Antennas and Prop., January, 1957, pp 100-109.

8. Hatkin, Leonard, "Analysis of Propagating Modes in Dielectric Sheets," Proceeding of the I.R.E., October, 1954, pp 1565-1568.

9. Zucker, F. S., "Theory and Applications of Surface Waves," Supplemento Al Vol. IX, Serie IX, Del Nuovo Cimento, November, 1952.